Digitized by the Internet Archive
in 2024

https://archive.org/details/physica-scripta_1956_10

QC
1
S923

634

ARKIV FÖR FYSIK

UTGIVET AV

KUNGL. SVENSKA VETENSKAPS-
AKADEMIEN

Band 10

Med 41 avhandlingar

ALMQVIST & WIKSELL / STOCKHOLM
1956

TIONDE BANDETS INNEHÅLL

Sid.

1. Arbman, E. and Svartholm, N., A high transmission beta-ray spectrometer of the double focusing type 1–18
2. Nilheden, G., The perturbations in the near ultra-violet band-system (D-X) of silicon monosulphide 19–36
3. Sato, M., On the characteristic of the weakening effect 37–44
4. ——, The wetting effect on quenched carbon steel within its elastic limit 45–48
5. Kronqvist, E., Paramagnetic susceptibility measurements on PdAg alloys 49–57
6. Bhar, B. N., Forsling, W. and Lindström, G., Molecular association and proton resonance in acetic acid 59–63
7. Erlandsson, G., Extended energy level tables for the rigid asymmetric rotor 65–88
8. Skavlem, S. and Espe, I., Application of the variational method to the calculation of proton-proton scattering in the region 0—5 Mev 89–96
9. Johansson, S. A. E., The decay scheme of Uranium 235 97–108
10. Pettersson, A. V., Optical problems concerning the use of interference in the determination of spectroscopic wave-numbers 109–112
11. Sugawara, M., On the electromagnetic properties of the deuteron 113–128
12. Olsson, O., A theoretical study of the time energy distribution of slowed-down neutrons 129–144
13. Heitler, W., The theory of chemical bond 145–156
14. von Ubisch, H., On the theory of the temperature jump in a rarefied gas and its experimental verification 157–163
15. Krantz, B.-Å. and Åslund, N., A method of indicating wave-numbers in spectrophotometric recording 165–173
16. Pauli, R., Investigation of the focusing properties of a double directional focusing magnetic spectrometer with conical pole surfaces 175–185
17. Borelius, G. and Sandin, A., On density fluctuations in solids and liquids 187–196
18. Åström, H. U., Isothermal measurements on the release of energy stored in cold-worked aluminium 197–211
19. Hertz, C. H., Untersuchung einer neuen kontinuierlich steuerbaren Gasentladung mit kalter Kathode 213–245
20. Johansson, K.-E., An investigation of the photoelectric absorption of gamma-rays in thallium-activated sodium iodide 247–278
21. Nordfors, B., On the K spectrum of aluminium and its oxide 279–289
22. Glad, S., Extension of the analysis of the third spectrum of iron, Fe III . 291–340
23. Norinder, H. and Siksna, R., Continued measurements of ions formed by corona discharge 341–353
24. Hartmann, B. and Wiedling, T., An excited level of high spin of Gd^{154} . 355–356
25. Hjalmar, E., Slätis, H. and Thompson, S. G., Photographic emulsion measurements of the energy distribution of neutrons from spontaneous fission of californium 252. I 357–368
26. Ahnlund, K., The position of the second excited level in C^{12} 369–372
27. Ahnlund, K., Angular distributions with high energy resolution. Experimental method 373–385
28. Bäckström, G., On the high energy gamma-transitions of W^{182} 387–391

29. Bäckström, G., On the energy of the 570 kev γ-ray of Bi^{207} 393–395
30. Norinder, H. and Salka, O., Long sparks from negative electrode with limited current in air at atmospheric pressure 397–423
31. Ahnlund, K., Angular distributions with high energy resolution: Long-range groups from $O^{18}(d, p)O^{19}$ 425–430
32. Uhler, U. and Åkerlind, L., The rotational analysis of the singlet system *A* of zirconium oxide 431–446
33. Kristiansson, K., Photo-electric mass determinations in nuclear emulsions. Part IV. Determinations of *K*-particle masses 447–465
34. Nilsson, S. B., On the Coulomb effect for the internal bremsstrahlung accompanying beta decay 467–477
35. Slätis, H., Low pressure diffusion cloud chamber tracks of fragments from the spontaneous fission of californium 252. I 479–488
36. Lindström, G. and Bhar, B. N., A spectrometer for high resolution nuclear magnetic resonance experiments 489–499
37. Reuterswärd, C., Direct-coupled amplifier and ratiometer for a single-beam mass spectrometer 501–524
38. Gerholm, T. R., On the annihilation of positrons in condensed materials 525–552
39. Edlén, B. and Risberg, P., The spectrum of singly-ionized calcium, Ca II 553–566
40. Bockasten, K., A study of CIV: Term values, series formulae, and Stark effect 567–582
41. Risberg, P., A revision of the term systems for Na I and K I based on hollow-cathode observations 583–606

ARKIV FÖR FYSIK Band 10 nr 1

Communicated 9 March 1955 by The Svedberg and Arne Westgren

A high transmission beta-ray spectrometer of the double focusing type

By E. Arbman and N. Svartholm[1]

With 14 figures in the text

1. Introduction

In recent years a number of beta-ray spectrometers have been constructed using the two-directional or double focusing property of inhomogeneous magnetic fields, first applied in beta-ray spectroscopy by Svartholm and Siegbahn [1]. The main advantage with this focusing principle is, apart from space focusing, that high resolution can be obtained. Consequently it has been used in designing spectrometers intended for high resolution and accurate measurements of beta and gamma ray energies.

To get high resolution, the electrons from the source must be limited to a rather narrow bundle. Spectrometers of this type, as described up to now, have been designed for a maximum transmission of about one per cent. They have shown to greatest advantage when adapted for measurements at very high resolution and transmission of fractions of a per cent.

The instrument to be described in the present paper was designed primarily to meet the needs of this Institute with respect to routine work in beta-ray spectroscopy. In order to make investigations of weak sources, and for use in coincidence measurements, the spectrometer was required to have a comparatively high maximum transmission (around 5 per cent). Furthermore, it needed to be adjustable for resolutions down to a few tenths of one per cent with a reasonable decrease in transmission when strong sources are available.

Since high transmission was stressed more than high resolution, it was realized that a particular form ($\beta=\frac{1}{4}$) of the double focusing principle would be most favourable in this case. Finally, the adoption of a relatively small mean radius (18 cm) was indicated for a number of concurring reasons, the handiness of the whole apparatus being one of them.

In this work one of the authors (N. S.) is responsible for the design of the spectrometer, while the experimental work including testing and calibration has been done by the other author.

2. Review of theory

The theory of the focusing properties and the application of inhomogeneous magnetic fields of cylindrical symmetry in beta-ray spectroscopy has been treated by various authors [2, 3, 4]. The spherical aberration and its contribution to the line shape is discussed in some detail in a paper by HEDGRAN *et al.* [5]. Here only some results of importance for the design of our spectrometer will be summarized.

---

[1] At present at Chalmers' Institute of Technology, Göteborg, Sweden.

According to the theory, every cylindrically symmetrical inhomogeneous magnetic field, the axial field component of which can be expanded as

$$B(r)=B(r_0)\left[1-\tfrac{1}{2}\left(\frac{r-r_0}{r_0}\right)+\beta\left(\frac{r-r_0}{r_0}\right)^2+\cdots\right] \tag{1}$$

has two-directional focusing properties. Charged particles, emerging from a point object on the circle $r=r_0$ in the symmetry plane are focused to an image after a traversed angular distance of $\pi\sqrt{2}$ radians. Central rays from an extended object give an inverted but true image. The magnification is unity. Particles which are emitted in orbits making finite angles with the circle $r=r_0$, $z=0$, strike the cylindrical surface $r=r_0$ after an angle $<\pi\sqrt{2}$. Hence the focusing system gives rise to aberration. The r and z coordinates of an electron in the focal plane $\varphi=\pi\sqrt{2}=$ $=255^\circ$ may be expressed by

$$\left.\begin{aligned} r&=r_0-\tfrac{2}{3}[(8\beta-1)\gamma_1^2+(3-8\beta)\gamma_2^2]r_0\\ z&=-\tfrac{4}{3}(3-8\beta)\gamma_1\gamma_2 r_0\end{aligned}\right\} \tag{2}$$

where γ_1 and γ_2 are the radial and axial aperture angles defined by shutters. The parameter β determines the aberration of the system, the magnitude of which is given by

$$\delta_{ab}=\tfrac{2}{3}[(8\beta-1)\gamma_1^2+(3-8\beta)\gamma_2^2]r_0. \tag{3}$$

It is seen to be independent of the parameter β if a square aperture is used (i.e. if $\gamma_1=\gamma_2$). When $\beta=\frac{3}{8}$ or $\frac{1}{8}$, δ_{ab} becomes independent of the angles γ_2 or γ_1 respectively, and the effect of the aberration can be reduced by diminishing the aperture in radial or axial dimension only. By using a circular aperture and $\beta=\frac{1}{4}$, the aberration width is one half of the value for $\beta=\frac{1}{8}$ or $\frac{3}{8}$. In this case, however, both the radial and the axial aperture angles have to be reduced in order to diminish the aberration width.

Spectrometers with field distributions corresponding to $\beta=\frac{3}{8}$ have been described by HEDGRAN *et al.* [5], by BARTLETT and BAINBRIDGE [6] and recently by STOKER *et al.* [7]. SHULL [8] and KURIE *et al.* [9] have used $\beta=\frac{1}{8}$. The spectrometer to be described in this paper is designed to have a field form corresponding to $\beta=\frac{1}{4}$.

The shape of the image from a point object, emitting mono-energetic radiation isotropically, and the intensity distribution of the image, can be calculated by the use of the expression (2). It is discussed for some β-values by HEDGRAN *et al.* [5]. When $\beta=\frac{3}{8}$, the image shape for any aperture used is a straight line of length $\frac{4}{3}\gamma_1^2 r_0$ in the radial direction. γ_1 is the radial aperture angle. When $\beta=\frac{1}{8}$, the image form is dependent on the shape of the aperture. A circular aperture gives an elliptical image pattern, and if a rectangular aperture is used the image is bounded by a section of a parabola. In the case $\beta=\frac{1}{4}$ and a circular aperture, the image is a triangle bounded by the straight lines $r-r_0=\pm z$; $r-r_0=-\frac{2}{3}\gamma_0^2 r_0$. If a square aperture with the angles $\gamma_1=\gamma_2=\gamma_0$ is used, the image boundaries are

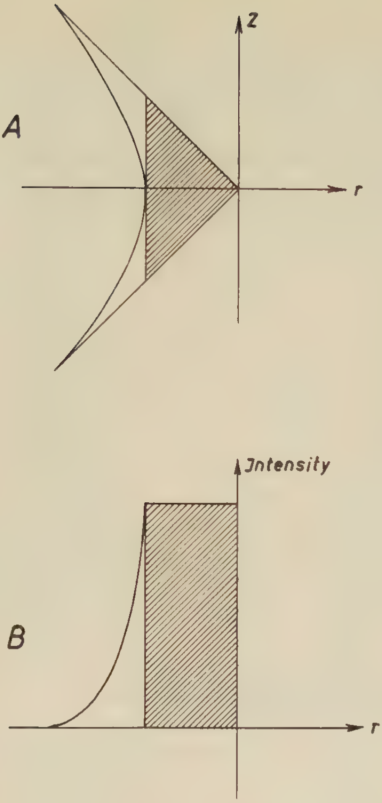

Fig. 1. The shape of the image (A), and the intensity distribution (B) from a point source for $\beta = \frac{1}{4}$ and square aperture with $\gamma = \gamma_1 = \gamma_2$. The shaded areas correspond to circular aperture of the same angle.

the straight lines $r - r_0 = \pm z$ and the curve $r - r_0 = -\frac{2}{3}\gamma^2 r_0$; $z = \pm\frac{4}{3} r_0 \gamma_0 \sqrt{\gamma^2 - \gamma_0^2}$, where the angle γ must satisfy the inequality $\gamma_0 \leq \gamma \leq \gamma_0 \sqrt{2}$.

The intensity distribution of the image as measured by a detector which is infinitesimally narrow in the radial, and sufficiently long in the axial direction, is generally a function of r. In the case $\beta = \frac{1}{4}$ and with a circular aperture, however, the intensity distribution is constant. Hence, when a source and counter slit of finite width are used, the intensity distribution of the image of a beta-line will have the shape of an equilateral triangle. Fig. 1 shows the image shape and intensity from a point source in the case $\beta = \frac{1}{4}$ for circular and square apertures.

3. Design and construction

The spectrometer was planned to become an easily handled instrument, intended for investigation of electrons of energies up to about 5 MeV. For this electron energy the magnet required must be capable of giving $B\varrho$ values of the order of

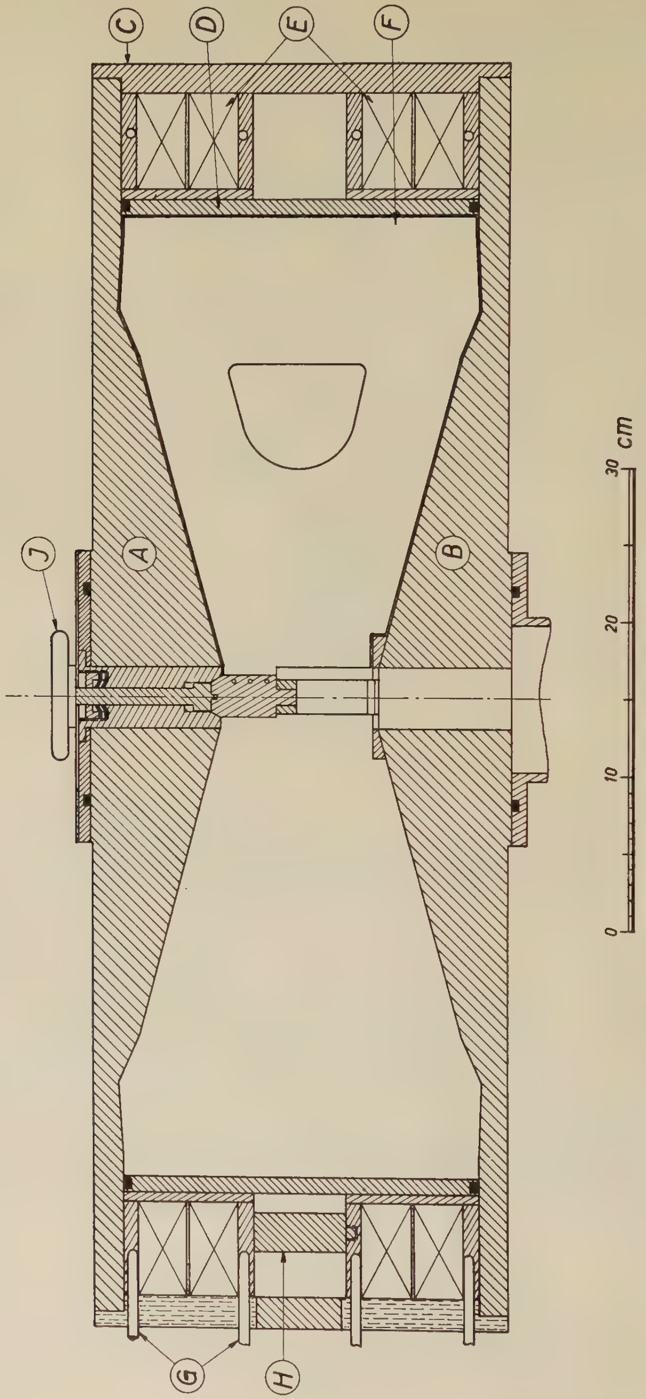

Fig. 2. Vertical section of the spectrometer. A and B = upper and lower pole shoes, C = circumferential iron yoke, D = brass cylinder, E = magnet coils, F = defining shutter, G = cooling tubes, H = distance bolt, J = knob and scale for adjustment of defining shutter.

20,000 gauss cm. To get the highest possible resolution when a large aperture is used, it is appropriate to have a field distribution corresponding to a value of the parameter $\beta = \frac{1}{4}$. This field can be realized by using conical pole surfaces. According to SVARTHOLM [3, 10], the pole distance $2z$ as a function of r can in this case be expressed by $2z = z_0 (r + r_0)/r_0$, where $2z_0$ is the pole distance at the radius $r = r_0$. In agreement with the expression for the aberration width in the case $\beta = \frac{1}{4}$, the radial and the axial dimensions of the pole gap must be chosen to be of equal magnitude.

The resolution of a spectrometer is a function of the magnet dimensions. A larger value of the mean radius r_0 corresponds to higher resolution. In our case, however, extremely high resolution was not aimed at, and in order to keep the dimensions of the magnet at reasonable values, a mean radius r_0 equal to 18 cm was adopted. With this value fixed for r_0 and a mean pole distance $2z_0$ equal to 20 cm, the available space between the pole pieces allows the use of a maximum solid angle of about six per cent of a sphere. The final design of the magnet can be seen in Fig. 2. It consists of three parts: Two symmetrical pole pieces with conical surfaces and a circumferential cylinder. This "closed" magnet design has some advantages compared to the central iron core type. The most important are that the field distribution, and hence the focusing properties, is practically independent of the field strength, and that edge effects are reduced, so that almost the whole space between the pole pieces from the centre up to the coils may be used for focusing of electrons. A disadvantage is the relative inaccessibility of the interior of the spectrometer.

The magnet pieces are machined of soft iron (Domnarfvet 311 F). The outer diameter of the 2 cm thick cylinder is 82 cm and the pole distance is 10 cm and 23 cm at the centre and at the periphery respectively. The magnet coils surround the spectrometer chamber. In order to make the interior more easily accessible, the coils are made in two sections, with a distance of 6 cm between them. Each section consists of two coils of 0.35 mm thick copper strips insulated with 0.1 mm fiber glass tape. They are wound on forms of brass in a manner similar to that described by COONROD *et al.* [11]. The forms are provided with cooling tubes, soldered into grooves in the form sides. The coils are connected in series and have a total resistance of 1.52 ohms.

The two pole pieces and a 9.5 mm thick brass cylinder, placed close inside the coil forms, constitute the walls of the vacuum chamber. The inside diameter of the brass cylinder is 62.5 cm. Rubber gaskets running in grooves along the edges of the cylinder form the vacuum seals. The chamber is evacuated through a hole at the centre of the bottom pole piece.

The pumping system consists of an oil diffusion pump combined with a two-stage rotating pump. By these pumps a minimum pressure of the order of 10^{-5} mm Hg can be obtained. About two hours are required to reduce the pressure from atmospheric to 10^{-4} mm Hg.

The sample is introduced into the spectrometer chamber through the space between the two coil sections by means of a vacuum lock device. Three aluminium shutters are used to limit the electron beam. The arrangement is shown in Fig. 3. Two shutters are placed at fixed angles 25° and 230° respectively from the source, and their apertures are set to permit a maximum transmission of 5 per cent. The third one is the defining shutter. It can be turned round the axis of the spectrometer by a knob and thus the aperture of the spectrometer may be changed in

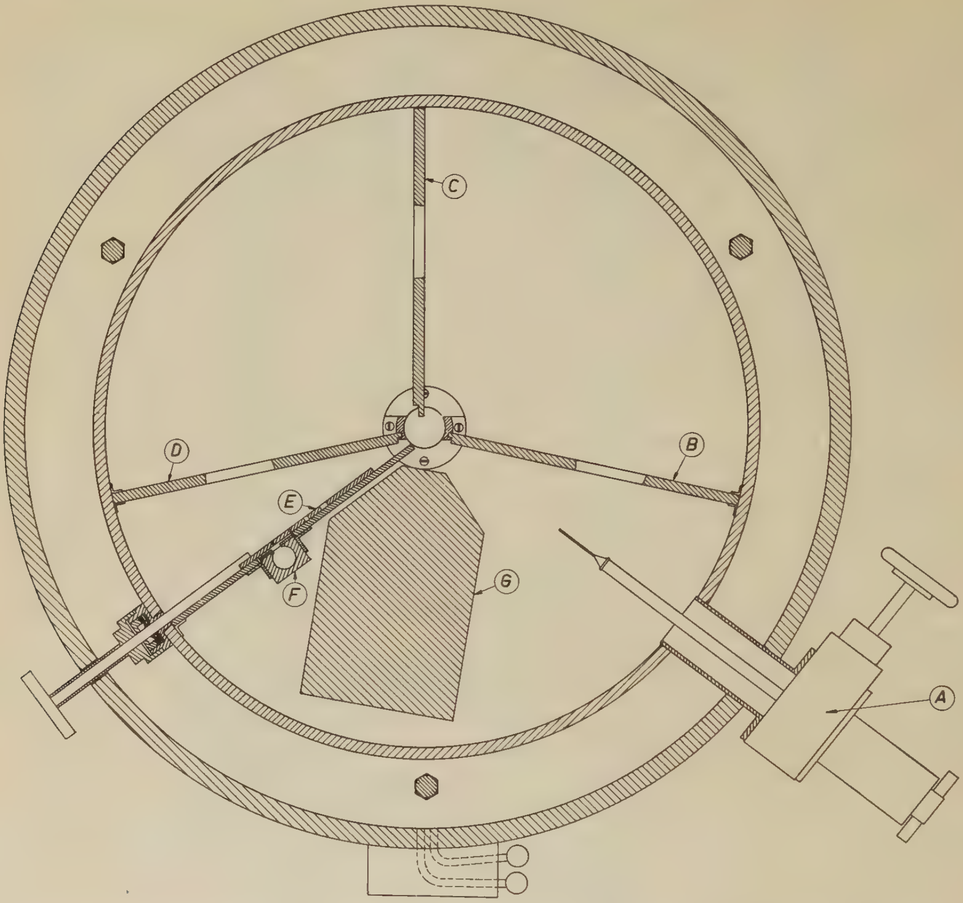

Fig. 3. Horizontal section of the spectrometer. A = vacuum lock device and sample holder, B and D = aluminium shutters in fixed positions, C = defining shutter, E = adjustable slit, F = counter, G = lead shield.

both axial and radial extension in a uniform manner. The position of the shutter is read on a scale on the top pole piece.

As detector, a side window Geiger counter with a window area of 4×1 cm^2 is used. The first measurements were performed with a Victoreen end window counter with a window diameter of 3.3 cm. About 15 cm of lead shield the counter from direct radiation from the source. The deflecting region of the spectrometer chamber is lined by 1.5 mm thick Plexiglas in order to reduce scattering from the walls.

The magnet current is supplied by an electronically regulated motor generator. Fig. 4 shows a block diagram of the principle used for the current stabilization. The difference between the voltage developed across an oil-cooled variable Kanthal resistor R and a reference voltage is fed to a Brown converter. The resulting alternating current, amplified by an a.c. amplifier controls a phase sensitive rectifier, which supplies the current necessary to produce the magnetic field of the

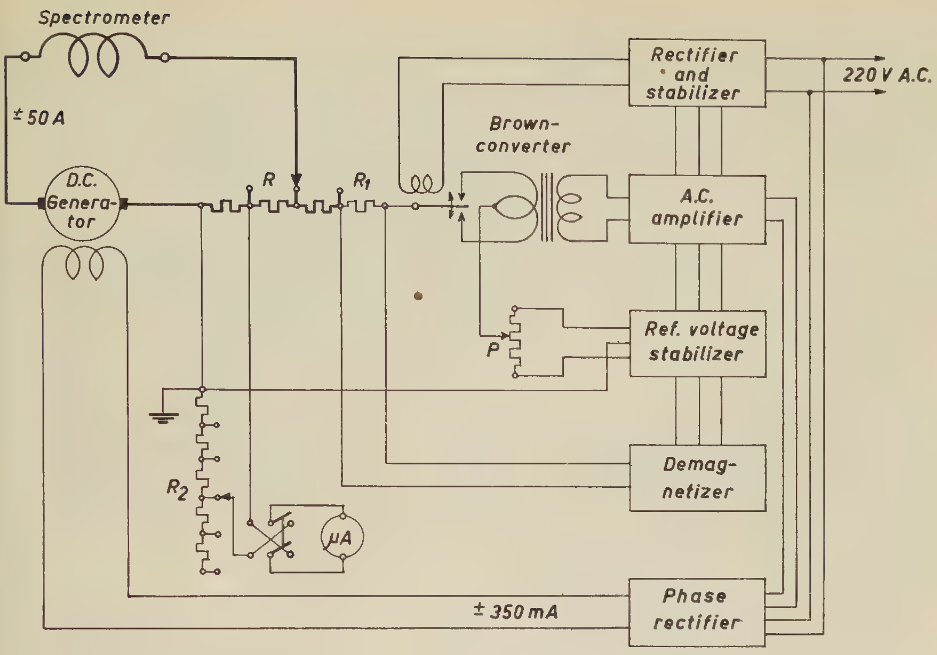

Fig. 4. Block diagram of the regulation circuits.

generator. By means of a ten-turn potentiometer P the magnet current can be varied continuously between the limits plus and minus a certain current value, the magnitude of which is determined by the resistor R.

The field is simply determined as a function of the current, which is read on a light-spot micro-ammeter. Accurate current readings can be obtained by a Leeds and Northrup potentiometer. To get reproducibility between the measured current values and the field strength the spectrometer must be effectively demagnetized, because of the remanence of the iron. Particularly in measurements at low field strength, it is of advantage to be able each time to start at the same point on the hysteresis curve. On account of that, the current stabilizer has been provided with a simple device which makes it possible to utilize the stabilizer for automatic demagnetization. Two equal condensers, charged to equal voltages but of opposite polarity, are alternately, by means of a relay, allowed to discharge through the resistor R_1 (Fig. 4). The result is a damped alternating current through the spectrometer. The time constant (about 45 sec.), and the frequency, have been experimentally adjusted to give the most effective demagnetization. The current changes during a demagnetization cycle are shown in Fig. 5.

The spectrometer is provided with a simple arrangement for automatic recording of spectra, particularly intended for investigation of conversion lines. The ten-turn potentiometer, which controls the magnet current, can be turned by a small synchronous motor. A gear train makes it possible to use 12 different sweep speeds corresponding to current changes ranging from 10 to 800 mA per min. The pulses from the Geiger counter are fed into a rate-meter (type 1138 A, E. K. Cole Ltd.), the output of which is connected to a Leeds and Northrup Speedomax recorder.

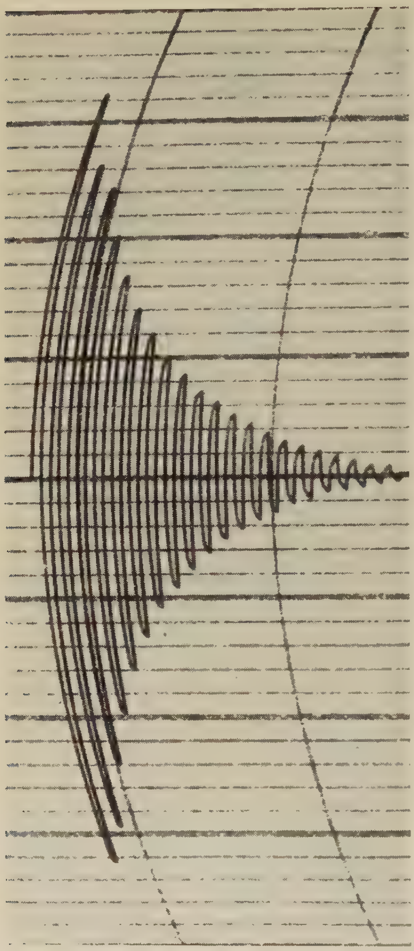

Fig. 5. Record of current changes during a demagnetizing cycle taken with an Esterline-Angus recorder.

For a chosen sweep speed the current through the spectrometer increases linearly with the time. The current, and hence the electron energy, can be calculated to an estimated accuracy of 1 per cent or better by interpolation on the recorder paper. A photograph of the complete spectrometer is shown in Fig. 6.

4. The field distribution and the focusing properties

The magnetic field distribution has been investigated experimentally by a Grassot fluxmeter and a small search coil. The search coil was movable in a brass frame along a diameter in the symmetry plane of the spectrometer and the frame together with the coil could be turned through 180° around this diameter.

Originally the pole pieces were machined to the shape shown by the dotted line in the lower part of Fig. 7. The measured field distribution was, however, found to deviate somewhat from the expected one, particularly in the outer part of the

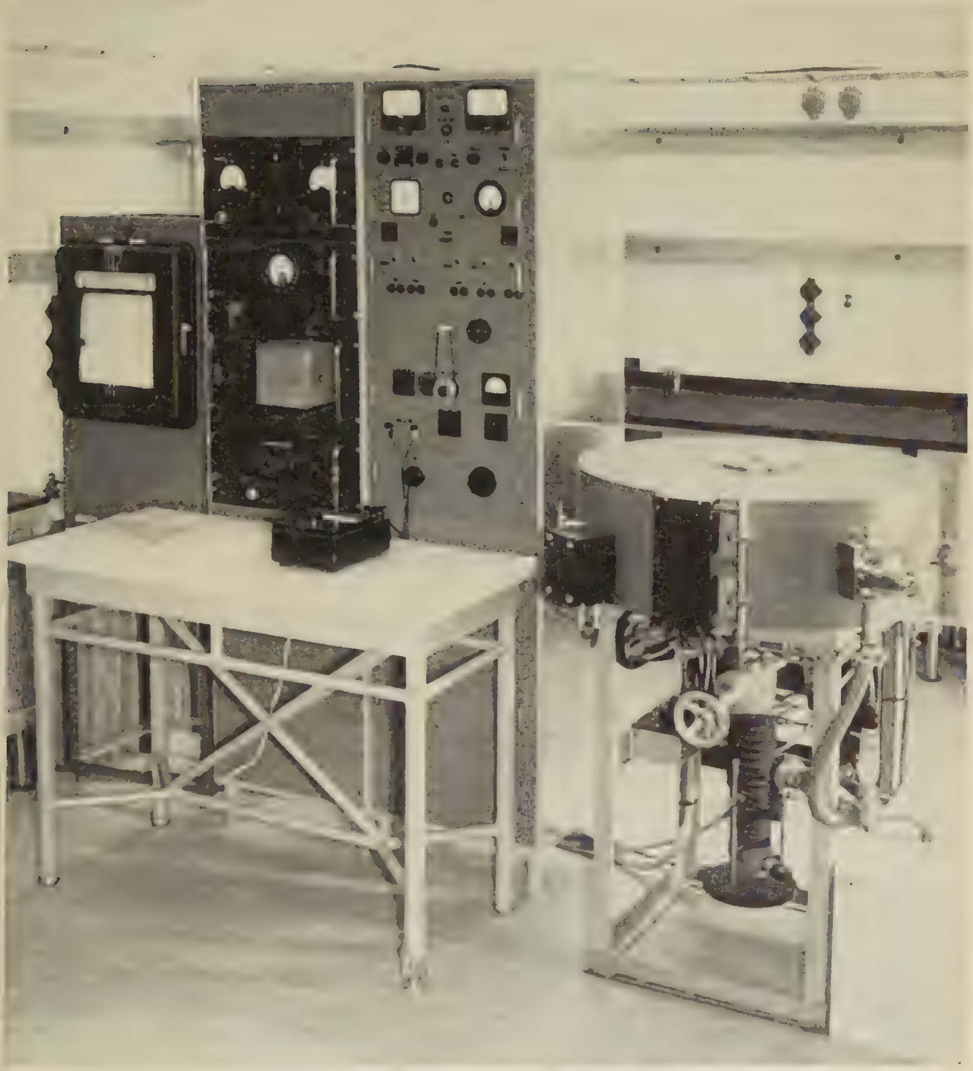

Fig. 6. General view of the spectrometer.

pole gap, where the distribution curve had a smaller curvature than predicted by the value $\beta = \frac{1}{4}$. In order to get better agreement with the theoretical shape, some iron was cut away from the outer part of the pole pieces. The final field distribution and the shape of the pole pieces are shown in Fig. 7. The field still deviates somewhat from the correct one. Particularly for r-values in the region $20 \le r \le 28$ the measured points lie between the two curves for $\beta = \frac{1}{4}$ and $\beta = \frac{3}{8}$. The distribution was considered tolerable in our case, however, because we thought that possible imperfections in the focusing properties might easily be corrected for by small adjustments of the shutters.

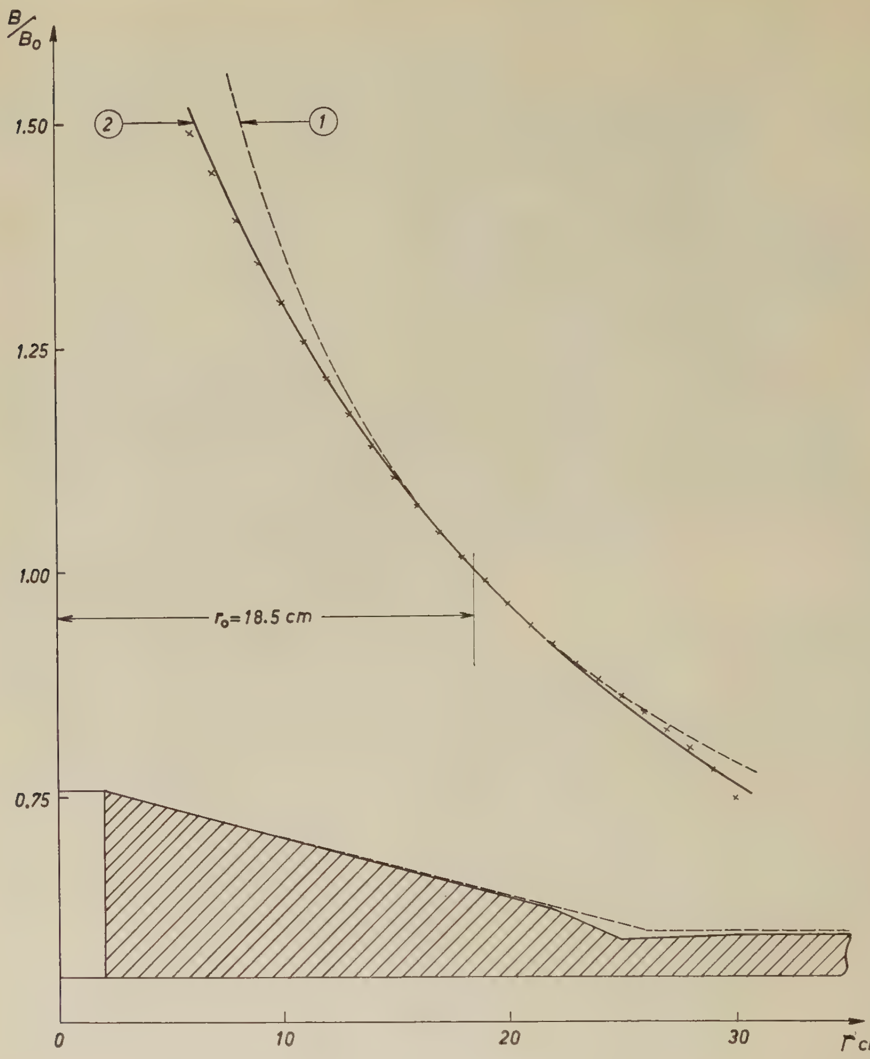

Fig. 7. Shape of pole shoe and magnetic field distribution. The curves 1 and 2 correspond to $\beta = \frac{3}{8}$ and $\beta = \frac{1}{4}$ respectively.

The distribution was investigated for different field strengths between 70 and 1100 gauss. Within the limits of the accuracy of our measurements ($\pm$ 0.1 %), it was found to be independent of the field strength, provided that the spectrometer was demagnetized before each measurement.

According to SVARTHOLM [10], the theoretical field distribution in the case of $\beta = \frac{1}{4}$ can be expressed by $B(r) = B(r_0)\,\frac{2\,r_0}{r + r_0}$; thus a straight line would be obtained when $1/B$ is plotted as a function of r. This line would cut the r-axis at

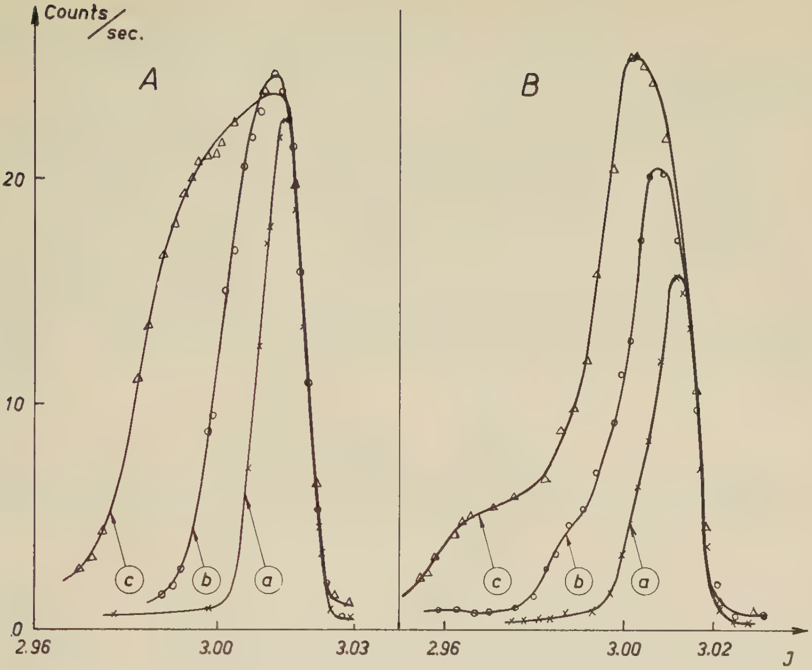

Fig. 8. Shape of F line from ThB in different field regions.

$r = -r_0$. The experimental points fit well to straight lines for r between 8 cm and 22 cm, but deviate somewhat for r-values outside that region. From the intersections of the lines with the r-axis, a value of r_0 equal to 18.5 cm is obtained, and, in agreement with this finding, the spectrometer has been adjusted for a mean radius of 18.5 cm.

Investigation of the focusing properties have been carried out by use of the well-known internal conversion lines from ThB in equilibrium with its decay products. The sources have been prepared by electrostatic collection of the activity on thin (2 mg/cm^2) aluminium foils. In order to get an idea of the consequences of the deviation from the correct field distribution, an experimental investigation of the line-shape was made when rays inside the cylinder surface $r = 18.5$ cm and rays outside this surface respectively were used. In Fig. 8 the line-shapes of the F line for three different apertures are shown. Fig. 8 A is obtained from inside rays, Fig. 8 B, from outside rays. In both cases the electron beam was bounded by a semi-circular aperture. All curves are obtained with a source of width 1 mm and the counter slit of width 2 mm. The curve pairs a, b, and c are obtained for transmissions corresponding to solid angles of 0.5, 0.9, and 1.6 per cent respectively. The contribution to the relative half-width due to the source and counter slit used is only about 0.2 per cent, and hence the main part of the line-width results from the effect of spherical aberration. The inequalities in line-shape obtained in the two field sections is clearly seen in Fig. 8. In the inner part the field corresponds to $\beta = \frac{1}{4}$, and here the intensity is approximately constant in agreement with theory. The only effect of an increase in solid angle is an increase of the image width towards lower energy. Some of the dissymmetry in the curve c may be due to the fact that the axial extension of the counter is only 3.3 cm, and accordingly some radiation may not be detected.

As seen from Fig. 8, the deviation in field distribution in the outer part of the pole gap does not reduce the resolution to any great extent. In order, however, to get a more symmetrical line-shape, composed of electrons focused in the two regions, it seemed advantageous to shut off some outside rays and so the aperture of the defining shutter has been adjusted to give the same total image width from both inside and outside rays.

After the adjustment of the shutters, the F and I lines were used to obtain experimental values of the resolving power for different widths of the counter slit and sample. Some results are collected in Table 1. Values of the half-width, calculated according to the expression

$$\left(\frac{\Delta B\varrho}{B\varrho}\right)=\frac{\delta_{ab}+\delta_s+\delta_{st}}{8r_0}$$

where δ_s and δ_{st} are the widths of source and slit respectively, are included for comparison. The height of the source was kept constant (20 mm).

Table 1.

Width of slit, mm	Width of source, mm	Relative half-width in per cent for different solid angles in per cent of a total sphere							
		½ %		1 %		2 %		4 %	
		measured	calc.	measured	calc.	measured	calc.	measured	calc.
2	2	0.50	0.44	0.64	0.60	0.92	0.94	1.3	1.5
4	4	0.70	0.71	0.85	0.87			1.5	1.7
8	8			1.3	1.4	1.6	1.7	1.8	2.4
20	16	2.3	2.6					2.9	3.5

When the spectrometer was first put into operation, an unexpectedly high counting rate of high energy electrons was observed. Obviously electrons of low momentum, describing trocoidal orbits, could pass the shutter system and the slit in front of the counter window. The effect appeared when the spectrometer was set to focus electrons of energies above about 2 MeV. A small contribution to the counting rate was found even when a narrow slit (2 mm) was used. Electrons in such orbits can be eliminated in several ways. A strip of metal foil placed along the cylinder surface $r = 18.5$ cm half-way between the source and the counter has proved effective.

5. Calibration

Due to the magnet iron the field strength is only approximately proportional to the current through the coils. Thus to enable the use of current readings as a measure of the field strength, the relation between field strength and current has

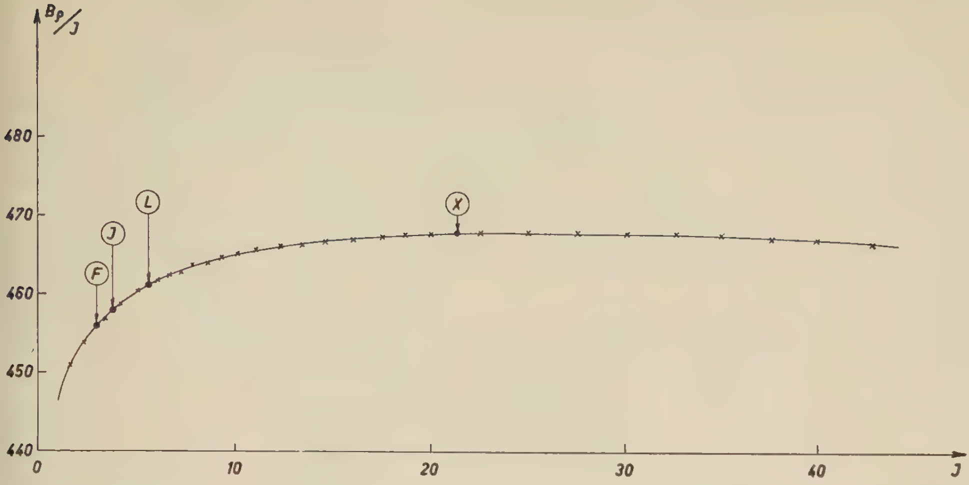

Fig. 9. Calibration curve for the spectrometer. The circles are the measured values for F, I, L and X lines from ThB.

been determined experimentally by fluxmeter and search coil. The coil was fixed with its centre at $r = 18.5$ cm and could be turned through 180°. In order to get the same relative accuracy in the whole field region of interest the sensitivity of the fluxmeter was decreased with increasing field by shunting the search coil. If S' is the deflection of the shunted fluxmeter, then the deflection S without shunt would be given by

$$S = S' \frac{R + R_c + R_s}{R_s}$$

where R_s is the resistance of the shunt, R_c is the resistance of the search coil and R is a resistance connected in series with the search coil to reduce the influence of small temperature changes in the coil. The resistors R and R_s were chosen so that the fluxmeter deflections could be kept approximately constant and could be read on the same part of the scale. Thus no corrections for the non-linearity of the scale and the fluxmeter deflections were needed. Values of the magnet current and the resistors could be determined with an accuracy of about 1 part in 10,000, and the deflection of the fluxmeter is measured with an estimated accuracy of 1 part in 1000 or better.

In Fig. 9 the deflections S divided by the magnet current are plotted as a function of the current in amperes. The curve has been normalized to fit the measured values of the F, I, L and X lines of ThB and its decay products, and gives gauss cm per ampere. The $B\varrho$ values used in normalizing the curve are those reported by LINDSTRÖM [12] for the F, I and L lines and by BROWN [13] for the X line.

After an excitation of the magnet by 45 amperes there is left a remanent magnetic field of about 6.7 gauss at $r = 18.5$ cm. This can, however, easily be removed by means of appropriate demagnetization, after which a reproducibility of about 0.1 per cent has been found for the F line of ThB, provided that the current

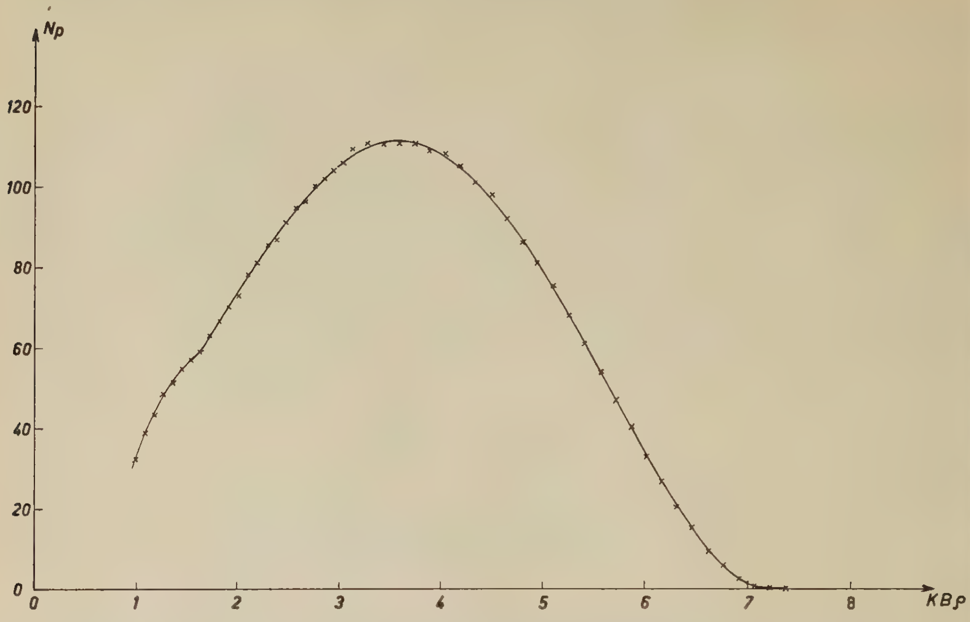

Fig. 10. β-spectrum from a sample of P^{32}. Spectrometer resolution 1 %. Counter window 3 mg/cm².

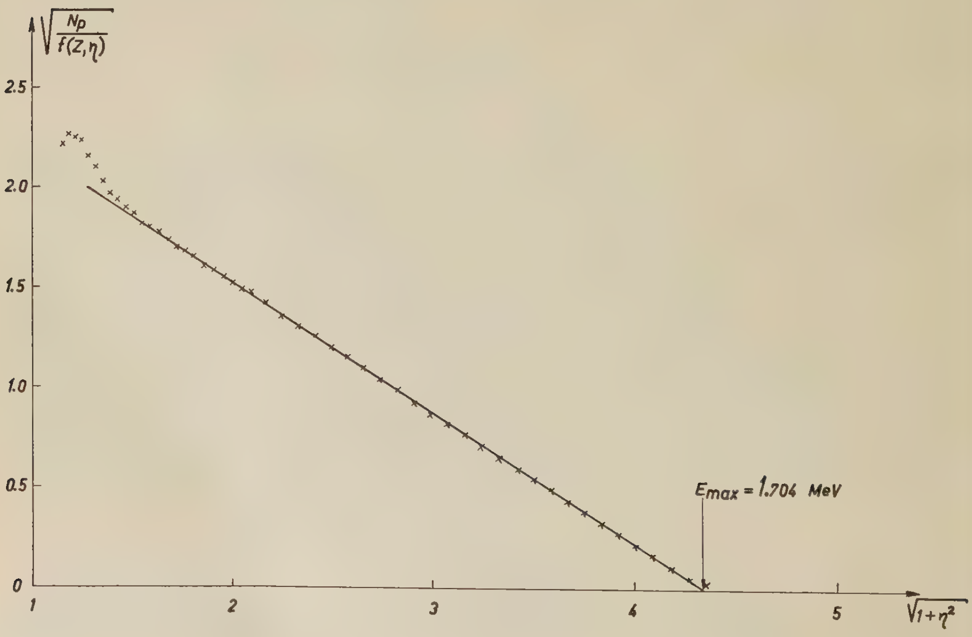

Fig. 11. Fermi plot of the β-spectrum of the P^{32} sample.

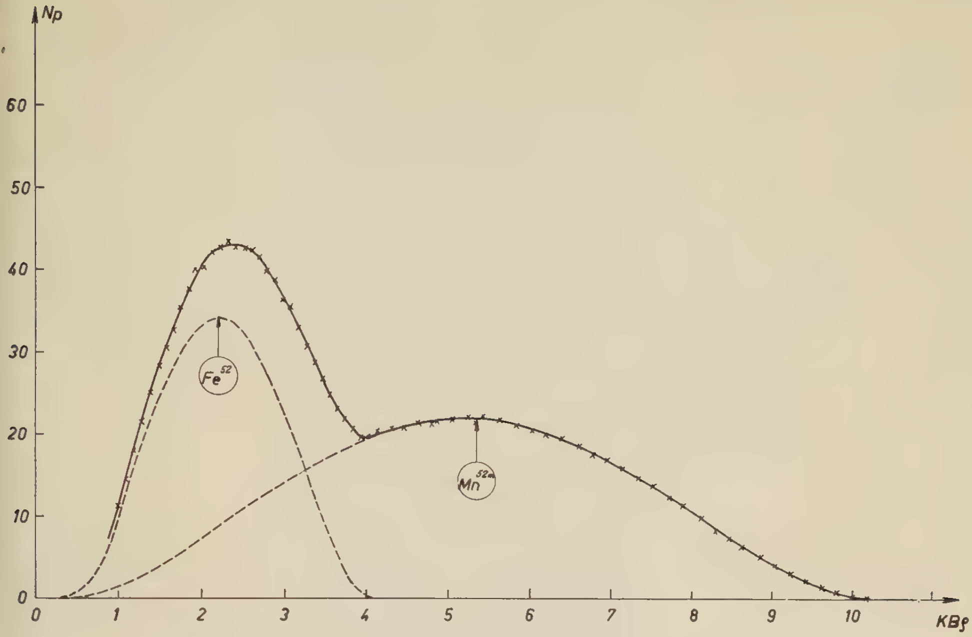

Fig. 12. Positron-spectra of F^{52} in equilibrium with Mn^{52m}. Spectrometer resolution 3 %.

always is changed from lower towards higher values. Thus the electron momentum may be determined from the current readings with an accuracy of 0.1 per cent by the use of the curve in Fig. 9. The energy of an electron line can, however, be determined with higher precision relative to a well established neighbouring line, used as a reference line.

6. Some results

The spectrometer has now been used for some time and the results of a few investigations will be briefly reported here as an illustration.

Beta-spectrum of P^{32}.—One of the first investigated continuous spectra was that of P^{32}. The nuclide P^{32}, being known as a pure β-emitter with an accurately investigated spectrum of the allowed type, seemed suitable as a test of the performance of the spectrometer. Carrier-free P^{32} was received from A.E.R.E., Harwell. Samples for the spectrometer were prepared by evaporation of a small quantity of the active H_3PO_4 solution on a thin Tygon film, the back-side of which was made conducting by a thin evaporated aluminium layer. The resulting β-spectrum for a resolution of the spectrometer set to 1 per cent is shown in Fig. 10. The experimental points are uncorrected for absorption in the counter window (~ 3 mg/cm^2). The Fermi plot (Fig. 11) becomes a straight line for electron energies higher than about 270 keV. There is, however, a marked excess of lower energy electrons. Remeasurement of the spectrum during several half-lives showed this excess to be more prominent with the time and that it could be ascribed to an activity with a decay period of about 25 days. It was concluded that the low energy electron

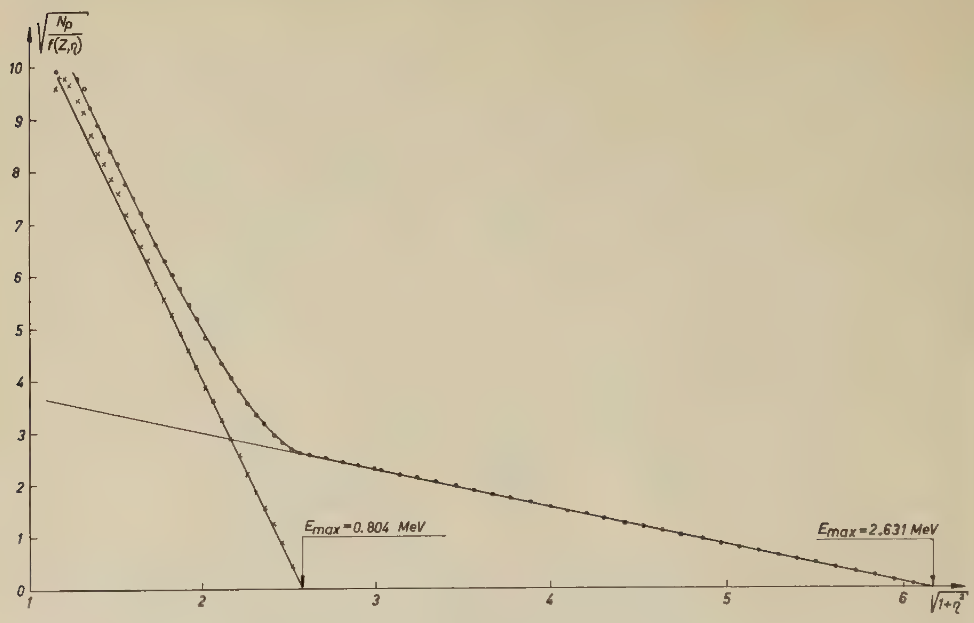

Fig. 13. Fermi plots of the positron spectra of Fe^{52} and Mn^{52m}.

excess was due to the presence of a small amount of P^{33} in the sample (cf. JENSEN *et al.* [14]). From the Fermi plot one gets 1.704 ± 0.010 MeV for the maximum electron energy in good agreement with recent values given in the literature.

Positron spectrum of Fe^{52}.—The positron distribution from 8.3 hr Fe^{52} in equilibrium with its decay product 21 min. Mn^{52m} is shown in Fig. 12. The source used had an area of 5 × 20 mm, on a thin Tygon film backing. Fe^{52} was produced by spallation of Ni with 160 MeV protons in the Uppsala synchrocyclotron. The iron activity was purified by repeated precipitations as $Fe(OH)_3$ with $Al(OH)_3$ carrier and extractions with isopropyl ether from 8*N* HCl solution. Decay curve analysis showed a pure 8.3 hr activity during ten half-lives.

The positron distribution can be resolved into two spectra by means of Fermi plot analysis (Fig. 13). According to an investigation by OSBORNE and DEUTSCH [15] the maximum positron energy in the disintegration of Mn^{52m} is 2.66 ± 0.05 MeV, and this value agrees within the experimental errors with the maximum energy 2.631 ± 0.015 MeV found here for the higher energy spectrum. For the lower energy component, which must then belong to the disintegration of Fe^{52}, we get a maximum positron energy of 0.804 ± 0.010 MeV. As the Fermi plot is seen to become a straight line the measurements confirm the result found by FRIEDLANDER and MILLER [16] that the disintegration of Fe^{52} is an allowed transition. The ratio between the areas under the two distribution curves is 0.57 ± 0.06. If it is assumed that ~ 100 per cent of the Fe^{52} disintegrations leads to the isomeric state of Mn^{52}, the branching ratio of positron emission to electron capture can be calculated as 1.3 ± 0.3 to be compared with the value 1.6 ± 0.4 given by FRIEDLANDER and MILLER.

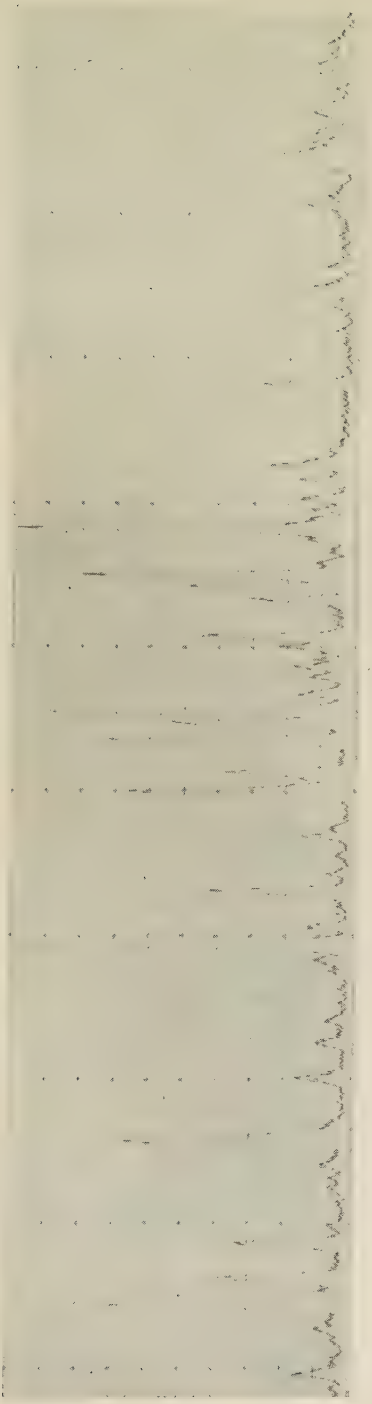

Fig. 14. Part of a record of conversion electron spectrum from neutron deficient lead isotopes and their decay products. Spectrometer resolution 0.3 %.

Conversion lines from Pb and Tl isotopes.—Recently an investigation of neutron deficient Pb and Tl isotopes with mass numbers < 200 was started [17], using the automatic device for recording of spectra. The Pb activities are produced in the synchrocyclotron of this Institute by $\mathrm{Tl}(p, xn)\mathrm{Pb}$ reactions of various proton energies. Records of the conversion lines within a selected energy interval are taken repeatedly and the decay periods and electron energies of the different lines can be calculated from the records. In this way it has been possible to identify the lines belonging to a certain isotope in the mixture of activities with half-lives ranging from 12 min. to several hours. Fig. 14 shows a record of conversion lines obtained from a sample consisting of a mixture of Pb isotopes and their decay products evaporated on to a thin aluminium foil, with the spectrometer adjusted to a resolution of 0.3 per cent. The time for recording the part of the spectrum shown in Fig. 14, ranging from 50 keV to about 300 keV, was in this case 40 minutes.

ACKNOWLEDGEMENT

The authors are indebted to Professor THE SVEDBERG for his interest in this work. We also wish to express our thanks to Dr. H. TYRÉN for many suggestions, to Civ.ing. B. HEDIN and Ing. G. HANSON for valuable assistance in the construction of the instrument, and to Mr. A. ÖSTLUND for the building and testing of the electronic current regulator. The work was financially supported by the Swedish Atomic Energy Commission. This support, as well as the permission to publish the results, is gratefully acknowledged.

The Gustaf Werner Institute for Nuclear Chemistry, University of Uppsala, Uppsala, Sweden.

REFERENCES

1. SIEGBAHN, K. and SVARTHOLM, N., Nature *157*, 872 (1946).
2. SVARTHOLM, N. and SIEGBAHN, K., Arkiv Mat. Astron. Fysik *33 A*, No. 21 (1946).
3. SVARTHOLM, N., Arkiv Mat. Astron. Fysik *33 A*, No. 24 (1946).
4. SHULL, F. B. and DENNISON, D. M., Phys. Rev. *71*, 681 (1947), 72, 256 (1947).
5. HEDGRAN, A., SIEGBAHN, K., and SVARTHOLM, N., Proc. Phys. Soc. (London) *63 A*, 960 (1950).
6. BARTLETT, A. A. and BAINBRIDGE, K. T., Rev. Sci. Instr. *22*, 517 (1951).
7. STOKER, P. H., ONG PING HOK, DE HAAN, E. F., and SIZOO, G. J., Physica *20*, 337 (1954).
8. SHULL, F. B., Phys. Rev. *74*, 917 (1948).
9. KURIE, F. N. D., OSABA, J. S., and SLACK, L., Rev. Sci. Instr. *19*, 771 (1948).
10. SVARTHOLM, N., Arkiv för Fysik *2*, No. 14, 20 (1950).
11. COONROD, L. G., CECCONI, W. E., GEDRAITIS, C., HARPER, K. R., and LEWIS, R. M., Rev. Sci. Instr. *20*, 408 (1949).
12. LINDSTRÖM, G., Phys. Rev. *83*, 465 (1951).
13. BROWN, W. L., Phys. Rev. *83*, 271 (1951).
14. JENSEN, E. N., NICHOLS, R. T., CLEMENT, J., and POHM, A., Phys. Rev. *85*, 112 (1952).
15. OSBORNE, R. K. and DEUTSCH, M., Phys. Rev. *71*, 467 (1947).
16. FRIEDLANDER, G. and MILLER, J. M., Phys. Rev. *84*, 588 (1951).
17. ANDERSSON, G., ARBMAN, E., BERGSTRÖM, I., and WAPSTRA, A. H., Phil. Mag. *46*, 70 (1955).

Tryckt den 9 september 1955

Uppsala 1955. Almqvist & Wiksells Boktryckeri AB

ARKIV FÖR FYSIK Band 10 nr 2

Communicated 9 February 1955 by ERIK HULTHÉN and ARNE WESTGREN

The perturbations in the near ultra-violet band-system (D–X) of silicon monosulphide

By GÖTE NILHEDEN

With 3 figures in the text

Abstract

The rotational analysis of the near ultra-violet bandsystem $D\,^1\Pi$–$X\,^1\Sigma^+$ has been extended to higher levels. Eight new bands have been analysed, namely the 7,0, 8,0, 8,1, 8,2, 9,1, 9,2, 10,1, and 10,2 bands. With special attention to the perturbations in the D state nine bands have been reanalysed, namely the 2,0, 3,0, 4,0, 4,1, 5,0, 5,1, 6,0, 6,1, and 7,1 bands.

The perturbations investigated arise from interactions with three electronic states, a $^3\Sigma^-$ state, a $^1\Pi$ or $^1\Delta$ state and a $^1\Sigma^-$ state. For the $^1\Pi$ or $^1\Delta$ state it has been possible to determine the v numbering. For the other two states it is impossible to give the v numbering, but in spite of that fairly good information has been obtained. For the $^3\Sigma^-$ state the constants derived are:

$$B_{e+v} = 0.221_6 - 0.002_9\, v,$$

$$\omega_e' \geq 407_2 \qquad x_e'\,\omega_e' = 1.7_7.$$

For the $^1\Pi$ or $^1\Delta$ state:

$$B_{v'} = 0.226_9 - 0.002_8\,(v' + \tfrac{1}{2}),$$

$$\omega_e' = 439._9 \qquad x_e'\,\omega_e' = 3.9_7.$$

For the $^1\Sigma^-$ state:

$$B_{i+v} = 0.213_3 - 0.001_8\, v,$$

$$\omega_e' \geq \quad 404._9 \qquad x_e'\,\omega_e' = 1.1_8.$$

Moreover, interactions with a fourth perturbing state seem to be present. For the moment no information can be given concerning this state. To get this information the analysis must be extended to even higher levels.

§ 1. Introduction

In a previous paper (LAGERQVIST, NILHEDEN and BARROW 1952) the rotational analysis of the D–X system of SiS was given. Two kinds of perturbations were then observed, one arising from the interaction with a $^3\Sigma^-$ state and the other from interaction with a $^1\Pi$ or $^1\Delta$ state.

When taking up some spectrograms in order to make a rotational analysis of the far ultra-violet bandsystem E–X (VAGO and BARROW 1946), I also obtained better plates of the higher levels of the D–X system than before. This paper presents a reanalysis of some bands in the D–X system and the new analysis of the 7,0, 8,0, 8,1, 8,2, 9,1, 9,2, 10, 1, and 10,2 bands made on the new plates with special attention to the perturbations. The analysis was very intricate since most of the bands overlap each other.

The structure of the $^3\Sigma^-$ interaction is mentioned in our previous paper (LAGERQVIST, NILHEDEN and BARROW 1952). The interactions from the $^1\Pi$ or $^1\Delta$ state with the $D\ ^1\Pi$ level are visible: One in the Q branch and one in the R and P branches. A new interaction only visible in the Q branch has been found. It seems to be a $^1\Sigma^-$ state interacting with the $D\ ^1\Pi$ level. In almost every perturbation extra lines have been found.

A fourth type of perturbing interaction may undoubtedly be predicted. To get information about this, the analysis has to be extended somewhat further, if possible to the levels with $v'=11$ and to higher J values in the levels with $v'=10$ and 9. At present it is very difficult to say anything about the state interacting with the $D\ ^1\Pi$ level, but it seems very complicated and might be a $^3\Pi$ state. New efforts will be made.

§ 2. Experimental

The spectrograms were taken in the same way as mentioned in our paper of 1952. It seems, however, that the result is closely connected with the gas-pressure in the absorption tube. The new plates were taken at a pressure of about 100 torr. The exposure time on Ilford Zenith plates was 40 mintes.

Table 1. Deslandres scheme of band origins.

10			38 977.63	739.43	38 238.20					
			455.70		455.02					
9			38 521.93	738.75	37 783.18					
			460.60		461.07					
8	38 805.40	744.07	38 061.33	739.22	37 322.11					
	464.02		464.44							
7	38 341.38	744.09	37 596.89							
	477.17		477.43							
6	37 864.21	744.75	37 119.46							
	477.91		477.15							
5	37 386.30	743.99	36 642.31							
	483.61		484.41							
4	36 902.69	744.79	36 157.90							
	489.79									
3	36 412.90									
	496.07									
2	35 916.83									
	501.23									
1	35 415.59	744.45	34 671.14							31 744.6
	506.95		507.26							
↑ 0	34 908.64	744.76	34 163.88	739.34	33 424.54	734.23	32 690.31	729.04	31 961.27	
v' v'' →	0		1		2		3		4	5

§ 3. Structure of the bands

A Deslandres scheme of bands-origins is given in Table 1. The wave numbers of the lines of the 7,0, 8,0, 8,1, 8,2, 9,1, 9,2, 10,1, and 10,2 bands are given in Tables 2–3, where overlapped lines are indicated with an asterisk.

§ 4. Determination of rotational constants

The rotational constants for the ground state have been determined by plotting $\Delta_2 F''(J)/(J+\frac{1}{2})$ against $(J+\frac{1}{2})^2$. The points were divided into two groups and for each group one point was determined by the weighted centre of gravity method (LAGERQVIST, LIND and BARROW 1950). The straight line through these two points gives the constants in the usual way. The results agree quite well with the equations given before (BARROW 1946):

$$B''_v = 0.3036_3 - 0.0014_9\,(v''+\tfrac{1}{2}),$$

$$D''_v = [2.01_5 - 0.01_0\,(v''+\tfrac{1}{2})]\cdot 10^{-7}.$$

In Table 4 the values now observed are found. The calculated values are from the equations above.

Table 4. Rotational constants for the $X\,^1\Sigma^+$ state.

v''	B_{obs}	B_{calc}	D_{obs}	D_{calc}
0	0.3030_0	0.3028_9	$-1.6_5\cdot 10^{-7}$	$-2.0_1\cdot 10^{-7}$
1	0.3014_3	0.3014_0	-1.7_2	-2.0_0
2	0.2997_2	0.2999_1	-1.5_7	-1.9_9

A control determination of the rotational constants for the upper levels agrees fairly well with our former results (LAGERQVIST, NILHEDEN and BARROW 1952).

The values were determined in the same way as in that paper and the values now observed for the levels with $v'=7$, 8, 9, and 10 are given in Table 5. There the calculated values are from the equation:

$$B_{v'} = 0.2664_7 - 0.0021_6\,(v'+\tfrac{1}{2})$$

(see LAGERQVIST, NILHEDEN and BARROW 1952).

Table 5. Rotational constants for the $D\,^1\Pi$ state.

v'	B_{obs}	B_{calc}
7	0.2501_7	0.2502_7
8	0.2480_4	0.2481_1
9	0.2460_2	0.2459_5
10	0.2438_9	0.2437_9

Table 2. Wave numbers for the 7,0, 8,0, 8,1 and 8,2 bands.

J	7,0			8,0			J	8,1			8,2		
	Q	R	P	Q	R	P		Q	R	P	Q	R	P
1							1						
2							2						
3				38805.21*			3						
4	38340.71*			04.58*			4						
5	40.03*			03.72*			5				37321.09*		
6	39.20*			02.91*			6	38059.34*			20.51*		
7	38.48*			01.75*			7	58.47*			19.48*		
8	37.53*			00.71*	38806.61		8	57.62*			18.33*		
9	36.11*	38340.71*		799.92	05.91		9	56.42*			17.38*		
10	35.11*	40.03*		99.09*	05.21*	38794.95*	10	55.29*			16.34	37321.09*	
11	34.03*	39.20*	38327.62*	97.88*	04.58*	92.85	11	54.32			15.29*	20.51*	
12	32.87*	38.48*	26.06*	96.95*	03.72*	90.71*	12	52.87*	38059.34*		13.87*	19.48*	37307.69*
13	31.19	37.53*	24.14*	95.72	02.91*	88.94*	13	51.56	58.47*		12.62*	18.33*	06.10*
14	29.72	36.11*	22.05*	94.27	01.75*	86.81*	14	50.02*	57.62*	38042.98*	10.92*	17.38*	04.09*
15	27.62*	35.11*	19.87*	92.85*	00.71*	84.87*	15	48.33	56.42*	40.99*	09.47*	16.34*	02.02*
16	26.06*	34.03*	17.95*	90.74*	799.09*	82.62*	16	46.52	55.29*	38.70*	07.69*	15.29*	299.49*
17	24.14*	32.87*	15.69*	88.94*	97.88*	80.34*	17	44.88*	53.70	36.50*	06.10*	13.87*	97.32*
18	22.05*	32.06	13.22*	86.81*	96.95*	77.83*	18	42.98*	52.29*	34.10*	04.09*	12.62*	94.61*
19	19.87*	30.25	11.03*	84.87*	94.95*	75.31*	19	40.99*	50.69*	31.51*	02.02*	10.92*	92.68*
20	17.95*	28.78*	07.88*	82.62*	92.85*	72.72*	20	38.72*	49.04*	28.60*	00.00*	09.47*	90.24*
21	15.69*	26.65*	05.25*	80.34*	90.71*	69.82*	21	36.50*	47.30	26.20*	297.77*	07.69*	87.36
22	13.22*	24.61*	02.38*	77.83*	88.94*	67.05*	22	34.10*	45.46	23.30*	95.46*	06.10*	84.65*
23	10.74*	22.62	299.41*	75.31*	86.81*	64.04*	23	31.51*	43.58*	20.30*	93.12	04.09*	82.04*
24	07.88*	20.30	96.46*	72.72*	84.87*	60.98*	24	29.06*	41.51*	17.17	90.56*	02.02*	78.88
25	05.25*	17.95*	93.13*	69.82*	82.62*	57.59*	25	26.20*	39.33	14.08	88.10*	00.00*	75.21*
26	02.38*	15.69*	89.30	67.05*	80.34*	54.24*	26	23.61*	36.90	10.79	85.24*	297.77*	71.98*
27	299.41*	13.22*	86.03*	64.04*	77.83*	50.96*	27	20.83*	34.54*	07.34	82.64	96.30*	69.23
28	96.46*	10.45*	82.60	60.98*	75.31*	47.23*	28	17.69*	32.16	03.85	79.53	93.99	65.78*
29	93.13*	07.88*	78.96	57.59*	72.72*	43.41*	29	14.71*	29.54	00.24*	76.56*	91.50*	62.14*
30	90.02*	05.25*	75.09	54.24*	69.82*	39.75*	30	11.56*	26.82	37996.49*	73.51	88.80	58.65*
31	86.69	02.38*	71.32	50.96*	67.05*	35.76*	31	08.17*	23.61*	92.60	70.12*	85.97*	55.09*
32	83.32*	299.41*	66.91*	47.45	64.04*	31.74*	32	04.77*	20.83*	88.80	67.08*	83.28*	51.10
33	79.62	96.46*	63.39*	43.90	60.98*	27.66*	33	01.19*	17.69*	84.86	63.48	80.15*	47.38*
34	75.87	93.13*	59.12*	40.23	57.59*	23.41*	34	37997.60*	14.71*	80.71*	60.01	77.54*	43.15*

37	_67.96*_	_84.92_	_50.41*_	28.32	47.23*	09.97*	37	85.97*	04.77*	67.68	48.81*	67.52*	30.54*
38	58.32 _62.35_	_80.86*_	40.55 _43.97*_	24.29	43.41*	05.35*	38	81.91*	01.19*	63.10	44.71*	64.03*	25.97*
39	52.29 _57.12_	_77.21_	34.66* _37.95_	19.90	39.75*	00.68*	39	77.71*	37 997.60*	58.45	40.74*	60.51	21.61*
40	_52.80*_	_73.07_	_33.22*_	15.47	35.76*	695.92*	40	73.35*	93.74*	53.73	36.62*	56.83*	16.73*
41	_48.42*_	_69.43*_	_28.16*_	11.05	31.74*	90.76*	41	_68.68*_ _75.91*_	89.91*	48.83	32.42*	52.83*	12.09
42	_43.97*_	_65.18_	_23.16*_	06.37 _12.38_	27.66*	85.55*	42	63.43 _68.68*_	85.97*	43.96	27.96	48.81*	07.30*
43	_39.23*_	_61.28*_	_17.98_	01.31 _04.30_	23.41*	80.32*	43	57.23 _61.86_	81.91*	38.90	23.13	44.71*	02.19*
44	_34.66*_	_57.12*_	_12.81*_	695.18 _97.16_	18.99*	74.95*	44	50.04* _56.03_	77.71*	33.64	17.65* _21.61*_	40.74*	197.15
45	_29.80*_	_52.80*_	_07.38*_	86.84* _91.99_	14.69*	69.56*	45	_50.64_	73.35*	28.29	_15.00_	36.62*	92.15*
46	_24.98*_	_48.42*_	_02.10*_	_86.84*_	09.97*	64.06*	46	_45.71*_	68.68*	22.86	_09.52*_	32.42*	86.83
47	_20.00*_	_43.97*_	_196.75*_	_81.65_	05.35*	58.69	47	_40.55*_	64.45	17.44*	_04.76*_	28.34*	81.83*
48	_14.72*_	_39.23*_	_90.84*_	_76.36_	00.68*	52.80	48	_35.47_	59.75*	11.71	_199.48*_	23.68	75.93
49	_09.70*_	_34.66*_	_85.43*_	_71.02_	695.92*	46.81	49	_30.25_	54.83	05.91	_94.41*_	18.98*	70.34*
50	_04.36*_	_29.80*_	_79.52*_	_65.36_	90.76*	40.80	50	_24.81_	50.07*	00.16	_89.20*_	14.36	64.38*
51	_198.92*_	_24.98*_	_73.64_	_60.09_	85.55*	34.81	51	_19.41_	45.07	894.14	_83.88*_	09.52*	58.72*
52	_93.62*_	_20.00*_	_67.62_	_54.20_	80.32*	28.59	52	_13.88_	39.93*	88.01	_78.33*_	04.76*	52.63*
53	_87.83*_	_14.72*_	_61.51*_	_48.35_	74.95*	22.41	53	_08.12*_	34.82	81.85	_72.83*_	199.48*	46.16
54	_81.95*_	_09.70*_	_55.40*_	_42.40_	69.56*	15.82*	54	_02.22_	29.52	75.72*	_67.37_	94.41*	39.74*
55	_75.85*_	_04.36*_	_49.05*_	_36.25_	64.06*	09.37	55	_896.37_	24.03	69.39	_61.75_	89.20*	33.49*
56	_69.71*_	_198.92*_	_42.68*_	_30.15_	57.55	02.80	56	_90.34_	18.40	62.90*	_55.88*_	83.07	27.53
57	_63.70*_	_92.84_	_36.04*_	_23.79_	52.07	596.12	57	_84.20_	12.68*	55.88*	_49.74*_	76.31*	20.54*
58	_57.48*_ 70.40	_87.34*_	_29.33*_	_17.22_	46.16	89.55	58	_77.96_	07.02*	49.28*	_43.68_	70.34*	14.13*
59	_50.71*_ 59.80*	_81.95*_	_22.65*_	_10.58_	40.31	81.88	59	_71.63_	01.10	42.31*	_37.49*_	63.60*	07.23*
60	_42.68*_ 49.94	_75.85*_	_15.69*_	_03.98*_	33.99	74.42	60	_64.92_	894.99	35.49*	_31.10*_	57.00	099.75*
61	_33.45*_ 41.41*	_69.71*_	_08.70_	_597.21*_	27.73	67.20	61	_58.29*_	88.76	28.42*	_24.70_	49.74*	92.28*
62	_22.65*_ 33.45	_63.70*_	_01.79*_	_90.41_	21.00	59.91*	62	_51.66*_	82.46	21.18*	_18.04*_	41.89	83.93*
63	25.87	_57.48*_	_094.46*_	_83.52_	13.84	52.33*	63	_45.08*_	75.72*	13.85*	_11.52*_	32.81* _46.96*_	75.21*

(Continued)

(Table 2, continued)

J	7,0			8,0			J	8,1			8,2		
	Q	R	P	Q	R	P		Q	R	P	Q	R	P
64	19.12	_51.29*_	_87.14*_	_76.32*_	05.73 _15.82*_	44.22*	64	_37.92*_	_68.36_ _77.35_	06.37*	_04.83_	23.50 _36.88_	66.09*
65	12.14*	_44.60*_	_79.89*_	_69.02_	597.21* _603.91*_	35.90	65	_30.96_	59.05 _65.81_	797.98*	_098.46_	12.21 _28.15*_	56.51* _70.37*_
66	05.02*	_38.20_	_71.80_	_61.56_	586.71 _93.59_	26.80 _37.02_	66	_23.78*_	48.68 _55.88*_	89.07* _99.16*_	_91.56*_	_20.54*_	46.00* _58.88*_
67	097.96	_31.68_	_64.73_	_53.88_	_84.80_	16.27 _24.12_	67	_16.25_	36.56* _47.17*_	79.27* _85.98*_	_84.46*_	_13.73_	33.50* _49.20*_
68	90.73*	_24.95*_	_57.01_	_45.98_	_76.32*_	04.68* _12.00*_	68	_08.55*_	_39.57*_	67.79* _74.55*_	_76.98*_	_07.23*_	_39.79*_
69	83.24	_17.91*_	_49.04*_	_38.07_	_68.43_	_01.40*_	69	_00.70_	_32.21*_	54.28 _65.07*_	_68.71*_	_00.29*_	_32.38*_
70	75.95	_10.93_	_41.51*_	_29.82_	_59.91*_	_492.79_	70	_792.60_	_24.77*_	_56.37*_	_60.28*_	_093.17*_	_23.72*_
71	68.20*	_03.68_	_33.10_	_21.07_	_52.33*_	_83.57_	71	_84.10*_ 805.53	_16.88_	_47.78*_	_51.34*_ 73.06	_85.57*_	_16.23*_
72	60.44*	_096.48*_	_24.89_	_12.00*_ 23.28	_44.22*_	_73.39*_	72	_775.10*_ 90.80	_09.51_	_39.52*_	_42.10_ 58.88*	_77.77*_	_08.03*_
73	52.87*	_89.25*_	_16.56*_	_01.40*_ 09.43	_36.63_	_64.22_	73	_64.52_ 77.60	_00.70*_	_29.96*_	_31.40*_ 46.00*	_70.37*_	_36 999.35_
74	44.88*	_81.72_	_08.17*_	_489.17_ 97.33*	_28.00_	_55.36*_	74	_52.78*_ 66.07	_791.34*_ 800.39	_21.46*_	_18.80_ 35.07*	_62.34_	_89.61_
75	36.70*	_73.07_ 88.22*	_37 999.45_	86.81	_18.97_ 28.75	_46.41*_	75	_39.52*_ 55.07*	_779.27*_ 89.07*	_12.19_	_03.97_ 25.82*	_52.24_	_81.84_
76	28.60*	_62.73_ 74.00*	_89.91*_	77.67	17.22	_36.99*_	76	_24.80*_ 44.33*	79.27*	_00.89*_ 09.77*	17.57*	_40.90*_ 51.05*	_71.96*_
77	20.30*	_50.02*_ 62.34*	_80.71*_ 96.49*	69.25*	06.68*	_27.12_ 36.99*	77	34.44	70.97*	_688.01*_ 98.15*	09.72	_27.91_ 40.90*	_60.66*_
78	11.56*	_35.06_ 52.29*	_69.05_ 80.71*	60.58*	497.33*	23.26	78	25.33*	62.22	87.02*	01.02*	32.30*	_48.73*_ 58.04
79	03.13	43.58*	_55.51_ 67.68*	51.55*	88.24*	11.56*	79	16.47	53.55*	76.90	36 992.58	23.71*	_34.04_ 47.54
80	37 994.30	34.54*	_39.93*_ 56.80*	42.22*	79.11	01.24*	80	07.58	45.21	67.17	83.98*	15.12	37.24*
81	85.51	26.20*	46.49	33.51*	69.98*	390.65*	81	699.16	36.19	57.56	75.55*	06.55*	28.22
82	75.91* _98.78_	17.69*	37.42*	24.21*	60.58*	80.75	82	90.09		48.16*			18.33*

85	*56.80**	37990.79	08.12	396.14*			85	61.84*					
86	*45.71**	79.43 *93.34*	898.15	86.33*			86	52.28					
87	*36.11*	65.97 *80.71**	87.58				87	42.39*					
88	*26.65*	*69.88*	74.27 *88.76**				88	30.41					
89	*16.68*	*59.75**	59.05* *75.19*				89	16.59					
90	*07.02**	*50.07**	*62.92**										
91	*896.96*	*40.55**	*51.08**										
92		*31.77*	*40.09**										
93		*22.32*	*30.26**										
94		*12.68**	*19.60*										
95		*02.98*	*08.68**										
96			*797.98**										
97			*86.94**										

Table 3. Wave numbers for the 9,1, 9,2, 10,1 and 10,2 bands.

J	9,1			9,2			J	10,1			10,2		
	Q	*R*	*P*	*Q*	*R*	*P*		*Q*	*R*	*P*	*Q*	*R*	*P*
1							1						
2							2						
3				37782.45			3						
4				82.05*			4						
5				81.59*			5						
6				81.01			6						
7				80.12*			7						
8				79.27*			8						
9				78.38*			9						
10				77.14*			10				38232.31*		
11	38514.80			76.00			11				31.04*		
12	13.47			74.55*			12	38968.58			29.80*		
13	12.00			73.06			13	67.08			28.16*		
14	10.34			71.67			14	65.40			26.54*		
15	08.72			69.97			15	63.72			24.98*	38232.31*	
16	06.68*			67.79*	37775.10*		16	61.99			23.16*	31.04*	
17	04.68*	38513.47		65.79*	73.86*		17	60.21*			21.26*	29.80*	38212.81*
18	02.71*	12.00*		63.85*	72.44*	37755.07*	18	58.36			19.36*	28.16*	10.57*
19	00.51*	10.34	38490.89*	61.79*	70.97*	52.78*	19	56.16	38965.70		17.38*	26.54*	08.11*
20	498.31*	08.72	88.24*	59.75*	69.30*	49.97*	20	54.11	64.32		15.15*	24.98*	05.41*
21	96.06*	06.68*	85.39*	57.39*	67.79*	47.16*	21	51.67	61.99*	38940.92*	12.81*	23.16*	02.74*
22	93.66*	04.68*	82.50*	55.07*	65.79*	44.33*	22	49.40	60.21*	38.18*	10.57*	21.26*	199.85*
23	90.89*	02.71*	79.61*	52.46*	63.85*	41.42*	23	46.68	57.84	35.10*	08.11*	19.36*	96.75*
24	88.24*	00.51*	76.50*	49.97*	61.79*	38.30*	24	43.94	55.67	32.10*	05.41*	17.38*	93.62*
25	85.39*	498.31*	73.39*	47.16*	59.75*	35.28*	25	40.92*	53.28	28.74*	02.74*	15.15*	90.84*
26	82.50*	96.06*	69.98*	44.33*	57.39*	32.14*	26	38.18*	51.02	25.25*	199.85*	12.81*	87.83*
27	79.61*	93.66*	66.54*	41.42*	55.07*	28.61*	27	35.10*	48.14	21.68*	96.75*	10.57*	84.27
28	76.50*	90.89*	62.95*	38.30*	52.46*	25.33*	28	32.10*	45.41	17.90*	93.62*	07.38*	80.49
29	73.39*	88.24*	59.27*	35.28*	49.97*	21.46*	29	28.74*	42.65	14.14*	90.65*	04.36*	76.38*
30	69.98*	85.39*	55.36*	32.14*	47.16*	17.49	30	25.25*	39.62	10.16*	87.34*	01.63	72.71*
31	66.54*	82.50*	51.55*	28.33*	44.33*	13.54*	31	21.68*	36.30	06.05*	83.77*	198.92*	68.54*
32	62.95*	79.61*	47.50*	25.33*	41.42*	09.77*	32	17.90*	32.98	01.68*	80.08	95.33	64.98
33	59.27*	76.05	43.37*	21.46*	38.30*	05.61*	33	14.14*	29.62	897.23*	76.38*	91.86	60.78

	47.50	65.73	29.92	10.37	28.12	92.64*	36	01.68*	17.29	85.23*	64.31	79.52*	47.35
37	43.37*	62.12	25.42	06.35	24.80*	88.01*	37	897.23*	12.96	75.59 78.10	59.80*	75.02	38.20 40.32*
38	39.13*	58.20	20.65	02.32*	20.79	83.49	38	92.59*	08.40	71.62*	55.40*	70.40*	34.99*
39	35.03	54.68	15.77	698.15*	16.96*	78.85	39	88.01	04.41	65.76*	50.71*	66.24*	29.20*
40	30.50	50.57	10.84*	93.79*	13.54*	74.01	40	82.78* 81.60	00.40	61.25	45.72* 44.60*	61.51*	23.50*
41	26.01	46.41*	05.78	89.13*	09.77*	69.01*	41	77.31 72.99	896.49	55.52*	40.32* 36.04*	57.48*	17.91*
42	21.34	42.22*	00.61	84.62	05.61*	64.16	42	69.85 65.76*	91.53	50.15*	33.45* 29.20*	53.82	12.14*
43	16.46	37.91	395.16	79.83	01.37*	58.90	43	60.25*	85.23*	44.82*	24.95* 23.50*	49.05* 49.05*	07.14*
44	11.56*	33.51*	90.00	75.10*	697.08*	53.59*	44	54.43	78.85 77.31	38.63	17.91*	42.68* 41.41*	01.79*
45	06.44	28.74	84.36*	70.17	92.64*	48.16*	45	49.04	71.62*	31.72*	12.14*	34.99* 34.99*	095.60* 95.60*
46	01.24*	24.21*	78.52	65.19	88.01*	42.39*	46	43.13	65.76*	23.26* 23.26*	07.14*	29.45	88.22 87.14*
47	396.14*	19.05	72.70	60.02*	83.29	37.10	47	37.40	60.25	15.45	01.79*	24.95*	79.89* 79.89*
48	90.65*	14.24	67.28	54.66	78.08	31.28	48	31.72	55.52	08.69	096.48*	19.70*	73.07*
49	85.00	09.19	61.19	49.27*	73.27	25.31	49	25.80	50.15*	01.75*	90.73*	15.12	67.02
50	79.36	03.55	54.78	43.87	68.22*	19.08*	50	19.71	44.82*	795.72*	85.79	09.96	61.20
51	73.57	398.17	48.13	38.15*	62.61*	12.95*	51	13.81	39.50	88.94*	79.89*	05.02*	55.29*
52	68.12	91.87	41.92*	32.26	56.68	07.19*	52	07.27	34.09	82.62*	74.00*	099.49	49.04*
53	62.37	84.36* 86.33*	35.11*	26.23*	49.27* 48.60*	00.44	53	00.71*	28.20	76.02	68.20*	94.46*	42.16
54	56.11*	77.56	27.62*	20.27	40.73 40.26	592.83*	54	794.27*		68.78	62.34*	89.25*	35.77
55	50.00	69.69	18.96 21.09	13.90*	32.26*	84.43* 83.78*	55	88.24		62.62	55.87	83.92	29.06*
56	43.00	62.87	11.03	07.19	25.31*	74.69* 73.94	56	81.37			49.04*		23.00*
57	35.11* 28.78*	56.11*	01.33*	599.80* 99.18*	19.08*	65.85*	57						16.56*
58	26.65* 17.95*	48.79	294.15	91.70* 88.30*	12.95*	56.84*							
59	17.16 07.88*	41.92*	85.46	82.66* 78.05*	05.41 01.59	49.34*							

(Continued)

(Table 3, continued)

J	9,1			9,2			J	10,1			10,2		
	Q	R	P	Q	R	P		Q	R	P	Q	R	P
60	06.38 _298.73_	_34.03*_ 31.19*	_76.75_	72.37* _68.71_	_596.97*_ 91.70*	_41.88_							
61	_90.02*_	_24.61*_ 22.05	_69.43*_	60.69* _60.69*_	_86.76*_ 82.66*	_33.22*_ 29.43*							
62	_81.97_	13.22*	_60.30_ 57.12*	_53.16*_	74.69*	_23.52*_ 18.54							
63	_74.07_	05.25*	_48.92_ 46.46*	_46.12*_	66.86*	_12.90_ 08.73*							
64	_66.91*_	297.84	36.74*	_38.85*_	59.61*	499.30							
65	_59.12*_	90.40	27.42	_31.23*_	52.64*	89.93							
66	_51.42_	83.32*	19.36*	_24.55*_	45.37	81.50*							
67	_43.97*_	75.87*	10.57*	_17.38_	37.89	73.31							
68	_36.74*_	68.56	02.10*	_09.58*_	30.99	64.83							
69	_28.74_	61.28*	193.62*	_02.10*_	23.52*	56.58							
70	_21.26*_	53.96	85.43*	_494.43_	16.40*	48.65							
71	_13.32_	46.46*	77.02			40.10							
72	_05.41*_	39.23*	68.54*			31.00*							
73	_196.75*_	31.63	59.80*										
74	_87.83*_	23.96	51.29*										
75	_78.30*_	16.21	42.60*										
76	_66.24*_	08.11*	33.45*										
77		199.85*	24.95*										
78		90.84*	15.69*										
79			06.33										
80			095.60*										

§ 5. Perturbations

1. Introduction

All the upper vibrational levels are perturbed: the lower are unperturbed. The perturbations were detected by forming the expressions:

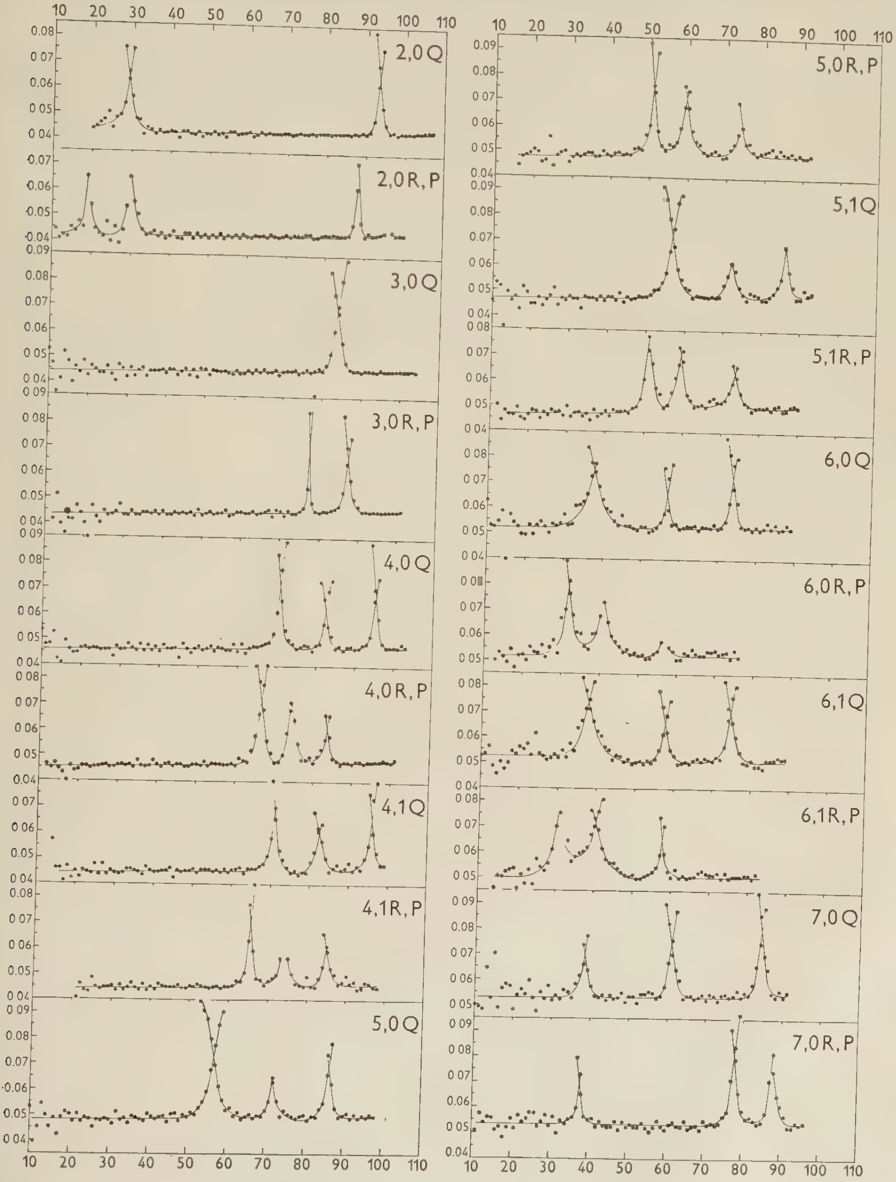

Fig. 1. $\frac{[Q(J-1)-Q(J)]}{2J}$ and $\frac{[R(J-2)-R(J-1)+P(J)-P(J+1)]}{4J}$ plotted against J.

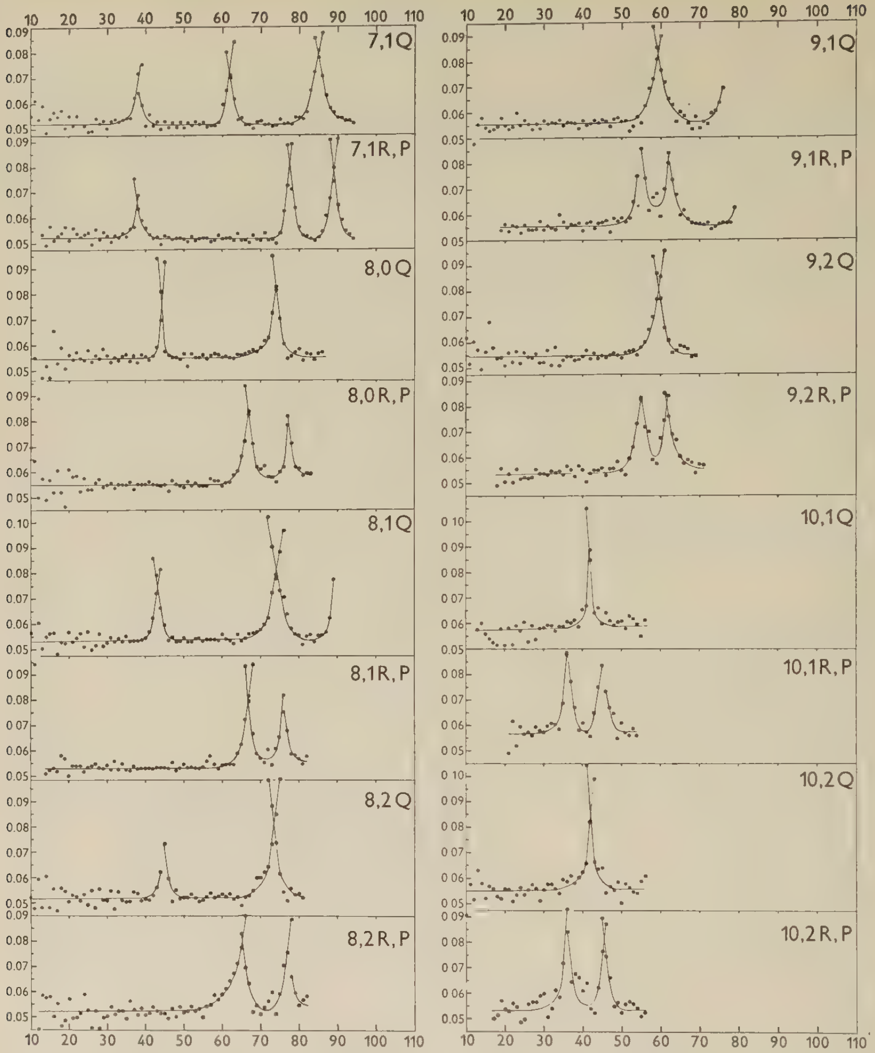

Fig. 2. $\frac{[Q(J-1)-Q(J)]}{2J}$ and $\frac{[R(J-2)-R(J-1)+P(J)-P(J+1)]}{4J}$ plotted against J.

$$\frac{Q(J-1)-Q(J)}{2J}=B''-B'-2J^2(D''-D'),\tag{1}$$

$$\frac{R(J-2)-R(J-1)+P(J)-P(J+1)}{4J}=B''-B'+6D''-2J^2(D''-D')\tag{2}$$

and plotting them against J (Figs. 1 and 2).

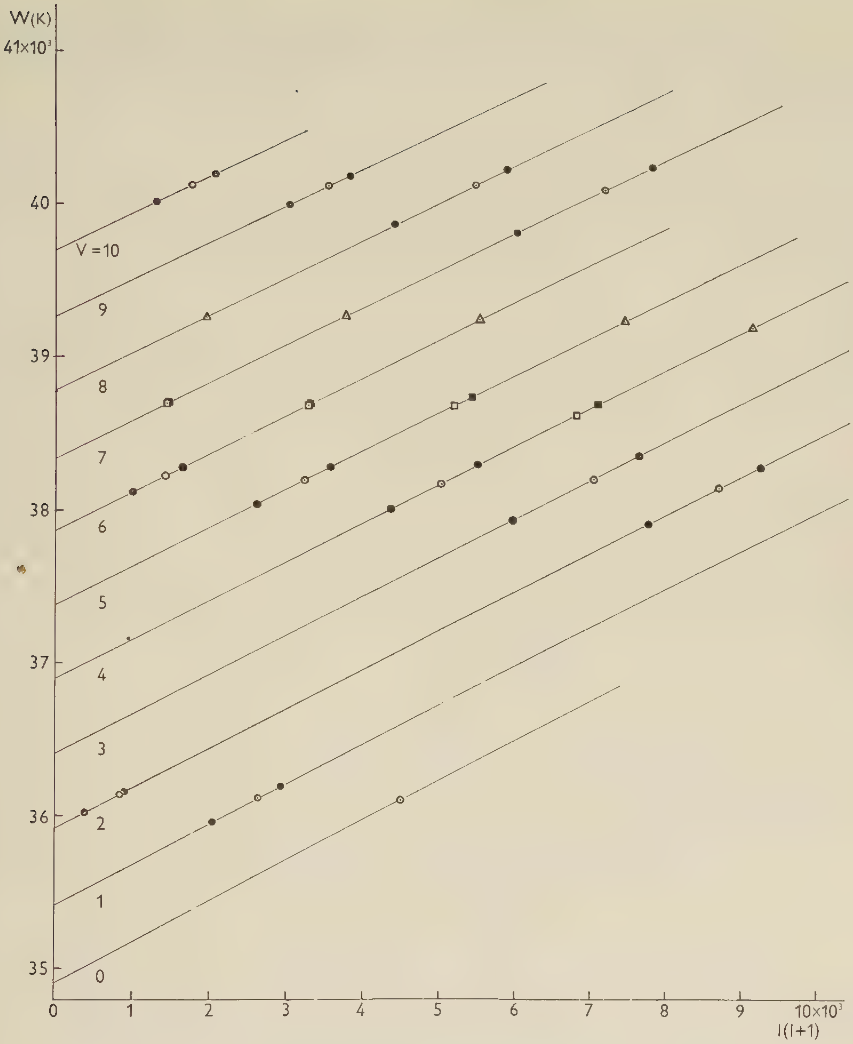

Fig. 3. Summary of the perturbations; term values plotted against $J(J+1)$.

Three perturbing states have now been investigated. They are called *e*, *F* and *I* in analogy with the CO molecule. As mentioned in our previous paper, *e* is a $^3\Sigma$ state and the *F* state a $^1\Pi$ or $^1\Delta$. The *I* state now discovered seems to be a $^1\Sigma$ state. The interaction is only found in the *Q* branch. In Fig. 3 the information about the perturbations is summarized. The figure shows the upper vibrational levels in a plot against $J(J+1)$. For the $^3\Sigma^-$ $^1\Pi$ interaction the positions where the perturbations culminate are marked, with a ⊙ when in the *Q* branch, and with a ● when the *R* and *P* branches. The $^1\Pi$ or $^1\Delta$ interaction with the $^1\Pi$ is indicated with a □ when in the *Q* branch, and with a ■ when in the *R* and *P* branches. Finally, the $^1\Sigma ^1\Pi$ interaction is marked with a △.

The more extra lines that are found, the better the determination of the B values of the perturbing state will be. The method is given by KOVÁCS (KOVÁCS 1937 and 1951).

2. Determination of constants

According to the method mentioned above, it is possible to determine the B and C values of the perturbing state, if extra lines are found at least at two consecutive J values. Extra lines have been found at almost every perturbation.

(a) The *e* ($^3\Sigma^-$) state

The treatment of such a perturbation is given by KOVÁCS (1951). The term values of a $^3\Sigma$ state are

$$\left.\begin{aligned} F_{J-1} &= C_{{}^3\Sigma} + B_{{}^3\Sigma}\,(J-1)\,J \\ F_J &= C_{{}^3\Sigma} + B_{{}^3\Sigma}\,J\,(J+1) \\ F_{J+1} &= C_{{}^3\Sigma} + B_{{}^3\Sigma}\,(J+1)\,(J+2) \end{aligned}\right\}. \tag{3}$$

The middle component will therefore be treated in the same way as in the case of a singlet-singlet interaction, i.e. the ordinate of an intersection point in Fig. 2 has the value

$$\frac{f_1+f_2}{2} = \tfrac{1}{2}\,(B_s + B') - B''$$

[$B_s = B_s(Q)$ when from the Q branch, $B_s = B_s(P)$ when in the R and P branches].

We have then $B_{{}^3\Sigma} = B_s(Q)$.

For the components

$$\left.\begin{aligned} B_{{}^3\Sigma} &= \frac{J}{J-1}\,B_s\,(P) \qquad (K = J-1) \\ B_{{}^3\Sigma} &= \frac{J}{J+1}\,B_s\,(P) \qquad (K = J+1) \end{aligned}\right\} \tag{4}$$

(where the $B_s(P)$ values are thus taken from the R and P branches).

For a singlet-singlet interaction the C values (the separation between the perturbed and the perturbing states at $J=0$) are calculated from

$$C_s(Q) = -2\,\sigma_0 + B' - \tfrac{1}{2}\,\{(J-1)\,[Q\,(J) + Q'(J)] - (J+1)\,[Q\,(J-1) + Q'(J-1)]\} \tag{5}$$

if the perturbation is found in the Q branch and from

$$\begin{aligned} C_s(P) = -2\,\sigma_0 + 2B'' + B' - \tfrac{1}{4}\,\{&(J-1)\,[P\,(J+1) + P'(J+1) + R\,(J-1) + R'(J-1)] - \\ &- (J+1)\,[P\,(J) + P'(J) + R\,(J-2) + R'(J-2)]\} \end{aligned} \tag{6}$$

if the perturbation is observed in the R and P branches.

For $C_s(Q)$ an approximate value is given by

$$C_s(Q) = B'(J^{*2} - 1) - B_s J^{*2} \qquad \text{(KOVÁCS 1937).} \tag{7}$$

J^* is J value where the curves in Figs. 1 and 2 cut each other. It is connected with J_0, the J value where the perturbation culminates, by the simple relation $J^* \sim J_0 + \frac{1}{2}$.

Now KOVÁCS (1951) has shown that $C_{^3\Sigma}$ can ce calculated in the following way

$$\left.\begin{aligned} C_{^3\Sigma} &= C_s(P) - B_s(P)\,J \qquad (\text{for } K = J+1) \\ C_{^3\Sigma} &= C_s(Q) \\ C_{^3\Sigma} &= C_s(P) + B_s(P)\,J \qquad (\text{for } K = J+1) \end{aligned}\right\} \qquad (8)$$

where $C_s(P)$ and $C_s(Q)$ are taken from (5) and (6) above.

The results of the calculation are given in Table 6. The $B_{^3\Sigma}$ (obs) values are means of the observed values (the number of observed values is given in brackets). The $B_{^3\Sigma}$(calc) are from the formula $B_{e+v} = 0.221_6 - 0.002_9\, v$, where B_e (for $v=0$) applies to the interaction with the $D\ {}^1\Pi$ level with $v'=0$.

The $C_{^3\Sigma}$ (a) values are means of the values calculated from the equations (5), (6) and (8) (the number of calculations is given in brackets). The $C_{^3\Sigma}$ (b) values are from the equation (7).

The values of $C_{^3\Sigma} + \sigma_0$ (means) are also given in Table 6.

Table 6. Summary of the *e–D* perturbations.

v_s	J^*			$B_{^3\Sigma}$ (obs)	$B_{^3\Sigma}$ (calc)	$C_{^3\Sigma}$ (a)	$C_{^3\Sigma}$ (b)	$C_{^3\Sigma} + \sigma_0$	Band
	RP	*Q*	*RP*						
$e+2$	19.5	28.9	30	0.214_9 (3)	0.215_9	38.4 (3)	38.3	35 955.2	2,0
$e+3$	88	93.2	93	213_4 (4)	213_1	401.4 (4)	414.1	36 320.8	2,0
$e+4$	77.2	83.8	87.3	210_2 (10)	210_2	329.7 (10)	331.7	36 743.6	3,0
$e+5$	66.0	70.8	74.1	207_5 (12)	207_4	239.2 (12)	247.4	37 143.7	4,0 4,1
$e+6$	50.9	56.7	59.6	204_6 (21)	204_5	156.6 (21)	160.8	37 545.4	5,0 5,1
$e+7$	31.6	37.6	40.4	202_4 (13)	201_7	69.4 (13)	71.4	37 933.6	6,0 6,1
$e+8$					198_8				
$e+9$	77.5	84.7	88.3	195_1 (15)	196_0	380.6 (15)	389.3	38 723.0	7,0 7,1
$e+10$	66.3	73.9	76.6	192_9 (21)	193_1	278.0 (20)	300.1	39 086.7	8,0 8,1 8,2
$e+11$	55	59.4	61.8	190_9 (10)	190_3	164.0 (11)	196.3	39 436.2	9,1 9,2
$e+12$	36.0	41.9	45.3	188_7 (9)	187_4	87.9 (9)	98.8	39 812.4	10,1 10,2

The vibrational constants are $\omega_e' \geqq 407._2$ $\omega_e' x_e' = 1.7_7$.

(b) The *F* (${}^1\Pi$ or ${}^1\Delta$) state

In our previous paper (LAGERQVIST, NILHEDEN and BARROW 1952) this state is named *f* but as it is probably a singlet one, we here prefer *F*. Compare also CO and SiO (see for example LAGERQVIST and UHLER 1952).

This perturbation is caused by the interaction between the $D\ {}^1\Pi$ levels and a ${}^1\Pi$ or ${}^1\Delta$ state. It is observed both in the Q branch at one J value and in the R and P branches at a J value which is somewhat larger than the one in the Q branch. The perturbation is observed in the levels with $v'=7$, 6, 5, and 4. Fortunately, however, the perturbation is not present in the level with $v'=3$, a fact that can be maintained with great certainty since, at the part of the 3,0 band where it would be situated, the lines are very distinct and separate.

This fact means that the interaction in the $D\,{}^1\Pi$ level with $v'=4$ is the level in the perturbing F state with $v_s=0$.

The constants can be derived in about the same way as in the case of the e (${}^3\Sigma^-$) state. The B values (here called B_{1_Π}) are calculated from

$$\frac{f_1+f_2}{2}=\tfrac{1}{2}(B_{1_\Pi}+B')-B''$$

where the B' belong to the upper and the B'' to the lower levels of the perturbed $D\,({}^1\Pi)$ state. There is no difference in the calculation whether the values come from the Q branch or from the R and P branches.

As regards the C values, $C_s(Q)$ and $C_s(P)$ are determined from the equations (5) and (6), whereupon C_{1_Π} can be taken from the formulas

$$\left.\begin{aligned} C_{1_\Pi}&=C_s\,(Q)+B_{1_\Pi}\\ C_{1_\Pi}&=C_s\,(P)+B_{1_\Pi}\end{aligned}\right\}. \qquad (10)$$

At every perturbation extra lines have been found.

A summary of the calculation is given in Table 7. The calculated B_{1_Π}(calc) values are from the formula

$$B_v=0.226_9-0.002_8\,(v+\tfrac{1}{2})$$

(number of observed values in brackets).

As before the C_{1_Π}(a) values are from the equations (5), (6), and (10) and the C_{1_Π}(b) from the approximate formula (7).

In Table 7 the means of the $C_{1_\Pi}+\sigma_0$ values are also given.

Table 7. Summary of the *F–D* perturbations.

v_s	J^*		B_{1_Π} (obs)	B_{1_Π} (calc)	C_{1_Π} (a)	C_{1_Π} (b)	$C_{1_\Pi}+\sigma_0$	Band
	RP	*Q*						
—	—	—	—	—	—	—	—	3,0
0	84.1	82.4	0.225_4 (11)	0.225_5	210.4 (11)	212.3	37 113.7	4,0 4,1
1	73.6	72.0	223_0 (5)	223_0	165.5 (5)	164.6	37 551.6	5,0 5,1
2	57.3	57.1	219_6 (9)	220_0	106.9 (8)	105.4	37 962.8	6,0 6,1
3	37.8	37.9	217_2 (8)	217_2	44.2 (8)	47.3	38 385.8	7,0 7,1

From Table 7 we obtain

$$\omega_e'=439._9 \qquad \omega_e'x_e'=4._0$$

and thus

$$r_e=2.2_3\ \text{Å}.$$

From Kratzer's relation $\left(D=\dfrac{4\,B_e^3}{\omega_e^2}\right)$ we obtain $D'=2.4_1\cdot10^{-7}$.

(c) The I ($^1\Sigma$) state

This perturbation is only present in the Q branch and must therefore be caused by a $^1\Sigma$ state. The interaction is observed in the $D\ ^1\Pi$ levels with $v'=8$, 7, 6, 5, and 4. In the level with $v'=3$, it is impossible to determine if the interaction is present or not, because at this point the 3,0 band is overlapped by the beginning of the 2,0 band. However, it may well be present, but a lower level than the one now discussed does not perturb. The conclusion is made because the point in the 3,0 band, where the perturbation would be situated, can be determined approximately by extrapolation and by using the slope-method (LAGERQVIST-UHLER 1952). Around this point ($J=38$) the $D\ ^1\Pi$ level with $v'=3$ does not seem to be disturbed.

The B values are found in the same way as for the other states

$$\frac{f_1+f_2}{2}=\tfrac{1}{2}(B_{1_\Sigma}+B')-B''$$

and

$$C_{1_\Sigma}=C_s\,(Q)$$

where $C_s\,(Q)$ is to be taken from equation (5).

A summary is given in Table 8. The calculated B_{1_Σ} (calc) values are from

$$B_{i+v}=0.213_3-0.001_8\ v$$

where B_i holds for the perturbation in the $D\ ^1\Pi$ level with $v'=4$. The C_{1_Σ}(a) values and the C_{1_Σ} (b) are calculated as before.

Table 8. Summary of the *I–D* perturbations.

v_s	J^*		B_{1_Σ} (obs)	B_{1_Σ} (calc)	C_{1_Σ} (a)	C_{1_Σ} (b)	$C_{1_\Sigma}+\sigma_0$	Band
	RP	Q						
i	—	95.5	0.213_0 (6)	0.213_3	384.7 (6)	396.5	37 290.2	4,0 4,1
$i+1$	—	86.2	211_5 (5)	211_5	297.0 (3)	320.0	37 706.9	5,0 5,1
$i+2$	—	74.2	209_9 (8)	209_7	203.0 (8)	234.9	38 073.4	6,0 6,1
$i+3$	—	61.3	207_2 (7)	207_9	153.3 (7)	159.1	38 495.9	7,0 7,1
$i+4$	—	44.0	205_9 (6)	206_0	80.2 (6)	81.3	38 886.1	8,0 8,1 8,2

In Table 8 the means of the $C_{1_\Sigma}+\sigma_0$ are also given. The vibrational constants are

$$\omega_e' \geqq 404._9 \quad \omega_e' x_e' = 1.1_8.$$

§ 6. Conclusions

A new comparison with CO and SiO is postponed until the fourth perturbation mentioned above and the rotational analysis of the E–X system of SiO has been carried out. (The analysis of the E–X system has begun.) The new perturbing $I\ ^1\Sigma$ state has been found in CO (SCHMID and GERÖ 1937) and in SiO (LAGERQVIST and UHLER 1952).

ACKNOWLEDGEMENTS

I take the opportunity of recording my thanks to Professor E. HULTHÉN for his keen and encouraging interest in my work and to Dr. A. LAGERQVIST for his great help and for valuable discussions.

Physics Department, University of Stockholm, February 1955.

REFERENCES

LAGERQVIST, A., NILHEDEN, G., and BARROW R. F., 1952. Proc. Phys. Soc. *A 65*, 419.
VAGO, E. E. and BARROW, R. F., 1946. Proc. Phys. Soc. *58*, 538.
LAGERQVIST, A., LIND, E., and BARROW, R. F., 1950. Proc. Phys. Soc. *A 63*, 1132.
BARROW, R. F., 1946. Proc. Phys. Soc. *58*, 606.
KOVÁCS, I., 1937. Z. Phys. *106*, 431.
KOVÁCS, I., 1951. Acta Phys. Hung. *1*, 97.
LAGERQVIST, A. and UHLER, U., 1952. Ark. Fys. *6*, 95.
SCHMID, R. and GERÖ, L., 1937. Z. Phys. *106*, 205.
HERZBERG, G., 1950. Molecular Spectra and Molecular Structure: I. Spectra of Diatomic Molecules. New York: van Nostrand.
M.I.T. Wavelength Tables, 1939. London: Chapman and Hall.

Tryckt den 9 september 1955

Uppsala 1955. Almqvist & Wiksells Boktryckeri AB

ARKIV FÖR FYSIK Band 10 nr 3

Communicated 27 April 1955 by Carl Benedicks

On the characteristic of the weakening effect

By Mizuho Sato

With 3 figures in the text

In connection with Benedicks' idea concerning the weakening effect on solid bodies due to wetting by liquids, the characteristic of this remarkable effect is discussed, assuming that fracture should occur by consuming the strain energy stored in Taylor's elementary prism for fracture.

In the previous paper [1] some experimental data on the wetting effect have briefly been communicated by Benedicks, showing that the weakening effect on paraffin and waxes can be represented by a curve composed of three parts, the first of which is a straight line (A) and the second is a curve (B) bent upwards while the third is a horizontal line (C), when the quantity δ proportional to the bending tensile strength and the surface tension γ of the wetting liquids are taken along the ordinate and the abscissa respectively, as shown in Fig. 1. It seems that this feature of the curve represents the characteristic of the weakening effect. In this note the reason why the curve should be divided into these three parts will be considered together with the dimensional independence of the effect—which has not yet been discussed in the previous paper.

As well known, the linear relationship such as (A) in Fig. 1 has experimentally been confirmed by Benedicks [2] for sugar, gypsum, marble, glass, steel and other brittle solids. In the previous paper of the present author, however, there were not sufficient plots to be used for confirming the linear relationship in the cases with paraffin and waxes because of lacking of liquids whose surface tensions are considerably smaller than that of methanol. Therefore, the author has tried with Kajima and Fujita to trace plainly such a line with Almond oil stone at 14°C using methanol, spindle oil, 10 per cent methanol, glycerine, distilled water and aqueous solutions of caustic soda, in order to verify the linear relationship. Data obtained are plotted in Fig. 2. The cross-section of the specimen was not a rectangle but a flat ellipse with major and minor axes of 9.5 mm and 3.0 mm respectively. Since the surface was somewhat oily, it was scratched with emery paper to increase the wettability. The specimens were left in the liquids for 5 minutes before the tests. The duration of loading was *c.* 3 sec. At least, 6–10 specimens in each of dry and wet states were tried. As seen in the figure, the relation between the bending tensile strength and the surface tension of wetting liquids is linear so far as the latter is smaller than 86.0 dyne/cm of 20 per cent solution of caustic soda, showing a similar straight line relationship as that observed by Benedicks for several other materials described above.

To illustrate such a weakening effect, Benedicks [2, 3] has proposed a theory of lines of force. According to him, a part of lines of force emanating from atoms on the solid surface is so bounded by atoms of wetting liquid that the mutual attraction between the solid atoms along the solid surface must decrease if the solid is wetted by the liquid. In intimate connection with this idea, the author wishes to consider the mechanism of fracture in the presence of a surrounding medium on the basis of TAYLOR's theory [4] of fracture.

If a specimen is stressed by bending as in Fig. 3, it is obvious that its lowest layer MN must be stretched in the greatest amount, and usually a crack starts at the lowest point R. As soon as this crack is formed, the surrounding liquid permeates it immediately by capillarity wetting its boundaries. This is also the case for natural flaws on the surface, whose existence is assumed in the modern theory of real solids. Such a crack or flaw is at first infinitesimally small, but under the successively increasing bending it grows up to finite length across the specimen layer by layer, until the fracture results. Let the extremity of this infinitesimally small crack be V, then the stresses concentrate at V storing strain energy. It may be supposed, therefore, that this crack goes a certain depth forward in the interior of the specimen, if this strain energy is consumed to be the work done in promoting the crack. From this point of view, therefore, the diminution of the strain energy is equal to the increasing amount of surface energy attributed to the new surfaces created by the proceeding of the crack.

We are now in the position to consider where the strain energy is stored, which converts its form into the surface energy. Concerning the relation between the breaking stress and the surface energy, the author wishes to suppose with TAYLOR that the elementary process in fracture consists in the slow elongation of the strongest bonds in an elementary or unit rectangular prism which may be regarded as made up of E/f layers of thickness λ_0, where E and f are YOUNG's modulus and the breaking stress respectively. According to TAYLOR, λ_0 is a characteristic elongation of the strongest atomic bond in order to effect fracture, as called by him under the name of the critical fracture distance which is constant for each solid regardless of the stress. In this mechanism of fracture, it has been assumed that the characteristic elongations are distributed in a statistical way among all the bonds whose total length is

$$r=\lambda_0 E/f,$$

but because of extremely rapid thermal vibration, the whole λ_0 soon concentrates on some one bond and then fracture occurs. On this basis, he has developed a theory of fracture, assuming that the product $\lambda_0 E$ measures the energy per unit area which is released when fracture occurs. Instead of using $\lambda_0 E$, it is convenient to take the product rf, in order to formulate the change of breaking stress due to wetting by liquids.

In his theory, TAYLOR has treated the case with glass, assuming that the wetting does not affect the modulus of elasticity on the basis of ANDEREGG's experimental data [5].[1] If this assumption is true, the length of the elementary prism is inversely proportional to the breaking stress because of constancy of E and λ_0. Against this, it is natural to consider that the modulus should be affected by water, when the bending or tensile test of glass is carried out in its wet state. In fact, BENEDICKS [6] has found experimentally that the elongation of a quartz fibre under static load is

---

[1] On this occasion, the author expresses his cordial thanks to Prof. BENEDICKS for his kindness of sending of a photocopy of ANDEREGG's original paper, which is unfortunately lacking in our library.

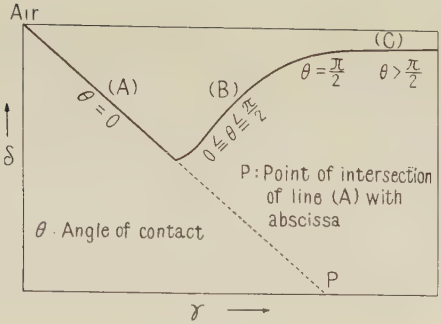

Fig. 1.

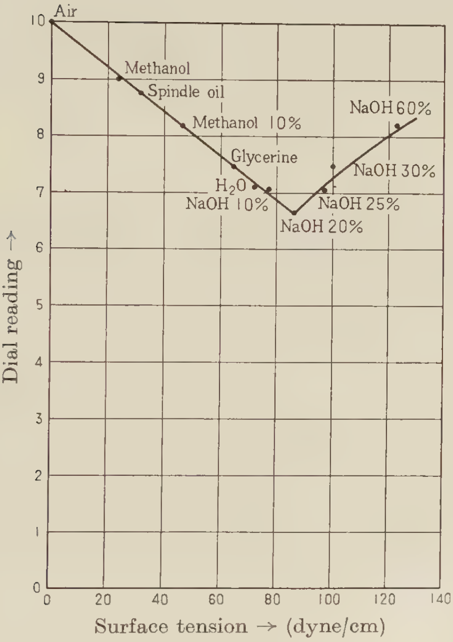

Fig. 2.

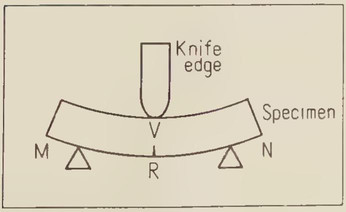

Fig. 3.

considerably increased by wetting, a phenomenon called by him liquostriction. This effect suggests that the modulus of glass will be decreased by the wetting of water, as seen in breaking stresses of glass and similar brittle solids. By this suggestion the author [7] has carried out an experiment to find any effect, observing whether the modulus of glass would be lowered by wetting of water or not. According to this experiment, the modulus was affected by the wetting as much as observed in the breaking stress, so that the ratio of the former to the latter seems to be unchanged in spite of the wetting, so long as the duration of loading in each test under dry and wet conditions is kept constant. Consequently, one may assume here that the length of the elementary prism will not be changed by the wetting in an equal duration of loading because of the constancy of the critical fracture distance.

Now, returning to the subject, the relation between the breaking stress and the surface energy will be formulated. As stated above, the energy $r f$ is no other than the strain energy w stored in the elementary prism with unit cross-sectional area at V in Fig. 3. Supposing that the crack created by the breaking stress proceeds perpendicularly layer by layer in depth l per unit width, we express the strain energy W converted into work done by creating new surfaces in the form of

$$W = w\,l = r\,f\,l.$$

Since r is assumed to be a constant of the specimen in dry and wet states for an equal duration of loading, we write the relation to be held in consuming of an equal amount of strain energy as follows:

$$f\,l = f'\,l' \quad \text{or} \quad \frac{l}{l'} = \frac{f'}{f}, \tag{1}$$

where f' and l' are f and l in wet state respectively. This relation expresses that the depth of crack is inversely proportional to the breaking stress. Consequently, the depth of crack must increase on account of the wetting by which the breaking stress is lowered, fracture occurring more easily than in dry state.

In the wet state of a solid, it may be assumed that the work done by the breaking all goes into new surfaces as an interfacial tension γ_{sl} between the solid and the wetting liquid, that is,

$$r\,f' = 2\,\gamma_{sl}, \quad \gamma_{sl} = \gamma_s - \gamma_l \cos\theta, \tag{2}$$

where γ_s and γ_l are the surface tensions of the solid and the liquid respectively, while θ is the angle of contact between them. As seen from this equation, the breaking stress of a given solid is expressed to be a function of the surface tension of wetting liquid and the angle of contact. Hence ve have the relation

$$\frac{\partial f'}{\partial \gamma_l} = -\frac{2}{r} \cos\theta,$$

showing that the breaking stress should be lowered due to wetting by liquids, so far as the angle of contact is smaller than $\pi/2$. It is obvious that the lowering for $\theta = 0$ is the greatest.

According to experiments, in the region of (A) shown in Fig. 1, the wettability of the specimen with wetting liquids is so good that the angle of contact between them can be assumed to be zero. In this case the relation is

$$f' = \frac{2}{r}(\gamma_s - \gamma_l), \tag{3}$$

implying that the breaking stress is linearly lowered with increasing surface tensions of wetting liquids.

If this test be carried out in dry state, the above equation becomes

$$f = \frac{2}{r}\gamma_s \tag{4}$$

putting $\gamma_l = 0$, which is nothing but the formula given by TAYLOR [4], if the product rf is replaced by the product of the modulus with the critical fracture distance.

Eliminating r between the above two equations, we have

$$\gamma_s = -\gamma_l \Big/ \frac{\Delta f}{f}, \tag{5}$$

where $\Delta f = f' - f$ is always negative in the weakening effect, and so γ_s is calculated to be positive because of negative sign on the right hand side; γ_s can be expressed as the ratio of γ_l to $-\Delta f/f$ which represents the weakening effect due to wetting by liquids. This is the formula to be used for determining the surface tension or the specific surface energy of glass and similar brittle solids. As seen from the above, though this formula has been derived by taking TAYLOR's theory of fracture into consideration, such an idea for determining the surface tension of solids is identical with that proposed by BENEDICKS [2, 3] in his theory applying lines of force, because in both theories the breaking stress is assumed to be a linear function of the surface tension of a solid. This identity will again be discussed on page 43.

Let us insert here an applicable example of the above formula, taking the experimental data of Almond oil stone given in Fig. 2. According to them, the values of $-\Delta f/f$ in methanol, spindle oil, 10 per cent methanol, glycerine, distilled water, 10 per cent and 20 per cent solutions of caustic soda are 10.0, 12.0, 18.0, 25.0, 28.0, 29.0 and 33.0 per cent respectively. Taking the surface tensions of these wetting liquids to be 22.7, 32.0, 47.0, 63.4, 72.5, 75.0 and 86.0 dyne/cm in order at room temperature of 14° C, we compute the surface tension of the specimen to be 227, 266, 261, 253, 259, 258 and 260 dyne/cm respectively, the mean value of which gives 254.9 dyne/cm. Thus, the required surface tension will be *c.* 255 dyne/cm at 14° C.

Instead of the above calculation, the surface tension of the specimen can easily be estimated by means of graphical representation, extrapolating the linear relationship shown by (A) up to the axis of surface tension to find the abscissa of the point of intersection, such as P in Fig. 1. As well known, this was initiated by BENEDICKS [2, 3] on the basis of his theory of lines of force, assuming that the breaking stress should actually vanish, if the specimen was wetted by a liquid whose surface tension is equal to that of the specimen. This is the same as the result deduced from (3) because of a definite length of r.

However it may be, if the surface tension of a liquid be above a certain value, the wettability becomes poor increasing the angle of contact. As seen from (2), the interfacial tension hereby increases with increasing surface tensions of wetting liquids. This is the reason why the breaking stress follows along an ascending curve, thus forming the second part (B) of the curve as shown in Fig. 1 or 2. This feature of the curve was already confirmed by BENEDICKS [2] in glass, marble and sugar II, and also by the author [1] in paraffin, beeswax and Japan wax. It is, however, not easy to find out the end point of this part, because the test near this point is usually accompanied by experimental difficulties, such as scarcity of liquids whose surface tensions are suitable for this test; besides, the effect of moisture or vapour in the vicinity of this point is relatively large.

Supposing that the angle of contact in the region of (B) changes from 0 to $\pi/2$, the end point is to be determined to be the position where the angle of contact is equal to $\pi/2$. At this point the interfacial tensions is equal to the surface tension of the specimen, showing that the breaking stress is independent of the surface tension of surrounding liquids, so far as the angle of contact is equal to $\pi/2$. By this reason, the curve (B) ascends towards the height corresponding to the breaking stress in dry condition. In our experiments in paraffin and waxes, it was preliminarily expected that the end point of the curve (B) should take the height as high as the level of the dry strength indicating the recovery of the weakening.

Against this expectation, it was actually observed that the end point was always lower than the level of the dry strength as shown in Figs. 1, 2 and 3, showing that the recovery is obstructed by the presence of surrounding liquid, even though the wettability is extremely poor. This would be caused by the presence of the vapour of surrounding liquid or moisture in air. In fact, BAKER and PRESTON [8] pointed out that the breaking stress of glass should decrease considerably by the presence of moisture in comparison with its vacuum strength. According to them, the strength of glass is greatest in the highest vacuum, the strength of the glass when tested in the 0.05 micron vacuum being greater than the strength when the glass is tested wet at atmospheric pressure by a factor of 2.04. It is, therefore, reasonable that the vacuum strength should be called dry strength. As described already, since in our experiment all tests in dry condition were carried out in the presence of air, it is natural to see that our dry strength is somewhat smaller than the vacuum strength. However it may be, it is sure that our dry strength is greater than the strength observed in the presence of surrounding liquid whose angle of contact with the specimen is equal to $\pi/2$, because the influence of moisture or liquid vapour due to surrounding liquid is greater than that of moisture contained in air. In our experiment each specimen was taken out from a desiccator[1] containing $CaCl_2$ and the test was carried out as soon as possible in order to reduce the influence of moisture, even though the moistening be inevitable. At all events, since the influence of vapour or moisture near the end point of the curve (B) is relatively larger than in dry test, the end point is situated below the level of dry strength.

If the angle of contact be over $\pi/2$, $\cos\theta$ takes negative sign, and so the interfacial tension becomes larger than the surface tension of the specimen. The breaking stress, therefore, would be larger than the dry strength showing a strengthening effect, if the boundary of the crack were covered by a liquid whose angle of contact with the specimen is larger than $\pi/2$. Against this expectation, in the cases with paraffin and waxes their breaking stresses were always lower than their dry strengths respectively, even though the surface tension of surrounding liquids is extremely large such as mercury. As reported in the previous paper, the wetting effects on paraffin due to distilled water and mercury were observed to be −18 and −19 per cent respectively, showing that they are approximately the same. This fact suggests that the wetting effect in the region of $\theta > \pi/2$ would be caused by vapour or moisture on the surface of the surrounding liquids. In fact, it was observed that the surface of the specimen is scarcely wetted by liquids whose angle of contact is larger than $\pi/2$ because of their extremely poor wettability, thus causing the third part (C) of the curve to be a horizontal line as shown in Fig. 1. This was confirmed in paraffin and waxes as reported in the previous paper.

---

[1] On this occasion, the author wishes to express his cordial thanks to Prof. BENEDICKS for his kind letter in which an effective absorbent was suggested.

Finally, a remark on the influence of dimensional difference in specimens will be added, taking our result obtained in paraffin into consideration. As seen in Figs. 4 and 5 of the previous paper, the weakening effect does not depend either on thickness or on width since the lines converged to a certain point on the abscissa. Concerning the effect of moisture on the strength of glass, BAKER and PRESTON [8] have proposed a simple rule, that moisture affects the strength by a ratio. Our result of observation supports this rule, showing that not only moisture but also surrounding liquid lowers the strength of paraffin by a certain ratio below the dry strength. In determining the weakening effect, specimens need not be the same in dimensions. In his paper on the wetting effect, BENEDICKS [3] has made graphs taking the bending tensile strength referred to dry state = 100 along the ordinate. This representation means nothing but the fact that the effect is independent of width and thickness of specimen, as determined directly by the author in the presence of wetting liquid, verifying the rule proposed by BAKER and PRESTON.

Let us consider the reason why this rule holds in the wetting effect. As described on page 38, the crack created in the lowest layer by bending causes the fracture of specimen, replacing its surface tension on the boundary of this crack by an interfacial tension between it and a surrounding liquid. Even if the work done by creating the first infinitesimal crack be dependent of the dimension of specimen, the essential part in the weakening should be owed to the decrease of its surface tension due to wetting by liquid as mentioned above. Since this decrease is independent of the dimensional difference of the specimens, the same effect should result so long as each specimen in dry and wet tests is equal in dimensions. This seems rather to be a matter of course, because the effect $-\Delta f/f$ is expressed by a ratio of γ_l to γ_s, which is independent of the dimension of specimen, as formulated in (5) indicating the relation of proportionality of two similar triangles drawn in the $f\gamma$-diagram.

The above is an exposition of the characteristic in the weakening effect. For the study of the wetting effect in full, the case of strengthening should be gone into in detail.

In conclusion, the author wishes to express his hearty thanks to Prof. CARL BENEDICKS of Stockholm for his valuable suggestion.

REFERENCES

1. M. SATO, Ark. Fys., *9*, Nr. 19 (1955), 335.
2. C. BENEDICKS and G. RUBEN, Jernk. Ann. *129* (1945), 37.
   C. BENEDICKS and R. HÄRDÉN, Ark. Fys. *3*, Nr. 22 (1951), 407.
   C. BENEDICKS, Proc. Internat. Symp. React. Solids, Gothenburg (1952), 477.

3. C. Benedicks, Compt. rend. *232* (1951), 2435; *233* (1951), 409, 482.
4. N. W. Taylor, J. Appl. Phys. *18* (1947), 943.
5. F. O. Anderegg, Ind. Eng. Chem. *31* (1939), 290.
6. C. Benedicks and R. Härdén, Ark. Fys. *3*, Nr. 22 (1951), 407.
   C. Benedicks, Proc. Internat. Symp. React. Solids, Gothenburg (1952), 477.
7. M. Sato, Proc. Japan Acad. *30* (1954), 455.
8. T. C. Baker and F. W. Preston, J. Appl. Phys. *17* (1946), 179.

Tryckt den 9 september 1955

Uppsala 1955. Almqvist & Wiksells Boktryckeri AB

ARKIV FÖR FYSIK Band 10 nr 4

Communicated 27 April 1955 by Carl Benedicks

The wetting effect on quenched carbon steel within its elastic limit

By Mizuho Sato

With 1 figure in the text

The change in Young's modulus of a quenched carbon steel due to wetting by several liquids is studied experimentally. It is found that the modulus is lowered by a group of liquids, while the reverse is the case with another group. The order of magnitude of this change is the same as that observed by Benedicks in his bending tensile test.

Applying the experimental data obtained in the weakening effect for determining the surface tension of the specimen, it is found that the surface tension of this steel is *c.* 350 dyne/cm at 18–20°C which agrees fairly well with Benedicks' result of determination.

In his interesting paper [1] on the wetting effect, Benedicks has pointed out that the bending tensile strength of a quenched carbon steel should be affected by the surrounding medium, and found that the changes due to distilled water and kerosene are *c.* -21 and $+28$ per cent respectively. It is therefore required to investigate whether the same effects can also be observed within its elastic limit or not. For this purpose, the author has carried out an experiment for finding the change in its Young's modulus due to wetting by several liquids. The result is reported below.

In order to find the change in the modulus, a bending test has been tried in the presence of a surrounding medium, measuring the change of load by means of a U-tube manometer connected with the oil chamber of the tester described in the previous paper [2]. The experiment has been performed at a room temperature of 18–20° C, repeating the tests in each of dry and wet states at least 10–12 times. The specimen is cut from a saw blade in the form of a rectangular plate of the cross-section of 6.725×0.637 mm. It is spanned between two supports 26 mm apart and loaded to the amount of bending of 10×10^{-2} mm. Analysis of this specimen gave as its composition 1.33 per cent carbon, 0.17 per cent silicon and 0.27 per cent manganese.

If the amount of bending of the given specimen remains the same in dry and wet states, the change in the modulus can be expressed in terms of the change in manometer reading. Data obtained are given in the figure in which the manometer reading and the surface tension of wetting liquids are taken along the ordinate and the abscissa respectively. As seen from this figure, the modulus is lowered by a group of liquids such as methanol, paraffin oil, toluene, glycerine and distilled water, while the reverse is the case with another group such as kerosene, spindle oil and soy bean oil. The wetting effects due to distilled water and kerosene are determined to be

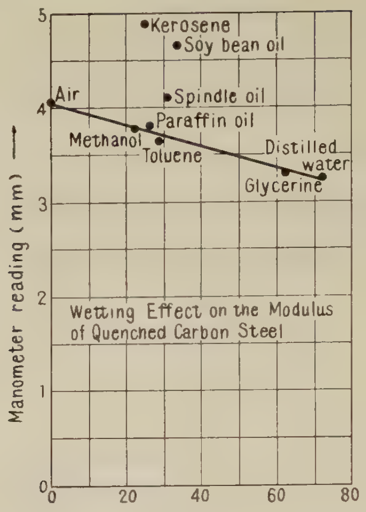

Fig. 1. Surface tension (dyne/cm)→.

c. −20 and +21 per cent respectively, showing a good agreement with the result obtained by BENEDICKS in his bending tensile test.

It is interesting to see that the above weakening effect has a regularity between the lowering of the modulus and the surface tension of wetting liquids as shown by a descending straight line. As for the origin of this effect, the author attributes the change in surface energy or tension of the specimen to the wetting by liquid. Since the wettability in the present case is excellent, the interfacial tension can be given by the difference of the surface tensions of the specimen and the wetting liquid, expressing that the larger the surface tension of the wetting liquid, the smaller the interfacial tension. For example, the interfacial tension between the specimen and distilled water is smaller than that in the state wetted by glycerine or methanol. Therefore, the work done in pushing down the specimen for giving a definite amount of bending should be lowered with increasing surface tension of the wetting liquids, as shown by a descending straight line drawn in the above figure.

Against this, there is no regular relation in the strengthening effect. In his explanation of the strengthening effect on the bending tensile strength due to wetting by kerosene and tar oil, BENEDICKS [1] considered that the strengthening might be caused by an increase of the interfacial tension, say in forming an adsorbed thin film on the solid surface. It is, however, natural to suppose that the surface tension of the specimen should also be decreased by the wetting of kerosene and tar oil. It seems, therefore, reasonable to consider some other factors to be applied for explaining the cause of this effect. In the same paper cited above, BENEDICKS remarked that other explanations might also be possible, if one considers the presence of surface fissures and their eventually increased cohesion when being filled by a wetting liquid. For real solids, the presence of surface fissures is allowable, but it is the essential point how to explain the increase of cohesion.

According to HARDY [3], in the boundary state of lubricant the chains of highly polarised molecules stretch through the lubricant from one solid to the other, showing that the total strength of all the chains of molecules in tension increases. So, if such lubricant permeates in a fissure of the lower surface of the solid, the chains of po- arised molecules may be stretched from one side of the fissure to the other side ttracting electrically along the chains, while the surface tension of its boundary hould be decreased by ANTONOFF's law. For the broadening of the fissure by means f bending, the former tends to resist it indicating the strengthening, while the atter shows the weakening. If the latter effect be overcome by the former one, the nodulus should be increased by the wetting.

The above consideration started from HARDY's point of view. It seems, however, nallowable to apply this idea to the present case immediately without examining he nature of the wetting liquids. At all events, as for the origin of the strengthening ffect, one is unfortunately not in a position as yet to establish a theory with certainty, ecause the phenomenon contains some important factors which are not clear at resent.[1] However that may be, it is interesting to note that the modulus of steel s affected by the presence of surrounding medium, indicating that this influence an be observed to have the same order of magnitude as in the case of its bending ensile strength.

The linear relationship observed in the weakening effect suggests that the surface ension γ_s of the specimen can be calculated by the following formula

$$\gamma_s = -\gamma_l \Big/ \frac{\Delta E}{E},$$

vhere γ_l is the surface tension of the wetting liquid and $\Delta E/E$ the relative change in he modulus E due to the wetting. Taking the manometer reading in dry condition, ve find the modulus of the specimen to be

$$E = 23.90 \times 10^{11}\ \text{dyne/cm}^2,$$

vhich seems to be of right order of magnitude, in comparison with the values 20.6–0.8 ton/mm² observed by BENEDICKS [4] for a carbon steel whose composition is .50 per cent carbon, 0.1–0.2 per cent silicon and 0.2–0.3 per cent manganese. In he following table our experimental data concerning the changes in the modulus ue to the wetting by methanol, glycerine and distilled water are given together vith the calculated values of the surface tension of the specimen.

Medium	Methanol	Glycerine	Distilled water
γ_l dyne/cm	22.7	62.5	72.0
$-\frac{\Delta E}{E} \times 10^2$	6.24	18.82	20.18
γ_s dyne/cm	363.8	332.1	356.7
Mean of γ_s	350.87 dyne/cm at 18–20°C		

---

[1] The fact that kerosene, spindle oil, soy bean oil and so on cause an increase of the strength Young's modulus) may depend on their power of penetration into even very fine fissures, ausing the appearance of additional cohesive forces as has been established by BENEDICKS nd EKELLUND-KAPPELER [Ark. Fys. *6*, Nr. 8 (1952), 73], added by C. B.

As seen from this table, the surface tension of our quenched carbon steel can be determined to be 350–351 dyne/cm at 18–20° C. According to BENEDICKS [1], the weakening effect on the bending tensile strength of his quenched carbon steel due to distilled water was -21 per cent as cited above. Consequently, if this datum is taken for $\gamma_l = 72.0$ dyne/cm, γ_s becomes 343 dyne/cm which is close to our result 350–351 dyne/cm determined here.

The above calculation for determining the surface tension of the specimen can be replaced by the graphical representation, extrapolating the linear relation between the lowering in the modulus and the surface tensions of the wetting liquids. The abscissa of the point of intersection of the straight line extended from the descending linear relation with the axis of surface tension is read to be *c.* 350 dyne/cm corresponding to the result of calculation. It is, however, inevitable that the result of calculation does not coincide exactly with that of graphical determination, because in the former the datum in dry state is assumed to be the standard by which the percentage change in the modulus due to wetting is computed, while in the latter all plots should be connected with a straight line by an interpolation supposing that the datum in the dry condition contains also an experimental error of the same order of magnitude as in the case of wet state. However that may be, it is interesting to see that the modulus of steel is lowered in the presence of a surrounding medium, showing that this lowering can be applied for determining the surface tension of a steel without destroying the specimen.

In conclusion, the author wishes to express his hearty thanks to Professor C. BENEDICKS of Stockholm for his valuable suggestion.

REFERENCES

1. C. BENEDICKS and R. HÄRDÉN, Ark. Fys. *3*, Nr. 22 (1951), 407.
2. M. SATO, Ark. Fys. *9*, Nr. 19 (1955), 335.
3. W. HARDY, Phil. Trans. A, *230* (1932), 1.
4. C. BENEDICKS, Recherches physiques et physico-chimiques sur l'acier au carbone, Thèse pour le Doctorat, Upsala (1904), 55. International Critical Table, *II* (1927), 516.

Tryckt den 9 september 1955

Uppsala 1955. Almqvist & Wiksells Boktryckeri AB

ARKIV FÖR FYSIK Band 10 nr 5

Communicated 13 April 1955 by G. BORELIUS and H. ALFVÉN

Paramagnetic susceptibility measurements on PdAg alloys

By EBBE KRONQVIST

With 5 figures in the text

Introduction

The magnetic susceptibility of PdAg alloys was first studied in this laboratory by SVENSSON [1], who measured the susceptibility at room temperature over the whole range of concentration. The present work contains measurements on Pd and three PdAg alloys with about 90, 80, and 70 atomic percent of Pd in the range from room temperature up to about 1000°K, mainly performed in 1948, as well as some measurements in 1952 on the same alloys after cold-working. During the time these measurements were being made an investigation on Pd and PdAg alloys in about the same range of temperature and concentration was published by WUCHER [2] as well as measurements at low temperatures by HOARE and MATTHEWS [3], and HOARE, MATTHEWS and WALLING [4].

The measurements

The alloy specimens used in the present work were made in 1937 by H. RUDBERG in connection with preliminary unpublished susceptibility measurements. They had the form of wires of about 12 cm length and a circular cross section of about 0.75 mm². The compositions of the samples were checked by resistance measurements. The magnetic susceptibility was measured with a magnetic balance described by GUSTAFSSON [5]. (In its present state the apparatus has been somewhat modified.) The susceptibilities were calculated per gram atom of the alloys. The apparatus was calibrated with a sample of pure Pd, for which the atomic susceptibility at 300°K was given the value 566×10^{-6} obtained from the work by GUSTAFSSON [5]. The measurements were performed with the specimens enclosed in evacuated tubes of quartz or Pyrex glass.

The results

The values of the paramagnetic atomic susceptibility χ_A for Pd and the alloys, obtained from the present measurements are given i Table 1.

In Fig. 1 the susceptibility χ_A has been plotted as a function of the content of Ag for some different temperatures. SVENSSON's and WUCHER's results, recalculated to the same χ_A value for Pd at 300°K as in the present determination by multiplying

Table 1.

(The figures above the vertical columns give the Pd concentrations of the alloys in at %.)

$T°K$	$\chi_A \times 10^6$			
	100	88.0	79.3	70.9
290	578	328	214.0	133.0
300	566	324	211.5	131.5
350	513.5	305	199.7	123.4
400	469	287.5	189.1	116.4
450	430.5	272.5	179.2	109.7
500	398.5	258.5	169.6	103.3
550	370.5	242.5	160.2	97.5
600	346	229.5	151.9	92.0
650	323.5	217.0	144.1	86.7
700	303.5	205.2	136.5	82.4
750	286	194.3	129.3	78.2
800	269	184.5	123.0	73.9
850	253	175.2	117.0	70.2
900	239.5	166.7	111.4	66.3
950	226.5	158.5	106.1	62.8
1000	215		101.0	

by the factors 0.980 and 1.018 respectively, have been inserted for comparison. The agreement between the different measurements seems to be satisfactory as far as the temperature variation of the susceptibilities is concerned. The rather considerable difference between the absolute values, which are about ten times the accuracy of the relative measurements, may be due to impurities or gases in the Pd. WUCHER has shown in a striking way how even very pure Pd specimens of different origins differ to a large extent [2], and the same experience has been reported by HOARE and MATTHEWS [3]. Fortunately for the understanding of paramagnetism, the temperature dependence of the susceptibility is more important than the absolute value.

Determination of the diamagnetic correction

In order to isolate the paramagnetic part of the susceptibility of the Pd ion, it is necessary to take into account the diamagnetism of both the Pd and the Ag atoms in the alloys. In several investigations on paramagnetism of alloys with a small content of the transition metal, no correction has been made for the diamagnetism of the transition metal itself. In the present case, however, this correction is important as the concentration of the transition metal is high and the paramagnetism of the alloys is rather weak.

In most cases it is very difficult to separate the diamagnetic part of the susceptibility for the transition metal atom from the measured paramagnetic susceptibility. In the case of AgPd alloys, however, it is possible to determine that the diamagnetism of the two components has about the same value. First a calculation using a method by SLATER and ANGUS [6] based on the electronic configuration $4d^{9.4}$ for the Pd ion gave the same result as the corresponding calculation for Ag. Further, experimental susceptibility determinations of the AgPd alloys on the Ag side, pre-

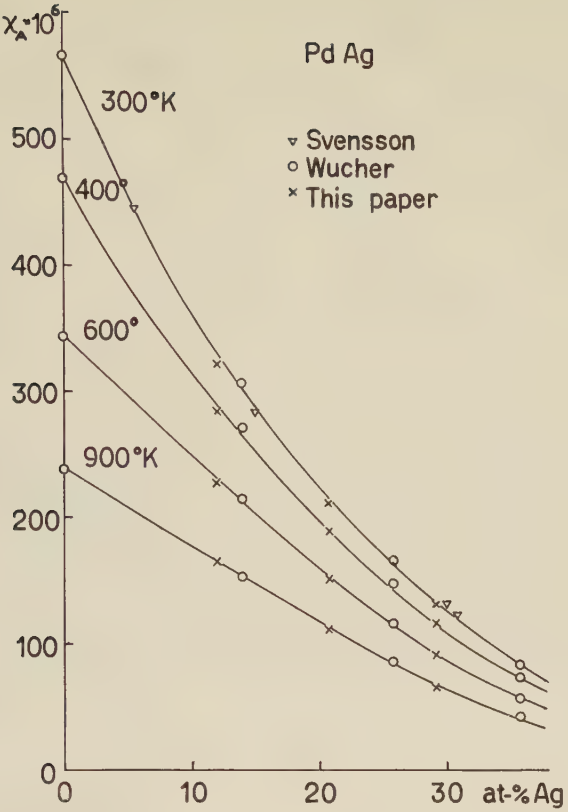

Fig. 1. Paramagnetic atom susceptibility of PdAg alloys as a function of the concentration of Ag at different temperatures.

viously performed by SVENSSON [1] and repeated by the author, show that the diamagnetic atomic susceptibility of Ag, -19×10^{-6}, is changed very little when small amounts of Pd are added to Ag. Linear extrapolation of the author's results from the Ag side to pure Pd gave the value -21×10^{-6} for the diamagnetic part of the susceptibility of Pd.

The influence of temperature on the diamagnetism of Ag and the Ag-rich AgPd alloys is comparatively small; the diamagnetism increased, according to measurements by the author, about 5 % from 300°K to 700°K. Thus it may be justifiable to use the same diamagnetic correction, -19×10^{-6}, for all the PdAg alloys in the whole temperature range. The paramagnetic part of the susceptibility for the Pd ion, χ_p, is then given by the equation

$$\chi_p = \chi_A + 19 \times 10^{-6}. \tag{1}$$

The temperature dependence of χ_p is shown in Fig. 2, where α/χ_p is plotted against the absolute temperature (α is the atomic fraction of Pd in the alloys). As can be seen all the curves bend, giving a successively increasing slope at increasing temperature.

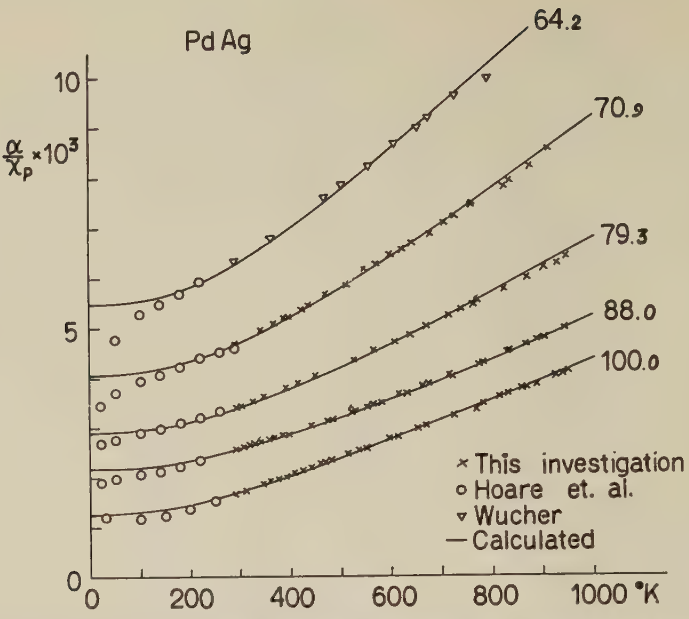

Fig. 2. The reciprocals of the atomic susceptibility per mole Pd as a function of the temperature. The fully drawn lines represent the susceptibility values, calculated from the collective electron theory (eq. (2)). The Pd concentrations in at % are marked on the curves.

Results compared with theories

There are two main approaches to the theoretical interpretation of magnetism in metals. First the well-known Curie-Weiss treatment, in which the atom ions are considered to be carriers of magnetic moments and the interchange interaction is represented by a "molecular field". The magnetic atomic moment is determined from the number of vacant electrons in the lowest unfilled shell and this number can be calculated, if it is assumed that the well-known quantum-mechanical formulae, which give so good agreement with experiments on metal ions, in salts and aqueous solutions, are also valid for metals. The Curie-Weiss treatment, originally developed entirely from an empirical point of view, has been given a firmer theoretical basis above all by HEISENBERG, who showed that the very strong interaction leading to ferromagnetism could be explained by quantum mechanics using the Heitler-London atomic model. On the whole the Curie Weiss theory seems to be a fairly good approach, especially for solid solutions with a low concentration of such paramagnetic transition metals as have a large number of vacant *d* electrons [7, 8]. WUCHER [2] has interpreted his results from paramagnetic measurements on PdAg alloys mainly with the Curie-Weiss treatment. He determined the value of the diamagnetic correction for the Pd ion, which was most consistent with Curie-Weiss' law. This value, -58×10^{-6}, is however quite incompatible with both theory and experiment, as has been shown previously in this paper. Even with this value Curie-Weiss' law was not valid for all the alloys. Further, in order to calculate a consistent number of vacant *d* electrons, WUCHER was forced to suppose that the "holes" in the *d* shell

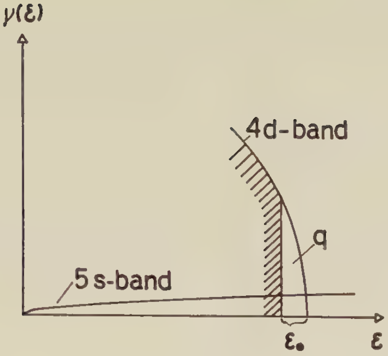

Fig. 3. The band structure of Pd at 0°K.

in the Pd atoms were coupled. This is, however, not considered to be in accordance with the linear electronic specific heat [9].

The second approach is derived from the energy band treatment of metals and is known as the collective electron theory for magnetism, developed mainly by STONER [10, 11, 12]. He supposed that magnetism arises from a number of electrons in a partially filled band of parabolic form or alternatively a number of "holes" in a more than half-filled band, in which latter case the energy is measured from the top of the band. The exchange interaction is further assumed to give a term in the energy expression proportional to the square of magnetization. The distribution of the electrons in the band is determined by application of Fermi-Dirac statistics. The collective electron theory for magnetism seems to be the most useful approach for those metals that have a small number of vacant *d*-electrons, and naturally also for binary alloys of such metals dissolved in a diamagnetic metal [12, 13, 14]. Evidently there is room for both theories.

As the number of vacant 4*d*-electrons for Pd is as low as about 0.6 per Pd atom in pure Pd and still less in the alloys, the theory of STONER should be applicable to the present measurements. The curves which STONER has calculated for the reciprocal of the susceptibility as function of the temperature are also in at least rough agreement with the measurements in Fig. 2, and therefore a more detailed comparison between the present experimental results and STONER's theory has been made.

From the band-structure in Fig. 3, generally accepted for Pd, the parameters q, θ_F and θ' are defined in the following way:

q = the average number of vacant d electrons per Pd atom,
θ_F = a characteristic Fermi-Direc temperature, satisfying the equation $k\theta = \varepsilon_0$ (Fig. 3) and

θ' = a temperature giving a measure of the interchange interaction energy such that $1/2\ k\theta'$ is the difference in energy per electron in the completely magnetized state, when the spins are parallel and the corresponding energy in the demagnetized state.

With these parameters the temperature variation of the paramagnetic susceptibiity is given, according to STONER, by the expression

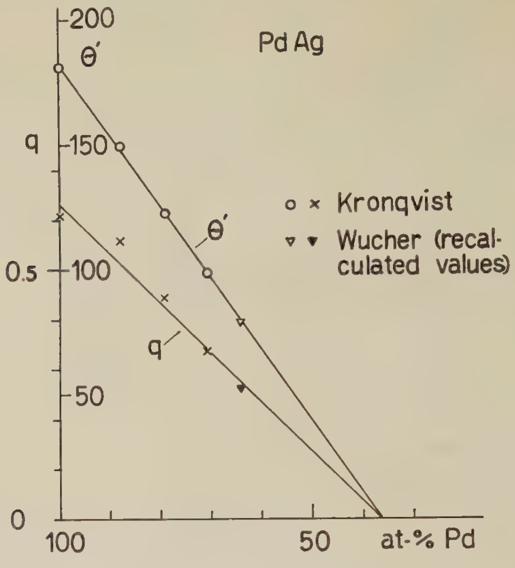

Fig. 4. The parameters q and θ' as functions of the Pd concentration.

Table 2.

α	θ_F	θ'	q
1.000	700	181	0.606
0.880	900	149	0.555
0.793	900	122	0.440
0.709	900	98	0.334
0.642[1]	900	79	0.255

$$\frac{\alpha}{\chi_p} = \frac{R\,\theta_F}{q\,M_B}\left(\frac{T}{\theta_F}\,\frac{F}{F'} - \frac{\theta'}{\theta_F}\right) \tag{2}$$

where R is the gas constant, M_B the Bohr magneton per gram atom, α is the atomic fraction of Pd and F/F' a function of T/θ_F, which is numerically determined [10], and which is $=1$ for $T/\theta_F = \infty$. In comparing the present experimental curves with formula (2), the three parameters were adjusted to obtain the best fit. In order to simplify the determination of the parameters, a graphical derivation of the experimental α/χ_p values was made, and the curves thus obtained were compared with the derivates of α/χ_p in eq. (2):

$$\frac{d}{d\,T}\left(\frac{\alpha}{\chi_p}\right) = \frac{R}{q\,M_B^2}\,\frac{d}{d\,T}\left(T\,\frac{F}{F'}\right) \tag{3}$$

which contains only two of the three parameters, namely q and θ_F (θ_F in the expression F/F'). This comparison permits the θ_F values to be determined. The uncertainty of the θ_F values, thus determined, may be as high as about 10 %, since their influence on the curves at the studied (medium and high) temperatures was rather small. Further a preliminary value of q was determined, which could be done more accurately, the uncertainty being assessed to about 2 %. In the final comparison with eq. (2) the last parameter, θ', the value of which at high concentrations of Ag was very much dependent on q, could be determined for the different alloys, after very small adjustments of the q values, in such a way that it decreased linearly with the content of Pd. The final parameter values are given in Table 2. Even considering the uncertainty of the determination, the θ_F value for Pd is lower than the constant value for the alloys. The variation of the two other parameters, q and θ', is plotted in Fig. 4.

---

[1] Calculated from WUCHER's measurements [2].

Both q and θ decrease linearly from $q = 0.635$ and $\theta' - 181$ for the pure metal Pd to zero for both constants at about $\alpha = 0.36$. It is most satisfactory that the value of q, and also its variation with the concentration of Pd, accurately determined by comparing the experiments with Stoner's theory, is altogether consistent with the information available at present about the PdAg alloys. Further, the similar dependence of θ' on the concentration of Pd, which, as mentioned above, is not necessary for, but compatible with good agreement between the measurements and eq. (2), means that θ' is proportional to q, and this is quite in accordance with the theoretical conceptions [15]. The magnitudes of θ_F and θ', calculated in this paper, are, however, small compared with other determinations [13, 3], which will be further discussed later.

With the parameter values in Table 2 quite satisfactory agreement is obtained between the present measurements from 290° to 1000°K, and Stoner's formula (2), which is shown in Fig. 2, where the full lines calculated from eq. (2) with the constants from Table 2 pass close to the measured point.

As mentioned above the susceptibility of Pd and PdAg has also been measured by Hoare, Matthews and Walling [3, 4], below room temperature. After having been interpolated to the same concentrations as used in the present work, and recalculated to the best fit to the present curves by multiplying by factors between 1.00 and 1.09, these susceptibilities have been plotted in Fig. 2. The values thus obtained for low temperatures deviate from the calculated curves, especially below 100°K, where the experimental susceptibility of Pd passes through a maximum. This is very difficult to explain with Stoner's theory. It is not possible, even with special parameters adopted for low temperatures, to derive curves from eq. (2) which agree with the experiments. The irregularities may indicate some over-simplification in the basic assumptions of the collective electron treatment. Another possibility is pointed out by Lidiard (16) who has tried to explain the most remarkable deviation from the theory, the temperature maximum for the paramagnetic susceptibility of Pd, as influenced by antiferromagnetism. His explanation was supported by a quantitative calculation.

The collective electron theory is supposed to give coordination of the magnetic and the associated thermal properties. In a detailed account of the magnetic and thermal properties of Pd and Pt, Wohlfarth [13] has determined the parameter θ_F from eq. (4)

$$\frac{\theta_F}{q} = \frac{\pi^2 R}{2\gamma} \tag{4}$$

derived from the collective electron theory on the basis of the same assumptions as eq. (2). γ in eq. (4) is the constant ratio between the electronic contribution to the specific heat and the absolute temperature, which is determined in the helium-hydrogen range. With the experimental value $\gamma = 31 \times 10^{-4}$ cal/mole degree^2 for Pd [17] inserted in eq. (4) $\frac{\theta_F}{q}$ is calculated to 3.5×10^3°K (about three times the corresponding ratio with the present parameter values inserted). Whereas WOHLFARTH in the case of Pd uses about the same value $q = 0.6$ as obtained in the present paper, he calculates $\theta_F \simeq 2 \times 10^3$°K, which is three times our value in Table 2. This is the reason why WOHLFARTH does not arrive at a good correspondence with the paramagnetic results.

HOARE and MATTHEWS [3] also determined the parameters for Pd in STONER's eq. (2) for paramagnetism from eq. (4), and in order to get a good agreement with experimental results they had to use a much lower θ_F value, 1020°K; and in order to obtain an experimental value of γ, they consequently had to insert the much too low value of $q = 0.29$. The corresponding curve agrees well with the measurements above 100°C; beyond this temperature the experiments gave curves quite different from anything resulting from eq. (2).

It appears that a complete coordination of both the paramagnetic and thermal properties of Pd in the collective electron theory as developed so far, is not possible. Further it is evident from this paper that the magnetic results at medium and high temperatures are most appropriate for comparison with the theory. The uncertainty in the determination of the thermal characteristics in the collective electron treatment is considerable, and the analysis of the experimental material very delicate, especially if, as seems probable, Pd is influenced by antiferromagnetism at low temperatures [16]. In fact, considering all complications, it is satisfactory enough that the parameters determined from the magnetic measurements, inserted in eq. (4), give a γ value of a correct order of magnitude.

Influence of cold-working

In order to study the influence of cold-working, the specimens were rolled to a decrease in cross-section of 70–85 %. The susceptibility measurements in this case were somewhat disturbed by ferromagnetic impurities, either introduced into the specimens during rolling or perhaps being made active by precipitation during cold-working. Thus the paramagnetic susceptibilities had to be determined by extrapolation of the measured values to infinite fields.

Repeated comparison between cold-worked and annealed specimens (1–2 hours' annealing at 500–900°C) showed that the influence of cold-working was small and in most cases beyond the accuracy of measurements. In Fig. 5 it is shown that the susceptibility of a cold-worked pure Pd sample was not changed by annealing in vacuum for one hour at 500°C. In this respect Pd and the Pd-rich alloys are different from binary alloys of other transition metals, e.g. Mn and Cr, dissolved in Cu, Ag or Au, where according to earlier measurements by the present author, the paramagnetism was appreciably changed by cold-working [7, 18]. It seems as if the cold-working effect increases with the number of vacant *d* electrons for the transition metal atom, which is 0.6 or less in the average per Pd atom in Pd and PdAg alloys, and between 4 and 5 for Cr and Mn atoms in the dilute alloys with the diamagnetic metals given above.

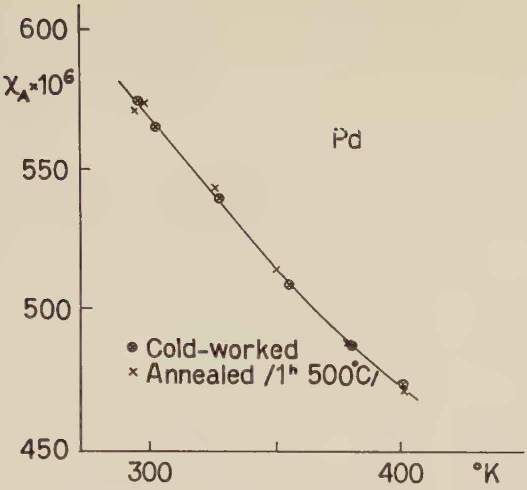

Fig. 5. The magnetic atomic susceptibility of a Pd sample.

Summary

The paramagnetic susceptibility of Pd and some Pd rich PdAg alloys has been determined from room temperature up to about 1000°K. The experimental results have been compared with the collective electron theory for magnetism, developed principally by STONER. Good agreement with this theory has been obtained in the interval of temperature studied. Further, it has been shown that cold-working does not appreciably change the paramagnetism of Pd and Pd-rich PdAg alloys.

The author wishes to express his gratitude to Professor G. BORELIUS and Dr. J. O. LINDE for valuable discussions.

Stockholm, Royal Institute of Technology, Department of Physics.

LITERATURE

1. B. SVENSSON, Ann. der Phys. *14* (1936) 699.
2. J. WUCHER, Ann. de Phys. *7* (1952) 317.
3. E. F. HOARE and J. C. MATTHEWS, Proc. Roy. Soc. *A 212* (1952) 137.
4. E. F. HOARE, J. C. MATTHEWS, and J. C. WALLING, Proc. Roy. Soc. *A 216* (1953) 502.
5. G. GUSTAFSSON, Ann. der Phys. *25* (1936) 545.
6. J. C. SLATER, Phys. Rev. *36* (1930) 57.
   W. R. ANGUS, Proc. Phys. Soc. *A 136* (1932) 569.
7. E. KRONQVIST and A. GIANSOLDATI, Ark. f. Fys. *7* Nr 26 (1953).
8. A. GIANSOLDATI, Ark. f. Fys. *8* Nr 12 (1954).
9. N. F. MOTT, Proc. Phys. Soc. *62* (1949) 416.
10. E. C. STONER, Proc. Roy. Soc. *A 165* (1938) 372.
11. —— Proc. Roy. Soc. *A 169* (1939) 339.
12. —— J. Phys. et Radium *12* (1951) 372.
13. E. P. WOHLFARTH, Proc. Leeds Phil. Soc. *5* (1949) 89.
14. —— Proc. Roy. Soc. *A 195* (1949) 434.
15. —— Rev. of Mod. Phys. *25* (1953) 211.
16. A. B. LIDIARD, Proc. Roy. Soc. *A 224* (1954) 161.
17. G. L. PICKARD and F. E. SIMON, Proc. Phys. Soc. *61* (1948).
18. E. KRONQVIST, Ark. f. mat., astr. o. fys. *34B* N:o 7 (1947).

Tryckt den 9 september 1955

Uppsala 1955. Almqvist & Wiksells Boktryckeri AB

ARKIV FÖR FYSIK Band 10 nr 6

Communicated 27 April 1955 by Manne Siegbahn and Erik Hulthén

Molecular association and proton resonance in acetic acid

By B. N. Bhar*, W. Forsling and G. Lindström

With 2 figures in the text

Studies of nuclear magnetic resonance spectra seem to be a helpful method in gaining some knowledge concerning the important property of molecular association in compounds endowed with hydrogen bonds. Several carboxylic acids, of which acetic acid can be taken as a typical example, are known to exist, under some circumstances, in the dimeric state by virtue of the property of association through a hydrogen bridge of the type O–H...O. Such a dimer can be represented as 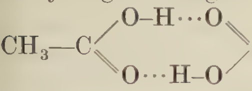. It is evident that the bridge protons of the COOH group and protons of the CH_3 group are in different chemical environments, and if subjected to a magnetic field, the two groups of protons would experience different diamagnetic shielding. The diamagnetic shielding of the bridge protons, because of their proximity to oxygen atoms, which have greater affinity for electrons, is less than that of the CH_3 group protons, and hence when a nuclear magnetic resonance (n-m-r) experiment is performed with an ensemble of such molecules, the bridge protons of the COOH group will resonate at a value of the externally applied magnetic field which is lower than that required for CH_3 group protons. Such a chemical shift, by virtue of which the proton peaks from different groups can be delineated as distinctly resolved lines in the n–m–r spectrum gives clearly an indication of the relative diamagnetic shielding of protons of the COOH and the CH_3 groups at any fixed value of the magnetic field. It is evident that any change in the O–H···O bridge, due to elongation or breaking up of the bridge leading to the monomeric state, would profoundly change the diamagnetic shielding of the COOH group protons. Hence the chemical shift would be different, which would manifest itself in altering the separation between the proton peaks from the two different groups.

With the purpose of observing the effect on the chemical shift due to alteration of the extent of association we have studied the proton spectra of acetic acid in its pure state and in different solutions in water, carbon tetrachloride, carbon disulphide and benzene.

The experimental method employed for the observation of the proton spectra was that of nuclear magnetic resonance absorption method introduced by Purcell *et al.* [1]. The magnetic field used was approximately 3285 gauss supplied by a permanent magnet, and the stimulating radio-frequency field was 13.997 Mc/s obtained from a crystal-controlled oscillator. The nuclear signals were detected by double-T bridge, essentially similar to that introduced by Grivet *et al.* [2]. The sample volume used was nearly 0.01 cc. The spectra as presented in Fig. 1 were recorded at a resolution of 1 part in 2 millions. The magnetic field was changed linearly through the resonance at a very slow rate of 3.5 milligauss/sec to avoid transients (wiggles). The details of the experimental technique and total arrangement of the set-up will be published later [3].

---

* Formerly associated with the University of Calcutta, India.

Acetic acid is said to exist as dimers in solutions of carbon disulphide, carbon tetrachloride and probably in benzene. If this is so, the diamagnetic shielding of the bridge protons, as stated earlier, would be the same in each of those solvents, and the separation of the proton peaks from the COOH group and the CH_3 group in the n-m-r spectra should be the same. From the proton spectra of acetic acid dissolved in carbon disulphide (CS_2) and carbon tetrachloride (CCl_4) as presented in Fig. 1 (*a*, *b*), it is experimentally observed that the separation of the two peaks in question is the same in each case, viz. 24.1 ± 0.2 milligauss. Fig. 1 (*c*) is the proton spectrum of acetic acid in benzene (50% by volume solution), where the solvent, unlike CS_2 and CCl_4, contains protons due to which a central peak between the COOH proton peak and CH_3 proton peak arises. The separation of the COOH peak from the CH_3 peak is here 24.5 ± 0.2 milligauss. Thus one can confirm that acetic acid exists as double molecules in benzene solution. The feasibility of low polymerisation with molecules greater than two seems to be ruled out because of the non-existence of any other proton peak, which would have arisen due to diamagnetic shielding different from that of the bridge protons. Studies of electric dipole moment measurements also lend support to the suggestion that acetic acid exists in benzene, even in dilute solutions, mainly as double molecules [4].

From the proton spectra of pure acetic acid (glacial), as presented in Fig. 1 (*d*), it is observed that the separation of the COOH proton peak from the CH_3 proton peak is also 24.1 ± 0.2 milligauss, i.e. the same as that in the case of acid dissolved in carbon disulphide, carbon tetrachloride and benzene. This leads to confirmation of the suggestion that acetic acid exists as dimers also in its pure state [5].

Proton spectra of acetic acid in CCl_4 in different dilutions were studied, but it was observed that practically no measurable change in the separation between COOH proton peak and CH_3 proton peak took place by altering the dilution. In alcohol, however, as in the case of methyl and ethyl alcohol [6] (ARNOLD and PACKARD), the effect of dissolution of alcohols in carbon tetrachloride has a profound influence on the chemical shift of the OH group, and the separation of the nuclear induction signals of the OH group from the neighbouring group progressively decreases as the dilution is increased.

Some interesting features were observed in the proton spectra of acetic acid diluted with water, which is known to alter the extent of association of the acid. Proton spectra of pure acetic acid and in different dilutions in water are presented in Fig. 1 (*d*, *e*, *f*, *g*, *h*, *i* and *j*), which clearly demonstrates the effect of dilution—a shift of the COOH group proton peak towards higher values of the externally applied magnetic field. The separation between the two peaks decreases with increasing dilution, but some "irregularities" are being observed within the region where the concentration of the acid is between 60% and 50% by volume, after which the separation concerned again decreases with increasing dilution. These observations were repeated taking particular care about the concentrations. On addition of water a fraction of the dimers breaks up to monomers and the equilibrium between the double and single molecules is due to a complex interaction between the associated and unassociated molecules [4]. Following a similar argument to that proposed by LIDDEL

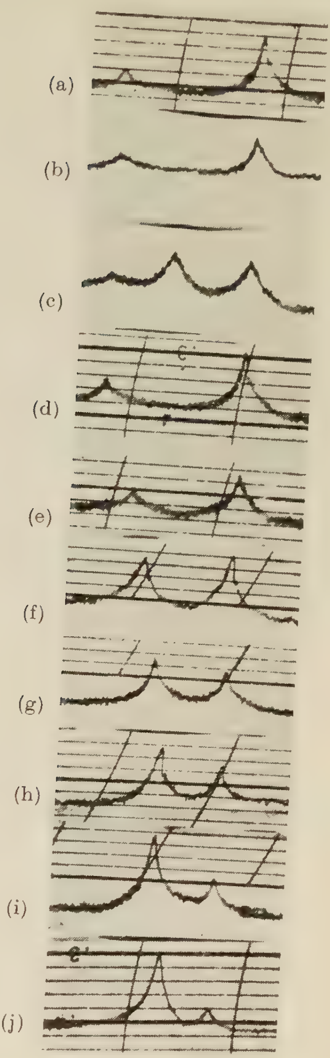

Resolved proton spectra of acetic acid (CH_3COOH),
various conditions, where the amplitude of the signals
tted against magnetic field, which increases linearly from
ight. The signals on the right hand side of the picture
n CH_3-group protons and the left hand ones are generally
OOH-group protons. The latter signals in case of aqueous
s, as shown in Fig. 1 (*e*, *f*, *g*, *h*, *i*, and *j*) for 90, 80, 70,
0 % concentration of the acid by volume respectively,
rimposed on proton peaks because of water as explained
ext. Signals in Fig. 1 (*a*) are from 70 % solution of acetic
carbon disulphide. Signals in Fig. 1 (*b*) are from 60 %
of acetic acid in carbon tetrachloride. Signals in Fig. 1 (*c*)
50 % solution of acetic acid in benzene. Signals in
Fig. 1 (*d*) are from pure acetic acid.

MSEY [7] when commenting on the temperature dependence of the chemical
the OH group in ethyl alcohol, if the correlation time for the life times of
erent states (associated and unassociated states in case of acetic acid) is
tly small, the hydrogen resonance of the COOH group will be observed at
ncy corresponding to the average shielding for the two states. Since the
will alter the distribution between the associated and unassociated states,
ance frequency of the COOH group protons, and hence its chemical shift,
dependent upon dilution. Moreover with dilution the water molecules would
ciate with acetic acid through hydrogen bonding and the protons of water
will exchange their positions with the protons of the COOH group in the

Table 1.

Proportion of acetic acid (by volume)	Separation in milligauss of COOH proton peak from CH_3.proton peak (± 0.2 milligauss)
Solution in Carbon disulphide (CS_2)	
70 %	24.1
Solution in Carbon tetrachloride (CCl_4)	
80 %	24.1
60 %	24.1
40 %	24.0
Solution in Benzene (C_6H_6)	
50 %	24.5
Pure (nearly 100 %) CH_3COOH	24.1
Solution in water	
90 %	18.9
80 %	14.3
70 %	11.3
65 %	10.4
55 %	9.6
50 %	9.9
45 %	8.2
40 %	7.5
35 %	7.1

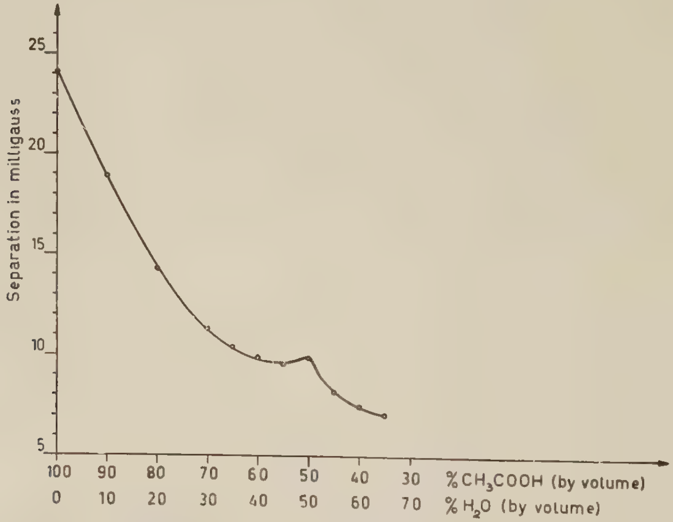

Fig. 2. The separation of the CH_3-group proton peak from the COOH-group proton peak as plotted against concentration of acetic acid.

acid [8]. Thus the proton line because of water will overlap on the dilution-dependent proton peak of the COOH group and the intensity of the peak will increase with dilution while the intensity of the peak because of CH_3 will decrease with decrease of the concentration of acetic acid. As the dissociation constant of acetic acid in water is very small (1.75×10^{-5}), it is dissociated to a very small extent under ordinary concentrations. A large percentage of the molecules will therefore remain either associating with themselves or with water molecules. The alternative formation of hydrogen bonds with water molecules, when the dimeric structure breaks up, as stated earlier, has also been suggested from studies of infra-red and Raman spectra of acetic acid in water [9, 10].

In Table 1 are presented the experimentally measured values of the separation in milligaus of the COOH proton peak and the CH_3 proton peak with different dilutions in water. In Fig. 2 we have plotted the separation concerned against dilution. It seems to us that if a smooth curve is drawn through the plotted points the nature of the curve would be similar to that of isothermals (p–v curves) of gases obeying van der Waals' equation of state. It was found by ARNOLD and PACKARD [6] that temperature changes have an effect in alcohols similar to dilution in regard to the chemical shift of the OH group. It seems suggestive that chemical shifts of the proton lines from OH group in alcohols or of COOH group in carboxylic acids are likely to be dependent on pressure, temperature remaining constant.

One of us (BHAR) wishes to record his profound gratitude to Professor MANNE SIEGBAHN, Director of the Nobel Institute of Physics, for his kind hospitality in extending all laboratory facilities to perform the work described here.

Nobel Institute of Physics, Stockholm 50, Sweden.

REFERENCES

1. PURCELL, E. M., TORREY, H. C., and POUND, R. V., Phys. Rev. *69*, 37 (1946).
2. GRIVET, P., SOUTIF, M. et BUYLE, M., *C. R. Acad. Sc. Paris 229*, 113 (1949).
3. LINDSTRÖM, G. and BHAR, B. N., Arkiv för fysik (to be published).
4. SMYTH, C. P., Dielectric Constant and Molecular Structure. New York, 1931.
5. LONGINESCU, G. G., Chem. Rev. *6*, 381 (1929).
6. ARNOLD, J. T. and PACKARD, M. E., J. Chem. Phys. *19*, 1608 (1951).
7. LIDDEL, U. and RAMSEY, N. F., J. Chem. Phys. *19*, 1608 (1951).
8. GUTOWSKY, H. S. and SAIKA, A., J. Chem. Phys. *21*, 1688–94 (1953).
9. EDSALL, J. T., J. Chem. Phys. *4*, 1 (1936) and *5*, 408 (1937).
10. HADZI, D. and SHEPPARD, N., Proc. Roy. Soc. (A) *216*, 247–66 (1953).

Tryckt den 9 september 1955

Uppsala 1955. Almqvist & Wiksells Boktryckeri AB

ARKIV FÖR FYSIK Band 10 nr 7

Communicated 26 January 1955 by Erik Hulthén and Oskar Klein

Extended energy level tables for the rigid asymmetric rotor

By Gunnar Erlandsson

The microwave spectroscopic work here has for some time been mainly confined to the rotational spectra of asymmetric top molecules. The analyses of such spectra require a great deal of time-consuming numerical work. Many of the computations involved are, however, very fit for handling in the electronic computing machine BESK. The machine has therefore been tried on a couple of problems, and been found very useful for the purposes. Especially, it has greatly reduced the labour concerning the evaluation of rotational energy-levels from given or assumed values of the rotational constants.

In order to facilitate the localization of the levels that may be involved in a particular spectrum, the machine has been used to extend the energy level tables given by King, Hainer and Cross for $J \leq 12$ [ref. 1, 2] up to $J = 40$. The extended tables are reproduced photographically on the following pages. They are arranged in the same manner as in [1] and [2], i.e. the columns represent the asymmetry values $\varkappa = -1.0$, -0.9 etc. to 0.0. The $2J+1$ levels for each value of J are labelled with the $K_{-1}K_1$ notations [1] representing the K-values of the corresponding symmetric rotor levels ($\varkappa = -1$ and $\varkappa = 1$.)

The machine program for the energy-level calculations was worked out by fil. lic. G. Ehrling at the Computation Machines Board. It employs the continued fraction method introduced by King *et al.* [1]. The representation type I is used throughout. The development for a certain root λ_m has in general been started with the corresponding constant k_m. In some cases, however, this development was found to diverge rapidly. For such incidents the machine was instructed to change to the development starting with k_{m+1}.

The accuracy obtainable with linear or quadratic interpolation in the tables, for intermediate values of $\varkappa$ is in general not sufficient for microwave spectroscopic purposes. Values obtained in this way are, however, useful as starting points for the calculation of better values manually or in BESK. The latter method is, of course, very advantageous, when several levels are needed, as is usually the case.

For the above-mentioned tabulation of energy-levels, the Computation Machines Board granted free machine-time. I am in this respect much obliged especially to

Dr. STIG COMÉT for his interest in the work and for helpful advice. I wish also to express my thanks to fil. lic. G. EHRLING for his skilful work with the machine program.

Department of Physics, University of Stockholm, Stockholm. January 1955.

REFERENCES

1. G. W. KING, R. M. HAINER, and P. C. CROSS, Journ. Chem. Phys. *11*, 27 (1943).
2. R. M. HAINER, P. C. CROSS and G. W. KING, Journ. Chem. Phys. *17*, 826 (1949).

Tryckt den 15 september 1955

Uppsala 1955. Almqvist & Wiksells Boktryckeri AB

-182.00000	-176.62675	-174.05264	-172.14059	-170.54123	-169.13722	-167.87108	-166.70918	-165.62972	-164.61760	-163.66183
-180.00000	-176.45315	-174.03124	-172.13718	-170.54061	-169.13710	-167.87105	-166.70917	-165.62972	-164.61760	-163.66183
-180.00000	-168.01370	-159.73225	-153.78725	-148.95244	-144.75236	-140.98191	-137.53101	-134.33116	-131.33574	-128.51113
-174.00000	-165.88121	-159.21118	-153.66822	-148.92452	-144.74566	-140.98030	-137.53062	-134.33107	-131.33572	-128.51113
-174.00000	-162.19770	-149.61538	-138.98786	-130.43517	-123.26733	-116.96351	-111.25160	-105.98416	-101.07095	-96.45076
-164.00000	-154.94857	-145.92298	-137.54037	-129.95461	-123.11921	-116.91967	-111.23910	-105.98074	-101.07007	-96.45054
-164.00000	-154.28945	-142.07023	-128.95839	-116.59016	-105.73889	-96.40933	-88.21348	-80.80521	-73.97192	-67.58808
-150.00000	-141.31362	-132.01189	-122.48585	-113.12367	-104.18710	-95.80364	-87.99803	-80.73395	-73.94996	-67.58182
-150.00000	-141.27042	-131.35706	-119.75043	-106.81982	-93.60593	-81.01402	-69.60670	-59.49031	-50.43434	-42.15984
-132.00000	-123.88257	-115.21409	-106.02715	-96.45870	-86.72523	-77.05949	-67.65782	-58.65379	-50.11378	-42.04875
-132.00000	-123.88113	-115.16588	-105.66009	-95.01995	-83.03646	-70.04085	-56.73316	-43.81238	-31.81930	-20.98868
-110.00000	-102.50714	-94.60672	-86.26611	-77.46776	-68.23437	-58.64784	-48.84666	-39.00167	-29.28432	-19.83904
-110.00000	-102.50711	-94.60472	-86.24134	-77.32005	-67.65892	-56.99471	-45.15424	-32.31884	-19.00188	-5.81546
-84.00000	-77.20457	-70.10207	-62.66487	-54.86144	-46.65997	-38.03764	-28.99565	-19.57521	-9.86592	0.00000
-84.00000	-77.20457	-70.10202	-62.66386	-54.85280	-46.61387	-37.85622	-28.42643	-18.10039	-6.67519	5.81546
-54.00000	-47.98814	-41.74037	-35.23609	-28.45111	-21.35702	-13.92120	-6.10845	2.11386	10.76557	19.83904
-54.00000	-47.98814	-41.74037	-35.23606	-28.45078	-21.35475	-13.90967	-6.06211	2.26982	11.21873	20.98868
-20.00000	-14.86424	-9.54767	-4.03480	1.69238	7.65498	13.87801	20.39119	27.22974	34.43429	42.04875
-20.00000	-14.86424	-9.54767	-4.03480	1.69238	7.65506	13.87848	20.39352	27.23940	34.46903	42.15984
18.00000	22.16389	26.46243	30.90709	35.51108	40.28980	45.26139	50.44741	55.87384	61.57235	67.58182
18.00000	22.16389	26.46243	30.90709	35.51108	40.28981	45.26140	50.44748	55.87422	61.57397	67.58808
60.00000	63.09440	66.28239	69.57189	72.97205	76.49345	80.14854	83.95205	87.92168	92.07896	96.45054
60.00000	63.09440	66.28239	69.57189	72.97205	76.49345	80.14854	83.95206	87.92169	92.07900	96.45076
106.00000	107.92623	109.90773	111.94919	114.05598	116.23434	118.49159	120.83635	123.27899	125.83207	128.51113
106.00000	107.92623	109.90773	111.94919	114.05598	116.23434	118.49159	120.83635	123.27899	125.83207	128.51113
156.00000	156.65868	157.33566	158.03248	158.75093	159.49307	160.26130	161.05849	161.88805	162.75413	163.66183
156.00000	156.65868	157.33566	158.03248	158.75093	159.49307	160.26130	161.05849	161.88805	162.75413	163.66183

-210.00000	-204.15050	-201.41309	-199.36339	-197.64535	-196.13621	-194.77487	-193.52536	-192.36434	-191.27559	-190.24733
-208.00000	-204.02590	-201.40059	-199.36170	-197.64509	-196.13616	-194.77486	-193.52536	-192.36434	-191.27559	-190.24733
-208.00000	-194.50688	-185.71135	-179.41414	-174.24643	-169.73913	-165.68650	-161.97460	-158.53122	-155.30678	-152.26537
-202.00000	-192.74710	-185.36961	-179.34883	-174.23327	-169.73638	-165.68592	-161.97448	-158.53120	-155.30677	-152.26537
-202.00000	-188.17345	-174.06657	-162.74395	-153.76358	-146.16584	-139.42846	-133.29790	-127.63277	-122.34271	-117.36450
-192.00000	-181.47756	-171.16835	-161.81532	-153.50551	-146.09757	-139.41091	-133.29353	-127.63173	-122.34248	-117.36445
-192.00000	-180.49959	-165.95700	-150.98956	-137.54566	-126.16040	-116.40566	-107.74142	-99.83587	-92.50425	-85.63475
-178.00000	-167.80136	-156.88522	-145.86205	-135.24402	-125.30570	-116.12344	-107.65507	-99.81112	-92.49762	-85.63312
-178.00000	-167.72457	-155.78011	-141.66364	-126.41543	-111.51943	-97.97450	-86.08454	-75.57164	-66.04701	-57.24198
-160.00000	-150.40055	-140.09177	-129.16870	-117.89359	-106.60726	-95.61436	-85.12103	-75.22412	-65.93355	-57.20830
-160.00000	-150.39754	-139.99252	-128.44501	-115.27713	-100.57176	-85.20100	-70.17667	-56.27538	-43.81848	-32.64884
-138.00000	-129.04778	-119.56238	-109.50640	-98.88277	-87.77757	-76.37034	-64.89810	-53.59894	-42.66510	-32.21755
-138.00000	-129.04771	-119.55745	-109.44641	-98.53686	-86.50620	-73.04178	-58.27542	-42.87343	-27.66402	-13.37474
-112.00000	-103.75890	-95.11394	-86.02802	-76.46070	-66.37956	-55.78257	-44.72455	-33.33072	-21.78478	-10.29596
-112.00000	-103.75889	-95.11378	-86.02503	-76.43570	-66.24959	-55.29160	-43.28190	-29.94939	-15.34913	0.00000
-82.00000	-74.55123	-66.78853	-58.68404	-50.20471	-41.31213	-31.96466	-22.12495	-11.77548	-0.94033	10.29596
-82.00000	-74.55123	-66.78853	-58.68394	-50.20355	-41.30411	-31.92483	-21.96979	-11.27668	0.41049	13.37474
-48.00000	-41.43326	-34.62038	-27.54004	-20.16735	-12.47289	-4.42175	4.02713	12.92019	22.30472	32.21755
-48.00000	-41.43326	-34.62038	-27.54004	-20.16732	-12.47257	-4.41969	4.03724	12.96107	22.44659	32.64884
-10.00000	-4.40936	1.37233	7.36140	13.57677	20.04055	26.77891	33.82312	41.21089	48.98786	57.20830
-10.00000	-4.40936	1.37233	7.36140	13.57677	20.04056	26.77898	33.82355	41.21302	48.99686	57.24198
32.00000	36.51804	41.17949	45.99653	50.98321	56.15587	61.53374	67.13965	73.00111	79.15171	85.63312
32.00000	36.51804	41.17949	45.99653	50.98321	56.15587	61.53374	67.13966	73.00118	79.15208	85.63475
78.00000	81.34751	84.79514	88.35137	92.02597	95.83027	99.77756	103.88356	108.16715	112.65130	117.36445
78.00000	81.34751	84.79514	88.35137	92.02597	95.83027	99.77756	103.88356	108.16715	112.65131	117.36450
128.00000	130.07813	132.21554	134.41725	136.68903	139.03757	141.47070	143.99769	146.62961	149.37996	152.26537
128.00000	130.07813	132.21554	134.41725	136.68903	139.03757	141.47070	143.99769	146.62961	149.37996	152.26537
182.00000	182.70932	183.43829	184.18856	184.96204	185.76096	186.58790	187.44592	188.33869	189.27067	190.24733
182.00000	182.70932	183.43829	184.18856	184.96204	185.76096	186.58790	187.44592	188.33869	189.27067	190.24733

J = 15

0,15	-240.00000	-233.68124	-230.77579	-228.58688	-226.74977	-225.13537	-223.67877	-222.34164	-221.09903	-219.93363	-218.8
1,15	-238.00000	-233.59268	-230.76856	-228.58605	-226.74966	-225.13535	-223.67877	-222.34164	-221.09903	-219.93363	-218.8
1,14	-238.00000	-222.99412	-213.72356	-207.05701	-201.54699	-196.72896	-192.39283	-188.41935	-184.73213	-181.27846	-178.0
2,14	-232.00000	-221.57126	-213.50426	-207.02182	-201.54089	-196.72786	-192.39262	-188.41931	-184.73213	-181.27846	-178.0
2,13	-232.00000	-216.02069	-200.49761	-188.59073	-179.15900	-171.09791	-163.90979	-157.35302	-151.28681	-145.61818	-140.2
3,13	-222.00000	-209.91152	-198.30413	-188.01903	-179.02503	-171.06736	-163.90295	-157.35153	-151.28650	-145.61812	-140.2
3,12	-222.00000	-208.51605	-191.54181	-174.87861	-160.61754	-148.76465	-138.52461	-129.33518	-120.90097	-113.05582	-105.6
4,12	-208.00000	-196.16976	-183.54222	-171.00778	-159.18736	-148.32160	-138.39956	-129.30205	-120.89270	-113.05390	-105.6
4,11	-208.00000	-196.03925	-181.78441	-164.98672	-147.56366	-131.35029	-117.18399	-104.86896	-93.86345	-83.77697	-74.3
5,11	-190.00000	-178.80137	-166.71161	-153.93608	-140.91485	-128.12272	-115.90518	-104.43213	-93.72914	-83.73925	-74.3
5,10	-190.00000	-178.79540	-166.51935	-152.61360	-136.59088	-119.16293	-101.75220	-85.54790	-71.11111	-58.28328	-46.6
6,10	-168.00000	-157.47615	-146.26788	-134.33942	-121.74372	-108.67811	-95.45466	-82.40766	-69.80781	-57.81835	-46.4
6,9	-168.00000	-157.47599	-146.25656	-134.20500	-121.00323	-106.16917	-89.59590	-72.01996	-54.55244	-38.17327	-23.4
7,9	-142.00000	-132.20412	-121.88806	-111.00320	-99.50195	-87.36576	-74.64785	-61.50263	-48.17207	-34.93303	-22.0
7,8	-142.00000	-132.20412	-121.88764	-110.99515	-99.43621	-87.03591	-73.47300	-58.36317	-41.68982	-24.09345	-6.5
8,8	-112.00000	-103.00724	-93.60747	-83.76373	-73.43199	-62.56272	-51.10969	-39.05104	-26.42102	-13.33697	0.0
8,7	-112.00000	-103.00724	-93.60746	-83.76342	-73.42830	-62.53758	-50.98842	-38.59854	-25.06185	-10.02641	6.5
9,7	-78.00000	-69.89659	-61.46959	-52.69065	-43.52631	-33.93676	-23.87499	-13.28798	-2.12326	9.65444	22.0
9,6	-78.00000	-69.89659	-61.46959	-52.69065	-43.52617	-33.93549	-23.86713	-13.25040	-1.97641	10.13920	23.4
10,6	-40.00000	-32.87789	-25.49832	-17.83916	-9.87461	-1.57433	7.09779	16.18509	25.73945	35.82140	46.4
10,5	-40.00000	-32.87789	-25.49832	-17.83916	-9.87461	-1.57429	7.09814	16.18714	25.74936	35.86211	46.6
11,5	2.00000	8.04569	14.29309	20.75937	27.46444	34.43150	41.68793	49.26644	57.20657	65.55676	74.3
11,4	2.00000	8.04569	14.29309	20.75937	27.46444	34.43150	41.68794	49.26651	57.20701	65.55897	74.3
12,4	48.00000	52.87226	57.89680	63.08656	68.45642	74.02372	79.80878	85.83575	92.13369	98.73805	105.6
12,3	48.00000	52.87226	57.89680	63.08656	68.45642	74.02372	79.80878	85.83576	92.13370	98.73813	105.6
13,3	98.00000	101.60063	105.30795	109.13101	113.08019	117.16758	121.40731	125.81612	130.41408	135.22561	140.2
13,2	98.00000	101.60063	105.30795	109.13101	113.08019	117.16758	121.40731	125.81612	130.41408	135.22561	140.2
14,2	152.00000	154.23003	156.52337	158.88535	161.32215	163.84090	166.44996	169.15922	171.98052	174.92823	178.0
14,1	152.00000	154.23003	156.52337	158.88535	161.32215	163.84090	166.44996	169.15922	171.98052	174.92823	178.0
15,1	210.00000	210.75996	211.54091	212.34463	213.17316	214.02886	214.91450	215.83336	216.78935	217.78724	218.8
15,0	210.00000	210.75996	211.54091	212.34463	213.17316	214.02886	214.91450	215.83336	216.78935	217.78724	218.8

J = 16

0.16	-272.00000	-265.21746	-262.13992	-259.81081	-257.85438	-256.13465	-254.58277	-253.15798	-251.83377	-250.59172	-249.4
1.16	-270.00000	-265.15502	-262.13577	-259.81041	-257.85433	-256.13464	-254.58277	-253.15798	-251.83377	-250.59172	-249.4
1.15	-270.00000	-253.48798	-243.76110	-236.70981	-230.85145	-225.72073	-221.10036	-216.86496	-212.93369	-209.25064	-205.7
2.15	-264.00000	-252.35974	-243.62287	-236.69114	-230.84867	-225.72029	-221.10028	-216.86495	-212.93369	-209.25064	-205.7
2.14	-264.00000	-245.75583	-228.95288	-216.51600	-206.59692	-198.04923	-190.40063	-183.41367	-176.94456	-170.89634	-165.1
3.14	-254.00000	-240.25584	-227.35058	-216.17556	-206.52923	-198.03588	-190.39803	-183.41318	-176.94447	-170.89632	-165.1
3.13	-254.00000	-238.33419	-218.87882	-200.74223	-185.84894	-173.50180	-162.71451	-152.96439	-143.98518	-135.61904	-127.7
4.13	-240.00000	-226.41858	-211.99844	-197.96487	-185.00923	-173.28256	-162.66122	-152.95212	-143.98251	-135.61850	-127.7
4.12	-240.00000	-226.20539	-209.35296	-189.81108	-170.47127	-153.32251	-138.67832	-125.86122	-114.26923	-103.56609	-93.5
5.12	-222.00000	-209.08291	-195.07276	-180.35126	-165.58555	-151.36955	-138.03746	-125.67544	-114.22006	-103.55415	-93.5
5.11	-222.00000	-209.07161	-194.72024	-178.10520	-159.02800	-139.08094	-120.11616	-103.21641	-88.37712	-75.05584	-62.8
6.11	-200.00000	-187.79058	-174.71704	-160.75932	-146.06745	-131.00486	-116.03264	-101.55070	-87.80580	-74.88395	-62.7
6.10	-200.00000	-187.79022	-174.69262	-160.47838	-144.61348	-126.57261	-106.86392	-86.90111	-68.06026	-51.12302	-36.0
7.10	-174.00000	-162.53903	-150.41928	-137.57888	-123.97010	-109.61767	-94.68168	-79.46096	-64.31987	-49.58929	-35.4
7.9	-174.00000	-162.53902	-150.41821	-137.55889	-123.81131	-108.85862	-92.19540	-73.58456	-53.68052	-33.71556	-14.8
8.9	-144.00000	-133.35525	-122.19330	-110.46586	-98.11564	-85.08350	-71.33285	-56.89399	-41.90744	-26.62856	-11.3
8.8	-144.00000	-133.35525	-122.19327	-110.46493	-98.10496	-85.01240	-71.00279	-55.73612	-38.76096	-19.96012	0.0
9.8	-110.00000	-100.25348	-90.09229	-79.47947	-68.37091	-56.71393	-44.44793	-31.51196	-17.86612	-3.52954	11.3
9.7	-110.00000	-100.25348	-90.09229	-79.47944	-68.37042	-56.70958	-44.42149	-31.38959	-17.41002	-2.13089	14.8
10.7	-72.00000	-63.24109	-54.14709	-44.68890	-34.83242	-24.53715	-13.75460	-2.42678	9.51349	22.13621	35.4
10.6	-72.00000	-63.24109	-54.14709	-44.68890	-34.83240	-24.53696	-13.75317	-2.41843	9.55273	22.29133	36.0
11.6	-30.00000	-22.32216	-14.37483	-6.13492	2.42437	11.33448	20.63272	30.36388	40.58238	51.35449	62.7
11.5	-30.00000	-22.32216	-14.37483	-6.13492	2.42437	11.33449	20.63277	30.36427	40.58464	51.36543	62.8
12.5	16.00000	22.50088	29.21439	36.15862	43.35448	50.82632	58.60284	66.71823	75.21379	84.14020	93.5
12.4	16.00000	22.50088	29.21439	36.15862	43.35448	50.82632	58.60284	66.71824	75.21388	84.14072	93.5
13.4	66.00000	71.22652	76.61430	82.17702	87.93045	93.89289	100.08582	106.53473	113.27025	120.32975	127.7
13.3	66.00000	71.22652	76.61430	82.17702	87.93045	93.89289	100.08582	106.53473	113.27026	120.32976	127.7
14.3	120.00000	123.85376	127.82082	131.91077	136.13465	140.50527	145.03763	149.74949	154.66212	159.80141	165.1
14.2	120.00000	123.85376	127.82082	131.91077	136.13465	140.50527	145.03763	149.74949	154.66212	159.80141	165.1
15.2	178.00000	180.38194	182.83120	185.35347	187.95531	190.64430	193.42933	196.32092	199.33164	202.47678	205.7
15.1	178.00000	180.38194	182.83120	185.35347	187.95531	190.64430	193.42933	196.32092	199.33164	202.47678	205.7
16.1	240.00000	240.81060	241.64354	242.50071	243.38428	244.29676	245.24112	246.22082	247.24004	248.30383	249.4
16.0	240.00000	240.81060	241.64354	242.50071	243.38428	244.29676	245.24112	246.22082	247.24004	248.30383	249.4

-306.00000	-298.75784	-295.50497	-293.03502	-290.95913	-289.13403	-287.48684	-285.97438	-284.56855	-283.24984	-282.00404
-304.00000	-298.71415	-295.50259	-293.03482	-290.95911	-289.13402	-287.48684	-285.97438	-284.56855	-283.24984	-282.00404
-304.00000	-285.99690	-275.81694	-268.36880	-262.15838	-256.71383	-251.80878	-247.31124	-243.13576	-239.22322	-235.53062
-298.00000	-285.11825	-275.73110	-268.35903	-262.15712	-256.71366	-251.80876	-247.31123	-243.13576	-239.22322	-235.53062
-298.00000	-277.39708	-259.45955	-246.50025	-236.06095	-227.01198	-218.89751	-211.47817	-204.60504	-198.17654	-192.11934
-288.00000	-272.51656	-258.32657	-246.30288	-236.02749	-227.00626	-218.89653	-211.47801	-204.60501	-198.17653	-192.11934
-288.00000	-269.95434	-248.02893	-228.67057	-213.22544	-200.32369	-188.94471	-178.61399	-169.08131	-160.19018	-151.83174
-274.00000	-258.54832	-242.27240	-226.77441	-212.75435	-200.21906	-188.92270	-178.60957	-169.08047	-160.19003	-151.83172
-274.00000	-258.21239	-238.48893	-216.25123	-195.34000	-177.53547	-162.39074	-148.97426	-136.73572	-125.38772	-114.75959
-256.00000	-241.24310	-225.17741	-208.44478	-191.97450	-176.43603	-162.08806	-148.89899	-136.71847	-125.38409	-114.75889
-256.00000	-241.22259	-224.56322	-204.88957	-182.73378	-160.63911	-140.64393	-123.28131	-107.94603	-93.99458	-81.05337
-234.00000	-219.98926	-204.90394	-188.76565	-171.88723	-154.84767	-138.24272	-122.47753	-107.71408	-93.93496	-81.03966
-234.00000	-219.98852	-204.85409	-188.21514	-169.26715	-147.78308	-125.21255	-103.49508	-83.92581	-66.62910	-51.03956
-208.00000	-194.76231	-180.70205	-165.74363	-149.85582	-133.15595	-115.97192	-98.77037	-82.00358	-65.98609	-50.85544
-208.00000	-194.76229	-180.69953	-165.69727	-149.50087	-131.56915	-111.32588	-89.17055	-66.57443	-45.11978	-25.77050
-178.00000	-165.59427	-152.54183	-138.78035	-124.23764	-108.85265	-92.62980	-75.70963	-58.39459	-41.08908	-24.18739
-178.00000	-165.59427	-152.54175	-138.77781	-124.20918	-108.66919	-91.82162	-73.11597	-52.22553	-29.80393	-7.26370
-144.00000	-132.50318	-120.48523	-107.89874	-94.68632	-80.77989	-66.10676	-50.61330	-34.31386	-17.34787	0.00000
-144.00000	-132.50318	-120.48523	-107.89864	-94.68477	-80.76641	-66.02705	-50.25970	-33.08172	-13.96250	7.26370
-106.00000	-95.49836	-84.57139	-73.18172	-61.28508	-48.82845	-35.74808	-21.96946	-7.41449	7.97453	24.18739
-106.00000	-95.49836	-84.57139	-73.18171	-61.28502	-48.82776	-35.74283	-21.93963	-7.27924	8.48158	25.77050
-64.00000	-54.58501	-44.82214	-34.68139	-24.12773	-13.11979	-1.60816	10.46695	23.17792	36.61024	50.85544
-64.00000	-54.58501	-44.82214	-34.68139	-24.12773	-13.11977	-1.60791	10.46868	23.18767	36.65597	51.03956
-18.00000	-9.76619	-1.25032	7.57171	16.72782	26.25067	36.17889	46.55878	57.44660	68.91163	81.03966
-18.00000	-9.76619	-1.25032	7.57171	16.72782	26.25067	36.17890	46.55885	57.44709	68.91442	81.05337
32.00000	38.95617	46.13610	53.55882	61.24628	69.22402	77.52212	86.17633	95.22979	104.73535	114.75889
32.00000	38.95617	46.13610	53.55882	61.24628	69.22402	77.52212	86.17633	95.22981	104.73547	114.75959
86.00000	91.58081	97.33194	103.26783	109.40510	115.76307	122.36439	129.23590	136.40986	143.92555	151.83172
86.00000	91.58081	97.33194	103.26783	109.40510	115.76307	122.36439	129.23590	136.40986	143.92556	151.83174
144.00000	148.10690	152.33373	156.69063	161.18929	165.84326	170.66840	175.68349	180.91103	186.37838	192.11934
144.00000	148.10690	152.33373	156.69063	161.18929	165.84326	170.66840	175.68349	180.91103	186.37838	192.11934
206.00000	208.53385	211.13904	213.82161	216.58850	219.44776	222.40879	225.48274	228.68294	232.02557	235.53062
206.00000	208.53385	211.13904	213.82161	216.58850	219.44776	222.40879	225.48274	228.68294	232.02557	235.53062
272.00000	272.86124	273.74617	274.65679	275.59540	276.56468	277.56774	278.60829	279.69074	280.82045	282.00404
272.00000	272.86124	273.74617	274.65679	275.59540	276.56468	277.56774	278.60829	279.69074	280.82045	282.00404

-342.00000	-334.30136	-330.87060	-328.25942	-326.06399	-324.13348	-322.39096	-320.79083	-319.30337	-317.90799	-316.58966
-340.00000	-334.27096	-330.86925	-328.25932	-326.06398	-324.13348	-322.39096	-320.79083	-319.30337	-317.90799	-316.58966
-340.00000	-320.52527	-309.88557	-302.03174	-295.46697	-289.70792	-284.51791	-279.75804	-275.33824	-271.19611	-267.28628
-334.00000	-319.85201	-309.83294	-302.02668	-295.46641	-289.70785	-284.51790	-279.75804	-275.33824	-271.19611	-267.28628
-334.00000	-310.96415	-292.02756	-278.52552	-267.54104	-257.98197	-249.39855	-241.54552	-234.26764	-227.45835	-221.04055
-324.00000	-306.70025	-291.24892	-278.41357	-267.52482	-257.97956	-249.39820	-241.54547	-234.26763	-227.45835	-221.04055
-324.00000	-303.38182	-279.05755	-258.71185	-242.71058	-229.19695	-217.19864	-206.27644	-196.18568	-186.76716	-177.90811
-310.00000	-292.56034	-274.38487	-257.47417	-242.45561	-229.14846	-217.18979	-206.27489	-196.18542	-186.76712	-177.90810
-310.00000	-292.04831	-269.21672	-244.43630	-222.32522	-203.97780	-188.24253	-174.15505	-161.23673	-149.22953	-137.96933
-292.00000	-275.27993	-257.03132	-238.25418	-220.15014	-203.39359	-188.10590	-174.12571	-161.23089	-149.22846	-137.96915
-292.00000	-275.24409	-256.01201	-232.98482	-207.90316	-184.14800	-163.50635	-145.65973	-129.69002	-115.02072	-101.34780
-270.00000	-254.07032	-236.82333	-218.36516	-199.25234	-180.30806	-162.21212	-145.29855	-129.60111	-115.00105	-101.34390
-270.00000	-254.06885	-236.72649	-217.35123	-194.91465	-170.00832	-145.08550	-122.29535	-102.30785	-84.52821	-68.26817
-244.00000	-228.87257	-212.73055	-195.48699	-177.15936	-158.02731	-138.63994	-119.61583	-101.42242	-84.28127	-68.20826
-244.00000	-228.87253	-212.72491	-195.38594	-176.42209	-155.01939	-130.93087	-105.60206	-81.12708	-58.98475	-39.33666
-214.00000	-199.72326	-184.64856	-168.69642	-151.78031	-133.85702	-115.02667	-95.60979	-76.09980	-57.00800	-38.71134
-214.00000	-199.72326	-184.64834	-168.68997	-151.70997	-133.42215	-113.24625	-90.54990	-65.72197	-40.38742	-16.37013
-180.00000	-166.64485	-152.64496	-137.94006	-122.45645	-106.10913	-88.82235	-70.58577	-51.53606	-32.00053	-12.44200
-180.00000	-166.64485	-152.64495	-137.93977	-122.45197	-106.07092	-88.60455	-69.67407	-48.65617	-25.17373	0.00000
-142.00000	-129.64903	-116.76845	-103.31101	-89.22003	-74.42695	-58.84994	-42.39982	-25.00582	-6.67329	12.44200
-142.00000	-129.64903	-116.76845	-103.31100	-89.21983	-74.42463	-58.83265	-42.30477	-24.59512	-5.24674	16.37013
-100.00000	-88.74230	-77.04657	-64.87469	-52.18181	-38.91455	-25.00851	-10.38562	5.04660	21.38709	38.71134
-100.00000	-88.74230	-77.04657	-64.87469	-52.18181	-38.91445	-25.00754	-10.37890	5.08330	21.55228	39.33666
-54.00000	-43.92850	-33.49543	-22.66975	-11.41532	0.31034	12.55781	25.38810	38.87583	53.11262	68.20826
-54.00000	-43.92850	-33.49543	-22.66975	-11.41532	0.31035	12.55784	25.38844	38.87811	53.12527	68.26817
-4.00000	4.78997	13.87496	23.28013	33.03459	43.17231	53.73339	64.76578	76.32758	88.49041	101.34390
-4.00000	4.78997	13.87496	23.28013	33.03459	43.17231	53.73339	64.76579	76.32768	88.49109	101.34780
50.00000	57.41153	65.05812	72.95974	81.13941	89.62391	98.44472	107.63922	117.25248	127.33958	137.96915
50.00000	57.41153	65.05812	72.95974	81.13941	89.62391	98.44472	107.63922	117.25248	127.33960	137.96933
108.00000	113.93514	120.04970	126.35890	132.88024	139.63405	146.64415	153.93878	161.55183	169.52456	177.90810
108.00000	113.93514	120.04970	126.35890	132.88024	139.63405	146.64415	153.93878	161.55183	169.52456	177.90811
170.00000	174.36006	178.84668	183.47058	188.24408	193.18148	198.29952	203.61800	209.16064	214.95628	221.04055
170.00000	174.36006	178.84668	183.47058	188.24408	193.18148	198.29952	203.61800	209.16064	214.95628	221.04055
236.00000	238.68576	241.44690	244.28977	247.22173	250.25126	253.38832	256.64467	260.03438	263.57455	267.28628
236.00000	238.68576	241.44690	244.28977	247.22173	250.25126	253.38832	256.64467	260.03438	263.57455	267.28628
306.00000	306.91188	307.84880	308.81287	309.80652	310.83259	311.89437	312.99577	314.14145	315.33708	316.58966
306.00000	306.91188	307.84880	308.81287	309.80652	310.83259	311.89437	312.99577	314.14145	315.33708	316.58966

J = 19

0.19	-380.00000	-371.84718	-368.23662	-365.48395	-363.16893	-361.13300	-359.29514	-357.60731	-356.03823	-354.56616	-353.
1.19	-378.00000	-371.82616	-368.23586	-365.48391	-363.16893	-361.13300	-359.29514	-357.60731	-356.03823	-354.56616	-353.
1.18	-378.00000	-357.07426	-345.96299	-337.69726	-330.77674	-324.70277	-319.22759	-314.20528	-309.54106	-305.16926	-301.
2.18	-372.00000	-356.56570	-345.93106	-337.69467	-330.77650	-324.70274	-319.22759	-314.20528	-309.54106	-305.16926	-301.
2.17	-372.00000	-346.47779	-326.65428	-312.57822	-301.03132	-290.95689	-281.90270	-273.61510	-265.93192	-258.74145	-251.
3.17	-362.00000	-342.81385	-326.13192	-312.51586	-301.02358	-290.95589	-281.90257	-273.61508	-265.93192	-258.74145	-251.
3.16	-362.00000	-338.62638	-312.03041	-290.87435	-274.26927	-260.10140	-247.46755	-235.94779	-225.29617	-215.34865	-205.
4.16	-348.00000	-328.45691	-308.35790	-290.09667	-274.13518	-260.07946	-247.46407	-235.94726	-225.29610	-215.34864	-205.
4.15	-348.00000	-327.70046	-301.57840	-274.50101	-251.50283	-232.59083	-216.17753	-201.37533	-187.75947	-175.08530	-163.
5.15	-330.00000	-311.19162	-290.64415	-269.82169	-250.17499	-232.29401	-216.11803	-201.36425	-187.75755	-175.08499	-163.
5.14	-330.00000	-311.13107	-289.03051	-262.45869	-234.75770	-209.84384	-188.69454	-170.23674	-153.53080	-138.09626	-123.
6.14	-308.00000	-290.03176	-270.47122	-249.57321	-228.22505	-207.48818	-188.04360	-170.08292	-153.49822	-138.09003	-123.
6.13	-308.00000	-290.02895	-270.29142	-247.81677	-221.59661	-193.54617	-166.92401	-143.54231	-123.09721	-104.65007	-87.
7.13	-282.00000	-264.86832	-246.49866	-226.80074	-205.89435	-184.30452	-162.82643	-142.16852	-122.72130	-104.56119	-87.
7.12	-282.00000	-264.86823	-246.48669	-226.59270	-204.47023	-179.13962	-151.29856	-123.48088	-97.97794	-75.49296	-55.
8.12	-252.00000	-235.74109	-218.50867	-200.20275	-180.72818	-160.09876	-138.58801	-116.75480	-95.26141	-74.63459	-55.
8.11	-252.00000	-235.74109	-218.50813	-200.18738	-180.56586	-159.14941	-135.07576	-108.12426	-79.88167	-52.67139	-28.
9.11	-218.00000	-202.67762	-186.56774	-169.59439	-151.66410	-132.67691	-112.57837	-91.46541	-69.67816	-47.76291	-26.
9.10	-218.00000	-202.67762	-186.56772	-169.59360	-151.65202	-132.57707	-112.03576	-89.37325	-63.90418	-36.13428	-7.
10.10	-180.00000	-165.69239	-150.73533	-135.06970	-118.62362	-101.30946	-83.02612	-63.68151	-43.25632	-21.90212	0.
10.9	-180.00000	-165.69239	-150.73533	-135.06967	-118.62298	-101.30232	-82.97443	-63.40888	-42.15393	-18.48021	7.
11.9	-138.00000	-124.79345	-111.04571	-96.70911	-81.72708	-66.03149	-49.53953	-32.15171	-13.75848	5.72834	26.
11.8	-138.00000	-124.79345	-111.04571	-96.70911	-81.72705	-66.03112	-49.53608	-32.12842	-13.63599	6.24972	28.
12.8	-92.00000	-79.98556	-67.51894	-54.56104	-41.06610	-26.97996	-12.23758	3.24013	19.55008	36.80828	55.
12.7	-92.00000	-79.98556	-67.51894	-54.56104	-41.06610	-26.97994	-12.23741	3.24155	19.55938	36.85806	55.
13.7	-42.00000	-31.27167	-20.16742	-8.65505	3.30279	15.74990	28.73824	42.33028	56.60230	71.64882	87.
13.6	-42.00000	-31.27167	-20.16742	-8.65505	3.30279	15.74990	28.73825	42.33034	56.60281	71.65214	87.
14.6	12.00000	21.34626	31.00082	40.98992	51.34388	62.09808	73.29420	84.98193	97.22141	110.08657	123.
14.5	12.00000	21.34626	31.00082	40.98992	51.34388	62.09808	73.29420	84.98194	97.22143	110.08673	123.
15.5	70.00000	77.86695	85.98039	94.36123	103.03360	112.02552	121.36990	131.10584	141.28035	151.95087	163.
15.4	70.00000	77.86695	85.98039	94.36123	103.03360	112.02552	121.36990	131.10584	141.28035	151.95088	163.
16.4	132.00000	138.28948	144.76755	151.45018	158.35577	165.50566	172.92486	180.64302	188.69568	197.12610	205.
16.3	132.00000	138.28948	144.76755	151.45018	158.35577	165.50566	172.92486	180.64302	188.69568	197.12610	205.
17.3	198.00000	202.61321	207.35965	212.25058	217.29899	222.51990	227.93093	233.55291	239.41081	245.53494	251.
17.2	198.00000	202.61321	207.35965	212.25058	217.29899	222.51990	227.93093	233.55291	239.41081	245.53494	251.9
18.2	268.00000	270.83768	273.75475	276.75795	279.85498	283.05481	286.36791	289.80668	293.38593	297.12368	301.
18.1	268.00000	270.83768	273.75475	276.75795	279.85498	283.05481	286.36791	289.80668	293.38593	297.12368	301.
19.1	342.00000	342.96252	343.95142	344.96895	346.01765	347.10051	348.22101	349.38325	350.59217	351.85373	353.
19.0	342.00000	342.96252	343.95142	344.96895	346.01765	347.10051	348.22101	349.38325	350.59217	351.85373	353.

J = 20

0.20	-420.00000	-411.39470	-407.60291	-404.70859	-402.27395	-400.13256	-398.19936	-396.42383	-394.77310	-393.22435	-391.
1.20	-418.00000	-411.38022	-407.60248	-404.70857	-402.27394	-400.13256	-398.19936	-396.42383	-394.77310	-393.22435	-391.
1.19	-418.00000	-395.64279	-384.04642	-375.36457	-368.08742	-361.69823	-355.93774	-350.65287	-345.74415	-341.14264	-336.
2.19	-412.00000	-395.26342	-384.02723	-375.36325	-368.08731	-361.69822	-355.93774	-350.65287	-345.74415	-341.14264	-336.
2.18	-412.00000	-383.95883	-363.33066	-348.64903	-336.52836	-325.93540	-316.40926	-307.68647	-299.59757	-292.02561	-284.
3.18	-402.00000	-380.86451	-362.98725	-348.61483	-336.52471	-325.93499	-316.40922	-307.68647	-299.59757	-292.02561	-284.
3.17	-402.00000	-375.70128	-347.00672	-325.14182	-307.87562	-293.02548	-279.74669	-267.62576	-256.41144	-245.93371	-236.
4.17	-388.00000	-366.24127	-344.21384	-324.66823	-307.80676	-293.01576	-279.74534	-267.62558	-256.41142	-245.93371	-236.
4.16	-388.00000	-365.15635	-335.62870	-306.56981	-282.87475	-263.31650	-246.16230	-230.62044	-216.29727	-202.95146	-190.
5.16	-370.00000	-348.97665	-326.02941	-303.19147	-282.10151	-263.17092	-246.13715	-230.61637	-216.29665	-202.95137	-190.
5.15	-370.00000	-348.87749	-323.59035	-293.41652	-263.52185	-237.82992	-216.12058	-196.93005	-179.42753	-163.20299	-148.
6.15	-348.00000	-327.87152	-305.84547	-282.41418	-258.87567	-236.48043	-215.81006	-196.86725	-179.41602	-163.20108	-148.
6.14	-348.00000	-327.86633	-305.52551	-279.55289	-249.44576	-218.73635	-191.05066	-167.21561	-146.13816	-126.89305	-109.
7.14	-322.00000	-302.74799	-282.00021	-259.68059	-236.09038	-212.08127	-188.67326	-166.56483	-145.98795	-126.86264	-109.
7.13	-322.00000	-302.74781	-281.97593	-259.27459	-233.53613	-204.00932	-172.85847	-143.39550	-117.40887	-94.48538	-73.
8.13	-292.00000	-273.64658	-254.11700	-233.28781	-211.07075	-187.60202	-163.41722	-139.33227	-116.09778	-94.14442	-73.
8.12	-292.00000	-273.64658	-254.11575	-233.25323	-210.71953	-185.69594	-157.23111	-126.24403	-95.49675	-67.42015	-42.
9.12	-258.00000	-240.60056	-222.24963	-202.85197	-182.29136	-160.46272	-137.38190	-113.34270	-88.95059	-64.93378	-41.
9.11	-258.00000	-240.60056	-222.24958	-202.84994	-182.26097	-160.22074	-136.14860	-109.10322	-78.98145	-47.68496	-17.
10.11	-220.00000	-203.62771	-186.46889	-168.45020	-149.48103	-129.45120	-108.24436	-85.79727	-62.22070	-37.90682	-13.
10.10	-220.00000	-203.62771	-186.46888	-168.45011	-149.47917	-129.43094	-108.10268	-85.09016	-59.62100	-30.98730	0.
11.10	-178.00000	-162.73786	-146.81701	-130.17857	-112.75185	-94.45064	-75.16975	-54.78783	-33.19497	-10.37199	13.

-178.00000	-162.73786	-146.81701	-130.17857	-112.75176	-94.44942	-75.15859	-54.71491	-32.82962	-8.93422	17.83730
-132.00000	-117.93685	-103.31871	-88.09714	-72.21507	-55.60432	-38.18223	-19.84753	-0.47779	20.06172	41.87492
-132.00000	-117.93685	-103.31871	-88.09714	-72.21507	-55.60426	-38.18159	-19.84222	-0.44412	20.23413	42.60189
-82.00000	-69.22831	-55.98923	-42.24252	-27.94125	-13.03014	2.55684	18.89973	36.09702	54.27075	73.56806
-82.00000	-69.22831	-55.98923	-42.24252	-27.94125	-13.03014	2.55687	18.90002	36.09925	54.28487	73.64315
-28.00000	-16.61461	-4.83842	7.36196	20.02521	33.19658	46.92960	61.28844	76.35121	92.21461	109.00043
-28.00000	-16.61461	-4.83842	7.36196	20.02521	33.19658	46.92960	61.28846	76.35131	92.21544	109.00585
30.00000	39.90267	50.12714	60.70076	71.65514	83.02708	94.85990	107.20518	120.12520	133.69637	148.01428
30.00000	39.90267	50.12714	60.70076	71.65514	83.02708	94.85990	107.20518	120.12520	133.69641	148.01456
92.00000	100.32242	108.90285	117.76318	126.92862	136.42848	146.29714	156.57541	167.31233	178.56775	190.41599
92.00000	100.32242	108.90285	117.76318	126.92862	136.42848	146.29714	156.57541	167.31233	178.56775	190.41600
158.00000	164.64385	171.48547	178.54164	185.83161	193.37778	201.20634	209.34835	217.84104	226.72968	236.07032
158.00000	164.64385	171.48547	178.54164	185.83161	193.37778	201.20634	209.34835	217.84104	226.72968	236.07032
228.00000	232.86638	237.87265	243.03064	248.35399	253.85847	259.56257	265.48816	271.66144	278.11421	284.88577
228.00000	232.86638	237.87265	243.03064	248.35399	253.85847	259.56257	265.48816	271.66144	278.11421	284.88577
302.00000	304.98959	308.06261	311.22613	314.48825	317.85839	321.34756	324.96876	328.73759	332.67295	336.79817
302.00000	304.98959	308.06261	311.22613	314.48825	317.85839	321.34756	324.96876	328.73759	332.67295	336.79817
380.00000	381.01316	382.05405	383.12503	384.22878	385.36843	386.54765	387.77074	389.04290	390.37039	391.76096
380.00000	381.01316	382.05405	383.12503	384.22878	385.36843	386.54765	387.77074	389.04290	390.37039	391.76096

= 21

21	-462.00000	-452.94345	-448.96939	-445.93332	-443.37902	-441.13218	-439.10361	-437.24037	-435.50800	-433.88256	-432.34663
21	-460.00000	-452.93353	-448.96915	-445.93331	-443.37902	-441.13218	-439.10361	-437.24037	-435.50800	-433.88256	-432.34663
20	-460.00000	-436.22861	-424.13397	-415.03315	-407.39881	-400.69420	-394.64828	-389.10076	-383.94748	-379.11619	-374.55435
20	-454.00000	-435.94866	-424.12254	-415.03249	-407.39877	-400.69420	-394.64828	-389.10076	-383.94748	-379.11619	-374.55435
19	-454.00000	-423.42690	-402.04594	-386.73188	-374.03013	-362.91667	-352.91778	-343.75931	-335.26435	-327.31064	-319.80945
19	-444.00000	-420.85945	-401.82397	-386.71337	-374.02844	-362.91650	-352.91776	-343.75931	-335.26435	-327.31064	-319.80945
18	-444.00000	-414.62256	-384.03151	-361.48988	-343.51267	-327.96265	-314.03332	-301.30890	-289.53054	-278.52169	-268.15499
18	-430.00000	-405.91759	-381.97440	-361.20874	-343.47800	-327.95842	-314.03281	-301.30884	-289.53054	-278.52169	-268.15499
17	-430.00000	-404.40514	-371.43124	-340.73597	-316.40374	-296.11316	-278.17826	-261.88261	-246.84630	-232.82572	-219.64914
17	-412.00000	-388.63396	-363.20419	-338.40674	-315.97016	-296.04379	-278.16789	-261.88115	-246.84611	-232.82569	-219.64914
16	-412.00000	-388.47612	-359.67922	-325.98762	-294.38490	-268.09161	-245.69884	-225.69205	-207.35957	-190.33151	-174.37305
16	-390.00000	-367.58745	-342.94652	-316.92095	-291.27651	-267.36014	-245.55669	-225.66727	-207.35563	-190.33094	-174.37298
15	-390.00000	-367.57822	-342.39962	-312.53513	-278.65950	-245.90980	-217.58143	-193.18847	-171.32311	-151.20595	-132.44526
15	-364.00000	-342.50990	-319.22915	-294.12799	-267.79353	-241.46290	-216.30643	-192.89800	-171.26586	-151.19597	-132.44373
14	-364.00000	-342.50955	-319.18188	-293.37571	-263.54689	-229.85632	-196.09488	-165.74038	-139.35770	-115.76448	-94.05777
14	-334.00000	-313.43847	-291.46806	-267.94047	-242.80610	-216.41713	-189.64770	-163.52898	-138.77734	-115.63767	-94.03400
13	-334.00000	-313.43846	-291.46533	-267.86659	-242.09204	-212.91173	-179.86433	-145.50804	-113.30428	-84.89287	-59.62370
13	-300.00000	-280.41270	-259.68638	-237.70238	-214.32049	-189.45550	-163.27392	-136.36217	-109.59656	-83.77809	-59.35674
12	-300.00000	-280.41270	-259.68627	-237.69743	-214.24864	-188.90982	-160.72757	-128.80801	-94.47006	-60.83829	-30.40883
12	-262.00000	-243.45419	-223.96578	-203.44433	-181.77627	-158.82672	-134.48002	-108.76521	-82.02861	-54.96283	-28.38338
11	-262.00000	-243.45419	-223.96578	-203.44409	-181.77122	-158.77327	-134.12234	-107.11025	-76.70354	-43.08437	-8.67481
11	-220.00000	-202.57488	-184.35776	-165.27657	-145.24352	-124.15020	-101.86567	-78.25431	-53.24995	-27.00257	0.00000
10	-220.00000	-202.57488	-184.35776	-165.27656	-145.24325	-124.14646	-101.83251	-78.04637	-52.27418	-23.57651	8.67481
10	-174.00000	-157.78185	-140.89250	-123.27273	-104.85208	-85.54548	-65.24864	-43.83379	-21.15422	2.91762	28.38338
9	-174.00000	-157.78185	-140.89250	-123.27273	-104.85207	-85.54528	-65.24640	-43.81585	-21.04474	3.44659	30.40883
9	-124.00000	-109.07950	-93.58857	-77.47778	-60.68912	-43.15377	-24.78885	-5.49289	14.85962	36.42114	59.35674
8	-124.00000	-109.07950	-93.58857	-77.47778	-60.68912	-43.15377	-24.78873	-5.49175	14.86829	36.47410	59.62370
8	-70.00000	-56.47069	-42.45795	-27.92029	-12.80949	2.93113	19.36897	36.58535	54.68005	73.77755	94.03400
7	-70.00000	-56.47069	-42.45795	-27.92029	-12.80949	2.93113	19.36898	36.58541	54.68056	73.78136	94.05777
7	-12.00000	0.04265	12.49136	25.38079	38.75099	52.64877	67.12939	82.25892	98.11753	114.80423	132.44373
6	-12.00000	0.04265	12.49136	25.38079	38.75099	52.64877	67.12939	82.25892	98.11755	114.80443	132.44526
6	50.00000	60.45917	71.25382	82.41245	93.96796	105.95863	118.42947	131.43401	145.03681	159.31691	174.37298
5	50.00000	60.45917	71.25382	82.41245	93.96796	105.95863	118.42947	131.43401	145.03681	159.31692	174.37305
5	116.00000	124.77793	133.82547	143.16549	152.82431	162.83253	173.22603	184.04735	195.34760	207.18909	219.64914
4	116.00000	124.77793	133.82547	143.16549	152.82431	162.83253	173.22603	184.04735	195.34760	207.18909	219.64914
4	186.00000	192.99822	200.20346	207.63323	215.30772	223.25032	231.48846	240.05459	248.98764	258.33493	268.15499
3	186.00000	192.99822	200.20346	207.63323	215.30772	223.25032	231.48846	240.05459	248.98764	258.33493	268.15499
3	260.00000	265.11955	270.38566	275.81075	281.40907	287.19717	293.19441	299.42369	305.91245	312.69399	319.80945
2	260.00000	265.11955	270.38566	275.81075	281.40907	287.19717	293.19441	299.42369	305.91245	312.69399	319.80945
2	338.00000	341.14150	344.37048	347.69432	351.12154	354.66200	358.32724	362.13090	366.08932	370.22231	374.55435
1	338.00000	341.14150	344.37048	347.69432	351.12154	354.66200	358.32724	362.13090	366.08932	370.22231	374.55435
1	420.00000	421.06380	422.15668	423.28111	424.43991	425.63636	426.87429	428.15824	429.49364	430.88706	432.34663
0	420.00000	421.06380	422.15668	423.28111	424.43991	425.63636	426.87429	428.15824	429.49364	430.88706	432.34663

J = 22

0.22	-506.00000	-496.49310	-492.33601	-489.15812	-486.48414	-484.13183	-482.00789	-480.05694	-478.24292	-476.54078	-474.9
1.22	-504.00000	-496.48632	-492.33588	-489.15811	-486.48414	-484.13183	-482.00789	-480.05694	-478.24292	-476.54078	-474.9
1.21	-504.00000	-478.82898	-466.22439	-456.70271	-448.71079	-441.69060	-435.35913	-429.54890	-424.15101	-419.08990	-414.3
2.21	-498.00000	-478.62434	-466.21763	-456.70237	-448.71077	-441.69060	-435.35913	-429.54890	-424.15101	-419.08990	-414.3
2.20	-498.00000	-464.89902	-442.79030	-426.82291	-413.53541	-401.90014	-391.42789	-381.83338	-372.93208	-364.59640	-356.7
3.20	-488.00000	-462.80579	-442.64888	-426.81301	-413.53463	-401.90007	-391.42789	-381.83338	-372.93208	-364.59640	-356.7
3.19	-488.00000	-455.40846	-423.13099	-399.89573	-381.16988	-364.90911	-350.32576	-336.99620	-324.65278	-313.11205	-302.2
4.19	-474.00000	-447.49092	-421.65977	-399.73233	-381.15272	-364.90730	-350.32557	-336.99618	-324.65278	-313.11205	-302.2
4.18	-474.00000	-445.43912	-409.05572	-377.04751	-352.04541	-330.95473	-312.21511	-295.15736	-279.40413	-264.70647	-250.8
5.18	-456.00000	-430.16302	-402.18849	-375.50727	-351.80955	-330.92246	-312.21093	-295.15685	-279.40407	-264.70646	-250.8
5.17	-456.00000	-429.91838	-397.30663	-360.31507	-327.46048	-300.56215	-277.37064	-256.49705	-237.31606	-219.47638	-202.7
6.17	-434.00000	-409.17743	-381.77801	-353.13331	-325.49598	-300.18248	-277.30770	-256.48755	-237.31475	-219.47621	-202.7
6.16	-434.00000	-409.16147	-380.87912	-346.79057	-309.47102	-275.31472	-246.46742	-221.34618	-198.59240	-177.56349	-157.9
7.16	-408.00000	-384.15230	-358.17990	-330.15183	-301.06430	-272.55534	-245.82463	-221.22236	-198.57141	-177.56033	-157.9
7.15	-408.00000	-384.15162	-358.09140	-328.82816	-294.51261	-257.00344	-221.45095	-190.60907	-163.64981	-139.20395	-116.5
8.15	-378.00000	-355.11544	-330.55609	-304.15094	-275.94463	-246.62049	-217.42704	-189.50546	-163.40890	-139.15915	-116.5
8.14	-378.00000	-355.11542	-330.55036	-304.00048	-274.58102	-240.73190	-203.34116	-166.56698	-133.72195	-104.94546	-78.9
9.14	-344.00000	-322.11301	-298.87351	-274.13459	-247.73560	-219.66015	-190.33511	-160.70716	-131.85068	-104.48893	-78.8
9.13	-344.00000	-322.11301	-298.87324	-274.12317	-247.57524	-218.51519	-185.59150	-148.77144	-111.18161	-76.44330	-45.8
10.13	-306.00000	-285.17100	-263.22250	-240.04333	-215.49226	-189.41186	-161.72515	-132.65386	-102.88044	-73.37680	-44.9
10.12	-306.00000	-285.17100	-263.22249	-240.04270	-215.47938	-189.28005	-160.89228	-129.18676	-93.43833	-55.61202	-19.2
11.12	-264.00000	-244.30382	-223.66510	-201.99617	-179.18845	-155.10661	-129.59361	-102.52519	-73.96379	-44.35235	-14.5
11.11	-264.00000	-244.30382	-223.66510	-201.99614	-179.18769	-155.09598	-129.50249	-101.98334	-71.64421	-37.39782	0.0
12.11	-218.00000	-199.51997	-180.23793	-160.08212	-138.96624	-116.78466	-93.40669	-68.67532	-42.43374	-14.62609	14.5
12.10	-218.00000	-199.51997	-180.23793	-160.08212	-138.96620	-116.78402	-93.39955	-68.61992	-42.11193	-13.19096	19.2
13.10	-168.00000	-150.82474	-132.96344	-114.35610	-94.93186	-74.60587	-53.27485	-30.81113	-7.05765	18.16336	44.9
13.9	-168.00000	-150.82474	-132.96344	-114.35610	-94.93186	-74.60584	-53.27443	-30.80700	-7.02724	18.34052	45.8
14.9	-114.00000	-98.22157	-81.85606	-64.85282	-47.15267	-28.68569	-9.36818	10.90178	32.25038	54.83546	78.8
14.8	-114.00000	-98.22157	-81.85606	-64.85282	-47.15267	-28.68569	-9.36816	10.90201	32.25250	54.85080	78.9
15.8	-56.00000	-41.71277	-26.92544	-11.59520	4.32762	20.90125	38.19471	56.29100	75.29152	95.32253	116.5
15.7	-56.00000	-41.71277	-26.92544	-11.59520	4.32762	20.90125	38.19471	56.29101	75.29163	95.32352	116.5
16.7	6.00000	18.70005	31.82176	45.40105	59.47943	74.10532	89.33583	105.23906	121.89751	139.41272	157.9
16.6	6.00000	18.70005	31.82176	45.40105	59.47943	74.10532	89.33583	105.23906	121.89751	139.41277	157.9
17.6	72.00000	83.01574	94.38079	106.12482	118.28204	130.89223	144.00214	157.66733	171.95469	186.94602	202.7
17.5	72.00000	83.01574	94.38079	106.12482	118.28204	130.89223	144.00214	157.66733	171.95469	186.94603	202.7
18.5	142.00000	151.23347	160.74822	170.56810	180.72056	191.23749	202.15628	213.52123	225.38556	237.81407	250.8
18.4	142.00000	151.23347	160.74822	170.56810	180.72056	191.23749	202.15628	213.52123	225.38556	237.81407	250.8
19.4	216.00000	223.35262	230.92149	238.72494	246.78403	255.12321	263.77109	272.76158	282.13527	291.94155	302.2
19.3	216.00000	223.35262	230.92149	238.72494	246.78403	255.12321	263.77109	272.76158	282.13527	291.94155	302.2
20.3	294.00000	299.37272	304.89869	310.59089	316.46422	322.53598	328.82642	335.35946	342.16378	349.27420	356.7
20.2	294.00000	299.37272	304.89869	310.59089	316.46422	322.53598	328.82642	335.35946	342.16378	349.27420	356.7
21.2	376.00000	379.29342	382.67835	386.16252	389.75485	393.46564	397.30696	401.29309	405.44112	409.77178	414.3
21.1	376.00000	379.29342	382.67835	386.16252	389.75485	393.46564	397.30696	401.29309	405.44112	409.77178	414.3
22.1	462.00000	463.11444	464.25931	465.43720	466.65104	467.90429	469.20094	470.54575	471.94438	473.40374	474.9
22.0	462.00000	463.11444	464.25931	465.43720	466.65104	467.90429	469.20094	470.54575	471.94438	473.40374	474.9

J = 23

0.23	-552.00000	-542.04341	-537.70274	-534.38297	-531.58930	-529.13151	-526.91219	-524.87353	-522.97785	-521.19902	-519.5
1.23	-550.00000	-542.03879	-537.70267	-534.38297	-531.58930	-529.13151	-526.91219	-524.87353	-522.97785	-521.19902	-519.5
1.22	-550.00000	-523.44119	-510.31686	-500.37302	-492.02325	-484.68735	-478.07027	-471.99726	-466.35470	-461.06374	-456.0
2.22	-544.00000	-523.29284	-510.31288	-500.37285	-492.02324	-484.68735	-478.07027	-471.99726	-466.35470	-461.06374	-456.0
2.21	-544.00000	-508.38837	-485.55581	-468.91969	-455.04342	-442.88542	-431.93935	-421.90847	-412.60060	-403.88278	-395.6
3.21	-534.00000	-506.71039	-485.46682	-468.91445	-455.04306	-442.88539	-431.93935	-421.90847	-412.60060	-403.88278	-395.6
3.20	-534.00000	-498.07903	-464.31320	-440.34171	-420.84085	-403.86257	-388.62286	-374.68693	-361.77762	-349.70441	-338.3
4.20	-520.00000	-490.96712	-463.28798	-440.24841	-420.83249	-403.86181	-388.62279	-374.68693	-361.77762	-349.70441	-338.3
4.19	-520.00000	-488.25508	-448.57493	-415.51024	-389.76337	-367.82569	-348.26700	-330.44191	-313.96904	-298.59252	-284.1
5.19	-502.00000	-473.56395	-443.00449	-414.52747	-389.63822	-367.81099	-348.26534	-330.44175	-313.96902	-298.59252	-284.1
5.18	-502.00000	-473.19419	-436.50432	-396.54473	-362.77619	-335.17415	-311.10092	-289.33119	-269.29077	-250.63408	-233.1
6.18	-480.00000	-452.63934	-422.34720	-391.09559	-361.59364	-334.98377	-311.07382	-289.32764	-269.29034	-250.63403	-233.1
6.17	-480.00000	-452.61248	-420.92618	-382.39823	-342.12452	-307.05840	-277.60491	-251.61503	-227.91493	-205.95244	-185.4
7.17	-454.00000	-427.67333	-398.84779	-367.76973	-335.97329	-305.45467	-277.29593	-251.56418	-227.90748	-205.95147	-185.4
7.16	-454.00000	-427.67206	-398.68799	-365.56039	-326.54437	-285.81515	-249.20522	-217.89618	-190.14562	-164.73747	-141.0
8.16	-424.00000	-398.67608	-371.37505	-341.91208	-310.51208	-278.30935	-246.89862	-217.38071	-190.05045	-164.72230	-141.0
8.15	-424.00000	-398.67604	-371.36348	-341.61935	-308.07201	-269.24793	-228.14690	-189.95587	-156.76598	-127.35576	-100.4
9.15	-390.00000	-365.70040	-339.80620	-312.13718	-282.52506	-251.10398	-218.68329	-186.57385	-155.90410	-127.18089	-100.3
9.14	-390.00000	-365.70040	-339.80561	-312.11204	-282.18635	-248.87567	-210.73074	-169.55241	-129.93472	-94.84451	-63.8
10.14	-352.00000	-328.77729	-304.23527	-278.23779	-250.61119	-221.18734	-189.99928	-157.58808	-125.02035	-93.42833	-63.5
10.13	-352.00000	-328.77729	-304.23525	-278.23624	-250.58013	-220.88260	-188.21560	-151.14392	-110.32907	-69.62880	-32.6
11.13	-310.00000	-287.92398	-264.73600	-240.32994	-214.57191	-187.29488	-158.32376	-127.60301	-95.44951	-62.69561	-30.4
11.12	-310.00000	-287.92398	-264.73600	-240.32987	-214.56982	-187.26663	-158.09130	-126.31451	-90.60245	-50.65320	-9.3
12.12	-264.00000	-243.15063	-221.35251	-198.51932	-174.54585	-149.30143	-122.62386	-94.33027	-64.29558	-32.65156	0.0
12.11	-264.00000	-243.15063	-221.35251	-198.51932	-174.54574	-149.29949	-122.60276	-94.17306	-63.43954	-29.24860	9.3

11	-214.00000	-194.46354	-174.11173	-152.87248	-130.65993	-107.37011	-82.87490	-57.01499	-29.60093	-0.45636	30.43567
10	-214.00000	-194.46354	-174.11173	-152.87248	-130.65992	-107.37000	-82.87347	-57.00131	-29.50411	0.07453	32.68479
10	-160.00000	-141.86680	-123.03094	-103.43136	-82.99631	-61.64047	-39.26072	-15.73024	9.10933	35.45322	63.51500
9	-160.00000	-141.86680	-123.03094	-103.43136	-82.99631	-61.64046	-39.26065	-15.72934	9.11729	35.50852	63.82640
9	-102.00000	-85.36319	-68.12170	-50.22353	-31.60811	-12.20415	8.07338	29.32742	51.68487	75.30513	100.38974
8	-102.00000	-85.36319	-68.12170	-50.22353	-31.60811	-12.20415	8.07339	29.32747	51.68536	75.30936	100.41944
8	-40.00000	-24.95461	-9.39195	6.73217	23.46896	40.87832	59.03112	78.01231	97.92531	118.89840	141.09416
7	-40.00000	-24.95461	-9.39195	6.73217	23.46896	40.87832	59.03112	78.01231	97.92533	118.89865	141.09626
7	26.00000	39.35757	53.15265	67.42246	82.21000	97.56538	113.54759	130.22693	147.68837	166.03625	185.40135
6	26.00000	39.35757	53.15265	67.42246	82.21000	97.56538	113.54759	130.22693	147.68837	166.03626	185.40146
6	96.00000	107.57236	119.50800	131.83775	144.59715	157.82751	171.57736	185.90431	200.87766	216.58209	233.12291
5	96.00000	107.57236	119.50800	131.83775	144.59715	157.82751	171.57736	185.90431	200.87766	216.58209	233.12291
5	170.00000	179.68903	189.67107	199.97096	210.61727	221.64320	233.08765	244.99672	257.42574	270.44206	284.12914
4	170.00000	179.68903	189.67107	199.97096	210.61727	221.64320	233.08765	244.99672	257.42574	270.44206	284.12914
4	248.00000	255.70702	263.63957	271.81675	280.26053	288.99639	298.05417	307.46919	317.28376	327.54934	338.32950
3	248.00000	255.70702	263.63957	271.81675	280.26053	288.99639	298.05417	307.46919	317.28376	327.54934	338.32950
3	330.00000	335.62590	341.41174	347.37106	353.51943	359.87489	366.45856	373.29543	380.41539	387.85478	395.65843
2	330.00000	335.62590	341.41174	347.37106	353.51943	359.87489	366.45856	373.29543	380.41539	387.85478	395.65843
2	416.00000	419.44534	422.98622	426.63073	430.38816	434.26929	438.28671	442.45533	446.79298	451.32132	456.06704
1	416.00000	419.44534	422.98622	426.63073	430.38816	434.26929	438.28671	442.45533	446.79298	451.32132	456.06704
1	506.00000	507.16508	508.36194	509.59328	510.86218	512.17222	513.52759	514.93325	516.39513	517.92042	519.51800
0	506.00000	507.16508	508.36194	509.59328	510.86218	512.17222	513.52759	514.93325	516.39513	517.92042	519.51800

= 24

24	-600.00000	-589.59419	-585.06956	-581.60788	-578.69450	-576.13122	-573.81652	-571.69013	-569.71280	-567.85727	-566.10370
.24	-598.00000	-589.59106	-585.06952	-581.60788	-578.69450	-576.13122	-573.81652	-571.69013	-569.71280	-567.85727	-566.10370
.23	-598.00000	-570.06282	-556.41082	-546.04395	-537.33612	-529.68441	-522.78164	-516.44581	-510.55854	-505.03770	-499.82352
.23	-592.00000	-569.95605	-556.40849	-546.04387	-537.33612	-529.68441	-522.78164	-516.44581	-510.55854	-505.03770	-499.82352
.22	-592.00000	-553.90368	-530.33653	-513.02068	-498.55361	-485.87222	-474.45195	-463.98443	-454.26981	-445.16969	-436.58356
.22	-582.00000	-552.57972	-530.28114	-513.01793	-498.55345	-485.87221	-474.45195	-463.98443	-454.26981	-445.16969	-436.58356
.21	-582.00000	-542.65585	-507.57312	-482.81527	-462.52169	-444.82154	-428.92380	-414.38053	-400.90465	-388.29845	-376.41881
.21	-568.00000	-536.35273	-506.87444	-482.76281	-462.51766	-444.82122	-428.92377	-414.38053	-400.90465	-388.29845	-376.41881
.20	-568.00000	-532.85505	-490.05971	-456.10407	-429.53213	-406.71696	-386.33034	-367.73434	-350.53978	-334.48297	-319.37448
.20	-550.00000	-518.83769	-485.67554	-455.49530	-429.46711	-406.71038	-386.32969	-367.73428	-350.53977	-334.48297	-319.37448
.19	-550.00000	-518.29209	-477.32235	-434.80799	-400.30154	-371.87804	-346.86969	-324.18658	-303.27975	-283.80213	-265.51023
.19	-528.00000	-497.97114	-464.66528	-430.85392	-399.61737	-371.78523	-346.85829	-324.18528	-303.27962	-283.80212	-265.51023
.18	-528.00000	-497.92709	-462.50502	-419.47645	-376.84074	-341.12333	-310.90431	-283.95322	-259.27416	-236.36507	-214.90692
.18	-502.00000	-473.07105	-441.22964	-407.00833	-372.59551	-340.23963	-310.76129	-283.93297	-259.27159	-236.36478	-214.90689
.17	-502.00000	-473.06876	-440.95085	-403.51535	-359.83428	-316.64185	-279.41701	-247.45936	-218.76226	-192.33154	-167.67826
.17	-472.00000	-444.11893	-413.91880	-381.22103	-346.55083	-311.59261	-278.18567	-247.23046	-218.72614	-192.32658	-167.67767
.16	-472.00000	-444.11885	-413.89624	-380.67624	-342.47234	-298.70653	-254.79406	-215.92195	-182.25878	-151.97120	-123.99551
.16	-438.00000	-411.17374	-382.47938	-351.69872	-318.68480	-283.84071	-248.46225	-214.14335	-181.88797	-151.90761	-123.98629
.15	-438.00000	-411.17373	-382.47809	-351.64579	-318.00713	-279.83926	-236.38576	-191.83165	-151.28562	-115.92425	-84.16790
.15	-400.00000	-374.27214	-347.00014	-318.01766	-287.11528	-254.14397	-219.35869	-183.74061	-148.69593	-115.32783	-84.05887
.14	-400.00000	-374.27214	-347.00008	-318.01398	-287.04424	-253.48272	-215.86922	-173.11295	-128.18610	-86.06639	-49.00481
.14	-358.00000	-333.43462	-307.56729	-280.26997	-251.37802	-220.68966	-188.03717	-153.53507	-117.89479	-82.34546	-48.06714
.13	-358.00000	-333.43462	-307.56729	-280.26978	-251.37264	-220.61902	-187.48552	-150.75823	-109.06905	-64.17113	-20.72222
.13	-312.00000	-288.67320	-264.23360	-238.57794	-211.57832	-183.07358	-152.86626	-120.76613	-86.76658	-51.34115	-15.53295
.12	-312.00000	-288.67320	-264.23360	-238.57793	-211.57801	-183.06806	-152.80819	-120.35498	-84.71729	-44.40211	0.00000
.12	-262.00000	-239.99536	-217.03121	-193.02162	-167.86312	-141.42880	-113.56025	-84.06163	-52.72213	-19.43605	15.53295
.11	-262.00000	-239.99536	-217.03121	-193.02162	-167.86310	-141.42847	-113.55572	-84.01988	-52.44097	-18.01500	20.72222
.11	-208.00000	-187.40594	-165.98071	-143.65143	-120.33193	-95.91879	-70.28567	-43.27536	-14.69144	15.69454	48.06714
.10	-208.00000	-187.40594	-165.98071	-143.65143	-120.33193	-95.91877	-70.28540	-43.27219	-14.66430	15.87429	49.00481
.10	-150.00000	-130.90822	-111.09578	-90.50034	-69.04898	-46.65534	-23.21573	1.39655	27.33936	54.81199	84.05887
.9	-150.00000	-130.90822	-111.09578	-90.50034	-69.04898	-46.65534	-23.21572	1.39674	27.34134	54.82831	84.16790
.9	-88.00000	-70.50446	-52.38588	-33.59082	-14.05718	6.28796	27.53126	49.77721	73.15398	97.82205	123.98629
.8	-88.00000	-70.50446	-52.38588	-33.59082	-14.05718	6.28796	27.53126	49.77722	73.15409	97.82318	123.99551
.8	-22.00000	-6.19626	10.14232	27.06137	44.61369	62.86098	81.87606	101.74608	122.57679	144.49894	167.67767
.7	-22.00000	-6.19626	10.14232	27.06137	44.61369	62.86098	81.87606	101.74608	122.57680	144.49900	167.67826
.7	48.00000	62.01519	76.48395	91.44482	106.94233	123.02829	139.76368	157.22108	175.48803	194.67189	214.90689
.6	48.00000	62.01519	76.48395	91.44482	106.94233	123.02829	139.76368	157.22108	175.48803	194.67190	214.90692
.6	122.00000	134.12904	146.63541	159.55114	172.91311	186.76419	201.15468	216.14430	231.80482	248.22386	265.51023
.5	122.00000	134.12904	146.63541	159.55114	172.91311	186.76419	201.15468	216.14430	231.80482	248.22386	265.51023
.5	200.00000	210.14462	220.59402	231.37403	242.51436	254.04953	266.01996	278.47356	291.46778	305.07255	319.37448
.4	200.00000	210.14462	220.59402	231.37403	242.51436	254.04953	266.01996	278.47356	291.46778	305.07255	319.37448
.4	282.00000	290.06143	298.35768	306.90864	315.73718	324.86982	334.33762	344.17733	354.43298	365.15810	376.41881
.3	282.00000	290.06143	298.35768	306.90864	315.73718	324.86982	334.33762	344.17733	354.43298	365.15810	376.41881
.3	368.00000	373.87907	379.92479	386.15126	392.57469	399.21388	406.09083	413.23156	420.66723	428.43567	436.58356
.2	368.00000	373.87907	379.92479	386.15126	392.57469	399.21388	406.09083	413.23156	420.66723	428.43567	436.58356
.2	458.00000	461.59725	465.29409	469.09894	473.02149	477.07296	481.26649	485.61760	490.14490	494.87092	499.82352
.1	458.00000	461.59725	465.29409	469.09894	473.02149	477.07296	481.26649	485.61760	490.14490	494.87092	499.82352
.1	552.00000	553.21572	554.46458	555.74936	557.07331	558.44015	559.85424	561.32076	562.84589	564.43712	566.10370
.0	552.00000	553.21572	554.46458	555.74936	557.07331	558.44015	559.85424	561.32076	562.84589	564.43712	566.10370

J = 25

0.25	-650.00000	-639.14534	-634.43645	-630.83283	-627.79974	-625.13096	-622.72087	-620.50675	-618.44775	-616.51552	-614.68
1.25	-648.00000	-639.14322	-634.43642	-630.83283	-627.79974	-625.13096	-622.72087	-620.50675	-618.44775	-616.51552	-614.68
1.24	-648.00000	-618.69182	-604.50589	-593.71539	-584.64935	-576.68174	-569.49321	-562.89451	-556.76251	-551.01175	-545.58
2.24	-642.00000	-618.61547	-604.50454	-593.71535	-584.64935	-576.68174	-569.49321	-562.89451	-556.76251	-551.01175	-545.58
2.23	-642.00000	-601.44936	-577.12818	-559.12486	-544.06561	-530.86031	-518.96552	-508.06115	-497.93959	-488.45705	-479.50
3.23	-632.00000	-600.41975	-577.09402	-559.12343	-544.06554	-530.86030	-518.96552	-508.06115	-497.93959	-488.45705	-479.50
3.22	-632.00000	-589.16169	-552.89903	-527.30799	-506.20993	-487.78499	-471.22794	-456.07655	-442.03354	-428.89392	-416.50
4.22	-618.00000	-583.65485	-552.43180	-527.27888	-506.20801	-487.78486	-471.22793	-456.07655	-442.03354	-428.89392	-416.50
4.21	-618.00000	-579.24636	-533.57179	-498.80010	-471.33513	-447.62305	-426.40279	-407.03327	-389.11538	-372.37711	-356.62
5.12	-600.00000	-565.98601	-530.22520	-498.43210	-471.30195	-447.62015	-426.40254	-407.03325	-389.11538	-372.37711	-356.62
5.20	-600.00000	-565.19950	-519.82392	-475.20084	-439.98590	-410.64184	-384.66548	-361.05837	-339.28027	-318.97870	-299.90
6.20	-578.00000	-545.17097	-508.74727	-472.45337	-439.60251	-410.59766	-384.66079	-361.05791	-339.28023	-318.97870	-299.90
6.19	-578.00000	-545.10040	-505.58982	-458.16817	-413.77330	-377.43529	-346.30597	-318.33770	-292.66063	-268.79638	-246.42
7.19	-552.00000	-520.34344	-485.32436	-447.90269	-411.00420	-376.96839	-346.24178	-318.32985	-292.65976	-268.79630	-246.42
7.18	-552.00000	-520.33942	-484.85387	-442.67421	-394.62283	-349.74348	-312.00360	-279.19300	-249.45508	-221.96836	-196.28
8.18	-522.00000	-491.44243	-458.18120	-422.08102	-384.11875	-346.57968	-311.38182	-279.09536	-249.44183	-221.96678	-196.28
8.17	-522.00000	-491.44227	-458.13871	-421.11097	-377.76027	-329.45403	-283.70965	-244.42954	-210.02861	-178.70855	-149.63
9.17	-488.00000	-458.53182	-426.88765	-392.80845	-356.22207	-317.95011	-279.82458	-243.56048	-209.87717	-178.68639	-149.63
9.16	-488.00000	-458.53181	-426.88495	-392.70155	-354.93871	-311.34546	-262.99450	-216.25396	-175.35915	-139.43949	-106.70
10.16	-450.00000	-421.65460	-391.51288	-359.37225	-324.98818	-288.28920	-249.89970	-211.31027	-174.11961	-139.20481	-106.66
10.15	-450.00000	-421.65460	-391.51275	-359.36396	-324.83361	-286.94434	-243.70898	-195.56693	-147.89194	-105.36184	-67.97
11.15	-408.00000	-380.83494	-352.15560	-321.80778	-289.58984	-255.26735	-218.73552	-180.42419	-141.54096	-103.59517	-67.62
11.14	-408.00000	-380.83494	-352.15560	-321.80730	-289.57666	-255.10076	-217.51945	-175.05794	-127.44269	-79.04965	-34.93
12.14	-362.00000	-336.08703	-308.87844	-280.25118	-250.05009	-218.07721	-184.10123	-147.97245	-109.94276	-70.96680	-32.46
12.13	-362.00000	-336.08703	-308.87844	-280.25116	-250.04924	-218.06243	-183.95184	-146.98208	-105.58190	-58.83903	-10.05
13.13	-312.00000	-287.41965	-261.71958	-234.79794	-206.53053	-176.76277	-145.29958	-111.90802	-76.39355	-38.85104	0.00
13.12	-312.00000	-287.41965	-261.71958	-234.79794	-206.53049	-176.76177	-145.28626	-111.79005	-75.64815	-35.49391	10.05
14.12	-258.00000	-234.83852	-210.70337	-185.50832	-159.15051	-131.50517	-102.41794	-71.69471	-39.09795	-4.39268	32.46
14.11	-258.00000	-234.83852	-210.70337	-185.50832	-159.15050	-131.50512	-102.41703	-71.68437	-39.01309	-3.86457	34.93
15.11	-200.00000	-178.34746	-155.84597	-132.42160	-107.98734	-82.43946	-55.65227	-27.47048	2.30142	33.90797	67.62
15.10	-200.00000	-178.34746	-155.84597	-132.42160	-107.98733	-82.43945	-55.65222	-27.46979	2.30861	33.96488	67.97
16.10	-138.00000	-117.94914	-97.15851	-75.56439	-53.09239	-29.65479	-5.14673	20.55918	47.62072	76.23747	106.66
16.9	-138.00000	-117.94914	-97.15851	-75.56439	-53.09239	-29.65479	-5.14673	20.55922	47.62119	76.24206	106.70
17.9	-72.00000	-53.64545	-34.64888	-14.95536	5.49888	26.78852	49.00213	72.24613	96.65053	122.37736	149.63
17.8	-72.00000	-53.64545	-34.64888	-14.95536	5.49888	26.78852	49.00213	72.24613	96.65056	122.37765	149.63
18.8	-2.00000	14.56224	31.67723	49.39206	67.76120	86.84817	106.72792	127.48992	149.24253	172.11932	196.28
18.7	-2.00000	14.56224	31.67723	49.39206	67.76120	86.84817	106.72792	127.48992	149.24253	172.11934	196.28
19.7	72.00000	86.67289	101.81558	117.46797	133.67610	150.49357	167.98336	186.22038	205.29491	225.31745	246.42
19.6	72.00000	86.67289	101.81558	117.46797	133.67610	150.49357	167.98336	186.22038	205.29491	225.31746	246.42
20.6	150.00000	162.68575	175.76299	189.26493	203.22979	217.70203	232.73376	248.38682	264.73549	281.87037	299.90
20.5	150.00000	162.68575	175.76299	189.26493	203.22979	217.70203	232.73376	248.38682	264.73549	281.87037	299.90
21.5	232.00000	242.60022	253.51704	264.77727	276.41178	288.45640	300.95308	313.95154	327.51139	341.70516	356.62
21.4	232.00000	242.60022	253.51704	264.77727	276.41178	288.45640	300.95308	313.95154	327.51139	341.70516	356.62
22.4	318.00000	326.41584	335.07582	344.00061	353.21397	362.74347	372.62139	382.88592	393.58283	404.76770	416.50
22.3	318.00000	326.41584	335.07582	344.00061	353.21397	362.74347	372.62139	382.88592	393.58283	404.76770	416.50
23.3	408.00000	414.13226	420.43786	426.93148	433.62999	440.55294	447.72320	455.16785	462.91927	471.01682	479.50
23.2	408.00000	414.13226	420.43786	426.93148	433.62999	440.55294	447.72320	455.16785	462.91927	471.01682	479.50
24.2	502.00000	505.74917	509.60197	513.56716	517.65483	521.87665	526.24629	530.77991	535.49685	540.42059	545.58
24.1	502.00000	505.74917	509.60197	513.56716	517.65483	521.87665	526.24629	530.77991	535.49685	540.42059	545.58
25.1	600.00000	601.26636	602.56721	603.90545	605.28445	606.70808	608.18090	609.70828	611.29665	612.95381	614.68
25.0	600.00000	601.26636	602.56721	603.90545	605.28445	606.70808	608.18090	609.70828	611.29665	612.95381	614.68

J = 26

0.26	-702.00000	-690.69674	-685.80339	-682.05782	-678.90500	-676.13072	-673.62523	-671.32338	-669.18272	-667.17379	-665.27
1.26	-700.00000	-690.69531	-685.80338	-682.05782	-678.90500	-676.13072	-673.62523	-671.32338	-669.18272	-667.17379	-665.27
1.25	-700.00000	-669.32652	-654.60184	-643.38727	-633.96289	-625.67930	-618.20497	-611.34336	-604.96658	-598.98589	-593.3
2.25	-694.00000	-669.27225	-654.60106	-643.38725	-633.96289	-625.67930	-618.20497	-611.34336	-604.96658	-598.98589	-593.3
2.24	-694.00000	-651.02623	-625.92773	-607.23156	-591.57914	-577.84950	-565.47992	-554.13852	-543.60988	-533.74481	-524.4
3.24	-684.00000	-650.23589	-625.90684	-607.23082	-591.57911	-577.84950	-565.47992	-554.13852	-543.60988	-533.74481	-524.4
3.23	-684.00000	-637.61982	-600.27746	-573.81431	-551.90397	-532.75218	-515.53482	-499.77464	-485.16401	-471.49062	-458.6
4.23	-670.00000	-632.88094	-599.96999	-573.79835	-551.90307	-532.75213	-515.53481	-499.77464	-485.16401	-471.49062	-458.6
4.22	-670.00000	-627.44109	-579.15647	-543.57114	-515.16191	-490.54055	-468.48272	-448.33766	-429.69509	-412.27439	-395.8
5.22	-652.00000	-615.01164	-576.67627	-543.35317	-515.14524	-490.53929	-468.48262	-448.33765	-429.69509	-412.27439	-395.8
5.21	-652.00000	-613.90341	-564.08109	-517.77082	-481.78234	-451.44602	-424.48145	-399.94334	-377.29031	-356.16238	-336.3
6.21	-630.00000	-594.23722	-554.61167	-515.93537	-481.57305	-451.42542	-424.47955	-399.94318	-377.29030	-356.16238	-336.3
6.20	-630.00000	-594.12666	-550.17297	-498.62924	-452.98372	-415.91814	-383.77405	-354.75543	-328.06840	-303.24286	-279.9
7.20	-604.00000	-569.48842	-531.13361	-490.49466	-451.26544	-415.67961	-383.74599	-354.75246	-328.06811	-303.24283	-279.9
7.19	-604.00000	-569.48153	-530.36516	-483.07271	-431.17063	-385.23136	-346.85044	-313.03304	-282.20005	-253.63753	-226.9
8.19	-574.00000	-540.64496	-504.15644	-464.50294	-423.28571	-383.37000	-346.54977	-312.99275	-282.19533	-253.63705	-226.9
8.18	-574.00000	-540.64466	-504.07890	-462.85214	-414.01761	-361.87836	-315.11638	-275.32680	-239.96512	-207.52478	-177.3
9.18	-540.00000	-507.77339	-473.02532	-435.45725	-395.15867	-353.53283	-312.91341	-274.92527	-239.90581	-207.51733	-177.3
9.17	-540.00000	-507.77338	-473.01989	-435.24977	-392.86451	-343.49704	-291.08968	-243.23504	-201.99748	-165.21028	-131.3
10.17	-502.00000	-470.92367	-437.76904	-402.29037	-364.21716	-323.65327	-281.75340	-240.49376	-201.44569	-165.12268	-131.3
10.16	-502.00000	-470.92366	-437.76876	-402.27244	-363.89673	-321.10039	-271.80700	-219.18249	-170.13486	-127.43583	-89.3

16	-460.00000	-430.12414	-398.49738	-364.93431	-329.18966	-291.00979	-250.45172	-208.42716	-166.64501	-126.67218	-89.20505
15	-460.00000	-430.12414	-398.49737	-364.93316	-329.15889	-290.63868	-247.97445	-199.18689	-146.50760	-96.30005	-52.15115
15	-414.00000	-385.39143	-355.28412	-323.53185	-289.94652	-254.28718	-216.30243	-175.97696	-133.99692	-91.84678	-51.10498
14	-414.00000	-385.39143	-355.28412	-323.53180	-289.94429	-254.24979	-215.94248	-173.79175	-125.84851	-73.36372	-22.14330
14	-364.00000	-336.73584	-308.17439	-278.19551	-246.65050	-213.35116	-178.05955	-140.51689	-100.62948	-58.87654	-16.53656
13	-364.00000	-336.73584	-308.17439	-278.19551	-246.65037	-213.34831	-178.02282	-140.20743	-98.83419	-51.99685	0.00000
13	-310.00000	-284.16402	-257.19684	-228.99706	-199.44245	-168.38292	-135.63007	-100.94621	-64.06000	-24.80227	16.53656
.13	-306.00000	-278.90678	-250.66740	-221.18019	-190.32373	-157.95051	-123.87747	-87.87249	-49.64477	-8.89062	34.46433
.12	-306.00000	-278.90678	-250.66740	-221.18019	-190.32373	-157.95048	-123.87689	-87.86473	-49.57092	-8.36918	37.16473
.12	-244.00000	-218.52145	-192.03359	-164.44835	-135.66192	-105.55028	-73.96277	-40.71249	-5.56239	31.78817	71.67736
.11	-244.00000	-218.52145	-192.03359	-164.44835	-135.66192	-105.55028	-73.96274	-40.71195	-5.55597	31.84603	72.08274
.11	-178.00000	-154.22850	-129.56827	-103.94259	-77.26178	-49.41989	-20.28995	10.28277	42.49082	76.57939	112.86391
.10	-178.00000	-154.22850	-129.56827	-103.94259	-77.26178	-49.41989	-20.28995	10.28280	42.49126	76.58428	112.90713
.10	-108.00000	-86.02981	-63.27922	-39.68133	-15.15840	10.38079	37.04462	64.96366	94.29796	125.24796	158.07094
.9	-108.00000	-86.02981	-63.27922	-39.68133	-15.15840	10.38079	37.04462	64.96366	94.29799	125.24828	158.07446
.9	-34.00000	-13.92676	6.82782	28.32189	50.62273	73.80897	97.97348	123.22736	149.70554	177.57490	207.04646
.8	-34.00000	-13.92676	6.82782	28.32189	50.62273	73.80897	97.97348	123.22736	149.70554	177.57492	207.04669
.8	44.00000	62.07961	80.74855	100.05695	120.06269	140.83318	162.44779	185.00101	208.60696	233.40568	259.57249
.7	44.00000	62.07961	80.74855	100.05695	120.06269	140.83318	162.44779	185.00101	208.60696	233.40569	259.57250
1.7	126.00000	141.98850	158.47965	175.51612	193.14709	211.42975	230.43122	250.23124	270.92573	292.63188	315.49546
1.6	126.00000	141.98850	158.47965	175.51612	193.14709	211.42975	230.43122	250.23124	270.92573	292.63188	315.49546
2.6	212.00000	225.79928	240.01856	254.69343	269.86489	285.58053	301.89616	318.87792	336.60522	355.17479	374.70650
2.5	212.00000	225.79928	240.01856	254.69343	269.86489	285.58053	301.89616	318.87792	336.60522	355.17479	374.70650
3.5	302.00000	313.51148	325.36327	337.58420	350.20743	363.27142	376.82125	390.91027	405.60244	420.97552	437.12571
3.4	302.00000	313.51148	325.36327	337.58420	350.20743	363.27142	376.82125	390.91027	405.60244	420.97552	437.12571
4.4	396.00000	405.12470	414.51219	424.18471	434.16786	444.49128	455.18972	466.30424	477.88406	489.98895	502.69273
4.3	396.00000	405.12470	414.51219	424.18471	434.16786	444.49128	455.18972	466.30424	477.88406	489.98895	502.69273
5.3	494.00000	500.63862	507.46402	514.49199	521.74070	529.23122	536.98820	545.04078	553.42386	562.17980	571.36089
5.2	494.00000	500.63862	507.46402	514.49199	521.74070	529.23122	536.98820	545.04078	553.42386	562.17980	571.36089
6.2	596.00000	600.05301	604.21773	608.50362	612.92153	617.48406	622.20594	627.10460	632.20088	637.52007	643.09340
6.1	596.00000	600.05301	604.21773	608.50362	612.92153	617.48406	622.20594	627.10460	632.20088	637.52007	643.09340
7.1	702.00000	703.36764	704.77247	706.21762	707.70672	709.24395	710.83422	712.48331	714.19818	715.98722	717.86083
7.0	702.00000	703.36764	704.77247	706.21762	707.70672	709.24395	710.83422	712.48331	714.19818	715.98722	717.86083

= 27

.27	-756.00000	-744.24835	-739.17039	-735.28284	-732.01028	-729.13049	-726.52961	-724.14002	-721.91770	-719.83206	-717.86083
.27	-754.00000	-744.24739	-739.17038	-735.28284	-732.01028	-729.13049	-726.52961	-724.14002	-721.91770	-719.83206	-717.86083
.26	-754.00000	-721.96561	-706.69848	-695.05953	-685.27669	-676.67706	-668.91688	-661.79232	-655.17075	-648.96011	-643.09340
.26	-748.00000	-721.92723	-706.69803	-695.05952	-685.27669	-676.67706	-668.91688	-661.79232	-655.17075	-648.96011	-643.09340
.25	-748.00000	-702.63261	-676.73309	-657.34032	-641.09397	-626.83965	-613.99506	-602.21645	-591.28062	-581.03290	-571.36089
.25	-738.00000	-702.03291	-676.72042	-657.33994	-641.09396	-626.83965	-613.99506	-602.21645	-591.28062	-581.03290	-571.36089
.24	-738.00000	-688.05307	-649.69608	-622.33058	-599.60273	-579.72253	-561.84403	-545.47451	-530.29586	-516.08839	-502.69273
.24	-724.00000	-684.03872	-649.49652	-622.32192	-599.60231	-579.72251	-561.84403	-545.47451	-530.29586	-516.08839	-502.69273
.23	-724.00000	-677.45516	-626.83869	-590.39566	-561.00590	-535.46718	-512.56889	-491.64665	-472.27831	-454.17434	-437.12571
.23	-706.00000	-665.91822	-625.04993	-590.26877	-560.99764	-535.46664	-512.56886	-491.64666	-472.27831	-454.17434	-437.12571
.22	-706.00000	-664.39142	-610.17141	-562.52125	-525.65558	-494.27880	-466.31324	-440.83916	-417.30833	-395.35205	-374.70650
.22	-684.00000	-645.16865	-602.27987	-561.33583	-525.54380	-494.26936	-466.31249	-440.83911	-417.30833	-395.35205	-374.70650
.21	-684.00000	-644.99902	-596.27016	-541.01565	-494.45716	-456.51462	-423.28767	-393.19855	-365.49341	-339.70187	-315.49546
.21	-658.00000	-620.50386	-578.66236	-534.83052	-493.43427	-456.39609	-423.27568	-393.19745	-365.49332	-339.70186	-315.49546
.20	-658.00000	-620.49230	-577.44773	-524.80076	-469.72643	-423.08549	-383.86641	-348.94317	-316.98349	-287.33234	-259.57250
.20	-628.00000	-591.72479	-551.83932	-508.50649	-464.12827	-422.04541	-383.72598	-348.92700	-316.98185	-287.33219	-259.57249
.19	-628.00000	-591.72425	-551.70202	-505.82678	-451.42250	-396.34864	-349.01900	-308.47426	-272.00659	-238.39684	-207.04669
.19	-594.00000	-558.89714	-520.88647	-479.63901	-435.53290	-390.70108	-347.84788	-308.29667	-271.98416	-238.39441	-207.04646
.18	-594.00000	-558.89712	-520.87589	-479.25162	-431.67655	-376.55864	-321.19763	-272.86211	-231.00057	-193.13461	-158.07446
.18	-556.00000	-522.07830	-485.76389	-446.76058	-404.79617	-360.29301	-315.07221	-271.46004	-230.76808	-193.10328	-158.07094
.17	-556.00000	-522.07830	-485.76329	-446.72325	-404.16295	-355.79688	-300.49166	-244.67718	-195.17324	-152.02947	-112.90713
.17	-514.00000	-481.30136	-446.58889	-409.63988	-370.15963	-327.90957	-283.25754	-237.73865	-193.43869	-151.72147	-112.86391
.16	-514.00000	-481.30136	-446.58887	-409.63721	-370.09106	-327.12869	-278.63215	-223.48568	-167.19123	-116.45741	-72.08274
.16	-468.00000	-436.58571	-403.44760	-368.41226	-331.25186	-291.67822	-249.45780	-204.85961	-159.16397	-114.28697	-71.67736
.15	-468.00000	-436.58571	-403.44760	-368.41212	-331.24635	-291.58863	-248.64589	-200.48798	-145.79035	-89.10628	-37.16473
.15	-418.00000	-387.94332	-356.39310	-323.20809	-288.21047	-251.17140	-211.80632	-169.86736	-125.50900	-79.78105	-34.46433
.14	-418.00000	-387.94332	-356.39310	-323.20808	-288.21013	-251.16373	-211.71118	-169.11408	-121.62585	-67.63954	-10.73911
.14	-364.00000	-335.38194	-305.45897	-274.11241	-241.19755	-206.53400	-169.89208	-130.98635	-89.54385	-45.60265	0.00000
.13	-364.00000	-335.38194	-305.45897	-274.11241	-241.19753	-206.53349	-169.88372	-130.89837	-88.89891	-42.31006	10.73911
.12	-310.00000	-284.16402	-257.19684	-228.99706	-199.44244	-168.38275	-135.62722	-100.91496	-63.81604	-23.40464	22.14330
.12	-252.00000	-227.68046	-202.37047	-175.98303	-148.41510	-119.54275	-89.21419	-57.23941	-23.37795	12.65721	51.10498
.11	-252.00000	-227.68046	-202.37047	-175.98303	-148.41510	-119.54274	-89.21401	-57.23700	-23.35396	12.83771	52.15115
.11	-190.00000	-167.28826	-143.70830	-119.18485	-93.62974	-66.93832	-38.98462	-9.61414	21.36670	54.20455	89.20505
.10	-190.00000	-167.28826	-143.70830	-119.18485	-93.62974	-66.93832	-38.98461	-9.61399	21.36851	54.22162	89.33267
.10	-124.00000	-102.98964	-81.21956	-58.62447	-35.12840	-10.64197	14.94128	41.75009	69.94298	99.71960	131.33668
.9	-124.00000	-102.98964	-81.21956	-58.62447	-35.12840	-10.64197	14.94128	41.75009	69.94309	99.72084	131.34818
.9	-54.00000	-34.78620	-14.91093	5.68234	27.05909	49.29593	72.48350	96.73045	122.16909	148.96359	177.32248
.8	-54.00000	-34.78620	-14.91093	5.68234	27.05909	49.29593	72.48350	96.73045	122.16910	148.96366	177.32327
.8	20.00000	37.32087	55.21266	73.72399	92.91099	112.83911	133.58548	155.24203	177.91992	201.75585	226.92133
.7	20.00000	37.32087	55.21266	73.72399	92.91099	112.83911	133.58548	155.24203	177.91992	201.75585	226.92138
.7	98.00000	113.33067	129.14749	145.49177	162.41109	179.96082	198.20603	217.22400	237.10780	257.97123	279.95605

20.6	98.00000	113.33067	129.14749	145.49177	162.41109	179.96082	198.20603	217.22400	237.10780	257.97123	279.
21.6	180.00000	193.24250	206.89072	220.97904	235.54708	250.64086	266.31433	282.63146	299.66910	317.52088	336.
21.5	180.00000	193.24250	206.89072	220.97904	235.54708	250.64086	266.31433	282.63146	299.66910	317.52088	336.
22.5	266.00000	277.05584	288.44013	300.18067	312.30949	324.86371	337.88687	351.43049	365.55634	380.33957	395.
22.4	266.00000	277.05584	288.44013	300.18067	312.30949	324.86371	337.88687	351.43049	365.55634	380.33957	395.
23.4	356.00000	364.77027	373.79399	383.09263	392.69086	402.61730	412.90543	423.59491	434.73321	446.37801	458.
23.3	356.00000	364.77027	373.79399	383.09263	392.69086	402.61730	412.90543	423.59491	434.73321	446.37801	458.
24.3	450.00000	456.38544	462.95094	469.71173	476.68533	483.89205	491.35566	499.10426	507.17149	515.59821	524.
24.2	450.00000	456.38544	462.95094	469.71173	476.68533	483.89205	491.35566	499.10426	507.17149	515.59821	524.
25.2	548.00000	551.90109	555.90985	560.03539	564.28817	568.68035	573.22611	577.94224	582.84885	587.97031	593.
25.1	548.00000	551.90109	555.90985	560.03539	564.28817	568.68035	573.22611	577.94224	582.84885	587.97031	593.
26.1	650.00000	651.31700	652.66984	654.06154	655.49558	656.97601	658.50756	660.09579	661.74741	663.47052	665.
26.0	650.00000	651.31700	652.66984	654.06154	655.49558	656.97601	658.50756	660.09579	661.74741	663.47052	665.

J = 28

0.28	-812.00000	-799.80011	-794.53743	-790.50789	-787.11559	-784.13029	-781.43400	-778.95668	-776.65269	-774.49034	-772.4
1.28	-810.00000	-799.79947	-794.53743	-790.50789	-787.11559	-784.13029	-781.43400	-778.95668	-776.65269	-774.49034	-772.4
1.27	-810.00000	-776.60808	-760.79569	-748.73212	-738.59072	-729.67500	-721.62893	-714.24140	-707.37501	-700.93439	-694.8
2.27	-804.00000	-776.58106	-760.79544	-748.73211	-738.59072	-729.67500	-721.62893	-714.24140	-707.37501	-700.93439	-694.8
2.26	-804.00000	-756.26535	-729.54281	-709.45079	-692.60994	-677.83063	-664.51083	-652.29487	-640.95173	-630.32130	-620.2
3.26	-794.00000	-755.81494	-729.53518	-709.45059	-692.60994	-677.83063	-664.51083	-652.29487	-640.95173	-630.32130	-620.2
3.25	-794.00000	-740.48253	-701.14477	-672.85441	-649.30540	-628.69560	-610.15527	-593.17593	-577.42891	-562.68707	-548.7
4.25	-780.00000	-737.13593	-701.01679	-672.84975	-649.30521	-628.69559	-610.15527	-593.17593	-577.42891	-562.68707	-548.7
4.24	-780.00000	-729.30755	-676.62444	-639.25808	-608.86291	-582.40133	-558.66038	-536.95963	-516.86454	-498.07660	-480.3
5.24	-762.00000	-718.71037	-675.36507	-639.18531	-608.85888	-582.40110	-558.66036	-536.95963	-516.86454	-498.07660	-480.3
5.23	-762.00000	-716.65318	-658.17407	-609.42836	-571.58157	-539.13289	-510.15790	-483.74409	-459.33312	-436.54682	-415.1
6.23	-740.00000	-697.96446	-651.77528	-608.68407	-571.52298	-539.12863	-510.15760	-483.74407	-459.33312	-436.54682	-415.1
6.22	-740.00000	-697.70942	-643.92024	-585.46508	-538.14180	-499.18699	-464.83445	-433.66192	-404.93269	-378.17138	-353.0
7.22	-714.00000	-673.38760	-627.91932	-580.95817	-537.55302	-499.12944	-464.82943	-433.66151	-404.93267	-378.17138	-353.0
7.21	-714.00000	-673.36862	-626.06254	-567.98899	-510.48360	-463.22469	-422.99202	-386.90276	-353.79692	-323.04802	-294.2
8.21	-684.00000	-644.68016	-601.22579	-554.12045	-506.72357	-462.66681	-422.92830	-386.89643	-353.79637	-323.04798	-294.2
8.20	-684.00000	-644.67918	-600.98962	-549.97981	-490.21695	-433.13624	-385.30789	-343.77910	-306.11933	-271.31123	-238.7
9.20	-650.00000	-611.90169	-570.46499	-525.35223	-477.39934	-429.56756	-384.71585	-343.70330	-306.11110	-271.31046	-238.7
9.19	-650.00000	-611.90165	-570.44497	-524.65624	-471.32261	-410.89889	-353.71164	-305.00891	-262.22694	-223.15865	-186.8
10.19	-612.00000	-575.11741	-535.49242	-492.77159	-446.72936	-398.29144	-350.01187	-304.33507	-262.13315	-223.14785	-186.8
10.18	-612.00000	-575.11741	-535.49117	-492.69668	-445.53779	-390.97732	-330.26631	-272.62257	-222.89765	-178.93481	-138.6
11.18	-570.00000	-534.36572	-496.42619	-455.91417	-412.48300	-365.97644	-317.26435	-268.56489	-222.09960	-178.81704	-138.6
11.17	-570.00000	-534.36572	-496.42613	-455.90827	-412.33676	-364.42806	-309.40297	-248.58591	-190.30035	-139.49291	-94.4
12.17	-524.00000	-489.66911	-453.36568	-414.88423	-373.94934	-330.22728	-283.57985	-234.75716	-185.70660	-138.53152	-94.2
12.16	-524.00000	-489.66911	-453.36568	-414.88387	-373.93625	-330.02342	-281.87113	-226.90845	-166.13710	-107.15361	-55.2
13.16	-474.00000	-441.04146	-406.37305	-369.82907	-331.19697	-290.19927	-246.50902	-199.96991	-151.18836	-101.88668	-54.1
13.15	-474.00000	-441.04146	-406.37305	-369.82905	-331.19607	-290.17970	-246.27693	-198.27517	-143.75153	-83.19029	-23.5
14.15	-420.00000	-388.49174	-355.48749	-320.84889	-284.40493	-245.93883	-205.17160	-161.77464	-115.55232	-66.96127	-17.5
14.14	-420.00000	-388.49174	-355.48749	-320.84889	-284.40487	-245.93737	-205.14852	-161.54331	-113.99085	-60.17868	0.0
15.14	-362.00000	-332.02595	-300.73482	-268.00840	-233.70418	-197.64694	-159.61590	-119.32857	-76.44716	-30.72515	17.5
15.13	-362.00000	-332.02595	-300.73482	-268.00840	-233.70418	-197.64685	-159.61412	-119.30533	-76.23672	-29.35847	23.5
16.13	-300.00000	-271.64827	-242.13268	-211.35083	-179.18122	-145.47751	-110.05998	-72.70263	-33.11619	9.05295	54.1
16.12	-300.00000	-271.64827	-242.13268	-211.35083	-179.18122	-145.47751	-110.05987	-72.70081	-33.09518	9.23266	55.2
17.12	-234.00000	-207.36167	-179.69353	-150.90616	-120.89460	-89.53405	-56.67391	-22.12885	14.33460	53.01658	94.2
17.11	-234.00000	-207.36167	-179.69353	-150.90616	-120.89460	-89.53405	-56.67390	-22.12873	14.33624	53.03419	94.4
18.11	-164.00000	-139.16828	-113.42634	-86.69583	-58.88543	-29.88751	0.42639	32.21206	65.66213	101.02049	138.6
18.10	-164.00000	-139.16828	-113.42634	-86.69583	-58.88543	-29.88751	0.42639	32.21207	65.66223	101.02184	138.6
19.10	-90.00000	-67.06971	-43.33775	-18.73553	6.81654	33.41171	61.16049	90.19567	120.67943	152.81384	186.8
19.9	-90.00000	-67.06971	-43.33775	-18.73553	6.81654	33.41171	61.16049	90.19567	120.67943	152.81392	186.8
20.9	-12.00000	8.93284	30.56723	52.96299	76.18924	100.32672	125.47063	151.73469	179.25675	208.20678	238.7
20.8	-12.00000	8.93284	30.56723	52.96299	76.18924	100.32672	125.47063	151.73469	179.25675	208.20678	238.7
21.8	70.00000	88.83844	108.28481	128.39078	149.21600	170.82989	193.31409	216.76576	241.30208	267.06663	294.2
21.7	70.00000	88.83844	108.28481	128.39078	149.21600	170.82989	193.31409	216.76576	241.30208	267.06663	294.2
22.7	156.00000	172.64637	189.81200	207.54095	225.88398	244.90009	264.65855	285.24156	306.74794	329.29835	353.0
22.6	156.00000	172.64637	189.81200	207.54095	225.88398	244.90009	264.65855	285.24156	306.74794	329.29835	353.0
23.6	246.00000	260.35609	275.14651	290.40807	306.18314	322.52093	339.47908	357.12594	375.54349	394.83159	415.1
23.5	246.00000	260.35609	275.14651	290.40807	306.18314	322.52093	339.47908	357.12594	375.54349	394.83159	415.1
24.5	340.00000	351.96713	364.28647	376.98785	390.10558	403.67947	417.75614	432.39078	447.64953	463.61281	480.3
24.4	340.00000	351.96713	364.28647	376.98785	390.10558	403.67947	417.75614	432.39078	447.64953	463.61281	480.3
25.4	438.00000	447.47913	457.23040	467.27684	477.64494	488.36541	499.47421	511.01386	523.03532	535.60043	548.7
25.3	438.00000	447.47913	457.23040	467.27684	477.64494	488.36541	499.47421	511.01386	523.03532	535.60043	548.7
26.3	540.00000	546.89181	553.97711	561.27227	568.79610	576.57044	584.62081	592.97740	601.67636	610.76157	620.2
26.2	540.00000	546.89181	553.97711	561.27227	568.79610	576.57044	584.62081	592.97740	601.67636	610.76157	620.2
27.2	646.00000	650.20493	654.52561	658.97185	663.55489	668.28778	673.18580	678.26698	683.55294	689.06988	694.8
27.1	646.00000	650.20493	654.52561	658.97185	663.55489	668.28778	673.18580	678.26698	683.55294	689.06988	694.8
28.1	756.00000	757.41828	758.87510	760.37371	761.91786	763.51189	765.16088	766.87084	768.64895	770.50394	772.4
28.0	756.00000	757.41828	758.87510	760.37371	761.91786	763.51189	765.16088	766.87084	768.64895	770.50394	772.4

-870.00000	-857.35199	-851.90451	-847.73296	-844.22091	-841.13009	-838.33841	-835.77334	-833.38768	-831.14862	-829.03228
-868.00000	-857.35156	-851.90451	-847.73296	-844.22091	-841.13009	-838.33841	-835.77334	-833.38768	-831.14862	-829.03228
-868.00000	-833.25314	-816.89338	-804.40499	-793.90497	-784.67309	-776.34110	-768.69057	-761.57935	-754.90873	-748.60692
-862.00000	-833.23420	-816.89324	-804.40499	-793.90497	-784.67309	-776.34110	-768.69057	-761.57935	-754.90873	-748.60692
-862.00000	-811.92071	-784.35590	-763.56271	-746.12690	-730.82234	-717.02716	-704.37373	-692.62319	-681.60997	-671.21367
-852.00000	-811.58545	-784.35132	-763.56262	-746.12690	-730.82234	-717.02716	-704.37373	-692.62319	-681.60997	-671.21367
-852.00000	-794.92619	-754.61577	-725.38416	-701.01141	-679.67101	-660.46826	-642.87869	-626.56300	-611.28657	-596.87912
-838.00000	-792.18025	-754.53456	-725.38168	-701.01132	-679.67101	-660.46826	-642.87869	-626.56300	-611.28657	-596.87912
-838.00000	-783.01954	-728.50628	-690.14763	-658.73019	-631.34183	-606.75641	-584.27601	-563.45339	-543.98087	-525.63590
-820.00000	-773.39358	-727.63790	-690.10644	-658.72823	-631.34173	-606.75641	-584.27601	-563.45339	-543.98087	-525.63590
-820.00000	-770.68186	-708.16425	-658.45906	-619.54464	-586.00363	-556.01326	-528.65676	-503.36370	-479.74599	-457.52464
-798.00000	-752.62448	-703.12238	-658.00256	-619.51444	-586.00174	-556.01315	-528.65675	-503.36370	-479.74599	-457.52464
-798.00000	-752.24838	-693.18094	-632.07582	-583.98133	-543.91165	-508.40674	-476.14192	-446.38397	-418.64981	-392.59662
-772.00000	-728.13752	-678.91710	-628.92430	-583.65161	-543.88427	-508.40467	-476.14178	-446.38396	-418.64981	-392.59662
-772.00000	-728.10699	-676.17440	-612.79314	-553.54381	-505.56454	-464.19130	-426.89956	-392.63462	-360.78105	-330.91781
-742.00000	-699.50917	-652.31348	-601.38192	-551.14344	-505.27496	-464.16310	-426.89713	-392.63443	-360.78104	-330.91781
-742.00000	-699.50747	-651.91855	-595.29796	-530.67417	-472.35663	-423.86199	-381.18651	-342.28422	-306.25924	-272.57506
-708.00000	-666.78561	-621.75475	-572.60180	-520.82617	-470.23481	-423.57430	-381.15512	-342.28127	-306.25900	-272.57504
-708.00000	-666.78554	-621.71790	-571.39942	-511.84997	-446.92814	-388.79133	-339.50841	-295.59383	-255.25330	-217.68636
-670.00000	-630.03986	-586.94935	-540.31302	-490.03458	-437.75238	-386.71365	-339.19971	-295.55735	-255.24969	-217.68606
-670.00000	-630.03986	-586.94684	-540.16792	-487.90516	-426.75525	-361.70115	-303.27061	-253.08894	-208.02924	-166.42021
-628.00000	-589.31629	-548.00510	-503.74632	-456.14601	-405.24338	-352.61514	-301.09560	-252.74252	-207.98611	-166.41584
-628.00000	-589.31629	-548.00497	-503.73371	-455.84731	-402.36405	-340.44942	-275.24038	-216.24318	-165.13811	-119.04704
-582.00000	-544.64088	-505.03499	-462.93903	-418.02132	-369.91725	-318.71563	-265.85376	-213.87333	-164.74132	-118.99630
-582.00000	-544.64088	-505.03499	-462.93818	-417.99155	-369.47660	-315.38352	-253.22832	-187.84049	-128.14265	-76.14537
-532.00000	-496.02963	-458.11144	-418.05143	-375.59549	-330.40950	-282.14583	-230.88206	-177.89285	-125.51088	-75.69073
-532.00000	-496.02963	-458.11143	-418.05139	-375.59321	-330.36193	-281.61248	-227.38893	-165.34787	-99.80293	-39.37308
-478.00000	-443.49286	-407.28003	-369.20070	-329.05295	-286.57619	-241.43474	-193.28213	-142.14795	-89.14224	-36.44538
-478.00000	-443.49286	-407.28003	-369.20069	-329.05281	-286.57224	-241.37460	-192.71411	-138.72151	-77.05193	-11.41584
-420.00000	-387.03749	-352.57069	-316.46275	-278.54686	-238.61500	-196.40085	-151.56425	-103.74627	-52.90772	0.00000
-420.00000	-387.03749	-352.57069	-316.46275	-278.54686	-238.61474	-196.39563	-151.49899	-103.19129	-49.69489	11.41584
-358.00000	-326.66833	-294.00381	-259.88807	-224.17954	-186.70601	-147.25326	-105.54794	-61.24090	-13.94964	36.44538
-358.00000	-326.66833	-294.00381	-259.88807	-224.17954	-186.70600	-147.25290	-105.54216	-61.17704	-13.43804	39.37308
-292.00000	-262.38876	-231.59376	-199.51151	-166.01985	-130.97258	-94.19164	-55.45536	-14.48069	29.09608	75.69073
-292.00000	-262.38876	-231.59376	-199.51151	-166.01985	-130.97258	-94.19162	-55.45495	-14.47501	29.15433	76.14537
-222.00000	-194.20126	-165.35088	-135.35789	-104.11586	-71.49873	-37.35514	-1.50005	36.29777	76.33488	118.99630
-222.00000	-194.20126	-165.35088	-135.35789	-104.11586	-71.49873	-37.35514	-1.50003	36.29817	76.34001	119.04704
-148.00000	-122.10767	-95.28282	-67.44538	-38.50218	-8.34370	23.16040	56.16758	90.87152	127.51593	166.41584
-148.00000	-122.10767	-95.28282	-67.44538	-38.50218	-8.34370	23.16040	56.16758	90.87154	127.51629	166.42021
-70.00000	-46.10938	-21.39533	4.21248	30.79560	58.44940	87.28674	117.44291	149.08263	182.41038	217.68606
-70.00000	-46.10938	-21.39533	4.21248	30.79560	58.44940	87.28674	117.44291	149.08263	182.41041	217.68636
12.00000	33.79257	56.30720	79.60538	103.75817	128.84842	154.97379	182.25076	210.82027	240.85574	272.57504
12.00000	33.79257	56.30720	79.60538	103.75817	128.84842	154.97379	182.25076	210.82027	240.85574	272.57506
98.00000	117.59734	137.82138	158.72536	180.37069	202.82883	226.18378	250.53540	276.00403	302.73693	330.91781
98.00000	117.59734	137.82138	158.72536	180.37069	202.82883	226.18378	250.53540	276.00403	302.73693	330.91781
188.00000	205.30429	223.14454	241.56619	260.62161	280.37166	300.88773	322.25452	344.57382	367.96980	392.59662
188.00000	205.30429	223.14454	241.56619	260.62161	280.37166	300.88773	322.25452	344.57382	367.96980	392.59662
282.00000	296.91291	312.27454	328.12291	344.50178	361.46195	379.06295	397.37530	416.48363	436.49090	457.52464
282.00000	296.91291	312.27454	328.12291	344.50178	361.46195	379.06295	397.37530	416.48363	436.49090	457.52464
380.00000	392.42278	405.20970	418.39159	432.00391	446.08781	460.69147	475.87192	491.69750	508.25127	525.63590
380.00000	392.42278	405.20970	418.39159	432.00391	446.08781	460.69147	475.87192	491.69750	508.25127	525.63590
482.00000	491.83357	501.94863	512.36901	523.12210	534.23966	545.75888	557.72375	570.18693	583.21239	596.87912
482.00000	491.83357	501.94863	512.36901	523.12210	534.23966	545.75888	557.72375	570.18693	583.21239	596.87912
588.00000	595.14500	602.49020	610.05256	617.85153	625.90969	634.25347	642.91411	651.92899	661.34350	671.21367
588.00000	595.14500	602.49020	610.05256	617.85153	625.90969	634.25347	642.91411	651.92899	661.34350	671.21367
698.00000	702.35685	706.83350	711.44008	716.18825	721.09151	726.16566	731.42938	736.90502	742.61972	748.60692
698.00000	702.35685	706.83350	711.44008	716.18825	721.09151	726.16566	731.42938	736.90502	742.61972	748.60692
812.00000	813.46892	814.97773	816.52980	818.12900	819.77982	821.48754	823.25836	825.09972	827.02065	829.03228
812.00000	813.46892	814.97773	816.52980	818.12900	819.77982	821.48754	823.25836	825.09972	827.02065	829.03228

J = 30

0.30	-930.00000	-916.90397	-911.27162	-906.95806	-903.32626	-900.12992	-897.24282	-894.59002	-892.12268	-889.80691	-887.6
1.30	-928.00000	-916.90368	-911.27162	-906.95806	-903.32626	-900.12992	-897.24282	-894.59002	-892.12268	-889.80691	-887.6
1.29	-928.00000	-891.90020	-874.99148	-862.07811	-851.21940	-841.67133	-833.05338	-825.13983	-817.78375	-810.88313	-804.3
2.29	-922.00000	-891.88698	-874.99140	-862.07811	-851.21940	-841.67133	-833.05338	-825.13983	-817.78375	-810.88313	-804.3
2.28	-922.00000	-869.59492	-841.17163	-819.67590	-801.64472	-785.81470	-771.54399	-758.45297	-746.29495	-734.89887	-724.1
3.28	-912.00000	-869.34736	-841.16891	-819.67585	-801.64472	-785.81470	-771.54399	-758.45297	-746.29495	-734.89887	-724.1
3.27	-912.00000	-851.39781	-810.10334	-779.91871	-754.72029	-732.64848	-712.78280	-694.58264	-677.69801	-661.88678	-646.9
4.27	-898.00000	-849.17905	-810.05228	-779.91739	-754.72025	-732.64848	-712.78280	-694.58264	-677.69801	-661.88678	-646.9
4.26	-898.00000	-838.61427	-782.46996	-743.05702	-710.60581	-682.28774	-656.85639	-633.59537	-612.04451	-591.88688	-572.8
5.26	-880.00000	-829.97413	-781.88175	-743.03398	-710.60488	-682.28770	-656.85639	-633.59537	-612.04451	-591.88688	-572.8
5.25	-880.00000	-826.47548	-760.20561	-709.58205	-669.53474	-634.88788	-603.87770	-575.57607	-549.39927	-524.94895	-501.9
6.25	-858.00000	-809.14921	-756.34577	-709.30752	-669.51939	-634.88705	-603.87766	-575.57606	-549.39927	-524.94895	-501.9
6.24	-858.00000	-808.60499	-744.12335	-680.89471	-631.92988	-590.67405	-553.99948	-520.63588	-489.84545	-461.13585	-434.1
7.24	-832.00000	-784.75157	-731.67213	-678.77178	-631.74941	-590.66125	-553.99865	-520.63583	-489.84544	-461.13585	-434.1
7.23	-832.00000	-784.70337	-727.76023	-659.38091	-598.91732	-550.04037	-507.44286	-468.92575	-433.49242	-400.52868	-369.6
8.23	-802.00000	-756.20990	-705.10229	-650.33470	-597.44983	-549.89408	-507.43065	-468.92484	-433.49236	-400.52867	-369.6
8.22	-802.00000	-756.20699	-704.46009	-641.82552	-573.06691	-513.98758	-464.59051	-420.66501	-380.48955	-343.23474	-308.3
9.22	-768.00000	-723.54737	-674.74972	-621.40048	-565.89047	-512.78759	-464.45515	-420.65234	-380.48852	-343.23467	-308.3
9.21	-768.00000	-723.54724	-674.68374	-619.40650	-553.41394	-485.03353	-426.39196	-376.23377	-331.05534	-289.40153	-250.5
10.21	-730.00000	-686.84447	-640.12910	-589.37643	-534.74585	-478.79124	-425.29157	-376.09768	-331.04158	-289.40036	-250.5
10.20	-730.00000	-686.84447	-640.12420	-589.10485	-531.14648	-463.41240	-395.32009	-336.57069	-285.57216	-239.24675	-196.2
11.20	-688.00000	-646.15212	-601.32123	-553.12502	-501.14072	-445.77020	-389.46920	-335.48274	-285.42849	-239.23152	-196.2
11.19	-688.00000	-646.15212	-601.32095	-553.09901	-500.55627	-440.78066	-372.18418	-304.14441	-244.99088	-193.15697	-145.8
12.19	-642.00000	-601.50022	-558.45201	-512.56733	-463.44991	-410.74235	-354.95243	-298.35853	-243.86462	-193.00182	-145.7
12.18	-642.00000	-601.50022	-558.45200	-512.56543	-463.38492	-409.83835	-348.98453	-279.98564	-211.80756	-152.10717	-99.4
13.18	-592.00000	-552.90714	-511.60535	-467.86775	-421.39043	-371.77693	-318.71280	-262.71797	-205.88697	-150.91411	-99.3
13.17	-592.00000	-552.90714	-511.60535	-467.86764	-421.38493	-371.66677	-317.56062	-256.19807	-187.05994	-118.63520	-58.3
14.17	-538.00000	-500.38472	-460.83412	-419.16172	-375.12916	-328.42315	-278.64825	-225.50468	-169.46936	-112.47020	-57.0
14.16	-538.00000	-500.38472	-460.83412	-419.16171	-375.12879	-328.41298	-278.50002	-224.20599	-162.75418	-93.65054	-24.9
15.16	-480.00000	-443.94090	-406.17289	-366.53809	-324.84159	-280.83632	-234.20115	-184.53700	-131.53453	-75.59764	-18.5
15.15	-480.00000	-443.94090	-406.17289	-366.53809	-324.84157	-280.83558	-234.18673	-184.36506	-130.18486	-68.94427	0.0
16.15	-418.00000	-383.58116	-347.64513	-310.05565	-270.64831	-229.22078	-185.51757	-139.20834	-89.88338	-37.20503	18.5
16.14	-418.00000	-383.58116	-347.64513	-310.05565	-270.64831	-229.22073	-185.51646	-139.19113	-89.70276	-35.87527	24.9
17.14	-352.00000	-319.30939	-285.26734	-249.75477	-212.63019	-173.72288	-132.82274	-89.66450	-43.90538	4.88303	57.0
17.13	-352.00000	-319.30939	-285.26734	-249.75477	-212.63019	-173.72288	-132.82267	-89.66314	-43.88710	5.06064	58.3
18.13	-282.00000	-251.12842	-219.05141	-185.66413	-150.84328	-114.44205	-76.28285	-36.14640	6.24485	51.25092	99.3
18.12	-282.00000	-251.12842	-219.05141	-185.66413	-150.84328	-114.44205	-76.28284	-36.14632	6.24632	51.26887	99.4
19.12	-208.00000	-179.04034	-149.00610	-117.80462	-85.32775	-51.44781	-16.01209	21.16514	60.31439	101.72920	145.7
19.11	-208.00000	-179.04034	-149.00610	-117.80462	-85.32775	-51.44781	-16.01209	21.16515	60.31449	101.73064	145.8
20.11	-130.00000	-103.04675	-75.13800	-46.19185	-16.11319	15.20958	47.90900	82.14464	118.11201	156.05575	196.2
20.10	-130.00000	-103.04675	-75.13800	-46.19185	-16.11319	15.20958	47.90900	82.14464	118.11201	156.05585	196.2
21.10	-48.00000	-23.14885	2.54789	29.16237	56.77813	85.49280	115.42170	146.70285	179.50390	214.03227	250.5
21.9	-48.00000	-23.14885	2.54789	29.16237	56.77813	85.49280	115.42170	146.70285	179.50390	214.03227	250.5
22.9	38.00000	60.65242	84.04765	108.24889	133.32915	159.37348	186.48205	214.77421	244.39417	275.51905	308.3
22.8	38.00000	60.65242	84.04765	108.24889	133.32915	159.37348	186.48205	214.77421	244.39417	275.51905	308.3
23.8	128.00000	148.35632	169.35824	191.06058	213.52656	236.82971	261.05639	286.30924	312.71182	340.41522	369.6
23.7	128.00000	148.35632	169.35824	191.06058	213.52656	236.82971	261.05639	286.30924	312.71182	340.41522	369.6
24.7	222.00000	239.96225	258.47722	277.59177	297.35989	317.84428	339.11850	361.26976	384.40286	408.64553	434.1
24.6	222.00000	239.96225	258.47722	277.59177	297.35989	317.84428	339.11850	361.26976	384.40286	408.64553	434.1
25.6	320.00000	335.46976	351.40266	367.83794	384.82076	402.40352	420.64764	439.62584	459.42538	480.15239	501.9
25.5	320.00000	335.46976	351.40266	367.83794	384.82076	402.40352	420.64764	439.62584	459.42538	480.15239	501.9
26.5	422.00000	434.87845	448.13298	461.79542	475.90241	490.49642	505.62720	521.35362	537.74623	554.89074	572.8
26.4	422.00000	434.87845	448.13298	461.79542	475.90241	490.49642	505.62720	521.35362	537.74623	554.89074	572.8
27.4	528.00000	538.18801	548.66688	559.46121	570.59932	582.11402	594.04372	606.43386	619.33885	632.82477	646.9
27.3	528.00000	538.18801	548.66688	559.46121	570.59932	582.11402	594.04372	606.43386	619.33885	632.82477	646.9
28.3	638.00000	645.39819	653.00331	660.83286	668.90697	677.24899	685.88620	694.85089	704.18171	713.92557	724.1
28.2	638.00000	645.39819	653.00331	660.83286	668.90697	677.24899	685.88620	694.85089	704.18171	713.92557	724.1
29.2	752.00000	756.50877	761.14138	765.90832	770.82162	775.89525	781.14554	786.59180	792.25714	798.16959	804.3
29.1	752.00000	756.50877	761.14138	765.90832	770.82162	775.89525	781.14554	786.59180	792.25714	798.16959	804.3
30.1	870.00000	871.51957	873.08036	874.68588	876.34013	878.04776	879.81420	881.64588	883.55050	885.53737	887.6
30.0	870.00000	871.51957	873.08036	874.68588	876.34013	878.04776	879.81420	881.64588	883.55050	885.53737	887.6

-992.00000	-978.45603	-972.63876	-968.18318	-964.43162	-961.12975	-958.14724	-955.40670	-952.85769	-950.46520	-948.20375
-990.00000	-978.45583	-972.63876	-968.18318	-964.43162	-961.12975	-958.14724	-955.40670	-952.85769	-950.46520	-948.20375
-990.00000	-952.54883	-935.08994	-921.75147	-910.53399	-900.66969	-891.76576	-883.58917	-875.98821	-868.85757	-862.12061
-984.00000	-952.53963	-935.08989	-921.75146	-910.53399	-900.66969	-891.76576	-883.58917	-875.98821	-868.85757	-862.12061
-984.00000	-929.28451	-899.98951	-877.79019	-859.16331	-842.80763	-828.06126	-814.53256	-801.96698	-790.18798	-779.06719
-974.00000	-929.10301	-899.98790	-877.79016	-859.16331	-842.80763	-828.06126	-814.53256	-801.96698	-790.18798	-779.06719
-974.00000	-909.90636	-867.60334	-836.45724	-810.43165	-787.62775	-767.09870	-748.28764	-730.83383	-714.48762	-699.06771
-960.00000	-908.13933	-867.57151	-836.45655	-810.43164	-787.62775	-767.09870	-748.28764	-730.83383	-714.48762	-699.06771
-960.00000	-896.11624	-838.49956	-797.98136	-764.48842	-735.23834	-708.95981	-684.91734	-662.63763	-641.79444	-622.15150
-942.00000	-888.45901	-838.10716	-797.96861	-764.48798	-735.23833	-708.95981	-684.91734	-662.63763	-641.79444	-622.15150
-942.00000	-884.03759	-814.34333	-762.77224	-721.54533	-685.78337	-653.74993	-624.50113	-597.43920	-572.15522	-548.35442
-920.00000	-867.53996	-811.46914	-762.60989	-721.53763	-685.78301	-653.74991	-624.50112	-597.43920	-572.15522	-548.35442
-920.00000	-866.76703	-796.82733	-731.92255	-681.95458	-639.46504	-601.60913	-567.14170	-535.31568	-505.62847	-477.72085
-894.00000	-843.22781	-786.20426	-730.53784	-681.85771	-639.45915	-601.60879	-567.14168	-535.31568	-505.62847	-477.72085
-894.00000	-843.15310	-780.81720	-707.91764	-646.55804	-596.60877	-552.73367	-512.97598	-476.36715	-442.28873	-410.30664
-864.00000	-814.78032	-759.59504	-701.02688	-645.69210	-596.53655	-552.72848	-512.97565	-476.36713	-442.28873	-410.30664
-864.00000	-814.77545	-758.57974	-689.66296	-617.62604	-557.94140	-507.43499	-462.19606	-420.72754	-382.23315	-346.18326
-830.00000	-782.18542	-729.44435	-671.76997	-612.67223	-557.28927	-507.37300	-462.19106	-420.72719	-382.23313	-346.18325
-830.00000	-782.18519	-729.32921	-668.60336	-596.25089	-525.49769	-466.38387	-415.10553	-368.58542	-325.59241	-285.44439
-792.00000	-745.53000	-695.02586	-639.95668	-580.91388	-521.52380	-465.82712	-415.04741	-368.58037	-325.59203	-285.44437
-792.00000	-745.52999	-695.01656	-639.46539	-575.18256	-501.33874	-431.46707	-372.34798	-320.23945	-272.55138	-228.21674
-750.00000	-704.87220	-656.36994	-604.03881	-547.46836	-487.64294	-427.98364	-371.83189	-320.18205	-272.54618	-228.21635
-750.00000	-704.87220	-656.36936	-603.98690	-546.37407	-479.62520	-405.16816	-335.73167	-276.32068	-223.40454	-174.68061
-704.00000	-660.24629	-613.61301	-563.75922	-510.21797	-452.71451	-392.41584	-332.47704	-275.81752	-223.34648	-174.67528
-704.00000	-660.24629	-613.61299	-563.75507	-510.08161	-450.95953	-382.65545	-307.92943	-238.60238	-178.77673	-125.12526
-654.00000	-611.67329	-566.85173	-519.27010	-468.56514	-414.27900	-356.23440	-295.64578	-235.43307	-178.27354	-125.06651
-654.00000	-611.67329	-566.85173	-519.26984	-468.55243	-414.03562	-353.90606	-284.70547	-209.84048	-140.42806	-80.16919
-600.00000	-559.16673	-516.14721	-470.72552	-422.62017	-371.45522	-316.78388	-258.47885	-197.72929	-137.27310	-79.66394
-600.00000	-559.16673	-516.14721	-470.72550	-422.61924	-371.43023	-316.43799	-255.73361	-186.08851	-111.14284	-41.56270
-542.00000	-502.73566	-461.53922	-418.22903	-372.57751	-324.29096	-272.98355	-218.21188	-159.85870	-99.05363	-38.40676
-542.00000	-502.73566	-461.53922	-418.22903	-372.57745	-324.28894	-272.94579	-217.78661	-156.85931	-87.07299	-12.08768
-480.00000	-442.38632	-403.05472	-361.84894	-318.57848	-273.00572	-224.82555	-173.64088	-119.00042	-60.76741	0.00000
-480.00000	-442.38632	-403.05472	-361.84894	-318.57848	-273.00558	-224.82231	-173.59270	-118.52512	-57.64648	12.08768
-414.00000	-378.12315	-340.71259	-301.63193	-260.71788	-217.77158	-172.54516	-124.72077	-73.88597	-19.56932	38.40676
-414.00000	-378.12315	-340.71259	-301.63193	-260.71788	-217.77158	-172.54493	-124.71648	-73.83104	-19.07007	41.56270
-344.00000	-309.94938	-274.52644	-237.61099	-199.06097	-158.70607	-116.33842	-71.69837	-24.45235	25.83357	79.66394
-344.00000	-309.94938	-274.52644	-237.61099	-199.06097	-158.70607	-116.33841	-71.69806	-24.44737	25.89170	80.16919
-270.00000	-237.86740	-204.50625	-169.81013	-133.65426	-95.89071	-56.34136	-14.78789	29.04374	75.50730	125.06651
-270.00000	-237.86740	-204.50625	-169.81013	-133.65426	-95.89071	-56.34136	-14.78787	29.04411	75.51260	125.12526
-192.00000	-161.87899	-130.65955	-98.24719	-64.53187	-29.38400	7.35095	45.86012	86.37449	129.18612	174.67528
-192.00000	-161.87899	-130.65955	-98.24719	-64.53187	-29.38400	7.35095	45.86012	86.37451	129.18651	174.68061
-110.00000	-81.98556	-52.99206	-22.93573	8.28061	40.77081	74.66979	110.13963	147.37822	186.63211	228.21635
-110.00000	-81.98556	-52.99206	-22.93573	8.28061	40.77081	74.66979	110.13963	147.37822	186.63214	228.21674
-24.00000	1.81184	28.49179	56.11384	84.76361	114.54102	145.56402	177.97351	211.94034	247.67534	285.44437
-24.00000	1.81184	28.49179	56.11384	84.76361	114.54102	145.56402	177.97351	211.94034	247.67534	285.44439
66.00000	89.51237	113.78850	138.89335	164.90188	191.90141	219.99467	249.30397	279.97691	312.19453	346.18325
66.00000	89.51237	113.78850	138.89335	164.90188	191.90141	219.99467	249.30397	279.97691	312.19453	346.18326
160.00000	181.11535	202.89533	225.39635	248.68345	272.83224	297.93150	324.08668	351.42463	380.10034	410.30664
160.00000	181.11535	202.89533	225.39635	248.68345	272.83224	297.93150	324.08668	351.42463	380.10034	410.30664
258.00000	276.62024	295.81004	315.61767	336.09874	357.31783	379.35065	402.28699	426.23465	451.32498	477.72085
258.00000	276.62024	295.81004	315.61767	336.09874	357.31783	379.35065	402.28699	426.23465	451.32498	477.72085
360.00000	376.02662	392.53085	409.55313	427.14003	445.34557	464.23305	483.87741	504.36855	525.81579	548.35442
360.00000	376.02662	392.53085	409.55313	427.14003	445.34557	464.23305	483.87741	504.36855	525.81579	548.35442
466.00000	479.33412	493.05628	507.19933	521.80104	536.90525	552.56326	568.83581	585.79563	603.53112	622.15150
466.00000	479.33412	493.05628	507.19933	521.80104	536.90525	552.56326	568.83581	585.79563	603.53112	622.15150
576.00000	586.54246	597.38514	608.55345	620.07660	631.98847	644.32870	657.14418	670.49106	684.43751	699.06771
576.00000	586.54246	597.38514	608.55345	620.07660	631.98847	644.32870	657.14418	670.49106	684.43751	699.06771
690.00000	697.65138	705.51641	713.61317	721.96244	730.58831	739.51897	748.78775	758.43454	768.50777	779.06719
690.00000	697.65138	705.51641	713.61317	721.96244	730.58831	739.51897	748.78775	758.43454	768.50777	779.06719
808.00000	812.66069	817.44927	822.37656	827.45500	832.69900	838.12543	843.75424	849.60927	855.71949	862.12061
808.00000	812.66069	817.44927	822.37656	827.45500	832.69900	838.12543	843.75424	849.60927	855.71949	862.12061
930.00000	931.57021	933.18300	934.84197	936.55127	938.31570	940.14087	942.03341	944.00127	946.05409	948.20375
930.00000	931.57021	933.18300	934.84197	936.55127	938.31570	940.14087	942.03341	944.00127	946.05409	948.20375

J = 32

0.32	-1056.00000	-1042.00814	-1036.00593	-1031.40832	-1027.53699	-1024.12959	-1021.05168	-1018.22338	-1015.59270	-1013.12350	-1010.
1.32	-1054.00000	-1042.00802	-1036.00593	-1031.40832	-1027.53699	-1024.12959	-1021.05168	-1018.22338	-1015.59270	-1013.12350	-1010.
1.31	-1054.00000	-1015.19868	-997.18870	-983.42502	-971.84873	-961.66816	-952.47822	-944.03857	-936.19272	-928.83206	-921.
2.31	-1048.00000	-1015.19231	-997.18867	-983.42502	-971.84873	-961.66816	-952.47822	-944.03857	-936.19272	-928.83206	-921.
2.30	-1048.00000	-990.98648	-960.80917	-937.90544	-918.68258	-901.80107	-886.57892	-872.61246	-859.63925	-847.47728	-835.
3.30	-1038.00000	-990.85426	-960.80822	-937.90543	-918.68258	-901.80107	-886.57892	-872.61246	-859.63925	-847.47728	-835.
3.29	-1038.00000	-970.45620	-927.11280	-894.99917	-868.14521	-844.60861	-823.41580	-803.99357	-785.97038	-769.08902	-753.
4.29	-1024.00000	-969.06760	-927.09311	-894.99881	-868.14520	-844.60861	-823.41580	-803.99357	-785.97038	-769.08902	-753.
4.28	-1024.00000	-955.55086	-896.58045	-854.91732	-820.37697	-790.19303	-763.06625	-738.24160	-715.23251	-693.70336	-673.
5.28	-1006.00000	-948.85573	-896.32211	-854.91033	-820.37676	-790.19303	-763.06625	-738.24160	-715.23251	-693.70336	-673.
5.27	-1006.00000	-943.37733	-870.60085	-818.01111	-775.57208	-738.68840	-705.62890	-675.43120	-647.48292	-621.36440	-596.
6.27	-984.00000	-927.79891	-868.51445	-817.91650	-775.56826	-738.68825	-705.62890	-675.43120	-647.48292	-621.36440	-596.
6.26	-984.00000	-926.72134	-851.37750	-785.13201	-734.03332	-690.27863	-651.23303	-615.65772	-582.79349	-552.12681	-523.
7.26	-958.00000	-903.56452	-842.53613	-784.25289	-733.98220	-690.27596	-651.23289	-615.65772	-582.79349	-552.12681	-523.
7.25	-958.00000	-903.45072	-835.36718	-758.54666	-696.40303	-645.24211	-600.05536	-559.04633	-521.25631	-486.05946	-453.
8.25	-928.00000	-875.21834	-815.79797	-753.50800	-695.90660	-645.20716	-600.05320	-559.04621	-521.25630	-486.05946	-453.
8.24	-928.00000	-875.21035	-814.23844	-738.95271	-664.49702	-604.12579	-552.35978	-505.76812	-462.99259	-423.25092	-386.
9.24	-894.00000	-842.69810	-785.83389	-723.74104	-661.24829	-603.78258	-552.33206	-505.76619	-462.99247	-423.25092	-386.
9.23	-894.00000	-842.69769	-785.63792	-718.93705	-640.64192	-568.44025	-508.64310	-456.07704	-408.16834	-363.81823	-322.
10.23	-856.00000	-806.09516	-751.63360	-692.05358	-628.60432	-566.05557	-508.37147	-456.05290	-408.16653	-363.81811	-322.
10.22	-856.00000	-806.09515	-751.61637	-691.19490	-620.02369	-540.96612	-470.23588	-410.44054	-357.02962	-307.92212	-262.
11.22	-814.00000	-765.47549	-713.14631	-656.47660	-595.14291	-530.96851	-468.29645	-410.20571	-357.00741	-307.92039	-262.
11.21	-814.00000	-765.47549	-713.14516	-656.37620	-593.18721	-519.02147	-439.99711	-370.08216	-310.02437	-255.80122	-205.
12.21	-768.00000	-720.87823	-670.51411	-616.50419	-558.31082	-495.86928	-431.25926	-368.38567	-309.81008	-255.78027	-205.
12.20	-768.00000	-720.87823	-670.51405	-616.49543	-558.03565	-492.66192	-416.65360	-337.83823	-268.30879	-207.88778	-152.
13.20	-718.00000	-672.32736	-623.84740	-572.25009	-517.10211	-457.89958	-394.77237	-329.87070	-266.75334	-207.68691	-152.
13.19	-718.00000	-672.32736	-623.84740	-572.24949	-517.07381	-457.38658	-390.40673	-313.30703	-234.67592	-165.28948	-104.
14.19	-664.00000	-619.83826	-573.21660	-523.88528	-471.51161	-415.64697	-355.82542	-292.29513	-227.19032	-163.82721	-104.
14.18	-664.00000	-619.83826	-573.21660	-523.88525	-471.50933	-415.58822	-355.06215	-286.98938	-209.25653	-130.75192	-61.
15.18	-606.00000	-563.42122	-518.66738	-471.52989	-421.74306	-368.95735	-312.71395	-252.57280	-188.83911	-123.60167	-60.
15.17	-606.00000	-563.42122	-518.66738	-471.52989	-421.74291	-368.95211	-312.62003	-251.58739	-182.83497	-104.74340	-26.
16.17	-544.00000	-503.08333	-460.23059	-415.26312	-367.96048	-318.04350	-265.14738	-208.80197	-148.57528	-84.78757	-19.
16.16	-544.00000	-503.08333	-460.23059	-415.26312	-367.96047	-318.04312	-265.13841	-208.67481	-147.41494	-78.29037	0.
17.16	-478.00000	-438.82964	-397.92777	-355.13879	-310.27480	-263.10441	-213.33494	-160.58519	-104.36839	-44.24218	19.
17.15	-478.00000	-438.82964	-397.92777	-355.13879	-310.27480	-263.10439	-213.33425	-160.57250	-104.21405	-42.95399	26.
18.15	-408.00000	-370.66379	-331.77441	-291.19480	-248.76191	-204.27871	-157.50222	-108.12462	-55.74488	0.14848	60.
18.14	-408.00000	-370.66379	-331.77441	-291.19480	-248.76191	-204.27870	-157.50217	-108.12360	-55.72907	0.32294	61.
19.14	-334.00000	-298.58850	-261.78190	-223.45862	-183.47554	-141.66195	-97.81082	-51.66586	-2.90106	48.90996	104.
19.13	-334.00000	-298.58850	-261.78190	-223.45862	-183.47554	-141.66195	-97.81082	-51.66579	-2.89976	48.92808	104.
20.13	-256.00000	-222.60581	-187.95876	-151.95063	-114.45495	-75.32218	-34.37306	8.61098	53.90226	101.84950	152.
20.12	-256.00000	-222.60581	-187.95876	-151.95063	-114.45495	-75.32218	-34.37306	8.61099	53.90234	101.85101	152.
21.12	-174.00000	-142.71729	-110.31150	-76.68626	-41.72947	-5.30939	32.73065	72.57977	114.47037	158.69451	205.
21.11	-174.00000	-142.71729	-110.31150	-76.68626	-41.72947	-5.30939	32.73065	72.57977	114.47038	158.69462	205.
22.11	-88.00000	-58.92414	-28.84518	2.32260	34.67851	68.33877	103.44088	140.14970	178.66597	219.23886	262.
22.10	-88.00000	-58.92414	-28.84518	2.32260	34.67851	68.33877	103.44088	140.14970	178.66597	219.23887	262.
23.10	2.00000	28.77268	56.43627	85.06668	114.75160	145.59338	177.71263	211.25330	246.38967	283.33629	322.
23.9	2.00000	28.77268	56.43627	85.06668	114.75160	145.59338	177.71263	211.25330	246.38967	283.33630	322.
24.9	96.00000	120.37240	145.52971	171.53864	198.47654	226.43183	255.51106	285.83916	317.56724	350.88043	386.
24.8	96.00000	120.37240	145.52971	171.53864	198.47614	226.43183	255.51106	285.83916	317.56724	350.88043	386.
25.8	194.00000	215.87443	238.43262	261.73260	285.84123	310.83622	336.80880	363.86726	392.14180	421.79139	453.
25.7	194.00000	215.87443	238.43262	261.73260	285.84123	310.83622	336.80880	363.86726	392.14180	421.79139	453.
26.7	296.00000	315.27826	335.14297	355.64384	376.83809	398.79218	421.58402	445.30596	470.06884	496.00767	523.
26.6	296.00000	315.27826	335.14297	355.64384	376.83809	398.79218	421.58402	445.30596	470.06884	496.00767	523.
27.6	402.00000	418.58350	435.65909	453.26846	471.45957	490.28805	509.81910	530.12989	551.31296	573.48086	596.
27.5	402.00000	418.58350	435.65909	453.26846	471.45957	490.28805	509.81910	530.12989	551.31296	573.48086	596.
28.5	512.00000	525.78980	539.97962	554.60330	569.69980	585.31429	601.49964	618.31843	635.84562	654.17229	673.
28.4	512.00000	525.78980	539.97962	554.60330	569.69980	585.31429	601.49964	618.31843	635.84562	654.17229	673.
29.4	626.00000	636.89691	648.10341	659.64571	671.55394	683.86301	696.61381	709.85468	723.64352	738.05060	753.
29.3	626.00000	636.89691	648.10341	659.64571	671.55394	683.86301	696.61381	709.85468	723.64352	738.05060	753.
30.3	744.00000	751.90457	760.02952	768.39350	777.01793	785.92767	795.15178	804.72466	814.68744	825.09007	835.
30.2	744.00000	751.90457	760.02952	768.39350	777.01793	785.92767	795.15178	804.72466	814.68744	825.09007	835.
31.2	866.00000	870.81261	875.75715	880.84480	886.08838	891.50276	897.10533	902.91668	908.96142	915.26941	921.
31.1	866.00000	870.81261	875.75715	880.84480	886.08838	891.50276	897.10533	902.91668	908.96142	915.26941	921.
32.1	992.00000	993.62085	995.28563	996.99806	998.76241	1000.58364	1002.46753	1004.42094	1006.45205	1008.57081	1010.
32.0	992.00000	993.62085	995.28563	996.99806	998.76241	1000.58364	1002.46753	1004.42094	1006.45205	1008.57081	1010.

-1122.00000	-1107.56032	-1101.37313	-1096.63348	-1092.64238	-1089.12945	-1085.95612	-1083.04007	-1080.32771	-1077.78180	-1075.37523
-1120.00000	-1107.56023	-1101.37313	-1096.63348	-1092.64238	-1089.12945	-1085.95612	-1083.04007	-1080.32771	-1077.78180	-1075.37523
-1120.00000	-1079.84951	-1061.28774	-1047.09875	-1035.16360	-1024.66674	-1015.19077	-1006.48803	-998.39729	-990.80658	-983.63444
-1114.00000	-1079.84510	-1061.28772	-1047.09875	-1035.16360	-1024.66674	-1015.19077	-1006.48803	-998.39729	-990.80658	-983.63444
-1114.00000	-1054.69833	-1023.63033	-1000.02156	-980.20246	-962.79497	-947.09693	-932.69263	-919.31173	-906.76675	-894.92129
-1104.00000	-1054.60257	-1023.62977	-1000.02155	-980.20246	-962.79497	-947.09693	-932.69263	-919.31173	-906.76675	-894.92129
-1104.00000	-1033.04782	-988.62961	-955.54401	-927.86070	-903.59089	-881.73398	-861.70033	-843.10757	-825.69093	-809.25806
-1090.00000	-1031.96972	-988.61751	-955.54383	-927.86070	-903.59089	-881.73398	-861.70033	-843.10757	-825.69093	-809.25806
-1090.00000	-1016.94369	-956.70052	-913.86259	-878.27066	-847.15131	-819.17536	-793.56789	-769.82896	-747.61349	-726.67131
-1072.00000	-1011.17221	-956.53239	-913.85879	-878.27057	-847.15131	-819.17536	-793.56789	-769.82896	-747.61349	-726.67131
-1072.00000	-1004.50887	-928.98196	-875.28566	-831.61200	-793.60165	-759.51377	-728.36567	-699.53000	-672.57614	-647.19310
-1050.00000	-989.92919	-927.50129	-875.23123	-831.61013	-793.60159	-759.51376	-728.36567	-699.53000	-672.57614	-647.19310
-1050.00000	-988.45461	-907.85873	-840.48606	-788.15156	-743.11072	-702.86913	-666.18259	-632.27792	-600.63014	-570.86246
-1024.00000	-965.76031	-900.69230	-839.94038	-788.12499	-743.10953	-702.86908	-666.18259	-632.27792	-600.63014	-570.86246
-1024.00000	-965.58982	-891.45599	-811.36819	-748.39572	-695.92303	-649.40228	-607.13377	-568.15790	-531.83942	-497.72753
-994.00000	-937.52186	-873.72115	-807.82619	-748.11786	-695.90641	-649.40139	-607.13372	-568.15790	-531.83942	-497.72753
-994.00000	-937.50896	-871.39622	-789.86262	-713.72412	-652.46895	-599.34328	-551.37344	-507.28046	-466.28523	-427.84863
-960.00000	-905.08369	-843.91489	-777.35274	-711.68705	-652.29305	-599.33113	-551.37271	-507.28042	-466.28523	-427.84863
-960.00000	-905.08298	-843.58943	-770.39993	-686.87953	-613.83698	-553.08061	-499.12092	-449.79375	-404.07327	-361.30265
-922.00000	-868.53862	-809.94619	-745.67360	-677.89375	-612.47401	-552.95200	-499.11112	-449.79311	-404.07323	-361.30265
-922.00000	-868.53859	-809.91505	-744.22530	-665.79430	-582.69918	-511.53938	-450.73788	-395.90792	-345.34551	-298.18997
-880.00000	-827.96092	-771.64517	-710.42838	-644.19392	-575.86535	-510.51560	-450.63461	-395.89956	-345.34494	-298.18993
-880.00000	-827.96092	-771.64293	-710.24012	-640.87090	-559.26763	-477.17523	-407.04993	-345.96487	-290.30329	-238.64579
-834.00000	-783.39517	-729.15119	-670.79119	-607.71879	-540.26926	-471.64710	-406.21629	-345.87709	-290.29597	-238.64530
-834.00000	-783.39517	-729.15106	-670.77325	-607.18471	-534.78753	-451.47015	-370.31593	-300.72278	-239.27144	-182.86204
-784.00000	-734.86860	-682.58901	-626.79875	-566.98339	-502.63445	-434.42933	-365.60817	-300.00806	-239.19472	-182.85565
-784.00000	-734.86860	-682.58900	-626.79741	-566.92267	-501.60428	-426.90094	-342.70329	-262.28201	-192.95576	-131.14651
-730.00000	-682.39868	-632.03951	-578.63381	-521.78803	-460.97336	-395.77831	-327.10140	-258.12524	-192.32627	-131.07929
-730.00000	-682.39868	-632.03951	-578.63373	-521.78268	-460.84118	-394.19070	-317.82578	-233.18531	-153.32329	-84.15721
-672.00000	-625.99703	-577.55500	-526.43470	-472.32587	-414.81220	-353.36030	-287.63762	-218.67356	-149.57900	-83.60010
-672.00000	-625.99703	-577.55500	-526.43470	-472.32549	-414.79918	-353.13829	-285.51002	-207.98429	-123.12829	-43.73506
-610.00000	-565.67171	-519.17068	-470.29311	-418.78416	-364.31540	-306.45082	-244.65244	-178.63985	-109.51801	-40.35002
-610.00000	-565.67171	-519.17068	-470.29311	-418.78414	-364.31437	-306.42723	-244.33599	-176.03261	-97.69924	-12.75499
-544.00000	-501.42841	-456.91107	-410.27099	-361.29239	-309.70610	-255.16597	-197.21556	-135.30587	-69.18265	0.00000
-544.00000	-501.42841	-456.91107	-410.27099	-361.29239	-309.70604	-255.16396	-197.18013	-134.90049	-66.16507	12.75499
-474.00000	-433.27125	-390.79374	-346.41174	-299.93871	-251.14715	-199.75303	-145.39073	-87.57963	-25.74929	40.35002
-474.00000	-433.27125	-390.79374	-346.41174	-299.93871	-251.14715	-199.75289	-145.38757	-87.53260	-25.26441	43.73506
-400.00000	-361.20331	-320.83160	-278.74672	-234.78514	-188.75053	-140.40275	-89.44092	-35.47644	22.00218	83.60010
-400.00000	-361.20331	-320.83160	-278.74672	-234.78514	-188.75053	-140.40274	-89.44069	-35.47210	22.05979	84.15721
-322.00000	-285.22689	-247.03433	-207.29913	-165.87672	-122.59535	-77.24785	-29.57955	20.73054	74.09946	131.07929
-322.00000	-285.22689	-247.03433	-207.29913	-165.87672	-122.59535	-77.24785	-29.57953	20.73086	74.10488	131.14651
-240.00000	-205.34375	-169.40929	-132.08652	-93.24701	-52.73931	-10.38248	34.04315	80.80964	130.26269	182.85565
-240.00000	-205.34375	-169.40929	-132.08652	-93.24701	-52.73931	-10.38248	34.04315	80.80966	130.26310	182.86204
-154.00000	-121.55527	-87.96219	-53.12237	-16.92154	20.77433	60.12437	101.32012	144.59608	190.24553	238.64530
-154.00000	-121.55527	-87.96219	-53.12237	-16.92154	20.77433	60.12437	101.32012	144.59608	190.24556	238.64579
-64.00000	-33.86252	-2.69749	29.58280	63.07990	97.91247	134.22075	172.17259	211.97192	253.87117	298.18993
-64.00000	-33.86252	-2.69749	29.58280	63.07990	97.91247	134.22075	172.17259	211.97192	253.87117	298.18997
30.00000	57.73363	86.38126	116.02069	146.74178	178.64930	211.86665	246.54094	282.85002	321.01251	361.30265
30.00000	57.73363	86.38126	116.02069	146.74178	178.64930	211.86665	246.54094	282.85002	321.01251	361.30265
128.00000	153.23251	179.27123	206.18464	234.05173	262.96441	293.03071	324.37905	357.16414	391.57531	427.84863
128.00000	153.23251	179.27123	206.18464	234.05173	262.96441	293.03071	324.37905	357.16414	391.57531	427.84863
230.00000	252.63355	275.97010	300.06928	324.99979	350.84148	377.68802	405.65058	434.86277	465.48760	497.72753
230.00000	252.63355	275.97010	300.06928	324.99979	350.84148	377.68802	405.65058	434.86277	465.48760	497.72753
336.00000	355.93630	376.47601	397.67024	419.57787	442.26725	465.81847	490.32646	515.90514	542.69320	570.86246
336.00000	355.93630	376.47601	397.67024	419.57787	442.26725	465.81847	490.32646	515.90514	542.69320	570.86246
446.00000	463.14039	480.78739	498.98392	517.77933	537.23090	557.40571	578.38317	600.25848	623.14741	647.19310
446.00000	463.14039	480.78739	498.98392	517.77933	537.23090	557.40571	578.38317	600.25848	623.14741	647.19310
560.00000	574.24549	588.90298	604.00734	619.59868	635.72350	652.43628	669.80144	687.89615	706.81417	726.67131
560.00000	574.24549	588.90298	604.00734	619.59868	635.72350	652.43628	669.80144	687.89615	706.81417	726.67131
678.00000	689.25136	700.82170	712.73800	725.03132	737.73763	750.89903	764.56535	778.79619	793.66398	809.25806
678.00000	689.25136	700.82170	712.73800	725.03132	737.73763	750.89903	764.56535	778.79619	793.66398	809.25806
800.00000	808.15776	816.54264	825.17383	834.07343	843.26705	852.78464	862.66163	872.94042	883.67248	894.92129
800.00000	808.15776	816.54264	825.17383	834.07343	843.26705	852.78464	862.66163	872.94042	883.67248	894.92129
926.00000	930.96453	936.06504	941.31304	946.72176	952.30652	958.08524	964.07914	970.31359	976.81936	983.63444
926.00000	930.96453	936.06504	941.31304	946.72176	952.30652	958.08524	964.07914	970.31359	976.81936	983.63444
1056.00000	1057.67149	1059.38826	1061.15415	1062.97355	1064.85158	1066.79420	1068.80847	1070.90283	1073.08754	1075.37523
1056.00000	1057.67149	1059.38826	1061.15415	1062.97355	1064.85158	1066.79420	1068.80847	1070.90283	1073.08754	1075.37523

J = 34

0.34	-1190.00000	-1175.11254	-1168.74035	-1163.85865	-1159.74777	-1156.12931	-1152.86056	-1149.85677	-1147.06274	-1144.44011	-1141.9
1.34	-1188.00000	-1175.11248	-1168.74035	-1163.85865	-1159.74777	-1156.12931	-1152.86056	-1149.85677	-1147.06274	-1144.44011	-1141.9
1.33	-1188.00000	-1146.50112	-1127.38702	-1112.77265	-1100.47859	-1089.66540	-1079.90338	-1070.93756	-1062.60190	-1054.78114	-1047.3
2.33	-1182.00000	-1146.49809	-1127.38702	-1112.77265	-1100.47859	-1089.66540	-1079.90338	-1070.93756	-1062.60190	-1054.78114	-1047.3
2.32	-1182.00000	-1120.41805	-1088.45279	-1064.13844	-1043.72289	-1025.78927	-1009.61526	-994.77304	-980.98441	-968.05637	-955.8
3.32	-1172.00000	-1120.34905	-1088.45246	-1064.13844	-1043.72289	-1025.78927	-1009.61526	-994.77304	-980.98441	-968.05637	-955.8
3.31	-1172.00000	-1097.67895	-1052.15227	-1018.09141	-989.57791	-964.57443	-942.05311	-921.40783	-902.24534	-884.29329	-867.3
4.31	-1158.00000	-1096.85094	-1052.14488	-1018.09131	-989.57791	-964.57442	-942.05311	-921.40783	-902.24534	-884.29329	-867.3
4.30	-1158.00000	-1080.31938	-1018.85032	-974.81553	-938.16885	-906.11277	-877.28683	-850.89599	-826.42681	-803.52470	-781.9
5.30	-1140.00000	-1075.41660	-1018.74202	-974.81348	-938.16880	-906.11276	-877.28683	-850.89599	-826.42681	-803.52470	-781.9
5.29	-1140.00000	-1067.45055	-989.47684	-934.58688	-889.66293	-850.52206	-815.40380	-783.30403	-753.58003	-725.79016	-699.6
6.29	-1118.00000	-1053.93487	-988.44646	-934.55593	-889.66202	-850.52204	-815.40380	-783.30403	-753.58003	-725.79016	-699.6
6.28	-1118.00000	-1051.95447	-966.34988	-897.94960	-844.29980	-797.95834	-756.51581	-718.71518	-683.76814	-651.13787	-620.4
7.28	-1092.00000	-1029.81416	-960.69828	-897.61727	-844.28617	-797.95781	-756.51579	-718.71518	-683.76814	-651.13787	-620.4
7.27	-1092.00000	-1029.56287	-949.14875	-866.42816	-802.49329	-748.64043	-700.77033	-657.23592	-617.07027	-579.62745	-544.4
8.27	-1062.00000	-1001.68872	-933.37854	-864.02566	-802.34089	-748.63265	-700.76997	-657.23590	-617.07027	-579.62745	-544.4
8.26	-1062.00000	-1001.66824	-930.01877	-842.57152	-765.27549	-702.92190	-648.37196	-599.00650	-553.58782	-511.33380	-471.6
9.26	-1028.00000	-969.34040	-903.68574	-832.65073	-764.04492	-702.83377	-648.36673	-599.00622	-553.58781	-511.33380	-471.6
9.25	-1028.00000	-969.33919	-903.15826	-823.04475	-735.22837	-661.59410	-599.63952	-544.22038	-493.45433	-446.35308	-402.2
10.25	-990.00000	-932.85897	-869.95751	-800.83127	-728.86405	-660.84484	-599.58017	-544.21649	-493.45411	-446.35307	-402.2
10.24	-990.00000	-932.85891	-869.90255	-798.47891	-712.71679	-626.83152	-555.23423	-493.17285	-436.85354	-384.81212	-336.2
11.24	-948.00000	-892.32737	-831.86108	-765.88637	-694.66784	-622.45221	-554.71592	-493.12873	-436.85047	-384.81195	-336.2
11.23	-948.00000	-892.32736	-831.85681	-765.54398	-689.32390	-600.77415	-516.98457	-446.44535	-384.06231	-326.88525	-273.7
12.23	-902.00000	-847.79617	-789.51994	-726.60882	-658.44036	-586.00343	-513.73610	-446.05400	-384.02751	-326.88276	-273.7
12.22	-902.00000	-847.79617	-789.51967	-726.57316	-657.44441	-577.28727	-487.71446	-405.61722	-335.60663	-272.83298	-214.8
13.22	-852.00000	-799.29623	-743.07306	-682.90654	-618.19151	-548.49758	-475.34410	-403.05566	-335.29438	-272.80475	-214.8
13.21	-852.00000	-799.29623	-743.07305	-682.90366	-618.06584	-546.53332	-463.45467	-373.71392	-292.88312	-223.13734	-159.9
14.21	-798.00000	-746.84730	-692.61302	-634.96346	-573.43293	-507.41230	-436.67990	-363.09248	-290.77622	-222.88110	-159.9
14.20	-798.00000	-746.84730	-692.61301	-634.96327	-573.42081	-507.12740	-433.58686	-348.46171	-258.91823	-179.04999	-109.4
15.20	-740.00000	-690.46252	-638.19960	-582.93720	-524.31267	-461.83076	-394.89789	-323.47337	-249.61905	-177.27721	-109.2
15.19	-740.00000	-690.46252	-638.19960	-582.93719	-524.31173	-461.79977	-394.39928	-319.23438	-232.70306	-143.50987	-64.4
16.19	-678.00000	-630.15096	-579.87285	-526.93364	-471.03873	-411.80115	-348.70192	-281.16680	-209.29604	-135.28478	-62.9
16.18	-678.00000	-630.15096	-579.87285	-526.93364	-471.03867	-411.79846	-348.64281	-280.42519	-203.97563	-116.46719	-27.7
17.18	-612.00000	-565.91902	-517.66060	-467.02397	-413.76161	-357.56029	-298.00974	-234.56796	-166.67360	-94.53267	-20.4
17.17	-612.00000	-565.91902	-517.66060	-467.02397	-413.76161	-357.56010	-298.00419	-234.47432	-165.68071	-88.21386	0.0
18.17	-542.00000	-497.77138	-451.58275	-403.25782	-352.58364	-299.29780	-243.06792	-183.45887	-119.90193	-51.83687	20.4
18.16	-542.00000	-497.77138	-451.58275	-403.25782	-352.58364	-299.29779	-243.06750	-183.44955	-119.77056	-50.59373	27.7
19.16	-468.00000	-425.71148	-381.65389	-335.67089	-287.57631	-237.14486	-184.09820	-128.08264	-68.63415	-5.14982	62.9
19.15	-468.00000	-425.71148	-381.65389	-335.67089	-287.57631	-237.14486	-184.09817	-128.08188	-68.62055	-4.97939	64.4
20.15	-390.00000	-349.74191	-307.88494	-264.28955	-218.79122	-171.19341	-121.25732	-68.68643	-13.10191	45.99569	109.2
20.14	-390.00000	-349.74191	-307.88494	-264.28955	-218.79122	-171.19341	-121.25732	-68.68638	-13.10076	46.01384	109.4
21.14	-308.00000	-269.86466	-230.28423	-189.13367	-146.26669	-101.51004	-54.65562	-5.44904	46.42782	101.38461	159.9
21.13	-308.00000	-269.86466	-230.28423	-189.13367	-146.26669	-101.51004	-54.65562	-5.44903	46.42790	101.38617	159.9
22.13	-222.00000	-186.08129	-148.85816	-110.21850	-70.03177	-28.14435	15.62681	61.50313	109.75755	160.73458	214.8
22.12	-222.00000	-186.08129	-148.85816	-110.21850	-70.03177	-28.14435	15.62681	61.50313	109.75755	160.73469	214.8
23.12	-132.00000	-98.39299	-63.61179	-27.55594	9.89110	48.86583	89.53003	132.07799	176.74691	223.83222	273.7
23.11	-132.00000	-98.39299	-63.61179	-27.55594	9.89110	48.86583	89.53003	132.07799	176.74691	223.83223	273.7
24.11	-38.00000	-6.80074	25.45090	58.84464	93.48430	129.49111	167.00816	206.20645	247.29342	290.52517	336.2
24.10	-38.00000	-6.80074	25.45090	58.84464	93.48430	129.49111	167.00816	206.20645	247.29342	290.52517	336.2
25.10	60.00000	88.69470	118.32669	148.97572	180.73384	213.70831	248.02536	283.83537	321.31990	360.70186	402.2
25.9	60.00000	88.69470	118.32669	148.97572	180.73384	213.70831	248.02536	283.83537	321.31990	360.70186	402.2
26.9	162.00000	188.09269	215.01302	242.83126	271.62847	301.49888	332.55322	364.92305	398.76676	434.27800	471.6
26.8	162.00000	188.09269	215.01302	242.83126	271.62847	301.49888	332.55322	364.92305	398.76676	434.27800	471.6
27.8	268.00000	291.39272	315.50774	340.40633	366.15904	392.84784	420.56891	449.43631	479.58708	511.18834	544.4
27.7	268.00000	291.39272	315.50774	340.40633	366.15904	392.84784	420.56891	449.43631	479.58708	511.18834	544.4
28.7	378.00000	398.59437	419.80913	441.69686	464.31805	487.74294	512.05386	537.34831	563.74330	591.38125	620.4
28.6	378.00000	398.59437	419.80913	441.69686	464.31805	487.74294	512.05386	537.34831	563.74330	591.38125	620.4
29.6	492.00000	509.69729	527.91574	546.69949	566.09931	586.17409	606.99282	628.63716	651.20499	674.81529	699.6
29.5	492.00000	509.69729	527.91574	546.69949	566.09931	586.17409	606.99282	628.63716	651.20499	674.81529	699.6
30.5	610.00000	624.70119	639.82637	655.41143	671.49765	688.13289	705.37317	723.28479	741.94714	761.45668	781.9
30.4	610.00000	624.70119	639.82637	655.41143	671.49765	688.13289	705.37317	723.28479	741.94714	761.45668	781.9
31.4	732.00000	743.60581	755.53999	767.83032	780.50875	793.61231	807.18436	821.27616	835.94907	851.27762	867.3
31.3	732.00000	743.60581	755.53999	767.83032	780.50875	793.61231	807.18436	821.27616	835.94907	851.27762	867.3
32.3	858.00000	866.41096	875.05575	883.95417	893.12895	902.60645	912.41753	922.59865	933.19347	944.25497	955.8
32.2	858.00000	866.41096	875.05575	883.95417	893.12895	902.60645	912.41753	922.59865	933.19347	944.25497	955.8
33.2	988.00000	993.11645	998.37293	1003.78129	1009.35514	1015.11028	1021.06516	1027.24162	1033.66577	1040.36933	1047.3
33.1	988.00000	993.11645	998.37293	1003.78129	1009.35514	1015.11028	1021.06516	1027.24162	1033.66577	1040.36933	1047.3
34.1	1122.00000	1123.72213	1125.49089	1127.31024	1129.18469	1131.11952	1133.12087	1135.19600	1137.35361	1139.60427	1141.9
34.0	1122.00000	1123.72213	1125.49089	1127.31024	1129.18469	1131.11952	1133.12087	1135.19600	1137.35361	1139.60427	1141.9

35

-1260.00000	-1244.66479	-1238.10758	-1233.08384	-1228.85318	-1225.12918	-1221.76502	-1218.67348	-1215.79776	-1213.09842	-1210.54672
-1258.00000	-1244.66476	-1238.10758	-1233.08384	-1228.85318	-1225.12918	-1221.76502	-1218.67348	-1215.79776	-1213.09842	-1210.54672
-1258.00000	-1215.15338	-1195.48653	-1180.44669	-1167.79369	-1156.66415	-1146.61606	-1137.38713	-1128.80655	-1120.75573	-1113.14837
-1252.00000	-1215.15129	-1195.48653	-1180.44669	-1167.79369	-1156.66415	-1146.61606	-1137.38713	-1128.80655	-1120.75573	-1113.14837
-1252.00000	-1188.14401	-1155.27638	-1130.25601	-1109.24380	-1090.78395	-1074.13388	-1058.85368	-1044.65727	-1031.34613	-1018.77587
-1242.00000	-1188.09453	-1155.27619	-1130.25601	-1109.24380	-1090.78395	-1074.13388	-1058.85368	-1044.65727	-1031.34613	-1018.77587
-1242.00000	-1164.34564	-1117.67967	-1082.64105	-1053.29666	-1027.55909	-1004.37311	-983.11600	-963.38363	-944.89605	-927.44980
-1228.00000	-1163.71583	-1117.67519	-1082.64100	-1053.29665	-1027.55909	-1004.37311	-983.11600	-963.38363	-944.89605	-927.44980
-1228.00000	-1145.70039	-1083.02277	-1037.77495	-1000.07099	-967.07704	-937.40041	-910.22570	-885.02591	-861.43688	-839.19446
-1210.00000	-1141.59708	-1082.95363	-1037.77385	-1000.07097	-967.07704	-937.40041	-910.22570	-885.02591	-861.43688	-839.19446
-1210.00000	-1132.22393	-1052.06884	-995.90862	-949.72326	-909.44875	-873.29842	-840.24583	-809.63270	-781.00620	-754.03877
-1188.00000	-1119.82095	-1051.36380	-995.89120	-949.72282	-909.44874	-873.29842	-840.24583	-809.63270	-781.00620	-754.03877
-1188.00000	-1117.21098	-1026.91603	-957.49417	-902.47163	-854.81924	-812.17171	-773.25456	-737.26347	-703.64949	-672.01748
-1162.00000	-1095.72556	-1022.57956	-957.29505	-902.46473	-854.81901	-812.17170	-773.25456	-737.26347	-703.64949	-672.01748
-1162.00000	-1095.36100	-1008.52407	-923.72480	-858.66589	-803.38697	-754.15639	-709.35083	-667.99207	-629.42254	-593.17277
-1132.00000	-1067.71679	-994.78791	-922.14473	-858.58377	-803.38338	-754.15625	-709.35082	-667.99207	-629.42254	-593.17277
-1132.00000	-1067.68480	-990.08603	-897.25339	-819.08606	-755.45299	-699.43690	-648.66308	-601.91199	-558.39474	-517.55650
-1098.00000	-1035.46637	-965.14734	-889.68478	-818.36498	-755.40970	-699.43469	-648.66298	-601.91199	-558.39474	-517.55650
-1098.00000	-1035.46435	-964.31317	-876.98233	-785.87863	-711.61176	-648.28487	-591.36449	-539.14460	-490.65412	-445.23337
-1060.00000	-999.05475	-931.66173	-857.55017	-781.59617	-711.21261	-648.25808	-591.36297	-539.14453	-490.65412	-445.23337
-1060.00000	-999.05465	-931.56689	-853.88073	-761.07444	-673.48699	-601.19643	-537.70572	-479.85305	-426.31498	-376.23561
-1018.00000	-958.57366	-893.78834	-822.84639	-746.62707	-670.83739	-600.94270	-537.68734	-479.85195	-426.31493	-376.28560
-1018.00000	-958.57366	-893.78038	-822.24248	-738.51989	-643.99364	-559.45462	-488.12210	-424.27103	-365.53083	-310.82014
-972.00000	-914.08027	-851.61579	-783.94565	-710.48574	-633.18164	-557.65971	-487.94500	-424.25763	-365.53000	-310.82010
-972.00000	-914.08027	-851.61526	-783.87680	-708.70540	-620.29482	-525.99391	-443.67667	-372.79067	-308.52001	-248.98055
-922.00000	-865.60945	-805.29588	-740.56333	-670.71099	-595.52693	-517.67890	-442.37141	-372.65965	-308.50995	-248.97994
-922.00000	-865.60945	-805.29586	-740.55730	-670.45992	-591.99021	-500.42042	-407.07996	-326.32257	-255.63987	-190.97010
-868.00000	-813.18346	-754.93409	-692.86613	-626.42889	-554.94862	-478.60707	-400.48706	-325.32716	-255.54012	-190.96255
-868.00000	-813.18346	-754.93409	-692.86570	-626.40239	-554.36077	-473.01297	-379.49796	-287.30992	-207.68498	-137.11490
-810.00000	-756.81710	-700.59859	-641.03078	-577.68921	-509.98746	-437.31731	-360.20486	-281.95515	-206.90676	-137.03877
-810.00000	-756.81710	-700.59859	-641.03075	-577.68699	-509.91662	-436.25548	-352.50429	-257.86293	-166.83724	-88.11207
-748.00000	-696.52055	-642.33488	-585.17914	-524.71270	-460.47881	-391.86679	-318.34683	-240.72475	-162.43329	-87.50192
-748.00000	-696.52055	-642.33488	-585.17914	-524.71255	-460.47208	-391.72550	-316.71692	-231.00724	-135.76071	-45.89141
-682.00000	-632.30103	-580.17443	-525.39296	-467.67293	-406.64935	-341.83528	-272.60042	-198.48975	-120.53772	-42.27651
-682.00000	-632.30103	-580.17443	-525.39296	-467.67292	-406.64883	-341.82061	-272.36614	-196.23722	-108.92694	-13.41811
-612.00000	-564.16377	-514.13973	-461.72889	-406.68858	-348.71614	-287.42195	-222.28777	-152.66213	-78.15424	0.00000
-612.00000	-564.16377	-514.13973	-461.72889	-406.68858	-348.71611	-287.42071	-222.26181	-152.31766	-75.24312	13.41811
-538.00000	-492.11263	-444.24723	-394.22749	-341.84199	-286.83266	-228.87677	-167.55762	-102.32158	-32.48928	42.27651
-538.00000	-492.11263	-444.24723	-394.22749	-341.84199	-286.83266	-228.87668	-167.55530	-102.28148	-32.02030	45.89141
-460.00000	-416.15054	-370.50922	-322.91863	-273.19225	-221.10577	-166.38432	-108.68253	-47.55216	17.60324	87.50192
-460.00000	-416.15054	-370.50922	-322.91863	-273.19225	-221.10577	-166.38431	-108.68236	-47.54840	17.65997	88.11207
-378.00000	-336.27973	-292.93506	-247.82478	-200.78299	-151.61226	-100.07399	-45.87406	11.35966	72.11378	137.03877
-378.00000	-336.27973	-292.93506	-247.82478	-200.78299	-151.61226	-100.07399	-45.87405	11.35995	72.11927	137.11490
-292.00000	-252.50192	-211.53197	-168.96315	-124.64720	-78.40898	-30.03887	20.71824	74.17933	130.74919	190.96255
-292.00000	-252.50192	-211.53197	-168.96315	-124.64720	-78.40898	-30.03887	20.71824	74.17935	130.74963	190.97010
-202.00000	-164.81848	-126.30560	-86.34714	-44.81030	-1.53908	43.65197	90.98659	140.73944	193.25536	248.97994
-202.00000	-164.81848	-126.30560	-86.34714	-44.81030	-1.53908	43.65197	90.98659	140.73944	193.25539	248.98055
-108.00000	-73.23049	-37.26045	0.01268	38.70781	78.96402	120.94592	164.85084	210.91912	259.44907	310.82010
-108.00000	-73.23049	-37.26045	0.01268	38.70781	78.96402	120.94592	164.85084	210.91912	259.44907	310.82014
-10.00000	22.26119	55.59989	90.10788	125.89132	163.07405	201.80209	242.24980	284.62831	329.19778	376.28560
-10.00000	22.26119	55.59989	90.10788	125.89132	163.07405	201.80209	242.24980	284.62831	329.19778	376.28561
92.00000	121.65585	152.27251	183.93165	216.72756	250.77002	286.18817	323.13570	361.79806	402.40257	445.23337
92.00000	121.65585	152.27251	183.93165	216.72756	250.77002	286.18817	323.13570	361.79806	402.40257	445.23337
198.00000	224.95292	252.75504	281.47845	311.20623	342.03501	374.07824	407.47066	442.37440	478.98753	517.55650
198.00000	224.95292	252.75504	281.47845	311.20623	342.03501	374.07824	407.47066	442.37440	478.98753	517.55650
308.00000	332.15192	357.04552	382.74371	409.31889	436.85520	465.45129	495.22416	526.31433	558.89306	593.17277
308.00000	332.15192	357.04552	382.74371	409.31889	436.85520	465.45129	495.22416	526.31433	558.89306	593.17277
422.00000	443.25246	465.14234	487.72366	511.05857	535.21920	560.29009	586.37136	613.58313	642.07153	672.01748
422.00000	443.25246	465.14234	487.72366	511.05857	535.21920	560.29009	586.37136	613.58313	642.07153	672.01748
540.00000	558.25420	577.04414	596.41516	616.41946	637.11757	658.58038	680.89179	704.15237	728.48433	754.03877
540.00000	558.25420	577.04414	596.41516	616.41946	637.11757	658.58038	680.89179	704.15237	728.48433	754.03877
662.00000	677.15689	692.74977	708.81557	725.39671	742.54241	760.31028	778.76845	797.99857	818.09976	839.19446
662.00000	677.15689	692.74977	708.81557	725.39671	742.54241	760.31028	778.76845	797.99857	818.09976	839.19446
788.00000	799.96027	812.25829	824.92265	837.98621	851.48706	865.46978	879.98710	895.10213	910.89151	927.44980
788.00000	799.96027	812.25829	824.92265	837.98621	851.48706	865.46978	879.98710	895.10213	910.89151	927.44980
918.00000	926.66415	935.56887	944.73452	954.18448	963.94588	974.05045	984.53572	995.44658	1006.83755	1018.77587
918.00000	926.66415	935.56887	944.73452	954.18448	963.94588	974.05045	984.53572	995.44658	1006.83755	1018.77587
1052.00000	1057.26837	1062.68082	1068.24954	1073.98853	1079.91405	1086.04509	1092.40410	1099.01797	1105.91931	1113.14837
1052.00000	1057.26837	1062.68082	1068.24954	1073.98853	1079.91405	1086.04509	1092.40410	1099.01797	1105.91931	1113.14837
1190.00000	1191.77277	1193.59352	1195.46632	1197.39583	1199.38746	1201.44753	1203.58353	1205.80440	1208.12100	1210.54672
1190.00000	1191.77277	1193.59352	1195.46632	1197.39583	1199.38746	1201.44753	1203.58353	1205.80440	1208.12100	1210.54672

J = 36

0.36	-1332.00000	-1316.21709	-1309.47484	-1304.30903	-1299.95860	-1296.12906	-1292.66948	-1289.49018	-1286.53279	-1283.75673	-1281.1
1.36	-1330.00000	-1316.21706	-1309.47484	-1304.30903	-1299.95860	-1296.12906	-1292.66948	-1289.49018	-1286.53279	-1283.75673	-1281.1
1.35	-1330.00000	-1285.80617	-1265.58624	-1250.12087	-1237.10889	-1225.66297	-1215.32880	-1205.83675	-1197.01123	-1188.73035	-1180.9
2.35	-1324.00000	-1285.80474	-1265.58623	-1250.12087	-1237.10889	-1225.66297	-1215.32880	-1205.83675	-1197.01123	-1188.73035	-1180.9
2.34	-1324.00000	-1257.87494	-1224.10096	-1198.37420	-1176.76516	-1157.77897	-1140.65275	-1124.93453	-1110.33028	-1096.63601	-1083.7
3.34	-1314.00000	-1257.83962	-1224.10085	-1198.37420	-1176.76516	-1157.77897	-1140.65275	-1124.93453	-1110.33028	-1096.63601	-1083.7
3.33	-1314.00000	-1233.04322	-1185.21103	-1149.19270	-1119.01677	-1092.54478	-1068.69389	-1046.82477	-1026.52239	-1007.49918	-989.5
4.33	-1300.00000	-1232.56828	-1185.20832	-1149.19267	-1119.01677	-1092.54478	-1068.69389	-1046.82477	-1026.52239	-1007.49918	-989.5
4.32	-1300.00000	-1213.10563	-1149.21261	-1102.73993	-1063.97663	-1030.04383	-999.51589	-971.55687	-945.62612	-921.34993	-898.4
5.32	-1282.00000	-1209.72173	-1149.16885	-1102.73934	-1063.97662	-1030.04383	-999.51589	-971.55687	-945.62612	-921.34993	-898.4
5.31	-1282.00000	-1198.85304	-1116.73975	-1059.24659	-1011.79174	-970.38099	-933.19709	-899.19070	-867.68772	-838.22404	-810.4
6.31	-1260.00000	-1187.59332	-1116.26429	-1059.23688	-1011.79153	-970.38098	-933.19709	-899.19070	-867.68772	-838.22404	-810.4
6.30	-1260.00000	-1184.21806	-1089.60184	-1019.09849	-962.66268	-913.69163	-869.83573	-829.79995	-792.76335	-758.16457	-725.5
7.30	-1234.00000	-1163.49465	-1086.36060	-1018.98088	-962.65922	-913.69153	-869.83572	-829.79995	-792.76335	-758.16457	-725.5
7.29	-1234.00000	-1162.97395	-1069.66906	-983.22735	-916.89351	-860.15753	-809.55802	-763.47690	-720.92215	-681.22387	-643.9
8.29	-1204.00000	-1135.60399	-1057.97038	-982.21482	-916.84993	-860.15589	-809.55796	-763.47690	-720.92215	-681.22387	-643.9
8.28	-1204.00000	-1135.55478	-1051.60007	-954.05669	-875.08956	-810.04206	-752.53191	-700.33990	-652.25079	-607.46651	-565.4
9.28	-1170.00000	-1103.45965	-1028.30361	-948.50596	-874.67751	-810.02115	-752.53098	-700.33986	-652.25078	-607.46651	-565.4
9.27	-1170.00000	-1103.45634	-1027.01721	-932.36648	-838.91593	-763.81127	-698.99504	-640.54557	-586.86026	-536.97350	-490.2
10.27	-1132.00000	-1067.12445	-995.05355	-915.86299	-836.16441	-763.60410	-698.98319	-640.54499	-586.86024	-536.97350	-490.2
10.26	-1132.00000	-1067.12428	-994.89348	-910.38013	-811.17483	-722.63960	-649.33970	-584.31247	-524.89708	-469.84865	-418.3
11.26	-1090.00000	-1026.69860	-957.42100	-881.30952	-800.14673	-721.11095	-649.21893	-584.30499	-524.89669	-469.84863	-418.3
11.25	-1090.00000	-1026.69860	-957.40652	-880.27728	-788.54617	-689.34768	-604.46391	-531.98627	-466.56395	-406.22873	-349.9
12.25	-1044.00000	-982.24649	-915.43394	-842.79078	-763.88000	-681.92524	-603.51918	-531.90855	-466.55891	-406.22846	-349.9
12.24	-1044.00000	-982.24649	-915.43292	-842.66147	-760.84051	-664.12417	-566.77561	-484.29805	-412.17247	-346.30196	-285.1
13.24	-994.00000	-933.80743	-869.25364	-799.75840	-724.53056	-643.78780	-561.60144	-483.66573	-412.11933	-346.29848	-285.1
13.23	-994.00000	-933.80743	-869.25358	-799.74613	-724.04653	-637.81502	-538.36032	-443.25013	-362.34200	-290.35197	-224.0
14.23	-940.00000	-881.40644	-818.99956	-752.33319	-680.75797	-603.57951	-521.67733	-439.49888	-361.89619	-290.31456	-224.0
14.22	-940.00000	-881.40644	-818.99955	-752.33226	-680.70191	-602.42046	-512.36191	-411.75186	-318.74538	-238.91499	-166.9
15.22	-882.00000	-825.06014	-764.74931	-700.70844	-632.44021	-559.25738	-480.63453	-398.01091	-315.94178	-238.59230	-166.9
15.21	-882.00000	-825.06014	-764.74931	-700.70838	-632.43509	-559.10181	-478.49991	-385.35310	-284.54030	-193.39832	-114.3
16.21	-820.00000	-764.77995	-706.55445	-645.02381	-579.79379	-510.32479	-435.91531	-356.23742	-273.17400	-191.26977	-114.1
16.20	-820.00000	-764.77995	-706.55445	-645.02380	-579.79341	-510.30859	-435.59322	-352.90440	-257.37240	-156.91425	-67.4
17.20	-754.00000	-700.57394	-644.45055	-585.37302	-523.01625	-456.95423	-386.60937	-311.28029	-230.83800	-147.52271	-65.8
17.19	-754.00000	-700.57394	-644.45055	-585.37302	-523.01622	-456.95286	-386.57237	-310.72598	-226.16156	-128.81965	-29.0
18.19	-684.00000	-632.44798	-578.46292	-521.82065	-462.24499	-399.38668	-332.78790	-261.83370	-185.82844	-104.83429	-21.4
18.18	-684.00000	-632.44798	-578.46292	-521.82065	-462.24498	-399.38659	-332.78447	-261.76500	-184.98234	-98.71176	0.0
19.18	-610.00000	-560.40640	-508.61005	-454.41272	-397.57482	-337.80092	-274.71646	-207.82917	-136.48374	-59.98931	21.4
19.17	-610.00000	-560.40640	-508.61005	-454.41272	-397.57482	-337.80091	-274.71620	-207.82236	-136.37230	-58.79373	29.0
20.17	-532.00000	-484.45245	-434.90575	-383.18301	-329.07333	-272.32125	-212.61052	-149.53828	-82.57273	-11.01116	65.8
20.16	-532.00000	-484.45245	-434.90575	-383.18301	-329.07333	-272.32124	-212.61050	-149.53772	-82.56108	-10.84544	67.4
21.16	-450.00000	-404.58864	-357.36052	-308.15684	-256.79016	-203.03620	-146.62195	-87.20746	-24.35665	42.50982	114.1
21.15	-450.00000	-404.58864	-357.36052	-308.15684	-256.79016	-203.03620	-146.62195	-87.20742	-24.35565	42.52787	114.3
22.15	-364.00000	-320.81689	-275.98244	-229.35359	-180.76268	-130.01091	-76.85901	-21.01375	37.89286	100.33729	166.9
22.14	-364.00000	-320.81689	-275.98244	-229.35359	-180.76268	-130.01091	-76.85901	-21.01375	37.89294	100.33889	166.9
23.14	-274.00000	-233.13873	-190.77787	-146.78832	-101.01964	-53.29453	-3.40137	48.91644	103.97612	162.17980	224.0
23.13	-274.00000	-233.13873	-190.77787	-146.78832	-101.01964	-53.29453	-3.40137	48.91644	103.97612	162.17992	224.0
24.13	-180.00000	-141.55537	-101.75181	-60.47290	-17.58347	27.07502	73.69073	122.49007	173.75015	227.81729	285.1
24.12	-180.00000	-141.55537	-101.75181	-60.47290	-17.58347	27.07502	73.69073	122.49007	173.75015	227.81730	285.1
25.12	-82.00000	-46.06778	-8.90830	29.58320	69.52804	111.06800	154.37066	199.63661	247.10967	297.09166	349.9
25.11	-82.00000	-46.06778	-8.90830	29.58320	69.52804	111.06800	154.37066	199.63661	247.10967	297.09166	349.9
26.11	20.00000	53.32325	87.74941	123.37237	160.30063	198.66072	238.60172	280.30139	323.97480	369.88645	418.3
26.10	20.00000	53.32325	87.74941	123.37237	160.30063	198.66072	238.60172	280.30139	323.97480	369.88645	418.3
27.10	126.00000	156.61709	188.21866	220.88837	254.72274	289.83411	326.35457	364.44122	404.28346	446.11321	490.2
27.9	126.00000	156.61709	188.21866	220.88837	254.72274	289.83411	326.35457	364.44122	404.28346	446.11321	490.2
28.9	236.00000	263.81320	292.49727	322.12612	352.78489	384.57261	417.60547	452.02145	487.98645	525.70306	565.4
28.8	236.00000	263.81320	292.49727	322.12612	352.78489	384.57261	417.60547	452.02145	487.98645	525.70306	565.4
29.8	350.00000	374.91115	400.58343	427.08138	454.47928	482.86343	512.33499	543.01391	575.04420	608.60131	643.9
29.7	350.00000	374.91115	400.58343	427.08138	454.47928	482.86343	512.33499	543.01391	575.04420	608.60131	643.9
30.7	468.00000	489.91056	512.47562	535.75063	559.79939	584.69596	610.52707	637.39549	665.42443	694.76380	725.5
30.6	468.00000	489.91056	512.47562	535.75063	559.79939	584.69596	610.52707	637.39549	665.42443	694.76380	725.5
31.6	590.00000	608.81113	628.17257	648.13092	668.73979	690.06133	712.16834	735.14700	759.10054	784.15444	810.4
31.5	590.00000	608.81113	628.17257	648.13092	668.73979	690.06133	712.16834	735.14700	759.10054	784.15444	810.4
32.5	716.00000	731.61259	747.67320	764.21976	781.29586	798.95207	817.24758	836.25240	856.05038	876.74335	898.4
32.4	716.00000	731.61259	747.67320	764.21976	781.29586	798.95207	817.24758	836.25240	856.05038	876.74335	898.4
33.4	846.00000	858.31473	870.97660	884.01501	897.46371	911.36187	925.75529	940.69816	956.25535	972.50561	989.5
33.3	846.00000	858.31473	870.97660	884.01501	897.46371	911.36187	925.75529	940.69816	956.25535	972.50561	989.5
34.3	980.00000	988.91735	998.08200	1007.51487	1017.24002	1027.28532	1037.68340	1048.47282	1059.69975	1071.42021	1083.7
34.2	980.00000	988.91735	998.08200	1007.51487	1017.24002	1027.28532	1037.68340	1048.47282	1059.69975	1071.42021	1083.7
35.2	1118.00000	1123.42029	1128.98871	1134.71778	1140.62193	1146.71783	1153.02502	1159.56659	1166.37018	1173.46932	1180.9
35.1	1118.00000	1123.42029	1128.98871	1134.71778	1140.62193	1146.71783	1153.02502	1159.56659	1166.37018	1173.46932	1180.9
36.1	1260.00000	1261.82341	1263.69616	1265.62241	1267.60697	1269.65540	1271.77420	1273.97106	1276.25518	1278.63773	1281.1
36.0	1260.00000	1261.82341	1263.69616	1265.62241	1267.60697	1269.65540	1271.77420	1273.97106	1276.25518	1278.63773	1281.1

-1406.00000	-1389.76941	-1382.84211	-1377.53424	-1373.06402	-1369.12895	-1365.57394	-1362.30690	-1359.26782	-1356.41504	-1353.71822
-1404.00000	-1389.76940	-1382.84211	-1377.53424	-1373.06402	-1369.12895	-1365.57394	-1362.30690	-1359.26782	-1356.41504	-1353.71822
-1404.00000	-1358.45941	-1337.68612	-1321.79517	-1308.42418	-1296.66187	-1286.04160	-1276.28641	-1267.21595	-1258.70500	-1250.66239
-1398.00000	-1358.45843	-1337.68612	-1321.79517	-1308.42418	-1296.66187	-1286.04160	-1276.28641	-1267.21595	-1258.70500	-1250.66239
-1398.00000	-1329.60986	-1294.92643	-1268.49295	-1246.28692	-1226.77428	-1209.17186	-1193.01556	-1178.00344	-1163.92601	-1150.63084
-1388.00000	-1329.58475	-1294.92636	-1268.49295	-1246.28692	-1226.77428	-1209.17186	-1193.01556	-1178.00344	-1163.92601	-1150.63084
-1388.00000	-1303.76697	-1254.74572	-1217.74613	-1186.73813	-1159.53138	-1135.01536	-1112.53409	-1091.66158	-1072.10265	-1053.64269
-1374.00000	-1303.41156	-1254.74409	-1217.74612	-1186.73813	-1159.53138	-1135.01536	-1112.53409	-1091.66158	-1072.10265	-1053.64269
-1374.00000	-1282.54943	-1217.41605	-1169.70974	-1129.88541	-1095.01288	-1063.63306	-1034.88934	-1008.22736	-983.26377	-959.72031
-1356.00000	-1279.79837	-1217.38855	-1169.70943	-1129.88541	-1095.01288	-1063.63306	-1034.88934	-1008.22736	-983.26377	-959.72031
-1356.00000	-1267.36373	-1183.47286	-1124.59778	-1075.86735	-1033.31815	-995.09940	-960.13833	-927.74486	-897.44352	-868.89002
-1334.00000	-1257.25867	-1183.15625	-1124.59241	-1075.86725	-1033.31815	-995.09940	-960.13833	-927.74486	-897.44352	-868.89002
-1334.00000	-1252.97483	-1154.42903	-1082.74739	-1024.86978	-974.57410	-929.50691	-888.35067	-850.26727	-814.68274	-781.18308
-1308.00000	-1233.12226	-1152.06402	-1082.67880	-1024.86807	-974.57406	-929.50691	-888.35067	-850.26727	-814.68274	-781.18308
-1308.00000	-1232.39003	-1132.67483	-1044.89506	-977.16281	-918.94839	-866.97321	-819.61281	-775.85956	-735.03073	-696.63692
-1278.00000	-1205.34832	-1122.94977	-1044.26019	-977.14001	-918.94765	-866.97319	-819.61281	-775.85956	-735.03073	-696.63692
-1278.00000	-1205.27374	-1114.58897	-1013.08318	-933.23243	-866.67602	-807.65237	-754.03430	-704.60238	-658.54779	-615.29684
-1244.00000	-1173.31825	-1093.16201	-1009.16376	-933.00189	-866.66608	-807.65199	-754.03428	-704.60238	-658.54779	-615.29684
-1244.00000	-1173.31289	-1091.22946	-989.37661	-894.33213	-818.13820	-751.75616	-691.75794	-636.59785	-585.30886	-537.21835
-1206.00000	-1137.06649	-1060.12868	-975.81066	-892.63210	-818.03304	-751.75101	-691.75772	-636.59784	-585.30886	-537.21835
-1206.00000	-1137.06620	-1059.86427	-967.97520	-863.31181	-774.18978	-699.60916	-632.97778	-571.97866	-515.40878	-462.47049
-1164.00000	-1096.70093	-1022.75298	-941.28370	-855.30956	-773.34081	-699.55305	-632.97479	-571.97852	-515.40877	-462.47049
-1164.00000	-1096.70092	-1022.72718	-939.57657	-839.60233	-737.14070	-651.86100	-577.98134	-510.92382	-448.97058	-391.14070
-1118.00000	-1052.29381	-980.96935	-903.13459	-818.66499	-732.35583	-651.38247	-577.94813	-510.92197	-448.97049	-391.14069
-1118.00000	-1052.29381	-980.96740	-902.89841	-813.73192	-709.20560	-610.27129	-527.29872	-453.69291	-386.15948	-323.34236
-1068.00000	-1003.88931	-934.94228	-860.48058	-779.64616	-693.37195	-607.26652	-527.00438	-453.67198	-386.15830	-323.34230
-1068.00000	-1003.88931	-934.94216	-860.45628	-778.74655	-683.96205	-577.92169	-482.29629	-400.73693	-327.21151	-259.22721
-1014.00000	-951.51552	-884.80611	-813.35549	-736.40242	-653.32089	-566.04151	-480.31096	-400.54552	-327.19793	-259.22646
-1014.00000	-951.51552	-884.80610	-813.35350	-736.28769	-651.14502	-551.79450	-446.05816	-353.14802	-272.51896	-199.00971
-956.00000	-895.19102	-830.64896	-761.96281	-688.54932	-609.61887	-524.90069	-437.10659	-351.78611	-272.39107	-199.00091
-956.00000	-895.19102	-830.64896	-761.96268	-688.53794	-609.29060	-520.87965	-418.23108	-313.70960	-222.97359	-143.03407
-894.00000	-834.92860	-772.52919	-706.46153	-636.26885	-561.31406	-480.82728	-394.93898	-306.92637	-222.02150	-142.94861
-894.00000	-834.92860	-772.52919	-706.46152	-636.26794	-561.27651	-480.12786	-388.67037	-283.85582	-180.97811	-92.03606
-828.00000	-770.73728	-710.48688	-646.95894	-579.78083	-508.45433	-432.29763	-350.59609	-263.88101	-175.84007	-91.37178
-828.00000	-770.73728	-710.48688	-646.95894	-579.78077	-508.45088	-432.20834	-349.35941	-255.13075	-149.04074	-48.03286
-758.00000	-702.62360	-644.55047	-583.52860	-519.24385	-451.29277	-379.13611	-302.05304	-219.40654	-132.11473	-44.18739
-758.00000	-702.62360	-644.55047	-583.52860	-519.24385	-451.29251	-379.12703	-301.88038	-217.47087	-120.75223	-14.07731
-684.00000	-630.59239	-574.74071	-516.22264	-454.76706	-390.03583	-321.59341	-248.85709	-171.06871	-87.68284	0.00000
-684.00000	-630.59239	-574.74071	-516.22264	-454.76706	-390.03581	-321.59265	-248.83813	-170.77694	-84.88526	14.07731
-606.00000	-554.64728	-501.07307	-445.07917	-386.42771	-324.82806	-259.91629	-191.22128	-118.11156	-39.78906	44.18739
-606.00000	-554.64728	-501.07307	-445.07917	-386.42771	-324.82806	-259.91624	-191.21958	-118.07749	-39.33711	48.03286
-524.00000	-474.79107	-423.55928	-370.12670	-314.28221	-255.77163	-194.28287	-129.42280	-60.67887	12.63785	91.37178
-524.00000	-474.79107	-423.55928	-370.12670	-314.28221	-255.77163	-194.28287	-129.42267	-60.67563	12.69342	92.03606
-438.00000	-391.02591	-342.20840	-291.38698	-238.37288	-182.94110	-124.81924	-63.67059	0.93241	69.55232	142.94861
-438.00000	-391.02591	-342.20840	-291.38698	-238.37288	-182.94110	-124.81924	-63.67059	0.93266	69.55784	143.03407
-348.00000	-303.35349	-257.02749	-208.87691	-158.73211	-106.39244	-51.61732	5.88673	66.48559	130.64871	199.00091
-348.00000	-303.35349	-257.02749	-208.87691	-158.73211	-106.39244	-51.61732	5.88673	66.48561	130.64916	199.00971
-254.00000	-211.77516	-168.02218	-122.60978	-75.38516	-26.16861	25.25386	79.14094	135.81110	195.66572	259.22646
-254.00000	-211.77516	-168.02218	-122.60978	-75.38516	-26.16861	25.25386	79.14094	135.81110	195.66575	259.22721
-156.00000	-116.29201	-75.19695	-32.59617	11.64799	57.69677	105.74120	156.01076	208.78549	264.41418	323.34230
-156.00000	-116.29201	-75.19695	-32.59617	11.64799	57.69677	105.74120	156.01076	208.78549	264.41418	323.34236
-54.00000	-16.90491	21.44456	61.15538	102.35135	145.17702	189.80308	236.43358	285.31609	336.75641	391.14069
-54.00000	-16.90491	21.44456	61.15538	102.35135	145.17702	189.80308	236.43358	285.31609	336.75641	391.14070
52.00000	86.38543	121.89940	158.63794	196.71195	236.25069	277.40633	320.36020	365.33142	412.58910	462.47049
52.00000	86.38543	121.89940	158.63794	196.71195	236.25069	277.40633	320.36020	365.33142	412.58910	462.47049
162.00000	193.57840	226.16511	259.84579	294.71920	330.90030	368.52415	407.75131	448.77523	491.83256	537.21835
162.00000	193.57840	226.16511	259.84579	294.71920	330.90030	368.52415	407.75131	448.77523	491.83256	537.21835
276.00000	304.67353	334.23970	364.77422	396.36436	429.11151	463.13467	498.57506	535.60242	574.42391	615.29684
276.00000	304.67353	334.23970	364.77422	396.36436	429.11151	463.13467	498.57506	535.60242	574.42391	615.29684
394.00000	419.67040	446.12145	473.41931	501.64016	530.87244	561.21987	592.80535	625.77640	660.31271	696.63692
394.00000	419.67040	446.12145	473.41931	501.64016	530.87244	561.21987	592.80535	625.77640	660.31271	696.63692
516.00000	538.56868	561.80897	585.77775	610.54050	636.17316	662.76473	690.42058	719.26706	749.45786	781.18308
516.00000	538.56868	561.80897	585.77775	610.54050	636.17316	662.76473	690.42058	719.26706	749.45786	781.18308
642.00000	661.36806	681.30104	701.84677	723.06026	745.00532	767.75667	791.40273	816.04942	841.82549	868.89002
642.00000	661.36806	681.30104	701.84677	723.06026	745.00532	767.75667	791.40273	816.04942	841.82549	868.89002
772.00000	788.06830	804.59665	821.62398	839.19508	857.36185	876.18506	895.73660	916.10253	937.38741	959.72031
772.00000	788.06830	804.59665	821.62398	839.19508	857.36185	876.18506	895.73660	916.10253	937.38741	959.72031
906.00000	918.66919	931.69492	945.10738	958.94124	973.23672	988.04087	1003.40933	1019.40873	1036.11991	1053.64269
906.00000	918.66919	931.69492	945.10738	958.94124	973.23672	988.04087	1003.40933	1019.40873	1036.11991	1053.64269
1044.00000	1053.17054	1062.59512	1072.29523	1082.29557	1092.62479	1103.31638	1114.40997	1125.95297	1138.00293	1150.63084
1044.00000	1053.17054	1062.59512	1072.29523	1082.29557	1092.62479	1103.31638	1114.40997	1125.95297	1138.00293	1150.63084
1186.00000	1191.57221	1197.29660	1203.18603	1209.25532	1215.52161	1222.00496	1228.72909	1235.72241	1243.01934	1250.66239
1186.00000	1191.57221	1197.29660	1203.18603	1209.25532	1215.52161	1222.00496	1228.72909	1235.72241	1243.01934	1250.66239
1332.00000	1333.87405	1335.79879	1337.77850	1339.81812	1341.92335	1344.10087	1346.35859	1348.70597	1351.15446	1353.71822
1332.00000	1333.87405	1335.79879	1337.77850	1339.81812	1341.92335	1344.10087	1346.35859	1348.70597	1351.15446	1353.71822

J = 38

0.38	-1482.00000	-1465.32177	-1458.20940	-1452.75946	-1448.16946	-1444.12884	-1440.47841	-1437.12361	-1434.00286	-1431.07336	-1428
1.38	-1480.00000	-1465.32176	-1458.20940	-1452.75946	-1448.16946	-1444.12884	-1440.47841	-1437.12361	-1434.00286	-1431.07336	-1428
1.37	-1480.00000	-1433.11304	-1411.78617	-1395.46958	-1381.73955	-1369.66082	-1358.75444	-1348.73611	-1339.42070	-1330.67967	-1322
2.37	-1474.00000	-1433.11237	-1411.78617	-1395.46958	-1381.73955	-1369.66082	-1358.75444	-1348.73611	-1339.42070	-1330.67967	-1322
2.36	-1474.00000	-1403.34799	-1367.75269	-1340.61220	-1317.80905	-1297.76988	-1279.69119	-1263.09675	-1247.67673	-1233.21611	-1219
3.36	-1464.00000	-1403.33021	-1367.75265	-1340.61220	-1317.80905	-1297.76988	-1279.69119	-1263.09675	-1247.67673	-1233.21611	-1219
3.35	-1464.00000	-1376.51246	-1326.28328	-1288.30116	-1256.46061	-1228.51882	-1203.33748	-1180.24390	-1158.80116	-1138.70642	-1119
4.35	-1450.00000	-1376.24833	-1326.28231	-1288.30116	-1256.46061	-1228.51882	-1203.33748	-1180.24390	-1158.80116	-1138.70642	-1119
4.34	-1450.00000	-1354.04097	-1287.63030	-1238.68382	-1197.79699	-1161.98397	-1129.75177	-1100.22299	-1072.82951	-1047.17831	-1022
5.34	-1432.00000	-1351.83440	-1287.61315	-1238.68366	-1197.79699	-1161.98397	-1129.75177	-1100.22299	-1072.82951	-1047.17831	-1022
5.33	-1432.00000	-1337.78315	-1252.25424	-1191.95999	-1141.94926	-1098.25972	-1059.00496	-1023.08842	-989.80390	-958.66446	-929
6.33	-1410.00000	-1328.82437	-1252.04574	-1191.95705	-1141.94921	-1098.25972	-1059.00496	-1023.08842	-989.80390	-958.66446	-929
6.32	-1410.00000	-1323.48625	-1221.39914	-1148.43022	-1089.09060	-1037.46544	-991.18448	-948.90616	-909.77481	-873.20368	-838
7.32	-1384.00000	-1304.61006	-1219.70999	-1148.39066	-1089.08975	-1037.46542	-991.18448	-948.90616	-909.77481	-873.20368	-838
7.31	-1384.00000	-1303.59634	-1197.63132	-1108.68923	-1039.46485	-979.75670	-926.40035	-877.75741	-832.80349	-790.84252	-751
8.31	-1354.00000	-1276.94798	-1189.75169	-1108.29842	-1039.45307	-979.75638	-926.40034	-877.75741	-832.80349	-790.84252	-751
8.30	-1354.00000	-1276.83657	-1179.10545	-1074.37771	-993.47585	-925.34611	-864.79474	-809.74407	-758.96526	-711.63750	-667
9.30	-1320.00000	-1245.04010	-1159.73389	-1071.70357	-993.34920	-925.34146	-864.79459	-809.74407	-758.96526	-711.63750	-667
9.29	-1320.00000	-1245.03155	-1156.90933	-1048.20206	-952.06639	-874.55694	-806.55887	-744.99718	-688.35455	-635.65823	-586
10.29	-1282.00000	-1208.87922	-1126.88427	-1037.44057	-951.04926	-874.50458	-806.55666	-744.99710	-688.35454	-635.65823	-586
10.28	-1282.00000	-1208.87873	-1126.45685	-1026.72714	-917.71878	-828.03045	-751.97073	-683.69119	-621.09237	-562.99185	-508
11.28	-1240.00000	-1168.57935	-1089.77814	-1002.78518	-912.19973	-827.57326	-751.94521	-683.69002	-621.09233	-562.99185	-508
11.27	-1240.00000	-1168.57933	-1089.73311	-1000.05989	-891.96682	-787.50074	-701.52400	-626.07329	-557.33884	-493.74987	-434
12.27	-1194.00000	-1124.22115	-1048.21668	-964.96996	-874.89926	-784.58443	-701.28907	-626.05943	-557.33817	-493.74984	-434
12.26	-1194.00000	-1124.22115	-1048.21304	-964.55033	-867.31964	-756.01176	-656.45111	-572.55182	-497.31710	-428.07920	-363
13.26	-1144.00000	-1075.85420	-1002.35758	-922.71838	-836.06441	-744.39208	-654.80196	-572.41923	-497.30906	-428.07881	-363
13.25	-1144.00000	-1075.85420	-1002.35734	-922.67150	-834.45580	-730.57458	-619.70769	-524.05360	-441.37838	-366.18231	-296
14.25	-1090.00000	-1023.50993	-952.35029	-875.92325	-793.34602	-704.21304	-611.86901	-523.06037	-441.29903	-366.17752	-296
14.24	-1090.00000	-1023.50993	-952.35028	-875.91913	-793.11876	-700.34583	-591.75533	-483.04937	-390.25381	-308.36724	-233
15.24	-1032.00000	-967.20909	-898.29466	-824.78607	-745.99924	-661.05764	-570.20792	-477.71597	-389.62878	-308.31843	-233
15.23	-1032.00000	-967.20909	-898.29466	-824.78578	-745.97471	-660.39268	-563.17599	-451.90485	-345.92636	-255.22946	-173
16.23	-970.00000	-906.96595	-840.25662	-769.48587	-694.12378	-613.42092	-526.60130	-434.60991	-342.25666	-254.82768	-173
16.22	-970.00000	-906.96595	-840.25662	-769.48585	-694.12164	-613.33713	-525.15869	-423.88360	-311.54097	-208.34361	-119
17.22	-904.00000	-842.79055	-778.28126	-710.14531	-637.95528	-561.12737	-478.86689	-390.57268	-297.85468	-205.80991	-119
17.21	-904.00000	-842.79055	-778.28126	-710.14531	-637.95512	-561.11897	-478.66075	-387.98736	-283.23506	-170.96937	-70
18.21	-834.00000	-774.69018	-712.40049	-646.84807	-577.67567	-504.41649	-426.43447	-342.90797	-253.46248	-160.31823	-68
18.20	-834.00000	-774.69018	-712.40049	-646.84807	-577.67566	-504.41579	-426.41143	-342.49605	-249.38183	-141.79799	-30
19.20	-760.00000	-702.67021	-642.63754	-579.65316	-513.41061	-443.52265	-369.48164	-290.59821	-206.03875	-115.69354	-22
19.19	-760.00000	-702.67021	-642.63754	-579.65316	-513.41060	-443.52260	-369.47953	-290.54798	-205.32034	-109.78130	0
20.19	-682.00000	-626.73468	-569.00968	-508.60350	-445.24834	-378.61376	-308.28050	-233.69594	-154.11359	-68.69966	22
20.18	-682.00000	-626.73468	-569.00968	-508.60350	-445.24834	-378.61376	-308.28034	-233.69097	-154.01934	-67.55333	30
21.18	-600.00000	-546.88671	-491.53000	-433.73112	-373.25294	-309.80778	-243.03904	-172.49132	-97.56023	-17.43492	68
21.17	-600.00000	-546.88671	-491.53000	-433.73112	-373.25294	-309.80778	-243.03903	-172.49091	-97.55030	-17.27445	70
22.17	-514.00000	-463.12867	-410.20859	-355.06041	-297.47222	-237.19010	-173.90434	-107.22840	-36.66440	38.45383	119
22.16	-514.00000	-463.12867	-410.20859	-355.06041	-297.47222	-237.19010	-173.90434	-107.22837	-36.66354	38.47165	119
23.16	-424.00000	-375.46247	-325.05336	-272.61026	-217.94269	-160.82439	-100.98259	-38.08217	28.29890	98.70995	173
23.15	-424.00000	-375.46247	-325.05336	-272.61026	-217.94269	-160.82439	-100.98259	-38.08217	28.29897	98.71158	173
24.15	-330.00000	-283.88960	-236.07053	-186.39552	-134.69271	-80.75932	-24.35288	34.82122	97.12832	163.03356	233
24.14	-330.00000	-283.88960	-236.07053	-186.39552	-134.69271	-80.75932	-24.35288	34.82122	97.12832	163.03369	233
25.14	-232.00000	-188.41126	-143.26512	-96.42802	-47.74468	2.96721	55.92434	111.38796	169.67864	231.19841	296
25.13	-232.00000	-188.41126	-143.26512	-96.42802	-47.74468	2.96721	55.92434	111.38796	169.67864	231.19842	296
26.13	-130.00000	-89.02842	-46.64116	-2.71725	42.88351	90.32517	139.80187	191.54635	245.84210	303.04104	363
26.12	-130.00000	-89.02842	-46.64116	-2.71725	42.88351	90.32517	139.80187	191.54635	245.84210	303.04104	363
27.12	-24.00000	14.25812	53.79805	94.72902	137.17736	181.29047	227.24225	275.24034	325.53633	378.44038	434
27.11	-24.00000	14.25812	53.79805	94.72902	137.17736	181.29047	227.24225	275.24034	325.53633	378.44038	434
28.11	86.00000	121.44770	158.04980	195.90446	235.12504	275.84355	318.21533	362.42537	408.69695	457.30400	508
28.10	86.00000	121.44770	158.04980	195.90446	235.12504	275.84355	318.21533	362.42537	408.69695	457.30400	508
29.10	200.00000	232.53978	266.11183	300.80382	336.71681	373.96835	412.69653	453.06545	495.27263	539.55960	586
29.9	200.00000	232.53978	266.11183	300.80382	336.71681	373.96835	412.69653	453.06545	495.27263	539.55960	586
30.9	318.00000	347.53390	377.98229	409.42272	441.94454	475.65158	510.66563	547.13119	585.22188	625.14949	667
30.8	318.00000	347.53390	377.98229	409.42272	441.94454	475.65158	510.66563	547.13119	585.22188	625.14949	667
31.8	440.00000	466.42969	493.65958	521.75748	550.80147	580.88216	612.10581	644.59830	678.51069	714.02692	751
31.7	440.00000	466.42969	493.65958	521.75748	550.80147	580.88216	612.10581	644.59830	678.51069	714.02692	751
32.7	566.00000	589.22681	613.14237	637.80501	663.28186	689.65078	717.00300	745.44654	775.11089	806.15351	838
32.6	566.00000	589.22681	613.14237	637.80501	663.28186	689.65078	717.00300	745.44654	775.11089	806.15351	838
33.6	696.00000	715.92499	736.42953	757.56268	779.38087	801.94954	825.34533	849.65892	874.99894	901.49740	929
33.5	696.00000	715.92499	736.42953	757.56268	779.38087	801.94954	825.34533	849.65892	874.99894	901.49740	929
34.5	830.00000	846.52401	863.52011	881.02824	899.09436	917.77173	937.12270	957.22102	978.15500	1000.03189	1022
34.4	830.00000	846.52401	863.52011	881.02824	899.09436	917.77173	937.12270	957.22102	978.15500	1000.03189	1022
35.4	968.00000	981.02365	994.41325	1008.19977	1022.41880	1037.11162	1052.32652	1068.12060	1084.56223	1101.73440	1119
35.3	968.00000	981.02365	994.41325	1008.19977	1022.41880	1037.11162	1052.32652	1068.12060	1084.56223	1101.73440	1119
36.3	1110.00000	1119.42374	1129.10825	1139.07559	1149.35113	1159.96426	1170.94938	1182.34715	1194.20624	1206.58571	1219
36.2	1110.00000	1119.42374	1129.10825	1139.07559	1149.35113	1159.96426	1170.94938	1182.34715	1194.20624	1206.58571	1219
37.2	1256.00000	1261.72413	1267.60449	1273.65429	1279.88872	1286.32539	1292.98490	1299.89160	1307.07464	1314.56938	1322
37.1	1256.00000	1261.72413	1267.60449	1273.65429	1279.88872	1286.32539	1292.98490	1299.89160	1307.07464	1314.56938	1322
38.1	1406.00000	1407.92469	1409.90142	1411.93459	1414.02926	1416.19129	1418.42754	1420.74613	1423.15676	1425.67120	1428
38.0	1406.00000	1407.92469	1409.90142	1411.93459	1414.02926	1416.19129	1418.42754	1420.74613	1423.15676	1425.67120	1428

-1560.00000	-1542.87415	-1535.57670	-1529.98469	-1525.27490	-1521.12874	-1517.38288	-1513.94033	-1510.73789	-1507.73168	-1504.88973
-1558.00000	-1542.87414	-1535.57670	-1529.98469	-1525.27490	-1521.12874	-1517.38288	-1513.94033	-1510.73789	-1507.73168	-1504.88973
-1558.00000	-1509.76699	-1487.88637	-1471.14409	-1457.05499	-1444.65983	-1433.46733	-1423.18585	-1413.62548	-1404.65436	-1396.17649
-1552.00000	-1509.76654	-1487.88637	-1471.14409	-1457.05499	-1444.65983	-1433.46733	-1423.18585	-1413.62548	-1404.65436	-1396.17649
-1552.00000	-1479.08875	-1442.57967	-1414.73192	-1391.33151	-1370.76572	-1352.21071	-1335.17811	-1319.35015	-1304.50631	-1290.48613
-1542.00000	-1479.07620	-1442.57965	-1414.73192	-1391.33151	-1370.76572	-1352.21071	-1335.17811	-1319.35015	-1304.50631	-1290.48613
-1542.00000	-1451.27581	-1399.82336	-1360.85765	-1328.18410	-1299.50701	-1273.66018	-1249.95417	-1227.94109	-1207.31046	-1187.83652
-1528.00000	-1451.08073	-1399.82278	-1360.85765	-1328.18410	-1299.50701	-1273.66018	-1249.95417	-1227.94109	-1207.31046	-1187.83652
-1528.00000	-1427.58457	-1359.85334	-1309.66168	-1267.71110	-1230.95689	-1197.87187	-1167.55771	-1139.43249	-1113.09351	-1088.24836
-1510.00000	-1425.83670	-1359.84270	-1309.66160	-1267.71110	-1230.95689	-1197.87187	-1167.55771	-1139.43249	-1113.09351	-1088.24836
-1510.00000	-1410.13912	-1323.07290	-1261.33160	-1210.03678	-1165.20523	-1124.91346	-1088.04075	-1053.86465	-1021.88674	-991.74580
-1488.00000	-1402.29834	-1322.93695	-1261.33000	-1210.03676	-1165.20523	-1124.91346	-1088.04075	-1053.86465	-1021.88674	-991.74580
-1488.00000	-1395.76313	-1290.49996	-1216.13953	-1155.32329	-1102.36467	-1054.86775	-1011.46592	-971.28561	-933.72711	-898.35718
-1462.00000	-1377.96060	-1289.31576	-1216.11695	-1155.32288	-1102.36466	-1054.86775	-1011.46592	-971.28561	-933.72711	-898.35718
-1462.00000	-1376.57918	-1264.62046	-1174.57824	-1103.79344	-1042.58022	-987.83803	-937.90975	-891.75322	-848.65872	-808.11609
-1432.00000	-1350.40141	-1258.40261	-1174.34146	-1103.78742	-1042.58008	-987.83803	-937.90975	-891.75322	-848.65872	-808.11609
-1432.00000	-1350.23726	-1245.22182	-1137.93587	-1055.79314	-986.04621	-923.95619	-867.46740	-815.33813	-766.73471	-721.06259
-1398.00000	-1318.62309	-1228.03452	-1136.16474	-1055.72467	-986.04406	-923.95613	-867.46740	-815.33813	-766.73471	-721.06259
-1398.00000	-1318.60967	-1224.02371	-1109.02486	-1012.04508	-933.04447	-863.39646	-800.25976	-742.12800	-688.01996	-637.24508
-1360.00000	-1282.56093	-1195.31950	-1100.80412	-1011.45239	-933.01885	-863.39553	-800.25973	-742.12800	-688.01996	-637.24508
-1360.00000	-1282.56010	-1194.64341	-1086.75689	-974.52776	-884.07625	-806.40294	-736.44513	-672.23389	-612.59494	-556.72266
-1318.00000	-1242.33250	-1158.49043	-1065.83936	-970.89678	-883.83627	-806.39154	-736.44468	-672.23387	-612.59494	-556.72266
-1318.00000	-1242.33246	-1158.41342	-1061.65160	-945.95714	-840.40025	-753.37011	-676.24083	-605.80031	-540.56141	-479.56864
-1272.00000	-1198.02742	-1117.17035	-1028.29363	-932.65563	-838.70352	-753.25778	-676.23516	-605.80008	-540.56140	-479.56864
-1272.00000	-1198.02742	-1117.16369	-1027.56874	-921.65008	-804.98077	-705.16757	-619.97852	-543.02318	-472.05123	-405.87561
-1222.00000	-1149.70119	-1071.49507	-986.46043	-893.80593	-796.97237	-704.30178	-619.92044	-543.02017	-472.05110	-405.87560
-1222.00000	-1149.70119	-1071.49461	-986.37229	-891.04789	-777.98190	-664.13228	-568.31151	-484.19075	-407.24159	-335.76323
-1168.00000	-1097.38890	-1021.62848	-940.02616	-851.57609	-756.32382	-659.32904	-567.83588	-484.15883	-407.23994	-335.76316
-1168.00000	-1097.38890	-1021.62846	-940.01782	-851.14045	-749.86107	-632.86864	-522.98109	-429.82357	-346.38690	-269.39130
-1110.00000	-1041.11368	-967.68338	-889.16993	-804.77203	-713.57228	-616.68799	-520.04359	-429.54917	-346.36887	-269.39041
-1110.00000	-1041.11368	-967.68338	-889.16929	-804.72076	-712.28192	-605.35353	-487.25674	-381.22779	-289.91716	-206.98526
-1048.00000	-980.89140	-909.73416	-834.09008	-753.34344	-666.62056	-573.26500	-475.45511	-379.39448	-289.75521	-206.97512
-1048.00000	-980.89140	-909.73416	-834.09004	-753.33861	-666.44035	-570.45433	-458.80690	-341.49911	-238.83038	-148.90721
-982.00000	-916.73323	-847.83146	-774.92645	-697.52740	-614.94943	-526.28973	-431.28611	-333.04081	-237.67635	-148.81201
-982.00000	-916.73323	-847.83146	-774.92645	-697.52702	-614.92971	-525.83464	-426.27293	-311.14165	-195.75340	-95.93121
-912.00000	-848.64725	-782.01104	-711.77420	-637.53041	-558.73848	-474.64898	-384.37636	-288.13974	-189.80295	-95.21178
-912.00000	-848.64725	-782.01104	-711.77420	-637.53039	-558.73671	-474.59290	-383.44555	-280.33076	-162.96832	-50.16038
-838.00000	-776.63944	-712.29880	-644.70002	-573.49693	-498.24564	-418.35280	-333.00812	-241.38832	-144.25073	-46.08372
-838.00000	-776.63944	-712.29880	-644.70002	-573.49693	-498.24551	-418.34720	-332.88137	-239.73273	-133.17117	-14.73284
-760.00000	-700.71428	-638.71401	-573.75224	-505.52783	-433.66515	-357.68029	-276.92321	-190.52513	-97.76900	0.00000
-760.00000	-700.71428	-638.71401	-573.75224	-505.52783	-433.66514	-357.67982	-276.90940	-190.27872	-95.08828	14.73284
-678.00000	-620.87521	-561.27126	-498.96676	-433.69584	-365.13332	-292.87153	-216.38157	-134.94934	-47.64841	46.08372
-678.00000	-620.87521	-561.27126	-498.96676	-433.69584	-365.13332	-292.87150	-216.38033	-134.92049	-47.21429	50.16038
-592.00000	-537.12489	-479.98177	-420.37086	-358.05495	-292.74799	-224.09820	-151.66138	-74.85600	7.10697	95.21178
-592.00000	-537.12489	-479.98177	-420.37086	-358.05495	-292.74799	-224.09820	-151.66129	-74.85322	7.16113	95.93121
-502.00000	-449.46541	-394.85430	-337.98564	-278.64622	-216.58161	-151.48316	-82.96846	-10.55013	66.41688	148.81201
-502.00000	-449.46541	-394.85430	-337.98564	-278.64622	-216.58161	-151.48316	-82.96845	-10.54991	66.42238	148.90721
-408.00000	-357.89843	-305.89581	-251.82765	-195.50145	-136.68922	-75.11710	-10.45024	57.73015	129.96394	206.97512
-408.00000	-357.89843	-305.89581	-251.82765	-195.50145	-136.68922	-75.11710	-10.45024	57.73016	129.96441	206.98526
-310.00000	-262.42529	-213.11183	-161.91006	-108.64570	-53.11357	4.93112	65.78480	129.81349	197.48022	269.39041
-310.00000	-262.42529	-213.11183	-161.91006	-108.64570	-53.11357	4.93112	65.78480	129.81349	197.48026	269.39130
-208.00000	-163.04706	-116.50686	-68.24345	-18.09898	34.11164	88.60805	145.65447	205.57418	268.77101	335.76316
-208.00000	-163.04706	-116.50686	-68.24345	-18.09898	34.11164	88.60805	145.65447	205.57418	268.77101	335.76323
-102.00000	-59.76463	-16.08455	29.16357	76.12257	124.95940	175.87143	229.09494	284.91717	343.69381	405.87560
-102.00000	-59.76463	-16.08455	29.16357	76.12257	124.95940	175.87143	229.09494	284.91717	343.69381	405.87561
8.00000	47.42128	88.15209	130.30395	174.00575	219.40782	266.68735	316.05571	367.76869	422.14114	479.56864
8.00000	47.42128	88.15209	130.30395	174.00575	219.40782	266.68735	316.05571	367.76869	422.14114	479.56864
122.00000	158.51006	196.20056	235.17185	275.53971	317.43898	361.02823	406.49615	454.07033	504.02969	556.72266
122.00000	158.51006	196.20056	235.17185	275.53971	317.43898	361.02823	406.49615	454.07033	504.02969	556.72266
240.00000	273.50121	308.05879	343.76241	380.71543	419.03806	458.87143	500.38319	543.77505	589.29346	637.24508
240.00000	273.50121	308.05879	343.76241	380.71543	419.03806	458.87143	500.38319	543.77505	589.29346	637.24508
362.00000	392.39431	423.72503	456.07156	489.52537	524.19269	560.19816	597.68957	636.84446	677.87928	721.06259
362.00000	392.39431	423.72503	456.07156	489.52537	524.19269	560.19816	597.68957	636.84446	677.87928	721.06259
488.00000	515.18899	543.19779	572.09586	601.96316	632.89252	664.99270	698.39261	733.24685	769.74365	808.11609
488.00000	515.18899	543.19779	572.09586	601.96316	632.89252	664.99270	698.39261	733.24685	769.74365	808.11609
618.00000	641.88495	666.47583	691.83239	718.02344	745.12876	773.24182	802.47329	832.95579	864.85061	898.35718
618.00000	641.88495	666.47583	691.83239	718.02344	745.12876	773.24182	802.47329	832.95579	864.85061	898.35718
752.00000	772.48194	793.55806	815.27866	837.70160	860.89395	884.93428	909.91553	935.94904	963.17009	991.74580
752.00000	772.48194	793.55806	815.27866	837.70160	860.89395	884.93428	909.91553	935.94904	963.17009	991.74580
890.00000	906.97972	924.44358	942.43254	960.99371	980.18172	1000.06050	1020.70566	1042.20776	1064.67675	1088.24836
890.00000	906.97972	924.44358	942.43254	960.99371	980.18172	1000.06050	1020.70566	1042.20776	1064.67675	1088.24836
1032.00000	1045.37811	1059.13158	1073.29217	1087.89639	1102.98657	1118.61224	1134.83196	1151.71586	1169.34904	1187.83652
1032.00000	1045.37811	1059.13158	1073.29217	1087.89639	1102.98657	1118.61224	1134.83196	1151.71586	1169.34904	1187.83652
1178.00000	1187.67694	1197.62138	1207.85597	1218.40671	1229.30376	1240.58240	1252.28436	1264.45954	1277.16855	1290.48613
1178.00000	1187.67694	1197.62138	1207.85597	1218.40671	1229.30376	1240.58240	1252.28436	1264.45954	1277.16855	1290.48613
1328.00000	1333.87605	1339.91238	1346.12254	1352.52212	1359.12918	1365.96485	1373.05412	1380.42688	1388.11942	1396.17649
1328.00000	1333.87605	1339.91238	1346.12254	1352.52212	1359.12918	1365.96485	1373.05412	1380.42688	1388.11942	1396.17649
1482.00000	1483.97533	1486.00405	1488.09068	1490.24040	1492.45923	1494.75421	1497.13366	1499.60754	1502.18793	1504.88973
1482.00000	1483.97533	1486.00405	1488.09068	1490.24040	1492.45923	1494.75421	1497.13366	1499.60754	1502.18793	1504.88973

J = 40

0.40	-1640.00000	-1622.42655	-1614.94401	-1609.20993	-1604.38035	-1600.12864	-1596.28736	-1592.75706	-1589.47293	-1586.39000	-1583.
1.40	-1638.00000	-1622.42654	-1614.94401	-1609.20993	-1604.38035	-1600.12864	-1596.28736	-1592.75706	-1589.47293	-1586.39000	-1583.
1.39	-1638.00000	-1588.42124	-1565.98670	-1548.81869	-1534.37051	-1521.65890	-1510.18025	-1499.63561	-1489.83028	-1480.62907	-1471.
2.39	-1632.00000	-1588.42093	-1565.98670	-1548.81869	-1534.37051	-1521.65890	-1510.18025	-1499.63561	-1489.83028	-1480.62907	-1471.
2.38	-1632.00000	-1556.83168	-1519.40730	-1490.85205	-1466.85428	-1445.76180	-1426.73041	-1409.25960	-1393.02367	-1377.79659	-1363.
3.38	-1622.00000	-1556.82284	-1519.40728	-1490.85205	-1466.85428	-1445.76180	-1426.73041	-1409.25960	-1393.02367	-1377.79659	-1363.
3.37	-1622.00000	-1528.05371	-1475.36565	-1435.41545	-1401.90852	-1372.49589	-1345.98340	-1321.66485	-1299.08135	-1277.91476	-1257.
4.37	-1608.00000	-1527.91045	-1475.36531	-1435.41545	-1401.90852	-1372.49589	-1345.98340	-1321.66485	-1299.08135	-1277.91476	-1257.
4.36	-1608.00000	-1503.18037	-1434.08366	-1382.64294	-1339.62749	-1301.93148	-1267.99323	-1236.89341	-1208.03623	-1181.00929	-1155.
5.36	-1590.00000	-1501.81155	-1434.07710	-1382.64289	-1339.62748	-1301.93148	-1267.99323	-1236.89341	-1208.03623	-1181.00929	-1155.
5.35	-1590.00000	-1484.45927	-1395.92048	-1332.71136	-1280.12932	-1234.15430	-1192.82460	-1154.99510	-1119.92697	-1087.11021	-1056.
6.35	-1568.00000	-1477.68887	-1395.83262	-1332.71049	-1280.12931	-1234.15430	-1192.82460	-1154.99510	-1119.92697	-1087.11021	-1056.
6.34	-1568.00000	-1469.82160	-1361.71256	-1285.87011	-1223.56642	-1169.27093	-1120.55614	-1076.02952	-1034.79934	-996.25280	-959.
7.34	-1542.00000	-1453.17738	-1360.89558	-1285.85734	-1223.56622	-1169.27092	-1120.55614	-1076.02952	-1034.79934	-996.25280	-959.
7.33	-1542.00000	-1451.32496	-1333.70828	-1242.53822	-1170.14418	-1107.41711	-1051.28511	-1000.06902	-952.70818	-908.47889	-866.
8.33	-1512.00000	-1425.70739	-1328.92881	-1242.39674	-1170.14114	-1107.41704	-1051.28510	-1000.06902	-952.70818	-908.47889	-866.
8.32	-1512.00000	-1425.46880	-1313.02387	-1203.72358	-1120.16631	-1048.77179	-985.13438	-927.20273	-873.71991	-823.83860	-776.
9.32	-1478.00000	-1394.06508	-1298.08294	-1202.57954	-1120.12982	-1048.77081	-985.13436	-927.20273	-873.71991	-823.83860	-776.
9.31	-1478.00000	-1394.04428	-1292.55582	-1171.99810	-1074.20372	-993.58574	-922.26391	-857.54276	-797.91625	-742.39264	-690.
10.31	-1440.00000	-1358.10983	-1265.43619	-1165.95382	-1073.86590	-993.57339	-922.26352	-857.54275	-797.91625	-742.39264	-690.
10.30	-1440.00000	-1358.10847	-1264.39024	-1148.22936	-1033.76373	-942.26743	-862.89168	-791.23378	-725.39964	-664.21564	-606.
11.30	-1398.00000	-1317.95898	-1228.88420	-1130.48075	-1031.47063	-942.14418	-862.88668	-791.23361	-725.39964	-664.21564	-606.
11.29	-1398.00000	-1317.95892	-1228.75507	-1124.30362	-1001.89128	-895.73416	-807.34668	-728.46981	-656.30155	-589.40096	-526.
12.29	-1352.00000	-1273.71149	-1187.82455	-1093.10789	-992.01666	-894.78318	-807.29418	-728.46753	-656.30147	-589.40096	-526.
12.28	-1352.00000	-1273.71149	-1187.81259	-1091.89167	-976.89150	-856.42766	-756.26570	-669.53116	-590.79640	-518.06792	-450.
13.28	-1302.00000	-1225.42934	-1142.35005	-1051.69599	-952.90779	-851.23716	-755.82698	-669.50633	-590.79529	-518.06788	-450.
13.27	-1302.00000	-1225.42934	-1142.34917	-1051.53443	-948.39386	-826.63345	-711.33295	-614.90560	-529.12954	-450.37370	-377.
14.27	-1248.00000	-1173.15162	-1092.63691	-1005.65332	-911.08625	-809.74769	-708.57301	-614.68574	-529.11703	-450.37315	-377.
14.26	-1248.00000	-1173.15162	-1092.63685	-1005.63686	-910.27885	-799.64835	-675.80748	-565.77299	-471.69781	-386.53549	-307.
15.26	-1190.00000	-1116.90410	-1038.81200	-955.10555	-864.84971	-767.18053	-664.50241	-564.25334	-471.58165	-386.52901	-307.
15.25	-1190.00000	-1116.90410	-1038.81200	-955.10420	-864.74581	-764.79096	-647.67389	-525.06945	-419.36601	-326.88717	-242.
16.25	-1128.00000	-1056.70435	-980.95915	-900.26700	-813.91164	-720.89175	-620.88396	-517.70228	-418.50399	-326.82433	-242.
16.24	-1128.00000	-1056.70435	-980.95915	-900.26691	-813.90107	-720.51843	-615.75385	-494.10218	-374.45525	-272.08898	-180.
17.24	-1062.00000	-992.56479	-919.13519	-841.29641	-758.48418	-669.89521	-574.55158	-472.87129	-369.72583	-271.59373	-180.
17.23	-1062.00000	-992.56479	-919.13519	-841.29640	-758.48329	-669.85058	-573.59275	-463.96291	-339.91242	-223.89454	-124.
18.23	-992.00000	-924.49435	-853.38007	-778.30189	-698.79741	-614.23780	-523.74514	-426.46572	-323.65949	-220.90212	-123.
18.22	-992.00000	-924.49435	-853.38007	-778.30189	-698.79735	-614.23346	-523.61422	-424.48308	-310.26034	-185.67873	-73.
19.22	-918.00000	-852.49967	-783.72269	-711.35882	-635.01707	-554.18789	-468.17610	-376.04550	-277.16671	-173.67367	-71.
19.21	-918.00000	-852.49967	-783.72269	-711.35882	-635.01707	-554.18754	-468.16181	-375.74091	-273.62890	-155.39903	-31.
20.21	-840.00000	-776.58569	-710.18448	-640.52150	-567.25848	-489.96820	-408.09083	-320.86072	-227.30349	-127.11137	-23.
20.20	-840.00000	-776.58569	-710.18448	-640.52150	-567.25848	-489.96818	-408.08953	-320.82411	-226.69547	-121.41992	0.
21.20	-758.00000	-696.75624	-632.78163	-565.83015	-495.60417	-421.73630	-343.76001	-261.05907	-172.79123	-77.96807	23.
21.19	-758.00000	-696.75624	-632.78163	-565.83015	-495.60417	-421.73630	-343.75991	-261.05545	-172.71174	-76.87197	31.
22.19	-672.00000	-613.01424	-551.52661	-487.31522	-420.11508	-349.60439	-275.38366	-196.94155	-113.59634	-24.42057	71.
22.18	-672.00000	-613.01424	-551.52661	-487.31522	-420.11508	-349.60439	-275.38365	-196.94125	-113.58790	-24.26575	73.
23.18	-582.00000	-525.36202	-466.42915	-405.00023	-340.83732	-273.65492	-203.10422	-128.74878	-50.02443	33.82897	123.
23.17	-582.00000	-525.36202	-466.42915	-405.00023	-340.83732	-273.65492	-203.10422	-128.74876	-50.02368	33.84648	124.
24.17	-488.00000	-433.80140	-377.49692	-318.90359	-257.80652	-193.95014	-127.02582	-56.65344	17.64725	96.50466	180.
24.16	-488.00000	-433.80140	-377.49692	-318.90359	-257.80652	-193.95014	-127.02582	-56.65344	17.64730	96.50630	180.
25.16	-390.00000	-338.33387	-284.73609	-229.03994	-171.05066	-110.53817	-47.22689	19.21875	89.21610	163.29880	242.
25.15	-390.00000	-338.33387	-284.73609	-229.03994	-171.05066	-110.53817	-47.22689	19.21875	89.21610	163.29893	242.
26.15	-288.00000	-238.96061	-188.15161	-135.42103	-80.59206	-23.45685	36.23204	98.77345	164.53500	233.97939	307.
26.14	-288.00000	-238.96061	-188.15161	-135.42103	-80.59206	-23.45685	36.23204	98.77345	164.53500	233.97940	307.
27.14	-182.00000	-135.68261	-87.74755	-38.05642	13.55130	67.26361	123.30331	181.93792	243.49397	308.37798	377.
27.13	-182.00000	-135.68261	-87.74755	-38.05642	13.55130	67.26361	123.30331	181.93792	243.49397	308.37798	377.
28.13	-72.00000	-28.50066	16.47278	63.04609	111.36476	161.59877	213.94883	268.65494	326.00839	386.36913	450.
28.12	-72.00000	-28.50066	16.47278	63.04609	111.36476	161.59877	213.94883	268.65494	326.00839	386.36913	450.
29.12	42.00000	82.58456	124.50662	167.88002	212.83626	259.52863	308.13770	358.87868	412.01173	467.85665	526.
29.11	42.00000	82.58456	124.50662	167.88002	212.83626	259.52863	308.13770	358.87868	412.01173	467.85665	526.
30.11	160.00000	197.57250	236.35166	276.43999	317.95578	361.03671	405.84460	452.57194	501.45069	552.76492	606.
30.10	160.00000	197.57250	236.35166	276.43999	317.95578	361.03671	405.84460	452.57194	501.45069	552.76492	606.
31.10	282.00000	316.46270	352.00596	388.72149	426.71497	466.10926	507.04857	549.70416	594.28194	641.03341	690.
31.9	282.00000	316.46270	352.00596	388.72149	426.71497	466.10926	507.04857	549.70416	594.28194	641.03341	690.
32.9	408.00000	439.25475	471.46790	504.72072	539.10677	574.73475	611.73210	650.24997	690.46983	732.61286	776.
32.8	408.00000	439.25475	471.46790	504.72072	539.10677	574.73475	611.73210	650.24997	690.46983	732.61286	776.
33.8	538.00000	565.94831	594.73608	624.43443	655.12522	686.90344	719.88046	754.18814	789.98470	827.46266	866.
33.7	538.00000	565.94831	594.73608	624.43443	655.12522	686.90344	719.88046	754.18814	789.98470	827.46266	866.
34.7	672.00000	696.54311	721.80933	747.85989	774.76522	802.60707	831.48114	861.50074	892.80167	925.54902	959.
34.6	672.00000	696.54311	721.80933	747.85989	774.76522	802.60707	831.48114	861.50074	892.80167	925.54902	959.
35.6	810.00000	831.03889	852.68662	874.99471	898.02244	921.83855	946.52351	972.17253	998.89967	1026.84349	1056.
35.5	810.00000	831.03889	852.68662	874.99471	898.02244	921.83855	946.52351	972.17253	998.89967	1026.84349	1056.
36.5	952.00000	969.43544	987.36707	1005.83686	1024.89311	1044.59179	1064.99842	1086.19049	1108.26078	1131.32195	1155.
36.4	952.00000	969.43544	987.36707	1005.83686	1024.89311	1044.59179	1064.99842	1086.19049	1108.26078	1131.32195	1155.
37.4	1098.00000	1111.73258	1125.84992	1140.38458	1155.37400	1170.86155	1186.89801	1203.54341	1220.86961	1238.96384	1257.
37.3	1098.00000	1111.73258	1125.84992	1140.38458	1155.37400	1170.86155	1186.89801	1203.54341	1220.86961	1238.96384	1257.
38.3	1248.00000	1257.93013	1268.13451	1278.63634	1289.46229	1300.64327	1312.21545	1324.22160	1336.71289	1349.75145	1363.
38.2	1248.00000	1257.93013	1268.13451	1278.63634	1289.46229	1300.64327	1312.21545	1324.22160	1336.71289	1349.75145	1363.
39.2	1402.00000	1408.02797	1414.22027	1420.59079	1427.15552	1433.93296	1440.94480	1448.21664	1455.77914	1463.66949	1471.
39.1	1402.00000	1408.02797	1414.22027	1420.59079	1427.15552	1433.93296	1440.94480	1448.21664	1455.77914	1463.66949	1471.
40.1	1560.00000	1562.02597	1564.10669	1566.24677	1568.45154	1570.72717	1573.08088	1575.52120	1578.05833	1580.70467	1583.
40.0	1560.00000	1562.02597	1564.10669	1566.24677	1568.45154	1570.72717	1573.08088	1575.52120	1578.05833	1580.70467	1583.

ARKIV FÖR FYSIK Band 10 nr 8

Communicated 25 May 1955 by Oskar Klein and Hilding Faxén

Application of the variational method to the calculation of proton–proton scattering in the region 0–5 Mev

By S. Skavlem and I. Espe

This paper gives a calculation of the proton–proton scattering on the basis of a Yukawa potential, corresponding to meson masses 300 m_e, 370 m_e and 400 m_e, respectively. The best fit with recent scattering experiments is obtained with a meson mass of 334 m_e. A simple explicit expression for the proton–proton S-wave function is worked out. The nuclear scattering phase shift and the S-wave function are both expanded in powers of k^2, the square of the relative wave number, and only two terms in these expansions are taken into account in the present work.

1. Introduction

Numerical integration is, as far as the present authors know, the only method which has been used hitherto in order to solve the radial wave equation of the proton–proton system for a given nuclear potential. In this paper it is shown that the equation

$$\left\{\frac{d^2}{dr^2}+k^2-\frac{\beta}{r}-\frac{2m}{\hbar^2}U(r)\right\}\psi(r)=0 \tag{1}$$

where

$$\beta=\frac{2mZZ'e^2}{\hbar^2};\quad k^2=\frac{2m}{\hbar^2}E \tag{2}$$

to a high digree of accuracy can be solved by means of a slight extension of a variational method given in two earlier papers [1, 2]. It turns out that, in order to obtain an accuracy corresponding to the accuracy of present experimental data, it is sufficient to perform the calculations with only one variational parameter in the trial wave function.

In the above equations Ze and $Z'e$ are the electrical charges of two colliding particles, E is the energy in the center of mass system, m is the reduced mass and $U(r)$ is an attractive potential of very short range. We will offer special interest to the case

$$U(r)=-A\frac{e^{-\varkappa r}}{r}, \tag{3}$$

the so-called Yukawa potential.

By means of the substitution

$$x = \varkappa r \tag{4}$$

where $\varkappa^{-1}$ is the range of the potential $U(r)$, equation (1) is written on dimensionless form

$$\left\{\frac{d^2}{d x^2} + q^2 - \frac{\beta_1}{x} + v(x)\right\} \phi(x) = 0. \tag{5}$$

Here

$$q = \frac{k}{\varkappa};\ \beta_1 = \frac{\beta}{\varkappa};\ v(x) = -\frac{2m}{\varkappa^2 \hbar^2} U\left(\frac{x}{\varkappa}\right). \tag{6}$$

$\phi(x)$ will have to satisfy the boundary conditions

$$\left.\begin{aligned} &\phi(0) = 0 \\ &\phi(x) \underset{x\to\infty}{\sim} \frac{1}{\sin\delta} \sin(qx - \alpha \log 2qx + \eta + \delta) \end{aligned}\right\} \tag{7}$$

where

$$\alpha = \frac{Z Z' e^2}{\hbar v};\ \eta = \arg \Gamma(1 + i\alpha) \tag{8}$$

and δ is the nuclear phase shift defined by (5) and (7). v is the relative velocity of the two particles. In the following we need the regular and the irregular S-wave coulomb wave functions $F(x)$ and $G(x)$, respectively, which are solutions of the equation

$$\left\{\frac{d^2}{d x^2} + q^2 - \frac{\beta_1}{x}\right\} \left\{\begin{matrix} F(x) \\ G(x) \end{matrix}\right\} = 0. \tag{9}$$

Asymptotically, for large x-values, $F(x)$ and $G(x)$ are defined by

$$\left.\begin{aligned} F(x) &\sim \sin(qx - \alpha \log 2qx + \eta) \\ G(x) &\sim \cos(qx - \alpha \log 2qx + \eta) \end{aligned}\right\}. \tag{10}$$

2. The variational method

We put $\phi(x)$ on the form

$$\phi(x) = G(x)(1 - e^{-x}) + \cot\delta \cdot F(x) - y(x) \tag{11}$$

where the new function $y(x)$ will have to satisfy the boundary conditions

$$y(0) = 0;\ y(\infty) = 0 \tag{12}$$

as can be seen from (7) and (10). The factor $(1 - e^{-x})$ is introduced in order to establish convergence of certain integrals which will appear soon. The equation for $y(x)$ is from (5) and (11)

$$y''+q^2\,y+v\,(x)\;y-\frac{\beta_1}{x}\,y=v\,(x)\,[G\,(x)\,(1-e^{-x})+\cot\delta\cdot F\,(x)]+ \\ +(2\,G'\,(x)-G\,(x))\,e^{-x}. \tag{13}$$

This is the Euler equation of the following variational principle. Require

$$J=\int_0^\infty\Big\{-y'^{\,2}+q^2\,y^2+v\,(x)\,[G\,(x)\,(1-e^{-x})-y]^2- \\ -\frac{\beta_1}{x}\,y^2-2\,(2\,G'-G)\,e^{-x}\,y-G^2\,e^{-2x}\Big\}\,d\,x \tag{14}$$

to be stationary under the accessory condition

$$N=\int_0^\infty v\,(x)\,F\,(x)\,[G\,(x)\,(1-e^{-x})-y]\,d\,x=\text{const.} \tag{15}$$

The variational equation

$$\delta\,J+2\,\lambda\cdot\delta\,N=0 \tag{16}$$

will then lead to Eq. (13) with $\lambda=\cot\delta$.

Further we define

$$L=\int_0^\infty\phi\left(\frac{d^2}{d\,x^2}+q^2+v\,(x)-\frac{\beta_1}{x}\right)\phi\,d\,x=L_1+\lambda\,L_2 \tag{17}$$

where

$$\left.\begin{aligned} L_1&=\int_0^\infty[G\,(1-e^{-x})-y]\left[\frac{d^2}{d\,x^2}+q^2+v\,(x)-\frac{\beta_1}{x}\right]\phi\,d\,x \\ L_2&=\int_0^\infty F\left[\frac{d^2}{d\,x^2}+q^2+v\,(x)-\frac{\beta_1}{x}\right]\phi\,d\,x \end{aligned}\right\}. \tag{18}$$

In L_1 we insert the expression (11) for $\phi\,(x)$. By partial integrations with due regard to the boundary conditions (12) and by making use of the equations (9) we get

$$L_1=J+\lambda\,N. \tag{19}$$

Partial integrations and application of the asymptotic expressions for $F\,(x)$ and $\phi\,(x)$ give for L_2 the formula

$$L_2=-q+\int_0^\infty v\,(x)\,F\,\phi\,d\,x. \tag{20}$$

From (11) we then obtain

$$L_2 = -q + N + q\,\delta_B \cdot \lambda \tag{21}$$

where δ_B is the Born-approximation for the eigenphase

$$\delta_B = \frac{1}{q} \int_0^\infty v(x)\, F^2\, d\,x. \tag{22}$$

Finally, we get for L

$$L = J + 2\,\lambda\, N + q\,\delta_B \cdot \lambda^2 - q\,\lambda. \tag{23}$$

On an infinitesimal variation of ϕ we obtain from (17) after partial integrations

$$\delta\, L = 2 \int_0^\infty \delta\,\phi \cdot \left(\frac{d^2}{d\,x^2} + q^2 + v(x) - \frac{\beta_1}{x} \right) \phi\, d\,x + q \cdot \delta\,\lambda. \tag{24}$$

The integral in (24) vanishes for an exact solution of (5). We now fix an approximate solution by requiring this integral to vanish for all possible $\delta\,\phi$, thus

$$\int_0^\infty \delta\,\phi \cdot \left(\frac{d^2}{d\,x^2} + q^2 + v(x) - \frac{\beta_1}{x} \right) \phi\, d\,x = 0. \tag{25}$$

The further development proceeds in the same way as in the case of the neutron–proton system, which is dealt with in an earlier paper [2]. We get a linear equation system (linear in λ and certain variational parameters c_ν which are contained in the trial wave function)

$$\left.\begin{aligned} &\frac{\partial J}{\partial c_\nu} + 2\,\lambda \frac{\partial N}{\partial c_\nu} = 0, \quad \nu = 1, 2, \ldots n \\ &N = q\,(1 - \delta_B \cdot \lambda) \end{aligned}\right\}. \tag{26}$$

(26) gives a non-stationary value of $\lambda = \cot\delta$. A stationary value λ_0 can then be calculated from the formula

$$\lambda_0 = \lambda - \frac{J + \lambda\, N}{q} \tag{27}$$

where λ, J and N are fixed by the approximate solution determined from (26).

3. Proton–proton scattering

We now specialize the foregoing considerations to the case $Z = Z' = 1$, $m = \dfrac{M}{2}$ where M is the proton mass, and

$$v(x)=b\frac{e^{-x}}{x}; \quad b=\frac{MA}{\hbar^2 \varkappa}. \tag{28}$$

As a trial function for $y(x)$ in (11) we choose the following expression [1, 2], which satisfies the boundary conditions (12)

$$y(x)=(1-e^{-x})\sum_{\nu=1}^{n} c_\nu e^{-\nu x}. \tag{29}$$

Here the c_ν's and λ are determined from the linear equation system (26), and the phase shift δ_0 from Eq. (27).

In order to find the integrals in (14) and (15) we expand them in powers of q^2. The equations (26) and (27) are also expanded in this way. Thus we get the $c_\nu' s$, $q\lambda$ and $q\lambda_0$ as power series in q^2. We neglect terms of order higher than q^2, corresponding to the shape-independent approximation formula [3]

$$c^2 k \cot \delta_0+\beta h(\alpha)=-\frac{1}{a}+\frac{1}{2} r_0 k^2. \tag{30}$$

For $F(x)$ and $G(x)$ we use the expansions [3]

$$\left.\begin{aligned} F(x)&=c\,q\,x\left[\frac{2}{z} I_1(z)-\frac{1}{12\beta_1^2} z^2 I_2(z)\cdot q^2\right]\\ G(x)&=\frac{1}{c}\left\{z K_1(z)+\tfrac{1}{2} h(\alpha)\cdot z I_1(z)-\frac{1}{\beta_1^2}\left[\tfrac{1}{6} z I_1(z)-\tfrac{1}{24} z^4 K_2(z)\right] q^2\right\}\end{aligned}\right\} \tag{31}$$

where

$$\left.\begin{aligned} c&=\left(\frac{2\pi\alpha}{e^{2\pi\alpha}-1}\right)^{1/2}\\ z&=2(\beta_1 x)^{1/2}\\ h(\alpha)&=Re\frac{\Gamma'(-i\alpha)}{\Gamma(-i\alpha)}-\ln\alpha.\end{aligned}\right| \tag{32}$$

I_n and K_n are the modified Bessel functions [4], $h(\alpha)$ is an even function of α which is zero for $\frac{1}{\alpha}=0$.

If we write

$$\left.\begin{aligned} J&=\sum_{\mu,\nu} J_{\mu\nu} c_\mu c_\nu+\sum_\nu J_\nu c_\nu+J_0\\ N&=\sum_\nu N_\nu c_\nu+N_0\end{aligned}\right\} \tag{33}$$

and remember that c and c^{-1} are factors in $F(x)$ and $G(x)$, respectively, we see from the expressions for J, N, δ_B that $J_{\mu\nu}$ and N_0 are independent of c, while δ_B, N_ν, J_ν and J_0 contain the factors c^2, c, c^{-1} and c^{-2}, respectively. Then it follows that c^{-2} appears as a factor in λ as well as in $J+\lambda N$.[1]

---

[1] In reference [1] it is shown that $J+\lambda N=J_0+\lambda N_0+{}^1/_2\sum_\nu J_\nu c_\nu$.

Consequently, multiplying the equation (27) with $c^2 q$ we get an equation of the form

$$c^2 q \cot \delta_0 = A_0(b, \varkappa) + A_2(b, \varkappa) \cdot \frac{1}{\alpha^2} + B(b, \varkappa) \cdot h(\alpha). \tag{34}$$

We add the function $\beta_1 h(\alpha)$ on both sides of this equation. On the right side we introduce the divergent Stirling's series for $h(\alpha)$ and take into account only the first term which is $\frac{1}{12} \cdot \frac{1}{\alpha^2}$. Introducing

$$q = \frac{k}{\varkappa}; \quad \frac{1}{\alpha^2} = \frac{4k^2}{\beta^2}; \quad \beta_1 = \frac{\beta}{\varkappa}$$

we get

$$c^2 k \cot \delta_0 + \beta h(\alpha) = a_0(b, \varkappa) + a_2(b, \varkappa) \cdot k^2. \tag{35}$$

4. Numerical results

The integrals in the expressions for J, N and δ_B were calculated by means of the power series [4] for I_1, I_2, K_1 and K_2. Only a few terms of these series had to be taken into account in order to obtain the desired accuracy.

The coefficients a_0 and a_2 cannot be obtained as explicit functions of $\varkappa$. Calculations were carried out for three different values of $\varkappa$, corresponding to meson masses 300, 370 and 400 electron masses, respectively. In either case the corresponding b-value was fitted to give the experimental phase shift value at 0.86 Mev [5]. The results are given in Table 2.

To test the accuracy of our variational method we calculated $\cot \delta_0$ for meson mass 400 m_e and $b = 1.575$ with one and two parameters in the trial wave function. The results are given in Table 1. The differences between the one and the two parameter results do not exceed 0.5 percent which is small in comparison to the errors in the experimental phase shift values (about 2 per cent). Hence the remaining calculations were performed with only one parameter in the trial wave function.

Comparison of (35) with (30) gives

$$-\frac{1}{a} = a_0(b, \varkappa); \quad \frac{1}{2} r_0 = a_2(b, \varkappa). \tag{36}$$

Using the experimental values for a and r_0 given in reference [3],

$$a = (-7.67 \pm 0.05) \times 10^{-13} \text{ cm} \quad \text{and} \quad r_0 = (2.65 \pm 0.07) \times 10^{-13} \text{ cm},$$

we get by means of interpolation

$$b = 1.55 \pm 0.01, \quad \varkappa = (9.06 \pm 0.25) \times 10^{12} \text{cm}^{-1}. \tag{37}$$

This (compare the last Eq. (32) in reference [2]) corresponds to a meson mass of

$$(350 \pm 10) \text{ m}_e. \tag{38}$$

The parameter c_1, corresponding to the present result, is found to be

Table 1.

Calculated values of cot δ_0 with one and two parameters in the trial wave function, respectively. In both cases it is assumed a Yukawa potential with depth and range corresponding to $b = 1.575$ and a meson mass of 400 m_e, respectively.

α	E (Mev)	$-c_1$	c_2	λ	$\Delta\lambda$	λ_0
0.30	0.278	0.6094		5.9675	0.1780	5.7894
		0.7271	0.0720	5.9206	0.1370	5.7889
0.22	0.516	0.5400		2.9728	0.1052	2.8676
		0.6746	0.0561	2.9417	0.0755	2.8661
0.1704	0.86	0.5100		2.8569	0.0734	1.7830
		0.6625	0.0591	2.8341	0.0533	1.7807
0.13	1.478	0.4963		1.2242	0.0526	1.1716
		0.5651	0.0604	1.2084	0.0408	1.1676
0.11	2.064	0.4958		0.9929	0.0441	0.9488
		0.6746	0.0597	0.9813	0.0365	0.9458
0.10	2.498	0.4984		0.8981	0.0404	0.8577
		0.6840	0.0585	0.8890	0.0349	0.8541
0.09	3.084	0.5039		0.8185	0.0371	0.7814
		0.6974	0.0560	0.8127	0.0339	0.7787
0.08	3.902	0.5138		0.8567	0.0342	0.7225
		0.7167	0.0515	0.7552	0.0335	0.7216
0.07	5.098	0.5309		0.7128	0.0322	0.6805
		0.7458	0.0431	0.7177	0.0341	0.6836

Table 2.

Calculated phase shift values for Yukawa potentials with ranges corresponding to meson masses 300, 370, and 400 m_e. The well depth parameter b is in either case fitted to the experimental phase shift value at 0.86 Mev.

α	E (Mev)	300 m_e ($b = 1.524$)			370 m_e ($b = 1.561$)			400 m_e ($b = 1.575$)		
		$-c_1$	λ_0	δ_0	$-c_1$	λ_0	δ_0	$-c_1$	λ_0	δ_0
0.30	0.278	0.5301	4.7385	11.91	0.5860	5.3955	10.51	0.6094	5.7894	9.81
0.22	0.516	0.4806	2.7450	20.02	0.5205	2.8239	19.50	0.5400	2.8676	19.21
0.1704	0.86	0.4637	1.7830	29.28	0.4929	1.7830	29.28	0.5100	1.7830	29.28
0.13	1.478	0.4677	1.1918	39.98	0.4887	1.1792	40.30	0.4963	1.1716	40.48
0.11	2.064	0.4731	1.0188	45.54	0.4894	0.9595	46.19	0.4959	1.9488	46.52
0.10	2.498	0.4815	0.8994	48.03	0.4924	0.8708	48.95	0.4984	0.8577	49.38
0.09	3.084	0.4937	0.8327	50.21	0.5010	0.7978	51.42	0.5039	0.7814	52.01
0.08	3.902	0.5119	0.7789	52.09	0.5130	0.7418	53.44	0.5138	0.7225	54.14
0.07	5.098	0.5390	0.7404	53.49	0.5325	0.7001	55.01	0.5309	0.6805	55.77

$$c_1 = \div \frac{1}{c}\left[0.293 + 0.000161 \cdot \frac{1}{\alpha^2} + 0.0468 \cdot h(\alpha)\right], \tag{39}$$

and for the radial S-wave function we have

$$\phi(x) = G(x)(1-e^{-x}) + \cot\delta_0 \cdot F(x) - c_1(1-e^{-x})e^{-x}. \tag{40}$$

The expressions (39) and (40) may perhaps be of interest in other problems than proton–proton scattering. However, it is to be remarked that the numerical coefficients in (39) are not stationary determined, in contradistinction to the expansion coefficients in (35).

The value (38) for the meson mass is somewhat higher than that found by other authors [3, 6, 7]. The reason for this is the following. The values

$$a = (-7.67 \pm 0.05) \times 10^{-13}\ \text{cm} \quad \text{and} \quad r_0 = (2.65 \pm 0.07) \times 10^{-13}\ \text{cm}$$

are found by means of the linear approximation fit (30).
From the parabolic approximation fit,

$$c^2 k \cot\delta_0 + \beta h(\alpha) = -\frac{1}{a} + \frac{1}{2} r_0 k^2 - P r_0^3 k^4, \tag{41}$$

on the other hand, one finds [3]

$$a = -7.70 \times 10^{-13}\ \text{cm}, \quad r_0 = 2.76 \times 10^{-13}\ \text{cm}, \quad P = 0.055. \tag{42}$$

Corresponding to (41) we get instead of (35)

$$c^2 k \cot\delta_0 + \beta h(\alpha) = a_0(b, \varkappa) + a_2(b, \varkappa) \cdot k^2 + a_4(b, \varkappa) \cdot k^4 \tag{43}$$

where a_0 and a_2 are the same functions as in (35). Extension of our calculations to higher order terms in k^2 does not disturb the terms allready found. Fitting b and $\varkappa$ in (36) with the values (42) for a and r_0, we get $b = 1.54$ and a $\varkappa$-value corresponding to a meson mass of

$$334\ \text{m}_e \pm 10\ \text{m}_e. \tag{44}$$

This result is in very good agreement with the values obtained by JACKSON and BLATT [3] and by YOVITS, SMITH and HULL [8].

Institute for Theoretical Physics, University of Oslo, Blindern, Norway.

REFERENCES

1. L. HULTHÉN, Arkiv. Mat. Astr. Fysik. *A 35*, No. 25, 1 (1948).
2. L. HULTHÉN and S. SKAVLEM, Phys. Rev. *87*, 297, (1952).
3. J. D. JACKSON and J. M. BLATT, Rev. Mod. Phys. *22*, 77 (1950).
4. G. N. WATSON, Theory of Bessel Functions. Cambridge University Press, London 1944.
5. M. TUVE, N. HEYDENBURG, and L. HAFSTAD, Phys. Rev. *56*, 1078 (1939).
6. L. E. HOISINGTON, S. S. SHARE, and G. BREIT, Phys. Rev. *56*, 884 (1939).
7. G. BREIT and R. D. HATCHER, Phys. Rev. *78*, 110 (1950).
8. M. C. YOVITS, R. L. SMITH, M. H. HULL, J. BENGSTON, and G. BREIT, Phys. Rev. *85*, 540 (1952).

Tryckt den 29 oktober 1955

Uppsala 1955. Almqvist & Wiksells Boktryckeri AB

ARKIV FÖR FYSIK Band 10 nr 9

Communicated 27 April 1955 by MANNE SIEGBAHN and BENGT EDLÉN

The decay scheme of Uranium 235

By SVEN A. E. JOHANSSON

With 5 figures in the text

Summary

The gamma-radiation from enriched U^{235} has been investigated by means of a coincidence scintillation spectrometer. Gamma-rays were found at 74, 110, 184, 200, 289, and 382 keV. The coincidence relations between the gamma-rays were investigated in detail. These measurements lead to a decay scheme which is in good agreement with the alpha-ray spectrum. The possibility to interpret the level scheme as a system of rotational bands is discussed.

Introduction

The uranium isotope with the mass 235 decays with a half-life of 7.1×10^8 years. The most recent measurement by GHIORSO [1] on the alpha-radiation shows a complex spectrum. There are alpha-groups with the energies of 4.58, 4.40, and 4.20 MeV. The intensities are 10, 86, and 4 per cent, respectively. There is possibly a fourth group at 4.47 MeV with an intensity of about 3 per cent.

A gamma-ray of 162 keV energy was found by MACKLIN [2]. Recently, BELL *et al.* [3] reported five gamma-rays with the energy values of 94, 143, 184, 289, and 386 keV. The 184 and 386 keV gamma-rays fit well into the level scheme found from the alpha-ray spectrum. The position of the other gamma-rays is not known, however.

In order to study the decay scheme of U^{235} more thoroughly, the gamma-radiation from a sample of enriched U^{235} was investigated by means of a coincidence scintillation spectrometer. This apparatus enables a detailed study of the coincidence relations among the various gamma-rays. Several new gamma-rays were found. The coincidence measurements establish a consistent decay scheme which is in very good agreement with the alpha-ray spectrum.

The apparatus

The coincidence scintillation spectrometer has been described elsewhere [4, 5]. One scintillation spectrometer is used to select a certain radiation component. A second spectrometer records the pulse height distribution of those pulses which are in coincidence with the selected ones. In the present work the apparatus was used only for gamma-gamma coincidence measurements.

The gamma-ray spectrometers consist of a sodium iodide crystal, one and a half inches in diameter and half an inch thick, in connection with a DuMont photomultiplier, type K 1177. The crystal is held in place on the top of the tube by a thin lucite ring. Thick silicone oil (10^6 cps) gives optical contact between crystal and tube. The oil also keeps the crystal firmly attached to the tube. The crystal is enclosed in a thin-walled aluminum container, which is coated on the inside with a thin layer of magnesium oxide. The container is cemented to the top of the tube to make the crystal hermetically sealed. The spectrometer was put together in a dry box in a helium atmosphere. The photomultiplier is painted with black glyptal in order to make it light-tight. The resolution of the spectrometers is five to seven per cent full width at half maximum for the Cs^{137} 661 keV line.

The source is mounted between the crystals of two gamma-ray spectrometers. The pulses from one of the spectrometers are led to a single channel analyzer, which selects pulses of a certain height. When the channel is set on a certain peak in the spectrum, one can select the corresponding gamma-ray from the rest of the radiation. The pulses from the other spectrometer are led to an integral discriminator. It consists essentially of a Schmitt-trigger circuit and a pulse-shaping circuit, which gives pulses of the same size and shape as the single channel analyzer. The output pulses from the single channel analyzer and the discriminator are led to a coincidence circuit. The output of the coincidence circuit is coupled to a discriminator, which discriminates between coincidence and single pulses. Finally, the discriminator triggers a pulse generator. The pulses from the generator are used in the pulse recording system to indicate the presence of coincidence events.

The determination of the pulse height distributions is performed by means of an oscilloscope, DuMont 404A. The pulse generator is connected to the triggering circuit of the oscilloscope. The coincidence pulses then appear on the screen. They are recorded by means of a DuMont oscilloscope camera, which takes still pictures of the screen. A base line is obtained by triggering the scope with a separate pulse generator for a short period of time during each exposure.

The pictures are run through a microphotometer in order to get quantitative results. The relative pulse height can be measured accurately from such a microphotometer trace. Before each run, the spectrometer was calibrated by taking pictures of some well known spectra. The calibration gives the energy scale of the spectrometer and makes it possible to get the energy values of the radiation to be examined. From the density values of the photometer curve the relative intensities of the corresponding pulse height spectrum can be calculated. The characteristic curve of the film must then be known. This curve was obtained in the following way: The pulses from a pulse generator are displayed on the screen of the oscilloscope. A series of pictures is taken with different values on the pulse frequency. The characteristic curve of the film is obtained by running the pictures in the photometer and plotting the density versus the frequency. The sweep speed, frequency, aperture of the camera and exposure time were kept about the same as in the measurements. The characteristic curve obtained in this way should therefore be directly applicable for determining the intensity values from the microphotometer curves. In doing so, a curve is divided in a number of pulse height intervals and the mean value of the density of each interval is determined from the curve. The characteristic curve gives the corresponding intensity values. In this way the density versus pulse-height curves from the photometer can be converted into intensity versus energy curves.

The oscilloscope works essentially as a multichannel analyzer. The method is

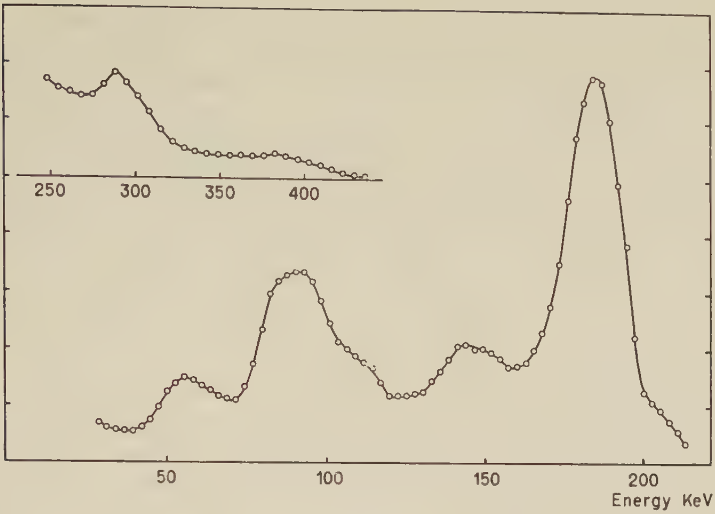

Fig. 1. Gamma-ray spectrum of U^{235}.

thus fast which is especially important in coincidence work where the counting rate is low. It gives energy values of high accuracy. The intensity values are less certain but pulse height distributions obtained in this way show good agreement with those recorded by means of a single channel analyzer.

Results

Fig. 1 shows the gamma-ray spectrum of U^{235}. There is a main peak at 184 keV corresponding to a gamma-ray of that energy. There are also two weak but well-defined peaks at 289 and 382 keV belonging to gamma-rays of those energies. At lower energies there are several peaks and bumps in the curve. There is a fairly strong peak at 95 keV. It is, however, much broader than expected for a single gamma-ray and it is not symmetrical in shape. It must therefore be made up of two or several components. There are finally two small bumps at 145 and 50 keV. The interpretation of the spectrum is as follows:

It is known that alpha-particles, when transversing matter, ionize the atoms and that X-rays subsequently are emitted. One can therefore expect the spectrum to contain *K* X-rays of uranium with an energy of about 96 keV. Hence it is likely that the 95 keV peak is partly due to uranium X-rays. To check this point, sources of different thickness were investigated. The source giving the spectrum of Fig. 1, was rather thin so that a considerable part of the alpha-particles escaped from the source. One should expect a higher yield of X-rays from a thick source, where almost all alpha-particles are stopped within the source. Fig. 2*a* shows a spectrum from a thick source. The 95 keV peak is higher, as expected. This fact indicates strongly that part of the 95 keV peak is due to the uranium X-rays. Another contribution to the peak should come from the X-rays emitted in the internal conversion of the gamma-rays. The thorium *K* X-rays have an energy of about 92 keV. Finally, the coincidence measurements reveal the existence of two gamma-rays at 74 and 110 keV. Hence the 95 keV peak is made up of components of four different energies.

It is well known that spectra from a scintillation spectrometer contain backscattering peaks. The high energy gamma-rays give a well defined peak around 200 keV because the radiation scattered in the backward direction has an energy close to 200 keV for a wide range of gamma-ray energies. Gamma-rays of lower energy give backscattering peaks of energies below 200 keV. The energy of the backscattering peak depends in this case upon the gamma-ray energy and upon the geometry used. Some evidence indicated that the 145 keV peak might be due to backscattering of the 184 keV gamma-ray. To investigate this point, spectra were recorded under different conditions. Fig. 2*a* shows the spectrum from a thick source (1 g of uranylnitrate). The 145 keV peak is rather high. Fig. 2*b* shows the spectrum from a very thin source. In this case the scattering in the source is eliminated but there still remains the scattering in the material surrounding the crystal, i.e. the aluminum container, the phototube etc. It can be seen that the peak is considerably reduced in height. Hence one may conclude that the scattering in the source contributes to the 145 keV peak. Fig. 2*c* shows the spectrum with the radiation from a thick source collimated in lead. This arrangement decreases the scattering from the surroundings but the scattering inside the source remains. A comparison between Fig. 2*a* and Fig. 2*c* shows that the collimation decreases the 145 keV peak. This indicates that also the scattering from the surroundings gives a contribution to the peak. It is quite possible that the combined scattering effect can account for the whole peak. In any case it must account for the greater part of it. If there is a gamma-ray at 145 keV at all, it must be very weak.

It is finally assumed that the bump in the spectrum at 50 keV is the Compton distribution of the 184 keV gamma-ray. This interpretation is supported by coincidence measurements. Part of the peak might also be due to one or several gamma-rays at 50 keV.

A series of gamma-gamma coincidence measurements was performed in order to investigate the coincidence relations in the decay. These measurements revealed the existence of some new gamma-rays. The 95 keV peak was found to contain two gamma-rays at 74 and 110 keV. The 184 keV peak was found to contain a second gamma-ray of slightly higher energy, about 200 keV. The coincidence measurements lead to a decay scheme, which agrees very well with the energy values of the alpha-radiation. The decay scheme is shown in Fig. 5. The dotted transitions are less certain than the others. They have not been completely resolved but there is some evidence for their existence. The coincidence measurements will now be described in detail.

The channel of the pulse analyzer was first set at 75 keV with a channel width of 20 keV. The corresponding coincidence spectrum is shown in Fig. 3*b*. By way of comparison the ordinary gamma-spectrum is shown in Fig. 3*a*. The coincidence spectrum contains a peak at 110 keV indicating coincidences between a gamma-ray at that energy and another one at about 75 keV. There is also a trace of the 95 keV peak. This peak is partly due to the uranium K X-rays which are caused by the ionization of the uranium atoms by the alpha-particles. Hence every gamma-ray should to some extent be in coincidence with these X-rays. Part of the 95 keV peak is probably due to the thorium K X-rays emitted in the internal conversion of some of the gamma-rays. One should therefore expect all the coincidence spectra to contain an X-ray peak. This is also the case. Fig. 3*b* shows a peak also at 190 keV. It can be

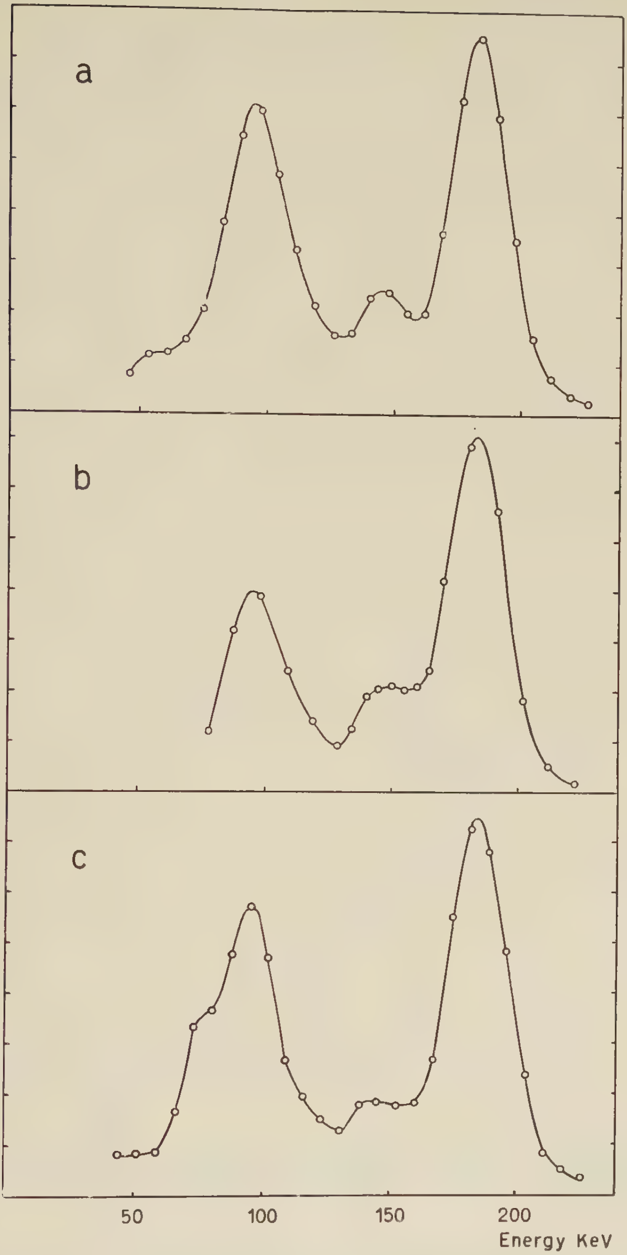

Fig. 2. Gamma-ray spectra.—*a*, for a thick source without collimation; *b*, for a thin source without collimation; *c*, for a thick source with collimation.

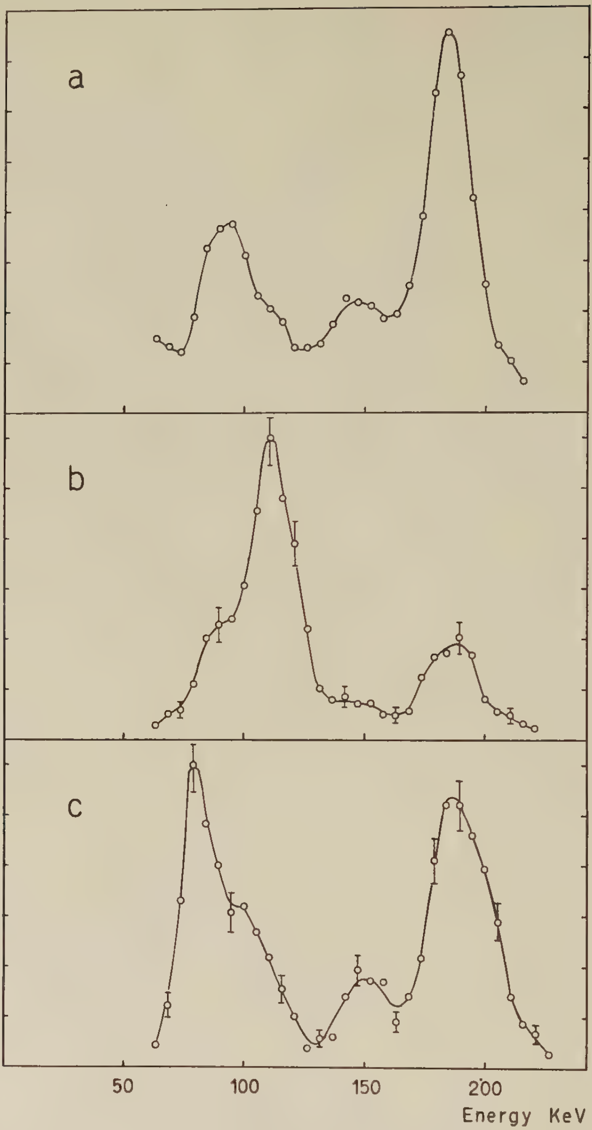

Fig. 3. Gamma-ray spectra.—*a*, ordinary spectrum; *b*, coincidence spectrum with the channel set at 75 keV; *c*, coincidence spectrum with the channel set at 105 keV.

resolved into two peaks due to gamma-rays at 184 and 200 keV. The 200 keV gamma-ray is assumed to be in coincidence with the 74 keV gamma-ray. The presence of the 184 keV gamma-ray can be explained as follows: With the channel set at 75 keV some of the selected pulses will come from the X-ray peak. Both the uranium and the thorium *K* X-rays are to some extent in coincidence with the 184 keV gamma-

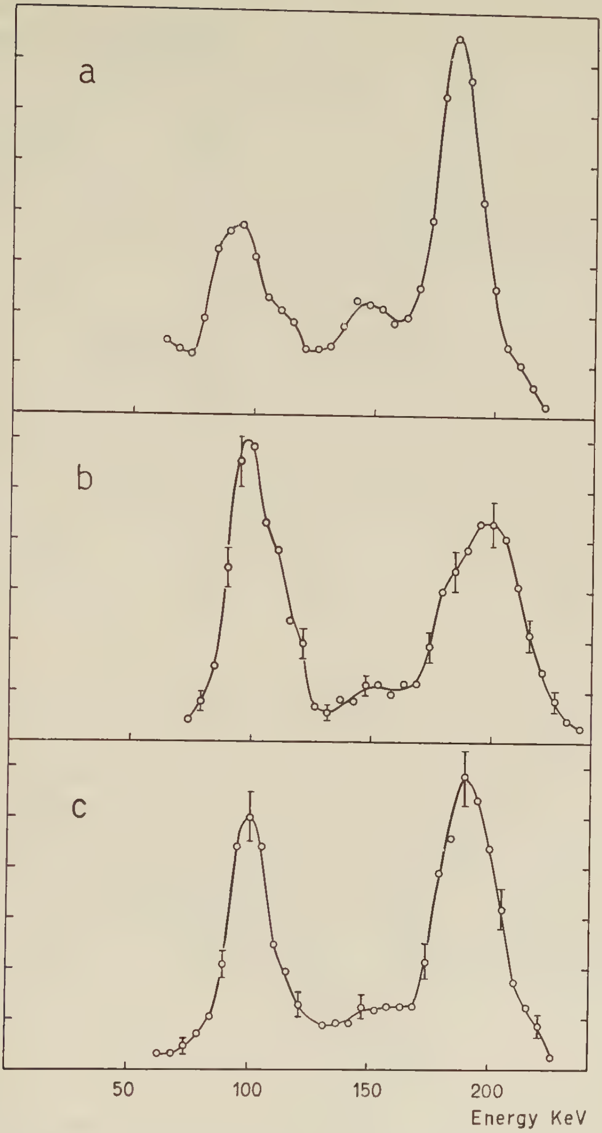

Fig. 4. Gamma-ray spectra.—*a*, ordinary spectrum; *b*, coincidence spectrum with the channel set at 180 keV; *c*, coincidence spectrum with the channel set at 195 keV.

ray; hence there appears a weak peak at 184 keV. The coincidence spectrum in Fig. 3*b* is accordingly in complete agreement with the proposed decay scheme.

Next the channel was set at 105 keV with a channel width of 20 keV. The coincidence spectrum shown in Fig. 3*c* was obtained. It contains a peak at 78 keV, showing coincidences between a gamma-ray of this energy and the 110 keV ray.

Their sum is close to 184 keV and the cascade is therefore assumed to start from the 184 keV level. One can also resolve a peak at about 95 keV, corresponding to the *K* X-rays. The peak at 190 keV is broad and non-symmetrical. It is presumably made up of the two components, 184 and 200 keV. The presence of the 184 keV gamma-ray has the same explanation as in the previous case. Some pulses from the X-ray peak come into the channel and are in coincidence with the 184 keV gamma-ray. The dotted transitions in the decay scheme may also give some contribution to the 190 keV peak. The presence of the 200 keV gamma-ray shows it to be in coincidence with the 110 keV ray. This coincidence spectrum is therefore in complete agreement with the proposed decay scheme.

Next the channel was set at 180 keV with a channel width of 20 keV. Hence the analyzer selects the 184 keV gamma-ray. However, some pulses due to the 200 keV ray will also come into the channel. The coincidence spectrum is shown in Fig. 4*b*. Fig. 4*a* shows an ordinary spectrum for comparison. The coincidence spectrum contains the usual X-ray peak. It is not perfectly symmetric. At the high-energy side there is an indication of another gamma-ray of somewhat higher energy. The two dotted transitions in the decay scheme may explain this coincidence effect. The high energy peak in the spectrum is shifted towards higher energy. It can be resolved into a peak at 200 keV and a weaker one at 184 keV. Hence this spectrum shows that the 184 and 200 keV gamma-rays are in coincidence. The 184 keV radiation in the coincidence spectrum is due to the fact that some pulses from the 200 keV ray come into the channel. This coincidence spectrum, too, supports the proposed decay scheme.

With the channel set at 195 keV the spectrum shown in Fig. 4*c* was recorded. The channel width was 20 keV. The spectrum consists of the X-ray peak and a peak around 185 keV. The latter consists of a 184 keV component plus a weak 200 keV component. The presence of the 200 keV gamma-ray is due to the fact that some pulses from the 184 keV ray are registered by the analyzer with the channel setting used. The gamma-rays at 74 and 110 keV are in coincidence with the 200 keV ray according to the preceding spectra but they do not show up in this spectrum because their branching ratio is small compared to that of the 184 keV gamma-ray. This coincidence spectrum, too, is in agreement with the proposed decay scheme.

Finally, a wide channel was used to select the gamma-rays above 200 keV. No coincidences were found except the accidental ones. Hence the 289 and 382 keV gamma-rays go directly to the ground state.

The decay scheme

The coincidence measurements are in complete agreement with the proposed decay scheme shown in Fig. 5. Together with the energy values of the alpha-radiation they determine the scheme in a univocal way. The transitions shown as dotted lines in the scheme have not been completely resolved. However, they can explain some features of the coincidence spectra, as discussed above. No alpha-ray group has been reported going to the 289 keV level. In the alpha-ray spectrum of GHIORSO [1] one can see, however, that the 4.40 MeV peak is not quite symmetrical. On the low energy side there is a bump. This may be due to a low intensity alpha-ray group. Assuming that the 4.40 MeV peak is of the same shape as the U^{234} peak, also present in the spectrum, one can by subtraction get the low intensity peak. The result of this

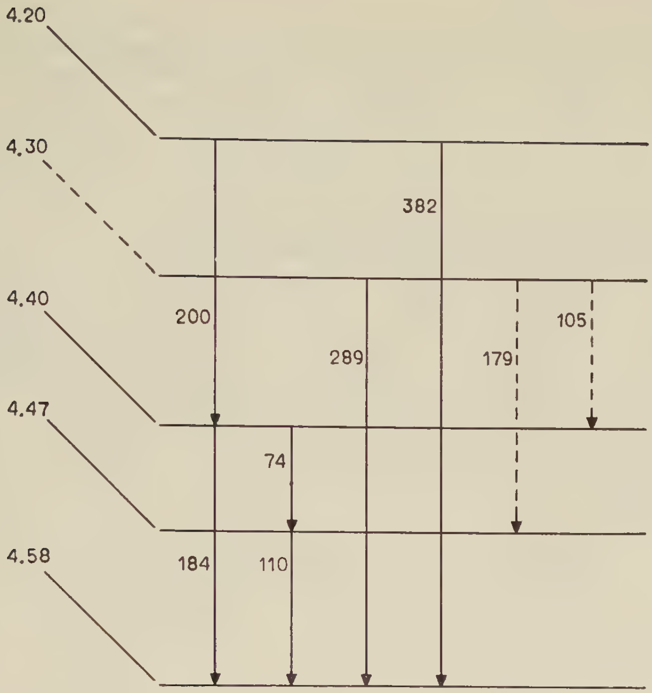

Fig. 5. Proposed decay scheme for U^{235}. Alpha-ray energies in MeV, gamma-ray energies in keV. The dotted transitions are only tentative.

rather uncertain procedure is a peak at about 4.30 MeV with an intensity of about six per cent. This is in good agreement with the proposed decay scheme.

In the decay of U^{235} the ground state alpha-transition is weaker than some of the transitions to the excited states. There are some other nuclei of the same type. This problem has been discussed by PERLMAN, GHIORSO and SEABORG [5] in connection with the systematics of alpha-radioactivity. If the logarithm of the half-life is plotted versus the energy for even-even nuclei, the experimental points fall on a series of parallel lines. Each line corresponds to a certain value of Z. If the same procedure is used for nuclei with even Z and odd number of neutrons, the experimental points will be much more scattered and nearly all will lie significantly above the curves for the respective elements as determined by the nuclei with even number of neutrons. There are some cases, among them U^{235}, where the ground state transition shows an appreciable departure from the curve, whereas in all these decays one or several alpha-groups have only a small departure factor. In the case of U^{235} the ground state transition is 1000-fold forbidden and the 4.40 MeV group 10-fold forbidden. It should be emphasized, however, that even nuclei showing no alpha fine structure are somewhat forbidden compared to the even-even nuclei.

According to the Gamow theory for the alpha-decay the transition probability depends on the spin change. To account for the observed degree of forbiddenness, however, one has to assume spin changes of 10 units or more. Such large changes are, of course, very improbable. According to the theory, the transition probability depends strongly on the nuclear radius. As discussed by PERLMAN *et al.* [5], however, a shrinkage of the nuclear radius cannot be assumed as a general explanation of the low transition probability in some nuclei with odd proton or neutron number.

PERLMAN *et al.* [6] have suggested an explanation for this phenomenon. They assume that the probability for formation of an alpha-particle inside the nucleus varies and that this causes the great variations in the transition probability. It is now possible to understand why nuclei with odd numbers of protons or neutrons sometimes have their ground state transitions highly forbidden. The odd nucleon, which in most cases is in the highest quantum state, must be a component of the alpha-particle, if the alpha-particle is to leave the nucleus with the full kinetic energy. The odd nucleon must therefore pair with a lower-lying nucleon of anti-parallel spin and some of the other nucleons may have to change quantum state. It is reasonable to assume that a transition of this type is slower than when the alpha-particle is assembled by lower-lying nucleons. In these cases one would therefore expect to find transitions to exited states, which are faster for their energies than the ground state transitions and therefore able to compete.

Table 1. Intensity and hindrance factor for the alpha-groups.

Energy, Mev	Intensity %	Hindrance factor
4.58	9	215
4.47	3	105
4.40	78	1
4.30	6	1.9
4.20	4	0.5

The spin of the U^{235} ground state is very probably 5/2 [7]. In the terms of the shell model this would mean that there are 6 neutrons in the $i_{11/2}$ shell and one in the $d_{5/2}$ shell. After the ground state alpha-transition the nucleus is therefore, according to the preceding discussion, presumably left with 5 neutrons in the $i_{11/2}$ shell. The 4.40 MeV alpha-group corresponds to a transition in which the odd neutron does not take part. The nucleus is therefore left with an odd neutron in the $d_{5/2}$ shell.

It is interesting to examine in greater detail the degree of forbiddenness of the various alpha-groups in the decay of U^{235}. In order to express the transition probability a hindrance factor is used which is inversely proportional to the transition probability when the dependence on the energy is already taken into account. This hindrance factor is then a measure of the alpha-particle formation probability; a large hindrance factor means that the formation probability is low. Table 1 gives the hindrance factors for the various alpha-groups with the value for the 4.40 MeV group arbitrarily put to 1. It is evident from the table that the five transitions are separated in two groups. The two high energy transitions (4.58 and 4.47 MeV) are rather highly forbidden with a hindrance factor of the same order of magnitude. The other three transitions form another group with about the same hindrance factor.

The fact that the alpha-groups are separated into two groups with respect to transition probability makes it interesting to discuss the decay of U^{235} from the standpoint of the strong surface coupling model [8, 9]. According to this model the levels occur in series. Each series corresponds to a certain particle state but the members of the series have different rotational energy. For odd-A nuclei the energies of the states are given by the equation

$$E_I = \frac{\hbar^2}{2J}[I(I+1) - I_0(I_0+1)], \quad I = I_0, I_0+1, I_0+2, \ldots$$

where I_0 is the angular momentum of the lowest state of the series, I the angular momentum of the state with the energy E_I, and $\frac{\hbar^2}{2J}$ the rotational energy quantum. The value of the rotational energy quantum can be obtained from rotational bands identified in neighbouring nuclei.

It is tempting to assume that the ground state and the first excited state belong to the same rotational band since the alpha groups going to these two states have the same degree of forbiddenness. The three higher excited states may form another band. The rotational bands in neighbouring nuclei, however, have a first excited state at about 40 keV and a second one at about 100 keV. Hence the 110 keV level should actually be the second excited state in the lowest rotational band. The first excited state has not been found in the present measurements. The reason for this is the low energy of the transition going from this state to the ground state. This gamma-ray must be practically completely converted. The gamma-rays of higher energy going to this state are probably too weak to be resolved. A similar interpretation can be given for the higher excited states. The 289 keV level may be the second excited state in a rotational band starting at the 184 keV level. The 386 keV level does probably not belong to this band. Its energy does not fit into the band and the intensity of the corresponding alpha group is too high. Spin considerations also exclude such an interpretation. This level may therefore correspond to a third particle state.

This tentative analysis shows that the decay scheme may contain levels at approximately 40 and 230 keV. There should in that case be alpha groups going to these levels. The resolution of the published alpha spectrum is not sufficient to decide whether this is the case or not. However, this possibility is not excluded.

Hence, the decay of U^{235} seems to be very complicated. If this decay is not radically different from that of neighbouring nuclei, it should contain low-energy gamma-rays. It would be particularly interesting to study this radiation in detail. Very thin sources of enough activity would be required. This is difficult to obtain, however, due to the low specific activity of U^{235}.

ACKNOWLEDGEMENTS

The present investigation was performed at the Institute for Atomic Research and Department of Physics, Iowa State College, Ames, Iowa, U.S.A. The author wants to express his sincere appreciation of the hospitality extended to him during his stay in Ames.

REFERENCES

1. A. Ghiorso, Phys. Rev. *82*, 979 (1951).
2. R. L. Macklin, Phys. Rev. *76*, 595 (1949).
3. R. R. Bell, R. C. Davis, J. E. Francis, and J. M. Cassidy, Oak Ridge Report ORNL-1164.
4. Sven A. E. Johansson, Iowa State College Report ISC-431.
5. Sven A. E. Johansson and S. Almquist, Arkiv för Fysik, *5*, 427 (1953).
6. I. Perlman, A. Ghiorso, and G. T. Seaborg, Phys. Rev. *77*, 26 (1950).
7. G. L. Stuckenbrocker and J. R. McNally, J. Opt. Soc. Am. *40*, 336 (1950).
8. A. Bohr, Phys. Rev. *81*, 134 (1951), Dan. Mat. Fys. Medd. *26*, No 14 (1952).
9. A. Bohr and B. R. Mottelson, Dan. Mat. Fys. Medd. *27*, No 16 (1953).

Tryckt den 24 oktober 1955

Uppsala 1955. Almqvist & Wiksells Boktryckeri AB

ARKIV FÖR FYSIK Band 10 nr 10

Communicated 11 May 1955 by ERIK HULTHÉN

Optical problems concerning the use of interference in the determination of spectroscopic wave-numbers

By A. VILHELM PETTERSSON

With 3 figures in the text

The spectrophotometric method [1] of recording spectra has the advantage over the photographic method that one gets the intensity of the spectral lines directly without having to go the roundabout way over photographic density curves. On the other hand, it is difficult to introduce a reference spectrum (e.g. iron). If two spectra are mixed by e.g. a semi-transparent mirror, the recording may be indistinct on account of overlapping, unless both spectra have only few lines.

By means of electronic devices one can separate the reference spectrum from the examined one even if they are fed simultaneously to the same phototube [2]. KRANTZ and ÅSLUND [3] have used this method in such a way that the reference lines are recorded as short, vertical scores or strokes and may thus be permitted to coincide with examined lines.

If one does not want the recording to be disturbed by the noise from the reference lines, two requirements must be fulfilled: (1) their intensity must be as nearly equal as possible, and (2) they should be narrow. Though the first requirement may be met by certain spectra, it has suggested the thought of using a continuous spectrum modulated by interference. Two ways of producing modulation are discussed here.

HULTHÉN's grating-interferometer [4] gives in certain mountings a pure, monotonous spectrum, the intensity of which varies according to the formula

$$I = \text{const} \times \cos^2 \frac{4\pi n d}{\lambda},^1$$

where d is the distance between the grating surface and the completely silvered back surface, and n is the index of refraction of the medium between them. The intensity contour for the modulated spectrum and the effective width of the dark fringes are thus independent of the reflecting power. It may thus be possible to make recordings in two different wave-length ranges without having to change the interferometer, in spite of a great difference in the reflecting power of the silvering in the ranges in question. The disadvantage of this method is the great width of the light fringes.

If the light from a Fabry-Perot interferometer is focussed by a lens whose focus coincides with the spectrograph slit, one gets narrow, light fringes that are concave towards the short wave end of the spectrum and separated by broad dark regions (Fig. 1). This method was chosen on account of the narrowness of the fringes. In a

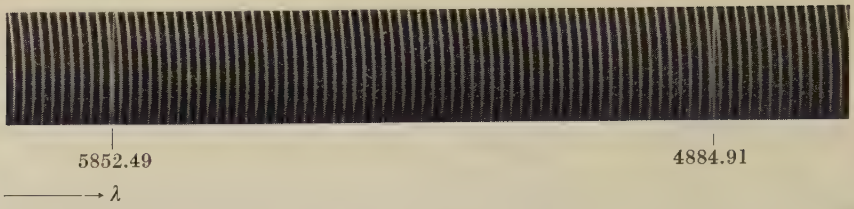

Fig. 1. This photograph was taken with an echelette grating. The fringes and the neon line 5852.49 belong to the 5th order, the neon line 4884.91 belongs to the 6th.

somewhat simpler form it was used by EDSER and BUTLER [5] as early as 1898. It has since been used in several ways, e.g. in the infrared by COOPER and STROUPE [6]. The fringe width depends chiefly upon the reflecting power of the interferometer plates, for the intensity varies according to

$$I = \frac{\text{const}}{1 + \dfrac{4\,r^2 \sin^2 \dfrac{\delta}{2}}{(1-r^2)^2}},$$

where r^2 is the reflecting power and

$$\delta = \frac{4\,\pi\, n\, d \cos\theta}{\lambda},[1]$$

where n is the index of refraction of the medium between the plates, d the distance between them, and θ the angle that the rays make (in the medium) with the normal to the plates. A further consideration is the broadening caused inter alia by the spectrograph and by the slits being not infinitely narrow. Theoretically, the intensity of the peaks of the fringes does not depend on r^2, but on account of these broadening effects it is increased if r^2 is reduced.

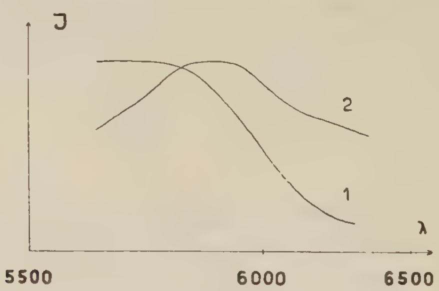

Fig. 2.

Curve 1 in Fig. 2 shows the relative current through the phototube at various wave-lengths, when the interferometer is not in the path of the rays. Its appearance will depend on the distribution between different wave-lengths of the intensity of the light source, on the dispersion of the spectrometer, and on the relative spectral sensitivity of the phototube. With an ordinary interferometer with silvered plates, a modulated curve would have been obtained, where the peaks would have formed a curve with approximately the same shape. To make possible a continuous recording over the whole range, one would have had to make the curve more plane by using a suitable filter. However, the plates used for the recordings were of multilayer type with maximal reflecting power in the green part of the spectrum. On account of the above-mentioned broadening effects, the decrease of the reflecting power towards the red end of spectrum counteracts the tendency in curve 1, Fig. 2. Thus the peaks formed curve 2 in Fig. 2. The two curves give relative values; the highest points in both have been put equal. This method of accommodation may, however, only be used to a certain value of r^2; if r^2 is still more decreased, the seeming increase of the peak intensity ceases, while the broadening continues.

---

[1] The formulas neglect the phase change caused by the reflections. This phase change and its dependence on the wave-length must be considered in some cases.

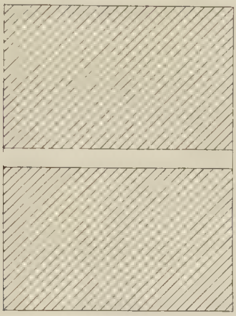

Fig. 3. The mirror at the slit of the spectrometer is silvered (not semi-transparent), except for a narrow horizontal band whose width is dependent on the focal length of the focussing lens of the interferometer. If the glass of the mirror is not plane, or if it is too thick, the fringes may be broadened.

As the formulas show, the difference between two fringes is constant if it is expressed in wave-numbers, provided that it is possible to neglect the dispersion of the medium between the plates. This is valid for the grating-interferometer as well as the Fabry-Perot interferometer.

The main feature of the optical arrangement is described in KRANTZ's and ÅSLUND's article. The mirror at the slit of the spectrometer must be placed as near the slit as possible and must be shaped according to Fig. 3. It cannot be replaced by a thinly silvered plate. The reason for this is the curvature of the fringes (Fig. 1); only the parts that run almost parallel with the spectrum lines (two such lines are visible in Fig. 1) can be used. The unsilvered band was 1.5 mm wide; the focal length of the lens focussing the light from the interferometer onto the slit was about 60 cm. Shorter focal length causes the curvature of the fringes to increase and thus necessitates a narrower unsilvered band, in addition to which the mirror has to be placed nearer the slit.

The adjustment of optical arrangements has been treated by e.g. TOLANSKY [7]. The following procedure is the most suitable for this case. A small source of light is first placed immediately in front of the centre of the collimator. Then one person can centre the optical system rapidly and accurately, if the optical elements in the interferometer part are placed in their proper turn (the zirconium oxide lamp, the condenser lens, the chopper etc.). Before the mirror at the slit is set in place, the (parallel-adjusted) interferometer and its focussing lens are adjusted in the following way. A source of light is placed immediately within the slit. The reflecting surface of the interferometer in combination with the focussing lens then throws an image of the slit near the latter. The lens is now moved to and fro; it is adjusted when the image is sharp. After this the slit is shortened by a diaphragm. The interferometer holder is turned round a horizontal axis and a vertical axis until the image coincides with the slit. While the latter is still shortened, the mirror is placed in such a way that the unsilvered band transmits the light. The interferometer part is now ready, and the examined light source with its optical arrangement is then adjusted in a similar manner.

The author wishes to express his gratitude to Professor E. HULTHÉN, fil. kand. B.-Å. KRANTZ, and fil. kand. N. ÅSLUND for valuable discussions.

Physics Department, University of Stockholm, May 1955.

REFERENCES

1. DIEKE, G. H., and CROSSWHITE, H. M., J. Opt. Soc. Am. *35*, 471 (1945).
2. ETZEL, H. W., J. Opt. Soc. Am. *43*, 87 (1953).
3. KRANTZ, B.-Å., and ÅSLUND, N., Arkiv för Fysik, *10*, 165 (1955).
4. HULTHÉN, E., Arkiv för Fysik *4*, 399 (1952).
5. EDSER, E., and BUTLER, C. P., Phil. Mag. *46*, 207 (1898).
6. COOPER, C. V., and STROUPE, J. D., J. Opt. Soc. Am. *41*, 427 (1951).
7. TOLANSKY, S., High Resolution Spectroscopy. London, 1947.

Tryckt den 24 oktober 1955

Uppsala 1955. Almqvist & Wiksells Boktryckeri AB

ARKIV FÖR FYSIK Band 10 nr 11

Communicated 25 May 1955 by OSKAR KLEIN and HILDING FAXÉN

On the electromagnetic properties of the deuteron[1]

By M. SUGAWARA[2]

The exchange current corrections to the quadrupole and magnetic moments of the deuteron have been calculated, assuming the sym. *ps–ps* meson theory and employing *T–D* formalism, neglecting the nucleon recoil energy in the energy denominator and retaining only the one meson amplitude. Also the non-additivity and the relativistic corrections have been estimated in the same approximation. It is shown that the exchange correction of the magnetic moment is rather unambiguous and is estimated as -0.85 % of its empirical value, while that of the quadrupole moment is somewhat ambiguous and may be estimated as from $+2$ % to zero or even a small negative value of its empirical value. The non-additivity and the relativistic corrections are estimated as $+0.26$ % and -0.41 %, respectively. The latter two effects are uncertain but almost cancel each other; thus the final estimate of the magnetic moment correction is rather definite and is -1.0 ± 0.3 %. This correction, in turn, determines the *D*-state probability as 2.4 ± 0.5 %. Including the over all errors, the final estimate of the *D*-state probability is 3 ± 1 %, a definitely smaller value than 4 %.

I. Introduction

Owing to rather many ambiguities in the theoretical estimates of the corrections to the electromagnetic properties of the deuteron, it has not been possible to give a rather definite estimate for the *D*-state probability of the deuteron ground state, which gives rise to a big ambiguity in determining the relative importance of the tensor force to the central one, both acting in the ground state of the deuteron.

In this paper, the present author attempted to give a somewhat definite answer to the above problem, assuming the symmetrical *ps–ps* meson theory. In order to make the physical content of the calculation as clearly as possible, the Tamm-Dancoff formalism was adopted. We therefore had to neglect all the renormalization effects, which would not modify the order of magnitude of the final result. We have conventionally classified the calculation into three parts. First of all, we investigate the effect of the virtual meson exchange (and also the consequent recoil motion of the nucleon) between the two nucleons in the deuteron, which will be treated in Section III after the development of the general theory in Section II and will be shown to be the major effect of the three. Secondly, the considerations are given in Section IV on the non-additivity problem of the nucleon moments in the deuteron and finally, in Section V, we discuss about the purely kinematical relativistic correction to the deuteron moment. Both of the latter effects are rather difficult to manage, but will be shown to be relatively small and cancel almost entirely with each other. Thus it will be possible to get a rather definite estimate of the required theoretical correction to the deuteron magnetic moment although the correction to the quadrupole moment is somewhat ambiguous. Numerical results and the relating discussions are given in Section VI, together with the comparisons with other papers published thus far on this topic.

---

[1] This work was done under the auspices of the Swedish Atomic Energy Committee.

[2] On leave of absence from Dept. of Physics, Hokkaido University, Sapporo, Japan.

II. Basic equations

The total Hamiltonian of the meson–nucleon system interacting with the external electromagnetic field is, assuming symmetrical *ps–ps* meson theory, given by

$$H = H_0 + H' + H'', \tag{1}$$

$$H_0 = \hbar c \left[\bar\psi\left(\sum_i \gamma_i \frac{\partial}{\partial x_i} + \varkappa\right)\psi\right] + \tfrac{1}{2}\sum_\alpha \left[c^2\pi_\alpha^2 + (\mathrm{grad}\,\phi_\alpha)^2 + \mu^2\phi_\alpha^2\right], \tag{2}$$

$$H' = i f \sum_\alpha \bar\psi\gamma_5\tau_\alpha\psi\phi_\alpha, \tag{3}$$

$$H'' = -ie\sum_\mu \bar\psi\frac{1+\tau_3}{2}\gamma_\mu\psi A_\mu + \frac{e}{\hbar c}\left[\sum_i A_i\left(\phi_1\frac{\partial\phi_2}{\partial x_i} - \phi_2\frac{\partial\phi_1}{\partial x_i}\right)\right] - $$
$$- icA_4(\phi_1\pi_2 - \phi_2\pi_1) - \tfrac{1}{2}\left(\frac{e}{\hbar c}\right)^2 A_4^2(\phi_1^2+\phi_2^2), \tag{4}$$

where we have used quite well-known notations. If we want to introduce the Pauli-term in order to represent the anomalous magnetic moments of the nucleons, we have only to add an extra term

$$\sum_{\mu\nu}\frac{i}{2}\bar\psi\frac{e}{2\varkappa}\left[(\mu_P-1)\frac{1+\tau_3}{2} + \mu_N\frac{1-\tau_3}{2}\right]\gamma_\mu\gamma_\nu\psi\left(\frac{\partial A_\nu}{\partial x_\mu} - \frac{\partial A_\mu}{\partial x_\nu}\right) \tag{5}$$

to the above Hamiltonian, where μ_P, μ_N and μ_D (which will be introduced later) are the total magnetic moments of a proton, a neutron and a deuteron in units of the nuclear magneton.

If we confine ourselves to a constant magnetic field $\bar H$ by putting

$$\bar A = -\tfrac{1}{2}[\bar x \times \bar H]$$

and $A_4 = 0$, we get from (4) the following magnetic moment operator $\bar\mu$ in units of $e/2\varkappa$:

$$\bar\mu = \varkappa\int\psi^*\frac{1+\tau_3}{2}[\bar x\times\bar\alpha]\psi\, d\bar x - \frac{\varkappa}{\hbar c}\int\left(\phi_1\left[\bar x\times\frac{\partial}{\partial\bar x}\right]\phi_2 - \phi_2\left[\bar x\times\frac{\partial}{\partial\bar x}\right]\phi_1\right)d\bar x, \tag{6}$$

where $\bar{\alpha}$ is the ordinary Dirac matrix. If, on the other hand, we introduce the pure electric field $\bar{E}$ varying rather slowly inside our meson–nucleon system by putting $\bar{A}=0$, $A_4 = i\phi$ and $\phi(\bar{x}) = \phi(0) - (\bar{x}\cdot\bar{E}) - \frac{1}{2}\sum_{ij} x_i x_j \frac{\partial}{\partial x_i} E_j$ we get the following electric quadrupole moment operator Q:

$$Q = \int (3z^2 - r^2)\left[\psi^* \frac{1+\tau_3}{2}\psi + \frac{1}{\hbar}(\phi_1 \pi_2 - \phi_2 \pi_1)\right] d\bar{x}. \tag{7}$$

As we can treat the interaction term H'' in (1) as a small perturbation, we shall first solve the meson–nucleon problem and then calculate the expectation values of $\bar{\mu}$ and Q obtained above. In order to solve the meson–nucleon problem, we use the ordinary Tamm-Dancoff formalism. Thus, to solve the basic Schrödinger equation of the meson–nucleon system

$$\int (H_0 + H')\, d\bar{x}\, |\Psi\rangle = E\, |\Psi\rangle, \tag{8}$$

we expand $|\Psi\rangle$ as follows:

$$|\Psi\rangle = \iint c(\bar{p}_1 \bar{p}_2)\, |\bar{p}_1 \bar{p}_2\rangle\, d\bar{p}_1\, d\bar{p}_1 + \iiint c(\bar{p}_1 \bar{p}_2 \bar{k})\, |\bar{p}_1 \bar{p}_2 \bar{k}\rangle\, d\bar{p}_1\, d\bar{p}_2\, d\bar{k}, \tag{9}$$

where the basic vector $|\bar{p}_1 \bar{p}_2 \bar{k}\rangle$, for example, is defined by $\frac{1}{\sqrt{2!}}\mathbf{a}^*_{\bar{p}_1}\mathbf{a}^*_{\bar{p}_2}\mathbf{a}^*_{\bar{k}}|0\rangle$, where $|0\rangle$ is the vacuum state and $\mathbf{a}^*_{\bar{p}_1}$ and $\mathbf{a}^*_{\bar{k}}$ are the ordinary creation operators of a nucleon having a positive energy and a momentum $\bar{p}_1$ and a meson having a wave vector $\bar{k}$, respectively. All the necessary summations or integrations are considered to be contained in the above notation and all the expansion coefficients c's are suitably symmetrized. In the expansion (9), we have considered only the one-meson amplitude, which will be sufficient in our present calculation because we are now only interested in the virtual exchange effect between two nucleons and the deuteron is a loosely bound system. The normalization condition is

$$\langle\Psi|\Psi\rangle = \iint |c(\bar{p}_1 \bar{p}_2)|^2\, d\bar{p}_1\, d\bar{p}_2 + \iiint |c(\bar{p}_1 \bar{p}_2 \bar{k})|^2\, d\bar{p}_1\, d\bar{p}_2\, d\bar{k}. \tag{10}$$

Upon substituting the expansion (9) into (8), we readily get the solution

$$c(\bar{p}_1 \bar{p}_2 \bar{k}) = \frac{1}{E - (E_{\bar{p}_1} + E_{\bar{p}_2} + \hbar c\, \omega_{\bar{k}})} \sqrt{\frac{\hbar c}{2\,\omega_{\bar{k}}\,(2\pi)^3}} \left(\frac{-if}{2\varkappa}\right) \times$$
$$\times \{\tau_\alpha^{(1)}(\bar{\sigma}^{(1)}\cdot\bar{k})\, c(\bar{p}_1 + \hbar\bar{k}, \bar{p}_2) + \tau_\alpha^{(2)}(\bar{\sigma}^{(2)}\cdot\bar{k})\, c(\bar{p}_1, \bar{p}_2 + \hbar\bar{k}\}, \tag{11}$$

where $\omega_{\bar{k}} = \sqrt{k^2 + \mu^2}$ and we have assumed that both nucleon momenta $\bar{p}_1$ and $\bar{p}^2$ can be considered as the non-relativistic ones, which enables us to approximate the formula

$$(u^*_{\bar{p}}\, i\gamma_4\gamma_5\, u_{\bar{p}'}) = \sqrt{\frac{(Mc^2 + E_{\bar{p}})(Mc^2 + E_{\bar{p}'})}{2E_{\bar{p}}\, 2E_{\bar{p}'}}} \left[\frac{ic\,\bar{\sigma}\cdot\bar{p}}{E_{\bar{p}} + Mc^2} - \frac{ic\,\bar{\sigma}\cdot\bar{p}'}{E_{\bar{p}'} + Mc^2}\right]$$

by

$$(u_{\bar{p}}^{*}\, i\gamma_4\gamma_5\, u_{\bar{p}'}) = \frac{i\,\bar{\sigma}(\bar{p}-\bar{p}')}{2Mc}, \tag{12}$$

where $u_{\bar{p}}$ and $u_{\bar{p}'}$ are the free particle Dirac spinors, M the mass of the nucleon and $\bar{\sigma}$ the Pauli spin matrix. In the above two formulas, we are using a somewhat arbitrary prescription. Correspondingly we are considering in (11) that the c's contain the ordinary spin and the charge spin basic vectors and the indices (1) and (2) mean that they apply to the former or the latter arguments of c's, respectively.

In the expectation values of Q (7) and $\bar{\mu}$ (6), there does not appear any cross term of $c(\bar{p}_1\bar{p}_2)$ and $c(\bar{p}_1\bar{p}_2\bar{k})$; they are given by

$$\begin{aligned}\langle\Psi|Q \text{ or } \bar{\mu}|\Psi\rangle = &\int c^{*}(\bar{p}_1\bar{p}_2)\langle\bar{p}_1\bar{p}_2|Q \text{ or } \bar{\mu}|\bar{p}_1'\bar{p}_2'\rangle c(\bar{p}_1'\bar{p}_2')\,d\bar{p}_1\,d\bar{p}_2\,d\bar{p}_1'\,d\bar{p}_2' + \\ &+\int c^{*}(\bar{p}_1\bar{p}_2\bar{k})\langle\bar{p}_1\bar{p}_2\bar{k}|Q \text{ or } \bar{\mu}|\bar{p}_1'\bar{p}_2'\bar{k}'\rangle c(\bar{p}_1'\bar{p}_2'\bar{k}')\,d\bar{p}_1\,d\bar{p}_2\,d\bar{k}\,d\bar{p}_1'\,d\bar{p}_2'\,d\bar{k}',\end{aligned} \tag{13}$$

where

$$\begin{aligned}\langle\bar{p}_1\bar{p}_2\bar{k}|Q|\bar{p}_1'\bar{p}_2'\bar{k}'\rangle = &-\hbar^2\left(3\frac{\partial^2}{\partial p_{1z}^2}-\frac{\partial^2}{\partial\bar{p}_1^2}\right)\frac{1+\tau_3^{(1)}}{2}\,\delta(\bar{p}_1-\bar{p}_1')\times \\ &\times\delta(\bar{p}_2-\bar{p}_2')\,\delta(\bar{k}-\bar{k}')+\text{term (2)}+\delta(\bar{p}_1-\bar{p}_1')\,\delta(\bar{p}_2-\bar{p}_2')\times \\ &\times\left(3\frac{\partial^2}{\partial k_z^2}-\frac{\partial^2}{\partial\bar{k}^2}\right)\delta(\bar{k}-\bar{k}')\,i\,(\delta_{12}-\delta_{21}),\end{aligned} \tag{14}$$

$$\begin{aligned}\langle\bar{p}_1\bar{p}_2\bar{k}|\bar{\mu}|\bar{p}_1'\bar{p}_2'\bar{k}'\rangle = &\frac{1+\tau_3^{(1)}}{2}\left(-i\left[\bar{p}_1\times\frac{\partial}{\partial\bar{p}_1}\right]+\bar{\sigma}^{(1)}\right)\delta(\bar{p}_1-\bar{p}_1')\,\delta(\bar{p}_2-\bar{p}_2')\,\delta(\bar{k}-\bar{k}')+ \\ &+\text{term (2)}+\varkappa\,\delta(\bar{p}_1-\bar{p}_1')\,\delta(\bar{p}_2-\bar{p}_2')\frac{1}{\omega_{\bar{k}}}\left[\bar{k}'\times\frac{\partial}{\partial\bar{k}'}\right]\delta(\bar{k}-\bar{k}')\,(\delta_{12}-\delta_{21}),\end{aligned} \tag{15}$$

and the similar expressions for $\langle\bar{p}_1\bar{p}_2)|Q|\bar{p}_1'\bar{p}_2'\rangle$ and $\langle\bar{p}_1\bar{p}_2|\bar{\mu}|\bar{p}_1'\bar{p}_2'\rangle$ as (16) and (15), respectively, with dropping the corresponding third terms and the δ-functions containing $\bar{k}$ and $\bar{k}'$, where we have used quite the analogous approximation as (12), namely

$$(u_{\bar{p}}^{*}\,\alpha\,u_{\bar{p}'}) = \frac{1}{2Mc}\{(\bar{p}+\bar{p}')+i[\bar{\sigma}\times(\bar{p}-\bar{p}')]\}, \tag{16}$$

and the symbols δ_{12} and δ_{21} mean that we must retain only the τ-spin combinations $\tau_1^{(1)}\tau_2^{(2)}$ and $\tau_2^{(1)}\tau_1^{(2)}$, respectively. We have also equated the terms which give the same contribution in the integral (13) already. If we have introduced the Pauli-term (5), then we must add the following term to (15)

$$\left[(\mu_P-1)\frac{1+\tau_3^{(1)}}{2}+\mu_N\frac{1-\tau_3^{(1)}}{2}\right]\bar{\sigma}^{(1)}\,\delta(\bar{p}_1-\bar{p}_1')\,\delta(\bar{p}_2-\bar{p}_2')\,\delta(\bar{k}-\bar{k}')+\text{term (2)} \tag{17}$$

and an analogous term to $\langle\bar{p}_1\bar{p}_2|\bar{\mu}|\bar{p}_1'\bar{p}_2'\rangle$.

III. Exchange current effect

Now we shall confine ourselves to the consideration about the exchange current effect. The second terms of (10) and (13) contain the self-meson effect and the exchange meson effect, the former of which contributes to the anomalous magnetic moments of nucleons and therefore produces the non-additivity correction and the latter of which gives rise to the correction due to the exchange current. There is, unfortunately, no satisfactory way of treating the former part. In this section, we shall first assume the exact additivity of nucleon moments in the deuteron and we, therefore, replace the self-meson terms in (10) and (13) by introducing the Pauli-term (5) or (17). Furthermore, in order to avoid the uncertainty in the knowledge of the meson theory of nuclear forces, we regard $c(\bar{p}_1\bar{p}_2)$ as the Fourier transform of the phenomenologically adjusted deuteron wave function. Then no infinities or ambiguities remain with respect to the exchange current contributions.

First of all, it is easily seen that the third terms in (14) and (15) (so-called meson contribution) vanish identically [1], because the factor $(\delta_{12}-\delta_{21})$ gives rise to the charge spin factor $\tau_1^{(1)}\tau_2^{(2)}-\tau_2^{(1)}\tau_1^{(2)}$, which will vanish identically in the deuteron ground state which belongs to a charge singlet state. Then only the recoil nucleons can contribute to the exchange current effect. Secondly, we shall approximate the energy denominator in (11) simply by $-\hbar c\,\omega_{\bar{k}}$, a consistent approximation as our previous ones (12) and (16) which were used to derive (11), (14) and (15). Then, it is more convenient to go over to the coordinate space, using

$$c(\bar{p}_1\bar{p}_2)=\frac{1}{(2\pi\hbar)^3}\int\!\!\int\psi(\bar{x}_1\bar{x}_2)\,e^{-\frac{i\,\bar{p}_1\bar{x}_1}{\hbar}}\,e^{-\frac{i\,\bar{p}_2\bar{x}_2}{\hbar}}\,d\bar{x}_1\,d\bar{x}_2\,, \tag{18}$$

$$c(\bar{p}_1\bar{p}_2\bar{k})=\frac{(\hbar)^{3/2}}{(2\pi\hbar)^{9/2}}\int\!\!\int\!\!\int\psi(\bar{x}_1\bar{x}_2\bar{x})\,e^{-\frac{i\,\bar{p}_1\bar{x}_1}{\hbar}}\,e^{-\frac{i\,\bar{p}_2\bar{x}_2}{\hbar}}\,e^{-i\bar{k}\bar{x}}\,d\bar{x}_1\,d\bar{x}_2\,d\bar{x}, \tag{19}$$

where $\psi(\bar{x}_1\bar{x}_2)$ is the deuteron wave function. The normalization integral (10) becomes

$$\langle\Psi|\Psi\rangle=\int\!\!\int|\psi(\bar{x}_1\bar{x}_2)|^2\,d\bar{x}_1\,d\bar{x}_2+\int\!\!\int\!\!\int|\psi(\bar{x}_1\bar{x}_2\bar{x})|^2\,d\bar{x}_1\,d\bar{x}_2\,d\bar{x} \tag{20}$$

and the expection values of Q and $\bar{\mu}$ (13) becomes

$$\begin{aligned}\langle\Psi|Q\text{ or }\bar{\mu}|\Psi\rangle=&\int\!\!\int\psi^*(\bar{x}_1\bar{x}_2)\,[Q\text{ or }\bar{\mu}]\,\psi(\bar{x}_1\bar{x}_2)\,d\bar{x}_1\,d\bar{x}_2+\\&+\int\!\!\int\!\!\int\psi(\bar{x}_1\bar{x}_2\bar{x})\,[Q\text{ or }\bar{\mu}]\,\psi(\bar{x}_1\bar{x}_2\bar{x})\,d\bar{x}_1\,d\bar{x}_2\,d\bar{x},\end{aligned} \tag{21}$$

where

$$Q=\frac{1+\tau_3^{(1)}}{2}\,(3\,z_1^2-r_1^2)+\text{term (2)}, \tag{22}$$

$$\bar{\mu}=\left[\mu_p\,\frac{1+\tau_3^{(1)}}{2}+\mu_N\,\frac{1-\tau_3^{(1)}}{2}\right]\bar{\sigma}^{(1)}-\frac{1+\tau_3^{(1)}}{2}\,i\left[\bar{x}_1\times\frac{\partial}{\partial\,\bar{x}_1}\right]+\text{term (2)}, \tag{23}$$

and

$$\psi(\bar{x}_1 \bar{x}_2 \bar{x}) = \frac{1}{(2\pi)^3} \int \frac{i f}{2 \hbar c \omega_{\bar{k}}} \sqrt{\frac{\hbar c}{2 \omega_{\bar{k}}}} [\tau_\alpha^{(1)} (\bar{\sigma}^{(1)} \bar{k}) e^{i \bar{k} (\bar{x} - \bar{x}_1)} + \\ + \tau_\alpha^{(2)} (\bar{\sigma}^{(2)} \cdot \bar{k}) e^{i \bar{k} (\bar{x} - \bar{x}_2)}] \psi(\bar{x}_1 \bar{x}_2) \, d\bar{k}, \tag{24}$$

and we have only to retain the cross terms of (1) and (2) in the second terms of (20) and (21). Remarking here again that $\psi(\bar{x}_1 \bar{x}_2)$ contains a charge singlet function, then we may rewrite (22) and (23) simply as

$$Q = \tfrac{1}{2} (3 z_1^2 - r_1^2 + 3 z_2^2 - r_2^2), \tag{25}$$

$$\bar{\mu} = (\mu_P + \mu_N) \tfrac{1}{2} (\bar{\sigma}^{(1)} + \bar{\sigma}^{(2)}) - \frac{i}{2} \left(\left[\bar{x}_1 \times \frac{\partial}{\partial \bar{x}_1} \right] + \left[\bar{x}_2 \times \frac{\partial}{\partial \bar{x}_2} \right] \right). \tag{26}$$

It is easily seen that, if we neglect the one meson amplitude $\psi(\bar{x}_1 \bar{x}_2 \bar{x})$ in (20) and (21), we then get the usual phenomenological expressions for deuteron moments:

$$\frac{\langle \Psi | Q | \Psi \rangle}{\langle \Psi | \Psi \rangle} = Q_{\text{phen.}} \equiv \frac{\sqrt{2}}{10} \int_0^\infty r^2 \left[u(r) \, w(r) - \frac{1}{2\sqrt{2}} w^2(r) \right] dr, \tag{27}$$

$$\frac{\langle \Psi | \mu_z | \Psi \rangle}{\langle \Psi | \Psi \rangle} = (\mu_D)_{\text{phen.}} \equiv (\mu_P + \mu_N) - \tfrac{3}{2} (\mu_P + \mu_N - \tfrac{1}{2}) \int_0^\infty w^2(r) \, dr, \tag{28}$$

where $u(r)$ and $w(r)$ are the S- and the D-deuteron wave functions which are normalized as $\int_0^\infty [u^2(r) + w^2(r)] \, dr = 1$. With using the normalized deuteron wave function as $\psi(\bar{x}_1 \bar{x}_2)$, we get from (20) and (21) as the total moments including the exchange current contribution

$$Q = \frac{Q_{\text{phen.}} + \Delta' Q}{1 + \Delta N}, \quad \mu_D = \frac{(\mu_D)_{\text{phen.}} + \Delta' \mu_D}{1 + \Delta N}, \tag{29}$$

where $\Delta' Q$, $\Delta' \mu_D$ and ΔN are the second terms of (21) and (20), respectively. Since these total moments must be compared with the empirical values of moments, we must subtract the following exchange current corrections ΔQ and $\Delta \mu_D$ from the measured values of Q and μ_D in order to get $Q_{\text{phen.}}$ and $(\mu_D)_{\text{phen.}}$ which can be used to determine the deuteron wave function with (27) and (28):

$$\Delta Q = \Delta' Q - Q_{\text{phen.}} \Delta N, \quad \Delta \mu_D = \Delta' \mu_D - (\mu_D)_{\text{phen.}} \Delta N, \tag{30}$$

where we get after a rather lengthy calculation

$$\Delta N = \alpha^2 \frac{2}{\pi} \left\{ \int\limits_0^\infty u^2(r) \left[K_0(x) - \frac{K_1(x)}{x} \right] dr + 4\sqrt{2} \int\limits_0^\infty u(r)\, w(r) \left[K_0(x) + \frac{2\, K_1(x)}{x} \right] dr - \right.$$

$$\left. - \int\limits_0^\infty w^2(r) \left[K_0(x) + \frac{5\, K_1(x)}{x} \right] dr \right\}, \tag{31}$$

$$\Delta' Q = \alpha^2 \frac{2}{\pi} \left\{ \tfrac{1}{5} \int\limits_0^\infty u^2(r) \left[K_0(x) + \frac{2\, K_1(x)}{x} \right] r^2\, dr - \frac{1}{5\sqrt{2}} \int\limits_0^\infty u(r)\, w(r) \, \times \right.$$

$$\left. \times \left[K_0(x) + \frac{5\, K_1(x)}{x} \right] r^2\, dr + \tfrac{1}{20} \int\limits_0^\infty w^2(r) \left[5\, K_0(x) + \frac{13\, K_1(x)}{x} \right] r^2\, dr, \right. \tag{32}$$

$$\Delta' \mu_D = \alpha^2 \frac{2}{\pi} (\mu_P + \mu_N) \left\{ \int\limits_0^\infty u^2(r) \left[K_0(x) - \frac{K_1(x)}{x} \right] dr + \sqrt{2} \int\limits_0^\infty u(r)\, w(r) \, \times \right.$$

$$\left. \times \left[K_0(x) + \frac{2\, K_1(x)}{x} \right] dr + \tfrac{1}{2} \int\limits_0^\infty w^2(r) \left[K_0(x) + \frac{5\, K_1(x)}{x} \right] dr + \right.$$

$$+ \alpha^2 \frac{2}{\pi} \left\{ \frac{3\sqrt{2}}{2} \int\limits_0^\infty u(r)\, w(r) \left[K_0(x) + \frac{2\, K_1(x)}{x} \right] dr - \right.$$

$$- \tfrac{3}{4} \int\limits_0^\infty w^2(r) \left[K_0(x) + \frac{5\, K_1(x)}{x} \right] dr, \tag{33}$$

where $\alpha^2 = (f^2/4\pi\hbar c)(\mu/2\varkappa)^2$; $x \equiv \mu r$ and $K_0(x)$ and $K_1(x)$ are the Hankel functions of an imaginary argument which have the properties

$$\frac{1}{4\pi} \int \frac{e^{i\,\bar{k}\cdot\bar{r}}}{\omega_k^3}\, d\bar{k} = K_0(\mu r) = K_0(x), \qquad \frac{d}{dx} K_0(x) = -K_1(x). \tag{34}$$

The expressions of ΔN and $\Delta' Q$ agree with those obtained by SESSLER [2]. It is remarked that all the integrals appearing in $\Delta' \mu_D$ are the same as those in ΔN, which simplifies the further calculation very much and at the same time enables us to get a rather definite estimate of $\Delta \mu_D$ (but not of ΔQ), as will be seen later. The value of ΔN will be shown to be actually small enough to guarantee the Taylor expansion in (29) to get (30). However, its effect is very important, although it has been neglected thus far [3, 4], since the second terms of (30) will be shown to be comparable with their first terms, as was shown by SESSLER [2] in the case of the quadrupole moment. The term containing the factor $(\mu_P + \mu_N)$ in $\Delta' \mu_D$ is due to the intrinsic magnetic moments of recoil nucleons which does not vanish even in the spherical symmetrical case ($w(r)=0$) because of the lack of the symmetry with respect to the intrinsic magnetic moments of two nucleons. The remaining term of $\Delta' \mu_D$ is due to the orbital motion of recoil nucleons, which vanishes in the pure S-state. On the other hand, $\Delta' Q$ does not vanish even when $w(r)=0$, since the meson emission depends upon the spin direction of the nucleon, which destroys the spherical symmetry in the one-meson amplitude.

IV. Non-additivity correction

Now let us consider the self-meson effect contained in the second terms of (10) and (13) and neglect the exchange term entirely for the sake of simplicity. It is easy to get the following expression for the expectation value of $\bar{\mu}$ with retaining the self-meson terms only:

$$\frac{\langle \Psi | \bar{\mu} | \Psi \rangle}{\langle \Psi | \Psi \rangle} = \frac{\iint c^* (\bar{p}_1 \bar{p}_2) [\bar{A}_1 + \bar{A}_2 + \bar{B}_1 + \bar{B}_2 + \bar{A}_1 n_2 + \bar{A}_2 n_1] c (\bar{p}_1 \bar{p}_2) \, d\bar{p}_1 \, d\bar{p}_2}{\iint c^* (\bar{p}_1 \bar{p}_2) [1 + n_1 + n_2] c (\bar{p}_1 \bar{p}_2) \, d\bar{p}_1 \, d\bar{p}_2}, \tag{35}$$

where

$$n_1 = \frac{1}{(2\pi)^3} \int \left(\frac{1}{E - (E_{\bar{p}_1 - \hbar \bar{k}} + E_{\bar{p}_2} + \hbar c \, \omega_{\bar{k}})} \right)^2 \frac{3 \hbar c}{2 \omega_{\bar{k}}} \left(\frac{f}{2 \varkappa} \right)^2 k^2 \, d\bar{k}, \tag{36}$$

$$\bar{A}_1 = \frac{1 + \tau_3^{(1)}}{2} \left\{ \bar{\sigma}^{(1)} - i \left[\bar{p}_1 \times \frac{\partial}{\partial \bar{p}_1} \right] \right\}, \tag{37}$$

$$\bar{B}_1 = \frac{1}{(2\pi)^3} \int \left[\frac{1}{E - (E_{\bar{p}_1 - \hbar \bar{k}} + E_{\bar{p}_2} + \hbar c \, \omega_{\bar{k}})} \right]^2 \frac{\hbar c}{2 \omega_{\bar{k}}} \left(\frac{f}{2 \varkappa} \right)^2 \times$$
$$\times \left[\frac{3 - \tau_3^{(1)}}{2} k^2 \left\{ -\tfrac{1}{3} \bar{\sigma}^{(1)} - i \left[(\bar{p}_1 - \hbar \bar{k}) \times \frac{\partial}{\partial (\bar{p}_1 - \hbar \bar{k})} \right] \right\} + \tfrac{4}{3} \tau_3^{(1)} k^2 \sigma^{(1)} \frac{\varkappa}{\omega_{\bar{k}}} \right] d\bar{k}, \tag{38}$$

and the corresponding expressions for n_2, $\bar{A}_2$ and $\bar{B}_2$, assuming naturally some cut-off procedure in the divergent integrals. If, on the other hand, we start from the one nucleon problem, we get

$$\frac{\langle \Psi | \bar{\mu} | \Psi \rangle_1}{\langle \Psi | \Psi \rangle_1} = \frac{\int c^* (\bar{p}_1) [\bar{A}_1 + \bar{B}_1'] c (\bar{p}_1) \, d\bar{p}_1}{\int c^* (\bar{p}_1) [1 + n_1'] c (\bar{p}_1) \, d\bar{p}_1}, \tag{39}$$

where we put the index 1 in order to stress that this is a single nucleon quantity and n_1' and $\bar{B}_1'$ can be obtained from n_1 and $\bar{B}_1$ simply by replacing the energy denominators by $E_1 - (E_{\bar{p}_1 - \hbar \bar{k}} + \hbar c \, \omega_{\bar{k}})$. Here it is clear that n's determine the relative probability of finding one meson to the one of finding no meson and $\bar{A}$'s and $\bar{B}$'s represent the normal and the anomalous parts of the magnetic moment of the nucleon.

If we make the same approximation as before with respect to the energy denominator, namely the replacement of all the energy denominators by $-\hbar c \omega_{\bar{k}}$, then $n_1 = n_1' \equiv n_1''$ and $\bar{B}_1 = B_1' \equiv \bar{B}_1''$ and we can easily show that

$$\frac{\langle \Psi | \bar{\mu} | \Psi \rangle_1}{\langle \Psi | \Psi \rangle_1} + \frac{\langle \Psi | \bar{\mu} | \Psi \rangle_2}{\langle \Psi | \Psi \rangle_2} =$$

$$= \frac{\iint c^* (\bar{p}_1) \, c^* (\bar{p}_2) \, [\bar{A}_1 + \bar{A}_2 + \bar{B}_1'' + \bar{B}_2'' + \bar{A}_1 n_2'' \, \bar{A}_2 n_1''] \, c (\bar{p}_1) \, c (\bar{p}_2) \, d \bar{p}_1 \, d \bar{p}_2}{\iint c^* (\bar{p}_1) \, c^* (\bar{p}_2) \, [1 + n_1'' + n_2''] \, c (\bar{p}_1) \, c (\bar{p}_2) \, d \bar{p}_1 \, d \bar{p}_2}, \tag{40}$$

neglecting the terms corresponding to the higher order processes. The only difference between (40) and (35) with double dashes is the one between $c(\bar{p}_1) \, c(\bar{p}_2)$ and $c(\bar{p}_1 \bar{p}_2)$, which means that the only remaining difference is due to the purely kinematical motions of nucleons in the deuteron ground state, which will be considered separately in the following section. Thus it can be concluded that we may assume the exact additivity of nucleon moments in the approximations we were concerned with in the previous section.

It is very difficult to proceed in the multi-meson effects and draw out the unambiguous results. We may, however, expect that the multi-meson effects are certainly important to the individual moments of nucleons, but would not contribute to the non-additivity so much since the deuteron is a loosely bound system.

Thus we shall confine ourselves only to the one-meson exchange process and look for another effect which gives rise to the non-additivity. Neglecting the purely kinematical effect, the only difference of the energy denominators in the deuteron moment (35) and in the individual moments (39) is the appearance of the deuteron binding energy W in the former. Then we may expand the energy denominator of the former as follows:

$$\frac{1}{E - (E_{\bar{p}_1 - \hbar \bar{k}} + E_{\bar{p}_2} + \hbar c \omega_k)} = \frac{1}{E_1 - (E_{\bar{p}_1 - \hbar \bar{k}} + \hbar c \omega_k)} + \frac{W}{[E_1 - (E_{p_1 - \hbar k} + \hbar c \omega_k)]^2}. \tag{41}$$

If we make the same approximation as before after the above expansion, we get

$$\frac{\langle \Psi | \bar{\mu} | \Psi \rangle}{\langle \Psi | \Psi \rangle} = \tag{42}$$

$$= \frac{\iint c^* (\bar{p}_1 \bar{p}_2) \, [(1 + n)(\bar{A}_1 + \bar{A}_2) + (\bar{B}_1 + \bar{B}_2) + \Delta n (\bar{A}_1 + \bar{A}_2) + \Delta \bar{B}_1 + \Delta \bar{B}_2] \, C (\bar{p}_1 \bar{p}_2) \, d \bar{p}_1 \, d \bar{p}_2}{\iint c^* (\bar{p}_1 \bar{p}_2) \, [1 + 2n + 2 \Delta n] \, C (\bar{p}_1 \bar{p}_2) \, d \bar{p}_1 \, d \bar{p}_2},$$

which gives

$$\Delta \mu_D = (\mu_P + \mu_N) \left[\frac{\Delta n \, (A_1 + A_2) + \Delta B_1 + \Delta B_2}{(1 + n)(A_1 + A_2) + (B_1 + B_2)} - \frac{2 \Delta n}{1 + 2n} \right] \tag{43}$$

as the non-additivity correction to the deuteron magnetic moment. In (43) we have replaced the expression obtained from (42) by putting all the Δ-terms zero by $(\mu_P + \mu_N)$, although our simple theory cannot naturally predict it and we have omitted all the double primes for simplicity. If we use the equality $A_1 + A_2 = 1$ and $B_1 + B_2 = -\frac{1}{3} n$ and $\Delta B_1 + \Delta B_2 = -\frac{1}{3} \Delta n$, which are easily shown from their definitions (36), (37) and (38), we get finally

$$\Delta \mu_D = (\mu_P + \mu_N) \left[\frac{(2/3) \Delta n}{1 + (2/3) n} - \frac{2 \Delta n}{1 + 2 n} \right], \tag{44}$$

where

$$\begin{gathered} n = \alpha^2 \frac{3}{\pi} \int\limits_0 \frac{k^4}{\omega^3_{\bar{k}}} \frac{d k}{\mu^2}, \\ \Delta n = -\left(\frac{2 W}{\hbar c \mu} \right) \alpha^2 \frac{3}{\pi} \int\limits_0 \frac{k^4}{\omega^4_{\bar{k}}} \frac{d k}{\mu}, \end{gathered} \tag{45}$$

which are necessary to be cut off arbitrarily at some value of k, which must naturally be smaller than $\varkappa$ for the internal consistency of the present investigation. Anyway it is important to remark that this correction $\Delta \mu_D$ is definitely positive.

V. Relativistic correction

Finally we shall consider the purely kinematical relativistic correction to the deuteron magnetic moment. This effect, together with the previous one, is rather difficult to estimate, because we do not know exactly the correct relativistic form of the two-nucleon interaction. Thus we are satisfied with the simple repetition of the old investigations by SACHS [5] and BREIT and others [6] in order to get the order of magnitude of this effect, because the pseudoscalar case has never been considered by these authors, although their methods are not quite satisfactory, for example, the basic equation (46) is not Lorentz invariant.

Our basic equation is

$$(-W + 2 M c^2) \varphi = \left[\sum_{i=1}^{2} (c \bar{\alpha}^{(i)} \bar{p}_i + \beta^{(i)} M c^2) - \bar{\mu} \cdot \bar{H} + V \right] \varphi, \tag{46}$$

where

$$\bar{\mu} = \sum_{i=1}^{2} \left\{ \frac{e}{2 \varkappa} \left[(\mu_P - 1) \frac{1 + \tau_3^{(i)}}{2} + \mu_N \frac{1 - \tau_3^{(i)}}{2} \right] \beta^{(i)} \bar{\sigma}^{(i)} + \frac{e}{2} \frac{1 + \tau_3^{(i)}}{2} [\bar{r}_i \times \bar{\alpha}^{(i)}] \right\} \tag{47}$$

and W is the binding energy of the deuteron and V is the static nuclear potential. This equation can be considered as the ordinary configuration space representation of our original Schrödinger equation using the relativistic Hamiltonian (1), where meson field quantities are, in order to discuss only the purely kinematical effect, replaced by the static nuclear potential V and the Pauli-term (5), since the non-additivity effect and the exchange current effect may now be neglected for the time being.

Here the most important point is that V can be considered to contain no β-factors, since in the approximation of one meson exchange the *ps–ps* theory is equivalent to the ps–pv theory, which gives no such factors, while the characteristic pair term can be considered to be damped almost entirely, although the latter term certainly gives rise to such factors in the static nuclear potential.

Now we decompose φ into four 4-component functions φ_1, φ_2, φ_3 and φ_4: φ_1 is the largest one, φ_2 is the small component with respect to the first particle, φ_3 is also the small one with respect to the second particle and φ_4 is the small one with respect to both particles. Then the coupled equations for φ_i's are

$$\begin{aligned} -(W+V)\,\varphi_1 &= (c\,\bar{\sigma}^{(1)}\,\bar{p}_1)\,\varphi_2 + (c\,\bar{\sigma}^{(2)}\,\bar{p}_2)\,\varphi_3\,, \\ [2\,M\,c^2-(W+V)]\,\varphi_2 &= (c\,\bar{\sigma}^{(1)}\,\bar{p}_1)\,\varphi_1 + (c\,\bar{\sigma}^{(2)}\,\bar{p}_2)\,\varphi_4\,, \\ [2\,M\,c^2-(W+V)]\,\varphi_3 &= (c\,\bar{\sigma}^{(1)}\,\bar{p}_1)\,\varphi_4 + (c\,\bar{\sigma}^{(2)}\,\bar{p}_2)\,\varphi_1\,, \\ [4\,M\,c^2-(W+V)]\,\varphi_4 &= (c\,\bar{\sigma}^{(1)}\,\bar{p}_1)\,\varphi_3 + (c\,\bar{\sigma}^{(2)}\,\bar{p}_2)\,\varphi_2\,, \end{aligned} \tag{48}$$

which give to the required order of approximation the following solutions:

$$\begin{aligned} \varphi_4 &= \frac{1}{(2\,M\,c^2)^2}\,(c\,\bar{\sigma}^{(1)}\,\bar{p}_1)\,(c\,\bar{\sigma}^{(2)}\,\bar{p}_2)\,\varphi_1\,, \\ \varphi_2 &= \frac{1}{2\,M\,c^2}\left[1+\frac{W+V}{2\,M\,c^2}+\frac{(c\,\bar{p}_2)^2}{(2\,M\,c^2)^2}\right](c\,\bar{\sigma}^{(1)}\,\bar{p}_1)\,\varphi_1\,, \\ \varphi_3 &= \frac{1}{2\,M\,c^2}\left[1+\frac{W+V}{2\,M\,c^2}+\frac{(c\,\bar{p}_1)^2}{(2\,M\,c^2)^2}\right](c\,\bar{\sigma}^{(2)}\,\bar{p}_2)\,\varphi_1\,. \end{aligned} \tag{49}$$

Then the deuteron magnetic moment, which is given by $(\varphi\,|\,\bar{\mu}\,|\,\varphi)/(\varphi\,|\,\varphi)$, can be written using the solution (49) as the expectation value of the following operator with respect to the largest component φ_1, which is just the ordinary normalized deuteron wave function:

$$\begin{aligned} &(\mu_P+\mu_N)\,\frac{\bar{\sigma}^{(1)}+\bar{\sigma}^{(2)}}{2}+\tfrac{1}{2}\,\bar{L}-(\mu_P-1+\mu_N)\,\frac{\bar{p}}{2\,M^2\,c^2}\left(\bar{p}\cdot\frac{\bar{\sigma}^{(1)}+\bar{\sigma}^{(2)}}{2}\right)+ \\ &\quad+\frac{W+V}{2\,M\,c^2}\left(\frac{\bar{\sigma}^{(1)}+\bar{\sigma}^{(2)}}{2}+\tfrac{1}{2}\,\bar{L}\right)+\frac{r\,V'}{8\,M\,c^2}\left[\frac{\bar{\sigma}^{(1)}+\bar{\sigma}^{(2)}}{2}-\frac{\bar{r}}{r^2}\left(\bar{r}\cdot\frac{\bar{\sigma}^{(1)}+\bar{\sigma}^{(2)}}{2}\right)\right], \end{aligned} \tag{50}$$

where $\bar{r}$, $\bar{p}$ and $\bar{L}$ are the relative coordinate, momentum and orbital angular momentum operators, respectively, and we have assumed that V is a function of r only, V' being the derivative of V with respect to r.

The first two terms in (50) give the phenomenological expression (28). The remaining terms are the required terms giving rise to the relativistic correction. Because there are rather many ambiguities in making the expectation value of these terms especially because the nuclear potential appears explicitly, we shall be satisfied with the central force case only. It can easily be seen that the admixture of a D-state would be a minor effect, whose magnitude would be the same order as the ambiguity in the static nuclear potential V. Then the relativistic correction becomes

$$\Delta \mu_D = -\tfrac{1}{6}(\mu_P + \mu_N + 1)\frac{\langle T \rangle}{Mc^2}, \tag{51}$$

using $\langle r V' \rangle = \langle 2T \rangle$ which can be shown by using the Schrödinger equation, where T is the relative kinetic energy and the bracket means the expectation value in the deuteron ground state. The relativistic correction is negative according to (51).

VI. Discussion and numerical results

Before entering into the numerical details, we shall compare our results obtained above with those obtained by the previous authors cited before.

As regards the exchange current effect, the extremely large results obtained by VILLARS [3] and DESER [4] are apparently due to having mixed up the unphysical and unpermissible divergences which may occur frequently in the present field theoretical calculations and must, therefore, be avoided carefully in order to retain the real physical effects only. Also they did not take account of the change of the normalization, the effect of which is very important quantitatively and will act as reducing the estimated corrections very much, as is seen from (30). On the other hand, the investigation by SESSLER [2], whose results are just the same as ours for the electric quadrupole moment, is lacking a little in its rigorousness and is too simple to be extended to the case of the magnetic moment. As for the multi-meson exchange effects which were neglected in our investigations, it may well be hoped that these would not affect the final results so much because the deuteron is a loosely bound system and the two nucleons are interacting rather apart from each other. The big value estimated by SESSLER [2] for this effect need not to be taken seriously, since he has not taken account of the pair damping effect.

With respect to the non-additivity correction, MIYAZAWA [1] calculated this effect together with the exchange current effect. His calculation is much more rough than ours with respect to the latter effect. As for the former part, his treatment of the nuclear force is basically different from ours. He also neglects the change of the normalization.

With respect to the kinematical relativistic effect, we employed simply the same procedure as was used by previous authors, simply because there are no other satisfactory ways to attack this problem. SACHS [5], for example, has got a similar result as ours (50) assuming the scalar meson field. In his case, however, owing to the appearance of the β-factor in the static nuclear potential, his result is just the one which can be obtained from (50) by replacing V by $-V$. The terms containing V are, however, the largest ones in the relativistic correction and so SACHS' result is just opposite in sign and is almost the same in magnitude as ours.

As regards the numerical values of our theoretical corrections, the non-additivity one (44) depends upon both the coupling constant $f^2/4\pi\hbar c$ and the

Table 1. The non-additivity correction to the deuteron magnetic moment $\Delta\mu_D/\mu_D$ for various values of the *ps–ps* coupling constant $f^2/4\pi\hbar c$ and the cut-off momentum $k_{\max}$.

	$f^2/4\pi\hbar c=10$	$f^2/4\pi\hbar c=15$
$k_{\max}=3\,\mu$	0.20 %	0.26 %
$k_{\max}=4\,\mu$	0.25 %	0.28 %
$k_{\max}=5\,\mu$	0.25 %	0.26 %

cut-off momentum $k_{\max}$. The values of $\Delta\mu_D/\mu_D$, μ_D being the observed deuteron moment, are listed in Table 1 for various values of these parameters. From this table we can take as the reasonable estimate for the non-additivity correction

$$\Delta\mu_D/\mu_D=+0.26\ \%. \tag{52}$$

With respect to the relativistic correction (51), we shall further restrict ourselves to the square well potential. Then we can derive the formula

$$\langle T\rangle=(V_0-W)\frac{r_0\alpha}{1+r_0\alpha}, \tag{53}$$

where V_0 and r_0 are the depth and the range of the square well potential and α is given by $\sqrt{MW}/\hbar$. In order to fit the low energy data, we may take $r_0=2.04\times10^{-13}$ cm and $V_0=35.39$ Mev,[1] which together with the value $W=2.226$ Mev, gives

$$\Delta\mu_D/\mu_D=-0.41\ \% \tag{54}$$

as the relativistic correction. It is seen that the above two effects are rather small in magnitude and fortunately they cancel out with each other almost entirely.

As regards the exchange current correction, our results (31) and (32) are just the same as those by SESSLER [2] and $\Delta'\mu$ contain only the same types of integral as those in ΔN. Thus we can readily get the numerical values simply by using the results of the numerical integration by SESSLER [2] whose values are contained in Table I in his original paper [2]. It is remarked here that $\Delta'\mu_D$ and ΔN (not $\Delta' Q$) are very sensitive to the *D*-state probability (P_D) to which $u(r)$ and $w(r)$ are fitted since the *S–D* mixed terms in $\Delta'\mu_D$ and ΔN are the major ones and these are solely dependent upon the inner behaviour of

---

[1] These values are due to the unpublished analysis, which will be contained in the article "Two-Nucleon Problem" in the new edition of the *Handbuch der Physik* by L. HULTHÉN and M. SUGAWARA.

Table 2. The exchange current correction to the deuteron moments for $f^2/4\pi\hbar c = 10$.

	$P_D = 3$ %		$P_D = 3.9$ %		Sessler's case ($P_D \approx 6$ %)	
	$n=3$	$n=4$	$n=3$	$n=4$	no hard core	with hard core
$\frac{\Delta \mu_D}{\mu_D}$	−0.91 %	−0.85 %	−1.24 %	−1.07 %	−0.88 %	−1.11 %
$\frac{\Delta Q}{Q}$	+1.96 %	+2.38 %	+0.57 %	+1.24 %	+3.08 %	−0.71 %

the deuteron wave function.[1] In order to know the effect of changing P_D, we have first assumed the analytic forms, dropping the normalization factor,

$$u(r) = \cos \varepsilon \; (1 - e^{-\beta r})\, e^{-\alpha r}, \quad w(r) = \sin \varepsilon \; (1 - e^{-\gamma r})^n\, e^{-\alpha r}/r, \tag{55}$$

where α is fixed by the binding energy and n is chosen as 3 or 4, of which $n=3$ corresponds to $r^{\ 1}$ dependence of the nuclear potential at the origin and $n=4$ to r^0 dependence. The above form of $w(r)$ does not satisfy the correct asymptotic behaviour but is one of the simplest forms which can approximate the correct asymptotic behaviour. In order only to simplify the calculation very much we have assumed the above form. The other three parameters ε, β and γ are then determined by the empirical values of the quadrupole moment and the deuteron effective range and the specified value of P_D, which we have assumed as 3.9 % and 3 %, since the present investigation will predict a value of about 3 % for P_D. Another point to be noted here is that the infinity of the integrand ($K_0(x)$ and $K_1(x)$) at $r=0$ is due to having carried out the integration over k up to infinity in (34). In order that our investigation be consistent, this integral must be cut off at least at $\varkappa$, which then gives a finite value to that integral at $r=0$. We have employed the straight cut-off method for K_0 and K_1/x at $r = \pi/\varkappa$ or the first zero point of $\sin kr/kr$ for $k=\varkappa$. The effect of this cut-off is large only in the first term in ΔN or $\Delta' \mu_D$, which gives rise to a very small effect upon $\Delta \mu_D$ owing to the almost perfect cancellation of that term in $\Delta \mu_D'$ and ΔN, while ΔQ is much influenced since $\Delta Q'$ is insensitive to such a detail near the origin and only ΔN is strongly affected. Generally speaking, $\Delta' Q$ is quite insensitive to the inner detail of the wave function, while $\Delta' \mu_D$ and ΔN are sensitive to it, the result being that ΔQ is sensitive to that inner detail but $\Delta \mu_D$ is rather insensitive to it. Remarking that the outer behaviour of the deuteron wave function is known very well and its many ambiguities lie in its inner behaviour, we can conclude that the estimation of ΔQ is much more ambiguous than that of $\Delta \mu_D$. The results of calculations are listed in Table 2, where those values obtained by using Sessler's values are also included and $f^2/4\pi\hbar c$ is put equal to 10.

---

[1] According to the private communication from Dr. SESSLER, his wave functions are adjusted to $P_D \approx 6$ %. The effect of changing P_D upon the deuteron wave function mainly consists in changing $w(r)$ (not $u(r)$) only at very small distances, from where comes the main contribution to $\Delta' \mu_D$ and ΔN. ΔQ is, on the other hand, an "outside" quantity and is almost intensitive to such a detail near the origin.

Let us first consider $\Delta \mu_D$. It is first noted from Table 2 that $\Delta \mu_D$ is always negative, which can also be inferred directly from the analytic expressions (31) and (33) by remarking that the S–D mixed terms are the major ones. It must be stressed here that this negative character is definite and is due to the effect of the change of the normalization ΔN in (30), since both $\Delta' \mu_D$ and ΔN are positive; this shows how the effect of ΔN is large quantitatively. By comparing the two cases in Sessler's case, the effect of a hard core is not so large to $\Delta \mu_D$. On the other hand, a nice agreement of our values for $P_D = 3$ % and those in Sessler's case seems to be inconsistent with the big effect of changing P_D upon $\Delta \mu_D$ which can be seen from comparing our two cases for $P_D = 3$ % and 3.9 %. This is, however, due to the different forms of the deuteron wave functions and shows how these have a large effect upon $\Delta \mu_D$. As our present investigation predicts $P_D \approx 3$ %, we may take as a reasonable estimate for the exchange current correction

$$\Delta \mu_D/\mu_D = -0.85\ \%, \tag{56}$$

which may rather give a reasonable upper limit (in magnitude) for this correction.

With respect to ΔQ, Sessler's case without hard core cannot be trusted, since he has not introduced the cut-off procedure and so his value is certainly overestimated. Our four cases show that ΔQ is very sensitive to P_D or the inner behaviour of $w(r)$. Thus, considering many ambiguities, we may estimate as, Q being the empirical value of the quadrupole moment,

$$\Delta Q/Q = 2\ \% \sim 0 \tag{57}$$

or even a small negative value, as is suggested by Sessler's case, although his values may be somewhat overestimated. It must also be remarked here that the effect of ΔN is again very important in this case, since the individual terms $\Delta' Q$ and $Q_{\text{phen.}} \Delta N$ are from two up to seven times larger than ΔQ; thus the change of the normalization ΔN reduces the correction very much.

The over all correction to μ_D is then from (52), (54) and (56)

$$\Delta \mu_D/\mu_D = -1.0 \pm 0.3\ \%, \tag{58}$$

where the error has been estimated somewhat arbitrarily. We may say that this value is rather free from ambiguities since the non-additivity and the relativistic corrections are minor ones and cancel out, while the exchange current effect is rather unambiguous. This correction then determines P_D as 2.4 % ±0.5 %. Since the exchange current correction seems to be overestimated, we get as a final estimate

$$P_D = 3\ \% \pm 1\ \%, \tag{59}$$

including the over all ambiguities. Two important conclusions are: (i) The present investigation predicts rather definitely a negative value for $\Delta \mu_D$, or the reduction of P_D from its phenomenological value 3.9 %. (ii) The correction does not seem so large as has been predicted thus far; the final estimate of P_D is at most 1 % reduction from its phenomenological value 3.9 %, namely 3 % ±1 %.

Although the ambiguity of ΔQ is rather large, its effect upon the phenomenological deuteron problem is much smaller than that due to the smaller ambiguity of $\Delta \mu_D$. The quadrupole moment is still a much more well-defined quantity than the *D*-state probability, although the present investigation has given it a rather narrow range than thus far expected.

The author should like to express his gratitude to Professor LAMEK HULTHÉN for his hospitality and to Mr. Z. SAWA for helping him in the numerical work.

Dept. of Mathematical Physics, Royal Institute of Technology, Stockholm, Sweden.

REFERENCES

1. H. MIYAZAWA, Prog. theor. Phys. *7*, 207 (1952).
2. A. M. SESSLER, Phys. Rev. *96*, 793 (1954).
3. F. VILLARS, Phys. Rev. *86*, 476 (1952).
4. S. DESER, Phys. Rev. *92*, 1542 (1953).
5. R. G. SACHS, Phys. Rev. *72*, 91 (1947).
6. G. BREIT and I. BLOCH, Phys. Rev. *72*, 135 (1947).
   G. BREIT and R. M. THALER, Phys. Rev. *89*, 1177 (1953).

Tryckt den 29 oktober 1955

Uppsala 1955. Almqvist & Wiksells Boktryckeri AB

ARKIV FÖR FYSIK Band 10 nr 12

Communicated 1 June 1955 by I. WALLER and O. H. FAXÉN

A theoretical study of the time energy distribution of slowed-down neutrons

By OLOF OLSSON

With 3 figures in the text

Introduction

We consider the time energy distribution of neutrons slowed-down by elastic impacts against free atoms at rest. Capture is neglected. The scattering of the neutrons is assumed to be isotropic in the center-of-mass system.

The validity of our considerations is thus confined to neutron energies lying approximately in the range between 1 ev and 10 Mev.

The theoretical background of this paper may be found in papers of WALLER[1] and in the review article of MARSHAK.[2] For the experimental side of the problem we refer to a paper of VON DARDEL.[3]

Integro-differential equation of the problem

Laplace transformation in time

At the time $t=0$ a pulse of neutrons with definite energy E_0 enters the moderator, which is assumed to be infinite, homogeneous and isotropic. We suppose the total number of neutrons to be 1 (unit source).

We introduce the following notation:

M = mass of a moderator atom, measured in units of the neutron mass;

E = energy of a neutron;

$u = \log (E_0/E) =$ logarithmic energy variable;

v = velocity of a neutron;

l = scattering mean free path of a neutron;

$\nu = v/l$;

$N(u, t)$ = number of neutrons in unit intervals at u and t;

---

[1] I. WALLER, Ark. Mat. Astr. Fys. *34* A; nr 3, 4, 5 (1946).

[2] R. E. MARSHAK, Rev. Mod. Phys. *19*, 185 (1947).

[3] G. F. VON DARDEL, Phys. Rev. *94*, 1272 (1954).

$\Psi(u, t) = \nu N(u, t) =$ the collision number;

$\alpha = (M+1)^2/4M$;

$q_M = 2 \log \frac{M+1}{M-1}$.

We now get:[1]

$$\frac{1}{\nu}\frac{\partial \Psi(u,t)}{\partial t} = -\Psi(u,t) + \alpha \int\limits_{\mathrm{Max}\,(u-q_M;\,0)}^{u} du'\,\Psi(u',t)\,e^{-(u-u')} + \delta(u)\,\delta(t). \tag{1}$$

We take the Laplace transform of (1) with respect to t and obtain:

$$(1+s/\nu)\,\Phi(u,s) = \alpha \int\limits_{\mathrm{Max}\,(u-q_M;\,0)}^{u} du'\,\Phi(u',s)\,e^{-(u-u')} + \delta(u), \tag{2}$$

where $\Phi(u,s) = \int\limits_0^\infty dt\,e^{-st}\,\Psi(u,t)$.

Outline of the work appearing in the following sections

We shall next take the Laplace transform of (2) with respect to u. Now (2) contains $\nu = v/l$, and l is a function of u that may be quite involved. In this paper we consider only two special cases:

I. l is proportional to v; i.e. ν is constant;

II. l is constant.

These two cases should be of importance if one tries to construct the solution for a general function l. For a rough estimate one may even directly use the formulas, derived in these two cases, by taking average values for ν or l.

In case I ORNSTEIN and UHLENBECK[2] have solved the problem for a hydrogen moderator ($M = 1$). We shall extend the result by getting an asymptotic solution, valid for large u and arbitrary M. The solution is obtained by means of the saddle point method.[3]

Case II has been treated by ORNSTEIN and UHLENBECK[4] for $M = 1$; here the exact solution is easily obtained. For other values of M, MARSHAK[5] gets an asymptotic solution, valid for large u, by means of the method of moments. Here we shall discuss an exact solution for arbitrary M in the form of a series, giving some insight into the statistical structure of the distribution function; but we have not succeeded in deriving the asymptotic expression for large u from our series.

---

[1] Cf. MARSHAK, l.c., eq. (11), (12).

[2] L. S. ORNSTEIN and G. E. UHLENBECK, Physica *4*, 478 (1937). Cf. MARSHAK, l.c., p. 195.

[3] The observation that this case can be treated by means of the saddle point method is due to Professor WALLER.

[4] ORNSTEIN and UHLENBECK, l.c. These authors actually give a solution for $M = 1$ and an arbitrary function l.

[5] MARSHAK l.c.

I. The scattering mean free path is proportional to the velocity

Laplace transformation in u. Laplace inversion

In this case $\nu = v/l$ is constant, and the Laplace transform of (2) with respect to u is:

$$(1+s/\nu)\,\chi(\eta,s) = \alpha\,\frac{1-e^{-(\eta+1)q_M}}{\eta+1}\,\chi(\eta,s)+1, \tag{3}$$

where $\chi(\eta,s) = \int_0^\infty d\,u\,e^{-\eta u}\,\Phi(u,s)$.

(3) gives:

$$\chi(\eta,s) = \frac{\nu}{s+\nu\left[1-\alpha\,\dfrac{1-e^{-(\eta+1)q_M}}{\eta+1}\right]}. \tag{4}$$

We now obtain the solution of our problem as the Laplace inverse of χ with respect to s and η:

$$\Psi(u,t) = \frac{1}{2\pi i}\int_{\eta_1-i\infty}^{\eta_1+i\infty} d\,\eta\,e^{\eta u}\,\frac{1}{2\pi i}\int_{s_1-i\infty}^{s_1+i\infty} d\,s\,e^{st}\,\chi(\eta,s). \tag{5}$$

The integration in s is immediate according to the calculus of residues and we get:

$$\Psi(u,t) = \nu\,e^{-\nu t}\,\frac{1}{2\pi i}\int_{\eta_1-i\infty}^{\eta_1+i\infty} d\,\eta\,\exp\left[\eta\,u+\nu\,t\,\alpha\,\frac{1-e^{-(\eta+1)q_M}}{\eta+1}\right]. \tag{6}$$

Sometimes it is convenient to subtract the delta function part corresponding to unscattered neutrons.

$$\Psi_\delta(u,t) = \nu\,e^{-\nu t}\,\delta(u);$$

$$\Phi_\delta(u,s) = \frac{\nu}{s+\nu}\,\delta(u); \tag{7}$$

$$\chi_\delta(\eta,s) = \frac{\nu}{s+\nu}.$$

We indicate by index 1 that the delta function part has been subtracted, e.g.

$$\Psi_1 = \Psi - \Psi_\delta.$$

According to (4), (5), (7) we may write:

$$\Psi_1(u,t) = \nu\,e^{-\nu t}\,\frac{1}{2\pi i}\int_{\eta_1-i\infty}^{\eta_1+i\infty} d\,\eta\,e^{\eta u}\left\{\exp\left[\nu\,t\,\alpha\,\frac{1-e^{-(\eta+1)q_M}}{\eta+1}\right]-1\right\}. \tag{6'}$$

Hydrogen moderator

We first consider the special case $M=1$. Then: $\alpha=1$, $q_M=\infty$.

(6) now becomes:

$$\Psi_1(u,t) = \nu e^{-\nu t}\frac{1}{2\pi i}\int_{\eta_1-i\infty}^{\eta_1+i\infty} d\eta\, e^{\eta u}\left[e^{\nu t/(\eta+1)}-1\right].$$

The integrand of Ψ_1 vanishes exponentially, when Re η (= the real part of η) $\rightarrow -\infty$, and vanishes as $1/\eta$, when Re η is finite and $|\eta|\rightarrow\infty$. Therefore we may close the integration path with an infinite semicircle to the left in the η-plane. The closed path may then be replaced by any closed path L_η around $\eta=-1$.

We may now write:

$$\Psi_1(u,t)=\nu e^{-\nu t}\frac{1}{2\pi i}\int_{L_\eta} d\eta\, e^{\eta u}\left[e^{\nu t/(\eta+1)}-1\right]=\nu e^{-\nu t}\frac{1}{2\pi i}\int_{L_\eta} d\eta\, e^{\eta u+\nu t/(\eta+1)}.$$

Making the substitution $\eta+1=y$, we get:

$$\Psi_1(u,t)=\nu e^{-\nu t-u}\frac{1}{2\pi i}\int_{L_y} dy\, e^{yu+\nu t/y},$$

where L_y is any closed path around $y=0$.

We now write the exponent of the integrand:

$$yu+\nu t/y = i\sqrt{\nu t u}\,(z-1/z),\ \text{with}\ z=y\frac{1}{i}\sqrt{u/\nu t}.$$

Substituting z for y, we find:

$$\Psi_1(u,t)=\nu e^{-\nu t-u}\sqrt{\nu t/u}\, i\cdot\frac{1}{2\pi i}\int_{L_z} dz\, e^{\frac{1}{2}2i\sqrt{\nu t u}\,(z-1/z)}. \tag{8}$$

L_z is any closed path around $z=0$.

The right hand side of (8) contains an integral representation of the Bessel function J_{-1}.[1]

(8) gives:

$$\Psi_1(u,t)=-\nu e^{-\nu t-u}\sqrt{\nu t/u}\, i\, J_1(2i\sqrt{\nu t u}). \tag{9}$$

---

[1] Cf. COURANT-HILBERT, Methoden der mathematischen Physik I, Berlin 1931, p. 413.

Introducing the Bessel function I_1[1] we get:

$$\Psi_1(u,t) = \nu e^{-\nu t - u} \sqrt{\nu t/u}\, I_1(2\sqrt{\nu t u}). \tag{9'}$$

This is the formula first derived by ORNSTEIN and UHLENBECK.[2]

Asymptotic formula for large u in the case of arbitrary M

We are now going to perform the integration in (6) for an arbitrary M. We confine ourselves to large values of u, and shall obtain an asymptotic formula by means of the saddle point method.

We introduce the notation:

$$\begin{aligned} \xi &= (\eta+1)\, q_M; \\ \varkappa &= \alpha\, q_M^2\, \nu t/u. \end{aligned} \tag{10}$$

Then (6) may be written:

$$\Psi(u,t) = \nu e^{-\nu t - u} \frac{1}{2\pi i} \int_{\eta_1 - i\infty}^{\eta_1 + i\infty} d\eta \exp\left\{\frac{u\varkappa}{q_M}\left[\xi/\varkappa + (1-e^{-\xi})/\xi\right]\right\}. \tag{11}$$

The saddle point value ξ_0 of ξ is determined by the equation:

$$\left[\frac{d}{d\xi}\left(\frac{\xi}{\varkappa} + \frac{1-e^{-\xi}}{\xi}\right)\right]_{\xi=\xi_0} = 0,$$

i.e.

$$\frac{1}{\varkappa} = \frac{1 - e^{-\xi_0} - \xi_0 e^{-\xi_0}}{\xi_0^2}$$

or

$$\varkappa = \frac{\xi_0^2 e^{\xi_0}}{e^{\xi_0} - 1 - \xi_0}. \tag{12}$$

In the study of (12) we confine ourselves to real values of ξ_0.

One easily finds that $d\varkappa/d\xi_0 > 0$. Hence $\varkappa$ is a steadily increasing function of ξ_0, and the inverse function ξ_0 *is a one-valued, steadily increasing function of* $\varkappa$.

When ξ_0 varies from $-\infty$ to $+\infty$, $\varkappa$ varies from 0 to $+\infty$; cf. (12). Thus the inverse function ξ_0 is *defined for* all values of $\varkappa$ between 0 and $+\infty$, and these are, according to (10), *all the physically attainable values of* $\varkappa$.

A graph of ξ_0 as a function of $\varkappa$ is given in Fig. 1.

From (12) we find:

$$\varkappa \sim \xi_0^2 \text{ or } \xi_0 \sim \sqrt{\varkappa}, \text{ when } \xi_0 \to +\infty. \tag{13}$$

Let A denote the exponent occurring in the integrand of (11). We expand A in a power series about the saddle point.

---

[1] Cf. WATSON, Theory of Bessel Functions, Cambridge 1944, p. 77.

[2] Cf. MARSHAK, l.c., eq. (41 a).

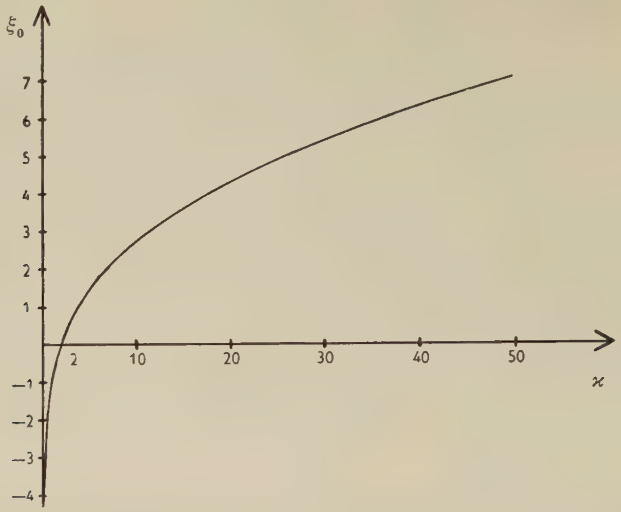

Fig. 1. The saddle point value $\xi_0 = (\eta_0 + 1)\, q_M$ defined as a function of $\varkappa = \alpha\, q_M^2\, \nu\, t/u$ by (12).

$$A = \frac{u\,\varkappa}{q_M}\left(\frac{\xi}{\varkappa} + \frac{1-e^{-\xi}}{\xi}\right) = \frac{u\,\varkappa}{q_M}\left[\left(\frac{\xi_0}{\varkappa} + \frac{1-e^{-\xi_0}}{\xi_0}\right) + \right.$$

$$\left. + {}^1/_2\left(\frac{d^2}{d\,\xi^2}\,\frac{1-e^{-\xi}}{\xi}\right)_{\xi=\xi_0}(\xi-\xi_0)^2 + \cdots\right].$$

Here we eliminate $\xi - \xi_0$ by means of (10) and $\varkappa$ by means of (12). *If we take into account only the first two terms,* we may write:

$$A = \frac{u}{q_M}\, f(\xi_0) + u\, q_M\, g(\xi_0)\,(\eta - \eta_0)^2, \tag{14}$$

with

$$f(\xi_0) = \frac{2\,\xi_0\,(e^{\xi_0} - 1 - \xi_0/2)}{e^{\xi_0} - 1 - \xi_0}, \tag{14'}$$

$$g(\xi_0) = \frac{e^{\xi_0} - 1 - \xi_0 - \xi_0^2/2}{\xi_0\,(e^{\xi_0} - 1 - \xi_0)}. \tag{14''}$$

As ξ_0 is a function of $\varkappa = \alpha\, q_M^2\, \nu\, t/u$, defined by (12), $f(\xi_0)$ and $g(\xi_0)$ are functions of t/u.

$$\begin{aligned} f(\xi_0) &= F\,(t/u),\\ g(\xi_0) &= G\,(t/u). \end{aligned} \tag{15}$$

$f(\xi_0)$ is shown graphically in Fig. 2. From (14′) and (13) we find the following asymptotic behaviour of $f(\xi_0)$.

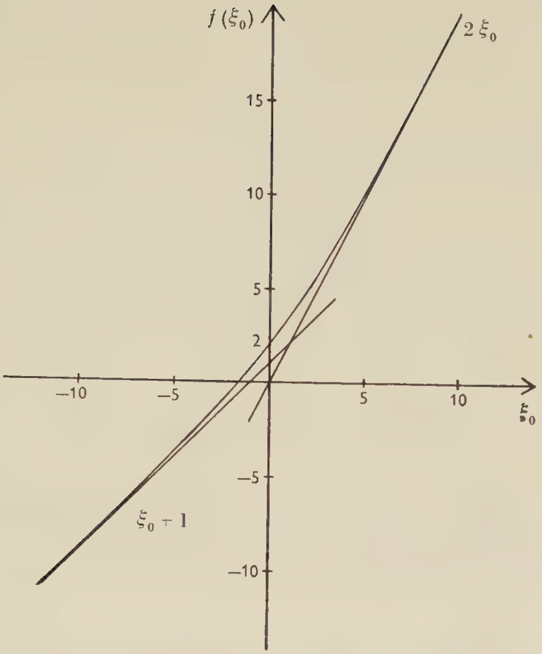

Fig. 2. Graph of $f(\xi_0)$, (14′). The straight lines are the asymptotes.

$$\left.\begin{aligned} & f(\xi_0) \sim 2\,\xi_0 \sim 2\sqrt{\varkappa}, \text{ when } \xi_0 \to +\infty. \\ & f(\xi_0) \sim \xi_0 + 1, \text{ when } \xi_0 \to -\infty. \end{aligned}\right\} \tag{16}$$

A graph of $g(\xi_0)$ is given in Fig. 3. $g(\xi_0)$ is positive for all values of ξ_0. The asymptotic behaviour of $g(\xi_0)$ is found from (14″) and (13).

$$\left.\begin{aligned} & g(\xi_0) \sim 1/\xi_0 \sim 1/\sqrt{\varkappa}, \text{ when } \xi_0 \to +\infty. \\ & g(\xi_0) \sim {}^1/_2 + 1/(2\,\xi_0), \text{ when } \xi_0 \to -\infty. \end{aligned}\right\} \tag{17}$$

From (11) and (14) we now find:

$$\begin{aligned} \Psi(u,t) &= \nu\, e^{-\nu t - u} \frac{1}{2\pi i} \int_{\eta_1 - i\infty}^{\eta_1 + i\infty} d\eta\, e^{(u/q_M) f(\xi_0) + u\, q_M\, g(\xi_0)(\eta-\eta_0)^2} \\ &= \nu\, e^{-\nu t - u + (u/q_M) f(\xi_0)} \frac{1}{2\pi i} \int_{\eta_1 - i\infty}^{\eta_1 + i\infty} d\eta\, e^{u\, q_M\, g(\xi_0)(\eta-\eta_0)^2}. \end{aligned}$$

We will integrate along *a path of steepest descent* through the saddle point; hence the imaginary part of the exponent in the last integrand must be constant, and thus zero, along the path. Therefore $\eta - \eta_0$ should be either real or

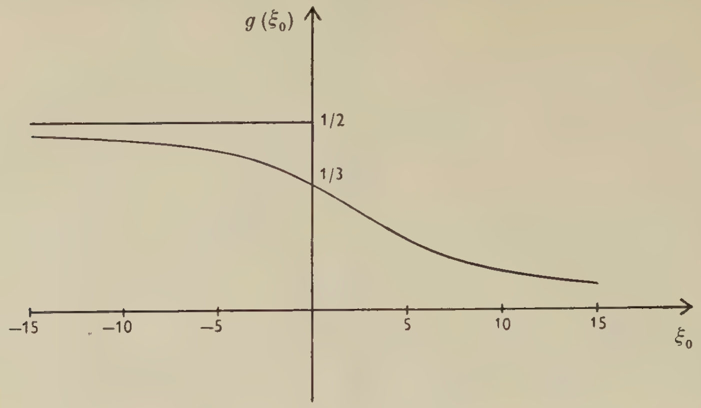

Fig. 3. Graph of $g(\xi_0)$, (14″).

purely imaginary along the path. As $g(\xi_0)$ is positive, we must choose our path so that $\eta - \eta_0$ becomes purely imaginary; i.e. our integration path should be *parallel to the imaginary axis.*

Putting $\eta - \eta_0 = ir$, r real, we have to evaluate the integral:

$$(1/2\pi i) \int_{-\infty}^{+\infty} i\, dr\, e^{-u q_M g(\xi_0) r^2} = \frac{1}{2\sqrt{\pi u q_M g(\xi_0)}} . \tag{18}$$

We now get the *asymptotic formula valid for large u:*

$$\boxed{\Psi(u,t) = \frac{\nu\, e^{-\nu t - u + (u/q_M) f(\xi_0)}}{2\sqrt{\pi u q_M g(\xi_0)}}} . \tag{19}$$

One obtains $N(u,t)$ from (19) by taking $\Psi(u,t)/\nu$.

If *both* u *and* $\varkappa = \alpha q_M^2 \nu t/u$ *are large*, ξ_0 is large too [cf. (13)]. Then we can use the asymptotic expressions for $f(\xi_0)$ and $g(\xi_0)$ with $\xi_0 \to \infty$ [cf. (16) and (17)] and get:

$$\Psi(u,t) = \frac{\nu}{2\sqrt{\pi}} (1/u)\, (\alpha \nu t u)^{1/4}\, e^{-\nu t - u + 2\sqrt{\alpha \nu t u}} . \tag{20}$$

By taking more terms in the exponent (14) we get an asymptotic expansion, with (19) or (20) as first term, when we perform the saddle point integration. We omit the details of the calculation.[1]

The result is that *the expression* (19) *should be multiplied by a factor* $(1 + \varepsilon)$. *In the first approximation* one must in (14) take account of additional terms containing $(\eta - \eta_0)^3$ and $(\eta - \eta_0)^4$. Then we get:

---

[1] Cf. BRILLOUIN, Ann. de l'Ec. Norm. *33*, 17 (1916).

$$\varepsilon = -(q_M/u)\, h(\xi_0). \tag{21}$$

Here $h(\xi_0)$ is a positive, steadily decreasing function of ξ_0;

$$h(-\infty) = 1/12; \quad h(0) = 81/1280; \quad h(+\infty) = 0.$$

$h(\xi_0)$ is given by the expression:

$$h(\xi_0) = \frac{3}{16} \frac{R_1(\xi_0)\,[5\,R_3^2(\xi_0) - 4\,R_4(\xi_0)\,R_2(\xi_0)]}{\xi_0\,R_2^3(\xi_0)}, \tag{22}$$

$$\text{with} \quad R_n(\xi_0) = e^{\xi_0} - 1 - \xi_0 - \cdots - \frac{\xi_0^n}{n!}.$$

When $\varkappa \to \infty$, i.e. when $\xi_0 \to \infty$, we have [cf. (13)]:

$$h(\xi_0) \sim \frac{3}{16\,\xi_0} \sim \frac{3}{16\sqrt{\varkappa}}.$$

Substituting this expression for $h(\xi_0)$ in (21) we get:

$$\varepsilon = -\frac{3}{16\sqrt{\alpha \nu t u}} \text{ for large values of } \varkappa = \frac{\alpha q_M^2 \nu t}{u}. \tag{23}$$

To permit an estimate of the magnitude of the additional terms (21) and (23), we have given in Table 1 the values of the constants q_M and α for several values of M.

As to the value of u, we make the following remark: If E varies between 1 and 10^7 *ev*, then $u_{\max} = \log 10^7 = 16$.

Table 1.

M	q_M	α
1	∞	1
2	2.20	1.13
12	0.334	3.52
16	0.250	4.52
238	0.0168	60.0
∞	0	∞

Asymptotic formula for large u in the case of a hydrogen moderator

If $M = 1$, then $\alpha = 1$, and $q_M = \infty$.

$$\therefore \varkappa = \alpha q_M^2 \nu t / u = \infty$$

and the formulae (20) and (23) may be used. These become:

$$\Psi(u,t) = \frac{\nu}{2\sqrt{\pi}}(1/u)(\nu t u)^{1/4} e^{-\nu t - u + 2\sqrt{\nu t u}}; \tag{24}$$

$$\varepsilon = -\frac{3}{16\sqrt{\nu t u}}. \tag{25}$$

On the other hand, Ψ_1 is in this case given by (9). Moreover, $\Psi = \Psi_1$ if $u > 0$.

Now

$$J_1(2i\sqrt{\nu t u}) = {}^1/_2\left[H_1^1(2i\sqrt{\nu t u}) + H_1^2(2i\sqrt{\nu t u})\right] \sim$$

$$\sim {}^1/_2\sqrt{\frac{2}{\pi\cdot 2i\sqrt{\nu t u}}}\left\{\exp\left[i\left(2i\sqrt{\nu t u}-\frac{3\pi}{4}\right)\right]+\exp\left[-i\left(2i\sqrt{\nu t u}-\frac{3\pi}{4}\right)\right]\right\}\sim$$

$$\sim\frac{i}{2\sqrt{\pi}}\frac{e^{2\sqrt{\nu t u}}}{(\nu t u)^{1/4}} \quad \text{for large } u.^1$$

If we put this asymptotic value of J_1 into (9), we get (24). This is a check of our formula (19).

If we take one term more in the asymptotic expansion of the Hankel function,[2] we obtain an additional term ε, which agrees exactly with (25). This is a check of (21).

II. The scattering mean free path is independent of the velocity

Laplace Transformation in *u*

If we assume the scattering mean free path to be a constant, l, (2) becomes:

$$[1+(ls/v_0)\,e^{1/2 u}]\,\Phi(u,s) = \alpha \int\limits_{\text{Max}(u-q_M;\,0)}^{u} du'\,\Phi(u',s)\,e^{-(u-u')} + \delta(u). \tag{26}$$

We take the Laplace transform of (26) and get:

$$\chi(\eta,s) + (ls/v_0)\,\chi(\eta-{}^1/_2,s) = \alpha\frac{1-e^{-(\eta+1)q_M}}{\eta+1}\chi(\eta,s)+1, \tag{27}$$

where
$$\chi(\eta,s) = \int_0^\infty du\, e^{-\eta u}\,\Phi(u,s).$$

We introduce the following notation:

$\zeta = 2\eta;$

$\lambda(\zeta,s) = \chi(\eta-{}^1/_2,s)$, i.e. $\chi(\eta,s) = \lambda(\zeta+1,s);$

---

[1] Cf. SOMMERFELD, Vorlesungen über theoretische Physik, VI, Wiesbaden 1947, pp. 91 and 102. — H means Hankel function.

[2] Cf. SOMMERFELD, l.c., p. 119.

$$k(\zeta, s) = -\frac{l\,s/v_0}{1 - \dfrac{2\,\alpha\,[1 - e^{-(\zeta+2)\,q_M/2}]}{\zeta+2}};$$

$$b(s) = v_0/l\,s.$$

(27) then becomes:

$$\boxed{\lambda(\zeta+1, s) = k(\zeta, s)\,\lambda(\zeta, s) - k(\zeta, s)\,b(s)}. \tag{28}$$

Our Laplace transform λ is thus a solution of this inhomogenous difference equation of the first order.

Formal solution of the difference equation. Subtraction of the delta function part

We first solve the homogeneous equation:

$$\lambda_0(\zeta+1) = k(\zeta)\,\lambda_0(\zeta).$$

(We have suppressed s in our notation.)

We choose a solution corresponding to the principal solution of NÖRLUND:[1]

$$\lambda_0(\zeta) = \frac{C}{k(\zeta)\,k(\zeta+1)\,\ldots}. \quad C \text{ is a constant.}$$

We now put:

$$\lambda(\zeta) = \frac{C(\zeta)}{k(\zeta)\,k(\zeta+1)\,\ldots}. \tag{29}$$

Introducing (29) into (28), we have:

$$C(\zeta+1) = C(\zeta) - b\,k(\zeta)\,k(\zeta+1)\ldots.$$

Here we choose a solution $C(\zeta)$, again corresponding to NÖRLUND's principal solution:

$$C(\zeta) = b\,k(\zeta)\,k(\zeta+1)\cdots + b\,k(\zeta+1)\,k(\zeta+2)\cdots + \cdots.$$

The solution of our inhomogeneous equation is thus:

$$\boxed{\lambda(\zeta) = b + \frac{b}{k(\zeta)} + \frac{b}{k(\zeta)\,k(\zeta+1)} + \cdots}. \tag{30}$$

Our Laplace transform is:

$$\chi(\eta) = \lambda(\zeta+1) = b + \frac{b}{k(\zeta+1)} + \frac{b}{k(\zeta+1)\,k(\zeta+2)} + \cdots.$$

---

[1] NÖRLUND, Differenzenrechnung, Berlin 1924, p. 40.

From this we subtract the delta function part $\lambda_\delta(\zeta+1)=b/(1+b)$, and get

$$\lambda_1(\zeta+1,s)=\sum_{n=0}^{\infty}(-1)^n b^{n+2}\left[1-\prod_{m=0}^{n} g(\zeta+m)\right], \tag{31}$$

with

$$g(\zeta)=1-\frac{2\alpha\left[1-\exp\left(-\frac{\zeta+3}{2}q_M\right)\right]}{\zeta+3}.$$

The series is absolutely convergent if $|b|<1$, i.e. if $|s|>v_0/l$.

Hydrogen moderator

If $M=1$, then $\alpha=1$, $q_M=\infty$. Thus $g(\zeta)=\frac{\zeta+1}{\zeta+3}$, and

$$\prod_{m=0}^{n} g(\zeta+m)=\frac{(\zeta+1)(\zeta+2)}{(\zeta+n+2)(\zeta+n+3)}.$$

We introduce this into (31), and make the Laplace inversion with respect to ζ. Using the calculus of residues and the formula $\Sigma(n+2)(n+1)(-x)^n=2/(1+x)^3$, we get:

$$\Phi_1(u,s)=\tfrac{1}{2}\frac{1}{2\pi i}\int_{\zeta_1\;i\infty}^{\zeta_1+i\infty} d\zeta\, e^{1/2\,\zeta u}\,\lambda_1(\zeta+1,s)=\frac{b^2(1+b)\,e^{\;3u/2}}{(1+b\,e^{\;u/2})^3}=\frac{v^3(s+v_0/l)}{v_0\,l^2(s+v/l)^3}.$$

We now take the Laplace inverse of Φ_1 with respect to s and find:

$$\Psi_1(u,t)=\frac{1}{2\pi i}\int_{s_1-i\infty}^{s_1+i\infty} ds\, e^{st}\,\frac{v^3(s+v_0/l)}{v_0\,l^2(s+v/l)^3}.$$

Calculating the residues, we obtain:

$$\Psi_1(u,t)={}^1\!/_2\,(v/l)^3\,t^2\left(1-\frac{v}{v_0}+\frac{2l}{t\,v_0}\right)e^{-vt/l}.$$

This formula may be found in the paper of MARSHAK.[1]

Arbitrary *M*. Laplace inversion

In the special case $M=1$, we thus got the correct result. We now write down the solution for an arbitrary M. The Laplace inversion may be performed because $|\lambda_1(\zeta+1,s)|^2$ [see (31)] is integrable along suitably chosen integration paths in the s- and ζ-planes. That $\lambda_1(\zeta+1,s)$ leads to a solution satisfying the initial conditions, will be seen later on in this paper.

---

[1] MARSHAK l.c., eq. (41 b). There is a misprint in MARSHAK's formula.

Observing that

$$\frac{1}{2\pi i}\int_{s_1-i\infty}^{s_1+i\infty} d s\, e^{s t} \frac{1}{s^{n+2}} = t^{n+1}/(n+1)!,$$

we thus get from (31):

$$\boxed{\Psi_1(u, t) = \sum_{n=0}^{\infty} (-1)^n \frac{v_0}{l}\left(\frac{v_0 t}{l}\right)^{n+1} \frac{1}{(n+1)!}\,\frac{1}{2}\,\frac{1}{2\pi i}\int_{\zeta_1-i\infty}^{\zeta_1+i\infty} d\zeta\, e^{1/_2 \zeta u}\,[1-\prod_{m=0}^{n} g(\zeta+m)]} . \quad (32)$$

The solution (32) is thus an expansion in powers of t. We now observe the following interesting fact:

If $u > r q_M$ *(*$r =$ *integer), the coefficients of* $t, t^2, \cdots, t^r$ *vanish.*

Proof: We consider the coefficient K_n of t^n, and assume that $n \leq r$. K_n contains the following integral as factor:

$$\frac{1}{2\pi i}\int_{\zeta_1-i\infty}^{\zeta_1+i\infty} d\zeta\, e^{1/_2 \zeta u}\,[1-\prod_{m=0}^{n-1} g(\zeta+m)],$$

where

$$g(\zeta) = 1 - \frac{2\alpha}{\zeta+3} + \frac{2\alpha \exp\left(-\dfrac{\zeta+3}{2} q_M\right)}{\zeta+3} .$$

We perform the multiplication $\prod_{m=0}^{n-1}$ and multiply through with $e^{1/_2 \zeta u}$. The integrand then is written as a number of terms of the type:

$$T = -\, e^{1/_2 \zeta u}\,(2\alpha)^{\mu+\nu}\,\frac{(-1)^{\mu}}{(\zeta+m_1+3)\cdots(\zeta+m_\mu+3)} \cdot$$
$$\cdot \frac{\exp\left[-\dfrac{\zeta+m_1'+3}{2} q_M - \cdots - \dfrac{\zeta+m_\nu'+3}{2} q_M\right]}{(\zeta+m_1'+3)\cdots(\zeta+m_\nu'+3)} \quad (33)$$

where $m_1, \cdots, m_\mu, m_1', \cdots, m_\nu'$ are different integers chosen among $0, 1, \ldots, n-1$.

The exponential factor contained in T and depending on ζ is $\exp[{}^1/_2\,\zeta(u-\nu q_M)]$. As $u > r q_M \geq n q_M \geq \nu q_M$, it is evident that *we may close our integration path with an infinite semicircle to the left.* This is true for every term T, and so for the whole integrand. But, like $g(\zeta)$, the complete integrand is analytic in the entire finite ζ-plane. (This is naturally due to the cancellation of every pole of T by a corresponding pole of another term, say, T'.) Therefore the coefficient K_n is zero according to Cauchy's theorem. This completes the proof.

The points $u = r q_M$ are thus points of discontinuity for Ψ_1. The same thing is true in the stationary case.[1]

Let us regard Ψ_1 as a function of t and consider u as a fixed parameter. The graph of the function has a contact with the t-axis at the point $t=0$. According to the above theorem, the order of the contact gets higher, as the values of the parameter u are made larger.

Now let $r q_M < u < (r+1) q_M$, and let us determine the coefficient, K_{r+1}, of t^{r+1}, *the first non-vanishing coefficient.* Our integrand is again composed of terms (33), where now $m_1, \cdots, m_\mu$, $m'_1, \cdots, m'_\nu$ are different integers, chosen among $0, 1, \ldots, r$. Our previous discussion proving that the integration path may be closed to the left is still valid for all terms but one, namely,

$$T_1 = -e^{1/2\,\zeta u}\,(2\,\alpha)^{r+1}\,\frac{\exp\left[-\dfrac{\zeta+3}{2}\,q_M - \cdots - \dfrac{\zeta+r+3}{2}\,q_M\right]}{(\zeta+3)\cdots(\zeta+r+3)}. \tag{34}$$

This term contains the factor $\exp\{-{}^1\!/_2\,\zeta\,[(r+1)\,q_M - u]\}$ making it necessary to close the integration path by an infinite semicircle *to the right.* Within the closed contour T_1 is analytic (all terms T clearly have their poles in the left half-plane). So the integral of T_1 is zero.

The remaining terms are on the contrary to be integrated along a contour to the left. As T_1 drops out, all residues will no longer cancel each other. According to (32) and (34) we get the following expression for K_{r+1}. (Observe that the first minus sign of T_1 corresponds to a plus sign in the remaining residues.)

$$K_{r+1} = (-1)^r\,(v_0/l)^{r+2}\,\frac{1}{(r+1)\,!}\,{}^1\!/_2\,(2\,\alpha)^{r+1}\times$$

$$\times\left\{\frac{1}{2\,\pi\,i}\oint_{|\zeta+3|=\varrho} d\,\zeta\,\frac{\exp\left[{}^1\!/_2\,\zeta\,u - \dfrac{\zeta+4}{2}\,q_M - \cdots - \dfrac{\zeta+r+3}{2}\,q_M\right]}{(\zeta+3)\cdots(\zeta+r+3)} + \right.$$

$$\left. + \cdots + \frac{1}{2\,\pi\,i}\oint_{|\zeta+r+3|=\varrho} d\,\zeta\,\frac{\exp\left[{}^1\!/_2\,\zeta\,u - \dfrac{\zeta+3}{2}\,q_M - \cdots - \dfrac{\zeta+r+2}{2}\,q_M\right]}{(\zeta+3)\cdots(\zeta+r+3)}\right\},$$

where $0 < \varrho < 1$, so that every closed contour contains only one pole. We calculate in the usual way the $(r+1)$ residues in the large bracket; it then turns out that these $(r+1)$ terms can be summed up by means of the binomial theorem. We get in this way after some elementary calculation:

$$K_{r+1} = \frac{(2\,\alpha)^{r+1}}{2\cdot r!\,(r+1)!}\,(v_0/l)^{r+2}\,\exp\left[-\frac{(r+1)\,(r+6)}{4}\,q_M + \frac{(r+3)\,u'}{2}\right](1-e^{-1/2\,u'})^r \tag{35}$$

where $u' = (r+1)\,q_M - u$.

The preceding discussion shows that Cauchy's theorem results in a certain simplification, when we calculate K_{r+1}. The same thing is naturally true for

---

[1] Cf. H. A. S. Eriksson, Ark. Mat. Astr. Fys. *33* B, nr 5 (1946).

higher coefficients. Let us assume, as before, that $r q_M < u < (r+1) q_M$ and let us consider an arbitrary coefficient K_n, $n \geq r+1$. We see from our previous discussion that a term (33) gives a contribution if ν in (33) satisfies the relations: $u - \nu q_M < 0$, $u - (\nu - 1) q_M > 0$. For in that case two complementary terms T must be integrated in different directions (one to the left, the other to the right) in the ζ-plane. This implies that ν must be the integral part of $(u/q_M + 1)$, i.e. $\nu = r+1$. The $(r+1)$ numbers $m_1', \cdots, m_\nu'$ are, according to (33), to be chosen among the numbers $0, 1, \cdots, n-1$. This choice can be done in $\binom{n}{r+1}$ different ways. To each of these choices corresponds

$$\binom{n-r-1}{0} + \cdots + \binom{n-r-1}{n-r-1} = 2^{n-r-1}$$

different choices of the numbers $m_1, \cdots, m_\mu$ in (33). Hence we must consider $2^{n-r-1}\binom{n}{r+1}$ different terms T. This seems to indicate that *the solution* (32) *is useful for practical calculations only for rather small values of* u/q_M *and* $v_0 t/l$.

The special case $u < q_M$

When $u < q_M$, the lower limit of the integral in the integral equation (26) is equal to zero. Therefore the integral equation may be solved by differentiation.[1] The result is:

$$\Phi_1(u, s) = \frac{\alpha v^3}{l^2 v_0} \frac{(s + v_0/l)^{2\alpha - 1}}{(s + v/l)^{2\alpha + 1}}. \tag{36}$$

In this case (31) gives:

$$\Phi_1(u, s) = \sum_{n=0}^{\infty} (-1)^n b^{n+2} \tfrac{1}{2} \frac{1}{2\pi i} \int_{\zeta_1 - i\infty}^{\zeta_1 + i\infty} d\zeta\, e^{1/2 \zeta u} \left[1 - \prod_{m=0}^{n} h(\zeta + m)\right], \tag{37}$$

with
$$h(\zeta) = 1 - \frac{2\alpha}{\zeta + 3},$$

for every term originating in the exponential expression $\exp\left(-\frac{\zeta+3}{2} q_M\right)$ of $g(\zeta)$ [see (31)] vanishes. As an example,

$$\int_{\zeta_1 - i\infty}^{\zeta_1 + i\infty} d\zeta \frac{\exp\left(1/2\, \zeta u - \frac{\zeta + 3}{2} q_M\right)}{\zeta + 3} = 0,$$

because the integration path may be closed with an infinite semicircle to the right (as $u < q_M$), and the integrand is analytic within the closed contour.

(37) may easily be evaluated by means of the calculus of residues. The result coincides with (36).

---

[1] Cf. MARSHAK, l.c., p. 194.

We remember that $\lambda_1(\zeta+1, s)$, (31), was obtained from $\lambda(\zeta+1, s)$, cf. (30), by subtraction of $\lambda_\delta(\zeta+1, s)$. Now $\lambda(\zeta+1, s)$ was obtained as a special solution of the difference equation (28). It is not *a priori* evident that this special solution λ should give a Φ_1 satisfying the initial conditions of the problem. But *from this section it is clear that our* Φ_1 *really agrees with the initial conditions. Since our problem obviously has a unique solution, we may conclude that the solution* (32) *is correct.*

The Laplace inverse of (36) is:

$$\Psi_1(u, t) = \frac{\alpha\, v^3}{l^2\, v_0}\,\frac{1}{2\pi i}\int_{s_1-i\infty}^{s_1+i\infty} d s\, e^{s t}\,\frac{(s+v_0/l)^{2\alpha-1}}{(s+v/l)^{2\alpha+1}}.$$

If *t is large*, we may neglect the contribution from the branch point $s=-v_0/l$, as $v_0 > v$. We thus get:

$$\Psi_1(u, t) = \frac{\alpha}{\Gamma(2\alpha+1)\, v_0\, l^{2\alpha+1}}(v_0-v)^{2\alpha-1}\, v^3\, t^{2\alpha}\, e^{-v t/l}.$$

We now introduce l as unit of length and v_0 as unit of velocity. We denote the velocity, time, and collision number, measured in the new system of units, by V, T and $\bar{\Psi}_1(u, T)$ respectively. Then we get:

$$\bar{\Psi}_1(u, T) = \frac{\alpha}{\Gamma(2\alpha+1)}(1-V)^{2\alpha-1}\, V^3\, T^{2\alpha}\, e^{-VT}.$$

Summary

The slowing-down of neutrons by elastic impacts against free atoms at rest is considered. Absorption is neglected. The integro-differential equation of the problem is Laplace transformed with respect to the time, t, and the logarithmic energy variable, u.

In *Part I* the scattering mean free path, l, of the neutrons is assumed to be proportional to the velocity. An asymptotic formula, giving the time energy distribution for large values of u, is derived by means of the saddle point method.

In *Part II*, l is assumed to be constant. A solution, giving a certain insight into the statistical structure of the distribution function, is studied.

ACKNOWLEDGEMENTS

I wish to express my gratitude to Professor IVAR WALLER for suggesting this investigation and for much good advice during the work.

I also wish to express my appreciation to the *Swedish Atomic Committee* for a grant.

Uppsala, Institute for Mechanics and Math. Physics.

Tryckt den 24 oktober 1955

Uppsala 1955. Almqvist & Wiksells Boktryckeri AB

ARKIV FÖR FYSIK Band 10 nr 13

Communicated 27 April 1955 by E. Hulthén and O. Klein

The theory of chemical bond[1]

By W. Heitler

With 2 figures in the text

Before I begin I am sure you will permit me to say a few words in remembrance of Fritz London who has given so much thought to the subject we are discussing. London was one of the rare scientists for whom theoretical work meant more than doing a few, simple or complicated, calculations. When a problem had fixed itself in his mind—and it never was an easy problem—he would ponder about it for months, or years, until he had understood it and its solution thoroughly and from all points of view. He never was given to premature publication. We have lost in him a profound thinker rather than a mere expert in theoretical physics or chemistry.

I shall now attempt to give a short qualitative survey of the theory of covalent chemical bond and its main stages of development. One can, of course, consider a complicated problem like a molecule from various points of view, but I shall limit myself to the trend of ideas which were London's as well as mine and which we had always favoured, namely the consideration of the interaction of atoms as a function of their distance. One can approach the problem also by considering first the solutions of the two-centre problem (in a diatomic molecule) and then building up the molecule by one-electron wave functions, as was first done by Hund and Mulliken. This is an approximation in its own rights if the molecule is in equilibrium (or near equilibrium) but the first method has the advantage of being valid also at large distances and therefore permitting an insight into the mechanism of chemical reactions.

1. Covalent bond and saturation

In classical physics the problem of the covalent bond was utterly unsolvable. There could be no answer to the question: why do *neutral* atoms attract each other so strongly? The mutual polarization of the atoms through electric multipole interaction proved much too weak. Moreover, the most striking feature of the chemical attraction is its *saturation* property expressed so forcibly by the concept of *valency*. This is a feature completely foreign to all classical laws. Only through quantum mechanics which claims to be a quantitative theory of all atomic and molecular phenomena the key to the solution could be found — and it might be guessed that it would be a typical quantum mechanical feature, with no classical analogue, that accounted for the attraction as well as the saturation. This feature was found to be the *exchange phenomenon* which, as was first pointed out by Heisenberg, was a consequence of the absolute identity of the elementary particles. It is a phenomenon very typical for quantum mechanics. The exchange contributes a large and dominant amount to the interaction energy, which in first approximation is given by the well-known exchange integral. Moreover, owing to the restrictions imposed by the Pauli principle, the exchange energy depends critically on the relative spin directions of the electrons involved. In the case of two interacting hydrogen atoms, the exchange energy is negative (attraction) if the spins are antiparallel (total spin zero) but positive for parallel spins (total spin 1). The total interaction energy turns out to be in first approximation

---

[1] Fritz London Memorial Lecture, given at the symposium in Stockholm, March 1955.

$$E = C \pm A. \tag{1}$$

C is the Coulomb interaction of the charge distributions of the two H-atoms. A is the exchange integral, a typical quantum mechanical quantity. C and A depend on the distance R of the atoms. For medium and large R both quantities are negative but A is numerically much larger than C. The $+(-)$ signs refer to antiparallel (parallel) spin directions. Thus, for parallel spins, we obtain a strong attraction. $C + A$ has a minimum at some distance R_0, and this and the minimum value of $C + A$ turn out to be in satisfactory agreement with the data of the H_2-molecule. When the spins are parallel the two H-atoms strongly repel each other. The existence of this repulsive state was a result new to chemistry which could be derived from quantum mechanics.[1] Thus we see that the chemical notation for a bond H–H means physically a pair of electrons with antiparallel spin belonging to the two atoms.

The critical spin dependence of E leads now also to an understanding of the saturation properties. Consider a complete H_2-molecule which has two electrons with antiparallel spin. Let now a third H-atom approach from a large distance. Whatever the spin direction of this third electron is, it can be exchanged only against the electrons of H_2 with the same spin:

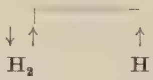

Otherwise either the Pauli principle would be violated or else the H_2-molecule would have to be broken up and be raised to the repulsive state with parallel spins (denoted by –H H–) and energy $C - A$. Thus a H_2 molecule cannot attract a third H-atom. The saturation properties therefore appear as a simple consequence of the exchange mechanism of quantum mechanics.

2. Activation energy

The fruitfulness of the quantum mechanical exchange mechanism for chemical problems is forcibly demonstrated if we consider the interaction of three H-atoms more in detail as was first done by London. To distinguish the atoms let us assume that the third atom is a deuterium atom D. If the two H-atoms are in a state with antiparallel spins (in the chemical notation H–H), we have seen that the D-atom is repelled at large distances. What happens now if we bring the D-atom nearer to H_2 so that the H–D distance is about the same as the H–H distance. There is no longer any reason why the electron pair should be formed between H–H. It may as well be formed between H–D, so that we may have a state –H H–D as well as H–H D– (without loss of energy). *Both* are unperturbed states of wave mechanics. The superposition principle of wave functions comes now into play and for mere reasons of symmetry we may expect that the true wave function is a superposition of both

---

[1] In (1) we have neglected the "overlap integral" S. The true formula is $E = (C \pm A)/(1 \pm S)$ where S also depends on R but is rather small compared with unity. In the following we shall neglect the overlap integrals throughout.

$$\{\text{H–H D–}\} + \{\text{–H H–D}\}. \tag{2}$$

That this is really so follows if we now remove the H-atom at the left. According to a well-known law of quantum mechanics the energy remains a minimum throughout as long as we change the distances adiabatically. Thus in the end we must be left with the *bound* H–D molecule, not with –H D– in the repulsive state. The state H–H D– *gradually* goes over into –H HD. In the intermediate region we must have a mixture (2), also called the *transition state*. It may well be denoted by ··H··H··D··. The existence of such *transition* states is a result of the superposition principle of wave mechanics and has since become an important concept in chemistry. The above considerations are corroborated by the quantitative treatment. If we denote the exchange integral between the H–H atoms by A_1, between the neighbouring H–D by A_2, and between the non-neighbours H D by A_3 the lowest energy of the 3 atoms is given by London's formula

$$E = C - \sqrt{A_1^2 + A_2^2 + A_3^2 - A_1 A_2 - A_1 A_3 - A_2 A_3}. \tag{3}$$

During an adiabatic change of distance the sign of the square root remains the same. When D is far away A_2, A_3 are small and $E = C + A_1 - \frac{1}{2}(A_2 + A_3)$. The negative sign of A_2 and A_3 shows that D is repelled. Similarly when the left hand H is removed $E = C + A_2 - \frac{1}{2}(A_1 + A_3)$. The plus sign $+A_2$ shows that we are left with an H–D-*molecule*. When the H–H and H–D distances are equal $A_1 = A_2 \equiv A$, but A_3 is small, and we have $E = C + A - A_3$. The energy is slightly higher $(-A_3)$ than that of a H_2 molecule. This is the above transition state.

Thus we see that an exchange reaction $H_2 + D \rightarrow H + HD$ can take place. For this purpose, however, first a certain repulsion has to be overcome which means that a certain *activation energy* has to be spent. The exchange mechanism of quantum mechanics therefore also yields a theory of the activation energies in chemical reactions.

3. Valency

We now generalize the above considerations to atoms with more than one electron. The first question we may ask is how many hydrogen atoms can be bound by a given atom. Since any pairs of electrons inside an atom can only repel another atom, it is obvious that the binding power of the atom must depend on those electrons in the outer shell which have, or can have, parallel spins. The number of these electrons will then also be the number of hydrogen atoms which can be attracted, i.e. the valency of the atom (more precisely, the valency against hydrogen). In general the ground state of an atom is the state with the highest multiplicity that is possible in the lowest electron configuration. ^4S of nitrogen (configuration s^2p^3) and ^3P of oxygen (s^2p^4) are examples. Thus the valency n is in general connected with the multiplicity $n+1$ of the ground state. This agrees in most cases with the chemical facts with one—most important—exception: The lowest configuration of carbon is

s^2p^2 and the ground state ^3P has only valency 2. We concluded therefore in the early stages of the theory of chemical bond that the well-known valency 4 of carbon must rest on an excited state, due to raising a 2*s*-electron into the *p*-shell. The lowest state of this sp^3-configuration is indeed ^5S. It was only comparatively recently that the excitation energy of this state was measured by SHENSTONE. It is 96 kcal/mole. The fact that an excited state is responsible for the four valencies of carbon is, of course, very important for the whole of organic chemistry. Before we consider the case of carbon more in detail some general facts concerning the interaction of atoms with several electrons must be discussed.

When calculating the interaction of an atom with several electrons with other atoms one can make essentially two different approximations within the framework of perturbation theory:

(a) We assume the atom to be in a *particular atomic state*, for example the ground state (or, if a low excited state has a higher valency (carbon) in this particular state). We ignore the presence of other atomic states which may influence the interaction. In this way we obtain a potential curve (energy as function of distance) starting from each atomic state.

(b) We neglect the interaction between the electrons in the outer shell of the atom. We permit these electrons to arrange themselves and their spins in such a way as to give the maximum binding energy. Thus we treat the atomic states arising from the same electron configuration as degenerate.

A criterion for the validity of (a) or (b) is the following: (a) is valid if the separation of the atomic states is large compared with the binding energy of the molecule. (b) is valid if the separation of the atomic states arising from the configuration considered is small compared with the binding energy. — In many cases both quantities are of the same order of magnitude and then neither (a) nor (b) is very good but the two approximations supplement each other and lead to different aspects of the same problem.

We can understand the relationship between these two approximations and arrive at an improvement (c) on both by the following consideration: We first consider the potential curves starting from various atomic states according to (a). For example, from ^4S of nitrogen (s^2p^3 configuration) 3 hydrogen atoms are attracted. From the excited states ^2D, ^2P which also arise from s^2p^3 the 3 H-atoms are repelled because these states have only valency 1. (Fig. 1, dotted curves; only ^4S and ^2D are shown.) Now this is not yet the true shape of the curves. According to quantum mechanics there is also a mutual "interaction" between these two curves which is the stronger the closer the curves are, provided that the total spin (and the total angular momentum etc., if this is an integral of the motion) are the same. This interaction of the potential curves can easily be obtained from perturbation theory. It always results in a mutual "repulsion" of the curves deepening the attraction curve still further and pushing the repulsion curve still higher (full-drawn curves of Fig. 1). In the case of NH_3 the effect is probably not very large because the curves are already rather far apart. By considering the mutual interaction of the potential curves we take a step towards approximation (b) because the influence of further states arising from the same configuration (^2D, ^2P) is taken into account. But we have also arrived at an improvement on (b) because the separation of the atomic states is no longer neglected. In general it will be sufficient to consider a few atomic states only and we call this procedure approximation (c).

The mutual interaction of the potential curves is most striking if the curves,

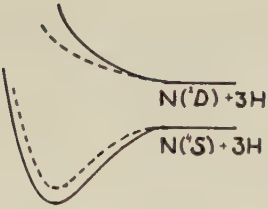

Fig. 1.

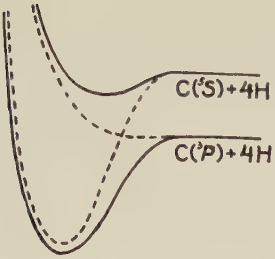

Fig. 2.

according to (a), would cross. This is the case for $C + 4\,H$. ^3P cannot attract 4 H-atoms. Only the ^5S-state has 4 valencies. The two curves "repel" each other strongly before reaching the crossing point and the result is that no crossing takes place at all. The curve starting from ^3P goes over gradually into that originally starting from ^5S (Fig. 2). This shows that a CH_4 molecule can be formed, after all, from the ^3P-state of carbon. It is not necessary to spend first the excitation energy of ^5S (96 kcal/mole). Nevertheless it is only through the strong influence of ^5S that the CH_4 molecule is formed.

Moreover, let us consider the wave function of the C-atom as we pass along the lower curve of Fig. 2. First this is ^3P. As we approach the crossing region we have a linear combination of ^3P and ^5S with coefficients changing with the distance. As we leave the crossing region the wave function becomes more and more ^5S because we join more or less the direct curve starting from ^5S. Thus, in the neighbourhood of the minimum (molecule) we expect the state of the carbon atom to be predominantly ^5S. The potential curve there is not very different from the dotted portion starting from ^5S, although it is reached from ^3P directly without prior excitation.

The above considerations also provide an explanation for a few facts which seem at first contrary to the idea that a bond is due to electron pairing. Quite generally we expect a saturated molecule to have total spin zero. For diatomic molecules consisting of two like atoms (N_2, C_2 etc.) the ground state should be a state with n pairs corresponding to the chemical formula $N\equiv N$ etc., and total spin zero. States, corresponding to $-N=N-$, $=N-N=$ etc., with total spin 1, 2, etc. have higher energy although in some of them the atoms are still attracted, giving rise to an excited molecular state. In fact the interaction energy of two such atoms for a total spin s in approximation (a) is given by

$$E = C + (n - s - s^2)\,A \tag{4}$$

where C and A are Coulomb and exchange integrals similar to those occurring in H_2. This formula is easily derived from the general theory of § 5. The above states of N_2 have energies $C + 3\,A$ ($N\equiv N$), $C + A$ ($-N=N-$, attractive), $C - 3\,A$ ($=N-N=$, repulsive), $C - 9\,A$ ($\equiv N\ N\equiv$, repulsive). It is perhaps unexpected that the quintet state is already repulsive although one pair is formed, but this seems to be in agreement with the facts as no such state is known.

There are now a few exceptions to the above results. The ground state of C_2 is $^3\Pi$ and not, as one would expect a singlet state. This is due to the strong influence of ^5S. Two carbon atoms in ^3P certainly form a stable molecular state with $s = 0$, but there is also an excited triplet state with energy $C(n=2, s=1)$[1] which is just slightly attractive. Now two carbon atoms, one in ^3P and one in ^5S can only have $s=1$ as the lowest multiplicity (two pairs) and in this state the interaction is strongly attractive. The curve starting from $^3P + {}^5S$ will cross the triplet curve starting from $^3P + {}^3P$. The result is that the latter is pushed down and even below the singlet curve from $^3P + {}^3P$. Thus the ground state of C_2 is a triplet, although the singlet to be expected is not far above it. Thus we see that approximation (c) yields always good results in agreements with facts.

Finally it may be mentioned that for many molecules the cooperation of ionic states is important. For example, a strong contribution to the binding energy of HCl arises from the state $H^+ + Cl^-$, in addition to H + Cl. Nevertheless it is clear that the molecule, when dissociated, goes over into normal H and Cl atoms. A discussion of this wide field is, however, outside the scope of this paper.

4. Directional properties

An advantage of approximation (b) often quoted is that it leads very simply to an understanding of the fact that the valencies of some atoms have preferential relative directions. Consider as an example nitrogen and the NH_3 molecule. The 3 decoupled p-electrons occupy 3 one-electron wave functions for which we can choose

$$xf(r),\ yf(r),\ zf(r). \tag{5}$$

These wave functions are largest along the x, y, z directions respectively. Now let these 3 electrons interact with 3 hydrogen atoms, placed at the same distance from N but as yet in arbitrary directions. The interaction of one N-electron with one H-atom gives rise to an exchange (and Coulomb) integral. Now this has the largest numerical value if the wave functions overlap as far as possible. Since each H-electron can form a pair with one N-electron only, it follows that the maximum binding energy is obtained when the 3 H-atoms are placed at right angles. (Each angle H–N–H is $\pi/2$.) This leads to the well-known pyramidal structure of NH_3. In reality the 3 H-atoms repel each other which flattens the pyramid a little. This simple explanation of the directional features was first given by SLATER and PAULING.

We can represent the above facts also in a slightly different way: The assumption of decoupled p-electrons means that we take the ^2D- and ^2P-states of nitrogen into account in addition to ^4S. ^4S alone does not exhibit any directional features in the approximation considered so far (see however below), on account of its spherical symmetry. The directional features are due to the influence of the excited states. Now we have seen that this influence is not very large, as far as the binding energy is concerned, but the small correction due to these excited states depends on the relative angles, formed by the 3 H-atoms. This is corroborated by the facts: The energy required to bend the valency angles is in many cases small compared with the binding energy. For example, to press the NH_3 pyramid flat requires only 6 kcal/mole whereas the total binding energy of NH_3 is ~ 250 kcal/mole.[2]

In addition to the influence of the excited states there is a further factor contributing to the directional properties inherent even in a single atomic state as has recently been shown by ARTMANN. When we consider the interaction of 3 or more atoms also electron exchanges can occur which affect all 3 atoms at the same time: Let us, for example, number the electrons of nitrogen 1, 2, 3 and those of the 3 H-atoms 4, 5, 6, respectively. We can then exchange two pairs, $1 \rightleftharpoons 4$ and $2 \rightleftharpoons 5$, at the same time. Accordingly a double exchange integral will occur which depends on the relative positions of 3 atoms simultaneously, and this also occurs in the full expression of the interaction energy. There are all sorts of higher exchanges, even if we have only two atoms with more than one electron each. Generally, such higher exchange integrals are much smaller than the ordinary exchange integrals (exchange of only two electrons) and are usually neglected for the calculation of binding energies, but they contribute to the directional effects. Consider now again an N-atom in the ^4S-state. The wave function can be built up approximately from the three single electron functions (5). The wave function is antisymmetrical in the 3 electrons and is easily seen to be

---

[1] In (4) it is assumed that the atoms are in non-degenerate states (except for the spin degeneracy). This formula should therefore be generalized for atoms in P-states, but this is of no importance for the above argument and does not change the result.

[2] Also for C-compounds a change of angles requires comparatively little energy, whereas for H_2O this is not the case.

$$\varphi = \text{const.}\ (\mathbf{r}_1 [\mathbf{r}_2\, \mathbf{r}_3])\, f(r_1)\, f(r_2)\, f(r_3) \tag{6}$$

where $\mathbf{r}_1, \ldots$ are the position vectors of the 3 electrons. Eq. (6) is evidently antisymmetrical. Now φ is spherically symmetrical in the sense that it remains invariant against a simultaneous rotation of all three $\mathbf{r}$'s in space but it does depend on the relative directions of $\mathbf{r}_1, \mathbf{r}_2, \mathbf{r}_3$. It has a *maximum* when $\mathbf{r}_1, \mathbf{r}_2, \mathbf{r}_3$ are *perpendicular to each other*. The ordinary exchange integral with another atom cannot show any preferential directions because (6) is spherically symmetrical. However, as soon as higher exchanges are taken into account, involving for example N and two hydrogen atoms ($1 \rightleftharpoons 4$, $2 \rightleftharpoons 5$, for example), the corresponding integrals depend on the angle H–N–H. Overlapping considerations show again that the preferential angle is $\pi/2$.

Thus in addition to the influence of the excited states, even an atom in one state can show preferential valency-directions if at least double exchanges are taken into account. It is not known yet which of the two causes is quantitatively more important.

Also the carbon atom is known to have directed valencies. The preferential directions are those of a tetrahedron. In this case, the method (b), which has also been widely applied here, is not a good approximation. We have in any case to consider the sp^3-configuration but if we assume the electrons to be decoupled, as has often been done, we include apart from ^5S also very high atomic states which can only have a very small influence on the bond problem. There are again two effects which both contribute to the stability of a tetrahedron.

(1) As we have seen (Fig. 2) two states mainly influence the bond, ^5S and ^3P (possibly also the other states of s^2p^2). It may be supposed that directional properties will result from the cooperation of these two states. This has indeed been shown to be the case by the late Mrs. PÖSCHL-NORDHEIM, who has made a detailed study of many compounds in approximation (c). She was able to show that the tetrahedral configuration of CH_4 is the most stable. For this purpose, however, an explicit calculation is required. (2) It is quite easy to see that the wave function of ^5S alone has a maximum if the position vectors $\mathbf{r}_1 \ldots \mathbf{r}_4$ of the 4 electrons point in the tetrahedral directions. This also leads to a stable tetrahedron if exchanges of two pairs of electrons are taken into account, much in the same way as for NH_3.

It is needless to say that the repulsion of the 4 hydrogen atoms in CH_4 alone suffices to make the tetrahedron stable, but the directional properties of carbon exhibit themselves also in other cases (for example in the inhibited rotation of the CH_2 groups in C_2H_4) for which the above considerations are required.

5. Calculation of binding energies

The preceding discussion has shown that it is in most cases sufficient to consider one atomic state only, if we are mainly interested in the binding energy of the molecule near the potential minimum. It is true that we ignore then one of the two contributing factors to the directional properties but this, as far as the energy is concerned, is usually of minor importance. A large body of chemical problems, in particular in organic chemistry, can be treated in this way. However, the method for the calculation of the interaction energy of a number of atoms to be described below is equally applicable in approximations (a) or (b) and only requires a generalization for approximation (c). The method was developped by RUMER, WEYL and the present author.

Consider a number of atoms $a, b, \ldots$ with $n_a, n_b \ldots$ valence electrons. For simplicity we assume that the atomic states are non-degenerate, i.e. are ${}^{n_a+1}S$ states and that a state with total spin $s = 0$ exists (complete saturation).[1] The first step is to consider the various ways in which electron pairs can be formed between these atoms. Two atoms with n_a and n_b electrons can form at most n_b pairs, if $n_a > n_b$, or n_a pairs if $n_a < n_b$. The number of pairs can also be less, leaving each of the atoms with a number of unpaired electrons available for pair formation with other atoms. We can then draw diagrams forming pairs of electrons between atoms in all possible manners and indicating each pair by a "valence-dash". Such a diagram we call "valence structure", and in general several valence structures exist for a given set of atoms (examples below). Now to each valence structure a definite spin wave function is attributed. If we denote the two spin wave functions of a single electron by α and β (spin component in z-direction $+\frac{1}{2}$ and $-\frac{1}{2}$), then the spin wave function of a pair of electrons 1 and 2 is $\alpha(1)\,\beta(2) - \alpha(2)\,\beta(1)$. If the two electrons belong to atoms a, b we denote this for short by $[ab]$. Two pairs between a and b can be symbolized by $[ab]^2$. It is seen that $[ab]$ changes sign, if electrons 1 and 2 are interchanged, or what comes to the same, if a and b are interchanged. The sign of the spin wave function must be taken into account and we do this by attributing an arrow to each valence-dash connecting atoms a, b etc. For example, for 4 hydrogen atoms $H_1 \ldots H_4$ the following valence structures exist

$$\varphi_1 = \begin{tikzcd} H_1 \arrow[d] & H_2 \arrow[d] \\ H_3 & H_4 \end{tikzcd}, \quad \varphi_2 = \begin{tikzcd} H_1 \arrow[r] & H_2 \\ H_3 \arrow[r] & H_4 \end{tikzcd}, \quad \varphi_3 = \begin{tikzcd} H_1 \arrow[dr] & H_2 \arrow[dl] \\ H_3 & H_4 \end{tikzcd} \tag{7}$$

or $\varphi_1 = [H_1H_3]\,[H_2H_4]$ etc.

For C_2H_2 also three structures exist

$$\varphi_1 = \begin{tikzcd} C_1 \arrow[r, shift left] \arrow[r] \arrow[r, shift right] \arrow[d] & C_2 \arrow[d] \\ H_1 & H_2 \end{tikzcd}, \quad \varphi_2 = \begin{tikzcd} C_1 \arrow[r, shift left] \arrow[r] \arrow[r, shift right] & C_2 \\ H_1 \arrow[r] & H_2 \end{tikzcd}, \quad \varphi_3 = \begin{tikzcd} C_1 \arrow[r, shift left] \arrow[r] \arrow[r, shift right] \arrow[dr] & C_2 \arrow[dl] \\ H_1 & H_2 \end{tikzcd} \tag{8}$$

or $\varphi_1 = [C_1C_2]^3\,[C_1H_1]\,[C_2H_2]$ etc.

We have arranged the atoms on a square for clarity's sake but this has nothing to do with the true arrangement of the atoms in space which so far is arbitrary.

---

[1] An unsaturated molecule ($s \neq 0$) can be treated simply by assuming a further atom with spin s which is infinitely far way so that its interaction integrals with all atoms vanish.

There is one further important point. It is at once verified that for any 4 atoms a linear relation between the spin functions exists

$$[ab]\,[cd] + [ac]\,[db] + [ad]\,[bc] = 0.$$

For the 3 φ's of (7) or (8) this means

$$\varphi_3 = \varphi_1 - \varphi_2.$$

Thus only two φ's of (7) or (8) are linearly independent which we may choose to be φ_1 and φ_2. It follows further that the independent valence structures correspond to spin wave functions which are *not orthogonal.* The non-observance of this fact has given rise to numerous mistakes in the literature.

It is now quite easy to calculate the interaction energy of such a system of atoms in first order perturbation theory. To each valence structure corresponds a completely antisymmetric unperturbed wave function. We have so many unperturbed degenerate wave functions as are independent valence structures. All we have to do then is to apply the standard procedure of perturbation theory for degenerate states. The non-orthogonality of the φ's gives rise to no difficulty.

The result is expressed in terms of Coulomb and exchange integrals. We only take into account exchanges of two electrons and neglect higher exchanges. This is justified if we are primarily interested in the binding energies. For each pair of atoms a, b there is then a Coulomb integral $-C_{ab}$ and an exchange integral $-A_{ab}$. We have reversed the signs because both are in general negative (thus C_{ab}, $A_{ab} > 0$). We obtain a set of linear equations for so many unknowns as are independent valence structures, and for the unknowns we can take the φ's themselves. Then the negative energy E of the system (= dissociation energy) is determined from the set of equations (for each φ_i):

$$E\,\varphi_i = \sum_{a,b} C_{ab}\,\varphi_i - \sum_{a,b} A_{ab}\,t_{ab}\,\varphi_i\,. \tag{9}$$

The integral A_{ab} is connected with an exchange of 2 electrons of d and b. This exchange is also to be carried out in the spin function φ_i and this is expressed by the operator $t_{ab} \cdot t_{ab}$ acting on φ_i exchanges any two electrons of a and b. The effect can be read off from the valence structure φ_i itself immediately: The starting point (or end point) of each valence dash starting from (or ending in) a has to be interchanged alternatively with each starting or end point beginning or ending in b. A bond $a \rightarrow b$ changes sign. For example, for the 4 hydrogen atoms (7) we have

$$t_{H_1H_2}\,\varphi_2 = -\varphi_2\,,\; t_{H_1H_2}\,\varphi_1 = \varphi_3 = \varphi_1 - \varphi_2.$$

For C_2H_2 (8) we have

$$t_{C_1C_2}\,\varphi_1 = -3\varphi_1 + \varphi_3 = -2\varphi_1 - \varphi_2$$

etc. We see that t_{ab} acting on any φ_i produces a linear combination of all the independent structures φ. Eq. (9) is then a set of linear homogeneous equations with the unknowns φ_i, and the determinant of this must vanish. This yields an algebraic equation for E, the highest root of which corresponds to the molecule.

In this way, for example, formula (2) of § 2 is very easily derived from (7) and (9). We have only to put the interaction integrals $C_{H_1H_4}$, $A_{H_1H_4}$ etc. of the fourth H-atom equal to zero. The same is true for formula (4) of § 3. If $s \neq 0$ it is useful to add a third atom, L say, with no interaction which consumes the resulting spin. For =N–N= the valence structure is then

$$\varphi = \begin{tikzcd} & \mathrm{L} \arrow[dl, shift right] \arrow[dl, shift left] \arrow[dr, shift right] \arrow[dr, shift left] & \\ \mathrm{N} \arrow[rr] & & \mathrm{N} \end{tikzcd}$$

and $t_{\mathrm{NN}}\varphi = -\varphi + 4\varphi$. The addition $+4\varphi$ is due to the interchange of the 2×2 bonds connecting L. Thus $E = C_{\mathrm{NN}} - 3A_{\mathrm{NN}}$ in agreement with (4) § 3, ($s = 2$).

Our method works equally simply in approximation (b). The electrons in the outer shell are treated independently and each electron occupies a one-electron state of the atom. All we have to do is to treat each such one-electron state like a separate "atom" with one electron. NH_3 is a 6-electron problem, formally equivalent with that of 6 interacting hydrogen atoms. Since such problems have been treated extensively in the literature and numerous applications been made we refrain from a more detailed discussion.

6. Binding energies of hydrocarbons

As a more quantitative application we consider the binding energies of the simple hydrocarbons CH_4, C_2H_2, C_2H_4, C_2H_6 and the radicals arising from these by removing one hydrogen atom. As has been explained in § 3 it is a permissible approximation to take only the ^5S-state of carbon into account, provided we confine our attention to the neighbourhood of the potential minimum. It is then, however, clear that E (eq. (9)) is the dissociation energy into excited carbon atoms, and if we wish to obtain the dissociation energy into normal atoms we have to replace E by $E + \nu V$, where $V = 96$ kcal/mole and ν is the number of C-atoms in the molecule. There is no difficulty in solving the equations (9). E is the largest root of an algebraic equation which is of first order for CH_4 (there is only one valence structure with a bond connecting C with each H-atom), of second order for C_2H_2 (the two structures φ_1, φ_2 of (8)) of third and fourth order respectively for C_2H_4 and C_2H_6. For simplicity we may neglect the interaction of non neighbours (although this is not necessary), but the interaction between the H-atoms in CH_4 and within the same CH_3 or CH_2 group must be taken into account. Since the H–H distances are known, the corresponding integrals are also known both from theory and experiment. We have $C_{\mathrm{HH}} + A_{\mathrm{HH}} = 11.5$ kcal (only this combination occurs). In the final formulae then 4 further unknown integrals occur, namely C_{CC}, A_{CC}, C_{CH}, A_{CH}. E appears then as a function of these integrals. In fact it turns out that E depends practically on 3 parameters only, and is, within the range of values that come into question, nearly independent of the ratio $A_{\mathrm{CC}}/A_{\mathrm{CH}}$.

There is little hope of calculating these integrals from the wave functions of the atoms. Instead a semi-empirical method suggests itself. We use 3 of the experimentally known data, for example, the energies of CH_4, C_2H_2 and C_2H_6 to determine the 3 remaining integrals and can then calculate all the other dissociation energies and compare them with the experiments. The result is summarised in the following table (all energies in kcal/mole):

Diss. En.	CH_4	C_2H_2	C_2H_4	C_2H_6	$CH_4 \rightarrow CH_3 + H$	$C_2H_2 \rightarrow C_2H + H$	$C_2H_6 \rightarrow C_2H_5 + H$
Experim.	395	391	541	670	102	121	98
Theoret.	(395)	(391)	546	(670)	105	128	97

The figures in brackets indicate that these are adjusted to fit the experimental data[1] by a suitable choice of the integrals. The agreement is surprisingly good, the error being nowhere greater than 6 %. Presumably some of the higher order effects which we have neglected are embodied in the empirical values of our integrals. The good agreement obtained for the energy of C_2H_4 shows that the theory *accounts very well for the single, double and triple bonds* C–C, C = C, C ≡ C. Furthermore, it accounts well for the observed differences of the dissociation energy of a hydrogen atom in the various compounds. For the latter result the excitation of ^5S and the H–H repulsion is largely responsible.

A few further observations may be made. The energies E are algebraic functions of the integrals and are therefore not additively composed of contributions due to individual bonds, not even, if the H–H interaction (which is quite substantial) and the excitation energy of ^5S are taken into account. (In the published figures of "bond energies" both effects are usually ignored. Such figures have no *physical* meaning.) That the binding energies are not additive follows also from the large differences in the dissociation energy of a hydrogen atom.

Nevertheless a certain approximate additivity obtains. One can calculate the energy required for substituting another atom in place of an H-atom in various compounds. These substitution energies differ only very slightly (1–2 kcal/mole) in the various compounds. Furthermore, the energy of a longer paraffin chain is certainly proportional to its length. It is very probable that the asymptotic value (per chain link) is already reached for rather short chains. HULTHÉN has verified this for a linear chain of hydrogen atoms and found that the energy of a chain of 8 atoms differs by only 5 % from that of an infinitely long chain (per atom).

The spin wave function of the molecule ψ is a linear combination of the valence structures φ_i. This is easily calculated once the energy of the molecule is obtained. It is of some interest because it has a bearing on the connexion with the chemical formula. For CH_4 only one structure exists and this coincides with the chemical formula. For C_2H_2 we find

$$\psi = \varphi_1 + 0.165\,\varphi_2 = 1.165\,\varphi_1 - 0.165\,\varphi_3 \tag{10}$$

(unnormalized) where $\varphi_1 = \mathrm{H{-}C = C{-}H}$, $\varphi_2 = \overline{\mathrm{H\ C = C\ H}}$, $\varphi_3 = \underline{\mathrm{H}\ \overline{\mathrm{C} \equiv \mathrm{C}}}\,\overline{\mathrm{H}}$. It is now very important to realize that φ_2, φ_3 are not orthogonal to φ_1. The coefficient of φ_2 does not therefore represent the probability of finding the structure φ_2 in the molecule. The structures φ_1, φ_2, φ_3 are *not mutually exclusive*, and do not contradict each other. The probability for finding a structure φ_i is given by

$$w_i = (\psi\varphi_i)^2/\psi^2\varphi_i^2. \tag{11}$$

---

[1] The experimental data of the above table are based on a heat of evaporation of diamond of 170 kcal. This seems at present the most likely value but the possibility cannot be excluded that this value is 141 kcal (no other value comes into question). If this should be the case the experimental figures change slightly, but 3 of the theoretical figures can again be adjusted and the agreement of the remaining data is about equally good (the small errors being on the other side). But it should be pointed out that no agreement can be reached if the heat of evaporation of diamond were either substantially larger than 170 or smaller than 140 kcal. Neither is this the case if the excitation energy of ^5S were substantially different from the true value.

It is easy to derive the products $(\varphi_1\varphi_2)$ etc. If $\varphi_1^2=1$, then $(\varphi_1\varphi_2)={}^4/_5$, $\varphi_2^2={}^8/_5$, $(\varphi_1\varphi_3)={}^1/_5$, $\varphi_3^2=1$. Even if the wave function ψ were identical with φ_1 the probability for φ_2 would not vanish. For the wave function (10) we find

$$w_1=0.98,\ w_2=0.60,\ w_3=0.004.$$

It is very satisfactory that the structure which corresponds to the chemical formula has a probability very close to unity and this is quite generally so. Nevertheless, other structures also occur with large probabilities (in the above example φ_2). These also contribute very substantially to the binding energy. It is not enough to calculate the expectation value of the energy for the state φ_1; this would be in striking disagreement with the experimental facts. On the other hand, the valence structure of the chemical formula always plays a dominant role, although it is accompanied by other structures. This provides the *physical* justification for the formulae found and used by chemists since the beginnings of chemistry.

Seminar für theoretische Physik, Universität Zürich.

Tryckt den 3 november 1955

Uppsala 1955. Almqvist & Wiksells Boktryckeri AB

ARKIV FÖR FYSIK Band 10 nr 14

Communicated 25 May 1955 by LISE MEITNER and OSKAR KLEIN

On the theory of the temperature jump in a rarefied gas and its experimental verification

By H. VON UBISCH

With 1 figure in the text

Abstract.—Earlier published measurements by the author on monatomic gases were in disagreement with the classical theory of the temperature jump, whereas those on diatomic gases fitted WEBER's version of this theory. The measurements on monatomic gases however support the more exact theory recently developed by WELANDER, whereas the behaviour of diatomic gases is dubious here. In view of the intricacy of the problem and some other evidence it is felt that improved experimental investigations would be highly desirable.

Fundamentals

The pioneering work on the temperature jump was performed by M. v. SMOLUCHOWSKI back in the 1890's. He showed that if heat is transferred from a wall to a gas, the distribution of temperature resembles that shown in Fig. 1. The temperature jump, $T_w - T'$, is caused by the restriction of the movement of the gas molecules by the boundary and is enlarged by any possible incompleteness of heat exchange during the impact of the molecules with the wall. This prevents the temperature of the gas from ever reaching the wall temperature T_w. The temperature in the gas may follow either a straight line ending up at T', or there may be a bend in this line so that it terminates at T_0. This question is the subject of the present paper.

It is generally assumed that the heat conduction in the gas at a sufficient distance from the wall follows the equation

$$q = K \frac{dT}{dx}, \tag{1}$$

where q is the heat transferred per unit time and unit of cross section, K is the *molar* heat conductivity of the gas and $\frac{dT}{dx}$ is the temperature gradient. The quantity

$$\Delta T = T_w - T'$$

is, by definition, the 'temperature jump'. It should be observed that this is a measurable quantity because it can be found by applying eq. (1) upon the system under investigation.

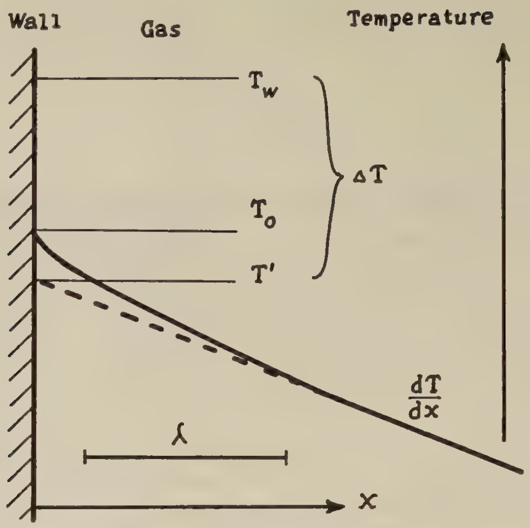

Fig. 1. Temperature distribution near a plane wall. This figure is drawn to scale for argon according to WELANDER's theory.

From the experimental point of view the phenomenon of the temperature jump belongs to the realm of rarefied gases or extremely narrow dimensions, because the possibility of observation requires that the distance between say two parallel walls should be comparable to the magnitude of the mean free path. Rarefying the gas in the system, would result into a decrease of heat transfer equivalent to a recess of each wall of about two times the mean free path, λ in Fig. 1. This can be judged from the figure.

Whereas v. SMOLUCHOWSKI measured the heat transfer, the existence of the jump was demonstrated later by P. LAZAREFF (1912) and by W. MANDELL & J. WEST (1924) by direct measurements of the temperature distribution. There has further been given some indication that the temperature may follow a bent line close to the wall.

The classical theory

The theoretical aim became to correlate ΔT with $\frac{dT}{dx}$ and λ, and as can be seen e.g. from the monography of E. H. KENNARD (1938), the following equation was agreed upon, at least as far as monatomic gases are concerned:

$$\Delta T = \frac{15}{8} \frac{2-a}{a} \lambda \frac{dT}{dx}. \tag{2}$$

Here, the accommodation coefficient a is the quantity which gives the ratio of the actual to the possible maximum energy exchanged by the molecules during the impact with the wall.

This formula is deduced in a somewhat elementary manner, based upon M. KNUD-

SEN's concept of free molecule heat transfer (cf. KENNARD). Using q from eq. (1), one is able to calculate the starting point of the temperature curve on the wall, because the point is given by the mean temperature of the molecules approaching the wall and rebounding from it. The slope of the curve in the immediate vicinity of the wall however, cannot so easily be calculated, and for the sake of simplicity the curve is considered to be straight, as it is far away from the wall.

For polyatomic gases, KENNARD and many others replace the factor $\frac{15}{8}$ in eq. (2) by a quantity which is some 20–30 % smaller, depending upon the gas, whereas S. WEBER (1939, 1942) considers the equation to be directly applicable. Two assumptions are here, in general, involved: (a) The accommodation coefficients for translational and rotational degrees of freedom are identical, or very nearly identical, as follows from an experiment on hydrogen carried out by M. KNUDSEN (1930). (b) The energy is distributed and exchanged independently over all degrees of freedom of the molecule, as assumed by A. EUCKEN.

Eq. (2) has frequently been used to determine accommodation coefficients, as can be seen from KENNARD. However, many cross-checks have not been made with KNUDSEN's formula for free molecule heat transfer (at considerably lower pressures), which offers another possibility of measuring accommodation coefficients.

Measurements on heat transfer

During the course of investigations on hot-wire manometers (v. UBISCH, 1951), extensive and sufficiently accurate measurements on many gases became available, to be used for the check indicated. They covered pressures between 0.1 and 180 mm of mercury which, because of the use of a wire as thin as 0.01 mm within a much wider tube, permitted extrapolation to free molecule heat transfer at lower pressures, and to molar heat conduction at the higher pressures. It was later shown that the apparatus was free from disturbing currents in the gas (v. UBISCH, 1952). Further, the essential points were that the wire temperature was kept constant at a reasonably low value, 9° above that of the tube, and that it was not expected that the lowest pressure of 0.1 mm would induce accommodation coefficients to change due to evaporation of adsorbed gas layers or impurities on the wire. Incidentally, a tungsten wire which was never reconditioned, proved to be constant within 1/1000 during a use of several months. (A platinum wire was inferior.)

The results (cf. p. 389 in the author's 1951 paper) were rather astonishing. Eq. (2) did not fit very well for the monatomic gases such as He, Ne and A, the deviations being identical; but it definitely did fit for the diatomic gases H_2, D_2 (with some reservation concerning the purity), N_2 and O_2. Furthermore it fitted for CH_4 and C_2H_6 reasonably well, whereas the results for CO_2, N_2O and SO_2 were somewhat off the equation. Without any doubt the modified eq. (2), as used by KENNARD for example, was unsuitable, the most critical proof being provided by H_2 and D_2.

This induced the author to contact the theoretical physicists at the University of Stockholm, and eventually the thesis of P. WELANDER (1954 a) was completed.

The theory of Welander

Using the Boltzman diffusion equation in calculating the movements of the molecules near the wall and the resulting temperature distribution, WELANDER could show that the curve should contain a bend and that eq. (2) therefore, should be changed into

$$\Delta T = \frac{75\,\pi}{128}\,\frac{2-k\,a}{a}\,\lambda\,\frac{d\,T}{d\,x}. \tag{3}$$

The first factor, $\frac{75\,\pi}{128}$, is only a more precise estimation of the term $\frac{15}{8}$ in eq. (2), and the small difference is unimportant here. The essentially new feature is the numerical factor k, which has the value 0.827.

WELANDER furthermore supported WEBER's general reasoning concerning the polyatomic gases, which led him to suppose that eq. (3) is valid here too.

It is of interest to compare this improved theory with the measurements at hand. We put WELANDER's k into v. UBISCH's eq. (32) and (33) and find

$$k = \frac{2}{k'}\left(c + \frac{k' - k''}{a}\right),$$

where

$$k' = \frac{15}{4}, \quad k'' = \frac{9\gamma - 5}{\gamma + 1}, \quad \gamma = \frac{c_p}{c_v},$$

and c is a constant introduced by v. UBISCH which can be determined experimentally. Using $\frac{9\gamma-5}{\gamma+1}$ as listed in table IV in that paper and replacing c by experimental values c' taken from fig. 9, a set of values for k, listed as k_1 in Table 1 below, is found:

Table 1. Experimental values for k.

Gas	k_1	k_2	Gas	k_1	k_2
He	0.75	0.88	O_2	1.02	0.94
Ne	0.75	0.68	CH_4	1.02	0.91
A	0.75	0.71	C_2H_6	1.09	1.00
H_2	1.00	0.70	CO_2	0.94	0.91
D_2	0.98	0.27	N_2O	0.76	0.63
N_2	1.02	0.95	SO_2	0.79	0.91

Experimental errors are estimated to be ± 0.07.

Evidently, values of k_1 for the rare gases give considerable support to WELANDER's theory, whereas those for the diatomic gases including CH_4 support eq. (2) and the classical theory, or suggest that there may be some errors in it which happen to cancel out. The relatively low accommodation coefficients found during this investigation for the triatomic gases, if compared with those for the other gases, suggest that their accommodation coefficients for internal energy appear to be fairly low (as pointed out in that paper), and because they thus do not fulfill the requirements of the theory, we will omit them here from further discussion.

Looking for ambiguities in the previous investigation, it appears that instead of

$$k'' = \frac{9\gamma - 5}{\gamma + 1}$$

an experimental value for k'' also listed in table IV could also be used. In effect, this means that in EUCKEN's well-known equation for the molar heat conductivity of gases,

$$K = \frac{9\gamma - 5}{4} c_v \eta,$$

one is exchanging the theoretical value of the constant,

$$\frac{9\gamma - 5}{4},$$

with an empirical value. Since this would change the slope $\frac{dT}{dx}$ in Fig. 1 of this paper, it will have a considerable effect on $T_w - T'$. Eventually, we arrive thus at the values listed under k_2 in Table 1.

It should be mentioned that $k' = k''$ for the rare gases according to theory, and these gases behave fairly simple, so the use of k_2 may not be justified here. Because of the smallness of their accommodation coefficients, the gases H_2, D_2 and also He are not very suitable for determinations of k. This follows from eq. (3), and it should explain the value of $k_2 = 0.27$ found for D_2.

With this in mind, it can be concluded that the values of k_2 for diatomic gases bring these into closer agreement with WELANDER's theory. In general, the theory is supported well enough by Table 1 to warrant renewed and more accurate investigations. A point to look for is a possible systematic difference between the rare gases and the diatomic gases, including the two hydrocarbons as is suggested by Table 1, not to mention the triatomic gases.

WELANDER (1954 b) has also applied his formula upon cylindrical geometry, and he has shown that in an experimental investigation there should be a tendency to arrive at diminished values of k, because of the ratio of mean free path to wire diameter may be far from zero. However, this effect cannot have been instrumental in the evaluation of the measurements cited, because k_1 is found to have the same value for all the rare gases, the range of pressures being identical.

On measurements of the actual temperatures in the gas near the wall

Possibly, this is a better method to explain the problem. In fact, WELANDER made a qualitative check on his formula by means of the measurements in air by LAZAREFF. It may be questioned whether LAZAREFF's investigations were sufficiently accurate and complete for this purpose, because measurements at more suitable pressures (cf. WELANDER) and for other gases for comparison are lacking. Later measurements of MANDELL & WEST suffer from a less fortunate design of the thermocouples used and especially of the geometry of the chamber (cf. WEBER 1939, p. 6–7).

The accommodation coefficients

The equality of the accommodation coefficients for the various degrees of freedom of a molecule has recently been questioned by K. SCHÄFER & K. H. RIGGERT (1953) who used the wire-ribbon method of A. EUCKEN & H. KROME. They found differences of at least 10% for the translational and rotational coefficients of e.g. N_2 and O_2, and a rise to as much as 35% (!) for a difference in temperature of 115° only.

If the rotational accommodation coefficients at walls are smaller, in contrast to coefficients for heat exchange in the gas itself, it is possible that this would result in an increase of $T_w - T_0$, without affecting $T_w - T'$ greatly (cf. Fig. 1), and this should, therefore, straighten the curve slightly.

Conclusion

The existing discrepancies on the temperature jump are really not unduly large, and as far as we can see WELANDER's theory is the best available at the moment. The discrepancies are of the same order of magnitude as those for EUCKEN's formula eq. (5), and are partly associated with that formula.

An attempt should be made to arrive at a substantial improvement through more accurate and more extensive experimental studies. By examining the principles of experiments carried out by LAZAREFF, MANDELL & WEST, v. UBISCH, SCHÄFER & RIGGERT and perhaps also by KNUDSEN a multi-purpose apparatus suggests itself. This would, indeed, make possible the most direct comparison of the results found by the different methods.

Here, provisions should be made to maintain sufficiently large ratios between wires, ribbons and enclosing vessels to allow properly for mean free path phenomena. There should be a careful geometrical design of apparatus to avoid thermomolecular currents. Reasonable lengths of the thinnest possible hot wires can be substituted for thermocouples as detectors, and they must be properly corrected for heat radiation and terminal losses. Modern principles of clean vacuum engineering should be used to make position of parts adjustable from outside during measurements.

The best gases to be investigated would be the rare gases and as many as possible of the diatomic gases, including some light hydrocarbons where vibrational frequencies are probably not yet excited at room temperature.

AB Atomenergi, Physics Department, Stockholm, May 1955.

REFERENCES

KENNARD, E. H., 1938: Kinetic Theory of Gases, esp. Chapter VIII. McGraw-Hill, New York.

KNUDSEN, M., 1930: Radiometerdruck und Akkommodationskoefficient. Ann. der Physik *6*, 129–185.

LAZAREFF, P., 1912: Über den Temperatursprung an der Grenze zwischen Metall und Gas. Ann. der Physik *37*, 233–246.

MANDELL, W. and WEST, J., 1924: On the temperature gradient in gases at various pressures. Proc. Phys. Soc. London *37*, 20–41.

SCHÄFER, K. and RIGGERT, K. H., 1953: Eine neue Methode zur Bestimmung partieller thermischer Akkommodationskoefficienten. Z. f. Elektrochemie *57*, 751–757.

UBISCH, H. v., 1951: On the conduction of heat in rarefied gases and its manometric application, I. Appl. Sci. Res., A *2*, 364–402.

—— 1952: Hot-wire manometers for chemical applications. Anal. Chem. *24*, 931–938, esp. p. 933.

WEBER, S., 1939: Über die Abhängigkeit des Temperatursprunges von dem Akkommodationskoefficienten nebst einigen verwandten Wärmeleitungsproblemen in Gasen. Kgl. Danske Vid. Selsk. Mat.-fys. Medd. *16*, nr 9, 1–37.

—— 1942: Über den Einfluss des Akkommodationskoefficienten auf die Wärmeleitung und Radiometerkraft in Gasen. Ibidem *19*, nr. 11, 1–39.

WELANDER, P., 1954 a: On the temperature jump in a rarefied gas. Arkiv för fysik *7*, nr. 44, 507–553.

—— 1954 b: Heat conduction in a rarefied gas: the cylindrically symmetrical case. Ibidem *7*, nr. 45, 555–564.

Tryckt den 3 november 1955

Uppsala 1955. Almqvist & Wiksells Boktryckeri AB

ARKIV FÖR FYSIK Band 10 nr 15

Communicated 11 May 1955 by ERIK HULTHÉN

A method of indicating wave-numbers in spectrophotometric recording

By BJÖRN-ÅKE KRANTZ and NILS ÅSLUND

With 6 figures in the text

Summary

An account is given of a method for indicating wave-number marks at constant intervals on a graphic recording of a spectrum. The wave-number marking is obtained by utilizing light interference. The marking is free of parallaxes, which has been attained by scanning the spectrum as well as the interference pattern with the same photo-multiplier and by using the same writing tool to record the spectrum and the marks. The signals from the photo-multiplier are separated by electronic means. The marks are obtained as thin vertical lines overlapping the spectrum (Fig. 1).

The method has been checked with the aid of a test apparatus (Fig. 2), and the wave-numbers of some neon lines (discharge tube) have been measured. A prism-spectrograph has been used. The results prove that the same degree of accuracy is obtained with this method as with the conventional photographic method of measuring wave-number, when the same spectrograph is used, but the method applied here enables a more rapid calculation of the wave-numbers. Furthermore, it should be possible to develop the apparatus to be used in combination with a spectrograph of greater dispersion, and this will also be attempted by the authors.

The utilization of light interference to determine wave-numbers in spectrophotometric recording was suggested to us by Professor ERIK HULTHÉN. We also wish to express our gratitude to him for much good advice and valuable help in the course of the work. In connection with the setting up of the optical part of the apparatus, especially the interferometer, we had the help of fil. mag. VILHELM PETTERSSON, for which we may here express our warm thanks.

Generation of the interference pattern. Description of the optical equipment

If a parallel beam of white light enters a Fabry-Perot interferometer at normal incidence only those wave-lengths will pass which fulfil the requirement

$$m\lambda = 2 \cdot d \cdot n$$

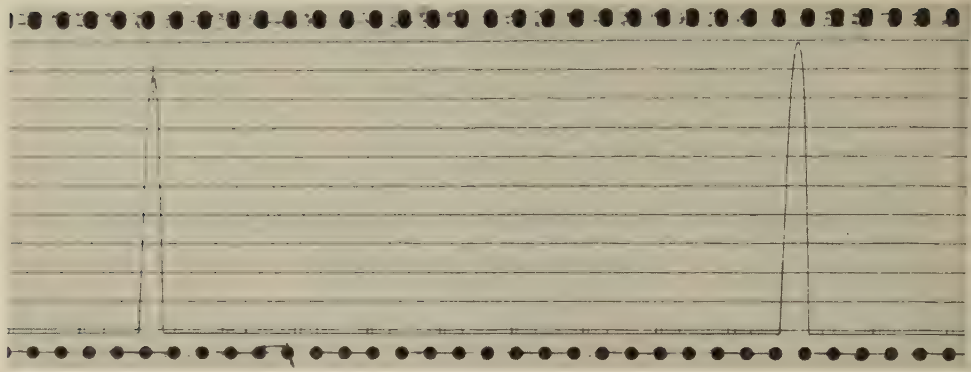

Fig. 1. A recording of two neon lines with wave-number marks. Each mark is threefold, due to discontinuities at the extinction of the glow-discharge tube. The highest mark corresponds to the ignition.

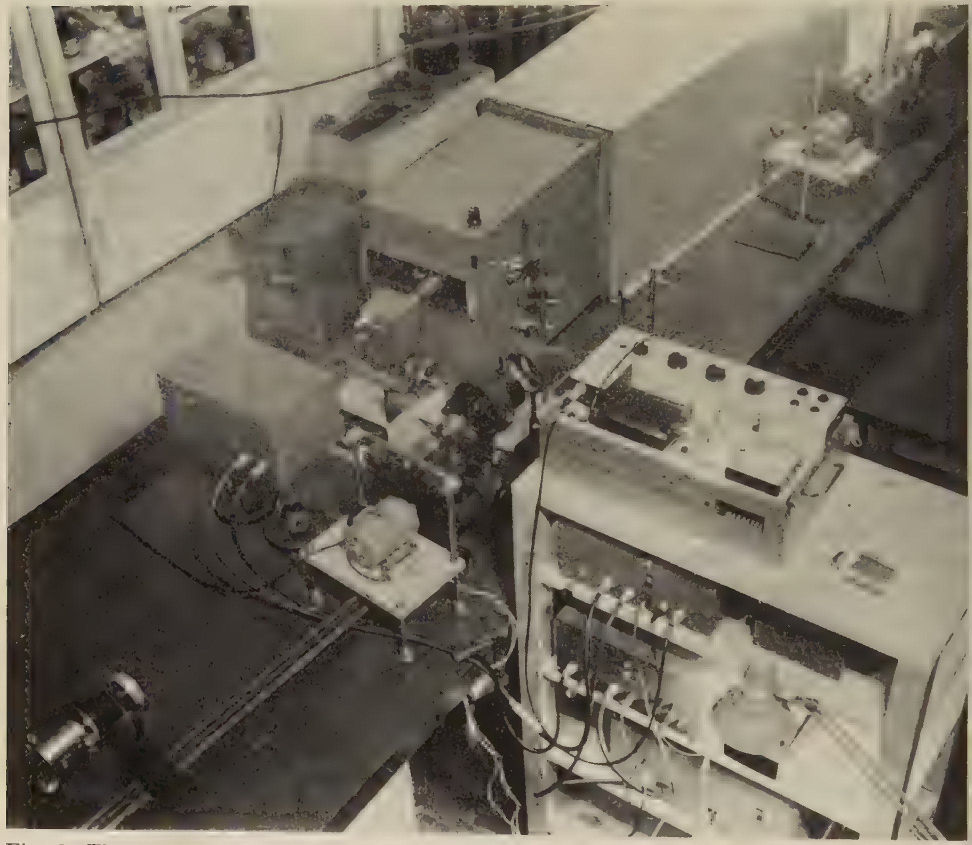

Fig. 2. The test apparatus. The entrance slit of the spectrograph is found in the centre of the picture. To the left there is the interference branch and to the right the spectral branch. The amplifiers and the recorder are found to the right, the photo-multiplier in the centre and the pre-amplifier to the left.

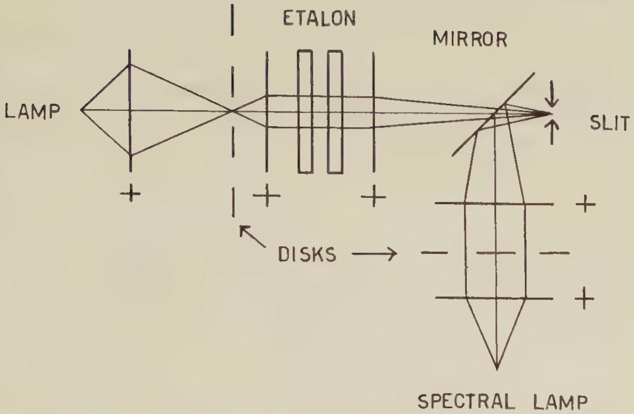

Fig. 3. Schematic diagram of the optical equipment.

i.e.

$$\frac{1}{\lambda}=\sigma=\frac{m}{2\cdot d\cdot n}\ \mathrm{cm}^{-1},$$

where d = separation between the plates of the interferometer and $n=n_{\mathrm{air}}$.

Thus the difference between the wave-numbers of two consecutive orders is a constant and equals $1/(2\cdot d\cdot n)$.

In the present apparatus the generation of interference lines has occurred in the following way.

The white light comes from a Zirconium oxide lamp, which has a continuous spectrum of high intensity (temp. $\cong 3000^\circ$ K). The diameter of the light spot is about 0.7 mm. The light is concentrated by a condenser lens at the focal point of another lens, which sends a parallel beam to the interferometer. The need for a high intensity and a small chromatic aberration necessitates a condenser lens of high quality. A Zeiss Biotar lens, $f=5$ cm, focal ratio 1 : 0.85, has been used. The lens has a variable stop, and thus it is possible to vary the intensity of the interference lines and also to limit the influence of non-parallel rays through the interferometer.

The diameter of the parallel beam through the interferometer is about 1 cm. The beam is focused by a third lens on the entrance slit of the spectrograph. A partly silvered mirror is placed obliquely close to the slit. The light from the interferometer passes through the unsilvered part of the mirror, and through its reflection at the silvered surface the light which is to be spectroscopically analysed also illuminates the slit (Fig. 3).

The prism-spectrograph has the focal lenght 440 cm, the dispersion in the focal plane is 7.7 Å/mm in yellow light. The photo-multiplier (1 P 21) is mounted on a motor-driven carriage, and the slit of the multiplier moves in the focal plane of the spectrograph at a speed of 0.075 mm/s.

The recorder

The investigated spectrum is recorded with an electronic recorder, type Brüel & Kjaer level recorder 2304. The recordings are made on waxed paper and the effective recording width is 50 mm. The recordings may be copied directly on photographic paper.

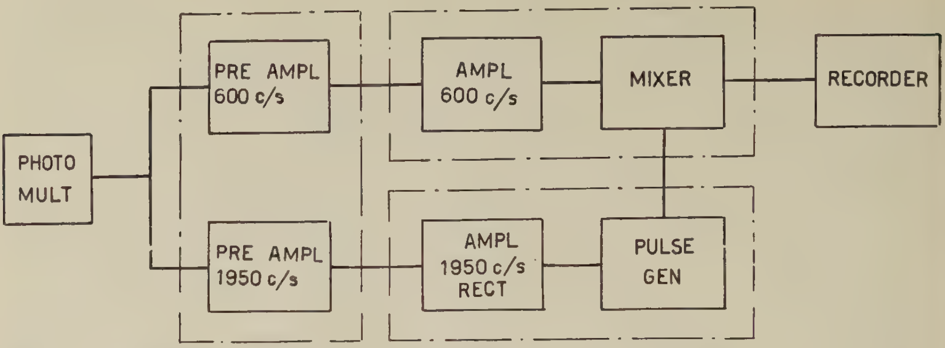

Fig. 4. Block diagram of the electronic equipment. The spectrum branch corresponds to the 600 c/s line.

The recorder is a level recorder, i.e. it records the modulation of a carrier frequency. This frequency has to exceed about 20 c/s and the effective voltage of the signal must exceed about 10 mV to be recorded. The recorder forms a servo system, and the components constituting the closed loop are a resistance bridge, an electronic amplifier and an electromagnetic system with a movable coil which directs the writing tool and also moves the potentiometer slider of the bridge.

The recorder is particularly well-suited to the present purpose thanks to its flexibility as regards damping and frequency-limiting. The writing speed may be made very high (about 1 m/s on the paper), which is valuable when marking the wave-numbers. The speed of the paper may be varied discontinuously from 0.003 mm/s to 100 mm/s, which makes it possible to meet different requirements of accuracy.

The applied variant of the recorder has a logarithmic amplitude scale with the total range 25 db. The following relations hold for the degree of accuracy obtaining when measuring the amplitude.

$$y = k \cdot \log \frac{x}{c}$$

where

x = input voltage
y = deflection on the recorder
k, c = constants.

i.e.

$$\Delta y = k \cdot \frac{\Delta x}{x} \cdot$$

Δy is independent of the size of the deflection ($\Delta y \simeq \pm 0.3$ db) and thus the relative error of amplitude is a constant. Thus it is possible to investigate a broad band of intensities, keeping the same relative accuracy for each determination.

Generation of a carrier

A high carrier frequency is favourable for the functioning of the recorder. A suitable, realizable frequency for the spectrum signal has been found to be 600 c/s. The carrier is introduced into the light beam by means of a rotating disk with

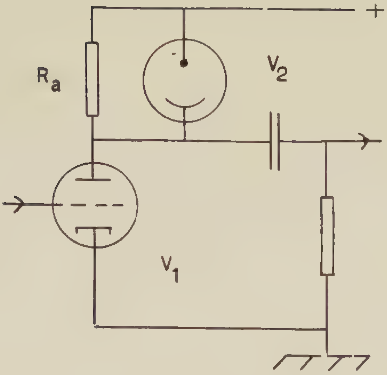

Fig. 5. Principle of pulse generator. $V_1 = 6V6$ (triod), $V_2 = VR–75$.

rectangular cogs. The spectrum light is formed into a parallel beam which illuminates a broad slit (opening about 2 cm^2). Close behind this slit the disk rotates and the slit is successively screened off by the cogs.

The slit has the shape of a half sine-wave. This arrangement gives the carrier the shape of a sine-wave, which is desirable in order to avoid distorting higher harmonics in the electronic equipment. Since the rectangular cogs pass the slit, moving almost rectilinearly (the diameter of the disk is large compared to the dimensions of the slit), the variations of the light flow through the slit and thus also of the intensity of the spectrum lines will be given by the following expression.

$$I = A \int_0^t \sin \omega t \, \mathrm{d}t = A \frac{1 - \cos \omega t}{\omega},$$

where A corresponds to the modulated amplitude.

In a similar way a carrier frequency of 1950 c/s is introduced into the interference light. In this case, however, the slit is rectangular, since there is no danger that the harmonics will disturb the other signal.

The electronic equipment

In the electronic equipment the two signals are separated by band-pass amplifiers. Fig. 5 is a block diagram of the two branches of the band-pass amplifiers.

Each of the amplifiers is divided into two parts, a pre-amplifier mounted close to the photo-multiplier and a main amplifier. The input and output stages of the pre-amplifiers are cathode-followers. This arrangement makes it possible to connect the photo-multiplier, which has a high output impedance, to the main amplifiers by fairly long cables.

The spectrum branch

Both the pre-amplifier and the main amplifier are one-stage, direct-coupled, single-tuned voltage amplifiers, resonance frequency 600 c/s. The effective gain per stage $= 20$ and $Q = 30$.

The interference branch

The pre-amplifier and the main amplifier constitute a staggered tuned pair, resonance frequency = 1950 c/s. The effective gain = 20 per stage and $Q = 30$. It is followed by a push-pull coupled amplifier, gain = 10, which feeds a balanced, bridge-coupled rectifier. The D.C. voltage from this rectifier is filtered by two RC-filters (time constant = 0.2 s). When this filtered voltage reaches a certain definite level it releases the wave-number marking in the following way (Fig. 5). The rectified signal, which is positive, is fed to the grid of the power-triod V_1. When the voltage drop in R_a reaches the ignition voltage of the glow-discharge tube V_2 this tube fires and the voltage falls discontinuously to the operating voltage of V_2. During the subsequent process V_2 is gradually extinguished. Also during the extinction some discontinuities occur, but these do not constitute any serious disturbance. The voltage step is differentiated by an RC-link, which also eliminates the D.C.-voltage. The pulse thus produced is finally mixed with the spectrum signal in a cathode-coupled mixer.

General considerations concerning the separation of two frequencies

The following requirements for the separation have been laid down: (1) minimum mutual influence between the two signals, (2) optimum signal-to-noise ratio (3) minimum distortion of the signals.

(1). For a minimum of mutual influence it is desirable that the band-widths should be as narrow as possible, and that the different signals should be of the same order of magnitude, i.e. the maximum light intensities of the two branches should be of approximately the same size. However, a lower limit of the band-widths is set by the changes in the carrier frequencies caused by changes in the line frequency, due to the fact that the cogged disks are driven by synchronous motors, fed from the power line.

The band-widths have been chosen in such a way that the relative amplification of the rejected signal equals 10^{-3} in each branch. The pass-band is in the case wide enough to allow the changes of the carrier mentioned above.

(2). For band-pass amplification a narrow band is generally desirable for an optimum signal-to-noise ratio.

In the present case the dominating noise consists of noise due to the instability of the light sources and the shot noise of the photo-multiplier. For the shot noise it holds that:

$$\overline{V_n^2} = 2 \cdot e \cdot (\sum i) \cdot M^2 \cdot R^2 \cdot |A|^2 \cdot B_n,$$

where

e = the electron charge
M = the current-amplification of the photo-multiplier
R = the effective input resistance
$\sum i$ = the sum of all currents from the photo-cathode
B_n = the noise band-width, defined as

$$B_n = \int_0^\infty \left|\frac{G}{A}\right|^2 df$$

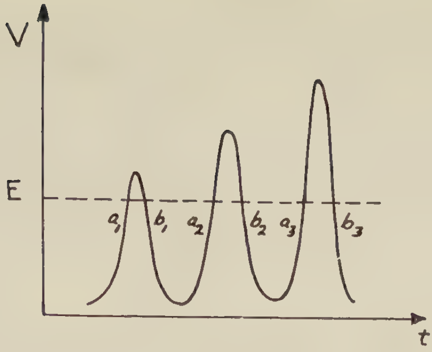

Fig. 6. Voltage variations corresponding to three interference lines of different intensities. E is the voltage level at which the marking is released.

G = the amplification at the frequency f
A = the amplification at resonance.

The signal-to-noise ratio is given by:

$$s_k^2 = \frac{i_k^2}{2\,e\,(\sum i)\,B_n},$$

where i_k is the signal current.

Where a spectrum signal $= 6 \times 10^{14}$ A coincides with an interference signal $= 10^{14}$ A, the actual B_n-values give $s = 100$ in each branch.

(3). A too narrow pass-band will cause a distortion of the line form and thus cause an uncertainty in the positions of the lines and the marks.

An approximate Fourier-analysis of the existing signals has been made in order to determine an optimum band-width. The interference lines are represented by the function:

$$I = \frac{(1-R)^2}{1+R^2-2\,R\cos\omega t} = \frac{1-R}{1+R}\left(1+2\sum_1^\infty R^n \cos n\,\omega\,t\right).$$

R is the reflecting power of the etalon plates, and $\omega = (2\pi)/T$, where T is the time between the passage of two interference lines.

If $\left|\frac{G}{A}\right| \geq 0.99$ for all frequencies, of which the amplitudes are $\geq 1\,\%$ of the fundamental frequency amplitude, the deviation from the true line form is $\leq 1\,\%$, i.e. the line will be approximated by a curve of which the ordinates are within 1 % of the true ones.

The amplifier fulfils this condition, and the test measurements show that no appreciable errors are caused by the distortion.

Method of measurement

Fig. 6 shows the D.C. voltage corresponding to the interference lines. The level E corresponds to the ignition voltage of the glow-discharge tube. If the photomultiplier carriage runs to the right, marks are released at the points a_1, a_2 and

a_3 in the diagram, and if it runs to the left, at the points b_3, b_2 and b_1. The mean positions of these marks, obtained in two separate recordings, give the positions of the interference lines, on the assumption that the light source is constant throughout the two recordings.

Before calculating the wave-number of a spectrum line the wave-number scale must be fixed with two reference lines. The wave-number of the unknown line is then determined by counting the number of marks from one reference line.

For the reading of a recorded spectrum we have used an apparatus consisting of a ground glass-plate illuminated from beneath and equipped with a graduated scale for interpolation.

Results and discussion of the measurements

The operation of the apparatus has been checked by measuring 4 neon lines in the interval 16 279–17 086 cm^{-1}. This interval had an extension of 40 mm in the focal plane of the spectrograph. The interval between two wave-number marks was 20.5 cm^{-1}, and on the recording paper the distance between the marks was about 12.5 mm. The precision with which the top of a spectrum line could be estimated on the paper was about 0.2 mm, equivalent to 0.33 cm^{-1}. In the focal plane this corresponds to 0.017 mm, i.e. an uncertainty which is to be expected in a photographic measurement by this optical equipment.

For the determination of the wave-mumbers the following formula holds:

$$\sigma_x = \sigma_0 + \frac{\sigma_n - \sigma_0}{n} n_x ,$$

where

σ_0 = wave-number of reference line 0
σ_n = ,, ,, ,, ,, ,, n
σ_x = wave-number of the unknown line
n_x = the number of marks between σ_x and σ_0
n = ,, ,, ,, ,, ,, σ_n ,, σ_0.

Differentiation gives:

$$|\Delta \sigma_x| \leq \left| \Delta n_x \frac{\sigma_n - \sigma_0}{n} \right| + \left| \Delta n \frac{\sigma_n - \sigma_0}{n^2} \right| .$$

According to what has been said above,

$$|\Delta n| = |\Delta n_x| = 2 \cdot \frac{0.2}{12.5} = 0.03.$$

Inserted values give

$$|\Delta \sigma_x| \leq 1 \text{ cm}^{-1}.$$

Five double measurements have been made on 4 neon lines (see Table 1), and as reference lines the lines 16 278.5 cm^{-1} and 17 086.7 cm^{-1} have been used. The mean deviation obtained for each line is given in the third column. The greatest error occurring in any measurement was 0.9 cm^{-1}.

Table 1.

International standards		$\|\Delta \sigma_x\|$ cm^{-1}	Remarks
λ_{vacuum} Å	σ_{vacuum} cm^{-1}		
6143.062	16 278.5		reference
6096.163	16 403.8	0.6	
6074.163	16 463.2	0.4	
5944.834	16 821.3	0.1	
5881.896	17 001.3		reference
5852.488	17 086.7	0.3	

REFERENCES

Candler, C., Modern Interferometers. Glasgow 1951.
Etzel U. W., J. Opt. Soc. Am. *43*, 87–90 (1953).
Brodersen, S., J. Opt. Soc. Am. *43*, 1216–20 (1953).

Tryckt den 24 oktober 1955

Uppsala 1955. Almqvist & Wiksells Boktryckeri AB

ARKIV FÖR FYSIK Band 10 nr 16

Communicated 10 March 1954 by MANNE SIEGBAHN and ERIK HULTHÉN

Investigation of the focusing properties of a double directional focusing magnetic spectrometer with conical pole surfaces

By R. PAULI

With 4 figures in the text

1. Introduction

As is well known, a magnetic sector field is double directional focusing if the field strength in the plane of symmetry decreases with increasing radius slower than $1/r$. Different field shapes fulfilling this condition can be used for a double focusing spectrometer, and the determination of which is the best one depends on both practical and principal considerations. HEDGRAN, SIEGBAHN and SVARTHOLM [1] for a large β-spectrometer chose a field shape where $H(r) = k/\sqrt{r}$. In a spectrometer for heavy particles where the maximum field strength must be high if the spectrometer is to be useful for work with nuclear reactions, it is often most economical to use a sector field with larger extension in the radial than in the axial direction, and then the $1/\sqrt{r}$-shape is not necessarily the best choice. For several reasons one may prefer to choose a field whose strength in the symmetry plane varies as

$$H(r) = H_c \frac{r_c + r_1}{r_1 + r}$$

where r_1 and r_c are defined in Fig. 1 and H_c is the field strength at the central radius r_c. This field shape can be realized by using conical pole surfaces, which have advantages from the constructional point of view, and also permits the astigmatism of the field to be changed at will, by simply varying the distance between the pole shoes, which is useful for certain applications [2]. Another advantage is that the spherical aberrations of this field shape are smaller than that of the $1/\sqrt{r}$-field as soon as the radial opening angle is larger than the axial opening angle, which for economical reasons is often the case for a heavy particle spectrometer.

Conical pole surfaces have been used in a large spectrometer for heavy particles built at the Nobel Institute [3, 4] which is used together with a Cockroft-Walton accelerator for investigation of nuclear reactions. Nuclear emulsion plates are used as detectors in the spectrometer, and in order to be able to place them correctly, we have experimentally determined the image plane along which at constant spectrometer current particles of different momenta are focused.

2. Experimental arrangements

Fig. 1 shows a schematic view of the spectrometer. The beam from the high tension set enters horizontally and hits a target at T, which serves as a source for the spectrometer. The sector angle of the pole shoes is 180° but in order to correct for the effect of the fringing fields, the spectrometer is considered as a sector of 191.4° with no fringing fields [4]. The central trajectory which is indicated in Fig. 1 will henceforth be referred to as the central axis. It has a radius of 40.0 cm. The form of the pole faces is strictly conical and the extensions of their surfaces cross each other along a circle of $r_1 = 40.0$ cm radius (see Fig. 1).

The coordinate frames used for definition of source and image positions are shown in Fig. 1. The object position is given by the frame x_1, y_1 with its origin at O_1. The x_1-axis is a continuation of the central axis of the spectrometer (it is a tangent to the central axis). On the image side of the spectrometer the coordinate frame x_2, y_2 is completely analogous to the x_1, y_1-frame on the object side.

The target spot T, Fig. 1, forms the object of the spectrometer and has the coordinates:

$$x_{10} = 29.8 \text{ cm}$$

$$y_{10} = 0 \quad \text{cm}$$

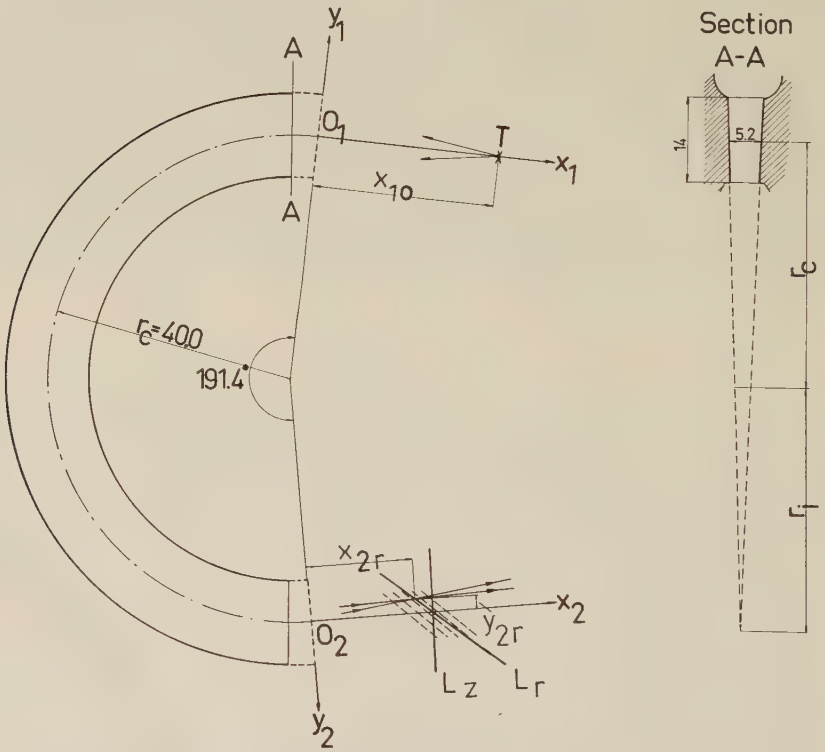

Fig. 1. Schematic view of the spectrometer. L_r and L_z are the radial and axial image loci of a source at T.

On the image side we used a camera in which nuclear plates could be placed in five different positions along the x_2-axis, which are shown with dotted lines in Fig. 1. The solid angle of the spectrometer was about 0.003 sterad.

3. Determination of the shape of spectral lines at different positions of the nuclear track plate

The high energy α-group (8.73 MeV) from ThC′ was used for the investigation. A platinum wire, 0.1 mm in diameter, served as a source. It was activated in the usual way by exposure to thoron gas when its potential was held at -1500 V. After activation, the platinum wire was mounted horizontally in the source position (T) of the spectrometer, and the α-group photographed at five somewhat different field strengths, so that five spectral lines were obtained, which were approximately evenly spaced along the plate. The procedure was repeated at the five possible positions of the plates, described above.

In Fig. 2 we have plotted some of the spectral lines obtained, in order to demonstrate their shapes. Their positions in the image area are shown in Fig. 3 with

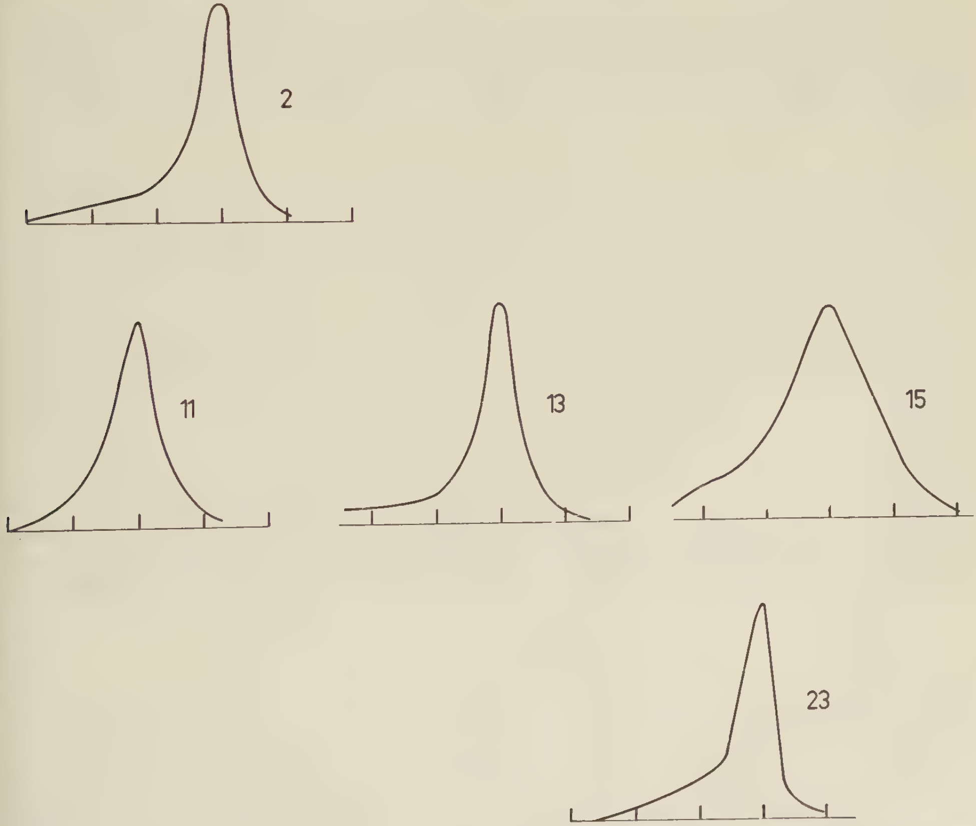

Fig. 2. Line shape at different positions in the image area (compare Fig. 3). Unit of the horizontal scales is $10^{-3} \times H_c r_c$.

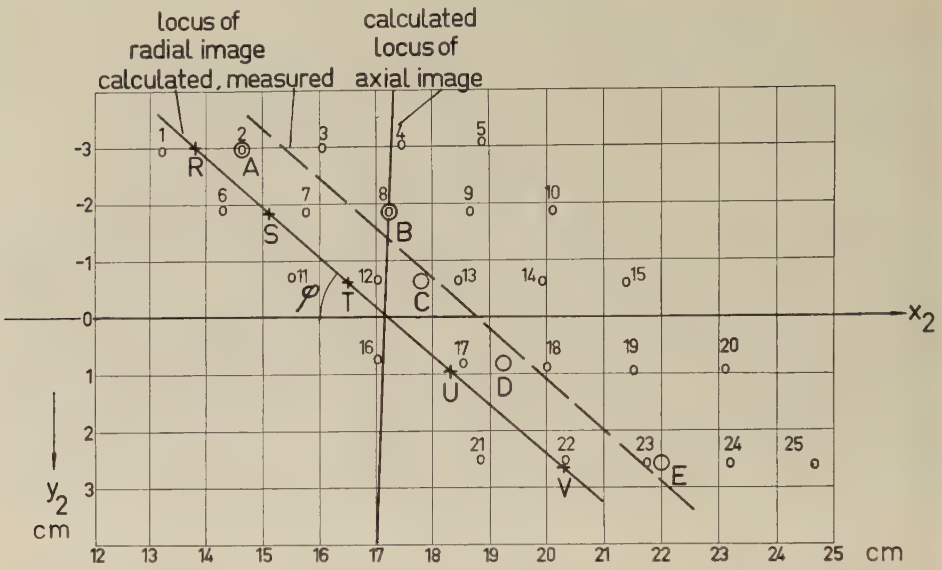

Fig. 3. Enlargement of the image area. Origin of the coordinate frame is shown in Fig. 1.

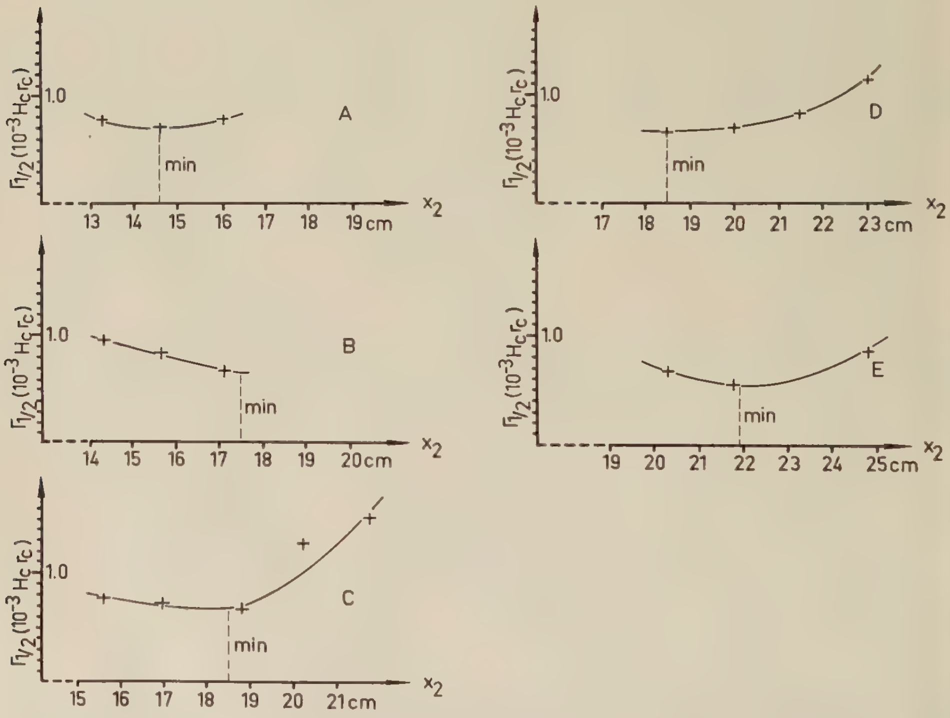

Fig. 4.

numbered circles corresponding to the numbering of the curves in Fig. 2. They all have a tail on the low energy side due to aberration and also to α-particles which have suffered some energy loss in the surface contaminations on the platinum. In the figure all lines are given the same height although the solid angle of the spectrometer was different at different line-positions due to cut off by the aperture of the vacuum chamber used. Line number 23, for example, has only about half the intensity of the other lines. The cut off due to aperture may explain the smaller width of this line compared to the other lines (smaller aberrations).

The spectral lines in Fig. 2 give the distribution of particles *along* the plate and their shapes characterize the focusing properties of the spectrometer in the *radial* direction. The exposed length of the activated platinum wire was only 1.3 mm; thus the distribution of α-particles *across* the plate (in the z-direction) would have shown the focusing properties of the spectrometer in the *axial* direction, but no such investigation was carried out.

4. Best position of the detecting nuclear track plate

At each field strength we obtained three to five spectral lines (all possibilities were not utilized). Their half-widths were measured and the curves A, B, C, D and E in Fig. 4 show the variation of the half-widths along the geometric lines 1–3, 6–8, 11–15, 17–20 and 22–25 of Fig. 3. The widths are given in units of 10^{-3} of $H_c r_c$ (H_c is the magnetic field strength in the symmetry plane at the central axis (see also Fig. 1).

The positions of the minima of the curves in Fig. 4 are indicated in Fig. 3 as points A, B, C, D and E. In order to obtain the best focus (that is the smallest radial widths of the spectral lines) the photographic plate used as a detector in the spectrometer should coincide with a line connecting these five points (see Fig. 3).

From Fig. 4 we see that *the experimental radial half-width* along the focal line ($ABCDE$, Fig. 3) varies between 0.55×10^{-3} and $0.73 \times 10^{-3}\, H_c r_c$. The source width is responsible for $0.06 \times 10^{-3}\, H_c r_c$ and aberrations and variations of the magnet current during exposure for the rest. The current is held constant within ± 0.3 ‰; thus aberrations should give rise to $0.4–0.6 \times 10^{-3}\, H_c r_c$ if widths due to different causes are assumed to add quadratically. If the aberrations are computed from eq. 7 of Ref. 4 for a field shape according to eq. (10), we get a base width of $0.3 \times 10^{-3}\, H_c r_c$ for a spectral line, corresponding to about $0.15 \times 10^{-3}\, H_c r_c$ half-width, at the actual values of the radial (3°) and the axial (3.8°) aperture angles. The observed widths are thus three to four times larger than the theoretical, probably partly explicable by aberrations at the entrance and exit of the spectrometer field.

5. Comparison with theory

It might be interesting to compare the experimental results with the predictions of first order equations given by Svartholm [5] for the movement of charged particles in an inhomogeneous magnetic field. An object at the point $x_1 = x_{10}$, $y_1 = 0$ emitting monoenergetic particles, the momentum of which corresponds to an $H\varrho$-value $= H(r_\varepsilon) \cdot r_\varepsilon$, gives one axial and one radial image, the coordinates of which are determined by the following equations:

$$x_{2r} = \frac{A_r \frac{x_{10}}{r_\varepsilon} + B_r}{C_r \frac{x_{10}}{r_\varepsilon} - A_r} \tag{1}$$

$$y_{2r} = \left(\frac{1}{C_r \frac{x_{10}}{r_\varepsilon} - A_r} + 1 \right) (r_\varepsilon - r_c) \tag{2}$$

$$x_{2z} = \frac{A_z \frac{x_{10}}{r_\varepsilon} + B_z}{C_z \frac{x_{10}}{r_\varepsilon} - A_z} r_\varepsilon \tag{3}$$

where:

$$A_{r,z} = \cos \frac{\pi \phi_0}{\phi_{r,z}} \tag{4}$$

$$B_{r,z} = \frac{\phi_{r,z}}{\pi} \sin \frac{\pi \phi_0}{\phi_{r,z}} \tag{5}$$

$$C_{r,z} = \frac{\pi}{\phi_{r,z}} \sin \frac{\pi \phi_0}{\phi_{r,z}} \tag{6}$$

$$\phi_r = \pi \left[1 + \frac{r_\varepsilon \cdot H'(r_\varepsilon)}{H(r_\varepsilon)} \right]^{-1/2} \tag{7}$$

$$\phi_z = \pi \left[- \frac{r_\varepsilon \cdot H'(r_\varepsilon)}{H(r_\varepsilon)} \right]^{-1/2} \tag{8}$$

and (see also Figs. 1 and 3):

x_{10} = the x_1-coordinate of the object (T). In the present case $x_{10} = 29.8$ cm.
x_{2r} = the x_2-coordinate of the radial image.
x_{2z} = the x_2-coordinate of the axial image.
r_ε = radius of the "optical axis" for the particles considered (see below).
r_c = radius of the central axis. In the present case $r_c = 40.0$ cm.
y_{2r} = the y_2-coordinate of the radial image.
ϕ_r = the focusing angle for the radial image.
ϕ_z = the focusing angle for the axial image.
ϕ_0 = the effective sector angle, $\phi_0 = 191.4°$ in the present case.
$H(r_\varepsilon)$ = magnetic field strength in the symmetry plane at $r = r_\varepsilon$.

The two essential parameters in the equations above are r_ε and $r_\varepsilon \cdot H'(r_\varepsilon)/H(r_\varepsilon)$. The radius r_ε is connected with the $H\varrho$-value of the particles emitted from the source. If this is called $(H\varrho)_\varepsilon$ then r_ε is defined by

$$r_\varepsilon H(r_\varepsilon) = (H\varrho)_\varepsilon .$$

Apparently a circle with the radius r_ε is a possible trajectory, and will have the properties of an optical axis. Therefore r_ε is called the radius of the optical axis for particles with a momentum corresponding to an $H\varrho$-value $= (H\varrho)_\varepsilon$. The second parameter is the so-called n-value of the spectrometer field for particles with $H\varrho$-value $= (H\varrho)_\varepsilon$:

$$n = -\frac{r_\varepsilon \cdot H'(r_\varepsilon)}{H(r_\varepsilon)} \tag{9}$$

and its value determines the focusing properties of the (inhomogeneous) magnetic field for such particles. $H'(r_\varepsilon)$ is the derivative of $H(r_\varepsilon)$ with respect to r at $r = r_\varepsilon$.

If the contours of the cross section of the poleshoes are of parabolic shape, the magnetic field strength can be made to vary with the radius in such a way, that n becomes independent of r_ε, so that n then has the same value for all particles whatever $H\varrho$-value they may have. The optical properties in such a case, with constant n, have been treated by JUDD [6].

In our case, however, the pole faces are conical surfaces (see Fig. 1) and then n is *not* independent of r_ε. Consequently the field has different n-values for particles of different $H\varrho$-values.

If the spectrometer field is to be anastigmatic, the n-value should be $=0.5$. In the present spectrometer the angles of the pole surfaces are chosen so that $r_1 = r_c$ (see Fig. 1) and then $n = 0.5$ for particles having the central axis ($r = r_c$) as their optical axis. For all other particles the spectrometer will be astigmatic. We are primarily interested in determining the locus along which the *radial* image moves when the $H\varrho$-value of the particles is changed at constant field, but we shall also calculate the locus of the *axial* image. (In the former case we have a cross over along an axially directed line, in the latter case along a radially directed line.)

We assume that the magnetic field strength in the symmetry plane of the spectrometer can be written as:

$$H(r) = H_c \frac{r_1 + r_c}{r_1 + r} \tag{10}$$

where $r =$ the radius at which the field strength is measured and H_c is the value of H at the central axis (radius $= r_c$). The meaning of r_1 is clear from Fig. 1 ($r_1 = 40.0$ cm in the present case).

We intend to calculate the trajectories of particles with $H\varrho$-values deviating a small amount from $H_c r_c$. It is then convenient to express the $H\varrho$-value of the particles emitted from the source in the following way:

$$(H\varrho)_\varepsilon = H_c r_c (1 + \varepsilon) \tag{11}$$

where ε is much smaller than 1.

The field strength varies with the radius according to eq. (10) and then it is easily shown that particles with $H\varrho = (H\varrho)_\varepsilon$ have an optical axis with the radius:

$$r_\varepsilon = \frac{r_1 \cdot r_c (1 + \varepsilon)}{r_1 - r_c \cdot \varepsilon} \tag{12}$$

Table 1. Coordinates of radial and axial image. Assumed values of r_1 and r_c 40.0 cm, of x_{10} 29.8 cm and of ϕ_0 191.4°.

ε	-0.020	-0.012	-0.004	0.0062	0.0167
x_{2r} (cm)	13.8	15.1	16.5	18.3	20.3
y_{2r} (cm)	-3.00	-1.84	-0.63	0.96	2.64
x_{2z} (cm)	17.3	17.3	17.2	17.1	17.0

and that

$$H(r_\varepsilon) = H_c \frac{r_1 - r_c \varepsilon}{r_1}.$$

The n-value from eq. (9) becomes:

$$n = -\frac{r_\varepsilon \cdot H'(r_\varepsilon)}{H(r_\varepsilon)} = \frac{r_\varepsilon (1+\varepsilon)}{r_1 + r_c}. \tag{13}$$

By means of eqs. (13), (10) and the eqs. (1) to (8) the coordinates of the images (x_{2r}, y_{2r} and x_{2z}) can be computed for every ε-value.

In our experiment we had particles of given $H\varrho$-value (α-particles from ThC′) and varied the field strength (that is H_c) of the spectrometer, but this had the same effect as if H_c had been kept constant and the velocity of the particles had changed, because the factor which determines the trajectories of the particles is the ratio $(1+\varepsilon)$ of the $H\varrho$-value of the particles to $H_c r_c$. If we assume that the spectrometer field strength is proportional to the current i_ε in the exciting coils, we have:

$$(1+\varepsilon) = \frac{i_c}{i_\varepsilon} \tag{14}$$

where i_c is the current in the coils at which $H_c r_c$ is equal to the $H\varrho$-value of the α-particles from ThC′. From the measured values of the current in our experiments we have used eq. (14) to calculate the corresponding ε-values and hence the image coordinates (from eqs. (1) to (8) and also eq. (13)). The result is shown in Table 1.

In Fig. 3 the calculated coordinates of the radial images are indicated by the points R to V, the coordinates of the axial images by M to Q. Although one cannot expect that the loci of the images shall be straight lines, Fig. 3 shows that the deviation from that shape is small.

The agreement between the calculated and measured image loci of the radial images is satisfactory. The lines are parallel and only 1.5 cm apart. This difference indicates that the effective sector angle of the field probably is somewhat smaller than 191.4°.

In order to extend the usefulness of eqs. (1) and (2) we have also calculated the derivatives of x_{2r} and y_{2r} with respect to ε. The derivatives show how the images are displaced when the particle energy is changed with the field unchanged, and are valid for a sector field where the pole-faces are conical surfaces. (The derivative of x_{2r} is given for $\varepsilon = 0$ only.) The ratio dy_{2r}/dx_{2r} at $\varepsilon = 0$ gives the tangent of the angle φ between the image locus and the extended central axis (see Fig. 3).

$$\left(\frac{d\,x_{2r}}{d\,\varepsilon}\right)_{\varepsilon=0} = \frac{\dfrac{x_{10}^2\,\phi_0}{2\,(r_1+r_c)} + \dfrac{x_{10}\,(r_1+r_c)}{r_1} + \dfrac{\phi_0\,r_c^2}{2\,r_1} + \dfrac{r_c\,x_{10}}{r_1}\sin^2\left(\dfrac{r_1}{r_1+r_c}\right)^{1/2}\cdot\phi_0 + \dfrac{1}{2}\left(\dfrac{x_{10}^2}{r_1^{1/2}\,(r_1+r_c)^{1/2}} - \dfrac{r_c^2\,(r_1+r_c)^{1/2}}{r_1^{3/2}}\right)\sin\left(\dfrac{r_1}{r_1+r_c}\right)\cdot\phi_0\cdot\cos\left(\dfrac{r_1}{r_1+r_c}\right)^{1/2}\cdot\phi_0}{\left[\dfrac{x_{10}\,r_1^{1/2}}{(r_1+r_z)^{1/2}\,r_c}\sin\left(\dfrac{r_1}{r_1+r_c}\right)^{1/2}\cdot\phi_0 - \cos\left(\dfrac{r_1}{r_1+r_c}\right)^{1/2}\cdot\phi_0\right]^2} +$$

$$+ \frac{\dfrac{(r_1+r_c)\,x_{10}}{r_1}\cos\left(\dfrac{r_1}{r_1+r_c}\right)^{1/2}\cdot\phi_0 + \dfrac{r_c\,(r_1+r_c)^{3/2}}{r_1^{3/2}}\sin\left(\dfrac{r_1}{x_1+r_c}\right)^{1/2}\cdot\phi_0}{\dfrac{x_{10}\cdot r_1^{1/2}}{(r_1+r_c)^{1/2}\,r_c}\sin\left(\dfrac{r_1}{r_1+r_c}\right)^{1/2}\cdot\phi_0 - \cos\left(\dfrac{r_1}{r_1+r_c}\right)^{1/2}\cdot\phi_0} \qquad (15)$$

and

$$\frac{d\,y_{2r}}{d\,\varepsilon} = \frac{r_1\,r_c\,(r_1+r_c)}{(r_1-r_c\,\varepsilon)^2}\cdot$$

$$\left[\frac{1}{\dfrac{x_{10}\,(r_1-r_c\,\varepsilon)^{3/2}}{r_c\cdot r_1\,(r_1+r_c)^{1/2}\,(1+\varepsilon)}\sin\left(\dfrac{r_1-r_c\,\varepsilon}{r_1+r_c}\right)^{1/2}\cdot\phi_0 - \cos\left(\dfrac{r_1-r_c\,\varepsilon}{r_1+r_c}\right)^{1/2}\cdot\phi_0} + 1\right] +$$

$$+\,\varepsilon\cdot\frac{r_c^2\cdot(r_1+r_c)^{3/2}}{(r_1-r_c\,\varepsilon)^{3/2}}\cdot\frac{\left(\dfrac{x_{10}\cdot(r_1-r_c\,\varepsilon)\cdot(2\,r_1+3\,r_c+r_c\,\varepsilon)}{r_c^2\cdot r_1\cdot(r_1+r_c)\cdot(1+\varepsilon)^2\cdot 2} + \dfrac{\phi_0}{2\,(r_1+r_c)}\right)\cdot\left(\sin\left(\dfrac{r_1-r_c\,\varepsilon}{r_1+r_c}\right)^{1/2}\cdot\phi_0 + \dfrac{x_{10}\,(r_1-r_c\,\varepsilon)^{3/2}\cdot\phi_0}{2\,r_c\,r_1\,(r_1+r_c)^{3/2}\,(1+\varepsilon)}\cos\left(\dfrac{r_1-r_c\,\varepsilon}{r_1+r_c}\right)^{1/2}\cdot\phi_0\right)}{\left[\dfrac{x_{10}\,(r_1-r_c\,\varepsilon)^{3/2}}{r_c\,r_1\,(r_1+r_c)^{1/2}\,(1+\varepsilon)}\sin\left(\dfrac{r_1-r_c\,\varepsilon}{r_1+r_c}\right)^{1/2}\cdot\phi_0 - \cos\left(\dfrac{r_1-r_c\,\varepsilon}{r_1+r_c}\right)^{1/2}\cdot\phi_0\right]^2} \qquad (16)$$

$$\operatorname{tg}\,\psi = \left(\frac{d\,y_{2r}}{d\,\varepsilon}\Big/\frac{d\,x_{2r}}{d\,\varepsilon}\right)_{\varepsilon=0} \qquad (17)$$

The dispersion D is defined by:

$$D = \frac{d\,y_{2r}}{r_c}\cdot\frac{H_c\,r_c}{d\,(H\,\varrho)_\varepsilon}\cdot\frac{1}{\sin\,\varphi} = \frac{d\,y_{2r}}{d\,\varepsilon}\cdot\frac{1}{r_c\,\sin\,\varphi}. \qquad (18)$$

We see from eq. (16) that D increases only slowly with ε. The calculated D-values for different ε-values are shown in Table 2.

A comparison of the calculated image positions R to V in Fig. 3 and the corresponding experimentally determined image positions A to E, Fig. 3, shows that calculated

Table 2.

$r_1 = r_c = 40.0$ cm, $x_{10} = 29.8$ cm $\varphi = 41°$.

ε	-0.02	0.00	0.02
D	5.50	5.85	6.24

and experimentally determined dispersion agree within 2 %. The discrepancy can be explained by (1) uncertainty in the experimental determination of the position of an image, and (2) by the fact that the spectrometer field strength is not exactly proportional to the exciting current but changes somewhat slower than the current because of the iron in the magnetic circuit, so that the real change in field strength was smaller than was assumed in the calculation of the positions of the points R to V.

6. The case $n = 0.57$

Mileikowsky [2] has proposed the use of astigmatic two-directional focusing as a means of eliminating line broadening caused by the angular energy spread among the particles emitted from nuclear reactions induced by beam bombardment. According to the same author one simple way to achieve astigmatism is to alter the ratio r_c/r_1 (Fig. 1) from the value 1 (which gives anastigmatism for particles with the central axis as their optical axis) to some other value. Mileikowsky proposes $r_c H_c'/H_c = -0.57$ as a suitable value and according to eq. (13) this corresponds to $r_c/r_1 = 0.57/0.43$.

We shall calculate the image loci for this case. We assume $r_c = 40.0$ cm and $r_1 = 40.(43/57) = 40.0.7544$. The air gap at $r = r_c$ is assumed to be the same as before, thus the fringing field around the central axis is the same as in the case $r_c = r_1$ and the effective sector angle still $= 191.4°$.

In Table 3 we have given the results of the calculations of the loci of the radial and axial images of objects situated at $x_{10} = 29.8$ cm, $y_{10} = 0.0$ cm for the three cases where the $H\varrho$-value of the focused particles is 1.02 $H_c r_c$, 1.00 $H_c r_c$ and 0.98 $H_c r_c$. The values of the dispersion D are also given. The equations (1) to (8) and (10), (13), (16) and (18) were used.

Table 3.

$r_1 = 0.7544\ r_c$ cm, $r_c = 40.0$ cm, $x_{10} = 29.8$ cm, $\phi_0 = 191.4°$, $\varphi = 31.4°$.

$(H\varrho)_\varepsilon$	0.98 $H^c rc$	1.00 $H_c r_c$	1.02 $H_c r_c$
ε	-0.02	0.00	0.02
x_{2r} (cm)	27.2	33.1	39.7
y_{2r} (cm)	-3.62	0.00	3.95
x_{2z} (cm)	5.9	5.7	5.4
D	8.16	9.03	9.98

7. Summary

The focusing properties of a large double directional focusing spectrometer for heavy particles built at the Nobel Institute have been investigated. The spectrometer uses a 180° sector field and the pole surfaces are conical, so that the field strength in the symmetry plane varies as $H(r) = H_c \frac{2 r_c}{r_c + r}$, where r_c is the mean radius of the sector and H_c the field strength at $r = r_c$. A field of this shape is double focusing but not exactly anastigmatic, and a point source will give one radial line image (axially directed) and one axial line image (radially directed). At a given spectrometer current particles of different momenta emitted from a point source on the central axis of the spectrometer will be focused radially along one surface (the radial image locus) and axially along another surface (the axial image locus) and these two surfaces intersect at the central axis. This axis consists of a part of the mean circle and the two tangents to this circle at the borders of the field.

In the present investigation the position of the radial image locus was experimentally determined. It was found to be approximately a plane inclined at an angle φ to the central axis, φ in the present case being 41°. The position of the locus was also calculated from first order equations and the agreement between calculations and measurements was good. The value of φ, the angle between spectrometer axis and axial image locus was calculated to be 93°.

The widths of spectral lines formed by monoenergetic particles emitted from a source of negligible width was experimentally determined and found to be three to four times larger than predicted from theory for a sector field of so large an angle that both source and image are within the field. The larger widths might be ascribed to aberrations at the entrance and exit of the actual sector field and also to energy spread among particles from the source.

Finally we used first order equations to calculate the image loci and radial dispersion for a magnetic sector field with conical pole faces where the angles between them had been chosen to give $r_c H'_c / H_c = -0.57$. (In the spectrometer investigated above the corresponding value was -0.50.)

This field shape is deliberately astigmatic and has been proposed by MILEIKOWSKY [2] in order to eliminate the broadening of spectral lines caused by the angular energy spread among particles emitted from nuclear reactions induced by particle bombardment.

REFERENCES

1. A. HEDGRAN, K. SIEGBAHN, and N. SVARTHOLM, Proc. Phys. Soc. *63*, 960 (1950).
2. C. MILEIKOWSKY, Ark. f. Fys. Bd *7*, nr 5, 57 (1953).
3. C. MILEIKOWSKY, Ark. f. Fys. Bd *4*, nr 16, 337 (1952).
4. C. MILEIKOWSKY, Ark. f. Fys. Bd *7*, nr 3, 33 (1953).
5. N. SVARTHOLM, Ark. f. Fys. Bd *2*, nr 14, 115 (1949).
6. D. L. JUDD, Rev. of Sci. Instr. Vol. *21*, No. 3, 213 (1950).

Tryckt den 24 oktober 1955

Uppsala 1955. Almqvist & Wiksells Boktryckeri AB

ARKIV FÖR FYSIK Band 10 nr 17

Read 1 June 1955

On density fluctuations in solids and liquids

By G. **Borelius** and A. **Sandin**

With 4 figures in the text

1. Introduction

In a recent paper [1] one of the present authors showed how by interpreting fusion as part of a structural transition beginning in the solid and continuing in the liquid state, it is possible to explain the existence of a lower limit of supercooling and to connect the thermal expansion with the increase of internal energy. In a second paper [2] it was shown that this structural transformation could be described as an order–disorder transition on the assumption that the thermal movements of the atoms with increasing temperature open up an increasing number of new sites for the atoms. It was also pointed out that the large number of new sites required to account for the great increase in structural entropy on one side and the relatively small increase in volume on the other, was inconsistent with the assumption that the new sites should be vacancies in the lattice. The mechanism was assumed to be density fluctuations causing local expansion of the crystal lattice, the influence of which on the macroscopically observable thermal expansion is largely compensated by local contractions. In the present paper we shall give a more quantitative treatment of the density fluctuations and deduce simple relationships between the change of volume with pressure, the ratio of increase in energy and volume at low temperatures, and the ratio of increase of energy and volume at the melting point. We shall also compare these relationships with the experimental data available in the literature.

The paper has been planned and written by Borelius. The study of the literature and the numerical treatment of experimental data for the tables were done by Sandin.

2. Introduction of two compressibility parameters

Thanks to extensive measurements by **Bridgman**, the variations of volume with pressure are known particularly for a large number of pure metals. As an example the fully drawn line in Fig. 1 gives the pressure as a function of the atomic volume for potassium at 20°C. From measurements at somewhat different temperatures the positions of curves for other temperatures are known only qualitatively, as for instance the dotted curve for absolute zero introduced in the figure.

So far no simple general formula has been found describing all these curves, i.e. we have no simple equation of state for solids. The relationships between variations of pressure p and volume V are mostly described for limited ranges of pressure by broken expansions of the form

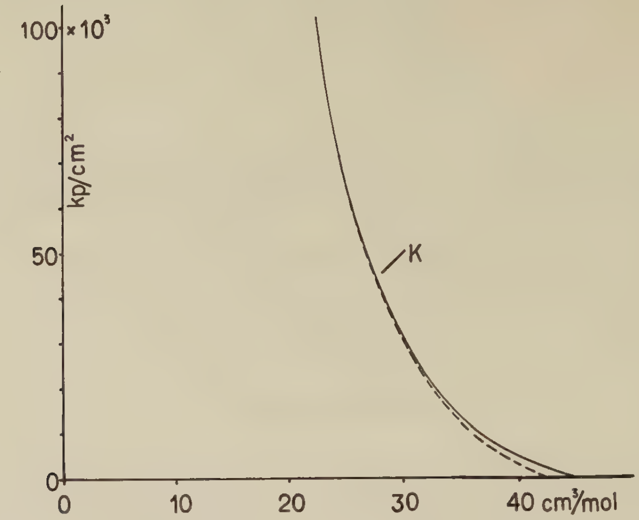

Fig. 1. Pressure versus volume for potassium.

$$\Delta V = a_1 \Delta p + a_2 (\Delta p)^2 \tag{1}$$

or

$$\Delta p = b_1 \Delta V + b_2 (\Delta V)^2 \tag{2}$$

with two mathematical relations between the four parameters. Two of these suffice to describe the properties of the solid near the initial state $\Delta p = \Delta V = 0$, properties which are a function of the values of the independent variables p and T in this initial state. The phenomenologic treatment of the solid state on this basis has been carried out in a comprehensive way by SLATER [3].

We have found, however, that a hyperbolic approximation of the form

$$(\Delta p + \alpha)(\Delta V + \beta) = \alpha\beta \tag{3}$$

allows a better adaption to the experimental isothermals than the parabolic approximation given by equations (1) and (2). Though the two parameters α and β are also functions of p and T, they can be treated as approximately constant over much wider ranges of pressure and temperature. The hyperbolic expression also offers certain mathematical advantages, which will be clear from the following. We shall denote the parameter α as pressure parameter and β as volume parameter. The parameter β, the value of which is also dependent on the mass considered, will be referred to one gram atom. In order to illustrate the possibilities of determining α and β from experimental results, we derive from eq. (3) the equations

$$\frac{2}{\alpha} = -\frac{d\left(\frac{dV}{dp}\right)}{dV} \tag{4}$$

and

$$\beta = -\alpha \frac{d V}{d p}. \tag{5}$$

From (5) we see that the compressibility coefficient $\varkappa$ near the initial state, $\Delta p = \Delta V = 0$, is given by

$$\varkappa = -\frac{1}{V}\frac{d V}{d p} = \frac{1}{V}\frac{\beta}{\alpha}. \tag{6}$$

Thus compressibility measurements give the ratio β/α, usually with an uncertainty of the order of a few percent. The determination of α and β separately implies measurements over a wide range of pressure, and even the best series of measurements give uncertainties of the order of tens percent. Erroneously high or low values of α give errors in the same direction also for β. For small variations Δp and ΔV the relations between α and β and the constants of the traditional equations (1) and (2) are given by

$$\alpha = -\frac{a_1}{a_2} = \frac{b_1^2}{b_2} \tag{7}$$

and

$$\beta = \frac{a_1^2}{a_2} = -\frac{b_1}{b_2}. \tag{8}$$

3. Changes of energy and volume by density fluctuations

We consider the fluctuations of a group of neighbouring atoms being a very small fraction f of a gram atom of a substance obeying equation (3). For the sake of simplicity we assume the parameters α and β to be constant. A change in volume $f \Delta V$ will then cause a change in pressure

$$\Delta p = \frac{\alpha}{1 + \dfrac{\Delta V}{\beta}} - \alpha. \tag{9}$$

According to the theory of fluctuations developed by EINSTEIN and SMOLUCHOWSKI [4] the probability of a concentration fluctuation is dependent on the increase in potential energy

$$\Delta u = -f \int_0^{\Delta V} \Delta p \, d(\Delta V). \tag{10}$$

Inserting the value of Δp from (9) and integrating, we obtain

$$\Delta U = \frac{\Delta u}{f} = \alpha\beta \left[\frac{\Delta V}{\beta} - \ln\left(1 + \frac{\Delta V}{\beta}\right)\right] \tag{11}$$

where ΔU is the potential energy converted to one gram atom. Fig. 2 shows $\Delta U/\alpha\beta$ as a function of $\Delta V/\beta$. As, according to the theory, for a group of atoms, two states

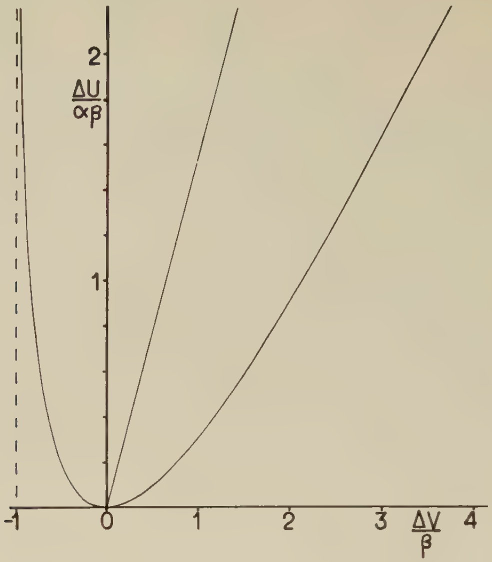

Fig. 2. Potential energy versus change of volume.

with positive and negative changes of volume respectively causing the same increase in potential energy will have the same probability, the average increase in energy $\overline{\Delta U}$ will be related to the average increase in volume $\overline{\Delta V}$ by the median to the two branches of the curve in Fig. 2. The equation of this median, in the range of variations of interest in our case, is given with very good approximation by

$$\frac{\overline{\Delta U}}{\alpha\beta} = \frac{3}{2}\,\frac{\overline{\Delta V}}{\beta} \tag{12}$$

which has been simply verified by a graphical test. This gives

$$\frac{\overline{\Delta U}}{\overline{\Delta V}} = \frac{3}{2}\alpha. \tag{13}$$

4. Experimental test of the theory and determination of the pressure parameter α

For a test of equation (13) we can compute values of $\Delta U/\Delta V$, on the one hand from measurements at low temperatures and on the other from measurements at the melting point. These values can be compared with each other and with values of α obtained from compressibility measurements.

In the first place we apply equation (13) to the density fluctuations caused by the lattice vibrations which dominate the increase of internal energy of solids at low temperatures and give the contribution to the specific heat described by the DEBYE formula. As U in equation (13) means potential energy and the total vibrational energy U_D is assumed to contain equal parts of kinetic and potential energy, we have to insert $U_D/2$ for U in this equation. If α_0 denotes the value of α for practically zero pressure, we obtain

$$\frac{3}{2}\alpha_0 = \frac{\Delta U_D}{2\,\Delta V}. \tag{14}$$

Inserting $\Delta U_D = C_D \Delta T$, where C_D is the vibrational (Debye) part of the atomic heat, and $\Delta V = \varepsilon V_r \Delta T$, where ε denotes the thermal volume expansion coefficient and V_r the atomic volume at the reference temperature used for the definition of $\varepsilon = dV/V_r\,dt$, we obtain

$$\alpha_0 = \frac{C_D}{3\,\varepsilon V_r} \quad \text{for} \quad T \to 0. \tag{15}$$

As found by GRÜNEISEN [5] the ratio of C_D to ε with decreasing temperature approaches a constant value, in the literature often denoted as Q_0. This means that α_0 also is constant. From experimental data collected from low temperature measurements by NIX and MACNAIR [6] we have calculated the values of $\Delta U/\Delta V$ for some metals with cubic lattices. Our choice of examples is limited by the fact that reliable values for the expansion coefficient at low temperatures seem so far only available for cubic metals, which have the same expansion in all directions of the crystal. For the alkali metals there are so far no measurements on thermal expansion at sufficiently low temperatures. The results obtained by equation (15) for α_0 in technical atmospheres (kp/cm²) are given in the first column of Table 1.

In the second place we apply equation (13) to the phenomenon of fusion. As in the earlier papers (1, 2) we assume fusion to be caused by increasing density fluctuations and the heat of fusion to be an increase of structural, that is potential, energy. We then have

$$\alpha = \frac{2}{3}\,\frac{\Delta U_f}{\Delta V_f} \tag{16}$$

Table 1. Pressure parameter α_0 at $p = 0$ in kp/cm².

	α_0 from eq. (14) $T \to 0$	α_0 from eq. (16) $T = T_m$	α_0 from eq. (4) Room temp.
Li	—	74×10^3	50×10^3
Na	—	29	23
K	—	14	14
Rb	—	10	9
Cs	—	8	5
Cu	240×10^3	280	300
Ag	150	180	210
Au	210	160	(210)
Al	120	110	—
Pb	61	51	74

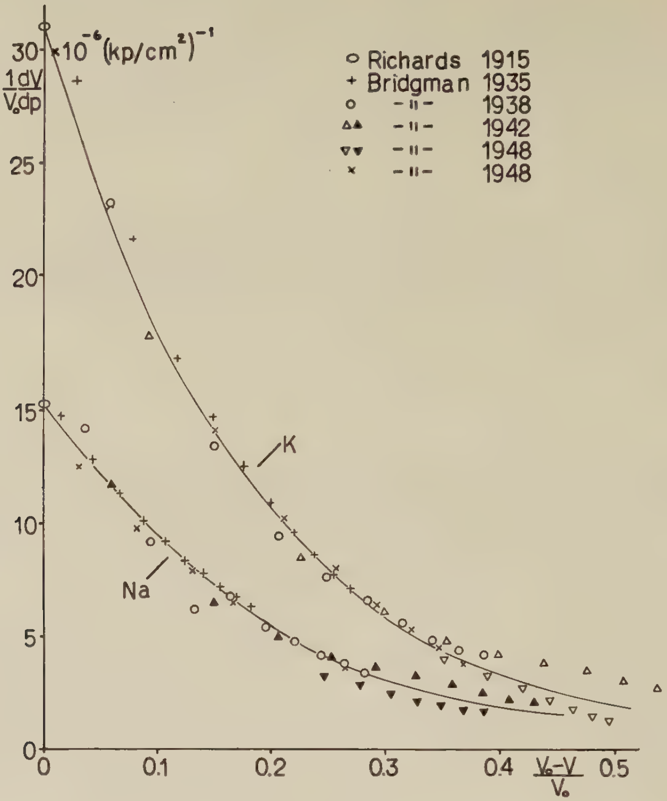

Fig. 3. Compressibility coefficient versus decrease of volume for sodium and potassium.

where ΔU_f and ΔV_f are the differences of atomic internal energy and atomic volume between liquid and solid at the melting point. $\Delta U_f/\Delta V_f$ can be obtained either from measurements of the latent heat of fusion, i.e. the change of entalpy ΔH, and the change of volume by the equation

$$\frac{\Delta U_f}{\Delta V_f} = \frac{\Delta H_f}{\Delta V_f} - p \tag{17}$$

or from the Clapeyron formula

$$\frac{\Delta U_f}{\Delta V_f} = T_m \frac{dp}{dT_m} - p \tag{18}$$

where T_m °K is the melting point at the equilibrium pressure p.

The values of α_0 for $p = 0$ inserted in the second column of Table 1 are obtained for Cu, Ag, Au, Al and Pb by means of equation (17) from data on ΔV_f and ΔU_f critically chosen from literature by KUBASCHEWSKI [7, 8] and for the alkali metals

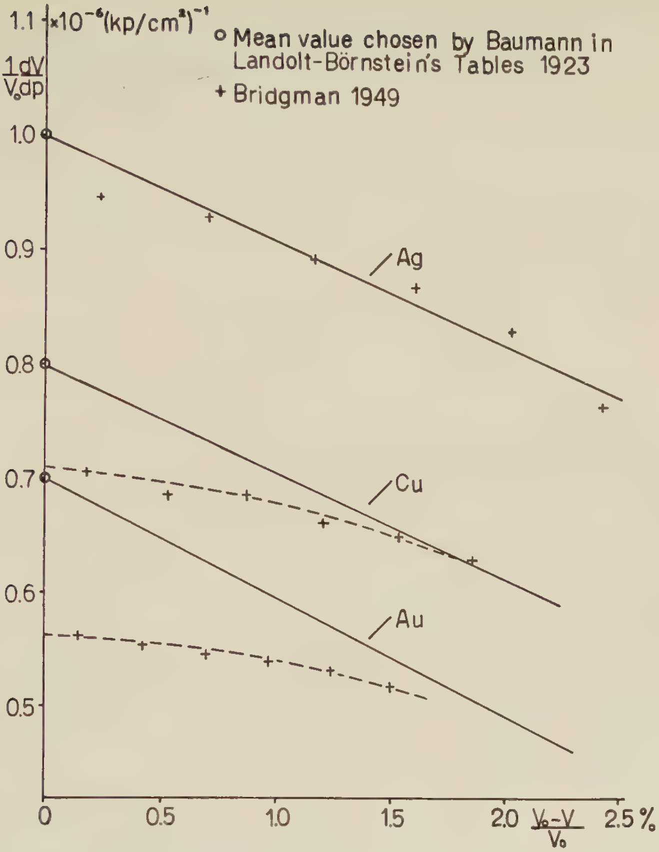

Fig. 4. Compressibility coefficient versus decrease of volume for copper, silver and gold.

by means of the Clapeyron formula from results of measurements by Bridgman on Na and K [9], Li [10], Rb and Cs [11].

In the third place we have calculated values for α_0 directly from compressibility measurements arranged as plots of the compressibility coefficient $\varkappa = dV/V_0dp$ against the relative decrease of volume $(V_0 - V)/V_0$ using equation (4). This calculation requires a rather high accuracy of the measurements over a wide range of pressure. We are for this purpose dependent on the investigations of Bridgman [12–18]. For the highly compressible alkali metals Cs, Rb, K, and Na, Bridgman's results are just accurate enough for a rough calculation and agree for $p = 0$ with earlier results of Richards [19]. For the less compressible metals Li, Cu, Ag, Au, Al, Pb, the measurements of Bridgman, whose methods are directed towards measurements at high pressures, seem to be less accurate for low pressures, a fact that was also pointed out by Bridgman himself. His results in the range where the decrease of volume is less than one or two percent are not always in agreement with the results obtained by other authors using low pressure methods. In these cases we have had to combine values of dV/V_0dp for high pressures from Bridgman's

Table 2. Pressure parameter α in kp/cm^2.

	Pressure in kp/cm^2	α from eq. (14) $T = T_m$	α from eq. (4) Room temp.
Na	0	29 000	23 000
	4 000	38 000	32 000
	8 000	47 000	40 000
	12 000	58 000	49 000
K	0	14 000	14 000
	4 000	25 000	20 000
	8 000	36 000	27 000
	12 000	51 000	34 000

measurements with values for low pressures taken from the critical survey of BAUMANN in the tables of LANDOLT-BÖRNSTEIN [20].

Fig. 3 shows the plots od dV/V_0dp against $(V_0 - V)/V_0$ for the most favourable cases, K and Na. We see that even in these cases the slopes, which we need for our calculation of α according to equation (4), are highly varying for the different series of measurements. We have used the slopes of the graphically smoothed curve. The errors may well be $\pm 20\,\%$ or more. The values of α_0 obtained from the initial slopes are inserted in column 3 of Table 1.

Fig. 4 shows plots of the same kind for the very difficult cases of Cu, Ag, and Au, where the changes in volume are only a few percent. The best thing to do in order to determine the initial slope is to draw a line connecting the results from the low pressure measurements with the results of BRIDGMAN for high pressures. The corresponding values for α_0 are given in the table.

In the case of Al there are two series of measurements by BRIDGMAN [17 and 18] which differ so widely that it is not possible to use them even in this way.

With regard to the fact that the mean values of α_0 vary, from Cu to Cs, in a ratio of 40:1 and to the uncertainty of the experimental results available, it is rather encouraging for the theory that the values in the three columns of Table 1, obtained in three independent ways, agree as well as they do. The largest deviations from the mean values found for Li, Cs, Au, and Pb, are about $\pm 20\,\%$. It is also worth of consideration that even from a theoretical point of view we cannot expect full agreement since we have treated α and β as fully independent of p and T which is allowed only in a first approximation.

For Na and K BRIDGMAN's results also allow a comparison of α-values for higher pressures obtained from the variations of the melting point by means of the Clapeyron formula and from the compressibility measurements respectively. The two sets of α are given in Table 2. The agreement is also in this case within the limits of the experimental uncertainty.

5. Determination and discussion of the volume parameter β

The parameter β is a sort of measure of the free part of the atomic volume V, that is the space not occupied by the rigid centres of the atoms. For our purpose the ratio β/V is more instructive than β itself. According to equation (6) which may be written

Table 3. Ratio of volume parameter β to volume V calculated by eq. [19] from compressibility coefficient $\varkappa$ and pressure parameter α.

	$\varkappa_0$ (kp/cm²)⁻¹	α_0 kp/cm²	$\frac{\beta_0}{V_0}$
Li	8.8×10^{-6}	74×10^3	0.65
Na	15	29	0.43
K	31	14	0.43
Rb	51	10	0.51
Cs	60	8	0.48
Cu	0.8	280	0.22
Ag	1.0	180	0.18
Au	0.7	160	0.11
Al	1.4	110	0.15
Pb	2.5	51	0.13

$$\frac{\beta}{V} = \alpha \varkappa \tag{19}$$

this ratio is obtained as the product of the pressure parameter α and the compressibility coefficient $\varkappa$. In order to calculate β/V we use the α-values for zero pressure obtained from melting data given in the second column in Table 1, which are probably those obtained with the best experimental accuracy, and the $\varkappa$-values for zero pressure already used for our determination of α_0 from compressibility measurements. Table 3 contains these values of α_0 and $\varkappa_0$ and the calculated values for β_0/V_0. It is interesting to observe that they deviate in both directions from the free fraction of volume of an arrangement of close-packed spheres, which is 0.26.

Another point of special interest is the order of magnitude of the free space opened up by the fluctuations. For a brief orientation we may consider Pb in the states just below and above the melting point. The increase in volume $\Delta V/V_0$ above that at absolute zero is 5.0 and 8.0 % respectively. The free volume β/V is 0.13 so that the average increase in free volume, $\Delta V/\beta$, is 0.38 and 0.65 respectively. In Fig. 2 the points on the median for $\Delta V/\beta = 0.38$ and 0.65 correspond to points on the positive branch of the energy curve with $\Delta V/\beta = 1.5$ and 2.3. This means that the half of the lattice which at a certain moment is expanded, has an average increase of the free volume as compared with that at absolute zero of 150 and 230 % respectively. This surprisingly high increase of the average volume of the one half of the lattice is balanced against a decrease of the other half annihilating on an average 70 and 85 % respectively of the free volume.

6. Concluding remarks

We have seen how a discussion of the density fluctuations in a simple way enables us to connect experimental results on the volume changes due to thermal dilatation, fusion and compression.

Another step towards a further development of the theory might be a discussion of the distribution function of the fluctuations and the probability for a large widening of the space for varying groups of neighbouring atoms. It may be possible in this way to estimate the number of new sites opened for the atoms and to account for the increase in structural entropy. It is interesting to remark that the increase in number of sites of the liquid as compared with the number of sites at absolute zero, that is the number of atoms, obtained from the calculations in the earlier papers [1, 2], is of the same order of 100 % as the increase in free volume.

Probably the way over an advanced fluctuation theory will also be the best way to attack such fundamental problems for the microscopic dynamics of solids as the spontaneous formation of dislocations, and of the vacancies, the existence of which is assumed for the explanation of the Kirkendall effect.

Stockholm, Physics Department, Royal Institute of Technology.

REFERENCES

1. G. Borelius, Arkiv f. Fysik *6*, 191 (1953).
2. —— Arkiv f. Fysik *6*, 207 (1953).
3. J. C. Slater, Introd. to Chem. Physics, 199 (1939).
4. M. v. Smoluchowski, Ann. Physik *25*, 105 (1908).
5. E. Grüneisen, Ann. Physik *26*, 211 (1908); *39*, 286 (1912).
6. F. C. Nix and D. MacNair, Phys. Rev. *60*, 597 (1941) and *61*, 75 (1942).
7. O. Kubaschewski, Trans. Faraday Soc. *45*, 934 (1949).
8. —— Z. Metallkunde *41*, 445 (1950).
9. P. W. Bridgman, Phys. Rev. *6*, 32 (1915).
10. —— Proc. Amer. Acad. *56*, 61 (1921).
11. —— Proc. Amer. Acad. *60*, 396, 403 (1925).
12. —— Proc. Amer. Acad. *58*, 180–206 (1923) and *70*, 313 (1935).
13. —— Proc. Amer. Acad. *60*, 401, 410 (1925).
14. —— Proc. Amer. Acad. *70*, 71 (1935).
15. —— Proc. Amer. Acad. *72*, 214, 221 (1938).
16. —— Proc. Amer. Acad. *74*, 434 (1942).
17. —— Proc. Amer. Acad. *76*, 4, 61, 75 (1948).
18. —— Proc. Amer. Acad. *77*, 199 (1949).
19. T. W. Richards, Journ. Amer. Chem. Soc. *37*, 1643 (1915).
20. Baumann in Landolt-Börnstein's Tables Hauptwerk, 80 (1923).

Tryckt den 24 oktober 1955

Uppsala 1955. Almqvist & Wiksells Boktryckeri AB

ARKIV FÖR FYSIK Band 10 nr 18

Communicated 1 June 1955 by G. Borelius and Erik Rudberg

Isothermal measurements on the release of energy stored in cold-worked aluminium

By H. U. Åström

With 5 figures in the text

1. Summary

The release of energy from room-temperature compressed high-purity aluminium bolts has been investigated in the temperature range 70 to 350°C by isothermal calorimetric measurements. The apparatuses were a Borelius type of micro-calorimeter.

At the lowest temperatures used, recovery was obtained in the specimens. By applying somewhat different formal equations for recovery suggested by Kuhlmann, Masing and Raffelsieper, and by Borelius, it is found that the equation of Borelius gives the best agreement with the experimental results. The energy of activation calculated from this equation is 27000 cal/mole.

At successively raised temperatures without renewed cold-work of the specimens, a second stage in the annealing process appears, which is distinctly separated in temperature from the recovery. From microscopic investigation it is found to depend on changes in the substructure of the metal which may be due to subgrain growth and polygonization. The experimentally determined energy of activation for this stage is 36000 cal/mole.

At about 350°C primary recrystallization was obtained in the specimens. The energy of activation for this stage is determined to 58000 cal/mole. The measurements indicate that the subgrain changes must advance to a certain point before the recrystallization process starts.

The influence of small amounts of impurities on the relaxation processes is briefly discussed.

2. Introduction

When a metal is cold-worked energy is stored in the metal structure. It was shown by Quinney and Taylor (1) in 1934 that this energy is only a smaller part of the total energy used in the cold-working process. The theoretical interpretation of the effect is the increase of the number of lattice imperfections in the metal on account of the deformation. The stored energy will, however, gradually be given off when the temperature is raised as the cold-worked state is thermodynamically unstable relative to the unstrained state. There seem to be three different processes, by which the fully annealed state may be approached. The one appearing at the lowest temperature range is called recovery. It does not imply any interface migration on a scale detectable by present methods, in contrast to the second process, which affects the substructure. At increasing temperature, the latter state changes to recrystallization and gradual grain growth, whereby the substructure in the metal is wiped out and the cold-working energy remaining in the lattice after the two first processes is given off completely. The existence of the second stage has not been made clear until in the last decade, but the other processes have been known for many years. A good review of theories and experimental results up to present time was recently given by BECK (2).

The relaxation of cold-worked metals as a function of temperature and time has been studied by various resistivity, magnetic, microscopic and calorimetric methods. In the present work the change of the internal energy with time and temperature of deformed high-purity aluminium has been studied by an isothermal calorimetric method. Isothermal measurements of the same kind have previously been reported by BORELIUS (3) and BORELIUS, BERGLUND and SJÖBERG (4) on recovery in some metals at 60 and 100°C. The measurements have now been extended over a larger range of temperature, from 70° to 350°C, in order to obtain all three relaxation stages. As a complement to the calorimetric investigation some microscopic work about the changes in the substructure was made.

3. Calorimetric method and measurements

The calorimetric apparatus was in principle the same as used in earlier investigations with the Borelius type of isothermal micro-calorimeter (5, 6). It consists essentially of a vapour thermostat providing an extremely constant temperature environment to a chamber containing specimen and measuring cell. The latter is a very sensitive differential thermopile consisting of a number of thermocouples, one set of junctions kept at constant temperature by thermal contact with the wall of the chamber, and the other set made to vary with the temperature of the sample. When the metal relaxes, heat is evolved in the sample causing a rise in its temperature, which is measured by following the difference in temperature across the measuring cell as a function of time. Absolute values of the heat liberated were obtained by calibrating the apparatus with a known amount of Peltier heat, evolved in the junction of a thermocouple located in an axial hole in the specimens. Owing to the small evolutions of heat connected with the annealing processes in a cold-worked metal (for recovery 0.001–0.03 calories per mole and hour), a lot of precautions must be taken to eliminate or reduce disturbing effects. These are discussed briefly in (4). For measuring temperatures from 70 to 100°C water was used as boiling liquid in the thermostats. At higher temperatures other substances must be chosen on which several claims must be placed besides their having a convenient boiling point. The following substances were used: bromobenzene 120–150°C, naphthalene 180–215°C, biphenyl 225–250°C and mercury about 350°C. There were five different thermostats and five different measuring devices operating.

The specimens were prepared from bars of polycrystalline aluminium. Two somewhat different degrees of purity have been used, the one in the following denoted *A* having the composition: < 0.002 % Cu, 0.0035 % Si, < 0.001 % Mg, and 0.0084 % Fe, and the one denoted *B*: < 0.002 % Cu, 0.0046 % Si, and 0.0048 % Fe. Most measurements were performed with aluminium *A* and where in the following no special note is made, this sort of aluminium was used. From the bars which had a diameter of about 15 mm, samples about 70 mm long were cut, in which a small axial hole was made for the junction of the thermocouple used for the Peltier calibration. Before cold-working, the samples were annealed and relatively slowly cooled down to room temperature. The grain size was about the same in *A* and *B* after this annealing.

The plastic deformation was made as compression at room temperature of the samples in a steel cylinder of convenient internal diameter in order to get samples, which after deformation filled up the space in the measuring cell as well as possible. This form of cold-working, however, does not give a homogeneous deformation of the specimen. Especially at the ends there will be too low a deformation compared with that in the rest of the bolts. In order to diminish this end effect we have placed the specimens between cylinders of high-purity aluminium during the deformation, whereby the flow in the end surface of the sample was made easier. For small and medium deformations it is to be expected that in this way the cold-working is more homogeneous. The compression was carried out very slowly in order to avoid rise of temperature in the specimens.

4. Calorimetric results

The release of stored energy from deformed aluminium was studied by isothermal measurements at successively raised temperatures from 70°C up to 350°C without renewed cold-work of the samples. As a check that no disturbing effects influenced the results after the main measurements at each temperature were completed, a dummy series was made at the same temperature and as far as possible under similar conditions. Samples of medium and high degrees of cold-work have been examined in this way. With increasing temperature they gave different types of rate of energy versus time curves. For the lowest temperatures, below 100°C, hyperbolic curves were obtained in agreement with BORELIUS *et al.* (4). Between 180°C and 250°C, however, the measurements gave an exponential relation between rate of energy and time. At the highest measuring temperatures used, about 350°C, exponential curves were also obtained but now there appeared a maximum of a form typical for a nuclea- and growth process. The energies released in measurements on highly and moderately deformed samples are given in Tables 1, 2, and 3. The values of Table 1 are also shown in a staple diagram (Fig. 1). The energy values have been obtained by graphical integration of the corrected measuring curves. As the first 20 minutes of each experiment were lost due to disturbances, the extrapolation of the curves to zero time might introduce an uncertainty of some percent in the values of the energies. In Fig. 1 the relative Brinell hardness values, measured on the surface of the specimen have also been plotted. No hardness determinations have, however, been made at the lowest temperatures, as it was feared that the plastic deformation under the Brinell ball would too much influence the energy values obtained at these temperatures. As can be seen from the figure, the hardness is practically constant up to 350°C, where a marked decrease occurs. Annealing at still higher temperatures produces only a slow further fall of the hardness curves. It was expected from this decrease at 350°C and the maximum form of the corresponding calorimetric curve that there was a primary recrystallization process in the metal at this temperature, which was also verified by microscopic examination. A further proof that we had to do with primary recrystallization was given by the magnitude of the energy of activation, mentioned in the following, which was quite in line with earlier deter-

Table 1. Results of calorimetric measurements. Aluminium *A*. 45 % compressed specimen.

Measuring temp. °C	Energy released cal/mole	Type of curve	Time const. h
73.0	0.86	Hyperbolic	
97.7	—		
130.4	—		
151.0	—		
182.9	1.20	Exponential	5.2
215.5	0.46	,,	3.3
250.1	0.56	,,	2.5
352.5	4.2	Max.-Exp.	3.3

Table 2. Aluminium *A*. 9 % compressed specimen.

Measuring temp. °C	Energy released cal/mole	Type of curve	Time const. h
73.2	0.26	Hyperbolic	
97.9	0.70	,,	
131.1	—		
151.5	—		
183.1	—		
215.2	—		
249.8	0.20	Exponential	1.5
352.8	2.0	Max.-Exp.	2.4

Table 3. Aluminium *A*. Spec. 1, 36.2 % compressed; spec. 2, 36.7 % compressed.

Measuring temp. °C		Energy released cal/mole	Type of curve	Time const. h
Spec. 1	182.7	0.40	Exponential	7.50
	353.0	4.5	Max.-Exp.	3.36
Spec. 2	205.0	0.30	Exponential	1.18
	346.7	3.1	Max.-Exp.	5.47

minations. At 353°C a number of recrystallization measurements were made on specimens with almost the same degree of cold-work (about 36 %) but with different pre-annealings and purities. Some of the curves have been plotted in Fig. 2 and will be discussed in sections 8 and 9.

Of the two other stages in the calorimetric series the first one is due to recovery and the second may be due to changes of some kind in the substructure, an assumption which we have tried to test by microscopic work (see section 5). The experimental results show, however, that these two stages are distinctly separate, as there

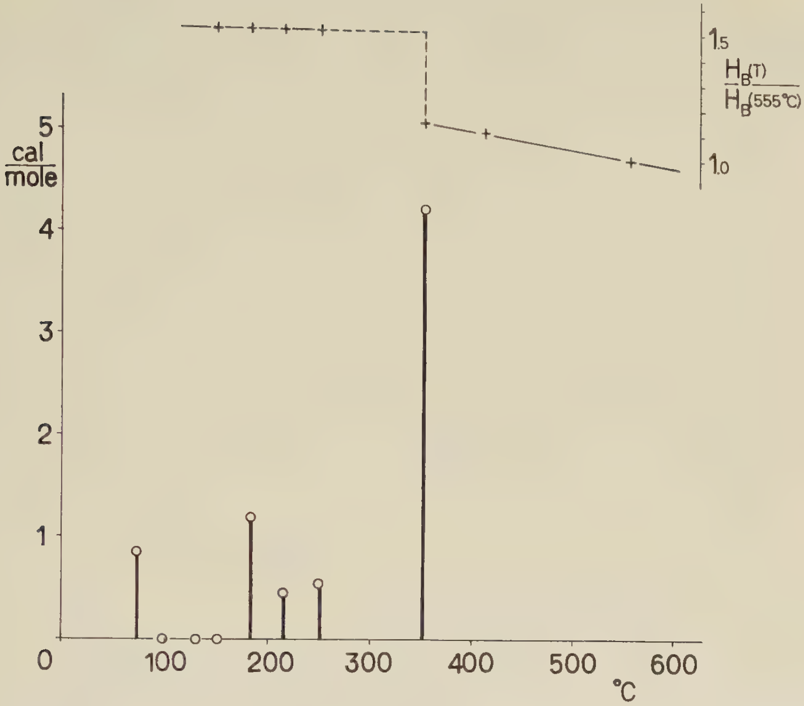

Fig. 1. Energy released by heat treatment of 45 % compressed high purity aluminium (cf. Table 1) and the corresponding relative hardness values.

are calorimetric measurements at temperatures between them with practically no evolution of heat. The transition from the second stage in the annealing process to recrystallization is probably more continuous (Fig. 1), and it is questionable whether the energies at 215° and 250° should be included in the substructure effect or not. As regards recovery, we measure of course at 70° and 100°C, only the last stages of this effect since it is known that not even very low temperatures are able to prevent a partial recovery from occurring during or immediately after the cold-working.

In order to obtain experimental information about the activation energies for the subgrain effect and the recrystallization, comparative measurements at different temperatures on two similar specimens were made (Table 3). The samples had been cold-worked in almost the same way and aged at 100°C to get rid of recovery. Measurements on the subgrain effect were made at 182.7° and 205.0°C. From the time constants of the exponential rate of energy curves an activation energy of 36000 calories per mole was calculated. Both specimens were then aged at 205°C to obtain equal initial conditions for recrystallization, which was then studied at 346.7° and 353.0°C. The time constants of the exponential curves obtained gave in this case an energy of activation of about 58000 calories per mole.

The hyperbolic relation between rate of energy evolved and time is valid exactly only for medium and large deformations. At very slight cold-working, deviations from this relation appear. As it seems possible to obtain valuable information about the

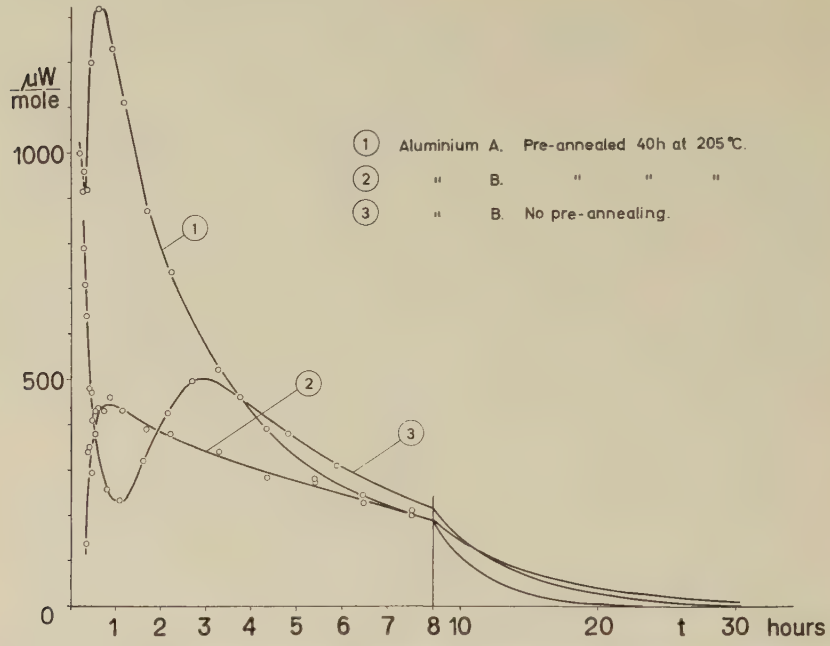

Fig. 2. Rate of energy versus time for primary recrystallization at 353°C in three high purity aluminium specimens deformed to the same degree (about 36 %).

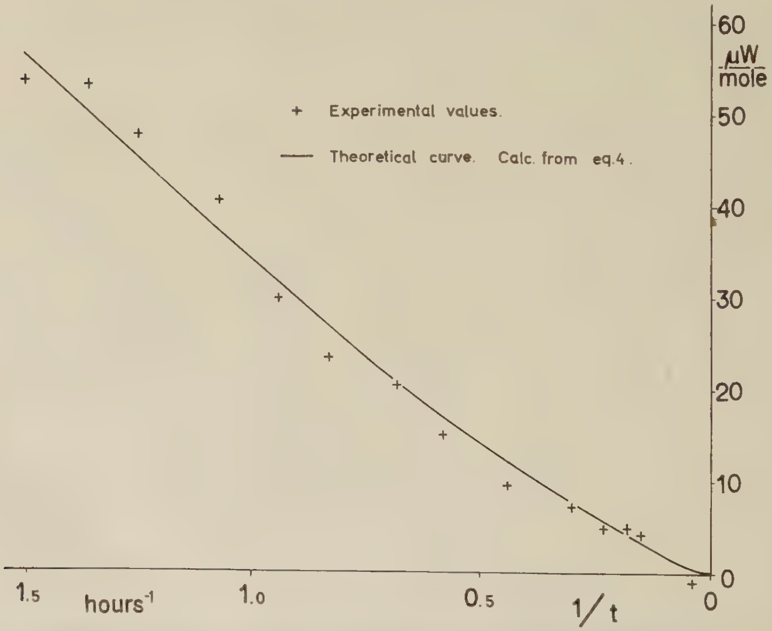

Fig. 3. Rate of energy versus the reciprocal of the time for a slightly deformed high purity aluminium specimen measured at 98°C.

kinetics of the recovery effect from this condition, some measurements were made at 70° and 100°C with very slightly deformed specimens. The results from such a measurement are plotted in Fig. 3, where the rate of energy is given as a function of the reciprocal of the time.

5. Microscopic investigation

For this part of the work a technique was needed which made it possible to study the approximate orientation of slip bands and crystallites at high magnifications. Most suitable appeared to be a method used among others by BECK and HU (7). When the samples had been electrolytically polished, they were oxidized anodically to produce a thin fine-grained oxide film on the polished surface, giving in polarized light under crossed nicols strong colour effects which were sensitive to rather small differences in orientation of the aluminium subgrains.

The specimens were prepared from aluminium A, and cold-worked in almost the same way as the calorimetric specimen in Table 1, but now a new sample was used for each annealing temperature. After deformation the cylinders were cut lengthwise (under intense cooling to avoid disturbing heating effects), and the layer which had been affected by the cutting, was removed by repeated polishing and etching. The specimens were annealed at various temperatures for times corresponding to the measurements in the thermostat. Figs. 4 a and 4 b show a specimen after cold-work. The deformed grains contain a lot of elongated continuous areas, sometimes almost parallel to each other, but without any visible structure inside or between them. These areas were thought to be an effect of the slip processes in the grains. The distance between the bands as well as their breadth were about 5 μ. After annealing at 180° and 250° (Figs. 5 a and 5 b) the banded appearance of the grains had partially or almost completely disappeared and been followed by a large number of small areas of a size from 3 μ to 7 μ. In polarized light the areas appeared in slightly varying shades of the dominating colour, and it was rather difficult to obtain a good reproduction of them on the photographic plates. These results are similar to those recently shown by PERRYMAN (8).

After annealing at 350°C, the specimens were recrystallized and the substructures had been wiped out.

6. Discussion of the recovery

In order to interpret the results obtained, we need a theoretical picture of what happens to the metal structure during cold-working and on subsequent annealing. It seems probable (9, 10) that the plastic deformation of polycrystalline face-centered metals generally involves a certain fragmentation due to fine slip in the region between the "coarse" or visible slip lines or bands. In the slip lines there may be groups of dislocations created by coarse slip and piled up against barriers of some sort. On account of the piled-up groups the blocks will be strained. The number of dislocations, n, in the groups and the distance between them, l, are determined from the degree of cold-working. At recovery n decreases but l probably remains constant. After thermal activation the dislocations may leave the piled-up groups by gliding in their slip planes (KUHLMANN (11)) or by climbing out of their slip planes (MOTT (12)). By dissolution of the dislocations the strain diminishes, however, with practically no influence on the substructure.

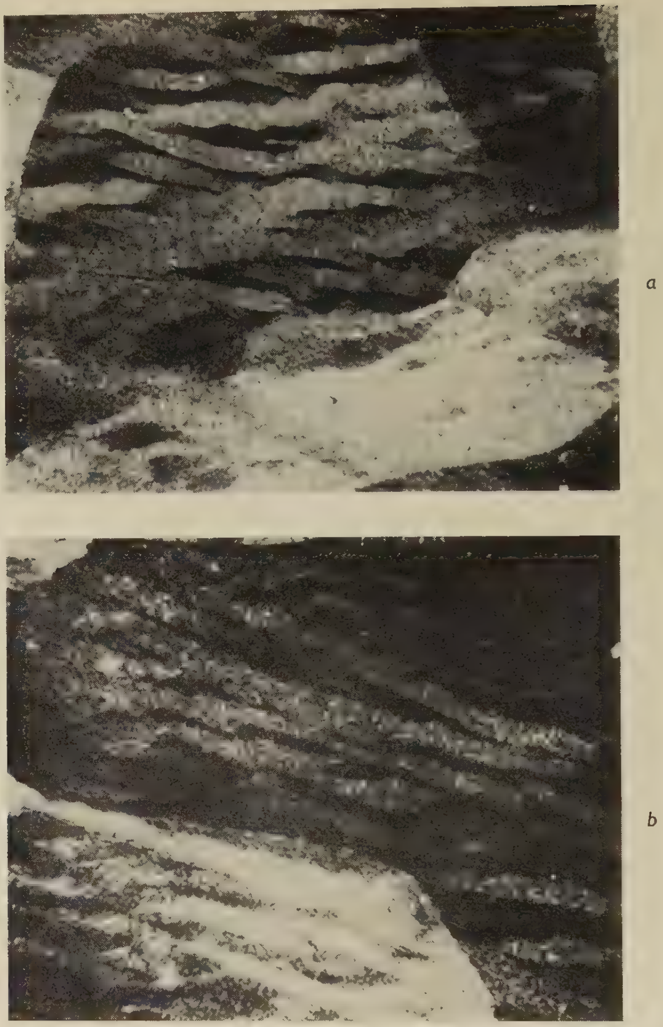

Figs. 4 a and b. High purity room-temperature compressed polycrystalline aluminium. Electrolytical polishing and anodic oxidation. Photographed in polarized light under crossed nicols. A similar picture is also valid after annealing at 100°C. × 750.

A formal theory of recovery has been developed by KUHLMANN, MASING and RAFFELSIEPER (13) suggesting that the rate of escape of dislocations from the piled-up groups is described by an equation of the form

$$\frac{dn}{dt} = A \cdot \exp\left\{-\frac{(E - \alpha \cdot n)}{RT}\right\} \tag{1}$$

where A and α are constants and E is the activation energy at the end of the recovery process. A similar formula for steady state creep has been given by COTTRELL and AYTEKIN (14). Integration of eq. (1) gives

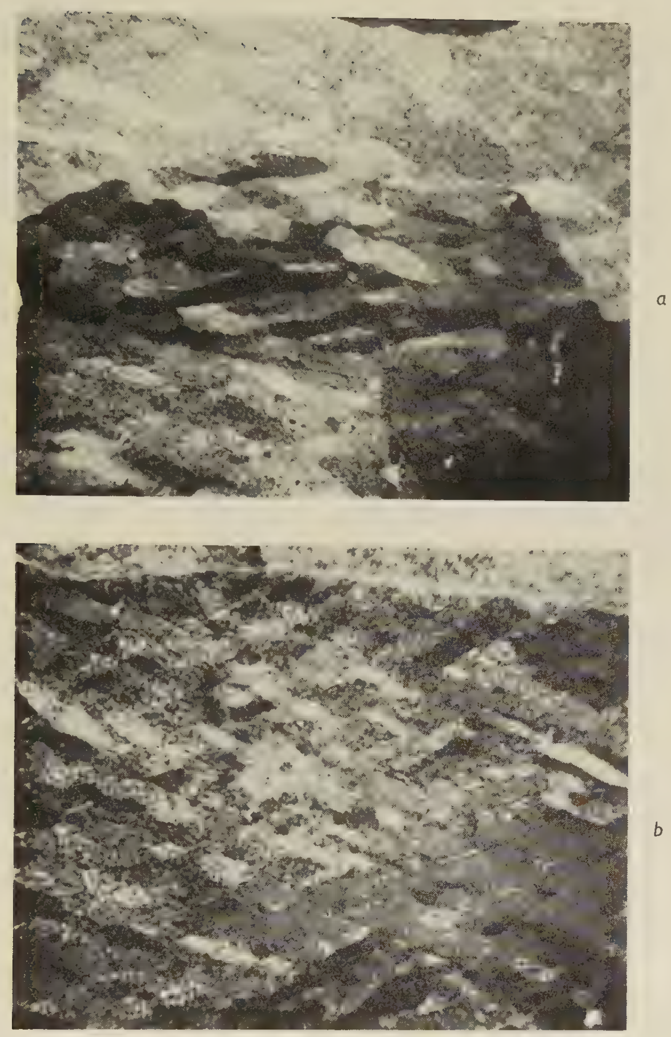

Figs. 5 a and b. High purity compressed aluminium annealed 25h at 250°C. Specimen preparation the same as in Figs. 4 a and b. × 750.

$$n = B - \frac{RT}{\alpha} \cdot \ln\,(t + t_0) \tag{2}$$

where t_0 is the duration of the foregoing recovery and B is constant for a given temperature. The rate of change of n is

$$\frac{dn}{dt} = -\frac{RT}{\alpha} \cdot \frac{1}{t + t_0}, \tag{3}$$

that is of hyperbolic form.

Borelius *et al.* (4) give an equation for recovery of a somewhat different form than that of Kuhlmann, Masing and Raffelsieper, namely

$$\frac{dQ}{dt} = -c \cdot Q \cdot \exp\left\{-\frac{(E-b\cdot Q)}{RT}\right\} \tag{4}$$

where Q is the heat per mole still to be given off for full recovery, t the time, c a constant of the order of frequency of the atomic vibrations, and b a dimensionless number.

By a simple transformation eq. (4) can be written in the form

$$\int_{\xi}^{\infty} \frac{e^{-\xi}}{\xi} \cdot d\xi = c \cdot (t+t_0) \cdot \exp\left\{-\frac{E}{RT}\right\} \tag{5}$$

where $\xi = \frac{b \cdot Q}{RT}$ and t_0 is again the duration of the foregoing recovery. It should be emphasized here that none of the mathematical formulae given will of course account for the recovery process in the immediate neighbourhood of $t = 0$.

When ξ in eq. (5) is large the integral can be replaced by $\frac{e^{-\xi}}{\xi}$ which leads to the following approximate expression

$$\frac{dQ}{dt} = -\frac{RT}{b} \cdot \frac{1}{t+t_0} \tag{6}$$

which is comparable to eq. (3). When ξ is small, however, the integral is approximately $\ln \frac{1}{\gamma \xi}$, where γ is Euler's constant, and the rate of Q is now obtained as an exponential function of the time

$$\frac{dQ}{dt} = -c \cdot \frac{RT}{b \cdot \gamma} \cdot \beta \cdot \exp\{-c \cdot \beta (t+t_0)\} \cdot \tag{7}$$

β is constant for a given temperature.

As mentioned earlier we have made some measurements on recovery with very slightly deformed specimens (a typical result is shown in Fig. 3). It seems from them as if an equation of Borelius' type should apply well, as the first part of the measured process is almost hyperbolic (cf. eq. (6), where t_0 can be neglected for these measurements) while, when Q has decreased to a certain level, changes towards an exponential relation between rate of energy and time appear. With an energy of activation of 26700 cal/mole, c equal to 8.3×10^{12} calculated from the Debye temperature in the theory of specific heats, and a b-value of 15000, estimated from the first hyperbolic part of the process in Fig. 3, eq. (4) gives good agreement with the experimental results. The values thus calculated are laid in as a curve in Fig. 3. The values of Q used in eq. (4) are obtained by graphical integration of the rate curve. It was thereby assumed that Q is zero when recovery is finished, which probably involves no considerable approximation in this case. By fitting eq. (4) to other similar measurements an average energy of activation of 28000 cal/mole was obtained.

We have also tried to adapt the equation which is obtained if we assume proportionality between n in eq. (1) and Q to the experimental values in Fig. 3. It is found that an equation of this form will give straight lines in a rate of energy versus $1/t$ diagram with slopes depending on the values of A and E. This equation does not, however, account for the experimental points in Fig. 3 equally well as eq. (4).

The dimensionless number b in eq. (4) is constant for a certain measurement but varies widely for the same material with different degrees of cold-working. In heavily deformed samples of aluminium, b is about 5000 while in slightly deformed ones it is of the order of 15000, both values referred to a measuring temperature of 70°C. We have not been able to explain this theoretically but the measurements will be continued to search an answer.

The energies of activation for recovery obtained here are much lower than the value 48000 cal/mole, which was determined by KUHLMANN, MASING and RAFFELSIEPER from tensile measurements on high-purity aluminium annealed at different temperatures between 100°C and 400°C. It seems, however, probable that not only recovery was obtained here but, for the highest temperatures considered, also the other relaxation stages. The energy of activation given may thus depend on all three relaxation processes. The value calculated from the curves in the lowest temperature range is about 25000 cal/mole, which is in closer agreement with our values.

Assuming an energy of 28000 cal/mole, we have an interesting possibility to distinguish between the two recovery mechanisms proposed. If the dislocations leave the piled-up groups by climbing out of their slip planes due to the migration of vacancies, this process may be connected with the energy of activation for self-diffusion which is about 37000 cal/mole. The other mechanism with gliding of the dislocations in their slip planes requires generally a very high thermal activation unless the dislocations in the groups intersect each other, and are cut through during gliding. The energy of activation for the dissolution of dislocations from such an arrangement must be less than that for self-diffusion as the vacancies needed are already present in the intersections. The energy for the migration of these vacancies may be as low as about 24000 cal/mole according to COTTRELL (15). As the energy obtained in this investigation is decidedly less than 37000 cal/mole, the last mechanism seems to be the most probable one, although it leads to a rather low energy for the jogs in the piled-up groups. This low energy has, however, been theoretically suggested in a paper by STROH (16).

7. Discussion of the release of energy due to changes in the substructure

An attempt will now be made to find a theoretical explanation of the energies released from the deformed samples when they are annealed in the temperature range 180° to 250°C. The calorimetric measurements show that the rate of energy obtained is here a simple exponential function of the time in contrast to the heat liberated in recovery. From the time constants of the exponential curves for two equally deformed specimens measured at different temperatures (Tab. 3) the energy of activation for the process was calculated. The value found was 36000 cal/mole, which is in fact the same value as has been ascribed to the self-diffusion effect in aluminium. Further it is obvious from the micrographs (Figs. 4 and 5) that the present release of energy is associated with changes in the substructure of the metal.

In order to interpret the results obtained, there seem to be two possibilities. One should be that the substructure effect is due to a growth of the subgrains which have been created already during the plastic deformation. The initial size of the subgrains is about 1–2 μ according to HEIDENREICH (9). When the strain of the initial grains has diminished or disappeared during recovery they can, however, grow. It is quite clear that we are not able to detect so small a structure after cold-work (Figs. 4 a and 4 b) with the microscopic technique used. After the proposed growth, the areas in Figs. 5 a and 5 b have a size of 3 to 7 μ. The question is now whether a subgrain growth of this extent is enough to explain the energy values obtained: 0.2–0.4 cal/mole for the two least deformed samples and for the heavily deformed specimen in Table 1, 1.2 cal/mole or even more, depending on whether the energies at 215° and 250°C are included or not (see section 4).

When the subgrain size increases, energy is set free due to the diminished grain-boundary surface. An estimate of the heat liberated in this growth process may be obtained from READ-SHOCKLEY's grain-boundary energy equation (17) which probably applies well to the sub-boundary case as the differences in orientation across those boundaries are very small. The equation is

$$E = \frac{G \cdot a}{4\pi(1-\sigma)} \cdot \theta \cdot (A - \ln \theta) \tag{8}$$

where E is the energy per unit of grain boundary, θ is the difference in crystal orientation, G is the modulus of rigidity, a the lattice constant, σ Poison's ratio, and A approximately constant $= 0.23$ (18).

LACOMBE and BEAUJARD (19) have disclosed by means of special etching methods the existence of substructures in high-purity aluminium with differences in orientation of about 0.3°. If this value is assumed as a mean value for θ during the growth process, and if the subgrain size increases from cubes of 1.5 to 5 μ, the internal energy should decrease by about 0.1 cal/mole according to eq. (8). This is somewhat less than the energies obtained from the specimens in Tables 2 and 3 but still of the same order of magnitude. It is, however, decidedly less than what was released in the heavily deformed sample and this might indicate that the subgrain growth provided that it is present, which seems rather likely, is not alone responsible for the energy obtained in the actual temperature range. The energy of activation determined, 36000 cal/mole, seems to be a reasonable value for sub-boundary migration on account of the special structure that these boundaries are assumed to have (20, 21).

The other possible mechanism, which would probably give a larger release of energy than the sub-boundary migration, is a thermally activated polygonization process. As the energy of activation for polygonization is the same as for self-diffusion, the present results do not contradict this assumption. The above discussion may be concluded by stating that there is a certain probability that both the processes suggested contribute to the values of energy obtained from our specimens in the temperature range 180° to 250°C.

As to the hardness values plotted in Fig. 1, they show no decrease until recrystallization is obtained at 350°C, although a fall in the values could be expected between 180° and 250°C. The reason may be that the hardness change due to the substructure effect has been too small to be observed with the experimental technique used. Another possibility may be that the subgrain growth and related phenomena are not always associated with any appreciable softening as suggested by HONEYCOMBE (22).

8. Discussion of recrystallization

As was pointed out in the foregoing the calorimetric measurements about 350°C gave rate of energy versus time curves of a form which is typical for a nucleation and growth process. The energy of activation determined from these curves was 58000 cal/mole for specimens of aluminium *A*. This value is in good agreement with the energy 59000 cal/mole, which was obtained by ANDERSON and MEHL (23) from microscopic investigations on primary recrystallization in 99.95 % Al.

In Fig. 2 we have collected some results of measurements at 353°C on specimens which all have been cold-worked to the same degree. They have, however, been pre-annealed in different ways as indicated in the figure. We shall here leave curve 1 out of consideration as it is to be discussed in the next section, and only compare curves 2 and 3, which have been obtained with specimens of material *B*. In the case of curve 2 the specimen was measured for 40 hours at 205°C, that is in the region of substructure changes. When after that the specimen was measured at 353°C, the typical recrystallization curve shown in Fig. 2 was obtained. The energies released are 1.3 cal/mole at 205° and 3.2 at 353°C. Another specimen was measured at 353° without pre-annealing and gave curve 3. The heat evolution starts now with an approximately exponential part which after a measuring time of about one hour changes into a bell-shaped curve. This shape points to two different processes operating, one predominating at shorter times and the other, the recrystallization process, predominating at longer times. By extrapolating the first part of the curve exponentially we find the energy due to the first process to be somewhere about 1.5 cal/mole, and that due to the recrystallization to be about 3.0 cal/mole. These energy values are practically the same in the two cases. We therefore make the assumption close at hand that the first part of curve 3 is mainly due to changes in the substructure, as recovery is probably so rapid at these temperatures that it can be left out of consideration here. It seems as if this pre-effect were necessary for the primary recrystallization process to start. One could perhaps suspect that the effect at 205°C is identical with the recrystallization process, but the separated energies of activation clearly indicate, that we have to do with two different relaxation stages.

The primary recrystallization and especially its nucleation have been the subject of many theoretical considerations. The model which at present seems to represent the best basis on which to describe the formation of recrystallization nuclei in severely deformed polycrystalline metals has been developed by COTTRELL (24) and CAHN (25). The essential part of it is the suggestion that the nuclei are pre-existing subgrains, which have either remained relatively strain-free with respect to their surroundings during the deformation or have become relatively strain-free during annealing. In this theory the time for the maximum rate of the process (which as a parameter is to be preferred to the so-called incubation time), must be intimately connected with the state of the substructure. We think that the experimental findings of this investigation support such an idea. It is thus clearly demonstrated that the substructure changes must advance to a certain point before the primary recrystallization starts. In the case of pre-annealing at 205°C some subgrains probably grow to a favourable starting position, thereby giving a more rapid recrystallization process.

It should be pointed out here that the total energies given off from the cold-worked specimens in this investigation are smaller than what was obtained by QUINNEY and TAYLOR (1), who determined the value of the stored energy in aluminium by a differential method. Though nothing definite can be said about the reason for this discrepancy, it may be due to different amounts of cold-work and/or to different degrees of purity of the aluminium metal used in the two investigations.

9. Effect of impurities

As mentioned previously most measurements on the relaxation processes were made with the aluminium denoted *A*, but in some cases aluminium *B* was also used. The compositions are given in section 3. The small differences in the amount of impurities between *A* and *B* appeared to have no observable influence on the recovery stage. Measurements on the substructure effect at 205°C and on the primary recrystallization at 353°C in their dependence on time revealed, however, a difference in the time constants of the exponential decrease between *B* and *A* in the ratio of two or three to one. The curves 1 and 2 in Fig. 2 show the results from the measurements at 353°C. The energies released here are somewhat different in the two cases: 4.5 cal/mole (curve 1) and 3.2 cal/mole (curve 2). It was, however, found that the added energies of subgrain effect and recrystallization were almost equally large in both cases (and also in the case of curve 3) which might give an evidence of the close connection between subgrain changes and recrystallization.

It seems not to be possible here to make any definite conclusions about the retarding effect on the two last relaxation stages from the compositional data of aluminium *A* and *B*. The explanation may, however, be the observation made by Kawashima and Nakamura (26) that the presence of impurities (Zn, Mn, Ti) generally reduces the recrystallization velocity, if the impurity content is within the range of solid solubility at the measuring temperature, while the presence of Fe as impurity increases this velocity.

ACKNOWLEDGEMENTS

I have had the favour to perform the present investigation at the Royal Institute of Technology, Department of Physics, under Professor BORELIUS' direction. I hereby want to express my sincere gratitude to him for all stimulating discussions and the valuable advice that I have always received.

The work has been subventioned by a grant from the *Swedish Council for Technical Research*.

Royal Institute of Technology, Department of Physics.

REFERENCES

1. H. QUINNEY and G. I. TAYLOR, Proc. Roy. Soc. A *163*, 157 (1937).
2. P. A. BECK, Advances in Physics *3*, 245 (1954).
3. G. BORELIUS, L'état solide. Inst. Solvay, Bruxelles 1952, p. 427.
4. G. BORELIUS, S. BERGLUND and S. SJÖBERG, Arkiv f. Fysik *6*, 143 (1952).
5. G. BORELIUS and S. BERGLUND, Arkiv f. Fysik *4*, 173 (1951).
6. H. U. ÅSTRÖM, Arkiv f. Fysik *8*, 495 (1954).
7. P. A. BECK and HSUN HU, J. Metals *4*, 83 (1952).
8. E. C. W. PERRYMAN, Acta Metallurgica *2*, 26 (1954).
9. R. D. HEIDENREICH, Bell Syst. tech. J., October 1951.
10. A. GUINIER and J. TENNEVIN, Progress in Metal Physics, II. 1951.
11. D. KUHLMANN, Zeit. Phys. *124*, 468 (1947); Proc. Phys. Soc. A *64*, 140 (1951).

12. N. F. Mott, Phil. Mag. *44*, 742 (1953).
13. D. Kuhlmann, G. Masing and J. Raffelsieper, Z. f. Metallk. *40*, 241 (1949).
14. A. H. Cottrell and V. Aytekin, J. Inst. Met. *77*, 389 (1950).
15. A. H. Cottrell, Dislocations and Plastic Flow in Crystals. Oxford 1953.
16. A. N. Stroh, Proc. Phys. Soc. B *66*, 2 (1953).
17. W. Shockley and W. T. Read, Phys. Rev. *75*, 692 (1949).
18. W. Shockley and W. T. Read, ibid. *78*, 275 (1950).
19. P. Lacombe and L. Beaujard, J. Inst. Met. *74*, 1 (1948).
20. W. L. Bragg, Proc. Phys. Soc. *52*, 105 (1940).
21. P. Lacombe and L. Beaujard, Progress in Metal Physics, II. 1951.
22. R. W. K. Honeycombe, J. Inst. Met. *80*, 45 (1951–52).
23. W. A. Anderson and R. F. Mehl, Trans. AIME *161*, 140 (1945).
24. A. H. Cottrell, Progress in Metal Physics, IV. 1953.
25. R. W. Cahn, Proc. Phys. Soc. A *63*, 323 (1950).
26. N. Kawashima and Y. Nakamura, Nippon Kinzoku Gakkai-Si, *16*, 662 (1952).

Tryckt den 6 december 1955

Uppsala 1955. Almqvist & Wiksells Boktryckeri AB

ARKIV FÖR FYSIK Band 10 nr 19

Mitgeteilt am 14. Sept. 1955 durch MANNE SIEGBAHN und BENGT EDLÉN

Untersuchung einer neuen kontinuierlich steuerbaren Gasentladung mit kalter Kathode

Von C. H. HERTZ

Mit 24 Abbildungen im Text

Zusammenfassung

In der vorliegenden Arbeit wird eine neue Möglichkeit untersucht, den Strom einer Gasentladung zwischen kalten Elektroden kontinuierlich zu steuern, indem man in der Gasentladungsstrecke an der Anodenseite unselbständige Entladungen erzeugt, welche durch die von der Kathode kommenden Elektronen gespeist werden. Als Kathode wird dabei eine negative Spitzenkorona verwand, und die kontinuierliche Regelung des Stromes in der Gasentladung durch ein besonderes Elektrodensystem an der Anodenseite der Gasentladungsstrecke bewirkt, an welchem durch Anlegen einer geeigneten Steuerspannung neue steuerbare Ionisationsbereiche in der Gasentladung entstehen. Die in diesen Bereichen unter kontrollierbaren Bedingungen entstehenden Ionen laufen zur negativen Spitze und erhöhen so den Koronastrom.

Wird eine solche Koronaentladung in Wasserstoff von 150 mm Hg Druck betrieben, so hat sie der Elektronenröhre sehr ähnliche Eigenschaften. Die elektrischen Daten der untersuchten „Koronaröhre“ sind etwa die folgenden: Spitzenspannung 950 Volt, Spitzenstrom 0,3–0,5 mA, Verstärkungsfaktor 50–100, innerer Widerstand 0 bis -250 kΩ. Die Arbeitsweise einer solchen Röhre wird untersucht und u. a. gezeigt, warum eine solche Gasentladungsröhre trotz eines relativ hohen Stromes zur Steuerelektrode einen sehr grossen oder sogar negativen Eingangswiderstand hat, was sich auf ihren negativen inneren Widerstand zurückführen lässt.

Die Einwirkung der Elektrodengeometrie, des Gasdruckes usw. auf die elektrischen Eigenschaften der Röhre werden besprochen and die möglichen technischen Anwendungen als Verstärkerröhre oder zur Stabilisierung hoher Spannungen werden diskutiert.

1. Einleitung

Seit langer Zeit ist immer wieder versucht worden (vgl. z. B. [1, 2]), den Strom in Gasentladungen kontinuierlich zu steuern, da von verschiedener Seite vermutet wurde, das eine solche Steuerung des Glimmentladungsstromes auf Grund der speziellen Eigenschaften des Glimmentladungsplasmas nur in sehr begrenztem Umfange möglich sei [3]. Weiterhin würden solche Gasentladungsröhren in der Technik viele Anwendungsgebiete finden, da viele Gasentladungen keine Glühkathode benötigen und oft einen geringen inneren Widerstand haben, weshalb sie zum Steuern hoher Ströme mit Vorteil verwendet werden können. Wichtige Entwicklungen auf dem Wege zu diesem Ziele waren insbesondere der Kopfverstärker [3] und Wandverstärker

[4], in denen eine Glimmentladung als Kathode verwendet wird, und schliesslich das Plasmatron [5], in welchem durch die Änderung der Leitfähigkeit eines Glimmentladungsplasmas zwischen Kathode und Anode der Röhre der Strom durch die Röhre gesteuert wird. Der Grund dafür, dass sich diese Röhren nicht eingeführt haben, dürfte teilweise an ihrem geringen Verstärkungsfaktor und teilweise an dem Gitterstrom liegen, der in solchen Röhren unvermeidlich ist. Ausserdem treten oft Schwierigkeiten durch langsame Zerstörung der Kathode auf, was besonders in den Fällen, wo Glühkathoden zur Verwendung kommen, einzutreten scheint.

Im Verlauf früherer Arbeiten des Verfassers [6, 7], in denen die Abhängigkeit der Spitzenkorona von einem isolierenden Lacküberzug auf der Gegenelektrode untersucht wurde, zeichnete sich eine neue Möglichkeit ab, den Strom einer Glimmentladung kontinuierlich zu steuern, was gleichzeitig eine Bestätigung für die in diesen Arbeiten gegebene Erklärung für den dort beschriebenen Effekt darstellen würde. Als Kathode diente hierbei eine negative Spitzenkorona und die Steuerung des Stromes durch die Gasentladungsröhre wird durch einen geeigneten Elektrodenaufbau an der Anodenseite der Röhre bewirkt. Im Folgenden soll nun der Aufbau und die Arbeitsweise einer solchen ,,Koronaröhre“ beschrieben und untersucht werden, welche technischen Möglichkeiten diese Art gasgefüllter Verstärker- und Regelröhre bietet.

2. Die Methode der steuerbaren sekundären Ionisationsbereiche

In einer früheren Arbeit [6, 7] ist vom Verfasser untersucht worden, wie sich der Koronastrom von einer negativen Koronaspitze zu einer ebenen Metallelektrode ändert, wenn man die ebene Elektrode mit einer dünnen Lackschicht überzieht. Es zeigt sich dabei, dass der Koronastrom unter sonst gleichen Bedingungen durch das Aufbringen der Lackschicht oft um ein Vielfaches wächst, was wegen der guten Isolationseigenschaften der Schicht zunächst nicht zu erwarten war.

Diese überraschende Erscheinung wurde auf folgende Weise erklärt. Durch die von der negativen Spitzenkorona kommenden Elektronen oder negativen Ionen wird die gut isolierende Lackschichtoberfläche auf ein beträchtliches negatives Potential gegenüber der darunterliegenden ebenen Elektrode aufgeladen, was wegen der geringen Dicke der Lackschicht zu grossen Feldstärken zwischen Lackschichtoberfläche und der ebenen Elektrode führt. Falls sich nun feine Poren in der Lackschicht befinden, so können weitere negative Ladungsträger, die von der Spitze kommend in diese Poren eintreten, wegen der hier herrschenden hohen Feldstärken wiederum das Gas ionisieren. Die auf diese Weise in dem Gasraum der Poren entstehenden positiven Ionen werden zur negativen Spitze gezogen und tragen so zur Vergrösserung des Koronastromes bei. Die Öffnung jeder Pore, in welcher diese Ionisation des Gases stattfindet, ist im Dunkeln sichtbar, da neben der Ionisation natürlich auch Anregung der Gasmoleküle stattfindet, was zu einer schwachen Lichtaussendung aus jeder Porenöffnung führt.

Um die Richtigkeit dieser Vorstellung näher zu prüfen sollte der Versuch gemacht werden, die in den Poren auftretenden hohen Feldstärken künstlich herzustellen und so den Effekt unter leichter kontrollierbaren Bedingungen zu untersuchen. Zu diesem Zwecke wurden in ein 1 mm dickes ebenes Messingblech 10 × 10 Löcher von 0,5 mm Durchmesser gebohrt (vgl. Abb 1), so dass sie ein Quadrat mit der Seitenlänge von 14 mm gleichmässig erfüllten. Sodann wurde in jedes Loch von unten ein spitzer Stift *A* (feine Nähnadeln) auf solche Weise eingeführt, dass seine Spitze mit der

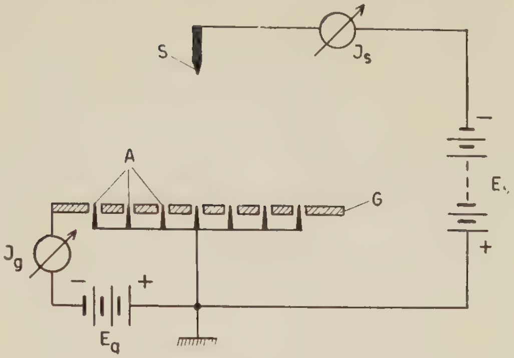

Abb. 1. Schematische Darstellung der Anordnung zur Erzeugung sekundärer Ionisationsbereiche in der Koronastrecke. Durch die Spannung E_g werden zwischen den Spitzen A und der Elektrode G Gebiete hoher Feldstärke erzeugt, in welchen die von der Spitzenkorona kommenden Elektronen das Gas ionisieren können.

Oberfläche der Platte G abschloss und G nirgends berührte. Danach wurden alle Spitzen A miteinander leitend verbunden.

Die in den Poren der Lackschicht aufgetretenen hohen Feldstärken können nun leicht dadurch nachgeahmt werden, das man zwischen die Spitzen A und der von diesen isolierten Metallplatte G eine geeignete Spannung E_g so legt, dass G negativ gegenüber A aufgeladen wird. Des geringen Krümmungsradius der Spitzen A und ihres kleinen Abstandes von G wegen lassen sich auf diese Weise hohe Feldstärken an den Spitzen A erhalten, welche durch Änderung der Spannung E_g geregelt werden können.

Bringt man nun über dieser Anordnung (Abb. 1) eine Koronaspitze S an und legt man zwischen diese und der Spitzenelektrode A eine so hohe Spannung E_s an, dass sich an S eine negative Koronaentladung ausbildet, so tritt in der unmittelbaren Nähe der Spitzen A eine dem in den Poren der Lackschicht gefundenen Effekt sehr ähnliche Erscheinung ein. In den Bereichen der hohen Feldstärke vor den Spitzen A, welche mit Hilfe der Spannungsquelle E_g und der Plattenelektrode G aufrecht erhalten werden, können auch hier wieder die von der Koronaspitze S kommenden negativen Ladungsträger das Gas ionisieren. Die hier erzeugten positiven Ionen wandern ihrerseits zum grössten Teil zur Koronaspitze S und bewirken so eine Vergrösserung des Koronastromes. — Da ebenfalls hier wieder neben der Ionisation auch Anregung der Gasmoleküle in den Bereichen hoher Feldstärke in der Nähe der Spitzen A auftritt, sieht man die Spitzen A im Dunkeln schwach leuchten. Abb. 2

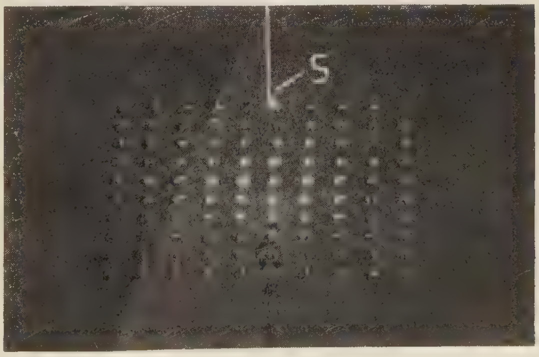

Abb. 2. Die in Abb. 1 beschriebene Anordnung schräg von oben gesehen. Spitzenabstand 5 mm, Spitzenspannung − 4 700 V, Spitzenstrom 102 μA. Umgebendes Gas: Luft von Atmosphärendruck. In den Bereichen hoher Feldstärke tritt neben Ionisation auch Anregung der Gasmoleküle auf, weshalb von allen diesen sekundären Ionisationsbereichen auch Licht ausgesendet wird. Etwa 2mal natürliche Grösse.

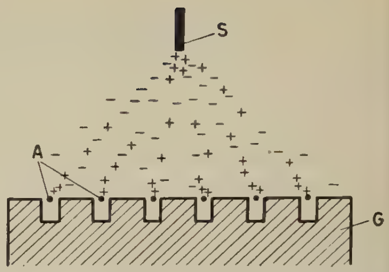

Abb. 4. Schematische Darstellung des endgültigen Elektrodenaufbaus in der Röhre (vgl. Fig. 5). Die Bereiche hoher Feldstärke (sekundäre Ionisationsbereiche) werden hier in der Nähe der dünnen Drähte A durch eine geeignete Gittervorspannung zwischen A und der Gitterelektrode G erzeugt.

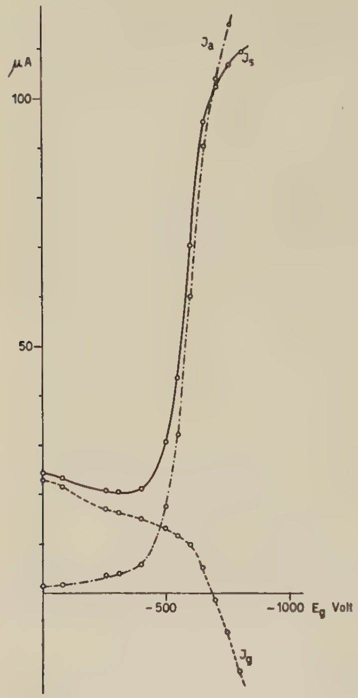

Abb. 3. Abhängigkeit des Spitzenstromes I_s von der „Gitterspannung" E_g (vgl. Abb. 1). Gleichzeitig ist der Strom I_a zu den Spitzen A und zur Gitterelektrode G, I_g, angegeben. $I_s = I_a + I_g$.

zeigt die Ansicht einer solchen Anordnung in Luft von Atmosphärendruck schräg von oben. Der Abstand der Koronaspitze S von G betrug dabei 5 mm, $E_s = -4700$ V, $E_g = -700$ V und der Koronastrom $I_s = 102\ \mu$A.

Durch das Anlegen der Spannung E_g zwischen die Elektroden A und G sind also auch hier wieder zusätzlich sekundäre Ionisationsbereiche in der Gasentladungsstrecke geschaffen worden, welche eine Erhöhung des Koronastromes bewirken. Diese sekundären Ionisationsbereiche können nun aber durch Änderung der Spannung E_g beeinflusst bzw. gesteuert werden; lässt man z.B. E_g gleich Null werden, so verschwinden sie vollkommen, der Koronastrom geht zurück und es sind auch keine Leuchterscheinungen mehr an den Spitzen A zu beobachten.

Die Abhängigkeit des Spitzenstromes I_s von der Spannung E_g bei konstanter Spitzenspannung E_s in der bisher besprochenen Anordnung (Abb. 1 u. 2) ist in Abb. 3 dargestellt. Neben dem Spitzenstrom I_s sind weiterhin noch seine beiden Komponenten I_a (Strom zur Spitzenelektrode A) und I_g (Strom zur Plattenelektrode G) angegeben, wobei $I_s = I_a + I_g$ ist. Auch hier war das umgebende Gas Luft von Atmospährendruck und der Abstand der aus 0,3 mm Pt-Draht gefertigten Koronaspitze von der ebenen Elektrode G 5 mm. Unterhalb einer Spannung von $E_g \simeq 400$ V ist der Spitzenstrom I_s praktisch konstant und verteilt sich nur verschieden auf die Elektroden G und A; die geringe Senkung von I_s bei wachsendem E_g unterhalb von $E_g = 400$ V ist dadurch zu erklären, dass bei steigendem E_g die Spannungsdifferenz zwischen der Elektrode G und der Koronaspitze S abnimmt, wodurch sich die Feldstärke bei S etwas vermindert.

Bei Spannungen $E_g > 400$ V ist aber eine deutliche Vergrösserung des Spitzenstromes I_s zu beobachten, was darauf zurückgeführt werden muss, dass hier Ionisation des Gases in der unmittelbaren Nähe der Spitzenelektrode A auftritt. Gleichzeitig können nun auch die oben erwähnten Leuchterscheinungen an den Spitzen A gefunden werden. Erhöht man E_g weiterhin, so nimmt der Strom I_g zur Elektrode G kontinuierlich ab, bis er bei $E_g = 690$ V schliesslich zu null wird. Auf diese Spannung stellt sich also die Elektrode G automatisch ein, wenn sie der Spitzenelektrode A gegenüber vollständig isoliert wird, da sich hier die auf der Elektrode G auftreffenden negativen Ladungsträger von der Koronaspitze und die positiven Ionen aus den sekundären Ionisationsbereichen gerade gegenseitig aufheben. Bei einer weiteren Steigerung der Gitterspannung E_g überwiegt dann, wie aus der Abb. 3 ersichtlich ist, der positive Ionenstrom zur Elektrode G.

Die in Abb. 3 gezeigte Abhängigkeit des Spitzenstromes von der Spannung E_g ist vollständig reproduzibel und hängt nicht davon ab, ob man die Spannung E_g beim Durchmessen der Kurve von null auf den Höchstwert steigert oder umgekehrt verfährt, d.h. die Kurve weist keine Hysterese auf. Der vorliegende Versuch zeigt also, dass man mit Hilfe der Spannung E_g den Koronastrom I_s innerhalb gewisser Grenzen steuern kann. Da die Elektrode G hierbei die Rolle einer Steuerelektrode spielt, sollen im Folgenden in Analogie mit der Elektronenröhre die Spannung E_g als Gitterspannung und die Elektrode G als Gitter bezeichnet werden.

Die mit der in Abb. 1 beschriebenen Anordnung gefundenen Resultate lassen nun vermuten, dass es eventuell mit Hilfe der steuerbaren sekundären Ionisationsbereiche möglich ist, den Strom einer Koronaentladung so zu steuern, dass sie als Verstärkerröhre Verwendung finden kann. Es soll deshalb im Folgenden untersucht werden, wie weit sich diese Vermutung verwirklichen lässt und welche Eigenschaften eine solche Röhre aufweist.

3. Aufbau der Koronaröhre

Bevor mit den Untersuchungen der Eigenschaften einer solchen Röhre begonnen werden konnte, war es notwendig, einen Elektrodenaufbau zu finden, welcher leicht herzustellen war und gute elektrische Eigenschaften hatte, d. h. einen hohen Verstärkungsfaktor $\mu_s = -(\partial E_s/\partial E_g)_{I_s}$ und eine grosse Steilheit $S_s = (\partial I_s/\partial E_g)_{E_s}$ aufwies. Es wurde deshalb dazu übergegangen, anstelle der feinen Spitzen A dünne Drähte zu benutzen, die in in der Elektrode G (Gitter) eingefrästen Schlitzen ausgespannt waren (vgl. Abb. 4 u. 5). Die untereinander leitend verbundenen Drähte A waren dabei von der Elektrode G isoliert, so dass durch Anlegung einer geigneten ,,Gitterspannung`` zwischen den Drähten (positiv) und dem Gitter (negativ) wieder hohe Feldstärken in der Nähe der Drähte erzeugt werden konnten. Wird nun über dieser Anordnung eine Koronaspitze angebracht und in gleicher Weise mit den Drähten A über eine Spannungsquelle verbunden, wie dies in Abb. 1 erfolgt ist, so findet auch hier bei genügend hoher Gitterspannung E_g Ionisation des Gases durch die von der Spitze kommenden negativen Ladungsträger in der unmittelbaren Nähe der Drähte A statt, wie dies in der früheren Anordnung an den Spitzen A der Fall gewesen ist. Neben dem einfacheren Aufbau werden aber hierbei weiterhin noch eine grössere Steilheit und ein grösserer Verstärkungsfaktor gewonnen.

Die Abb. 5a zeigt ein solches Elektrodensystem schräg von oben. Die verwendete Elektrode G war dabei 15 × 15 mm gross und die Schlitzbreite 0,3 mm. Die Korona-

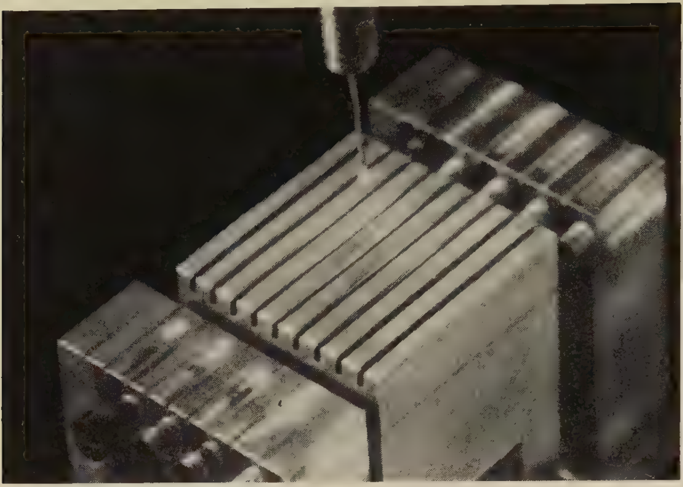

Abb. 5*a*. Ansicht der in Abb. 4 beschriebenen Anordnung schräg von oben. Spitzenabstand 5 mm, Spitzenspannung – 4700 V, Spitzenstrom 160 μA. Umgebendes Gas: Luft von Atmosphärendruck. Etwa 2mal natürliche Grösse.

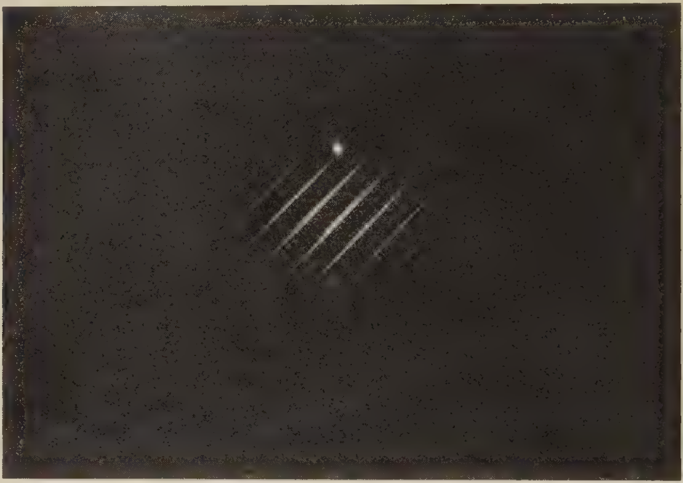

Abb. 5*b*. Ansicht der in Abb. 5*a* gezeigten Anordnung im Dunkeln. Die sekundären Ionisationsbereiche senden auch hier wieder wegen Anregung der Gasmoleküle Licht aus.

spitze *S* wurde 5 mm über *G* angebracht. In jedem Schlitz ist ein 0,015 mm dicker Wolframdraht *A* ausgespannt; wegen ihres geringen Durchmessers sind diese Drähte *A* jedoch nur schlecht zu erkennen. Diese können aber gut im Dunkeln gesehen werden (Abb. 5*b*), da sich an ihnen bei genügend hoher Gitterspannung E_g die leuchtenden sekundären Ionisationsbereiche ausbilden. Auch hier war wieder das die Anordnung umgebende Gas Luft von Atmosphärendruck, die Spannungen $E_s = -4700$ V, $E_g = -500$ V und die Ströme $I_a = 165$ μA, $I_g = -5$ μA. Aus der I_s-E_g Kennlinie (Abb. 6) für diese Anordnung können wir ersehen, das sie eine fast dreimal grössere Steilheit S_s (ca. $1{,}7 \cdot 10^{-6}$ A/V) aufweist, als mit der ursprünglichen Anordnung (Abb. 3) erreicht worden ist, obwohl in beiden Fällen sonst gleiche Bedingungen (gleiche Spitze, Spitzenabstand 5 mm, $E_s = -4700$ V) vorlagen. Der Verstärkungsfaktor einer solchen Anordnung ist aber immer noch nicht sehr gross, in der in Abb. 5 gezeigten Aufstellung wurde er zu etwa 5 bestimmt.

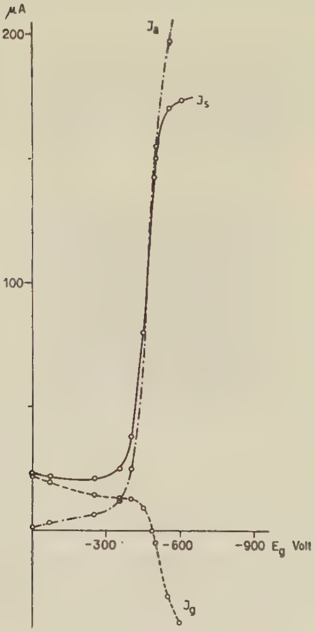

Abb. 6. Abhängigkeit des Spitzenstromes I_s von der Gitterspannung E_g in der in Abb. 5 gezeigten Anordnung. Gleichzeitig sind die Ströme I_a und I_g zu den dünnen Drähten *A* (Anode) und zum Gitter *G* angegeben.

Nach längeren Vorversuchen, über deren Ergebnis noch kurz weiter unten berichtet werden wird, wurde schliesslich der folgende Normalelektrodenaufbau gewählt, der, wenn nichts anderes ausdrücklich erwähnt, bei allen hier beschriebenen Ergebnissen zur Verwendung kam.

Das der Koronaspitze *S* gegenüberliegende Elektrodensystem ist in Abb. 7 dargestellt. Die Gitterelektrode *G* bestand aus einer 8 mm dicken, 18 × 19 mm grossen Messingplatte, in welche 12 Schlitze gefräst waren. Die Breite der Schlitze betrug 0,5 mm, ihre Tiefe ca. 1,5 mm. Quer zu den Schlitzen war auf beiden Seiten eine Messingleiste *L* zur Befestigung der Drähte *A* angebracht. Da diese von *G* isoliert sein mussten, wurde zwischen *G* und *L* ein 0,5 mm Pertinaxplättchen gelegt und das ganze mit Araldit zusammengeleimt. Die 0,015 mm dünnen Wolframdrähte *A* liessen sich dann unter dem Mikroskop leicht in den Schlitzen ausspannen, indem man den Draht so um die Anordnung herumwickelt, dass in jedem Schlitz ein Draht zu liegen kommt. Danach werden die Drähte an den Aussenseiten der Leisten *L* mit Araldit in ihrer Lage festgehalten. Der Anfang und das Ende des Drahtes wird dabei unter den Klemmschrauben *K* befestigt. Die für die elektrischen Eigenschaften des Elektrodensystems wichtige Höhe der Drähte in den Schlitzen wird hierbei durch die obere Kante der Leisten *L* bestimmt. Aus Vorversuchen ging hervor, dass die günstigste Lage für die Drähte *A* ca. 0,05 – 0,15 mm unter der Oberfläche der Elektrode *G* war.

Die Koronaspitze *S* war in dieser Röhre aus einem 0,3 mm dicken Tantaldraht gefertigt. Der Draht war vorher an seinem unteren Ende senkrecht zu seiner Längsachse platt angeschliffen (vgl. z. B. Fig. 4), wodurch eine Änderung der Spitzenform auf Grund von Kathodenzerstäubung vermieden wurde. Da der Tantaldraht unter Einfluss der Koronaentladung besonders in Wasserstoff Kristallisationserscheinungen zeigte, wodurch er spröde wurde und längere Stücke leicht zerbrachen, wurde als

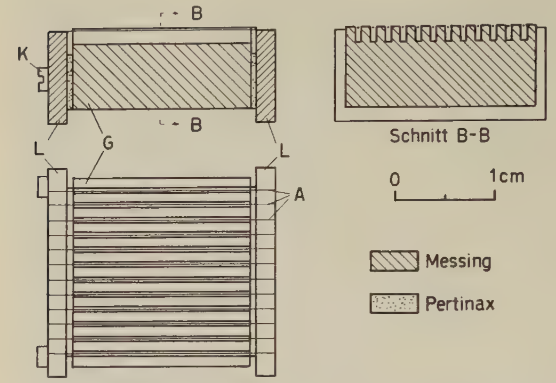

Abb. 7. Das Gitter-Anoden-Elektrodensystem.

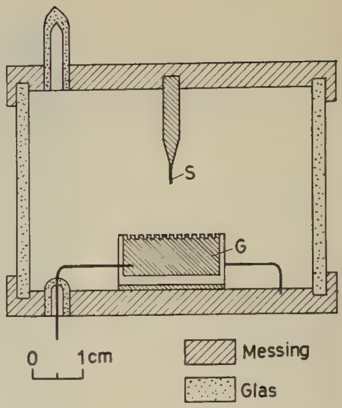

Abb. 8. Koronaröhre im Schnitt. Füllgas in der Röhre 150 mmHg Wasserstoff.

Spitze nur ein etwa 5 mm langes Stückchen des Drahtes verwandt, welches in einer Messinghalterung eingeklemmt war. Auf diese Weise wurde ein Abbrechen der Spitze selbst bei kräftigen Erschütterungen der Anordnung vermieden. Diese Spitze wurde dann so über dem oben beschriebenen Elektrodensystem angebracht, dass das untere Ende des Tantaldrahtes 10 mm über der Mitte der Elektrode *G* zu liegen kam.

Vorversuche in verschiedenen Gasen hatten gezeigt, dass die Anordnung besonders günstige elektrische Eigenschaften zeigte, wenn als umgebendes Gas Wasserstoff von erniedrigtem Drucke gewählt wurde. Deshalb wurden die Elektroden in ein Glasrohr von 55 mm Durchmesser eingebaut, welches oben und unten von einer mit Araldit angeleimten Messingplatte abgeschlossen war (Abb. 8). Nach Füllung des Gefässes mit dem gewünschten Gas konnte eine solche Röhre abgeschmolzen werden und wies auch nach mehreren Monaten keine wesentlichen Änderungen ihrer elektrischen Eigenschaften auf. — Die so aufgebaute Röhre ist zweifellos unnötig gross ausgefallen; es war jedoch für die Versuche vorteilhaft, die Entladung in der Röhre beobachten zu können, weshalb ein Glasrohr als Gefässwand gewählt wurde. Um aber Einwirkungen statischer Aufladungen der Glaswände auf die Koronaentladung zu verhindern, ist ein verhältnismässig grosser Abstand von der Koronaspitze zur Gefässwand nötig, weshalb die Röhre die vorliegende Grösse erhalten musste. — Soweit nichts anderes ausdrücklich erwähnt, wurde bei den im Folgenden beschriebenen Versuchen eine solche Röhre verwendet, die mit gereinigtem Wasserstoff (weniger als 0,4 % O_2) von 150 mm Hg Druck gefüllt war. — Für einen Teil der Untersuchungen war es dagegen wünschenswert, die Geometrie der Elektroden leicht verändern zu können. In diesen Fällen wurde das Elektrodensystem in einem Rezipienten aufgestellt.

4. Eigenschaften der Röhre

a) *Gleichstromdaten*

Zur näheren Untersuchung der Eigenschaften der auf diese Weise hergestellten Röhre sollten zunächst ihre Kennlinien aufgenommen werden. Dies geschieht am besten in der bei den Elektronenröhren üblichen Weise durch Messung der Abhängig-

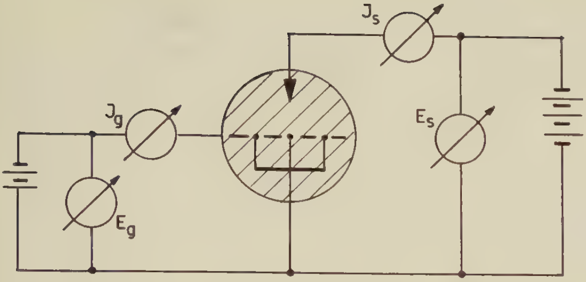

Abb. 9. Schaltung zur Messung der Röhrenkennlinien.

keit des Spitzenstromes I_s sowie des Gitterstromes I_g von der Spitzenspannung E_s und der Gitterspannung E_g. Die hierfür benutze Schaltung ist in Abb. 9 wiedergegeben. Um die Analogie mit der Elektronenröhre (Triode) weiterhin zu verdeutlichen, wird im Folgenden das in Abb. 9 verwandte, der Elektronenröhre ähnliche Symbol für die Koronaröhre benutzt. Wie weiter unten noch deutlicher hervortreten wird, treten also anstelle der Anode die Koronaspitze (Kathode) und anstelle der Kathode die dünnen Drähte A, d. h. die Anode der Koronaröhre. Aus demselben Grunde soll deshalb in den folgenden Überlegungen die Gitter- und Spitzenspannung immer positiv gerechnet werden.

Die Abhängigkeit des Spitzenstromes I_s von der Spitzenspannung E_s bei verschiedenen Gittervorspannungen ist in Abb. 10*a* wiedergegeben. Die hierbei verwandte Röhre hatte den oben beschriebenen Normalelektrodenaufbau und war mit 150 mm Hg reinem Wasserstoff gefüllt. Aus den Kennlinien ist zu ersehen, dass erst bei Gitterspannungen von mehr als -30 Volt die sekundären Ionisationsbereiche zu wirken beginnen. Bei Gitterspannungen zwischen -40 und -45 Volt findet sich ein Gebiet, wo die Kennlinien eine gute Linearität des Verstärkungsfaktors $\mu_s = -(\partial E_s/\partial E_g)_{I_s}$ vermuten lassen. Der Punkt P, der für die unter b) beschriebenen Wechselstrommessungen als Arbeitspunkt der Röhre gewählt wurde, wurde deshalb in dieses Bereich verlegt.

Aus den Kennlinien der Abb. 10*a* können ähnlich wie bei der Elektronenröhre die Daten der Röhre im Arbeitspunkt P bestimmt werden, welche bei allen im Folgenden gemachten Berechnungen verwendet werden:

Verstärkungsfaktor	$\mu_s = -(\partial E_s/\partial E_g)_{I_s} = 47{,}6$
Steilheit	$S_s = (\partial I_s/\partial E_g)_{E_s} = -3{,}5 \cdot 10^{-4}$ A/V
Innerer Widerstand	$R_s = (\partial E_s/\partial I_s)_{E_g} = -136$ kΩ

wobei also hier und im Folgenden die Gitter- und Spitzenspannung als positive Spannungen behandelt werden. — Besondere Beachtung verdient hierbei der negative innere Widerstand R_s der Koronaröhre, eine Eigenschaft, welche wichtige Konsequenzen für das elektrische Verhalten der Röhre hat.

An dieser Stelle sollte noch erwähnt werden, dass bei Spitzenströmen I_s von weniger als 300 μA manchmal Kippschwingungen in der Entladung auftraten, deren Form oft gewisse Ähnlichkeit mit Trichelpulsen [8] hatte. Diese lassen sich aber ohne Schwierigkeiten vermeiden, wenn man bei Spitzenströmen von mehr als 300 μA arbeitet.

Da bei Gitterspannungen von weniger als -50 V immer ein Teil des Spitzenstromes zur Oberfläche der Gitterelektrode hinfliesst, sind in der Röhre ein grosser Gitter-

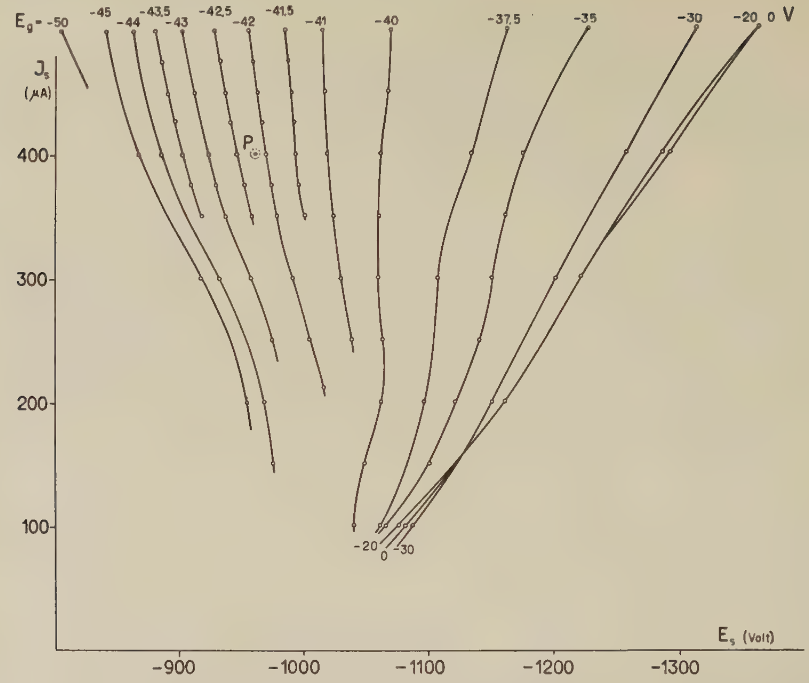

Abb. 10*a*. Abhängigkeit des Spitzenstromes von der Spitzenspannung bei verschiedenen Gittervorspannungen.

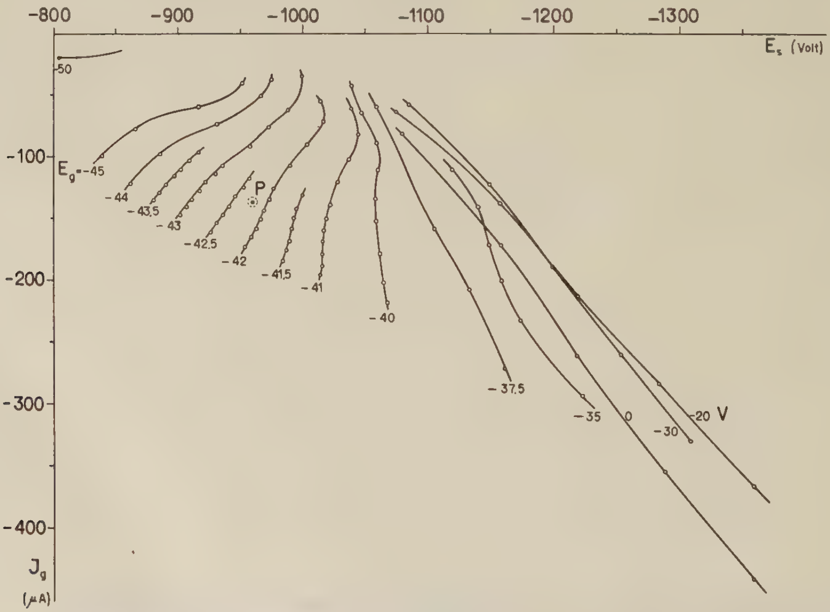

Abb. 10*b*. Abhängigkeit des Gitterstromes von der Spitzenspannung bei verschiedenen Gittervorspannungen.

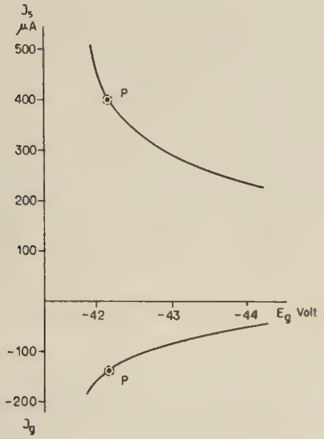

Abb. 11. Abhängigkeit des Spitzen- und Gitterstromes von der Gitterspannung in der Nähe des Arbeitspunktes der Röhre. Spitzenspannung konstant = 960 V. Steilheit S_s im Arbeitspunkt: $-3{,}5 \cdot 10^{-4}$ A/V.

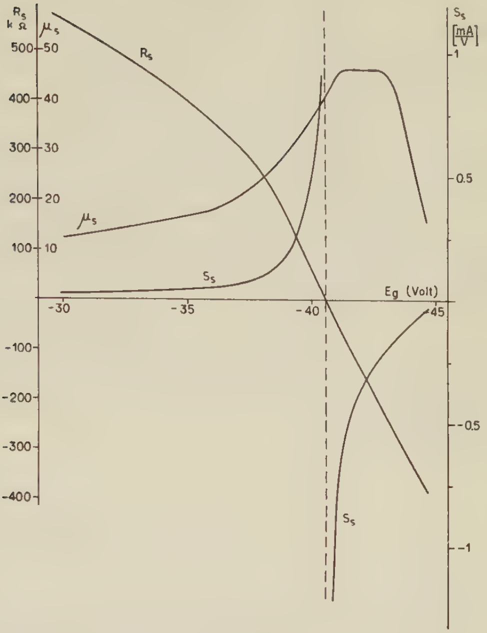

Abb. 12. Abhängigkeit des Verstärkungsfaktors μ_s, des inneren Widerstandes R_s und der Steilheit S_s von der Gittervorspannung E_g bei konstantem Spitzenstrom $I_s = 400$ μA.

strom I_g und ebenfalls auch eine Abhängigkeit des Gitterstromes von der Anoden- und Gitterspannung zu erwarten. Die Abb. 10*b* zeigt diese Gitterstromkennlinien. Bei Gitterspannungen von weniger als -50 V muss dabei für die folgenden Überlegungen der Gitterstrom negativ gerechnet werden, da er entgegen der Richtung des Gitterpotentiales E_g die Gitterbatterie durchläuft. Auch für das Gitter kann man wieder aus den Kennlinien der Abb. 10*b* gewisse Daten herauslesen, die später für das Verständnis der elektrischen Eigenschaften der Röhre nötig sein werden. Diese sind für den bereits oben gewählten Arbeitspunkt P gegeben durch

Gitterverstärkungsfaktor $\mu_g = -(\partial E_g/\partial E_s)_{I_g} = 1{,}758 \cdot 10^{-2}$

Gittersteilheit $S_g = (\partial I_g/\partial E_g)_{E_s} = 2{,}07 \cdot 10^{-6}$ A/V

Innerer Gitterwiderstand $R_g = (\partial E_s/\partial I_g)_{E_g} = 8{,}5$ kΩ

Der beträchtliche Gitterstrom, der in der Röhre fliesst, lässt zunächst einen sehr geringen Eingangswiderstand der Röhre erwarten. Dies ist jedoch, wie weiter unten gezeigt wird, nicht der Fall.

Die Abb. 11 gibt schliesslich für den Bereich des Arbeitspunktes P den Spitzenstrom I_s und den Gitterstrom I_g in Abhängigkeit von der Gitterspannung bei konstanter Spitzenspannung. Im Gegensatz zu den bekannten Kurven der Elektronenröhre ist hier die Steilheit des Spitzenstromes $(\partial I_s/\partial E_g)_{E_s}$ negativ. Wie aus Abb. 12

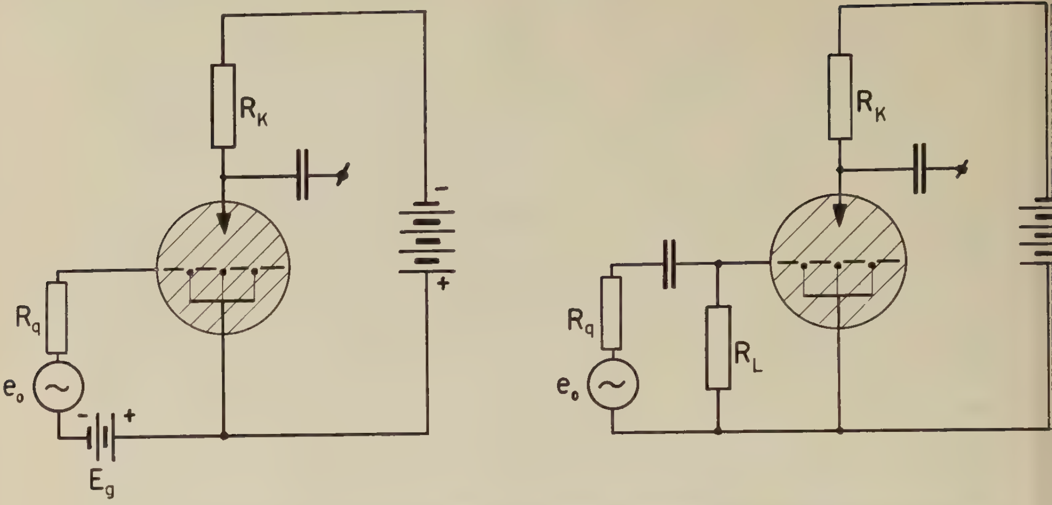

Abb. 13. Anwendung der Röhre in einer RC-Verstärkerschaltung, *a* links mit Gitterbatterie, *b* rechts ohne Gitterbatterie.

hervorgeht, welche Steilheit S_s, Verstärkungsfaktor μ_s und inneren Widerstand R_s der Röhre bei verschiedenen Gitterspannungen und konstantem Spitzenstrom darstellt, ist dies jedoch nicht immer der Fall, sondern die Werte dieser Grössen schwanken stark je nach Wahl des Arbeitspunktes der Röhre. Wie weiter unten bewiesen wird, gilt für die Grössen S_s, μ_s und R_s jedoch immer die Barkhausenbedingung $S_s \cdot R_s = \mu_s$. Die Werte der Abb. 12 sind direkt den in Abb. 10*a* und *b* wiedergegebenen Kennlinien entnommen.

b) *Die Verstärkung von Wechselspannungen tiefer Frequenzen*

Um die Anwendbarkeit der Koronaröhre für die Verstärkung von Wechselspannungen zu untersuchen, wurde sie in einem Kreise verwendet, welcher der von der Elektronenröhre her bekannten Schaltung des RC-Verstärkers sehr ähnlich ist (Abb. 13). In Abb. 13*a* wird die nötige Gitterspannung E_g einer separaten Gitterbatterie entnommen. Diese für den praktischen Gebrauch unbequeme Methode kann jedoch leicht umgangen werden, indem man den hohen negativen Gitterstrom der Röhre durch einen geeigneten Gitterableitwiderstand R_L (Abb. 13*b*) fliessen lässt, wobei die nötige negative Gittervorspannung durch den Spannungsabfall in R_L erzeugt wird. Der in der Abb. 13 eingezeichnete Widerstand R_q soll den inneren Widerstand der Signalquelle und ev. anderer Elemente, die in den Gitterkreis eingeschaltet sind, darstellen.

Die mit dieser Schaltung erreichte Spannungsverstärkung wurde dann in folgender Weise gemessen: als Signalquelle wurde ein Tongenerator mit vernachlässigbar kleinem innerem Widerstand verwendet, der eine sinusförmige Wechselspannung konstanter und bekannter Amplitude abgab. Die Frequenz des Tongenerators war hierbei 200 Hz. Am Ausgang des Koronaröhrenverstärkers wurde dann die Amplitude der verstärkten Wechselspannung mit Hilfe eines sorgfältig geeichten Kathodenstrahloszillographen gemessen, woraus sich die Verstärkung mit einer Genauigkeit von besser als ±3% berechnen liess. Bei der Berechnung des Widerstandes R_k in den folgenden Messungen wurde der Eingangswiderstand des Oszillographen, der wechselstrommässig gesehen parallel zu R_k liegt, mitgerechnet. Der Ausgangskondensator wurde stets so gross gehalten, dass sein Wechselstromwiderstand neben den anderen Widerständen des Kreises zu vernachlässigen war.

Um das beim praktischen Betriebe der Röhre in einer der in Abb. 13 wiedergegebenen Schaltungen auftretende etwas unübersichtliche Verhalten besser verstehen zu können, ist es vorteilhaft, die in der Röhre auftretenden Vorgänge erst einmal theoretisch zu betrachten. Es soll dabei davon ausgegangen werden, dass die Röhre von einem Ruhestrom I_s durchflossen wird, welcher durch die Spitzenspannung E_s und die Gitterspannung E_g bestimmt wird. Das gleiche gilt für den Gitterstrom, der auch eindeutig von diesen beiden Grössen abhängt.

Analog zu den bekannten Herleitungen für die Elektronenröhre können wir dann eine kleine Änderung ΔI_s des Spitzenstromes I_s näherungsweise durch das erste Glied einer Taylorentwicklung des Spitzenstromes nach den beiden Variablen E_s und E_g darstellen (vgl. z.B. [9]):

$$\Delta I_s = \left(\frac{\partial I_s}{\partial E_s}\right)_{E_g} \Delta E_s + \left(\frac{\partial I_s}{\partial E_g}\right)_{E_s} \Delta E_g .$$

In der gleichen Weise findet man für den Gitterstrom I_g, da dieser ja ebenfalls durch E_s und E_g eindeutig bestimmt ist :

$$\Delta I_g = \left(\frac{\partial I_g}{\partial E_s}\right)_{E_g} \Delta E_s + \left(\frac{\partial I_g}{\partial E_g}\right)_{E_s} \Delta E_g .$$

Setzt man hier in bekannter Weise $\Delta I_s = i_s$, $\Delta I_g = i_g$, und $\Delta E_s = e_s$, $\Delta E_g = e_g$ und führt weiterhin die folgenden Grössen ein:

$$S_s = \left(\frac{\partial I_s}{\partial E_g}\right)_{E_s} = \text{Steilheit}, \qquad R_s = \left(\frac{\partial E_s}{\partial I_s}\right)_{E_g} = \text{innerer Widerstand},$$

$$S_g = \left(\frac{\partial I_g}{\partial E_g}\right)_{E_s} = \text{Gittersteilheit}, \qquad R_g = \left(\frac{\partial E_g}{\partial I_g}\right)_{E_s} = \text{innerer Gitterwiderstand}$$

so können die oben angeführten Gleichungen folgendermassen ausgedrückt werden:

$$i_s = \frac{1}{R_s} \cdot e_s + S_s \cdot e_g , \tag{1}$$

$$i_g = S_g e_s + \frac{1}{R_g} e_g . \tag{2}$$

Weiterhin kann man auf ähnliche Weise eine kleine Änderung ΔE_s der Spitzenspannung E_s als Funktion kleiner Änderungen der Gitterspannung und des Spitzenstromes darstellen:

$$\Delta E_s = \left(\frac{\partial E_s}{\partial E_g}\right)_{I_s} \cdot \Delta E_g + \left(\frac{\partial E_s}{\partial I_s}\right)_{E_g} \cdot \Delta I_s$$

und auf die gleiche Weise für E_g:

$$\Delta E_g = \left(\frac{\partial E_g}{\partial E_s}\right)_{I_g} \cdot \Delta E_s + \left(\frac{\partial E_g}{\partial I_g}\right)_{E_s} \Delta I_g \, .$$

Setzen wir nun hier

$$\mu_s = -\left(\frac{\partial E_s}{\partial E_g}\right)_{I_s} = \text{Verstärkungsfaktor}$$

$$\mu_g = -\left(\frac{\partial E_g}{\partial E_s}\right)_{I_g} = \text{Gitterverstärkungsfaktor}$$

und führen wieder kleine Buchstaben für die Grössen ΔE_s, ΔE_g, ΔI_s und ΔI_g ein, so finden wir

$$e_s = -\mu_s e_g + R_s i_s \, , \tag{3}$$

$$e_g = R_g i_g - \mu_g e_s \, . \tag{4}$$

Aus der Gl. (1) und (3) findet man dann die bekannte Barkhausenbedingung

$$\mu_s = S_s \cdot R_s \tag{5}$$

und ebenfalls für den Gitterkreis aus Gl. (2) und (4)

$$\mu_g = S_g \cdot R_g . \tag{6}$$

Legt man die in Abb. 13*a* angegebenen Schaltung für die weiteren Betrachtungen zu Grunde, so findet man in gewohnter Weise

$$e_s = -i_s \cdot R_k \tag{7}$$

und für den Gitterkreis:

$$e_0 = e_g + i_g \, R_q \tag{8a}$$

wobei e_0 die Spannungsänderung der Signalquelle, e_g die am Gitter auftretende Spannungsänderung und R_q der Widerstand des äusseren Gitterkreises ist.

Setzt man erst vorläufig einmal $R_q = 0$, also $e_g = e_0$, so erhält man aus Gl. (1), (7) und (5) die von der Elektronenröhre her bekannte Beziehung für die Spannungsverstärkung G_0 der Röhre:

$$G_0 = \frac{e_s}{e_g} = -\frac{\mu_s R_k}{R_k + R_s} . \tag{9}$$

Gegenüber der Elektronenröhre tritt aber hier wegen des negativen inneren Widerstandes der Koronaröhre ein wichtiger Unterschied auf. Während bei der ersteren eine desto höhere Verstärkung erzielt wird, je grösser der Anodenwiderstand R_k gewählt wird, steigt die Spannungsverstärkung der Koronaröhre, wenn man $R_k \rightarrow R_s$ laufen lässt, da sich damit der Nenner $R_s + R_k$ wegen des negativen Zeichens von R_s verkleinert. Voraussetzung ist jedoch, dass R_k immer grösser als $|R_s|$ ist.

Dass dies tatsächlich der Fall ist zeigt die Abb. 14, die die Abhängigkeit der Verstärkung G_0 von dem Widerstand R_k bei sonst unveränderten Bedingungen wiedergibt, d. h. die Spitzen- und Gitterspannung der Röhre wurden unabhängig von R_k konstant gehalten, so dass die Röhre immer in dem in Abb. 10 angegebenen Arbeits-

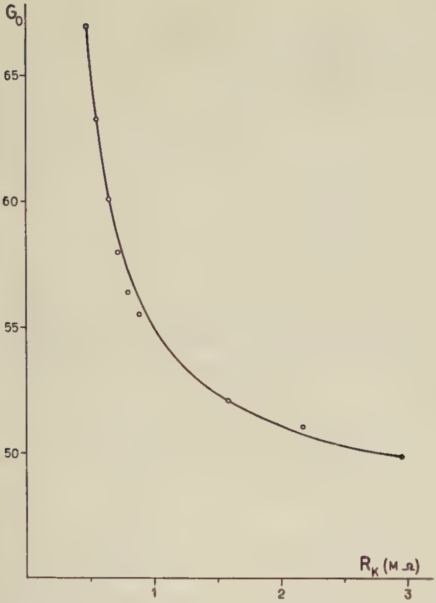

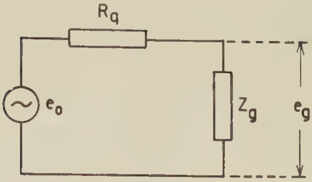

Abb. 15. Ersatzschaltbild des Gitterkreises.

Abb. 14. Abhängigkeit der Verstärkung G_0 vom Kathodenwiderstand R_k in Abb. 13. Der Widerstand $R_q = 0$. Ausgezogene Kurve: berechnete Werte; Punkte: gemessene Werte.

punkt P arbeitete. Die ausgezogene Kurve gibt die theoretisch zu erwartende Verstärkung G_0 wieder, welche mit Hilfe der aus den Kennlinien (Abb. 10) entnommenen Röhrendaten für den Arbeitspunkt aus Gl. (9) berechnet werden kann, während die Punkte die experimentell gemessene Verstärkung darstellen. Der Widerstand R_k wurde hierbei von 2,95 auf 0,47 MΩ erniedrigt. Die Linearität der Verstärkung ist bei Eingangswechselspannungen von weniger als 1–2 Volt sehr gut.

Wenn schliesslich $R_k = |R_s|$ gemacht wird (im vorliegenden Beispiel also $R_k = 136$ kΩ), so sollte man eine unendliche Verstärkung erwarten, da dann der Nenner der Gl. (9) null wird. Lange bevor dieser Punkt erreicht wird, treten aber bereits heftige Eigenschwingungen in der Röhre auf, die das Arbeiten mit der Röhre bei so kleinem R_k unmöglich machen. Es sind jedoch unter günstigen Bedingungen mit Koronaröhren Verstärkungen von bis zu 4000 erreicht worden, obwohl der Verstärkungsfaktor μ_s der Röhre unter 100 lag. Dieses sind jedoch technisch uninteressante Ausnahmefälle, da unter so extremen Verhältnissen die Verstärkung auf Grund des Millereffektes und der inneren Eigenschaften der Röhre sich als stark frequenzabhängig erweist.

Für $R_k < |R_s|$ wird der Nenner der Gl. (9) negativ, und es ist deshalb kein stabiles Arbeiten der Röhre mehr zu erwarten und wurde auch nicht gefunden. Dies ist in guter Übereinstimmung mit den bei (10) angegebenen Stabilitätsbedingungen.

Während also bei der Elektronenröhre die wahre Spannungsverstärkung immer kleiner als der Verstärkungsfaktor ist, ist die mit der Koronaröhre erreichte Verstärkung immer grösser als ihr Verstärkungsfaktor, soweit in einem Arbeitspunkt gemessen wird, wo R_s negativ ist. Für beide Röhren gilt aber, dass bei $R_k \to \infty$ die Verstärkung gleich dem Verstärkungsfaktor wird.

Ist $R_q \neq 0$, so gestalten sich die Verhältnisse wegen des hohen Gitterstromes der Röhre etwas komplizierter. Es tritt hier zunächst die Frage nach dem Eingangswiderstand der Röhre auf: ist dieser nämlich klein gegenüber R_q, so fällt der grösste

Teil der Spannung e_0 der Signalquelle an dem Widerstand R_q ab und $e_g \ll e_0$. Da unter diesen Umständen die Koronaröhre als Verstärkerröhre kaum anwendbar wäre, ist eine nähere Untersuchung des Eingangswiderstandes notwendig.

Der Eingangswiderstand $Z_g = e_g / i_g$ der Röhre lässt sich am einfachsten aus der Gl. (2) und (9) herleiten:

$$Z_g = \frac{e_g}{i_g} = \frac{R_g}{1 + \mu_g G_0} = \frac{R_g}{1 - \frac{\mu_g \mu_s R_k}{R_k + R_s}} \tag{10}$$

Da μ_s μ_g, und R_g Röhrenkonstanten sind, zeigt sich also, dass auch der Eingangswiderstand ausschliesslich von dem äusseren Widerstand R_k abhängt. Wird dabei R_k so gewählt, dass $(\mu_g \mu_s R_k)/(R_k + R_s) < 1$ ist, so stellt der Eingangswiderstand der Röhre einen positiven Widerstand dar, was wegen des relativ hohen Gitterstromes zu erwarten war. Aus Gl. (10) geht jedoch hervor, dass bei fallendem R_k der Eingangswiderstand der Röhre wächst, um bei $(\mu_g \mu_s R_k)/(R_k + R_s) = 1$ unendlich gross zu werden. Wird R_k weiterhin vermindert, so wird $(\mu_g \mu_s R_k)/(R_k + R_s) > 1$ und der Eingangswiderstand der Röhre somit negativ.

Die Konsequenzen dieses Verhaltens des Eingangswiderstandes der Röhre kann man sich leicht an dem in Abb. 15 gegebenen Ersatzbilde des Gitterkreises klar machen. Ist e_0 die Spannung der Signalquelle, so findet man für die Spannung am Gitter e_g:

$$e_g = \frac{e_0}{1 + \frac{R_q}{Z_g}} \tag{11}$$

wobei R_q wieder der äussere Widerstand des Gitterkreises ist. Solange Z_g einen positiven Widerstand darstellt, so ist immer $e_g < e_0$. Bei $Z_g = \infty$ wird $e_g = e_0$ (Fall der Elektronenröhre). Für negative Werte des Eingangswiderstandes findet man dagegen $e_g > e_0$, d. h. es findet bereits im Gitterkreis eine Verstärkung statt. Diese Überlegungen werden bei höheren Frequenzen ($f > 500$–1000 Hz) dadurch komplizierter, dass dann der Eingangswiderstand Z_g sowie der innere Widerstand R_s der Röhre komplex werden.

Die Verstärkung im Gitterkreis kann nun direkt berechnet werden. Aus Gl. (2) und (8a) erhält man für den Gitterstrom i_g:

$$i_g = \frac{e_0 + \mu_g e_s}{R_g + R_q} \tag{12}$$

und hieraus zusammen mit Gl. (4)

$$e_g = \frac{R_g e_0 - R_q \mu_g e_s}{R_g + R_q}. \tag{13}$$

Setzt man hier nun $e_s = G_0 e_g = -\frac{\mu_s R_k}{R_k + R_s} e_g$ so erhält man für die Verstärkung e_g/e_0 im Gitterkreise:

$$\frac{e_g}{e_0}=\frac{1}{1+\frac{R_q}{R_g}\left(1-\frac{\mu_g\,\mu_s\,R_k}{R_k+R_s}\right)}. \tag{14}$$

Ist $(\mu_g\mu_s R_k)/(R_k+R_s)>1$, so tritt wie erwartet eine Verstärkung im Gitterkreise auf, da dann der Nenner der Gl. (13) kleiner als 1 wird. Aus Gl. (14) geht weiterhin hervor, dass bei $R_q=0$ die Gitterverstärkung natürlich gleich 1 wird.

Die Verstärkung im Gitterkreis kann nun direkt gemessen werden, indem man bei konstantem und bekanntem e_0 die Spannung e_g am Gitter der Röhre bei verschiedenen Werten von R_k und R_q mit einem Kathodenstrahloszillographen mit hohem Eingangswiderstand misst und e_g/e_0 berechnet. Folgende Werte der Gitterverstärkung wurden experimentell ermittelt:

Tabelle 1.

R_k / R_q	0,55	0,645	0,72	0,795	0,875	1,585	2,95	$M\Omega$
51,2 $k\Omega$	3,159	1,708	1,193	—	0,930	0,643	0,560	
106 $k\Omega$	*	3,980	1,695	—	0,872	0,484	0,388	
199 $k\Omega$	*	*	*	1,218	0,755	0,330	0,247	

Aus diesen Werten lässt sich dann der Eingangswiderstand mit Hilfe von Gl. (11) berechnen. Die Resultate sind in Abb. 16 wiedergegeben, in welcher die aus den in Tabelle 1 wiedergegebenen Messergebnissen berechneten Z_g-Werte als Punkte eingetragen sind, während die ausgezogene Kurve nach der Gl. (10) unter Verwendung der aus den statischen Röhrenkurven (Abb. 10) entnommenen Daten für μ_s, μ_g, R_s und R_g berechnet wurde.

Es ist an dieser Stelle vielleicht von Interesse, die Richtung des Gitterstromes für verschiedene Z_g-Werte zu betrachten. Aus Abb. 15 finden wir für den Gitterwechselstrom:

$$i_g=\frac{e_0}{R_q+Z_g}.$$

Ist $Z_g>0$ so hat i_g die gleiche Richtung wie e_0, ist dagegen $Z_g<0$ und $|Z_g|>R_q$ so fliesst i_g immer in der entgegengesetzten Richtung, in welcher e_0 den Strom zu treiben versucht.

Die durch die Einführung des Widerstandes R_q eingetretene Gitterverstärkung muss natürlich auch die Gesamtverstärkung $G=e_s/e_0$ der Röhre ändern, da ja je nach dem Eingangswiderstand Z_g der Röhre e_g grösser oder kleiner als e_0 ist. Unter Verwendung der Gl. (9) und (14) erhält man also für die Gesamtverstärkung:

$$G=\frac{e_s}{e_0}=-\frac{\mu_s R_k}{R_k+R_s}\cdot\frac{1}{1+\frac{R_q}{R_g}\left(1-\frac{\mu_g\,\mu_s\,R_k}{R_k+R_s}\right)} \tag{15}$$

---

* Eigenschwingungen in der Röhre.

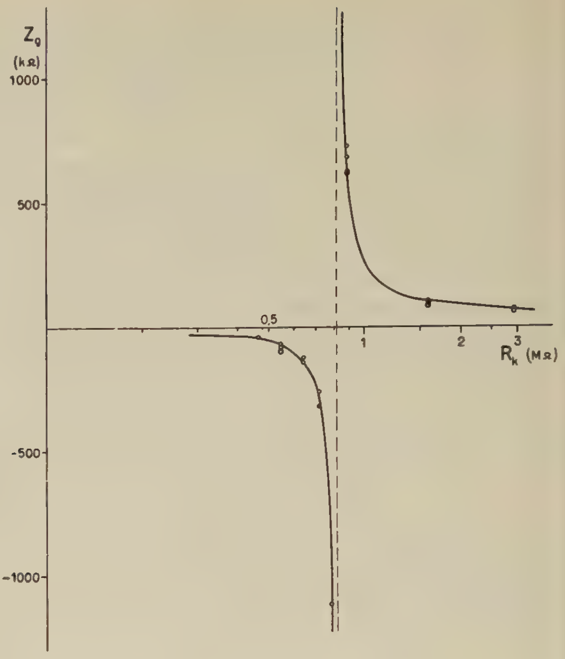

Abb. 16. Der Eingangswiderstand Z_g der Röhre in Abhängigkeit vom Kathodenwiderstand R_k der Abb. 13. Ausgezogene Kurve: berechnete Werte; Punkte: gemessene Werte.

Wie zu erwarten hängt G ausser von den Röhrendaten im Arbeitspunkt nur von R_k und R_q ab. Diese Abhängigkeit ist in Abb. 17 dargestellt, wo wieder die ausgezogenen Linien die aus Gl. (15) und den Röhrendaten für verschiedene Widerstände R_q berechneten Werte darstellen, während die Punkte die tatsächlich gemessene Gesamtverstärkung angeben. Innerhalb der Fehlergrenzen stimmen also Theorie und Experiment überein. — Im Punkte $(\mu_g \mu_s R_k)/(R_k+R_s)=1$ $(Z_g=\infty)$ ist, wie zu erwarten, die Verstärkung G unabhängig von R_a, da dort die Gitterverstärkung $e_g/e_0=1$ ist. Ist Z_g negativ, also $(\mu_g \mu_s R_k)/(R_k+R_s)>1$, so wird, wie aus Gl. (14) hervorgeht, die Gitterverstärkung bereits bei umso grösseren R_k-Werten unendlich, je grösser R_q gewählt wird. Wird aber die Gitterverstärkung unendlich, so muss nach Gl. (15) notwendigerweise auch die Gesamtverstärkung G unendlich werden, was auch aus Abb. 17 hervorgeht. Dies führt wieder dazu, dass kräftige Eigenschwingungen in der Röhre auftreten [10], welche sich auch in einer Veränderung des Aussehens der Spitzenkorona bemerkbar machen.

Für die praktische Anwendung der Röhre kann diese Instabilität bei zu kleinen R_k- und zu grossen R_q-Werten Schwierigkeiten mit sich führen. Sollen nämlich zwei solche Verstärkerstufen in der bei RC-Verstärkern üblichen Weise hintereinander geschaltet werden, so setzt sich der Wechselstromwert des Widerstandes R_k der ersten Röhre aus dem Kathodenwiderstand (Spitzenwiderstand) der ersten Röhre und dem hierzu parallelen Gitterwiderstand der zweiten Röhre zusammen. Da zur Vermeidung von Schwingungen und zur Einstellung einer geeigneten Gitterspannung der Gitterableitwiderstand der zweiten Röhre nicht zu gross sein darf, ist es schwer, den wirksamen Wechselstromwiderstand R_k der ersten Röhre genügend gross zu machen, um Eigenschwingungen in der ersten Röhre zu verhindern. Es wäre also hierzu nötig,

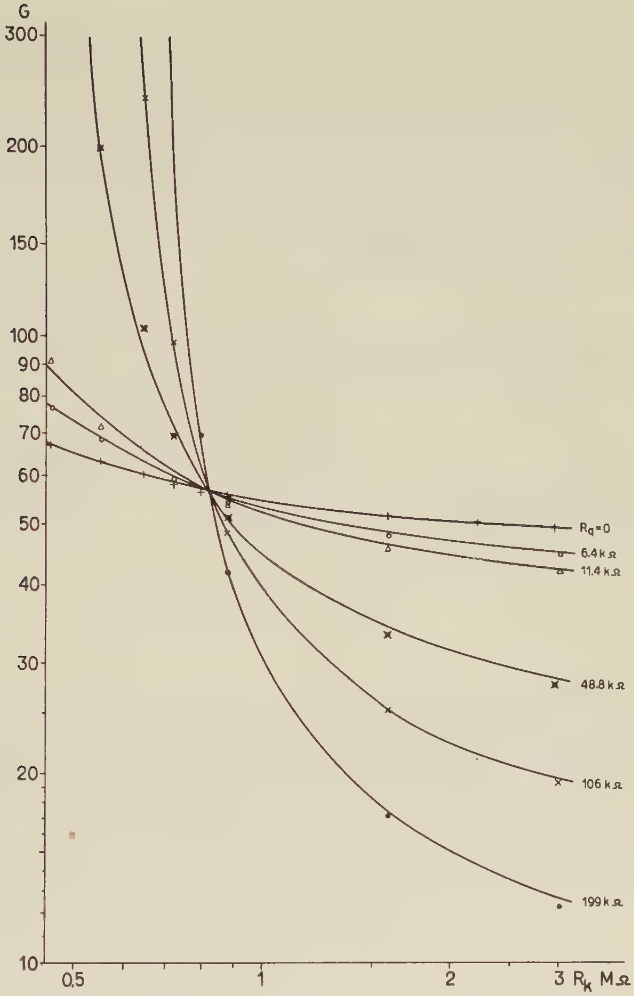

Abb. 17. Die Verstärkung G in Abhängigkeit vom Kathodenwiderstand R_k für verschiedene Werte des Widerstandes R_q (vgl. Abb. 13). Ausgezogene Kurve: berechnete Werte; Punkte: gemessene Werte.

durch Änderung der Geometrie und des Gasdruckes Röhren herzustellen, die hierfür geeignete elektrische Daten aufweisen. Allerdings könnte diese Schwierigkeit auch durch Einführung von Drosseln hoher Induktivität direkt umgangen werden.

Da alle im Koronaröhrenverstärker (Abb. 13) verwandten Widerstände relativ grosse Werte haben, muss weiterhin darauf geachtet werden, dass die Kapazitäten der Zuleitungen so klein wie möglich gehalten werden, da der Wechselstromwiderstand solcher Kapazitäten selbst bei verhältnismässig tiefen Frequenzen leicht in der Grössenordnung der ohmschen Widerstände des RC-Verstärkers liegt. Hierauf ist auch besonders zu achten, wenn man Wechselstrommessungen mit der Röhre macht, um Theorie und Experiment zu vergleichen. Bei den in Abb. 14, 16 und 17 wiedergegebenen Messungen wurden durch geeigneten Aufbau alle Leitungskapazitäten kleiner als 5 pF gehalten, so dass sie bei einer Frequenz von 200 Hz neben den ohmschen Widerständen vernachlässigt werden konnten.

Um schliesslich noch auf die in Abb. 13*b* dargestellte Schaltung eines RC-Verstärkers einzugehen, in der die für das Arbeiten der Röhre notwendige negative Gittervorspannung E_g durch den Gitterstrom I_g im Gitterableitwiderstand R_L hervorgerufen wird, können folgende Beziehungen gefunden werden. Ausser der Gl. (8a) gelten alle Gleichungen (1)–(7) und (9), welche als Ausgangspunkt für die Überlegungen gedient haben, die den in Abb. 13*a* dargestellte RC-Verstärker betroffen haben. Für den Gitterkreis der in Abb. 13*b* angegebenen Schaltung findet man aber, wenn man den Gitterkondensator genügend gross wählt, so dass sein Wechselstromwiderstand vernachlässigbar ist:

$$e_g(R_q + R_L) = e_0 R_L - R_L R_q i_g. \tag{8b}$$

Für die Verstärkung im Gitterkreis erhält man hieraus unter Zuhilfenahme der Gl. (4) und (9):

$$\frac{e_g}{e_0} = \frac{1}{1 + \frac{R_q}{R_L} + \frac{R_q}{R_g}\left(1 - \frac{\mu_g \mu_s R_k}{R_k + R_s}\right)} \tag{16}$$

und damit für die Gesamtverstärkung

$$G = \frac{e_s}{e_0} = -\frac{\mu_s R_k}{R_k + R_s} \cdot \frac{1}{1 + \frac{R_q}{R_L} + \frac{R_q}{R_g}\left(1 - \frac{\mu_g \mu_s R_k}{R_k + R_s}\right)}. \tag{17}$$

Die Einführung des Widerstandes R_L anstelle der Gitterbatterie bewirkt also keine wesentliche Änderung, der Verstärker kommt aber nicht so leicht in Eigenschwingungen, da die Gitterverstärkung e_g/e_0 (vgl. Gl. 16) erst bei kleineren Werten des Widerstandes R_k unendlich wird, als dies bei der in Abb. 13*a* dargestellten Schaltung der Fall ist (vgl. Gl. 14 und 15). Diese Tatsache kann leicht durch das Experiment bestätigt werden. — Der Eingangswiderstand der Röhre $Z_g = e_g/i_g$ ist natürlich unabhängig von der Art des Gitterkreises und ergibt sich auch hier wieder zu dem in Gl. (10) gefundenen Werte.

c) *Die Abhängigkeit der Verstärkung von der Frequenz*

Da in der hier zur Untersuchung vorliegenden Röhre nicht nur Elektronen sondern auch positive Ionen den Stromtransport durch die Röhre besorgen, ist zu erwarten, dass, ähnlich wie bei der Elektronenröhre bei sehr hohen Frequenzen, die Trägheit der Ladungsträger eine obere Grenze für die Frequenz der zu verstärkenden Wechselspannungen setzt. Diese Grenze wird aber der viel schwereren positiven Ionen wegen wesentlich tiefer liegen, als dies für die Elektronenröhre der Fall ist. Um eine Frequenzgrenze zu erhalten, die so hoch wie möglich liegt, ist es daher naheliegend ein Gas zu benutzen, welches erstens keine negativen Ionen bildet, wodurch auch die Elektronen auf ihrem Wege zur Spitze verlangsamt würden, und zweitens ein so kleines Atomgewicht wie möglich hat. Aus dem ersteren Grunde scheidet Luft als Füllgas sofort aus. Geeignet dagegen wären z.B. Stickstoff oder Wasserstoff; wegen des wesentlich geringeren Atomgewichtes wurde zu Gunsten von Wasserstoff entschieden, der sich auch sonst in Vorversuchen als vorteilhafter erwiesen hatte, weil eine mit Wasserstoff gefüllte Röhre einen höheren Verstärkungsfaktor aufwies als eine mit

Stickstoff gefüllte. In diesem Zusammenhang wäre natürlich auch an Füllung mit Edelgasen, z.B. Helium zu denken, da wegen des geringeren Ionisationspotentials von He die zum Betriebe der Röhre nötige Spitzenspannung vermutlich gesenkt werden könnte. WEISSLER [11] hat jedoch gefunden, dass es in reinem Argon keine negative Spitzenkorona gibt, sondern direkt ein Funkendurchschlag einsetzt. Dies dürfte nach den von WEISSLER angegebenen Gründen für alle Edelgase gelten, so dass für die Füllung der Koronaröhre nur Mischung von Edelgasen und anderen Gasen, z.B. Wasserstoff, in Frage käme. In der vorliegenden Arbeit konnten jedoch diese Fragen noch nicht aufgenommen werden und es wurden deshalb alle Untersuchungen mit Wasserstoff vorgenommen.

Um die zu erwartende Frequenzgrenze der Röhre ungefär abzuschätzen soll zunächst versucht werden, die Laufzeit der positiven Ionen von der Anode der Röhre zur Spitzenkatode zu berechnen. Da die Laufzeit der Elektronen in umgekehrter Richtung sehr viel kleiner als die Ionenlaufseit ist, ist im wesentlichen nur die letztere für die Bestimmung der Frequenzgrenze ausschlaggebend.

Die Laufzeit eines positiven Ions von der Anode zur Spitzenkathode der Röhre ist von der Feldverteilung zwischen diesen beiden Elektroden bestimmt, da seine Geschwindigkeit v in jedem Punkt proportional der Feldstärke F ist [3]. Bezeichnen wir diesen Proportionalitätsfaktor mit b so erhalten wir für die Laufzeit T:

$$T=\int\frac{ds}{v}=\int\frac{ds}{bF}, \tag{18}$$

wobei das Integral längs des Ionenweges s von Anode zur Spitzenkathode berechnet werden muss.

Da nun die Feldverteilung zwischen Spitze und Anode nicht bekannt ist, kann die Laufzeit T nur annäherungsweise bestimmt werden. Zunächst lässt sich hier eine untere Grenze für die Laufzeit angeben, da sich mit Hilfe einer Methode der Variationsrechnung [12] beweisen lässt, dass diese bei vorgegebener Spitzenspannung am kleinsten wird, wenn das Feld zwischen den beiden Elektroden konstant und somit auch die Geschwindigkeit der Ionen konstant ist. Da in der vorgegebenen Röhre der Anoden-Spitzenabstand 10 mm und die Spitzenspannung etwa 1000 Volt war, so erhalten wir für die Feldstärke F bei konstanter Feldverteilung

$$F=\frac{1000-200}{1}=800\ \mathrm{V/cm},$$

wenn man in Betracht zieht, dass ein Spannungsabfall von ca. 200 V in dem sehr begrenzten Gebiete des Kathodenfalles vor der Spitze [3] stattfindet. Da die Geschwindigkeit der positiven Ionen in Wasserstoff von 150 mm Hg $v=30\cdot F$ cm/sec [3] ist, erhält man für die kürzest denkbare Laufzeit $T=1/30800\cong 4\cdot 10^{-5}$ sec und somit für die im besten Fall erreichbare Frequenzgrenze, bei der sich die Laufzeiteffekte schon stark bemerkbar machen, $f=1/T=$ ca. 25 kHz.

Diese Frequenzgrenze wird nun natürlich nie erreicht, da das Feld zwischen Koronaspitze und Anode in keiner Weise konstant ist. Zu einer etwas besseren Näherung kann man kommen, wenn man das Feld zwischen Koronaspitze und Anode durch die Beziehung $F=k/r^2$ beschreibt. Hierbei wird die Konstante k durch die Spitzenspannung $V=1000$–200 V, dem Spitzenabstand $d=10$ mm und einem grob geschätzten Radius der äusseren Begrenzung des Faradayschen Dunkelraumes r

in der Spitzenkorona von 0,5 mm bestimmt. Unter Verwendung dieser Werte und der Gl. (18) ergibt sich die Laufzeit T zu

$$T = \frac{(d-r)\,(d^3 - r^3)}{3\,b\,V\,r} \cong 2{,}5 \cdot 10^{-4}\,\mathrm{sec}$$

und damit für die Frequenz, bei der die Laufzeiten schon wesentlich das Arbeiten der Röhre beeinflussen, 4 kHz.

Wegen der positiven Raumladungen, die von den langsamen positiven Ionen zwischen Koronaspitze und der planen Gitter-Anodenelektrode herrühren, dürfte das Feld aber noch schneller als $1/r^2$ von der Koronaspitze zur Anode abfallen. Dadurch verlängert sich die Laufzeit weiterhin. Nimmt man z. B. eine Feldverteilung $1/r^3$ an, so ergibt sich unter denselben Voraussetzungen wie vorher $T \cong 2 \cdot 10^{-3}$ und als Frequenz $1/T$ ca. 0,5 kHz.

Es sollte nun erwartet werden, dass die Verstärkung der Röhre etwa zwischen diesen beiden Frequenzwerten abfällt.

In der vorliegende Röhre dürfte aber auch ein anderer Effekt die Frequenzgrenze noch weiter nach unten zu verschieben, als dies nach diesen überschlagsmässigen Rechnungen zu erwarten ist. Wird nämlich die Gitterspannung in der Röhre im Zeitpunkt t etwas negativer gemacht, so werden von diesem Augenblicke an mehr positive Ionen in den sekundären Ionisationsbereichen erzeugt. Nach der Zeit $t+T$ erreicht dieser verstärkte Ionenstrom die Koronaspitze und befreit dort etwas mehr Elektronen durch Ionenstoss, als dies vor der Zeit $t+T$ der Fall gewesen ist. Diese grössere Anzahl Elektronen laufen in einer gegen T zu vernachlässigen Zeit zu den sekundären Ionisationsbereichen, wo nun noch mehr Ionen befreit werden, die ihrerseits zur Spitze eilen. Dieser Aufbauprozess läuft einigemale hin und her, bis der Spitzenstrom den Wert erreicht hat, welcher dem neuen Gitterspannungswerte entspricht. Für die Frequenzgrenze der Röhre dürfte also ein Vielfaches der Ionenlaufzeit T ausschlaggebend sein. Der hier beschriebene Prozess geht in Wirklichkeit jedoch sicher kontinuierlicher vor sich, da ja schon im Augenblick t, wo der verstärkte Ionenstrom von den sekundären Ionisationsbereichen aus zur Koronaspitze zu laufen beginnt, das Feld vor der Koronaspitze auf Grund der erhöhten positiven Raumladung im Entladungsraum vergrössert wird und somit schon gleich mehr Elektronen in der negativen Korona erzeugt werden. Dies dürfte die Einstellung auf den neuen Wert des Koronastromes beschleunigen.

Die experimentell gefundene Abhängigkeit der Verstärkung von der Frequenz für den Fall $R_k - 4{,}07$ MΩ und $R_a = 0$ zeigt Abb. 18*a*. Die bei dieser Messung verwandte Schaltung findet sich in Abb. 13*a*. Neben der Verstärkung ist auch noch der Phasenwinkel φ angegeben, welcher die Phase zwischen der Ausgangswechselspannung und der um 180° verschobenen Eingangsspannung angibt. Da auch die Koronaröhre ebenfalls wie die Elektronenröhre als RC-Verstärker immer eine Phasenverschiebung von 180° zwischen Eingangs- und Ausgangswechselspannung einführt, kann φ auch als Phasenwinkel zwischen der wirklich erhaltenen Ausgangswechselspannung und einer idealen Ausgangswechselspannung betrachtet werden, die man erhalten würde, wenn keine Trägheitseffekte auf Grund der langen Laufzeiten der Ionen in der Röhre auftreten würden. In den vorliegenden Messungen wurde φ mit Hilfe eines Kathodenstrahloszillographen bestimmt, an dessen x-Ablenkung nach geeigneter Verstärkung die Eingangswechselspannung gelegt wurde, während die y-Platten mit der Ausgangswechselspannung des Koronaverstärkers betrieben wur-

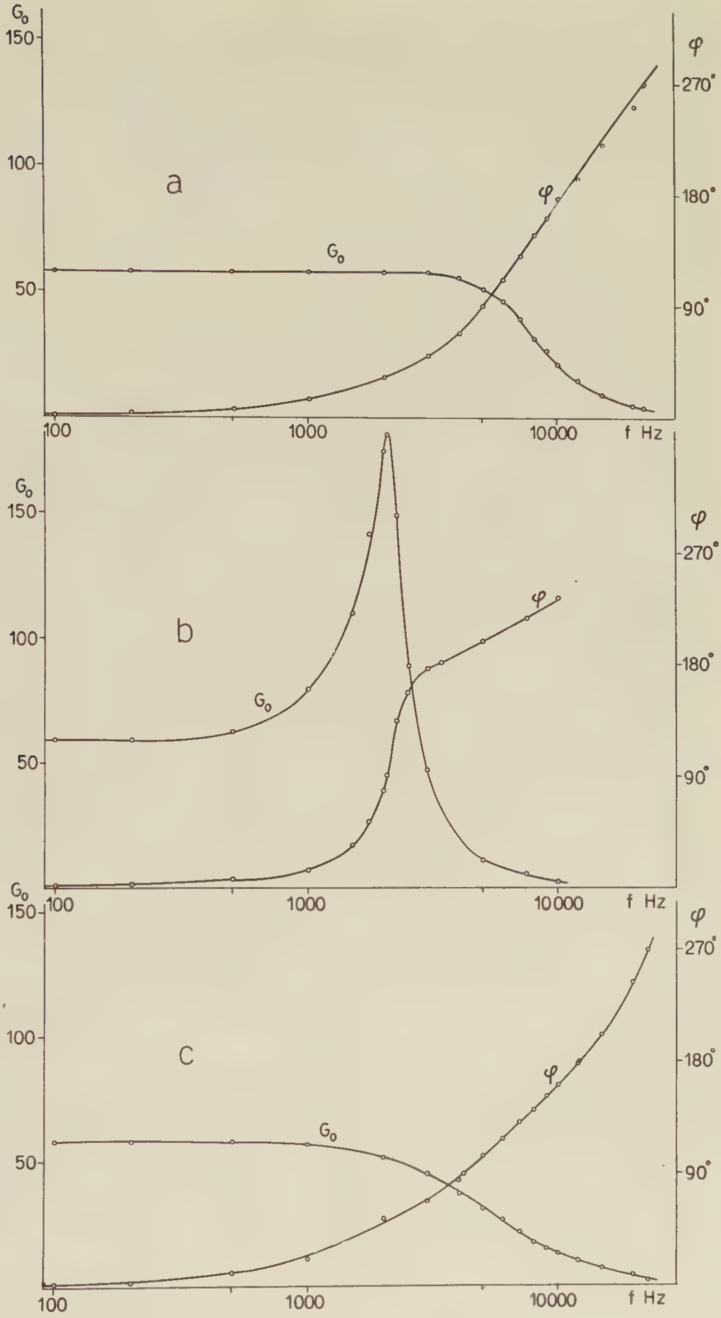

Abb. 18. Abhängigkeit der Verstärkung G_0 von der Frequenz der verstärkten Wechselspannung. *a*) $R_k = 4\,\mathrm{M\Omega}$, $C = 20$ pF; *b*) $R_k = 4\,\mathrm{M\Omega}$, $C = 240$ pF; *c*) $R_k = 0{,}77\,\mathrm{M\Omega}$, $C = 20$ pF (vgl. Abb. 19). $\varphi + 180°$ gibt die Phasenverschiebung zwischen Eingangs- und Ausgangswechselspannung des Verstärkers an.

den. Aus der sich auf dem Leuchtschirm ausbildenen Ellipse kann man dann leicht die Phase zwischen den beiden Wechselspannungen bestimmen.

Aus Abb. 18*a* ist zu entnehmen, dass die Verstärkung G_0 erst bei unerwartet hohen Frequenzen (3–5 kHz) zu fallen beginnt. Dies ist umso unverständlicher, da die Messung der Phase zeigt, dass die Ausgangsspannung bei einer Frequenz von z.B. 3 kHz schon um 50° hinter der Phase der Wechselspannung herläuft, die im idealen Falle erwartet werden muss. Da diese Phasenverschiebung nur durch die langen Ionenlaufzeiten in der Röhre erklärt werden kann, muss die Erklärung für das merkwürdige Verhalten der Verstärkung bei den höheren Frequenzen in einem anderen Effekt gesucht werden.

Einen Hinweis auf diesen Effekt gibt Abb. 18*b*, in welcher die experimentell bestimmte Abhängigkeit der Verstärkung G_0 und des Phasenwinkels φ von der Frequenz für den Fall dargestellt ist, dass ein Kondensator $C = 240$ pF parallel zum Ausgang der Röhre geschaltet wurde. Die sonstigen Bedingungen waren dieselben wie bei Abb. 18*a*. Man findet hier eine Resonanzstelle in der Verstärkungskurve, die mit einer Art Sprung der Phase φ von 0 auf 180° zusammenfällt. Es ist also zu erwarten, dass es sich hier um ein Resonanzphänomen handelt, bei welchem die Koronaröhre die Rolle einer Selbstinduktion spielt. Die Überhöhung der Röhrenverstärkung an der Resonanzstelle ist dabei von der Grösse der Eingangwechselspannung abhängig.

Bei der Diskussion der Laufzeiterscheinungen hat es sich gezeigt, dass die Einstellung des Koronastromes auf einen neuen Wert nach einer plötzlichen kleinen Erhöhung der Gitterspannung sich verhältnismässig langsam vollzieht, wobei sich die Ionendichte im Entladungsraum vergrössert. Die Erhöhung der Ionendichte in der Entladung kommt aber einer Speicherung von elektrischer Energie gleich. Diese elektrische Energie muss wieder an den äusseren Kreis abgegeben werden, sobald der Koronastrom aus irgendwelchen Gründen sinkt. Geschieht dies z.B. auf Grund einer plötzlichen Erniedrigung der Gitterspannung, so kann sich der Koronastrom erst verhältnismässig langsam auf den neuen Wert einstellen, da ja erst die überschüssigen Ladungsträger aus dem Entladungsraum verschwinden müssen, ein Vorgang, der dem bereits ausführlich beschriebenen bei einer Erhöhung der Gitterspannung ganz ähnlich verläuft.

Es zeigt sich also, dass die Koronaröhre einer Selbstinduktion ähnliche Trägheit besitzt, wobei sie anstelle von magnetischer elektrische Energie aufspeichert. Diese Eigenschaft ist für Gasentladungen allgemein bekannt und wurde kürzlich von van Geel [13] theoretisch näher untersucht. Von Hölscher [14] wurde eine dem hier beschriebenen Resonanzeffekte ganz ähnliche Erscheinung in anderen Gasentladungen gefunden.

Aus diesen Überlegungen geht ohne weiteres hervor, dass der innere Widerstand der Koronaröhre bei höheren Frequenzen komplex wird. Dieses bedingt auf Grund der Barkhausenbedingung Gl. (5), dass mindestens die Steilheit oder der Verstärkungsfaktor oder beide ebenfalls komplexe Werte annehmen müssen. Das Gleiche muss weiterhin für die Grössen R_g, S_g und μ_g gelten, so dass die Verhältnisse so kompliziert werden, dass eine rechnerische Erfassung der Vorgänge in der Koronaröhre bei höheren Frequenzen nur schwer möglich erscheint.

Da die Koronaröhre in Wechselstromkreisen eine der Selbstinduktion sehr ähnliche Wirkung hat, kann man den Ausgangskreis des RC-Verstärkers (Abb. 13) durch das in Abb. 19 wiedergegebene Ersatzschaltbild wechselstrommässig darstellen, wobei L die Selbstinduktion und den inneren Widerstand der Koronaröhre bezeichnet. Die Kapazität C entspricht der Röhrenkapazität zwischen Koronaspitze und Anode

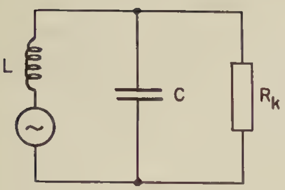

Abb. 19. Ersatzschaltbild des Anodenkreises des RC-Verstärkers (vgl. Abb. 13).

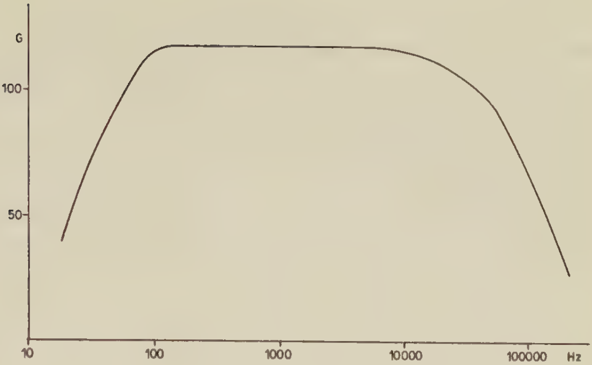

Abb. 20. Vgl. Text.

(20 pF), wozu eine eventuell aussen parallel zur Röhre geschaltete Kapazität hinzugerechnet werden muss. Durch Bestimmung der Resonanzfrequenz bei verschiedenen Kapazitäten C konnte die Induktanz der Koronaröhre gemessen werden und ergab sich zu etwa 25 Hy. — Weiterhin ist nach dem Ersatzschaltbild (Abb. 19) zu erwarten, dass der Widerstand R_k dämpfend auf jede Schwingung im Kreise einwirkt und zwar um so mehr, je kleiner R_k gewählt wird. Dies wurde ebenfalls durch das Experiment bestätigt.

Die unerwartet hohe Frequenzgrenze der Röhre lässt sich nun leicht dadurch verstehen, dass die Eigenkapazität der Röhre zwischen Spitze und Anode, die ja parallel zur ,,Selbstinduktion'' der Röhre liegt, Anlass zu einer Resonanz im Kreise gibt, die gerade so liegt, dass sie den Abfall der Röhrenverstärkung, der eigentlich schon bei wesentlich tieferen Frequenzen beginnt, in das Bereich höherer Frequenzen verschiebt. Dies lässt sich teils dadurch zeigen, dass man die in Abb. 18*a* gezeigte Kurve mit verschiedenen Parallelkapazitäten C aufnimmt und teils, indem man den Widerstand R_k verkleinert, wodurch die Dämpfung des Kreises sehr vergrössert wird. Die Abb. 18*c* zeigt die Abhängigkeit der Verstärkung von der Frequenz bei $R_k = 0{,}77$ MΩ, wobei C wieder 20 pF war und auch sonst alle Bedingungen die gleichen wie bei Abb. 18*a* waren. Wegen der wesentlich grösseren Dämpfung im Kreise tritt keine ausgeprägte Resonanz mehr ein und die Frequenzabhängigkeit der Röhrenverstärkung ist deshalb wesentlich verschlechtert.

Ausser den hier besprochenen Faktoren, die auf die Frequenzabhängigkeit der Verstärkung einwirken, kann auch noch der Millereffekt [15] unter gewissen Bedingungen die Frequenzgrenze der Röhre herabsetzen. Der hohen Röhrenverstärkung und der relativ grossen Widerstände im Röhrenkreise wegen können nämlich bereits verhältnismässig kleine Kapazitäten zwischen Anode und Koronaspitze die Verstärkung der Röhre bei hohem Widerstand R_q des Gitterkreises wesentlich beeinflussen. Die in Abb. 17 erhaltenen hohen Verstärkungen bei $R_q = 50$ kΩ und höher und $R_k < 0{,}7$ MΩ fielen daher schon bei Frequenzen über 1–2 kHz recht wesentlich ab.

d) *Rauschen der Koronaröhre*

Soll eine Röhre in einem Verstärker zur Verwendung kommen, so ist es wichtig, ihre Rauscheigenschaften zu kennen, da hiervon abhängt, wie kleine Wechselspannungen noch mit ihr verstärkt werden können. Aus diesem Grunde sollte auch das Rauschen der Koronaröhre untersucht werden.

Die Rauschspannung, die am Ausgang des Koronaverstärkers (Abb. 13*a*) auftrat, wurde deswegen nach geeigneter Verstärkung mit Hilfe eines Thermokreuzes gemessen. Der hierzu notwendige Messverstärker war ein Zweiröhren-RC-Verstärker mit negativer Rückkopplung, dessen Ausgang auf das Gitter eines Kathodenverstärkers gegeben wurde. Die über den Kathodenwiderstand von 3 kΩ auftretende Wechselspannung wurde dann mit einem Thermokreuz gemessen. Die Frequenzabhängigkeit der Spannungsverstärkung des Messverstärkers ist in Abb. 20 wiedergegeben, die äquivalente Bandbreite des Verstärkers war 90 kHz (16).

Die Eichung des Verstärkers geschah mit einem Tongenerator bei einer Frequenz von 2000 Hz, welcher an den Eingang des Messverstärkers angeschlossen wurde. Bei verschiedenen bekannten Ausgangsspannungen des Tongenerators wurde dann die am Ausgange des Verstärkers am Thermokreuz auftretende Spannung gemessen und so eine Eichkurve aufgenommen. Danach wurde der Ausgang des Koronaröhrenverstärkers (Abb. 13*a*) mit einer sehr kurzen Leitung auf den Eingang des Messverstärkers gegeben und so die effektive Rauschspannung $\sqrt{\overline{E^2}}$ bestimmt. Da weiterhin der äussere Widerstand R_k (1,43 MΩ) des Koronaröhrenverstärkers (Abb. 13*a*) bei diesen Messungen sehr viel grösser als der innere Widerstand R_s der Koronaröhre gehalten wurde, wird die gesamte von der Koronaröhre erzeugte Rauschleistung in den äusseren Widerstand R_k abgegeben und kann also aus der Rauschspannung leicht berechnet werden. — Bei allen Messungen wurde durch sorgfältige Schirmung genau darauf geachtet, dass keine 50-periodischen Streuwechselfelder die Messergebnisse fälschten. Da das Rauschen des Messverstärkers und das Widerstandsrauschen im Widerstand R_k ganz erheblich kleiner als das Rauschen der Koronaröhre war, konnte das Messverstärkerrauschen vernachlässigt werden.

Für die im Vorhergehenden besprochene Normalröhre wurde auf diese Weise im Arbeitspunkt P (Abb. 10) ein mittlere Rauschspannung von 12,5 $\mathrm{mV_{eff}}$ gefunden. Dies bedeutet, dass die Röhre eine Rauschleistung von ungefähr $1{,}1 \cdot 10^{-10}$ Watt an den äusseren Kreis abgab. Bei diesen Messungen war $R_k = 1{,}43$ MΩ und $R_q = 0$. Wurde der Widerstand des Gitterkreises R_q wesentlich erhöht, so trat hierdurch eine gewisse Steigerung der Rauschspannung auf (im vorliegenden Beispiel bei $R_q = 10$ kΩ z.B. $\sqrt{\overline{E^2}} = 17\ \mathrm{mV_{eff}}$); eine sehr wesentliche Vergrösserung der Rauschspannung kann hierdurch jedoch nicht auftreten, da der Widerstand des Gitterkreises dem Verteilungsrauschen (siehe unten) entgegenwirkt.

Um festzustellen, ob das Rauschen der Röhre frequenzabhängig ist, wurde ein selektiver Verstärker [17] zwischen die zweite Röhre und den Kathodenverstärker des Messverstärkers geschaltet. Auf diese Weise wurde nur ein schmales Frequenzband kräftig verstärkt und gemessen, während alle Rauschfrequenzen die ausserhalb des Frequenzbandes des selektiven Verstärkers lagen, nicht wesentlich verstärkt wurden und somit wenig zu der mit dem Thermokreuz gemessenen Wechselspannung beitrugen. Die spezielle Art des selektiven Verstärkers [17] liess es zu, das Frequenzband, in welchem der selektive Verstärker kräftig verstärkte, im Bereich der Frequenzen von 0 bis 5 kHz kontinuierlich zu verschieben. Dabei trat eine gewisse Änderung der Bandbreite des selektiven Verstärkers ein, für die bei jeder Messung korrigiert wurde. Die äquivalente Bandbreite des selektiven Verstärkers war im Mittel etwa 200 Hz.

Durch eine Anzahl Messungen bei verschiedener Frequenzeinstellung des selektiven Verstärkers konnte auf diese Weise festgestellt werden, dass innerhalb eines Mess-

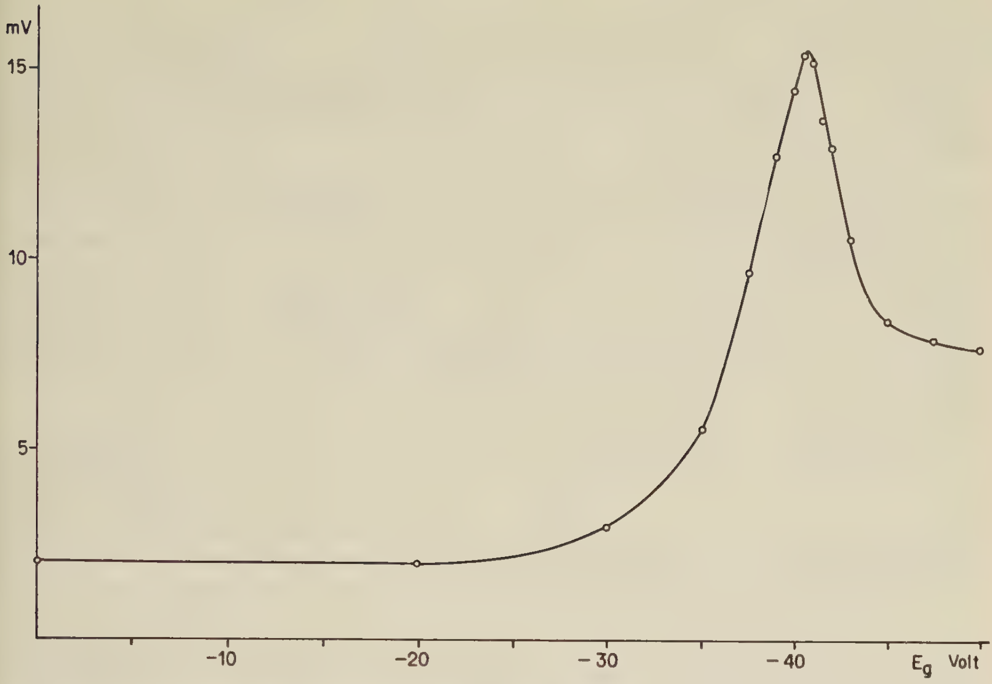

Abb. 21. Abhängigkeit des Röhrenrauschens von der Gitterspannung E_g bei konstantem Spitzenstrom $I_s = 400\ \mu A$.

fehlers von etwa 10 % die Rauschspannung der Koronaröhre im Bereiche von 0–5 kHz unabhängig von der Frequenz war, d. h. dass sog. ,,weisses" Rauschen vorlag. Dies stimmt mit der bei [16] gemachten Angabe überein, dass die von Gasentladungen abgegebenen Rauschspannungen im allgemeinen unabhängig von der Frequenz sind.

Bei Vorversuchen wurde festgestellt, dass das Rauschen der Koronaröhre im allgemeinen etwa proportional mit der in der Röhre erreichten Verstärkung wächst. Es war deshalb von Interesse festzustellen, was der eigentliche Grund für das hohe Rauschen der Röhre ist, besonders da das Rauschen der negativen Korona alleine ($E_g - 0$) wesentlich geringer ist. Es wurde deshalb die Abhängigkeit der Rauschspannung von der Gitterspannung E_g bei konstantem Spitzenstrom I_s untersucht (Abb. 21). Dabei wurde gefunden, dass das Rauschen bei steigender Gittervorspannung auf einen Höchstwert ansteigt um danach wieder abzufallen. Der Anstieg des Rauschens fällt ungefähr mit dem Punkte zusammen, bei dem die sekundären Ionisationsbereiche wirksam werden, und das Rauschmaximum tritt etwa beim günstigsten Arbeitspunkt der Röhre ein. Es ist deshalb anzunehmen, dass es sich hierbei um ein durch die Röhre verstärktes Verteilungsrauschen handelt, was dadurch entsteht, dass der Gitterstrom I_g und der Anodenstrom I_a statistische Schwankungen aufweisen, da der Spitzenstrom $I_s - I_a + I_g$ einmal etwas mehr zum Gitter und einmal etwas mehr zur Anode hinfliesst. Diese Schwankungen werden dann durch die Verstärkerwirkung der Röhre verstärkt und addieren sich dem normalen Rauschen der negativen Korona, welches ebenfalls durch das Einsetzen der sekundären Ionisationsbereiche etwas verstärkt wird. Die Tatsache, dass der Widerstand des Gitter-

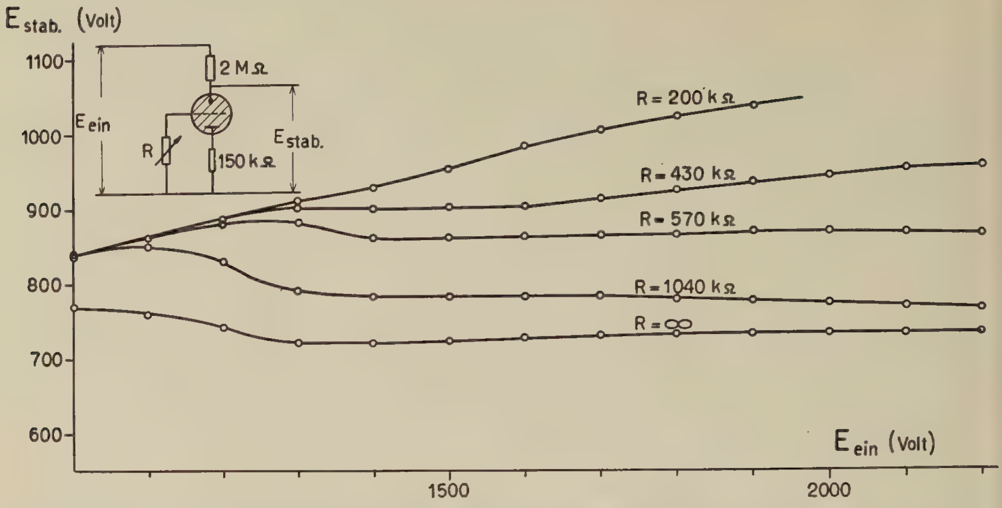

Abb. 22. Anwendung der Röhre zur Stabilisierung hoher Spannungen. Durch die Änderung des Widerstandes R kann die stabilisierte Ausgangsspannung E_{stab} geregelt werden. Oben links die verwendete Schaltung.

kreises R_q die Rauschspannung nur verhältnismässig wenig beinflusst, zeigt jedoch, dass der Anteil des durch die Röhre verstärkten Koronarauschens verhältnismässig gering ist. Der grösste Teil der gefundenen Rauschspannung rührt also vom Verteilungsrauschen her. Dies erklärt, dass in erster Näherung das Rauschen proportional der Verstärkung gefunden wurde. Experimentell wurde festgestellt, dass sich eine Eingangswechselspannung von 0,2 mV unabhängig von der Röhrenverstärkung immer gerade aus dem Rauschen hervorhob.

Wie zu erwarten ist das Rauschen vom Gasdruck, Spitzenstrom usw. abhängig, jedoch sind die zu beobachtenden Änderungen nicht sehr wesentlich. Allgemein scheint zu gelten, dass bei fallendem Gasdruck das Rauschen zunimmt; dies gilt besonders für Drucke unter 150 mm Hg. Die Abhängigkeit des Rauschens vom Spitzenstrom zeigt keine so klare Tendenz.

e) *Stabilisierung hoher Spannungen mit der Koronaröhre*

Die Stabilisierung von hohen Spannungen besonders für den Betrieb von GM-Röhren mit Hilfe von Koronaentladungen ist seit längerer Zeit bekannt [18, 19, 20]. Im allgemeinen wird hierzu eine positive Koronaentladung an einem Draht in einem konzentrischen Zylinder verwendet; die Gasfüllung ist gewöhnlich Wasserstoff. Die so hergestellten Röhren haben den Nachteil, dass ihre Brennspannung durch den Gasdruck und die Geometrie fest bestimmt ist. Gerade für den Betrieb von GM-Röhren ist es aber wünschenswert, die stabilisierte Spannung in gewissen Grenzen ändern zu können. Weiterhin ist oft ein relativ hoher Widerstand in Serie mit der Koronastabilisatorröhre nötig, um eine genügend gute Stabilisierung zu erhalten. Wegen des geringen inneren Widerstandes R_s der Koronaröhre ist es deshalb naheliegend, dieselbe auch auf ihre Stabilisierungseigenschaften zu untersuchen.

Abb. 22 gibt eine für die Koronaröhre geeignete Stabilisatorschaltung und die damit erhaltenen Ergebnisse wieder. Die hier verwendete Koronaröhre gleicht geometrisch vollständig der im obigen beschriebenen, der Gasdruck war aber nur 110 mm Hg. Als Gitterableitwiderstand R kann hierbei ein gewöhnliches Potentiometer mit einem Widerstand von 5 $M\Omega$ verwendet werden. Der Anodenwiderstand von 150 kΩ ist ein Hilfswiderstand, der den negativen inneren Widerstand der Röhre ausgleicht (Abb. 10).

Abb. 22 gibt ferner die über die Röhre abgenommene stabilisierte Spannung E_{stab} in Abhängigkeit von der Eingangsspannung E_{ein} bei verschiedenen Einstellungen des Widerstandes R an. Man sieht, dass durch die Änderung von R die stabilisierte Spannung kontinuierlich zwischen etwa 720 und 900 Volt geändert werden kann und trotzdem eine gute Stabilisierung der Ausgangsspannung erreicht wird, obwohl der mit der Röhre in Serie liegende Widerstand nicht allzu gross ist. Der Koronastrom durch die Röhre betrug in dem günstigsten Stabilisierungsbereich ($E_{\text{ein}} = 1500$ V) etwa 300 μA. Bei Spitzenströmen von wesentlich unter 200 μA treten manchmal kleine Schwingungen in der Röhre auf, die mit einem Kondensator ausgeglichen werden müssten. — Bei gewissen Einstellungen von R kann die Stabilisierung weiterhin noch verbessert werden, wenn der Anodenwiderstand von 150 kΩ gleichzeitig mit R etwas geändert wird (*z. B.* bei $R = 1040$ kΩ).

Aus Abb. 22 geht weiterhin hervor, dass es nicht möglich ist, eine einheitliche Zahlenangabe für die Güte der mit der Koronaröhre erreichten Stabilisation anzugeben, da dies ganz davon abhängt, mit welcher Eingangsspannung E_{ein} und welchem Gitterwiderstand R man gerade arbeitet. Die Güte der Spannungsstabilisation muss also von Punkt zu Punkt gemessen oder direkt aus Abb. 22 entnommen werden.

Durch Änderung von Geometrie, Gasart und Gasdruck der Röhre kann die Höhe der stabilisierten Spannung oberhalb einer unteren Grenze von etwa 600 V sehr wesentlich verändert werden. Wird z.B. Luft von Atmosphärendruck als Füllgas verwendet, findet man ähnliche Stabilisationseigenschaften der Röhre bei einer Spannung von 6000 Volt. Allerdings muss dann mit recht viel höheren Widerständen R und R_k gearbeitet und eventuell noch zur Erhöhung der Gitterwirkung ein Widerstand zwischen Gitter und negativen Pol der Eingangsspannung gelegt werden.

Bevor ein endgültiges Urteil über die Anwendbarkeit der Koronaröhre als Spannungsstabilisator abgegeben werden kann, müssen jedoch noch ausführlichere Untersuchungen besonders über die Konstanz der Röhreneigenschaften bei längerem Betrieb gemacht werden. Da der gegenwärtige Aufbau der Röhre (Abb. 8) eine genügende Reinigung der Röhrenelemente vor dem Abschmelzen durch Ausheizen usw. nicht zulässt, ist zu erwarten, dass sich bei längerem Betriebe Schmutz auf den Elektroden ansammelt und die Gasfüllung der Röhre verunreinigt wird. Dadurch verändern sich dann die Kennlinien der Röhre, was durch einen Dauerbetrieb der Röhre von einigen 100 Stunden bestätigt werden konnte.

4. Die Abhängigkeit der Röhreneigenschaften von dem Aufbau der Röhre

Im Vorhergehenden ist bereits angedeutet worden, dass die Eigenschaften der Röhre sehr wesentlich von ihrem geometrischen Aufbau, Gasfüllung usw. abhängen. Die spezielle Elektrodenform, die für die oben erwähnten Messungen angewandt wurde, sind deshalb gewählt worden, weil die so hergestellte Röhre eine gute Betriebsstabilität, einen einfachen Aufbau und eine gute Reproduzierbarkeit aufwies. Auf besonders hohen Verstärkungsfaktor, geringe Spitzenspannung E_s im Arbeitspunkt usw. ist dabei kein besonderer Wert gelegt worden. — Im Folgenden sollen nun kurz die verschiedenen Konstruktionselemente der Röhre besprochen und die Einwirkung ihrer Ausführung auf die Eigenschaften der Röhre zumindestens qualitativ angegeben werden.

a) *Kathode*

Im Verlaufe der Untersuchungen wurden verschiedene Formen der Kathode untersucht. Neben der oben beschriebenen einfachen Spitze wurden Mehrfachspitzen und auch dünne Drähte, welche parallel zur Gitter-Anodenelektrode gespannt wurden, angewandt. Diese letzteren Formen konnten bei Drucken in der Grössenordnung von 760 mm Hg unter gewissen Voraussetzungen verwendet werden, bei einem Druck von 150 mm Hg wird die Korona in diesen Fällen jedoch sehr unruhig. Deshalb wurde bisher auschliesslich nur eine einzelne Spitze als Kathode verwendet.

Da die Spitze von positiven Ionen getroffen wird, muss erwartet werden, dass an ihr eine gewisse Kathodenzerstäubung auftritt. Um dieser entgegenzuwirken wurde als Spitzenmaterial ein Metall gewählt, welches eine geringe Kathodenzerstäubung aufweist [3]. Da die Spitzenkorona an Aluminium- und Magnesiumspitzen unruhig war, was vermutlich auf Oxydschichten zurückgeführt werden muss, wurde schliesslich Tantal gewählt, welches sich gut bewährte. Dauerversuche mit 0,3 mm dickem Tantaldraht zeigten bei einem Koronastrom von 300 μA erst nach etwa 1000 Stunden eine leichte Verformung der Spitze, nach 4000 Stunden konnte jedoch unter dem Mikroskop eine deutliche Einwirkung der Kathodenzerstäubung festgestellt werden. — Da die Kathodenzerstäubung die Spitzenform verändert und diese wiederum für die elektrischen Eigenschaften der Röhre wichtig ist, wurde die Form der Spitze von vornherein so gewählt, wie sie sich nach längerem Betriebe der Röhre auf Grund der Kathodenzerstäubung einstellt. Wie schon oben berichtet, wurde die Spitze deshalb senkrecht zu ihrer Längsachse flach angeschliffen, so dass sie die Form eines Zylinders mit ebenem Boden (Abb. 4) hatte. Die negative Korona bedeckt dann diese ebene Fläche in einer dünnen Schicht, wie dies von Glimmentladungen bei tieferen Drucken her bekannt ist.

Weiterhin wurde festgestellt, dass der Verstärkungsfaktor der Röhre mit dem Durchmesser der Spitze wächst, solange nur die Bodenfläche der zylindrischen Spitze noch ganz von der Korona bedeckt wird. Da ein möglichst dicker Draht ebenfalls aus Gründen der Kathodenzerstäubung vorzuziehen war, wurde schliesslich ein 0,3 mm dicker Tantaldraht, der in einer Messingfassung befestigt war, gewählt.

Als Abstand zwischen Spitze und Gitter-Anodenelektrode wurde aus rein praktischen Gründen zunächst 10 mm gewählt, obwohl dies sicher nicht der günstigste Wert für die Erreichung einer möglichst hohen Frequenzgrenze ist. Auch der Verstärkungsfaktor μ_s ist von diesem Abstande abhängig, der Gang dieser Abhängigkeit ist aber für verschiedene Gasdrucke in der Röhre verschieden.

Abschliessend kann festgestellt werden, dass die vorliegende Kathodenform sicher nicht die bestmögliche ist und das hier noch wesentliche Verbesserungen zu erwarten sind, welche besonders auch die Lebensdauer der Röhre günstig beeinflussen können.

b) *Gitter-Anodenelektrode*

Die Verstärkung der Röhre muss natürlich von dem Sitze der sekundären Ionisationsbereiche, d. h. der Gitter-Anodenelektrode, stark abhängig sein. Es wurden

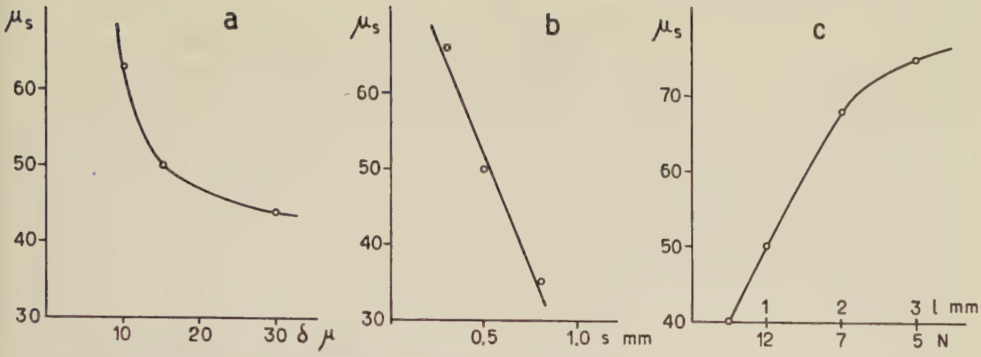

Abb. 23. Abhängigkeit des Verstärkungsfaktors μ_s von gewissen geometrischen Abmessungen der Röhre (vgl. Text).

deshalb Versuche mit verschiedenen Formen dieser Elektrode gemacht, wobei aber immer die Methode der dünnen Drähte in Schlitzen zum Aufbau der Gitter-Anodenelektrode verwendet wurde.

In vorbereitenden Untersuchungen wurde festgestellt, dass die Lage der dünnen Anodendrähte in den Schlitzen der Gitterelektrode so gewählt werden muss, dass sie 0–0,2 mm unter der Oberfläche der Gitterelektrode liegen. Nur unter diesen Umständen erhält man einen guten Verstärkungsfaktor: liegen die Drähte höher oder tiefer so fällt der Verstärkungsfaktor stark ab, während er innerhalb des angegebenen Bereiches ziemlich konstant ist. Dies gilt ziemlich unabhängig von der Dicke der Drähte. Es wurden daher in allen Elektrodensystemen dei Drähte so montiert, dass sie 0,1 mm unter der Oberfläche der Gitterelektrode lagen.

Die Abb. 23 gibt den Verlauf des Verstärkungsfaktors, wenn jeder der verschiedenen Parameter der Gitteranodenstruktur für sich geändert wird. Hierbei wurde der Koronaspitzenabstand $d = 10$ mm, der Gasdruck $p - 150$ mm Hg, die Grösse der Gitterelektrode 18×19 mm und der Spitzenstrom $I_s = 400\ \mu$A konstant gehalten. Geändert wurde der Durchmesser der Wolframdrähte δ bei konstanter Anzahl und Breite der Schlitze (Abb. 23*a*), die Breite der Schlitze s bei konstanter Anzahl der Schlitze (12 Stück) und konstantem Durchmesser der Wolframdrähte (15 μ) (Abb. 23*b*) und schliesslich der Schlitzabstand l oder die Anzahl der Schlitze N bei konstanter Breite der Schlitze (0,5 mm) und konstantem Drahtdurchmesser (15 μ) (Abb. 23*c*). Der in den ersten zwei Fällen beobachtete Gang des Verstärkungsfaktors ist durch die Änderung der Feldstärke an den Anodendrähten bei Änderung der beiden Parameter δ und s zu verstehen. Die in Abb. 23*c* gezeigte Einwirkung der Schlitzanzahl auf die Verstärkung ist dagegen wohl dadurch zu erklären, dass bei geringerer Schlitzanzahl die Ionisierungswahrscheinlichkeit und damit die Empfindlichkeit für Gitterspannungsschwankungen in den noch verbleibenden sekundären Ionisationsbereichen steigt, da die Stromdichte dort wächst. Der innere Widerstand R_s wurde bei allen diesen Messungen als ziemlich konstant zwischen 0 und -100 kΩ gefunden. Da die dünnen Drähte in den Schlitzen nur von Elektronen getroffen werden, ist nicht zu erwarten, dass die Lebensdauer der Röhre durch frühzeitige Zerstörung der Drähte beeinträchtigt wird, was durch Dauerversuche bestätigt wurde. Schwieriger ist dagegen zu vermeiden, dass sich mit der Zeit einzelne punktförmige Entladungen auf den Drähten bilden, was die Verstärkung und Frequenzgrenze der Röhre sehr

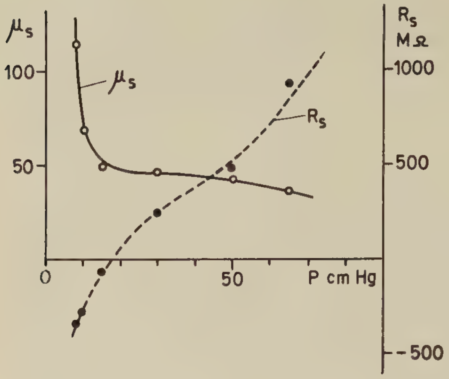

Abb. 24. Abhängigkeit des Verstärkungsfaktors μ_s und des inneren Widerstandes R_s vom Gasdruck.

beeinflusst. Es ist deshalb wichtig, auf wirkliche Sauberkeit bei der Herstellung der Röhre zu achten.

c) *Gasfüllung*

Bei der Wahl des Füllgases für die Röhre muss zunächst darauf geachtet werden, dass ein Gas zur Verwendung kommt, welches ein so geringes Atomgewicht wie möglich hat und keine negativen Ionen bildet. Diese beiden Forderungen müssen gestellt werden, weil die Frequenzgrenze der Röhre im wesentlichen von der Laufzeit der Ionen von Anode zu Kathode abhängt. Würden sich negative Ionen in der Röhre bilden, so würde auch noch die sonst sehr kurze Laufzeit der Elektronen in der entgegengesetzten Richtung wesentlich verlängert. Aus diesen Gründen scheidet Luft als Füllgas aus. Auf Grund seines geringen Atomgewichtes wurde dem Wasserstoff schliesslich der Vorzug gegeben, besonders da sich bei Vorversuchen mit Wasserstoff ein grösserer Verstärkungsfaktor der Röhre als mit Stickstoff ergab. Auf diesem Gebiete sollten aber noch ausführlichere Untersuchungen vorliegen, bevor man eine endgültige Aussage über das günstigste Füllgas der Röhre machen kann.

Die Abhängigkeit des Verstärkungsfaktors μ_s und des inneren Widerstandes R_s der Röhre vom Gasdruck zeigt Abb. 24. Das kräftige Ansteigen der Verstärkung bei $p < 150$ mm Hg ist von einem gleichzeitigen Ansteigen des Rauschens der Röhre begleitet, bei Gasdrucken von weniger als 80 mm Hg wird die Entladung leicht instabil. Die Frequenzgrenze der Röhre steigt, wie zu erwarten, mit fallendem Gasdruck.

5. Diskussion

Die Ergebnisse der Untersuchungen zeigen, dass die hier verwendete Methode der sekundären Ionisationsbereiche prinzipiell zum Bau einer Gasentladungsverstärkerröhre mit kalter Kathode zu verwenden ist. Die Befürchtung, dass eine Gasentladungsverstärkerröhre wegen ihres Gitterstromes notwendigerweise einen geringen Eingangswiderstand haben müsse, hat sich in diesem Fall als unbegründet erwiesen. Als weiterer Vorteil der Koronaröhre gegenüber der Elektronenröhre muss fernerhin die Vermeidung der thermischen Trägheit einer Heizkathode und der Wegfall des Heizstromes genannt werden. Typisch für die Koronaröhre ist weiterhin, dass alle mit ihr im Zusammenhang stehenden Kreise hochohmig sind, was je nach Anwendungszweck vor- oder nachteilig sein kann.

Als Nachteile der Koronaröhre sind zunächst ihre hohe Betriebsspannung und ihre relativ tiefe Grenzfrequenz zu nennen. Durch Anwendung einer anderen Kathode und eines anderen Füllgases sowie durch Änderung des Kathoden-Anodenabstandes können beide Grössen vermutlich günstiger gestaltet werden als dies in der vorliegenden Röhre der Fall ist; es erscheint aber fraglich, ob diese Verbesserungen soweit getrieben werden können, dass die Koronaröhre neben anderen heute existierenden Verstärkeranordnungen technische Vorteile bietet. Schliesslich wäre hier noch das relativ hohe Rauschen der Koronaröhre in Betracht zu ziehen; der geringen äquivalenten Bandbreite der Koronaröhre wegen (im vorligenden Fall bestenfalls etwa 7 kHz) dürfte dies aber keine so wesentliche Rolle spielen, wenn mehrere Röhren in RC-Verstärkerschaltung hintereinander geschaltet werden. Die Koronaröhre ist jedoch auch hierin der Elektronenröhre unterlegen.

Auf dem Gebiete der Stabilisierung hoher Spannungen scheint die vorliegende Röhre jedoch im Vergleich mit den heute bekannten Methoden einige Vorteile zu bieten, da sie die Stabilisierung in einem sehr einfachen Kreis möglich macht und weiterhin den Vorteil einer einfachen Änderung der stabilisierten Spannung bietet. Durch weitere Arbeit an der Röhre im Hinblick auf dieses Ziel dürfte eine technisch gut verwendbare Form geschaffen werden können.

Herrn Professor S. von Friesen möchte ich an dieser Stelle für sein stetes förderndes Interesse meinen besten Dank ausdrücken. Weiterhin sei Herrn fil. dr. L. Stigmark für wertvolle Diskussionen gedankt.

Physikalisches Institut der Universität Lund, im September 1955.

LITERATUR

1. A. Güntherschulze und F. Keller, Z. f. Physik *72*, 133 (1931).
2. A. Gemant, Z. techn. Physik *14*, 187 (1933).
3. A. von Engel und M. Steenbeck, Elektrische Gasentladungen (1932).
4. E. Lübcke und W. Schottky, Wiss. Veröff. Siemens-Werke *IX*, 390 (1930).
5. E. O. Johnson und W. M. Webster, Proc. I. R. E. *40*, 645 (1952).
6. C. H. Hertz, Arkiv för Fysik *9*, 1 (1954).
7. C. H. Hertz, Z. angew. Physik *7*, 183 (1955).
8. G. W. Trichel, Phys. Rev. *54*, 1078 (1938).
9. G. P. Harnwell, Principles of Electricity and Electromagnetism (1949).
10. K. Küpfmüller, Einführung in die theoretische Elektrotechnik (1951).
11. G. L. Weissler, Phys. Rev. *63*, 97 (1943).
12. Courant-Hilbert, Methoden der mathematischen Physik I (1931).
13. C. van Geel, Dissertation Technische Hochschule Delft (1955).
14. I. G. A. Hölscher, Private Mitteilung, Technische Hochschule Delft.
15. E. K. Sandeman, Radio Engineering II (1949).
16. F. E. Terman und J. M. Petit, Electronic Measurements (1952).
17. O. G. Villard, Electronics *22*, 77 (July 1949).
18. I. H. Blifford, R. G. Arnold und H. Friedman, Electronics *22*, 111 (December 1949).
19. S. W. Lichtman, Proc. I. R. E. *39*, 419 (1951).
20. A. I. L. Collison und D. W. Hill, Journ. Scient. Instr. *32*, 13 (1955).

Tryckt den 26 oktober 1955

Uppsala 1955. Almqvist & Wiksells Boktryckeri AB

ARKIV FÖR FYSIK Band 10 nr 20

Communicated 1 June 1955 by MANNE SIEGBAHN and ERIK HULTHÉN

An investigation of the photoelectric absorption of gamma-rays in thallium-activated sodium iodide

By KARL-ERIK JOHANSSON

With 13 figures in the text

Summary

The photoelectric absorption of gamma rays in thallium-activated sodium iodide has been determined in the energy range 0.4–1.3 MeV by one absolute and one relative method through graphical analysis of the pulse height distributions from various isotopes. Corrections were made for electron and K X-ray escape. The measurements were performed with two or more crystals of different sizes to make an extrapolation to zero crystal extension possible. In this way the influence of secondary and higher absorption processes could be eliminated. Then the fraction of the photons primarily absorbed by the photoelectric effect could be obtained. It was also shown that the same result of the extrapolation was reached with both collimated and uncollimated radiation. In the absolute method the photoelectric absorption coefficients were calculated with the aid of the scattering coefficients from the Klein-Nishina formula. In the relative method isotopes with two or more gamma energies of known relative intensities were used. The pulse height distribution curves were analysed graphically. After the above corrections had been made, the ratio between the photoelectric absorption coefficients for two gamma-energies could be calculated. The agreement between the results of the two methods was good. The photoelectric absorption coefficients according to the present investigation are compared with previous theoretical and experimental values.

I. Introduction

Since the introduction of the scintillation counter in its present form about 1948 it has proved to be a very useful instrument for measuring the intensity of radioactive radiations, and for many purposes superior to the apparatus previously used. This is especially true as regards gamma rays, since its sensitivity for this type of radiation is considerably higher than that of the GM counter. When a suitable phosphor—for instance, thallium-activated sodium iodide—is used, part of the gamma radiation is absorbed via the photoelectric effect. When a gamma photon is absorbed in this way, its entire energy is transformed to light energy in the crystal. Since the magnitude of the pulse from the photomultiplier is proportional to the quantity of light energy incident on the cathode surface, it will then also be proportional to the energy of the gamma quantum. This latter energy can therefore be determined from the position of the photoelectric peak in the pulse height distribution. The area under the peak may be taken as a measure of the number of quanta absorbed photoelectrically.

The aim of the present investigation was to determine experimentally the photoelectric absorption in sodium iodide for various gamma energies. In the energy range considered (0.4–1.3 MeV) the absorption of gamma rays is mostly due to the Compton effect. The relative magnitudes of the two types of absorption have been determined by analysing experimental pulse height distributions. The photoelectric absorption coefficients could then be determined from the Compton scattering coefficients as calculated by means of the Klein-Nishina formula. The matter is complicated by the fact that the absorption depends not only on the energy of the gamma quantum but also on the size and shape of the crystal, and the manner in which the ray strikes the crystal. During the course of the present investigation a paper has been published by MAEDER *et al.* [1] which treats the same problems mainly from theoretical considerations. LIDÉN and STARFELT [2] have investigated the absorption of continuous gamma and X-ray spectra below 1 MeV.

In addition to the above method, a relative method has also been used for determining the photoelectric absorption in sodium iodide. Isotopes with two or more gamma lines of known relative intensities were used. The pulse height distribution has a peak for each energy. The areas under them could be measured after their separation by a graphical method. The relative values of the corresponding photoelectric absorption coefficients could then be obtained. As in the method previously mentioned, it is necessary to take into account the size and shape of the crystal, and the geometry of the configuration. Measurements on isotopes with two or more gamma energies of known relative intensities have also been used to evaluate the relative total absorption of different gamma energies in a particular crystal. When the latter is known it can be used to evaluate the relative intensities of different gamma lines in the spectra of other isotopes. The method is described in more detail in an appendix, where examples of its application are also given (see Zn^{65} and Cs^{134}).

In connection with the present investigation of the photoelectric absorption, the gamma energies for the isotopes Sc^{46}, Zn^{65}, Nb^{95}, and Cs^{134}, and the half-life of Au^{198} were also determined. The results are presented under the respective isotopes in the Appendix.

The account of the present investigation commences with a review of earlier experimental and theoretical work on the determination of photoelectric absorption coefficients. This is followed by a brief description of the spectrometer used. The general shape of the pulse height distribution is discussed, and in that connection losses due to electron and K X-ray escape from the crystal as well. The percentage ratio p of the area of the photoelectric peak to the combined area of the photoelectric peak and the Compton distribution varies not only with the energy concerned but also with the size of the crystal, mainly on account of secondary absorption processes. Correction to infinitely small crystal size is therefore necessary. Measurements on collimated radiation from Au^{198} showed that the value of p for medium-sized crystals varies linearly with respect to crystal height. It was thus possible to extrapolate p to $h = 0$ (p_0). Extrapolation to $h = 0$ for points obtained with uncollimated radiation was found to give the same value. It has been assumed that the same applies to other gamma energies up to 1.3 MeV, and extrapolation was accordingly performed throughout on values for uncollimated radiation. The measured, corrected, and extrapolated values (p, p_{corr}, p_0) for the various energies are assembled in Table 2 and Fig. 2. The photoelectric absorption coefficients are then determined from the theoretical Compton scattering coefficients. Subsequently there is an account of the relative method mentioned in the Introduction, a method based on the comparison of two photoelectric peaks in a pulse height distribution recorded for an isotope with two or more lines of known relative intensity. Finally, the results of the two methods are summarised and compared with theoretical values calculated by DAVISSON and EVANS [3], WHITE [4], and VICTOREEN [5], as well as a few experimental values obtained by MAEDER *et al.* [1].

II. Earlier experimental and theoretical investigations

Only few experimental studies have been made of the photoelectric absorption within the energy range considered here. Most determinations were made by measuring the cross section of total absorption and then subtracting the theoretically computed cross sections of Compton scattering by the Klein-Nishina formula. As a relatively small portion of the absorption is caused by the photoelectric effect the accuracy of the determined values of the photoelectric absorption coefficients is fairly small. Among the papers concerning gamma ray absorption measurements during the last years the following may be mentioned: COWAN [6], DAVISSON and EVANS [7], and WYARD [8].

Several theoretically calculated data on photoelectric absorption coefficients have been published. Various kinds of approximations must then be performed. They are in most cases fairly uncertain, which prejudices the results obtained. DAVISSON and EVANS [3] have published a review of the interaction of gamma radiation with matter. There the different formulas and simplifying approximations for the calculations of the photoelectric coefficients are discussed. Another review is given by WHITE [4].

For our purpose the result of HULME, MCDOUGALL, BUCKINGHAM, and FOWLER [9] is of greatest interest. It is obtained from the Dirac relativistic equation for a bound electron in the K shell. Exchange interactions between atomic electrons were neglected. The two K electrons were treated separately and the total absorption of the K shell was obtained by doubling the result for one K electron. No simple formula can be given for the cross section as a function of the energy. Numerical values are calculated for the two gamma energies 0.354 MeV and 1.13 MeV and for the three atomic numbers, $Z = 26$, 50, and 84.

In the reviews referred to above DAVISSON and EVANS and WHITE published tables and diagrams of absorption coefficients for some elements. The cross section for the photoelectric absorption in the K shell was calculated by means of the Sauter-Stobbe combined formula for energies less than about 0.35 MeV. The values were found to fit smoothly into the interpolated data from the calculation by HULME *et al.* For energies greater than 2 MeV the extrapolated values agree well with those obtained from the Hall formula. The "screening effects" from electrons nearer the nucleus than the photoelectron were taken into account by attributing an "effective atomic number", $Z - s$ to the nucleus. s is called the "inner screening number" and has been evaluated for the various shells by SLATER.

The photoelectric absorption occurs mainly in the K shell. The formulas mentioned above apply to this part of the total photoelectric absorption. The cross sections for higher shells were calculated by the Stobbe formulas.

Victoreen [5] developed an empirical formula for the calculation of the photoelectric absorption coefficients in various elements. If this formula is applied to NaI(Tl) the following simple expression is obtained:

$$\mu_p = 0.0506 \frac{E_\gamma - 0.0255}{E_\gamma^4} \text{ cm}^{-1} \tag{1}$$

where E_γ is the gamma energy expressed in mass units ($mc^2 = 0.511$ MeV).

III. Apparatus

a. Phosphor

Thallium-activated sodium iodide crystals were used as phosphors for all the measurements reported here. The crystals used were kept in paraffin oil as a protection against atmospheric moisture. Before use, the surfaces of the crystal were polished by rubbing them against blotting paper moistened with methyl-ethyl ketone, and were then immediately dipped in paraffin oil to obtain a protective layer. For a few experiments the crystal surfaces were roughened with fine emery cloth; but there was no appreciable difference in the spectral resolution. The crystal was placed on the flat surface of the photo-multiplier. The intervening layer of paraffin oil ensured good optical contact. In order to reduce light losses from the crystal it was covered over with a thin aluminium hood, the inside of which was coated with magnesium oxide by holding it over burning magnesium. Another type of reflector used in some experiments was an internally polished aluminium hood. The former type was found to be somewhat more effective. The paraffin oil and the aluminium shield did not provide complete protection for the crystal, which acquired a surface coating that absorbed part of the light emitted. This effect was noticeable in that the position of, for instance, a photoelectric peak in the pulse height distribution shifted somewhat in two successive series of measurements. This is obviously a source of error which impairs the accuracy of the measurements. It can be avoided only by airtight mounting of the crystal. Two cylindrical crystals mounted in this way by the Harshaw Chemical Company have been used for most of the measurements reported here. The dimensions of one crystal were $\varnothing \frac{1}{2}'' \times \frac{1}{2}''$, and of the other $\varnothing \frac{3}{4}'' \times \frac{3}{4}''$.

b. Electronic equipment

A photomultiplier of type Du Mont 6292 was used. This type was found to be particularly suitable on account of the good resolution obtainable—an essential consideration for the present measurements. The high voltage was provided by a carefully stabilised unit, and was usually kept at 1000–1200 V. A voltage divider then provided the voltage steps for the successive stages. The voltage from the cathode to the first dynode was greater than that between the subsequent successive dynodes. The anode of the photomultiplier was connected to a cathode-follower, which was built into the light-proof bakelite container surrounding the photomultiplier. From the cathode-follower the pulses proceeded to a linear pulse amplifier with stepwise variable amplification. The gain was usually about 50. The anode voltage was well stabilised to ensure constant amplification. The pulses were then sorted according to height in a single channel differential discriminator of a type described by C. W. JOHNSTONE [10]. This was found to function very well. The stability of the channel width was good, even when the channel was narrow. The discriminator was set to take pulses up to 50 V. The channel width was generally 1 V. The counting rate for the mechanical register was reduced by a preceding scale-of-64 unit. The whole apparatus was allowed to warm up for at least 2 hours before measurements commenced, in order to achieve stable conditions.

c. The source and its position

The source consisted of a small quantity of the active material placed between two strips of tape. Its extention could be neglected. When the radiation was not collimated, the activity of the sample was usually of the order of 0.01–0.1 μC, but measurements could have been carried out with even weaker sources. The position of the source is of great importance when investigating the various absorption processes that occur in the crystal. For the present measurements it was placed directly on the reflector, unless otherwise stated. For the mounted crystals its distance from the crystal was about 3 mm. The experimental conditions are easily reproducible with this arrangement. Furthermore, since a large part of the radiation meets the crystal it is possible to use weak sources. The isotopes used in the present investigation were easily obtainable in a highly active form. In many other cases, however, it may be very difficult to obtain such high activity, and it is then very advantageous to have an apparatus capable of using very weak sources.

From measurements on isotopes with simple, known decay schemes it is possible, for particular geometrical arrangement, to calibrate a crystal for subsequent application to other gamma spectra.

When the primary absorption processes in the crystal are investigated it is necessary to correct the measurements for various effects, in ways which are described later. The corrections are rendered more complicated and uncertain by the present geometrical arrangement, since total irradiation of the crystal entails edge effects, but on the other hand collimation corrections are also difficult to apply.

IV. Method for determining absolute photoelectric absorption coefficients

a. The general shape of the pulse height distribution

In all experiments β-radiation was absorbed by means of aluminium foil of suitable thickness, so the recorded distribution corresponded solely to the gamma radiation from the source. The absorption of gamma radiation in the aluminium foil was negligible, as was also Compton scattering in the foil.

In the energy range 0.4–1.3 MeV the entire absorption of gamma radiation in the crystal is attributable to the photoelectric effect and the Compton effect, pair production being negligible.

The linear relation between the energy absorbed in the crystal and the pulse from the photomultiplier might lead us to expect a pulse of a definite height for each gamma quantum absorbed photoelectrically. However, it is found that the pulse height is spread around the expected value for the energy in question according to a Gaussian distribution. This scattering is due to statistical fluctuation in the light emission from the crystal, in the incidence of the light flashes on the cathode surface, in the number of electrons emitted from the cathode, and the amplification produced by the multiplier. It is important that these scattering effects are reduced to a minimum if the resolution is to be as good as possible. The usual criterion of the resolution is the width of the peak at half maximum height, given as a percentage of the pulse height. The most satisfactory result was obtained with the mounted crystals and the Du Mont photomultiplier. As an instance of the resolution attained it may be mentioned that for the 0.662 MeV line of Ba^{137} it was somewhat better than 8 %. BORKOWSKI and CLARK [11] have investigated the resolving power of various photomultipliers of type RCA 5819 and various sizes of NaI crystals. Their best value for the line mentioned was 7–8 %, with crystals mounted like those used in the present instance. Direct mounting of the crystal on the photocathode gave a value of 6.8 %.

When gamma quanta lose part of their energy to electrons by the Compton effect, a distribution of pulse heights results which extends from $E=0$ to

$$E_c = \frac{E_\gamma}{1 + \dfrac{m_0 c^2}{2 E_\gamma}} \tag{2}$$

where E_c is the maximum energy of the recoil electron and E_γ the energy of the gamma quantum, in MeV. $m_0 c^2$ is the energy corresponding to the rest mass of the electron (0.511 MeV). The distribution has a maximum at an energy approximately 0.25 MeV less than that of the photoelectric peak. The scattered gamma photon may either pass out of the crystal or be absorbed by it. In the latter case the secondary absorption process may contribute to the photoelectric peak; the probability of this occurring increases with the crystal size. The influence of these secondary processes has been eliminated as far as possible by an extrapolation procedure, which is described later.

At about 0.2 MeV each pulse height distribution manifests a peak. It is due to back-scattering, primarily from the window of the crystal holder and multiplier. The ratio of the scattered photon's energy, E_s, to that of the primary photon, E_γ, is

$$\frac{E_s}{E_\gamma} = \frac{1}{1 + \dfrac{h\nu_0}{m_0 c^2}(1 - \cos\theta)} \tag{3}$$

where θ is the angle between the directions of the primary and scattered photons. This ratio varies with both E_γ and θ. For back-scattering θ is between 90° and 180°. Within this interval the variation with θ is relatively small, and the peak is consequently well-defined. The diagrams of pulse height distributions indicate that the back-scattering peak is superposed on the Compton distribution. The two can be separated quite accurately by a graphical procedure. Back-scattering of gamma radiation in connection with the scintillation spectrometer has recently been treated by HINE and MCCALL [12].

The counting rate does not immediately fall to zero when the discriminator threshold is raised above the highest gamma energy in the spectrum under investigation. This may be due to the presence of impurities in the radioactive source, or to random coincidences, when two pulses occur in such close succession that they act as a single pulse. In order to reduce the probability of such coincidences the counting rate was kept rather low. When two gamma photons are emitted in cascade they usually follow one another in a period that is shorter than the resolving time of the spectrometer. If they both strike the crystal they are therefore registered as a single pulse. With the present geometrical arrangement the probability of such coincidences is quite large. This circumstance accounts for the relatively high surplus count for isotopes which emit two gamma photons in cascade (Co^{60}, Sc^{46}, and Cs^{134}). The problems involved have recently been considered in a paper by LU and WIEDENBECK [13]. The requisite correction for these coincidences is difficult to estimate at all accurately, so in the present investigation it has been made graphically on the pulse height distributions. Due regard has been paid to the fact that the correction is somewhat larger for lower pulses than for higher. As may be seen from the pulse height distributions the correction is relatively small, and the procedure mentioned may therefore be regarded as satisfactory. It leads to a reduction of the areas of both the photoelectric peak and the Compton distribution, so their ratio does not change greatly. The same applies to the areas of two photoelectric peaks, provided they are of the same order of magnitude (cf. Co^{60}).

Where measurements were not extended to weak gamma rays of higher energies (the isotopes Au^{198} and Cs^{134}), a graphical correction was made to eliminate their contributions in the pulse height distributions.

After subtraction of the back-scattering peak and the correction for surplus counts, the areas under the photoelectric peak and Compton distribution were measured with a planimeter. These two areas are denoted in the following by P and C. The percentage ratio of P to $P+C$ is called p, i.e.

$$p = \frac{100\,P}{P+C}. \tag{4}$$

If the spectrum includes two or more gamma energies it is first necessary to divide it up graphically. The procedure is described under the respective isotopes in the Appendix.

b. Electron escape and *K* X-ray escape

When a gamma quantum is absorbed photoelectrically, the whole of its energy is delivered to an orbital electron of an atom, generally one in the K shell. If the binding energy of the released electron is E_k, it will leave the atom with an energy $E_\gamma-(E_k+E_a)$, where E_a is the excitation energy of the atom. If the absorption occurs near the crystal surface the photo-electron may leave the crystal without surrendering its entire energy. The pulse registered in such a case is within the interval $0-E_\gamma$, and thus contributes to the Compton distribution if the lost energy is greater than the energy difference that corresponds to the half-width of the photoelectric peak at its base.

When the ionised atom returns to its ground state the change is accompanied by the release of an X-ray photon of energy E_k. This is usually absorbed in the crystal, as its energy is low (29 keV for iodine). But sometimes it may leave the crystal, and in such a case the corresponding pulse is lower by an amount equivalent to 29 keV. The escape peak should therefore occur at $E_\gamma-E_k$, but on account of the inadequate resolution cannot be distinguished from the photoelectric peak.

K X-ray escape, and to some extent electron escape, help to make the photoelectric peak somewhat unsymmetric; this is clearly discernible in the pulse height distributions in the Appendix. The discrepancy occurs in the upward sloping left lower part of the peak. This part of the curve has a smaller inclination than the corresponding part of the peak's other side. The counting rate is therefore somewhat greater for points to the left of the maximum ordinate than for points at the same distance to the right of it. The deviation from symmetry does not impair the accuracy with which the position of the photoelectric peak may be determined.

Lidén and Starfelt [2] have computed the proportion of photoelectric pulses, both primary and secondary, which is lost on account of the two escape processes mentioned above. The calculation has been carried out for a crystal of dimensions $\varnothing 1.5 \times 1.5$ cm and for radiation collimated in the direction of the crystal axis. For K X-ray escape the result obtained was about 3 % over the entire range 0.2–1.0 MeV. The correction for electron escape varies from about 1 % at 0.2 MeV to 7 % at 1.0 MeV, and is thus quite large for high gamma energies. A theoretical calculation of the corresponding corrections for the geometrical configuration used in the present investigation would be complicated and somewhat uncertain, and for this reason the above values have been used as the basis for the correction applied here. Its magnitude varies with the size of the crystal. This has been taken into consideration by assuming that the correction factor is directly proportional to the ratio between the area of the crystal surface and its volume. Only that part of the crystal which is irradiated has been included in the calculation. This means that for collimated radiation the correction has been taken to be inversely proportional to the height of the crystal, where this is not too small ($h > 2$ mm). Cf. also the measurements on Au^{198}.

The correction for K X-ray escape has actually been made in the pulse height diagram, since the peak as determined comprises both the photoelectric peak and the K X-ray escape peak. The pulses that do not attain their full height—corresponding to E_γ—on account of electron escape are distributed over the range corresponding to $0–E_\gamma$. Some of them therefore fall under the photoelectric peak, and contribute to its area as measured. The calculated correction for electron escape must therefore be reduced by an amount which can be computed if it is assumed that the anomalous pulses referred to are uniformly distributed over the energy range $0–E_\gamma$.

c. Secondary absorption processes

It has already been mentioned that the entire energy of a gamma photon may be transformed to light energy in the crystal despite initial Compton scattering, owing to the occurence of secondary absorption processes. The resulting pulse is of the same magnitude as that arising by photoelectric absorption. There is consequently an increment to the photoelectric peak at the cost of the Compton distribution, compared with the hypothetical case where only primary processes occur. The secondary absorption decreases as the dimensions of the crystal diminish, so it is possible to apply a correction for this type of absorption by extrapolating p to p_0, the value corresponding to an infinitely small crystal.

In order to investigate the variation of p with crystal size experiments were carried out with several crystals, employing collimated radiation from Au^{198} ($E_\gamma = 0.412$ MeV). The collimator was a lead cylinder of diameter 120 mm and height 67 mm,

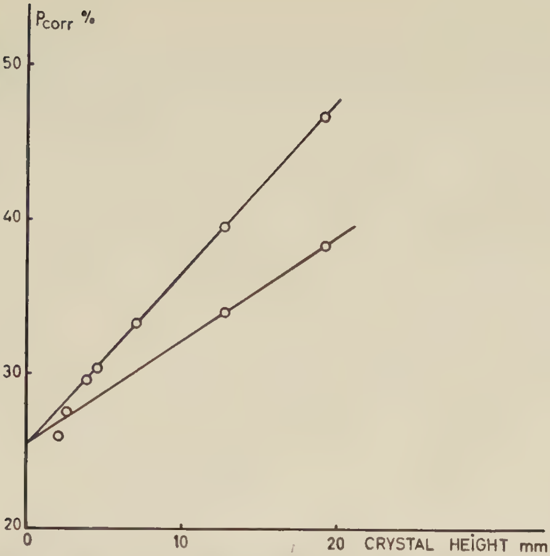

Fig. 1. Percentage ratio, p_{corr}, of the area of the photoelectric peak to the combined area of the photoelectric peak and the Compton distribution for the Au^{198} 0.412 MeV gamma ray as a function of the crystal height, h; collimated radiation (upper line) and uncollimated radiation (lower line). Corrections for electron and K X-ray escape have been made.

with an axial hole 3 mm in diameter. The source was situated at the upper end of the central hole, and the crystal was about 10 mm from the lower opening.

The correction for electron escape has been based on a figure (1.6 % of the area of the photoelectric peak) that was derived for a crystal of dimensions ⌀ 1.5 × 1.5 cm. This was taken from the previously mentioned computations of LIDÉN and STARFELT, with due regard to the fact that some of the pulses included in the computed correction have already been included in the photoelectric peak. The ratio of height to width was not the same for the crystals used in the present case. The cross section was chosen so that the collimated ray did not encounter the peripheral part of the crystal. In accordance with what was stated above about the correction for electron escape, it may be regarded as inversely proportional to the crystal height. The results of the measurements are presented in Table 1, which gives p, the measured values, and p_{corr}, the values as corrected for electron escape.

Table 1. Percentage ratio of the area of the photoelectric peak to the combined area of the photoelectric peak and the Compton distribution for the Au^{198} 0.412 MeV gamma line with NaI(Tl) crystals of various sizes and collimated radiation; p, the measured values, and p_{corr}, the values as corrected for electron escape.

Crystal	⌀ 3/4″ × 3/4″	⌀ 1/2″ × 1/2″	$h = 7 \times 12 \times 12$ mm	$h = 4.5 \times 7.0 \times 7.5$ mm	$h = 3.8 \times 10 \times 13.5$ mm	$h = 2.5 \times 10 \times 11$ mm	$h = 2.0 \times 7 \times 7$ mm
p %	46.3 ± 0.7	39.0 ± 0.7	32.4 ± 0.2	28.8 ± 0.2	27.9 ± 0.3	25.1 ± 0.3	23.1 ± 0.3
p_{corr} %	46.9 ± 0.7	39.7 ± 0.7	33.3 ± 0.2	30.3 ± 0.2	29.7 ± 0.3	27.5 ± 0.3	25.9 ± 0.3

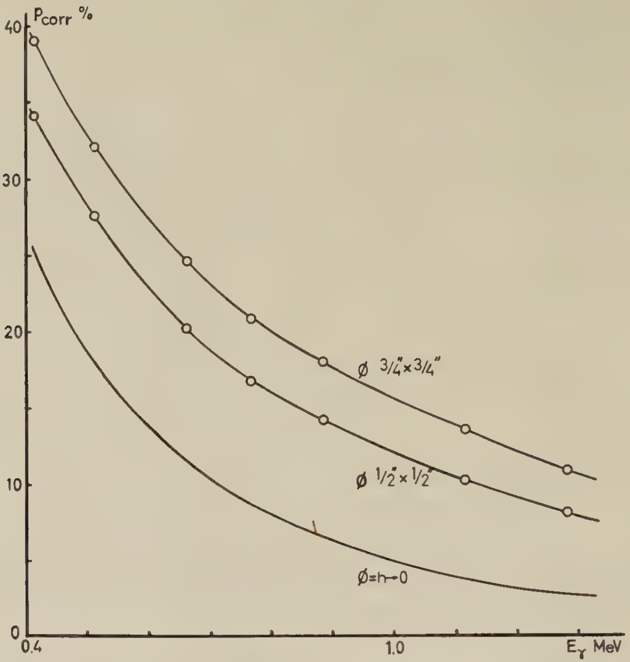

Fig. 2. Percentage ratio, p_{corr}, of the area of the photoelectric peak to the combined area of the photoelectric peak and the Compton distribution for the two NaI(Tl) crystals Ø $\frac{1}{2}''$ × $\frac{1}{2}''$ and Ø $\frac{3}{4}''$ × $\frac{3}{4}''$. Corrections have been made for electron and K X-ray escape. The third curve is drawn according to the extrapolated values, p_0, for an infinitely small crystal.

The corrected values (p_{corr}) have also been plotted against crystal height, h, in Fig. 1. It will be seen that p_{corr} varies linearly with h down to about $h = 3$ mm. For lower h the experimental points lie below the straight line. This is presumably attributable to the correction for electron escape in the form referred to above not being valid for such low values of h: it seems that it should be larger. Extrapolation of the straight line to $h = 0$ gives $p_0 = 25.4$ %. MAEDER *et al.* give $p_0 = 24.5 \pm 1.5$ %, without a correction for electron escape. The present measurements give the same figure after extrapolation by means of the experimental points. The result obtained, that $p_{\mathrm{corr}} - p_0$ is proportional to h, conforms with the theoretical expectations for crystals that are not too large. See also MAEDER *et al.*

Fig. 1 also includes the points obtained from measurements with the source placed directly on the mounted crystals. In this case too p may be expected to vary linearly with h, since the two crystals are similar in shape. If the straight line through the two points obtained is extrapolated to $h = 0$, about the same value is obtained for p_0 as with collimated radiation, i.e. $p_0 = 25.6$ %. It therefore seems permissible to determine p_0 by extrapolating to $h = 0$ by means of these two accurately determined values of p. Measurements on Nb^{95} were carried out with crystals of various heights up to $h = 20$ mm, in addition to the two mounted crystals. It was found that the relation between p and h was linear in this case as well, within the limits of error.

There is reason to suppose that the above process of extrapolation is also applicable to gamma energies up to 1.3 MeV, and accordingly p_0 has been determined in the

Table 2. Percentage ratio of the area of the photoelectric peak to the combined area of the photoelectric peak and the Compton distribution with the NaI(Tl) crystals $\varnothing \frac{1}{2}'' \times \frac{1}{2}''$ and $\varnothing \frac{3}{4}'' \times \frac{3}{4}''$, uncollimated radiation; p, measured values, and p_{corr}, the values as corrected for electron escape. p_0, the values after extrapolation of p_{corr} to zero crystal extension.

		Au^{198} 0.412 MeV	Na^{22} 0.511 MeV	Cs^{137} 0.662 MeV	Nb^{95} 0.767 MeV	Sc^{46} 0.892 MeV	Zn^{65} 1.112 MeV	Na^{22} 1.28 MeV
Crystal $\varnothing\, ^1/_2'' \times {}^1/_2''$	p %	33.5 ±0.3	26.9 ±0.3	19.4 ±0.1	16.0 ±0.2	13.4 ±0.2	9.4 ±0.1	7.0 ±0.1
	p_{corr} %	34.1 ±0.4	27.5 ±0.5	20.1 ±0.2	16.7 ±0.3	14.1 ±0.3	10.1 ±0.2	8.0 ±0.2
Crystal $\varnothing\, ^3/_4'' \times {}^3/_4''$	p %	38.1 ±0.5	31.5 ±1.3	23.9 ±0.2	20.1 ±0.2	17.2 ±0.3	12.7 ±0.1	10.2 ±0.2
	p_{corr} %	39.0 ±0.6	32.0 ±0.4	24.5 ±0.3	20.7 ±0.3	17.9 ±0.4	13.4 ±0.2	10.8 ±0.3
	p_0 %	25.4 ±1.0	18.6 ±0.8	11.5 ±0.4	8.7 ±0.4	6.4 ±0.3	3.7 ±0.3	2.7 ±0.3

Table 3. Compton scattering coefficients, μ_c, as obtained by applying the Klein-Nishina formula on NaI(Tl) and photoelectric absorption coefficients, μ_p, as calculated from (5).

E_γ	0.412 MeV	0.511 MeV	0.662 MeV	0.767 MeV	0.892 MeV	1.112 MeV	1.28 MeV
μ_c cm^{-1}	0.295	0.271	0.241	0.225	0.210	0.188	0.175
μ_p cm^{-1}	0.101 ±0.005	0.059 ±0.006	0.0310 ±0.0016	0.0212 ±0.0013	0.0143 ±0.0008	0.0072 ±0.0006	0.0049 ±0.0004

same way for these higher energies as for $E_\gamma = 0.412$ MeV. The values as corrected for electron escape, p_{corr}, which are used for the extrapolation are to be found in Table 2. The table also contains the values of p before correction and the values obtained as a result of the extrapolation.

The relation between p_{corr} and E_γ for the two mounted crystals with uncollimated radiation is presented graphically in Fig. 2, as is also that between p_0 and E_γ.

The extrapolated values of p_0 can be applied directly to determination of the photoelectric absorption coefficient, μ_p, for a particular energy if the Compton scattering coefficient, μ_c, is known for the same energy. The latter may be obtained by applying the Klein-Nishina formula [14] to NaI(Tl), taking 0.3 % of the Na atoms to be replaced by Tl atoms. The derivation of the formula assumes that all the electrons in the crystal are completely free, and this assumption may be regarded as well

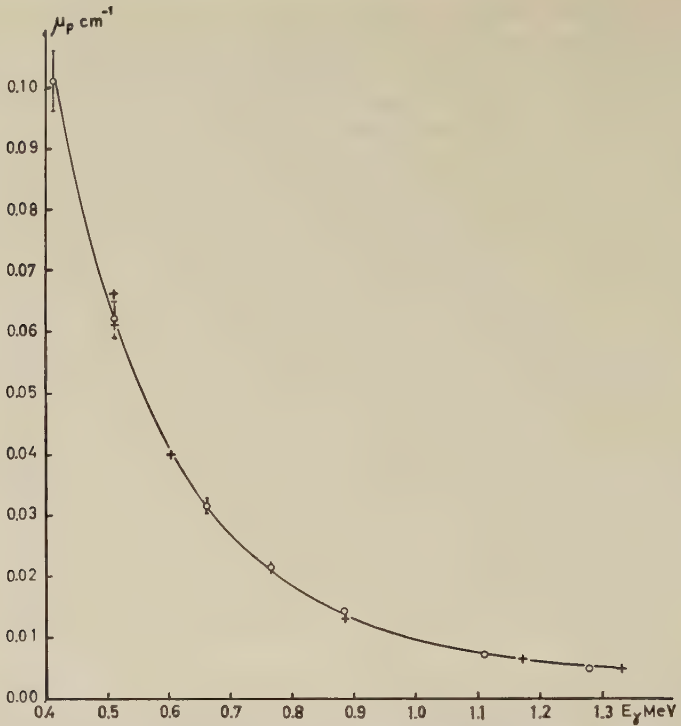

Fig. 3. Photoelectric absorption coefficients as a function of the gamma energy according to the present investigation. O and + are points from the absolute and relative method respectively.

justified for incident gamma quanta of energies such as those treated here. It is thus possible to calculate the total scattering cross-section with sufficient accuracy from the uncorrected Klein-Nishina formula (see also MAEDER *et al.*). The following equation then applies

$$\mu_p = \mu_c \cdot \frac{p_0}{100 - p_0}. \tag{5}$$

Table 3 contains the values of μ_p calculated from (5), together with the values of μ_c used for the calculation.

The relation between μ_p and E_γ is represented graphically in Fig. 3.

V. Method for determining relative photoelectric absorption coefficients

As mentioned in the Introduction, this investigation has given particular consideration to isotopes with two gamma lines whose relative intensities are well defined. It is then possible to compare the photoelectric absorption for different energies in the interval considered.

Four isotopes have been used—Na^{22}, Sc^{46}, Co^{60}, and Cs^{134}. The pulse height distribution was analysed graphically in a manner described in the Appendix, and the areas under the separate photoelectric peaks then measured. The correction for electron escape is made in the way already described. The measurements were made with the two mounted crystals and uncollimated radiation. It has already been pointed out that secondary absorption processes cause an enlargement of the photoelectric peak at the cost of the Compton distribution, and a correction must be made for this effect before two photoelectric peaks can be compared. The correction is easily made as follows. Let the area of the photoelectric peak (corrected for electron escape) be denoted by P, and that of the corresponding Compton distribution by C. Suppose that if only primary absorption processes were involved the corresponding quantities would be P_0 and C_0. Then the following relationships apply:

$$P = \frac{p_{\text{corr}}}{100}(P+C),\ \ P_0 = \frac{p_0}{100}(P_0+C_0).$$

And since $P + C = P_0 + C_0$ we have

$$P_0 = \frac{p_0 \cdot P}{p_{\text{corr}}}. \tag{6}$$

That is, the area of the photoelectric peak must be multiplied by p_0/p_{corr}, which has previously been determined as a percentage and may be obtained from Fig. 2.

The intensity of a gamma ray decreases exponentially during passage through an absorbing medium. The rate of decrease depends on the energy of the quantum, and the ratio of the intensities of two components of different energy changes as they pass through the medium. For a thin crystal the ratio between the areas of two photoelectric peaks after correction for escape losses and secondary processes leads directly to the ratio between the respective photoelectric absorption coefficients, if the intensities of the two incident components are known. If the extension of the crystal is not negligible it is necessary to compute the ratio as it would have been if the crystal had been infinitely small. It is easy to deduce the following relationship:

$$\frac{\mu_p'}{\mu_p''} = \frac{P_0'}{P_0''} \cdot \frac{\mu'}{\mu''} \cdot \frac{I_0''}{I_0'} \cdot \frac{e^{-\mu'' a} - 1}{e^{-\mu' a} - 1} \tag{7}$$

where μ_p is the coefficient of photoelectric absorption, μ the coefficient of total absorption, P_0 the area of the photoelectric peak after correction for escape losses and secondary absorption processes, I_0 the intensity of the gamma ray incident on the crystal, and a the path traversed by the ray in the crystal. The superscripts $'$ and $''$ refer to the two energies under comparison.

This correction is primarily significant for measurements with the isotope Na^{22}, as the difference in the gamma energies for this isotope, and accordingly the difference in the absorption of them, as well are rather large.

When calculating the ratio I_0'/I_0'' of two intensities from the decay scheme for a particular isotope it is necessary to take into account possible internal conversion of gamma quanta. However, for the gamma radiation of the present investigation such internal conversion is negligible.

The measurements were carried out with crystals of two different sizes in order to obtain a check on the results and the corrections applied.

Na^{22}

For Na^{22} the ratio between the areas of the photoelectric peaks at $E_\gamma = 0.511$ MeV and 1.28 MeV after correction for electron escape $P'/P'' = 10.6 \pm 0.2$ and 9.8 ± 0.3 for the crystals of dimensions $\varnothing\,\frac{1}{2}'' \times \frac{1}{2}''$ and $\varnothing\,\frac{3}{4}'' \times \frac{3}{4}''$ respectively. These figures become $P_0'/P_0'' = 20.5$ and 21.2 respectively if a correction is made for secondary absorption in accordance with (6). Calculation of μ_p'/μ_p'' by means of formula (7) gives the values 12.1 and 12.6 for the two crystals. The ratio of the intensities of the two gamma lines has been taken to be 1.8, from the consideration that 10 % of the decay occurs through K capture to the excited level at 1.28 MeV in Ne^{22}. If it is instead assumed that the entire decay is accounted for by positron emission to the level mentioned the respective values are 10.9 and 11.3. The mean ratio of the photoelectric absorption coefficients for the gamma energies 0.51 and 1.28 MeV is thus 12.4 or 11.1, according to which of the above assumptions is made.

Co^{60}

The results for Co^{60} were dealt with in the same way as those for Na^{22}. For $E_\gamma' = 1.17$ MeV and $E_\gamma'' = 1.33$ MeV, $P'/P'' = 1.27 \pm 0.04$ for the $\varnothing\,\frac{1}{2}'' \times \frac{1}{2}''$ crystal and 1.22 ± 0.03 for the $\varnothing\,\frac{3}{4}'' \times \frac{3}{4}''$. $P_0'/P_0'' = 1.30$ and 1.28 (by (6)). The total absorption was almost the same for the two energies, so that correction according to (7) leads to no alteration of these values. It may be seen from the account of Co^{60}'s decay in the Appendix that the numbers of gamma quanta with energies 1.17 and 1.33 MeV are equal. The ratio of the photoelectric absorption coefficients is therefore 1.29 ± 0.05.

Sc^{46}

The intensities of the Sc^{46} lines with $E_\gamma = 0.89$ and 1.12 MeV are approximately equal (cf. Appendix). The ratio of the areas of the photoelectric peaks in the pulse height distribution, corrected for electron escape, was 1.44 ± 0.02 and 1.40 ± 0.02 for the crystals $\varnothing\,\frac{1}{2}'' \times \frac{1}{2}''$ and $\varnothing\,\frac{3}{4}'' \times \frac{3}{4}''$. Formula (6) gives $P_0'/P_0'' = 1.82$ and 1.83. Correction according to (7) raises these figures about 1 %. The mean ratio of the photoelectric absorption coefficients for the gamma energies 0.89 and 1.12 MeV is thus $\mu_p'/\mu_p'' = 1.85$.

Cs^{134}

The ratio of the photoelectric peaks for $E_\gamma = 0.60$ and 0.80 MeV was found to be 1.80 ± 0.07 for crystal $\varnothing\,\frac{1}{2}'' \times \frac{1}{2}''$ and 1.72 for the crystal $\varnothing\,\frac{3}{4}'' \times \frac{3}{4}''$ after correction for electron escape. The effect of secondary absorption processes was eliminated by calculating P_0'/P_0'' according to (6), the values obtained being 2.14 and 2.13. In accordance with what is stated in the Appendix about the decay of the isotope, the intensity of the 0.60 MeV line is about 3 % greater than that of the 0.80 MeV line. The corresponding value of I_0'/I_0'' was used to determine μ_p'/μ_p'' by means of (7). The result was $\mu_p'/\mu_p'' = 2.25$ and 2.24 in the two cases. The mean ratio of the photoelectric absorption coefficients for the gamma energies 0.60 and 0.80 MeV is thus 2.25.

The ratio of the areas of two photoelectric peaks in a pulse height distribution may be determined quite accurately if the spectrum is not too complicated and the two lines not too close together. This may be seen from the fact that there is little variation in the results of different series of measurements. The correction for electron escape is relatively small, and therefore does not cause any considerable increase of the error in the ratio of the areas under the photoelectric peaks. But in correcting for secondary absorption in accordance with (6) the p_0 values obtained by extrapolation are used. The margin of error for P_0'/P_0'' is therefore greater than that for P'/P'', especially if the lines compared are widely separated and the correction therefore large. Of the four values for P_0'/P_0'', that for Na^{22} is the most uncertain. However, it should be noted that the two values of P'/P'' obtained for each isotope by using the two different crystal sizes differ appreciably, whereas the corresponding pairs of values for P_0'/P_0'' (after extrapolation) are almost equal in all cases. This indicates that the corrections are of the correct order of magnitude at least. Correction in accordance with (7) for the different attenuation rates of different gamma energies passing through the crystal is small for all the isotopes except Na^{22}. It may be concluded from this discussion that the method described here for determining the relative coefficients of photoelectric absorption for two gamma energies in a spectrum yields results of a satisfactory accuracy.

The four values of μ_p'/μ_p'' obtained above may be used for an approximate determination of the relative coefficients of photoelectric absorption in a thallium-activated sodium iodide crystal for gamma energies between 0.50 and 1.35 MeV. In plotting a curve of μ_p against E_γ an arbitrary value of μ_p was adopted for the highest gamma energy considered, 1.33 MeV (Co^{60}). A point of the curve was then obtained at 1.17 MeV. It was easy to extrapolate from these points to $E_\gamma = 1.12$ MeV. By means of the value of μ_p'/μ_p'' for Sc^{46} the curve could then be extended to $E_\gamma = 0.89$ MeV and from there extrapolated to $E_\gamma = 0.80$ MeV. The value of μ_p'/μ_p'' for Cs^{134} then gave a point for $E_\gamma = 0.60$ MeV, and a final point at $E_\gamma = 0.51$ MeV was obtained from the value for Na^{22}. The latter point is double, because of the two possible assumptions regarding the decay scheme, as already mentioned.

VI. Conclusions

The results obtained by the two different methods are shown in Fig. 3. The points obtained by the second method have been normalised so that the photoelectric absorption coefficient for $E_\gamma = 0.662$ MeV is the same for both methods ($\mu_p = 0.0310$ cm^{-1}). It will be seen from the figure that the agreement between the results of the two methods is good. The curve in the figure has been drawn to fit all the points as well as possible. It thus represents the variation of the photoelectric absorption coefficients in NaI(Tl) for gamma rays with energies between 0.4 and 1.3 MeV, according to the present measurements.

As may be seen from equation (5), the value of μ_p is highly dependent on the extrapolated value p_0, especially when p_0 is small. However, it is worth mentioning that a systematic error in the extrapolation does not to any great extent influence the accuracy of the determination of p_0 by the relative method. The good agreement between the values obtained by the two methods may accordingly be taken as proof that the extrapolation used here will give fairly correct values of p_0.

In Table 4 the values for a series of gamma energies are compared with those calculated theoretically by DAVISSON and EVANS, WHITE, and the empirical values of VICTOREEN. The table also includes some values determined experimentally by MAEDER *et al.* The calculated absorption coefficients are for a NaI crystal with a

Table 4. Comparison of the photoelectric absorption coefficients for NaI(Tl) from the present investigation with some earlier theoretical and experimental values.

Energy E_γ MeV	Compton scattering coefficient μ_c cm^{-1}	Photoelectric absorption coefficient, μ_p cm^{-1}				
		Davisson-Evans [3]	White [4]	Victoreen [5]	Maeder [1] (exper.)	Present investigation
0.412	0.295	0.113	0.101	0.0941	0.096 ± 0.008	0.101 ± 0.005
0.511	0.271	0.063	0.055	0.0494		0.062 ± 0.003
0.6	0.253	0.043	0.038	0.0310		0.041
0.662	0.241	0.034	0.0300	0.0228	0.024 ± 0.003	0.0313 ± 0.0012
0.7	0.235	0.0300	0.0260	0.0195		0.0272
0.767	0.225	0.0246	0.0214	0.0147		0.0207 ± 0.0012
0.8	0.291	0.0225	0.0195	0.0130		0.0182
0.892	0.210	0.0182	0.0160	0.0098		0.0135 ± 0.0010
1.0	0.199	0.0143	0.0126	0.0068		0.0095
1.112	0.188	0.0117	0.0111	0.0048	0.0054 ± 0.0014	0.0072 ± 0.0006
1.28	0.175	0.0092	0.0083	0.0032		0.0052 ± 0.0007

thallium content of 0.3 %. The values of Maeder *et al.* were obtained by the same method as that first described here; they are not corrected for stray radiation from the collimator, nor for electron and K X-ray escape and Bremsstrahlung losses.

It may be seen from the table that the values of μ_p calculated by Davisson and Evans are all somewhat higher (about 10 %) than those calculated by White, and that those obtained from Victoreen's equation are considerably lower than the figures in either of the other series. The difference between White's and Victoreen's figures is 0.005–0.007 cm^{-1} throughout, and this corresponds to a rather large percentage difference in view of the fact that the order of magnitude of μ_p is 0.01 cm^{-1} at about $E_\gamma = 1.0$ MeV.

White's values are nearest to those of the present investigation in the range 0.4–0.8 MeV. For $E_\gamma > 0.8$ MeV the values obtained here are somewhat lower, but not so low as Victoreen's. One reason for low values at the higher energies is that Bremsstrahlung losses have not been taken into account, these being greater for the higher energies. According to an estimate made by Maeder *et al.* for a crystal of size $R = h = 5$ mm, 4 electrons of 100 with an initial energy of 1.11 MeV undergo Bremsstrahlung losses greater than 100 keV, while 13 leave the crystal with an energy greater than 100 keV (electron escape). That is to say, for this particular case the correction for Bremsstrahlung losses is about $\frac{1}{4}$ of that for electron escape. It is reasonable to suppose that the corrections should be in about the same proportion for the crystals used in the present investigation. Therefore, in view of the small size of the correction applied for electron escape, it seems unlikely that taking Bremsstrahlung losses into account would raise the μ_p values so much that they would agree with those calculated by Davisson and Evans or by White.

The photoelectric absorption coefficients of Table 4 are plotted against the gamma energy in Fig. 4. The curve is drawn on the basis of the values from the present investigation.

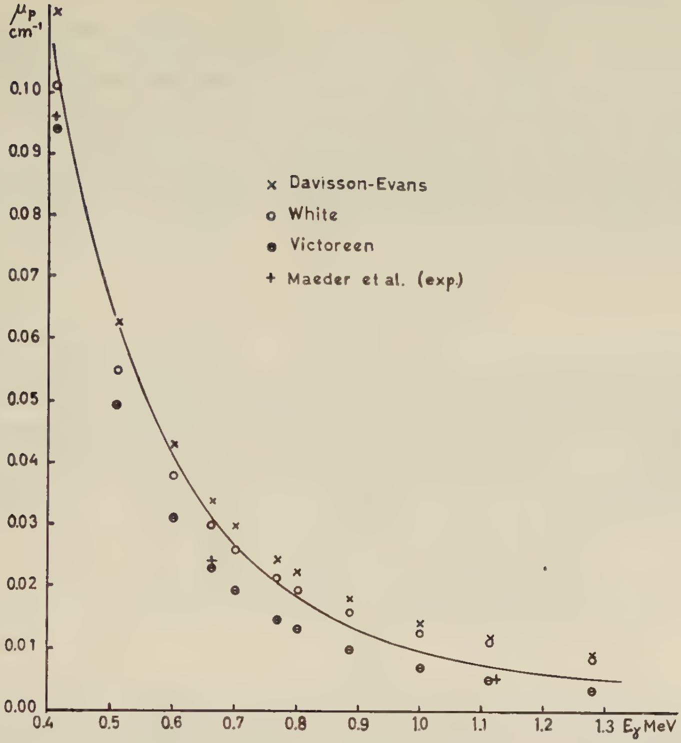

Fig. 4. Comparison of the photoelectric absorption coefficients according to the present investigation (drawn curve) with some earlier values.

VII. Appendix

This appendix contains an account of the measurements performed on various isotopes. Under each isotope there is first a brief account of the manner in which the transitions occur, according to the published results of recent research. Complete references may be obtained by consulting the special publications referred to at the end of this paper.

As mentioned in the Introduction, certain gamma energies were determined for the isotopes Nb^{95}, Zn^{65}, Sc^{46} and Cs^{134}. For this purpose the spectrometer was calibrated for the following lines, which have been accurately determined with crystal spectrometers: Au^{198}, 0.412 MeV; Zn^{65}, 0.511 MeV; Cs^{137}, 0.662 MeV; Co^{60}, 1.172 and 1.332 MeV. The relation between pulse height and gamma energy was found to be linear in the range of energies investigated. Each series of measurements included determination of the positions of the photoelectric peaks for the above seven isotopes. To obviate the effect of long-period drift in the spectrometer the measurements on the different isotopes were carried out in as rapid succession as possible. The figures stated below under each isotope are the means of several series of measurements.

Subsequently there is under each isotope an account of the graphical analysis of the pulse height distribution, and the resulting values of p are stated.

The gamma energy concerned, together with the geometrical arrangement, determine the total absorption in a particular crystal. The energy dependence was investigated by means of isotopes with two or more gamma lines. The results used were those obtained with the two mounted crystals and with the source central and directly against the reflector. The sum of the areas of a photoelectric peak (P) and the corresponding Compton distribution (C) is a measure of the total number of gamma quanta of the relevant energy which are absorbed in the crystal. The ratio R of the total absorption for two gamma energies (1 and 2) of relative intensities I_1 and I_2 is given by

$$R = \frac{I_2}{I_1} \cdot \frac{P_1 + C_1}{P_2 + C_2}. \tag{8}$$

On the other hand, if this ratio is known for two lines in a spectrum it can be used to calculate their relative intensities, when the above areas have been determined from the pulse height distribution. An example of such a calculation is given under Zn^{65}. If the percentage p is already known for the crystal and geometric arrangement used for the measurements on the two energies (Fig. 2), it is only necessary to measure the areas of the photoelectric peaks. It is easy to see that

$$P + C = \frac{100\,P}{p} \quad \text{and} \quad \frac{P_1 + C_1}{P_2 + C_2} = \frac{P_1}{P_2} \cdot \frac{p_2}{p_1}. \tag{9}$$

Au^{198}

Small pieces of pure gold were activated by slow neutron bombardment for 1 week at Harwell. This gives rise to the isotope Au^{198}, which has a half-life of 2.70 days. A transition with a maximum energy of 0.97 MeV produces an excited state of Hg^{198}. The ground state is attained by emission of a gamma photon whose energy MULLER *et al.* [15] found to be 0.411770 ± 0.000036 MeV using a crystal spectrometer. Some authors [16–19] state that this is the only way in which the decay can occur, while others [20–23] have detected a weak β-transition to a level at 1.09 MeV in Hg^{198}. The nucleus may proceed from this level to the ground state either directly or via a level at 0.412 MeV ($E_\gamma = 1.09$ and 0.68 MeV). Rather different values are given for the relative intensities of the gamma lines, but in any case more than 99 % of all the gamma quanta emitted have an energy of 0.412 MeV.

During the present measurements a very weak gamma line was detected at about 0.67 MeV. Its contribution to the pulse height distribution was insignificant, and it was easily eliminated graphically when determining the areas of the photoelectric peak and Compton distribution corresponding to the energy 0.412 MeV. A pronounced peak occurs at about 75 keV. This is due to X-radiation from mercury, which arises from the internal conversion of some of the gamma radiation. The back-scattering peak previously mentioned occurs at 0.16 MeV. The presence of these two peaks renders the separation of the Compton distribution in this region somewhat uncertain. In order to carry out extrapolation to zero energy a comparison was made with the shapes of Compton distributions recorded for other isotopes, and with theoretical curves for various crystal sizes. The shape of the pulse height distribution is shown in Fig. 5.

Measurements were performed in the manner described previously, with a weak source placed directly on the crystal mounting. The extension of the source was

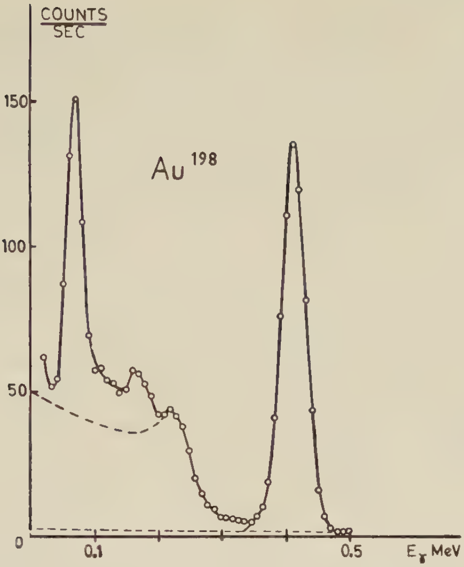

Fig. 5. Pulse height distribution for X-rays and gamma-rays of Au^{198}. NaI(Tl) crystal ⌀ $\frac{3}{4}''\times\frac{3}{4}''$, uncollimated radiation.

negligible. Six series of measurements with the crystal of dimensions ⌀ $\frac{1}{2}''\times\frac{1}{2}''$ gave the result $p = 33.5 \pm 0.3\,\%$. From five series of measurements with the crystal of dimensions ⌀ $\frac{3}{4}''\times\frac{3}{4}''$ $p = 38.1 \pm 0.5\,\%$.

In connection with these measurements on gold it was decided to investigate the applicability of the scintillation spectrometer to the determination of this isotope's half-life. For this purpose a piece of gold was placed directly on the crystal mounting, in a central position. The pulse height distribution was recorded each day for a week. The area of the photoelectric peak was taken as the measure of the source's activity. The logarithm of this quantity was plotted against time. The points were found to lie very nearly on a straight line, and the value of the isotope's half-life obtained from the slope of this line was 2.697 days. The estimated margin of error is 0.005. LOCKETT and THOMAS [24] have recently obtained the figure 2.697 ± 0.003 days, using an electroscope. SAXON and HELLER [18] and SILVER [25] obtained the value 2.69 days; SINCLAIR and HOLLOWAY [26] 2.73 ± 0.02 days; and CAVANAGH *et al.* [23] 2.66 ± 0.01 days. The accuracy of the determination can of course be improved by making measurements at more frequent intervals and by extending the measurements of several half-life periods. One of the series of measurements was carried out on a piece of gold which contained some silver as impurity, and which had been activated three times during the course of a year. Since the silver isotope formed, Ag^{110}, has a half-life of 270 days, its activity remains practically constant for one week. At the time of the measurements, about two months after the last activation, the activities of the silver and gold isotopes were about the same. The photoelectric peak for gold was thus superposed on the pulse height distribution for the silver isotope, but could nevertheless be measured quite accurately, since the curve for silver could be determined when the activity of the gold had sunk to a negligible level. The experiment shows that the scintillation spectrometer can be used for accurate determination of

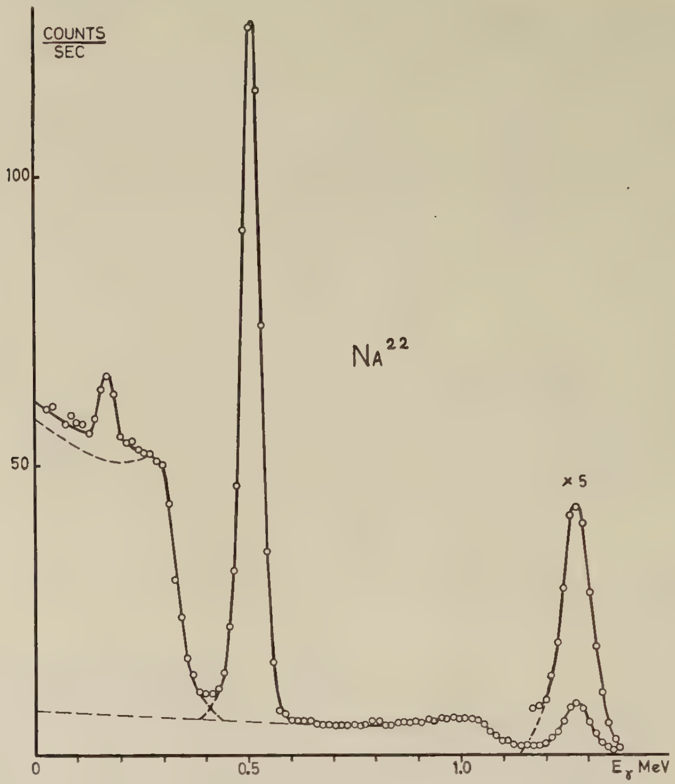

Fig. 6. Pulse height distribution for gamma-rays of Na^{22}.
NaI(Tl) crystal ∅ ¾″ × ¾″, uncollimated radiation.

half-lives of suitable durations even when another gamma-active isotope is present, provided the half-life of the latter is known or long in comparison with that to be determined.

Na^{22}

Na^{22} was obtained from the Radiochemical Centre, Amersham, in the form of an aqueous solution of NaCl.

The isotope decays with a half-life of 2.6 years, by a single β^{+}-transition to Ne^{22} followed by emission of a single gamma quantum to the ground state [27]. ALBURGER [28] gives the gamma energy as 1.277 ± 0.004 MeV. Recently SHERR and MILLER [29] investigated the activity of Na^{22} and found that 10% of it involves K-capture to the above-mentioned excited state of Ne^{22}.

A very small volume of the active solution was sucked up by means of a capillary tube and applied to a piece of a blotting paper. This source was enclosed in aluminium of 0.7 mm thickness to absorb positrons, and placed on top of the crystal mounting. The pulse height distribution is shown in Fig. 6. There are photoelectric peaks at 1.28 and 0.51 MeV. The curve has been corrected for background. The Compton distribution for the higher energy is well defined down to about $E_{\gamma} = 0.5$ MeV. Its extrapolation to zero pulse height was possible by comparing with other experimental Compton distributions and with theoretical curves. The photoelectric peak and Compton distribution for $E_\gamma = 0.511$ MeV have not been drawn standing on the axis, since their shapes are equally well discernible from the measured curve.

Four series of measurements were made with the ⌀ $\frac{1}{2}'' \times \frac{1}{2}''$ crystal. For the 0.511 MeV line p was 26.9 ± 0.4 % and for the 1.28 MeV line 7.0 ± 0.1 %, the corresponding values resulting from four series of measurements with the ⌀ $\frac{3}{4}'' \times \frac{3}{4}''$ crystal were $p = 31.5 \pm 1.3$ % and 10.2 ± 0.2 %. The half width was about 10.5 % and 5.5 % for the respective peaks.

In accordance with what was stated above, the activity of Na^{22} was attributed entirely to emission of a positron and subsequently a gamma photon of energy 1.28 MeV. If it is ensured that all the positrons are absorbed near the source, each positron, when annihilated gives rise to two gamma photons of energy 0.511 MeV. These may be regarded as emanating from the same point as the corresponding 1.28 MeV photon, so there are twice as many 0.511 MeV photons incident on the crystal as there are 1.28 MeV photons, i.e. $I_1/I_2 = 2$. The ratio of the total absorption coefficients for the two energies as computed from this result and the formula (8) is 1.45 ± 0.05 for the ⌀ $\frac{1}{2}'' \times \frac{1}{2}''$ crystal and 1.62 ± 0.08 for the ⌀ $\frac{3}{4}'' \times \frac{3}{4}''$. It will be seen from these figures that the absorption is about 50 % greater at the lower energy.

If it is assumed that the transition to the 1.28 MeV level in Ne^{22} occurs to 10 % through K-capture, the ratio of the two gamma intensities becomes 1.8:1, instead of 2:1. The computed ratio of the total absorption coefficients in the two cases is then 1.61 ± 0.06 and 1.80 ± 0.09 for the respective crystals.

Cs^{137}

Cs^{137} was obtained from the Radiochemical Centre in the form of an aqueous solution of the chloride. The half-life of the isotope is 33 years. It decays by two β-transitions to Ba^{137}, in part (8 %) direct to the ground state and in part via a Ba isomer with a half-life of 26 min. to the ground state with emission of a gamma photon [30]. MULLER *et al.* [15] found the energy of the gamma photon to be 0.66160 ± 0.00014 MeV, using a crystal spectrometer.

A very small volume of the active solution was applied to a piece of blotting paper, which was then placed between two pieces of cellulose tape. The pulse height distribution is shown in Fig. 7. Besides the pronounced photoelectric peak at 0.662 MeV there is a well-defined back-scattering peak at about 0.19 MeV. Since some of the gamma radiation is converted internally the source also emits X-rays (cf. Au^{198}). The peak which this radiation gives rise to is not drawn in the figure. For the ⌀ $\frac{1}{2}'' \times \frac{1}{2}''$ crystal $p = 19.4 \pm 0.1$ %, and for the ⌀ $\frac{3}{4}'' \times \frac{3}{4}''$ crystal $p = 23.9 \pm 0.2$ %. The half width of the peak is about 8.0 %.

Nb^{95}

Nb^{95} occurs as a fission product from uranium. It was obtained in the form of a hydrochloric solution from the Radiochemical Centre. The decay, which has been investigated several times, takes place by a single β-transition to a metastable state of Mo^{95}, followed by gamma emission to the ground state. The half-life is about 35 days. A small quantity of an isomer of Nb^{95} is also present. It is transformed to 35-days Nb^{95} by emission of a totally converted 0.230 MeV photon. Its half-life is 84 hours, and accordingly the weak activity of this isomer soon disappears. It is

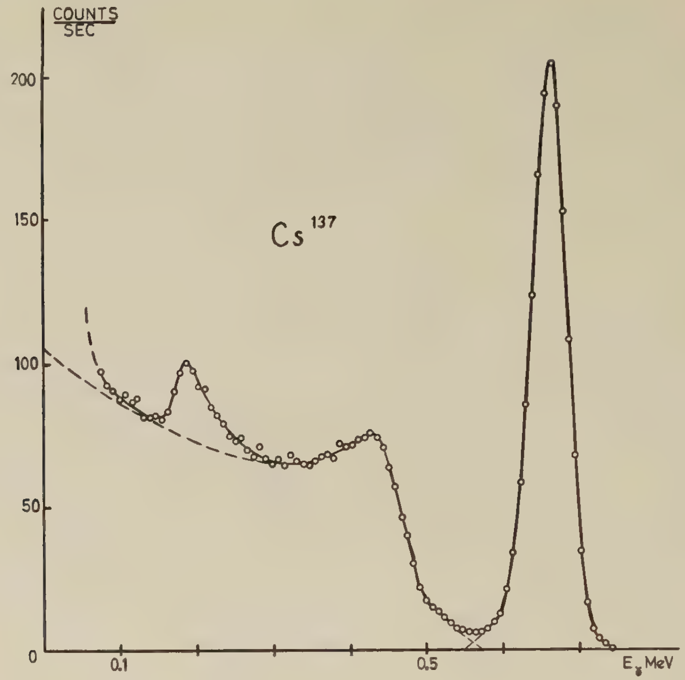

Fig. 7. Pulse height distribution for gamma-rays of Cs^{137}. NaI(Tl) crystal ⌀ $\frac{3}{4}'' \times \frac{3}{4}''$, uncollimated radiation.

unnoticeable in the present measurements. The values given for the gamma energy vary somewhat. RALL [31] obtained 0.75 MeV, HUDGENS and LYON [32] 0.758 ± 0.02 MeV, LEVINGER [33] 0.776 MeV, SLÄTIS and ZAPPA [34] 0.745 MeV, MANDEVILLE *et al.* [35] 0.76 ± 0.02, CORK *et al.* [36] 0.768 MeV (together with two cascade energies of 0.016 and 0.702 MeV), and MITTELMAN [37] 0.764 MeV. The value obtained here was $E_\gamma = 0.767 \pm 0.002$ MeV, which is in good agreement with the above values, especially those of CORK *et al.* and of MITTELMAN.

A small amount of the active material was made into a suitable source in the same way as with Cs^{137}, and examined in the scintillation spectrometer in the manner already described for uncollimated radiation. For the ⌀ $\frac{1}{2}'' \times \frac{1}{2}''$ crystal $p = 16.0 \pm 0.2\,\%$, and for the ⌀ $\frac{3}{4}'' \times \frac{3}{4}''$ crystal $p = 20.1 \pm 0.2\,\%$. The pulse height distribution s shown in Fig. 8. p was also determined with unmounted crystals, for which purpose the source was placed on top of the reflector. As already mentioned, the relation between p and the crystal height was found to be linear. The extrapolated value of p, p_0, was 8.2%.

The half width of the photoelectric peak at $E_\gamma = 0.767$ MeV was about 8 %.

Zn^{65}

Zinc metal was bombarded with slow neutrons at Harwell for four weeks. This leads to the formation of Zn^{65} and Zn^{67}, and a little Zn^{69m}. The half-lives are 250 days, 57 mins. and 13.8 hours. After a short time the only appreciable isotope is

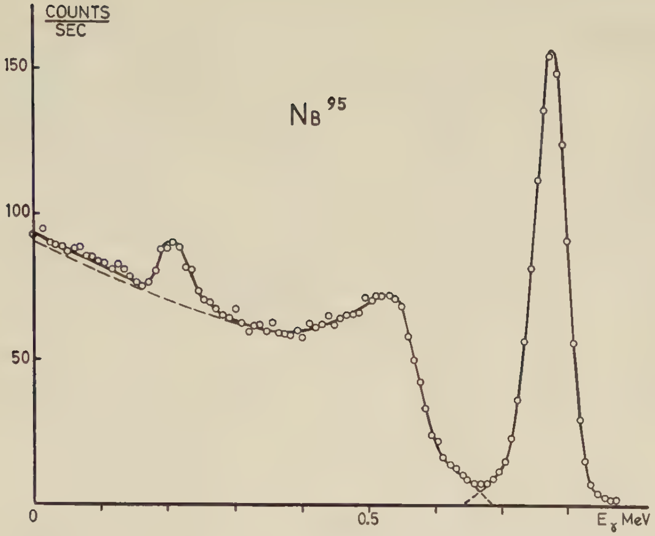

Fig. 8. Pulse height distribution for gamma-rays of Nb^{95}. NaI(Tl) crystal ∅ $\frac{3}{4}'' \times \frac{3}{4}''$, uncollimated radiation.

Zn^{65}. This decays by K-capture and by positron emission. About 55 % of the K-captures go to the ground state and about 45 % to an excited state of Cu^{65}, followed by transition to the ground state through emission of a gamma ray [38–41]. The intensity of β^+ is given by GOOD and PEACOCK [38] as 2.2 % of all disintegrations. MAJOR [40] gives the figure 2.5 ± 0.1 % and GRIFFITHS [41] 0.8 %. PERKINS and HAYNES [42] give 1.74 ± 0.2 %.

There have been several determinations of the energy of the gamma ray. The following are some of the most recent results: JENSEN *et al.* [43] 1.118 MeV, MANN *et al.* [44] 1.114 MeV, HEDGRAN *et al.* [45] 1.125 MeV, WAGGONER *et al.* [46] 1.112 ± 0.007 MeV, GOOD [47] 1.127 ± 0.009 MeV. The present measurements give $E_\gamma = 1.112 \pm 0.003$ MeV.

A small piece of the activated zinc was used as source. The pulse height distribution obtained with the scintillation spectrometer is shown in Fig. 9. The photoelectric peak for 1.11 MeV is well defined, as are also the maximum and the edge of the Compton distribution. At 0.51 MeV there is a photoelectric peak arising from the annihilation radiation of the positrons. Since it is superposed on an almost horizontal section of the main curve its position and area are easily determined. With this area known the magnitude of the corresponding Compton distribution can be calculated without difficulty, since the percentage ratio is known from the measurements on Na^{22}. When this distribution is subtracted from the original pulse height distribution the distribution corresponding to 1.11 MeV can be extrapolated to zero energy. The effect of the back-scattering peak at 0.22 MeV can easily be eliminated from the curve. At $E_\gamma = 1.11$ MeV p was 9.4 ± 0.1 % for the ∅ $\frac{1}{2}'' \times \frac{1}{2}''$ crystal and 12.7 ± 0.1 % for the ∅ $\frac{3}{4}'' \times \frac{3}{4}''$ crystal. The half widths of the photoelectric peaks at 0.51 and 1.11 MeV were approximately 11.0 and 6.9 % respectively.

If all the positrons are annihilated near the source it is possible to calculate the relative numbers of nuclei that disintegrate by positron emission and by K-capture

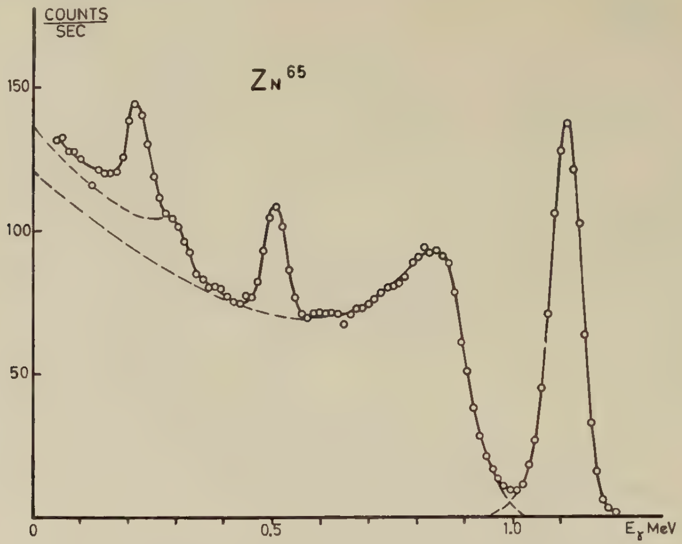

Fig. 9. Pulse height distribution for gamma-rays of Zn^{65}.
NaI(Tl) crystal ∅ $\frac{3}{4}''\times\frac{3}{4}''$, uncollimated radiation.

from the areas of the photoelectric peaks at 0.511 and 1.11 MeV. If the areas of the photoelectric peak and Compton distribution for 0.511 MeV are denoted by P_1 and C_1, and for 1.11 MeV by P_2 and C_2, the ratio $2\,(P_2 + C_2)/(P_1 + C_1)$ is 30.3 ± 1.5 for the ∅ $\frac{1}{2}''\times\frac{1}{2}''$ crystal and 25.2 ± 2.0 for the ∅ $\frac{3}{4}''\times\frac{3}{4}''$ crystal. The absorption at 1.11 MeV is about the same as at 1.28 MeV, and it is therefore permissible to use the values obtained for the ratios of the total absorption coefficients at 0.51 and 1.28 MeV for Na^{22} (1.61 and 1.80 respectively) for the two energies 0.51 and 1.28 MeV in the present case. The ratio of the number of gamma photons of energy 1.11 MeV and the number of positrons emitted is then 49.7 % and 45.5 % for the two crystals. The mean is 47.1 %. As already mentioned, 45 % of the disintegrations by K-capture are stated to proceed to the excited level. Using this value, we arrive at the result that 1.0 ± 0.1 % of the Zn^{65} nuclei disintegrate by positron emission.

Sc^{46}

Sc^{46}—with a half-life of 85 days—was obtained by bombardment of scandium oxide with slow neutrons for two weeks at Harwell. Sc^{46m} is also formed, but since it decays to Sc^{46} with a half-life of 20 secs. it very rapidly disappears.

A decay scheme for Sc^{46} has been given by PEACOCK and WILKINSON [16]. According to this scheme 98 % of the nuclei undergo a β-transition ($E_{\max} = 0.36$ MeV) to an excited level of Ti^{46} at 2.01 MeV, followed by emission in cascade of two gamma photons of energies 0.89 ± 0.005 and 1.12 ± 0.005 MeV to attain the ground state. 2 % of the nuclei undergo β-transition ($E_\gamma = 1.49$ MeV) to a 0.89 MeV level. More recently, different values have been published for the two β-components. MOON *et al.* [48] found that only 0.06 % of the transitions are to the lower level; PORTER and COOK [49] set an upper limit at 0.5 %; and SCHMIDT and KEISTER [50]

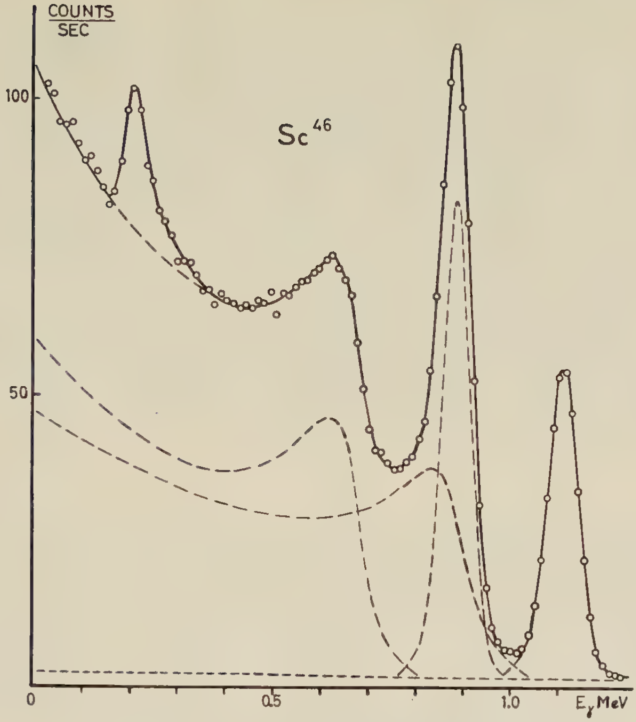

Fig. 10. Pulse height distribution for gamma-rays of Sc^{46}. NaI(Tl) crystal $\varnothing\ \frac{3}{4}'' \times \frac{3}{4}''$, uncollimated radiation.

$0.22 \pm 0.05\,\%$. It therefore seems that the β-component with the higher energy is very weak, and negligible in the present investigation. LINDQVIST [51] found the gamma energies to be 0.885 ± 0.002 MeV and 1.119 ± 0.002 MeV. The present measurements lead to the values 0.892 ± 0.003 and 1.118 ± 0.003 MeV, which are in good agreement with Lindqvist's and earlier results [16, 52].

The gamma radiation from a small sample of the active material was examined with the spectrometer. The pulse height distribution is shown in Fig. 10. The photoelectric peak for the higher energy is well separated, and is thus easily measured. The shape of the corresponding Compton distribution may be obtained from the results for Zn^{65}. Series of measurements for Sc^{46} and Zn^{65} were carried out alternately without alteration of the experimental arrangement. The pulse height distribution for Zn^{65} is drawn to such a scale that its photoelectric peak is of the same size as the 1.12 MeV peak in the Sc curve. After correcting for the slight energy difference it is then possible to draw the Compton distribution. The photoelectric peak for 0.89 MeV is superposed on this distribution, but can be drawn standing on the axis after subtraction, whereupon its position and area can be determined. Its shape is very similar to that of the 1.12 MeV peak. The half width is somewhat less, which was to be expected. Consideration of the resolution at different energies provides a check on the shape of photoelectric peaks. The corresponding Compton distribution is obtained in an analogous manner to the photoelectric peak by continuing the subtraction of the Zn distribution from the original Sc curve. The back-scattering peak is well separated and is easy to eliminate graphically. After this graphical analysis of the original curve it is possible to determine p for the 0.89 MeV peak. For $\varnothing \frac{1}{2}'' \times \frac{1}{2}''$ and $\varnothing \frac{3}{4}'' \times \frac{3}{4}''$ crystals p was 13.4 ± 0.2 % and 17.3 ± 0.3 % respectively. It may be seen from Fig. 2, where p is plotted against energy, that these points accord well with the curves for the two crystals. This shows that it is possible to obtain good quantitative resolution of two gamma lines in a spectrum by the method described here.

The proportion of internal conversion for the two gamma transitions of 0.89 and 1.12 MeV is insignificant (*c.* 1.10^{-4}). Consequently, from what was said above about the decay scheme, the intensities of the primary gamma radiations are equal. The ratio of the coefficients of total absorption at 0.89 and 1.12 MeV is 1.03 ± 0.01 for the $\varnothing \frac{1}{2}'' \times \frac{1}{2}''$ crystal and 1.03 ± 0.02 for the $\varnothing \frac{3}{4}'' \times \frac{3}{4}''$ crystal. These results indicate that with the present experimental arrangement about 3 % more of the gamma radiation of energy 0.89 MeV is absorbed than of the 1.12 MeV radiation. There is no detectable difference between the two crystals in this respect, owing to the fact that the energies concerned are relatively high and relatively close together.

Co^{60}

Co^{60} was obtained by bombarding cobalt metal with slow neutrons for 8 weeks at Harwell. The isotope Co^{60} thus formed has a half life of 5.3 years, and there is in addition a small quantity of Co^{60m}, which is soon (half life 10 mins.) transformed to Co^{60}. Co^{60} decays to an excited state of Ni^{60} with emission of β-particles of maximum energy 0.31 MeV. The ground state is attained by emission of two gamma photons in cascade. LIND *et al.* [53] have determined the gamma energies by means of a crystal spectrometer, and found them to be 1.1715 ± 0.0010 MeV and 1.3316 ± 0.0010 MeV. DZHELEPOV *et al.* [54] give the same values. LINDSTRÖM *et al.* [55] give the values 1.1728 ± 0.0005 and 1.3325 ± 0.0003 MeV.

A very small piece of the activated metal was placed between two pieces of cellulose tape for investigation by means of the spectrometer. The pulse height distribution obtained is shown in Fig. 11. The photoelectric peaks are close together, but the resolution is sufficiently good for the 1.33 MeV peak to be measureable. The 1.17 MeV peak is also distinct, but it is superposed on the Compton edge corresponding to the other energy. The shape of this Compton distribution has been obtained by comparison with the curves for Na^{22} ($E_\gamma = 1.28$ MeV), after correction for the slight energy difference. The pulse height distribution can then be divided up graphically in the manner described under Sc^{46}.

The half width of the photoelectric peak at 1.33 MeV is about 6.7 %. Proceeding from the equal intensities of the 1.17 and 1.33 MeV radiations, the ratio of the total absorptions at these energies was calculated in the manner described under preceding isotopes. For the $\varnothing \frac{1}{2}'' \times \frac{1}{2}''$ crystal the ratio was 1.00 ± 0.05 and for the $\varnothing \frac{3}{4}'' \times \frac{3}{4}''$ crystal 0.98 ± 0.05. The margin of error is rather large, on account of the difficulty in determining the areas of such closely adjacent peaks. However, the values obtained indicate that the total absorption is in both crystals practically the same for the gamma energies 1.17 and 1.33 MeV.

Cs^{134}

The isotope Cs^{134} is formed when cesium is bombarded with slow neutrons. Its half-life is 2.3 years. Cs^{134m} is also formed, but its half-life is relatively short (3.15 hours), and it rapidly decays to Cs^{134} or directly to the ground state of Ba^{134}. A

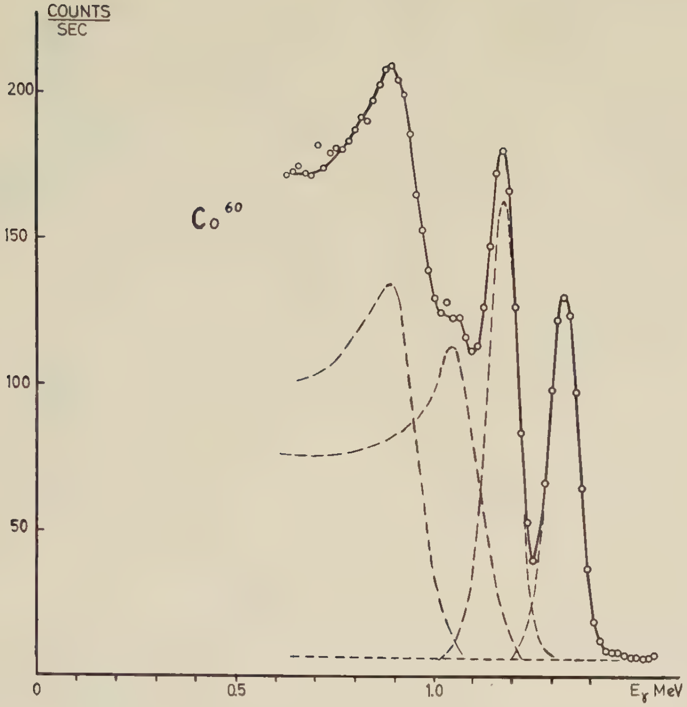

Fig. 11. Pulse height distribution for gamma-rays of Co^{60}. NaI(Tl) crystal ∅ $\frac{3}{4}''$ × $\frac{3}{4}''$, uncollimated radiation.

decay scheme was formulated by Elliot and Bell [56], and their results have been confirmed by Siegbahn and Deutsch [57]. There are two alternative beta transitions to excited states of Ba^{134}, followed by transition to the ground state by emission of gamma rays (see Fig. 12*a*). The respective papers referred to above give the gamma energies as 0.568 ± 0.015, 0.602 ± 0.015 and 0.794 ± 0.015 MeV (the relative intensities being 0.26 : 1.0 : 1.0), and 0.566 ± 0.01, 0.603 ± 0.01, and 0.798 ± 0.015 MeV. Weak cross-over gamma radiation was detected at *c.* 1.35 MeV. Its position in the decay scheme could not be established with certainty. If the lowest excited level of Ba^{134} is 0.602 MeV, it might be produced by a transition from the 1.964 MeV level to the 0.602 MeV level. Meem and Maienschein [58] arrived at the value 34 ± 5 % for the relative frequency of the weaker beta transition. Waggoner *et al.* [46] give an experimental scheme as shown in Fig. 12*b*. Two weak lines were observed at 1.037 and 1.170 MeV. These could not be fitted into the beta-transition branches, and they were accordingly ascribed to K-capture. Schmidt and Keister [59] found seven gamma lines: 561.5 ± 1.0, 566.5 ± 0.8, 601.2 ± 0.5, 793.1 ± 0.7, 1037.2 ± 2.6, 1164.4 ± 2.9, and 1365.7 ± 3.3 MeV. The last three lines were weak. On the basis of these results the decay scheme of Fig. 12*c* was drawn up. Shpinel [60] gives the energies γ_1 0.570, γ_2 0.601, γ_3 0.793, γ_4 1.024, γ_5 1.11, γ_6 1.35, with the relative intensities $\gamma_1 : \gamma_2 : \gamma_3 : \gamma_6 = 0.35 : 0.94 : 1.0 : 0.017$. By particularly accurate measurements Cork *et al.* [61] have detected altogether eleven gamma lines, of which all except one were interpreted as lines in the spectrum of Cs^{134}. On the basis of

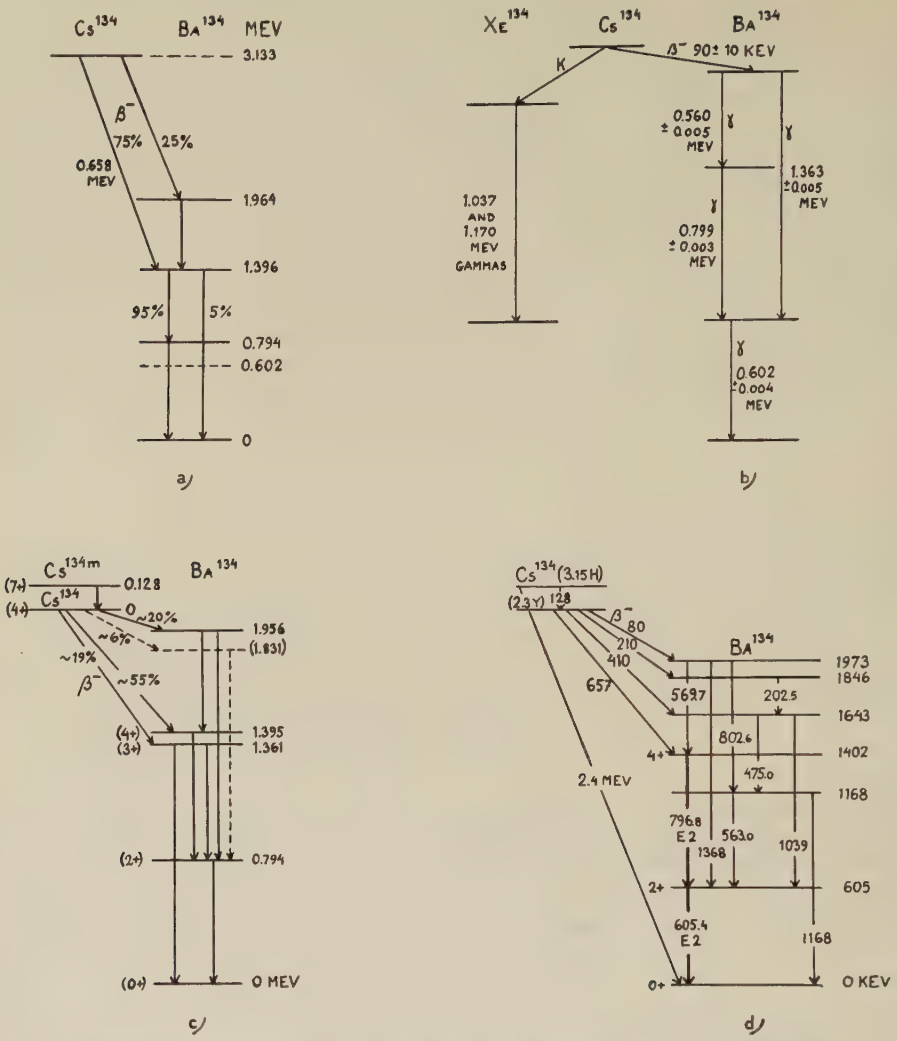

Fig. 12. Decay scheme of Cs¹³⁴ according to *a*, ELLIOT and BELL [56]; *b*, WAGGONER *et al.* [46]; *c*, SCHMIDT and KEISTER [59]; *d*, CORK *et al.* [61].

these measurements and others carried out in conjunction with them on the beta spectrum they arrived at the decay scheme of Fig. 12*d*. The relative abundances of the beta transitions are 81, 6, 3, 10, in decreasing order of energy.

Cesium chloride was bombarded with slow neutrons at Harwell. A small quantity of the activated compound was investigated with the scintillation spectrometer in the manner already described. The measurements were on the whole restricted to energies below 0.90 MeV, since the principal object of the investigation was the determination of photoelectric absorption coefficients at 0.60 and 0.80 MeV. The counting rate above 0.80 MeV was low, which indicates that gamma lines in that

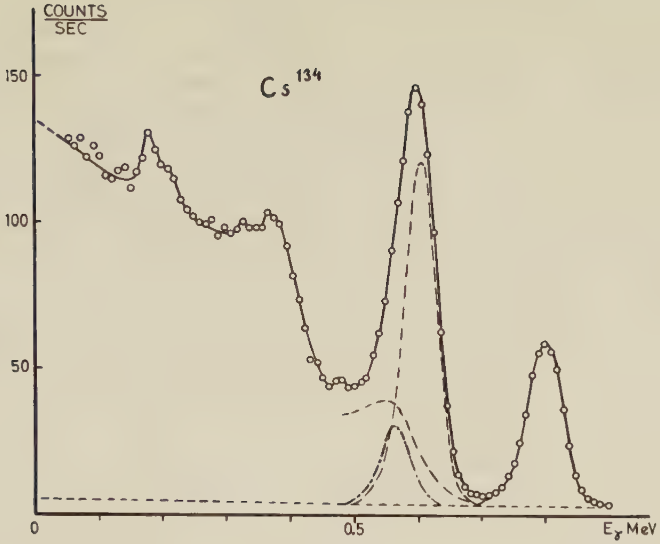

Fig. 13. Pulse height distribution for gamma-rays of Cs^{134}. NaI(Tl) crystal ∅ $\frac{3}{4}''$ × $\frac{3}{4}''$, uncollimated radiation.

range of energies are weak: it was estimated that the number of gamma photons with energies greater than 0.80 MeV was less than 5 % of the number associated with the 0.60 MeV line. The photoelectric peaks at 0.60 and 0.80 MeV are quite distinct in the pulse height distribution (Fig. 13). From the shape of the left side of the 0.60 MeV peak it can be deduced that there is a relatively strong line with an energy somewhat lower than 0.60 MeV. The shape and area of this peak can be determined approximately by a graphical method. According to the papers of SCHMIDT and KEISTER and of CORK *et al.* referred to above there are two lines closely adjacent—the energies being given as 0.562, 0.567 and 0.563, 0.570 MeV in the respective publications. It was of course impossible to resolve these lines with the scintillation spectrometer. They form a single peak in the pulse height distribution. By comparison with the positions of the two larger peaks the energy corresponding to this peak was determined to be 0.566 ± 0.004 MeV. This figure is nearer the higher of the above two energies, which suggests that the line with the higher energy is the stronger—a conclusion according with CORK's decay scheme. The energies of the two strong lines as determined here are 0.603 ± 0.001 and 0.797 ± 0.002 MeV. These values are in good agreement with the results referred to above. CORK states that there are two lines below 0.56 MeV—at 0.203 and 0.475 MeV. The photoelectric peak corresponding to the former of them would fall within the back-scattering peak of the present distribution. Most of the recorded series of measurements do in fact evidence a slight irregularity on the right of the back-scattering peak. It is possible that this slight irregularity corresponds to a weak line. The energy appears to be about 0.21 MeV. There is a very small peak at 0.475 ± 0.003 MeV, which is not always clearly discernible on account of the statistical fluctuation in the counting rate. However, it is possible to determine its position quite accurately from the curves where it is clearly discernible. The peak might be due to some other active isotope with a long half-life, but it probably arises from a weak gamma line in the spectrum of Cs^{134}. As already mentioned, Cork *et al.* detected a weak gamma line at 0.475 MeV. It thus seems that the present result is a confirmation of theirs. It is difficult to estimate the intensity of the line, but it appears to have less than 1 % of the intensity of the 0.60 MeV line.

The diversity of the decay schemes that have been put forward for Cs^{134} makes a calculation of the intensity ratio of the two strongest lines impossible. According to Elliot and Bell it is 1:1, according to Waggoner the intensity of the 0.60 MeV line is somewhat greater, which also accords with Cork's diagram. On the other hand, Schmidt and Keister take 0.794 MeV to be the lowest energy level for Ba^{134}, which means that the line with this energy should be the most intense.

The graphical resolution of the pulse height distribution was much the same as that described for Sc^{46}. Nb^{95} was utilised to obtain the shape of the Compton distribution for the 0.80 MeV line. A correction for the energy difference 0.767 to 0.797 MeV was applied. The separation of the 0.57 and 0.60 MeV peaks was of course somewhat uncertain. The right side of the 0.60 MeV peak is not much affected by the smaller peak, so it is possible to determine its shape. Then, when the position of the axis of symmetry had been determined the peak could be completed, and the form of the lesser peak obtained by subtraction. The areas of the different photoelectric peaks were measured after this graphical analysis had been carried out. If these areas are denoted by P_1, P_2, and P_3, for the energies 0.57, 0.60, and 0.80 MeV respectively, then for the $\varnothing\ \frac{1}{2}'' \times \frac{1}{2}''$ crystal $P_2/P_1 = 4.57 \pm 0.06$, $P_2/P_3 = 1.83 \pm 0.03$, and $P_3/P_1 = 2.50 \pm 0.10$. The corresponding figures for the $\varnothing\ \frac{3}{4}'' \times \frac{3}{4}''$ crystal were 4.82 ± 0.08, 1.74 ± 0.03, 2.76 ± 0.03. In order to be able to calculate the relative intensities of the different gamma lines it is necessary to know the relative total absorptions for the different gamma energies concerned. This method has already been applied to Na^{22}, Sc^{46}, and Co^{60}, and resulted in values of the total relative absorption for 0.5 and 0.9 MeV, as well as other energies. The values for the three most intense lines in the Cs spectrum can be estimated by graphical interpolation. The magnitudes of the Compton distributions corresponding to the various peaks have been calculated as for Co^{60}, p being known. The ratio of the intensities of the 0.57, 0.60, and 0.80 MeV lines was found to be 0.19 : 1.0 : 0.96. The result that the 0.60 MeV line is the strongest is in good agreement with the decay schemes of Waggoner and of Cork. It was therefore decided to adopt these values in calculating photoelectric absorption coefficients by the relative method.

ACKNOWLEDGEMENTS

The present investigation has been carried out at the Department of Physics, Chalmers University of Technology, Gothenburg. The author wishes to express his sincere appreciation to Professor N. F. Ryde for his interest and support in this work and to Dr. S. A. E. Johansson, University of Lund, for many valuable discussions. The work was assisted by a grant from the Swedish Atomic Energy Commission.

Department of Physics, Chalmers University of Technology, Gothenburg (Sweden).

REFERENCES

1. D. Maeder, R. Müller, and V. Wintersteiger, Helv. Phys. Acta *27*, 3 (1954).
2. K. Lidén and N. Starfelt, Arkiv för Fysik *7*, 427 (1954).
3. C. M. Davisson and R. D. Evans, Rev. Mod. Phys. *24*, 79 (1952).
4. G. R. White, Nat. Bur. Stand. Report No. 1003 (May 1952).
5. J. A. Victoreen, Journ. Appl. Phys. *20*, 1141 (1949).
6. C. L. Cowan, Phys. Rev. *74*, 1841 (1948).
7. C. M. Davisson and R. D. Evans, Phys. Rev. *81*, 404 (1951).
8. S. J. Wyard, Proc. Phys. Soc. (London), A *66*, 382 (1953).
9. H. R. Hulme, J. McDougall, R. A. Buckingham, and R. H. Fowler, Proc. Roy. Soc. A *149*, 131 (1935).
10. C. W. Johnstone, Nucleonics *11* No. 1, 36 (1953).
11. C. J. Borkowski and R. L. Clark, Rev. Sci. Instr. *24*, 1046 (1953).
12. G. J. Hine and R. C. McCall, Nucleonics *12* No. 4, 27 (1954).
13. D. C. Lu and M. L. Wiedenbeck, Phys. Rev. *94*, 501 (1954).
14. O. Klein and Y. Nishina, Z. Phys. *52*, 853 (1929).
15. D. E. Muller, H. C. Hoyt, D. J. Klein, and J. W. M. Du Mond, Phys. Rev. *88*, 775 (1952).
16. C. L. Peacock and R. G. Wilkinson, Phys. Rev. *74*, 297 (1948).
17. K. Siegbahn and A. Hedgran, Phys. Rev. *75*, 523 (1949).
18. D. Saxon and R. Heller, Phys. Rev. *75*, 909 (1949).
19. C.-Y. Fan, Phys. Rev. *87*, 252 (1952).
20. L. G. Elliot and J. L. Wolfson, Phys. Rev. *82*, 333 (1951).
21. P. E. Cavanagh, Phys. Rev. *82*, 791 (1951).
22. A. R. Brosi, B. H. Ketelle, H. Zeldes, and E. Fairstein, Phys. Rev. *84*, 586 (1951).
23. P. E. Cavanagh, J. F. Turner, D. V. Booker, and H. J. Dunster, Proc. Phys. Soc. (London) *64* A, 13 (1951).
24. E. E. Lockett and R. H. Thomas, Nucleonics *11* No. 3, 14 (1953).
25. L. M. Silver, Phys. Rev. *76*, 589 (1949).
26. W. K. Sinclair and A. F. Holloway, Nature *167*, 365 (1951).
27. W. M. Good, D. Peaslee, and M. Deutsch, Phys. Rev. *69*, 313 (1946).
28. D. E. Alburger, Phys. Rev. *76*, 435 (1949).
29. R. Sherr and R. H. Miller, Phys. Rev. *93*, 1076 (1954).
30. M. A. Waggoner, Phys. Rev. *82*, 906 (1951).
31. W. Rall, Phys. Rev. *71*, 321 (1947).
32. J. E. Hudgens and W. S. Lyon, Phys. Rev. *75*, 206 (1949).
33. J. S. Levinger, NNES 9, paper 94 (1951).
34. H. Slätis and L. Zappa, Arkiv för Fysik *6*, No. 9 (1952).
35. C. E. Mandeville, E. Shapiro, R. I. Mendenhall, E. R. Zucker, and G. L. Conklin, Phys. Rev. *89*, 559 (1953).
36. J. M. Cork, J. M. Le Blanc, D. W. Martin, W. H. Nester, and M. K. Brice, Phys. Rev. *90*, 579 (1953).
37. P. S. Mittelman, Phys. Rev. *91*, 484 (1953).
38. W. M. Good and W. C. Peacock, Phys. Rev. *69*, 680 (1946).
39. S. E. Furberg, Nature *168*, 1005 (1951).
40. J. K. Major, Phys. Rev. *86*, 631 (1952).
41. G. M. Griffiths, Phys. Rev. *83*, 852 (1951).
42. J. F. Perkins and S. K. Haynes, Phys. Rev. *92*, 687 (1953).
43. E. N. Jensen, L. J. Laslett, and W. W. Pratt, Phys. Rev. *76*, 430 (1949).
44. K. C. Mann, D. Rankin, and P. N. Daykin, Phys. Rev. *76*, 1719 (1949).
45. A. Hedgran, K. Siegbahn, and N. Svartholm, Proc. Phys. Soc. (London) *63* A, 960 (1950).
46. M. A. Waggoner, M. L. Moon, and A. Roberts, Phys. Rev. *80*, 420 (1950).
47. M. L. Good, Phys. Rev. *81*, 891 (1951).
48. M. L. Moon, M. A. Waggoner, and A. Roberts, Phys. Rev. *79*, 905 (1950).
49. F. T. Porter and C. S. Cook, Phys. Rev. *81*, 640 (1951).
50. F. H. Schmidt and G. L. Keister, Phys. Rev. *91*, 483 (1953).
51. T. Lindqvist, Arkiv för Fysik *6*, No. 13 (1953).
52. A. E. Miller and M. Deutsch, Phys. Rev. *72*, 527 (1947).
53. D. A. Lind, J. R. Brown, and J. W. M. Du Mond, Phys. Rev. *76*, 591 and 1838 (1949).
54. B. Dzhelepov, N. Zhukovskii, and Y. Kholnov, Doklady Akad Nauk. SSSR *77*, 233 (1951).

55. G. LINDSTRÖM, A. HEDGRAN, and D. E. ALBURGER, Phys. Rev. *89*, 1303 (1953).
56. L. G. ELLIOT and R. E. BELL, Phys. Rev. *72*, 979 (1947).
57. K. SIEGBAHN and M. DEUTSCH, Phys. Rev. *73*, 410 (1948).
58. J. L. MEEM and F. MAIENSCHEIN, Phys. Rev. *76*, 328 (1949).
59. F. H. SCHMIDT and G. L. KEISTER, Phys. Rev. *86*, 632 (1952).
60. V. S. SHPINEL, Zhur. Eksptl. i Teoret. Fiz. *21*, 853 (1951).
61. J. M. CORK, J. M. LE BLANC, W. H. NESTER, D. W. MARTIN, and M. K. BRICE, Phys. Rev. *90*, 444 (1953).

Tryckt den 12 november 1955

Uppsala 1955. Almqvist & Wiksells Boktryckeri AB

ARKIV FÖR FYSIK Band 10 nr 21

Communicated 14 September 1955 by MANNE SIEGBAHN and GUNNAR HÄGG

On the *K* spectrum of aluminium and its oxide

By BERTIL NORDFORS

With 4 figures in the text

Abstract

An X-ray tube with two targets has been constructed, making it possible to obtain suitable reference lines in an easy way. In the *K* spectrum of aluminium and its oxide the lines α_2, α_1, α_3, α_4 and β have been recorded and measured. The difficulty of avoiding oxidation of an aluminium target is discussed. An interesting change in intensity and line shape of the satellite lines α_3 and α_4 in oxide as compared to metal is reported and discussed.

The X-ray tube

When relative measurements in the wavelength region above 4 Å are made, one of the difficulties is to find suitable reference lines. The present work was carried out with a large bent crystal vacuum spectrograph designed by SANDSTRÖM [1], and at first the reference lines were obtained in one of two ways: either the target was changed after the recording of the "unknown" line to one giving the desired reference lines, or the target consisted of an alloy or mixture of two or more elements. Neither method is good, however. In the first case there is always a risk that the spectrograph setting is changed during the opening and shutting of the tank, while in the second the choice of elements for reference lines is rather limited and chemical effects might disturb the lines. Thus a new solution had to be attempted.

An X-ray tube was constructed according to Fig. 1. It has two filaments and two targets placed next to each other, thus constituting a type of twin tube. The filament current can be switched from one filament to the other, and the focal spot on one or the other target is put in its proper position by moving the X-ray tube perpendicularly to the direction of the X-ray beam in a manner described by SANDSTRÖM ([2], p. 132 and Fig. 3). The proper position can be determined with an accuracy better than 0.1 mm. Thus two different target materials can be placed in the tube at the same time, and the changing over from one to the other is easily effected without destroying the vacuum in the tank. The method has worked very well.

In connection with the construction of the new X-ray tube the voltage set was changed to give positive high tension instead of negative. This implies that the targets, now on the high voltage side, must be cooled in a special way. As before water is used for cooling, and outside the spectrometer tank several metres of plastic cooling

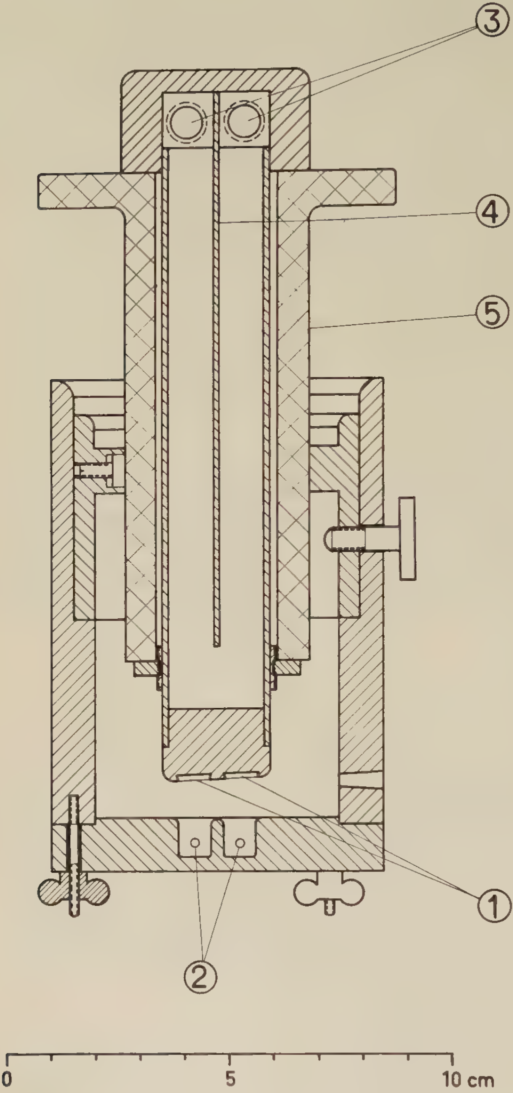

Fig. 1. The X-ray tube. *1* are two slits for the targets, *2* the cathodes, *3* the cooling tubes, *4* a brass wall for the circulation of the cooling-water, and *5* a porcelain cylinder.

tube are rolled on an insulated cylinder. In this way the current through the cooling-water amounts to only 4 mA at 20 kV. Since the X-ray tube is placed inside the tank, the cooling tube (which here is flexible copper tubing) must be prevented from touching the inside walls of the tank as the X-ray tube moves along its track. This was achieved by supplying the pipes with circular plexiglas collars (diameter 12 cm, thickness 2 cm) spaced 10 to 20 cm apart. In this way the cooling pipes are always kept at least 4 cm from the walls of the tank, no matter how they are bent.

The cathodes consist of coated platinum spirals, and as the filament current is consequently low (2–3 A) the natural cooling by radiation and conduction of the heat is sufficient.

For the registration of the X-rays an argon–alcohol filled Geiger counter was used (SANDSTRÖM [2] p. 131). For all measurements here described the crystal employed was quartz $10\bar{1}0$. The pressure in the spectrograph tank and the X-ray tube was usually below 2×10^{-5} mm during recordings. Both the tube voltage and emission were well stabilized (SANDSTRÖM [2] p. 131).

The Al $K\alpha_1\alpha_2$ lines

Former wavelength measurements of the Al $K\alpha_1\alpha_2$ lines have yielded results that differ from one another more than the accuracy of the measurements would indicate. For two reasons it was thus desirable to re-measure these lines. Firstly they have been and will probably also continue to be the most important ones for determining the metric value of the X-unit. A new value, based on the wavelength found in the present investigation, will be published elsewhere. Secondly the energy difference between the satellite lines $K\alpha_3$ and $K\alpha_4$, treated in the next paragraph, and their parent line α_1 was to be measured.

The wavelengths were measured for metal and oxide independently of each other. The earlier measurements were made for metal only or aimed directly at the wavelength difference between metal lines and oxide lines.

The respective target materials were spectroscopically standardized aluminium metal from Johnson, Matthey and Co. and aluminium coated with a 20 μ layer of Al_2O_3. As the depth of penetration for electrons is only 0.7 μ at the voltage used, this thickness is quite sufficient to ensure radiation from oxide only. In the case of metal it was soon found that greatest care is necessary in order to avoid a disturbing oxidation of the target surface. A "natural" oxide film is formed instantly on any aluminium surface exposed to air, and in the present case this could not be avoided (the only way would be to evaporate aluminium onto the target in a very high vacuum, but with the spectrograph used here this was impossible). The natural layer is, however, extremely thin, its thickness being around 0.01 μ. It is thus around 60 times less than the depth of penetration for the electrons, counted to the point where their energy equals the excitation potential of the $K\alpha$ lines. The results in this investigation are given with a reservation for the slight disturbance which may be caused by this thin natural oxide layer.

There are reasons to believe that the oxide layer reaches a depth several times greater than 0.01 μ under the influence of the focal spot in case the vacuum is not sufficiently good. As will be pointed out in the next paragraph the satellite lines $K\alpha_3$ and $K\alpha_4$ change their shapes and relative intensity in a very marked way when aluminium metal is changed into oxide. A strong wavelength displacement also occurs. For these reasons the lines form a very sensitive indicator of the presence of oxide. Repeated recordings of the metal lines at a pressure of 5×10^{-5} mm revealed that they changed their shape from one recording to the next in a manner indicating an increasing oxide layer on the target. At pressures below 10^{-5} mm no such effect could be traced, however, and it can be concluded that the vacuum is then sufficiently good to prevent any detectable oxidation.

In order to reach the best possible results it is thus necessary to start with the purest aluminium metal obtainable, to clean the target surface carefully immediately before closing the spectrograph tank and to maintain a vacuum better than 10^{-5} mm. Efficient cooling of the target is possibly also important. It is quite likely that the discrepancies in earlier measurements of the Al K spectrum are due to varying degrees of oxidation or to other impurities in the metal.

When the present measurements were made all the precautions mentioned above were taken. As reference lines the Ag $L\alpha_1$ and β_1 lines were chosen, the second target consisting of silver. As these lines had to be recorded in the second order while the aluminium lines were recorded in the first, corrections for refraction in the crystal were applied. The wavelengths were further corrected for anomalous dispersion. HAGLUND's [3] determinations were used for the wavelengths of the reference lines.

The Al $K\alpha_1$ and α_2 lines are not completely resolved in the spectrogram, but the shape of the compound line is such as to make a graphical resolution fairly reliable. It has to be assumed, however, that the lines are symmetrical.

The wavelengths represent mean values of five determinations in the case of metal and three determinations in the case of oxide. The errors represent greatest fluctuations from the mean value. The results together with some earlier measurements are listed in Table 1.

Table 1. The Al $K\alpha_1\alpha_2$ lines. Wavelength values in X.U.

Line and target		HAGLUND [4]	SIEGBAHN [5]	SHEARER [6]	CAUCHOIS [7]	Present results
α_2	metal	8324.62 ± 0.20	8324.59	8322.35 ± 0.25	8323.82 ± 0.20	8324.30 ± 0.20
	oxide					8322.76 ± 0.20
α_1	metal	8322.18 ± 0.20	8322.19	8319.88 ± 0.07	8321.37 ± 0.20	8321.96 ± 0.20
	oxide					8320.47 ± 0.20

The present results coincide within the limits of error with those of HAGLUND and SIEGBAHN, while the wavelengths obtained by CAUCHOIS are slightly shorter. SHEARER's results lie very close to the author's oxide measurements, but as the former got his aluminium radiation from impurities in a nickel target it is to be expected that the lines are strongly disturbed.

Table 1 shows that the oxide displacement amounts to 1.5 X.U. or in terms of Rydberg units 0.020 Ry. An earlier measurement by BÄCKLIN [8] gave the result 1.7 X.U.

The Al $K\alpha_3\alpha_4$ lines

The satellite lines in X-ray spectra are known to originate from transitions in atoms where two of the inner electrons are missing. Several theories of the mechanism of these transitions have been put forward. KENNARD and RAMBERG [9] treated the $K\alpha$ satellites in the case of sodium theoretically. They suggested the following hole transitions for the lines $K\alpha_3$, α_3' and α_4:

$$K\alpha_3 \quad 1s2p\ {}^3P \rightarrow (2p)^2\ {}^3P$$

$$K\alpha_3' \quad 1s2s\ {}^3S \rightarrow 2s2p\ {}^3P$$

$$K\alpha_4 \quad 1s2p\ {}^1P \rightarrow (2p)^2\ {}^1D$$

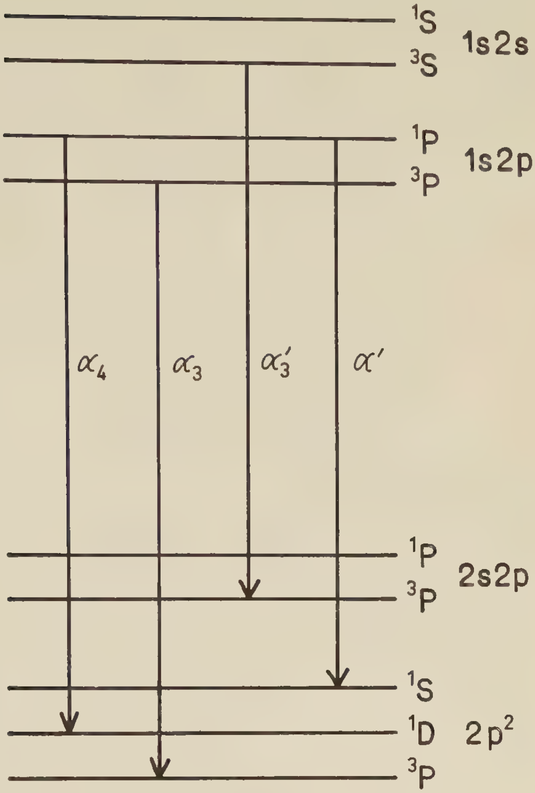

Fig. 2. Energy level diagram showing the transitions according to KENNARD and RAMBERG.

In Fig. 2 an energy level diagram is shown for these transitions.

CANDLIN [10] calculated the $K\alpha$ satellites for eleven elements between $Z=19$ and $Z=42$ and predicted several lines in the $\alpha_3\alpha_4$ group; of interest in connection with the present investigation are the lines α_3'', α_3, α_3' and α_4, the last one consisting of two components. CANDLIN's notations for the hole transitions are:

$$K\alpha_3'' \quad 1s_{1/2}2p_{3/2}(1) \rightarrow 2p^2{}_{3/2}(0)$$

$$K\alpha_3 \quad 1s_{1/2}2p_{3/2}(2) \rightarrow 2p^2{}_{3/2}(2)$$

$$K\alpha_3' \quad 1s_{1/2}2p_{3/2}(1) \rightarrow 2p^2{}_{3/2}(2)$$

$$K\alpha_4 \quad \begin{cases} 1s_{1/2}2p_{1/2}(0) \rightarrow 2p_{1/2}2p_{3/2}(1) \\ 1s_{1/2}2p_{1/2}(1) \rightarrow 2p_{1/2}2p_{3/2}(2) \end{cases}$$

Not all these lines have been observed as far down in the periodic system as $Z=13$; in the present investigation only α_3 and α_4 have been found. It seems quite likely, though, that at least α_3, which in metal is strongly asymmetrical, is complex. Extrapolation of CANDLIN's theoretical curves in Fig. 2 of his paper [10] would suggest that α_3 consists of four lines: α_3, α_3', α_3'' and one of the components of α_4 above (the transition $1s_{1/2}2p_{1/2}(0) \rightarrow 2p_{1/2}2p_{3/2}(1)$).

As to experimental work the papers by PARRAT [11] and SHAW and PARRAT [12] are the most important ones. They do not go further down than $Z=16$, however. In the case of aluminium wavelength measurements have been made by WETTERBLAD [13], FORD [14] and KUNZL [15], who all used photographic registration. In Table 2 their results are mentioned in connection with the present ones.

Table 2. The Al $K\alpha_3\alpha_4$ lines. Wavelength values in X.U.

Line and target		WETTERBLAD	FORD	KUNZL	Present results
α_3	metal	8265.8	8265.48	8270	8268.7 ± 0.4
	oxide				8265.1 ± 0.5
α_4	metal	8250.1	8253.75	8254	8256.8 ± 0.6
	oxide				8253.7 ± 0.5

When recording the satellite lines α_3 and α_4 the target materials were indentical with those used for the $\alpha_1\alpha_2$ lines. As to precautions against excessive oxidation of the metal, the same steps as before were taken. Here, too, the Ag $L\alpha_1$ and β_1 lines were chosen as reference lines. The author's wavelength values are mean values of five separate determinations, and as previously the errors indicate greatest fluctuations from the mean.

The wavelengths reported by WETTERBLAD and FORD lie close to the present oxide values, and it can safely be assumed that their targets consisted mainly of oxide instead of pure metal. KUNZL's α_3 value is higher than the present metal value, while his α_4 value coincides with the present oxide value. From the photometric curves in his paper [15] it appears that the α_3 and α_4 lines are hardly resolved at all, and his limits of error (not published) must be very wide. Furthermore he used an air-filled ion tube, and consequently all his measurements on aluminium should be referred to oxide rather than to metal.

The wavelength displacement in oxide as compared to metal was measured separately and was found to be 3.6 ± 0.2 X.U. for α_3 and 3.1 ± 0.2 X.U. for α_4, or in terms of Rydberg units 0.048 Ry and 0.041 Ry respectively. This is around twice the displacement of the parent line, which according to Table 1 is 1.5 X.U. or 0.020 Ry. Such an effect is to be expected according to the KENNARD-RAMBERG [9] theory, which is thus confirmed by the present results. An earlier measurement of the oxide displacement of α_3 and α_4 was made by CARLSSON [16]. He found 3.1 X.U. for α_3 and 2.6 X.U. for α_4.

The distance to the parent line α_1 was also measured, and the results are given in Table 3.

When studying the relative intensities of α_3 and α_4, a most interesting change in intensity and line shape in oxide as compared to metal was observed. This has already been briefly mentioned in a research note (NORDFORS [17]). Fig. 3 shows one of the five recordings of $\alpha_3\alpha_4$. The α_3 line in metal is strongly asymmetrical, and as pointed out before it is quite likely that it consists of two or more lines. A graphical resolution is, however, impossible as nothing is known about the components, not even their number. In the case of α_3 in oxide the asymmetry is slight though still present. The rise in intensity to the long wavelength side of α_3 is due to Ag $L\alpha_1$, as the second target gives a weak contribution even when it is not in its proper position.

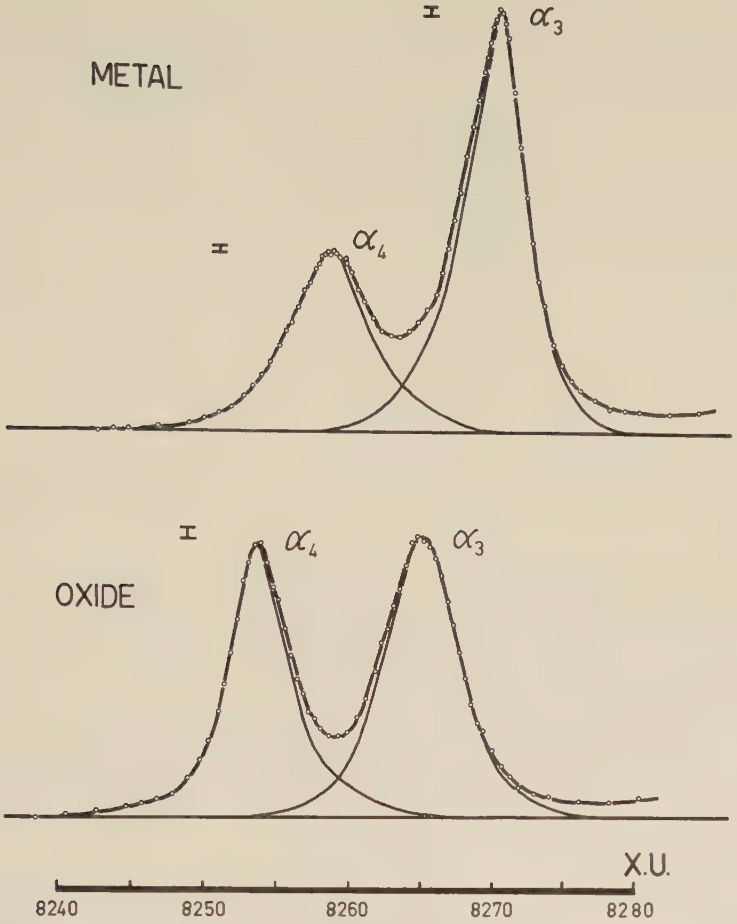

Fig. 3. The Al $K\alpha_3\alpha_4$ lines in metal and oxide. The vertical lines at the peaks indicate the statistical uncertainty.

Table 3. Wavelength- and energy-difference between $\alpha_3\alpha_4$ and their parent line α_1.

Target	α_1—α_3		α_1—α_4	
	$\Delta\lambda$ X.U.	$\Delta\frac{\nu}{R}$ Ry	$\Delta\lambda$ X.U.	$\Delta\frac{\nu}{R}$ Ry
Metal	53.2	0.707	65.1	0.862
Oxide	55.4	0.735	66.8	0.888

According to PARRAT [18] the intensity of a satellite line relative to its parent line is a function of tube voltage. When the recordings of Int. $\alpha_3\alpha_4$/Int. $\alpha_1\alpha_2$ were made, the tube voltage was hence kept constant at 2.25 kV in order to make comparisons between metal and oxide possible. The excitation potential for $K\alpha_1\alpha_2$ is 1.55 kV and for the satellites due to *KL*-ionization 1.62 kV ($K_z + L_{z+1} = 1.55$ keV + 0.07 keV = 1.62 keV). Thus the voltage used was safely above the excitation potential. When recording Int. α_4/Int. α_3, which was done separately and at higher voltages for the sake of intensity, the tube voltage ranged for the five recordings from 4.0 kV to 7.2 kV. This did not influence the relative intensity α_4/α_3, and it can be concluded that for these lines the intensity varies according to one and the same function of voltage (at least within the voltage limits given above; no experiments were made with extremely high or low voltages).

Table 4. Relative intensities of Al $K\alpha_3$ and α_4.

Target	Area values			Peak values		
	$\alpha_3/\alpha_{1,2}$	$\alpha_4/\alpha_{1,2}$	α_4/α_3	$\alpha_3/\alpha_{1,2}$	$\alpha_4/\alpha_{1,2}$	α_4/α_3
Metal	0.052	0.028	0.54	0.044	0.019	0.44
Oxide	0.045	0.037	0.82	0.038	0.037	0.98

The results of the intensity measurements are given in Table 4. In this wavelength region the natural width of the lines is such as to make broadening effects negligible. Other factors that may influence the values of the relative intensities, such as X-ray absorption in the target and reflection properties of the crystal, are also unimportant because of the short distances between the lines measured.

The intensities have been measured relative to the compound line $\alpha_1\alpha_2$, since the graphical resolution of the doublet gives very uncertain results as to the intensity ratio of the components. According to the classical theory this should be 1:2, but CAUCHOIS [7] has experimentally found signs that it may be lower, so this assumption could not safely be made.

The area values were measured with a planimeter.

As is seen from Table 4 the peak ratio α_4/α_3 varies much more than the area ratio. This is due to an inverse change in line width (listed in Table 5).

Table 5. Line width of Al $K\alpha_3$ and α_4.

	Metal		Oxide	
	α_3	α_4	α_3	α_4
Width at half maximum (in X.U.)	5.3	6.9	6.2	4.9

Relative to the parent line the intensity of α_3 decreases and that of α_4 increases in oxide as compared to metal. The explanation of this intensity change is not clear. There seems to be no reason to assume that the transition probability for the two neighbouring lines should change in opposite directions when the metal is changed into oxide (the valence electrons are one 3*p* and two 3*s*). If we assume, however, that α_3 is composed of two or more lines, another explanation is possible. If one (or more) of the components of α_3 is so strongly shifted towards shorter wavelengths as to form

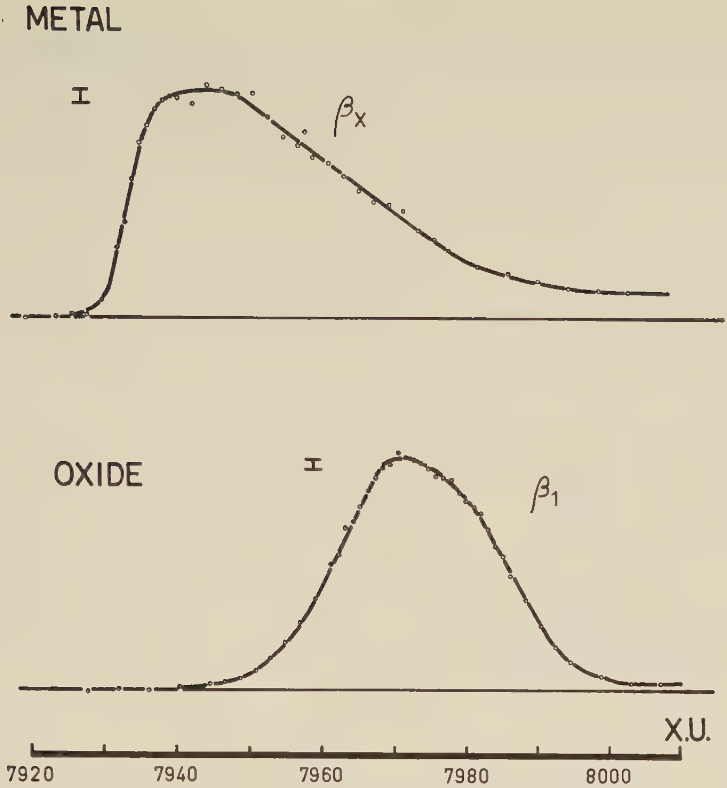

Fig. 4. The Al $K\beta$ line in metal and oxide.

a component of α_4 instead, the intensity effect found in this investigation would appear. There is one sign pointing in this direction. According to the KENNARD-RAMBERG theory [9] the oxide shift of α_4 ought to be as great as that of α_3. In the present case the shift found for α_4 is definitely less than that for α_3, a result also obtained by CARLSSON [16]. This may possibly be due to a component added to the long wavelength side of α_4. Against this suggestion, however, speaks the fact that the width of α_4 is smaller in oxide than in metal. Thus a fully convincing explanation cannot be found at present.

The Al $K\beta$ line

Finally the β line was recorded in metal and oxide under the same conditions as mentioned before. The two curves are reproduced in Fig. 4, each curve representing the sum of two different recordings. The common nomenclature is used: the metal line is designated β_x and the oxide line β_1.

In Fig. 4 it is interesting to notice that the intensity background is higher on the long wavelength side of the lines than on the short wavelength side (most clearly seen in the case of metal). This is due to the K-absorption in the target.

The present results are listed in Table 6 together with some earlier measurements. The wavelength of the β_x edge is measured at the point of inflection.

Table 6. The Al $K\beta$ line. Wavelength values in X.U.

Line	KARLSSON and SIEGBAHN [19]	KUNZL [15]	FARINEAU [20]	Present results
β_x maximum				7944
β_x edge	7935.4	7940	7937	7932.6
β_1 maximum				7972

Photometric curves have been published by KUNZL, DAS GUPTA [21] and FARINEAU. The first-named has such a low resolution that the shape of the β line cannot be studied, while the second has not given any wavelength values. His curves for β_x and β_1 are strikingly alike in shape and both coincide with the shape of the present oxide line. There remains the curve of the β_x line published by FARINEAU. He has found a second maximum (almost resolved) on the long wavelength side of β_x at a distance of circa 23 X.U. from the main maximum. The present investigation gives a distance of 28 X.U. between maxima of β_x and β_1, and it is thus not impossible that the structure found by FARINEAU is due to oxidation of the target.

ACKNOWLEDGEMENTS

The work with the bent crystal vacuum spectrograph is being sponsored by the Swedish Natural Science Research Council, whom the author wishes to thank for making it possible for him to continue his postgraduate studies.

Further his thanks are due to the head of the Department of Physics, Professor PER OHLIN, who supervises the author's work.

His introduction to the subject of X-ray spectroscopy the author owes to Laborator ARNE ELD SANDSTRÖM, whose constant encouragement and expert advice have been vital to the success of the investigation.

Grateful acknowledgements are also due to Fil. Kand. GÖRAN WASSBERG and Fil. Stud. HANS BJÖRKEGREN, who assisted in recording the curves.

Department of Physics, University of Uppsala, Sweden, August 1955.

REFERENCES

1. A. E. SANDSTRÖM, Arkiv f. Fysik *4*, 517 (1952).
2. —— Arkiv f. Fysik *8*, 129 (1954).
3. PH. HAGLUND, Arkiv f. Mat., Astr. o. Fysik *28 A*, No. 8 (1941).
4. —— Zs. f. Phys. *94*, 369 (1935).
5. M. SIEGBAHN, the values published in [4].
6. J. SHEARER, Phil. Mag. *21*, 501 (1936).
7. Y. CAUCHOIS, C. R. *221*, 25 (1945).

8. E. BÄCKLIN, Zs. f. Phys. *33*, 547 (1925).
9. E. H. KENNARD and E. RAMBERG, Phys. Rev. *46*, 1040 (1934).
10. D. J. CANDLIN, Proc. Phys. Soc. *A 68*, 322 (1955).
11. L. G. PARRAT, Phys. Rev. *50*, 1 (1936).
12. C. H. SHAW and L. G. PARRAT, Phys. Rev. *50*, 1006 (1936).
13. T. WETTERBLAD, Zs. f. Phys. *42*, 611 (1927).
14. O. R. FORD, Phys. Rev. *41*, 577 (1932).
15. V. KUNZL, Zs. f. Phys. *99*, 481 (1936).
16. E. CARLSSON, Zs. f. Phys. *76*, 471 (1932).
17. B. NORDFORS, Proc. Phys. Soc. *A 68*, 654 (1955).
18. L. G. PARRAT, Phys. Rev. *49*, 132 and 502 (1936).
19. H. KARLSSON and M. SIEGBAHN, Zs. f. Phys. *88*, 76 (1934).
20. J. FARINEAU, Ann. de Physique *10*, 20 (1938).
21. K. DAS GUPTA, Ind. Journ. of Physics *20*, 226 (1946).

Tryckt den 4 januari 1956

Uppsala 1956. Almqvist & Wiksells Boktryckeri AB

ARKIV FÖR FYSIK Band 10 nr 22

Communicated 14 September 1955 by MANNE SIEGBAHN and BENGT EDLÉN

Extension of the analysis of the third spectrum of iron, Fe III

By SVEN GLAD

With 2 plates and 3 figures in the text

Summary

The Fe III spectrum has been studied in the region 8600–2600 Å by using a condensed hollow cathode discharge. This produces the Fe III spectrum with good intensity and at the same time it is possible to separate the Fe III lines from those of Fe I and Fe II by studying the shape of the lines. A comparison with the vacuum spark shows that the strongest Fe IV lines in the visible region appear only as very faint traces in the hollow cathode. About 2000 lines, experimentally classified as Fe III, have been measured between 8600 and 2600 Å. Analysis of the new data has led to the classification of terms arising from the configurations $3d^5\,5s$, $3d^5\,6s$, $3d^5\,4d$, $3d^5\,5d$, and $3d^5\,5p$. In connection with this analysis about 100 of the hazy lines observed by EDLÉN and SWINGS in the vacuum ultraviolet around 1400–1600 Å and due to $3d^5\,4p - 3d^5\,5s$ and $3d^5\,4p - 3d^5\,4d$ have been classified. In the (^6S) system terms attributable to the configurations $3d^5\,7s$, $3d^5\,6p$, $3d^5\,6d$, $3d^5\,5f$, $3d^5\,6g$ and $3d^5\,6h$ have been found. From the last three members of the series $3d^5\,(^6S)\,ns\,^7S$ $(n = 5, 6, 7)$ an ionization potential of 247 221 cm^{-1} or 30.643 volts has been calculated. The tables contain about 200 new levels and approximately 800 newly-classified lines.

Introduction

Using a vacuum spark and a spark in nitrogen EDLÉN and SWINGS (1942) made an exhaustive investigation of the Fe III spectrum. Their analysis, which gave practically all terms of the configurations $3d^6$, $3d^5\,4s$, and $3d^5\,4p$ as well as several of the higher terms built on $3d^5\,(^6S)$, was mainly concentrated to the vacuum region and the ultraviolet. The spectrograms in the visible region were obtained with a Hilger E1 quartz-prism spectrograph and a small glass-prism spectrograph. Owing to low dispersion and overlapping of lines the measurements in this region were rather uncertain. As the spectrum of Fe III in the visible range is of considerable astrophysical interest it was desirable to reobserve this part of the spectrum at high dispersion.

Experimental procedure

A vacuum spark was at first used as a light source. The sparks were produced by the discharge of a 0.2 μF condenser through a spark gap of 0.5–1 mm. The voltage applied was 45000–80000 volts. Various amounts of inductance in the circuit were

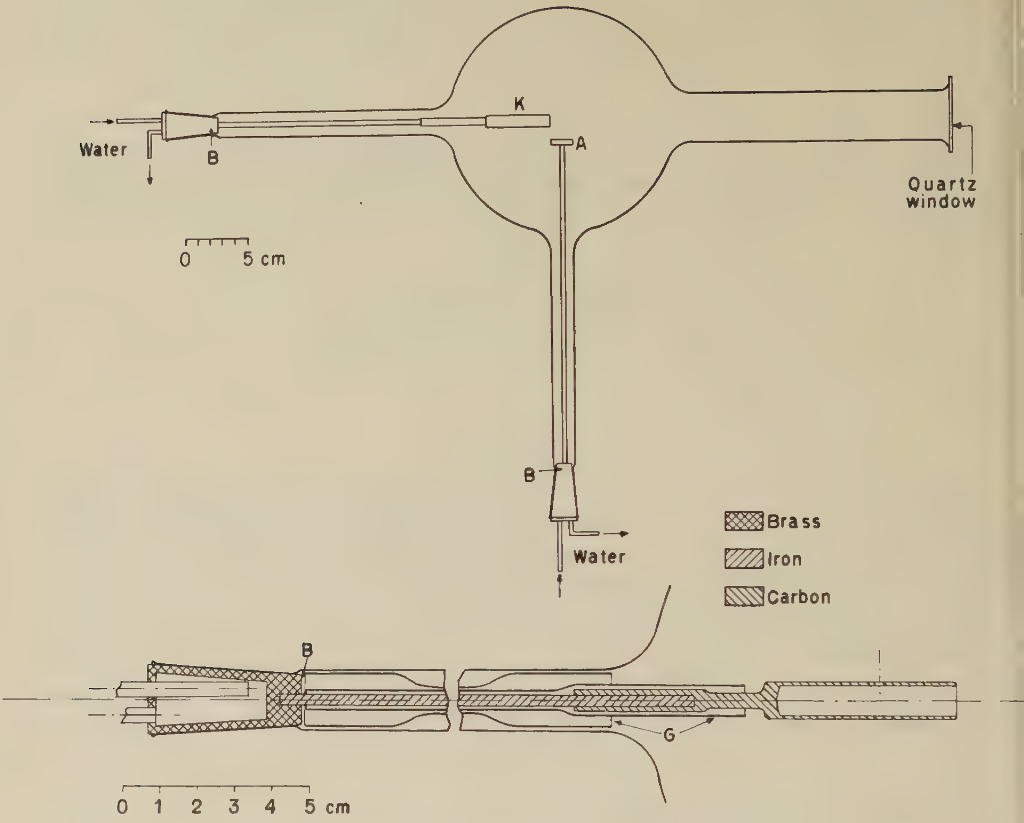

Fig. 1. The discharge tube. *A*, anode; *K*, hollow cathode; *G*, glass tubes to prevent sparking to the ground joints *B*.

used in order to separate lines of various stages of ionization. The effect of increasing the inductance is, however, partly counteracted by an increase of the break-down voltage. By using a Marx impulse generator to ignite the spark, it was possible to hold the break-down voltage more constant, but in spite of this the separation of Fe III from the neighbouring ionization stages was rather uncertain. Moreover, many lines are too hazy in the vacuum spark to be measured with any accuracy. It was therefore desirable to get a light source giving sharper lines than the vacuum spark and at the same time permitting an experimental separation of Fe III from Fe I, Fe II, and Fe IV. For this purpose various modifications of the hollow cathode discharge have been tried. Normal continuous discharge with helium gas gives the arc and first spark spectra and usually no more. Using a condensed discharge, however, Paschen (1923) succeeded in exciting Al III in a hollow cathode. He used an induction coil to charge a condenser of 12 000 cm, connected to the discharge tube through a spark gap. By using a capacity about 1000 times larger in the present experiments this form of discharge gave a Fe III spectrum with good intensity. A similar arrangement has been used by Gartlein and Gibbs (1931) for the production of the second spark spectra of Ge and Cu, and by KOPFERMANN and WITTKE (1937, 1940) for an investigation of the hyperfine structure in scandium III.

The light source is shown in Fig. 1. It consists of a large pyrex bulb with two tubes for the electrodes and two tubes for the circulation of the gas (the latter ones are not drawn in the figure). A is the anode; K is the hollow cathode consisting of a graphite tube fitted with an inner thin-walled iron cylinder. Both electrodes are supported by iron rods covered with glass tubes (G) to prevent sparking to the ground joints (B). It was impossible to make the cathode entirely of iron because the temperature in the hollow cathode was so high that the iron cylinder softened. The electrodes were connected to a 10 μF condenser through a rotating spark gap giving 20–30 sparks per second. The condenser was charged by a full-wave rectifier to 800–1800 V.

A striking distinction between the Fe III lines and those of Fe I and Fe II was obtained if a hole was bored in the side of the hollow cathode tube. The size and the form of the hole were not critical, but usually a 3 mm hole was bored as shown in Fig. 1. During every spark across the external spark gap the charge of the condenser passed through the light source giving rise to an oscillatory discharge which at a helium pressure of 6–12 mm Hg was concentrated inside the hollow cathode. A luminous layer appeared along the walls of the cathode, while the inner space of the cylinder was traversed by a very great number of small sparks. It appeared that these sparks gave almost exclusively the spectrum of doubly-ionized iron, while the neutral and singly-ionized iron was confined to the luminous layer along the walls. The light source was focused end-on on the slit of a stigmatic spectrograph. The intensity distribution along a diameter of the cathode tube was then reproduced in each spectral line. Thus, the Fe III lines have nearly the same intensity from end to end, while the Fe I and Fe II lines are much stronger at their ends and often disappear in the central part. These different shapes are clearly seen on Plate II. Spectrogram a was taken with a vacuum spark while b was obtained with the condensed hollow cathode discharge. In this region two different types of transitions appear, namely $4f-5g$ and $4s-4p$. In the short-wave part of the upper spectrogram (a) the transitions $4f-5g$ are very diffuse and form an almost continuous spectrum which is resolved into a large number of lines in the hollow cathode discharge. The transition $4s-4p$ on the other hand gives rise to a multiplet ($a\ {}^5P-4p\ {}^5P$) of sharp lines in either case.

Plate IIe and f shows a part of the spectrum where the vacuum spark contains a number of strong lines which are missing or appearing as faint traces on plates taken with the hollow cathode tube. This group of lines is probably due to the transitions $5f-6g$ and $5g-6h$ in Fe IV which should fall in this range.

The spectrograms also contain carbon lines which have the same shape as the Fe III lines. In order to be able to pick out with certainty all carbon lines a pure carbon spectrum was photographed with the same spectrographs and the same light source using a pure graphite cylinder as the cathode. The result of this investigation has been published in an earlier paper (GLAD 1953). Ti and V lines which were recorded when the cathode consisted of only a graphite tube disappeared when the iron cylinder was placed in the graphite tube. The cylinders were usually made of pure iron from Johnson, Matthey & Co., Ltd, but a set of spectrograms was also taken with tubes of commercial iron. In this case the plates also contained the strongest lines of the following elements: Si, Mg, Ca, Ba, P, S, Cl and Mn. All these foreign lines had the same shape as Fe I and Fe II. With the exception of the Ca lines they all disappeared when a cylinder of pure iron was used. If any Fe III-like lines were due to impurities they might be expected to show a change in relative intensity with the two kinds of iron. As no such effect has been observed it is thought that all the lines given in Table 1 are due to Fe III.

The first observations were made with a large glass-prism spectrograph having a dispersion of 7.7 Å/mm at 6800 Å and 1.0 Å/mm at 4100 Å. This spectrograph has been described in detail by MINNHAGEN (1944). Later on the region 8600–2600 Å was photographed with a 15000 lines per in., 21-foot grating in a Wadsworth mounting (Jarrell-Ash) giving a dispersion of about 5 Å/mm in the first order. Eastman spectroscopic plates of different types have been used.

The reduction of the measurements in the region 6000–2600 Å was made with the vacuum-arc values of BURNS and WALTERS (1929, 1931) as standards. Since the filling gas contained 0.1 % neon, the strongest Ne I lines were recorded on the spectrograms. By admitting a small amount of argon into the system, some plates were also supplied with an argon spectrum. In the long-wavelength range Ne I and A I lines were used as standards. The wavelengths were taken from BURNS, ADAMS and LONGWELL (1950) for neon and from MEGGERS and HUMPHREYS (1934) for argon.

The wavelengths

The Fe III spectrum was photographed from 8600–2600 Å, but the investigation has been concentrated to the region above 3000 Å where the superiority of the new spectrograms is most pronounced. At the same time this region is the most interesting from the astrophysical point of view. The wavelength material is collected in Tables 1–4. Table 1 gives wavelength and intensity of all lines in the region 8600–3000 Å which have been classified experimentally as Fe III. The lines above 3000 Å for which the term combination has been identified are collected in Table 2. For the sake of completeness the previously identified lines in this region are also included. Table 3 covers the region 3000–1966 Å and contains all the newly-classified lines in this region and also some previously identified lines which have been included because they have been used in the present calculation of improved term values. Table 4 gives the classified lines of the group of hazy lines at 1600–1400 Å observed by EDLÉN and SWINGS.

The wavelengths in the astronomical region were published some time ago in the form of a mimeographed table covering the region 8600–3000 Å and containing all measured Fe III lines with an intensity figure of 1 or more (on a scale from 0 to 20). This list is now given in Table 1. Some lines measured on only one plate were omitted from the mimeographed table, but in so far as their reality has now been established by level combinations they are included in Table 1, which contains about 1700 lines. The wavelengths for three lines, $\lambda\lambda$ 3955.150, 3300.196, and 3212.181, have been slightly changed as compared with the preliminary list.

The intensity and character of the lines are indicated by numbers and letters in the column marked I. The meaning of the symbols is explained at the beginning of the table. In the preliminary list the symbol h was used for all lines which are not sharp, but in Table 1 the classification of the lines with regard to their appearance has been refined by introducing the symbol (h) for those lines that are only slightly hazy. Some lines marked h are probably unresolved blends of two or more lines.

The wavelengths are, as a rule, weighted means of measurements on two or more spectrograms. For wavelengths given with three decimal places the error is estimated to be definitely less than 0.02 Å. For other wavelengths the error may range from

Table 1.

Wavelengths of Fe III lines in the region 8600–3000 Å.

Notation for indicating the appearance of the lines:

(h) = slightly hazy
h = hazy
l = slightly shaded to longer waves
s = slightly shaded to shorter waves
w = wide

h l = hazy, shaded to longer waves
h s = hazy, shaded to shorter waves
w h = wide and hazy
v w h = very wide and hazy

An intensity figure in parenthesis means that the line is blended, the intensity being only partially due to Fe III.

A brace connecting two intensity figures means that the separation of the lines is uncertain.

An asterisk after the wavelength indicates that the term combination responsible for the line has been identified. The identifications are to be found in Table 2.

I	λ	I	λ	I	λ	I	λ
1	8 603.07	1	7 619.67	1 w h	6 478.16	4	6 353.40
1	8 593.31	1	7 603.70	2	6 476.60	(1) h	6 351.67
2	8 568.42*	2 h	7 322.88*	1	6 474.50	2 (h)	6 345.19*
5	8 563.49*	6 h	7 320.14*	1	6 473.48	1 w h	6 343.89
2 w h	8 554.48	1 h	7 319.56*	1	6 466.32	2 (h)	6 341.71
1	8 542.57	5 h	7 317.63*	2 h	6 463.67	(3) h	6 340.33
1	8 515.29*	4	7 265.14*	2 h	6 463.37	1	6 339.55
2	8 512.72*	3	7 007.62	(1)	6 462.05	2	6 319.16
3	8 509.06*	1 w	7 006.49	2	6 461.40	1	6 318.47
1 w h	8 505.95	3	6 892.07	2	6 460.60	1 h	6 311.60
2	8 481.38*	1	6 789.91	1 h	6 459.63	1 h	6 311.14
2	8 479.71*	1 w h	6 769.30	1 h	6 459.19	1 h	6 308.50
1	8 477.13*	1	6 767.61	2	6 456.98	1 (h)	6 307.74
1	8 416.50*	1 w h	6 764.04	2	6 454.27	1 h	6 306.56
1	8 359.22*	(1) h	6 751.84	1	6 451.72	6	6 294.50
(2) h	8 282.47	1 h	6 747.92	1	6 450.06	3	6 294.33
2	8 261.85	1	6 737.66	1 h	6 447.39	1 h	6 289.94
3	8 259.91	(1)	6 730.80	(2) h	6 440.54	1 (h)	6 288.35*
6 w h	8 238.98	(1)	6 726.32	1	6 430.31	1 (h)	6 287.49
2 h	8 237.52	1	6 652.25	1 w h	6 429.69	4	6 285.38
8 w h	8 236.75*	1	6 529.36	2	6 427.37	1 (h)	6 283.75*
(9) w h	8 235.45*	1 h	6 527.98	1 h	6 426.82	2 w h	6 283.02
3 w h	8 234.94	1	6 524.29	(1) h	6 420.27	2	6 281.20*
1 w h	8 233.02	3	6 522.98	(3)	6 417.95	1 h	6 277.19
5 w h	8 231.79	1 h	6 521.85	2 w h	6 415.12	1 h	6 275.59
5 w h	8 230.88	1 h	6 520.95	(1) h	6 413.75	2 h	6 275.32
1 w h	8 227.33	(2) h	6 519.85	1 h	6 412.46	2	6 273.68
2 h	8 224.18	1 h	6 513.94	2	6 409.38	1 h	6 267.38
1	8 123.68	1	6 509.25	1	6 406.81	2 h	6 264.38
1	8 119.79	2	6 507.35	1 (h)	6 404.52	2	6 263.89
1 w h	8 018.51	1 h	6 504.63	1 (h)	6 396.17	5	6 259.81
3 w h	8 017.92*	(1) h	6 503.48	2	6 381.09	1	6 257.68
3 w h	8 014.69*	2	6 499.84	(2) h	6 372.57	2 h	6 256.63
1 w h	8 012.57	1	6 499.28	1	6 370.47	1 h	6 253.78
2 w h	8 011.22*	(1) h	6 486.05*	1	6 370.02	(3) h	6 250.76
2 w h	8 007.88*	2	6 485.25	(1) h	6 369.37	3	6 244.85
5 v w h	7 921.17*	1 h	6 484.06	3	6 368.40	2 h l	6 236.75
1 h	7 914.93	3	6 479.83	5	6 357.81	1 h s	6 235.34

(Table 1, cont.)

I	λ	I	λ	I	λ	I	λ
(1) h	6 233.87	2	6 123.30	1 h	6 040.50	9	5 968.48
1 (h)	6 228.29	3	6 122.04	2 h	6 040.21	2	5 968.04
1 w (h)	6 227.49*	2	6 121.45	3	6 039.08*	2	5 967.48
(1)(h)	6 225.58*	(3)	6 121.00	2	6 037.80	3	5 964.76
1 hs	6 222.38	5	6 117.47*	13	6 036.56*	1	5 963.33*
3 h	6 220.30	3	6 113.42	4	6 035.53*	4	5 962.46*
3	6 219.22	2	6 110.17	3	6 033.89	1	5 961.06
2 h	6 215.65	5	6 109.78	3	6 033.62	3	5 959.46*
1	6 211.28	5	6 109.13	16	6 032.59*	1	5 958.56
4	6 208.37*	5	6 106.37	5	6 031.97	5	5 957.36
1	6 206.09*	1 hl	6 104.79	9	6 031.02*	6	5 956.81*
5 s	6 203.04*	2 l	6 101.26	(7)	6 030.00	1 (h)	5 956.17
4 w	6 201.92	3	6 097.40*	7	6 028.87*	7	5 955.41
6	6 201.37*	2	6 095.74	2	6 027.52	2	5 954.86
6	6 195.43	6	6 092.16*	3	6 024.82	14	5 953.62*
7	6 194.79*	5	6 089.08	1	6 022.85*	10	5 952.31*
2	6 194.56*	4	6 087.45	2 hs	6 022.14	3	5 951.50*
1	6 189.91	1	6 084.91	3	6 021.51	4	5 950.51*
7	6 186.56	2	6 084.23*	6 l	6 020.78*	2 w	5 949.26*
1	6 186.06*	2 wh	6 083.07	4	6 020.44	1 (h)	5 947.70
9	6 185.26*	3	6 082.04*	3	6 019.50	1 h	5 946.99
2	6 184.52	1 (h)	6 080.85	1 wh	6 017.44	5	5 946.65*
(1)	6 183.92	2	6 079.56	2	6 015.87	2 hs	5 945.86
5	6 181.70*	6	6 077.78*	8	6 015.29*	8	5 944.28
2	6 177.52	2 h	6 075.67	6	6 014.48*	3 (h)	5 941.63
3	6 176.20	3	6 075.04	2	6 013.64*	8 s	5 940.10*
3	6 174.11	2	6 073.40	1	6 011.68	7	5 938.90*
(3)	6 172.74	3	6 073.06	1 h	6 010.40	3 l	5 937.36
1	6 171.36	1	6 072.44	2 w	6 009.88	1 h	5 935.53
3	6 170.79	4	6 070.41	3	6 007.80*	2	5 933.01*
9	6 169.74*	1	6 069.27	3	6 007.49	1	5 931.71
1 wh	6 166.57	3	6 068.78	2	6 007.11	18	5 929.69*
7	6 165.68	2 (h)	6 067.81	2 h	6 006.24	2	5 929.28
5	6 165.46*	5	6 066.76	1	6 005.35	2	5 928.79
1	6 161.41	2 hl	6 062.95	2	6 004.64*	(3)	5 927.77
1	6 160.45	2 hs	6 062.25	6	6 000.10*	2	5 927.06
2	6 158.79*	4	6 059.01*	18	5 999.54*	3	5 925.09
5	6 157.37	6	6 058.46*	2	5 997.96	5	5 924.68
4	6 154.36*	2	6 057.64*	1 hs	5 996.64	4	5 924.07
4	6 152.04	8	6 057.13*	3	5 995.81*	(1)	5 922.23
(3)	6 151.30	9	6 056.36*	5	5 994.59*	1	5 921.99
9	6 149.99*	(2) h	6 055.90	3	5 993.97	5 l	5 920.99*
1	6 149.01	4	6 054.77*	1 h	5 990.19	7	5 920.39*
2	6 147.10	11	6 054.18*	12 h	5 989.08*	10	5 920.13*
1 h	6 146.56	3 (h)	6 052.99	1	5 986.37	7	5 919.90*
2	6 142.10	3	6 050.58	4	5 985.35	9	5 918.96*
2	6 141.91	11	6 048.72*	(3)	5 984.82*	7	5 918.06*
3	6 141.09	6	6 048.34*	7 h	5 984.54*	1 (h)	5 917.04
2 h	6 140.44	7	6 047.91*	9 h	5 981.01*	3	5 916.29
4 s	6 139.68	7	6 047.73*	12	5 979.32*	2	5 915.47*
1 (h)	6 135.50	2 h	6 045.17	6 h	5 978.48*	3	5 915.11
3 l	6 134.40	3	6 044.48	(5) h	5 976.78*	2 (h)	5 911.74
1	6 132.93	3	6 044.17*	2 (h)	5 973.43	7	5 910.52
4	6 132.40	7	6 042.94*	5	5 971.30	1 (h)	5 908.68
1	6 127.45			3 l	5 969.54	(5)(h)	5 907.25*

(Table 1, cont.)

I	λ	I	λ	I	λ	I	λ
2	5 905.36	7	5 817.43*	(4)	5 686.44	1 h	5 552.93
3	5 904.16	5	5 816.96*	1	5 685.17*	2 s	5 539.76
4	5 901.74*	2	5 815.75	1	5 684.47*	(5) w (h)	5 536.53
7	5 901.33*	5	5 813.31*	5	5 683.57*	1 l	5 534.10
7	5 900.70*	6	5 812.19*	4	5 681.88*	3	5 530.77
(3)	5 899.11	1	5 810.32	4	5 678.36*	1	5 527.65
9	5 898.68*	1	5 809.71	2	5 677.03	1 (h)	5 525.16*
3	5 895.69	5	5 805.16*	7	5 675.75	4	5 524.46
2	5 893.64	3	5 803.40*	3	5 672.88*	2	5 521.69*
(15)	5 891.91*	6	5 799.92*	4	5 672.14*	1 w	5 519.48*
(5)	5 889.77*	8	5 795.87*	3	5 671.24*	2 s	5 517.25
1 h	5 887.55	2	5 793.42	1	5 666.78	5	5 515.62
3 (h)	5 886.87	8	5 788.79*	2	5 666.21	1 (h)	5 514.05
5	5 886.66*	4	5 787.76*	3	5 665.26*	1	5 509.97
3 (h)	5 885.85*	5 w	5 786.43	4	5 661.40*	(5)	5 505.29
3 (h)	5 885.65*	3	5 785.67*	2	5 655.81	(4) (h)	5 502.84
1	5 883.36*	4	5 774.07*	1 (h)	5 655.18	3	5 491.24
9	5 876.26*	5	5 773.29*	2	5 654.33	1	5 490.12*
2	5 867.06	1	5 772.87	(6)	5 651.48	1	5 489.73*
4	5 864.08*	4	5 770.78	(4) (h)	5 649.09	4	5 485.74
2	5 863.70	2	5 770.56	1	5 635.51*	6	5 485.53*
1 h	5 863.07	(4)	5 768.39*	1 (h)	5 634.88	3	5 479.28
(1) h	5 862.11	(1) (h)	5 767.01	1	5 632.44	(1)	5 478.52*
6	5 860.95*	10	5 756.38*	1	5 631.32*	3	5 475.00
2	5 860.76*	(4) w	5 755.63*	2	5 630.40	(4) (h)	5 473.49
1 h	5 858.68	1	5 754.58*	1 h	5 630.09	1 h s	5 471.53
4	5 857.65*	2	5 753.65	2	5 628.25	2	5 470.70
2	5 857.26	3 (h)	5 751.63	6	5 626.55	2 h l	5 469.31
10	5 854.62*	4	5 749.81*	(2) h	5 623.57	2	5 465.01
6	5 853.48*	9	5 744.19*	2 (h)	5 621.40	(7)	5 460.81*
3	5 852.09*	3 l	5 743.08	1	5 620.52	1	5 459.92
3	5 851.46*	3 w	5 742.29*	4	5 619.09	1	5 454.06
2	5 850.29*	8	5 741.47	4	5 617.98	3	5 453.66
9	5 848.76*	6	5 740.42	7	5 617.35	5 l	5 452.95
1 h	5 846.03	4	5 734.84*	4	5 616.10	1	5 450.64
3	5 845.07	8	5 733.41*	5 w	5 613.59	2	5 448.91
(5)	5 843.33	(3)	5 731.81*	2	5 612.38	1 w h	5 448.45
2	5 843.15*	(3)	5 730.09	4	5 612.11	2	5 447.96
4	5 840.86	2 l	5 728.42	3	5 609.21	2	5 447.21
7	5 838.04*	6	5 722.46*	1	5 608.37	(3) (h)	5 444.48
(1) h	5 836.56	3	5 722.02*	1 (h)	5 607.58	1 (h)	5 441.91*
1	5 835.91	2	5 721.66	1	5 597.69	3	5 437.57
7	5 835.09	11	5 719.88	2 l	5 595.60	3	5 437.28
18	5 833.93*	5	5 713.97*	1 w h	5 592.68	1	5 433.96
1	5 832.41	7	5 712.92*	(2)	5 586.49	1	5 433.63
2 (h)	5 831.70	7	5 705.15*	2	5 585.66	(1)	5 431.52
5	5 831.24	5	5 701.06*	2	5 584.77	1	5 426.64*
6	5 830.61*	1	5 699.59	2 w	5 583.42	2 h	5 424.76
7	5 829.02	(4)	5 695.68*	6	5 575.05	1	5 422.59
1 (h)	5 827.33	3	5 693.52	8	5 573.47*	1	5 420.55
(3) (h)	5 826.38	4	5 692.43*	(2) (h)	5 572.64	2 s	5 420.00*
1	5 824.52	2	5 691.82	3	5 569.09	1	5 418.60
3	5 822.88*	1 (h)	5 688.59	4	5 562.42	(2)	5 415.61*
7	5 821.38*	3	5 687.88	3	5 556.15	4	5 413.75
8	5 818.49*	3	5 686.87*	1 w h	5 553.68	2	5 412.62

(Table 1, cont.)

I	λ	I	λ	I	λ	I	λ
1 h l	5 410.18	1 s	5 317.72	5	5 225.64*	2	5 092.368*
1	5 406.32	4	5 311.783	(7)	5 222.42*	2 (h)	5 090.57*
(3)	5 402.06*	9	5 310.877*	2	5 222.000*	2	5 088.93*
1 (h)	5 399.80	7	5 309.923*	2 (h)	5 221.45*	7	5 086.718*
1	5 394.89	2	5 309.41	5	5 219.124*	3 (h)	5 083.67*
1	5 392.59*	2	5 308.71	8	5 218.12*	(8)	5 078.92*
1 h s	5 390.86	4	5 307.194	(2)	5 217.33	6	5 077.671*
1	5 388.40*	10	5 306.758*	1 l	5 213.24	7	5 073.896*
1	5 384.55	2 (h)	5 304.42	1 (h)	5 212.09	4	5 069.158*
4	5 382.36*	6	5 303.722*	2 (h)	5 211.84*	3	5 066.539*
2	5 381.70*	14 w	5 302.599*	(4) s	5 210.46*	3	5 065.931
5	5 381.22*	1	5 301.68	1	5 207.94	6	5 063.459*
2	5 381.00*	12	5 299.926*	1 h	5 206.86	2	5 054.786*
4	5 380.44*	11	5 298.115*	(3)(h)	5 205.73	4	5 054.230*
6	5 379.13*	1	5 297.60	3	5 205.35	1	5 046.70
6	5 378.21*	4	5 296.360	(10)	5 199.08	(5)	5 040.81
3	5 376.44	2	5 295.03*	2	5 198.376	3	5 033.390
11 l	5 375.47*	1 h	5 293.66	8	5 194.07*	1 h s	5 026.32
1	5 374.33	2	5 290.73	5	5 193.85*	4	5 024.88
7	5 372.41*	5	5 289.718*	1 (h)	5 187.61*	1 (h)	4 997.96
2	5 368.69	3	5 289.349	2 h	5 181.04	1 (h)	4 996.55*
10	5 368.06*	1	5 285.22	(3)	5 178.60*	2	4 988.56
12	5 363.76*	12	5 284.829*	3 (h)	5 165.79	3	4 987.575
8	5 363.35*	16	5 282.295*	12	5 156.117*	5 w	4 968.50
2	5 361.70	1	5 280.61	4	5 154.821	2	4 965.243
1	5 361.12	1 h	5 279.37	(7)	5 149.38*	(8)	4 948.16
3 l	5 360.26*	4	5 279.17	1	5 146.109	3	4 941.08
4 s	5 357.52*	3	5 276.782*	2	5 141.050	6	4 940.410
3	5 354.98*	15	5 276.475*	3	5 137.814	4	4 936.332
12	5 353.77*	2	5 273.657*	7 l	5 136.09*	2	4 934.64
4	5 352.66*	(14)	5 272.98*	4	5 131.999*	3 (h)	4 927.38
1	5 352.13*	9	5 272.370*	3	5 129.03	2 (h)	4 918.25
1 (h)	5 351.39	(7)	5 266.66*	(2) h	5 128.84	1 h	4 908.77
5	5 350.78*	(7)	5 263.38	6	5 127.638*	2 (h)	4 907.05
3 w	5 348.49*	(13) l	5 260.34	9	5 127.352*	2	4 895.89
11	5 346 88*	(2) h	5 259.54	5	5 125.612*	3	4 895.21
2	5 345.20	(8)	5 257.23*	2	5 124.16*	3	4 866.76
5 s	5 344.42*	1	5 256.09*	3	5 122.98*	3 h	4 858.53
(4)	5 343.38	3 s	5 254.51*	5	5 120.65*	3	4 856.08
1	5 342.02	(6) l	5 248.15	6 s	5 116.44*	2	4 850.496
1	5 341.57	18	5 243.306*	4	5 115.758	5	4 841.806
8	5 340.54*	2	5 242.391	(3) h	5 114.92	3	4 837.748
2	5 336.13	4 s	5 241.45*	3	5 114.64*	2	4 832.344
1	5 335.60	6	5 240.548*	5	5 113.918	3 l	4 828.93
7	5 334.34*	3 (h)	5 239.19	2 (h)	5 113.33*	2	4 818.50
3	5 333.37	3 (h)	5 237.57	3	5 111.719*	1	4 818.02
(2)	5 332.69	10	5 235.661*	9	5 111.068*	3	4 787.37
(8)	5 330.73*	2	5 235.218*	5 l	5 109.38*	2	4 777.77
7	5 329.13*	7	5 230.783*	3	5 108.86*	3	4 766.145
2	5 327.59	(6)	5 229.92*	7	5 105.331*	2	4 760.477
5	5 326.87	2	5 229.416*	(2)(h)	5 104.40*	1	4 752.72*
10	5 322.74*	4	5 229.143*	(2)	5 100.35*	2 h s	4 748.35
(7)	5 322.16	6 w	5 228.63*	6	5 099.327*	2 h	4 747.51
4	5 320.35	(5)	5 227.81*	1	5 095.63	3	4 746.876
1	5 319.19*	(4)	5 226.16*	3	5 094.577*	2 (h)	4 740.98

(Table 1, cont.)

I	λ	I	λ	I	λ	I	λ
4 (h)	4 733.82	2	4 365.642*	2 h s	4 335.10	2 h	4 295.37
(3)	4 729.01	3 h s	4 365.44	2 (h)	4 334.53*	3 (h)	4 295.018*
1 (h)	4 724.82	1 (h)	4 365.002	3 (h)	4 334.313*	⎧ 1 (h)	4 293.82
5 (h)	4 723.59	3 h s	4 364.74	2 h	4 334.02	⎩ 1 (h)	4 293.67*
2	4 706.873	2 hs	4 363.96	6 (h)	4 333.830	2 (h)	4 293.359
3 w	4 698.35	4 (h)	4 363.378	3 (h)	4 333.547	2 (h)	4 293.102
2	4 676.16	3 (h)	4 362.872	4 (h)	4 333.255	1 (h)	4 292.00*
1 h	4 623.95	3 w h	4 362.07	1 w	4 333.00*	6	4 291.094
4 h	4 619.753	3 (h)	4 361.024	2 w h	4 332.20	2 (h)	4 290.647
3	4 570.341*	1 (h)	4 360.77	4 h	4 332.026	6	4 289.188
5	4 569.722*	1 (h)	4 360.54	4 h	4 331.712	2 h	4 287.668
5 w	4 543.84	2 h s	4 359.79	7 (h)	4 331.245	14 (h)	4 286.161*
1	4 536.24	4 (h)	4 359.230	3 (h)	4 330.585*	3 (h)	4 283.997
1 h	4 501.68	4 (h)	4 358.916	⎧ 3 h	4 330.26	3	4 283.794
6	4 492.974	(4) w h	4 358.40	⎩ 5 h	4 330.10	3 h	4 282.804
5	4 463.105	2 h	4 357.302	3 (h)	4 329.783	1 h	4 279.05
(2) h	4 449.66	2	4 355.721	6 h	4 329.481	1 h	4 278.45
1	4 447.807	3 (h)	4 355.45	1 (h)	4 328.78	1 (h)	4 275.98
1	4 442.595*	⎧ 2 h	4 353.99	5 h	4 328.426	2 h	4 275.561
2	4 436.470*	⎩ 2 h	4 353.89	3 (h)	4 328.135	12 (h)	4 273.405*
9	4 431.015*	4 (h)	4 353.415	⎧ 4 h	4 327.62	2 (h)	4 272.905
12	4 419.599*	6	4 352.568*	⎩ 4 h	4 327.51	3 (h) s	4 268.15*
5	4 414.137	4 h l	4 351.19	⎧ 3 (h)	4 326.87*	3	4 266.78*
3	4 411.890	1 (h)	4 350.89	⎩ (3) (h)	4 326.75	2 h	4 264.465
4	4 404.150*	2 h l	4 350.54	3 h	4 325.04	⎧ 3 h	4 263.81
2	4 402.050*	2 (h)	4 349.952	3 h	4 324.862	⎩ 3 h	4 263.71
9	4 395.759*	2 (h)	4 349.682	4 (h)	4 324.492	3	4 263.385*
5	4 382.508*	1 h	4 349.38	2 h	4 324.133	4 s	4 263.18*
1 h	4 382.06	6	4 348.794*	9	4 323.682	2	4 262.137
2 h	4 381.249	4 h	4 348.293	1	4 322.518	7 (h)	4 261.398*
2 (h)	4 379.51	4 w h	4 347.36	7 l	4 322.142	3	4 260.31*
⎧ 2 h	4 379.21	3 (h)	4 346.264	8	4 321.892	⎧ 2 (h)	4 259.30
⎩ 2 h	4 379.05	2 (h)	4 346.075	⎧ 4 h	4 321.03	⎩ 1 (h)	4 259.18*
1 h	4 378.51	(3) (h) s	4 344.43*	⎩ 3 h	4 320.91	4	4 258.818*
1 h	4 377.95	2 h	4 342.95	2	4 320.562	(2) (h)	4 258.33*
2 (h)	4 377.618*	⎧ 4 h	4 342.57	2	4 320.157	1 h	4 257.96
2	4 375.448	⎩ 2 h	4 342.46	2 h	4 318.05	3	4 256.334*
1 w h	4 374.86	3 (h)	4 342.046	(6) w h	4 317.19	6	4 255.113
⎧ (4) h	4 374.28	2 (h)	4 341.252	2	4 316.471*	4	4 254.96
⎩ 2 w h	4 374.09	1 (h)	4 340.97	3 (h)	4 316.071*	⎧ 3	4 254.17
18 (h)	4 372.81*	3 h	4 340.530	2 (h)	4 314.635	⎩ 3	4 254.06
(14) (h)	4 372.53*	5 h	4 340.151	1 (h)	4 312.23	4	4 253.650
(11) (h)	4 372.31*	2 w h	4 339.91	2 (h)	4 311.97*	4	4 253.478*
⎧ 9 (h)	4 372.14*	4 (h)	4 339.396*	2 (h) s	4 311.41*	1 (h)	4 252.45
⎩ 9 (h)	4 372.04*	2 h	4 339.18	20 (h)	4 310.362*	2	4 251.982*
4	4 371.339*	2 h	4 338.98	2 h	4 307.14	3	4 251.485*
5 (h)	4 370.708	1 h	4 338.39	18 (h)	4 304.775*	(4)	4 250.20*
(7)	4 369.72	⎧ 5 w h	4 338.12	2 (h)	4 304.039	12	4 249.717*
2 h l	4 369.01	⎩ 2 h	4 338.02	2 (h)	4 303.773	8	4 248.777*
4 l	4 368.461	4 (h) l	4 337.32*	1 (h)	4 303.42	8	4 248,339*
3 (h)	4 367.712	⎧ 4 (h)	4 336.78	1 h	4 301.40	2	4 247.867*
2 (h)	4 366.77	⎩ 3 (h)	4 336.65*	5	4 301.121	(2)	4 246.14*
⎧ 3 (h)	4 366.52	2 (h)	4 336.311	2 (h)	4 297.786	1	4 245.72*
⎩ 3 (h)	4 366.42	2 (h)	4 335.882	16 (h)	4 296.854*	2 (h)	4 244.506*
(1) (h)	4 365.88	3 (h)	4 335.551	(3) (h)	4 295.81	12	4 243.754

(Table 1, cont.)

I	λ	I	λ	I	λ	I	λ
8	4 243.406*	2 s	4 185.49	2 (h)	4 151.09	1	4 117.637
3	4 243.156	(4)	4 184.98*	2 (h)	4 150.95	1	4 117.073
3 (h)	4 242.487	3	4 184.159*	3	4 150.575	6	4 116.714
2	4 241.951	5	4 184.005*	4 w	4 149.647	7	4 115.620
3 h	4 241.252	3	4 183.728	4 w	4 148.746*	(2) (h)	4 114.50
8	4 240.666*	7	4 182.098	2	4 148.316*	6	4 113.212
9	4 238.619*	2	4 181.510*	(4) (h)	4 147.76	4	4 113.078
13	4 235.556	3	4 180.768	2 w	4 147.17*	3	4 112.79
2	4 232.560	3	4 180.496	6	4 146.694	5	4 112.304
1 (h)	4 231.68	2 l	4 179.57	3	4 146.127	1	4 111.72
2	4 231.180	8	4 179.130	8	4 145.641*	2 h	4 110.794
5 h l	4 230.43	2 (h)	4 177.96	3	4 144.887	3	4 110.340
2 h	4 228.371	4	4 177.87*	4	4 144.435	3	4 105.473*
4	4 226.938	5	4 177.403*	4 w	4 142.638*	1	4 103.865
11	4 222.269*	7	4 176.835	3	4 142.159*	1 (h)	4 103.507*
(3)	4 220.23*	2	4 176.102*	6	4 141.519	8	4 103.037*
2 h	4 220.038	1	4 175.357	9	4 140.481*	4 (h)	4 102.150
1 h	4 215.11	3	4 174.809*	6	4 140.180	3 (h)	4 100.964*
3	4 214.651	13	4 174.259*	13	4 139.349*	6	4 100.479*
3 (h)	4 213.932	1	4 173.760*	5	4 139.066	4	4 099.257
2	4 213.07*	(4) w (h)	4 172.63	2	4 138.786	3 (h)	4 098.51
3 (h)	4 211.652	3	4 170.582*	2	4 138.424	7	4 097.584*
5	4 211.08	4	4 170.215	4	4 137.964	8	4 096.790
2 h	4 210.94	2	4 169.665*	15	4 137.762*	3	4 096.54*
9	4 210.672*	7	4 168.449*	7	4 137.133*	1 (h)	4 096.18*
4	4 209.406*	4	4 167.666	5	4 136.821	(5)	4 095.87*
5	4 208.830	13	4 166.843*	2	4 135.821*	4 (h)	4 095.36*
4 (h)	4 207.548	1	4 166.38	3	4 135.630	5	4 095.26*
(2)	4 207.06*	2	4 166.135	4	4 135.089	2	4 094.995*
2	4 205.908*	4	4 165.853	6 w	4 134.268*	1	4 094.47
6	4 204.511*	9	4 164.921*	4	4 133.103	3	4 094.36*
5	4 203.826*	18	4 164.731*	3	4 131.698	3	4 094.138
8	4 200.204	2 (h)	4 164.14	2	4 131.504	1	4 093.857
3	4 199.981	2 (h)	4 163.93	4 (h)	4 129.911	6	4 093.224*
2 (h)	4 197.464	4	4 163.35*	5 (h)	4 129.397	3	4 093.048*
2 (h)	4 197.304	2 (h)	4 163.21*	2 (h)	4 128.545	4	4 092.628*
5	4 196.033	2	4 162.89*	2	4 128.317	7	4 092.339*
4	4 195.643	2	4 162.73	(3) h l	4 127.816	5 w	4 091.479
2 (h)	4 195.470*	2	4 162.59*	2	4 127.154	5	4 090.986*
3	4 194.703*	3	4 162.217	4	4 126.996*	2 h	4 090.708
6	4 194.11*	6	4 161.353*	4	4 126.518*	1	4 090.427*
6	4 193.95*	2	4 160.894	5	4 123.515	4 (h)	4 089.94*
2	4 192.834	2	4 159.843*	2 (h)	4 123.309	2 (h)	4 089.77
6	4 192.270	3 (h)	4 158.706	1 (h)	4 123.00*	2 (h)	4 089.62
4 h	4 191.123	4 (h)	4 158.271	11	4 122.780*	2	4 088.082
3 h	4 190.781	1	4 157.106*	11	4 122.025*	1 (h)	4 086.365*
3 w h	4 190.12	1	4 156.946	2	4 121.583	6	4 085.466
2 (h)	4 189.616	2 (h)	4 155.34*	6	4 121.345*	1	4 082.76*
8	4 189.112*	2 (h)	4 155.18	(10)	4 120.90*	6	4 082.474*
3	4 188.899*	9	4 154.963*	7 w	4 119.858*	1 (h)	4 081.983*
1	4 188.53	3 w	4 153.764	5 w	4 119.363*	1	4 081.513*
6	4 188.044	6 w	4 153.105	5	4 118.866*	12	4 081.005*
2 h l	4 187.44	(5)	4 152.16*	6	4 118.716*	(2)	4 080.17
4	4 186.786	1 (h)	4 151.588	5	4 118.401*	5 w	4 079.73
3	4 186.527			3	4 118.105	2 (h)	4 079.299*

(Table 1, cont.)

I	λ	I	λ	I	λ	I	λ
2	4 078.961	1 (h)	4 014.219	1	3 936.759	1 (h)	3 671.790
3 w	4 078.61	2	4 012.823	1 (h)	3 934.992	2 (h)	3 670.875
2 h	4 077.912	7	4 008.771*	1 (h)	3 915.895	4 (h)	3 667.636
4 w	4 072.21	1	4 007.674	1	3 912.822*	(2) h	3 664.00
(6)	4 070.36	2 w (h)	4 006.92*	6 l	3 910.866	1	3 662.367
4	4 069.213*	2	4 005.613*	2 h	3 906.285	7	3 652.668
8 w	4 065.977*	8	4 005.022*	2 h	3 905.796	1	3 628.16
(2)	4 065.37	1 h	4 004.553	4	3 894.860	2	3 625.533
1 h	4 065.130	2	4 003.543*	3 (h)	3 892.445	(1)(h)	3 620.48
6	4 063.077	7	4 003.231*	1	3 881.472	1 (h)	3 620.285*
4 (h)	4 061.731*	5	4 002.367*	1 (h)	3 869.364	6	3 611.748*
5	4 060.248	3	4 002.054	1 (h)	3 849.538	1	3 606.263*
1	4 060.005*	1 (h)	4 001.149*	1 (h)	3 845.827*	11	3 603.883*
1 h	4 059.133	5 l	4 000.767*	1	3 841.785	11	3 600.944*
(6)	4 057.50*	{ 6	3 999.88*	3	3 839.618	5	3 599.439*
1 h	4 056.85	{ 6	3 999.79*	(4)	3 828.43*	{ 2	3 598.20*
1 h	4 056.472	2 (h)	3 999.368	4 (h)	3 812.480	{ 1	3 598.12*
11	4 053.114*	1 (h)	3 999.10*	1	3 795.255*	7	3 593.127*
4	4 052.511*	6	3 993.146*	6	3 793.526*	1	3 591.19*
4	4 051.624	1	3 988.995	2 w h	3 791.613	{ 6	3 589.70
5	4 051.015	3 (h)	3 987.894	4	3 791.261	{ 3 h	3 589.56
2 (h)	4 050.047	1 h s	3 987.32	5	3 789.370*	1 h	3 588.038
1 (h)	4 048.00	1 h	3 986.836	2 h	3 788.261	4	3 587.549*
(1)(h)	4 047.54	4 (h)	3 985.822	7	3 786.997*	(10)	3 586.04*
2 h	4 045.290	2 (h)	3 984.812*	1	3 785.543*	2	3 575.633*
2 h s	4 045.08	1	3 984.641	1	3 785.228	1	3 574.15*
4	4 043.536	1 (h)	3 984.25*	5 (h)	3 778.015	1	3 572.32*
(1) l	4 043.17	7	3 980.093*	1 (h)	3 773.089	1	3 569.45*
1 w h	4 042.67	10 w	3 979.423*	1	3 765.22*	{ 1 h	3 568.47
(2)	4 041.86*	8	3 978.406*	(3)	3 761.97	{ 2 h	3 568.31
4	4 039.821	2 h	3 978.077	1	3 758.703	1	3 562.690*
6	4 039.151*	(6)	3 976.95*	1	3 755.451*	2 l	3 561.119
2 h	4 038.31	3	3 975.149	1 (h)	3 754.231*	1	3 560.11*
1 l	4 037.35	2 h	3 974.758	6	3 753.168*	2 (h)	3 559.742
3 h s	4 037.03	2 h	3 973.141	2	3 747.84	1	3 559.275
3	4 036.345	5	3 971.126*	(7)	3 747.42*	5	3 557.367
2	4 035.810*	4	3 970.511*	(2) w	3 746.52*	(1)	3 547.77
10	4 035.425*	9	3 969.490*	1	3 740.593	(1)(h)	3 544.56*
7	4 033.871	11	3 968.718*	2 w (h)	3 739.65	(4) l	3 543.25
1	4 033.624	1 (h)	3 966.342	1 (h)	3 737.550	1 h	3 538.840
4 (h)	4 033.058	2 (h)	3 964.283	(3)	3 729.41	3	3 528.044*
5	4 030.993	5	3 963.991	2	3 717.277*	5	3 525.184*
2 (h)	4 025.652*	1 (h)	3 958.737	2 w	3 713.05	1	3 523.83*
4	4 024.999*	1	3 955.67*	3	3 700.152*	3	3 517.576
3 h	4 023.897	3	3 955.150*	4	3 698.802	7	3 515.536*
8	4 022.326*	1 (h)	3 954.801	(1)	3 697.31	2	3 514.881*
1	4 021.725*	16	3 954.326*	2	3 696.209*	1	3 514.286*
3	4 019.356	6	3 953.814*	1	3 695.883*	(2)	3 512.73
2 (h)	4 018.760	2 h	3 952.899	1	3 695.650	8	3 506.936*
4	4 017.983	(7)	3 952.59	2 (h)	3 692.237	1	3 505.891*
2 (h)	4 017.705	1	3 951.503*	5	3 690.556*	2	3 504.417*
5	4 017.510	1 (h)	3 949.28*	3	3 685.400*	10	3 501.756*
4 w	4 016.489*	(6)	3 947.05*	2 (h)	3 683.818	1	3 501.268*
2	4 015.778	3	3 946.124	1 h l	3 679.38	(3)	3 500.60
5	4 015.271	2 h	3 939.343	2 (h)	3 678.483	9	3 500.285*

(Table 1, cont.)

I	λ	I	λ	I	λ	I	λ
9	3 499.589*	3	3 373.534*	7	3 304.302*	6	3 218.340*
2	3 497.598*	1	3 371.571	3	3 303.597*	8	3 215.633*
1	3 496.715*	(1) (h)	3 370.53*	2	3 302.567*	2	3 212.181*
(4)	3 496.27*	1	3 368.163	1	3 302.212	3	3 206.951*
1 l	3 493.857*	3	3 367.581*	3	3 300.196*	1 (h)	3 206.29*
4	3 491.176*	6	3 364.996*	1	3 294.960*	6	3 204.763*
3	3 489.492*	1	3 362.21*	2	3 294.805*	2	3 201.893*
1 w h	3 489.07	(3) h	3 361.70	4	3 294.524*	2	3 201.637*
5	3 488.913*	7	3 360.868*	1	3 294.370*	2	3 199.216
1	3 487.256	3	3 360.736	2	3 294.176	5	3 198.822*
4	3 486.234	(2) (h)	3 360.20	3 (h)	3 293.185	2	3 197.669
2	3 484.324	4	3 359.194*	(7)	3 292.04*	1	3 190.514*
3	3 482.305*	6	3 358.777*	1 l	3 290.415	3	3 189.745*
2 w h	3 481.81	5	3 357.419*	10	3 288.808*	1 (h)	3 185.95*
3	3 479.505	1	3 355.006	1	3 284.290*	2	3 182.508
3	3 478.913	3	3 354.821*	1	3 283.785*	(10)	3 178.01*
1	3 474.291	2	3 353.525	3	3 283.296*	3	3 176.838*
(2)	3 472.59	2	3 351.154	6	3 280.556*	10	3 175.993*
3	3 464.141	3	3 350.898	1	3 278.250	1	3 174.331*
3	3 458.906*	1	3 350.471	1	3 277.650	10	3 174.089*
1 (h)	3 458.756	3 h	3 349.110	11	3 276.079*	2 w	3 172.473
1 (h)	3 458.503	4	3 348.535	3 l	3 274.949*	1	3 170.95*
2 l	3 457.485	7	3 347.734*	2 (h)	3 273.86*	1	3 170.639
2	3 455.837	1	3 347.484	5	3 273.600*	⎧ 3	3 169.43*
2	3 455.204*	2 l	3 346.749	1 (h)	3 273.13*	⎩ 3	3 169.35
2 w (h)	3 454.37*	1	3 346.331	(2)	3 271.47*	1	3 167.553*
2	3 452.749*	2 s	3 345.435	2 s	3 270.24*	3	3 165.596
⎧ 1 h	3 449.96	2 l	3 344.291*	2	3 269.051	4	3 164.687*
⎩ 1 h	3 449.84	2 (h)	3 343.790	13	3 266.885*	4	3 150.339
3	3 441.733*	2	3 342.584	3	3 265.471	2	3 148.894
1	3 437.149	9	3 339.386*	1	3 265.304*	2 (h)	3 146.997
3 l	3 435.815	1	3 339.036	1	3 264.250*	1	3 144.180*
3	3 435.023	7 s	3 338.717*	1	3 263.065*	1 h	3 143.685
1	3 434.604	1	3 337.186	5	3 262.455*	2	3 143.386*
2 (h)	3 433.369	2	3 334.510	2 h	3 259.699	2 h s	3 139.58
5	3 432.997*	3	3 333.318*	2	3 258.555	⎧ 4	3 136.49*
2	3 427.455*	(4)	3 331.62*	1	3 256.550*	⎩ 10	3 136.43*
1	3 424.467*	7	3 329.899*	2	3 255.485*	2	3 130.858*
⎧ 3	3 422.085*	1	3 327.348	(2)	3 255.25*	4	3 129.121
⎩ 3	3 422.000*	1	3 325.54*	1	3 252.730	2 s	3 128.418
1	3 421.282	3	3 324.732*	1	3 249.058*	1	3 127.634
5	3 419.500*	2	3 323.344	2	3 245.191	1	3 126.953
4	3 410.716*	(3)	3 321.24	1	3 242.376	8	3 123.152*
1	3 409.452*	2	3 320.276*	1	3 240.157	1	3 121.189
4	3 406.197*	1	3 317.840	(3)	3 239.03*	8	3 121.055
3	3 403.528*	3	3 315.846*	4	3 238.711*	3	3 120.862*
8	3 396.704*	1	3 314.926	1	3 238.053	(2)	3 120.03*
2	3 391.639*	1	3 311.536*	5	3 237.203*	2	3 119.259*
1	3 388.385	1	3 311.02*	(2)	3 236.61*	4	3 118.754*
3	3 386.853*	5 w	3 309.40	1	3 235.475*	(2)	3 118.26*
1	3 385.701	1	3 309.020*	3 w h	3 233.18	2 (h)	3 117.90
(2) (h)	3 383.76	1	3 307.824*	(2)	3 230.16*	3	3 117.118
7	3 382.179*	5	3 307.547*	1	3 227.492	2	3 114.876
1	3 378.862	4	3 306.991*	2 h	3 224.152	1	3 113.839*
(2) h	3 378.17	9	3 305.220*	2 h	3 220.571	7	3 111.616*

(Table 1, cont.)

I	λ	I	λ	I	λ	I	λ
(3)	3 110.88*	2	3 083.92	2	3 039.576*	6	3 008.511*
8	3 110.074*	3	3 070.091*	2	3 035.788*	8 1	3 007.793*
(3)	3 108.85*	1	3 068.032*	2	3 027.491*	5 (h)	3 007.600*
6	3 107.977*	1	3 066.817*	6	3 027.006*	6 (h)	3 007.461*
1	3 102.548*	1	3 065.023*	2	3 026.129*	12 (h)	3 007.275*
3	3 100.470*	1	3 060.159*	7	3 023.883*	5 (h)	3 007.22*
1 w (h)	3 099.01*	1	3 060.013*	(3)	3 022.00*	3 (h)	3 007.14*
1	3 096.97*	1	3 059.368*	2	3 021.886	7 (h)	3 007.06*
1	3 094.761*	2	3 055.554*	6	3 018.789*	2 (h)	3 006.99*
2	3 094.303*	5	3 054.138*	2 1	3 017.31*	4	3 006.142*
(4)	3 091.63*	3	3 050.467*	6	3 015.260*	(3)	3 004.13*
2	3 090.754*	(2) w	3 046.71*	2	3 013.97	(4)	3 002.99*
1	3 088.746	1	3 046.194*	15	3 013.167*	12	3 001.617*
3	3 088.264	3	3 045.877*	1	3 012.465	2	3 000.839*
3	3 084.07*						

Table 2.

Classified Fe III lines in the region 8568–3000 Å.

The notation for the shape of the lines is the same as used in Table 1. In addition, the following abbreviations are used:

m = masked by
bl = blended by
aff = affected by
* in column 2: λ from EDLÉN and SWINGS (1942 and unpublished material).
* in column 5: classified by EDLÉN and SWINGS (1942).

Intensity	λ_{air} (obs)	σ (obs)	σ (calc)	Combination
2	8 568.42	11 667.56	7.56	$6p\ ^7P_4 - 6d\ ^7D_4$
5	8 563.49	11 674.27	4.27	$6p\ ^7P_4 - 6d\ ^7D_5$
1	8 515.29	11 740.36	0.34	$6p\ ^7P_3 - 6d\ ^7D_2$
2	8 512.72	11 743.90	3.91	$6p\ ^7P_3 - 6d\ ^7D_3$
3	8 509.06	11 748.95	8.95	$6p\ ^7P_3 - 6d\ ^7D_4$
2	8 481.38	11 787.30	7.30	$6p\ ^7P_2 - 6d\ ^7D_1$
2	8 479.71	11 789.62	9.63	$6p\ ^7P_2 - 6d\ ^7D_2$
1	8 477.13	11 793.21	3.20	$6p\ ^7P_2 - 6d\ ^7D_3$
1	8 416.50	11 878.16	8.16	$6p\ ^7P_4 - 7s\ ^7S_3$
1	8 359.22	11 959.55	9.55	$6p\ ^7P_3 - 7s\ ^7S_3$
0	8 324.89	12 008.87	8.84	$6p\ ^7P_2 - 7s\ ^7S_3$
8 w h	8 236.75	12 137.37	7.4	$5g\ ^5G - 6h\ ^5H$
9 w h bl Fe I	8 235.45	12 139.29	9.3	$5g\ ^7G - 6h\ ^7H$
3 w h aff Fe III	8 017.92	12 468.63	8.6	$5f\ ^5F_5 - 6g\ ^5G_6$
3 w h	8 014.69	12 473.66	3.7	$5f\ ^5F_4 - 6g\ ^5G_5$

(Table 2, cont.)

Intensity	λ_{air} (obs)	σ (obs)	σ (calc)	Combination
2 w h	8 011.22	12 479.05	9.0	$5f\ {}^5F_3 - 6g\ {}^5G_4$
2 w h	8 007.88	12 484.27	4.3	$5f\ {}^5F_2 - 6g\ {}^5G_3$
0 w h	8 004.46	12 489.60	9.6	$5f\ {}^5F_1 - 6g\ {}^5G_2$
5 v w h	7 921.17	12 620.93	1	$5f\ {}^7F\ - 6g\ {}^7G$
2 h	7 322.88	13 652.07	1.8	$5d\ {}^5D_2 - 5f\ {}^5F_2$
			2.1	$5d\ {}^5D_3 - 5f\ {}^5F_3$
6 h	7 320.14	13 657.18	6.8	$5d\ {}^5D_4 - 5f\ {}^5F_4$
			7.0	$5d\ {}^5D_2 - 5f\ {}^5F_3$
			7.2	$5d\ {}^5D_0 - 5f\ {}^5F_1$
			7.3	$5d\ {}^5D_3 - 5f\ {}^5F_4$
1 h	7 319.56	13 658.26	8.3	$5d\ {}^5D_1 - 5f\ {}^5F_2$
5 h	7 317.63	13 661.86	1.86	$5d\ {}^5D_4 - 5f\ {}^5F_5$
4	7 265.14	13 760.56	0.47	$b\ {}^1G_4 - z\ {}^1H_5$
0 (h)	6 718.81	14 879.48	9.43	$e\ {}^3G_4 - x\ {}^5G_5$
0 (h)	6 610.75	15 122.70	2.61	$e\ {}^3D_2 - v\ {}^5F_1$
0 (h) bl Fe II	6 595.09	15 158.60	8.74	$e\ {}^3D_2 - v\ {}^5F_2$
0 (h)	6 549.49	15 264.15	4.19	$e\ {}^3D_3 - v\ {}^5F_2$
1 h bl Fe II	6 486.05	15 413.45	3.46	$e\ {}^3D_3 - v\ {}^5F_4$
2 (h)	6 345.19	15 755.61	5.57	$e\ {}^3G_4 - w\ {}^5F_4$
1 (h)	6 288.35	15 898.03	8.06	$e\ {}^3D_1 - v\ {}^5D_1$
1 (h)	6 283.75	15 909.66	9.57	$e\ {}^3D_2 - v\ {}^5D_1$
2	6 281.20	15.916.12	6.32	$c\ {}^3G_4 - z\ {}^3I_5$
0 (h)	6 279.68	15 919.97	9.92	$e\ {}^3F_4 - x\ {}^5G_4$
1 w (h)	6 227.49	16 053.39	3.30	$e\ {}^3D_3 - v\ {}^5D_3$
1 (h) bl Fe II	6 225.58	16 058.32	8.44	$e\ {}^3D_3 - v\ {}^5D_2$
4	6 208.37	16 102.83	2.86	$e\ {}^5P_1 - w\ {}^5D_2$
1	6 206.09	16 108.75	8.75	$e\ {}^5P_1 - w\ {}^5D_0$
5 s	6 203.04	16 116.66	6.66	$e\ {}^5P_1 - w\ {}^5D_1$
6	6 201.37	16 121.00	1.02	$e\ {}^3G_3 - q\ {}^3F_2$
7	6 194.79	16 138.13	8.15	$e\ {}^3G_4 - q\ {}^3F_3$
2	6 194.56	16 138.74	8.61	$e\ {}^3G_3 - q\ {}^3F_3$
m Fe I	—	16 146	6.46	$e\ {}^3G_4 - q\ {}^3F_4$
1	6 186.06	16 160.91	0.86	$e\ {}^5P_2 - w\ {}^5D_2$
9	6 185.26	16 163.00	3.00	$e\ {}^5P_2 - w\ {}^5D_3$
5	6 181.70	16 172.31	2.33	$e\ {}^3G_5 - q\ {}^3F_4$
9	6 169.74	16 203.65	3.64	$e\ {}^3G_5 - u\ {}^3H_6$
			3.69	$e\ {}^3G_4 - u\ {}^3H_5$
5 aff Fe III	6 165.46	16 214.90	4.73	$e\ {}^5P_3 - w\ {}^5D_3$
2	6 158.79	16 232.45	2.40	$e\ {}^5P_1 - y\ {}^5S_2$
4	6 154.36	16 244.15	4.14	$e\ {}^3G_3 - u\ {}^3H_4$
9	6 149.99	16 255.68	5.67	$e\ {}^5P_3 - w\ {}^5D_4$
m Fe I	—	16 290	0.40	$e\ {}^5P_2 - y\ {}^5S_2$
5	6 117.47	16 342.11	2.13	$e\ {}^5P_3 - y\ {}^5S_2$
3	6 097.40	16 395.90	5.89	$e\ {}^3D_2 - s\ {}^3D_3$
6	6 092.16	16 410.01	0.08	$b\ {}^1G_4 - z\ {}^1G_4$

(Table 2, cont.)

Intensity	λ_{air} (obs)	σ (obs)	σ (calc)	Combination
2	6 084.23	16 431.39	1.39	$g\,^5F_1 - w\,^5G_2$
3	6 082.04	16 437.29	7.28 7.29	$e\,^3D_1 - s\,^3D_2$ $y\,^5G_3 - 4d\,^5D_3$
6	6 077.78	16 448.81	8.79	$e\,^3D_2 - s\,^3D_2$
4	6 059.01	16 499.77	9.78	$e\,^3D_1 - s\,^3D_1$
6	6 058.46	16 501.28	1.34	$e\,^3D_3 - s\,^3D_3$
2	6 057.64	16 503.52	3.54	$f\,^5G_3 - x\,^5G_2$
8	6 057.13	16 504.91	4.90	$f\,^5G_2 - x\,^5G_2$
9	6 056.36	16 507.01	7.04	$f\,^5G_3 - x\,^5G_3$
4	6 054.77	16 511.34	1.29 1.39	$e\,^3D_2 - s\,^3D_1$ $f\,^5G_4 - x\,^5G_3$
11	6 054.18	16 512.95	2.95	$f\,^5G_4 - x\,^5G_4$
m Fe II	—	16 525	5.99	$5p\,^5P_1 - e\,^5P_2$
11	6 048.72	16 527,84	7.88	$f\,^5G_5 - x\,^5G_5$
6	6 048.34	16 528.87	8.86	$e\,^3D_1 - p\,^3F_2$
7	6 047.91	16 530.07	29.92	$f\,^5G_5 - x\,^5G_4$
7	6 047.73	16 530.55	0.63	$5p\,^5P_2 - e\,^5P_3$
3	6 044.17	16 540.30	0.37	$e\,^3D_2 - p\,^3F_2$
7	6 042.94	16 543.67	3.70	$e\,^3D_2 - p\,^3F_3$
3	6 039.08	16 554.23	4.24	$e\,^3D_3 - s\,^3D_2$
13	6 036.56	16 561.14	1.17	$f\,^5G_6 - x\,^5G_6$
4	6 035.53	16 563.96	3.99	$f\,^5G_6 - x\,^5G_5$
16	6 032.59	16 572.05	1.81 2.00	$f\,^3I_6 - x\,^3I_7$ $5s\,^5S_2 - 5p\,^5P_3{}^*$
9	6 031.02	16 576.35	6.35	$f\,^3I_7 - x\,^3I_7$
7	6 028.87	16 582.26	2.26 2.36	$e\,^3D_3 - p\,^3F_4$ $5p\,^5P_2 - e\,^5P_2$
1	6 022.85	16 598.84	8.84	$y\,^5G_2 - 4d\,^5D_1$
6 l	6 020.78	16 604.54	4.46	$f\,^3I_5 - x\,^3I_6$
8	6 015.29	16 619.70	9.72	$f\,^3I_6 - x\,^3I_6$
6	6 014.48	16 621.94	1.95	$5p\,^5P_3 - e\,^5P_3$
2	6 013.64	16 624.27	4.26	$f\,^3I_7 - x\,^3I_6$
3 aff Fe III	6 007.80	16 640.42	0.36	$5p\,^5P_2 - e\,^5P_1$
2	6 004.64	16 649.19	9.15	$e\,^3D_3 - p\,^3F_3$
6	6 000.10	16 661.78	1.81	$f\,^3I_5 - x\,^3I_5$
18	5 999.54	16 663.32	3.32	$5s\,^5S_2 - 5p\,^5P_2{}^*$
3	5 995.81	16 673.70	3.68	$5p\,^5P_3 - e\,^5P_2$
5	5 994.59	16 677.10	7.07	$f\,^3I_6 - x\,^3I_5$
12 h	5 989.08	16 692.44	2.4 2.9	$5d\,^7D_5 - 5f\,^7F_6$ $5d\,^7D_5 - 5f\,^7F_5$
3 bl Fe I	5 984.82	16 704.32	4.30	$g\,^5F_2 - w\,^5G_2$
7 h	5 984.54	16 705.10	5.0 5.5	$5d\,^7D_4 - 5f\,^7F_5$ $5d\,^7D_4 - 5f\,^7F_4$
9 h	5 981.01	16 714.94	4.8 5.3	$5d\,^7D_3 - 5f\,^7F_4$ $5d\,^7D_3 - 5f\,^7F_3$
12	5 979.32	16 719.68	9.69	$5s\,^5S_2 - 5p\,^5P_1{}^*$
6 h	5 978.48	16 722.04	1.9 2.4	$5d\,^7D_2 - 5f\,^7F_3$ $5d\,^7D_2 - 5f\,^7F_2$

(Table 2, cont.)

Intensity	λ_{air} (obs)	σ (obs)	σ (calc)	Combination
5 h bl Fe I	5 976.78	16 726.78		$5d\ ^7D_1 - 5f\ ^7F_{21}$
1	5 963.33	16 764.51	4.49	$f\ ^5D_2 - v\ ^5F_1$
4	5 962.46	16 766.95	6.95	$g\ ^5F_2 - w\ ^5G_3$
3	5 959.46	16 775.40	5.43	$f\ ^5D_1 - v\ ^5F_1$
6	5 956.81	16 782.87	2.87	$e\ ^3I_7 - u\ ^3H_6$
14	5 953.62	16 791.87	1.87	$4d\ ^5D_4 - 5p\ ^5P_3$*
10	5 952.31	16 795.55	4.77 5.54	$4d\ ^5D_2 - 5p\ ^5P_3$ $4d\ ^5D_3 - 5p\ ^5P_3$
3	5 951.50	16 797.84	7.81	$f\ ^5D_0 - v\ ^5F_1$
4	5 950.51	16 800.62	0.62	$f\ ^5D_2 - v\ ^5F_2$
2 w	5 949.26	16 804.16	4.16	$e\ ^3I_6 - u\ ^3H_6$
5	5 946.65	16 811.54	1.56	$f\ ^5D_1 - v\ ^5F_2$
8 s	5 940.10	16 830.08	0.08 0.14	$e\ ^3I_6 - u\ ^3H_5$ $f\ ^5G_2 - y\ ^5H_3$
7	5 938.90	16 833.46	— 3.68	— $f\ ^5D_3 - v\ ^5F_2$
2	5 933.01	16 850.17	0.18	$e\ ^3I_5 - u\ ^3H_5$
18	5 929.69	16 859.63	9.63 9.83	$5s\ ^7S_3 - 5p\ ^7P_2$* $f\ ^5D_2 - v\ ^5F_3$
5 l	5 920.99	16 884.39	4.31	$4d\ ^5D_1 - 5p\ ^5P_2$
7	5 920.39	16 886.09	6.09	$4d\ ^5D_2 - 5p\ ^5P_2$*
10	5 920.13	16 886.85	6.86	$4d\ ^5D_3 - 5p\ ^5P_2$*
7	5 919.90	16 887.50	7.58	$f\ ^5G_3 - y\ ^5H_4$
9	5 918.96	16 890.18	0.17 —	$e\ ^3I_5 - u\ ^3H_4$ —
7	5 918.06	16 892.75	2.70 2.89	$g\ ^5F_3 - w\ ^5G_3$ $f\ ^5D_3 - v\ ^5F_3$
2	5 915.47	16 900.14	0.39	$c\ ^3D_3 - y\ ^5D_3$
5 (h) bl C II	5 907.25	16 923.66	3.32 —	$c\ ^3D_2 - y\ ^5D_3$ —
4	5 901.74	16 939.45	9.45	$4d\ ^5D_0 - 5p\ ^5P_1$*
7	5 901.33	16 940.64	0.68	$4d\ ^5D_1 - 5p\ ^5P_1$*
7	5 900.70	16 942.46	2.46	$4d\ ^5D_2 - 5p\ ^5P_1$*
9	5 898.68	16 948.25	8.28	$f\ ^5G_4 - y\ ^5H_5$
15 bl C II	5 891.91	16 967.71	7.74	$5s\ ^7S_3 - 5p\ ^7P_3$*
5 bl C II	5 889.77	16 973.90	4.15	$g\ ^5F_3 - w\ ^5G_4$
5 aff Fe III	5 886.66	16 982.86	2.95	$f\ ^5D_3 - v\ ^5F_4$
3 (h)	5 885.85	16 985.19	5.13	$y\ ^3G_3 - 4d\ ^5D_3$
3 (h)	5 885.65	16 985.77	5.90	$y\ ^3G_3 - 4d\ ^5D_2$
0	5 884.49	16 989.12	9.07	$f\ ^5D_4 - v\ ^5F_3$
1	5 883.36	16 992.38	2.61	$c\ ^3D_2 - y\ ^5D_2$
9	5 876.26†	17 012.91	2.69	$f\ ^5G_5 - y\ ^5H_6$
0	5 871.34	17 027.16	7.08	$v\ ^5D_4 - h\ ^5F_5$
4	5 864.08	17 048.26	8.30	$e\ ^3G_3 - s\ ^3G_3$
6	5 860.95	17 057.36	7.31	$e\ ^3G_4 - s\ ^3G_4$
2	5 860.76	17 057.91	7.77	$e\ ^3G_3 - s\ ^3G_4$
4	5 857.65	17 066.97	6.97	$e\ ^3G_4 - s\ ^3G_5$

---

† λ 5 876.26 was measured on vacuum spark spectrograms because it is masked by He in the hollow cathode.

(Table 2, cont.)

Intensity	λ_{air} (obs)	σ (obs)	σ (calc)	Combination
10	5 854.62	17 075.79	5.79	$f\ {}^5G_6 - y\ {}^5H_7$
6	5 853.48	17 079.13	9.13	$f\ {}^5D_4 - v\ {}^5F_4$
3	5 852.09	17 083.19	3.18	$e\ {}^3G_5 - s\ {}^3G_4$
3	5 851.46	17 085.01	5.00	$g\ {}^5F_4 - w\ {}^5G_4$
2	5 850.29	17 088.42	8.41	$f\ {}^3I_6 - t\ {}^3H_6$
9	5 848.76	17 092.91	2.84 2.95	$e\ {}^3G_5 - s\ {}^3G_5$ $f\ {}^3I_7 - t\ {}^3H_6$
2 aff Fe III	5 843.15	17 109.30	9.05	$f\ {}^3I_5 - t\ {}^3H_5$
7	5 838.04	17 124.30	4.31	$f\ {}^3I_6 - t\ {}^3H_5$
18	5 833.93	17 136.35	6.33	$5s\ {}^7S_3 - 5p\ {}^7P_4$*
6	5 830.61	17 146.12	6.11	$f\ {}^3I_5 - t\ {}^3H_4$
3	5 822.88	17 168.86	8.80	$e\ {}^3F_3 - q\ {}^3F_2$
7	5 821.38	17 173.30	3.33	$g\ {}^5F_4 - w\ {}^5G_5$
m Ne I	—	17 176	6.60	$e\ {}^3F_4 - q\ {}^3F_3$
8	5 818.49	17 181.81	1.75	$f\ {}^5D_4 - v\ {}^5F_5$
7	5 817.43	17 184.97	4.91 5.16	$e\ {}^3F_4 - q\ {}^3F_4$ $e\ {}^3F_2 - q\ {}^3F_2$
5	5 816.96	17 186.36	6.39	$e\ {}^3F_3 - q\ {}^3F_3$
5	5 813.31	17 197.14	7.16	$e\ {}^5P_2 - x\ {}^5P_3$
6	5 812.19	17 200.45	0.42	$g\ {}^5F_5 - w\ {}^5G_5$
5	5 805.16	17 221.29	1.30	$e\ {}^5P_1 - x\ {}^5P_2$
3	5 803.40	17 226.51	6.51	$g\ {}^5F_1 - u\ {}^5F_2$
6	5 799.92	17 236.84	6.80	$f\ {}^3G_5 - p\ {}^3F_4$
8	5 795.87	17 248.87	8.89	$e\ {}^5P_3 - x\ {}^5P_3$
8	5 788.79	17 269.98	9.98	$g\ {}^5F_5 - w\ {}^5G_6$
4	5 787.76	17 273.05	3.04	$e\ {}^5P_1 - x\ {}^5P_1$
3	5 785.67	17 279.30	9.30	$e\ {}^5P_2 - x\ {}^5P_2$
4	5 774.07	17 313.99	4.00	$g\ {}^5F_1 - u\ {}^5F_1$
5	5 773.29	17 316.35	6.38	$f\ {}^3G_4 - p\ {}^3F_3$
4 bl Fe II	5 768.39	17 331.07	1.03 1.04 1.06	$e\ {}^5P_3 - x\ {}^5P_2$ $e\ {}^5P_2 - x\ {}^5P_1$ $f\ {}^5G_5 - w\ {}^5F_5$
10	5 756.38	17 367.20	7.17	$f\ {}^5G_6 - w\ {}^5F_5$
4 w bl Fe II	5 755.63	17 369.48	9.33	$f\ {}^3G_3 - p\ {}^3F_2$
1	5 754.58	17 372.65	2.66	$f\ {}^3G_3 - p\ {}^3F_3$
4	5 749.81	17 387.06	7.05	$f\ {}^5G_4 - w\ {}^5F_4$
9	5 744.19	17 404.06	4.02	$f\ {}^5G_5 - w\ {}^5F_4$
3 w	5 742.29	17 409.83	9.95	$g\ {}^5F_2 - u\ {}^5F_3$
4	5 734.84	17 432.45	2.42	$f\ {}^5G_3 - w\ {}^5F_3$
8	5 733.41	17 436.80	6.77	$f\ {}^5G_4 - w\ {}^5F_3$
3 bl Fe I	5 731.81	17 441.66	1.59	$g\ {}^5F_3 - u\ {}^5F_4$
6	5 722.46	17 470.15	0.13	$f\ {}^5G_3 - w\ {}^5F_2$
3	5 722.02	17 471.48	1.49	$f\ {}^5G_2 - w\ {}^5F_2$
5	5 713.97	17 496.10	6.08	$g\ {}^5F_4 - u\ {}^5F_5$
7	5 712.92	17 499.31	9.29 9.42	$f\ {}^5G_2 - w\ {}^5F_1$ $g\ {}^5F_2 - u\ {}^5F_2$
0 (h) aff Fe III	5 706.51	17 518.99	9.15	$v\ {}^5F_5 - i\ {}^5G_6$

(Table 2, cont.)

Intensity	λ_{air} (obs)	σ (obs)	σ (calc)	Combination
7	5 705.15	17 523.16	3.17	$g\,^5F_5 - u\,^5F_5$
5	5 701.06	17 535.74	5.70	$g\,^5F_3 - u\,^5F_3$
m C III	—	17 551	1.45	$f\,^5D_2 - v\,^5D_1$
4 bl C III	5 695.68	17 552.29	2.44	$g\,^5F_4 - u\,^5F_4$
4	5 692.43	17 562.34	2.39 2.43	$f\,^5D_1 - v\,^5D_1$ $f\,^5D_3 - v\,^5D_4$
3	5 686.87	17 579.49	9.53	$g\,^5F_5 - u\,^5F_4$
1	5 685.17	17 584.74	4.77	$f\,^5D_0 - v\,^5D_1$
1	5 684.47	17 586.91	6.91	$g\,^5F_2 - u\,^5F_1$
5	5 683.57	17 589.69	9.73	$f\,^5D_2 - v\,^5D_3$
4	5 681.88	17 594.91	4.87	$f\,^5D_2 - v\,^5D_2$
4	5 678.36	17 605.84	5.81	$f\,^5D_1 - v\,^5D_2$
3	5 672.88	17 622.83	2.79	$f\,^5D_3 - v\,^5D_3$
4	5 672.14	17 625.13	5.17	$g\,^5F_3 - u\,^5F_2$
3	5 671.24	17 627.94	7.93	$f\,^5D_3 - v\,^5D_2$
3	5 665.26	17 646.54	6.55	$g\,^5F_4 - u\,^5F_3$
4	5 661.40	17 658.56	8.61	$f\,^5D_4 - v\,^5D_4$
0	5 642.10	17 718.98	8.97	$f\,^5D_4 - v\,^5D_3$
1	5 635.51	17 739.70	9.96	$c\,^3G_4 - x\,^3F_3$
1	5 631.32	17 752.89	3.02	$c\,^3G_3 - x\,^3F_2$
8	5 573.47	17 937.15	7.31	$c\,^3G_5 - y\,^3H_6{}^*$
1 (h)	5 525.16	18 094.00	3.93	$e\,^5D_4 - v\,^5F_4$
2	5 521.69	18 105.39	5.42 5.55	$e\,^3F_4 - s\,^3G_5$ $e\,^3F_3 - s\,^3G_4$
1 w	5 519.48	18 112.62	2.44	$e\,^3F_2 - s\,^3G_3$
m Fe II	—	18 196	6.55	$e\,^5D_4 - v\,^5F_5$
1	5 490.12	18 209.47	9.55	$e\,^5D_3 - v\,^5F_4$
1	5 489.73	18 210.77	0.69	$e\,^5D_2 - v\,^5F_3$
6 aff Fe III	5 485.53	18 224.70	4.76	$c\,^3G_4 - y\,^3H_5{}^*$
0 bl Fe II	5 483.49	18 231.48	1.24	$e\,^5D_1 - v\,^5F_2$
1 bl C II	5 478.52	18 248.04	7.93	$f\,^5D_4 - p\,^3F_4$
0	5 478.00	18 249.77	9.81	$b\,^1G_4 - z\,^1F_3$
7 bl Hg I	5 460.81	18 307.23	7.25	$c\,^3G_3 - y\,^3H_4{}^*$
0	5 457.23	18 319.22	9.22	$c\,^3G_4 - y\,^3H_4$
1 (h)	5 441.91	18 370.78	0.79	$5p\,^5P_2 - e\,^5D_2$
1	5 426.64	18 422.49	2.49	$h\,^5G_2 - w\,^5G_2$
2 s	5 420.00	18 445.06	5.41	$c\,^3G_4 - x\,^3F_4$
2 bl Fe II	5 415.61	18 460.01	0.01	$c\,^3G_5 - x\,^3F_4$
m Fe I, II	—	18 461	1.99	$5p\,^5P_2 - e\,^5D_3$
3 bl Fe II	5 402.06	18 506.31	6.40	$h\,^5G_6 - w\,^5G_6$
1	5 392.59	18 538.80	8.80	$h\,^5G_3 - w\,^5G_3$
1	5 388.40	18 553.23	3.31	$5p\,^5P_3 - e\,^5D_3$
4	5 382.36	18 574.06	4.07	$e\,^5G_2 - x\,^5G_2$
2	5 381.70	18 576.34	6.34	$e\,^5G_3 - x\,^5G_3$
5	5 381.22	18 578.00	7.57 7.90	$e\,^5G_2 - x\,^5G_3$ $e\,^5G_3 - x\,^5G_4$
2	5 381.00	18 578.74	8.60	$e\,^5G_4 - x\,^5G_5$

(Table 2, cont.)

Intensity	λ_{air} (obs)	σ (obs)	σ (calc)	Combination
4	5 380.44	18 580.67	0.64	$e\,^5G_4 - x\,^5G_4$
6	5 379.13	18 585.22	— 5.59	— $e\,^5G_5 - x\,^5G_6$
6	5 378.21	18 588.37	8.41	$e\,^5G_5 - x\,^5G_5$
11 l	5 375.47	18 597.85	7.85	$g\,^5G_6 - v\,^5F_5$
7	5 372.41	18 608.44	8.45	$e\,^5G_6 - x\,^5G_6$
10	5 368.06	18 623.53	3.53	$g\,^5G_4 - v\,^5F_3$
12	5 363.76	18 638.44	8.44 8.44	$g\,^5G_5 - v\,^5F_4$ $g\,^5G_2 - v\,^5F_1$
8	5 363.35	18 639.87	9.82	$g\,^5G_3 - v\,^5F_2$
3 l	5 360.26	18 650.64	0.62	$e\,^5F_1 - x\,^5G_2$
4 s	5 357.52	18 660.18	0.17	$e\,^5F_2 - x\,^5G_3$
3	5 354.98	18 669.00	8.93	$5p\,^5P_3 - e\,^5D_4$
12	5 353.77	18 673.24	— 3.41	— $e\,^5D_4 - v\,^5D_4$
4	5 352.66	18 677.12	7.14	$e\,^5F_3 - x\,^5G_4$
1	5 352.13	18 678.94	8.97	$h\,^5G_4 - w\,^5G_4$
5	5 350.78	18 683.68	3.49 3.70	$f\,^5F_2 - w\,^5D_2$ $f\,^5F_1 - w\,^5D_0$
3 w	5 348.49	18 691.66	1.61	$f\,^5F_1 - w\,^5D_1$
11	5 346.88	18 697.31	7.29 7.53	$f\,^5F_2 - w\,^5D_1$ $h\,^5G_5 - w\,^5G_5$
0	5 346.41	18 698.93	9.03	$g\,^5G_3 - v\,^5F_3$
5 s	5 344.42	18 705.91	5.81	$e\,^5F_4 - x\,^5G_5$
8	5 340.54	18 719.51	9.51	$f\,^5F_3 - w\,^5D_2$
m Fe I	—	18 721	1.65	$f\,^5F_3 - w\,^5D_3$
7	5 334.34	18 741.27	1.06 —	$g\,^5G_5 - v\,^5F_5$ —
8 bl Ne I	5 330.73	18 753.94	3.70 3.93	$f\,^5F_4 - w\,^5D_3$ $e\,^5F_5 - x\,^5G_6$
7	5 329.13	18 759.59	9.59	$h\,^5G_6 - u\,^5F_5$
10	5 322.74	18 782.09	2.09	$e\,^5I_4 - y\,^5H_3$
0	5 320.80	18 788.94	9.03	$e\,^5D_3 - v\,^5D_4$
1	5 319.19	18 794.64	4.64	$f\,^5F_4 - w\,^5D_4$
9	5 310.877	18 824.05	4.04	$e\,^5I_5 - y\,^5H_4$
7	5 309.923	18 827.43	7.43	$f\,^5F_5 - w\,^5D_4$
10	5 306.758	18 838.66	8.66	$4d\,^7D_3 - 5p\,^7P_2$*
m Fe II	—	18 840	0.89	$e\,^5I_4 - y\,^5H_4$
6	5 303.722	18 849.44	9.39	$e\,^5D_3 - v\,^5D_3$
14 w	5 302.599	18 853.43	3.42	$4d\,^7D_2 - 5p\,^7P_2$*
12	5 299.926	18 862.94	2.94	$4d\,^7D_1 - 5p\,^7P_2$*
11	5 298.115	18 869.39	9.39	$e\,^5I_6 - y\,^5H_5$
2	5 295.03	18 880.37	0.39	$e\,^5I_5 - y\,^5H_5$
m Fe II	—	18 898	8.08	$e\,^5G_3 - y\,^5H_3$
5	5 289.718	18 899.34	9.31	$e\,^5G_2 - y\,^5H_3$
12	5 284.829	18 916.82	6.83	$e\,^5I_{76} - y\,^5H_6$
16	5 282.295	18 925.90	5.89	$4d\,^7D_4 - 5p\,^7P_3$*

(Table 2, cont.)

Intensity	λ_{air} (obs)	σ (obs)	σ (calc)	Combination
0	5 277.30	18 943.82	3.82	$e\,^5I_7 - y\,^5H_7$
3	5 276.782	18 945.67	5.73	$e\,^5D_2 - v\,^5D_2$
15	5 276.475	18 946.78	6.77	$4d\,^7D_3 - 5p\,^7P_3$*
2	5 273.657	18 956.90	6.88	$e\,^5G_3 - y\,^5H_4$
14 bl Fe I	5 272.98	18 959.35	9.35 9.62	$e\,^5I_8 - y\,^5H_7$ $e\,^5G_4 - y\,^5H_4$
9	5 272.370	18 961.53	1.53	$4d\,^7D_2 - 5p\,^7P_3$*
7 bl Fe I	5 266.66	18 982.07	1.91 2.07	$e\,^5F_2 - y\,^5H_3$ $e\,^5D_1 - v\,^5D_1$
8 bl Fe II	5 257.23	19 016.13	5.97	$e\,^5G_4 - y\,^5H_5$
1	5 256.09	19 020.25	0.28	$h\,^5G_5 - u\,^5F_5$
3 s	5 254.51	19 025.96	5.78	$e\,^5G_5 - y\,^5H_5$
0	5 246.17	19 056.21	6.12	$e\,^5F_3 - y\,^5H_4$
18	5 243.306	19 066.63	6.63	$4d\,^7D_5 - 5p\,^7P_4$*
4 s	5 241.45	19 073.40	3.22	$e\,^5G_5 - y\,^5H_6$
6	5 240.548	19 076.66	6.64	$h\,^5G_5 - u\,^5F_4$
10	5 235.661	19 094.47	4.48	$4d\,^7D_4 - 5p\,^7P_4$*
2	5 235.218	19 096.09	6.08	$e\,^5G_6 - y\,^5H_6$
7	5 230.783	19 112.28	2.31	$e\,^5H_7 - x\,^5G_6$
6 bl Fe I	5 229.92	19 115.45	5.36	$4d\,^7D_3 - 5p\,^7P_4$*
2	5 229.416	19 117.27	7.29	$e\,^5H_6 - x\,^5G_6$
4	5 229.143	19 118.27	8.27	$f\,^5H_4 - w\,^5G_3$
6 w	5 228.63	19 120.14	0.11 0.14	$e\,^5H_6 - x\,^5G_5$ $f\,^5H_5 - w\,^5G_4$
5 bl Fe II	5 227.81	19 123.14	3.07	$e\,^5G_6 - y\,^5H_7$
4 bl Fe II	5 226.16	19 129.20	9.01	$e\,^5H_5 - x\,^5G_5$
5	5 225.64	19 131.07	1.05	$e\,^5H_5 - x\,^5G_4$
7 bl Fe II	5 222.42	19 142.90	2.84 3.18	$e\,^5H_4 - x\,^5G_3$ $e\,^5F_4 - y\,^5H_5$
2	5 222.000	19 144.42	4.40	$e\,^5H_4 - x\,^5G_4$
2 (h)	5 221.45	19 146.43	6.41	$h\,^5G_4 - u\,^5F_4$
5	5 219.124	19 154.97	4.94	$e\,^5H_3 - x\,^5G_2$
8	5 218.12	19 158.67	8.44 8.61 8.72	$e\,^5H_3 - x\,^5G_3$ $f\,^5H_3 - w\,^5G_2$ $f\,^5H_7 - w\,^5G_6$
2 (h)	5 211.84	19 181.75	1.80	$h\,^5G_3 - u\,^5F_3$
4 s bl Fe II	5 210.46	19 186.83	6.83	$f\,^5H_6 - w\,^5G_5$
m Fe II	—	19 240	0.52	$h\,^5G_4 - u\,^5F_3$
8	5 194.07	19 247.37	7.03	$a\,^5D_2 - 4p\,^5P_3$*
5	5 193.85	19 248.18	7.96	$a\,^5D_3 - 4p\,^5P_3$*
1 (h)	5 187.61	19 271.33	1.27	$h\,^5G_3 - u\,^5F_2$
3 bl Fe II	5 178.60	19 304.86	5.10	$h\,^5G_2 - u\,^5F_1$
12	5 156.117	19 389.04	9.06	$a\,^5D_4 - 4p\,^5P_3$*
7 bl Fe II	5 149.38	19 414.40	4.45	$e\,^5G_6 - w\,^5F_5$
7 l	5 136.09	19 464.65	4.55 4.58	$e\,^5G_5 - w\,^5F_4$ $e\,^5H_4 - y\,^5H_3$
4	5 131.999	19 480.16	0.18	$e\,^5H_3 - y\,^5H_3$

(Table 2, cont.)

Intensity	λ_{air} (obs)	σ (obs)	σ (calc)	Combination
6	5 127.638	19 496.72	6.75	$a\,^5D_2 - 4p\,^5P_2$*
9	5 127.352	19 497.81	7.68	$a\,^5D_3 - 4p\,^5P_2$*
5	5 125.612	19 504.43	4.46	$e\,^5G_4 - w\,^5F_3$
0 (h)	5 124.40	19 509.04	8.99	$e\,^5F_4 - w\,^5F_5$
2	5 124.16	19 509.97	10.03	$e\,^5H_5 - y\,^5H_4$
3	5 122.98	19 514.45	4.42	$c\,^3D_3 - y\,^3F_4$
5	5 120.65	19 523.35	3.38	$e\,^5H_4 - y\,^5H_4$
6 s	5 116.44	19 539.41	9.43	$e\,^5G_3 - w\,^5F_2$
3 aff Fe III	5 114.64	19 546.26	6.32	$a\,^5D_1 - 4p\,^5P_2$*
2 (h)	5 113.33	19 551.28	1.24	$e\,^5F_3 - w\,^5F_4$
3	5 111.719	19 557.44	7.48	$e\,^5H_6 - y\,^5H_5$
9	5 111.068	19 559.93	9.93	$e\,^5F_5 - w\,^5F_5$
5 l	5 109.38	19 566.41	6.38	$e\,^5H_5 - y\,^5H_5$
3	5 108.86	19 568.38	8.46	$e\,^5G_2 - w\,^5F_1$
7	5 105.331	19 581.91	1.95	$e\,^5F_4 - w\,^5F_4$
2 (h) bl Fe II	5 104.40	19 585.48	5.55	$e\,^5F_2 - w\,^5F_3$
m Fe II	—	19 599	9.94	$e\,^5H_7 - y\,^5H_6$
2 bl Fe II	5 100.35	19 601.03	0.96	$e\,^5F_3 - w\,^5F_3$
6	5 099.327	19 604.97	4.92	$e\,^5H_6 - y\,^5H_6$
0	5 096.15	19 617.19	7.21	$e\,^5F_1 - w\,^5F_2$
3	5 094.577	19 623.25	3.26	$e\,^5F_2 - w\,^5F_2$
m Fe II	—	19 626	6.93	$e\,^5H_7 - y\,^5H_7$
2	5 092.368	19 631.76	1.67	$e\,^5F_4 - w\,^5F_3$
			1.96	$5p\,^5P_1 - f\,^5D_0$
2 (h)	5 090.57	19 638.70	8.67	$e\,^5F_3 - w\,^5F_2$
2	5 088.93	19 645.01	5.01	$e\,^5F_1 - w\,^5F_1$
m Fe II	—	19 651	1.06	$e\,^5F_2 - w\,^5F_1$
7	5 086.718	19 653.56	3.63	$a\,^5D_2 - 4p\,^5P_1$*
m Fe II	—	19 654	4.34	$5p\,^5P_1 - f\,^5D_1$
3 (h) bl Fe I	5 083.67	19 665.36	5.28	$5p\,^5P_1 - f\,^5D_2$
8 bl Fe II	5 078.92	19 683.75	3.73	$5p\,^5P_3 - f\,^5D_4$
6	5 077.671	19 688.58	8.59	$5p\,^5P_2 - f\,^5D_3$
7	5 073.896	19 703.23	3.20	$a\,^5D_1 - 4p\,^5P_1$*
4	5 069.158	19 721.64	1.65	$5p\,^5P_2 - f\,^5D_2$
3	5 066.539	19 731.84	1.75	$c\,^3D_2 - y\,^3F_3$
6	5 063.459	19 743.84	3.99	$a\,^5D_0 - 4p\,^5P_1$*
0	5 057.56	19 766.87	6.60	$c\,^3D_2 - y\,^3F_2$
2	5 054.786	19 777.72	7.48	$c\,^3D_1 - y\,^3F_2$
4	5 054.230	19 779.89	9.91	$5p\,^5P_3 - f\,^5D_3$
0	5 045.79	19 812.98	2.97	$5p\,^5P_3 - f\,^5D_2$
1 (h)	4 996.55	20 008.22	8.48	$c\,^3G_3 - z\,^1G_4$
0 bl Fe II	4 824.86	20 720.21	0.39	$e\,^5P_3 - v\,^5D_4$
0	4 821.63	20 734.08	4.16	$e\,^5P_2 - v\,^5D_2$
0	4 810.79	20 780.80	0.75	$e\,^5P_3 - v\,^5D_3$
1	4 752.72	21 034.72	4.96	$a\,^3S_1 - z\,^3P_2$
3	4 570.341	21 874.07	4.19	$b\,^1D_2 - z\,^1D_2$*

(Table 2, cont.)

Intensity	λ_{air} (obs)	σ (obs)	σ (calc)	Combination
5	4 569.722	21 877.04	6.85	$b\,{}^{1}G_{4} - y\,{}^{1}G_{4}$*
1	4 442.595	22 503.05	2.78	$b\,{}^{1}G_{4} - y\,{}^{1}F_{3}$
0	4 441.41	22 509.06	9.07	$b\,{}^{1}D_{2} - x\,{}^{3}F_{3}$
2	4 436.470	22 534.11	4.10	$b\,{}^{1}D_{2} - x\,{}^{3}F_{2}$
9	4 431.015	22 561.86	1.84	$a\,{}^{5}P_{2} - 4p\,{}^{5}P_{3}$*
12	4 419.599	22 620.14	0.15	$a\,{}^{5}P_{3} - 4p\,{}^{5}P_{3}$*
4	4 404.150	22 699.48	9.42	$c\,{}^{3}D_{2} - y\,{}^{3}P_{1}$
2	4 402.050	22 710.31	0.30	$c\,{}^{3}D_{1} - y\,{}^{3}P_{1}$
9	4 395.759	22 742.81	2.83 3.04	$a\,{}^{5}P_{1} - 4p\,{}^{5}P_{2}$* $b\,{}^{1}G_{4} - v\,{}^{3}F_{3}$
5	4 382.508	22 811.58	1.56	$a\,{}^{5}P_{2} - 4p\,{}^{5}P_{2}$*
2 (h)	4 377.618	22 837.06	7.03	$v\,{}^{3}H_{6} - f\,{}^{3}G_{5}$
18 (h)	4 372.81	22 862.15	2.1 2.3	$4f\,{}^{5}F_{5} - 5g\,{}^{5}G_{6}$* $4f\,{}^{5}F_{5} - 5g\,{}^{5}G_{5}$*
14 (h) bl C II	4 372.53	22 863.64	3.6 3.8	$4f\,{}^{5}F_{4} - 5g\,{}^{5}G_{5}$* $4f\,{}^{5}F_{4} - 5g\,{}^{5}G_{4}$*
11 (h) bl C II	4 372.31	22 864.79	4.8	$4f\,{}^{5}F_{3} - 5g\,{}^{5}G_{43}$*
9 (h)	4 372.14	22 865.66	5.7 5.9	$4f\,{}^{5}F_{2} - 5g\,{}^{5}G_{3}$* $4f\,{}^{5}F_{2} - 5g\,{}^{5}G_{2}$*
9 (h)	4 372.04	22 866.19	6.2	$4f\,{}^{5}F_{1} - 5g\,{}^{5}G_{2}$*
4	4 371.339	22 869.86	9.87	$a\,{}^{5}P_{3} - 4p\,{}^{5}P_{2}$*
2	4 365.642	22 899.70	9.71	$a\,{}^{5}P_{1} - 4p\,{}^{5}P_{1}$*
6	4 352.568	22 968.49	8.44	$a\,{}^{5}P_{2} - 4p\,{}^{5}P_{1}$*
6	4 348.794	22 988.42	8.35	$c\,{}^{3}D_{3} - y\,{}^{3}P_{2}$
3 (h) s bl Fe II	4 344.43	23 011.54	1.28	$c\,{}^{3}D_{2} - y\,{}^{3}P_{2}$
0 (h)	4 340.25	23 033.65	3.50	$u\,{}^{3}H_{4} - h\,{}^{5}F_{4}$
4 (h)	4 339.396	23 038.20	8.25	$u\,{}^{3}H_{5} - h\,{}^{5}F_{5}$
0 (h)	4 338.31	23 043.97	3.86	$u\,{}^{3}H_{4} - i\,{}^{5}G_{5}$
4 (h) l	4 337.32	23 049.22	9.40	$u\,{}^{3}H_{4} - h\,{}^{5}F_{3}$
3 (h) aff Fe III	4 336.65	23 052.80	2.67	$b\,{}^{1}G_{4} - v\,{}^{3}F_{4}$
2 (h)	4 334.53	23 064.09	4.17	$u\,{}^{3}H_{6} - h\,{}^{5}F_{5}$
3 (h)	4 334.313	23 065.22	5.14 5.21	$u\,{}^{3}H_{4} - i\,{}^{5}G_{4}$ $u\,{}^{3}H_{4} - i\,{}^{5}G_{3}$
1 w	4 333.00	23 072.21	2.37	$v\,{}^{3}H_{5} - f\,{}^{3}G_{4}$
3 (h)	4 330.585	23 085.08	5.06	$v\,{}^{3}H_{5} - f\,{}^{3}G_{5}$
3 (h) aff Fe III	4 326.87	23 104.91	5.13	$u\,{}^{3}H_{5} - i\,{}^{5}G_{4}$
2	4 316.471	23 160.56	0.52	$b\,{}^{3}F_{2} - z\,{}^{5}G_{2}$
3 (h)	4 316.071	23 162.71	2.81	$b\,{}^{3}F_{4} - z\,{}^{5}G_{4}$
0	4 313.64	23 175.77	6.00	$c\,{}^{3}G_{3} - x\,{}^{3}H_{4}$
2 (h)	4 311.97	23 184.73	4.67	$p\,{}^{3}F_{2} - g\,{}^{5}D_{3}$
2 (h) s	4 311.41	23 187.74	7.97	$c\,{}^{3}G_{4} - x\,{}^{3}H_{4}$
20 (h)	4 310.362	23 193.39	3.4	$4f\,{}^{7}F_{6} - 5g\,{}^{7}G_{76}$*
18 (h)	4 304.775	23 223.48	3.5 3.6	$4f\,{}^{7}F_{5} - 5g\,{}^{7}G_{6}$* $4f\,{}^{7}F_{5} - 5g\,{}^{7}G_{5}$*
16 (h)	4 296.854	23 266.29	6.3	$4f\,{}^{7}F_{4} - 5g\,{}^{7}G_{54}$*
3 (h)	4 295.018	23 276.24	6.25	$s\,{}^{3}D_{2} - g\,{}^{5}D_{3}$
1 (h) aff Fe III	4 293.67	23 283.58	3.83	$f\,{}^{5}G_{5} - v\,{}^{5}F_{4}$

(Table 2, cont.)

Intensity	λ_{air} (obs)	σ (obs)	σ (calc)	Combination
1 (h)	4 292.00	23 292.63	2.64	$v\ {}^3H_4 - f\ {}^3G_4$
14 (h)	4 286.161	23 324.34	4.3	$4f\ {}^7F_3 - 5g\ {}^7G_4{}^*$
			4.5	$4f\ {}^7F_3 - 5g\ {}^7G_3{}^*$
12 (h)	4 273.405	23 393.96	3.9	$4f\ {}^7F_2 - 5g\ {}^7G_3{}^*$
			4.1	$4f\ {}^7F_2 - 5g\ {}^7G_2{}^*$
3 (h) s	4 268.15	23 422.75	2.56	$f\ {}^5G_6 - v\ {}^5F_5$
			3.75	$c\ {}^3G_4 - x\ {}^3H_5$
3	4 266.78	23 430.28	0.33	$w\ {}^5F_1 - i\ {}^5G_2$
0	4 265.35	23 438.12	8.35	$c\ {}^3G_5 - x\ {}^3H_5$
m Fe II	—	23 446	6.27	$w\ {}^5F_1 - h\ {}^5F_2$
3	4 263.385	23 448.94	8.94	$w\ {}^5F_1 - h\ {}^5F_1$
4 s	4 263.18	23 450.07	0.08	$w\ {}^5F_2 - h\ {}^5F_3$
0	4 261.73	23 458.03	8.13	$w\ {}^5F_2 - i\ {}^5G_2$
7 (h)	4 261.398	23 459.87		$4f\ {}^7F_1 - 5g\ {}^7G_{21}$
3	4 260.31	23 465.88	5.89	$w\ {}^5F_2 - i\ {}^5G_3$
1 (h) aff Fe III	4 259.18	23 472.12	1.89	$w\ {}^5F_3 - h\ {}^5F_4$
4	4 258.818	23 474.08	4.07	$w\ {}^5F_2 - h\ {}^5F_2$
2 (h) bl Fe II	4 258.33	23 476.80	6.74	$w\ {}^5F_2 - h\ {}^5F_1$
3	4 256.334	23 487.79	7.79	$w\ {}^5F_3 - h\ {}^5F_3$
4	4 253.478	23 503.56	3.53	$w\ {}^5F_3 - i\ {}^5G_4$
			3.60	$w\ {}^5F_3 - i\ {}^5G_3$
2	4 251.982	23 511.82	1.78	$w\ {}^5F_3 - h\ {}^5F_2$
3	4 251.485	23 514.57	4.61	$s\ {}^3G_5 - g\ {}^3G_5$
4 bl Fe I	4 250.20	23 521.71	1.61	$w\ {}^5F_4 - h\ {}^5F_4$
12	4 249.717	23 524.36	4.27	$s\ {}^3G_4 - g\ {}^3G_5$
			—	—
8	4 248.777	23 529.56	9.58	$5p\ {}^5P_1 - 6s\ {}^5S_2$
8	4 248.339	23 531.99	1.97	$w\ {}^5F_4 - i\ {}^5G_5$
2	4 247.867	23 534.60	4.58	$s\ {}^3G_5 - g\ {}^3G_4$
m Fe I	—	23 537	7.17	$s\ {}^3G_4 - g\ {}^3G_3$
			7.51	$w\ {}^5F_4 - h\ {}^5F_3$
2 bl Fe I	4 246.14	23 544.18	4.24	$s\ {}^3G_4 - g\ {}^3G_4$
1	4 245.72	23 546.53	6.64	$s\ {}^3G_3 - g\ {}^3G_3$
2 (h)	4 244.506	23 553.24	3.25	$w\ {}^5F_4 - i\ {}^5G_4$
8	4 243.406	23 559.34	9.33	$w\ {}^5F_5 - h\ {}^5F_5$
8	4 240.666	23 574.56	4.54	$w\ {}^5F_5 - i\ {}^5G_6$
9	4 238.619	23 585.95	5.95	$5p\ {}^5P_2 - 6s\ {}^5S_2$
0 bl Fe I	4 237.09	23 594.48	4.57	$w\ {}^5F_5 - h\ {}^5F_4$
11	4 222.269	23 677.28	7.27	$5p\ {}^5P_3 - 6s\ {}^5S_2$
3 bl Fe I	4 220.23	23 688.69	8.81	$t\ {}^3D_3 - e\ {}^3F_4$
2	4 213.07	23 728.99	9.24	$c\ {}^3G_5 - x\ {}^3G_5$
9	4 210.672	23 742.49	2.48	$y\ {}^5H_7 - g\ {}^5H_7$
4	4 209.406	23 749.63	9.72	$v\ {}^5D_4 - g\ {}^5D_4$
2 bl Fe I	4 207.06	23 762.86	3.17	$c\ {}^3G_4 - x\ {}^3G_4$
2	4 205.908	23 769.38	9.16	$b\ {}^3G_5 - z\ {}^5G_5{}^*$
			9.47	$y\ {}^5H_6 - g\ {}^5H_7$
6	4 204.511	23 777.28	7.19	$v\ {}^5D_3 - g\ {}^5D_3$
			7.77	$c\ {}^3G_5 - x\ {}^3G_4$

(Table 2, cont.)

Intensity	λ_{air} (obs)	σ (obs)	σ (calc)	Combination
5	4 203.826	23 781.16	1.11	$y\,{}^5H_6 - g\,{}^5H_6$
2 (h)	4 195.470	23 828.52	8.55	$y\,{}^5H_5 - g\,{}^5H_6$
3	4 194.703	23 832.87	2.85	$v\,{}^5D_2 - g\,{}^5D_2$
6	4 194.11	23 836.27	6.01 6.58	$c\,{}^3G_3 - x\,{}^3G_3$ $v\,{}^5D_1 - g\,{}^5D_1$
6	4 193.95	23 837.15	7.21	$y\,{}^5H_5 - g\,{}^5H_5$
8	4 189.112	23 864.68	4.64 —	$p\,{}^3F_3 - f\,{}^3D_3$ —
3	4 188.899	23 865.90	5.92	$y\,{}^5H_7 - i\,{}^5G_6$
4 bl Fe I	4 184.98	23 888.25	8.22	$y\,{}^5H_4 - g\,{}^5H_4$
3	4 184.159	23 892.93	2.91	$y\,{}^5H_6 - i\,{}^5G_6$
5	4 184.005	23.893.81	3.42 3.56	$b\,{}^3G_4 - z\,{}^5G_5$* $y\,{}^5H_4 - g\,{}^5H_5$
2	4 181.510	23 908.06	7.85	$b\,{}^3G_3 - z\,{}^5G_3$
m Fe II	—	23 923	3.30 3.37	$y\,{}^5H_6 - i\,{}^5G_5$ $p\,{}^3F_2 - f\,{}^3D_1$
0	4 178.54	23 925.08	5.14	$y\,{}^5H_5 - h\,{}^5F_5$
4 aff Fe III	4 177.87	23 928.89	8.93	$p\,{}^3F_3 - f\,{}^3D_2$
5	4 177.403	23 931.57	1.53	$p\,{}^3F_4 - f\,{}^3D_3$
2	4 176.102	23 939.03	9.12	$c\,{}^3G_5 - x\,{}^3H_6$
3	4 174.809	23 946.44	6.44	$y\,{}^5H_3 - g\,{}^5H_3$
13	4 174.259	23 949.59	9.59	$y\,{}^5H_7 - f\,{}^5I_8$
1	4 173.760	23 952.46	2.45	$s\,{}^3D_1 - f\,{}^3D_1$
3	4 170.582	23 970.71	0.74	$y\,{}^5H_5 - i\,{}^5G_5$
2	4 169.665	23 975.99	— 6.33	— $y\,{}^5H_7 - f\,{}^5I_7$
7	4 168.449	23 982.98	2.98	$5p\,{}^7P_4 - 5d\,{}^7D_3$*
13	4 166.843	23 992.22	1.60 2.02 2.24	$t\,{}^3D_2 - e\,{}^3F_3$ $y\,{}^5H_5 - i\,{}^5G_4$ $5p\,{}^7P_4 - 5d\,{}^7D_4$*
9	4 164.921	24 003.29	3.32	$y\,{}^5H_6 - f\,{}^5I_7$
18	4 164.731	24 004.39	4.39	$5p\,{}^7P_4 - 5d\,{}^7D_5$*
4	4 163.35	24 012.36	2.45	$s\,{}^3D_3 - f\,{}^3D_3$
2 (h)	4 163.21	24 013.18	3.38	$y\,{}^5H_6 - f\,{}^5I_6$
2 aff Fe III	4 162.89	24 015.02	4.95	$s\,{}^3D_2 - f\,{}^3D_1$
2 aff Fe III	4 162.59	24 016.71	6.73	$y\,{}^5H_4 - h\,{}^5F_4$
6	4 161.353	24 023.87	3.84	$s\,{}^3D_2 - f\,{}^3D_2$
2	4 159.843	24 032.59	2.63	$y\,{}^5H_4 - h\,{}^5F_3$
1	4 157.106	24 048.42	8.37 8.44	$y\,{}^5H_4 - i\,{}^5G_4$ $y\,{}^5H_4 - i\,{}^5G_3$
2 (h) aff Fe III	4 155.34	24 058.61	8.53	$y\,{}^5H_5 - f\,{}^5I_5$
9	4 154.963	24 060.82	0.82	$y\,{}^5H_5 - f\,{}^5I_6$
5 bl Fe I	4 152.16	24 077.08	6.74 —	$s\,{}^3D_3 - f\,{}^3D_2$ —
4 w	4 148.746	24 096.87	6.65 6.7	$w\,{}^5F_4 - j\,{}^5G_5$ $b\,{}^1G_4 - u\,{}^3F_4$
2	4 148.316	24 099.37	9.26 9.48	$x\,{}^5P_2 - f\,{}^5P_3$ $y\,{}^5H_3 - i\,{}^5G_2$

(Table 2, cont.)

Intensity	λ_{air} (obs)	σ (obs)	σ (calc)	Combination
2 w	4 147.17	24 106.04	5.73	$y\,^5H_4 - f\,^5I_4$
0	4 146.97	24 107.19	7.24	$y\,^5H_3 - i\,^5G_3$
8	4 145.641	24 114.92	4.88	$y\,^5H_4 - f\,^5I_5$
4 w	4 142.638	24 132.40	2.30	$w\,^5F_5 - j\,^5\mathrm{G}_6$
3	4 142.159	24 135.19	5.18	$t\,^3D_1 - e\,^3F_2$
9	4 140.481	24 144.97	4.97	$5p\,^7P_3 - 5d\,^7D_2$*
13	4 139.349	24 151.57	1.57	$5p\,^7P_3 - 5d\,^7D_3$*
15	4 137.762	24 160.84	0.83	$5p\,^7P_3 - 5d\,^7D_4$*
7	4 137.133	24 164.51	4.53	$y\,^5H_3 - f\,^5I_4$
m Fe I	—	24 165	5.23	$x\,^5P_2 - f\,^5P_2$
2	4 135.821	24 172.18	2.15	$x\,^5P_1 - f\,^5P_1$
6 w	4 134.268	24 181.26	1.40	$x\,^5P_3 - f\,^5P_3$
4	4 126.996	24 223.87	3.89	$x\,^5P_2 - f\,^5P_1$
4	4 126.518	24 226.67	6.58	$v\,^5F_5 - g\,^5D_4$
1 (h)	4 123.00	24 247.37	7.37	$x\,^5P_3 - f\,^5P_2$
11	4 122.780	24 248.64	8.64	$5p\,^7P_2 - 5d\,^7D_1$*
11	4 122.025	24 253.08	3.08	$5p\,^7P_2 - 5d\,^7D_2$*
6	4 121.345	24 257.08	7.10	$x\,^5G_6 - g\,^5H_7$
10 bl He I	4 120.90	24 259.70	9.68	$5p\,^7P_2 - 5d\,^7D_3$*
7 w	4 119.858	24 265.84	5.92	$x\,^5G_5 - g\,^5H_6$
5 w	4 119.363	24 268.75	8.74 8.76	$x\,^5G_6 - g\,^5H_6$ $x\,^5G_3 - g\,^5H_4$
5	4 118.866	24 271.68	1.68	$x\,^5G_2 - g\,^5H_3$
6	4 118.716	24 272.56	2.54	$x\,^5G_4 - g\,^5H_5$
5	4 118.401	24 274.42	— 4.58	— $x\,^5G_5 - g\,^5H_5$
0 bl Fe I	4 109.09	24 329.42	9.20	$v\,^5F_4 - g\,^5D_4$
3	4 105.473	24 350.85	0.80	$u\,^3H_4 - g\,^3G_3$
1 (h)	4 103.507	24 362.52	2.51 2 58	$x\,^5G_5 - h\,^5F_5$ $b\,^1G_4 - u\,^3F_3$
8	4 103.037	24 365.31	5.33	$x\,^5G_6 - h\,^5F_5$
3 (h)	4 100.964	24 377.63	— 7.72	— $x\,^5G_5 - i\,^5G_6$
6	4 100.479	24 380.52	0.54	$x\,^5G_6 - i\,^5G_6$
0	4 097.92	24 395.74	5.71	$x\,^5G_4 - h\,^5F_4$
7	4 097.584	24 397.74	7.75 7.86	$x\,^5G_5 - h\,^5F_4$ $u\,^3H_5 - g\,^3G_4$
3	4 096.54	24 403.93	3.81	$u\,^3H_6 - g\,^3G_5$
1 (h)	4 096.18	24 406.10	6.07	$x\,^5G_4 - i\,^5G_5$
5 bl Fe I	4 095.87	24 407.94	8.11	$x\,^5G_5 - i\,^5G_5$
4 (h)	4 095.36	24 410.99	0.93 —	$x\,^5G_6 - i\,^5G_5$ —
5	4 095.26	24 411.60	1.61	$x\,^5G_4 - h\,^5F_3$
2	4 094.995	24 413.16	3.17	$x\,^5G_3 - h\,^5F_3$
3 aff Fe III	4 094.36	24 416.97	7.03	$v\,^5F_4 - g\,^5D_3$
0	4 093.62	24 421.34	1.22	$x\,^5G_3 - i\,^5G_2$
6	4 093.224	24 423.73	3.68	$y\,^5H_7 - j\,^5G_6$

(Table 2, cont.)

Intensity	λ_{air} (obs)	σ (obs)	σ (calc)	Combination
3	4 093.048	24 424.78	4.72	$x\,{}^5G_2 - i\,{}^5G_2$
4	4 092.628	24 427.28	7.35	$x\,{}^5G_4 - i\,{}^5G_4$
			7.42	$x\,{}^5G_4 - i\,{}^5G_3$
7	4 092.339	24 429.01	8.91	$x\,{}^5G_3 - i\,{}^5G_4$
			8.98	$x\,{}^5G_3 - i\,{}^5G_3$
			9.39	$x\,{}^5G_5 - i\,{}^5G_4$
0	4 091.78	24 432.36	2.48	$x\,{}^5G_2 - i\,{}^5G_3$
5	4 090.986	24 437.09	7.16	$x\,{}^5G_3 - h\,{}^5F_2$
1	4 090.427	24 440.42	—	—
			0.66	$x\,{}^5G_2 - h\,{}^5F_2$
4 (h) aff Fe III	4 089.94	24 443.37	3.33	$x\,{}^5G_2 - h\,{}^5F_1$
1 (h)	4 086.365	24 464.72	4.61	$b\,{}^3F_3 - z\,{}^5H_3$
1	4 082.76	24 486.32	6.27	$x\,{}^5G_3 - f\,{}^5I_4$
6	4 082.474	24 488.03	7.98	$y\,{}^5H_6 - j\,{}^5G_5$
1 (h)	4 081.983	24 490.99	0.95	$x\,{}^5G_6 - f\,{}^5I_7$
1	4 081.513	24 493.80	3.86	$x\,{}^5G_4 - f\,{}^5I_5$
12	4 081.005	24 496.85	6.84	$5p\,{}^7P_4 - 6s\,{}^7S_3$*
m Fe I	—	24 498	8.19	$x\,{}^5G_5 - f\,{}^5I_6$
2 (h)	4 079.299	24 507.09	7.09	$v\,{}^5F_3 - g\,{}^5D_3$
m Fe I	—	24 552	2.81	$y\,{}^5H_5 - j\,{}^5G_4$
4	4 069.213	24 567.84	7.89	$v\,{}^5F_3 - g\,{}^5D_2$
8 w	4 065.977	24 587.39	7.41	$v\,{}^5F_2 - g\,{}^5D_1$
4 (h)	4 061.731	24 613.09	3.11	$y\,{}^5H_4 - j\,{}^5G_3$
1	4 060.005	24 623.56	3.54	$v\,{}^5F_1 - g\,{}^5D_1$
6 bl Fe II	4 057.50	24 638.75	8.39	$b\,{}^3F_4 - z\,{}^5H_4$
11	4 053.114	24 665.42	5.43	$5p\,{}^7P_3 - 6s\,{}^7S_3$*
4	4 052.511	24 669.09	9.07	$y\,{}^5H_3 - j\,{}^5G_2$
2 bl Fe I	4 041.86	24 734.08	3.88	$a\,{}^1G_4 - z\,{}^3F_3$
6	4 039.151	24 750.69	0.63	$c\,{}^3F_2 - z\,{}^3F_2$*
2	4 035.810	24 771.18	1.11	$c\,{}^3F_3 - z\,{}^3F_2$
10	4 035.425	24 773.54	3.54	$5p\,{}^7P_2 - 6s\,{}^7S_3$*
2 (h)	4 025.652	24 833.68	3.59	$c\,{}^3F_2 - z\,{}^3F_3$
4	4 024.999	24 837.71	7.60	$a\,{}^1G_4 - z\,{}^3F_4$*
8	4 022.326	24 854.21	4.07	$c\,{}^3F_3 - z\,{}^3F_3$*
1	4 021.725	24 857.92	7.77	$c\,{}^3F_4 - z\,{}^3F_3$
4 w	4 016.489	24 890.33	0.27	$a\,{}^3S_1 - y\,{}^5P_1$
7	4 008.771	24 938.25	8.30	$x\,{}^5G_6 - j\,{}^5G_6$
2 w (h)	4 006.92	24 949.79	9.89	$f\,{}^3G_5 - t\,{}^3H_6$
2	4 005.613	24 957.91	7.79	$c\,{}^3F_3 - z\,{}^3F_4$
			8.16	$b\,{}^1G_4 - w\,{}^3H_5$
8	4 005.022	24 961.60	1.49	$c\,{}^3F_4 - z\,{}^3F_4$*
2	4 003.543	24 970.82	0.75	$x\,{}^5G_4 - j\,{}^5G_5$
7	4 003.231	24 972.76	2.79	$x\,{}^5G_5 - j\,{}^5G_5$
5	4 002.367	24 978.15	8.16	$b\,{}^1D_2 - y\,{}^3G_3$
1 (h)	4 001.149	24 985.76	5.79	$f\,{}^3G_5 - t\,{}^3H_5$
5 l	4 000.767	24 988.14	8.14	$x\,{}^5G_4 - j\,{}^5G_4$
6	3 999.88	24 993.69	3.65	$x\,{}^5G_3 - j\,{}^5G_3$
6	3 999.79	24 994.24	4.31	$x\,{}^5G_2 - j\,{}^5G_2$

(Table 2, cont.)

Intensity	λ_{air} (obs)	σ (obs)	σ (calc)	Combination
1 (h)	3 999.10	24 998.56	8.48	$f\ ^3G_4 - t\ ^3H_5$
6	3 993.146	25 035.83	5.54 —	$f\ ^3G_4 - t\ ^3H_4$ —
2 (h)	3 984.812	25 088.19	8.16	$y\ ^5S_2 - f\ ^5P_3$
1 (h)	3 984.25	25 091.72	1.82	$f\ ^3G_3 - t\ ^3H_4$
7	3 980.093	25 117.93	7.94	$5p\ ^5P_1 - 5d\ ^5D_0{}^*$
10 w	3 979.423	25 122.16	2.18	$5p\ ^5P_1 - 5d\ ^5D_1{}^*$
8	3 978.406	25 128.59	8.63	$5p\ ^5P_1 - 5d\ ^5D_2{}^*$
6 bl Fe I	3 976.95	25 137.81	8.01	$c\ ^3G_5 - w\ ^3G_5{}^*$
0 bl Fe I	3 974.39	25 154.00	4.13	$y\ ^5S_2 - f\ ^5P_2$
0 (h)	3 972.65	25 164.99	4.96	$b\ ^3G_4 - z\ ^5H_3$
5	3 971.126	25 174.65	4.62	$w\ ^5D_4 - f\ ^5P_3$
4	3 970.511	25 178.55	8.55	$5p\ ^5P_2 - 5d\ ^5D_1$
9	3 969.490	25 185.03	5.00	$5p\ ^5P_2 - 5d\ ^5D_2{}^*$
11	3 968.718	25 189.93	9.93	$5p\ ^5P_2 - 5d\ ^5D_3{}^*$
0 (h) aff Fe III	3 959.13	25 250.94	1.03	$b\ ^3G_3 - z\ ^5H_3$
1	3 955.67	25 273.01	3.25	$c\ ^3G_3 - w\ ^3G_4$
3	3 955.150	25 276.34	6.32	$5p\ ^5P_3 - 5d\ ^5D_2$
16	3 954.326	25 281.61	1.25 1.53 1.70	$5p\ ^5P_3 - 5d\ ^5D_3{}^*$ $w\ ^5D_3 - f\ ^5P_2$ $5p\ ^5P_3 - 5d\ ^5D_4{}^*$
6	3 953.814	25 284.88	5.22	$c\ ^3G_4 - w\ ^3G_4{}^*$
1	3 951.503	25 299.67	9.82	$c\ ^3G_5 - w\ ^3G_4$
1 (h)	3 949.28	25 313.92	3.89	$v\ ^5F_2 - f\ ^3D_2$
6 bl Fe I	3 947.05	25 328.23	7.33 8.53 8.55	$b\ ^3G_4 - z\ ^5H_4{}^*$ $w\ ^5D_1 - f\ ^5P_1$ $c\ ^3G_3 - w\ ^3G_3{}^*$
m Fe I	—	25 340	0.52 1.13	$c\ ^3G_4 - w\ ^3G_3{}^*$ $v\ ^5F_1 - f\ ^3D_1$
m Fe I	—	25 342	2.33	$w\ ^5D_2 - f\ ^5P_1$
1	3 912.822	25 549.77	9.68	$c\ ^3D_1 - z\ ^1D_2$
1 (h)	3 845.827	25 994.84	4.88	$b\ ^3F_4 - z\ ^5F_4$
4 bl Fe I	3 828.43	26 112.93	3.15	$c\ ^3G_4 - y\ ^1F_3{}^*$
1	3 795.255	26 341.21	1.44	$c\ ^3G_3 - v\ ^3F_3$
6	3 793.526	26 353.22	3.41	$c\ ^3G_4 - v\ ^3F_3{}^*$
5	3 789.370	26 382.12	1.89	$b\ ^1G_4 - t\ ^3F_4$
7	3 786.997	26 398.65	9.06	$c\ ^3G_3 - v\ ^3F_2{}^*$
1	3 785.543	26 408.79	8.78	$b\ ^3G_5 - z\ ^5F_5$
0	3 776.13	26 474.60	4.54	$b\ ^3F_2 - z\ ^5S_2$
1	3 765.22	26 551.31	1.37	$b\ ^3F_2 - z\ ^5F_2$
1	3 755.451	26 620.40	0.21	$b\ ^1G_4 - t\ ^3F_3$
1 (h)	3 754.231	26 629.05	9.29	$b\ ^1D_2 - z\ ^1F_3$
6	3 753.168	26 636.59	6.51	$b\ ^1G_4 - y\ ^1H_5{}^*$
7 bl Fe II	3 747.42	26 677.44	7.64	$c\ ^3G_5 - v\ ^3F_4{}^*$
2 w bl Fe I	3 746.52	26 683.88	3.82	$b\ ^3G_4 - z\ ^5F_4$
2	3 717.277	26 893.76	4.1	$b\ ^1D_2 - w\ ^3D_1$

(Table 2, cont.)

Intensity	λ_{air} (obs)	σ (obs)	σ (calc)	Combination
3	3 700.152	27 018.23	8.18	$b\,{}^1G_4 - x\,{}^1G_4{}^*$
2	3 696.209	27 047.05	7.12	$c\,{}^3G_3 - v\,{}^3D_2$
1	3 695.883	27 049.43	9.38	$b\,{}^3F_4 - z\,{}^5D_4$
5	3 690.556	27 088.48	8.29	$b\,{}^1G_4 - x\,{}^1F_3{}^*$
3	3 685.400	27 126.38	6.58	$c\,{}^3G_4 - v\,{}^3D_3$
0	3 672.31	27 223.04	2.98	$b\,{}^1D_2 - w\,{}^3D_2$
1 (h)	3 620.285	27 614.26	4.06	$b\,{}^3G_5 - z\,{}^5D_4{}^*$
6	3 611.748	27 679.53	9.62	$b\,{}^3F_3 - z\,{}^3F_2{}^*$
1	3 606.263	27 721.63	1.7	$c\,{}^3G_5 - u\,{}^3F_4$
11	3 603.883	27 739.94	9.88	$b\,{}^3F_2 - z\,{}^3F_2{}^*$
11	3 600.944	27 762.58	2.58	$b\,{}^3F_3 - z\,{}^3F_3{}^*$
5	3 599.439	27 774.18	3.99	$b\,{}^3F_4 - z\,{}^3F_3{}^*$
2	3 598.20	27 783.72	3.74	$y\,{}^5P_3 - 4d\,{}^5D_3{}^*$
1	3 598.12	27 784.34	4.51	$y\,{}^5P_3 - 4d\,{}^5D_2$
7	3 593.127	27 822.97	2.84	$b\,{}^3F_2 - z\,{}^3F_3{}^*$
1	3 591.19	27 837.98	7.72	$y\,{}^5P_2 - 4d\,{}^5D_2$
4	3 587.549	27 866.23	6.30	$b\,{}^3F_3 - z\,{}^3F_4{}^*$
10 bl Fe I	3 586.04	27 877.98	7.71	$b\,{}^3F_4 - z\,{}^3F_4{}^*$
2	3 575.633	27 959.09	8.98	$b\,{}^3F_3 - z\,{}^5P_3$
1	3 574.15	27 970.66	0.39	$b\,{}^3F_4 - z\,{}^5P_3$
1	3 572.32	27 985.05	4.96	$y\,{}^5P_1 - 4d\,{}^5D_0$
1	3 569.45	28 007.49	7.28	$y\,{}^5P_3 - 5s\,{}^5S_2$
1	3 562.690	28 060.67	0.49	$y\,{}^5P_2 - 5s\,{}^5S_2$
1	3 560.11	28 081.02	0.76	$y\,{}^5D_0 - 4d\,{}^5D_1$
1 (h) bl Fe I	3 544.56	28 204.20	4.72	$y\,{}^5P_1 - 5s\,{}^5S_2$
3	3 528.044	28 336.21	6.26	$c\,{}^3D_3 - x\,{}^3P_2$
5	3 525.184	28 359.20	9.19	$c\,{}^3D_2 - x\,{}^3P_2{}^*$
1	3 523.83	28 370.10	0.07	$c\,{}^3D_1 - x\,{}^3P_2$
7	3 515.536	28 437.04	6.98	$a\,{}^1G_4 - z\,{}^3G_5{}^*$
2	3 514.881	28 442.33	2.39	$b\,{}^3G_5 - z\,{}^3F_4{}^*$
1	3 514.286	28 447.15	7.16	$b\,{}^3G_5 - z\,{}^3H_6$
8	3 506.936	28 506.77	6.81	$c\,{}^3F_2 - z\,{}^3G_3{}^*$
1	3 505.891	28 515.26	5.64	$c\,{}^3G_4 - w\,{}^3H_4$
2	3 504.417	28 527.25	7.29	$c\,{}^3F_3 - z\,{}^3G_3{}^*$
10	3 501.756	28 548.93	8.84 9.00	$c\,{}^3F_3 - z\,{}^3G_4{}^*$ $b\,{}^3G_3 - z\,{}^3F_3{}^*$
1	3 501.268	28 552.91	2.54	$c\,{}^3F_4 - z\,{}^3G_4$
9	3 500.285	28 560.93	0.87	$c\,{}^3F_4 - z\,{}^3G_5{}^*$
9	3 499.589	28 566.61	6.65	$b\,{}^3G_4 - z\,{}^3F_4{}^*$
2	3 497.598	28 582.87	3.13	$c\,{}^3G_5 - w\,{}^3H_5$
1	3 496.715	28 590.09	89.98	$y\,{}^5D_4 - 4d\,{}^5D_3$
4 bl Fe II	3 496.27	28 593.72	3.65	$y\,{}^5D_4 - 4d\,{}^5D_4{}^*$
1 l	3 493.857	28 613.47	3.53	$y\,{}^5D_1 - 4d\,{}^5D_2$
4	3 491.176	28 635.45	5.29 6.06	$y\,{}^5D_2 - 4d\,{}^5D_3{}^*$ $y\,{}^5D_2 - 4d\,{}^5D_2$
3	3 489.492	28 649.26	9.40	$b\,{}^3G_5 - z\,{}^3H_5$
5	3 488.913	28 654.03	4.03	$c\,{}^3D_1 - x\,{}^3P_1{}^*$

(Table 2, cont.)

Intensity	λ_{air} (obs)	σ (obs)	σ (calc)	Combination
3	3 482.305	28 708.39	8.25	$y\,{}^5D_3 - 4d\,{}^5D_4$*
3	3 458.906	28 902.59	2.66	$b\,{}^3G_4 - z\,{}^3H_4$*
2	3 455.204	28 933.56	3.68	$c\,{}^3F_2 - z\,{}^3D_3$
2 w (h)	3 454.37	28 940.54	0.72	$b\,{}^1G_4 - u\,{}^3G_3$*
2	3 452.749	28 954.14	4.16	$c\,{}^3F_3 - z\,{}^3D_3$
m Fe I	–	28 957	7.86	$c\,{}^3F_4 - z\,{}^3D_3$*
3	3 441.733	29 046.81	7.06	$c\,{}^3D_3 - x\,{}^3D_3$
5	3 432.997	29 120.72	0.97	$b\,{}^1D_2 - z\,{}^1P_1$*
2	3 427.455	29 167.80	7.68	$c\,{}^3D_3 - y\,{}^5G_3$
1	3 424.467	29 193.25	3.25	$c\,{}^3D_1 - x\,{}^3P_0$
3	3 422.085	29 213.58	3.70	$b\,{}^3F_3 - z\,{}^3P_2$
3	3 422.000	29 214.30	4.28	$a\,{}^3F_2 - z\,{}^5G_2$*
5	3 419.500	29 235.65	5.45	$a\,{}^3F_2 - z\,{}^5G_3$*
			5.89	$c\,{}^3F_3 - z\,{}^3D_2$*
4	3 410.716	29 310.95	0.58	$c\,{}^3D_3 - y\,{}^5G_4$*
			0.94	$c\,{}^3D_2 - x\,{}^3D_1$*
1	3 409.452	29 321.82	1.82	$c\,{}^3D_1 - x\,{}^3D_1$
4	3 406.197	29 349.84	9.88	$c\,{}^3D_3 - x\,{}^3D_2$*
3	3 403.528	29 372.85	2.81	$c\,{}^3D_2 - x\,{}^3D_2$*
8	3 396.704	29 431.86	1.94	$a\,{}^3H_6 - z\,{}^3H_6$*
2	3 391.639	29 475.81	5.79	$a\,{}^3F_4 - z\,{}^5G_4$
3	3 386.853	29 517.46	7.46	$a\,{}^3F_4 - z\,{}^5G_5$
7	3 382.179	29 558.25	8.39	$c\,{}^3G_5 - v\,{}^3G_5$*
3	3 373.534	29 633.99	4.18	$a\,{}^3H_6 - z\,{}^3H_5$*
1 (h) bl Fe II	3 370.53	29 660.40	0.34	$a\,{}^3H_5 - z\,{}^3H_6$
3	3 367.581	29 686.38	6.37	$a\,{}^3H_4 - z\,{}^3F_4$*
6	3 364.996	29 709.18	8.85	$a\,{}^3S_1 - y\,{}^3P_0$
1	3 362.21	29 733.77	4.05	$c\,{}^3G_3 - v\,{}^3G_4$
7	3 360.868	29 745.67	6.02	$c\,{}^3G_4 - v\,{}^3G_4$*
4	3 359.194	29 760.50	0.62	$c\,{}^3G_5 - v\,{}^3G_4$*
6	3 358.777	29 764.19	4.72	$c\,{}^3G_3 - v\,{}^3G_3$*
5	3 357.419	29 776.23	6.41	$c\,{}^3D_3 - w\,{}^3D_3$*
			6.69	$c\,{}^3G_4 - v\,{}^3G_3$*
3	3 354.821	29 799.29	9.34	$c\,{}^3D_2 - w\,{}^3D_3$*
7	3 347.734	29 862.37	2.58	$a\,{}^3H_5 - z\,{}^3H_5$*
2 l	3 344.291	29 893.11	3.38	$a\,{}^3H_4 - z\,{}^3H_5$
9	3 339.386	29 937.02	7.22	$a\,{}^5F_1 - z\,{}^5G_2$*
7 s	3 338.717	29 943.02	2.97	$a\,{}^3S_1 - y\,{}^3P_1$
3	3 333.318	29 991.51	1.58	$a\,{}^3H_5 - z\,{}^3H_4$*
			2.26	$c\,{}^3G_4 - t\,{}^3F_4$*
4 bl Fe I	3 331.62	30 006.76	6.86	$c\,{}^3G_5 - t\,{}^3F_4$*
7	3 329.899	30 022.30	2.38	$a\,{}^3H_4 - z\,{}^3H_4$*
1	3 325.54	30 061.67	1.46	$c\,{}^3D_3 - x\,{}^5F_4$
3	3 324.732	30 068.97	8.98	$y\,{}^5F_5 - 4d\,{}^5D_4$*
2	3 320.276	30 109.32	9.63	$b\,{}^1D_2 - w\,{}^3G_3$
3	3 315.846	30 149.54	9.82	$c\,{}^3G_3 - t\,{}^3F_2$*
1	3 311.536	30 188.78	8.78	$c\,{}^3D_3 - x\,{}^5F_2$

(Table 2, cont.)

Intensity	λ_{air} (obs)	σ (obs)	σ (calc)	Combination
1	3 311.02	30 193.52	3.64	$b\,^1D_2 - y\,^1D_2$
1	3 309.020	30 211.73	1.71	$c\,^3D_2 - x\,^5F_2$
1	3 307.824	30 222.66	2.59	$c\,^3D_1 - x\,^5F_2$
5	3 307.547	30 225.19	5.32	$a\,^5F_2 - z\,^5G_2{}^*$
4	3 306.991	30 230.27	0.58	$c\,^3G_4 - t\,^3F_3{}^*$
9	3 305.220	30 246.46	6.49	$a\,^5F_2 - z\,^5G_3{}^*$
7	3 304.302	30 254.87	4.83	$a\,^3S_1 - y\,^3P_2$
3	3 303.597	30 261.32	1.48	$c\,^3G_5 - y\,^1H_5$
2	3 302.567	30 270.76	0.97	$c\,^3D_3 - z\,^1F_3$
3	3 300.196	30 292.51	2.46	$y\,^5F_4 - 4d\,^5D_3{}^*$
1	3 294.960	30 340.64	0.49	$c\,^3D_1 - x\,^5F_1$
2	3 294.805	30 342.07	2.23	$b\,^3F_3 - y\,^5F_2{}^*$
4	3 294.524	30 344.66	4.65	$a\,^1F_3 - z\,^3F_3{}^*$
1	3 294.370	30 346.08	6.34	$a\,^5F_3 - z\,^5G_2$
7 bl Fe I	3 292.04	30 367.57	7.51	$a\,^5F_3 - z\,^5G_3{}^*$
10	3 288.808	30 397.40	7.48	$a\,^5F_3 - z\,^5G_4{}^*$
1	3 284.290	30 439.21	9.05	$a\,^3F_3 - z\,^5H_4$
1	3 283.785	30 443.89	3.89	$a\,^5F_4 - z\,^5G_3{}^*$
3	3 283.296	30 448.43	8.37	$a\,^1F_3 - z\,^3F_4{}^*$
6	3 280.556	30 473.86	3.86	$a\,^5F_4 - z\,^5G_4{}^*$
0 bl Fe II	3 278.07	30 496.99	7.11	$a\,^5F_5 - z\,^5G_4{}^*$
11	3 276.079	30 515.50	5.53	$a\,^5F_4 - z\,^5G_5{}^*$
3 1	3 274.949	30 526.03	5.35 6.12	$y\,^5F_3 - 4d\,^5D_3$ $y\,^5F_3 - 4d\,^5D_2{}^*$
2 (h)	3 273.86	30 536.15	6.25	$b\,^3F_4 - y\,^5F_3$
5	3 273.600	30 538.61	8.78	$a\,^5F_5 - z\,^5G_5{}^*$
1 (h)	3 273.13	30 543.04	3.14	$e\,^3G_5 - t\,^3H_6$
0 w	3 272.02	30 553.34	3.17	$e\,^3G_4 - t\,^3H_5$
2 bl Fe I	3 271.47	30 558.53	8.7	$c\,^3D_2 - w\,^3D_1$
2 s	3 270.24	30 569.97	9.6	$c\,^3D_1 - w\,^3D_1{}^*$
0 (h)	3 268.03	30 590.66	0.69	$e\,^3G_3 - t\,^3H_4$
13	3 266.885	30 601.38	1.39	$a\,^5F_5 - z\,^5G_6{}^*$
1	3 265.304	30 616.20	6.58	$c\,^3G_3 - x\,^1G_4$
1	3 264.250	30 626.08	6.22	$c\,^3D_2 - w\,^3F_2{}^*$
1	3 263.065	30 637.20	7.10	$c\,^3D_1 - w\,^3F_2{}^*$
5	3 262.455	30 642.93	3.15	$c\,^3G_5 - x\,^1G_4{}^*$
1	3 256.550	30 698.49	8.66	$c\,^3G_4 - x\,^1F_3{}^*$
2	3 255.485	30 708.53	8.73	$y\,^5F_2 - 4d\,^5D_2{}^*$
2 aff Fe III	3 255.25	30 710.71	0.51	$y\,^5F_2 - 4d\,^5D_1$
1	3 249.058	30 769.28	9.14	$b\,^3F_4 - y\,^5F_4$
0 bl Fe I	3 241.57	30 840.38	39.58 0.81	$y\,^5F_1 - 4d\,^5D_1$ $y\,^5F_1 - 4d\,^5D_0$
3 bl Fe I	3 239.03	30 864.56	4.66	$c\,^3D_3 - w\,^3D_2{}^*$
4	3 238.711	30 867.57	7.89	$c\,^3D_3 - w\,^3F_3{}^*$
5	3 237.203	30 881.95	2.26	$b\,^1D_2 - y\,^1F_3$
2 bl Fe II	3 236.61	30 887.63	7.59	$c\,^3D_2 - w\,^3D_2$

(Table 2, cont.)

Intensity	λ_{air} (obs)	σ (obs)	σ (calc)	Combination
1	3 235.475	30 898.44	8.47	$c\,{}^3D_1 - w\,{}^3D_2$
2 bl Fe I	3 230.16	30 949.31	9.18	$t\,{}^3D_3 - e\,{}^3D_3$
6	3 218.340	31 062.94	3.04	$b\,{}^1G_4 - w\,{}^1G_4$*
8	3 215.633	31 089.09	9.32	$b\,{}^3D_1 - z\,{}^5G_2$*
2	3 212.181	31 122.50	2.37 2.52	$e\,{}^3I_7 - t\,{}^3H_6$ $b\,{}^1D_2 - v\,{}^3F_3$
3	3 206.951	31 173.26	3.26	$b\,{}^3D_2 - z\,{}^5G_2$*
1 (h)	3 206.29	31 179.65	9.56	$e\,{}^3I_6 - t\,{}^3H_5$
6	3 204.763	31 194.54	4.43	$b\,{}^3D_2 - z\,{}^5G_3$*
2	3 201.893	31 222.50	2.50	$b\,{}^3D_3 - z\,{}^5G_3$*
2	3 201.637	31 225.00	5.19	$b\,{}^3G_4 - y\,{}^5F_3$
5	3 198.822	31 252.48	2.47	$b\,{}^3D_3 - z\,{}^5G_4$*
1	3 190.514	31 333.86	3.82	$b\,{}^3G_5 - y\,{}^5F_4$
3	3 189.745	31 341.41	1.40	$a\,{}^1G_4 - y\,{}^3D_3$*
1 (h)	3 185.95	31 378.72	8.72	$t\,{}^3D_2 - e\,{}^3D_1$
10 bl Fe I	3 178.01	31 457.18	7.35	$b\,{}^3F_3 - z\,{}^3G_4$*
3	3 176.838	31 468.74	8.76	$b\,{}^3F_4 - z\,{}^3G_4$*
10	3 175.993	31 477.11	7.09	$b\,{}^3F_4 - z\,{}^3G_5$*
0	3 174.61	31 490.82	0.99	$c\,{}^3\mathrm{F}_2 - y\,{}^3D_2$
1	3 174.331	31 493.59	3.84	$c\,{}^3D_3 - x\,{}^5D_3$
10	3 174.089	31 495.99	6.06	$b\,{}^3F_2 - z\,{}^3G_3$*
1	3 170.95	31 527.13	7.15	$t\,{}^3D_1 - e\,{}^3D_2$
3 aff Fe III	3 169.43	31 542.26	1.95	$c\,{}^3F_2 - y\,{}^3D_1$
1	3 167.553	31 560.97	0.97	$b\,{}^3G_5 - y\,{}^5F_5$*
4	3 164.687	31 589.56	9.67	$a\,{}^5F_2 - z\,{}^5H_3$*
0 bl Fe I	3 162.07	31 615.70	5.44	$c\,{}^3D_3 - x\,{}^5D_2$
0	3 158.14	31 655.01	4.9	$c\,{}^3D_2 - x\,{}^5D_1$
1	3 144.180	31 795.58	5.54 5.77	$a\,{}^3F_3 - z\,{}^5F_4$ $a\,{}^1F_3 - z\,{}^3P_2$
2	3 143.386	31 803.61	3.57	$a\,{}^3F_3 - z\,{}^5D_3$*
4	3 136.49	31 873.58	3.06	$a\,{}^5F_3 - z\,{}^5H_4$
10	3 136.43	31 874.20	4.08	$b\,{}^3F_4 - z\,{}^3D_3$*
2	3 130.858	31 930.88	0.94	$a\,{}^1G_4 - y\,{}^3F_4$
8	3 123.152	32 009.65	— 10.15	— $a\,{}^3F_2 - z\,{}^5D_1$
3	3 120.862	32 033.14	3.44	$b\,{}^3G_5 - z\,{}^3G_4$*
2 bl Fe II	3 120.03	32 041.68	1.77	$b\,{}^3G_5 - z\,{}^3G_5$*
2	3 119.259	32 049.60	9.47	$a\,{}^3F_2 - z\,{}^5D_2$
4	3 118.754	32 054.80	4.83	$c\,{}^3F_4 - y\,{}^3F_4$*
2 bl Fe II	3 118.26	32 059.85	60.03	$z\,{}^3P_2 - 5s\,{}^5S_2$
1	3 113.839	32 105.39	5.52	$a\,{}^3F_2 - z\,{}^5D_3$
7	3 111.616	32 128.32	8.43	$a\,{}^5F_4 - z\,{}^5H_5$*
3 bl Fe I	3 110.88	32 135.97	6.15	$b\,{}^3G_4 - z\,{}^3G_3$*
8	3 110.074	32 144.25	4.40	$b\,{}^3F_3 - z\,{}^3D_2$*
3 bl Fe II	3 108.85*	32 156.91	7.08	$a\,{}^3F_4 - z\,{}^5F_5$*
6	3 107.977	32 165.94	6.03	$b\,{}^3G_4 - z\,{}^3G_5$*

(Table 2, cont.)

Intensity	λ_{air} (obs)	σ (obs)	σ (calc)	Combination
1	3 102.548	32 222.23	2.22	$b\,{}^3G_3 - z\,{}^3G_3$
3	3 100.470	32 243.81	3.77	$b\,{}^3G_3 - z\,{}^3G_4$
1 w (h)	3 099.01	32 259.01	8.77	$c\,{}^3D_3 - x\,{}^3G_3{}^*$
			9.90	$c\,{}^3F_2 - y\,{}^3F_2$
1	3 096.97	32 280.25	0.38	$c\,{}^3F_3 - y\,{}^3F_2$
0 bl Fe II	3 096.82	32 281.80	1.70	$c\,{}^3D_2 - x\,{}^3G_3{}^*$
1	3 094.761	32 303.30	3.18	$a\,{}^3F_3 - z\,{}^5F_2$
2	3 094.303	32 308.08	7.86	$a\,{}^3F_4 - z\,{}^5F_4$
4 bl Fe I	3 091.63	32 335.98	6.02	$a\,{}^5F_5 - z\,{}^5H_6$
2	3 090.754	32 345.18	4.91	$a\,{}^3H_4 - y\,{}^5F_3{}^*$
3	3 084.07	32 415.30	4.90	$b\,{}^3F_3 - y\,{}^5D_2{}^*$
m Fe I	–	32 419	9.35	$b\,{}^3F_2 - z\,{}^3D_1{}^*$
3	3 070.091	32 562.86	3.02	$b\,{}^3G_4 - z\,{}^3D_3{}^*$
0	3 069.65	32 567.57	7.65	$a\,{}^3F_2 - z\,{}^5F_1$
1	3 068.032*	32 584.71	4.79	$t\,{}^3G_5 - f\,{}^5H_5$
1	3 066.817*	32 597.62	7.51	$t\,{}^3G_4 - f\,{}^5H_4$
1	3 065.023*	32 616.70	6.70	$t\,{}^3G_3 - f\,{}^5H_3$
1	3 060.159	32 668.54	8.81	$z\,{}^5P_1 - 4d\,{}^5D_1{}^*$
1	3 060.013	32 670.10	0.04	$z\,{}^5P_1 - 4d\,{}^5D_0$
1	3 059.368*	32 676.98	7.09	$t\,{}^3G_4 - f\,{}^5H_5$
2	3 055.554	32 717.78	7.78	$a\,{}^5F_1 - z\,{}^5D_0{}^*$
5	3 054.138	32 732.95	3.09	$a\,{}^5F_1 - z\,{}^5D_1{}^*$
3	3 050.467	32 772.34	2,41	$a\,{}^5F_1 - z\,{}^5D_2{}^*$
2 w bl Fe II	3 046.71	32 812.7	2.53	$z\,{}^5P_2 - 4d\,{}^5D_3$
			3.30	$z\,{}^5P_2 - 4d\,{}^5D_2$
1	3 046.194	32 818.28	8.31	$g\,{}^5G_6 - u\,{}^5F_5$
3	3 045.877*	32 821.72	1.41	$c\,{}^3G_4 - u\,{}^3G_4{}^*$
2	3 039.576	32 889.76	9.80	$z\,{}^5P_1 - 5s\,{}^5S_2$
2	3 035.788	32 930.79	0.82	$b\,{}^3G_3 - z\,{}^3D_2{}^*$
0	3 027.76	33 018.0	7.88	$g\,{}^5G_5 - u\,{}^5F_4$
2	3 027.491	33 021.03	1.19	$a\,{}^5F_2 - z\,{}^5D_1{}^*$
6	3 027.006	33 026.32	5.96	$t\,{}^3G_5 - h\,{}^5G_4$
			6.55	$a\,{}^3H_6 - z\,{}^3G_5{}^*$
2	3 026.129	33 035.90	6.07	$z\,{}^5P_2 - 5s\,{}^5S_2$
			6.30	$b\,{}^3G_5 - y\,{}^5D_4$
7	3 023.883	33 060.43	0.51	$a\,{}^5F_2 - z\,{}^5D_2{}^*$
3 bl Fe II	3 022.00*	33 081.0	0.79	$c\,{}^3G_5 - u\,{}^3G_5{}^*$
6	3 018.789	33 116.22	6.56	$a\,{}^5F_2 - z\,{}^5D_3{}^*$
2 1	3 017.31	33 132.4	2.03	$b\,{}^3G_3 - y\,{}^5D_3$
6	3 015.260	33 154.97	5.15	$a\,{}^5F_4 - z\,{}^5F_5{}^*$
15	3 013.167	33 178.00	8.40	$a\,{}^5F_5 - z\,{}^5F_5{}^*$
6	3 008.511	33 229.35	9.55	$a\,{}^5F_3 - z\,{}^5F_4{}^*$
8 l	3 007.793	33 237.28	7.58	$a\,{}^5F_3 - z\,{}^5D_3{}^*$
5 (h)	3 007.600	33 239.41	9.4	$4d\,{}^5D_0 - 4f\,{}^5F_1{}^*$
6 (h)	3 007.461	33 240.95	0.6	$4d\,{}^5D_1 - 4f\,{}^5F_1{}^*$
			0.9	$4d\,{}^5D_1 - 4f\,{}^5F_2{}^*$
			1.7	$4d\,{}^5D_4 - 4f\,{}^5F_4{}^*$

(Table 2, cont.)

Intensity	λ_{air} (obs)	σ (obs)	σ (calc)	Combination
12 (h)	3 007.275	33 243.00	2.7 3.0	$4d\ {}^5D_2 - 4f\ {}^5F_2$* $4d\ {}^5D_4 - 4f\ {}^5F_5$*
5 (h)	3 007.22	33 243.6	3.6	$4d\ {}^5D_2 - 4f\ {}^5F_3$*
3 (h)	3 007.14	33 244.5	4.4	$4d\ {}^5D_3 - 4f\ {}^5F_3$*
7 (h)	3 007.06	33 245.4	5.4	$4d\ {}^5D_3 - 4f\ {}^5F_4$*
2 (h)	3 006.99	33 246.2	6.62	$a\ {}^3H_5 - z\ {}^3G_4$*
4	3 006.142	33 255.54	5.87	$a\ {}^3H_4 - z\ {}^3G_3$*
3 bl Fe I	3 004.13	33 277.8	7.86	$b\ {}^3F_4 - y\ {}^5P_3$*
4 bl Fe I	3 002.99	33 290.5	0.59	$a\ {}^5F_1 - z\ {}^5F_1$*
12	3 001.617	33 305.67	5.93	$a\ {}^5F_4 - z\ {}^5F_4$*
2	3 000.839	33 314.30	3.96 4.75	$a\ {}^5F_4 - z\ {}^5D_3$* $z\ {}^5P_3 - 5s\ {}^5S_2$

Table 3.

Newly-classified Fe III lines in the region 3000–1966 Å.

The notation in column 1 is that used in Tables 1 and 2.

* in column 2: λ from EDLÉN and SWINGS (unpublished material).
* in column 5: the line was classified by EDLÉN and SWINGS (1942) but is included here because it has been used in the present term calculation.
† in column 5: the line is due to two transitions, one of which was identified by EDLÉN and SWINGS (1942).

Intensity	λ_{air} (obs)	σ (obs)	σ (calc)	Combination
1	2 997.042*	33 356.50	6.42	$t\ {}^3G_5 - h\ {}^5G_6$
2	2 980.716	33 539.20	9.34	$a\ {}^5F_2 - z\ {}^5S_2$
1	2 978.091*	33 568.75	8.79	$e\ {}^5I_8 - x\ {}^3I_7$
3	2 965.645	33 709.63	9.68	$a\ {}^5F_2 - z\ {}^5F_3$
1	2 956.303*	33 816.15	6.20	$v\ {}^3H_6 - f\ {}^5H_7$
1	2 951.999*	33 865.45	5.34	$v\ {}^3H_5 - f\ {}^5H_4$
4	2 943.197	33 966.72	6.56 6.80	$v\ {}^3H_5 - f\ {}^5H_6$ $b\ {}^3G_4 - y\ {}^5P_3$
2 (h)	2 941.817	33 982.66	2.62	$v\ {}^3H_4 - f\ {}^5H_3$
1 (h)	2 939.269	34 012.11	2.22	$z\ {}^5D_4 - 4d\ {}^5D_3$
1	2 922.467*	34 207.66	7.83	$v\ {}^3H_6 - h\ {}^5G_5$
1 bl Fe II	2 901.41*	34 455.9	5.86	$v\ {}^3H_5 - h\ {}^5G_5$
3	2 900.535	34 466.30	6.34	$z\ {}^5F_3 - 4d\ {}^5D_2$
1	2 896.333	34 516.30	6.58	$a\ {}^5F_1 - z\ {}^3F_2$
2	2 892.524	34 561.75	1.63	$z\ {}^5F_2 - 4d\ {}^5D_1$
1	2 883.220	34 673.27	3.41	$c\ {}^3G_4 - w\ {}^1G_4$
1 (h) bl Fe II	2 879.64	34 716.4	6.55	$v\ {}^3H_5 - h\ {}^5G_6$
1 (h)	2 871.985	34 808.91	8.75	$u\ {}^3D_3 - f\ {}^5F_3$
3 w (h)	2 870.22	34 830.3	0.05	$u\ {}^3D_2 - f\ {}^5F_3$
2 (h)	2 866.799	34 871.87	1.75	$u\ {}^3D_2 - f\ {}^5F_1$
1 (h)	2 862.511	34 924.10	4.27	$u\ {}^3D_1 - f\ {}^5F_2$

(*Table 3, cont.*)

Intensity	λ_{air} (obs)	σ (obs)	σ (calc)	Combination
1	2 862.405	34 925.40	5.40	$a\ ^1I_6 - z\ ^3H_6$
			5.70	$a\ ^5F_3 - z\ ^3F_2$
2	2 859.608	34 959.56	9.64	$b\ ^3F_3 - y\ ^3F_4$
1 h	2 859.47	34 961.2	1.1	$4f\ ^5F_5 - 6g\ ^5G_6$
1 v w h	2 859.29	34 963.5	2.4	$4f\ ^5F_4 - 6g\ ^5G_5$
			3.5	$4f\ ^5F_3 - 6g\ ^5G_4$
			4.5	$4f\ ^5F_2 - 6g\ ^5G_3$
			4.8	$4f\ ^5F_1 - 6g\ ^5G_2$
2 w	2 851.47	35 059.3	8.69	$z\ ^5D_3 - 4d\ ^5D_3$
			9.46	$z\ ^5D_3 - 4d\ ^5D_2$
3	2 850.873	35 066.67	6.72	$z\ ^5F_4 - 4d\ ^5D_3$*
2 bl Fe I	2 840.98	35 188.8	8.76	$a\ ^5F_4 - z\ ^3F_4$
			8.89	$b\ ^3F_3 - y\ ^3F_2$
1 (h)	2 838.589	35 218.41	8.50	$u\ ^3G_4 - f\ ^5F_5$
5	2 838.377	35 221.04	1.17	$z\ ^5F_5 - 4d\ ^5D_4$*
1 (h) bl Fe I	2 835.92	35 251.5	1.29	$u\ ^3G_4 - f\ ^5F_4$
2 (h)	2 833.373	35 283.25	3.34	$u\ ^3G_4 - f\ ^5F_3$
2	2 820.180	35 448.30	8.39	$a\ ^5F_3 - z\ ^3H_4$
5	2 815.761	35 503.92	3.69	$c\ ^3D_1 - v\ ^3D_2$
			4.58	$c\ ^3F_2 - y\ ^3P_2$
2 (h)	2 811.824	35 553.63	3.66	$u\ ^3G_3 - f\ ^5F_3$
2 (h)	2 808.974	35 589.71	9.68	$u\ ^3G_3 - f\ ^5F_2$
5	2 802.773	35 668.44	8.68	$b\ ^3D_1 - z\ ^3F_2$
2	2 796.866	35 743.77	3.98	$b\ ^1F_3 - x\ ^3F_4$
5	2 779.483	35 967.30	7.37	$b\ ^3D_3 - z\ ^3F_4$
2	2 709.949	36 890.13	0.18	$4d\ ^7D_2 - 4f\ ^7F_1$
4	2 709.243	36 899.74	9.70	$4d\ ^7D_1 - 4f\ ^7F_1$
2	2 706.210	36 941.09	1.19	$4d\ ^7D_3 - 4f\ ^7F_2$*
7	2 705.117	36 956.02	5.95	$4d\ ^7D_2 - 4f\ ^7F_2$*
2	2 704.424	36 965.49	5.47	$4d\ ^7D_1 - 4f\ ^7F_2$*
3	2 702.657	36 989.65	9.73	$4d\ ^7D_4 - 4f\ ^7F_3$
7 bl Fe II	2 701.13	37 010.6	0.61	$4d\ ^7D_3 - 4f\ ^7F_3$*
m Fe II	—	37 019	19.89	$4d\ ^7D_5 - 4f\ ^7F_4$
8	2 700.045	37 025.44	5.37	$4d\ ^7D_2 - 4f\ ^7F_3$*
7	2 698.414	37 047.81	7.74	$4d\ ^7D_4 - 4f\ ^7F_4$*
2	2 698.261	37 049.91	50.12	$a\ ^5F_1 - y\ ^5F_1$
4 bl Fe II	2 697.34	37 062.6	2.57	$4d\ ^7D_5 - 4f\ ^7F_5$*
7	2 696.905	37 068.55	8.62	$4d\ ^7D_3 - 4f\ ^7F_4$*
9	2 695.314	37 090.42	0.42	$4d\ ^7D_4 - 4f\ ^7F_5$*
10	2 695.150	37 092.68	2.68	$4d\ ^7D_5 - 4f\ ^7F_6$*
4	2 682.388	37 269.14	9.42	$a\ ^3F_3 - z\ ^3G_4$
3	2 675.118	37 370.42	0.30	$x\ ^1F_3 - e\ ^3F_3$
1	2 674.419	37 380.19	0.09	$x\ ^1F_3 - e\ ^3F_4$
2 bl Fe II	2 668.23	37 466.9	7.29	$a\ ^5F_2 - y\ ^5F_2$
3	2 665.351	37 507.35	7.62	$b\ ^1F_3 - y\ ^3G_3$
3	2 655.286	37 649.53	9.90	$a\ ^5F_2 - y\ ^5F_3$
2	2 303.725*	43 394.60	4.66	$x\ ^5F_5 - e\ ^5F_5$

(Table 3, cont.)

Intensity	λ_{air} (obs)	σ (obs)	σ (calc)	Combination
0	2 294.83*	43 562.8	3.00	$x\ ^5F_5 - e\ ^5G_5$
2	2 291.710*	43 622.10	1.80 2.03	$a\ ^3D_1 - y\ ^5F_1$ $x\ ^5F_3 - e\ ^5F_4$
5	2 290.126*	43 652.26	1.98 2.74	$b\ ^1F_3 - v\ ^3F_3$† $x\ ^5F_3 - e\ ^5F_3$
3	2 289.139*	43 671.08	0.86	$x\ ^5F_4 - e\ ^5F_3$
3 aff Fe III	2 285.04*	43 749.4	9.24	$x\ ^5F_3 - e\ ^5G_4$
5 aff Fe III	2 284.92*	43 751.7	— 1.98	— $x\ ^5F_3 - e\ ^5G_3$
3 w	2 284.64*	43 757.1	7.55	$x\ ^5F_4 - e\ ^5G_5$
4	2 280.298*	43 840.38	0.36	$y\ ^5G_6 - e\ ^5F_5$
5	2 272.751*	43 985.95	5.84	$y\ ^5G_6 - e\ ^5G_6$
2	2 272.549*	43 989.86	9.99	$5p\ ^7P_4 - 6d\ ^7D_5$
2	2 271.558*	44 009.05	8.70	$y\ ^5G_6 - e\ ^5G_5$
1	2 264.459*	44 146.99	6.83	$5p\ ^7P_3 - 6d\ ^7D_3$
3 bl Fe II	2 264.188*	44 152.27	1.87 2.15	$5p\ ^7P_3 - 6d\ ^7D_4$ $c\ ^3F_3 - x\ ^5D_2$
3	2 263.477*	44 166.16	6.13	$x\ ^1D_2 - e\ ^3D_2$
3	2 262.888*	44 177.65	7.64 8.04	$x\ ^1D_2 - e\ ^3D_1$ $a\ ^1F_3 - x\ ^3F_3$†
0	2 262.07*	44 193.7	3.88	$5p\ ^7P_4 - 7s\ ^7S_3$
1 aff Fe III	2 259.24*	44 248.9	9.04	$5p\ ^7P_2 - 6d\ ^7D_1$
2	2 258.936*	44 254.92	4.94	$5p\ ^7P_2 - 6d\ ^7D_3$
m Fe I	—	44 314	4.35	$y\ ^5G_5 - e\ ^5F_4$
1	2 251.104*	44 408.88	8.89	$y\ ^5G_5 - e\ ^5G_6$
4	2 250.456*	44 421.66	1.74	$y\ ^5G_4 - e\ ^5F_3$
4 w	2 249.97*	44 431.2	1.75	$y\ ^5G_5 - e\ ^5G_5$
0	2 249.45*	44 441.6	1.56	$y\ ^5G_5 - e\ ^5G_4$
3	2 243.215*	44 565.05	4.64 —	$y\ ^5G_3 - e\ ^5F_3$ —
2 w	2 234.47*	44 739.4	9.05	$y\ ^5G_2 - e\ ^5F_2$
2	2 230.373*	44 821.62	1.65	$y\ ^5G_2 - e\ ^5G_2$
	λ_{vac} (obs)			
3	1 966.074*	50 862.78	2.95	$a\ ^3S_1 - w^3P_2$

0.02 to 0.05 Å depending on the character of the line. The classified lines are marked with an asterisk after the wavelength.

Table 2 contains 800 classified lines. About 200 of these lines were previously identified and may be found in the paper of EDLÉN and SWINGS (1942) or in the "Revised Multiplet Table" (C. E. MOORE 1945). The wave-numbers in column 3 have been calculated from wavelengths with three decimal places, even in cases where only two decimal places have been retained in column 2. Vacuum corrections to three decimal places were taken from the tables given by EDLÉN (1953). σ_{calc} in

Table 4.

Classified Fe III lines due to transitions 4*p*–5*s* and 4*p*–4*d*.

The notation in columns 1 and 5 is the same as used in Tables 1 and 2.

Intensity	λ_{vac} (obs)	σ (obs)	σ (calc)	Combination
7 h	1 611.763	62 043.9	3.51	$4p\ ^5P_1 - 4d\ ^5D_2{}^*$
7 h	1 611.723	62 045.4	5.29	$4p\ ^5P_1 - 4d\ ^5D_1{}^*$
			6.52	$4p\ ^5P_1 - 4d\ ^5D_0{}^*$
9 h	1 607.723	62 199.8	9.62	$4p\ ^5P_2 - 4d\ ^5D_3{}^*$
			200.39	$4p\ ^5P_2 - 4d\ ^5D_2{}^*$
3 h	1 606.014	62 266.0	6.28	$4p\ ^5P_1 - 5s\ ^5S_2{}^*$
5 h	1 602.000	62 422.0	3.16	$4p\ ^5P_2 - 5s\ ^5S_2{}^*$
6 h	1 601.289	62 449.7	9.34	$4p\ ^5P_3 - 4d\ ^5D_3{}^*$
			50.11	$4p\ ^5P_3 - 4d\ ^5D_2{}^*$
10 h	1 601.211	62 452.8	3.01	$4p\ ^5P_3 - 4d\ ^5D_4{}^*$
1 h	1 597.631	62 592.7	2.92	$z\ ^5F_3 - e\ ^5F_3$
6 h	1 595.597	62 672.5	2.88	$4p\ ^5P_3 - 5s\ ^5S_2{}^*$
0 h	1 595.180	62 688.9	9.42	$z\ ^5F_3 - e\ ^5G_4$
0 h	1 594.844	62 702.1	1.84	$z\ ^5F_2 - e\ ^5F_2$
1 h	1 593.897	62 739.3	9.32	$z\ ^5F_1 - e\ ^5F_2$
1 h	1 593.741	62 745.5	5.37	$z\ ^5F_1 - e\ ^5F_1$
1 h	1 592.913	62 778.1	8.67	$z\ ^5S_2 - e\ ^5F_2$
1 h	1 592.721	62 785.6	4.72	$z\ ^5S_2 - e\ ^5F_1$
			5.67	$z\ ^5F_2 - e\ ^5G_3$
2 h	1 591.803	62 821.8	1.92	$z\ ^5F_1 - e\ ^5G_2$
m Fe II	–	63 094	4.60	$y\ ^5P_2 - e\ ^5D_2$
0 h	1 583.973	63 132.4	2.59	$y\ ^5P_3 - e\ ^5D_3$
3 h	1 583.199	63 163.3	3.36	$z\ ^5F_4 - e\ ^5F_4$
0 h	1 582.621	63 186.3	5.80	$y\ ^5P_2 - e\ ^5D_3$
0 h	1 582.419	63 194.4	4.07	$z\ ^5F_4 - e\ ^5F_3$
1 h aff Fe III	1 581.057	63 248.8	8.21	$y\ ^5P_3 - e\ ^5D_4$
2 h bl Fe II	1 580.690	63 263.5	3.20	$z\ ^5F_5 - e\ ^5F_5$
5 w h	1 580.237	63 281.7	0.76	$z\ ^5F_4 - e\ ^5G_5$
			2.54	$z\ ^5D_3 - e\ ^5G_4$
			2.73	$y\ ^3F_2 - f\ ^3G_3$
2 h	1 578.759	63 340.9	1.33	$z\ ^5D_2 - e\ ^5G_3$
2 h	1 577.926	63 374.3	3.86	$y\ ^3F_3 - f\ ^3G_4$
3 h bl Fe II	1 577.084	63 408.2	8.68	$z\ ^5F_5 - e\ ^5G_6$
0 h	1 572.984	63 573.4	4.24	$z\ ^5H_7 - e\ ^5H_6$
5 h	1 572.841	63 579.2	9.22	$z\ ^5H_7 - e\ ^5H_7$
3 h	1 572.776	63 581.8	0.95	$y\ ^3F_4 - f\ ^3G_5$
1 h	1 571.255	63 643.4	4.12	$w\ ^3D_2 - h\ ^5G_2$
1 h	1 569.066	63 732.2	—	—
			3.32	$z\ ^5H_6 - e\ ^5H_5$
3 h	1 568.820	63 742.2	2.22	$z\ ^5H_6 - e\ ^5H_6$
m Fe IV	—	63 747	7.20	$z\ ^5H_6 - e\ ^5H_7$
1 w h	1 567.650	63 789.8	90.65	$y\ ^5D_1 - e\ ^5D_1$
3 w h	1 565.100	63 893.7	2.94	$y\ ^5D_2 - e\ ^5D_2$
2 h	1 564.512	63 917.7	7.66	$z\ ^5H_5 - e\ ^5H_5$
0 h	1 564.281	63 927.1	6.56	$z\ ^5H_5 - e\ ^5H$[illegible]

(Table 4, cont.)

Intensity	λ_{vac} (obs)	σ (obs)	σ (calc)	Combination
0 h	1 561.179	64 054.2	3.43	$y\,^5D_3 - e\,^5D_3$
			4.45	$y\,^5D_4 - e\,^5D_4$
2 h	1 560.857	64 067.4	7.70	$z\,^5H_4 - e\,^5H_3$
			8.46	$z\,^3F_4 - e\,^3F_4$
3 h	1 560.483	64 082.7	3.08	$z\,^5H_7 - e\,^5G_6$
			3.30	$z\,^5H_4 - e\,^5H_4$
2 h	1 559.463	64 124.6	4.41	$z\,^3H_4 - e\,^3I_5$
m Fe II	–	64 162	2.39	$z\,^3F_3 - e\,^3F_3$
0 h	1 558.310	64 172.1	2.18	$z\,^3F_3 - e\,^3F_4$
2 h	1 557.561	64 202.9	2.10	$x\,^5F_1 - h\,^5G_2$
			—	—
2 h	1 556.902	64 230.1	28.99	$z\,^3F_2 - e\,^3F_2$
			0.07	$z\,^5H_3 - e\,^5H_3$
1 h	1 556.756	64 236.1	5.49	$y\,^3F_4 - e\,^3D_3$
8 h	1 556.493	64 247.0	6.80	$z\,^5H_7 - e\,^5I_8$
1 h	1 556.427	64 249.7	50.40	$y\,^3G_4 - f\,^5H_4$
5 h	1 556.075	64 264.3	4.23	$y\,^5G_6 - f\,^5H_7$
3 h	1 555.861	64 273.1	3.51	$z\,^3H_5 - e\,^3I_6$
			3.92	$z\,^5H_6 - e\,^5G_5$
0 h	1 555.166	64 301.8	2.31	$z\,^1I_6 - f\,^5H_5$
0 h	1 552.681	64 404.7	4.71	$x\,^5F_4 - h\,^5G_5$
8 h	1 552.067	64 430.2	0.31	$z\,^5H_6 - e\,^5I_{76}$
4 h	1 551.377	64 458.9	9.38	$4p\,^7P_4 - 4d\,^7D_3$*
2 h	1 551.149	64 468.3	8.07	$z\,^5H_5 - e\,^5G_4$
2 h	1 551.085	64 471.0	0.85	$x\,^5F_5 - h\,^5G_6$
8 h	1 550.862	64 480.3	0.26	$4p\,^7P_4 - 4d\,^7D_4$*
5 h	1 550.450	64 497.4	7.04	$z\,^3H_6 - e\,^3I_7$
12 h	1 550.196	64 508.0	8.11	$4p\,^7P_4 - 4d\,^7D_5$*
5 h	1 548.251	64 589.0	9.61	$y\,^5G_5 - f\,^5H_6$
8 h	1 547.640	64 614.5	4.65	$z\,^5H_5 - e\,^5I_6$
0 h	1 547.494	64 620.6	19.99	$w\,^3D_3 - h\,^5G_4$
4 h	1 546.928	64 644.3	4.65	$y\,^5G_4 - f\,^5H_5$
0 h	1 546.570	64 659.2	60.02	$y\,^3G_5 - h\,^5G_5$
4 h	1 546.120	64 678.0	—	—
			8.71	$w\,^3D_3 - h\,^5G_3$
3 h	1 545.411	64 707.7	7.97	$y\,^5G_3 - f\,^5H_4$
4 h	1 544.232	64 757.1	7.11	$z\,^5F_3 - f\,^5G_4$
			—	—
3 w h	1 544.067	64 764.0	3.98	$y\,^5G_2 - f\,^5H_3$
6 h	1 543.640	64 781.9	2.64	$z\,^5H_4 - e\,^5I_5$
2 h	1 542.965	64 810.3	0.94	$z\,^5H_3 - e\,^5G_2$
1 h	1 542.625	64 824.6	5.03	$y\,^3D_3 - e\,^3D_3$
5 h	1 541.818	64 858.5	7.95	$z\,^5D_4 - f\,^5F_5$
2 h aff Fe III	1 540.815	64 900.7	899.90	$z\,^3H_5 - e\,^3G_4$
1 h	1 540.428	64 917.0	6.55	$y\,^5G_6 - h\,^5G_6$
0 h	1 540.362	64 919.8	20.71	$y\,^3G_5 - h\,^5G_6$

(Table 4, cont.)

Intensity	λ_{vac} (obs)	σ (obs)	σ (calc)	Combination
7 h	1 540.165	64 928.1	8.16	$z\,{}^5H_3 - e\,{}^5I_4$
5 h	1 539.480	64 957.0	7.29	$4p\,{}^7P_3 - 4d\,{}^7D_2$*
8 h	1 539.128	64 971.9	2.05	$4p\,{}^7P_3 - 4d\,{}^7D_3$*
10 h	1 538.632	64 992.8	2.93	$4p\,{}^7P_3 - 4d\,{}^7D_4$*
1 h	1 536.830	65 069.0	9.25	$y\,{}^5D_4 - f\,{}^5D_4$
2 h	1 536.640	65 077.1	6.27	$z\,{}^3H_6 - e\,{}^3G_5$
1 h	1 536.591	65 079.1	8.91	$y\,{}^5G_5 - h\,{}^5G_5$
2 h	1 536.421	65 086.3	5.82	$y\,{}^5G_4 - h\,{}^5G_4$
4 h	1 535.421	65 128.7	8.48	$y\,{}^5F_5 - g\,{}^5G_6$
4 h	1 533.439	65 212.9	2.42	$y\,{}^5F_4 - g\,{}^5G_5$
7 h	1 531.864	65 279.9	9.96 80.03	$4p\,{}^7P_2 - 4d\,{}^7D_1$* $y\,{}^5D_3 - f\,{}^5D_3$
8 h	1 531.644	65 289.3	7.44 9.48	$y\,{}^5G_3 - h\,{}^5G_3$ $4p\,{}^7P_2 - 4d\,{}^7D_2$*
6 h	1 531.293	65 304.3	4.24	$4p\,{}^7P_2 - 4d\,{}^7D_3$*
0 h	1 530.431	65 341.1	1.29	$z\,{}^5F_4 - f\,{}^5G_5$
2 h aff Fe III	1 530.220	65 350.1	49.34 0.23	$x\,{}^3D_3 - h\,{}^5G_4$ $z\,{}^5D_3 - f\,{}^5G_4$
3 h	1 529.764	65 369.6	70.16	$y\,{}^5F_3 - g\,{}^5G_4$
0 h	1 528.884	65 407.2	8.06	$x\,{}^3D_3 - h\,{}^5G_3$
1 h aff Fe III	1 527.767	65 455.0	5.96	$z\,{}^5F_5 - f\,{}^5G_6$
3 h aff Fe III	1 527.260	65 476.7	6.85 7.27	$z\,{}^5G_6 - e\,{}^5H_6$ $y\,{}^5F_2 - g\,{}^5G_3$
6	1 527.145	65 481.7	1.83	$z\,{}^5G_6 - e\,{}^5H_7$
2 h	1 526.016	65 530.1	29.78 0.56	$y\,{}^5F_5 - e\,{}^5D_4$ $z\,{}^5G_5 - e\,{}^5H_5$
6	1 525.801	65 539.4	9.46	$z\,{}^5G_5 - e\,{}^5H_6$
2	1 525.634	65 546.5	6.48	$z\,{}^5S_2 - f\,{}^5F_3$
1	1 525.343	65 559.0	8.88	$z\,{}^5G_4 - e\,{}^5H_4$
6 aff Fe III	1 525.041	65 572.0	1.59 2.23 3.25	$y\,{}^5F_1 - g\,{}^5G_2$ $z\,{}^5G_4 - e\,{}^5H_5$ $z\,{}^5G_3 - e\,{}^5H_3$
1	1 524.799	65 582.4	2.50	$z\,{}^5S_2 - f\,{}^5F_2$
5	1 524.658	65 588.5	8.18 8.85	$z\,{}^5S_2 - f\,{}^5F_1$ $z\,{}^5G_3 - e\,{}^5H_4$
5	1 524.522	65 594.3	4.42	$z\,{}^5G_2 - e\,{}^5H_3$
0 h aff Fe III	1 521.891	65 707.7	7.27	$x\,{}^5F_5 - g\,{}^5F_5$
5 h	1 518.842	65 839.6	40.21	$z\,{}^5G_6 - e\,{}^5F_5$
0 h	1 517.771	65 886.1	5.85	$y\,{}^5F_2 - e\,{}^5D_1$
0 h	1 516.790	65 928.7	8.91	$x\,{}^5F_4 - g\,{}^5F_4$
0	1 516.591	65 937.4	7.21	$z\,{}^5D_3 - f\,{}^5F_4$
3 h	1 516.222	65 953.4	3.76	$z\,{}^5G_5 - e\,{}^5F_4$
5 h	1 515.481	65 985.7	5.69	$z\,{}^5G_6 - e\,{}^5G_6$
0 h	1 514.948	66 008.9	8.55	$z\,{}^5G_6 - e\,{}^5G_5$
2	1 514.563	66 025.7	5.31 6.14	$z\,{}^5D_2 - f\,{}^5F_3$ $z\,{}^5G_4 - e\,{}^5F_3$
5 w h	1 513.539	66 070.3	1.16 1.52	$z\,{}^5G_5 - e\,{}^5G_5$ $z\,{}^5G_3 - e\,{}^5F_2$

(Table 4, cont.)

Intensity	λ_{vac} (obs)	σ (obs)	σ (calc)	Combination
2 h	1 512.896	66 098.4	8.74	$z\,{}^5G_2 - e\,{}^5F_1$
0	1 512.830	66 101.3	0.65	$z\,{}^5D_1 - f\,{}^5F_2$
3 h	1 512.346	66 122.4	1.64 2.64	$z\,{}^5D_0 - f\,{}^5F_1$ $z\,{}^5G_4 - e\,{}^5G_4$
0 h	1 512.262	66 126.1	5.38	$z\,{}^5G_4 - e\,{}^5G_3$
2 h bl Fe II	1 512.192	66 129.2	30.36	$z\,{}^5H_7 - f\,{}^5G_6$
5 h	1 511.617	66 154.3	2.97 4.12 5.35	$y\,{}^5G_6 - g\,{}^5F_5$ $z\,{}^5G_3 - e\,{}^5G_2$ $z\,{}^5G_3 - e\,{}^5G_3$
2 h	1 511.133	66 175.5	5.29	$z\,{}^5G_2 - e\,{}^5G_2$
2 h aff Fe III	1 507.530	66 333.7	4.45	$z\,{}^5H_6 - f\,{}^5G_5$
10 h	1 505.166	66 437.9	8.41	$4p\,{}^7P_4 - 5s\,{}^7S_3$*
2 h	1 502.964	66 535.2	5.76	$z\,{}^5H_5 - f\,{}^5G_4$
1 h	1 498.825	66 718.9	9.10	$z\,{}^5H_4 - f\,{}^5G_3$
1 h	1 495.210	66 880.2	0.11	$z\,{}^5H_3 - f\,{}^5G_2$
9 h	1 493.640	66 950.5	1.08	$4p\,{}^7P_3 - 5s\,{}^7S_3$*
7 h	1 486.265	67 282.8	3.27	$4p\,{}^7P_2 - 5s\,{}^7S_3$*
6 h	1 469.881	68 032.7	2.97	$z\,{}^5G_6 - f\,{}^5G_6$
0 h	1 468.526	68 095.5	5.58	$z\,{}^5G_5 - f\,{}^5G_6$
4 h	1 467.751	68 131.5	1.69	$z\,{}^5G_5 - f\,{}^5G_5$
4 h	1 466.492	68 189.9	90.33	$z\,{}^5G_4 - f\,{}^5G_4$
0 h	1 465.820	68 221.2	0.30	$z\,{}^5G_3 - f\,{}^5G_4$
3 h	1 465.763	68 223.9	4.65	$z\,{}^5G_3 - f\,{}^5G_3$
3 h	1 465.309	68 245.0	4.46 5.82	$z\,{}^5G_2 - f\,{}^5G_2$ $z\,{}^5G_2 - f\,{}^5G_3$

column 4 were obtained from the term values given in Tables 5 and 6 and those given by Edlén and Swings (1942). The notation in the last column is that used by hese authors. If a calculated transition is expected to be too weak to explain the observed line completely the computed wave-number and the designation are displaced up or down.

In Table 3 about 75 newly-classified lines are listed. Below 3000 Å the spectrograms from the hollow cathode discharge are weaker than those used by Edlén and Swings. Therefore the wavelengths of some lines (denoted with an asterisk) which are too weak to be measured on the present plates are taken form their working lists unpublished). The line 1966.074 is one of the few unidentified lines appearing in heir published wavelength list.

In the vacuum region at 1400–1600 Å Edlén and Swings, using a spark in nirogen, observed a large number of hazy lines which are doubtless attributable to he transitions $4p-4d$ and $4p-5s$. All classified lines of this type (about 100) are ollected in Table 4. The wavelengths are mean values of measurements made by Edlén and Swings and by the author using the old plates.

The term analysis

The main result of the present analysis is the classification of terms arising from the configurations $3d^5 5s$, $3d^5 6s$, $3d^5 4d$, $3d^5 5d$, and $3d^5 5p$. As mentioned above the transitions $4p-4d$ and $4p-5s$ give rise to a group of lines between 1400 and 1600 Å. From this wavelength material, however, the only terms of the configurations $3d^5 4d$ and $3d^5 5s$ that had been identified by EDLÉN and SWINGS were those built on $3d^5(^6S)$ of Fe IV. They also found the corresponding high odd terms $5p\,^5P$, ^7P from combinations with $4d\,^5D$, ^7D and $5s\,^5S$, ^7S. The latter transitions fall between 5000 and 6200 Å, in which region the condensed hollow cathode discharge gives many strong lines. By using the two groups of lines mentioned above it has now been possible to identify $3d^5(^4G)4d\,^5F$, ^5G, ^5H, ^5I, $3d^5(^4G)5s\,^5G$ and the corresponding odd triad $3d^5(^4G)5p\,^5F$, ^5G, ^5H.

From the positions of the terms $3d^5\,^4P$ and $3d^5\,^4D$ in Fe IV as estimated by EDLÉN (1941) it was possible to predict the approximate position of $3d^5(^4P)5s\,^5P$ and $3d^5(^4D)5s\,^5D$. In this way their combinations with the known $3d^5(^6S)5p\,^5P$ could be found. After that the corresponding odd terms $3d^5(^4P)5p\,^5S$, ^5P, ^5D and $3d^5(^4D)5p\,^5D$, ^5F were located. Of the $4d$ terms arising from ^4P and ^4D only $3d^5(^4P)4d\,^5F$ and $3d^5(^4D)4d\,^5D$, ^5G could be established.

As the interfamily lines are very few and weak, the quintet system based on $3d^5(^4F)$ had to be constructed independent of the foregoing systems. The even terms $3d^5(^4F)4d\,^5G$, ^5H, $5s\,^5F$ and the odd $3d^5(^4F)5p\,^5F$, ^5G have been found.

The separation between the two terms of different multiplicity obtained by adding an s-electron should be proportional to the multiplicity of the limit. The $4s$ terms of Fe III follow this law very well and therefore the same may be expected for $5s$. As the distance between $5s\,^7S$ and $5s\,^5S$ was known, the position of the $5s$ triplets arising from the quartet limits could be predicted with good accuracy. From a comparison with the corresponding transitions in $4s-4p$ it was then possible to identify the terms $3d^5(^4G)5s\,^3G$ and $3d^5(^4D)5s\,^3D$ in combinations with the odd terms $3d^5(^4G)5p\,^3F$, ^3G, ^3H and $3d^5(^4D)5p\,^3D$, ^3F. After that the even terms $3d^5(^4G)4d\,^3F$, ^3I and $3d^5(^4D)4d\,^3G$ were found. The triplet system was at first built up independent of the quintet system and was connected to the main term system only by lines in the vacuum region 1400–1600 Å. Later on, however, intercombination lines were found in the visible region.

Of the triplet terms based on the doublet limits only $3d^5(^2I)5s\,^3I$ and $3d^5(^2I)5p\,^3H$, ^3I have been located. They are connected to the other triplet terms by several interfamily lines.

The transitions $5p-5d$, $6s$ give many lines between 3900 and 4300 Å. EDLÉN and SWINGS have classified $5p\,^5P$, $^7P-5d\,^5D$, ^7D and $5p\,^7P-6s\,^7S$. As in the region 5000–6200 Å the combinations between terms built on the (^4G) limit give rise to strong multiplets. They permitted the identification of the same terms as in the case of the $4d$ and $5s$ configurations. In addition the following $6s$ states were established: $3d^5(^6S)6s\,^5S$, $3d^5(^4P)6s\,^5P$ and $3d^5(^4D)6s\,^5D$, ^3D.

There are many unclassified lines in the region in which the transitions $4d-4f$ and $4f-5g$ fall, but it has not been possible to group them into multiplets. Of higher states only those belonging to the (^6S) system have been established.

Table 5.

Even terms of Fe III.

The table contains all newly-established terms and, in addition, the following previously known terms, $4d\,^{5,7}D$, $5s\,^{5,7}S$, $5d\,^{5,7}D$, $6s\,^{7}S$, and $5g\,^{5,7}G$, for which the level values have been recalculated in the present investigation. Values are referred to $3d\ ^5D_4 = -0.8$.

Configuration	Symbol	Term value	Separation
$3d^5(^2S)4s$	$a\ ^3S_1$	98 661.88	
$3d^5(^6S)4d$	$4d\ ^7D_5$	147 353.90	+27.85
	$^7D_4$	147 326.05	+20.88
	$^7D_3$	147 305.17	+14.76
	$^7D_2$	147 290.41	+ 9.52
	$^7D_1$	147 280.89	
$3d^5(^6S)5s$	$5s\ ^7S_3$	149 284.20	
$3d^5(^6S)4d$	$4d\ ^5D_4$	151 537.00	+ 3.67
	$^5D_3$	151 533.33	− 0.77
	$^5D_2$	151 534.10	− 1.78
	$^5D_1$	151 535.88	− 1.23
	$^5D_0$	151 537.11	
$3d^5(^6S)5s$	$5s\ ^5S_2$	151 756.87	
$3d^5(^4G)4d$	$e\ ^5H_7$	179 220.65	+ 4.98
	$^5H_6$	179 215.67	+ 8.90
	$^5H_5$	179 206.77	+13.35
	$^5H_4$	179 193.42	+15.60
	$^5H_3$	179 177.82	
$3d^5(^4G)4d$	$e\ ^5F_5$	179 579.03	−50.94
	$^5F_4$	179 629.97	−30.71
	$^5F_3$	179 660.68	15.41
	$^5F_2$	179 676.09	6.05
	$^5F_1$	179 682.14	
$3d^5(^4G)4d$	$e\ ^5G_6$	179 724.51	−22.86
	$^5G_5$	179 747.37	− 9.81
	$^5G_4$	179 757.18	− 2.74
	$^5G_3$	179 759.92	+ 1.23
	$^5G_2$	179 758.69	
$3d^5(^4G)4d$	$e\ ^5I_8$	179 888.23	−15.53
	$^5I_7$	179 903.76	0.00
	$^5I_6$	179 903.76	+11.00
	$^5I_5$	179 892.76	+16.85
	$^5I_4$	179 875.91	
$3d^5(^4G)5s$	$f\ ^5G_6$	181 771.79	−36.11
	$^5G_5$	181 807.90	−16.97
	$^5G_4$	181 824.87	− 4.35
	$^5G_3$	181 829.22	+ 1.36
	$^5G_2$	181 827.86	
$3d^5(^4P)4d$	$f\ ^5F_5$	182 379.06	−32.79
	$^5F_4$	182 411.85	−32.05
	$^5F_3$	182 443.90	−36.02
	$^5F_2$	182 479.92	− 5.68
	$^5F_1$	182 485.60	
$3d^5(^4G)4d$	$e\ ^3F_4$	182 417.90	+ 9.79
	$^3F_3$	182 408.11	+16.36
	$^3F_2$	182 391.75	
$3d^5(^4G)4d$	$e\ ^3I_7$	182 851.25	+21.29
	$^3I_6$	182 829.96	+20.10
	$^3I_5$	182 809.86	
$3d^5(^4G)5s$	$e\ ^3G_5$	183 430.48	−25.87
	$^3G_4$	183 456.35	+ 0.46
	$^3G_3$	183 455.89	
$3d^5(^4P)5s$	$e\ ^5P_3$	184 950.82	−51.73
	$^5P_2$	185 002.55	−58.00
	$^5P_1$	185 060.55	
$3d^5(^4D)4d$	$g\ ^5G_6$	186 596.50	+143.21
	$^5G_5$	186 453.29	+ 75.15
	$^5G_4$	186 378.14	+ 75.50
	$^5G_3$	186 302.64	+ 34.75
	$^5G_2$	186 267.89	
$3d^5(^4D)4d$	$e\ ^5D_4$	186 997.80	+115.62
	$^5D_3$	186 882.18	+ 91.20
	$^5D_2$	186 790.98	+ 79.76
	$^5D_1$	186 711.22	
	$^5D_0$	—	
$3d^5(^4D)5s$	$f\ ^5D_4$	188 012.60	− 96.18
	$^5D_3$	188 108.78	− 33.06
	$^5D_2$	188 141.84	+ 10.94
	$^5D_1$	188 130.90	+ 22.38
	$^5D_0$	188 108.52	
$3d^5(^4D)4d$	$f\ ^3G_5$	189 023.73	+ 12.69
	$^3G_4$	189 011.04	+ 56.28
	$^3G_3$	188 954.76	
$3d^5(^4D)5s$	$e\ ^3D_3$	189 678.27	−105.45
	$^3D_2$	189 783.72	11.51
	$^3D_1$	189 795.23	

(Table 5, cont.)

Configuration	Symbol	Term value	Separation
$3d^5(^6S)5d$	$5d\ ^7D_5$	190 424.92	+ 12.15
	$^7D_4$	190 412.77	+ 9.26
	$^7D_3$	190 403.51	+ 6.60
	$^7D_2$	190 396.91	+ 4.44
	$^7D_1$	190 392.47	
$3d^5(^6S)6s$	$6s\ ^7S_3$	190 917.37	
$3d^5(^6S)6s$	$6s\ ^5S_2$	192 006.14	
$3d^5(^6S)5d$	$5d\ ^5D_4$	193 610.57	+ 0.45
	$^5D_3$	193 610.12	+ 4.93
	$^5D_2$	193 605.19	+ 6.45
	$^5D_1$	193 598.74	+ 4.24
	$^5D_0$	193 594.50	
$3d^5(^2I)5s$	$f\ ^3I_7$	196 880.67	− 4.54
	$^3I_6$	196 885.21	− 15.26
	$^3I_5$	196 900.47	
$3d^5(^4F)4d$	$f\ ^5H_7$	200 002.90	+ 97.67
	$^5H_6$	199 905.23	+ 21.64
	$^5H_5$	199 883.59	+ 79.58
	$^5H_4$	199 804.01	+102.99
	$^5H_3$	199 701.02	
$3d^5(^4F)4d$	$h\ ^5G_6$	200 655.22	+260.69
	$^5G_5$	200 394.53	+ 69.77
	$^5G_4$	200 324.76	− 58.72
	$^5G_3$	200 383.48	− 53.66
	$^5G_2$	200 437.14	
$3d^5(^4F)5s$	$g\ ^5F_5$	201 891.64	− 27.09
	$^5F_4$	201 918.73	−110.85
	$^5F_3$	202 029.58	−125.75
	$^5F_2$	202 155.33	−272.91
	$^5F_1$	202 428.24	
$3d^5(^6S)5g$	$5g\ ^7G_7$	207 640.0	0.0
	$^7G_6$	207 640.0	− 0.1
	$^7G_5$	207 640.1	0.0
	$^7G_4$	207 640.1	− 0.2
	$^7G_3$	207 640.3	− 0.2
	$^7G_2$	207 640.5	
	$^7G_1$	—	
$3d^5(^6S)5g$	$5g\ ^5G_6$	207 642.1	− 0.2
	$^5G_5$	207 642.3	− 0.2
	$^5G_4$	207 642.5	0.0
	$^5G_3$	207 642.5	− 0.2
	$^5G_2$	207 642.7	
$3d^5(^6S)6d$	$6d\ ^7D_5$	210 410.52	+ 6.71
	$^7D_4$	210 403.81	+ 5.04
	$^7D_3$	210 398.77	+ 3.57
	$^7D_2$	210 395.20	+ 2.33
	$^7D_1$	210 392.87	
$3d^5(^6S)7s$	$7s\ ^7S_3$	210 614.41	
$3d^5(^6S)6g$	$6g\ ^7G_{7-1}$	219 739	
$3d^5(^6S)6g$	$6g\ ^5G_6$	219 741.1	0.0
	$^5G_5$	219 741.1	− 0.1
	$^5G_4$	219 741.2	− 0.1
	$^5G_3$	219 741.3	0.0
	$^5G_2$	219 741.3	
$3d^5(^4G)5d$	$g\ ^5H_7$	222 590.06	− 11.64
	$^5H_6$	222 601.70	− 8.66
	$^5H_5$	222 610.36	+ 5.34
	$^5H_4$	222 605.02	+ 0.58
	$^5H_3$	222 604.44	
$3d^5(^4G)5d$	$h\ ^5F_5$	222 698.29	− 35.24
	$^5F_4$	222 733.53	− 15.90
	$^5F_3$	222 749.43	− 23.99
	$^5F_2$	222 773.42	− 2.67
	$^5F_1$	222 776.09	
$3d^5(^4G)5d$	$i\ ^5G_6$	222 713.50	− 30.39
	$^5G_5$	222 743.89	− 21.28
	$^5G_4$	222 765.17	− 0.07
	$^5G_3$	222 765.24	+ 7.76
	$^5G_2$	222 757.48	
$3d^5(^4G)5d$	$f\ ^5I_8$	222 797.17	− 26.74
	$^5I_7$	222 823.91	− 10.06
	$^5I_6$	222 833.97	+ 2.29
	$^5I_5$	222 831.68	+ 9.15
	$^5I_4$	222 822.53	
$3d^5(^4G)6s$	$j\ ^5G_6$	223 271.26	− 37.31
	$^5G_5$	223 308.57	− 17.39
	$^5G_4$	223 325.96	− 3.95
	$^5G_3$	223 329.91	+ 2.84
	$^5G_2$	223 327.07	
$3d^5(^4G)6s$	$g\ ^3G_5$	224 037.93	− 19.97
	$^3G_4$	224 057.90	+ 7.07
	$^3G_3$	224 050.83	
$3d^5(^4P)6s$	$f\ ^5P_3$	226 381.11	− 65.97
	$^5P_2$	226 447.08	− 58.66
	$^5P_1$	226 505.74	

(Table 5, cont.)

Configuration	Symbol	Term value	Separation	Configuration	Symbol	Term value	Separation
$3d^5(^4D)6s$	$g\ ^5D_4$	229 420.93	− 87.83	$3d^5(^4D)6s$	$f\ ^3D_3$	230 192.06	− 64.29
	$^5D_3$	229 508.76	− 60.80		$^3D_2$	230 256.35	+ 8.89
	$^5D_2$	229 569.56	+ 39.69		$^3D_1$	230 247.46	
	$^5D_1$	229 529.87					
	$^5D_0$	—					

Table 6.

Odd terms of Fe III.

The table contains all newly-established terms and, in addition, those previously known terms for which the levels have now been recalculated. Values are referred to $3d\ ^5D_4 = -0.8$.

Configuration	Symbol	Term value	Separation	Configuration	Symbol	Term value	Separation
Recalculated terms				$3d^5(^6S)4f$	$4f\ ^7F_6$	184 446.58	+ 30.11
$3d^5(^6S)4p$	$4p\ ^5P_3$	89 083.99	−249.72		$^7F_5$	184 416.47	+ 42.68
	$^5P_2$	89 333.71	−156.88		$^7F_4$	184 373.79	+ 58.01
	$^5P_1$	89 490.59			$^7F_3$	184 315.78	+ 69.42
$3d^5(^2D)4p$	$x\ ^3P_1$	134 548.58	−539.22		$^7F_2$	184 246.36	+ 65.77
	$^3P_0$	135 087.80			$^7F_1$	184 180.59	
$3d^5(^2D)4p$	$x\ ^3D_2$	135 278.24	+ 61.87		$^7F_0$	—	
	$^3D_1$	135 216.37		$3d^5(^6S)4f$	$4f\ ^5F_5$	184 780.0	+ 1.3
$3d^5(^2F)4p$	$w\ ^3D_3$	135 704.77	−1088.25		$^5F_4$	184 778.7	+ 1.0
	$^3D_2$	136 793.02			$^5F_3$	184 777.7	+ 0.9
$3d^5(^2F')4p$	$u\ ^3G_3$	146 890.24			$^5F_2$	184 776.8	+ 0.3
$3d^5(^2D')4p$	$t\ ^3D_3$	158 729.09	+312.58		$^5F_1$	184 776.5	
	$^3D_2$	158 416.51	+159.94	*New terms*			
	$^3D_1$	158 256.57		$3d^5(^4G)5p$	$x\ ^5G_6$	198 332.96	− 2.82
$3d^5(^2G')4p$	$v\ ^3H_6$	166 186.70	+248.03		$^5G_5$	198 335.78	− 2.04
	$^3H_5$	165 938.67	+220.27		$^5G_4$	198 337.82	+ 1.56
	$^3H_4$	165 718.40			$^5G_3$	198 336.26	+ 3.50
$3d^5(^2G')4p$	$t\ ^3G_5$	167 298.80	+ 92.30		$^5G_2$	198 332.76	
	$^3G_4$	167 206.50	+122.18	$3d^5(^6S)6p$	$6p\ ^7P_4$	198 736.25	+ 81.39
	$^3G_3$	167 084.32			$^7P_3$	198 654.86	+ 49.29
$3d^5(^6S)5p$	$5p\ ^7P_4$	166 420.53	+168.59		$^7P_2$	198 605.57	
	$^7P_3$	166 251.94	+108.11	$3d^5(^4G)5p$	$y\ ^5H_7$	198 847.58	+ 26.99
	$^7P_2$	166 143.83			$^5H_6$	198 820.59	+ 47.44
$3d^5(^6S)5p$	$5p\ ^5P_3$	168 328.87	− 91.32		$^5H_5$	198 773.15	+ 56.35
	$^5P_2$	168 420.19	− 56.37		$^5H_4$	198 716.80	+ 58.80
	$^5P_1$	168 476.56			$^5H_3$	198 658.00	
				$3d^5(^4G)5p$	$w\ ^5F_5$	199 138.96	− 72.96
					$^5F_4$	199 211.92	− 49.72
					$^5F_3$	199 261.64	− 37.71
					$^5F_2$	199 299.35	− 27.80
					$^5F_1$	199 327.15	

(Table 6, cont.)

Configuration	Symbol	Term value	Separation
$3d^5(^4G)5p$	$q\ ^3F_4$	199 602.81	+ 8.31
	$^3F_3$	199 594.50	+ 17.59
	$^3F_2$	199 576.91	
$3d^5(^4G)5p$	$u\ ^3H_6$	199 634.12	− 25.92
	$^3H_5$	199 660.04	− 39.99
	$^3H_4$	199 700.03	
$3d^5(^4G)5p$	$s\ ^3G_5$	200 523.32	+ 9.66
	$^3G_4$	200 513.66	+ 9.47
	$^3G_3$	200 504.19	
$3d^5(^4P)5p$	$w\ ^5D_4$	201 206.49	+ 40.94
	$^5D_3$	201 165.55	+ 2.14
	$^5D_2$	201 163.41	− 13.80
	$^5D_1$	201 177.21	+ 7.91
	$^5D_0$	201 169.30	
$3d^5(^4P)5p$	$y\ ^5S_2$	201 292.95	
$3d^5(^4P)5p$	$x\ ^5P_3$	202 199.71	− 82.14
	$^5P_2$	202 281.85	− 51.74
	$^5P_1$	202 333.59	
$3d^5(^4D)5p$	$v\ ^5F_5$	205 194.35	+102.62
	$^5F_4$	205 091.73	+ 90.06
	$^5F_3$	205 001.67	+ 59.21
	$^5F_2$	204 942.46	+ 36.13
	$^5F_1$	204 906.33	
$3d^5(^4D)5p$	$v\ ^5D_4$	205 671.21	− 60.36
	$^5D_3$	205 731.57	− 5.14
	$^5D_2$	205 736.71	+ 43.42
	$^5D_1$	205 693.29	
	$^5D_0$	—	
$3d^5(^4D)5p$	$s\ ^3D_3$	206 179.61	− 52.90
	$^3D_2$	206 232.51	− 62.50
	$^3D_1$	206 295.01	
$3d^5(^4D)5p$	$p\ ^3F_4$	206 260.53	− 66.89
	$^3F_3$	206 327.42	+ 3.33
	$^3F_2$	206 324.09	
$3d^5(^6S)5f$	$5f\ ^7F_6$	207 117.3	− 0.5
	$^7F_5$	207 117.8	− 0.5
	$^7F_4$	207 118.3	− 0.5
	$^7F_3$	207 118.8	− 0.5
	$^7F_2$	207 119.3	
	$^7F_1$	—	
	$^7F_0$	—	
$3d^5(^6S)5f$	$5f\ ^5F_5$	207 272.43	+ 5.0
	$^5F_4$	207 267.4	+ 5.2
	$^5F_3$	207 262.2	+ 5.2
	$^5F_2$	207 257.0	+ 5.3
	$^5F_1$	207 251.7	
$3d^5(^2I)5p$	$x\ ^3I_7$	213 457.02	− 47.91
	$^3I_6$	213 504.93	− 57.35
	$^3I_5$	213 562.28	
$3d^5(^2I)5p$	$t\ ^3H_6$	213 973.62	− 35.90
	$^3H_5$	214 009.52	− 37.06
	$^3H_4$	214 046.58	
$3d^5(^4F)5p$	$w\ ^5G_6$	219 161.62	+ 69.56
	$^5G_5$	219 092.06	+ 88.33
	$^5G_4$	219 003.73	+ 81.45
	$^5G_3$	218 922.28	+ 62.65
	$^5G_2$	218 859.63	
$3d^5(^4F)5p$	$u\ ^5F_5$	219 414.81	− 56.36
	$^5F_4$	219 471.17	− 94.11
	$^5F_3$	219 565.28	− 89.47
	$^5F_2$	219 654.75	− 87.49
	$^5F_1$	219 742.24	
$3d^5(^6S)6h$	$6h\ ^7H_{8-2}$	219 779.4	
	$6h\ ^5H_{7-3}$	219 779.8	

Calculation of term values

For the levels attributed to the configurations $3d^5 4s$ and $3d^5 4p$ Edlén and Swings (1942) give a term system which is well tied together. Table 2 contains several lines in the visible and near ultraviolet which are transitions between previously known terms. These wavelengths could be used in computing improved values of some terms. However, if any term values used by Edlén and Swings in their term calculation are changed the whole system must be recalculated. A comparison of wavelengths obtained from the vacuum spark and from the hollow cathode shows that some energy levels are sensitive to the properties of the light source. Therefore a recalculation of the whole term system using wavelength values from both the spark and the hollow cathode would surely not lead to any improvement. For a few $4p$ terms, however, which have not been used in the calculating scheme of EDLÉN and SWINGS, improved term values have been computed from combinations with new even terms or with previously known terms whose values are judged to be independent of the character of the light source. All improved term values are included in Tables 5 and 6.[1]

Those terms in the (^6S) system that are due to electron configurations higher than $4p$ give rise to several strong multiplets in the region now investigated. These wavelengths have been used to recalculate the quintet and septet systems. The former was attached to the main term system in the way described below. In calculating the septet terms the value of $4d\,^7D_5$ as given by EDLÉN and SWINGS was used as a starting point. Because no new intercombination lines between the quintet and septet systems have been found the two systems are still connected through the transitions $4s\,^5S - 4p\,^7P$ only. The value of $4d\,^7D$ with respect to the ground state $3d\,^5D_4$ is determined by the transitions $4p - 4d$ falling in the region 1600–1400 Å where measurements cannot be relied upon to better than about 0.5 cm^{-1}.

Tables 5 and 6 also contain the new even and odd terms, respectively. The levels due to the configurations $3d^5 5s$, $3d^5 6s$, $3d^5 4d$, $3d^5 5d$ and $3d^5 5p$ were computed through successive approximations in the same way as EDLÉN and SWINGS (1942) have done for the $3d^5 4s$ and $3d^5 4p$ terms. It was, however, inconvenient to treat all the new terms as one group because the interfamily lines are few and generally very weak. Therefore the terms were divided into three groups which were treated separately. The first group, including terms based on the limits ^6S, ^4P, ^4D and ^2I, was attached to the old system through combinations of $4d\,^5D$ and $5s\,^5S$ with $3d^5 4p$ terms. For the two other groups, consisting of the (^4G) and (^4F) systems, respectively, an approximate connexion with the remaining term system was obtained through the transitions $4p - 4d$, $5s$ falling in the region 1600–1400 Å. After that the interfamily lines between the (^4G) system and the (^4F)$4p$ terms could be found and these lines gave the final connexion for the (^4G) system. In a similar manner the terms built on the ^4F-limit were tied to the main system through combinations with the terms $v\,^3H$ and $g\,^5G$. The designation of term symbols for the configurations $5s$, $6s$ and $5p$ was made by comparison with the $4s$ and $4p$ states. The naming of the $4d$ and $5d$ terms is uncertain in some cases. This is particularly true in the case of the two overlapping terms ^5F and ^5G of the configuration $3d^5(^4G)5d$.

Rydberg series and ionization potential

The term values for the leading components of the terms built on the lowest term $3d^5(^6S)$ of Fe IV and the corresponding values of n^* are given in Table 7. By using a Ritz formula on the last three members of the series $3d^5(^6S)ns\,^7S$ an ionization potential of 247 221 cm^{-1} or 30.643 volts has been calculated. With this limit the term value of $6h\,^7H$ deviates only 8 cm^{-1} from a hydrogen-like value.

Table 8 contains Rydberg denominators and weighted mean values for the quintet

---

[1] It should be noted that the values given in Tables 5 and 6 correspond to $3d\,^5D_4 = -0.8$ as in the paper by EDLÉN and SWINGS. Consequently, all values should be increased by 0.80 cm^{-1} to bring them on level with the *Fe* III table in "Atomic Energy Levels", National Bureau of Standards, Circular 467, Washington, 1952.

Table 7.

Term values and Rydberg denominators for terms based on the ^6S limit.

	$n=4$		$n=5$		$n=6$		$n=7$	
	T	n^*	T	n^*	T	n^*	T	n^*
$ns\ ^7S_3$	217 133.0	2.1327	97 936.8	3.1756	56 303.6	4.1882	36 606.6	5.1942
$ns\ ^5S_2$	206 221.9	2.1884	95 464.1	3.2164	55 214.9	4.2293		
$np\ ^7P_4$	164 375.2	2.4512	80 800.5	3.4961	48 484.8	4.5133		
$np\ ^5P_3$	158 137.0	2.4991	78 892.1	3.5382				
$nd\ ^7D_5$	99 867.1	3.1447	56 796.1	4.1700	36 810.5	5.1798		
$nd\ ^5D_4$	95 684.0	3.2128	53 610.4	4.2921				
$nf\ ^7F_6$	62 774.4	3.9665	40 103.7	4.9626				
$nf\ ^5F_5$	62 441.0	3.9770	39 948.6	4.9722				
$ng\ ^7G_{7-1}$			39 580.9	4.9952	27 482	5.9948		
$ng\ ^5G_6$			39 578.9	4.9953	27 479.9	5.9950		
$nh\ ^7H_{8-2}$					27 441.6	5.9992		
$nh\ ^5H_{7-3}$					27 441.2	5.9992		

Table 8.

Term values and Rydberg denominators for terms arising from the configurations $3d^5\,ns$ and based on the quartet limits.

	$n=4$		$n=5$		$n=6$	
	T	n^*	T	n^*	T	n^*
$3d^5\ (^4G)\ ns\ ^{5,3}G$	213 298	2.1518	97 060	3.1899	55 896	4.2034
$3d^5\ (^4P)\ ns\ ^{5,3}P$	213 272	2.1519	(96 903)	3.1925	(55 807)	4.2068
$3d^5\ (^4D)\ ns\ ^{5,3}D$	213 050	2.1531	96 843	3.1935	55 780	4.2078
$3d^5\ (^4F)\ ns\ ^{5,3}F$	213 733	2.1496	(97 053)	3.1900		

and triplet terms arising from the configurations $3d^5ns$ and based on the quartet limits. For $3d^5\,(^4P)\,5s$, $6s$ and $3d^5\,(^4F)\,5s$ only the quintet terms are known. The values of the corresponding triplet terms have then been estimated by assuming the separation between the quintet and triplet terms to be constant for a given n-value. Fitting a Ritz formula to the first three series of Table 8 gives the following values of the limits referred to the ground level $3d^5\,^6S$ of Fe IV $3d^5\,^4G$ 32 260 cm^{-1}, $3d^5\,^4P$ 35 290 cm^{-1} and $3d^5\,^4D$ 38 325 cm^{-1}. If the curve n–n^* versus T for $ns\ ^{5\,3}F$ is assumed to be parallel with the curve for $ns\ ^{5,3}D$ the value 52 460 cm^{-1} is obtained for the limit $3d^5\,^4F$.

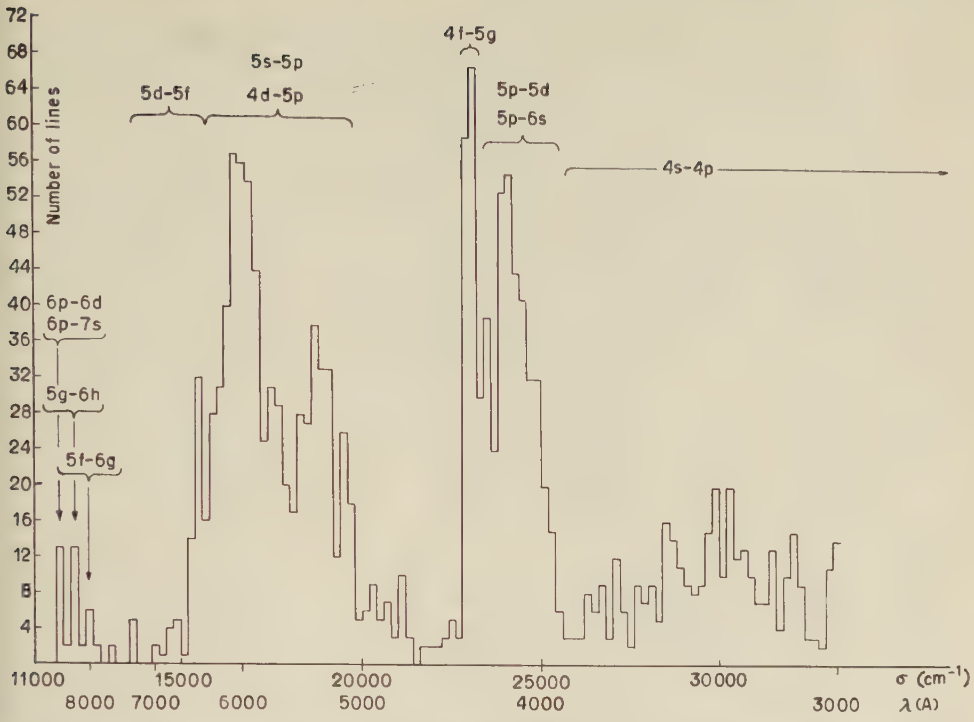

Fig. 2. The number of measured Fe III lines per interval of 200 cm^{-1} plotted against the wave-number.

Discussion

In order to give a survey of the Fe III spectrum between 8600 and 3000 Å the number of measured Fe III lines is plotted against the wave-number in Fig. 2. The regions in which the different types of transitions fall are marked in the figure. Since the intensity of interfamily lines has been found to decrease strongly with increasing n-values the lines in the visible region are generally due to transitions between terms with the same limit. For that reason there is a great probability that unidentified lines in a given range are due to the type of transition assigned to this region in Fig. 2.

The energy level diagram of Fig. 3 gives approximate positions of the terms that have been located and assigned to a configuration. Terms with the same limit are connected with a line and the notation of the limit appears at the top of the figure.

No terms of the configuration $3d^{n-2}4s^2$ have been found. The position of $3d^4 4s^2\,{}^5D$ has been estimated to about 145000 cm^{-1} according to the method given by Catalán, Rohrlich and Shenstone (1954). It should give combinations with several $3d^5 4p$ terms in the visible and near ultraviolet regions but no transitions of this type could be identified.

In the (${}^6S$), (${}^4G$), and (${}^4D$) systems the two terms of different multiplicity obtained by adding an s-electron are known for $n=4$, 5 and 6. The separations, ΔT, between

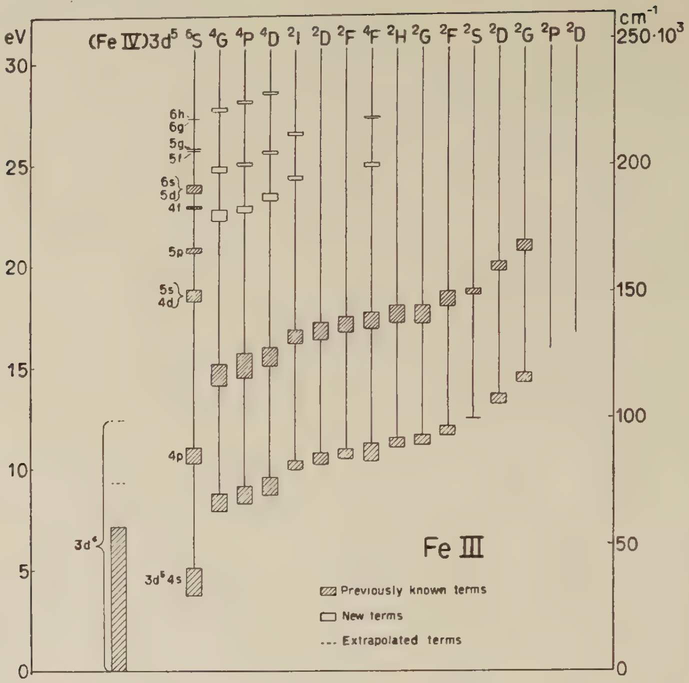

Fig. 3. Energy level diagram of Fe III.

Table 9.

The separation (ΔT) between the two terms of different multiplicity obtained by adding an s-electron to a given limit-term. (M is the multiplicity of the limit-term.)

$3d^5$	$3d^5\,ns$	M	$4s$		$5s$		$6s$	
			ΔT	$\Delta T/M$	ΔT	$\Delta T/M$	ΔT	$\Delta T/M$
^6S	$^5S-{}^7S$	6	10 911	1819	2472	412	1089	181
^4G	$^3G-{}^5G$	4	7 248	1812	1640	410	741	185
^4D	$^3D-{}^5D$	4	7 252	1813	1654	414	734	184

these two terms are listed in Table 9, where column 3 contains the multiplicity, M, of the limit-term. The quotient $\Delta T/M$ is nearly constant as the theory predicts.

For the purpose of comparison the fine structure intervals of a number of terms of the configurations $3d^5\,ns$ are collected in Table 10. The data are taken from KIESS (1953) for Cr I and from CURTIS (1938, 1952) for Mn II.

Table 10.

Fine structure intervals in the configurations $3d^5 ns$ in Cr I, Mn II and Fe III.

	Cr I		Mn II		Fe III		
	4s	5s	4s	5s	4s	5s	6s
$^5G_6 - {}^5G_5$	− 4.34	+ 6.39	− 24.05	− 21.73	− 41.22	− 36.11	− 37.31
$^5G_5 - {}^5G_4$	+ 0.25	+ 10.15	− 12.35	− 9.72	− 20.39	− 16.97	− 17.39
$^5G_4 - {}^5G_3$	+ 2.77	+ 11.54	− 4.93	− 2.27	− 7.22	− 4.35	− 3.95
$^5G_3 - {}^5G_2$	+ 3.52	+ 10.59	− 0.80	+ 1.46	− 0.56	+ 1.36	+ 2.84
$^3G_5 - {}^3G_4$	+ 141.06	—	− 148.62†	− 23.25	− 34.72	− 25.87	− 19.97
$^3G_4 - {}^3G_3$	+ 63.69	—	− 94.00†	− 2.03	+ 3.74	+ 0.46	+ 7.07
$^5P_3 - {}^5P_2$	− 7.04	—	− 29.91	− 32.73	− 58.31	− 51.73	− 65.97
$^5P_2 - {}^5P_1$	− 9.06	—	− 31.90	− 31.97	− 68.73	− 58.00	− 58.66
$^3P_2 - {}^3P_1$	+ 46.83	—	− 90.01	+ 34.76	− 121.46	—	—
$^3P_1 - {}^3P_0$	+ 13.02	—	− 63.59	+ 106.49	− 86.86	—	—
$^5D_4 - {}^5D_3$	− 21.60	—	− 69.35	− 64.34	− 141.10	− 96.18	− 87.83
$^5D_3 - {}^5D_2$	+ 4.05	—	− 1.89	− 16.70	− 0.93	− 33.06	− 60.80
$^5D_2 - {}^5D_1$	+ 13.35	—	+ 22.44	+ 4.38	+ 49.57	+ 10.94	+ 39.69
$^5D_1 - {}^5D_0$	+ 9.48	—	+ 18.30	+ 6.14	+ 40.79	+ 22.38	—
$^3D_3 - {}^3D_2$	− 45.18	—	− 5.24†	− 68.20	− 145.64	− 105.45	− 64.29
$^3D_2 - {}^3D_1$	+ 2.75	—	− 13.19†	− 2.09	+ 27.13	− 11.51	+ 8.89
$^5F_5 - {}^5F_4$	+ 15.44	—	− 8.6	—	− 23.25	− 27.09	—
$^5F_4 - {}^5F_3$	+ 13.63	—	+ 141.9	—	− 76.38	− 110.85	—
$^5F_3 - {}^5F_2$	+ 9.12	—	+ 55.9	—	− 121.02	− 125.75	—
$^5F_2 - {}^5F_1$	+ 2.79	—	+ 28.1	—	− 288.10	− 272.91	—

† Perturbed because of configuration interaction.

Acknowledgments

I should like to express my sincere gratitude to Professor Bengt Edlén for the constant interest with which he has followed my investigations, for valuable suggestions and for placing at my disposal unpublished material of Fe III. I wish also to thank Fil. Dr. Lennart Minnhagen who from my earliest studies at this Laboratory has shown great interest in my work. To Fil. Mag. Kjell Bockasten I am greatly indebted for his valuable experimental assistance.

The work has been assisted by grants from the Swedish Natural Science Research Council, which is gratefully acknowledged.

The Physical Laboratory, University of Lund, June 1955.

REFERENCES

BURNS, K., ADAMS, K. B., and LONGWELL, J., J. Opt. Soc. Am. *40*, 339, 1950.
BURNS, K. and WALTERS, JR., F. M., Publ. Allegheny Obs. *6*, 159, 1929.
—— Ibid. *8*, 39, 1931.
CATALÁN, M. A., ROHRLICH, F., and SHENSTONE, A. G., Proc. Roy. Soc. London *A 221*, 421, 1954.
CURTIS, C. W., Phys. Rev. *53*, 474, 1938.
—— J. Opt. Soc. Am. *42*, 300, 1952.
EDLÉN, B., Actualités Scientifiques et Industrielles, No. 895, Part I, p. 55 (Hermann et C^{ie}, Paris, 1941).
EDLÉN, B. and SWINGS, P., Astrophys. J. *95*, 532, 1942.
EDLÉN, B., J. Opt. Soc. Am. *43*, 339, 1953.
GARTLEIN, C. W. and GIBBS, R. C., Phys. Rev. *38*, 1907, 1931.
GLAD, S., Ark. Fysik *7*, 7, 1953.
KIESS, C. C., Bur. Stand. J. Res. *51*, 247, 1953.
KOPFERMANN, H. and WITTKE, H., ZS f. Phys. *105*, 16, 1937.
MEGGERS, W. F. and HUMPHREYS, C. J., Bur. Stand. J. Res. *13*, 293, 1934.
MINNHAGEN, L., The Stark Effect of Certain Multiplets. Diss. (Lund 1944), p. 56.
MOORE, C. E., A Multiplet Table of Astrophysical Interest, Part I. Princeton, 1945.
PASCHEN, F., Ann. d. Phys. (4) *71*, 142, 1923.
WITTKE, H., ZS f. Phys. *116*, 547, 1940.

Description of Plates I–II

I. Spectrograms obtained with a stigmatic 21-foot concave grating spectrograph (1st order) and a condensed hollow cathode discharge. The cathode consisted of a graphite tube containing a thin-walled iron cylinder. *a–d*: Magnification 3 times. *e*, *f*: Magnification 6 times.

II. A comparison between spectrograms obtained with the vacuum spark (*a*, *c*, *e*) and the condensed hollow cathode discharge (*b*, *d*, *f*). *a*, *b*, *c*, *e*, *f*: Large glass-prism spectrograph; magnification 3 times. *d*: 21-foot concave grating spectrograph (2nd order); magnification 6 times.

Tryckt den 21 januari 1956

Uppsala 1956. Almqvist & Wiksells Boktryckeri AB

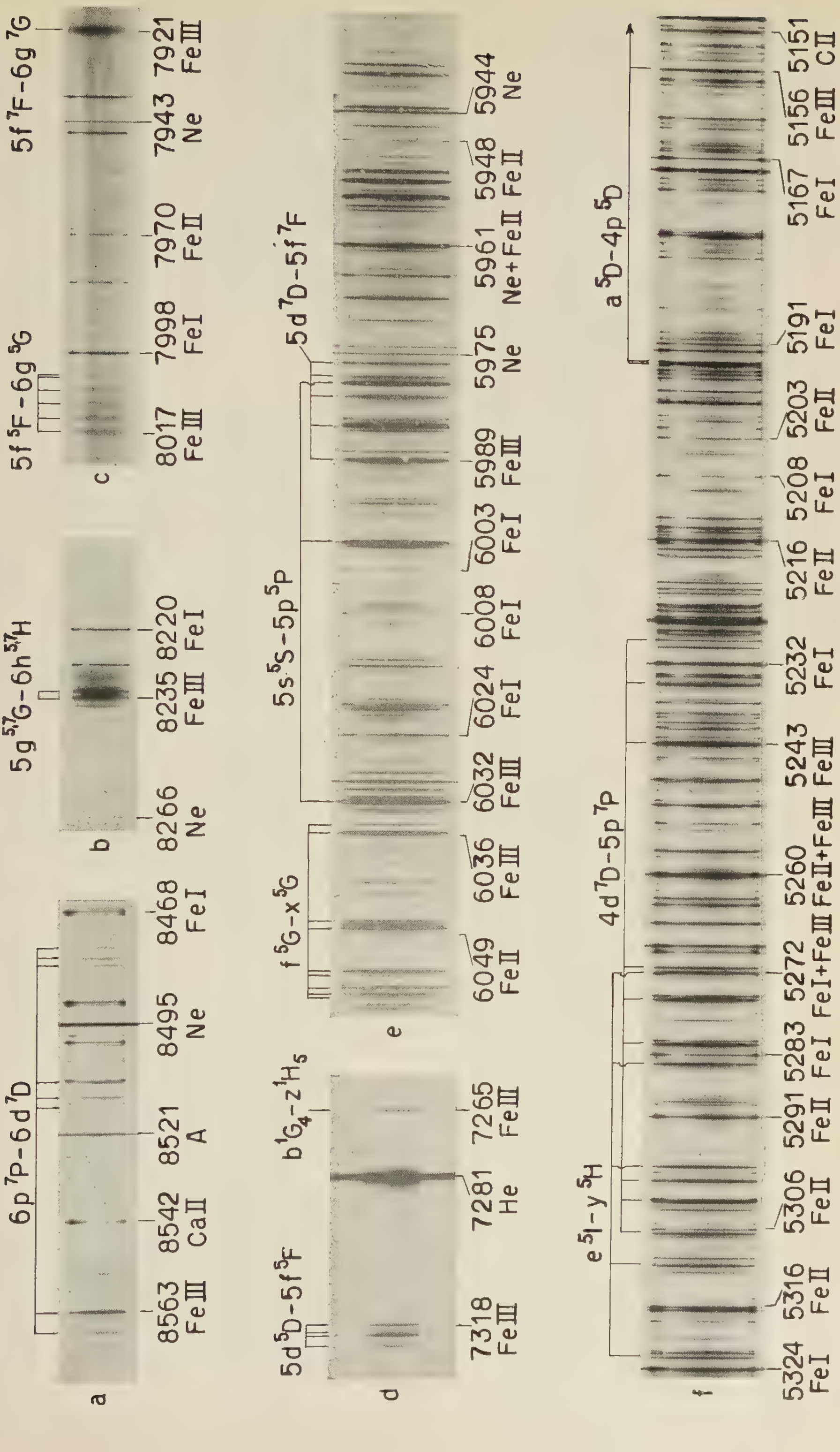
5f 7F-6g 7G
5f 5F-6g 5G
7921 FeIII
7943 Ne
7970 FeII
7998 FeI
8017 FeIII
c
5g 5,7G-6h 5,7H
8220 FeI
8235 FeIII
8266 Ne
b
6p 7P-6d 7D
8468 FeI
8495 Ne
8521 A
8542 CaII
8563 FeIII
a
5d 7D-5f 7F
5s 5S-5p 5P
f 5G-x 5G
5944 Ne
5948 FeII
5961 Ne+FeII
5975 Ne
5989 FeIII
6003 FeI
6008 FeI
6024 FeI
6032 FeIII
6036 FeIII
6049 FeII
e
b 1G4-z 1H5
5d 5D-5f 5F
7265 FeIII
7281 He
7318 FeIII
d
a 5D-4p 5D
4d 7D-5p 7P
e 5I-y 5H
5151 CII
5156 FeIII
5167 FeI
5191 FeI
5203 FeII
5208 FeI
5216 FeII
5232 FeI
5243 FeIII
5260 FeII+FeIII
5272 FeI+FeIII
5283 FeI
5291 FeII
5306 FeII
5316 FeII
5324 FeI
f

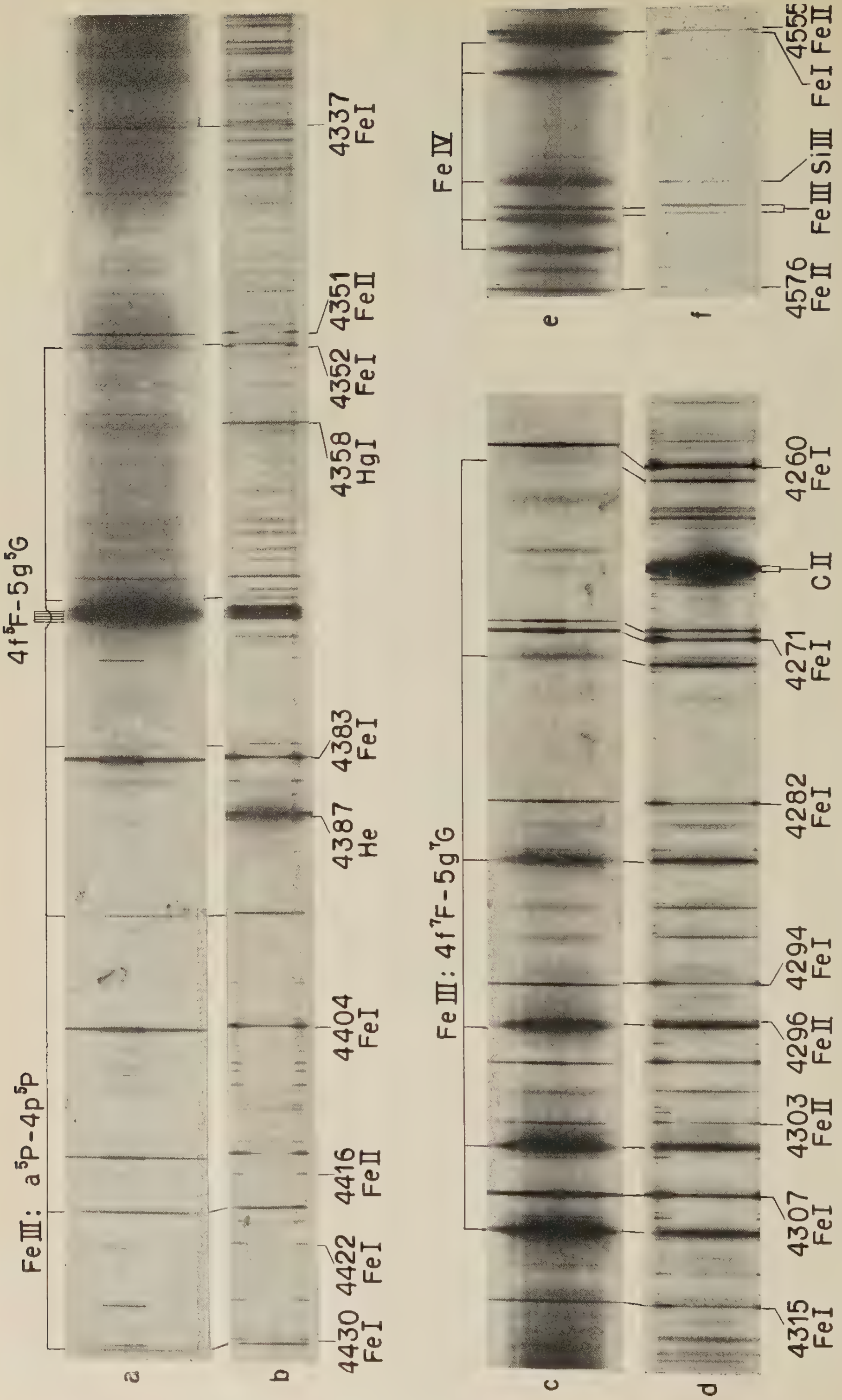
Fe III: a^{5}P-4p^{5}P
4f^{5}F-5g^{5}G
4337 FeI
4351 FeII
4352 FeI
4358 HgI
4383 FeI
4387 He
4404 FeI
4416 FeII
4422 FeI
4430 FeI
a
b
Fe IV
4555 FeII
FeI
SiIII
FeIII
4576 FeII
e
f
Fe III: 4f^{7}F-5g^{7}G
4260 FeI
CII
4271 FeI
4282 FeI
4294 FeI
4296 FeII
4303 FeII
4307 FeI
4315 FeI
c
d

ARKIV FÖR FYSIK Band 10 nr 23

Read 11 May 1955

Continued measurements of ions formed by corona discharge

By Harald Norinder and Reinhards Siksna

With 14 figures in the text

1. Introduction

It has been known for a long time that ions will be formed by corona discharge. However, there are not too many investigations concerning properties of these ions in spite of the importance of knowing them for the explanation of different phenomena related to corona discharge.

As one of the first papers where an attempt to measure the mobility of small ions formed by point discharge is described, Franck's doctor's thesis (1906) [2] must be mentioned. The experimental arrangement used by Franck seems to be worth a reproduction in a modern version. Young [20] has attempted to investigate the large ions formed by corona, and he has established a large number of groups with mobilities down to 10^{-5} cm sec^{-1}/volt cm^{-1}, stating that "nearly all mobilities were found below 10^{-2}, the ions apparently being generated in equal numbers, except now and then a greater number of a certain mobility was formed". The fickleness of Young's results could be understood by regarding that the transformation of corona ions with time has not been respected. Nolan and O'Keeffe [5, 6, 7] measured the ions produced in discharge at liquid surfaces and have concluded that part of ions formed are of multiple charge. Koller [4] measured ions formed by a cylindric corona device, stating concentrations up to 10^7 cm^{-3} without noting the mobility of the ions measured. Israël and Schulz [3] measured the mobility composition of the ions formed by an ion producer made by the firm of AEG and constructed for medical purposes. Corona discharge was its acting mechanism, but detailed data of the mobility distribution of the ions are not given in the publication, indicating only that beside small ions with concentrations up to 6.5×10^5 cm^{-3} large ions with concentrations up to 8.5×10^4 cm^{-3} were present. Series of investigations of corona ions have been carried out at this institute [8, 9, 10, 14, 15]. The results of our investigations quoted can be summarized as follows: Beside small ions a fraction of charged particles with mobilities of large ions was established in the room where corona was acting. For the development of this fraction some time was necessary, it was transformed with time and in a different way in the case of positive or negative corona. Some peculiarities were established when alternating the polarity of the corona potential and by using alternating corona potential [18]. Continued measurements of ions formed by corona in different devices and carried out from different points of view will be considered in the present paper.

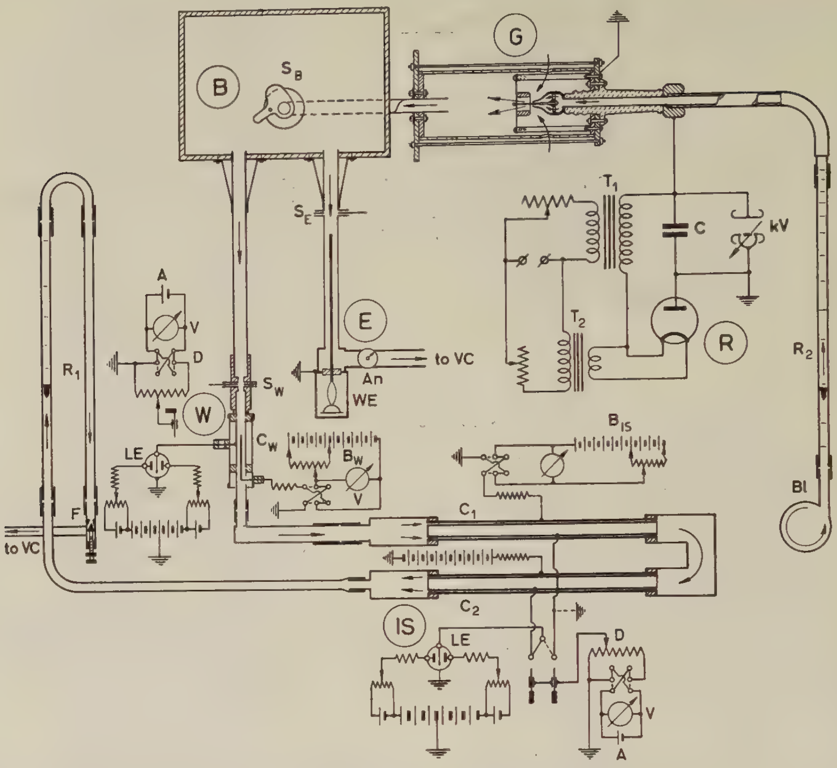

Fig. 1. Schematic diagram of the experimental arrangement. (*G*) generator of corona ions, *Bl* air blower, R_2 rotameter; (*R*) rectifier, T_1 high tension transformer, T_2 heating transformer, *C* condenser, *kV* Starke-Schröder high-tension voltmeter; (*B*) suction box, S_B slide; (*W*) small-ion counter with Weger condenser C_W, *LE* Lindemann electrometer, *D* calibration device, S_W slide; (*E*) Ebert ion counter, *WE* Wulf bifilar electrometer, *An* anemometer, S_E slide; (*IS*) Israël large-ion counter, C_1, C_2 cylindrical condensers, *LE* Lindemann electrometer, *D* calibration device, R_1 rotameter, *F* valve to adjust the air-flow, *VC* vacuum cleaner.

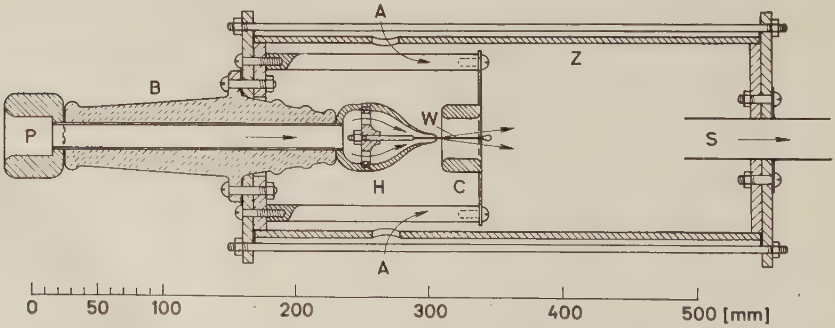

Fig. 2. Schematic diagram of the generator of corona ions. *Z* bakelite cylinder, *B* bushing, *H* head of the corona electrode, *W* corona wire, *C* cylindrical grounded electrode, *P* pipe for pressed air, *S* pipe for suction of ionized air to the suction box and the ion counters respectively.

2. Experimental arrangement

2.1. *Ion counters.*—The measuring devices used were in general the same as for our earlier investigations: a small-ion counter with a Weger condenser [15] and an Israël large-ion counter [9]. A part of the measurements with the large-ion counter was carried out with the condensers of the counter connected in series, as shown in Fig. 1 and by alternating the adjusted limiting mobility by variation of the potential of the first condenser. Thus two advantages were obtained: (1) The scanning of the small ions with the lower end of the limiting mobility was obviated in this connection. The effect of scanning the small ions is considered by us [14] and as shown it may be of advantage in some cases, yet it may also be troublesome. (2) By alternation of the adjusted limiting mobility of the counter by variation of the potential of the first condenser at constant air-flow through the counter it was attempted to remove disturbances arising when the limiting mobility was adjusted by the air-flow. In this last case different transformations of the ions could be expected during their travelling through the connection tubes to the counter. However, part of the present measurements was carried out by alternation of the limiting mobility by changing the air-flow at constant potential of both condensers connected in this case in parallel for the air-flow, because a more rapid operation may be obtained in such an arrangement and the number of adjusted mobilities could be increased. Because the aspiration through the measuring ion counters was too slow to replace the air sufficiently speedily in the suction box, an Ebert ion counter was also joined to the suction box for maintaining a sufficient air-flow (200 l/min) through it.

2.2. *Generator of corona ions.*—The generator used by us during an earlier work [15] was completed and the new construction is shown in Fig. 2. Against the ends of a bakelite tube Z of 15 cm diameter and of 38 cm length two bakelite disks were pressed with three bolts. The disks were tightened with rubber washers. In the centre of one of the disks a porcelain bushing B was fastened. A brass tube with the head H for the corona wire at one end and an aluminium cylinder P with rounded edges at the other end was put into the bushing. The corona wire W, a piece of a 0.5 mm or 0.25 mm thick kanthal wire, extended 3 cm out from the nozzle of the head. A brass sphere of 5 mm diameter was fixed to the free end of the corona wire to prevent discharge on the sharp end. Through the nozzles of the head with the inner diameter of 3 mm it was possible to blow air along the corona wire. The air-flow through the nozzle was measured by the rotameter R_2 (Fig. 1). Axially to the corona wire an aluminium cylinder C with the inner diameter of 30 mm and with rounded edges was placed. This cylinder was connected with the second terminal of the high tension source through the ground. A brass connection tube S of 30 mm diameter was fixed to the other bakelite disk. This tube was connected with the suction box. Air was drawn in across the corona wire, through two apertures A made in the bakelite tube Z.

3. Small ions

3.1. *Concentration of ions formed. Dependence on the diameter of the corona wire.*—As could be expected, the starting of the production of small ions was established at a lower potential applied to the corona wire if its diameter was smaller, because the field on the surface of the wire is in the case of a wire with a smaller diameter higher at the same potential applied. The concentration of small ions measured in dependence on the corona potential applied is shown in Figs. 3 and 4 for two wires with diameters of 0.25 mm and of 0.5 mm respectively. The increase of the concentration is more rapid in dependence on the increase of the potential in the case of a wire with a diameter of 0.25 mm. Up to $U = 10$ kV this increase is very steep, after

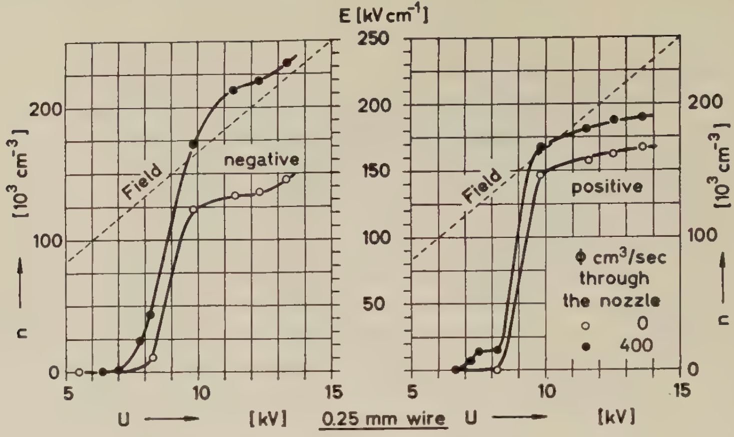

Fig. 3. Dependence of the concentration of small ions formed n on the corona potential U; 0.25 mm corona wire.

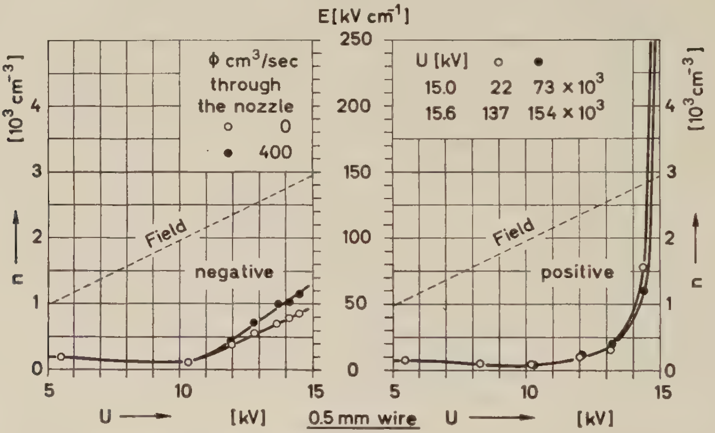

Fig. 4. Dependence of the concentration of small ions formed n on the corona potential U; 0.5 mm corona wire.

reaching 10 kV it is flatter. In the case of the wire of 0.5 mm diameter the increase of the concentration is small for positive ions up to 14 kV when a marked increase was stated.

3.2. *Influence of the air-flow along the corona wire.*—As already mentioned, through a nozzle of the corona head it was possible to blow air along the corona wire. When using an air-flow of 400 cm³/sec the speed of the air coming from the nozzle along the corona wire is 5600 cm/sec. Results when blowing air are also shown in Figs. 3 and 4. For 0.25 mm corona wire (Fig. 3) the concentration of both—negative and positive small ions measured—increases; the increase of the concentration of negative ions being more pronounced. For 0.5 mm corona wire the increase of the concentration of ions is somewhat different from that of the 0.25 mm wire when blowing air, as

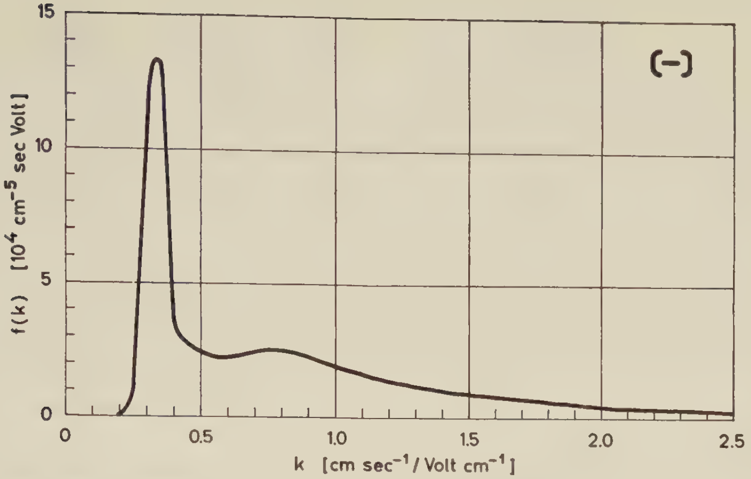

Fig. 5. Distribution function of mobilities $f(k)$ for negative small ions formed by corona.

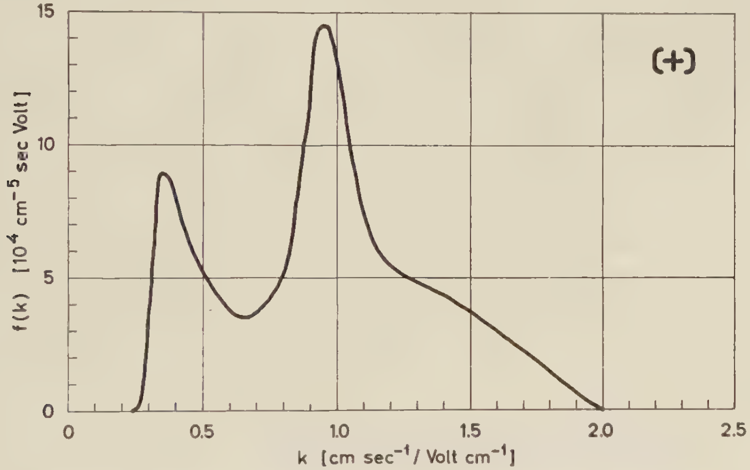

Fig. 6. Distribution function of mobilities $f(k)$ for positive small ions formed by corona.

shown in Fig. 4. The ions of the sign opposite to the polarity of the corona potential applied were not measured when blowing air along the corona wire, because during the measurements considered here we have had a conception that ions only of the sign of the corona potential applied could be present. By our experiments of using alternating corona potential [18] it was shown that ions of both polarities were present when blowing air through the corona device. Therefore, the presence of ions of both polarities must be examined when blowing air also in the case of direct current corona of one polarity. It is not excluded that some new insights into the process of production of ions by corona discharge might be obtained by such an examination. As the dependence of the development stages of the corona phenomena ranged over

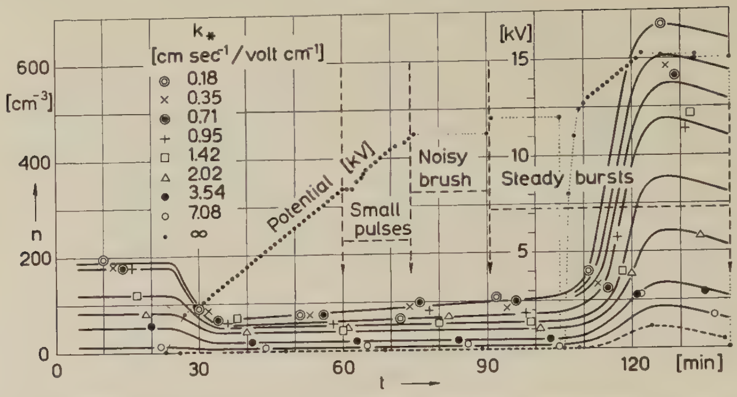

Fig. 7. Number of small ions measured with a Weger condenser periodically adjusted for chosen limiting mobilities k_*, during positive corona discharge when gradually increasing corona potential.

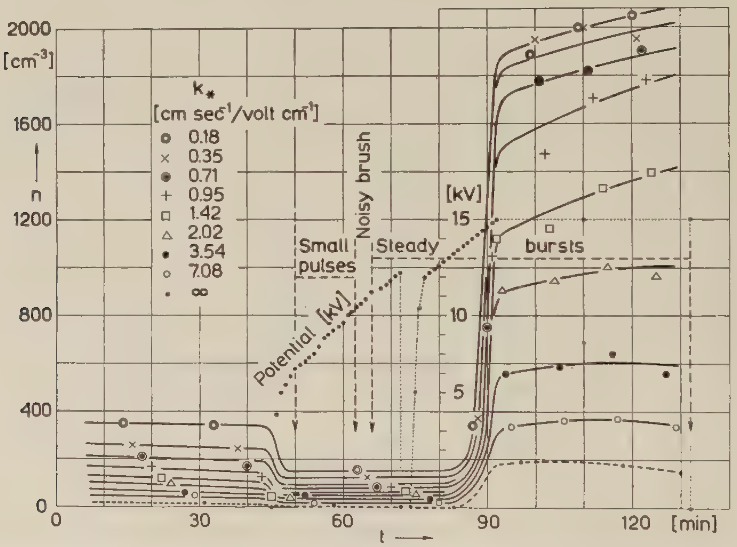

Fig. 8. Number of small ions measured with a Weger condenser periodically adjusted for chosen limiting mobilities k_*, during positive corona discharge when gradually increasing corona potential.

a larger diapazon of the potential applied in the case of a wire with a large diameter, the following measurements were carried out by using corona wire with a diameter of 0.5 mm.

3.3. *Mobility.*—From our earlier measurements of small ions with respect to their mobilities [15] we have got an idea that the atmospheric small ions may be divided into two groups with different properties [11]. It was proposed to call the ions of the first group *initial small ions* and those of the second group *affected small ions*, as the latter ions may be considered as transformed with time from the former. Thus it seemed to be of great importance to investigate in more detail the small ions from that point of view and it seemed that ions formed by corona might be suitable for this purpose. The arrangement of satisfactory conditions for measurements was, however, not easy because of disturbances caused by different troubles in the apparatuses used. The inconstancy of the corona potential was one of the principal causes by which the measurements were troubled. The inconstancy of the corona potential applied may not be caused only by the variation of the potential source, but also by the corona discharge itself. The variations of the potential source can be obviated by stabilization. The constancy of the discharge may not be obtained so easy. The events under examination might also be influenced by variation of the humidity of the air while measuring. Results from one of the best series are shown in the following figures: the distribution function of mobilities of negative corona ions (Fig. 5) is in general similar to that obtained earlier [15]; the distribution function of positive ions produced by corona is shown in Fig. 6 with two marked peaks—a shape of mobility distribution of positive ions observed also by Tyndall, Grindley and Scheppard [19], Erikson [1], Zeleny [21, 22], and Pollermann [13]. Such marked separation into two peaks was not always shown. Some peculiar conditions must be present in the considered case. Usually the median mobility of positive small-ions produced by corona was 0.82–0.88 cm $\sec^{-1}$/volt cm^{-1}, in some cases 1 cm $\sec^{-1}$/volt cm^{-1}.

3.4. *Development stages of positive corona.*—In the case of positive corona when gradually increasing the corona potential, some irregularities were observed in the range between 9.8–10 kV for 0.5 mm corona wire. As shown in Fig. 4, no small ions were produced in this range of the potential applied, but a noise was heard coming from the discharge gap. By increasing the potential still more the noise ceased. As shown in [16, 17], a phase of positive corona called noisy brush was the cause of the noise. By a detailed investigation of the development stages of positive corona [12, 16, 17] it was shown that the particular phases can be very sensitively indicated by an oscillograph connected with the corona device. Small pulses were already indicated at 5–8 kV. By increasing the potential their frequency and magnitude also increased. At *c.* 10 kV big pulses appeared, superposed at the beginning on the small pulses, later on with increasing frequency of the big pulses a deflection of the zero line was caused and therefore, the small pulses were observed only on the trails of the big pulses. At *c.* 12 kV the frequency of the big pulses decreased and quick oscillations appeared on the trails of the big pulses. At the place of the zero line of the oscilloscope screen these quick oscillations with small amplitudes were now observed.

3.5. *Concentration of small ions during different stages of positive corona.*—Now it was of interest to see how the production of ions varies during different stages of positive corona. Results of two series of measurements by using periodical alternation of chosen limiting mobilities of the Weger condenser are shown in Figs. 7 and 8. As may be seen, as soon as the corona potential was switched on, the number of ions measured decreased. No production of small ions was observed during the phases of small pulses, noisy brush and at the beginning of steady bursts. An increase of the concentration of small ions was established only when the potential was high enough (13–14 kV) during the steady corona. The diminishing of the concentration of small ions when the potential was just applied and before the great increase is partly due to the removing by the electrodes of the small ions usually present in the air.

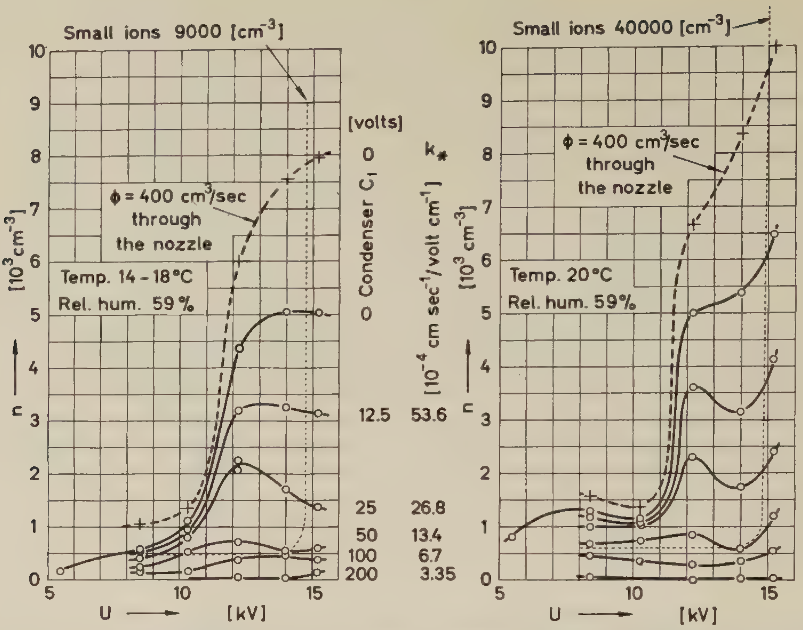

Fig. 9. Number of ions measured with the large-ion counter. Limiting mobility k_* adjusted by alternating the potential applied to the first condenser C_1. Dependence on the corona potential U.

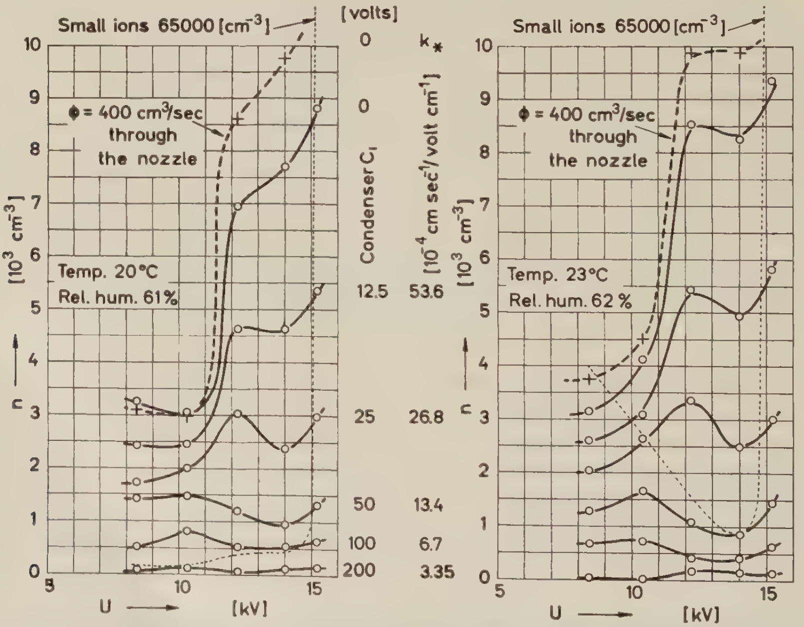

Fig. 10. Number of ions measured with the large-ion counter. Limiting mobility k_* adjusted by alternating the potential applied to the first condenser C_1. Dependence on the corona potential U.

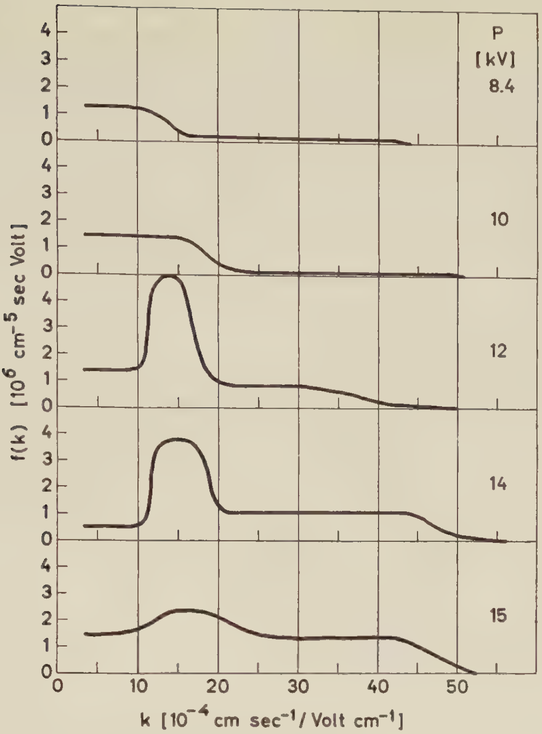

Fig. 11. Distribution function of mobilities $f(k)$ for positive large ions formed by corona. Dependence on the corona potential P.

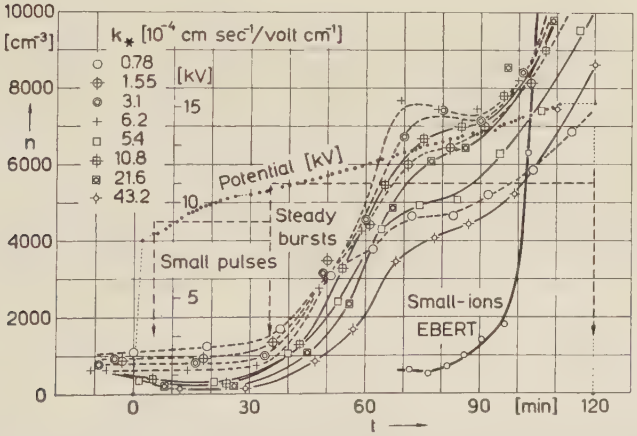

Fig. 12. Number of charges measured with an Israël large-ion counter adjusted periodically for chosen limiting mobilities k_* during positive corona discharge when gradually increasing corona potential.

4. Fraction of positive large ions

Only positive large ions were measured, and therefore only these ions will be considered below.

4.1. *Mobility groups.*—The first series of measurements were carried out by using the scheme shown in Fig. 1 with variation of the adjusted limiting mobility by alternation of the potential applied to the first condenser. The number of ions was measured in dependence on the corona potential applied. Results of 4 such series are shown in Figs. 9 and 10. The concentration of small ions was simultaneously measured with the Weger condenser and the results are also plotted on the figures. Small ions were produced in a considerable quantity only at a corona potential of 14.7–15 kV, however, large ions were established at a potential of 10 kV or even below that. When air was blown along the corona wire, the concentration of large ions measured increased, such measurements were carried out only at zero potential of the first condenser. The distribution functions with respect to the mobilities of the series without air-blowing were sufficiently similar one to another for all the four series considered, and therefore average distribution functions were computed and plotted in Fig. 11 for different corona potentials. At a corona potential of 8.4 kV a band of large ions is stated in the range of mobilities between 3 and 12 × 10^{-4} cm sec^{-1}/volt cm^{-1}; this band may be attributed to the large ions present in the air without corona acting. By increasing the potential up to 10 kV, the band is enlarged in the direction of higher mobilities, at a potential of 12 kV a marked peak between (10÷18) × 10^{-4} cm sec^{-1}/volt cm^{-1} is shown with a lower trail up to $k = 45 \times 10^{-4}$ cm sec^{-1}/volt cm^{-1}. When increasing the potential up to 14 kV the peak is lower and broader and the trail of the high mobilities spreads more to higher mobilities. More marked the same variations are shown for a potential of 15 kV, when the small ions were

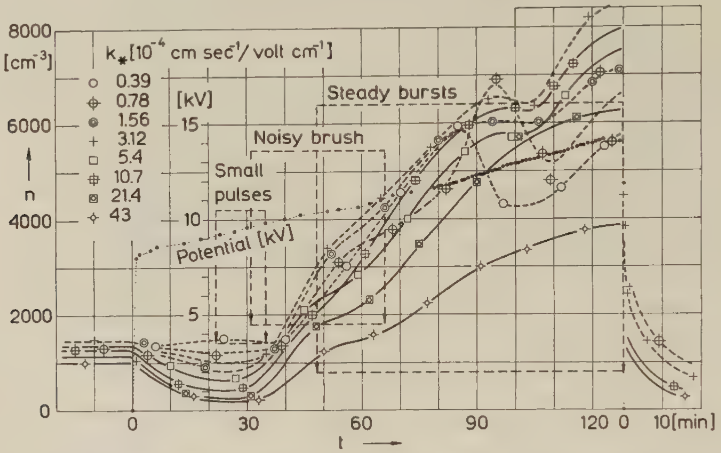

Fig. 13. Number of charges measured with an Israël large-ion counter adjusted periodically for chosen limiting mobilities k_*, during positive corona discharge when gradually increasing corona potential.

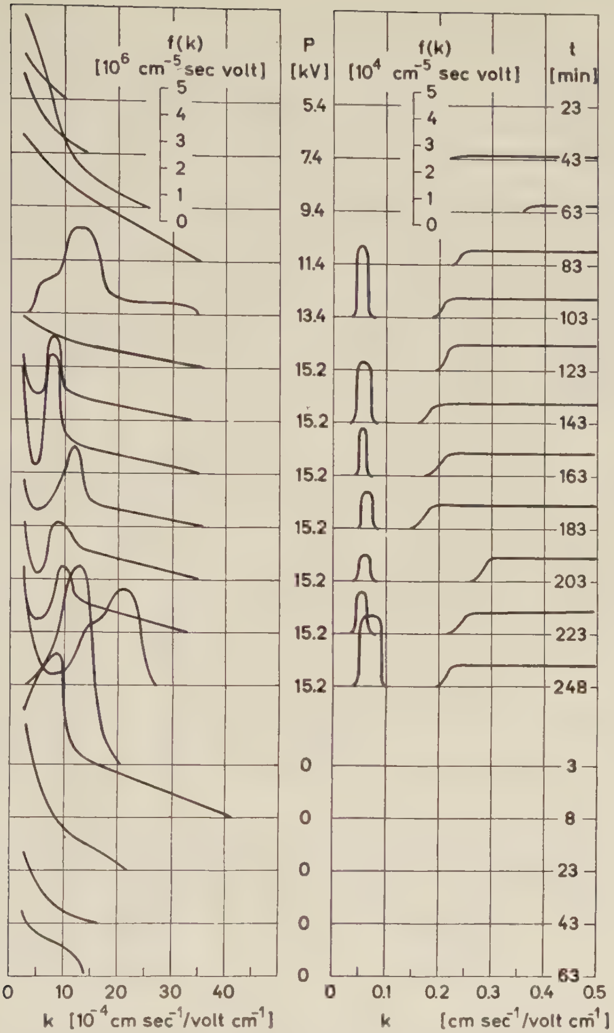

Fig. 14. Distribution functions of mobilities $f(k)$ of large, intermediate and small ions formed in a room by positive corona discharge, calculated from measurements carried out with a large-ion counter by adjusting periodically the limiting mobilities with alternation of the air-flow through the two condensers connected in parallel for the air-flow.

also established. The band and the peak considered are the same as established in the air from a room where corona was acting [15], they are only displaced a little to higher mobilities. It seems that by the measuring arrangement used here, namely by changing the adjusted limiting mobilities with alternation of the potential applied to the first condenser, more disturbances were eliminated and therefore the data obtained by using this arrangement may be regarded as more definite.

4.2. *Variation of the concentration of large ions measured during different stages of positive corona.*—In the following series (Figs. 12 and 13) it was attempted to measure the concentration of large ions formed by the corona generator during different stages of positive corona by using the large-ion counter with both the condensers connected in parallel for the air-flow and by variation of the adjusted limiting mobility by alternation of the air-flow, as used during our earlier investigations [8, 9, 10]. The particular stages of the positive corona were determined by the oscillograph. No definite influence may be seen during individual stages. It could be of importance to note here that no special influence on the concentration of the large ions measured was stated during the noisy brush phase when very intense pulses were observed. That very intensive processes of formation and transformation of large ions were present in the corona gap is shown by the trends of the measured concentration-time curves. However, difficulties arose by calculating the mobility distribution from these curves. Therefore, only the ranges of the mobility bands were estimated and results of this estimation are shown in Table 1.

Table 1. Ranges of mobility of positive large ions formed by the generator of corona ions.

Ions	Range of mobility bands $[10^{-4}$ cm sec^{-1}/volt cm$^{-1}]$	Concentration [cm^{-3}]
Large	3–4 6–40	some thousands 1000–9000
Intermediate	100–200 400–800	some hundreds some thousands

The ranges of the bands coincide sufficiently with those from our earlier series, when ions have been measured in the air from a large room where corona was acting [15]. For comparison a non-published series from those measurements is given in Fig. 14. The bands shown on the right-hand side of the figure are those scanned by the lower end of the adjusted limiting mobility and the bands on the very right-hand side are those of the small ions. The lower range of these last bands at about 0.2 cm sec^{-1} /volt cm^{-1} agrees sufficiently with that shown in Fig. 6 measured with the Weger condenser. This coincidence is surprising because the methods by which the bands were computed in the two cases were very different and the scanning of small ions with the large-ion counter [14] cannot be regarded as promising very definite results.

We wish to thank the Swedish Natural Science Research Council for placing means at the disposal of the Institute to perform this investigation. Credit is due to Mr. A. Metnieks and Dr. H. A. Watson who assisted in the observations and calculations.

Institutet för högspänningsforskning vid Uppsala Universitet, May 1955.

REFERENCES

1. Erikson, H. A., Factors affecting the nature of ions in air. *Phys. Rev., 34,* 635–643 (1929).
2. Franck, J., Über die Beweglichkeit der Ladungsträger der Spitzenentladung. *Ann. Phys.* (Leipzig), (4), *21,* 972–1000 (1906).
3. Israël, H. und Schulz, L., Das Ionengerät der AEG. *Der Balneologe, 1,* 503–506 (1934).
4. Koller, L. R., Ionization of the atmosphere and its biological effects. *J. Frankl. Inst., 214,* 543–568 (1932).
5. Nolan, J. J. and O'Keeffe, J. G., The ions produced by discharge at liquid surfaces. *Proc. Roy. Irish Acad.* (A), *39,* 21–30 (1929).
6. —— Electric discharge from water drops. *Proc. Roy. Irish Acad.* (A), *40,* 86–98 (1932).
7. —— Multiply charged large ions. *Proc. Roy. Irish Acad.* (A), *41,* 26–40 (1933).
8. Norinder, H. and Siksna, R., Ions formed by corona discharge. *IVA,* (Stockholm), *23,* 234–245 (1952).
9. —— Ions formed in a room by negative wire corona. *Ark. fys., 6,* Nr 14, 127–140 (1952).
10. —— Ions formed in a room by positive wire corona. *Ark.* fys. *6,* Nr 25, 255–261 (1953).
11. —— Mobility of atmospheric small ions during summer nights at Uppsala. *J. Atmosph. Terr. Phys., 4,* 93–105 (1953).
12. —— Indication of the development stages of positive corona discharge in the atmospheric air. *IVA* (Stockholm), *26,* 46–57 (1955).
13. Pollermann, M., Die Tröpfchenbildung an Ionen in der Wilsonschen Nebelkammer. *Ann. Phys.* (Leipzig) (6), *5,* 329–348 (1950).
14. Siksna, R., Mobility spectra of ions formed in a room by negative corona discharge. *Ark. fys., 5,* Nr 26, 545–564 (1952).
15. —— Mobility spectra of ions formed in a room by positive corona discharge. *Ark. fys., 6,* Nr 28, 279–286 (1953).
16. —— Two different breakdowns between a positive electrode with small curvature and a plane. *Ark. fys., 9,* Nr 6, 77–82 (1954).
17. —— Some peculiarities of the current-potential characteristics of positive corona discharge. *Ark. fys., 9,* Nr 7, 83–91 (1954).
18. —— Charged condensation nuclei formed in a room by corona discharge when alternating the polarity of the corona potential and by using alternating corona potential. *Geofisica pura e applicata, 31,* 39–49 (1955).
19. Tyndall, A. M., Grindley, G. C., and Scheppard, P. A., The mobility of ions in air. Part V. The transformation of positive ions at short ages. *Proc. Roy. Soc.* (London) (A), *121,* 185–194 (1928).
20. Young, W. M., Mobility of the ions in the corona discharge. *Phys. Rev., 28,* 129–141 (1926).
21. Zeleny, J., The mobilities of ions in dry and moist air. *Phys. Rev., 36,* 35–43 (1930).
22. —— The aging of ions in air and nitrogen. *Phys. Rev., 38,* 969–976 (1931).

Tryckt den 31 januari 1956

Uppsala 1956. Almqvist & Wiksells Boktryckeri AB

ARKIV FÖR FYSIK Band 10 nr 24

Communicated 26 October 1955 by E. HULTHÉN

An excited level of high spin of Gd^{154}

By B. HARTMANN and T. WIEDLING

Slattery *et al* [1] have reported an excited level of 1.54 Mev energy in Gd^{154}, which decays through emission of two cascaded gamma rays of 1.42 Mev and 123 kev energy respectively. Because of the fact that they could not detect any coincidences between betas in the decay of Eu^{154} and the gamma ray deexciting the 1.54 Mev level, they drew the conclusion that this latter level had a mean life longer than microseconds. Among other measurements of Gd^{154} we may mention those by Church and Goldhaber [2], who found transitions of 123.4 kev and 247.7 kev. Sunyar [3] reports a mean life of 4.2×10^{-9} sec of the 123 kev level.

A disintegration scheme like this one is of great interest because of the fact that if the first gamma ray starts from an excited state of rather long mean life it is very probable that the atom is in its ground state and thus no complications due to atomic excitation are to be expected in a gamma-gamma correlation measurement. Further, as the mean life of the first excited state is known a more detailed investigation of this state by correlation methods is possible.

We have started a gamma-gamma correlation measurement of Gd^{154} because of the reasons just mentioned. As is common in experiments of this kind we used scintillation spectrometers. The mother substance of Eu^{154} used is strongly mixed with Eu^{152} as we only had access to a pile irradiated europium source of natural isotope abundance. As is well-known Eu^{152} decays with several gamma lines up to rather high energies (up to 1.09 Mev). For that reason we put the discriminator of one channel just below the 1.4 Mev peak and the differential discriminator of the other channel accepted only the 123 kev line. However, it is a problem here that the 123 kev gamma-ray intensity of Gd^{152} is about seven times [4] higher than that of Gd^{154}, thereby making it necessary not to use too strong a source.

Hitherto we have only measured on sources of $EuCl_3$ dissolved in water,[1] and have got the following result:

$$A_2 = 0.219 \pm 0.005$$

$$A_4 = -0.003 \pm 0.007$$

---

[1] We wish to express our thanks to Dr. L. Holm, Nobel Institute of Physics, who put this source at our disposal.

where A_2 and A_4 are the coefficients in $W(\theta) = 1 + A_2 P_2(\cos\theta) + A_4 P_4(\cos\theta)$. The experimental coefficients A_2 and A_4 are corrected for the angular resolution of the counters.

As the Gd^{154} nucleus is of the even-even type the ground state spin is zero and the first excited state probably has the spin 2. Under the assumption of pure multipole character of the transitions and $I = 6$ for the 1.54 Mev level the theoretical Legendre coefficients [5] are

$$A_2 = 0.2208$$

$$A_4 = -0.0018.$$

These numbers are in agreement with those experimentally found within the experimental errors.

Of course we cannot disregard at this point of our investigation the possibility that we have an attenuation effect of the correlation or a mixture in the first transition. However, we can immediately say that the spins 0, 1, 2 or 3 of the 1.54 Mev level are not possible for in these cases we can expect a not found cross-over transition and further this level has too long a half life for these spin values. For this reason spin 4 is not possible either and further this value should give pure multipole radiation. Slattery *et al.* proposed the level at 1.54 Mev to be a second excited state but according to Scharff-Goldhaber's [6] systematics an even-even nucleus cannot as a rule be expected to have a higher spin of the second excited state than 4 and then we must have a short half life contrary to the experimental results. However, as was earlier pointed out Church and Goldhaber have found two transitions of low energies in Gd^{154} which possibly deexcite the first and second excited states. The 1.54 Mev level must then be of higher order and may be a long-lived excited state. We can thus conclude that a spin of 6 of this excited state is probable.

We wish to express our gratitude to Professor Erik Hulthén for his encouraging interest in this work. We also wish to thank Atomkommittén for financial support.

Department of Physics, University of Stockholm, October 1955.

REFERENCES

1. SLATTERY, R. E., LU, D. C. and WIEDENBECK, M. L., Phys. Rev. *96*, 468 (1954).
2. CHURCH, E. L. and GOLDHABER, M., Bull. Am. Phys. Soc. *29*, 38, (April 29, 1954).
3. SUNYAR, A. W., Phys. Rev. *98*, 653 (1955).
4. ANDERSSON, B., Personal communication (Department of Physics, Chalmers University of Technology, Sweden).
5. LLOYD, S. P., Phys. Rev. *83*, 716 (1951).
6. SCHARFF-GOLDHABER, G. and WENESER, J., Phys. Rev., *98*, 212 (1955).

Tryckt den 31 januari 1956

Uppsala 1956. Almqvist & Wiksells Boktryckeri AB

ARKIV FÖR FYSIK Band 10 nr 25

Communicated 9 November 1955 by Manne Siegbahn and Erik Hulthén

Photographic emulsion measurements of the energy distribution of neutrons from spontaneous fission of californium 252. I

By Elis Hjalmar, Hilding Slätis and Stanley G. Thompson[1]

With 9 figures in the text

Contents

1. Introduction 357
2. Earlier investigations of energy distributions of fission neutrons 358
3. The californium sample 359
4. The experimental arrangement 359
5. Computation of the neutron energy 360
6. Observed energy distribution of neutrons from Cf^{252} 362
7. Neutron energy distribution corrections 362
8. Energy distribution distortion caused by the finite size of the source . . . 364
9. Result 366

Acknowledgments 367
Summary 367

1. Introduction

The isotopes of the transuranium elements decay by fission as well as by the other processes which occur in the lighter elements. The fission may be a result of excitation, such as by neutron capture, or it may occur spontaneously. Spontaneous fission is known for about fifteen nuclides [1]. The half-lives for this mode of decay range from $\sim 1.5 \times 10^{17}$ years for Th^{232} to 3 hours for Fm^{256}. For a detailed study of the spontaneous fission process the californium isotopes are particularly suitable. The half-lives for α decay and spontaneous fission of some californium isotopes are seen in Table 1.

Table 1. Alpha and spontaneous fission decay half-lives for californium isotopes.

Nuclide	α decay	Spontaneous fission	Reference
Cf^{248}	225 days	7000 years	1
Cf^{250}	12 years	5000 years	2
Cf^{252}	2.1 years	60 years	3
Cf^{254}	–	80 ± 15 days	3 a

---

[1] On leave from the University of California, Radiation Laboratory.

It is obvious that Cf^{252} provides a favourable ratio between the two modes of decay, and that this nuclide is especially suited for a study of spontaneous fission.

The fragments formed in fission emit almost immediately a few neutrons. The number of neutrons per fission in Cf^{252} is 3.82 ± 0.12 [4].

The purpose of our investigation was to determine the energy distribution of these neutrons by use of photographic emulsion technique.

2. Earlier investigations of energy distributions of fission neutrons

Earlier investigations of the distribution in energy of the neutrons emitted by fission have been made for neutrons from the fission of U^{235} and Pu^{239} induced by thermal neutrons. According to Nereson [5], Richards studied the spectrum of neutrons from $U^{235} + n$ using Ilford half-tone plates. Nicodemus and Staub [6] measured the neutron energy distribution by use of a high pressure ionization chamber, in which the proton recoil energy was measured. Nereson [5] used Ilford C2 plates for a study of the energy region 0.4–7 MeV, and Bonner, Ferrell, and Rinehart [7] carried out experiments with a cloud chamber filled with hydrogen gas at a pressure of 1/3 of an atmosphere and water vapor. In this way the energy region 0.05–0.7 MeV was covered. Hill [8] used a "Ranger" for measuring the range distribution of knock-on protons from thin paraffin layers. In this way the region 0.4–7 MeV was investigated. Watt [9] used a proton recoil counter for the range 3.3–17 MeV and combined the data with those obtained by Hill and by Bonner, Ferrell and Rinehart. It was found that the energy distribution in the whole interval 0.075–17 MeV fitted the formula

$$N(E) = \text{const.} \cdot e^{-E} \sinh \sqrt{2E}, \tag{1}$$

where E is the neutron energy in MeV.

Newer data have been obtained at Los Alamos by Barton, using an expansion cloud chamber filled with low pressure hydrogen plus water vapor for the energy region below 700 keV, by Cranberg and Nereson, who used a neutron time-of-flight method for the interval 0.2–3 MeV, and by Frye and Rosen, who used photographic emulsions for the energy region 0.3–12 MeV. These data have been combined by Leachman [10], who gives the following formula (derived by M. Goldstein and B. Carlson) for the distribution of energy of neutrons from thermal fission of U^{235}

$$N(E) = \text{const.} \cdot e^{-E/0.965} \sinh \sqrt{2.29 \cdot E}. \tag{2}$$

The empirically determined constants in this formula differ very little from those of Watt (formula (1)). Fig. 1 shows a comparison of this formula with experimental data as well as a representation of the simpler formula

$$N(E) = \text{const.} \cdot \sqrt{E} \cdot e^{-E/1.29}. \tag{3}$$

It is seen that this formula fits the experimental data almost as well as formula (2).

Theoretically the form of the neutron energy distribution curve can be understood assuming the neutron velocities are the vector sum of the resulting velocities of the

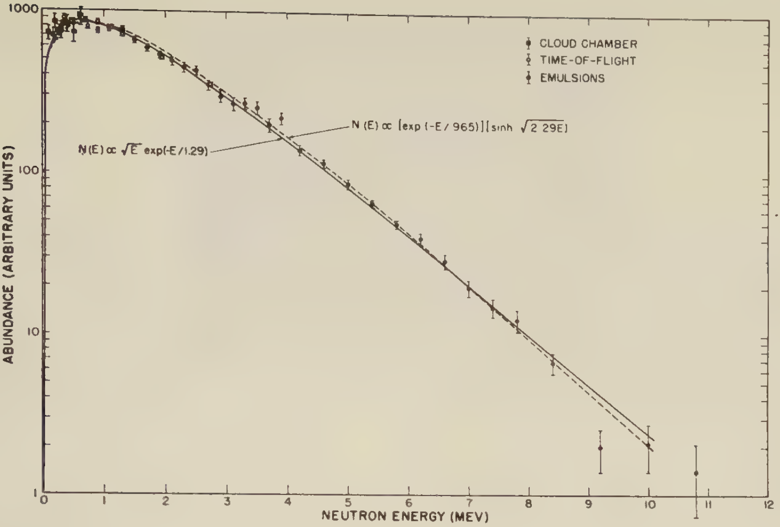

Fig. 1. Comparison of semi-empirical expressions of the energy spectrum of fission neutrons with recent measurements of thermal neutron induced fission of U^{235} according to Leachman [10].

neutron emitting fission fragments and a Maxwell-Boltzmann distribution velocity proportional to $\sqrt{E'}e^{-E'/Q}$, where Q is an energy corresponding to the "temperature" of the fragment and E' the neutron energy in the c.m. system. According to Watt [9], this explanation was first given by N. Feather.

3. The californium sample

The Cf^{252} source used in this work was prepared at Berkeley[1] following the neutron irradiation of Pu^{239} in the Materials Testing Reactor in Idaho (see for example [11]). The source also contained some Cf^{250}, similarly produced in the irradiation. The spontaneous fission rate of the sorce was approximately 30 per minute and essentially all fissions were produced by Cf^{252}, which is easily seen from the data in Table 1. Considering the number of neutrons per fission [4], 3.82, the rate of emission of neutrons was about 100 per minute.

The essentially weightless source was prepared by the evaporation of a solution of the californium isotopes on a thin platinum foil which was covered with another foil in order to prevent alpha particles from escaping. The diameter of the active deposit was about 3 mm.

4. The experimental arrangement

The source was placed in the center of a wooden box of dimensions $35 \times 35 \times 50$ cm^3 on a 5×10 cm^2 Type C2 Ilford Photographic Emulsion for Nuclear Research of 100 μ

---

[1] University of California, Radiation Laboratory.

thickness. The plate was exposed to the neutrons for 14 days. After the emulsion was developed for 15 minutes in ID-19, it was examined for proton recoil tracks using an Ortholux Research Microscope (magnification 300).

5. Computation of the neutron energy

The position of the californium sample on the Ilford plate was automatically recorded by means of the blackening caused by the emitted gamma rays. This auto-radiogram showed a circular spot with a more intense peripheral boundary (Fig. 2). Figs. 3 and 4 show the position of the data of interest when measuring the position and the length l of a proton recoil track and the angle ϑ between the direction of motion of the neutron and that of the proton. v is the angle between the proton track and the emulsion plane, and φ is the projection on the emulsion plane of the angle ϑ.

Because of the finite size of the sample the starting point of the neutron path is not known accurately. The starting point lies inside a circle, the diameter of which is 3 mm. The angle φ is therefore uncertain by an amount $<$ arc sin (r/R), where r is the radius of the peripheral boundary of the sample and R is the distance between the center of the sample and the starting point of the proton recoil track.

As a consequence of this it is not possible to use tracks which are found in the neighborhood of the sample. On the other hand, because of the small number of proton recoil tracks observed, one has to make some kind of compromise for the lower limit distance R, which is chosen for the tracks taken into consideration. We have used tracks for which $R \geq 6$ mm. The largest error in φ will therefore be arc sin $(1.5/6) = 14.5°$. The influence of this error will be discussed later (page 364).

Because of the small thickness of the emulsion, 0.1 mm, the position of the sample next to the emulsion and the condition $R \geq 6$ mm mentioned above, the neutron paths are practically in the plane of the emulsion. The finite size of the sample has therefore no influence on the computation of v, which is found from the simple formula $v = \text{arc tan } (h/l_H)$.

Simple geometric considerations give

$$\cos \vartheta = \cos v \cdot \cos \varphi \tag{4}$$

and the usual momentum and energy conservation equations for an elastic impact between a neutron and a proton give

$$E_n = E_p/\cos^2\vartheta, \tag{5}$$

where E_n and E_p are the energies of the neutron and that of the proton, respectively.

The best determinations of E_n are made for head on collisions or from impacts for which v and φ are small angles. Again, because of the small number of tracks observed, we have to take into consideration tracks for which these angles are quite large, viz. $|v| \leq 20°$ and $|\varphi| \leq 40°$. The limit $|v_0|$ for $|v|$ has been chosen smaller because the largest errors in the measurements are connected to the measurement of h.

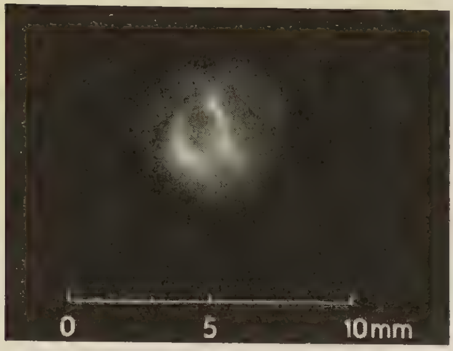

Fig. 2. Autoradiograph of the californium sample on the photographic emulsion. Compare Fig. 3.

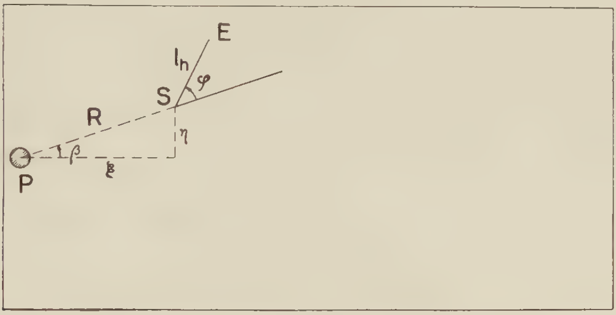

Fig. 3. Position P of the californium sample on the photographic plate and some of the data recorded for a proton recoil track. S = starting, E = endpoint, l_h = projection on the emulsion plane of the length l of the track.

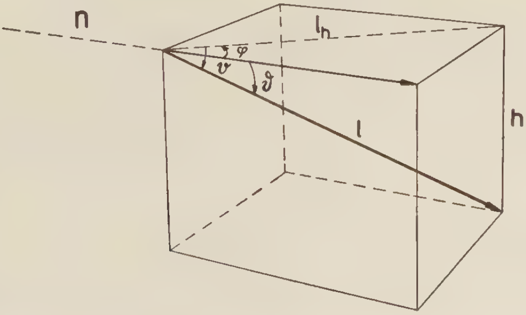

Fig. 4. Position of the neutron path n, the proton track l and the projection l_h of l in a plane parallel to the emulsion plane.

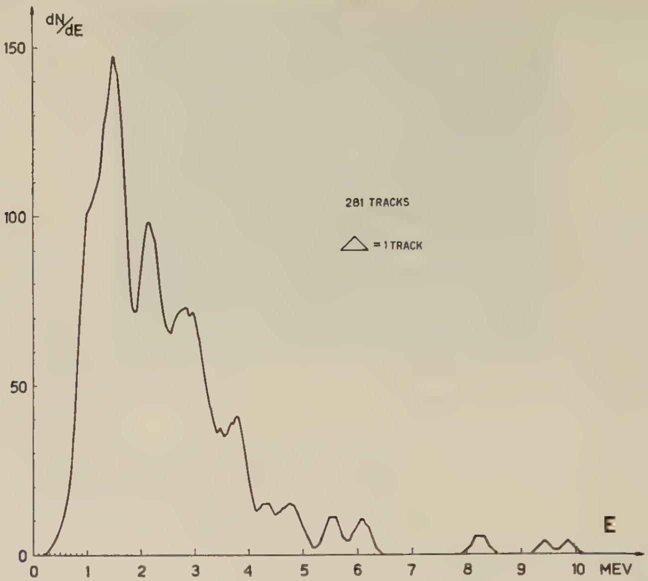

Fig. 5. Observed (uncorrected) energy distribution of neutrons from Cf^{252}.

6. Observed energy distribution of neutrons from Cf^{252}

A total of 281 tracks fulfilled the conditions described above. Fig. 5 shows the energy distribution of the corresponding neutrons from the fission of californium 252. Each neutron energy value is represented by a triangle of the shape marked on the figure, and the triangles are integrated. This method has been used previously in [12], for instance.

7. Neutron energy distribution corrections

Because of the differing probability that long tracks be acceptable for measurement, depending on the finite thickness of the emulsion, Richards [13] showed that for track lengths $l \geq d/\sin v_0$, where d is the emulsion thickness, the probability W that a track which starts in the emulsion (and hence be acceptable for measurement) also ends within the emulsion, is $W = d/2l \sin v_0$. For track lengths $l \leq d/\sin v_0$ this probability is $W = 1 - l \sin v_0/2d$. These relations are derived under the condition of small values for $|v_0|$. Fig. 6 shows a curve for the correction factor as well as the distribution curve corrected for the finite emulsion thickness (curve b).

The neutron energy distribution curve found has to be corrected also for the differing probability for impacts for different neutron energies. The probability for an impact between a neutron and a proton is proportional to the cross section σ for neutrons. The curve in Fig. 6 for the neutron cross section correction factor has been constructed by use of the data given in [14], and curve c gives the final energy

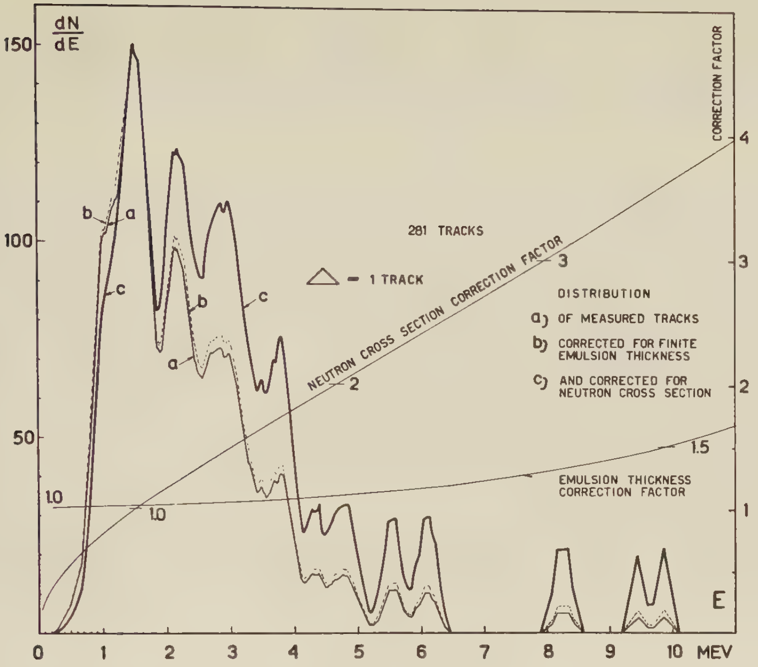

Fig. 6. Energy spectrum of neutrons from spontaneous fission of Cf^{252}.

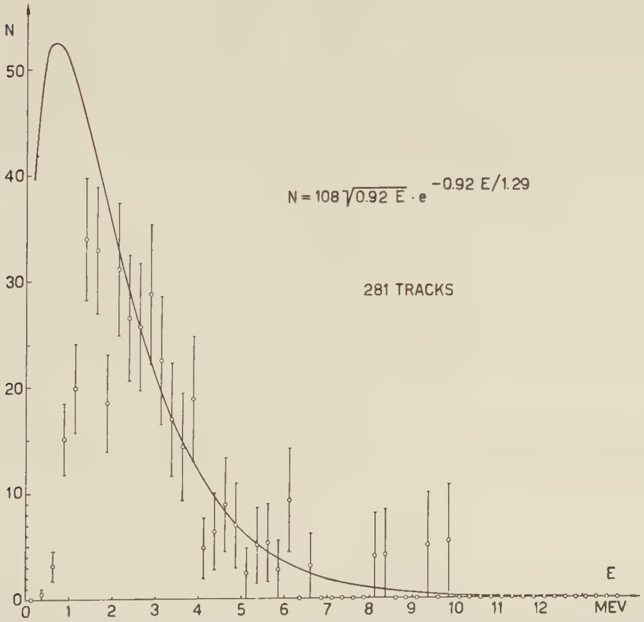

Fig. 7. Number of tracks per 0.25 MeV interval. The formula $N = 108\sqrt{0.92\,E}\cdot e^{\;0.92\,E/1.29}$, which fits the experimental data for $E \geq 2$ MeV, is obtained by use of the method of least squares.

spectrum of neutrons, corrected for finite emulsion thickness and for varying neutron cross section. Fig. 7 shows the same spectrum in another representation, viz. the number of tracks per 0.25 MeV energy interval as well as the statistical errors for each point. The smooth curve is explained in the figure as well as below (Section 9).

8. Energy distribution distortion caused by the finite size of the source

As mentioned before the californium sample covered a circular area with a diameter of 3 mm. The activity was concentrated in the periphery of the circle, as shown by the autoradiograph (Fig. 2). As a consequence, most of the neutrons are emitted from the boundary of the sample, and the maximum error in φ will be $\pm$ arc sin (r/R), as already mentioned on page 360. For small r/R values the error in φ statistically will have the + sign as frequently as the − sign, even if the distribution of the activity is not a symmetrical one. In cases where the $|\varphi|$ value has been taken too small the corresponding neutron energy will also be found too small, and vice versa. This circumstance will cause a distortion of the neutron distribution. We shall now compute this influence.

If the correct value of the projection in the emulsion plane of the deflection angle is $\varphi \pm$ arc sin (r/R) (this corresponds to a maximum error in φ), the formulas (4) and (5) give the observed neutron energy E_C for a circular source as

$$E_C = \frac{E_p}{\cos^2 v \cos^2 \varphi}\left(1 \pm \frac{2\,r}{R} \tan \varphi\right), \tag{6}$$

when we neglect higher powers of r/R. The probability for the proton to be emitted in a direction limited by φ and $\varphi + d\varphi$, v and $v + dv$ is proportional to $\cos v \cos \vartheta\, dv\, d\varphi = \cos^2 v \cos\varphi\, dv\, d\varphi$. Hence, the mean value M of $|\tan \varphi|$, if we have $|v| \leq v_0$, $|\varphi| \leq \varphi_0$, will be

$$M = \frac{\int\limits_0^{v_0} dv \int\limits_0^{\varphi_0} d\varphi \cdot \tan \varphi \cos^2 v \cos \varphi}{\int\limits_0^{v_0} dv \int\limits_0^{\varphi_0} d\varphi \cdot \cos^2 v \cos \varphi}. \tag{7}$$

For $|\varphi_0| = 40°$ we get $M = 0.366$. For $2\,r = 3$ mm and $R \geq 6$ mm we obtain, if we for brevity put $\Delta = (2r/R) \tan \varphi$

$$\Delta_{\max} = 0.183 \tag{8}$$

For $R = 6$ mm we have the largest error in E_C. Formula (6) shows that we then have, on an average, in the neutron energy a maximum relative error equal to

$$\frac{\delta E_C}{E_C} = 0.183.$$

When R increases, the relative error in E_C decreases proportional to $1/R$. The number of tracks found in the emulsion layer will also be proportional to $1/R$. Hence, if the distribution function of the energy E_0 of point source neutrons is N_0,

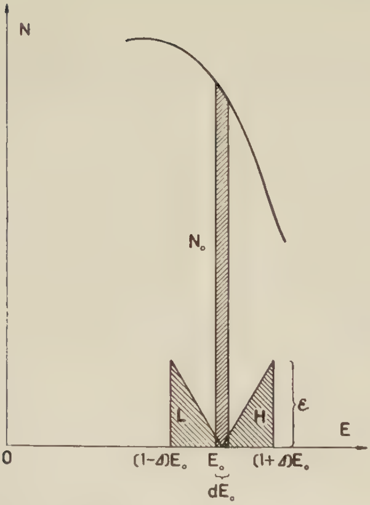

Fig. 8. Influence of the finite size of the source on the measured neutron energy distribution. $N_0 dE_0$ = number of tracks with an energy between E_0 and $E_0 + dE_0$. The hypotenuse in the triangle L is the energy distribution found for the half of those tracks, depending on too low a value for φ. The hypotenuse in the triangle H is the corresponding energy distribution for tracks, which have been computed for a value of φ which has been too high.

the number $N_0 dE$ of neutrons of an energy between E_0 and $E_0 + dE$ is experimentally found to be distributed in the energy interval $(1-\Delta)E_0$ to $(1+\Delta)E_0$ in such a way that the number of neutrons is proportional to $|E - E_0|$. (See Fig. 8.) Obviously,

$$N_0 dE_0 = \varepsilon E_0 \Delta. \tag{8}$$

Experimentally we get a distribution curve which is the sum of the distribution curve for the neutrons whose energy of which is determined too low, namely

$$N_L = \int\limits_{E_C}^{\frac{E_C}{1-\Delta}} \frac{E_0 - E_C}{E_0\,\Delta}\,\varepsilon \tag{9}$$

and the distribution for the neutrons whose energy of which is determined too high

$$N_H = \int\limits_{\frac{E_C}{1+\Delta}}^{E_C} \frac{E_C - E_0}{E_0\,\Delta}\,\varepsilon. \tag{10}$$

Considering (8), we get

$$N_L = \frac{1}{\Delta^2} \int\limits_{E_C}^{\frac{E_C}{1-\Delta}} \frac{E_0 - E_C}{E_0^2}\, N_0\, d E_0 \tag{9'}$$

and

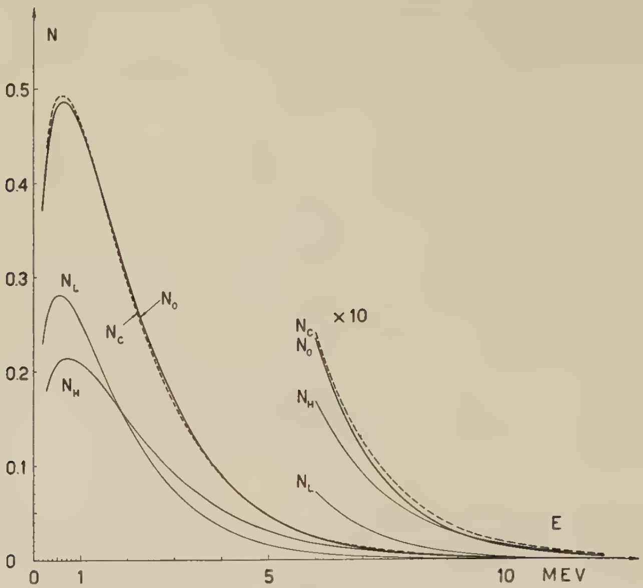

Fig. 9. Comparison of the semiempirical neutron energy distribution $N_0 = \sqrt{E} \cdot e^{-E/1.29}$ with the experimental neutron energy distribution N_C expected when the source has a circular shape. For details see the text.

$$N_H = -\frac{1}{\Delta^2} \int\limits_{\frac{E_C}{1+\Delta}}^{E_C} \frac{E_0 - E_C}{E_0^2} N_0 \, d E_0 . \tag{10'}$$

Fig. 9 shows the semiempirical distribution $N_0 = \sqrt{E} \cdot e^{-E/1.29}$ (point source), as well as the distributions N_L, N_H, and $N_C = N_L + N_H$ for a circular source, computed for $\Delta = 0.2$ and N_0. It is seen that the experimentally found distribution N_C for a circular source is very close to that for a point source. In addition, the curve N_C represents a maximum deviation from the curve N_0, because we have used $\Delta = 0.2$ instead of $\Delta = 0.183$ and, especially, because we have computed N_C supposing the errors in $|\varphi|$ would always be $\pm(r/R)$. However, as the activity is spread over a periphery and in addition over the circular surface, the errors in $|\varphi|$ will not often reach the value $\pm(r/R)$.

The result obtained shows that in our measurements a correction for the finite size of the californium source is not important.

9. Result

The energy distribution found for neutrons from spontaneous fission of californium is shown in Fig. 7. Because of the difficulty of detecting short tracks in photographic emulsions, the lower energy part, say below $E < 2$ MeV, should not be considered. The real maximum of the neutron energy distribution can hardly be determined accurately by nuclear research emulsions. The distribution above 2 MeV fits the formula

$$N = 108 \cdot \sqrt{0.92\,E} \cdot e^{-0.92\,E/1.29}, \tag{11}$$

which was determined by use of the method of least squares. The exponent denominator 1.29 is used in order to facilitate a comparison with the formula (3). The probable errors are ±11.5 for the factor 108 and ±0.06 for the coefficient 0.92.

As mentioned before, formula (3) represents the energy distribution for neutrons from thermal neutron fission of U^{235}. A comparison between (11) and (3) shows that the distributions are the same, if the energies in (3) are multiplied by 0.92, that is, the energies of the californium fission neutrons might be higher by a factor 1/0.92 or about 9 percent higher than the energies of the neutrons from thermal fission of U^{235}. However, the statistics are still insufficient to decide the reality of such a small difference in the compared energy distributions. The mean result is that the energy distributions are almost the same in those parts of the spectrum where the photographic method is reliable.

Summary

1. Earlier investigations of the energy distribution of neutrons from fission of U^{235} with thermal neutrons are briefly given.

2. The energy distribution of neutrons from the spontaneous fission of Cf^{252} was investigated by measuring the proton recoil tracks in a photographic emulsion.

3. The energy distribution was corrected for the finite thickness of the emulsion layer and for the varying neutron cross section.

4. The influence of the finite size of the californium sample on the energy distribution was computed. It was shown that the correction for the finite sample size was negligible.

5. The energy distribution of neutrons from spontaneous fission of Cf^{252} was found to be similar to that for neutrons from thermal neutron fission of U^{235}.

ACKNOWLEDGMENTS

It is a pleasure to acknowledge various helpful discussions with Dr. R. Leachman and Dr. T. Maris.

Nobel Institute of Physics, Stockholm 50, Sweden.

REFERENCES

1. R. A. Glass, S. G. Thompson, and G.T. Seaborg, J. Inorg. and Nuclear Chem. *1*, 3, 1955.
2. A. Ghiorso, S. G. Thompson, G. R. Choppin, and B. G. Harvey, Phys. Rev. *94*, 1081, 1954.
3. H. Diamond, L. B. Magnusson, J. F. Mech, C. M. Stevens, A. M. Friedman, M. H. Studier, P. R. Fields, and J. R. Huizenga, Phys. Rev. *94*, 1083, 1954.

3a. B. G. Harvey, S. G. Thompson, G. R. Choppin, and A. Ghiorso, Phys. Rev. *99*, 337, 1955.

4. D. A. Hicks, J. Ise, Jr., and R. V. Pyle, Phys. Rev. (in print). Private communication by D. A. Hicks.
5. N. Nereson, Phys. Rev. *85*, 600, 1952.
6. D. B. Nicodemus and H. H. Staub, Phys. Rev. *89*, 1288, 1953.
7. T. W. Bonner, R. A. Ferrell, and M. C. Rinehart, Phys. Rev. *87*, 1032, 1952.
8. D. L. Hill, Phys. Rev. *87*, 1034, 1952.
9. B. E. Watt, Phys. Rev. *87*, 1037, 1952.
10. R. B. Leachman, A/Conf. 8/P/592, U.S.A., 29 June 1955.
11. S. G. Thompson, A. Ghiorso, B. G. Harvey, and G. R. Choppin, Phys. Rev. *93*, 808, 1955.
12. H. Slätis, E. Hjalmar, and R. Carlsson, Phys. Rev. *81*, 641, 1951; Arkiv f. Fysik *3*, 315, 1951.
13. H. T. Richards, Phys. Rev. *59*, 796, 1941.
14. *Neutron Cross Section Compilation* (AECU-2040). Suppl. 1, Nov. 20, 1952.

Tryckt den 14 februari 1956

Uppsala 1956. Almqvist & Wiksells Boktryckeri AB

ARKIV FÖR FYSIK Band 10 nr 26

Communicated 26 October 1955 by MANNE SIEGBAHN

The position of the second excited level in C^{12}

By KATARINA AHNLUND

With 3 figures in the text

Introduction

The exact position of the "7.68 MeV" excited level in C^{12} has a special astrophysical interest as it very critically affects the yield for the conversion, by a sequence of reactions, of three alpha particles into one C^{12} nucleus (Salpeter [1, 2]). This might be a predominant process in hot stars where the original hydrogen content is practically exhausted. The level position would also indirectly govern the formation of the elements heavier than carbon. The C^{12} level in question corresponds to a maximum in the cross section of the $Be^8 + \alpha \rightarrow C^{12}$ reaction (Fig. 1). Due to this a considerable amount of C^{12} could be formed by alpha particles in the high energy tail of the alpha energy distribution corresponding to a central stellar temperature of the order of 10^8 °K, even though the Be^8 breaks up into two alpha particles in less than 4×10^{-15} seconds [3]. The lower the position of the excited level in C^{12}, the higher will be the probability for the reaction to occur for a given temperature of this order of magnitude.

The most accurate determinations of the exact resonance position have been made by the energy of the low cross-section $N^{14}(d, \alpha)C^{12}$ reaction to this state. By this method Dunbar *et al.* [4] and Sperduto *et al.* [5] found a level position at 7.68 ± 0.03 MeV excitation. A measurement at the Nobel Institute by Pauli [6] gave 7.66 ± 0.02 MeV. In this paper two new determinations of the same reaction are reported, which confirm the lower value obtained by Pauli.

Experimental procedure

The measurements were made during a survey of proton groups from thin separated $N^{14}O^{17}$ targets bombarded with 0.855 MeV deuterons [7]. Information about the general experimental arrangements is given in ref. 7. During these bombardments a spectrum of alpha groups were recorded in the photographic plates simultaneously with the proton spectrum. Among them were the alphas from the $N^{14}(d, \alpha)C^{12}$ transition leading to the second excited level in C^{12}. The identity of this alpha group was verified by the difference in energy between alpha particles ejected in two different laboratory angles θ to the bombarding deuteron beam. Figs. 2 and 3 show the alpha distributions obtained from this reaction at the two angles $\theta = 61.0°$ and $\theta = 134.7°$. In both cases a near-lying peak with known Q-value falling in the same photographic

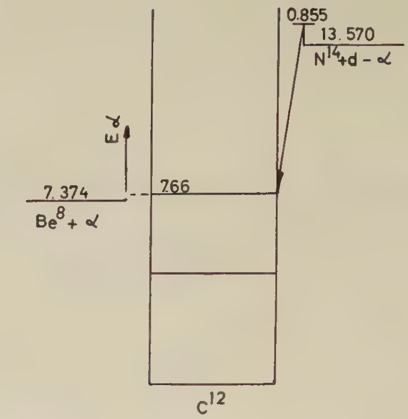

Fig. 1. The lower part of the energy level scheme of C^{12} with the reactions treated in the text.

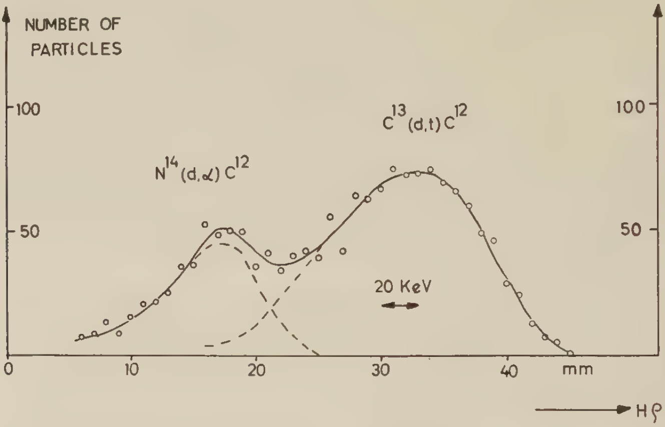

Fig. 2. Spectrum of alpha particles from $N^{14}(d, \alpha)C^{12}$ and of tritons from $C^{13}(d, t)C^{12}$ collected in one nuclear emulsion plate. $\theta_{lab} = 61.0°$ $2\Delta\theta = 3.4°$. Deuteron energy is 0.855 MeV. The number of tracks/0.4 mm on the plate is given in the ordinate.

plate was used to make an accurate calibration of the alpha energy scale. At $\theta = 61.0°$ one can use the triton group from $C^{13}(d, t)C^{12}$ with $Q = 1310 \pm 3$ keV [8] and at $\theta = 134.7°$ the proton group from $O^{17}(d, p)O^{18}$ with $Q = 3835 \pm 8$ keV [7].

The evaluation of the peaks was made in the way reported earlier. The peaks were read at the extrapolated high-energy edges and the calculations of Q were done for the corresponding minimum spectrometer angle $\theta - \Delta\theta$. A small correction for an external layer on the target was incorporated. The layer should be the same for the three types of target nuclei, C^{13}, N^{14} and O^{17}, as, by the isotope separation, all were collected simultaneously—in form of the ions $C^{13}O^{18}$, $N^{14}O^{17}$ and $N^{15}O^{16}$—on an iron plate placed at mass number 31 [9].

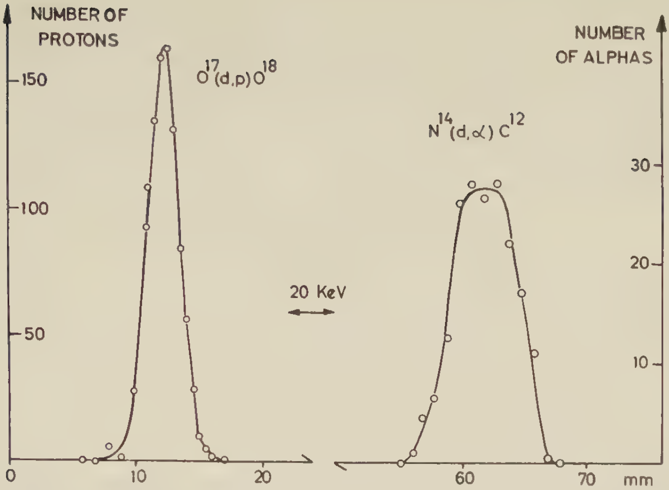

Fig. 3. Spectrum of alpha particles from $N^{14}(d, \alpha)C^{12}$ and of protons from $O^{17}(d, p)O^{18}$ collected in one nuclear emulsion plate. $\theta_{\text{lab}} = 134.7°$ $2\Delta\theta = 3.4°$. Deuteron energy is 0.855 MeV. The number of tracks/0.4 mm on the plate is given in the ordinate.

Results and discussion

The following results are obtained for the Q-value of the $N^{14}(d,\alpha)C^{12}$ transition:

$$\text{at} \quad 61.0°: \quad Q = 5907 \pm 18 \text{ keV}$$
$$\text{at} \quad 134.7°: \quad Q = 5917 \pm 18 \text{ keV}.$$

The total probable error in Q is composed of partial errors of somewhat different magnitude for the two angles. Beside the contributions from the usual sources of error [7], we have in the first determination as in Fig. 2 an additional error in the position of the N^{14} peak due to incomplete resolution of the two peaks. The contribution of this partial error to the error in Q has been estimated to be ± 17 keV. In the last determination as in Fig. 3 the distance between the peaks is so large that the uncertainty in the dispersion in the plate gives an error of ± 14 keV in Q. The mean value from these two determinations is

$$N^{14}(d, \alpha)C^{12} \quad Q_2 = 5912 \pm 13 \text{ keV}.$$

In ref. 4 the level width of the corresponding excited C^{12} level was given as less than 25 keV. With our method to read the peaks at the extrapolated high energy edges—which is preferable for other reasons [10]—we should get a high Q value if the level has a considerable width. If the width were 25 keV our measured Q values should be lowered by 6 keV. However, the half-widths of the experimental alpha distributions are found to be directly proportional to the maximum target layer for the corresponding angle θ, which indicates a smaller width than 25 keV of the level in the residual nucleus. As to the calibration reactions, no similar effects will enter in our case.

The measured Q-value shows a good agreement with the value 5910 ± 15 keV, which was obtained by Pauli. To get the excitation in C^{12} we subtract this value from the Q-value of the ground state transition of $N^{14}(d, \alpha)C^{12}$, which has hitherto not been measured directly. A calculation from the known mass values gives $Q_M = 13570 \pm 24$ keV [11]. The excitation of the second C^{12} level is then $E^* = 7658$ keV with an estimated probable error of ± 27 keV.

REFERENCES

1. Salpeter, E. E., Astrophys. J. *115*, 326 (1952).
2. Salpeter, E. E., Phys. Rev. *98*, 1183 (1955).
3. Treacy, P. B., Proc. Phys. Soc. *68A*, 204 (1955).
4. Dunbar, D. N. F., Pixley, R. E., Wenzel, W. A., and Whaling, W., Phys. Rev. *92*, 649 (1953).
5. Sperduto, A. and Fader, W. J., M. I. T. Progress Report (May 1953).
6. Pauli, R., Ark. f. Fys. *9*, nr 36, 571 (1955).
7. Ahnlund, K., Phys. Rev. *96*, 999 (1954).
8. v. Patter, D. M., Rev. Mod. Phys. *26*, 402 (1954).
9. Ahnlund, K., Thulin, S. and Pauli, R., Ark. f. Fys. *8*, nr 48, 489 (1954).
10. Mileikowsky, C., Ark. f. Fys. *7* nr 8, 89 (1953).
11. Ajzenberg, F. and Lauritsen, T., Rev. Mod. Phys. *27*, 77 (1955).

Tryckt den 14 februari 1956

Uppsala 1956. Almqvist & Wiksells Boktryckeri AB

ARKIV FÖR FYSIK Band 10 nr 27

Communicated 23 November 1955 by MANNE SIEGBAHN and G. BORELIUS

Angular distributions with high energy resolution

Experimental method

By KATARINA AHNLUND

With 12 figures in the text

Introduction

By means of the equipment of the Cockcroft-Walton accelerator at the Nobel Institute, including a double-focusing magnetic heavy-particle spectrometer, angular distributions of particle groups from nuclear reactions can be measured even if these groups be very close to each other in energy (some tens keVs). A device for turning the rotatable spectrometer automatically was outlined in an introductory paper (ref. 1) together with a discussion of the monitoring problem. The present report mainly deals, firstly, with practical arrangements and constructions and secondly, with the experimental procedures developed. The various factors which must be controlled in this kind of measurement are also discussed.

General principles

Fig. 1 defines the various directions and angles in the laboratory coordinate system. In the following paragraphs coordinates without any subscript refer to this system. The target spot is placed at the axis of rotation of the heavy-particle spectrometer. By the bombardment reaction products are emitted in all directions. Only those which are analysed by the spectrometer are indicated in the figure. The differential cross-section for particles emitted in the solid angle interval $d\omega = 2\pi \sin\theta \, d\theta$ at θ is measured as

$$\frac{d\sigma}{d\omega} = \frac{\frac{dN_2}{d\omega}}{n_1 \cdot N_0} =$$

$$= \frac{\text{number of secondary particles emitted/sec, sterad}}{\text{number of primary particles/cm}^2\text{, sec} \times \text{number of exposed target nuclei}} \qquad (1)$$

where, for an unpolarized beam, $dN_2/d\omega$ is a function of θ.

The number of detected particles N_{pl} in a nuclear emulsion plate at the exit of the spectrometer is

$$N_{pl} = \Delta\omega \cdot \frac{dN_2}{d\omega} \qquad (2)$$

where $\Delta\omega$ is the solid angle of the spectrometer. By a comparison of the relative numbers of counted tracks in the directions θ_A and θ_B we obtain:

$$\frac{\left(\frac{d\sigma}{d\omega}\right)_A}{\left(\frac{d\sigma}{d\omega}\right)_B}=\frac{\left(\frac{N_{pl}}{n_1}\right)_A}{\left(\frac{N_{pl}}{n_1}\right)_B}\cdot\frac{\Delta\omega_B}{\Delta\omega_A}\cdot\frac{N_{0B}}{N_{0A}}\,. \tag{3}$$

Thus, if we can keep the solid angle $\Delta\omega$ and the number of exposed target nuclei N_0 in the two directions A and B constant during measurements, we can obtain the relative differential cross-sections by comparing the number of tracks in the plate per unit bombardment for the two cases. In our arrangement $\Delta\omega$ will be the same for all values of θ. N_0 is a quantity that may vary in the course of a run, because the target substance may, for example, gas away due to heating. To compensate for a possible decrease in N_0, θ is changed between θ_A and θ_B several times during a run. In actual experiments we use about 10 periods. According to ref. 1, such a change should take place every 5 minutes. In practice it was found to be more correct to let the change be made according to the charge accumulated on the target. After a certain number of microcoulombs have been received from the incident beam when the spectrometer is in position θ_A, a change is made to the position θ_B and vice versa.

The theoretically relevant cross-sections are those related to the center-of-mass system. Before an analysis of the data can be made we transfer the experimentally measured quantities in equation (3) to the center-of-mass system. We have simple dynamic and geometrical relations between the solid angles $\Delta\omega$ and $\Delta\omega_{cm}$ and the angles θ and θ_{cm} as measured in the two systems (ref. 2). The subscript cm refers to the center-of-mass system. The following relations hold:

$$\sin(\theta_{cm}-\theta)=\frac{V}{v_{cm}}\cdot\sin\theta \tag{4}$$

$$\frac{\Delta\omega}{\Delta\omega_{cm}}=\frac{\sin\theta\,d\theta}{\sin\theta_{cm}\,d\theta_{cm}} \tag{5}$$

where (ref. 3)

$$\frac{V}{v_{cm}}=\sqrt{\frac{M_1 M_2}{M_0 M_3}\Big/\left(1+\frac{M_0+M_1}{M_0}\cdot\frac{Q}{E_1}\right)}\,. \tag{6}$$

The M's are the relativistic masses of the participating nuclei denoted in the usual way: E_1 is the kinetic energy of the bombarding particle and Q is the reaction energy of the reaction studied.

Experimental set-up

Geometry

A view of the target arrangement is shown in Fig. 2. The beam of bombarding protons or deuterons from the accelerator enters the target chamber through its fixed, lower part. See also Figs. 3 and 4. The vertical axis of the chamber is also the axis of rotation of the spectrometer. Secondary particles can enter the rotatable spectrometer through an exit in the upper part of the chamber, which turns with it. The solid angle of the spectrometer is about 1/4000.

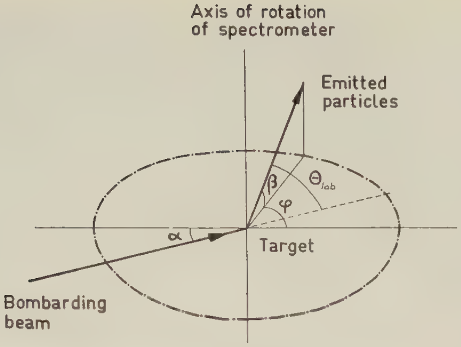

Fig. 1. Schematic representation of the angles α, β, φ and θ_{lab}.

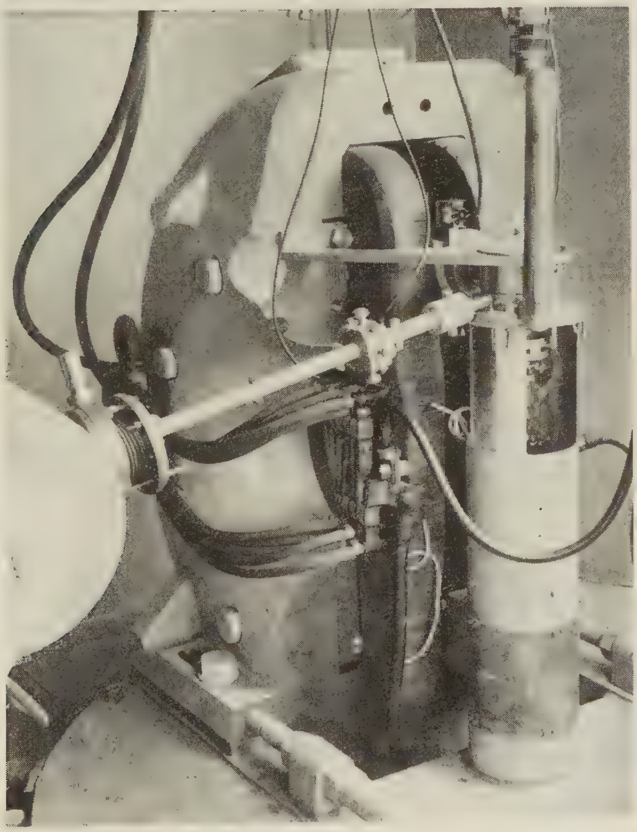

Fig. 2. General view of the system around the target, with the analysing magnet to the left, entrance tube with defining slits, target chamber and spectrometer.

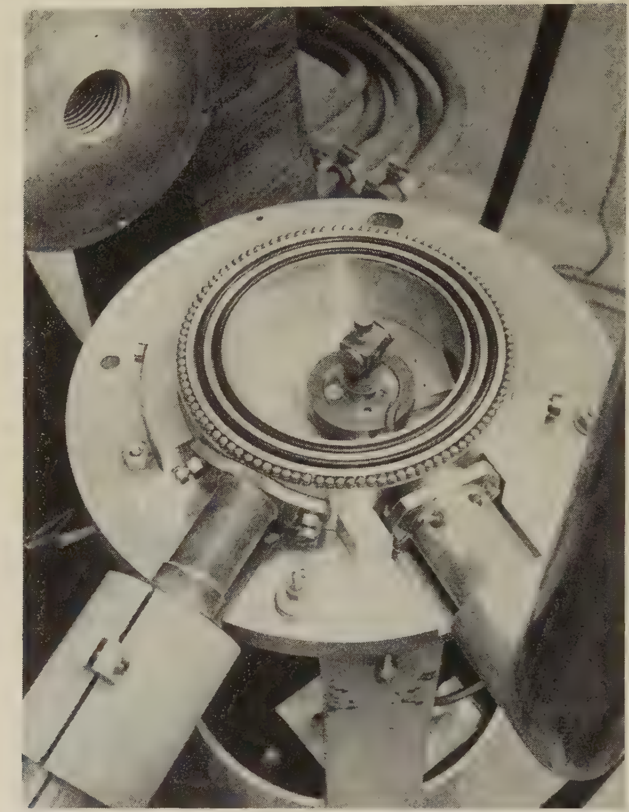

Fig. 3. The fixed, lower part of the chamber with gaskets and ball bearings. The screen is removed from the target holder. The bombarding beam enters at lower left of figure, upper left shows entrance to spectrometer. The tube to the lower right is a pumping line.

The incident beam, which in all earlier work has been horizontal, must now enter the target chamber in an upward direction. By analysis of the conditions for proper entrance of secondary particles into the spectrometer, it was found that the minimum elevation of the incident beam away from the horizontal was 10.2°. This angle is denoted by α in Fig. 1. This means that the vertical beam from the accelerator should be deflected 100.2° by our 90° homogeneous-field magnetic analyser, instead of 90° as has earlier been the case. To accomplish this one could not merely increase the field strength of this magnet, as the beam would then strike the wall of the corresponding vacuum chamber above the opening leading to the vacuum tube to the target. Instead, the analyser was tilted 5.1°, i.e. half of the amount of the desired extra deflection. Fig. 5 shows this arrangement whereby the original entrance and exit could be used. The maximum deviation from the mean radius is thus only about 40 % of the space available.

The spectrometer table was raised about 1 dm to bring the target to the proper height, corresponding to the elevation 5.7° of the emitted particles (ref. 4). In Fig. 1 this angle is denoted by β. Both α and β are fixed during all the experiments. The

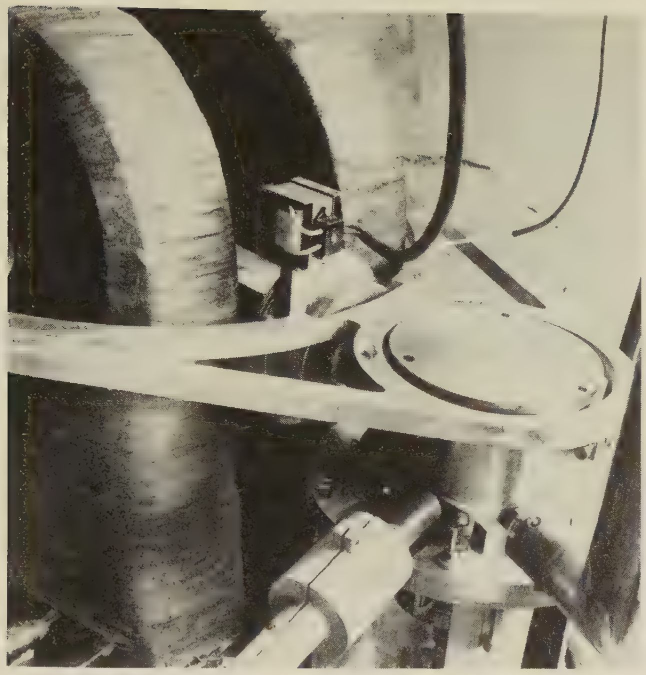

Fig. 4. The target chamber with its upper part fixed to the spectrometer by a brass frame. The small electromagnet operates the shutter which is mentioned in the text.

laboratory angle θ between incoming beam and emitted particles is geometrically a function of α, β and φ:

$$\cos\theta = \cos\alpha\,\cos\beta\,\cos\varphi + \sin\alpha\,\sin\beta. \qquad (7)$$

The quantity $(\theta - \varphi)$ is given in Fig. 6 for our values of α and β, as a function of the experimentally varied parameter φ, the angular reading along the spectrometer periphery. We see that the range over which θ can be varied is some degrees smaller than the range of φ.

Target system

A sectional view of the target chamber is shown in Fig. 7. The target support was also used in an earlier chamber. It can hold up to 5 different target plates. It is electrically isolated from its surroundings and connected with a current integrator. A screen to prevent secondary electrons from passing between the target chamber and the target has entrance and exit of adjustable sizes and is kept at a potential of–400 Volts to the chamber. To save the target, the cooling trap in the cover is filled with liquid oxygen during the runs. Occasionally, this cover is replaced by a cover with a sink to enable a gamma detector to be placed near the target, or by a lucite cover which permits direct inspection of the target during bombardment.

A brass frame fixes the upper part of the chamber to the spectrometer. It is seen in Figs. 2 and 4. After proper adjustment of the relative heights of ball bearings and

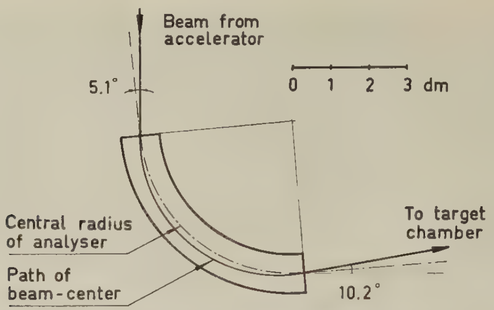

Fig. 5. Schematic view of the passage of the incident beam through the analysing magnet. The beam comes vertically down from the accelerator and leaves the magnet with 10.2° elevation to the horizontal.

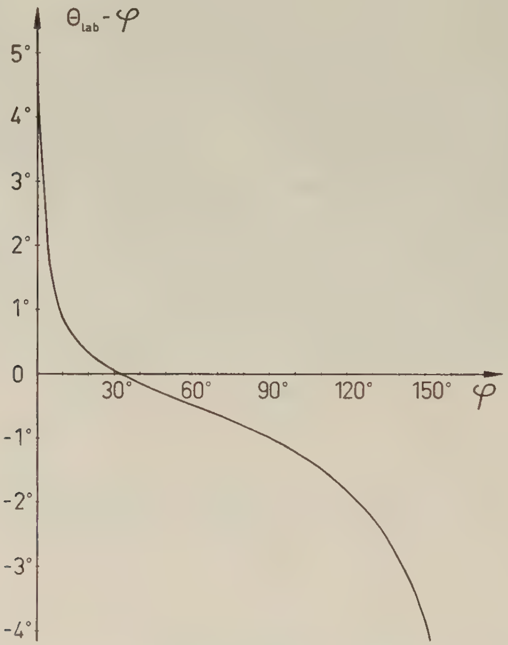

Fig. 6. The angle difference $\theta_{lab} - \varphi$ as a function of φ according to equation (7) for $\alpha = 10.2°$, $\beta = 5.7°$.

gaskets between the two parts of the chamber, we can now move the spectrometer between different angular positions without any disturbances in the vacuum system. The turning is done under high tension and with the bombarding beam on the target.

An iron screen for magnetic shielding can be placed around the stainless steel chamber. Magnetic shielding is also needed around the vacuum tube of the incident particles to reduce the stray field from the spectrometer, especially when this instrument is placed at the extreme backward angles of φ.

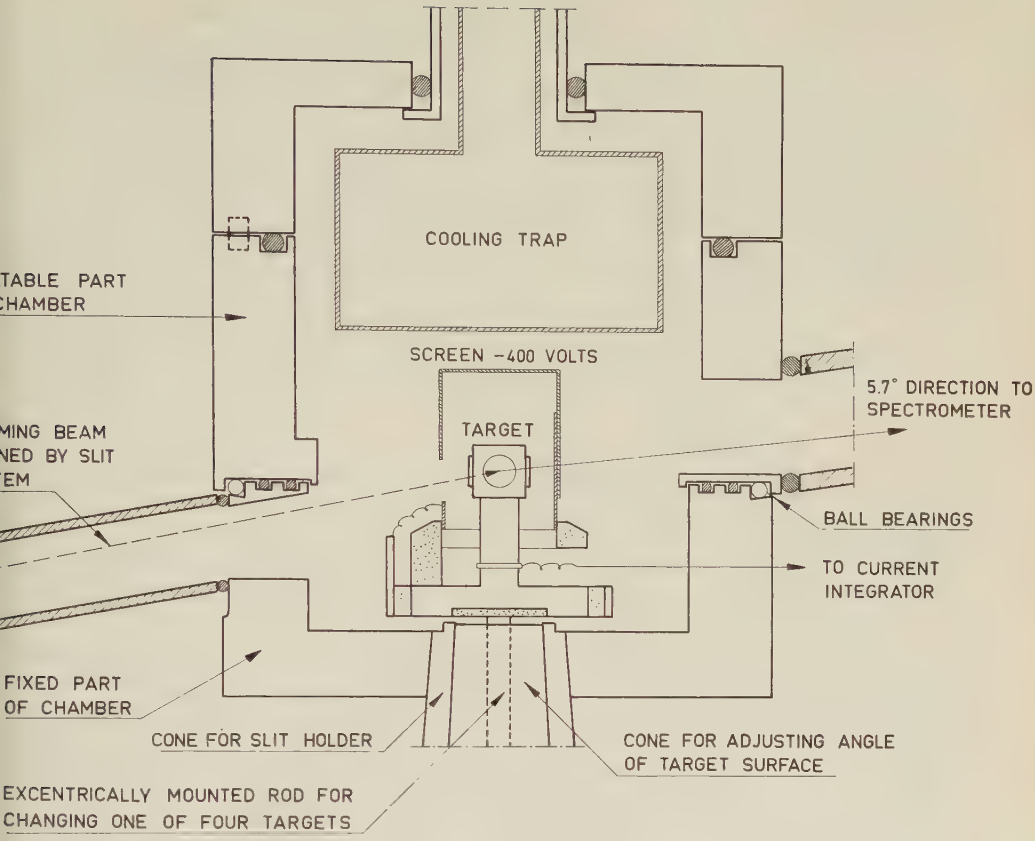

Fig. 7. Vertical section of the target chamber. The dotting indicates insulating material.

To extend φ to such angles, the lower defining slit system (seen in Fig. 2) has been reconstructed with much smaller external dimensions than before and also placed at a more favorable position along the target tube. Since some material has been removed from the flank of the spectrometer, it is now possible to vary φ continuously between 0° and 138°.

Between the target chamber and the spectrometer there is an electrically operated shutter (seen in Fig. 4), which confines the detection of emitted particles to the proper time intervals. Between each exposure the shutter is closed for 45 seconds to allow for necessary rearrangements of the spectrometer position and field etc. As the shutter is in the entrance field of the magnetic spectrometer, an ordinary camera shutter could not be used, therefore a special brass construction is employed. The operation is performed by means of a small electromagnet.

Detector

Nuclear emulsion plates are used for detection of the particles which have passed the spectrometer. Six plates can be placed vertically in the camera for successive

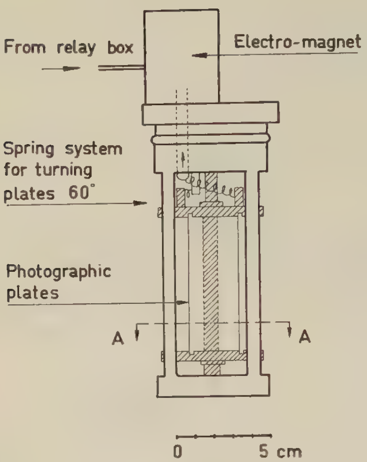

Fig. 8. Plate-holder for a maximum of six nuclear emulsion plates 1″ × 3″.

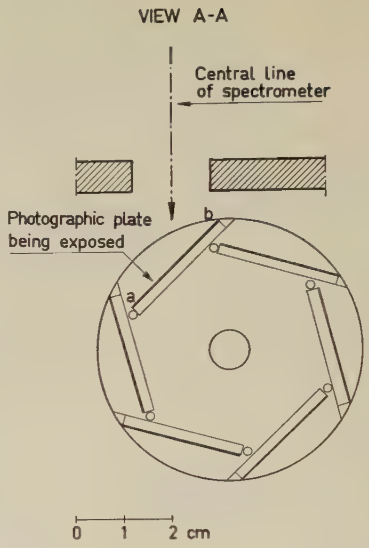
VIEW A-A
Central line of spectrometer
Photographic plate being exposed
a
b
0
1
2 cm

Fig. 9. Horizontal section of the camera showing the arrangement of the photographic plates.

exposures (Figs. 8 and 9). They are arranged approximately around the sides of a hexagon. This arrangement was chosen to ensure that the plate under exposure would not be screened by the other plates. In the figure, the dashed parts of the camera can pivot around the axis. When the small electromagnet in the top of the camera is operated, the rotatable plate holder moves 60° and the exposed plate is replaced in the detecting position by another plate. By switching the current to the electromagnet on and off, one can alternatively collect particles on one or the other of two neighbouring plates, one for the spectrometer direction φ_A and the other for φ_B.

Adjustment and measurements

Each partial measurement implies a measurement of the ratio between the values of $d\sigma/d\omega$ for two different angles. Cf. equation (3). We perform this by making alternating exposures in the angles: θ_A, θ_B, $\theta_A \ldots \theta_A$. The particles emitted into the spectrometer during the periods when it is in the angle θ_A position, are all collected on one photographic plate and the ones received by the spectrometer at angle θ_B, are collected on another. The plates are afterwards scanned for individual tracks under a microscope. By making a series of such comparisons each time between two angles, one can cover a whole range of angles and give the variation of $d\sigma/d\omega$—referred to some reference angle—as a function of θ. A discussion of the experimental accuracy for the various parameters will be given with reference to equation (3).

Alignments and angles

The geometrical direction of the incoming beam to (a) the vertical axis of rotation of the spectrometer table and (b) the axis of the target chamber—which should coincide—was adjusted very accurately with katetometer and plumb lines. The remaining inaccuracies should give no notable error in the angle measurements. However, to prevent the lower part of the chamber from being inclined or twisted when the upper part follows the rotation of the spectrometer it was found necessary to strengthen the supporting cylinder by three stays, one fixed to the analysing magnet and two to the outer, fixed periphery of the spectrometer. (These stays are not seen on the photographs.) The twisting is then reduced to less than 0.2 ‰ in φ and the deviation of the target axis from the rotational axis of the spectrometer is only of the order of 0.1 mm. The important point here is that by these measures one has prevented the bombarded spot on the target from moving on the possibly inhomogeneous target surface after the changes in direction of the spectrometer, thus making $N_{0_A} \neq N_{0_B}$. There is practically no other reason to fear such small disturbances in geometry.

The error in θ lies chiefly in the measurement of φ, which is made to $\pm 0.3°$. A certain value of φ can be reproduced manually to $\pm 0.05°$.

Current to the target

We proceed to study the measurement of the quantity n_1 appearing in equation (3), which is essentially done as a determination of the number of primary particles arriving at the target during the time interval when the spectrometer is open. It is measured as the number of discharges in the current integrator. To make this correct, several preventive measures are made.

The electrically negative screen around the target prevents secondary electrons from passing between the target holder and other parts of the chamber. Its potential lies well below the limit above which a change in the screen potential is followed by a change in registered current. Leakage from the system target–current integrator was found to be very small, always less than 0.01 μA and it could be compensated for by a proper biasing voltage to the integrator.

Impurities of other particle types in the primary beam could make the integrator count more charges than those which are actually relevant to our measurements. Only additional particles which have the appropriate momentum-to-charge ratio can pass through the magnetic analyser and reach the target. When we work with a proton beam, no such particles can arrive, but with the deuteron beam we always get a slight contamination of H_2^+. One gets an estimation of how big this can be by measuring the currents indicated in the following table:

Table 1.

	Mass 1		Mass 2	
	Current	Ion	Current	Ion
Proton beam	I_{1p}	H^+	I_{2p}	H_2^+
Deuteron beam	I_{1d}	H^+	I_{2d}	H_2^+, D^+

If we assume that the ratio I_{1p}/I_{2p} is also conserved when the ion source is fed with heavy hydrogen, we get for the percentage of H_2^+ in the analysed deuteron beam:

$$\frac{I_{2p} \cdot I_{1d}}{I_{1p} \cdot I_{2d}} \cdot 100 \text{ percent.}$$

This quantity was checked now and then during the experiments and it was never found to exceed 0.3 %. Changes in this small number are completely unimportant during a single run.

Finally, all the sources of error discussed in this section will be cancelled to a very large extent as our procedure is always to compare the results taken at two angles with alternating exposures. Therefore they are considered to be practically zero.

Number of target nuclei

A similar cancelling will occur for N_0, the number of target nuclei in the bombarded spot. We use thin target layers separated on to or evaporated on metal plates or metal foils. Long-time effects, e.g. due to gasing or shooting away of material, will therefore have a much reduced influence on our results. Discontinuous changes in N_0 during a run are very improbable as we keep the current practically constant.

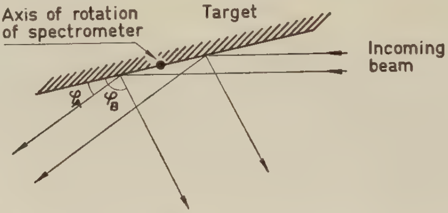

Fig. 10. Schematic representation of the target surface with the margin rays of in- and outgoing beams.

The surface density of target nuclei is not at all uniform, especially when we use targets from the isotope separator. We therefore do not turn the target plate when we change φ. Fig. 10 shows how the incoming beam hits the same target spot, while the spectrometer angle is alternately φ_A and φ_B. The different amount of slowing-down for the particles emitted in different directions will have no practical importance as we use very thin target layers, only some keVs.

This is true only as long as we do not use very oblique angles of emergence for the emitted particles. In this case, part of the bombarded target area might be eclipsed because of unevenness in the surface, thus giving false results.

To avoid too oblique angles of incidence it is necessary to use a thin foil target backing for the region of small φ-values. Special attention must then be devoted to the measurement of the current to the target. The foil is placed normal to the bombarding beam and particles emitted "backwards" through the foil are analysed. Of course no bombarding particles must hit the frame which holds the foil, this would spoil the current measurement.

When the spectrometer is turned to the neighbourhood of the incident beam, i.e. for large values of φ, it is of great importance that the beam should not be influenced by its stray field, thus displacing the spot on the target plate when φ is changed between φ_A and φ_B. With iron shielding around the entrance tube and $\varphi = 135°$ we measured a displacement of the target spot of 1.5 mm, when a 400 A spectrometer current was turned on and off. As this was definitely too great, the iron screen is replaced by a 4 mm thick mumetal tube in order to assure good precision also for the measurements in the extreme backward angles.

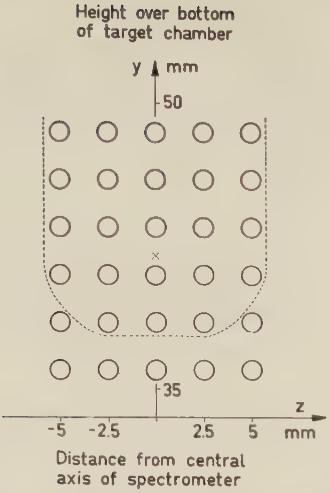
Height over bottom of target chamber
y
mm
50
35
z
-5
-2.5
2.5
5
mm
Distance from central axis of spectrometer

Fig. 11. Positions of ThC′ source in a plane through the axis of the target chamber and directed towards the spectrometer. The cross denotes the section of this plane and a 5.7° direction from the middle of the spectrometer entrance.

Solid angle

It was mentioned earlier that $\Delta\omega$, the solid angle of the spectrometer, is the same for all values of φ. The frame between the upper part of the target chamber and the spectrometer is adjusted so that the entrance channel for the particles from the target is always directed towards the vertical central axis of the target. This is not very critical as the limiting aperture of the spectrometer lies inside the field.

An investigation was made of how far from the ideal source position the source could be displaced without a resulting change in the solid angle. A preliminary calculation showed that the linear dimension of this "plateau" for $\Delta\omega$ would be about 12 mms. An experimental determination was also made by means of a small ThC′ source which was in turn placed in different positions around the target center, as indicated in Fig. 11. For each position an exposure of definite time of the 8.776 MeV alpha line was made, and the number of detected alpha tracks were counted. The dotted curve in Fig. 11 encloses the region within which the solid angle $\Delta\omega$ was found to be independent of source position. During the angular distribution measurements it is necessary to ensure that the target spot, as seen from the two relevant spectrometer directions, is well within this plateau (cf. Fig. 10). The dimensions of the target spot can easily be changed by the micrometer screws of the slit system in front of the target chamber.

Fig. 12 shows the distribution of tracks in a horizontal strip of the detecting plate—i.e. a strip with one value of $B\varrho$—for one of the Th curves taken with the source placed within the plateau. From this figure we see that all particles are quite well focused in the horizontal direction perpendicular to the beam. In fact, without the double directional focusing property of the spectrometer we could not perform this type of relative intensity measurements. In the vertical direction of the plate we correct the readings for the decrease in solid angle towards the ends of the plate by means of the correction curve given in ref. 5. The stated inaccuracy in this curve, $\pm 5\,\%$, will contribute only a few per cent probable error in our results, as the spectro-

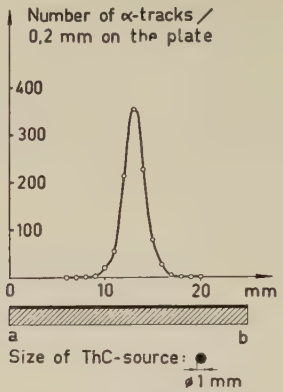

Fig. 12. Number of alpha tracks from ThC′ 8.776 MeV along one horizontal strip of the plate. The narrower such a line, the better are the double-focusing properties of the spectrometer. The letters *a* and *b* indicate the plate edges as shown in Fig. 9.

meter field is always adjusted to give peaks in the same position on the photographic plates. With some effort, the correction curve of ref. 5 can be replaced by a more accurate one.

Each plate covers an energy region which is 8 % of the energy being analysed. Since it is better not to use the areas towards the edges, where $\Delta\omega$ decreases rapidly, for intensity measurements, only a region corresponding to 6 % is used. The resolution as given by the half-width of a line from a thin radioactive source is about 0.2 % in energy, using the present position of the plates which, as found lately (ref. 6), is not exactly at the best focus. The experimental half-widths of peaks from nuclear reactions are considerably broader, due to several broadening factors such as angular energy spread, layer thicknesses etc. If two peaks differ by more than some 3 % in energy they are usually well resolved and no additional inaccuracy enters in the intensity measurement of one peak due to the presence of the other. For near-lying groups from one single reaction, a simultaneous detection on one set of plates can be made.

Other experimental factors

The operation of the shutter is not exactly simultaneous with a discharge of the current integrator because it takes some fraction of a second before the impulse from the integrator has passed through the relay system. This will cause an error in the exposure time which is not necessarily the same every time. We put it at ± 1 %, but this figure could be considerably reduced without much effort.

In the reading of the plates, apart from the statistical errors, we have sometimes had a little difficulty in judging what background should be subtracted. This case enters e.g. when we study proton lines in the energy regions in which protons from the $D + d$ reaction occur. The length of tracks is quite different for different types of particles, e.g. alpha particles give no background on proton plates and vice versa.

If the cross-section for the reaction which we study changes rapidly with the bombarding energy E_1, it is of course very important to keep E_1 as constant as possible during the runs. An increase of the external layer on the target by pump oil will decrease the effective E_1. The cooling trap reduces this effect.

Conclusion

The resulting inaccuracy in the angular distribution measurements is better to be judged for each reaction individually, as it can differ greatly with yield, reaction energy etc. It will be of the order of a few percents. The first problem investigated is the angular distribution of protons from $O^{18}(d, p)O^{19}$. This work will be described in a separate paper.

ACKNOWLEDGEMENTS

My thanks are due to Professor M. Siegbahn for having supported this work in many ways. Valuable assistance was given by Doctor B. Saraf, Bombay and Civ.ing. B. Sjögren during different phases of the work. Ing. B. Höijer gave technical assistance.

REFERENCES

1. Mileikowsky, C., Ark. f. Fys. 1955 (in press).
2. Haxby, R. O., Allen, J. S., and Williams, J. H., Phys. Rev. *55*, 142 (1939).
3. Heydenburg, N. P. and Inglis, D. R., Phys. Rev. *73*, 230 (1948).
4. Mileikowsky, C., Ark. f. Fys. *7*, nr 3, 33 (1953).
5. Pauli, R. T., Ark. f. Fys. *9*, nr 36, 571 (1955).
6. Pauli, R. T., Ark. f. Fys. *10*, nr 16, 175 (1955).

Tryckt den 14 februari 1956

Uppsala 1956. Almqvist & Wiksells Boktryckeri AB

ARKIV FÖR FYSIK Band 10 nr 28

Communicated 23 November 1955 by Manne Siegbahn and Erik Hulthén

On the high energy gamma-transitions of W^{182}

By Gunnar Bäckström

With 4 figures in the text

The decay of Ta^{182} has been extensively studied by a number of workers, the main contribution being that of Murray, Boehm, Marmier and DuMond [1]. In this investigation the γ-spectrum was taken with a large, transmission type crystal spectrometer, yielding a relative energy half-width of $0.3\ E \times 10^{-4}$ (E is expressed in kev). As is seen from this formula the width increases to 3 % at 1 mev, in addition to the complications occasioned by high background. In order to cover this high energy region they use a homogeneous field lens spectrometer, capable in this case of momentum resolution down to 0.25 % and provided with a proton resonance arrangement for the field measurement. In the examination of the conversion and photoelectron spectra the high energy part is again unfavoured because of low conversion coefficients and in the latter case high background, making it necessary to sacrifice some resolution. The two different instruments now provided the means of determining the intensities for their respective regions, and the parts were linked together by scintillation spectrometer methods. The decay scheme arrived at in this way, supported by earlier coincidence experiments, is reproduced in Fig. 1 and the report on the intensities in Table 1.

The level scheme of W^{182} has recently been successfully interpreted by Alaga, Alder, Bohr and Mottelson [2], who have correlated all but one or two of the levels by describing them as the low energy part of four different rotational series. In view of the great interest in principle of this decay, it was considered well motivated to make a check on the consistency of the scheme with respect to the somewhat neglected high energy part of the spectrum, at the same time improving the absolute accuracy of the transition energies.

The instrument used in the present investigation was an iron-pole double focusing spectrometer [3] with $\varrho = 50$ cm and with relative momentum half-widths down to 0.2 %, this value corresponding to a sample area 0.3 cm^2 and a solid angle of 0.15 % of 4π. The geometry made possible a very effective shielding of the detector from direct γ-radiation.

The sample was produced by an $(n\gamma)$ process in the Harwell pile. The activity, estimated at 30 mC, was packed into a Cu capsule 0.4 cm in diameter, the walls being just thick enough to absorb the β-distribution. The photoelectric uranium converter was prepared by painting a 0.01 cm Al foil with an alcoholic solution of uranyl nitrate, which was transformed to oxide by heating in an oven at 500° C. After this treatment the foil was rubbed with a cloth in order to remove irregularities in

Table 1. Transitions in W^{182}

Initial and final energy levels	γ-ray energy (kev)	γ-ray intensity	α total	Decay fraction per cent	Multi-polarity
ED	33.36 ± 0.01	Weak	—	—	$(E1)$
HG	42.71 ± 0.01	Weak	—	—	$(E1)$
KJ	65.71 ± 0.01	7.5	4.0	11.0	$M1\,(+E2)$
FD	67.74 ± 0.01	85	0.31	31	$E1$
HF	84.67 ± 0.02	5	(8)	13.0	$M1\,(+E2)$
BA	100.09 ± 0.02	40	5.0	65	$E2$
JH	113.66 ± 0.02	7.5	2.2	7.0	$M1$
KI	116.40 ± 0.02	1.7	—	—	—
HD	152.41 ± 0.03	35	0.07	11.0	$E1$
JG	156.37 ± 0.04	11.5	—	(3.5)	$(E1)$
KH	179.36 ± 0.05	16	0.58	7.5	$M1\ +E2$
JF	198.31 ± 0.06	7.5	0.36	2.9	$E2$
KG	222.05 ± 0.07	35	0.07	11.5	$E1$
CB	229.27 ± 0.08	20	0.24	7.5	$E2$
KF	264.09 ± 0.10	22	0.17	7.5	$E2$
EC	927 ± 1	—	—	0.5	$(E3)$
FC	960 ± 1	—	—	0.5	$(E3)$
GC	1003 ± 1	—	0.006	2.4	$(M1+E2)$
DB	1122 ± 1	100	0.006	29	$M1+E2$
EB	1155 ± 1	6.5	0.005	1.9	$(M2)$
FB	1189 ± 1	45	0.007	13.5	$M2+E3$
DA	1222 ± 1	95	0.0035	28	$E2$
GB	1231 ± 1	50	0.0035	14	$E2$
FA	1289 ± 1	—	—	(5.0)	$(M2)$
HA	1375 ± 2	—	—	(0.25)	$(E3)$
IA	1437 ± 4	—	—	(0.25)	—
KB	1454 ± 4	—	—	(0.25)	$(M2+E3)$

Table 2. Results of the energy determinations.

Transition	Energy kev	Reference line	Energy mean value kev
DB	1121.7 ± 0.3	Bi^{207}	
DB	1121.4 ± 0.3	Bi^{207}	
DB			1121.6 ± 0.2
FB	1189.3 ± 0.3	Bi^{207}	
FB	1189.5 ± 0.3	DB	
FB			1189.3 ± 0.2
DA	1222.0 ± 0.3	Bi^{207}	
DA	1222.0 ± 0.3	DB	
DA			1221.8 ± 0.2

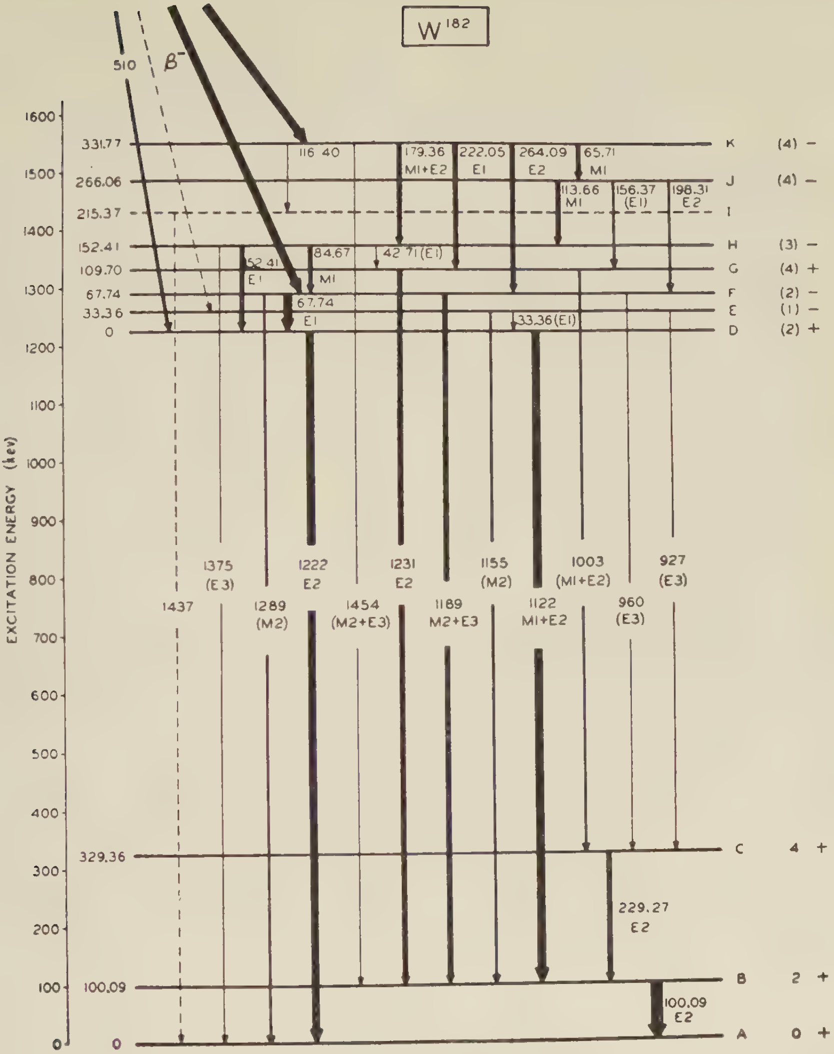

Fig. 1.

the oxide surface and the painting was repeated. What thickness of U can be produced by this method is mainly a question of time. In this experiment U foils of 3.4 and 4.4 mg/cm² were used and the number of layers necessary was 10–13.

In the precision measurements the Ta sample and the converter could be exchanged for a Bi^{207} standard, giving a reference line at 976 kev electron energy. The spectrometer geometry was set to a resolution of $\Delta B\varrho/B\varrho = 0.21\%$. After careful demagnetization the reference and the Ta line were recorded in order of increasing energy. For the Ta spectrum a background curve was taken under the same conditions but without the uranium converter layer. The reference line was normalized to the $B\varrho$

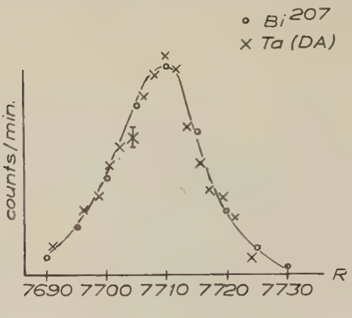

Fig. 2.

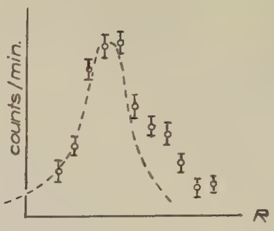

Fig. 3.

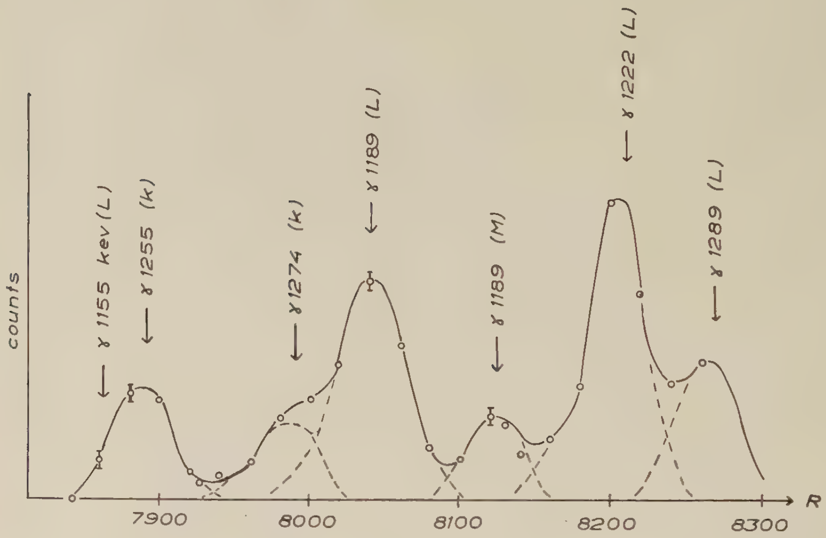

Fig. 4.

of the Ta line after which its shape was calculated it being assumed that the Bi-line too had suffered energy loss by emission from a U foil of 3.4 mg/cm². The two profiles were normalized vertically and brought to coincidence. Fig. 2 gives an idea of the agreement in shape obtained in this way. In the cases where only adjacent Ta lines were compared, the profiles were simply normalized to the same height and width before comparison.

The result will be seen from Table 2.

The errors involved are dominated by the counting statistics, which is worse than expected of 30 mC because of decay branching. An inspection of the table shows that the energy difference between transitions DB and FB is 67.8(5) kev, and the corresponding transition according to Table 1 is 67.74 kev. The difference for DB and DA is here 100.4(5) kev, to be compared with 100.09 of the decay scheme, a result which is within the limits of error and supports the present interpretation of the decay. By taking advantage of the more precise energy differences the number of statistically independent measurements may be effectively doubled. The adjusted mean values obtained in this way are given in the last column of Table 2.

The GB line, which is not found in the above table, has been resolved from DA and the energy difference shown to be right within 1 kev.

The FA gamma ray is very elusive. In the internal conversion spectrum the FA K-line at 1220 kev is very near the GB L-line at 1219, which is comparable in intensity. In spite of this fact, the authors cited have measured the K/L ratio for FA. The corresponding gamma has not been found however. Therefore an attempt was made to detect it in a photoelectron spectrum. As it could not be expected to be completely resolved with either a U, Pb or Au converter, U was chosen as yielding the best intensity. Fig. 3 shows the result obtained with a 4.4 mg/cm² U converter. The group is dominated by the FB L-line, the true shape of which has been inferred from the normalization of a stronger line. It seems convincing that the FA gamma ray exists, with an intensity of about 2.

The three hypothetical transitions HA, IA and KB are situated well above all lines strong enough to mask them. It was attempted to measure their intensities, using a 42 mg/cm² Pb converter (0.8 × 1.5 cm) at a transmission of about 0.5%. No traces could be seen of the lines searched for, and it must be concluded that their intensities must be less than 0.3 units. This figure was arrived at by comparison with a strong line run at the same geometry.

In a survey run two peaks were found that cannot be explained as purely statistical effects (Fig. 4). The electron energies are 1139 ± 2.5 kev and 1158 ± 2.5 kev. The only interpretation seems to be that they are K-lines, the corresponding γ-transitions being $E_\gamma = 1254$ kev and $E_\gamma = 1273$ kev. These are, within the limits of error, energies that could be expected from the level scheme.

The line at 1254 kev (intensity = 4) must be interpreted as a transition from E to A, of multipolarity $E1$ (unequivocal), if the assignment of spin and parity to E can be trusted. It is at present not possible to make any comments on whether the $E1$ transition is reasonable or not, as E happens to be one of the levels that are not systematized on the basis of the collective model.

$E_\gamma = 1273$ kev (intensity = 3) fits well as a difference between H and B, with spins 3— (uncertain) and 2+. In general one would thus expect an $E1$ transition, retarded in this case by first order K-forbiddenness. It is interesting to compare it to the strong 152.4 $E1$ gamma-ray, which goes between the same spins and parities, but has a favourable ΔK.

My thanks are due to Professor Kai Siegbahn, who suggested this investigation.

Uppsala, in October 1955.

REFERENCES

1. MURRAY, BOEHM, MARMIER and DUMOND, Phys. Rev. *97*, 1007–1016 (1955).
2. ALAGA, ALDER, BOHR and MOTTELSON, Kgl. Danske Videnskab. Selskab., Mat. fys. Medd. *29* N:o 9 (1955).
3. HEDGRAN, Arkiv för Fysik *5*, 1–27 (1952).

Tryckt den 16 februari 1956

Uppsala 1956. Almqvist & Wiksells Boktryckeri AB

ARKIV FÖR FYSIK Band 10 nr 29

Communicated 23 November 1955 by MANNE SIEGBAHN and ERIK HULTHÉN

On the energy of the 570 kev γ-ray of Bi^{207}

By GUNNAR BÄCKSTRÖM

With 3 figures in the text

As most β-spectrometers now in use have no field-measuring devices but depend for the energy determination on comparison between pairs of lines close in energy, much work has been devoted to the construction of a set of reference lines as closely spaced as possible. The list of standard lines [1] measured with a precision of the order of 1 in 10^4 is represented graphically in Fig. 1.

Bi^{207} also exhibits a γ-transition of 570 kev, the K-conversion line of which may be used as an energy standard (Fig. 2) [2]. Its $B\varrho$ being about 2840 gauss cm, it fills a gap between ThC″ L and the Cs^{137} K-line in the table of previously existing standards. Besides it is an especially great advantage to have two known lines in the same source, as this makes a convenient check of linearity possible. Additional desirable features are the absence of a continuous spectrum, its long half-life (8 years) and the high specific activity available. For the above reasons the present investigation was made.

The instrument was a large, double-focusing type, $\varrho = 50$ cm, essentially a copy of the one at the Nobel Institute, Stockholm [3]. In this experiment the shutter sice chosen was 2×9 cm, the detector slit width 0.2 cm and the sample width 0.2 cm. These data imply a relative half-width of the lines $\Delta B_\varrho / B_\varrho = 0.21\%$.

The sample was produced in the cyclotron at Oak Ridge, separated and electroplated on a copper foil 0.012 cm thick.[1] The source was thin enough not to show any noticeable thickness effects at the resolution used. A Th-deposit on a 0.2 cm Al strip produced the main reference line, ThC″ L.

Table 1. The $B\varrho$ of the Bi^{207} K-conversion line

Reference line	$B\varrho$ gauss cm	
ThC″ L . . .	2838.7	Preliminary
	2839.5	
	2839.1	
Bi 976 kev . .	2838.6	Careful demagnetization
ThC″ L . . .	2838.8	
	2838.8	
	2839.0	

---

[1] I am indebted to Dr D. E. Alburger, Brookhaven, for providing the Bi^{207} sample.

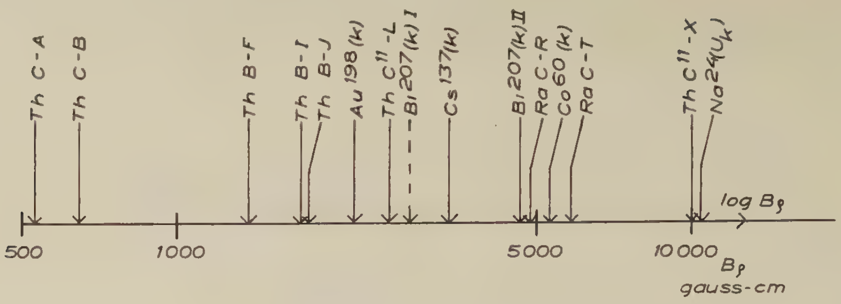

Fig. 1. Standard lines.

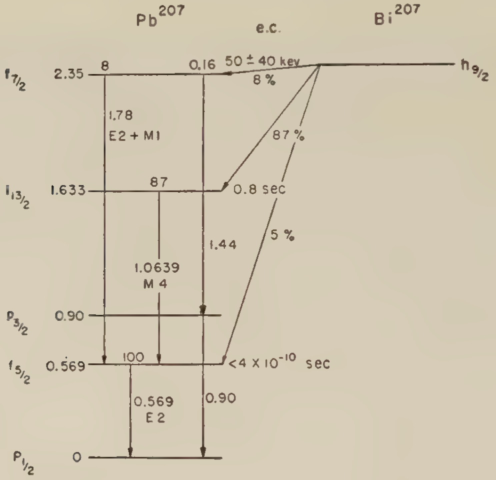

Fig. 2. Decay scheme of Bi^{207}.

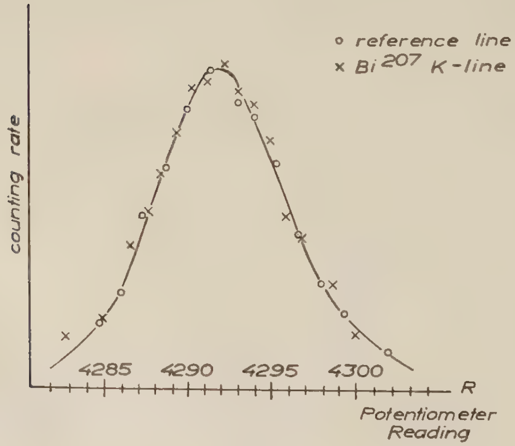

Fig. 3.

At the beginning of each run the spectrometer iron was demagnetized by the conventional method of damped oscillations. The two lines to be compared were then recorded, the field being steadily increased. The profiles were normalized and fitted together.

A few preliminary runs gave results of an unexpectedly great spread of energy. As it was soon realized that the demagnetization was a critical process, more care was taken to reduce the residual field. In order to make an estimate of the reproducibility obtainable, the same line was recorded several times, the field being reduced to less than 0.05 % between the runs. The root-mean-square deviation was found to be 1 in 10^4. This standard of demagnetization was kept throughout the succeeding measurements.

An example of the degree of coincidence between two compared line profiles, when they are normalized to the same height and widths, is given in Fig. 3.

The results of the determinations are shown in Table 1. The first three runs are preliminary involving a less careful demagnetization. In the mean value these are given the statistical weight 1/3.

As a mean value of the Bi^{207} standard line we obtain from Table 1 $B\varrho$ 2838.9 ± 0.4 gauss cm. The corresponding electron energy is found to be 481.71 ± 0.1 kev and the γ-energy 569.7 ± 0.1 kev.[1]

The discussion of errors being the same for identical instruments, reference is made to the previously mentioned publication on the Nobel Institute spectrometer [3].

In two cases, the ThC″ M-line was included in the run, yielding the mean value $B\varrho = 2891.9 \pm 0.5$ gauss cm for the M-line.

I wish to thank Professor Kai Siegbahn for his kind interest in this investigation.

Uppsala, in September 1955.

REFERENCES

1. Siegbahn, (editor) Beta and Gamma Ray Spectroscopy, 227. North Holland Publishing Company (1955).
2. Alburger D. E. and Sunyar A. W., Phys. Rev. *99*, 695–702 (1955).
3. Hedgran A., Arkiv för Fysik *5*, 1–27 (1952).

---

[1] After this investigation was finished, a note appeared in the *Physical Review* [2], reporting the determination of the energy of the 570 kev line by Marmier and Boehm of the California Institute of Technology. They have found the value $E_\gamma = 569.7 \pm 0.2$ kev, which supports the result given above.

Tryckt den 16 februari 1956

Uppsala 1956. Almqvist & Wiksells Boktryckeri AB

ARKIV FÖR FYSIK Band 10 nr 30

Read 11 May 1955

Long sparks from negative electrode with limited current in air at atmospheric pressure

By Harald Norinder and Oskars Salka

With 16 figures in the text

---

1. Introduction and arrangement of the experiments 397
2. Circuit calculations 398
3. Experimental results 400
  a. Predischarge 400
  b. Development of the spark 406
  c. Arc stage 408
  d. The discharge with the thin point electrode 409
  e. The variation of potential and current 410
  f. Calculation of the resistance of the spark 412
  g. Diameter of the channels 414
4. Discussion 416
  a. Predischarge 416
  b. Spark 419
  c. Arc stage 421
5. Summary 422

---

1. Introduction and experimental arrangement

Experimental study of the processes involved in the development of a discharge is rendered extremely difficult by the explosive rapidity of the phenomenon, and is in fact possible only to a limited extent. There is unfortunately no method of studying the mechanism which will give comprehensive information about all its stages. The ideal method would be to obtain a moving picture of the process, with at least 10 pictures per microsecond. This is of course impossible with any apparatus at present available, in view of the extreme rapidity of the process and the low light intensity (the predischarge is but weakly luminous). We must be content to reach our goal indirectly, by observation of various phenomena which are connected with the discharge and which may be produced under special conditions. For instance, the test gap may be subjected to a brief voltage pulse by connecting a spark gap in parallel with it, so that the discharge can only build up to a certain definite stage. If the voltage across the test gap persists for a longer time, the spark is transformed by the current that flows to a bright arc, which makes investigation of the first stages impossible.

The discharge (in air at atmospheric pressure) is a collective name applied to various processes that follow one another in a certain order until the discharge as a whole is completed. It seems sufficient to divide a discharge into three stages. During the *predischarge* a complex flow of charge prepares the interelectrode space for the initiation of the spark. The *spark* covers the interval from the start of the plasma channel (leader) to the completion of the spark channel. A suitable term for the final stage is the *arc stage*. During this stage the interelectrode channel acts as a variable resistor to the discharge of the source of potential (e.g. a condenser).

The aim of the present investigation was to extend that previously reported [1], and in particular to examine more closely the predischarge and the development of sparks in air at atmospheric pressure from the electrodes of negative polarity. For this purpose use was made of a method whose value does not appear to have been fully appreciated. The principle is that only a limited amount of energy is made available for the spark, sufficient for the formation of the spark channel but not for the transition to a light arc. This will probably make it possible to follow the first stage separately, and to obtain further grounds for explaining the discharge mechanism.

The limitation of current has been achieved experimentally by a device similar to that of Allibone and Meek [2], which involves connection of a large resistor in series with the spark gap. The electrode pairs used were point-plate and sphere-plate, and the voltage was provided by an impulse generator (2500 $\mu\mu$F, max. 1.1 MV), with a 1.5 MΩ water resistor in series (Fig. 1*a*). In order to prevent any corona effects disturbing the test gap, the water resistor was terminated at one end by a sphere (diam. 15 cm), to which the actual discharge electrode was connected. The electrodes used were (1) a 5 mm brass rod with 30° taper at the end—referred to subsequently as the thick point electrode, (2) a 0.75 mm copper wire with a rounded end (thin point electrode), and (3) a sphere of 25 cm diameter.

The experiments were performed with long sparks (up to 52 cm) from electrodes of negative polarity. Gaps of length less than 5 cm were not considered. The current (via a shunt) and the voltage (via small pick-up capacitors) were measured by means of a cathode-ray oscillograph. Since it was difficult to ensure complete screening of the pick-up plate from parasitic fields, the accuracy of the voltage recording was not high. There is as yet no better means of measuring the voltage: a potential divider parallel to the spark gap alters the character of the discharge. In order to avoid effects arising from over-voltage, all the tests were performed with the minimum breakdown voltage. At the same time as the voltage and current were recorded with the oscillograph, the discharge was photographed on both stationary and rotating film in a camera with a quartz-rocksalt lens system (F = 1:5, f = 18 cm).

2. Circuit calculations

The experimental arrangement of Fig. 1*a* may be replaced by the equivalent circuit of Fig. 1*b*. The individual elements are:

C_1 Impulse generator (2500 $\mu\mu$F).
C_2 Interelectrode capacity (15–50 $\mu\mu$F).
R_1 Series water-resistor (1.5 MΩ).
R_2 Resistance of the spark.

When the voltage is first applied to the circuit the spark resistor R_2 is infinite, and the interelectrode capacity C_2 is charged up from the generator through the

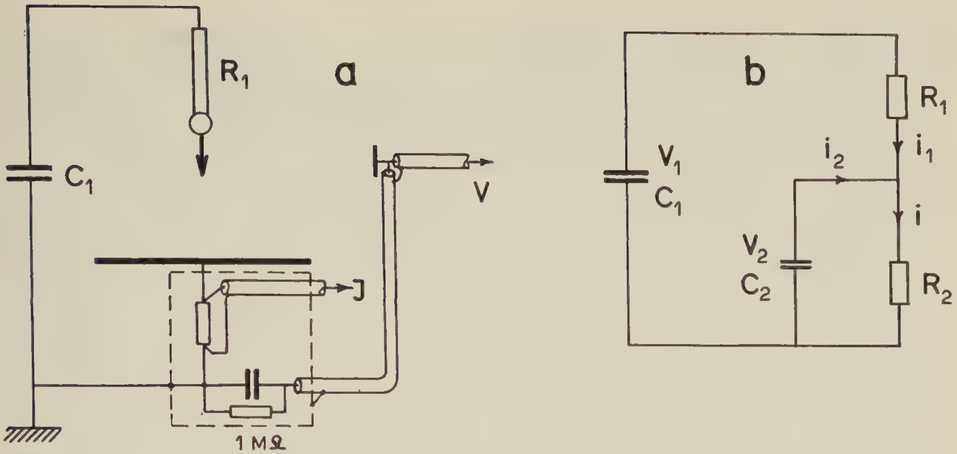

Fig. 1. The experimental arrangement (*a*) and equivalent circuit (*b*).

series resistor R_1. Let the generator potential at breakdown be V_1, and the gap potential V_2. The problem under consideration may be formulated as follows: at time $t=0$ there are two potentials (V_1 across the generator and V_2 across the electrodes) operative in the circuit; an expression is required for the spark current i. It is this current that is measured experimentally by means of the cathode-ray oscillograph.

Three equations are valid:

$$i = i_1 + i_2,$$

$$V_1 - \frac{1}{C_1}\int i_1\,dt = i_1 R_1 + i R_2,$$

$$i R_2 = V_2 - \frac{1}{C_2}\int i_2\,dt.$$

Combination of them gives

$$C_1 C_2 R_1 R_2 \frac{d^2 i}{d t^2} + (C_1 R_1 + C_2 R_2 + C_1 R_2)\frac{d i}{d t} + i = 0$$

which, integrated, gives

$$i = A e^{a_1 t} + B e^{a_2 t} \tag{1}$$

where

$$a_{1,2} = \frac{-(C_1 R_1 + C_2 R_2 + C_1 R_2) \pm \sqrt{(C_1 R_1 + C_2 R_2 + C_1 R_2)^2 - 4 C_1 C_2 R_1 R_2}}{2 C_1 C_2 R_1 R_2}.$$

The time constant $C_2 R_2$ is very small compared with $C_1 R_1$ (about 5 μs as compared with *c.* 4000 μs). This allows us to write with sufficient approximation

$$a_1 = -\frac{1}{C_1 R} \qquad a_2 = -\frac{1}{C_2 r}$$

where the following abbreviations have been made:

$R = R_1 + R_2$ for the circuit resistance when R_1 and R_2 act in series;

$r = \dfrac{R_1 R_2}{R_1 + R_2}$ for the resistance when R_1 and R_2 are in parallel.

The constants of integration may be calculated from the initial conditions. For $t = 0$ we have

$$i = \frac{V_2}{R_2}$$

$$i_2 = \frac{V_2}{R_2} - \frac{V_1 - V_2}{R_1},$$

from which we obtain

$$A = \frac{V_1}{R} \qquad B = \frac{V_2}{R_2} - \frac{V_1}{R}$$

and eqn. (1) takes the form

$$i = \frac{V_1}{R} e^{-\frac{t}{C_1 R}} - \frac{V_1}{R} e^{-\frac{t}{C_2 r}} + \frac{V_2}{R_2} e^{-\frac{t}{C_2 r}}. \tag{2}$$

3. Experimental results

a. The predischarge

In order to ascertain the type of predischarge involved, reference must be made to the spark, which is undoubtedly dependent on the predischarge. Photographs show that three different kinds of predischarges may be distinguished:

1. With a channel such that the spark invariably develops along it.
2. Where the channel is not such that the spark follows it—except for short unimportant sections near the electrodes.
3. Where about half the spark follows the predischarge channel, the other half taking another path.

The first kind of predischarge usually has a single channel which bridges the interelectrode gap, and in whose track the spark immediately follows. It is impossible to photograph this type separately. The predischarge and spark are superposed in the photograph. The shape of the predischarge is only indirectly distinguishable. The result is mostly predictable, but sometimes there is some uncertainty. This first kind of predischarge may be divided into three types. Type 1 is easily discernible in photographs (Fig. 2*a*). The predischarge appears as a long upper luminous cone and a shorter lower one. The channel commences from the upper electrode, as a point or short stem, which diverges to a maximum thickness, beyond which it is constricted to a fine filament. The second luminous cone proceeds from the site of the convergence, and in its symmetry more resembles an ellipsoid, terminating at a luminous base point on the plate. The most luminous parts are the start and base points, and the fine filament at the constriction; elsewhere the luminosity is low.

Type 2 differs from type 1 in that the lower luminous cone develops more as a

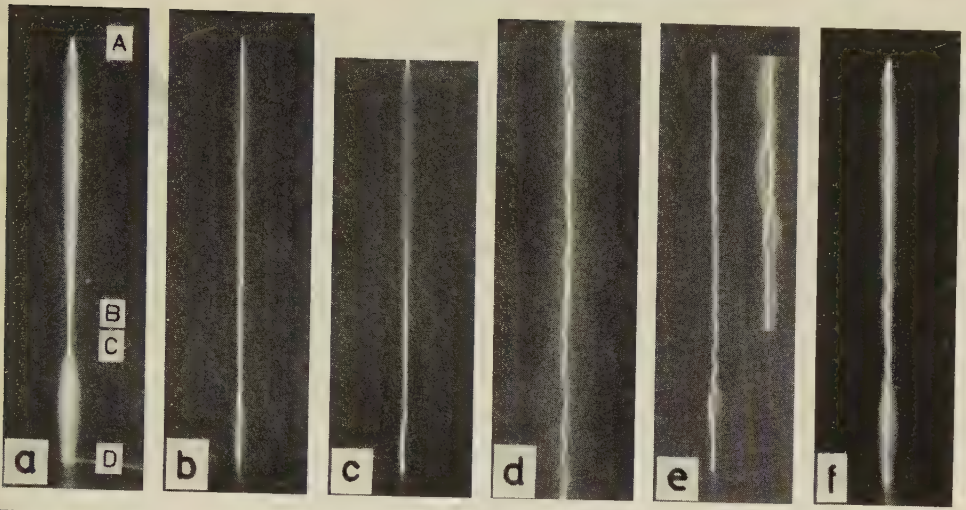

Fig. 2. Discharge type 1: *a*—predischarge; *b*, *c*—spark; *d*—spark, enlarged 1.3 ×; *e*, *f*—arc.

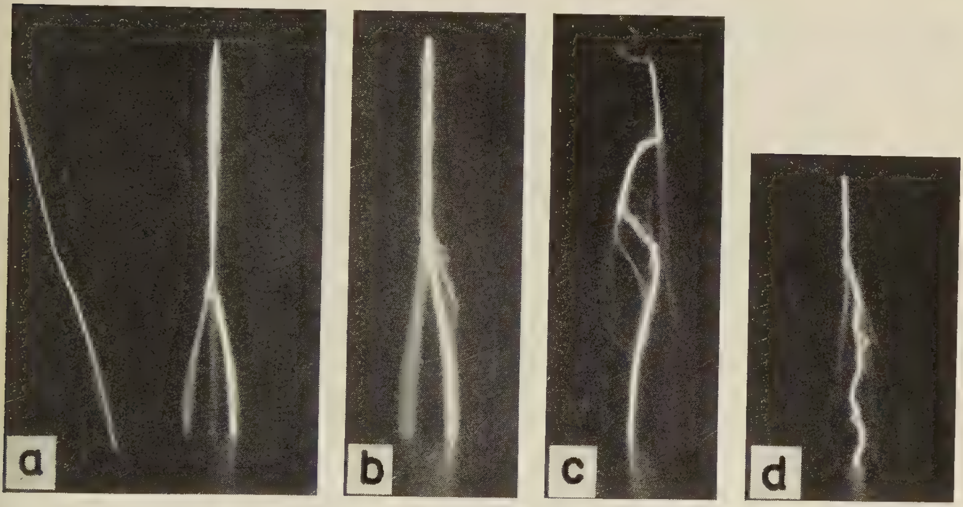

Fig. 3. Discharge type 2: *a*—predischarge and spark; *b*, *c*, *d*—arc.

bunch of diverging threads, with no tendency to branch (Fig. 3*a*). The "blunted" ends of these threads meet the plate in small luminous base points.

Type 3 includes several variants, and occurs when the gap is short (*c*. 5 cm). It is impossible to photograph the predischarge without the spark, which is considerably more luminous, so in all the places where the two are superposed it is impossible to reconstruct the shape of the predischarge. Some different variants are shown in Fig. 4, and it is clear from them that the discharge is a combination of intensely uminous spark channels and more weakly luminous conical formations, position, ength and number of the respective components being widely variable.

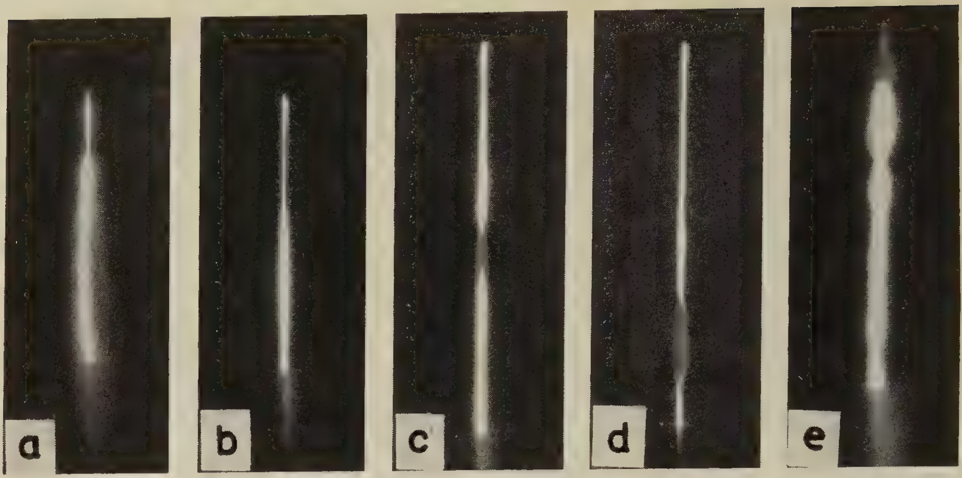

Fig. 4. The variants of discharge type 3.

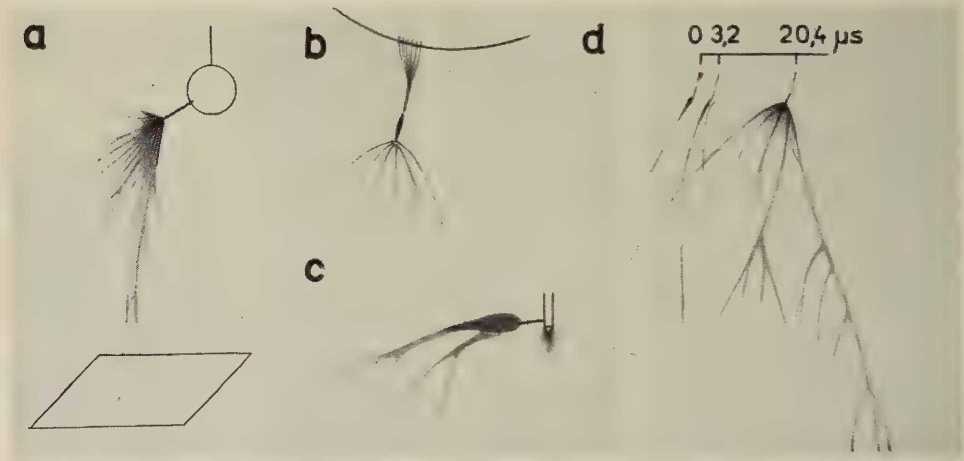

Fig. 5. The forms of the predischarge in discharge type 4.

As regards *the second kind* of predischarge, where the spark does not follow the path of the predischarge, it is easy to distinguish the two in photographs and to trace the predischarge more exactly. There are two types. In type 4 a stem forms at the upper electrode, with a fan-shaped crown of threads growing from its lower end. On photographs taken at a large distance the stem appears to be a luminous cylinder of relatively high intensity (Fig. 5*a*). With the camera nearer it is found that the stem has a complex structure. An example taken with the spherical electrode is reproduced in Fig. 5*b*: from the sphere there proceed several threads which lower down bunch together and form a luminous cone. Fig. 5*c* is another example, where the predischarge has started from the cylindrical side surface of the thick point electrode, and where two luminous cones have formed from the stem that descends

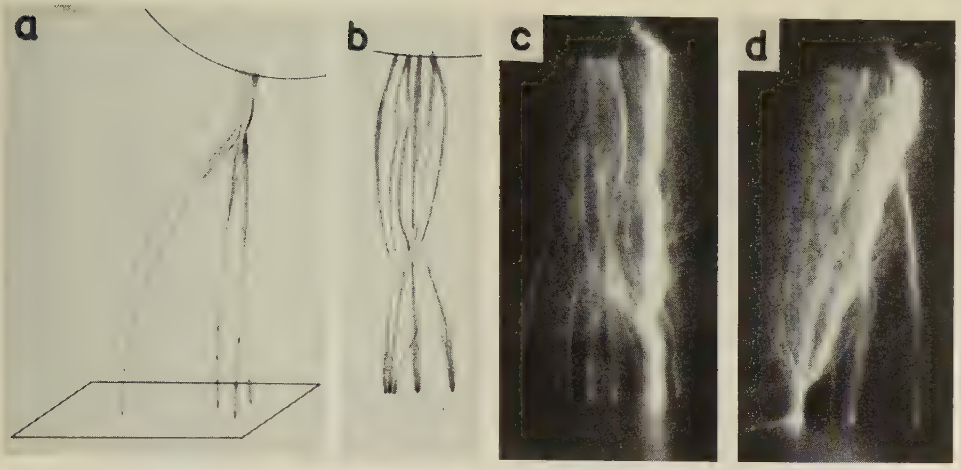

Fig. 6. Discharge type 5: *a*—transitional form of predischarge between types 4 and 5; *b*—predischarge; *c*, *d*—spark and arc.

from the electrode. The first stem, together with part of the filamentous formation, may be so strongly ionised that another stem and bunch of threads arise from it. Several such channels may be connected together in series. In this case the stem is complex, with a long, crooked path (Fig. 6*d*).

The crown of threads has two characteristic features: it diverges, and tends to branch out towards the plate. Depending on the energy, they either extend a certain distance across the gap or traverse it completely, meeting the plate in small luminous points (Fig. 5*a*). The development of the crown of threads often takes place in several stages, as is apparent from Fig. 5*d*. In the first stage the stem is well visible, and only a single thread develops. After 3.2 μs the predischarge again brightens (second stage), the preceding thread elongates, and a new thread appears. The third stage commences after 17.2 μs: the outline of the stem is diffuse, the stem resembles a cylindrical channel, the number of threads increases, and one of them reaches the plate—none of them follows the track of preceding threads, however. The ionisation presumably decays during the first 17.2 μs, and the conductivity of the path no longer differs from that of the surrounding air.

The other type of the second kind—type 5—does not have a cylindrical stem (Fig. 6*b*). Threads diverge from several points of the sphere, running roughly in the direction of the field. In one particular region they show a tendency to cluster together, but everywhere else they diverge. The threads invariably reach the plate.

Types 4 and 5 exemplify two characteristic forms of the second class of predischarge. Between these two extremes there are a number of variants which more or less resemble one or the other of these two types (Fig. 6*a*).

We may also distinguish two types of the *third kind* of predischarge, where the spark follows in the track of the predischarge only a short distance. Type 6 is somewhat similar to type 1: the initial point develops into short intense channels, after which come the first and second luminous cones. The difference from type 1 occurs in the upper part of the first cone, which is so faintly luminous that it is scarcely detectable in the photograph (Fig. 7). This is analogous to the Faraday dark space.

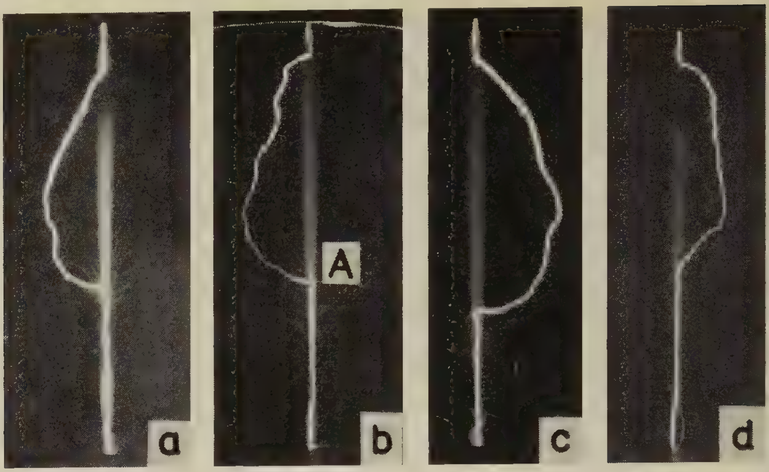

Fig. 7. Discharge type 6: *b*—predischarge and spark (rotating film); *a*, *c*, *d*—all stages.

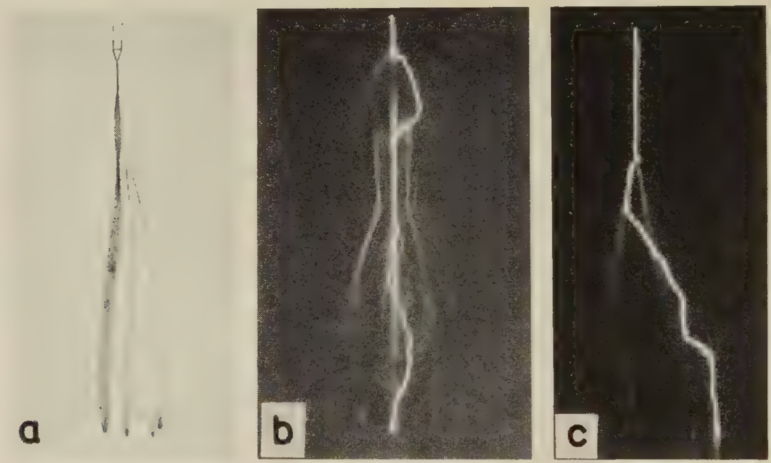

Fig. 8. Discharge type 7: *a*—predischarge; *b*—predischarge and spark; *c*—arc.

Type 7 is a mixture of types 1 and 4: an intense channel is followed by a cone, after which there are several diverging threads, with a tendency to branch towards the plate (Fig. 8*a*). They meet the plate in small points of light.

It should be emphasised that the threads mentioned in connection with types 2, 4, 5, and 7 proceed from the upper electrode, and move towards the lower, either directly or after changing direction. Their branching and divergence also take place in the same direction. These threads are the basic threads of the initial stage.

Also discernible in the photographs are threads of another kind—*subsidiary threads*. They occur only in types 1 and 6, and in appearance resemble the basic threads, apart from the initial and final points, which may be classified as follows.

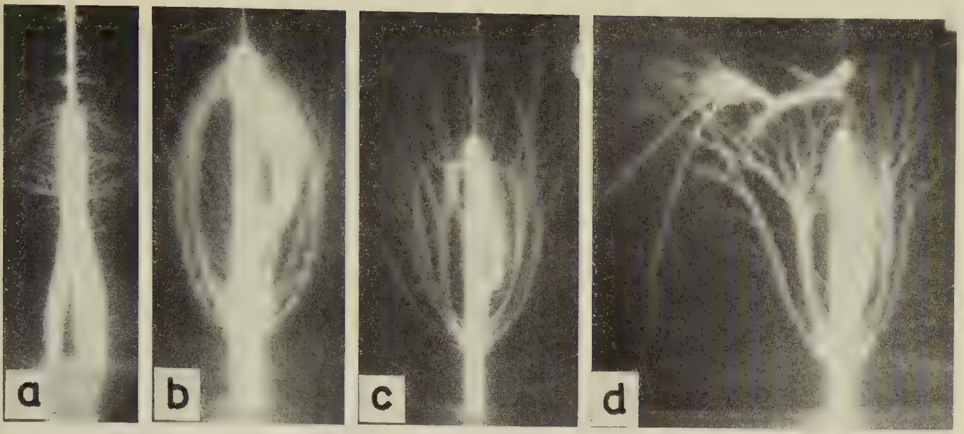

Fig. 9. Subsidiary threads of the discharge.

(1) The initial points may be on the upper part of the upper luminous cone. The subsidiary threads either proceed towards the plate or return to the cone lower down (Figs. 9*a*, *b*).

(2) The subsidiary threads may develop in the gap space and run to the upper cone. Their points of entry there can be either in the upper or lower part (Figs. 9*a*, *c*).

(3) Some of the subsidiary threads originate in free space and some of them at the upper electrode, and they run to the lower part of the upper cone (Fig. 9*c*).

There is always a thickening of the thread at its termination, and this leads to an increase in brightness. There are never any subsidiary threads from the lower cone, and even the upper cone lacks them when the interelectrode gap is less than 10 cm. It may be observed that the threads do not terminate at the place where the cone converges, but anywhere on the cone at a distance of more than 2–4 cm from the point of convergence. An increase in the energy of the spark causes the subsidiary threads to be denser, and they are at the same time forced upwards. It is characteristic of these threads that they originate somewhere in the gap or at the upper electrode and proceed to the upper cone; they never terminate at the basic threads or the spark. Fig. 9*d* illustrates how the basic and subsidiary threads cross one another without coalescing.

Which of the various types of predischarge occurs depends on various factors connected with the parameters of the discharge arrangement. These factors include the voltage, the gap length, the shape of the electrodes, and the capacity of the electrodes. However, even when these factors are kept constant the type of predischarge is not unambiguously defined: there is a certain arbitrariness about which type occurs. This fact is evident in the results of the experiments with the thick point electrode and the spherical electrode. The thin point electrode is treated separately in a later section.

For the thick point electrode the manner in which the type of predischarge varies with the length of the gap (δ) may be summarised as follows:

Gap length (cm)	5–10	10–15	15–25	> 25
Type of predischarge	3	1, 2	6	4, 7

Increasing the interelectrode capacity by coupling a further spherical electrode (25 or 50 cm diameter) at some distance and in parallel with the test electrode favours the occurrence of type 1. When the capacity is made larger in this way type 1 occurs for gap lengths of from 5 up to 25 cm, the upper cone becoming longer and the lower shorter as the gap increases. When an overvoltage is applied types 4 and 7 may appear already for gap smaller than 20 cm.

The predischarge for the spherical electrode (D = 25 cm) is much more variable and irregular. No direct correlation between type of predischarge and length of gap is apparent: a particular type may occur for both short and long gaps. However, the different types do seem to be restricted to particular ranges of gap lengths. Types 1, 6, and 7 did not occur for the range of gaps investigated, 8–52 cm. The other types occurred for the following gaps:

type 2: $\delta = 8$–20 cm
type 3: only for $\delta = 8$ cm
type 4: from $\delta = 12$ cm up to the largest values
type 5: $\delta = 10$–20 cm

It may be seen that type 4 is the only one that occurs for long gaps.

b. Development of the spark

A necessary, though not sufficient, condition for the development of a spark is the occurrence of a predischarge. The predischarge must possess certain characteristics which lead to the development of the spark and help the formation of plasma channels. It should be noted that the term leader is used here to denote growing plasma channels, and not the threads or "cone" of the predischarge.

Type 1.—As already mentioned, a characteristic of this type of predischarge is that the development of plasma channels within the cone is facilitated. In the upper cone the spark always travels along the axis (Fig. 2), while in the lower one its course is more complicated—there are often two plasma channels, one from the tip of the upper cone and the other from the base point at the plate. The ends of the two plasma channels are often not in line, in which case there is a discontinuity in the middle of the cone. Quite frequently the two ends are separate from one another (Fig. 2*b*). Between the ends there is either nothing discernible or something resembling an arc. There are thus two or three parts to the spark: one upper and either one or two lower. As to the order and rapidity of their development it was not possible to make any measurements from rotating films for the shorter gaps ($\delta = 5$–10 cm). Presumably the time was of the order of 10^{-7} sec. For wider gaps the value was 1–2 μs, and the process was probably as follows: a channel developed from the upper cone and ran into the lower cone, the time taken for this stage being the greater part of the total 1–2 μs. The subsequent processes (the growth of the upper and lower channels) was very rapid, probably occupying a time of the order of 10^{-7} sec.

Type 2.—Two leaders commence, presumably at the same instant, from above and below (Fig. 3). The upper one travels along the axis of the cone, the lower follows in the track of one of the threads. After reaching the branching point the upper leader does not necessarily travel in the path of the same thread as the lower leader follows. It often deviates to another thread. When the distance between the two leaders is sufficiently small a spark bridges the gap between their ends (Fig. 3*a*), or it may be an arc-like channel, with a light intensity less than that of the leaders elsewhere.

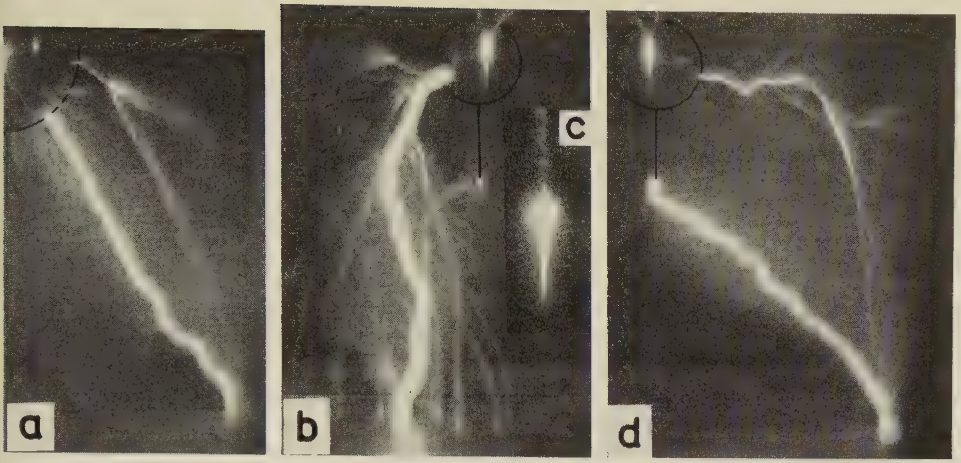

Fig. 10. Discharge type 4: *a*—sphere electrode; *b*, *d*—sphere with fine point; *c*—corona round the thin point, 0.7 natural size.

Type 3.—Includes several variants. In all variants the spark seldom crosses the gap as a uniform channel. Usually only a part of the gap is strongly luminous, and elsewhere there are fainter cones of the predischarge, along whose axes a spark channel develops (Fig. 4).

Type 4.—The stem and perhaps a small part of the adjacent threads have similar characteristics to the canal of type 1, that is, they favour the development of leaders within the predischarge channel. But the stem does not extend far from the electrode, even when it is composite, and the threads subsequently lack this property. Consequently the stem from negative electrodes cannot initiate a leader. In this case the leader commences at the plate. It is therefore necessary that the predischarge threads reach the plate, whereupon a plate stem may appear which initiates the lower leader. The characteristic feature of the lower (positive) leader is that it never follows the predischarge thread, instead making a path of its own with a typical zig-zag course. Slightly later than the positive leader the upper (negative) leader appears, of a smoother shape and at first in a stem or in a succession of stems. Subsequently it creates its own channel, which is zig-zag like that of the positive leader. Between the two growing leaders there appears a diffuse glowing cloud, consisting of many fine threads, constricted at the ends. The two leaders meet in the upper part of the gap, often quite near the electrode, and their junction is often marked by some kind of discontinuity, e.g. loops, or a thickening. It may happen that the stem whose threads initiate the positive leader is not concerned in the formation of the negative leader; the positive leader may travel towards another place on the electrode, from which the corresponding glowing cloud develops more easily. In this latter case the negative leader is usually quite short. The two cases are compared in fig. 10. The time required for the formation of the leaders is relatively long. For a gap 40 cm long the times measured were between 6 and 18 μs.

Type 5.—As already mentioned, an important difference between predischarges of types 4 and 5 is the absence of an electrode stem in type 5. The several threads proceed directly from the sphere (type 5 occurs only with the spherical electrode), each of them with a luminous base point; they thus do not provide an initial channel for the later negative leader. Furthermore, the spark process commences with the appearance of a positive leader. With a contraction on the positive leader the glowing cloud extends across to the sphere, in the form of a very divergent bundle of fine filaments. (Figs. 6*c*, *d*.) The positive leader commences at the plate and travels within the cloud towards the sphere. It is not until the positive leader has almost reached the sphere that the negative leader appears. This upper leader is therefore short, and the meeting point of the two leaders very near the sphere. It may even happen that the only feasible interpretation of the photograph is that the negative leader is absent.

Type 6.—Types 1 and 6 are similar as far as the dark space in the upper cone, but the dark space seems to have an inhibiting effect, so that the spark is only able to utilise a part of the predischarge channel for its development. The continuation of the spark beyond the dark space does not follow in the track of a predischarge channel. The spark develops as follows (Fig. 7): a plasma channel develops in the lower cone, and projects into the upper as well. The time elapsing between the predischarge and the start of the channel, and the time of initiating for the channel, is too short to be determinable with the help of the rotating film. The positive leader appears next, commencing from a luminous point A where one of the subsidiary threads meets the constriction of the upper cone. It is interesting to note that the positive leader initially has no direct contact with the already existent plasma channel on the constriction, but instead enters the plasma channel through a small arc-like glow. In the meanwhile an upper (negative) leader has started from the more intensely luminous stem and between the two leaders lies the glowing cloud. From the fact that the meeting point of the leaders is in the upper part of the gap it may be concluded that the negative leader commences after the positive. When the two leaders have met the spark completely bridges the gap. The development of the leaders occupies 2.5–3.7 μs for a gap length of 15 cm, and 3.5–5.6 μs for $\delta = 40$ cm.

Type 7.—As with type 5, the spark here utilises only a part of the predischarge channels for its development, i.e. only the stem and the lower part of the cone. Neither the dark space within the cone nor the crown of the threads into which the cone merges are made use of; with the help of the leader the spark creates its own channel in this region. Fig. 8*b* is a photograph of a completed spark: the two leaders unite in the ionised part of the cone that is situated in the centre of the gap.

c. The arc stage

After the completion of the spark stage there is a channel of variable resistance through which the condenser can discharge. This latter process is here referred to as the arc stage, and in the cases under consideration it may last for several milliseconds. It is interesting to follow the change in the spark channel during this time. As mentioned in the next section, the current falls on an average from 3 to 0.5 A in 10–20 μs. This latter current then decays with a time constant of about 1000 μs. So after 20 μs the current may be regarded comparatively constant.

If the discharges are also photographed with stationary film it is found that the various types all have something of the same character, despite the individual differences. Further channels are visible in the stationary photographs: they appear as thick threads, invariably undulatory. It is not possible to say whether the actual paths are in the form of a spiral or an irregular wave. Their general course follows the preceding (already crazed?) spark channels (Figs. 2*e*, 3*d*, 7*c*, *d*, 8*c*). They have ıe same undulatory appearance when they pass through the cones (Fig. 2*f*), and ven in places where there is no spark channel (Figs. 3*c*, 4*d*). There can hardly be ıy doubt that these lines on the photographs arise from the arc stage, since they re never visible in the photographs with rotating film.

These undulatory lines were found to occur for all types of discharge, though less ronounced for type 4. They do not occur in the electrode stem, nor in other channels here the luminous intensity is high; in such places the after current causes a widening nd intensification of the photographic image. In photographs taken with a large perture the undulatory lines disappear in misleadingly thick lines due to overxposure.

The duration of the undulatory channels was not determined.

d. Discharges with the thin point electrode

A characteristic of these discharges is the presence of cones in the predischarge. or a gap length up to 25 cm type 1—only with cones—is the predominant type of ischarge; the ionisation in the predischarge channel is sufficiently intense for the park to follow the same channel. Type 6 occurs for $\delta = 25$–40 cm. The upper cone ontributes only partially to the development of the spark; the conditions in its ark space are unfavourable for the passage of a spark. Even in the case of gaps onger than 40 cm one or more cones may occur in the upper part of the predischarge, ut these do not bridge the gap—they are associated with a crown of threads in ıe lower part of the gap. Type 7 occurs, or a combination of types 4 and 7. With ıis electrode there is never the simpler kind of predischarge—e.g. type 4 or type 5—here the stem is short or perhaps entirely absent and the threads alone bridges ıe interelectrode gap.

It is noteworthy that the predischarge never comes from the side of the thin point lectrode, as it often does with the thick point electrode. The only thing observable t the side surfaces of the thin electrode is a corona-like phenomenon, which is oncentrated at single glowing points (Fig. 9*c*). Short filaments may be visible at ght angles to the surface of the wire, but these do not develop farther. The subsidiary ıreads in the upper cone of the predischarge extend farther upwards on account of ıese short lateral threads (Fig. 9*c*). Whenever a predischarge develops it always oes so from the tip of the thin point electrode, and if the potential is less than the reakdown value a corona is visible there (Fig. 10*c*). It develops only in the immediate eighbourhood of the tip, and consists of a glow that fades into the surrounding space. ometimes it is penetrated by a short streamer, which does not have terminal threads, owever.

As already mentioned, the thin wire, 18 cm long, was connected to a 15 cm sphere t its upper end as a shield against corona. With this arrangement and a gap 37 cm ong the spark often occurred not between the electrode tip and the plate but along longer path between the sphere and the plate. The following figures may illustrate ıis. In Figs. 10*b*, *d* the discharge commences from the sphere, with a predischarge f type 4; the threads reach the plate, and there initiate the positive leader, which sually runs to the negative leader that grows from the stem at the sphere (Fig. 10*b*). ess frequently the positive leader goes to the tip of the point electrode (Fig. 10 *d*), ı which case the negative leader is usually short. Fig. 11*a* shows a case where a here (D = 25 cm) has been placed on the plate. Although the distance from the oint to the plate is only 37 cm, the spark crosses the longer gap (65 cm) between

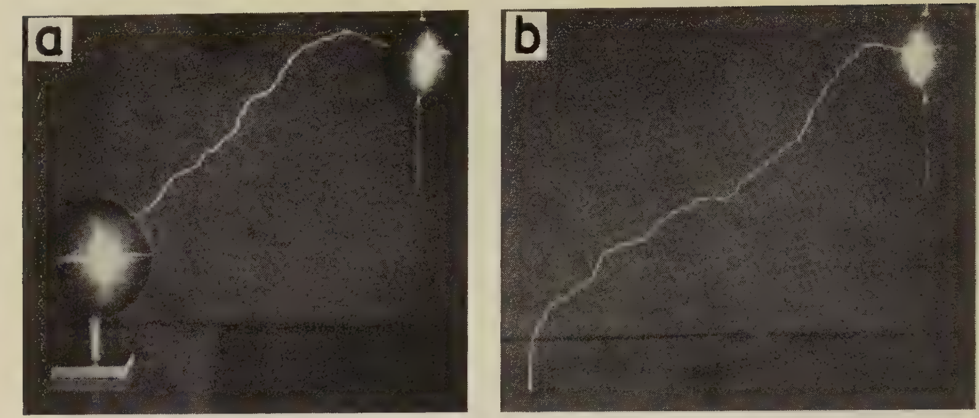

Fig. 11. Discharge with a composite electrode of sphere and thin point.

the two spheres. This effect can be enhanced by having a point on the anode surface. With this arrangement the positive leader is initiated even for weak terminal threads. An example is given in fig. 11*b*: the spark traverses 100 cm between the negative sphere and the positive point electrode rather than the 37 cm between the negative point and the plate.

In all the four figures referred to it may be observed that the threads arise as a rule from the sphere and not from the point, despite the much greater field intensity at the point.

e. The variation of potential and current

It might be expected that the different types of discharge would have correspondingly different potential and current curves. However, the curves obtained with the oscillograph are not so diverse as the photographs, and may be divided into two groups. In the first group the curves for potential and current are both smooth (Figs. 12 and 13 (upper)). These figures and the circuit of fig. 1*b* suggest that the process is as follows: At the point A the impulse generator C_1 is coupled in. The resistor R_2 has as yet infinite resistance. The capacitor C_2 (interelectrode) begins to charge up; the potential rises and the current sinks, the time constant being the same for both curves: R_1C_2 (25–75 μs). At point B the spark channel begins to grow. The current then increases over the period necessary for the growth of the spark, rising to a maximum value at the point C, where the development of the spark is (and of the resistance R_2) complete. The calculation of the current can commence at C, and from that instant the current obeys equation (2). Since a movement of charge is associated with each predischarge channel, the smoothness of the curve must indicate that the predischarge is present only during the interval of time between B and C, and not between A and B or after C. The interval BC, which represents the combined formation time of the predischarge and the spark, is shorter than 1 μs. Since the process is subject to abrupt changes during the time BC, there is generally no part of the oscillogram to correspond to BC. No appreciable change of potential occurs during this interval of time, and consequently the electrode is still subject to the entire breakdown potential at the instant C. This type of curve occurs as a rule for short gaps, i.e. for types 1, 2, 3, and to some extent type 6.

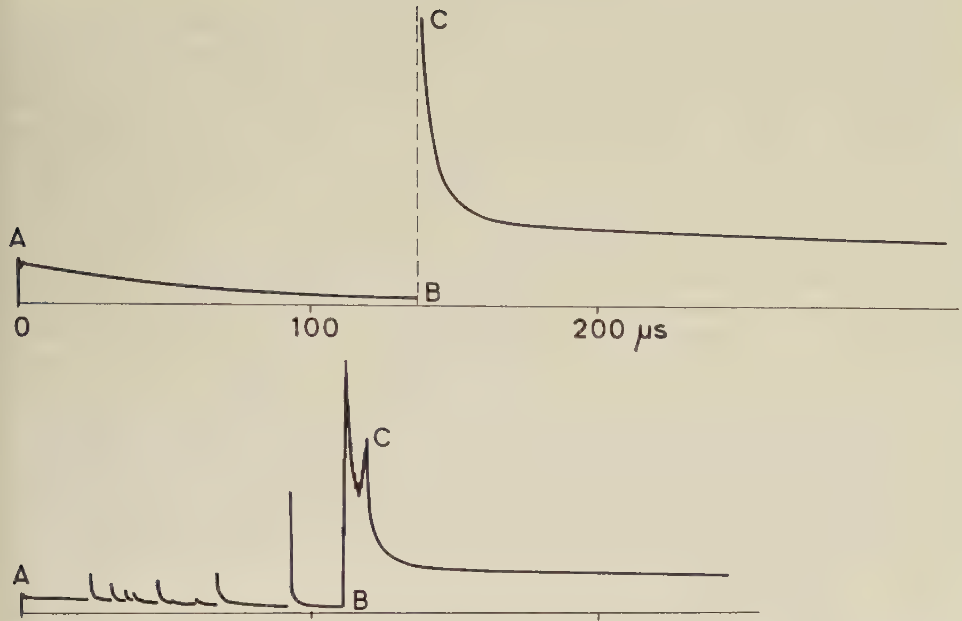

Fig. 12. Current oscillograms: above—smooth curve; below—with distinct predischarge pulses, and irregular current variation during the development of the leaders.

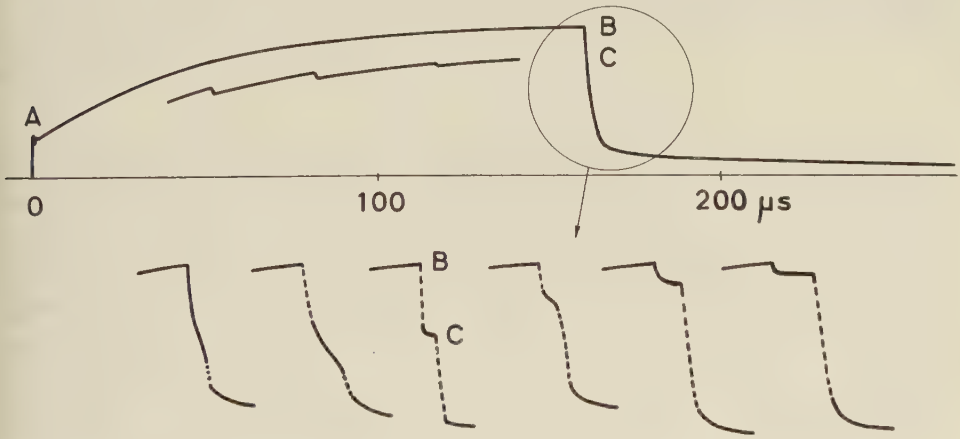

Fig. 13. Voltage oscillograms with and without step.

For longer gaps (types 4, 5, 7, and sometimes 6) the potential and current curves are irregular (Figs. 12 and 13 (lower)). Even during the charging of the electrode (AB) there may be short single pulses (with a duration of the order of 1 μs) while the potential is still less than the breakdown value. This indicates that isolated predischarge channels develop without contributing to the growth of the spark. The currents involved are small. These pulses appear as small depressions in the voltage curve, which indicates that the amount of charge these channels draw from the electrode is so small that the drop in voltage is practically imperceptible. In contrast, the branches of the predischarge which develop shortly before the start of the leader draw considerable current, even though they do not initiate the spark. The lower current curve of Fig. 12 shows a typical example: shortly before the commencement of the leader a predischarge channel develops with a current amplitude equal to half the maximum current; nevertheless 19 μs elapsed before the decisive predischarge channel arose (instant B). The spark grows during the interval BC, and from the instant C the current flows across the gap (resistance R_2) that the spark has crossed. The current passes through a minimum in the interval BC when the spark is growing, presumably in connection with the growth of the two leaders. Corresponding to the current minimum there is a step in the potential curve (Fig. 13), a persistence of the potential at a value about half the maximum or a little higher followed by further decline. The discharge of Fig. 12 has several successive predischarges. Most of them are separate predischarges with a single current pulse. But some of the pulses may be such as contribute to the successive growth of the same predischarge.

The step in the potential curve may be of various forms (Fig. 13), which indicates that the union of the leaders does not always take place in the same way. In Fig. 13 the places where the potential collapses smoothly are drawn with a continuous line, while the irregular parts are dotted.

f. Calculation of the resistance of the spark

The method employed here enables the resistance of the spark (R_2) to be calculated solely on the basis of the current curve. The current equation (2) is utilised:

$$i = \frac{V_1}{R} e^{-\frac{t}{C_1 R}} - \frac{V_1}{R} e^{-\frac{t}{C_2 r}} + \frac{V_2}{R_2} e^{-\frac{t}{C_2 r}} . \qquad (2)$$

This signified that the current consists of three components. The components are presented graphically in Fig. 14*a*. The third component, $(V_2/R_2)e^{-t/C_2 r}$, may be derived from the current curve, and from its curve the time constant $C_2 r$ determined. The spark resistance is easily calculated from the latter.

Of course, it is not necessary to transform the oscillogram to absolute values in order to derive T from an exponential curve such as

$$I = I_0 e^{-\frac{t}{T}} . \qquad (3)$$

It is sufficient to know the ordinates I_1 and I_2 for times t_1 and t_2 in the same units (e.g. millimetres). The time constant can then be determined from

$$T = \frac{t_2 - t_1}{\ln I_1 - \ln I_2} . \qquad (4)$$

If T may be variable the times t_1 and t_2 should not be far apart, for T then constitutes a mean value for the intermediate time interval.

The calculating procedure may be illustrated from a current oscillogram (Fig. 14*c*). The initial current (V_1/R) is determined to begin with. For this purpose several

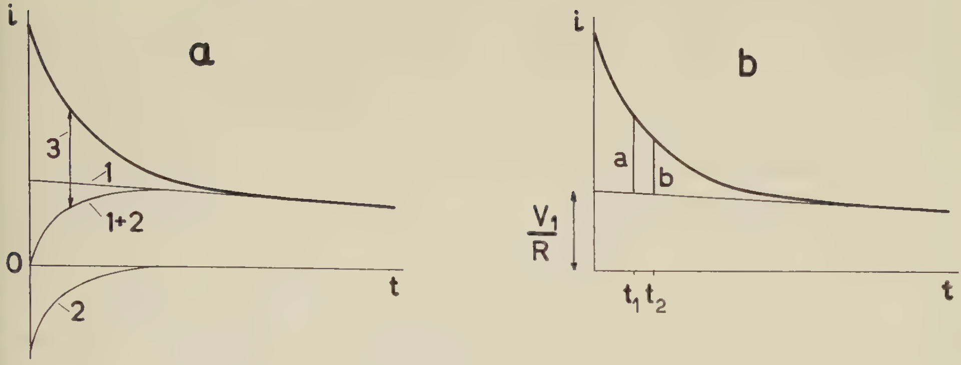

Fig. 14. The components of the spark current.

ordinates are measured for times greater than four times the time constant C_2r. The last two current components in equation (2) are then negligible, leaving only the first component, $(V_1/R)e^{-t/C_1R}$, for which the time constant (C_1R) may easily be determined with the help of equation (4). From C_1R the initial current (V_1/R) is determined from equation (3). The fact that the resistance involved in C_1R $(R = R_1 + R_2)$ is not constant on account of the variability of R_2 does not entail any great error.

The V_1/R value obtained is marked on the oscillogram at $t = 0$, and from it an exponential curve may be drawn that coincides with the current curve for large t. Since the time constant is large it is in practice sufficient to draw a straight line instead of the curve. The ordinates a and b corresponding to two neighbouring times t_1 and t_2 are then measured. It is first necessary to estimate the required time constant $(T = C_2r)$. If this value is called T_e,

$$\frac{V_1}{R}e^{-\frac{t_1}{T_e}}+a=\frac{V_2}{R_2}e^{-\frac{t_1}{T}}$$

$$\frac{V_1}{R}e^{-\frac{t_2}{T_e}}+b=\frac{V_2}{R_2}e^{-\frac{t_2}{T}}$$

from which it is easy to calculate T with the help of equation (4). If the value thus calculated does not coincide with the estimated (T_e), the calculation may be repeated with the new value of $T_e = T$ replacing and so on, until successive approximation gives a value of T that is sufficiently close to the estimated (T_e).

Finally it is a simple matter to determine R_2 from the value of T thus arrived at, since

$$T = C_2r = \frac{C_2R_1R_2}{R_1+R_2}$$

and C_2 and R_1 are known. The interelectrode capacity (C_2) is determinable in two ways—by direct measurement with a bridge, and from an analysis of the discharge curve (AB in Fig. 13).

The method put forward here has the advantage that the resistance may be calculated solely from the current curve. The absolute value of the current is nowhere required in the calculation: it is sufficient to insert the ordinates measured in mm for instance, in the equations used. This allows the errors involved in measurements and calculations to be reduced to a minimum. A disadvantage is that the spark resistance can only be determined for the time interval corresponding to the third component, $(V_2/R_2)e^{-t/C_2r}$, i.e. for about the first 15 μs in the case under consideration. It is theoretically possible to utilise the persisting first component subsequently, and thus to calculate R_2 from RC_1, R_1 and C_1 being known. But unfortunately R_2 is small compared with R_1, which is moreover variable since it is a water resistance. The calculation of R_2 in this way is therefore attended by large errors. Another disadvantage is associated with the inexactness of the current equation (2), which is strictly applicable only when $C_1R_1 \gg C_2R_2$. It is often difficult to decide from the oscillogram at which point the plasma channel has bridged the gap, whereupon equation (2) may be employed. On account of these sources of error the value obtained for the spark resistance cannot be regarded as more than the order of magnitude.

The values of R_2 as determined for different gap lengths from 20 oscillograms evidence a pronounced spread. The *initial value* is from 70 to 150 kΩ, on an average 100 kΩ. It is remarkable that for gap lengths of 7 to 40 cm these values are independent of the gap length, both for the point electrode and the sphere, and that in the interval immediately afterwards (some 15 μs) the spark resistance has a marked tendency to increase—in some cases to five times the initial value. However, this observation should be regarded as no more than preliminary. The phenomenon is so complicated that further comprehensive experiments are needed to clarify it.

g. Diameter of the channels

Several successive luminous phenomena are superposed in a stationary picture of a discharge. The same applies to a photograph with rotating film, if the speed of the processes exceeds the resolving power of the rotating film. If the successive stages are of about the same luminosity it is impossible to distinguish between them in the photograph. If on the other hand the luminosities are different, as is mostly the case, the photograph of a spark does not show uniform channels, but a relatively intense core surrounded by an aureole which may or may not have the same shape as the core. But the exposure of the film must be suitable. If it is too long, the distinction disappears, and the spark seems to be uniform. In order to arrive at a correct exposure it is necessary to take several photographs with different lens apertures. This enables us, moreover, to judge how far the channels are uniformly luminous.

At the initial stage—the commencement of the spark—the intense core may be called the *spark channel*; later, after an alteration in the core, it is called the *arc channel*.

The aureole around the core may arise from various phenomena. For discharges of types 1, 2, 3, and to some extent 6 the aureole corresponds to the *predischarge channel*. For types 4, 5, 7, and in part 6, the predischarge channel is separately visible in the photographs; the rather indistinct halo surrounding the spark channel in the photographs is a satelite effect of the spark and is referred to as the *spark aureole*.

The spark channel.—In all cases where the spark does not follow in the track of the predischarge channel (types 4, 5, 7, and in part 6), the spark channel is a uniform filament with a sharp outline and fairly constant width. In types 1, 2, 3, and in part 6 the channel is irregular: (a) The width is variable—sometimes small at the

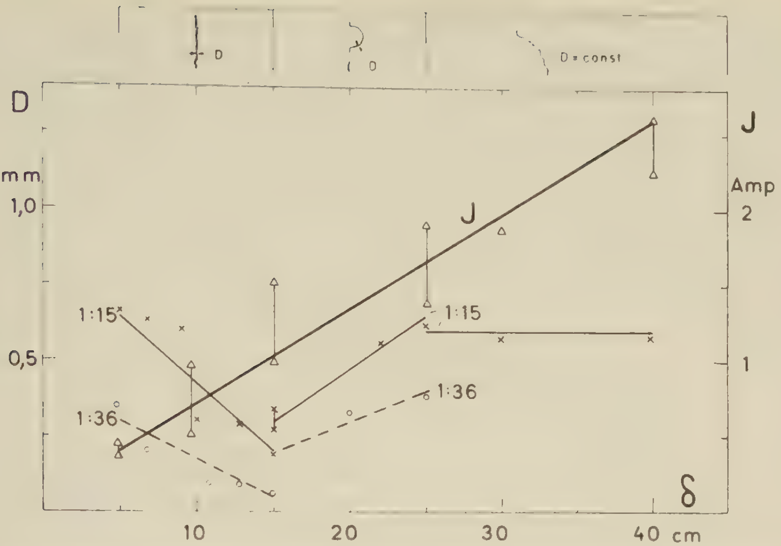

Fig. 15. The diameter of the spark channel (D) for various gap lengths (δ). The numbers give the camera lens aperture. I—mean initial current in the spark channel.

top and the bottom and large in the middle, sometimes the other way about (Fig. 2*c*). (b) The path is erratic, as if the spark jumped from one track to another (Fig. 2*e*). (c) The channel is mainly split up into fine filaments of *c*. 0.1 mm diameter (Fig. 2*d*).

Consequently, in a graphical presentation of the changes in the channel diameter with gap length and with current, it is only possible to use the width at places where it is not markedly variable. Fig. 15 is a synopsis of selected values, with the positions of measurement indicated schematically. These values are averages taken from several photographs. It may be observed that as the gap becomes longer the width of the spark decreases for type 1, increases for type 6, and remains constant for types 4, 5, and 7. The measurements have as a rule been made on photographs taken with aperture 1:15. With a smaller aperture (1:36) there was a decline in the width of the spark, more marked for type 1 than for type 5. It was not possible to employ the lens's full aperture (1:5) for the determination of the diameter, since the film was then overexposed, and the superposed aureole obscured the spark channel.

The arc channel.—It is not clear what should be regarded as the diameter of the channel in this case. The overall width occupied by erratic path may be quite large, e.g. in type 1 it may fill the whole of the predischarge channel, with a diameter of 25 mm. The meandering thread itself is of fairly constant thickness, rather like that of the spark channel, on an average about 0.6 mm.

The predischarge channel and the spark aureole.—Fig. 16 shows the diameters, measured with the largest lens aperture. The values denoted by a and c are the maximum diameters of the upper and lower cones respectively. Both increase with gap length and with current. Reduction of the lens aperture to 1:15 reduces the width of channel a in the photographs:

for $\delta = 5$ cm from 6.5 mm to 3 mm,
$\delta = 15$ cm from 10 mm to 8 mm,
$\delta = 25$ cm from 15 mm to 13 mm.

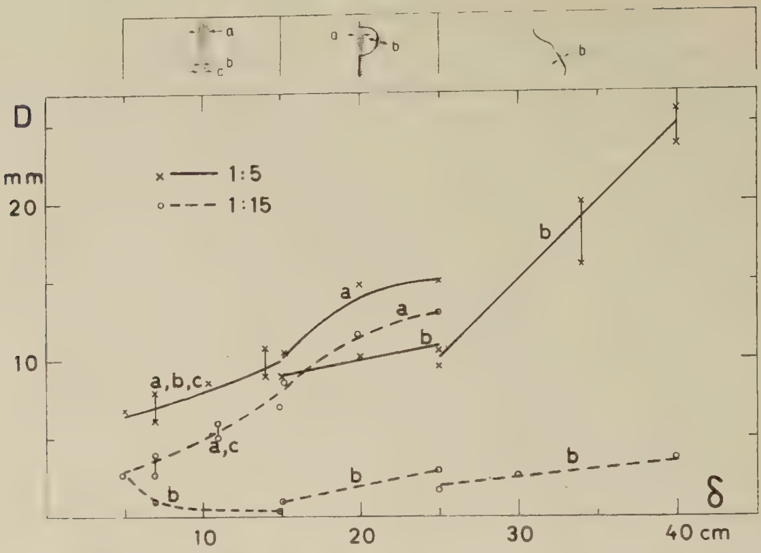

Fig. 16. The diameter of (*a*) the upper cone, (*c*) the lower cone, (*b*) the spark aureole. The solid curve is for aperture 1:5, the dashed curve for 1:15.

These figures show that the cones become more uniformly luminous as the gap length (δ) increases.

The diameter of the spark aureole is denoted by *b* for all types. This also increases as the gap becomes longer. But the luminosity is low—changing the lens aperture from 1:5 to 1:15 reduces the width to a few millimeters for all types.

4. Discussion

a. The predischarge

The thousand or so discharges photographed by us have been divided into 7 types, which can be arranged in two groups. The first group (types 1, 2, 3, 6, 7) comprises discharges where the spark either completely or partially follows in the track of the predischarge. To the second group (types 4, 5) are assigned discharges where the predischarge channel does not exert a direct influence on the development of the spark. In this case the predischarge contributes to the growth of the plate stems, and thus creates conditions for the commencement of leaders. However, the leaders do not follow the same path as the predischarge: other factors determine their paths.

In order to ascertain which of the particular forms of discharge in the first group is relevant in a particular case, it is sufficient to know how the predischarge grows. For the second group this is of no significance: here it is necessary to follow the development of the leaders. The first group corresponds to small and medium gaps; the second occurs only for the largest gaps.

The various types of predischarge depend on the configuration of the discharge space and the kind of charge supply. The principal factor is the instantaneous field configuration, which depends on the shape and capacity of the electrodes, the inter-electrode gap, and the energy instantaneously available to the spark. The actual flow of charge is greatly affected by the ionisation by collision that takes place (both at the electrodes and in the gap). Even when the parameters of the test arrangement are kept constant there is no single definite field configuration, because of the numerous possible combinations of the various elements concerned. For instance, it is not only the quantity of charge that is important, but also the manner in which it is distributed, the channels it follows, and the further processes it gives rise to. According to their size, type, time and order of formation, etc., the channels favour a particular subsequent development. All this compels us to conclude that it must be impossible to summarise the predischarge by a single formula--and much less so then the complete discharge process. So it is understandable why neither of the two theories that are current can provide a really satisfactory explanation of the process in long sparks. The theories must be based on an oversimplification; the real process is of a much more complex nature.

Experiment shows that at negative discharge the predischarge always starts from a brightly luminous point on the cathode. Never once in our experiments did it originate in the interelectrode space or at the anode. From the point of initiation on the cathode there develop either faint filaments or more luminous cones; combinations of the two may also occur. It can scarcely be doubted that both these phenomena represent some kind of motion of electrons: the predischarge lasts such a short time that the ions formed may be regarded as practically motionless.

An important characteristic of negative discharges is the alternation of convergence and divergence along the predischarge channel. Such variation of the width is found not only for single channels—e.g. the cones, where there is continual variation of the cross section—but also in a crown of threads. The individual threads diverge from one another in some places and in others converge (Figs. 6*a*, *b*). The cause of this behaviour appears to be the presence of positive ions arising from ionisation by collision—cf. our previous paper [1b]. On account of their large mass these ions move much more slowly than the secondary electrons that are simultaneously produced. Consequently a positive space charge develops in the predischarge channels, and associated with it is a field that tends to constrict the stream of the following electrons. The possibility of such convergence of the channels by the space charge they give rise to may even be confirmed by calculation [3].

The electrons start from the brightly luminous points on the cathode. The paths they take may differ considerably from case to case, depending on whether the field is weakly or strongly divergent:

1. Threads may form without appreciable ionisation by collision (type 5). The convergence of the threads in the middle of the gap (Fig. 6*b*) indicates the occurrence of ionisation there. Positive charge in the path of the first thread attracts following threads, so a divergent crown of threads forms.

2. The field is sufficiently strong to bring about ionisation by collision at the cathode. A stem develops, and this extends downwards to the region where the ionisation ceases, whereupon it branches out into threads (type 4). The divergence of the thread bundle indicates the absence of ionisation. The threads may be short (Figs. 5*b*, *c*), or may extend to the plate electrode (Figs. 5*a*, *d*), depending on the amount of charge received from the stem. The number of electrons emitted by the cathode presumably also has some influence.

3. The configuration of the field allows more extensive ionisation by collision in the gap (types 1, 2, 3, 6, 7). The electrons from the cathode produce a charge in the stem, but the field is not sufficiently strong to produce further ionisation beyond

this stage and the flow of electrons diverges, giving rise to the upper divergent part of the cone (Fig. 2*a*) and the subsequent dark space—where such occurs (Fig. 7*a*). In the meantime the electrons have again begun to accelerate, and soon produce a second region of ionisation by collision, corresponding to the lower convergent part of the cone. The ionisation is most intense at the tip of the cone, as evidenced by the high luminosity and the smallness of the cross section.

Fig 5*d* shows that the predischarge may proceed in a series of jumps. This suggests that the primary electrons from the cathode come in bursts of very short duration (10^{-7}–10^{-8} sec). There is no quasi-continuous emission of electrons—lasting for several microseconds—from the cathode. If conditions at the base point are favourable there may be several pulses of cathode electrons. When the interval between two successive pulses is short (a few microseconds) the second pulse follows and extends the channel left by the first pulse. If the interval is somewhat longer (e.g. 20 μs) the preceding channel has already lost its condcutivity, and the new pulse forms its own crown of threads.

The conditions in the lower cone of types 1 and 5 are not so amenable to analysis as those in the upper cone. The lower cone is presumably formed through a movement of charge. The divergence of the upper part indicates that no ionisation occurs there, but on the other hand convergence of the lower part is no evidence of ionisation, for the threads (without ionisation) impinging on the anode are usually converging as well. The manner in which the spark grows in the lower cone supports this point of view: cases occur where the spark moves along the surface of the cone instead of along the axis.

As regards the subsidiary threads, it is difficult to attain clarity. They represent a kind of charge movement where ionisation by collision does not occur, though there is a luminous excitation. The rotating film shows that the subsidiary threads occur either at the same time as the cone or immediately afterwards (10^{-7} sec). This indicates that these threads involve electron pulses, not a movement of ions. Most of the subsidiary threads run out from the space. This suggests that free electrons are present in the space at the instant the cone is formed, and that the modified and intensified field due to the cone sets them in motion, thus giving rise to the luminous threads. These threads thus indicate the form of the local field lines, and we may conclude that the inner end of each subsidiary thread must terminate at a place where there is *positive charge*. In a plasma channel the distributions of the two types of charge are similar, which means that the channel is externally neutral; consequently neither a basic thread nor subsidiary thread can terminate at such a channel. This conclusion is of great importance as regards the development of the discharge: from the point of view of the field configuration *a plasma channel cannot be regarded as identical with a metal conductor*. Comparison of Figs. 9*c* and 4*d* provides a convincing proof of this; whereas there is a pronounced corona around the metal wire (D = 0.75 mm), there is none whatsoever around the spark channel (D = 0.4 mm).

Certain phenomena associated with the predischarge may be interpreted in the light of this conclusion:

(1) The free electrons in the ionised glowing cloud never travel directly to the surface of the positive leader. They move in fine filaments that form a sort of brush at the end of the leader (Fig. 6*d*).

(2) No subsidiary threads are attached to the convergent end of the first cone (Fig. 2*a*). This accords with the supposition made above, that a plasma channel occurs there.

(3) Since subsidiary threads never terminate at the lower cone, and since this does not consist of plasma, it must contain a preponderance of negative charge.

(4) A discharge of the kind shown in Fig. 9*a* consists of plasma only in the lower part: the upper part has a preponderance of positive charge.

(5) It is not correct to suppose that the plasma channel by its high conductivity raises the potential of the negative electrode almost to that of the plate.

A few remarks may be made about discharges with the thin point electrode. For a slightly convergent field—e.g. near a spherical electrode or the lateral surface of a thick point electrode—the critical value is attained when the electrode potential has reached its maximum value. The electrons from the cathode are emitted into an almost charge-free space. The initial growth of the predischarge depends mainly on the divergence of the field.

There is a marked contrast in the case of a highly divergent field. The critical value is attained long before the potential has reached its maximum value. The already initiated ionisation does not assist the predischarge, since the field farther away from the electrode tip is too weak for necessary transport of charge. The space charge is delayed near the electrode, presumably in the form of negative ions. By the time the potential has reached its maximum value the surrounding space is filled with negative charge. This space charge retards the electron emission, and the predischarge is thus unable to commence during the period that the potential retains its maximum value. If the two cases are compared, it will be seen that a highly convergent field requires a higher potential for breakdown than does a slightly convergent field. If both configurations occur simultaneously—e.g. when a composite electrode of sphere and point is used—the predischarge develops more easily where the field is only moderately convergent (at the sphere), and the spark travels from the sphere, even though the distance between plate and point is much smaller (Fig. 11).

The case of the negative leader is similar—the flow of electrons has to contend with a negative space charge. This appears to be the explanation of the inertia of negative leaders.

b. The spark

The experiments reveal two kinds of spark growth.

In the first kind the spark develops entirely within the predischarge channel. The diameter and other characteristics of the channel are not uniform—it is divisible lengthwise into several elements. Let us consider the development of the spark of discharge type 1 more closely.

The current in the element BC (Fig. 2*a*) arising from ionisation by collision during the predischarge is of high cross-sectional density, because the cross section is small. Consequently this element has already become a plasma channel of high temperature and low resistance at the conclusion of the predischarge. The subsequent spark follows this channel, occupying the whole of its width. The diameter of this element is fairly constant: its values for $\delta = 5$–15 cm are given in Fig. 15. The diameter decreases from 0.65 to 0.2 mm as the length of the gap increases, while the average initial current rises from 0.4 to 1 A. The current density thus rises from 134 to 3200 A/cm^2.

In the element AB the spark develops in another manner. The ion density in the cone channel is insufficient to transform the entire channel to a plasma channel. Along the axis of the cone (probably owing to greater ion density there) the spark forms its own channel, a core whose structure suggests that it is made up of several simultaneously initiated ionisation paths a few millimetres long. It is not possible to say whether the ionisation is by collision or thermal. Separate processes occur simultaneously yet independently and somewhat displaced with respect to one another (Fig. 2*e*). End to end they form a thin ($D = 0.1$ mm) zig-zag spark filament. Several such filaments may occur side by side, together forming a "rope" some 2 mm in diameter, which in the photographs has the appearance of a core within the cone (Fig. 2*d*).

The question of how the spark develops in the lower cone (element CD) may be left open for the present. The available experimental material is insufficient for a consideration of the processes involved.

The second kind of spark development, which occurs in types 4 and 5, is fundamentally different. The spark makes its way across the gap without the assistance of the predischarge channel. The growth is from both electrodes simultaneously. This brings us to leaders. The spark is said to grow with the aid of two leaders—a negative (the upper) and a positive (the lower). The positive leader commences by the initiation of a plate stem by the threads of the predischarge. The end of a thread that strikes the plate is transformed into a plasma channel; the brightly luminous base point of the thread probably plays an important part in this. At the same time there appears a glowing cloud—a diffuse, weakly luminous phenomenon, closely resembling the silent discharge; it represents a diffuse movement of charge. The photographs suggest that the glowing cloud consists of fine filaments which run from the tip of the cathode stem to the end of the positive leader. The growth of the positive leader may be explained as follows: the region of the glowing cloud is either ionised or filled with a swarm of electrons from the electrode stem. The charge is drawn to the positive leader through fine brush-like channels. The whole picture is strongly reminiscent of the spark-figure stage in Lichtenberg figures. The charge is conducted to the plate by the leader. The current density here is of the order of 500 A/cm^2, since the cross section is about 0.001 cm^2 and the current about 0.5 A. The thermal ionisation that occurs and the increasing current account for the maintenance and growth of the positive leader. The leader finally has a cross section of 0.003 cm^2, which, with an average current of 2 A, corresponds to a current density of 670 A/cm^2. Thus it seems that the current density is fairly constant while the positive leader grows.

The growth of the negative (upper) leader proceeds in an analogous way, except that instead of the collection of charge by the positive leader there is an emission of electrons, which likewise occurs in fine luminous channels. There is little branching of the channels in the negative leader, and it is always directed towards the plate. The channels of the positive leader are much branched, on the other hand, and directed towards the cathode. The necessary current for the emission of electrons comes from the cathode, and is conducted through the stem and the fine channels. The current is the same as in the positive leader, and the cross section of the stem some 0.01 cm^2, so the current density is less than in the positive leader—it increases from 50 to 200 A/cm^2. The negative leader is therefore relatively inert; it does not start until the positive leader is near, i.e. until the current density has risen. The negative leader therefore commences later, and the junction of the two leaders is usually in the upper half of the gap. When the two leaders have come close together some other phenomenon presumably occurs, for there is often a thickening at the junction, and often a discontinuity or branching of the channel.

The oscillograms taken with large gaps manifest a discontinuity, both in the current and potential curves. The current first rises rapidly, then falls to a minimum, whereupon it again rises to a maximum, finally decreasing steadily (Fig. 12). Corresponding to the minimum in the current curve there is a step in the potential curve (Fig. 13). The current during the first stage is that required for the development of the leader; this process is accompanied by rising current and rising conductivity. The actual growth of the leader on the other hand requires less current, which accounts for the minimum in the current curve. We may therefore conclude that the step in the potential curve corresponds to the growth of the leader. For types of discharge where there is no leader—e.g. type 1—there is no such step.

c. The arc stage

When the spark has bridged the gap the discharge is self maintainable. When the conditions are favourable for the further development the resistance of the gap falls to the value it has for an arc. This decrease in the resistance does not occur in the cases here under consideration. It was observed that there was actually an initial rise in the resistance. The methods used did not permit observation for more than 15 μs, so it is uncertain how the resistance subsequently varied.

At the same time there is a change in the structure of the channel. The spark does not follow the previous channel; this applies to all types of discharge. Instead of the previous fairly straight path there is an erratic path of about the same cross section (0.003 cm^2). We have not observed when this change takes place; presumably it does not occur during the discharge of the capacitor C_2, but during the subsequent stage of comparatively constant lower current.

The factors governing the change in the resistance of a spark channel are known theoretically. The heating due to the initial consumption of energy rises the temperature of the channel and gives rise to thermal ionisation, which raises the ion density in the plasma and accordingly lowers the resistance. In the present case, where all the parameters are variable, it is impossible to decide whether the energy supplied is sufficient to ensure a further rise in the temperature and the degree of ionisation. Either the initial power is insufficient to start the arc or the declining power is insufficient to maintain an arc. Calculation gives an initial value of the power in the neighbourhood of 500 kW, which falls to 10 kW after 15 μs. It therefore seems plausible to attribute the increase in resistance in our case to the sharp decline in the rate of energy consumption.

As long as it is not possible to clarify all the factors involved in the variation of resistance and to draw up a complete balance of energy, it must be regarded as an open question how the spark with its relatively large resistance of positive character changes to the arc with its small resistance of negative character.

It has frequently been demonstrated that the type of the discharge is determined by the associated circuit. The discussion below is concerned with this question.

Each stage of the discharge requires a certain amount of energy or a certain current, and in the absence of constraints is completed in a certain period of time. In the experiments described here the time occupied by the predischarge was less than 1 μs, and by the spark up to 5.6 μs. The duration of the arc stage is unrestricted, on the other hand, lasting until the condenser is discharged. The first two stages therefore demand a rapid supply of energy, and the last a slower. To begin with the available energy is stored in two capacitors—the impulse generator C_1 and the interelectrode capacitor C_2. Although the latter is small (15–50 $\mu\mu$F), the energy stored in it (0.02 Ws for $\delta = 5$ cm, 2.7 Ws for $\delta = 40$ cm) suffices for the consumption in the first two stages. This energy (in C_2) is immediately available for the first two stages, whereas that of the primary source (C_1) is not, owing to the series resistor R_1 and the larger time constant (1000 μs). This means that the whole of the energy stored in C_1 is supplied to the arc stage. It is evident that the series resistor does not affect the predischarge stage, and only affects the spark stage very slightly. But for the arc stage it is very important. It has long been recognised that a series resistor of a certain size is necessary for the establishment of a stable arc. It is incorrect to derive the value of the initial current from the generator potential (V_1) and the total resistance ($R_1 + R_2$). When R_1 is large the current at $t = 0$ is almost determined only by the electrode potential (V_2) and the spark resistance (R_2), and may attain much higher values than V_1/R.

Briefly, when the predischarge and the growth of the spark is the chief subject of attention the interelectrode capacity is important, and both parameters (R_1 and C_2) should always be stated.

5. Summary

A complete discharge process—from negative electrode with limited current in air at atmospheric pressure—may be divided into three stages: the predischarge, the spark, and the arc stage. Some 1000 photographs of discharges have been classified in 7 types, which may be divided into 2 groups. In the first group the spark develops in the channel of the predischarge. In the second group the spark develops outside the predischarge channel, with the aid of positive and negative leaders.

The distinctive thing about the predischarge of type 1 is that it consists of two cones, of diameter 6.5 mm at $\delta = 5$ cm and 10 mm at $\delta = 15$ cm. The predominant type of predischarge at large gap lengths (type 4) is one that grows from the cathode as a stem with a crown of threads. An important observation is the alternation of divergence and convergence, both in a channel and between the individual elements of the predischarge. The initial emission from the cathode occurs as a burst from a point on the electrode; and a predischarge may in fact be built up of a series of such electron bursts (a displacement of up to 17.2 μs has been observed). Very thin point electrodes retard the development on account of the negative space charge that develops as the potential rises. Two types of threads have been observed: firstly the basic threads, which run from the cathode to the plate, and indicate the form of the undisturbed field. Secondly there are the subsidiary threads between points in the interelectrode space and certain parts of the cone—they indicate the disturbed field.

The growth of the spark is only regular in the cases where it takes place outside the predischarge channel with the aid of leaders (types 4, 5, 7); the diameter of the spark was in these cases d = 0.6 mm, the current density 670 A/cm^2. It is interesting that there is a step in the potential curve, corresponding to the development of the leaders. Where the spark follows in the track of the predischarge its growth is complicated and variable from point to point along the spark. The diameter at the most stable parts of the spark was d = 0.65 mm for $\delta = 5$ cm, d = 0.2 mm for $\delta =$ 15 cm, with corresponding current densities 134 and 3200 A/cm^2. The time for the development of the spark was: for type 1 ($\delta = 12.7$ cm) 1–2 μs; for type 6 2.5–3.7 μs ($\delta = 15$ cm) and 3.5–5.6 μs ($\delta = 40$ cm); for type 4 ($\delta = 40$ cm) 6–18 μs. The spark resistance has been computed by means of a new method: the initial value is of the order of 100 kΩ. 15 μs later the resistance has increased—the subsequent variation was not investigated.

The energy stored in the interelectrode capacitance (15–50 μμF) was 0.02 Ws for $\delta = 5$ cm, 2.7 Ws for $\delta = 40$ cm. In the arc stage the power developed is initially 500 kW, but 15 μs later it has fallen to 10 kW.

It is definitely established that a plasma channel cannot be regarded as identical with a thin metal wire as regards their effects on the surrounding field, since a plasma channel is externally neutral.

REFERENCES

1a. NORINDER, H. and SALKA, O., Mechanism of positive spark discharges with long gaps in air at atmospheric pressure. *Arkiv för fysik, Vol. 3*, No. 19, Stockholm 1951.

b. —— Mechanism of long-gap negative spark discharges in air at atmospheric pressure. *Arkiv för fysik, Vol. 5*, No. 24, Stockholm 1952.

c. —— Screens in long discharge gaps. *Arkiv för fysik, Vol. 6*, No. 17, Stockholm 1953.

2. ALLIBONE, T. E. and MEEK, J. M., The development of the spark discharge. *Proc. Roy. Soc., A*, 166, 924, and *A*, 169, 937, London 1938.

3. PUCHER, W., Form der negativen Vorentladung in Luft bei Atmosphärendruck für Stossspannung. *Arkiv för fysik, Vol. 6*, No. 37, Stockholm 1953.

Tryckt den 2 mars 1956

Uppsala 1956. Almqvist & Wiksells Boktryckeri AB

ARKIV FÖR FYSIK Band 10 nr 31

Communicated 25 January 1956 by MANNE SIEGBAHN

Angular distributions with high energy resolution: Long-range groups from $O^{18}(d, p)O^{19}$

By KATARINA AHNLUND

With 4 figures in the text

Introduction

The reaction $O^{16}(d, p)O^{19}$ gives two proton groups leading to the ground level and irst excited level in O^{19}, which levels are only 94 ± 8 keV apart in energy as was ound at the Nobel Institute in 1954 [1]. This is a typical case where only a measuring nethod with high energy resolution can give the angular distributions for each of the wo groups separately, all the more as both groups are near in energy to a strong roton group from $O^{16}(d, p)O^{17}$. In view of this we chose this reaction as the first roblem to study with the equipment for measuring angular distributions which was lescribed in refs. 2 and 3. Some theoretical work has lately been devoted to the strucure of nuclei of mass 18 and 19 (see e. g. ref. 4) and more experimental material is eeded.

Experimental arrangements

For all data concerning the equipment and the experimental procedure in general, ve refer to [2] and [3]. Only such details which specially relate to the actual reaction $)^{18}(d, p)O^{19}$ need to be considered here.

The O^{18} targets were prepared by electromagnetic isotope separation of water from .E.R.E., Harwell, 25 times enriched in O^{18}. H_2O^{18} ions of mass number 20 were colected. Separations on thick backings of steel and stainless steel have been performed t the Nobel Institute and, later on, separation on thin 0.15 mg/cm² Al foils were lone at Chalmers' Tekniska Högskola, Gothenburg.

By bombardment of these targets with deuterons we got a series of proton groups oth from the target nucleus O^{18} and from several inevitable contaminants on the arget. In our earlier work with $O^{18}(d, p)O^{19}$ we have surveyed all these groups in letail [5] and therefore the identification of the O^{18} groups raises no problem. Fig. 1 hows the proton spectrum from the two groups in question, as detected in one nuclear mulsion plate—type Ilford C2, 50 μ thick—placed behind the heavy-particle spectroneter.

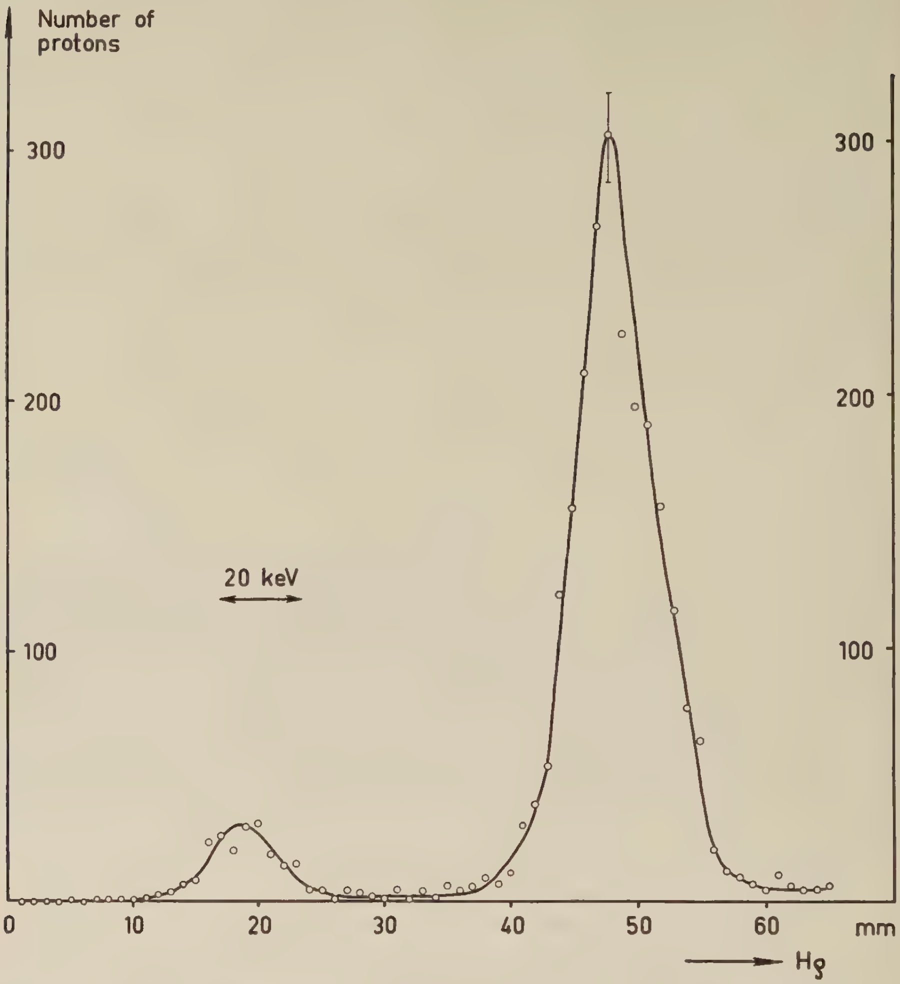

Fig. 1. Typical proton spectrum from $O^{18}(d, p)O^{19}$ showing the two peaks for the transitions leading to the ground state and first excited state in O^{19}. $E_d = 800$ keV, $\varphi = 60°$, thick target backing of Fe.

Excitation function of $O^{18}(d, p)O^{19}$

Before deciding what deuteron energy should be used, an investigation was made of how the proton yield varied with the bombarding energy in the region 790 to 880 keV. Two sequences of photographic plates were taken during two subsequent days. The same target spot was bombarded and the spectrometer direction was $\varphi = 60°$. As we wanted to know only the general character of the excitation curve, we confined the scanning of the plates to the proton group of highest intensity—the ground state group—and some 1000 to 1500 tracks were counted in each plate. Fig. 2 shows the

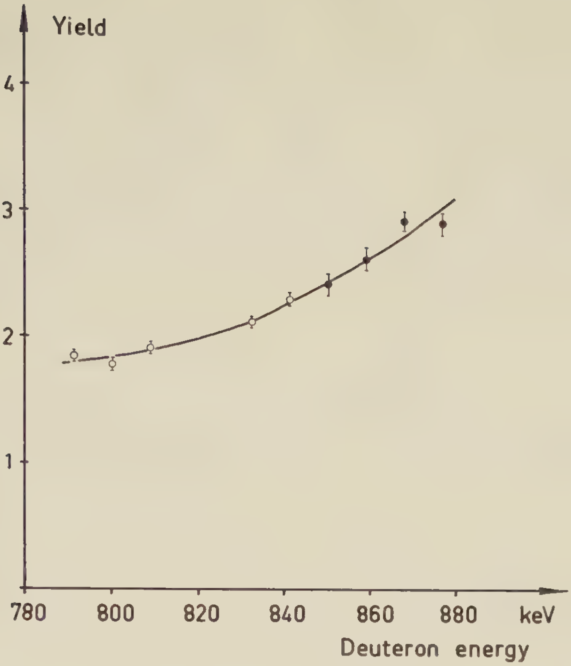

Fig. 2. Relative yield of the ground state transition $O^{18}(d, p)O^{19}$ for deuteron energy 790 to 880 keV.

result with the statistical error of each point. An additional error enters due to the fitting of two sets of points. As no special resonance could be seen in this region we chose to use the deuteron energy 800 keV for the angular distribution measurements. Here the excitation curve is comparatively flat and hence small variations in the energy of the primary particles will have very little influence on the final results.

Angular distributions

Each partial measurement consists of a comparison between the intensities of protons ejected from the target in two directions, one of which is a reference direction. In this investigation the angular reading φ at the periphery of the spectrometer table could be varied in steps of 7.5° between 0° and 127.5°. Later we shall use 10° more in the backward direction, but these extreme angles of φ could at present not give data with high accuracy as the ultimate magnetic screening of mu-metal around the entrance tube was not yet completed. For the same reason we estimate the probable errors of the points taken at $\varphi = 127.5°$ and $\varphi = 120°$ to be larger than the errors of the other points on the angular distribution curves. φ is nearly equal to θ_{lab}—see [3].

For the angles of $\varphi > 30°$ the thick target backings and for $\varphi < 30°$ the thin foil backings were used. A thick backing of highly polished steel (from a combination gauge block) was used in the region 30° to 60° to reduce the risk of slowing down the emitted particles due to unevenness in the surface. This would be accentuated by these oblique angles of emergence. Control points taken with foil backings showed

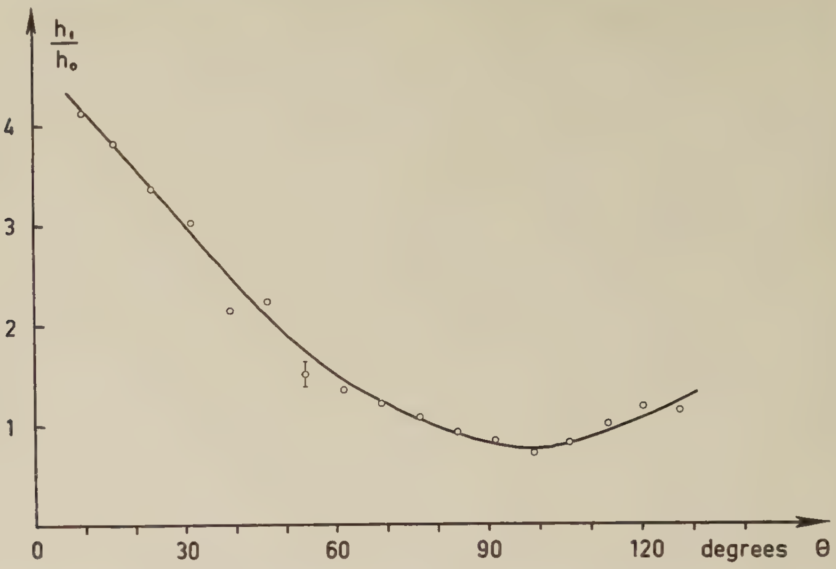

Fig. 3. The intensity ratio between the two proton peaks in one plate as a function of the angle θ in the center-of-mass system. $E_d = 800$ keV.

that no such effect was present. The foil target was placed perpendicular to the incident beam and particles emitted backwards through the foil were analysed by the spectrometer. In this case a special brass net with fine meshes was placed behind the foil and connected to the current integrator. In this way we could measure the intensity of the incident beam and analyse the emitted particles simultaneously.

The plates were scanned for proton tracks under a microscope. In each plate about 10,000 tracks forming the big peak were present and about 1500 tracks corresponding to the small peak. Since the data making up an angular distribution curve, such as the one given in Fig. 4, are obtained from about 40 photographic plates, we chose to count only a fraction of all the available tracks—at least for the moment. Some 20 % of the tracks of the big peak and 60 % of the small one are as yet counted.

The number of tracks counted in the big peak on each plate was divided by the measured value of the deuteron charge having reached the target during the exposure time, and transferred to the center-of-mass system. The ratios between each couple of angles obtained in this way were all related to the common reference angle $\theta = 90°$ The results are seen as the points I_0 in Fig. 4. Each point corresponds to one measured intensity ratio.

For the small peak an other procedure of evaluation was used in order to get accurate results in spite of the smaller number of tracks. As the two peaks in one plate were exposed simultaneously under the same experimental conditions their heights are practically directly proportional to the number of tracks in the peak and therefore a measure of the intensity. The intensity ratio between the two peaks was investigated and the points in Fig. 3 were obtained. Here each point is generally the mean value of the data from two plates. The angular distribution of the small peak I_1 was then calculated by combining Fig. 3 with a curve through the points I_0 in Fig. 4. A certain value of $I_1(\theta)/I_1(90)$ is established as

$$\frac{I_1(\theta)}{I_1(90)}=\frac{I_1(\theta)}{I_0(\theta)}\cdot\frac{I_0(90)}{I_1(90)}\cdot\frac{I_0(\theta)}{I_0(90)}=\frac{h_1(\theta)}{h_0(\theta)}\cdot\frac{h_0(90)}{h_1(90)}\cdot\frac{I_0(\theta)}{I_0(90)}, \tag{1}$$

i.e. by two data taken fram Fig. 3 and one from the curve I_0 in Fig. 4. The characteristics of the two curves I_0 and I_1 are seen to show a marked difference in their behaviour especially in the region below 90°. I_0 is less asymmetric around 90°. As all other conditions were equal this would correspond to different properties of the two lowest levels in O^{19}.

Evaluation in Legendre polynomials

In the wave mechanical representation of the nuclear reaction the angular dependence of the emitted particles occurs in terms of Legendre polynomials of the first kind. We write the function $I(\theta)$ as

$$I(\theta)=\sum_i a_i P_i(\cos\theta) \tag{2}$$

and calculate the coefficients a_i by 20-part numerical integration of the expression

$$a_i=\tfrac{1}{2}(2i+1)\int_{-1}^{+1} I\cdot P_i\cdot d(\cos\theta) \tag{3}$$

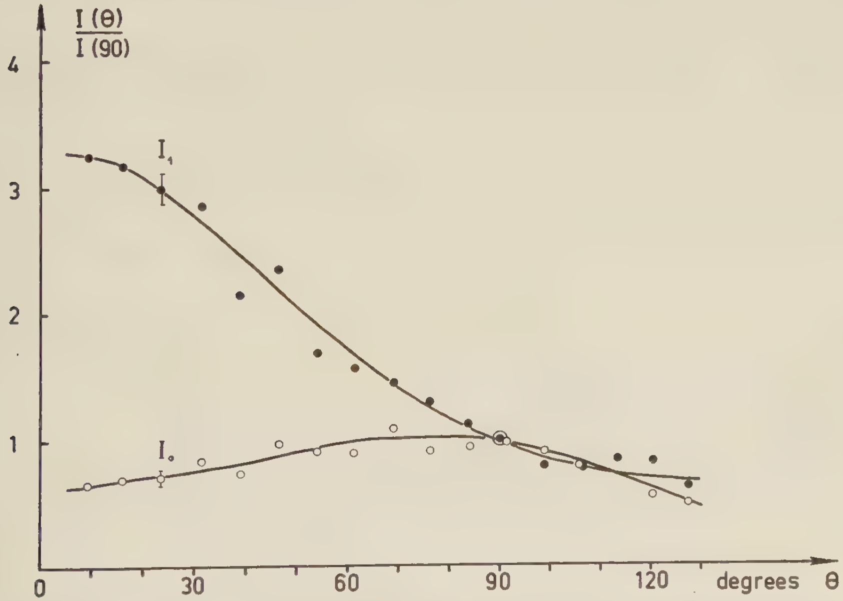

Fig. 4. Angular distributions of the two proton groups of longest range from $O^{18}(d,p)O^{19}$ at $E_d = 800$ keV, referred to the center-of-mass system. I_0 is the group to the ground state, and I_1 to the first excited state in O^{19}. The curves are drawn according to equations (4) and (5) in the text.

where I is obtained from a curve drawn to give a good fit with the experimental points (ref. 7). The series were found to converge rapidly. If we neglect the terms in P_n, for which a_n is less than the experimental error, we get for the angular distributions:

$$I_0 = 0.76 + 0.35\,P_1 - 0.48\,P_2 \tag{4}$$

$$I_1 = 1.29 + 1.21\,P_1 + 0.58\,P_2 + 0.22\,P_3. \tag{5}$$

The curves in Fig. 4 were drawn according to these equations.

Sources of error

A discussion of the instrumental sources of error in the angular distribution measurements was given in [3]. The largest error in the present investigations is statistical. For each point, the statistical errors from the counting of two plates enter. It is difficult to reduce these errors. A doubling of the number of counted tracks would change the statistical errors in I_0 with only about one-third.

An additional error comes from the fact that the two peaks in the same plate are not always completely resolved. This is partly due to differences in angular energy spread and target angles for different values of θ, partly to the quality of the target itself. Generally the foil targets gave the best resolution. Unfortunately, it is considerably more difficult to work with such targets. Furthermore, a certain proton background may be present in the plate, e.g. due to protons from the $D + d$ reaction. This should only be the case for the thick backings. The personal error of the microscopist is judged to be small.

The total probable error in the present data is of the order of 4–7 %.

The angular resolution is determined by the opening angle 3.6° of the spectrometer. For details see ref. 6.

ACKNOWLEDGEMENTS

Separated O^{18} targets were kindly prepared by Dr. S. Thulin, Stockholm, and Civ.ing. O. Almén, Gothenburg.

Civ.ing. B. Sjögren has given valuable assistance in the experimental work.

REFERENCES

1. Ahnlund, K. and Mileikowsky, C., Ark. f. Fys. *8*, nr 14, 161 (1954).
2. Mileikowsky, C., Ark. f. Fys. (1956), in press.
3. Ahnlund, K., Ark. f. Fys. *10*, nr 27. 373 (1956).
4. Elliott, J. P. and Flowers, B. H., Proc. Roy. Soc. A *229*, 536 (1955).
5. Mileikowsky, C. and Ahnlund, K., Phys. Rev. *96*, 996 (1954).
6. Pauli, R. T., Ark. f. Fys. *9*, nr 36, 571 (1955).
7. Redman, W. C., Phys. Rev. *79*, 6 (1950).

Tryckt den 16 februari 1956

Uppsala 1956. Almqvist & Wiksells Boktryckeri AB

ARKIV FÖR FYSIK Band 10 nr 32

Communicated 9 November 1955 by Erik Hulthén and Gustaf Ising

The rotational analysis of the singlet system *A* of zirconium oxide

By Ulla Uhler and Lars Åkerlind

With 2 figures in the text

Abstract

A rotational analysis of the ultra-violet band-system *A* of zirconium oxide has been carried out. The bands probably form a $^1\Sigma$–$^1\Sigma$ transition. The 0,0, 0,1, 1,0 and 2,1 bands have been analysed. A perturbation was found in the level $v' = 2$. The isotope effect has been studied and lines belonging to the isotopes Zr^{91}, Zr^{92} and Zr^{94} besides the main isotope Zr^{90}, have been identified.

The derived constants may be summarized in the following formulae:

$$\begin{aligned} B_v'' &= 0.4241 - 0.0023\,(v'' + \tfrac{1}{2}) \quad D'' = 0.33 \text{ K} \\ B_v' &= 0.3951 - 0.0019\,(v' + \tfrac{1}{2}) \quad D' = 0.35 \text{ K} \\ r_e'' &= 1.711 \text{ Å} \\ r_e' &= 1.772 \text{ Å} \\ \omega_e' &= 843.2_7 \text{ K} \\ \omega_e' x_e' &= 3.0_4 \text{ K}. \end{aligned}$$

The possibility that the bands are due to a $^1\Delta$–$^1\Delta$ transition is discussed.

Introduction

To the molecule ZrO several band-systems are attributed. In view of the astrophysical importance of this molecule much work has been devoted to the study of these systems. Lowater [1] has given the vibration analysis of the three strongest triplet systems. An extensive investigation by Afaf [2] reports the vibrational analysis of two more triplet systems and a strong and conspicuous singlet system in the ultra-violet part of the spectrum which he designates system *A*. He also mentions several systems in the red and infra-red regions, but is unable to give definite analyses of these bands. Rotational analyses of the three strong triplet systems have recently been given by Lagerqvist, Uhler and Barrow [3] and Uhler [4].

The present investigation gives the rotational analysis of the singlet system *A*. The obtained *B* and *D* values are of the same magnitude as those for the triplet systems. The bands 0,0, 0,1, 1,0 and 2,1 have been analysed. It was possible to check the analysis through the occurrence of a perturbation in an upper level.

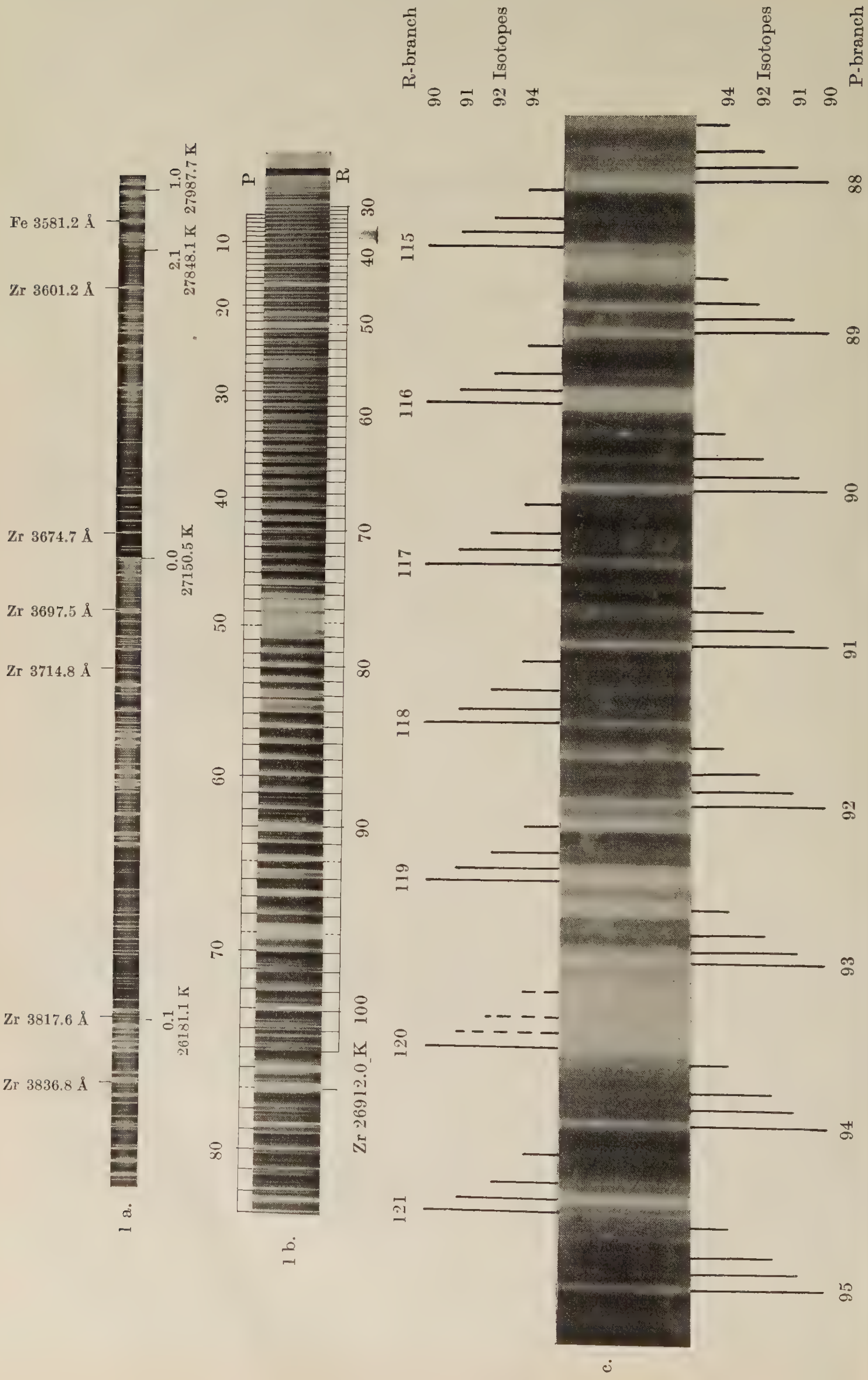

Fig. 1. *a*. The singlet system *A* of ZrO. *b*. The 0,0 band. *c*. Isotopes in part of the 0,0 band.

Experimental

The best source of light has proved to be an arc burning between zirconium rods 3 mm in diameter. The arc was fed with 440 V, 1 A D.C. In order to stabilize the current a choke was used in the circuit, thanks to which the arc could be kept burning for hours. This was a considerable advantage because an isolating layer of oxide was formed on the rods which made it very difficult to start the arc after an interruption. We also tried other sources of light, a carbon arc containing ZrO_2 and a copper arc with the same substance. The carbon arc gave a strong spectrum of ZrO but was less suitable, for our purposes, as only the 0,0 band appeared freely. The 0,1 and 1,0 bands are blended by strong CN bands. In order to avoid these impurities a copper arc was tried. An intense atomic line of Cu masks part of the 0,0 band. The spectrum obtained in this way is several times weaker than that arising from zirconium rods.

For a general survey the bands were photographed in a large quartz spectrograph (the dispersion in the ultra-violet region is about 7 Å/mm). The final plates were taken in a Wood's 21 ft. concave grating in the first order (165000 lines in all). The dispersion is about 1.27 Å/mm. The exposure time for the grating spectrograms was 3 hours. Ilford Thin Film Half Tone plates were used. Iron lines served for comparison.

The structure of the bands

The appearance of the bands is shown in Fig. 1. The bands are degraded to longer wave-lengths. The sequences do not overlap and the vibrational analysis is thus fairly easy. Every band has only one head. The 1,1 head is too weak to be observed.

Each band consists of two intense branches of equal intensity, one *R*-branch and one *P*-branch. The rotational structure is not fully resolved in the vicinity of the heads and no *R* lines have been identified before the turn of the head. Some series of weak lines, belonging to less abundant isotopes of zirconium, could also be identified. As is seen in the figure, there are many intense atomic lines, some of which originate from zirconium and the others from iron. The zirconium rods available were very short and had to be mounted in an iron holder, and this arrangement unfortunately gave iron lines in the spectrum.

A small perturbation was found in the level $v' = 2$, thus confirming the analysis.

In view of the simple structure of the bands and the absence of satellite branches and Λ-type doubling, the system is regarded as a $^1\Sigma$–$^1\Sigma$ transition. This question will be further discussed below.

The rotational analysis

Tables 1–3 give the wave-numbers of the 0,0, 0,1, 1,0 and 2,1 bands. Lines overlapped by other band-lines or weak atomic lines (Fe, Zr) are marked with an asterisk. Table 4 shows part of the combination differences of the main isotope. The agreement is generally good. For the weaker isotopes the discrepancies are somewhat greater, due to considerable overlapping of the weak lines with stronger ones and also to the less accurate measurements of weak and sometimes diffuse lines. However, in most cases the errors in the combination differences seldom amount to more than 0.2 K.

Table 1. Wave-numbers of the 0,0 band.

J	$Zr^{90}O^{16}$		$Zr^{91}O^{16}$		$Zr^{92}O^{16}$		$Zr^{94}O^{16}$	
	R	P	R	P	R	P	R	P
4		27 140.94						
5		39.88						
6		38.64						
7		37.52						
8		36.28						
9		35.03						
10		33.66						
11		32.16						
12		30.71						
13		29.21						
14		27.63						
15		25.98						
16		24.27						
17		22.56						
18		20.72						
19		18.85						
20	27 149.25	16.86						
21	48.76	14.92						
22	48.32	12.80						
23	47.78	10.62						
24	47.19	08.56						
25	46.63	06.31						
26	45.85	04.10						
27	45.09	01.64						
28	44.30	099.30						
29	43.35	96.91						
30	42.44	94.44						
31	41.49	91.87						
32	40.46	89.24						
33	39.29	86.54						
34	38.19	83.83						
35	36.94	81.08						
36	35.65	78.22						
37	34.38	75.31						
38	32.94	72.32						
39	31.52	69.38						
40	30.00	66.27						27 067.15*
41	28.45	63.19						64.01*
42	26.81	59.92						60.81*
43	25.16	56.70						57.57*
44	23.39	53.38						54.22*
45	21.52	50.05						50.85*
46	19.68	46.65					27 120.03	47.45*
47	17.78	43.12					18.07	43.92*
48	15.83	39.56				27 040.02*	16.13	40.40*
49	13.73	36.02				36.54*	14.16	36.74
50	Atom	Atom				Atom	12.03	Atom
51	09.51	28.70				29.30*	09.89	29.60
52	07.28	24.95				25.49*	07.78	25.93
53	05.04	21.09				21.62*	05.44	22.13*
54	02.70	17.21				17.74*	03.21	18.24*

(Table 1. Cont.)

J	$Zr^{90}O^{16}$		$Zr^{91}O^{16}$		$Zr^{92}O^{16}$		$Zr^{94}O^{16}$	
	R	P	R	P	R	P	R	P
55	27 100.32	27 013.25				27 013.79*	27 100.79	27 014.29*
56	097.90	09.38				09.75*	098.35	10.35*
57	95.37	05.22				05.80*	95.84	06.30*
58	92.82	01.16				01.50*	93.32	02.19
59	90.17	26 997.04				26 997.66*	90.70	26 998.31*
60	87.53	92.87*				93.47*	88.10	94.07*
61	84.79	88.57*				89.22*	85.37	89.77*
62	81.99	84.19*				84.86*	82.48	85.45*
63	79.21	79.78*				80.43*	79.62	81.03*
64	76.25	75.30*				75.97*	76.97	76.61*
65	73.27	Atom				Atom	73.82	72.10*
66	70.28	66.15*				66.87*	70.94	67.64*
67	67.15*	61.75				62.45	67.84	63.30
68	64.01*	56.96				57.80	64.70	58.40
69	60.81*	Atom				Atom	61.48	53.91
70	57.57*	47.45*				48.33*	58.31	48.96
71	54.22*	42.58*			27 054.59	43.45*	55.01	44.06
72	50.85*	37.68*			51.20	38.47*	51.64	39.15
73	47.49*	32.64*			47.80	33.46*	48.27	34.24
74	43.92*	27.62*			44.23	28.48*	44.78	29.23
75	40.40*	22.54*			40.78	23.27*	41.32	24.16
76	36.64*	17.39*			Atom	18.29*	Atom	19.06
77	Atom	Atom			Atom	12.68*	Atom	13.81
78	29.30*	06.89			29.74	07.82	30.39	08.63
79	25.49*	01.57*			25.93*	02.47	26.56	03.32
80	21.62*	896.24*			22.13*	897.10	22.66	898.06
81	17.74*	90.81*			18.24*	91.72	18.75	92.54
82	13.79*	85.27*		26 885.71	14.29*	86.22	14.68	87.10
83	09.75*	79.71*		80.16	10.35*	80.70	10.87	81.52
84	05.80*	Atom		Atom	06.30*	Atom	06.79	76.01
85	01.50*	68.38*		68.89	02.16*	69.47	02.66	70.41
86	26 997.25*	62.68*		63.22	26 997.66*	63.70	26 998.31*	64.74
87	92.87*	56.90*		57.42	93.47*	57.95	94.07*	58.94
88	88.57*	50.95		51.54	89.22*	52.10	89.77*	53.18
89	84.19*	45.14		45.69	84.86*	46.21	85.45*	47.28
90	79.78*	39.13		39.68	80.43*	40.25	81.03*	41.28
91	75.30*	33.14		33.69	75.97*	34.34	76.61*	35.36
92	Atom	27.08		27.58	Atom	28.17	72.10*	29.27
93	66.15*	20.92		21.40	66.87*	22.12	67.64*	23.09
94	61.46	14.71		15.34	Atom	15.86	62.92	16.98
95	56.55	08.42		09.03	57.40	09.62	57.95	10.71
96	Atom	02.09		02.72	Atom	03.37	53.14	04.78*
97	46.85	795.71		796.33	47.45*	796.95	48.33*	798.19*
98	41.92	89.29		89.92	42.58*	90.59	43.45*	91.70*
99	36.93	82.78		83.42	37.68*	84.10	38.47*	85.67*
100	32.00	76.20		76.87	32.64*	77.55	33.46*	79.14*
101	26.75	69.59		70.23	27.62*	70.97	28.48*	72.29*
102	21.55	62.89	26 922.02	63.47	22.54*	64.27	23.27*	65.65*
103	Atom	56.17	Atom	56.88	17.39*	57.48	18.29*	58.78*
104	11.14	Atom	Atom	Atom	Atom	Atom	12.68*	Atom
105	05.60	42.51	06.03	43.15	06.40	43.84*	07.31	45.32*

(Table 1. Cont.)

J	$Zr^{90}O^{16}$		$Zr^{91}O^{16}$		$Zr^{92}O^{16}$		$Zr^{94}O^{16}$	
	R	P	R	P	R	P	R	P
106	26 900.19	26 735.54	26 900.65	26 736.27	26 901.07	26 736.98*	26 901.57*	26 738.40*
107	894.63	28.61	895.12	29.30	895.65	29.87*	896.24*	31.47*
108	89.12	21.54	89.54	22.21	90.10	22.75*	90.81*	24.30*
109	83.51	14.51	83.99	15.37*	84.48	16.04*	85.27*	17.48
110	77.78	07.28	78.32	08.09*	78.79	08.83*	79.71*	10.41
111	72.11	00.05	—	00.79*	73.17	01.69	Atom	03.18
112	66.25	692.74	66.75	693.63	67.47	94.60	68.38*	695.87
113	60.36	85.39	60.79	86.14	61.39	87.20	62.68*	Atom
114	54.40	78.19	54.96	79.08	Atom	79.80	56.55	81.60
115	48.48	70.85	49.04	Atom	49.61	72.22	Atom	73.80
116	42.50	Atom	42.94	64.04	43.58	64.78	44.60	66.46
117	36.28	55.57	36.84	56.51	37.39	57.31	38.43	58.73
118	30.11	47.89*	30.77	Atom	31.28	49.70	32.41	51.37
119	23.91	40.21	24.42	41.13	25.10	42.01	26.19	43.82
120	17.71	32.46	Atom	33.46	Atom	34.20	19.89	36.17
121	11.11	24.68	11.76*	Atom	12.45	26.37	13.58	28.19
122	04.78*	16.80	05.37	17.75	06.01	18.59	07.05	20.58
123	798.19*	08.83	798.73*	09.87	799.39	10.71	00.80	12.51
124	91.70*	Atom	Atom	01.86	Atom	02.63	794.24	04.54
125	84.94	592.73	85.67*	593.86	86.32	594.70	87.62	596.40
126	78.34	84.60	79.14*	85.77	79.69	86.71	81.00	88.44
127	71.65	76.47	72.29*	77.46	72.95	78.54	74.19	80.32
128	64.88	68.12	65.65*	69.39	Atom	70.34	Atom	72.13
129	58.01	60.04	58.78*		59.39	62.12	60.68	63.85
130	51.00		Atom		52.42		53.85	
131	43.84*		Atom		45.32*		46.64	
132	36.98*		37.65		38.40*		39.73	
133	29.87*		30.47		31.47*		32.74	
134	22.75*		23.46		24.30*		25.56	
135	15.37*		16.04		16.86			
136	08.09*		08.83*		09.73			
137	00.60*							
138	693.22							
139	85.92							

J	The 0,1 band						The 1,0 band					
	$Zr^{90}O^{16}$		$Zr^{92}O^{16}$		$Zr^{94}O^{16}$		$Zr^{90}O^{16}$		$Zr^{92}O^{16}$		$Zr^{94}O^{16}$	
	R	*P*	*R*	*P*	*R*	*P*	*R*	*P*	*R*	*P*	*R*	*P*
16		26 155.19										
17		Atom										
18		51.70										
19		49.85										
20		47.96										
21		45.94										
22	26 179.56	43.99										
23	79.07	42.07										
24	78.61	Atom										
25	78.15	37.96*										
26	77.54	35.77*										
27	76.94	33.59*					27 980.47	27 938.20				27 936.06
28	76.15	31.49*					Atom	35.59*				33.61
29	75.41	Atom					78.63	32.86*				30.92
30	74.59	26.61					77.68	30.35*				28.09
31	73.68	24.21					76.73	27.54*				25.68
32	72.82	21.76*					75.66	24.87*		27 923.77		22.78
33	71.82	19.39*					74.45	21.97		20.83		19.99
34	70.71	Atom					73.17	19.08		Atom		16.94
35	69.53	13.90				Atom	71.73	Atom		Atom	27 969.41*	14.12*
36	Atom	11.15*		26 113.02*		26 114.84*	70.39	13.30	27 969.41*	12.17	67.95*	11.08
37	Atom	08.38*		10.20*		12.07*	68.94	10.25	67.95*	09.14	66.57	08.34
38	Atom	05.52*		07.48*		09.31*	67.37	07.09	66.37	06.20	64.97	05.23*
39	64.69	02.68*		04.79*		06.51*	65.72	03.96	64.54	02.94	63.32	02.14*
40	63.54	99.82		01.76*		03.63*	64.11	00.72	63.05*	899.72	61.75	898.89*
41	Atom	97.01		098.59*		00.76*	62.23	897.46	61.18*	96.46	59.98	95.46*
42	60.68	93.89		95.85	26 164.38	097.70*	60.51	94.03	59.44	93.07	Atom	92.06*
43	59.21*	90.89		92.70	Atom	94.62*	Atom	90.67	Atom	89.74	56.45	88.70*
44	57.57*	87.77		89.43	60.98	91.50*	56.77	87.21*	55.52	86.38*	54.43	85.48
45	55.94*	84.44		86.44	59.21*	88.42*	54.80	Atom	53.62	82.82	—	81.83*
46	Atom	81.22		83.03	57.57*	85.10*	52.76	79.94	51.51	79.14	Atom	78.10
47	52.45*	77.92		79.75*	55.94*	81.86*	Atom	Atom	Atom	Atom	Atom	74.08*
48	50.71*	Atom		76.51	Atom	78.63*	48.39*	72.37*	47.24	71.73	46.21*	Atom
49	48.93	71.25		Atom	52.45*	75.23*	46.21*	68.60*	44.83	68.05	Atom	66.68

(*Table 2. Cont.*)

J	The 0,1 band						The 1,0 band					
	$Zr^{90}O^{16}$		$Zr^{92}O^{16}$		$Zr^{94}O^{16}$		$Zr^{90}O^{16}$		$Zr^{92}O^{16}$		$Zr^{94}O^{16}$	
	R	P	R	P	R	P	R	P	R	P	R	P
50	26 147.21	26 167.75		26 169.72	26 150.71*	26 071.82*	Atom	27 864.92	27 942.73	27 864.19	27 941.72	Atom
51	45.17	64.29		66.36	48.72	68.27*	27 941.54	61.17	40.42	Atom	Atom	27 959.55
52	43.23	Atom		Atom	46.54*	64.70*	Atom	57.15	37.91	56.42	37.04	55.54
53	41.07	Atom		59.18*	44.53	Atom	36.65	53.18	35.59*	52.30	34.41	Atom
54	38.85	53.38		Atom	42.68	57.59*	34.18	49.10	32.86*	head	31.99	47.39
55	36.72	49.57		51.76	Atom	53.78*	31.56	45.04*	30.35*	44.18	29.42	43.40
56	34.53	46.02*		48.10	37.96*	50.05*	28.95	40.97*	27.54*	40.01*	26.85	39.33
57	32.21	42.24*		44.47*	35.77*	Atom	26.24	36.55	24.87*	35.66*	24.24*	34.97
58	Atom	38.33*		40.43*	33.59*	42.88*	23.38	32.20*	22.25	31.38*	21.28	30.67*
59	27.54	34.38*		36.42*	Atom	Atom	20.53	27.83*	19.57	27.31*	18.50	26.54*
60	25.05	Atom	26 126.97	32.89*	Atom	34.87*	17.72*	Atom	Atom	Atom	Atom	21.85*
61	22.61	Atom	24.36	28.60*	26.20	Atom	Atom	18.79*	Atom	18.32*	—	17.62*
62	20.07	22.16*	21.76*	24.32*	23.77	Atom	11.56	14.25*	10.48	13.64*	09.62	12.80*
63	Atom	18.09	19.39*	20.27*	Atom	22.67	08.34	09.50*	07.40	08.91*	06.40	08.34*
64	14.84*	Atom	Atom	15.72*	18.44	18.62	05.23*	04.84*	04.16	04.24*	03.47	03.73*
65	12.07*	09.69*	13.90*	11.54*	15.73	Atom	02.14*	00.06*	01.07	799.50	00.20	798.84*
66	09.31*	05.34*	11.15*	07.37	13.02*	09.69*	898.89*	795.27*	897.90	94.63*	896.92	94.05*
67	06.51*	00.89*	08.38*	03.20	10.20*	05.34*	95.46*	90.41*	94.49	89.68*	93.60	89.19*
68	03.63*	25 996.48*	05.52*	25 998.75	07.48*	00.89*	92.06*	85.44*	90.96	84.77*	90.05	84.22
69	00.76*	92.07*	02.68*	94.24	04.79*	25 996.48*	Atom	80.44*	87.98*	79.75*	Atom	79.38
70	097.70*	87.52*	099.61	89.92	01.76*	92.07*	85.03	75.42	Atom	74.82	Atom	74.55*
71	94.62*	82.88*	96.69	85.21	098.59*	87.52*	81.34	70.24	Atom	69.64*	79.55	69.23*
72	91.50*	78.31*	93.38*	80.63	95.27	82.88*	77.72	65.11*	Atom	64.58*	Atom	63.99*
73	88.42*	73.58*	90.36	75.85	92.07	78.31*	74.08	Atom	73.08	Atom	72.37*	58.71*
74	85.10*	68.80*	87.10	70.95	89.07	73.58*	Atom	54.44*	69.35	53.88*	68.60*	53.41*
75	81.86*	64.01*	83.90	66.13	85.76	68.80*	66.31	49.06*	65.45	48.40*	64.56	47.81
76	78.63*	59.15*	80.51	Atom	82.42	64.01*	62.30	43.59*	61.39	43.08	Atom	42.69*
77	75.23*	54.31	77.24	56.67	79.07	59.15*	58.37	38.08	57.49	37.73*	56.64	37.18*
78	71.82*	49.30	Atom	51.92	75.95	54.08	Atom	32.61*	53.41	32.12*	52.70	31.69*
79	68.27*	44.40	70.29	46.79	72.14	Atom	50.23	26.92	49.31	26.40*	48.56	26.08*
80	64.70*	39.36	66.80	41.63	68.71	44.00	46.03	21.19*	45.04*	20.81	44.42*	20.55*
81	Atom	34.17	63.16	36.63	65.18	38.98	41.78	15.43	40.97*	Atom	40.26	Atom
82	57.59*	28.96	59.52	31.45	Atom	33.82	37.47	09.65*	36.75*	09.32*	36.04	08.85*
83	53.78*	Atom	Atom	26.25	58.07	28.58	33.15*	03.74	32.20*	03.31	31.67*	02.98*

88	34.38*	896.75	36.42*	Atom	Atom	01.72	10.17	73.28	[illegible]		[illegible]	
89	30.44*	91.21	32.89*	893.84	34.87*	896.29	05.44	67.18	04.84*		04.24*	Atom
90	26.31*	85.64	28.60*	88.19	Atom	90.76	00.72*	60.79*	00.06*		799.33	
91	22.16*	79.98	24.32*	82.77	Atom	85.11	795.82*	54.42	795.27*		94.65*	
92	17.82*	Atom	20.27*	Atom	22.16*	79.30	90.89	47.91	90.41*		89.68*	
93	Atom	68.44	15.72*	71.15	17.82*	Atom	85.80	41.29	85.44*		84.77	
94	09.23*	Atom	11.54*	65.29	Atom	67.80	80.79	34.90	80.44*		79.75*	
95	04.78*	56.69	06.98	59.37	09.23*	Atom	75.72*	28.17	75.02*		74.55*	
96	00.31*	Atom	02.69	53.55	04.78*	56.10	70.24	21.57	69.64*		69.23*	
97	25 995.74*	44.73	25 998.19	47.62	00.31*	50.01	65.11*	14.69	64.58*		63.99*	
98	91.43*	38.64	93.63	41.52	25 995.74*	44.10	Atom	07.98	Atom		58.71*	
99	Atom	32.62	88.99	35.42*	91.43*	37.98	54.44*	Atom	53.88*		53.41*	
100	82.04*	26.44	84.35	29.24	Atom	32.06	49.06*	594.20	48.40*		47.81	
101	77.25*	20.22	79.47	23.15*	82.04*	25.78	43.40*	Atom	42.69*		42.47	
102	72.47*	13.95	74.84	Atom	77.25*	19.62	37.73	80.09	37.18*		36.93*	
103	67.65*	Atom	69.98	10.14	72.47*	13.01	32.12*	72.97	31.69*		31.29*	
104	62.77	01.16	65.17	03.80	67.65*	06.78	26.40*	65.78	26.08*		25.75*	
105	57.93	794.81	60.36	797.62	62.41	00.42	20.55*	58.50			19.61*	
106	52.79	88.30	55.27	91.13	57.42		Atom	51.06			13.91*	
107	47.78		50.31		52.44		08.86*	43.71			07.79*	
108							02.98	36.18			Atom	536.50
109							696.71*	Atom			695.83*	Atom
110							90.58	21.01			90.10	21.49
111							84.57*	13.30			84.05*	Atom
112							Atom	05.74			Atom	06.42
113							71.89	497.96		498.15		498.61
114							65.24*	90.05		90.35		90.95
115							58.93	82.17		82.54		82.86
116							52.43*	Atom		Atom		75.04
117							45.80	66.10		66.44		67.11
118							39.20	58.01		58.52		59.02
119							32.54*	49.82		50.33		50.85
120							Atom	41.52		41.92		42.55
121							18.88	33.15		33.80		34.30
122							11.98*	24.87		25.45		26.04
123							04.91	16.54		17.01		17.84
124							597.91	Atom		08.78		09.22
125							90.71	399.47		00.12		00.67
126							83.58	90.69		391.13		391.75
127							76.39	81.98		82.47		83.05
128							68.91	73.27		74.00		74.61
129							61.42	64.37		64.89		65.65
130								55.53		56.21		56.96

Table 3. Wave-numbers of the 2,1 band.

J	$Zr^{90}O^{16}$		$Zr^{92}O^{16}$		$Zr^{94}O^{16}$	
	R	P	R	P	R	P
9		27 832.72				27 830.67*
10		31.38				29.33*
11		30.12*				27.83*
12		28.71*				26.54*
13		27.31*				25.03
14		25.76*				Atom
15		24.14*				21.85*
16		22.29*		27 821.43*		20.24
17		20.54*		19.59*		—
18		18.79*		17.62*		16.82*
19		16.82*		15.66*		15.03*
20		14.85*		13.64*		13.08
21		12.79*		11.50*		11.10*
22	27 845.72	10.63*		09.50*		08.91*
23	45.04*	08.34*		07.13*		06.48
24	44.42*	06.12*		04.84*		04.24*
25	43.68	03.73*		02.98*		01.79
26	42.77	01.49*		00.72*		—
27	41.78*	799.15*		798.29*		797.51*
28	40.97*	96.63*		95.82*		95.01*
29	40.01*	94.05*	27 838.97*	93.34*	27 837.80*	92.35*
30	38.97*	91.54*	37.80*	90.89*	36.75*	89.68*
31	37.80*	88.76*	36.75*	87.98*	35.66*	86.94*
32	36.75*	86.05*	35.66*	85.44*	Atom	84.22*
33	35.66*	83.32*	Atom	82.58*	33.15*	81.69
34	Atom	80.44*	33.15*	79.75*	Atom	78.84
35	32.72*	77.46	31.67*	76.68	30.67*	75.72*
36	31.38*	74.55*	30.12*	73.85*	29.33*	72.79*
37	29.92	71.52	28.71*	Atom	27.83*	69.95*
38	28.23*	68.47*	27.31*	67.78	26.37	66.80*
39	26.54*	65.11*	25.76*	—	24.87*	63.66*
40	24.87*	61.90*	24.14*	Atom	Atom	Atom
41	Atom	58.71*	22.29*	57.82	21.43*	57.18*
42	21.43*	55.39	20.54*	54.66	19.59*	53.88*
43	19.59*	52.00	18.79*	51.25	17.62*	50.35*
44	17.62*	48.40*	16.82*	47.81*	15.66*	47.04*
45	15.66*	Atom	14.85*	44.47	13.64*	43.59*
46	13.64*	41.37	12.79*	Atom	11.50*	39.95*
47	11.50*	37.73*	10.63*	36.93*	09.50*	36.29*
48	09.50*	33.97	08.34*	33.35	07.55	32.61*
49	07.13*	30.15	06.12*	29.46	05.23	28.88*
50	04.84*	26.40*	03.73*	25.75*	02.98*	25.06*
51	02.46	22.48	01.49*	21.77	00.72*	21.19*
52	00.06*	Atom	799.15*	17.83	798.29*	17.17
53	797.51*	Atom	96.63*	13.91*	95.82*	Atom
54	95.01*	10.33	94.05*	09.65*	93.34*	09.25
55	92.35*	06.30	91.54	05.80	—	05.30
56	89.68*	Atom	88.76*	Atom	87.98*	Atom
57	86.94*	697.85*	86.05*	97.20*	85.44*	696.71*
58	84.22*	93.63	83.32*	693.14	82.58*	92.44
59	81.39	89.13	80.44*	88.71	79.75*	87.89

Table 3. Cont.)

J	$Zr^{90}O^{16}$		$Zr^{92}O^{16}$		$Zr^{94}O^{16}$	
	R	P	R	P	R	P
60	*78.24*	84.57*	77.79	84.06*	*77.14*	83.60
61	75.72*	80.15	74.82*	79.61*	73.85*	79.10*
62	72.79*	*75.38*	71.86	74.94*	Atom	*74.94**
63	69.95*	71.18	69.23*	70.45	68.47*	Atom
64	66.80*	Atom	66.09	65.87	65.11*	65.24*
65	63.66*	61.79	Atom	61.34	61.90*	60.79*
66	Atom	Atom	Atom	Atom	58.71*	Atom
67	57.18*	52.43*	56.51		55.39*	51.75
68	53.88*	47.37	53.41*		52.32	46.76
69	50.35*	42.70	49.64		49.06*	42.16
70	47.04*	37.68	46.22		45.62	36.97
71	43.59*	32.54*	42.69*		42.09	31.97
72	39.95*	27.84	39.46		—	27.23
73	36.29	22.36	35.67		35.08	—
74	32.61*	17.21	32.12*		31.29*	16.40
75	28.88*	11.98*	Atom		27.47	11.41
76	25.06*	06.64	24.54		23.63	Atom
77	21.21*	Atom	20.27		19.61*	Atom
78	16.95	595.89	—		16.05	595.47
79	Atom	90.20	12.42		11.90	89.73
80	08.86*	84.64			07.79	
81	04.54				03.54	

Table 4. Combination differences ($Zr^{90}O^{16}$).

J	$v''=0$		$v''=1$		$v'=0$	
	From 0,0	From 1,0	From 0,1	From 2,1	From 0,0	From 0,1
25	43.09		42.84	42.93	40.32	40.19
30	51.48		51.20	51.25	48.00	47.98
35	59.97	59.87	59.56	—	55.86	55.63
40	68.33	68.26	67.68	67.83	63.73	63.72
45	76.74	76.83	76.35	76.25	71.47	71.50
50	85.03	85.04	84.64	84.65	—	79.46
55	93.32	93.21	92.83	—	87.07	87.15
60	101.60	101.74	—	101.24	94.66	—
65	110.10	109.96	109.50	—	—	102.32
70	118.23	—	117.88	117.81	110.12	110.18
75	126.53	—	125.95	125.97	117.86	117.85
80	134.68	134.80	134.10		125.32	125.34
85	143.12	143.07	142.29		133.12	132.92
90	151.05	151.02	150.46		140.65	140.67
95	159.37	159.22	—		148.13	148.09
100	167.34	—	—		155.80	155.60
105	175.60	175.34	174.47		163.09	163.12
110	183.46	183.41			170.50	
115	—	—			177.63	
120	199.23	199.39			185.25	
125	207.10	207.22			194.21	

Evaluation of the rotational constants

The rotational energy of a $^1\Sigma$-term may be written

$$F(J) = B\,J(J+1) - D\,J^2(J+1)^2.$$

The B and D values are obtained graphically from the equation

$$\frac{\Delta_2 F(J)}{J+\frac{1}{2}} = 4\,B - 8\,D\,(J+\tfrac{1}{2})^2.$$

The derived values are given in Table 5. No estimation of B and D has been made for the isotope 92, $v'=2$, as the $\Delta_2\,F(J)$ values were too widely scattered to provide a reliable determination. In the case of the isotope 91, $v'=0$ and $v''=0$, the obtained values are very uncertain because of the long extrapolation. The B values for isotope 90 may be combined in the equations

$$B_v'' = 0.4241 - 0.0023\,(v''+\tfrac{1}{2})$$
$$B_v' = 0.3951 - 0.0019\,(v'+\tfrac{1}{2}).$$

The corresponding internuclear distances are:

$$r_e'' = 1.711\ \text{Å}$$
$$r_e' = 1.772\ \text{Å}.$$

Table 5. B and D values.

	$Zr^{90}O^{16}$	$Zr^{91}O^{16}$	$Zr^{92}O^{16}$	$Zr^{94}O^{16}$
B_0''	0.4229	0.4242	0.4213	0.4200
B_1''	0.4206		0.4192	0.4177
B_0'	0.3942	0.3951	0.3928	0.3915
B_1'	0.3922		0.3909	0.3897
B_2'	0.3904			0.3874
D_0''	0.34×10^{-6}	0.41×10^{-6}	0.32×10^{-6}	0.32×10^{-6}
D_1''	0.32		0.29	0.28
D_0'	0.35	0.41	0.34	0.33
D_1'	0.35		0.35	0.34
D_2'	0.31			0.26

The obtained B values are of a reasonable order of magnitude as compared with those of the triplet systems (e.g. $B_0 = 0.4147$ for $X\ ^3\Delta$).

An estimate of α may be obtained from the expression by Pekeris [5]

$$\alpha_e = \frac{6\sqrt{\omega_e\,x_e\,B_e^3}}{\omega_e} - \frac{6\,B_e^2}{\omega_e}.$$

The derived values are

$$\alpha_e'' = 0.0027 \qquad \alpha_e' = 0.0020.$$

The agreement with the observed values is satisfactory.
The D values obtained from Kratzer's relation are

$$D_e'' = 0.32 \times 10^{-6} \qquad D_e' = 0.35 \times 10^{-6}.$$

in good agreement with the experimental values.

Calculation of the origins

The band-origins have been calculated with the formula

$$2\sigma_0 = R(J-1) + P(J) + 2(B'' - B')\,J^2.$$

When the right-hand side expression is plotted against J^2, a straight line is obtained, whose intercept gives $2\sigma_0$. The obtained values are:

$$\begin{aligned} 0{,}0 &: \sigma_0 = 27144.7_1 \text{ K} \\ 0{,}1 &: \sigma_0 = 26174.9_5 \\ 1{,}0 &: \sigma_0 = 27981.9_0 \\ 2{,}1 &: \sigma_0 = 27843.2_5. \end{aligned}$$

The following values for the vibrational constants have been derived:

$$\omega_e'' - 2\,\omega_e'' x_e'' = 969.7_6 \text{ K}$$

$$\omega_e' = 843.2_7 \text{ K}, \ \omega_e' x_e' = 3.0_4 \text{ K}.$$

The isotope effect

Zirconium has the following five stable isotopes: $Zr^{90}:Zr^{91}:Zr^{92}:Zr^{94}:Zr^{96}$, with the relative abundances 51.46:11.23:17.11:17.40:2.80 [6]. The main lines are thus due to the molecule $Zr^{90}O^{16}$. Lines arising from $Zr^{92}O^{16}$ and $Zr^{94}O^{16}$ have been identified in all bands. The weak lines from $Zr^{91}O^{16}$ have been reported only in the strongest band (0,0) at high J values.

The isotope shift is the sum of the vibrational and rotational displacements. The vibrational shift may be written approximately

$$\Delta\sigma_v = \sigma_v{}^{90} - \sigma_v{}^{i} \sim (1-\varrho)[(v' + \tfrac{1}{2})\omega' - (v'' + \tfrac{1}{2})\omega''],$$

where $\varrho = \sqrt{\mu^{90}/\mu^{i}}$ (μ = the reduced mass of the molecule). The approximate rotational isotope displacement may be obtained from the expression

$$\Delta\sigma_r = \sigma_r{}^{90} - \sigma_r{}^{i} \sim (1-\varrho^2)(\sigma^{90} - \sigma_{\text{origin}}).$$

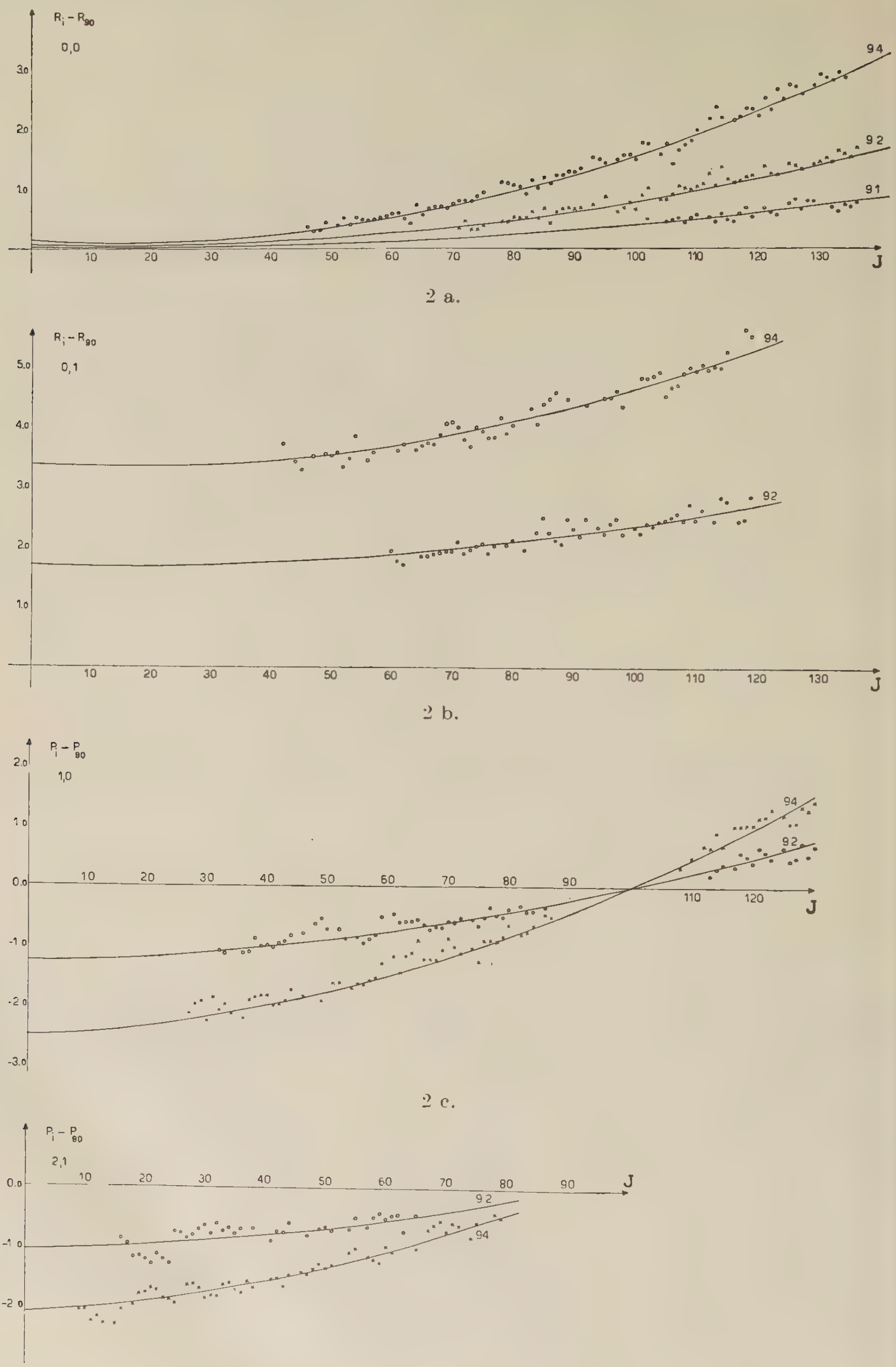

2 a.

2 b.

2 c.

2 d.

Fig. 2. Isotope effect in the 0,0, 0,1, 1,0 and 2,1 bands.

Fig. 2 shows the observed isotope shift in the respective bands.

The lines correspond to the theoretical shifts obtained from $\varrho = 0.99917$ ($Zr^{91}O^{16}$), $\varrho = 0.99836$ ($Zr^{92}O^{16}$) and $\varrho = 0.99678$ ($Zr^{94}O^{16}$).

Assuming $B_v^i = \varrho^2 \cdot B_v{}^{90}$, the values in Table 5 may be used to estimate experimental values of ϱ. These values are given in Table 6.

Table 6. Observed ϱ-values.

Level	ϱ_{92}	ϱ_{94}
$v'' = 0$	0.9981	0.9966
$v'' = 1$	0.9983	0.9966
$v' = 0$	0.9982	0.9966
$v' = 1$	0.9983	0.9968
$v' = 2$		0.9962

The agreement with the theoretical formulae establishes the identity of the emitting molecule of this band spectrum beyond doubt.

Perturbation

In the level $v' = 2$ a small perturbation has been found at $J = 69$. The displacement is only about 0.3 K. No extra lines have been found and no perturbations in the levels $v' = 0$ and $v' = 1$. Thus it is unfortunately not possible to draw any conclusions about the perturbing state.

Discussion

The rotational analysis of singlet system A has shown that the bands may be fully explained as being due to a $^1\Sigma$–$^1\Sigma$ transition as assumed by Afaf [2]. He designates the system $b\ {}^1\Sigma - a\ {}^1\Sigma$. However, in the corresponding molecule, TiO, no $^1\Sigma$ state has been identified. The triplet systems of the two molecules show great similarities and there is perhaps reason to assume that also the singlets are analogous. The lowest state of TiO is generally admitted to be a $^1\Delta$ term (Phillips [7]). Thus one might tentatively suggest that system A of ZrO is a $^1\Delta$–$^1\Delta$ transition. The weak Q-branch may have too low an intensity to be seen, and the absence of Λ-type doubling is not surprising either.

The relative agreement between the vibrational constants between the state b $^1\Sigma$ ($\omega_e = 843$) and the upper level of the triplet β-system ($\omega_e = 846$) might indicate that the level b is identical with one of the sub-level of $B\ {}^3\Pi$. A comparison between the B-values shows, however, that the agreement of the ω_e-values is wholly accidental. Thus it is impossible to get any correlation between the triplet and singlet systems in this way. Also the perturbation failed to resolve this question. Thus the relations between singlets and triplets are unknown, and the problem of the ground-state of ZrO still awaits its final solution.

To the head of the Institute, Professor Erik Hulthén, we wish to express our thanks for his keen interest in the work. We are also indebted to Bergsingenjör C. G. Carlsson, Metallografiska Institutet, for valuable help in supplying zirconium rods.

Physics Department, University of Stockholm, October 1955.

REFERENCES

1. LOWATER, F., Proc. Phys. Soc. *44*, 51, 1932.
2. AFAF, M., Proc. Phys. Soc. *A 63*, 1156, 1950.
3. LAGERQVIST, A., UHLER, U., and BARROW, R. F., Arkiv för Fysik *8*, 281, 1954.
4. UHLER, U., Arkiv för Fysik *8*, 265, 1954.
5. PEKERIS, C. L., Phys. Rev. *45*, 98, 1934.
6. HOLLANDER, J. M., PERLMAN, I., and SEABORG, G. T., Rev. Mod. Phys. *25*, 469, 1953.
7. PHILLIPS, J. G., Astrophys. J. *111*, 314, 1950.

Tryckt den 3 april 1956

Uppsala 1956. Almqvist & Wiksells Boktryckeri AB

ARKIV FÖR FYSIK Band 10 nr 33

Communicated 22 February 1956 by Manne Siegbahn and Bengt Edlén

Photo-electric mass determinations in nuclear emulsions

Part IV. Determinations of *K*-particle masses

By Krister Kristiansson

With 9 figures in the text

Introduction

The determination of the mass of a *K*-particle, stopping in a nuclear emulsion, can be made by measurements of its ionization and residual range. The ionization can be determined by photo-metric measurements of the grain density of the track. Such photo-metric mass determinations have been described in several papers [2, 6, 7, 8, 9]. The construction of the photo-meter and the methods of measurement vary, and the accuracy of the results is different for different instruments.

The photo-electric apparatus built in Lund has been described in papers published in the last few years [1, 3, 5]. The method used for the determination of the mass of a particle has been given, at least in its earlier forms, in some papers dealing with other investigations [2, 3]. In connection with the publication of results of some new mass determinations of *K*-particles it may be of interest to give a complete description of the photo-metric method of determining masses as now used in this laboratory.[1]

The apparatus

The photo-electric apparatus consists in principle of two parts, a microscopic part for the measurements proper and an electronic part for their registration. The microscopic part consists of a Leitz microscope BST 48/77 with the objective Ks 100 ×. The place of the ordinary eye piece is taken by an eye piece of special construction. There is a slit in its image plane, and above this slit a photo-multiplier which registers the amount of light passing through. The dimensions of the slit referred to the objective plane are $2.5\,\mu \times 30\,\mu$. The slit admits a very small part of the field of view around the image of a $30\,\mu$ long section of the track which is to be measured. The amount of light through the slit is proportional to the area of the slit minus the projected area of the track. If the slit and the track are moved relative to one another to a position where the track falls outside the slit, the amount of light which now passes through it is proportional to the total slit area. The difference between the two measurements is proportional to the projected area of the track. The result is affected by a possible background of grains not related to the track. In order to decrease the effect of this background measurements are made on both sides of the track and the mean value of the readings is used in the calculations. The main features of this part of the apparatus have been described in a paper by v. Friesen and Kristiansson [1]. Some minor improvements in order to increase the speed with which measurements can be made have been described in two later papers [3, 5].

---

[1] The following papers describing the photo-electric method of measurement in Lund are referred to in this paper:

1. v. Friesen and Kristiansson: Photo-electric determination of the density of tracks in nuclear emulsions. Arkiv f. Fysik *4*, 505 (1952).
2. Kristiansson: Photo-electric determination of the mass of the Bristol $\varkappa_1$-meson. Phil. Mag. *44*, 267 (1953).
3. Kristiansson: Photo-electric mass determinations in nuclear emulsions. Part I. An investigation of the accuracy of mass determinations. Arkiv f. Fysik, *8*, 311 (1954).
4. v. Friesen: Photo-electric mass determination in nuclear emulsions. Part II. A new correction for local variations in the emulsion with a report on the photo-electric identification of K-particles. Arkiv f. Fysik *8*, 305 (1954).
5. v. Friesen and Stigmark: Photo-electric mass determinations in nuclear emulsions. Part III. Description of the new experimental arrangements. Arkiv f. Fysik *8*, 121 (1954).

The photo-multiplier is connected to a Leeds and Northrup Speedomax recorder via a linear amplifier. This amplifier and the high tension supply for the photo-multiplier have been described by v. Friesen and Stigmark [5]. They also give a detailed description of a measurement on a section of a track.

Choice of the optimum slit dimensions

Slits of different dimensions can be used in the photo-metric apparatus. The most suitable slit for any special experiment can therefore be chosen before a measurement is begun. The significance of the dimensions of the slit has been discussed in paper [3]. A long and narrow slit cannot easily be placed in the right position relative to the track. A short and wide slit gives poor information about the number of grains in the track, since the area of the track section is small compared to the area of the slit. A short slit means a large number of measurements for a given length of track and a slow rate of progress.

The length of the slit has been $30\,\mu$ referred to the objective plane in most measurements published up till now [2, 3, 4]. No reason to change the length has been encountered hitherto.

The width of the slit is important as soon as the track does not run parallel to the surface of the emulsion. In paper [3] the mean track width, MTW, has been investigated as a function of the angle of dip for different slit widths. The result of this investigation can be summarized as follows. MTW for tracks in a G5 emulsion may, at a first approximation, be assumed to be independent of the dip angle if the width of the slit is approximately $2.5\,\mu$ and the length $30\,\mu$. This width has been used in the present measurements. The dimensions of the slit given above, $30\,\mu \times 2.5\,\mu$, represent the size of the image of the slit in the objective plane. Its actual dimensions are 3 mm × 0.25 mm.

An approximate but sufficiently accurate estimate of the influence of the dip angle on MTW for a slit $2.5\,\mu$ wide has been obtained by an investigation on the influence of the defocusing upon the measured MTW. Fig. 1 shows the apparent loss in mean track width as a function of the defocusing of a horizontal track located very accurately in the middle of the slit before the defocusing took place. The loss in MTW is the same if the track is defocused up to down. The expected change

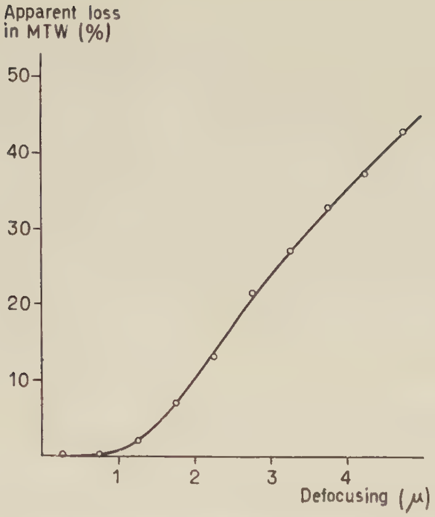

Fig. 1. The influence of the defocusing on the measurement of mean track width (MTW).

n be calculated in principle for a track with a known dip angle since the loss in TW is known from Fig. 1 as soon as we know the amount of defocusing. The focusing is determined from the dip angle and the distance to the centre of the t, where the track is kept exactly in focus. Fig. 2 shows the result of two such lculations. The MTW is given as a function of tan α', where α' is the dip angle in e processed emulsion. Curve 1 applies for tracks which have a very high grain nsity and can be approximated by a compact cylinder. Curve 2 has been calculated r tracks in which the grains are completely separated from one another. In this se one must take into consideration that the number of grains in the visible

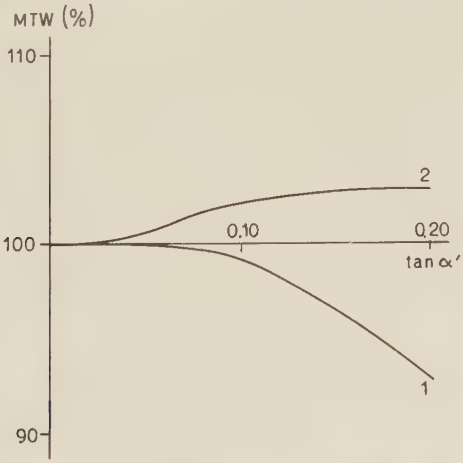

g. 2. The influence of the dip angle (α') on the MTW of different tracks in a processed emulsion. Tracks which can be approximated by a compact cylinder. 2. Thin tracks with completely resolved grains.

section of the track increases as $\cos^{-1}\alpha$ where α is the dip angle in the unprocessed emulsion. The shrinkage factor of the emulsion is 2.4 ± 0.2, determined by measurements of the ranges of μ-mesons from π-μ-meson decays.

A real track represents something between a dense cylinder and a track with completely separated grains. The corresponding curve must therefore lie between the two curves in the figure. The K-particle measurements are made near the ends of the tracks, where the tracks are dense and the individual grains are not separated in most cases. The relation between MTW and dip angle can therefore be expected to lie just above the curve for a compact cylinder in Fig. 2.

The largest dip angle that a track has had in a short interval has been such that $\tan \alpha' = 0.09$. The error in MTW from the steepnes of this track cannot exceed 0.5 % at this range. The dip angle is much less on the average; and the errors caused by the dip in the mean values of the MTW are completely negligible.

Testing of the photo-metric apparatus

The following tests were made before the measurement of a K-particle was started.

1) Check of the registering system and the microscope lamp. The reading of the Speedomax recorder must remain constant when the microscope lamp is on and the beam of light passes through the instrument in the same way as when a measurement is being made. This provides a check of the constancy of the beam of light and also of the constancy of the recording system when the light flux remains unchanged. A very small amount of noise exists, however, depending upon the Shot-effect in the photo-multiplier tube. The amplitude of the noise is low, $\simeq 0.1$ % of the reading when the light intensity is suitable for measurements. The noise is added both to the reading of the track and the reading of the background. The difference in amplitude of the noise of the two readings is too low to be observable. In the MTW, which is proportional to the difference between these two readings divided by the reading of the background, the error caused by Shot-noise is so much reduced that it is completely negligible.

2) Check of the linearity of the registering system. This check is made by a special arrangement, which belongs to the amplifier and has been described earlier [5]. It gives two voltages, one exactly twice as large as the other. If these two voltages are applied to the registering system one after the other, they should give two readings on the Speedomax recorder, one eaxctly twice as large as the other when the system is linear. The linearity requirement of the apparatus has been such that any deviation from the factor 2 must not exceed 1 %. The small imperfections in linearity which may still remain after the adjustment are of small importance. The reason for this is that a measurement on a K-particle is always made relative to a known particle. The measurements of the tracks of the particles used for comparison are made with the same amplification. Possible errors will therefore influence the MTW of all the tracks in the same way. The present mass determination has been made by comparing the MTW of the K-particle track and proton tracks.

3) Check of the background measurement. A measurement of the MTW consists of one measurement with the track in the slit and two measurements of the empty slit one on each side of the track [1, 5]. The slit is moved relative to the track by means of a plane parallel glass plate in the microscope located between the objective and the eye piece. The glass plate turns round an axis parallel to the track. The

turning of the glass plate causes a small change in the manner in which light passes through the instrument. This implies that there may be a remote possibility that different amounts of light could reach the photo-cathode for the three positions of the glass plate even if the illumination is quite uniform. In addition, the light may fall in areas of the cathode surface which have different sensitivity. This would give differences in the photo-current even if the amount of light is the same in all three cases. The microscope and the photo-multiplier must be adjusted until the turning of the glass plate does not give any errors whatsoever in the MTW. This has been checked by the use of a clean emulsion (an undeveloped but fixed emulsion) on the microscope stage. Measurements in this emulsion have been made in the usual way. The conditions for the acceptance of an adjustment have been

$$u(b_1) \simeq u(b_2) \simeq u(t)$$

and $\frac{1}{2}/u(b_1)+u(b_2)/-u(t) \leq 0.001 \cdot u(t)$.

$u(b_1)$ and $u(b_2)$ are the two measurements of the backgrounds, $u(t)$ being the measurement in the middle (normally the measurement of the track). The small errors left after the adjustment will be eliminated at the first approximation in the same way as the errors described earlier, since the mass determinations of the K-particles are made relative to other particles.

4) Check of the reproducibility. The standard deviation of the measurements of the integrated MTW has been estimated at about 0.3 % in paper [3]. The term "integrated MTW" of a track with a residual range R means the sum of all measurements of mean width from the end of the track to the residual range R. The tracks were 3–4 mm long in the average. The reproducibility of the measurements has been checked by measuring every K-particle track twice in the work described here. Table 1 shows the differences found for the two measurements of integrated mean width of four K-particles. The mean value of the differences is 0.45 %. The mean value of their residual ranges is about 6 mm. The result indicates that the standard deviation given above (0.3 %) applies to these measurements, even if the statistics are very poor in this case.

Table 1.

Particle	Difference %
KLu7	0.44
KLu8	0.35
KLu12	0.76
KLu13	0.26
Mean value	0.45

The choice of the comparison tracks

The position in the emulsion of the comparison tracks relative to the position of the K-particle track is important if the mass determination is to be as accurate as possible.

The existence of a small variation in the mean level of the width of tracks expected to show the same ionization in an emulsion has been discussed earlier [3].

This variation manifests itself in the following way. When we compare the MTW values of tracks from local regions of a plate with the average MTW of the whole plate, we quite often find that in some regions the MTW level is consistently higher than the average while in other regions it is below average. The deviations are too large to be explained as due to the normal distribution of measurements round the mean. The same phenomenon has been studied by v. Friesen [4]. He found that a correlation existed between the mean level of the MTW and the coefficient of light absorption in the emulsion. He further found that areas with practically the same absorption coefficient quite often had a diameter of a few centimeters in the emulsion studied by him.

The emulsions in which the K-particles have been found are of a very high quality. For this reason errors due to the type of irregularities in the emulsion just described are probably quite small. If, however, a measurement is to reach the highest degree of accuracy it is necessary to take the above-mentioned facts into account and choose the comparison tracks accordingly. The comparison tracks have been chosen as close to the K-particle as possible in order to get the same mean level for all the tracks. Protons have been used to provide the comparison tracks. A circular area with a radius of about 2 cm with the K-particle in the centre has been scanned for such tracks. The protons have been identified by means of gap counting. The exposure has been high enough to give a sufficient number of proton tracks inside this area.

Measurements of depth and mean track width

The positions of the tracks have been determined relative to the surface of the emulsion in order to enable a depth correction to be made for differences in development and transparency. These measurements have been made using the dial of the ordinary focusing screw of the microscope. The number of measurements along a track has depended upon its length. A track of a range of 10 mm was measured in 25 places. The intervals between the measurements have been least near the end of the track. It is very important when measuring the depth that the water content of the emulsion is kept in equilibrium with the relative humidity of the air. If the conditions of equilibrium are not fulfilled the emulsions will swell or shrink during the depth measurements. The emulsion has therefore been stored at the corresponding humidity for some days before the measurements took place.

How the measurements of MTW are made has been described earlier [5]. The order in which the different tracks have been measured can be illustrated by the following example from the determination of the mass of one of the K-particles.

1) Measurement of 4 comparison protons
2) ,, ,, the$K$-particle
3) ,, ,, 3 comparison protons
4) ,, ,, the K-particle
5) ,, ,, 2 comparison protons
6) ,, ,, 3 tracks of relativistic heavy primaries for the determination of the depth correction.

The tracks of highest statistical weight for the mass determination have been measured between the two measurements on the K-particle. The order of the measurements reduces the influence of a possible continuous change in the apparatus. Such a change has not been observed, however, on any occasion.

The speed with which the photo-metric measurements proceed has been 4–4.5 mm/hour. The total length of all tracks necessary for a complete mass determination is 120–140 mm when the residual range of the K-particle is 6 mm. The mean range of the K-particles described in this paper is about 6 mm. The time required for a measurement of a K-particle including the calibrations is thus about 30 hours. Approximately the same amount of time is necessary for the reading of the Speedomax recording and the calculation of the mass.

The time required for a complete photo-metric mass determination is accordingly quite considerable. But there hardly seems to exist any other method to determine masses by measurements of ionization and range which is much quicker if the same accuracy is wanted. A gap measuring method which is both accurate and fast is described by Fowler and Perkins [10]. They state that the measurements take two days when the calibration is done. But the calibration is not very easy to perform and their method can therefore not be much faster than the photo-metric method. Furthermore, it can be used only when the residual ranges of the tracks are considerable.

Determination of the depth correction

Tracks of particles with the same ionization, which are found at different depths in the emulsion, do not show the same MTW owing to differences in the development and in the passage of light through the emulsion. The differences can be eliminated if every MTW value is multiplied by a certain correction factor. This factor is a function of the distance of the track from the surface [2, 3, 7, 8, 11, 12]. Different methods to determine the correction factor as a function of the depth in the emulsion have been discussed in earlier papers. All the methods are based on measurements of tracks of the same ionization at different depths. A depth–MTW curve is plotted and the correction factor obtained from this curve.

The correction was described for the first time in connection with a measurement of the Bristol-$\varkappa_1$-meson [2]. Three series of correction factors were determined, one from proton tracks and two from μ-meson tracks at different degrees of ionization. The three series did not coincide completely. If the difference was purely statistical in nature or if a real difference existed could not be decided at the time.

An important step forward in the development of the method of correction was taken by Waldeskog [11]. He showed that it was possible to use relativistic heavy primaries to determine the correction factor. The correction factor from heavy primaries has also been studied by Norlind, who found that tracks of minimum ionizing α-particles, Li-nuclei and F-nuclei gave the same factor (12). He found, however, a small difference between the different kinds of tracks nearest the surface (down to $^1/_3$ of the thickness of the emulsion).

The correction factors in the present investigation of K-particles have been determined from measurements on both protons and heavy primaries. The protons which have been chosen as comparison particles have also been used to construct a depth –MTW curve. The range interval $0 < R < 3$ mm has been used for this purpose. Details of such a determination of the correction factor from protons are given in [3].

The number of protons is small (about 10 particles) and, if they are not evenly distributed over the different depths in the emulsion, gaps will appear in the depth –MTW curve. In order to draw the curve correctly in these gaps, the following procedure has been used: Tracks of heavy primaries passing obliquely through the emulsion have been measured. At the depths, where the depth–MTW curve from the protons is missing or is statistically uncertain, the analogous curve from the heavy primaries has been used. The heavy primary curve has been normalized to fit the proton curve as closely as possible at such depths where it exists.

The heavy primaries have been chosen to have a MTW roughly the same as the MTW of a proton track near its end. Their ionization must not change on their way through the emulsion. Consequently, they must be relativistic or nearly relativistic. A kinetic energy of 400 MeV/nucl. has been chosen as a lower limit. The energy has been determined by scattering measurements. The lengths of the primary tracks have been about 10 mm.

Before we can be allowed to use a correction which has been determined from a mixture of information from protons and heavy primaries, we must show that the two different kinds of particles give the same correction factor. Appendix I describes an investigation of the influence of the ionization on the correction factors and also a study of the accuracy of the correction. The results of this special investigation show that the correction may be constructed in the way just described.

Construction of the best proton track for the comparison

An ideal proton track relative to which the mass of the K-particle can be measured should be such that the following conditions are fulfilled:

1) The error in the MTW shall be much less than the corresponding error in the measurement of the K-particle. This is accomplished by constructing the track for the comparison as a mean value of several proton tracks. It has been required that this track must be based on at least ten times as many measurements as the number of measurements of the K-particle itself.

2) The residual range of the comparison track must be related to the range of the K-particle track as the proton mass to the K-particle mass.

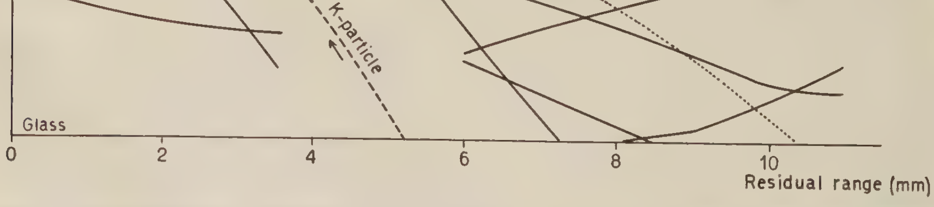

Fig. 3. The construction of a mean proton track for comparison purposes. The figure shows a vertical section of the emulsion with the tracks used. The tracks denoted by ———— and ------- are the protons and the K-particle respectively. The dotted line is the ideal position of the comparison track. The protons used approximate this line as nearly as possible.

3) It is suitable to use such proton tracks that each section of the K-particle track is compared with sections of the proton tracks lying at the same depth in the emulsion. In this case errors of the correction factor influence all the tracks in the same manner and the error in the mass, due to inaccuracies in the correction factor, has been reduced to a minimum.

The first two conditions are easily fulfilled. But to find tracks which also fulfill the third condition and which in addition lie close to the K-particle, is, as a rule, not possible. For this reason the track with which the K-particle finally is compared has been constructed out of sections of proton tracks found at suitable depths. Fig. 3 illustrates such a construction of a comparison track. The figure shows a vertical section of the emulsion with the tracks used in the mass calculation. The K-particle comes from the glass and passes through the emulsion up into the opposite emulsion where it has been identified. Its mass has been determined very roughly by gap counting to about half the proton mass. The ideal tracks for a comparison should pass the emulsion at the position shown by the dotted line. Such particles do not exist. The proton track has instead been built up from those sections of the proton tracks which are shown in the figure. The vertical mean position of those sections will follow the ideal direction at least approximately.

Calculation of the *K*-particle masses

For two particles with the same velocity and the same charge the following relation holds:

$$\frac{m_1}{m_2} = \frac{R_1}{R_2} \tag{1}$$

where m_1 and m_2 are the masses of the particles and R_1 and R_2 their residual ranges. This equation is the basis of several methods to calculate the mass of a particle from measurements of ionization and residual range [3, 7, 8, 13]. All the methods aim at determining points along the tracks with the same velocity as accurately as possible and comparing the residual ranges from those points.

A method which has been found suitable for calculations from photo-metric measurements according to the Lund method has been described earlier [3]. It will be recapitulated very briefly here.

The mean track width $S(R, m)$ as a function of the residual range R of a particle of mass m can be written as a power series.

$$S(R, m) = S_0 + A\frac{R}{m} + B\left(\frac{R}{m}\right)^2 + \cdots \tag{2}$$

The coefficients S_0, A, B ... are independent of the mass and the residual range of the particle. The number of terms necessary in the series is determined essentially by the range of the particles but the quality and development of the emulsion are also important. The largest residual range of any of the present K-particles has been 8 mm. Such a range requires three terms. Two terms are sufficient for a range less than about 2 mm. The coefficients S_0, A and B have been calculated by making use of the comparison proton.

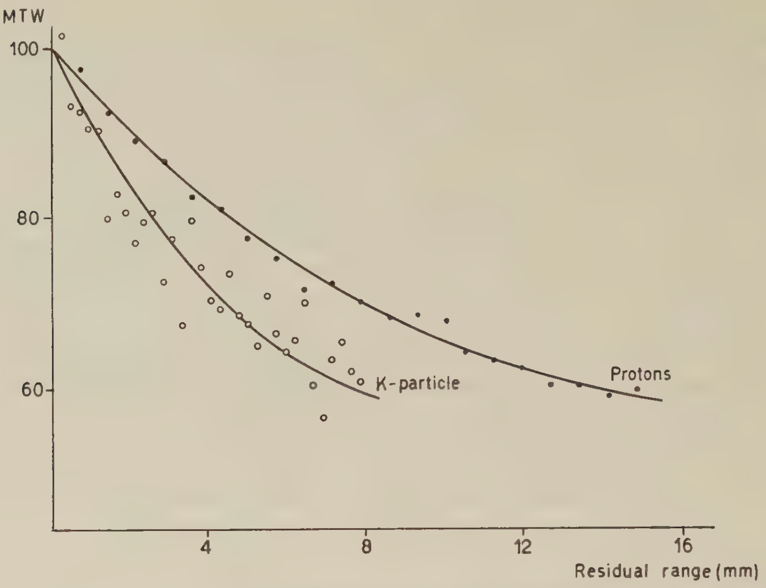

Fig. 4. A MTW–range relation showing the fit of an approximation of the second degree to the measured points. The MTW has been normalized to 100 at $R=0$.

The mass of the unknown particle has been calculated by the method of least squares with the condition that function (2) shall fit the measured values of MTW as well as possible. This condition gives the following equation for the mass

$$0=\sum_{n}[S_i - S(R_i,\ m)]\frac{\partial S(R_i,\ m)}{\partial m} \tag{3}$$

where S_1, R_1; S_2, R_2; ... S_i, R_i; .... S_n, R_n represent measurements of MTW and residual range. The details of the calculations are given in paper [3].

Fig. 4 illustrates how an approximation of the second degree fits the measurements.

Discussion of the errors in the mass determination

Errors which appear in a photo-metric mass determination have been discussed in paper [3]. The errors of the mean track width may be divided into three categories:

1) Errors due to the photo-metric apparatus and the technique of measurement, including errors in the depth correction.
2) Errors from irregularities in the emulsion.
3) Errors from the statistical distribution of the grains in the track.

The first two sources of error have been reduced as much as possible by the choice of a suitable method for the mass measurements. Errors from the instrument and the method of measurement have been reduced by a very accurate check of the

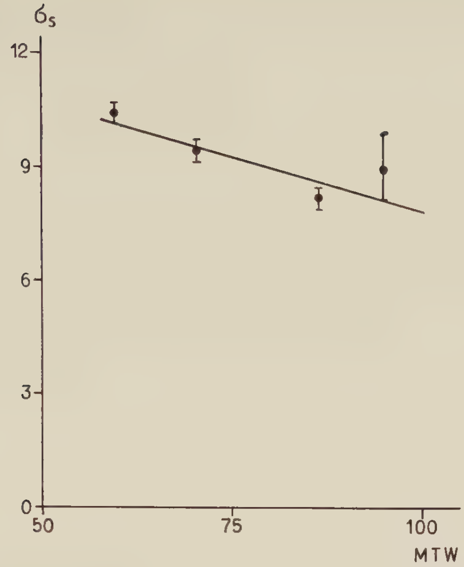

Fig. 5. The standard deviation of MTW (σ_s) versus MTW.

pparatus and by treating the K-particle track and the comparison track in exactly he same way. An error from a lack of reproducibility of the measurements remains 0.3 %). The error in the depth correction has been eliminated by an accurate determination of the correction factors and by the use of a comparison track which raverses the emulsion in the same way as the track of the K-particle.

The errors from such irregularities in the emulsion which appear as variations in he MTW mean level and which are extended over areas of the order of a few square entimeters have been reduced by the choice of comparison tracks as close to the -particle as possible.

The error arising from the statistical distribution of the measured MTW values emains and cannot be avoided. It depends chiefly on the random distribution of he grains in the track. In Fig. 5 the standard deviation of the measurements of TW (σ_s) is given as a function of mean track width. The measurements are reerred to a cell length of 30 μ = the length of the slit.

The standard deviation is approximately constant within the actual interval of ean track width ($60 \leq S \leq 100$). The error of the integrated MTW is thus aproximately equal to $\bar{\sigma}_s\sqrt{n}$ where n is the number of measurements and $\bar{\sigma}_s$ is the ean value of σ_s of the track in question. In $\bar{\sigma}_s\sqrt{n}$ a very slight correlation between djacent measurements has not been taken into consideration. If the increase in tegrated MTW is uniformly distributed along the track, the new MTW will be $(R, m) + \bar{\sigma}_s/\sqrt{n}$.

A method of transforming an error in MTW into an error in mass has been disussed in the earlier paper [3]. The assumptions made there are not, however, in ll details suitable for a calculation of errors of the K-particles. he calculations have therefore been modified to some extent.

The increase in mean track width $\bar{\sigma}_s/\sqrt{n}$ along the track is equivalent to a change in mass σ_m which can be written

$$\sigma_m = \alpha\left(R,\ m,\ \frac{\partial S(R,\ m)}{\partial m}\right)\cdot\frac{\bar{\sigma}_s}{\sqrt{n}} \tag{4}$$

The transformation factor is a function of the residual range, the mass of the particle, and the resolving power of the emulsion $\partial S(R,\ m)/\partial m$.

In order to follow the methods used in the calculation of the masses, an "effective" increase in the mean track width is defined in the range interval R to $R+\Delta R$. This increase is equal to $(\bar{\sigma}_s/\sqrt{n})\ [\partial S(R,\ m)/\partial m]\Delta R$. The factor $\partial S(R,\ m)/\partial m$ can be regarded in this case as the statistical weight of the MTW in the interval ΔR. The total effective increase along a track with the residual range R is

$$\Delta I_{\text{eff}} = \int_0^R \frac{\bar{\sigma}_s}{\sqrt{n}}\,\frac{\partial S(R,\ m)}{\partial m}\,dR \tag{5}$$

If this integral is compared with the formula (3) for the mass calculation it is seen that they are very similar. One of them (3) is the sum of products of mean track width and statistical weight, the other (5) of products of the standard deviation of the mean track width and statistical weight.

The same effective increase in the integrated MTW is obtained if the mass increases from m to $m+\sigma_m$.

$$\Delta I_{\text{eff}} = \int_0^R \frac{\partial S(R,\ m)}{\partial m}\,[S(R,\ m+\sigma_m) - S(R,\ m)]\,dR \simeq \sigma_m \int_0^R \left(\frac{\partial S(R,\ m)}{\partial m}\right)^2 dR \tag{6}$$

It is possible to calculate the transformation factor $\alpha[R,\ m,\ \partial S(Rm)/\partial m]$ from equations (5) and (6).

Fig. 6 shows the product $\alpha(\bar{\sigma}_s/\sqrt{n})$. It gives the percentage error in mass for a particle with the mass 966 m_e as a function of its residual range. Only the normal statistical distribution of the measurements is taken into account in curve 1. This curve gives the minimum error to be expected in the determination of the mass of a particle with this mass by photo-metric measurement. It is valid for those emulsions only in which the present K-particles have been found. As these emulsions are normally developed and have a normal background of electron tracks, it can be assumed that this curve is very nearly correct for most other normal emulsions. Curve 2 includes the error from the lack of reproducibility inherent in the apparatus and the measurements (0.3 %). Curve 3 takes also into account the range straggling of the particles. It represents the total error of the present measurements if the error from the comparison particles can be neglected.

The range straggling can be found from a formula given by Linhard and Scharf [14]

$$|\Delta R|^2 = 4\pi z^2 e^4 NZ \int_0^E \left(\frac{dE}{dR}\right)^{-3}\cdot\frac{1-\dfrac{\beta^2}{2}}{1-\beta^2}\,dE \tag{7}$$

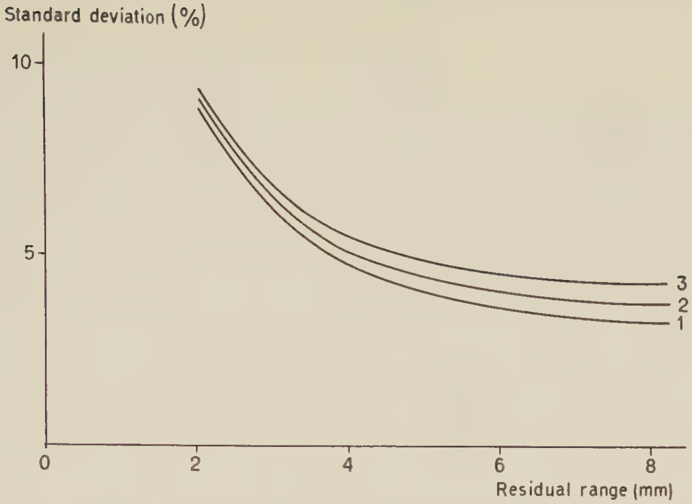

Fig. 6. The standard error in the mass measurements of a K-particle. The following errors are taken into account: Curve 1, the statistical errors from the random distribution of the grains in the track. Curve 2, the statistical error + the error from the lack of reproducibility of the instrument readings. Curve 3, the statistical error + the error from the instrument + the error from the range straggling.

where $|\Delta R|$ is the standard deviation of the range straggling, ze the charge of the particle, NZ the electron density of the absorber, dE/dR the ionization of a particle with the velocity β, the energy E and the residual range R. The formula has been tabulated by Barkas and Young for protons in nuclear emulsions [15]. The transformation to other masses can be easily done by a formula given in the same paper. The range straggling of the K-particles treated in this paper can in all cases be put equal to 2%.

The error in the mass of the mean comparison proton is small. The errors are given as a function of the residual range of the mean proton in Table 2. The statistical distribution of the measurements, the non-reproducibility of the readings of the instrument, and the range straggling have been taken into consideration. The number of measurements on the individual protons on which the mean proton is based has been taken as 10 times the number of measurements on the K-particles in question.

Table 2.

Residual range of the mean proton mm	Standard deviation in the mass m_e
6	41
9	31
12	28
15	27

Systematic errors

The best way to investigate the systematic errors is to measure the mass ratio between known particles. The possible existence of systematic errors has been studied in [3]. Measurements were made of the ratios between the masses of π-mesons and protons and between μ-mesons and protons. In both cases the results were such that there was no reason to assume the existence of any systematic errors.

There has been no change either in the apparatus or in the method of measurements or calculations after this investigation. It seems reasonable to assume therefore that a determination of the mass ratio between K-particles and protons can be made without any systematic errors.

The Masses of the *K*-particles

The K-particles have been found in emulsions exposed by the Sardinian expedition 1953, flight No. 25, II, PD. The type of emulsion is Ilford G5 on glass with a thickness of 600 μ. The plateau value of the blob density is 20 blobs/100 μ.

Table 3 shows the results of the mass measurements. The first four particles have been measured by the author. The particles Br2 and Lu10 have been measured by v. Friesen. Preliminary results of the measurements of those six particles have been published at the conference on elementary particles at the University of Pisa in June 1955 [16]. The last particle K3 has been lent to Lund by the Copenhagen group [18]. The error in the mass of this particle is large, the emulsion not being quite satisfactory. The particles Br2 and K3 do not belong to the plates of the Sardinian expedition [17, 18].

The mean value of the first six particles in the table is $975 \pm 23\ m_e$.

Particle Lu13 has been measured photo-metrically by B. Dobovišek [19]. Her mass values are somewhat lower than the mass given in the table. Her diverging result seems to depend upon a somewhat defective adjustment of the apparatus [20].

Norlind has undertaken the measurements of the secondaries with the excepion of Br2 and K3, which have been measured in Bristol and Copenhagen respectively [21].

Fig. 7 shows the mass distribution of the six particles which are included in the mean value. Every particle is represented by a rectangle. The area is the same for all of them and the length of the base is $2\sigma_m$. The dotted distribution is the distri-

Table 3.

Particle No.	Mass (m_e)	Residual range, mm	Measured by	Secondary
Lu7	1034 ± 45	8.0	K. K.	$g^* = 1$
Lu8	953 ± 50	5.4	K. K.	$g^* = 1.00$ $p\beta = 160 \pm 15$ MeV/c
Lu12	925 ± 50	5.2	K. K.	$g^* = 1.0$
Lu13	991 ± 75	2.6	K. K.	star; $P(DT) + \pi$
Br2	955 ± 70	5.8	v. F.	μ-meson $p\beta = 12$ MeV/c
Lu10	985 ± 70	1.8	v. F.	star; $P + ? + \pi$
K3	1106 ± 160	2.5 (1.0)	K. K.	see reference [18]

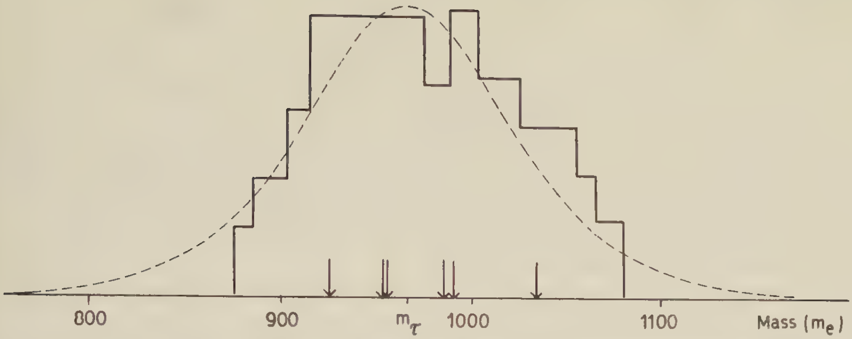

. 7. The mass distribution of six K-particles. Each particle is represented by a rectangle. e area is the same for all of them and the length of the base is $2\sigma_m$. The dotted line distribution he one to be expected if all the K-particles have the same mass equal to that of the τ-meson (966 m_e). The exact positions of the six masses are marked in the figure by arrows.

tion to be expected if all the particles had the same mass equal to that of the neson (966 m_e).

The agreement between the two distributions is good. The number of particles small and it is hardly possible to draw any extensive conclusions from the agree- ent. There is, however, nothing in the experiments to contradict the assumption at all K-particles have the same mass within narrow limits of error and that this ss is equal to the τ-meson mass [26].

A comparison is made in Table 4 between some mass measurements in different oratories. Only such measurements which have been made directly on the primary rticle have been included. The table shows that the results published here are good agreement with other measurements.

The errors given in the fourth column of the table are not directly comparable. some cases only the pure statistical errors are taken into account, in others stematic errors are also included.

Table 4.

Institute	Method	No. of particles	Mass	Reference
ome	Scattering	24	960 ± 36	[22]
ome	Gap measurements	6	965 ± 25	[22]
openhagen	Scattering	18	935 ± 40	[18]
openhagen	Gap measurements	5	986 ± 25	[18]
aris (École normale supe- rieure)	Photo-metric measurements	4	1018 ± 38	[8]
aris (École Polytechnique)	4 methods in emulsions	30	926 ± 25	[23]
aris (École Polytechnique)	Cloud chamber	22	935 ± 15	[24]
erkeley	Magnetic spectrometer	{459 177	971 ± 1.3 962.9 ± 1.9	[25]
und	Photo-metric measurements	6	975 ± 23	All errors included

APPENDIX

Influence of the ionization on the correction factor

The correction for depth which has been used in the photo-metric measurements of the K-particles has been determined from measurements of tracks of particles with different ionization. One would not be allowed to mix measurements in this way and use the same correction independent of ionization, if the correction factors change with ionization in one way or other.

Figures 8 and 9 show five depth–MTW curves from the same emulsion. The MTW is plotted as a function of the distance to the surface in the processed emulsion. The curves have not been drawn in the regions nearest to the surface down to a depth of 40 μ, because of a much too wide spread of the individual values, which means that the correction is very unreliable in this interval. The tracks from which the curves have been determined had different MTW. The mean track width at a depth of 100 μ has been normalized to 100 in the figures. Table 5 gives information about the tracks from which the curves have been determined.

The normalization of the mean track width in the table has been such that the mean width of the end of a proton track is equal to 100. The unit of ionization in the table is the ionization in tracks of relativistic singly charged particles (J_0). Both mean track width and ionization are given approximately only.

The measurements in Fig. 9 have a lower statistical weight than the measurements in Fig. 8. The number of developed grains per point in the diagram is smaller. The solid curves drawn in Fig. 9 are therefore not taken directly from the points

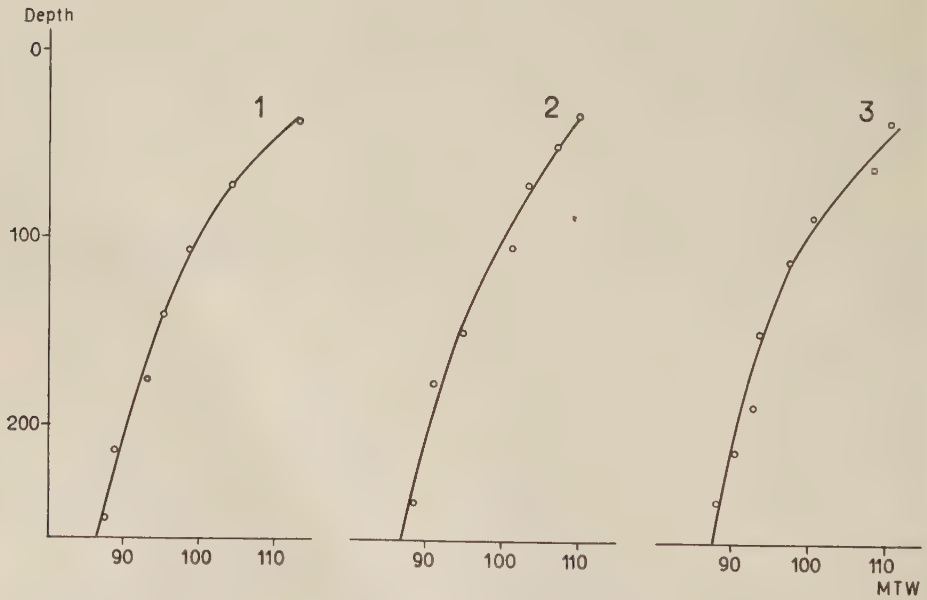

Fig. 8. The depth–MTW relation for tracks of relativistic heavy primaries (1) and for proton tracks (2 and 3).

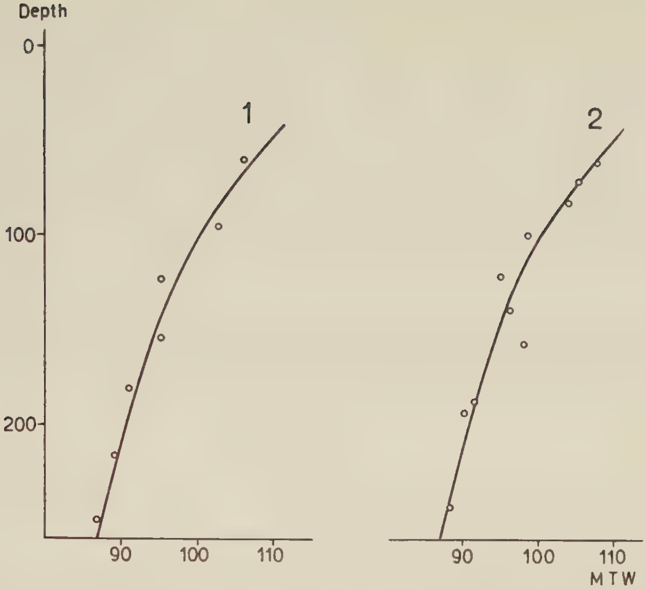

Fig. 9. The depth–MTW relation for tracks of relativistic α-particles (1) and for tracks of singly charged relativistic particles (2).

but are a mean value of the three curves in Fig. 8. Suitable normalization has made the agreement between the curves and the points as good as possible. This agreement seems to be rather good. No significant difference is to be seen.

The conclusion which can be drawn from a comparison of the five depth–MTW curves is that the correction factor is independent of the ionization in an interval of mean track width which covers completely all tracks of singly charged particles.

The accuracy of the correction factors

An estimate of the accuracy of the correction is obtained by a comparison between depth–MTW curves determined from different tracks in the same emulsion. Such a comparison has been made in Table 6. The correction factors $K(1)$, $K(2)$, and $K(3)$ have been calculated from data taken from the curves in Fig. 8.

Table 5.

Curve No.	Tracks used	Total length of the tracks mm	Mean value of the mean track width	Mean value of the ionization J_0
Fig. 8, 1	Relativistic heavy primaries	25	105	20
,, 8, 2	Protons $0 < R < 3$	24	93	11
,, 8, 3	Protons $6 < R < 10$	32	70	6
,, 9, 1	Relativistic α-particles	22	51	4
,, 9, 2	Relativistic particles $z = 1$	30	15	1

Table 6.

Depth μ	$K(1)$	$K(2)$	$K(3)$
60	0.935	0.941	0.931
120	1.027	1.024	1.024
180	1.086	1.087	1.087
240	1.140	1.136	1.131

The error in mean track width resulting from inaccurate correction has been discussed in paper [3]. It was stated there that the error can amount to 1 %, only under very exceptional conditions. Table 6 confirms this statement.

Summary

Photo-metric measurements of the mass of K-particles stopping in nuclear emulsions are described. The paper discusses the method of measurement and the errors which normally appear in such mass measurements. The errors are eliminated as far as possible by accurate checking of the instrument and a suitable choice of the tracks used for comparison.

The result of the mass measurements of six K-particles is $975 \pm 23\ m_e$, thus in good agreement with other mass determinations.

ACKNOWLEDGEMENT

I wish to express my sincere gratitude to my teacher, Professor Sten von Friesen, for suggesting this investigation and for much valuable advice and many stimulating discussions during the course of the work.

Department of Physics, University of Lund, February 1956.

REFERENCES

1. v. Friesen and Kristiansson, Arkiv f. Fysik *4*, 505 (1952).
2. Kristiansson, Phil. Mag. *44*, 267 (1953).
3. Kristiansson, Arkiv f. Fysik *8*, 311 (1954).
4. v. Friesen, Arkiv f. Fysik *8*, 305 (1954).
5. v. Friesen and Stigmark, Arkiv f. Fysik *8*, 121 (1954).
6. Kayas and Morellet, Journ. Phys. et Rad. *14*, 353 (1953).
7. Morellet, Suppl. Nuovo Cimento *1*, 209 (1955).
8. Van Rossum, Ann. de Phys. *10*, 643 (1955).
9. Artom and Gentile, Preliminary report of the Pisa Conference on elementary particles, Milano 1955, p. 87.
10. Fowler and Perkins, Phil. Mag. *46*, 587 (1955).
11. Waldeskog, Arkiv f. Fysik *7*, 475, (1954).
12. Norlind, Kungl. Fysiografiska Sällskapets i Lund Förhandlingar *24*, 12 (1954).
13. Lattes, Occhialini and Powell, Proc. Phys. Soc. *61*, 173 (1948).
14. Linhard and Scharff, Dan. Mat. Fys. Medd. *27*, 15 (1953).
15. Barkas and Young, Emulsion tables I, USRL–2579 Rev. Sept. 1954, Berkeley, California.

16. v. FRIESEN and KRISTIANSSON, Preliminary report of the Pisa Conference on elementary particles. Milano 1955, p. 295.
17. O'CEALLAIGH, Phil. Mag. *42*, 1032 (1951).
18. BØGGILD, HOOPER, ORTEL and SCHARFF, Dan. Mat. Fys. Medd. *30*, no 3 (1955).
19. DOBOVIŠEK, Bull. Scient. Yougoslavic *2*, 44 (1955).
20. DOBOVIŠEK, Reports from J. Stefan Institute *2*, 39 (1955).
21. NORLIND, private communication.
22. CASTAGNOLI, CORTINI and MANFREDINI, Preliminary report of the Pisa Conference on elementary particles, Milano 1955, p. 253.
23. HOANG, JAUNEU, JOUVIN, KAYAS, LEPRINCE-RINGUET, MORELLET, ORKIN-LECOURTOIS and TREMBLEY, Suppl. Nuovo Cimento *1*, 172 (1955).
24. ARMENTEROS, GREGORY, HENDEL, LAGARRIGUE, LEPRINCE-RINGUET, MULLER and PEYROU, Nuovo Cimento *1*, 915 (1955).
25. BIRGE, PETERSON, STORK and WHITEHEAD, Phys. Rev. *100*, 430 (1955).
26. POWELL, Preliminary report of the Pisa Conference on elementary particles, Milano, 1955, p. 135.

Tryckt den 27 mars 1956

Uppsala 1956. Almqvist & Wiksells Boktryckeri AB

ARKIV FÖR FYSIK Band 10 nr 34

Communicated 14 September 1955 by Axel E. Lindh and Ivar Waller

On the Coulomb effect for the internal bremsstrahlung accompanying beta decay

By S. Bertil Nilsson

Summary

Reference is made to the elementary picture of the radiative beta-decay due to Knipp and lenbeck, and to the modifications of the Born-approximation formula suggested by this cture to include the Coulomb effect. The main part of the paper is devoted to a more con- tent theoretical treatment of allowed transitions, in which the Coulomb field is taken into nsideration from the outset and not only in the end result. The calculation reported here is ll approximate in considering only that contribution to the Coulomb effect which comes from e proper beta transition. A numerical integration in the case of S^{35} shows a not inconsiderable crease over the photon yield predicted by the elementary picture in the corresponding ap- oximation (which is commonly employed to compare with experiment). However, in this proximation at least, the increase is not large enough to account for the very high yield served in some recent experimental work.

I. Introduction

In the radiative beta-decay

$$N \rightarrow P + \nu + e + \gamma \tag{1}$$

nucleus of proton number Z-1, say, is converted into a nucleus of proton num- r Z under emission of a neutrino, an electron, and a photon. The theory of is process of internal bremsstrahlung was developed in the Born approximation Knipp and Uhlenbeck [1] and by Bloch [2] for an allowed transition, and by ang and Falkoff [3] for forbidden transitions and different types of interaction.

Let the outgoing electron have momentum p and relativistic energy $W_p =$ $^2 + m^2)^{1/2}$ far from the nucleus; the photon energy and momentum $= k$ (units th $\hbar = c = 1$ are employed). It is advantageous to introduce also the sum

$$W_e = W_p + k, \tag{2}$$

ich would be the electron energy in the corresponding non-radiative transition. e are here interested in the probability per unit time, $S(k)\,dk$, for the emis- n of a photon in the energy interval dk around k. As remarked by Knipp d Uhlenbeck [1] for an allowed transition, the result of a second-order pertur- tion calculation with Z formally equal to zero can be factored in the sug- stive form

$$S(k) = \int_m^{W_0} d\, W_e\, P(W_e)\, \Phi(W_e, k), \tag{3}$$

with $P = P_0$ and $\Phi = \Phi_0$ given by

$$P_0(W_e) = \frac{G^2 M^2}{2\pi^3} (W_0 - W_e)^2 p_e\, W_e, \tag{4}$$

$$\Phi_0(W_e, k) = \begin{cases} \dfrac{\alpha}{\pi k} \left[\dfrac{W_p^2 + W_e^2}{p_e\, W_e} \ln \dfrac{W_p + p}{m} - \dfrac{2p}{p_e} \right] & \text{for } W_e > m + k, \\ 0 & \text{for } W_e < m + k. \end{cases} \tag{5}$$

Here α is the fine-structure constant, G the beta coupling constant, M a nuclear matrix element (see below), and p_e the momentum corresponding to the energy W_e (i.e. $W_e^2 = p_e^2 + m^2$).

The factorization in (3) has been chosen in such a way that $P_0(W_e)$ represents the beta energy spectrum, with upper limit W_0: $P_0(W_e)\, d\, W_e$ is the ordinary expression, neglecting the effect of the electrostatic nuclear field, for the beta-decay probability per unit time if the emitted electron is to have an energy between W_e and $W_e + d\, W_e$. One may thus picture $\Phi_0(W_e, k)\, dk$ as the probability that a beta-particle born with energy W_e will lead to the creation of a photon with energy between k and $k + dk$. This is confirmed by a direct calculation [1] using outgoing Dirac waves with a singularity at the origin, and is in approximate agreement with classical radiation theory [3].

The result, which is true also for the angular distribution, means that, at least for allowed transitions with $Z = 0$, the decay (1) can be successfully treated as if consisting of two independent real processes. If the same simplifying assumption is tried when $Z \neq 0$, the following modifications suggest themselves to account for the influence of the Coulomb field.

(i) The beta-spectrum corrected for the Coulomb effect should be substituted in place of the original spectrum [1]. That is, the first factor $P(W_e)$ in (3) is now to be understood as meaning

$$P(W_e) = P_Z(W_e) = P_0(W_e)\, F(Z, W_e), \tag{6}$$

where F is the Coulomb correction factor occurring in beta theory [4] and approximated by [5]

$$F(Z, W_e) = \frac{2\pi\alpha Z\, W_e / p_e}{1 - e^{-2\pi\alpha Z\, W_e/p_e}}. \tag{7}$$

When only this modification is made in (3), the resulting expression will be labelled (3-i); the Coulomb influence on the gamma-radiation process is then neglected.

(ii) More exactly, Φ_0 too should be replaced by a modified function Φ_Z. It is consistent with the provisional assumption of two real processes to regard the increased radiation, due to the motion in the Coulomb field, as being analogous to an external bremsstrahlung. If it is then possible to apply the usual Sommerfeld-Elwert correction [6, 7, 8] to the Born approximation Φ_0, we get

$$\Phi_Z(W_e,k)=\Phi_0(W_e,k)\frac{F(Z,W_p)}{F(Z,W_e)}, \tag{8}$$

with F defined by (7) and with $W_p=W_e-k$ as in (2). In fact the result of combining (8) and (6) in Eq. (3)—leading to the form (3-ii)—agrees well with an estimate by Knipp and Uhlenbeck [1] for low-velocity electrons.

However, it must be borne in mind that in a consistent quantum-mechanical treatment the decay (1) is not described as built up of two real processes. One may rather speak of a first step in the form of a *virtual* transition, without conservation of energy. An argument along the lines indicated above cannot, therefore, give a real theoretical justification for the use of either (3-i) or (3-ii). In spite of that it has been shown by Cutkosky [9] and by Ford and Lewis [10] that a formula which is correct up to terms proportional to the first power of αZ does coincide with the same approximation of (3-ii). This is true for allowed transitions; forbidden transitions will exhibit also an extraordinary Coulomb effect [9, 10; cf. 11].

The following investigation of allowed transitions was undertaken with a view to obtaining approximate corrections[1] to results based on the naïve assumption of two independent processes. We shall not use expansions in powers of αZ. The present paper is of a rather preliminary character, in that it corresponds to the above consideration (i) only. Thus, though the Coulomb field will be considered from the beginning and not just in the end result, we shall here make the same approximation, that its influence on the proper radiation process can be neglected. The result is to be compared with Eq. (3-i). The case of S^{35}, for which recent experimental values are available, will be chosen as a numerical example.

II. Matrix element

We shall follow the perturbation method of references 1–3. In the lowest order of approximation the decay (1) proceeds in two steps, so that altogether three states are involved:

(a) The initial neutron state $|1\rangle=|N\rangle$.

(b) An intermediate state $|m\rangle=|P\nu q\rangle$ containing the final proton and neutrino as well as a virtual electron in a state labelled q.

(c) The final state $|2\rangle=|P\nu p k\rangle$ with the electron p and photon k, the proton and neutrino being unchanged.

The transition from $|1\rangle$ to $|m\rangle$ is effected by the beta interaction H_β, and from $|m\rangle$ to $|2\rangle$ by the electron-radiation coupling H_γ. These combine to the total matrix element

$$H=\sum_m\frac{\langle 2|H_\gamma|m\rangle\langle m|H_\beta|1\rangle}{E_1-E_m}, \tag{9}$$

from which the transition probability per unit time is obtained as

$$w=2\pi\sum_{\substack{\text{final}\\\text{states}}}|H|^2\,\delta(E_2-E_1). \tag{10}$$

---

[1] As remarked above, Eq. (3-ii) has been shown in references 9 and 10 to be correct to order αZ. I was not aware of this result in the calculations reported here.

With self-explanatory notations for the Dirac wave-functions belonging to the several particles, the matrix elements appearing in (9) are given by

$$\langle P\nu q|H_\beta|N\rangle = G\sum_N\int d^3x\,\bar{\psi}_q\lambda_a B\bar{\psi}_\nu\,\bar{\psi}_P\lambda_a\psi_N, \tag{11}$$

$$\langle p k|H_\gamma|q\rangle = \frac{ie}{\sqrt{2k}}V^{-1/2}\int d^3x\,e^{-i\mathbf{k}\cdot\mathbf{x}}\,\bar{\psi}_p\gamma_r\psi_q. \tag{12}$$

As usual $\bar{\psi}=\psi^*\beta=\psi^*\gamma_4$. The λ_a are Dirac matrices characteristic of the particular type of beta-interaction assumed, with coupling constant G; a summation over a is implied. In a more comprehensive formulation we should use a combination of the different sets of matrices λ_a, each with its own coupling parameter, but such a generalization will not be indicated explicitly. The matrix B has been inserted to ensure the correct transformation properties [12]. In H_γ the index r represents the polarization of the emitted photon, of momentum $\mathbf{k}$, and the coupling constant e is the absolute value of the electronic charge expressed in rationalized units ($e^2/4\pi=\alpha=1/137$). The integrals are to be extended over the large normalization volume V.

In the case of an allowed transition (11) reduces to

$$\langle P\nu q|H_\beta|N\rangle = G\,M_a\,\bar{\psi}_q(0)\,\lambda_a B\,\bar{\psi}_\nu(0), \tag{13}$$

where M_a is a nuclear matrix element:

$$M_a=\sum_N\int d^3x\,\bar{\psi}_P\lambda_a\psi_N. \tag{14}$$

For a neutrino of momentum $\boldsymbol{\nu}$ we may write (cf. e.g. [13])

$$B\bar{\psi}_\nu(\mathbf{x}) = V^{-1/2}v(\nu)\,e^{-i\boldsymbol{\nu}\cdot\mathbf{x}},\qquad B\bar{\psi}_\nu(0)=V^{-1/2}v(\nu), \tag{15}$$

with $v(\nu)$ a Dirac spinor satisfying $\gamma_\mu\nu_\mu v(\nu)\equiv\gamma\nu\,v(\nu)=0$. In Born's approximation the electron is likewise treated as a free particle and described by a plane wave, e.g. for momentum $\mathbf{q}$:

$$\psi_q(\mathbf{x}) = V^{-1/2}u(q)\,e^{i\mathbf{q}\cdot\mathbf{x}}, \tag{16}$$

with

$$(i\gamma q+m)\,u(q)=0. \tag{17}$$

However, we now want to take account of the fact that the electron is not really free, but moves in the electrostatic field of the nuclear charge Ze (the screening being neglected). The Coulomb wave-function corresponding to (16) has the asymptotic form of a plane wave plus an ingoing spherical wave. An approximate expression has been given by Furry and others [14; cf. 15]; we will, in this preliminary calculation, keep only the main term, which means disregarding certain relativistic effects. Then

$$\psi_q(\mathbf{x}) = V^{-1/2}N(q_0)\,u(q)\,e^{i\mathbf{q}\cdot\mathbf{x}}\,F(-i\alpha Z q_0/q, 1; -iqr-i\mathbf{q}\cdot\mathbf{x}). \tag{18}$$

Here $q_0=\pm W_q=\pm(q^2+m^2)^{1/2}$, F is a confluent hypergeometric function, and N a normalization factor:

$$F(a,c;z) = 1 + \frac{a}{c}\frac{z}{1} + \frac{a(a+1)}{a(c+1)}\frac{z^2}{2!} + \cdots, \tag{19}$$

$$N(q_0) = \Gamma(1 + i\alpha Z q_0/q)\, e^{\pi\alpha Z q_0/2q}. \tag{20}$$

Even apart from other corrections, (18) involves an error when q_0 is negative, . for positron states. With a modification of the transition scheme (a)–(c) we ould then say that a virtual positron is first created together with an ordinary ctron and a photon, and is afterwards absorbed by the neutron, turning it o a proton and a neutrino. Consequently the field of importance for the tion of the positron is that of the original nucleus, of proton number Z-1. e use of Z instead, as in (18), involves an error which is, however, not significant in view of the other approximations made here.

Since $F = 1$ for $\mathbf{x} = 0$, the matrix element (13) of H_β will now be

$$\langle P\nu q | H_\beta | N\rangle = V^{-1} G M_a N^*(q_0)\, \bar{u}(q)\, \lambda_a v(\nu), \tag{21}$$

ich differs from the plane-wave expression only by the factor N^*. A similar luction of H_γ is not possible when Coulomb waves are used. It might, however, argued that the Coulomb distortion of the wave is most pronounced near the cleus and should therefore be more important in H_β than in H_γ, especially small k (long wave-lengths). As a first step it is then possible to use the rected form (21) for H_β while retaining plane waves in H_γ. This corresponds the modification (i) in the Introduction. As already mentioned, this approximan will be adopted in the present paper.

With the help of plane waves according to (16) the matrix element (12) is dily evaluated:

$$\langle p k | H_\gamma | q\rangle = \frac{i e}{\sqrt{2k}} V^{-1/2}\, \bar{u}(p)\, \gamma_r u(q)\, \delta_{\mathbf{q}-\mathbf{p}-\mathbf{k}}, \tag{22}$$

ere the δ-symbol is unity for $\mathbf{q} - \mathbf{p} - \mathbf{k} = 0$ and zero otherwise.

It remains to write down the energy differences appearing in Eqs. (9) and). With W_0 equal to the nucler energy difference, we have

$$E_2 - E_1 = W_p + k + \nu - W_0 \equiv \nu - W_0 + W_e, \tag{23}$$

$$E_1 - E_m = W_0 - \nu - q_0 = W_e - q_0. \tag{24}$$

e last equality is a consequence of the δ-function in (10).

The total matrix element (9) is obtained from (21), (22) and (24) as

$$H = \frac{i e G M_a}{\sqrt{2k}} V^{-3/2} \sum_{(q)} \frac{N^*(q_0)}{W_e - q_0}\, \bar{u}(p)\, \gamma_r u(q)\, \bar{u}(q)\, \lambda_a v(\nu), \tag{25}$$

h the only remaining sum extended over the four states belonging to the omentum $\mathbf{q} = \mathbf{p} + \mathbf{k}$. Using appropriate projection operators for the positive and gative energy states respectively, we can perform the summation in the usual nner, and obtain

$$H=\frac{i e G M_a}{\sqrt{2k}}\,V^{-3/2}\,\frac{1}{2W_q}\,\bar{u}(p)\,\gamma_r\,L(q)\,\lambda_a\,v(\nu), \tag{26}$$

with

$$L(q)=\frac{N^*(W_q)}{W_e-W_q}(-i\gamma q+m)-\frac{N^*(-W_q)}{W_e+W_q}(-i\gamma q'+m). \tag{27}$$

The four-vectors q and q' are given by

$$q=(\mathbf{q}, W_q), \qquad q'=(\mathbf{q}, -W_q).$$

III. Transition rate

We are now in a position to evaluate the transition rate (10) in the present approximation. With $u=u(p)$ and $v=v(\nu)$ we get from (26)

$$w=-2\pi\sum_{\substack{\text{final}\\ \text{states}}} V^{\;3}\,\frac{e^2 G^2 M_a M_b^*}{8kW_q^2}\,\bar{u}\gamma_r L(q)\,\lambda_a v\bar{v}\bar{\lambda}_b\,\bar{L}(q)\,\gamma_r u\,\delta(\nu-W_0+W_e), \tag{28}$$

where $\bar{\lambda}_a=\beta\lambda_a^*\beta$. $\bar{L}$ differs from L only in having N in place of N^*.

The sum over final states involves a summation over the spins of the particles and over their momenta. A typical momentum sum is of the form

$$\sum_{\mathbf{p}}\cdots\rightarrow\frac{V}{(2\pi)^3}\int d^3p\cdots=\frac{V}{(2\pi)^3}\int_0^\infty p^2\,dp\int d\Omega_p\cdots, \tag{29}$$

while the spin sums for the electron and neutrino are performed with the help of projection operators, e.g.

$$\sum_1^2 v\bar{v}=\sum_1^4\frac{-i\gamma\nu'}{2\nu}\,\beta v\bar{v}=\frac{-i\gamma\nu'}{2\nu} \tag{30}$$

where ν' stands for the four-vector $(-\mathbf{r},\nu)$. Anticipating the result of integrating over the angles, we may replace (30) by $\frac{1}{2}\beta$.

The integration over the magnitude of the neutrino momentum can be carried out immediately on account of the δ-factor in (28). If we sum also over the escape directions of the neutrino and photon, the probability per unit time for a transition to a state with photon energy between k and $k+dk$ is obtained as

$$w=\frac{e^2G^2|M_a|^2}{8(2\pi)^6}\,k\,dk\int_{(W_e<W_0)} p^2\,dp\,\frac{(W_0-W_e)^2}{W_p W_q^2}\int d\Omega_p\sum_r \mathrm{Sp}\{L(q)\,\beta\,\bar{L}(q)\,\gamma_r(i\gamma p-m)\gamma_r\}. \tag{31}$$

We have here assumed the nucleons to be non-relativistic and in consequence retained only such matrices λ_a as couple the large spinor components together, which is effectively equivalent to replacing $\lambda_a\beta\bar{\lambda}_b$ by $\beta\delta_{ab}$.

The effect of the Coulomb field is contained in the matrices L and $\bar{L}$. Eq. (27) gives

$$L(q)\,\beta\,\bar{L}(q) = 2\,W_q\left\{\frac{|N(W_q)|^2}{(W_e - W_q)^2}\,(m - i\gamma q) - \frac{|N(-W_q)|^2}{(W_e + W_q)^2}\,(m - i\gamma q')\right\}, \qquad (32)$$

where, from (20) and (7),

$$|N(q_0)|^2 = \frac{2\pi\alpha Z q_0/q}{1 - e^{-2\pi\alpha Z q_0/q}} = F(Z, q_0). \qquad (33)$$

After summing over the two directions of polarization according to

$$\tfrac{1}{2}\sum_{r} \gamma_r (i\gamma p - m)\gamma_r = \beta W_p - m - i\gamma(\mathbf{k})\,\mathbf{p}\cdot\mathbf{k}/k, \qquad (34)$$

the spurs in (31) can be evaluated immediately. It is not necessary to give all details of the following reduction, which is straightforward. In the integral over the magnitude of the electron momentum, write

$$\frac{p^2\,d\,p}{W_p} = p\,d\,W_p = p\,dW_e,$$

with a corresponding adjustment of the integration limits. Then in (32) reduce to a common denominator, which will be the square of

$$W_e^2 - W_q^2 = 2\,(k\,W_p - \mathbf{k}\cdot\mathbf{p}) \equiv 2\,k\,(W_p - \xi) \equiv 2\,k\,\eta. \qquad (35)$$

It is convenient to use ξ or η so defined as integration variable in summing over the directions of the outgoing electron, so that, θ being the angle between the electron and the photon,

$$\sin\theta\,d\,\theta = -\,d\,\xi/p = d\eta/p.$$

Collecting all terms we get, with $w = S(k)\,d\,k$ as before,

$$S(k) = \frac{\alpha\,G^2 M^2}{2\pi^4}\,\frac{1}{k}\int_{m+k}^{W_0} d\,W_e\,(W_0 - W_e)^2 \int_{-p}^{p} d\,\xi\,\{X\,F(Z, W) - Y\,[F(Z, W) - F(Z, -W)]\}, \qquad (36)$$

where $W = W_q > 0$ is defined by (35) in terms of ξ or η:

$$W^2 = W_e^2 - 2\,k\,\eta = W_p^2 + k^2 + 2\,k\,\xi, \qquad (37)$$

and

$$\left.\begin{aligned} 2\,X &= (W_e^2 + W_p^2)/\eta - W_e\,(1 + m^2/\eta^2),\\ 4\,Y &= \frac{k^2}{W\,W_e}\,[W_p - 4\,\eta^2\,X/(W_e + W)^2]. \end{aligned}\right\} \qquad (38)$$

Further, by (33),

$$F(Z, W) - F(Z, -W) = 2\,\pi\,\alpha\,Z\,W/q, \qquad (39)$$

with $q^2 = W^2 - m^2$. In (36) we have also written $e^2/4\pi = \alpha$ and $|M_a|^2 = M^2$.

We may use the mean value theorem and (39) to write (36) as

$$S(k) = \frac{\alpha G^2 M^2}{2\pi^4}\,\frac{1}{k}\int\limits_{m+k}^{W_0} d\,W_e\,(W_0 - W_e)^2 \left\{F(Z,\overline{W})\int\limits_{-p}^{p} d\xi\,X - 2\pi\alpha Z\int\limits_{-p}^{p} d\xi\,W\,Y/q\right\}, \tag{40}$$

where $\overline{W}$ is some interior point in the W-interval, and

$$\int\limits_{-p}^{p} d\xi\,X = (W_e^2 + W_p^2)\ln\frac{W_p + p}{m} - 2\,p\,W_e. \tag{41}$$

The result (36) or (40) deviates from the older formula (3-i) in two respects. (i) In the main term, containing the factor X, the Coulomb factor F is to be taken at the point $\overline{W}$ and not at W_e; otherwise this term is identical with (3-i) on account of (41). Since $W < W_e$ in the whole integration interval, and F is a decreasing function of the energy, this modification tends to increase the photon yield. (ii) A negative correction term is added, working in the opposite direction. —For $Z=0$ $(F \equiv 1)$ the two formulas coincide, as is also the case for $Z \neq 0$ and $k \to 0$.

Let us, for the purpose of a numerical evaluation, seek an approximate expression for $\overline{W}$ in (40). In the ξ-interval corresponding to a fixed value of W_e we can put, roughly, $F(Z, W) = \text{const.}\ W/q$, so that

$$\int\limits_{-p}^{p} \frac{W}{q}\,X\,d\xi \approx \frac{\overline{W}}{\overline{q}}\int\limits_{-p}^{p} X\,d\xi. \tag{42}$$

When p and k are much less than W_p, the integrals are given with sufficient accuracy by the first few terms in expansions of the form

$$\int\limits_{-p}^{p} X\,d\xi = \frac{p}{W_p}\left\{\frac{2\,W_e}{3\,W_p}\,p^2 + k^2 + \cdots\right\}, \tag{43}$$

etc., whence it is easy to derive

$$\overline{W} = W_p\left\{1 + \frac{2}{5}\left(\frac{k}{W_p} + \frac{k^2}{2\,p^2 + 3\,k^2}\right)\frac{p^2}{m^2} + \cdots\right\}. \tag{44}$$

Similarly,

$$\int\limits_{p}^{p} \frac{W\,Y}{q}\,d\xi = \frac{k^2}{2}\left\{\frac{W_p}{W_e} - \frac{1}{3}\,\frac{p^2}{W_e^2} - \frac{13}{30}\,\frac{k^2}{W_e^2} + \cdots\right\}. \tag{45}$$

The expressions given in (44) and (45) presuppose $p > k$, but there is no difficulty in extending the formulas to the case $p < k$. Combining them with (40) and (41) we are left with an approximate expression for $S(k)$ containing only one integration.

IV. Comparison with experiment: S^{35}

In experimental work on internal bremsstrahlung one can obtain direct information about the number of photons per beta-decay, i.e. the ratio $S(k)/\lambda$, with λ equal to the total probability of beta-emission in unit time:

$$\lambda = \int_m^{W_0} P_Z(W_e)\, d\, W_e = \frac{G^2 M^2}{2\pi^3} f(Z, W_0), \tag{46}$$

$$f(Z, W_0) = \int_m^{W_0} d\, W_e (W_0 - W_e)^2 p_e W_e F(Z, W_e). \tag{47}$$

On division by λ our formula (36) becomes

$$\frac{S(k)}{\lambda} = \frac{\alpha}{\pi f} \frac{1}{k} \int_{m+k}^{W_0} d\, W_e (W_0 - W_e)^2 \int_{-p}^{p} d\xi \{X F(Z, W) - 2\pi\alpha Z W\, Y/q\}, \tag{48}$$

while Eq. (3-i) gives

$$\frac{S(k)}{\lambda} = \frac{\alpha}{\pi f} \frac{1}{k} \int_{m+k}^{W_0} d\, W_e (W_0 - W_e)^2 F(Z, W_e) \int_{-p}^{p} d\xi\, X. \tag{49}$$

Since the Coulomb factor F is contained in both numerator and denominator, the relative yield $S(k)/\lambda$ is not so sensitive to the value of Z as the absolute yield $S(k)$.

When the Z-dependence, i.e. the Coulomb effect, is not disregarded in comparing theory and experiment, it is usual [16–19] to employ Eq. (49) or some equivalent formula (e.g. the experimental beta-spectrum may be used in place of $P_Z(W_e)$, Eq. (6)). In contrast to earlier results, a marked increase over the expected photon yield, especially towards the high-energy limit, is indicated in recent observations by Lidén, Starfelt, and Svantesson [18, 19] for P^{32} and S^{35}.

We shall here consider the decay of S^{35}, which is accepted to be an allowed transition, with maximum energy $W_0 \approx 1.326\, m$ (c being put $= 1$). For such low energies we have always $k < W_p$, so that the approximation (44), (45) can be used.[1] The different expressions for $S(k)/\lambda$ are now amenable to a numerical integration. With $W_0 = 1.326\, m$ and $Z = 17$, one obtains from (7) and (47)

$$f(17, W_0) = 1.213 \cdot 10^{-2} m^5.$$

---

[1] In the numerical evaluation of (48), the values following from the approximation (44), (45) where checked by using also another approximation. With an error of, at most, one half per cent, the Coulomb factor $F(Z, W)$ in (33) can be approximated by a formula of the form

$$F(Z, W) \approx a\, W/q + c/(1 + d\, m^2/q^2),$$

with the constants determined by the asymptotic behaviour,

$$a = 2\pi\alpha Z, \quad b = a/(1 - e^{-a}), \quad c = b - a, \quad d = (b-1)/2.$$

The ξ-integration can now be performed exactly, leaving one numerical integration as before. The values in column (a) of the table below were computed in this way. The approximation (44), (45) leads to deviations of about one or two per cent.

We give the dimensionless quantity $k S(k)/\lambda$ evaluated from (48) and from the old formula (49), which is equivalent to Knipp and Uhlenbeck's theory in the form (3-i). For comparison the result of using the Knipp-Uhlenbeck formula modified in accordance with (3-ii) — $F(Z, W_e)$ replaced by $F(Z, W_p)$ — and approximate experimental values according to Starfelt and Svantesson [19] are also appended. In the table, column (a) refers to the approximate theory developed here, (b) to the Knipp-Uhlenbeck theory (3-i), and (c) to the modified Knipp-Uhlenbeck theory (3-ii).

k/m	$10^5 \cdot k S(k)/\lambda$ (a)	(b)	(c)	Exp.
0	28.4	28.4	28.4	—
0.10	6.55	5.53	6.96	9–10
0.18	1.27	0.99	1.54	2.3–3.3
0.22	0.39	0.30	0.54	0.8–1.0
0.326	0	0	0	—

The k-values picked out suffice to illustrate the general behaviour. There is a not inconsiderable increase in photon yield over the Knipp-Uhlenbeck theory (3-i) when the decay is not treated as consisting of two distinct real processes. In the rather arbitrary approximation chosen here, however, we do not come up to the yield predicted by the modified Knipp-Uhlenbeck theory, in which the Coulomb influence is taken into consideration in both steps (this is immediately evident from Eq. (48)). As we see, even this latter curve lies well below the experimental points. All four curves tend to coincide for small values of k.

V. Conclusion

Though the result of the present calculation is an improvement on the formula (3-i) commonly used, it cannot lay claim to agreement with the experimental data. This is not surprising in view of the approximation still involved, but the gap between theory and experiment makes it a matter of uncertainty whether the discrepancy will vanish on consistently following up the calculation of the Coulomb effect. A continued investigation of this question is being prepared.

Pending a definitive theoretical analysis, the modified Knipp-Uhlenbeck formula (3-ii) seems best suited as a reference formula with which to compare experimental results.

The present investigation was carried out at the Institute of Theoretical Physics in Lund, and I wish to express my gratitude to Professor T. Gustafson, Director of the Institute. I am also grateful to Mr. N. Svantesson for drawing my attention to this problem, and to him as well as to Dr. K. Lidén and Mr. N. Starfelt for helpful information on the experimental situation.

Institutionen för Teoretisk Fysik, Lund.

REFERENCES

1. Knipp, J. K. and Uhlenbeck, G. E., Physica *3*, 425 (1936).
2. Bloch, F., Phys. Rev. *50*, 272 (1936).
3. Wang Chang, C. S. and Falkoff, D. L., Phys. Rev. *76*, 365 (1949).
4. Fermi, E., Zs. Physik *88*, 161 (1934).
5. Kurie, F. N. D., Richardson, J. R., and Paxton, H. C., Phys. Rev. *49*, 368 (1936).
6. Elwert, G., Ann. Physik *34*, 178 (1939).
7. Sommerfeld, A., Atombau und Spektrallinien, II, Sec. VII. 2–3. Vieweg & Sohn, Braunschweig 1939.
8. Guth, E., Phys. Rev. *59*, 325 (1941).
9. Cutkosky, R. E., Diss., Carnegie Institute of Technology, Pittsburgh, Pa., 1953 (unpublished). I am obliged to Dr. Cutkosky for an opportunity to study his work.
10. Ford, G. and Lewis, R. R., private communication to Dr. K. Lidén. (To be published in the Phys. Rev.)
11. Cutkosky, R. E., Phys. Rev. *95*, 1222 (1954).
12. Pauli, W., Ann. Inst. Henri Poincaré *6*, 109 (1936).
13. Blatt, J. M. and Weisskopf, V. F., Theoretical Nuclear Physics, p. 714. John Wiley & Sons, 1952.
14. Furry, W. H., Phys. Rev. *46*, 391 (1934).
15. Sommerfeld, A., Atombau und Spektrallinien, II, Sec. V. 8. Vieweg & Sohn, 1939.
16. Wu, C. S., Phys. Rev. *59*, 481 (1941).
17. Novey, T. B., Phys. Rev. *84*, 145 (1951); *89*, 672 (1953).
18. Lidén, K. and Starfelt, N., Phys. Rev. *97*, 419 (1955).
19. Starfelt, N. and Svantesson, N. L., Phys. Rev. *97*, 708 (1955).

Tryckt den 27 mars 1956

Uppsala 1956. Almqvist & Wiksells Boktryckeri AB

ARKIV FÖR FYSIK Band 10 nr 35

Communicated 7 December 1955 by MANNE SIEGBAHN and ERIK HULTHÉN

Low pressure diffusion cloud chamber tracks of fragments from the spontaneous fission of californium 252. I

By HILDING SLÄTIS

With 9 figures in the text

Introduction

The diffusion cloud chamber has already become a widely used tool for investigation of a large number of nuclear reactions and measurement of the ranges and energies of fast charged nuclear particles, such as electrons, positrons, mesons, protons, deuterons etc. It has been used in connection with accelerators for quantitative measurements as well as just for demonstration of nuclear events. The formation of tracks in a continuously sensitive cloud chamber seems to be a phenomenon which in a most simple and impressive manner demonstrates the nature and reality of nuclear events.

Professor S. G. Thompson, visiting the Nobel Institute of Physics, suggested a study of the spontaneous fission of californium 252 using a diffusion chamber made for demonstration purposes at our institute. Prof. Thompson prepared a weak sample on an aluminum foil of 150 μg/cm^2 thickness. The number of α particles emitted was about 60/minute and the number of fissions about two in the same time. Details concerning Cf^{252} are given in [1]. As the fission tracks in the atmospheric pressure diffusion chamber were quite short, about 16 mm, it was then decided to build a low pressure diffusion cloud chamber. The cloud chambers as well as some of the fission tracks obtained with these chambers will be presented here.

Development of the diffusion cloud chamber

As is well known, the first continuously working cloud chamber was constructed by Langsdorf [2] in 1938. In a rectangular glass chamber, alcohol was vaporized near the roof of the chamber and was moved by diffusion toward the chamber floor, which was cooled by means of a refrigerating liquid pumped through a coil cooled by solid carbon dioxide. In a region near the bottom of the chamber a supersaturation of the vapor was maintained continuously, and in this sensitive region tracks of the paths of charged particles were created by condensation of vapor on the ions formed along the paths of the particles. The floor of the chamber was made of two glass sheets between which the refrigerating liquid was pumped. Photographs were taken through this glass bottom. The roof of the chamber was of metal in order to facilitate the heat conduction necessary for the evaporation of the alcohol. The inactive gas of the chamber was carbon dioxide. Langsdorf computed theoretically the temperature and the vapor density distribution, as well as the degree of supersaturation. A very simple diffusion cloud chamber, the so called "beaker

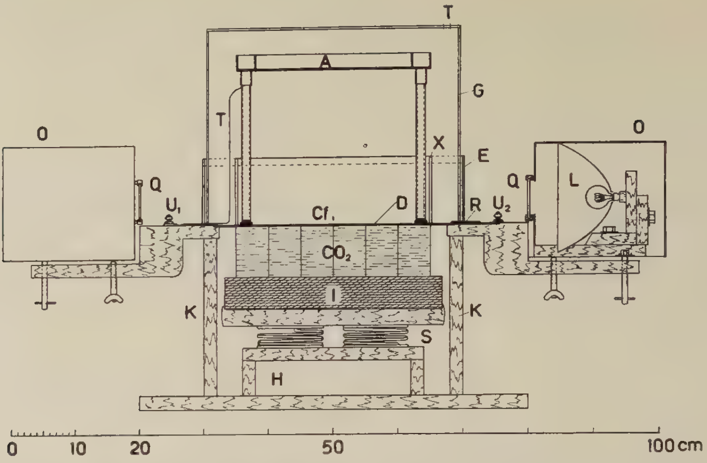

Fig. 1. Design of the atmospheric pressure diffusion cloud chamber for demonstration purposes.

chamber" was described by Needels and Nielsen [3]. It consisted of a glass beaker on a cake of dry ice and was covered with a carboard wet with alcohol. A clearing electric field (50 to 100 volts/cm) was placed across the sensitive region (an electric field was already used by Langsdorf).

Really successful diffusion cloud chambers were constructed by Cowan [4]. He introduced the more convenient method of taking photographs through a glass window at the roof of the cahmber, whereas the bottom was made of aluminum blackened by an anodizing process or of black Bakelite cooled by direct contact with blocks of dry ice (−78°C). With argon and methyl alcohol in the chamber, the sensitive layer was about 3 inches deep in the center of the chamber at the optimum roof temperature of 39°C. Miller, Fowler, and Shutt [5] have constructed diffusion cloud chambers with hydrogen at pressures up to 15 atmospheres. Fowler, Shutt, Thorndike, and Whittemore [6] at Brookhaven have used diffusion cloud chambers filled with hydrogen gas at a pressure of about 20 atmospheres in connection with the Cosmotron for investigation of meson production in n-p collisions. Schluter and Wright [6 a] have built the University of Chicago diffusion cloud chamber characterized by 30 atmospheres of hydrogen operating pressure and a magnetic field of 12,600 gauss. The theory of the diffusion cloud chamber has been further developed by Shutt [7]. Simple types of diffusion cloud chambers have been described by Barnard and Atkinson [8], Kuehner [9], Voisin [10], Wilner [11], Milojević, Cerinco, and Lalović [12]. The last authors describe a chamber cooled by means of liquid air. Diffusion cloud chambers are used extensively also in Harwell. A 9-in. chamber is described by Snowden and Bevan [13] and has been employed to determine the factors affecting its operation with various gases up to a pressure of 11 atmospheres [14]. The system of stereoscopic photography and reprojection used with the Harwell 18 inch diffusion cloud chamber has been constructed by Whitby [15].

The demonstration diffusion chamber

Fig. 1 shows the design of the atmospheric diffusion chamber built for demonstration purposes. The chamber G is made of 3 mm thick glass. The lower parts of the

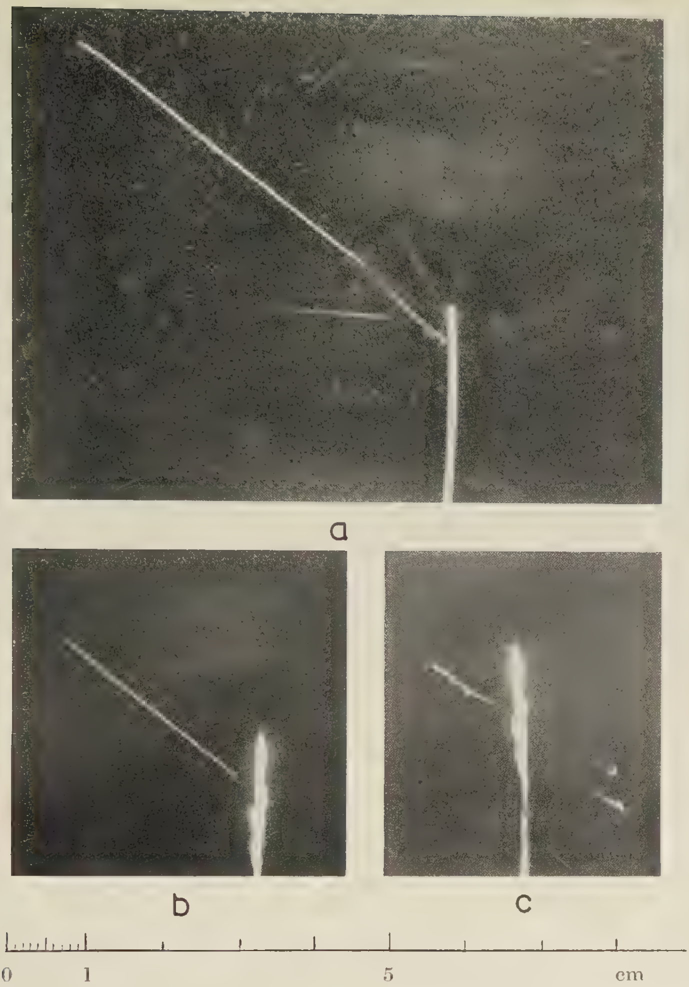

Fig. 2. (*a*) α tracks from ThC′. An electron track crosses the long α track. The active deposit is at the end of a copper wire (vertical line). (*b*) α track from Cf^{252}. (*c*) Fission tracks from Cf^{252}. Pressure in all cases is 1 atm.

walls consist of two glass sheets. The walls are resting on a rubber seal R. An inner glass collar X is used in order to diminish disturbances from the outer glass walls. A rectangular brass container A filled with methyl alcohol is supported by glass pillars. By means of a wire T connected to the contact U_1 and by means of the contact U_2 connected to the chamber floor D of copper, it is possible to apply electric cleaning fields between the top and the bottom of the chamber. The temperature distribution in the chamber is measured by means of a thermoelement (not reproduced in the figure), of which one junction can be inserted through the hole T at the chamber roof (the other junction being kept in a beaker filled with melting ice). The radioactive sample is at the center Cf of the sensitive region. The floor is cooled by dry

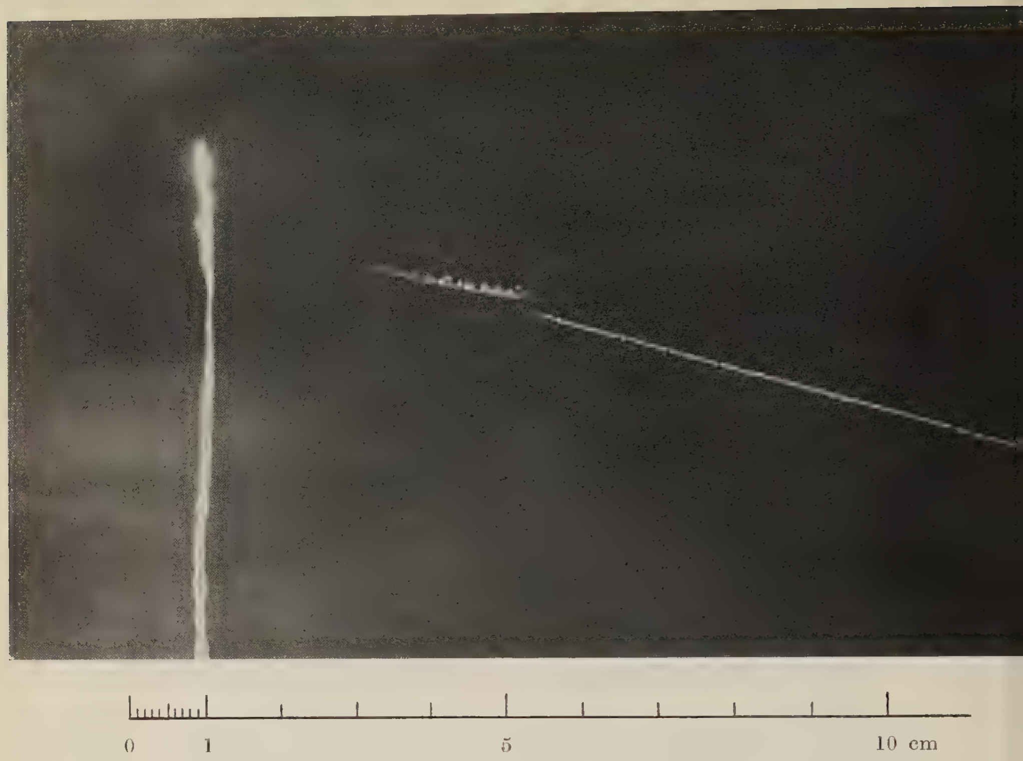

Fig. 3. An old α track from Cf^{252} and a long proton track ($E \approx 2.5$ MeV), probably a recoil from a neutron. Pressure 1 atm.

ice CO_2, which is resting on a heat insulator I resting on a wooden disk. This assembly is pressed by the springs S against the chamber floor D. The side walls of the CO_2 supply space are made of wood, the front and the back walls of plexiglass. The lighting device consists of two 35-watt electric lamps in the foci of parabolic reflectors L. Heat absorbing glass disks Q are inserted in the light beams. The directions of the beams can be adjusted by means of screws. The arrangements for photographing the tracks are the same as for the low pressure chamber and are described below.

The size of the dry ice pieces is 5 × 8 × 25 cm. Six pieces of dry ice maintain operation of the diffusion cloud chamber for about 12 hours.

Fig. 2 shows photographs of (*a*) α tracks from ThC′ and a track of an electron crossing the long α track. The active deposit is located at the end of a copper wire (vertical line in the figure). (*b*) α track from californium 252. (*c*) tracks of fragments from the spontaneous fission of californium 252. The californium sample holder is heated by a light projector in order to prevent condensation of alcohol on the foil. The heat of the foil causes a slight turbulence in the gas, destroying the first parts of the tracks.

Fig. 3 shows an old, disappearing α track from californium and a long proton track, probably caused by recoil from a neutron.

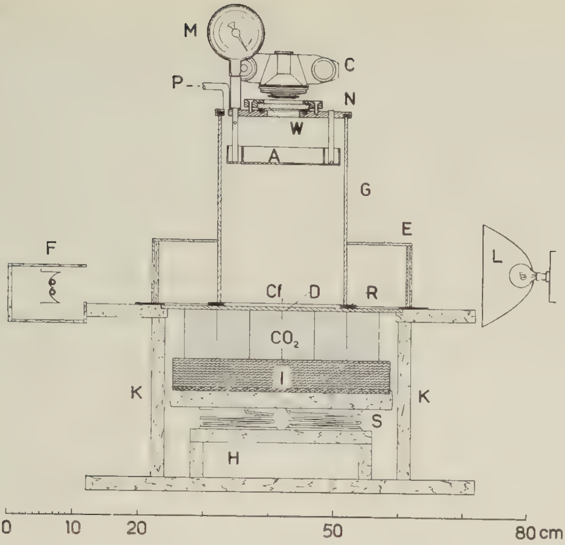

Fig. 4. Design of the low pressure diffusion cloud chamber.

The low pressure diffusion cloud chamber

The design of the low pressure diffusion cloud chamber is shown in Fig. 4. The lower part of the apparatus is the same as that in the demonstration equipment. The diffusion chamber consists of a glass cylinder G surrounded by a lower protection E of glass, both resting on rubber seals against the bottom disk. The roof of the cylinder is a disk of brass carrying the circular container A, which is filled with methyl alcohol through the tube N. The cylinder is evacuated through P and the pressure in the chamber is shown by the gauge M. A glass window W permits photographs of tracks to be taken with the camera C. The light for the continuous observation is provided by two 35-watt electric lamps L as before, and a commercial xenon flash light tube, "Brown-Hobby" type BH100, is used when photographs are taken. The xenon tube has been placed in front of a reflector in the cover F.

The low pressure chamber worked very satisfactorily at all pressures from 1 to 0.1 atmospheres. A constant voltage of only 12 volts between top and bottom maintained continuous working conditions. The use of the glass shielding E prevents disturbing heat conduction through the lower part of the cylinder G and hence also prevents gas flows near the wall of the cylinder.

The photographic arrangement consisted of a Contaflex 1:2.8 camera, aperture 1:16, time adjustment 0.008 sec, and Ilford HP3 film.

Figs. 5–9 show tracks of fragments from the spontaneous fission of californium 252. The pressure in the chamber was 0.2 atmospheres.

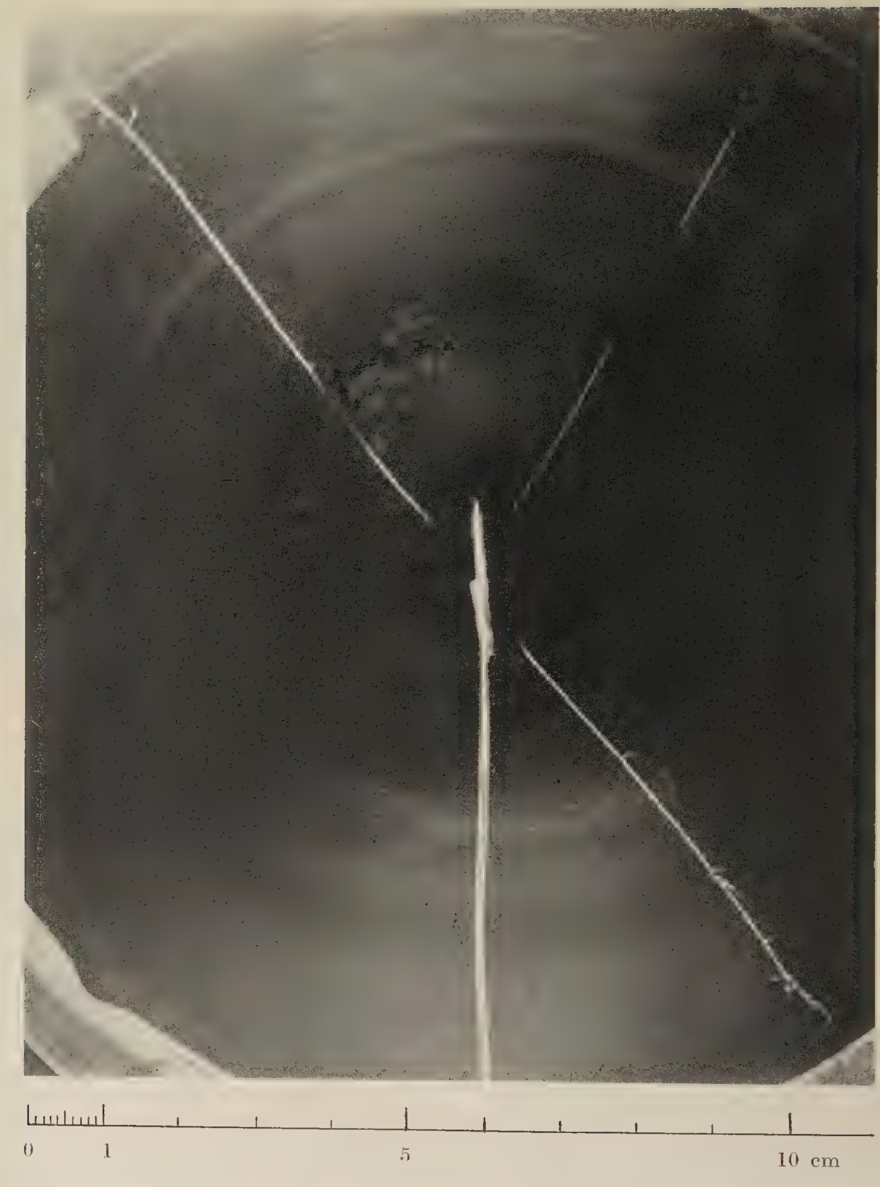

Fig. 5. Spontaneous fission tracks (forked) and an α track from Cf^{252}. The vertical line is the sample holder. The concentric circles are reflections of the top window and the alcohol container in the wet bottom. The pressure is 0.2 atm.

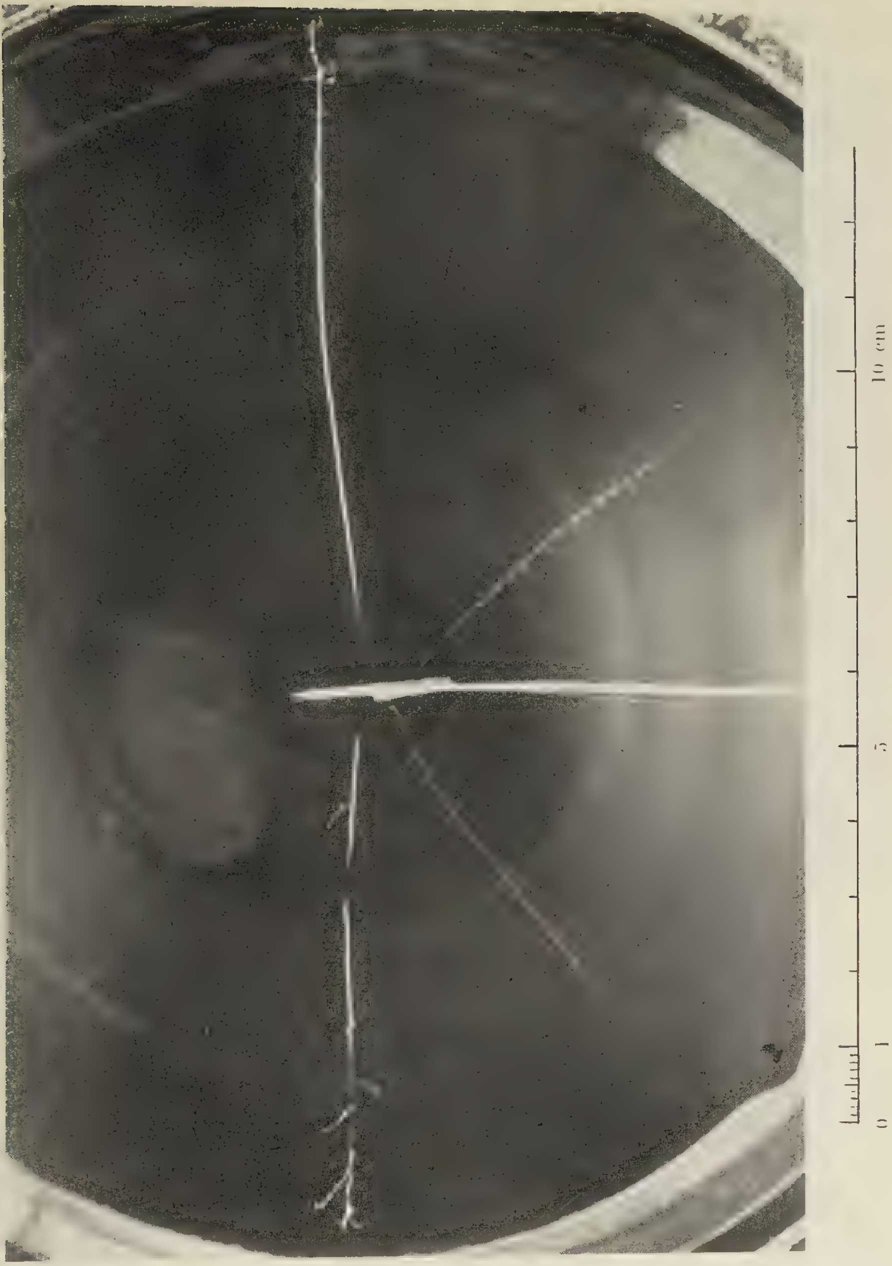

Fig. 6. Fission and α tracks from Cf^{252}.

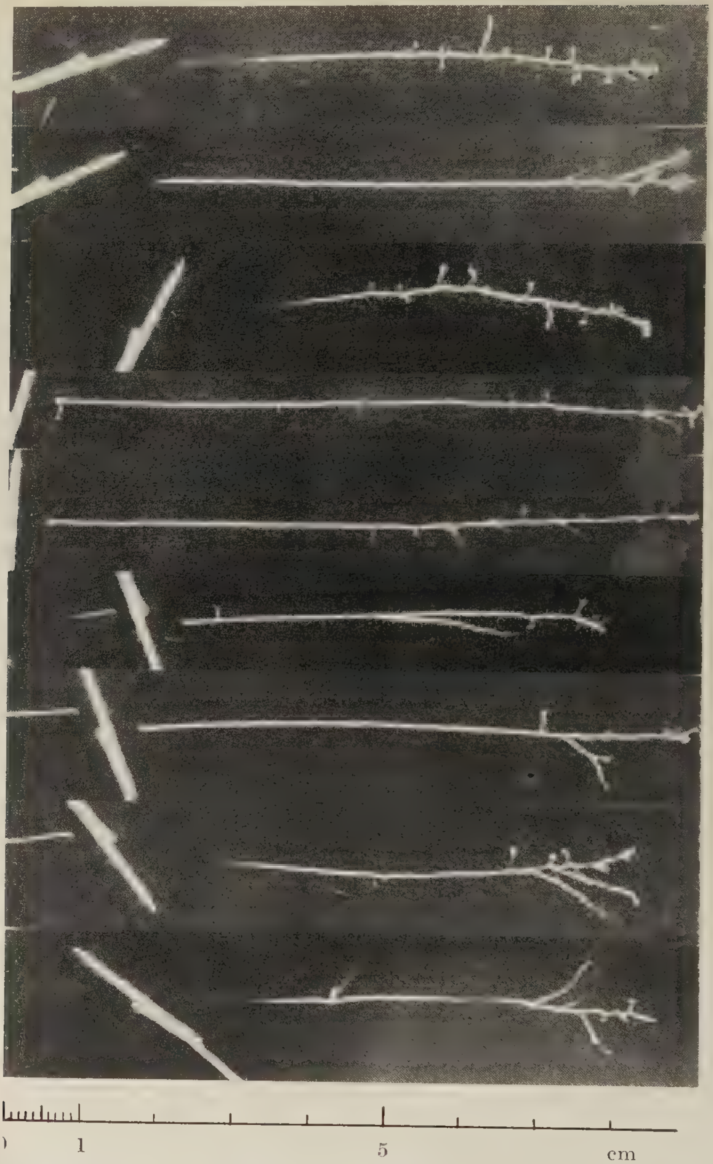

Fig. 7. A number of Cf^{252} fission tracks. The sample is the heavy line to the left. It is obvious that the more branches, the shorter the range of the fragment. The pressure is 0.2 atm.

Summary

The development of the diffusion cloud chamber is briefly given. A diffusion cloud chamber for demonstration purposes and a low pressure diffusion chamber have

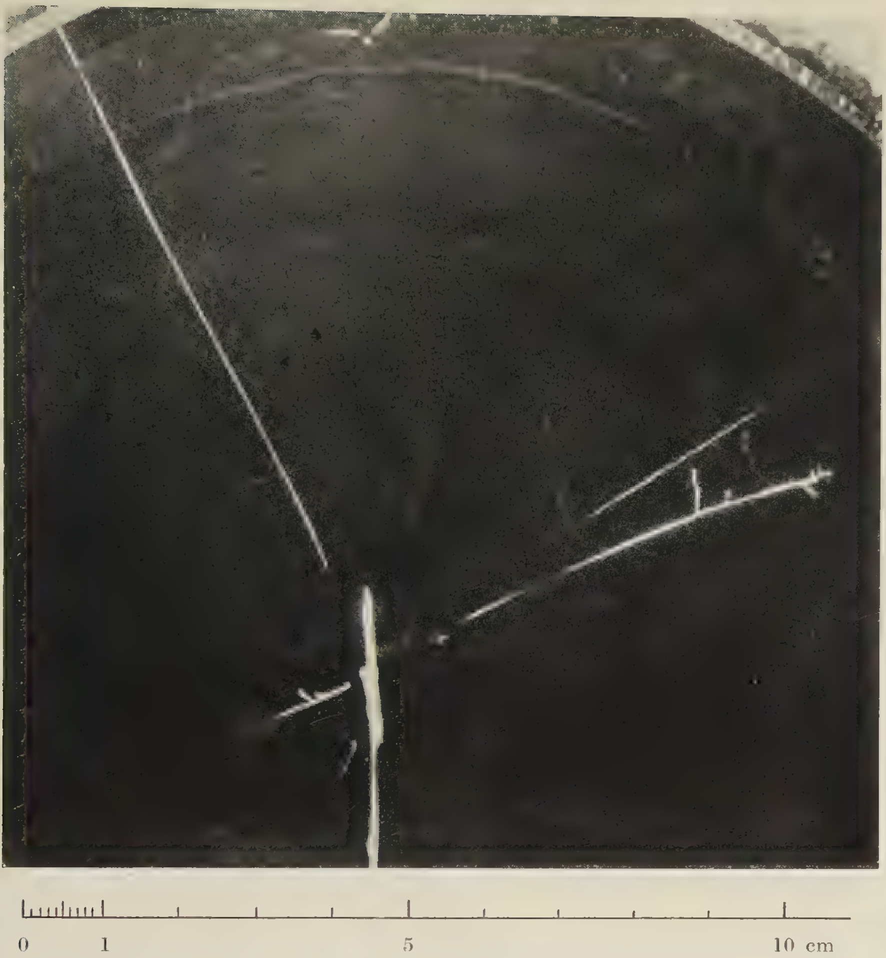

Fig. 8. Fission and α tracks from Cf^{252}.

een constructed. Tracks of α particles and fission fragments from californium 252 nd electrons and protons are shown, the first two types of tracks at a pressure of .2 atmospheres.

Nobel Institute of Physics, Stockholm 50.

REFERENCES

1. E. Hjalmar, H. Slätis, and S. G. Thompson, Phys. Rev. *100*, 1542, 1955 and Arkiv f. Fysik *10*, 357, 1956.
2. A. Langsdorf, Rev. Sci. Inst. *10*, 91, 1939.
3. T. S. Needels and C. E. Nielsen, Rev. Sci. Inst. *21*, 976, 1950.
4. E. W. Cowan, Rev. Sci. Inst. *21*, 991, 1950.
5. D. H. Miller, E. C. Fowler, and R. P. Shutt, Rev. Sci. Inst. *22*, 280, 1951.

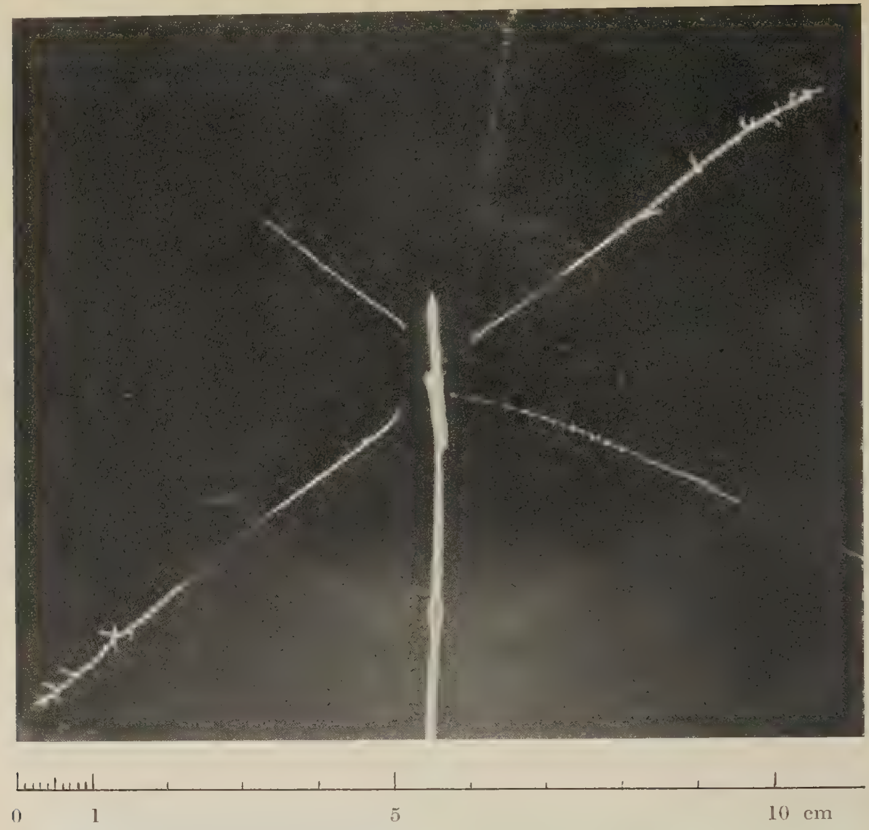

Fig. 9. Fission tracks and two α tracks from Cf^{252}. The α track to the right is old and has started to disappear.

6. W. B. Fowler, R. P. Shutt, A. M. Thorndike, and A. L. Whittemore, Phys. Rev. *95*, 1026, 1954, Rev. Sci. Inst. *25*, 996, 1954.
6a. R. A. Schluter and S. C. Wright, Rev. Sci. Inst. *26*, 1053, 1955.
7. R. P. Shutt, Rev. Sci. Inst. *22*, 730, 1951.
8. A. J. Barnard and J. R. Atkinson, Nature *169*, 170, 1952.
9. A. L. Kuehner, J. Chem. Educ. *29*, 511, 1952.
10. A. Voisin, J. Phys. et Rad. *14*, 459, 1953.
11. T. Wilner, Elementa *36*, 265, 1953.
12. A. B. Milojević, M. A. Cerineo, and B. J. Lalović, Bull. Inst. Nucl. Sci. ‘‘Boris Kidrich’ *3*, 23, 1953.
13. M. Snowden and A. R. Bevan, J. Sci. Inst. *30*, 3, 1953.
14. A. R. Bevan, A.E.R.E. GP/R 1215, 1953.
15. H. C. Whitby, A.E.R.E. GP/R 1129, 1953.

Tryckt den 12 april 1956

Uppsala 1956. Almqvist & Wiksells Boktryckeri AB

ARKIV FÖR FYSIK Band 10 nr 36

Communicated 23 November 1955 by Manne Siegbahn and G. Borelius

A spectrometer for high resolution nuclear magnetic resonance experiments

By G. Lindström and B. N. Bhar

With 4 figures in the text

General introduction

Soon after the discovery of "nuclear induction" [1] and "nuclear magnetic resonance absorption" [2], the methods found their immediate application to the precise determination of magnetic moments of stable as well as some radioactive nuclei. These measurements were mostly based upon an accurate comparison of resonance frequencies of the subject nuclei with that of protons taken as standard. In the course of such precise derminations of nuclear moments it was found that the choice of a compound can have an effect upon the frequency at which nuclear resonance occurs. Identical nuclei immersed in a certain externally applied magnetic field can lead to different resonance frequencies if they are situated in different chemical environments. Such shift in resonance frequencies, which were independently and almost simultaneously observed by a number of investigators [3, 4, 5, 6], is now well known as the "chemical shift" in nuclear magnetic resonance phenomena. The studies of these chemical shifts and other fine structure of resonance lines, as will be discussed below, may be called in general "high resolution nuclear magnetic resonance" spectroscopy.

It is now well established that the nuclear magnetic resonance frequencies depend upon the electronic environment of the nucleus. The resonance frequency of the nuclear moment is shifted from that value which it would have if the nucleus were devoid of all its neighbouring orbital electrons. By the interaction of the externally applied magnetic field with the orbital electrons, the field at the position of the nucleus is slightly modified in value from that of the externally applied one; in other words, the electrons around a given nucleus create a "diamagnetic shielding". The electronic distribution around nuclei of the same species is different if they are contained in different chemical compounds. Not only in chemically different molecules would the nuclei of the same nuclear species experience different diamagnetic shielding, but even nuclei of the same species, when contained in different chemical environments n the same molecule and hence in regions of different diamagnetic shielding, would manifest the chemical shift effect. In certain cases where the natural linewidth of the spins in question is extremely narrow as in liquids and gases, it is possible to observe discrete resonance lines from each of these chemically non-equivalent nuclei. From the extent of the shift of different resonance lines from one taken as reference (often the proton resonance from water is chosen for that purpose) one can have a fair estimate of the electron distribution in the molecule [7, 8, 9, 10, 11]. The areas under these chemically shifted resonance lines are proportional to the number of nuclei present in the non-equivalent group. This information coupled with the fairly well characterized proton chemical shifts of certain organic groups like olefinic, aromatic and aliphatic groups is of immense value in the study of molecular structure of hydrocarbons. Also, in fluorocarbons from the well-characterized resonance shifts of certain fluorine groups like $-\mathrm{CF}_3$, $>\mathrm{CF}_2$, $-\!\!>\mathrm{C}-\mathrm{F}$ etc., one can determine the distribution of fluorine in the molecule [12].

It should be mentioned here that in molecules, in addition to shifts due to effects of diamagnetism originating from the interaction of the orbital electrons with the magnetic field, the nuclei may experience shifts due to induced paramagnetism which can appear when there exist several low lying electronic states of the molecule near the ground state. Because these two effects are linearly proportional to the applied magnetic field, it is impossible to distinguish them from one another. In addition to chemical shifts originating from the electronic environment of the nuclei, a chemically shifted nuclear resonance line may be further split to give a complex line structure due to coupling interaction of neighbouring nuclei via the electron cloud. In fluids the direct interaction among the neighbouring groups of spins averages out due to rapid and random rotations of a molecule. The indirect interaction due to spin–spin coupling via the bonding electrons (now termed as J-coupling) is invariant to rotation and therefore can be observed in liquids and vapours. The method of high resolution nuclear magnetic resonance spectroscopy has revealed this new kind of nuclear interaction that can exist within a molecule [13, 14, 15]. As first proposed by Gutowsky *et al.*, if two groups of non-equivalent electron-coupled magnetic nuclei are represented by $X_m Y_n$, then the resonance lines from group X and group Y generally would be split into $2nI_y + 1$ and $2mI_x + 1$ respectively. I_x and I_y are the spin quantum numbers of the nucleus X and Y respectively. This splitting is independent of the applied field or of temperature and states of aggregation of the sample. By noting the number into which a resonance line of one group of nuclei is split by its neighbouring group of nuclei by the spin–spin coupling, the nuclear spin quantum number of a nucleus can be accurately assigned [16]. The presence or absence of proper splitting due to spin–spin coupling often helps in confirming or rejecting the presence of certain chemical groups like ethyl, isopropyl etc. within a molecule.

If nuclei of any group are undergoing rapid chemical exchange, i.e. if the electronic environment of the nuclei in question is changing at a sufficiently rapid rate, then the fine structure of nuclear resonance line, as mentioned above, obliterates and the chemically shifted resonance lines may coalesce to form a common line. Gutowsky and Saika [17] have presented a theory of chemical shifts in cases when such dissociation and chemical exchange are taking place. Their theory may be approximately valid for certain electrolytes, but is inadequate to explain certain chemical shifts such as in case of acetic acid–water system according to our previous findings [18, 19], which were subsequently corroborated by Shoolery [20]. In previous communications we have discussed some aspects of our observations with reference to molecular association by virtue of hydrogen bonding. In what follows we shall describe the experimental part and the technique of high resolution nuclear magnetic resonance.

Experimental arrangement and technique

Chemical shift and other features of the high resolution nuclear magnetic resonance spectra are best studied by the "nuclear induction" method of Bloch or by the Purcell method for "nuclear magnetic resonance absorption". The principles and other details of these methods are adequately described in their original works [21, 22]. Some modifications of the experimental method of these basic designs have since then been introduced, the most recent one being the double resonance technique in the field of high resolution n.m.r., in which the effect of simultaneous resonance of two species of nuclei in the same molecule is observed [23].

In our work we have employed the nuclear magnetic resonance absorption method and nuclear signals were detected by the double-T bridge as shown in Fig. 2. The bridge was originally proposed by Tuttle [24] in high frequency work and introduced by Grivet *et al.* [25] in the nuclear magnetic resonance work. The advantage of this type of bridge over the Purcell bridge is that the balance of the bridge in regard to ndependent adjustment of amplitude and phase balance can be done quite easily. This can be seen from a brief analysis of the bridge that will be given here while describing the bridge. In this bridge we have also incorporated an arrangement for rotating the sample for line-narrowing as has been proposed by Bloch [36]. The description of the arrangement for rotating the sample ("spinning sample" as it is often called) will be given below.

A block diagram of the experimental arrangement is given in Fig. 1. The sample containing the subject nuclei was placed in the coil L of the bridge. A portion of the bridge containing the coil was placed between the pole-gap of the magnet. The axis of the coil was perpendicular to the magnetic field. Arrangements for slight variation of the spatial orientation of the coil axis were also provided by mechanical devices. The bridge was fed by a crystal-controlled oscillator through co-axial cable

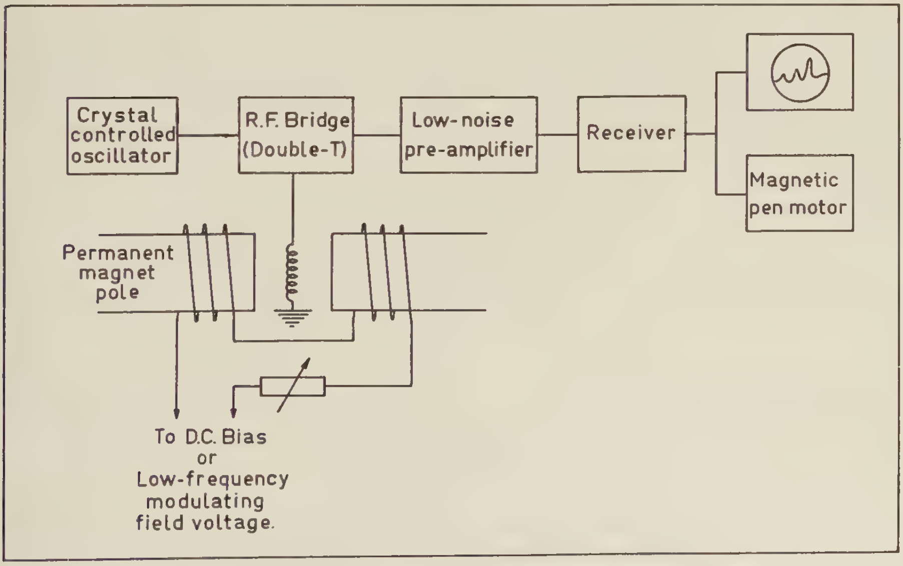

Fig. 1. Block diagram of the experimental arrangement.

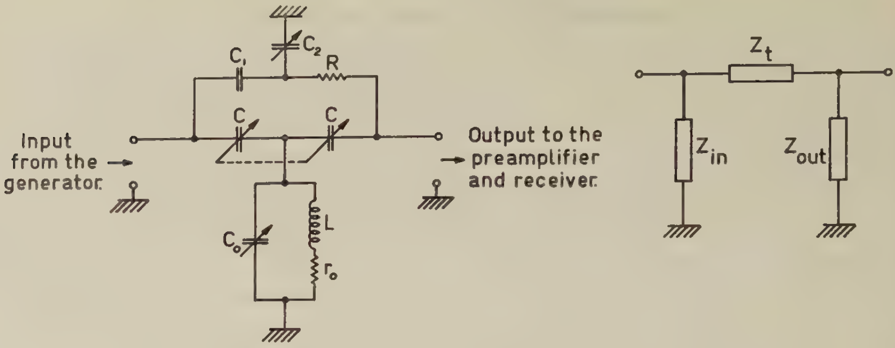

Fig. 2. Principle of the double-T bridge.

and an attenuator so that the power of rf oscillation feeding the bridge and the coil in turn can be adjusted to the desired level. If the bridge is balanced to a frequency f and γ is the gyromagnetic ratio of the subject nuclei, then the resonance occurs at magnetic field H given by the well-known relation $2\pi f = \gamma H$. In high resolution n.m.r. the frequency is kept constant and resonance signals from nuclei residing in regions of different diamagnetic shielding are observed by varying H. The resonance unbalances the bridge and gives rise to a nuclear signal, either absorption, dispersion, or a mixture of the two, according to the amplitude and phase balance of the bridge. The nuclear signals from the bridge were led to a low-noise preamplifier, the high tension of which was supplied from a stabilized power supply. The preamplified signal was then fed to a high gain receiver (National HRO-50 T); the output from the audiostage was displayed on the oscilloscope or when necessary the d-c voltage across a high resistor in the detector circuit was coupled to a D.C. amplifier followed by a magnetic pen motor of the Brush Development Comp., U.S.A.

Before going into the details it may be mentioned here at the outset that the essential requirements in this technique are that the frequency stability of the stimulating radio-frequency field, the magnetic field stability, and magnetic field homogeneity over the sample volume should be exceedingly high (at least a part or so in ten millions).

The stability of the magnetic field can be obtained by the use of a permanent magnet, although a proton-controlled electromagnet [27] can be used, but it seems that the use of a permanent magnet is less troublesome, especially when the cooling arrangement necessary in an electromagnet when working at high field is considered. In our work we have employed a permanent magnet giving a field of approximately 3285 gauss with a gap width of 38 mm. The description of the magnet will be given below.

Regarding frequency stability of the rf field, we have used a crystal-controlled oscillator of fundamental frequency 6.993 Mc/s; the second harmonic oscillation 13.997 Mc/s was used for our purpose. Particular care for the stability of oscillation was taken by using stable power source from battery supply. We have also tried a General Radio 805-C signal generator but it proved to be unsatisfactory in the high resolution n.m.r. because of its relatively poor frequency stability.

Variation of the crystal frequency or of the magnetic field of the permanent magnet due to variation of temperature was reduced by controlling the temperature the room in which the experiment was housed to within ±$^1/_2$°C by a contact-ercury thermometer arrangement. A very high stability of the crystal frequency rther could be obtained by housing the crystal in a specially designed commercially ailable crystal oven. The effect of seasonal variation of temperature on the field rength of the permanent magnet [28] in delocalizing the homogeneity of the magnet as however observed. It may be pointed out that the start time stability of the agnetic field will be extremely good even with the simple temperature control used, ecause a magnet of this size has a temperature–time constant that is great.

he magnet

The permanent magnet has been designed so that it could be used for many fferent types of experiments necessitating a stable magnetic field. Fig. 3 shows drawing of the permanent magnet.

By combining the relation $\oint H_s\, ds = 0$ with the condition for constancy of flux is easy to show that the volume of permanent-magnet material required is, (neglect-g the reluctance of the iron in the yoke)

$$A_p\, l_p = \frac{H_g^2\, A_g\, l_g \cdot q}{H_p\, B_p}$$

here B_p is the flux density in the permanent-magnet steel, A_p and A_g are the oss sections of the permanent-magnet steel and air-gap respectively, q is the leakage ctor, and H_g and H_p are the field strengths in the air-gap and in the permanent-agnet material respectively.

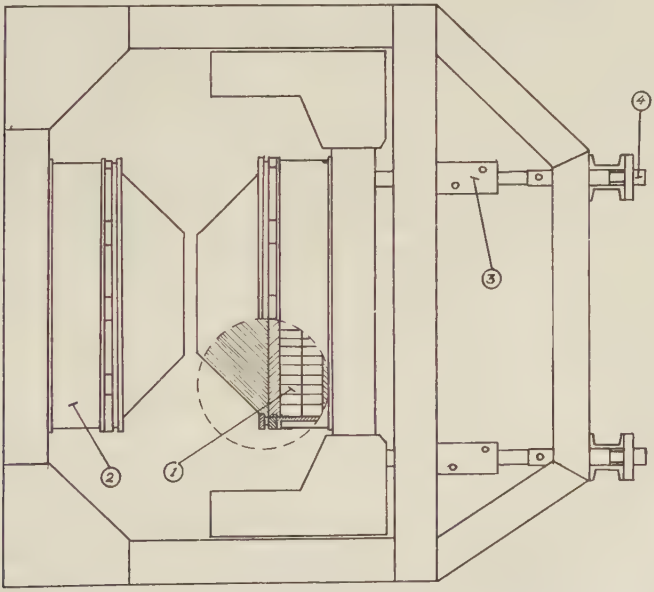

g. 3. Diagram of the permanent magnet. Portion marked ① contains the permanent magnet aterials. Portion marked ② contains the magnetizing coils. Screw arrangements marked ③ and ④ make possible motion of one of the pole pieces laterally.

For the magnetic material used in this magnet (trade name Ticonal[1]), $B_p \cdot H_p = 5 \cdot 10^6$ gauss oersted. The magnetic material is manufactured in rectangular bars 25 mm × 25 mm × 60 mm. They are polished so that the length is 60 ± 0.05 mm. Each pole consists of two layers with 750 pieces of these bars. The whole magnet therefore contains 3000 pieces comprising 112,500 mm^3 of this material.

The diameter of the pole pieces seen in the picture is 80 cm and they are 3 cm thick and with a leakage factor of 1.8 and an air gap of 4 cm. The relation gives a field strength of about 4000 gauss, which is in fair agreement with observed values.

Fig. 3 shows the dimensions of the magnet and the tapering pole tips in it, the tapered ends being of 40-cm diameter. With the pole tip and with the same air gap as before (4 cm) the field strength may go up to about 7000 gauss. The pole at the right hand side in the figure can be laterally moved so that the air gap can be changed from zero to 50 cm with the possibility of varying the field strength within a wide range.

It may also be pointed out that the change of the pole gap is being made by means of three screws having very low pitch, which enables one to adjust the geometrical configurations of the pole pieces to achieve a good homogeneity of the magnetic field.

The permanent-magnet pieces are placed inside two cylinders of non-magnetic material around which the magnetizing coils are wounded. Around each pole there are ten parallel copper coils with 35 turns. The magnet can be magnetized with about 2000 amperes, which means 140,000 ampere turns.

The bridge

The double-T bridge, unlike the Purcell bridge, does not contain any dummy circuit and the independent adjustment of amplitude and phase balance is easier than that in the latter one. As the balance of all high frequency bridges is dependent upon frequency, any frequency drift or frequency modulation effect of the stimulating radio field should be avoided. The use of a crystal-controlled frequency however ensures this. Regarding the bridge in Fig. 2*a*, since each T network can be transformed into a π network, the double-T would be equivalent to a π network (Fig. 2*b*). The transformed impedance Z_t should be infinite or $1/Z_t$ should be zero at the balance condition. The bridge would be balanced in amplitude and phase if the real and imaginary part, i.e. the resistive and reactive part of $1/Z_t$, are separately equal to zero.

Now it can be shown that for amplitude balance of the bridge

$$R\,R_p\,c^2\,w^2\left(1+\frac{c_2}{c_1}\right)-1=0 \tag{1}$$

and for phase balance of the bridge

$$L\,w^2\left(2\,c+c_0+\frac{c^2}{c_1}\right)-1=0, \tag{2}$$

where R_p is the equivalent shunt resistance of the coil and w is the angular frequency of rf oscillation at which the bridge is balanced. With the bridge balanced in amplitude, any unbalance in phase due to inequalities in (2) results in a signal at the output of the bridge that would be of the dispersion type. This balance can be achieved y varying c_0, while doing so it does not affect the amplitude balance condition as (1) loes not contain c_0. Similarly the absorption type of signal can be obtained by unalancing the bridge by varying c_2, which operation does not affect phase balance ondition as (2) does not contain c_2. Thus the amplitude and phase balance of the ridge can be done quite independently.

---

[1] Manufactured by Fagersta Bruks Aktiebolag, Fagersta, Sweden.

The actual values of the components used in the bridge are given below:

c variable from 10–20 $\mu\mu$f
c_0 ,, ,, 10–200 $\mu\mu$f
c_2 ,, ,, 10–350 and c_1 was equal to 150 $\mu\mu$f
R was 70 ohms and L was nearly 2 μH.

The coil containing 20 turns of 28 swg copper wire was 9 mm long and 3 mm inside iameter. The Q of the coil was about 100 at 14 Mc/s. The condensers were of conventional variable type, the control knobs of which were mounted on shafts some 60 cm ong. The grounded ends of all connections were brought to a common point.

On the two sides of the brass box shielding the rf coils each containing 10 turns f wire were mounted for the purpose of modulating the magnetic field at low frequency.

A line-narrowing experiment

Experiments in the field of high resolution nuclear magnetic resonance work may e termed as "line-narrowing" experiments [26, 29]. As the resolution of closely paced lines is often obliterated by the adverse line broadening effect of the inhomogeneity of the magnetic field, it is necessary at the very outset of such experiments o explore the best homogeneous part of the magnetic field and to make it homogeneous to at least 1 part in a ten millions for successful observation of a resolved icture of n.m.r. spectra.

With the purpose of finding the most homogeneous part of the magnetic field, we irst started with a somewhat bigger sample of ethyl alcohol ($CH_3\ CH_2\ OH$) of nearly .1 cc and displayed the proton resonance absorption signal on the oscilloscope sing the conventional modulation method. For increasing the homogeneity of the agnetic field over the sample volume, which revealed itself in the narrowness of he resonance line, we resorted to various procedures, (i) changing the geometrical onfigurations between the pole faces, (ii) changing the position of the sample in he space between the pole faces, and (iii) decreasing the sample volume. While ecreasing the sample volume care was taken to decrease the rf power, if necessary, o that the line may not be broadened by the saturation effect. The lines were first bserved on an oscilloscope and then written by a magnetic pen-motor, which enabled s to measure the width of the lines rather quickly. The magnetic field was varied hrough resonance by passing current through the magnet coils which were originally sed in parallel to magnetize the magnet. In series with the coils was a helical potentioeter, which was varied by means of a motor. This arrangement of varying the magetic field was later replaced by a saw-tooth voltage generator, as it was found that he former arrangement was a source of noise. To determine the rate of change of agnetic field through resonance a milliammeter was connected in series with the agnet coils, the meter being properly calibrated in terms of the corresponding magetic field change.

In the efforts of narrowing the line more and more, the resonance signal from a sample volume of 0.02 cc just showed the splitting into three components arising from three groups of protons, viz. the OH-group protons, the CH_2-group protons, and the CH_3-group protons [30]. By decreasing the sample volume, we no doubt gained in homogeneity over the sample volume, but sacrificed to some extent the signal strength. It seemed worth while also not to decrease what is called the filling factor [22] of the coil by only decreasing the sample volume relative to the volume of the space inside the coil. Thus, we also used a smaller rf coil while decreasing the sample volume. However, care was taken that the sample was in the central region of the rf coil so that inhomogeneities arising from the ends of the rf coil have no adverse effect on the sample. The sample volume with which the main three peaks from ethyl alcohol were resolved was nearly 0.01 cc contained in a test tube of 2 mm inside diameter and 3 mm outside diameter. While using such small sample volume, we had to adjust also the optimum rf power in compliance, however, with the speed with which the magnetic field was swept through resonance. The speed should be slow enough so that a peak is reached when the resonance effect from its preceding one was over and that the speed of the passage through resonance does not give rise to transients according to the condition [31] that $T_2 \sqrt{|\gamma| \left(\frac{\partial H_0}{\partial t}\right)_{\text{res}}} < 1/2$. The speed used was nearly 5.8 milligauss/sec. To increase further the homogeneity of the magnetic field over the sample volume we have tried to use small compensating coils, 10 on each side of the brass box shielding the rf coil. By passing small currents from storage batteries through them, it was possible to annul inhomogeneity over the sample volume to some extent. By using the compensation coils the homogeneity was no doubt improved, but it seemed to be more time-consuming every time to adjust the currents through all of these coils. Thus we thought it worth while to achieve our goal of "line-narrowing" still further by imparting macroscopic motion to the sample as has been proposed by Bloch.

According to Bloch [26], when the sample is rapidly rotated in a magnetic field the magnetic field inhomogeneities over the sample partially average out when the nuclei are carried through the distribution of the field in a time short compared to the transversal relaxation time. The rotational speed necessary to narrow the line is dependent upon the inhomogeneity of the field and the gyromagnetic ratio of the subject nuclei. For a proton sample rotational frequencies from 50 r.p.m. to some hundreds are in general necessary for increasing the resolution. The rotation is executed by blowing air at high pressure against the vanes mounted on a shaft at the other end of which a test tube containing the sample is rigidly coupled. By varying the flow of air the rotational speed is changed. Fig. 4 shows the interesting result of rotating the sample; the upper picture is the signal from a stationary sample ethyl alcohol and the lower one is from the same sample when it is rotated. By rotating the sample not only the three major peaks have come out sharply, but also the finer details of splittings due to indirect spin–spin coupling are vividly discernible. The finer splittings are field-independent as has been mentioned earlier. We have observed that the spacing between the component lines is 1.35 ± 0.25 milligauss.

Here, the proton peak because of OH group does not show any splitting into possible finer components. According to Anderson [32] the explanation is that protons of OH groups are undergoing rapid exchanges with H^+ or OH^- ions which may be present as impurities in the alcohol. It has been mentioned already that obliteration of fine details and coalition of otherwise different lines into a single line take place

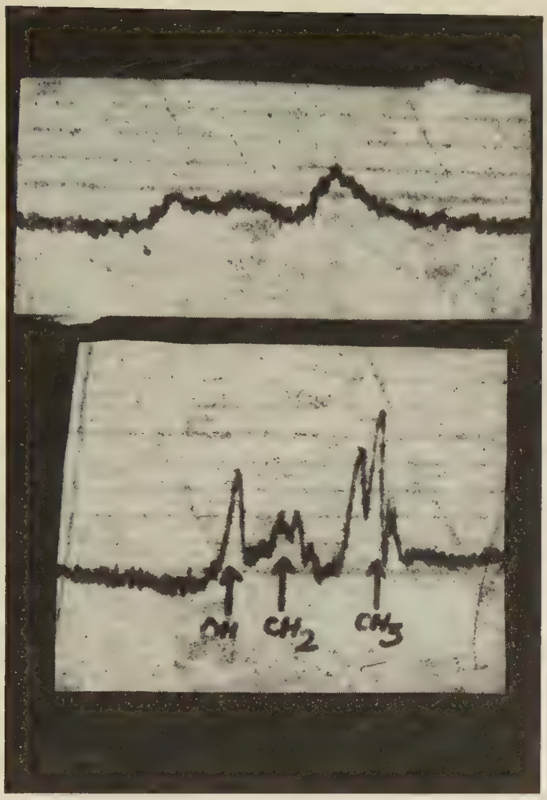

g. 4. The effect of line-narrowing by rotating a sample of ethyl alcohol in the magnetic field. e upper trace is the signal from a stationary sample. The lower one is the signal from the sample when it is rotated.

ıen rapid exchange of chemically non-equivalent nuclei is going on. We have also served such effects and have described them with some associated phenomena in r previous communications [18, 19].

Concluding remarks

With the experimental arrangement described above it has been possible for us observe some resolved proton spectra with finer details in a rather low field of e order of 3000 gauss. It is, however, advantageous to perform high resolution n.m.r. rk at higher field strength of the order of 7000 gauss in which a smaller sample lume can be used and thereby the homogeneity of the magnetic field over the mple can be increased. The intensity of the signal is not sacrificed by using smaller mple volume when working at higher field strength as the signal strength increases 7/4 power of the magnetic field.

Summary

An apparatus for high resolution nuclear magnetic resonance experiments for the studies of "chemical shift" and other details of the nuclear resonance lines in liquids is described here with detailed procedures, experimental technique and design of the radio-frequency bridge and permanent magnet used in the experiment. The origin of the "chemical shift" and fine components of nuclear magnetic resonance spectra is also discussed here. Bloch's method of "line-narrowing" by macroscopic motion of the sample is utilized here to observe the splitting of nuclear resonance lines originating from electron-coupled spin–spin interaction of non-equivalent protons in ethyl alcohol. The resolution of the apparatus is at present of the order of one part in 10 millions.

ACKNOWLEDGEMENTS

The work described here and in our previous communications has been supported by grants from the Swedish Natural Science Research Council and the Swedish Atomic Energy Committee for which we express our gratitude. Ing. J. Mednis and especially Ing. B. Johansson have given us technical assistance for which we thank them heartily. One of us (B. N. B.) wishes to express his profound gratitude to the authorities of the University of Calcutta for the award of the 1954 Ramgopal Ghosh Scholarship, and to Professor Manne Siegbahn, N. L. Director of the Nobel Institute of Physics, for his kindness in giving him a place in his laboratory to work on nuclear magnetic resonance.

Nobel Institute of Physics, Stockholm 50, Sweden.

REFERENCES

1. F. Bloch, W. W. Hansen and M. E. Packard, Phys. Rev. *69*, 127 (1946).
2. E. M. Purcell, H. C. Torrey and R. V. Pound, Phys. Rev. *69*, 37 (1946).
3. W. D. Knight, Phys. Rev. *76*, 1259 (1949).
4. K. Siegbahn and G. Lindström, Arkiv f. Fys. *1*, 193 (1949).
5. W. G. Proctor and F. C. Yu, Phys. Rev. *77*, 717 (1950).
6. W. C. Dickinson, Phys. Rev. *77*, 736 (1950).
7. H. S. Gutowsky, D. W. McCall, B. R. McGarvey and L. H. Meyer, J. Am. Chem. Soc. *74*, 4809 (1952).
8. L. H. Meyer and H. S. Gutowsky, J. Phys. Chem. *57*, 481 (1953).
9. L. H. Meyer, A. Saika and H. S. Gutowsky, J. Am. Chem. Soc. *75*, 4567 (1953).
10. H. S. Gutowsky and D. W. McCall, J. Chem. Phys. *22*, 162 (1954).
11. H. S. Gutowsky, R. L. Rutledge, Milton Tamres and Scott Searles, J. Am. Chem. Soc. *76*, 4242 (1954).
12. J. N. Shoolery, Analytical Chemistry *26*, 1400 (1954).
13. H. S. Gutowsky and D. W. McCall, Phys. Rev. *82*, 748 (1951).
14. H. S. Gutowsky, D. W. McCall and C. P. Slitcher, Phys. Rev. *84*, 589 (1951).
15. E. L. Hahn and D. E. Maxwell, Phys. Rev. *84*, 1246 (1951).
16. R. A. Ogg and James D. Ray, J. Chem. Phys. *22*, 147 (1954).
17. H. S. Gutowsky and A. Saika, J. Chem. Phys. *21*, 1688 (1953).
18. B. N. Bhar, W. Forsling and G. Lindström, Arkiv f. Fys. *10*, 59 (1955).
19. B. N. Bhar and G. Lindström, J. Chem. Phys. (in print).
20. J. N. Shoolery, (Private communication for which we wish to express our thanks to Dr. Shoolery).
21. F. Bloch, W. W. Hansen and M. E. Packard, Phys. Rev. *70*, 474 (1946).
22. N. Bloembergen, E. M. Purcell and R. V. Pound, Phys. Rev. *73*, 679 (1948).
23. A. L. Bloom and J. N. Shoolery, Phys. Rev. *97*, 1261 (1955).

W. N. Tuttle, Proc. I.R.E. *28*, 23 (1940).
P. Grivet, M. Soutif and M. Buyle, C. R. Acad. Sc. (Paris), *229*, 113 (1949).
F. Bloch, Phys. Rev. *94*, 496 (1954).
M. E. Packard, Rev. Sci. Inst. *19*, 439 (1948).
R. V. Pound, Phys. Rev. *79*, 685 (1950).
W. A. Anderson and J. T. Arnold, Phys. Rev. *94*, 497 (1954).
J. T. Arnold, S. S. Dharmatti and M. E. Packard, J. Chem. Phys. *19*, 507 (1951).
B. A. Jacobsohn and R. K. Wangsness, Phys. Rev. *73*, 942 (1948).
W. A. Anderson, (1955 Radio-frequency and Microwave Spectroscopy Conference at Cambridge).

Tryckt den 25 april 1956

Uppsala 1956. Almqvist & Wiksells Boktryckeri AB

ARKIV FÖR FYSIK Band 10 nr 37

Communicated 14 March 1956 by MANNE SIEGBAHN and IVAR WALLER

Direct-coupled amplifier and ratiometer for a single-beam mass spectrometer

By CARL REUTERSWÄRD

With 10 figures in the text

Abstract

Design considerations and details of construction are given for an amplifier intended for ecision measurements on isotopes of low abundance by rapid scanning of the mass spectrum. ırther, for continuous accurate determination of isotope ratio, the single-beam mass spectroeter is converted to a two-isotope ratio meter by combining an automatic switching device th a null method of comparing voltages.

I. Introduction

The advances in mass spectrometry are intimately linked to the development of ethods for measuring small currents accurately and rapidly. In the beginning, the ıadrant electrometer was the tool, exact, but sluggish and cumbersome, and the sults could hardly compare with the contemporary achievements of photographic tensitometry by the mass spectrograph, and would nowadays be classified as only ıalitative. The arrival of special thermionic tubes for the measurement of minute ırrents, particularly the space-charge grid electrometer tetrode, in the early 1930's ıanged the situation radically, and turned the mass spectrometer into a versatile strument of precision. Methods of eliminating the effects of battery drifts were veloped (DuBridge & Brown 1933, Barth 1934, Penick 1935),[1] and the principle cancellation of cathode drifts and flicker was invented (Du Bridge & Brown 1933, owling & O'Ceallaigh 1935, Seaton 1948, O'Meara 1951), but apparently not nerally noticed.[2] Later, the construction of the electrometer tubes was perfected chnically through reducing the surface leakage as well as the size, and by subtuting an oxide cathode for the thoriated tungsten filament (Lafferty & Kingdon 46, Victoreen 1949, Hughes & Lander 1953), but this development had little imrtance to the field of mass spectrometry. The cause of this fact was the contemporaneous advances in amplifying technique, embraced in the concept of negative feedback (Vance 1936, Roberts 1939), which promoted accuracy, speed and automatic operation of all electric equipment, and removed the indispensability of the special electrometer tube for measurements where the ultimate current sensitivity it not essential. For a survey of actually adopted methods of current amplification and recording in mass spectrometry, see Bonne & Margoloff 1951. The introduction of the electron multiplier (Cohen 1943, Leland 1950), finally, eliminated the remaining superiority in this last respect, also raising the detecting sensitivity to the limit of making possible the counting of individual ions (White & Collins 1954). Furthermore, the carrier frequency technique of amplification (Hull, Gunn 1932, Sutherland 1949, Thomas & Finch 1950, McAdam *et al.*, Nonaka *et al.* 1951) provided the means of practically eliminating the amplifier zero drift, thus widening the span of measuring ranges. The full exploitation of the accuracy of the feedback amplifier demanded recourse to bridge methods of measurement, with a resulting precision of measurement amounting to 0.01 % (Nier *et al.* 1947, Wanless & Thode 1953).

---

[1] It is not the intention to give here a full bibliography of the wide field of current amplification d measurement. The references in this introduction are those thought to be particularly inuctive of the course of development, or useful for general survey thereof. Additional references pear in the text following.

[2] Other cases of (partial) cathode effect cancellation are reported by Lafferty & Kingdon 1946, ıker 1947, Prescott 1949, Bishop & Harris 1950; see also: MIT Rad. Lab. Ser., *18* (1948), Ch. 11.

Some of these trends and achievements are reflected in the design of the instrumentation, the description of which is to follow. As to the particular choice made of methods and devices, it was governed by the particular objects of use, and there was no intention of constructing any all-purpose instrument for mass spectrometry. In particular, the general conditions of spectrometer operation were not those of a plant for large-scale routine work, and the lack of personnel gave a preference to direct-reading (subjective) methods of gathering the data of measurement, in contrast to the largely automatic recording systems generally employed in mass spectrometry.

The general specifications of the present *amplifier* were set by the original intention of making accurate measurements on the rare isotope of potassium (Reuterswärd 1951), and are the following:

1) Error of individual reading: 0.3 % or rather better.
2) Input (ion collector) current: as small as possible.
3) Output load: recording galvanometer of 1 mA span.
4) Response time: less than 1 s, corresponding to a "RC-period", τ, equal to about 0.1 s.[1]

In an attempt to find the causes of differences and variations of the isotopic constitution of the yield of different types of ion sources, accurate measurements of isotope ratio were to be made during changes of ion source trimming as well as during gradual exhaustion of the source in long-time runs. To this end, the single-beam mass spectrometer was converted into a *two-isotope ratio meter* through combining an automatic beam switching device with an electric null method of measuring the ratio of voltages.

---

[1] The response to a step-signal, $1 - \exp(-t/RC)$, is correct within 0.3 % after lapse of $t = -RC \ln 0.003 - 5.8\ RC$.

II. The amplifier

1. The input circuit

The object of this circuit[1] is to transform the current to be measured, i, into a voltage, u, which is sensed by the input tube of the amplifier. It consists essentially of a resistor, R, which is shunted by the capacitance, C, of the grid and the collector electrode of the mass spectrometer. If grid current is absent, the only d.c. in the resistor is i. This, being composed of quanta $e = 1.6 \times 10^{-19}$ As, introduces an irregular a.c., the shot-effect (Schottky), the mean square of which is

$$\overline{\Delta i^2} = 2 e i \Delta f \tag{1}$$

in any small frequency band Δf. In the circuit considered, the noise current develops the mean square voltage on R and C,

$$(\overline{\Delta u^2})_{\text{shot}} = \frac{2 e i R^2}{1 + (2 \pi f R C)^2} \Delta f. \tag{2}$$

If the band-width of the measuring apparatus is determined by the input circuit only, the total shot noise current is obtained by taking the integral of (2) over all frequency intervals Δf:

$$(\overline{\Delta i^2})_{\text{shot, total}} = \frac{e i}{2 R C} \,. \tag{3}$$

With the specifications above, identifying τ with RC, and the error with therms value of the noise current, this gives the minimum current, $i = 9 \times 10^{-14}$ A, and the minimum noise current, 3×10^{-16} A. This result stands independent of the method of measurement.

In the case of our input circuit, there exists in the resistance R a thermal noise source (Schottky, Nyquist) of mean power

$$\bar{p} = 4 k T R \Delta f. \tag{4}$$

There results another noise voltage on R and C, the mean square of which is:

$$(\Delta \overline{u^2})_{\text{therm}} = \frac{4 k T R \Delta f}{1 + (2 \pi f R C)^2} \,. \tag{5}$$

In order that the thermal noise should not materially affect the precision of measurement, the resistance R has to satisfy the inequality: $(\overline{\Delta u^2})_{\text{therm}} \leqslant (\overline{\Delta u^2})_{\text{shot}}$, i.e. according to (2) and (5):

$$i R \gg 2 k T / e = 0.050 \text{ V}. \tag{6}$$

---

[1] General considerations on the use of thermionic tubes in measuring small currents are found at various places, e.g. Macdonald, Schintlmeister, Harris & Bishop.

For any measurement, the input resistance should thus be so high, that the current to be measured develops more than 0.05 V; otherwise there occurs loss in accuracy or speed of measurement. In the present case of $i = 9 \times 10^{-14}$ A, $R \gg 6 \times 10^{11}\ \Omega$.

Adding (2) and (5), and integrating as before, one obtains the total noise voltage effective in the input circuit:

$$(\Delta \overline{u^2})_{\text{noise, total}} = \frac{2kT}{e} \cdot \frac{eR}{\tau} \cdot \left(1 + iR\frac{e}{2kT}\right). \qquad (7)$$

It is then found, that with $R = 10^{12}\ \Omega$, the input noise voltage has the rms value $\frac{1}{3}$ mV.

In this case however, the maximum value of $C = \tau / R = 0.1$ pF, which is quite unattainable in the primitive electrometer circuit, where R connects the input grid to earth, because C will then be larger than the input capacitance of the tube (several pF).

The principal object of the amplifier following the input tube is, then, to supply the input circuit with a feedback signal, which has the effect of reducing the capacitive loading of the input resistor R. With the circuitry adopted, the effect of the capacitance of the input conductor is reduced by the factor $1/A$, A being the voltage gain in the amplifier-feedback loop. Thus, with $A > 1000$, a 20 pF input capacitance is reduced to less than 0.02 pF actively shunting R. In addition there comes the self-capacitance of the resistor, which has to be about 0.1 pF in order to comply with the condition above.[1]

2. The input amplifier stage

In order that the input circuit should not be loaded with undesirable current noise, superposed on that of eq. (7), which is principally unavoidable, the amplifier tube should present the input lead with a high internal resistance and a small grid current. "Electrometer tubes" are specifically designed to meet these requirements (Schintlmeister; Victoreen giving an account of recent achievements). At the time when the design of the present amplier was taken up, electrometer tubes could not be obtained commercially, but as shown by Nielsen, several other amplifying tubes can be operated at conditions of very small grid current. In addition, the anode current shot noise[2] must be kept small enough, which makes some low frequency pass filter necessary (usually found in the output measuring instrument). The general condition, that the tube noise should be small as compared to the inherent signal noise, is—according to (8)— in the case considered, rather less stringent than the specifications for an electrometer tube. Ordinary amplifying tubes have been adopted to similar measuring tasks (Anker, Nier *et al.*, Thode *et al.*, Caldecourt, Dowben).

On the whole, the requirements on the input tube in the feedback amplifier are less than those of electrometer tubes proper, just as the demand on low input ca-

---

[1] In fact, the capacitance as measured in a hf bridge was 0.5 pF, making the speed somewhat less than desired. Five resistors could be connected in series in order to obtain $10^{12}\ \Omega$ with a time-constant of 0.1 s. Alternatively, according to a method due to Taïeb, the capacitance of the input circuit could be largely neutralised by controlling the electrostatic field around the resistor reducing the time-constant to 1/150 s in the case of a $10^{12}\ \Omega$ electrometer circuit. It requires a regular cylindrical geometry, and was not applicable to the resistor switching arrangement employed. The reduction of τ could be driven much further with the feedback network of Pelchowitch & Zaalberg van Zelst.

[2] A good review of the topic of tube noise is found in the cited work of Harris & Bishop.

Table 1. Data of type 959 amplifier tube in current amplifier service.

Voltages referred to negative end of filament:

$$u_f = 0.68 \text{ V}, \; u_1 = u_f , \; u_2 = 3.17 \text{ V}, \; u_3 = -2.59 \text{ V}, \; u_a = 4.87 \text{ V}.$$

Currents:

$$i_f = 42 \text{ mA}, \; i_2 = 58 \; \mu\text{A}, \; i_3 = -8 \cdot 10^{-15} \text{ A}, \; i_a = 22 \; \mu\text{A}.$$

Conductances and transconductances in μA/V:

$$\begin{array}{lll}
\dfrac{\partial i_f}{\partial u_f} = 38\,000 & \dfrac{\partial i_2}{\partial u_f} = 213 & \dfrac{\partial i_a}{\partial u_f} = 87 \\[2ex]
 & \dfrac{\partial i_2}{\partial u_2} = 13.6 & \dfrac{\partial i_a}{\partial u_2} = 18.2 \\[2ex]
 & \dfrac{\partial i_2}{\partial u_a} = -6.6 & \dfrac{\partial i_a}{\partial u_a} = 14.7 \\[2ex]
 & \dfrac{\partial i_2}{\partial u_3} = -10.5 & \dfrac{\partial i_a}{\partial u_3} = 21.4
\end{array}$$

pacitance is lightened by the use of inverse feedback. The internal grid resistance should only be much higher than the effective amplifier input resistance, i.e. R/A ($< 10^9 \, \Omega$), and the shot-effect of the grid current should be much less than the shot-effect of the current i. Operation of tubes such as type 959 at electrode voltages below 6 V, possible because of the very small transconductance practicable, virtually eliminates the ion component of the grid current and makes the noise distribution of this current rather normal. Then, the necessary condition on grid current is that it be much smaller than i, i.e. 9×10^{-14} A.

The type 959 was selected for this work. Out of a batch of 5 tubes (war surplus make with 50 h guaranteed lifetime) tested in an electrometer circuit (Nielsen), two had to be discarded on account of unsuitable plate current characteristics. Of the remaining, two were investigated more thoroughly in order to determine proper operating data and inserted in two identical amplifiers, one of which was utilised in the mass spectrometer work. In service this tube showed large zero-point drift, and it became necessary to season it thoroughly. The zero-point plate current was, at the beginning, continuously increasing, but this trend could be influenced by changing the filament current. A sufficiently large reduction in the latter would make the trend change the sign. At an intermediate filament current, neither activation nor deactivation obtains (Lafferty & Kingdon). After this seasoning, the characteristics were again determined, and the results are reproduced here in Table 1.

As calculation according to theory (Penick) shows, this specimen of type 959 could be incorporated into a circuit balanced against power supply variations. This was not done, however, as the following amplifier stage is not of the balanced type, which would be necessary, because the voltage gain of the 959 stage is only 1.6. Instead, the filamentary cathodes of the three first stages are heated from the common d.c. supply of the amplifier, and the amplifier balanced as a whole, by adjusting the resistors in the circuit of the number 2 grid (space-charge grid) of the 959; cf. the circuit diagram of Fig. 1. Without this balance, a change of filament heating current to 0.01 % would displace the amplifier zero as much as 1 mV.

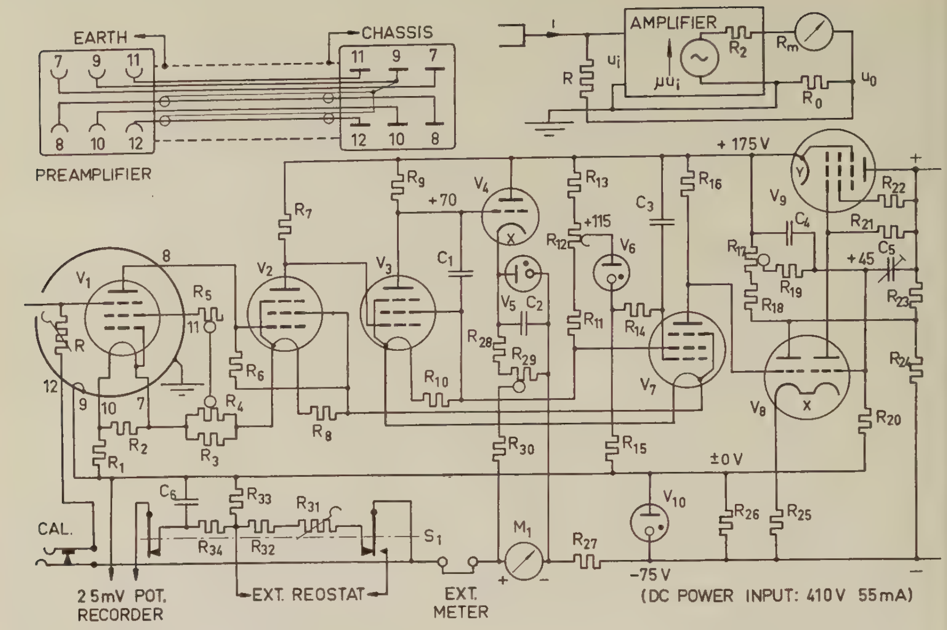

Fig. 1. Amplifier and associated operating current stabilizer.

V_1 959 (selected)
V_2–V_3 1S5 (1U5)
V_4 6SN7GT (both sections)
V_5 LS 75/5 (Luma)
V_6 85A1
V_7 1S5 (1U5)
V_8 6SL7GT
V_9 6Y6G
V_{10} VR–75
C_1–C_2 10 000 pF paper
C_3 0.1 μF paper
C_4 300 pF mica
C_5 30 pF var.
C_6 400 μF electrolytic
M_1 1 mA = panel meter
S_1 3-pos. toggle switch

R (see note (4))
R_1 55 Ω
R_2 75–155 Ω adj.
R_3 100 Ω
R_4 10 kΩ pot.
R_5 50 kΩ var.
R_6 1 MΩ
R_7 5 MΩ C
R_8 400 Ω
R_9 3 MΩ C
R_{10} 500 Ω
R_{11} 1200 Ω
R_{12} 10 × 10 Ω pot.
R_{13} 1200 Ω
R_{14} 50 kΩ C
R_{15} 5 kΩ
R_{16} 1 MΩ C

R_{17} 100 kΩ C pot.
R_{18} 500 kΩ C
R_{19} 2 MΩ C
R_{20} 1 MΩ C
R_{21} 500 kΩ C
R_{22} 100 Ω C
R_{23} 100 kΩ C
R_{24}–R_{25} 200 kΩ C
R_{26} 3000 Ω
R_{27} 15 kΩ
R_{28} 150 kΩ C
R_{29} 10 kΩ pot.
R_{30} 200 kΩ C
R_{31} 9900 Ω var.
R_{32} 98.00 Ω
R_{33} 2.00 Ω
R_{34} 200 Ω C

Notes.—(1) "*C*" denotes a deposited-carbon resistor of common type, the other resistors being of wire-wound construction; (2) heaters "*x*" are at + 65 V, and heater "*y*" is at + 175 V; (3) the potentiometer R_{29} carries a meter-scale vernier graduated in tenths of a meter-scale deflection; (4) resistances less than 10^{10} Ω may require a capacitive shunt of a few pF.

The balanced electrometer tube circuits can be made to balance out tube noise (esp. flicker effect) and drift in tube characteristics (DuBridge & Brown, Dowling & O'Ceallaigh, O'Meara) as well. In the present case this was not tried, because similar effects of the second stage would be equally noisome and need separate treatment. Then, too, the resulting loss in performance was taken as allowable in view of the rather large signal noise in the input. The stability of direct-coupled amplifiers are

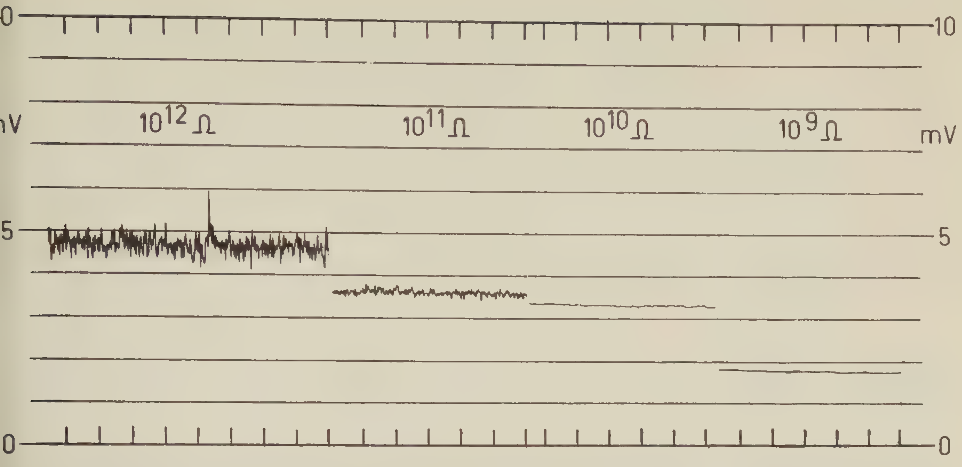

Fig. 2. Records of noise at the output of the amplifier, taken with a Honeywell-Brown potentiometric recorder. Frequency band width of the recorder was about 10 Hz. Horizontal scale is 10 s to the division.

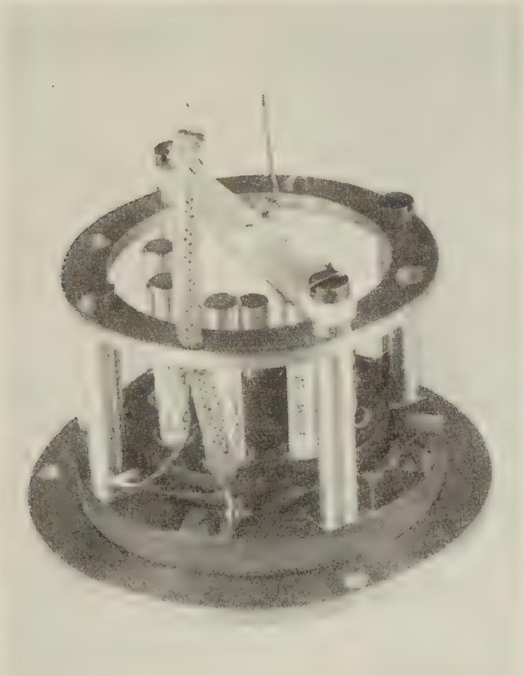

Fig. 3. The input resistor switch. The resistors are mounted, self-supporting, on the rotor. Contacts are made by springs to gold-plated caps soldered to their ends. The signal spring s fastened to the horizontal rod of trolitul, and the input lead (top right) secured directly to it. The feedback voltage is introduced by the shielded wire in front.

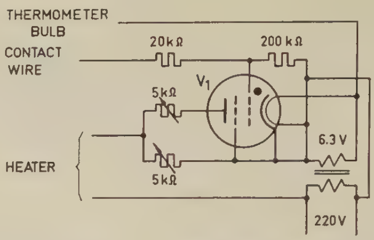

Fig. 4. Thermostat for the input stage. A Standard Radio type G4S/2 is used for the gas tetrode.

generally reported to be about 0.5 mV (Nier *et al.*, Thode *et al.*, Caldecourt, Dowben), as compared with 0.02 mV in completely balanced electrometer tubes (O'Meara). Fig. 2 shows the noise of the present amplifier as recorded by a fast instrument at the output. The rms value of the noise is estimated at less than 0.1 mV with $< 10^{10}$ ohms input resistor, about 0.1 mV with 10^{11} Ω, and about 0.3 mV with 8×10^{11} Ω.

The amplifier tube type 959 was cleaned with ethyl alcohol and mounted in a brass can by soldering to the leads. It is kept dry by a continuous stream of air, which has passed one tube of silica gel and two tubes of phosphorous pentoxide. Arrangements are made for dehydrating the gel at intervals without disassembling the flow line. The brass can also contains a rotary switch by which the input resistors can be exchanged. In order to reduce surface and dielectric leakage as far as possible, the high resistance ends of the resistors have no supports, the resistors themselves acting as the switching elements. Details of the switch are displayed in Fig. 3.

The resistors, specimens of 10^9 to 10^{12} Ω from Welwyn[1] exhibit large internal differences as to temperature coefficient of resistance (0.7 % per degree C observed). Therefore, the brass box is made a thermostat, comprising a mercury contact thermometer[2] attached to the wall of the box, a heater winding, and a thyratron relay. The thermostat is operated at about 5°C above room temperature, and is surrounded by a thermally insulating sheath. The electric circuit diagram is depicted in Fig. 4.

3. The voltage amplifier

The general layout of the amplifier (Fig. 1) started from an instrument described by Nier *et al.* 1947, in which several batteries were used for heating of the input tube cathode and for the coupling of the amplifying stages. In the present amplifier, a common mains powered d.c. source supplies all necessary currents to the amplifier, with exception of the cathode heater of the output stage, which is fed directly from the mains transformer.

As seen in Fig. 1, the collector current amplifier and the d.c. stabilizing amplifier constitute one unit, powered by a conventional mains transformer and rectifier unit.[3] The stabilizer tends to keep the filament current constant, thereby providing fixed voltages at various points within the amplifier, yet leaving the negative bias voltage of the output stage to take care of itself. This negative voltage, while insulated from the mains voltage changes, is dependent on the current in the output circuit. Yet, because of the high feedback gain (>1600), the interaction of the negative voltage through the output stage is negligible. The stabilizer is balanced against changes in the rectifier output voltage by the resistor network R_{17}, R_{18}, R_{19}, R_{20}, R_{23}, R_{24} such that the whole stabilizing amplifier serves only on large voltage changes. The balance is observed with an oscilloscope connected to the output of the collector current amplifier and adjusted on R_{17} such that the 100 Hz mains ripple just disappears. Because of the limited frequency range of the resistor network, high frequency disturbances are handled by a capacitive dividing network C_4, C_5, which is trimmed to minimum noise.

---

[1] Type PY3623 obtained through AB. Bergman & Beving, Stockholm.

[2] Miniature size with fixed contact wires and adjustable mercury charge, manufactured to order by AB. E. Schlaug, Stockholm.

[3] A complete circuit diagram was published by LENNANDER 1954. Two corrections to data appearing there are appropriate: (1) The resistor R_{27} shall have the resistance 200 kΩ; (2) the screen grid of V_8 is connected not to the point shown, but to the screen grid of V_5. The amplifier described here has undergone a few small alterations.

High-frequency noise is reduced further by some filtering at both sides of the mains transformer, and through a single hf filter link in the positive lead of the rectified voltage. However, in the present state the amplifier is still rather sensitive to hf noise (manifest in the spurious pips of the zero traces in Fig. 2), and it is expected that ordinary choke ripple filters in both positive and negative supply voltages would be profitable.

The choice of type 1S5 for the filamentary amplifying tubes was governed by availability reasons at the time of construction. It should be replaced by type 1U5, which is less microphonic. Some trouble was experienced with faulty contacts in the sockets of V_2 and V_3. It was remedied by point-welding bits of brass wire to the pins of the tubes and soldering them to the socket lugs. The amplifier is then not very sensitive to mechanical shock, except for the brass can containing the 959. This is solidly fastened to the spectrometer body.

The main amplifier chassis is mounted on a panel rack carrying other electronic equipment. The proper earthing of the circuits thus became a problem. It was found necessary to insulate the circuits from the chassis and make the necessary interconnections by wire leads. Thus, the cable between the main amplifier and the input circuit can carries one insulated wire which earths the input grid bias voltage at the inside of the can wall; the cable harness constituting a separate grounding lead for the amplifier chassis. Inside this harness, there run separately shielded cables for the feedback lead and the anode current of the 959, as shown in Fig. 1.

The step potentiometer R_{12} is used for fine adjustment of the amplifier balance by varying the filament current, the coarse adjustment being made once on the potentiometer R_4, which is located at the rear of the chassis. The amplifier zero is set with the variable resistor R_5 at the front panel. For stable zero, the amplifier should be operated for one hour before use. The zero drift encountered with the present instrument in such circumstances was ≈ 1 mV per hour.

4. The feedback loop

A little reflection on the block diagram of the amplifier (top right of Fig. 1) will yield the following expressions, connecting the input current i, the input voltage u_i and the output voltage u_o:[1]

---

[1] For introduction into the theory of feedback amplifiers, the reader is referred to textbooks, such as Reich.

$$\frac{u_i}{i} = \frac{R}{A+1}, \text{ where } A = \mu \cdot \frac{R_0}{R_0 + R_2 + R_m}, \tag{8}$$

$$u_0 = -iR \frac{\mu R_0}{(\mu+1) R_0 + R_2 + R_m} = -\frac{iR}{1 + 1/A}. \tag{9}$$

The first of these equations gives us the input resistance, $A + 1 = A$ times smaller than R; the second shows that the meter is connected in series with a virtual resistance at least μ times larger than the output load resistance, and the meter resistance will in practice only very slightly affect the current calibration. Both A and μ are large numbers with the present amplifier.

The total gain A in the feedback loop thus depends on the voltage measuring range switched into the output circuit through R_{31}, and on the resistance of the auxiliary equipment connected at EXT. METER of Fig. 1. Without any such external load, the following gain was measured:

R_3:	100	250	500	10000 Ω
Loop gain; A:	4000	10000	15000	36000

From this, $R_2 = 700\ \Omega$

The exact calculation of the transfer function of the amplifier is made difficult by the multiple feedback paths provided by the common filament current bleeder. There are also several paths of interaction with the stabilizer. At d.c. signals, the balancing of the amplifier against variations in the filament current effectively removes the internal feedback (leaving only the external one through the input resistor), but at frequencies above 1 Hz the amplifier becomes unbalanced through the disappearance of the cathode temperature changes. Measurement shows the unbalance against filament current changes to be equivalent to about 10 ohms at the input. The general effect of the internal feedback is then to raise the gain about 50 % at these frequencies.

The best way of investigating the properties of the amplifier is to observe the response to high-impedance current signals such as the collector current of a mass spectrometer. The general performance in use shows that it meets the requirements well, making possible rapid reading of the panel-mounted meter, or scanning a narrow mass peak in 10 seconds ($10^{12}\ \Omega$ input resistor). Sample spectra were given in a previous communication (Reuterswärd 1951).

5. The output circuit

This circuit contains what is essentially a voltage measuring device, in the diagram of Fig. 1 represented by the meter M_1 and a bank of precision wire-wound resistors, R_{31}, which are connected by means of a rotary switch making good contacts. The panel mounted meter (British Physical Laboratories, mod. S.50, 0–500 μA, shunted) is of good quality, has a long scale with 50 divisions and is equipped with a mirror. In order to eliminate errors made in estimating tenths of divisions and exploit fully the meter accuracy, readings can be made by means of a vernier arrangement; a graduated potentiometer knob (R_{29}), by which the meter current can be changed by known amounts, making the deflection coincide exactly with an adjacent division mark. The different measuring ranges could be calibrated with an internal accuracy of better than 0.1 % by reading meter deflections.

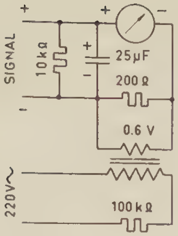

g. 5. Eliminator of rest friction of pen in Esterline-Angus graphic meter of 1 mA nge and 1 kΩ input resistance. A 10 VA heating current transformer, 127/6.3, is employed, d the resistors chosen to give 0.6 V secondary voltage. The resistor shunting the signal input, controls the damping.

By means of a toggle switch, three arrangements in the output circuit are available:) the internal meter and the internal load resistor, R_{31}; (2) an external potentio-etric recorder of 2.5 mV range, connected through RC filter to give about the me ranges as the internal meter; (3) the internal resistor exchanged for an external ecade resistor or voltage attenuator, use of the potentiometric recorder still per-itted.

An external meter of 1 mA range can be connected in series with the internal one. this way a graphic instrument (Esterline-Angus) with an internal resistance of kΩ was used with hardly any change in calibration or performance of the amplifier. or mass spectrometer work it proved necessary to reduce the pen-paper friction superposing a 50 Hz a.c. on the current to be measured. In Fig. 5, the diagram of e circuit employed is reproduced.[1]

6. Connections for measurement and calibration

In order to give exact measurements, the amplifier proper and the adjoining circuits ave to be calibrated. The meter scale has to be corrected for division errors. The itput circuit constituting essentially a voltmeter, the different voltage measuring nges have to be known. Also the input resistors have to be investigated. Several ethods of performing these checks are listed in the following.

. *Calibration of voltage ranges.*

1. Meter scale and multiplier resistances are calibrated, without using the amplifier, common potentiometer and Wheatstone bridge. In addition, according to (9), e amplifier gain A has to be known for precise measurements. A practical circuit r determining A is shown in Fig. 6a; the potentiometer ratio $\beta = 1/A$.

2. Calibrating voltage is introduced into the feedback line as shown in Fig. 6b. nowledge of A not necessary. The voltage, e, is obtained from a calibrated decade tentiometer (the input current, i, must be zero, of course).

3. Calibrating current introduced through external high-ohmic resistance as own in Fig. 6c. The ratio R_{I}/R must be known, and the same is true of the gain, , for precise work.

---

[1] A similar device was used by Sulzer & Waynick.

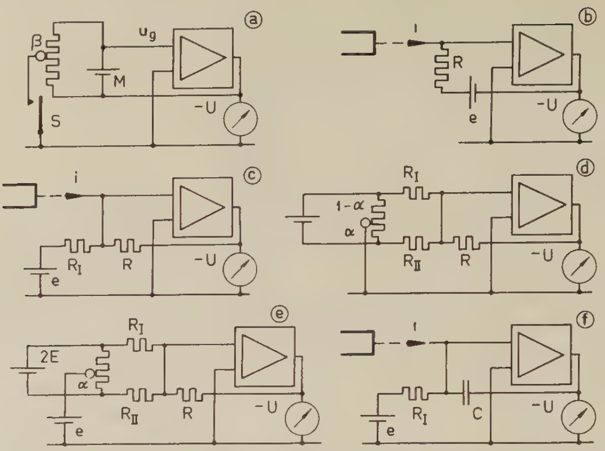

Fig. 6. Amplifier calibrating circuits; (*a*) measuring amplifier gain, (*b*) calibrating in terms of input voltage, (*c*) calibrating in terms of input current, (*d*) measuring high-ohmic resistances in bridge circuit, (*e*) testing resistors for linearity of response, (*f*) calibrating resistance in terms of time and capacitance.

B. Calibration of input resistor.

1. The same set-up as for A3, Fig. 6c, will also calibrate the input resistor, or rather calibrate the instrument as a whole. However it is essential, that the calibrating resistor, R_I, have a linear response.

2. The input resistor is measured in a Wheatstone bridge arrangement. The amplifier itself provides a suitable null detector in a set-up shown in Fig. 6d. The resistor in the feedback line is not essential in this application of the amplifier, except for stabilizing the amplification, and should have a sufficiently high resistance not to impair the sensitivity. The reference resistor has to be operated in a range of linear response. If no such resistor is available, the circuit of Fig. 6e can be used for investigation of the response characteristic. If the resistors R_I and R_{II} are true ohmic, the ratio e/U is independent of the voltage $2E$, applied to these resistors in series. By this method, the Welwyn resistors used were tested and found linear to 0.1 % in the voltage range 0.1 to 10 V.

3. By means of a high-quality capacitor, an external resistor can be calibrated in absolute units in the circuit of Fig. 6f.

C. Measurement of ion currents.

1. The straight-forward method is that of Fig. 6b, with the calibrating voltage zero. With a calibrated voltage e of reversed polarity, the current can be measured by compensating the voltage drop in the input resistor, the amplifier being used a a null detector.

2. With the actual amplifier, the calibrating resistors were connected to the input circuit in a plug-in manner, in order to evade the necessity of an extra switch o high insulation, and were not removed for ion current measurement. The effective measuring circuit is then that of Fig. 6c, with $e = 0$. The auxiliary resistor carrie a shunt current to earth, which has to be taken into account as a small correction in the calibration of the instrument.

III. The peak height ratio meter

1. General

The feedback amplifier allows measurements of a very high short-term reproducibility. The noise level being about 0.1 mV, an output signal of only 1 V is representative of the input current to 0.01 %. Full use of this precision can be made only with electric bridge arrangements. Thus, the ratio of two isotope currents may be determined by using two ion collectors and two amplifiers, the outputs of which are compared with aid of a precision attenuator and null galvanometer (Nier *et al.*, Wanless & Thode) or a direct-reading ratio meter (Stevens & Inghram). Sometimes this method is objectionable, e.g. in case isotope ratios are desired on an absolute basis; then the isotope ions should have identical paths and reach the same collector. A similar case obtains in absorption photometry, when separate phototubes in the two light paths cannot be tolerated because of possible differences in spectral response characteristics. Methods of comparing directly, currents which are recieved alternatingly have been devised by Ahlers & Freedman, Hales and Tait & Chalklin for application to absorption photometry, and by the present author for mass spectrometric work (reported in 1953). Characteristic of the present method is the absence of any amplifying element in the comparator circuit, which is connected to the output circuit of the feedback amplifier.

2. The basic principles of the ratiometer

When making absolute intensity ratio determinations in a mass spectrometer, the magnetic field is changed in order to bring the ions of different isotopes to the collector, the ion accelerating voltage being kept constant. A continuous field sweep will result in a record of the spectrum shown schematically in Fig. 7a. For precision measurements, the tops of the mass peaks should be flat, and the base line should be straight. In order to determine the ratio of the isotopes, A:B, the top currents, i_A and i_B, are measured alternatingly, thus reducing the effects of drifts in the ion source yield, and the same repeated with the base currents, i_{A0} and i_{B0}. Then, the desired ratio is given by:

$$q = (i_A - i_{A0}) : (i_B - i_{B0}). \tag{10}$$

The sloping of the base line can have several causes; in the present instrument it reflects a small influence of the magnetic field on the amplifier input tube. The proper method of measuring i_{A0} and i_{B0} is then to displace the mass spectrum $\frac{1}{2}$ mass unit by a small change in accelerating voltage.

The measurement of the currents i, usually made by reading the output meter or a continuous record of the spectrum, is performed automatically by the ratiometer, the schematic diagram of which appears in Fig. 7b. By switching in the magnet circuit, the two peaks are alternatingly introduced into the galvanometer circuit—the smaller one, A, in full, but the larger one, B, reduced in a known ratio by the attenuator. The capacitor C_I is charged to a steady voltage, if $i_A = q i_B$ (not considering the base corrections), and the galvanometer will then read zero. If $i_A \neq q i_B$, C_I carries an alternating current of the switching period, which is rectified in

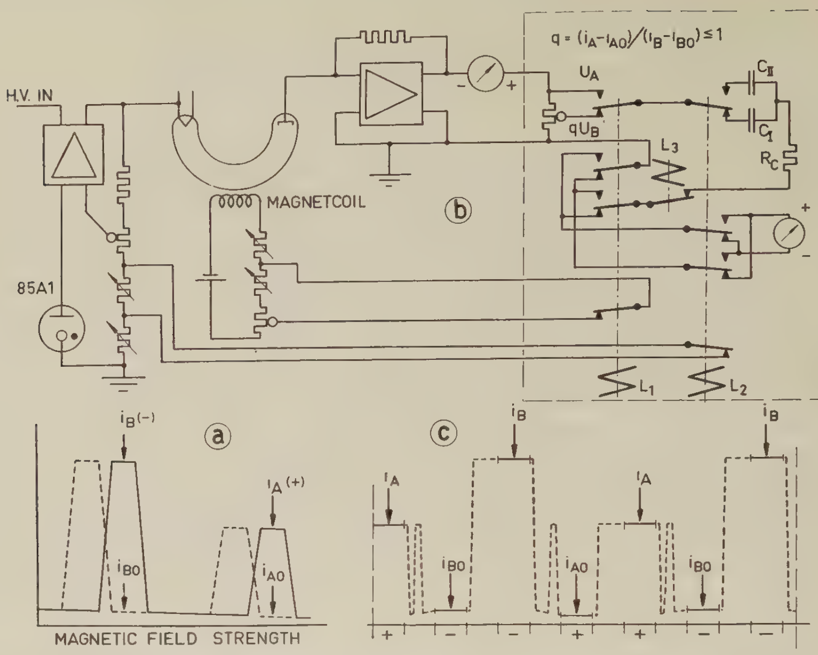

Fig. 7. (*a*) Schematic mass spectrum; (*b*) circuitry for peak ratio measurement; (*c*) course of the collector current.

the galvanometer circuit, whence a deflection is obtained, indicating the remaining unbalance. The base line corrections may be applied through small compensating voltages introduced at U_A and $q\,U_B$, which are adjusted, again using the galvanometer as null indicator, with the spectrum displaced and the capacitor bypassed.

3. The design of the ratiometer

The switching frequency is determined by the response times of the magnet and of the amplifier; the capacitor charging time constant, $C_I R_C$, and the galvanometer period will have to be selected accordingly. The averaging action of the necessarily long galvanometer period (about 8 s) will reduce amplifier and ion current noise and enhance the sensitivity and precision of the amplifier. However, an error in the base corrections reacts directly on the q measured. In the actual instrument, this drawback is eliminated by intercalating base corrections between the peak top measurements by the actions of two sets of switches, one (L_1) switching between isotopes, the other (L_2) between top and base. Each switching action is accompanied by a current reversal in the galvanometer circuit. It is also necessary to switch between two capacitors, C_I and C_{II}, the steady charges of which will correspond to the peak top and base currents, respectively. The galvanometer period is sufficient to average the current $i_A - i_{A0} - i_B + i_{B0}$; when this is made zero by adjusting the attenuator, the ratio, q, is obtained free from any base correction error. However, when $i_{A0} \neq i_{B0}$, the galvanometer current oscillates, and the sensitivity of the balance indication

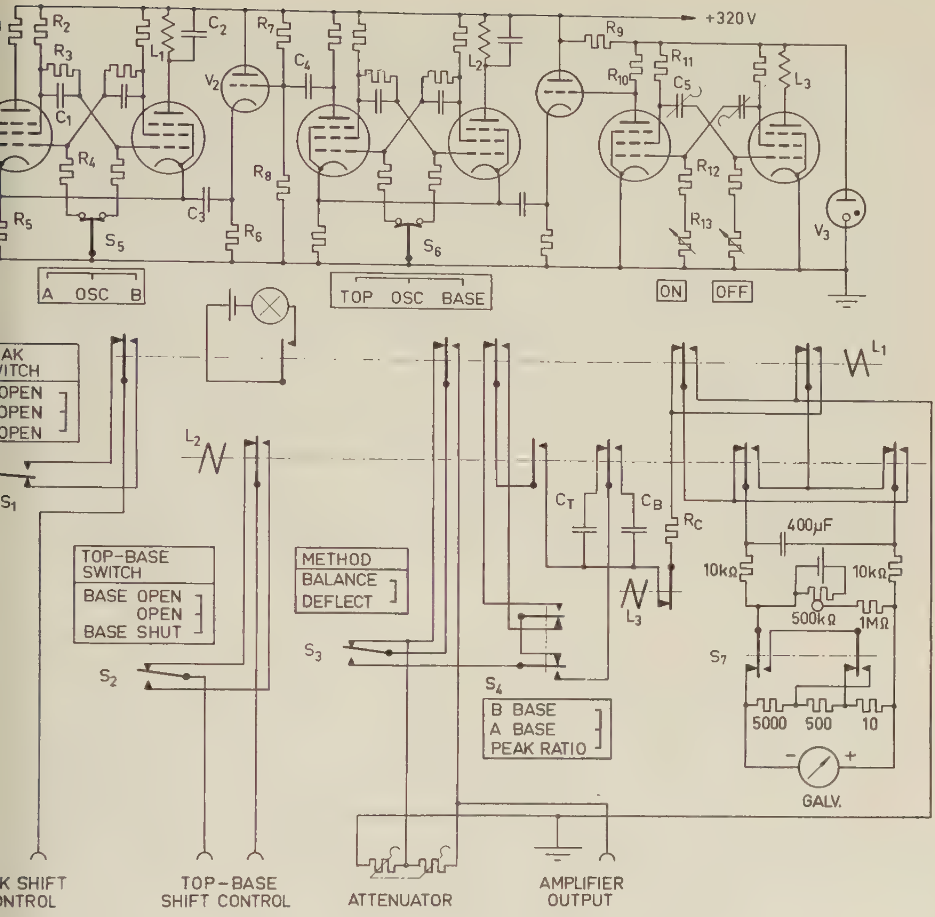

Fig. 8. Wiring diagram of the ratiometer.

mponents of driving unit (upper part of the diagram):

V_1 6K6GT (6 in number)
V_2 6J5 (2)
V_3 VR-150
C_1 200 pF mica (4)
C_2 1 μF (2)
C_3 300 pF mica (2)
C_4 500 pF mica
C_5 2 or 6 μF (2)
R_1 5 kΩ (2)
R_2 30 kΩ (4)
R_3–R_4 300 kΩ (8)

R_5 10 kΩ (2)
R_6 50 kΩ (2)
R_7–R_8 2 MΩ
L_1–L_2 RT 5018/313 } (Svenska Relä-
L_3 RT 5051/254 } fabriken AB, Sthlm)
R_9 6700 Ω
R_{10} 5 kΩ
R_{11} 20 kΩ (2)
R_{12} 100 kΩ (2)
R_{13} 2 MΩ var. (2)*

mponents of ratiometer unit (lower part of the diagram):

S_1–S_6 RMA-1101 } (L. M. Ericsson)
S_2 RMA-1201 }

R_C 150 kΩ
C_T–C_B 10 μF (small leakage)

The dials may be graduated in seconds (0–3, or 0–10, according to C_5) of "on" and f" times.

may be impaired. If necessary, a manually adjusted zero control could be inserted in one of the output leads of the attenuator. The main advantage of the automatic base correction is the fact, that changes in the amplifier zero cannot *systematically* corrupt the result.

In Fig. 7c, the temporal succession of the collector currents and the signs of their action on the galvanometer are displayed. As only the stationary currents, i_A, i_{A0}, etc., are to be used in the null circuit, the transient currents must be kept away by means of an on-off switch (L_3) in series with the capacitors.

The complete wiring diagram of the ratiometer panel and chassis appears in Fig. 8. The switches are operated by relays, L_1–L_3, which are driven by amplifier tubes in scale-of-two circuits[1] as explained in the upper part of the diagram. The periodicity is governed by a relaxation oscillator, giving the galvanometer "on" and "off" intervals. The first scaling circuit, with L_2, performs the switching between top and base, the second, with L_1, the alternation of the peaks; thus reducing the need for speed in the magnet switching. The relays L_1 and L_2 are bypassed capacitively in order to delay their action, thus insuring that the galvanometer circuit be opened in advance. The adopted method of switching control assures complete symmetry of operation. The lower half of the diagram gives the circuitry of the relay switches and the manual controls for eliminating the automatic switching action, in order to perform the necessary adjustments of the spectrum and the ratiometer circuits.

4. The operation of the ratiometer

The operation of the ratiometer at the outset presents some difficulties because of the number of adjustments, which in the usual way of measurement are performed one after another, and now have to be managed, all at one time, before starting the balancing procedure. In order to assure ease of operation, rather stringent requirements are put on the resolution and stability of the spectrum as to mass scale. The effects of fluctuations of the ion source yield, however, are reduced, and a small steady rise or falling-off of the primary intensity does little harm to the precision of measurement. It should be borne in mind however, that the method is likely to be of value only when a precision of one percent or better is attainable.

The first adjustment to be made is the locating of the measuring points at corresponding sections of the isotope peaks. With switch S_3 in pos. DEFLECT, the panel meter of the amplifier is read, and the attenuator coarsely adjusted to give equal maximum deflections in the two peaks, which are switched in by S_5. At the same time the peak phasing switch S_1 has to be put in the proper position (according to which of A and B is the heavier isotope) and the peak control (a variable resistor in the magnet current circuit) given a preliminary adjustment. During these preparations,

---

[1] The scaling circuits are proportioned to yield a minimum ratio, $r = e_2/(-e_1)$, of screen and grid voltages in the quenched tube, i.e., designed for a high stability rather than high signal sensitivity. The approximate condition is

$$u_k/u_B = 1 - \sqrt{e/u_B}, \text{ giving } r = (u_B/u_k)^2.$$

Here u_B = the B-supply voltage; u_k, the cathode potential; and e, the screen voltage in the conducting tube; the grid voltage being adjusted to the limiting case of no grid current flow. In the actual case, $u_k/u_B = 0.5$, and $r = 4$. The same formula, with e_a for e_2, would apply to the conventional Eccles-Jordan trigger circuit.

S_6 is in the OSC. pos., but the base control in the ion accelerating voltage supply is set for zero mass shift. Now the automatic switching is started by putting S_5 in the OSC. pos., the mass spectrum displaced about one half peak width, and by vernier controls the two peaks adjusted to give equal final deflections in about half maximum height; thus the positions of the two ion beams at the collector slit are made exactly equal. Finally, the switching is arrested in the position A by switch S_5, the half height width of the peak determined, and the mass scale set for the mid-point (rather than the maximum point) of the peak. The spectrometer may then be said to be tuned for peaks A and B.

Next, the galvanometer scale is adjusted for correct zero position, and the zero made independent of galvanometer sensitivity (controlled by S_7) through adjusting (by the 500 kΩ potentiometer) the current which compensates the current generated in the 400 μF electrolytic capacitor of the ripple filter in the galvanometer circuit. This adjustment will have to be repeated frequently until the conditions in the capacitor have become stationary, and the compensating current is then left on for weeks.

S_4 is then set for A BASE, S_5 is set for OSC, the proper zeroing mass shift set, and S_3 shifted to BALANCE; now the galvanometer reads the base of A only, and this is made zero by adjusting the zero control in the amplifier. S_4 may then be shifted to B BASE, in order to ascertain that this zero correction be sufficiently small. The zero corrections thus established, the circuit is set in operation through shifting S_4 into the PEAK RATIO pos.

After about three complete switching periods (during which the peak B intensity may be read on the output meter), the galvanometer is observed for gross unbalance and corresponding adjustment made in the attenuator, until perceptibly steady deflection near the zero position is obtained, and read. Next, the attenuator setting is changed in order to give a deflection of opposite sign, which, too, is read. A linear interpolation between the readings will give the ratio q.

One determination of q thus performed, the whole procedure of adjustment is repeated, all over again, to check for spectrometer, amplifier, and galvanometer drift. When all are operating properly, the ratio q is determined repeatedly, and the zero checked only occasionally by switching at S_4. In practice however, it was experienced that the galvanometer zero drift limited the precision of measurement and had to be checked at short intervals. The source of the drift was the electrolytic capacitor, which acts as an erratic source of e.m.f. A paper capacitor would be preferred, or the whole ripple filter can be left out if a galvanometer of proper period is available. However, the combination of a smoothing RC circuit and a relatively rapid galvanometer makes possible quick change of sensitivity, and provides some protection of the galvanometer from overloads due to incautious operation.

5. Sensitivity of the peak height ratio measuring equipment

The precision with which ratio measurements are made depends on—in addition to the geometrical qualities of the spectrum (flatness of peak tops and linearity of base line, stability of mass calibration)—the current sensitivity of the galvanometer, the quality of the attenuator and the capacitors, and so on. Some of these factors will be analysed here with reference to the prototype instrument.

A. *The null circuit.*

The capacitance, C, of the two storage capacitors, C_T and C_B, should be chosen as large as practical in order to give a high sensitivity; there is, however, no point in raising the product $R_C C$ above the length of the interval of each switching period in which the circuit is closed (the "on" interval, T). R_C was taken much larger than the attenuator resistance, a simple means of warranting constant resistance in the null circuit—which is essential lest there should be any small base current residue to compensate. The output resistance of the attenuator varied from 0 to 2.8 kΩ, $R_C = 150$ kΩ, and $C = 10$ μF, making $R_C C = T = 1.5$ s.

The d.c. leakage in the charged capacitor C_T produces a ripple current in the galvanometer. By using a high quality paper condenser,[1] having an intrinsic time constant of the order of magnitude 10000 T, the ripple due to the maximum charging voltage, 10 V, is reduced to an equivalent of 1 mV, which will not affect the precision of the null reading. This high insulation is not necessary for C_B, which in operation carries only a very small direct voltage.

B. *Deflection sensitivity and period; noise characteristic.*

The theory of the galvanometer deflections has been worked out on the following assumptions:

(a) The "on" and "off" intervals are equal to T;
(b) the base currents are compensated to zero;
(c) the null detector (galvanometer and associated ripple filter) has a time response equal to that of a simple exponential of time constant $4T$ (which is equivalent to that of the ripple filter followed by a rapid galvanometer);
(d) the null circuit time constant $R_C C = T$ ($R_C = 150$ kΩ, $C = 10$ μF).

The galvanometer current is then derived solely from the inequality of the two voltages, U_A, qU_B, at the input of the null circuit. Let k denote the static sensitivity of the galvanometer (the deflection a due to the current i being $a = ki$), then the mean deflection due to the constant unbalance, $U_A - qU_B = \Delta$, is ($k = 1.25 \times 10^9$ A/mm):

$$\bar{a} = 0.1155 \frac{kC}{T} \Delta = 100 \text{ mm per V.} \qquad (11)$$

With the components used, the effective series resistance, $(0.1155\, C/T)^{-1}$, is 1.3 MΩ.

Superposed on this mean deflection there is a ripple of period $4T$ and amplitude $0.36\,\bar{a}$, the minimum, $0.65\,\bar{a}$, occurring at begin of the "on" interval, and the maximum, $1.37\,\bar{a}$, at the end of the same.

Of interest, further, are the rate at which the deflection a increases as the result of the sudden introduction of a *fixed increment* Δ in U_A, and the rate of decay of the deflection caused by an *accidental increment*, δ, in U_A during one halfperiod ($4T$); the initial conditions in either case being those of steady balance, $\Delta = 0$, and $a = 0$. As the mean deflection of any half-period is proportional to the maximum and minimum deflections, either of these may be used for reading. The following Table 2 gives the readings in terms of half-period means, which are to be compared to the steady-state reading of eq. (11).

---

[1] AB Rifa, type PKH 6011B/170; leakage resistance measured: 750 MΩ.

Table 2. The galvanometer response, $\bar{a}T/kC$, to a step-function signal Δ, and to an accidental signal δ.

Half-period number	Step-function	Accidental
First	$0.100\ \Delta$	$0.100\ \delta$
Second	$0.100\ \Delta$	$0.100\ \delta$
Third	$0.114\ \Delta$	$0.014\ \delta$
Fourth	$0.114\ \Delta$	$0.014\ \delta$
Fifth	$0.115\ \Delta$	$0.002\ \delta$

In order to calculate the noise, or rms error, in the galvanometer deflection, we consider the case of equal noise in U_{A} and $q\,U_{\mathrm{B}}$. The samples of these voltages, collected during intervals T, are subject to a rms error, μ; consideration of the decay of the contribution of the individual samples according to Table 2, gives the rms deviation of the half-period mean galvanometer deflection by:

$$(T/k\,C)\sqrt{\overline{a^2}} = \sqrt{0.020\,\overline{\delta^2}} = (0.144\,\mu)^2. \tag{12}$$

Thus, if any galvanometer deflection is interpreted as due to an unbalance voltage according to (11), then according to (12) the relative rms error in q is:

$$\sqrt{\overline{(\delta\,q)^2}}\,/q = \sqrt{\overline{\Delta^2}}\,/U_{\mathrm{A}} = 1.23\,\mu/U_{\mathrm{A}}. \tag{13}$$

Now $\mu = U_{\mathrm{A}}(\omega_F T\ \tanh\ \tfrac{1}{2})^{-\frac{1}{2}} = 1.47\ U_{\mathrm{A}}(\omega_F T)^{-\frac{1}{2}}$, ω_F being an equivalent noise band-width (Davenport et al., eq. (3.7), for $\alpha = 1/T$ and $\omega_F T \gg 1$). Similarly, if U_{A} and $q\,U_{\mathrm{B}}$ are measured directly with an ideal integrating device during the time interval T^*, the error is, for each peak, $U_{\mathrm{A}}(2/\omega_F T^*)^{\frac{1}{2}}$ (ibid., eq. (3.12) and table I); in order to give q with the relative error (13), $T^* = 1.22\ T$. The ratiometer provides one such determination in every interval of length $8\,T$.

The noise here considered can be assumed to originate from the ion source. It usually dominates in application of a thermionic source, except in the most sensitive measuring ranges, where the amplifier noise also acquires importance. This noise is introduced in both U_{A} and U_{A0}, eq. (13) being valid for this kind of noise also.

The noise in the galvanometer deflection should be distinguished from the periodic ripple due to non-compensation of the peak bases and q-unbalance, which, if having a moderate amplitude, does not prevent the reading of the mean deflection. However, in practice it is found advantageous to read the last figure of the q ratio from the unbalance deflection and, to that end, reduce the ripple further by using a more efficiently damped galvanometer[1] at some sacrifice of speed of response.

C. Stability of mass calibration.

Fig. 9A shows the result of a measurement of the peak profile. In this case the switching between the peaks was carried out through changing the accelerating voltage only, the magnetic field remaining constant; the ordinate gives the relative

---

[1] The galvanometer employed has the following characteristics: internal resistance 1000 Ω, external aperiodic resistance 6500 Ω, period 8.6 s. The damping was controlled in an auxiliary coil of the galvanometer movement.

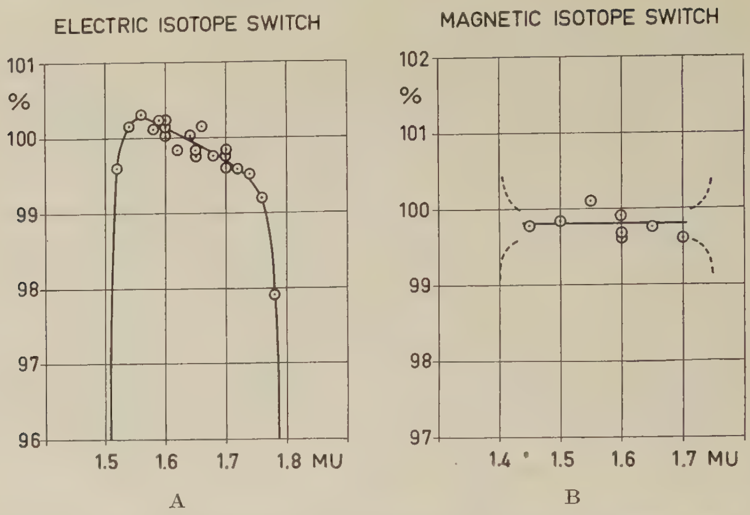

Fig. 9. Ratio readings obtained by the ratiometer. Ion source, powdered orthoclase on Pt filament; ions, $^{39}K^+$ and $^{41}K^+$ at 1100 V; slits, 0.25 and 0.7 mm; radius of ion path in 180° spectrometer, 80 mm.

A. Peak profile. Electric mass sweep in one peak; 100 % ratio = 14.43.

B. Measurement of peak height ratio with variation of mass adjustment. Electric mass sweep common to both peaks; 100 % ratio = 14.06. (The difference in ratio is due to the discriminating effect of electric mass switching.)

intensity distribution of the 39 peak in potassium. As visible, the peak has a plateau of width 0.2 mass units (MU), but the plateau has a rather large slope (4.8 % per MU), which makes exact ratio measurements difficult. In order to achieve a precision of 0.1 %, the switching of the peaks has to be performed between corresponding points of the peaks to within 0.02 MU. This has to be ascertained by the procedure of adjustment of the spectrometer tuning described above. The cause of the slope was, in this case, improper adjustment of the ion source, which introduces a masking effect on the ion beams. With due attention to this matter, the slope, in practice, can be reduced to that caused by the electric mass scanning.

Fig. 9B gives an example of the null reading in peak height ratio measurement when measured at different, but corresponding, points of the peaks. The abscissa gives the position on a mass scale with arbitrary zero; the ordinate, the galvanometer reading in percent of equivalent ratio change, the attenuator being set to the constant ratio 1/14.06. It is evident that the ratio measured is independent of peak position in an interval of 0.25 MU, or rather more than the extension of the plateau. Outside thereof, the measurements scatter widely, due to effects of mass scale fluctuations and the abrupt changes of slope at the edges of the plateau. From the diagram, the ratio is found within an error of about 0.1 %.

The mass scale stability is thus of high importance when the peaks are narrow or their tops sloping. A source of trouble was found in the relay contacts carrying the magnet current. Ordinary high-power solid contacts are useless, and telephone relay contacts may become erratic in operation. A Hg-relay should offer a reliable solution to the problem.

6. General remarks on the merits of the ratiometer

The merit of the peak height ratio measuring system described above should be assessed by comparing with the usual procedure of reading output current meters. Such instruments in favourable instances allow of a reading accuracy of 0.1 % and would compete with balancing methods in much mass spectrometric work, where deficiencies of the ion source do not allow of any higher precision. If no composite switching devices, similar to those of the ratiometer, are available, the scanning for the isotope peak tops and switching of ranges are lengthy and the accurate reading of deflections fatiguing. If the yield of the ion source is slowly rising or falling, the measurements have to be repeated with regard to timing, or the direct readings will have to be corrected for time. Also, corrections will have to be applied for errors of scale division and variable amplifier gain. The final result is found only after some calculations. 10 minutes may be necessary for collecting the data of 10 independent ratio determinations, and the work spent in following slow changes in the ratio for some time becomes considerable. In contrast to this, the ratiometer requires a close attention to the proper tuning and setting of the spectrometer and its controls during, perhaps, 5 minutes, but thereafter the isotope ratio is monitored with ease just by observing the galvanometer null deflection and the attenuator reading, which is proportional to the ratio. The effects of adjustment of the ion source, or of varying the base reference point are directly visible in the galvanometer deflection, which for fixed peak height U_B may be made to read the change in q. Reading the deflection for the interval $8\,T$ (about 12 s) will, by a mental averaging process, give the ratio to 0.1 %, if only the mass calibration of the spectrometer can be relied upon to hold with sufficient accuracy to eliminate the need for frequent checks.

Most of these favours are, however, not inherent with the ratio balancing feature, but with the method of composite and automatic switching, which will make comparing peak deflections an equally rapid and convenient procedure. Combined with a graphic display of the peaks compared, this method does away with the need for a long-time stability of the mass scale (Siri, Ezoe, Pelchowitch). Utilising the approach of Taylor, the ratiometer described has been used in connection with a potentiometric recorder and a peak top scanning device to obtain objective balance indica-

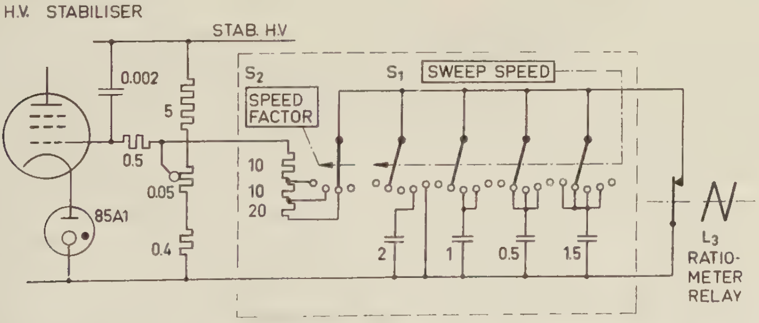

Fig. 10. Peak top scanning unit. Resistances given in MΩ, capacitances in μF. The switch dials are graduated:

S_1: Off—0.27—0.20—0.13—0.08 per cent mass per second.
S_2: × 0— × 0.25— × 0.5— × 1.

tion. In this way, the purpose of the operation of the mass spectrometer is only the collection of information regarding the isotope currents, the measurement proper being postponed to the visual inspection of the record, which allows of a better exploitation of the spectrometer operating time and reduces the demands on the qualification of the operator.

7. Peak height comparator

The conversion of the ratiometer into a peak height comparator of a type similar to that of Taylor is effected by means of the auxiliary appliance depicted in Fig. 10. The automatic switching is performed by the relays, L_1 and L_3, of the ratiometer unit, the switch S_3 being set to DEFLECT, and the recorder connected in series with the attenuator (now operated as a variable resistance) as shown in Fig. 1. In order that the recorder should make no deflection during the sweep retrace, the recorder driving voltage is intercepted by a switching element of the relay L_3. As now the peaks are to be switched after each peak scanning period, and no top-base switching intercalated, the relays L_1 and L_2, and their respective manual controls, S_5 and S_6, are interchanged by means of a 6-pole change-over switch (not shown in any of the diagrams). In operation, the scanning rate is set by the switches of the scanning unit, and the exact scanning interval length adjusted through the "on" time control of the ratiometer unit, the starting point of the sweep being controlled in the accelerating voltage stabilizer.

No biassing-off of the main part of the peak top signal fed to the recorder, as devised by Taylor, was utilized in the operation of the peak height comparator. It could easily be accomplished by introducing an adjustable, constant e.m.f. in series with the recorder input. The gain in accuracy achieved by that means, of course depends on properties of the mass spectrum.

IV. Concluding remarks

It is stressed that the instrumentation here presented was designed and constructed for operation in connection with specific mass spectroscopic work,[1] but it would, presumably, serve well in other applications, without large alterations. Some hints in this respect follow.

The current amplifier, because of its low weight and small power consumption, would serve as a general laboratory or mobile instrument for high precision measurement of currents in the range $10^{-13} \ldots 10^{-6}$ A. In order to widen the range of applications, the first two stages should be redesigned to accept special subminiature tubes, e.g. types Victoreen 5800 and CK-522 (Hughes & Lander), thus giving an improved zero stability when working with input resistors of $10^{10}\ \Omega$, or less, resistance, and in addition reducing microphony. The measuring ranges could easily be extended in the other direction too. An output range of 25 V is accomplished simply by increasing the multiplier resistance, R_{31} of Fig. 1, and a 50 V range is possible, if the negative supply voltage is increased by 30 V, the positive being reduced by the same amount (the VR tubes, V_5 and V_6, exchanged for VR-105's). In the latter case, it is wise to use two tubes 12AT7 in parallel for V_4, and to insert V_5 in the grid circuit of V_4 (cf. Miller), operating the cathode of this tube at earth level, in order to attain a larger transconductance, improving the amplifier gain at low output resistances.

---

[1] To be reported in a separate publication.

The ratiometer here described, is really an unnecessarily comprehensive device or the intended application, as a pure peak height comparator would have served qually well, being not so particular about the stability of the spectrum mass calibraion. It is expected, that the instrument will be more valuable in certain applications f optics, e.g. absorption photometry and stellar photometry, in cases when the im is at highest ratio accuracy. The switching frequency should be as high as posible, in order to reduce the demands on capacitor insulation. The switching will hen advantageously be performed not by relays but by some rotary movement, arrying mirrors, prisms, or filters necessary for switching in the light paths. The mplifier employed must always be well stabilized by a large amount of inverse eedback, and have a sufficient speed of response (cf. references in Sect. II.2). olystyrene capacitors of improved insulation and less capacitance could be applied f the galvanometer were substituted by a more current sensitive null indicator, g., a vacuum tube ammeter of sensitivity 10^{-12} A, employing capacitive or contact nodulation. In applications of mass spectrometers and spectrophotometers to autonatic process control, a switching null detector for measuring voltage ratios, like he peak height ratiometer here described, will have a particular field of service.

Physics Department, University of Uppsala.

REFERENCES

hlers and Freedman (1953), Nature *172*, 260.
. S. Anker (1947), Electronics, *June*, 138, 140.
. Barth (1934), Z. Physik *87*, 399.
. O. Bishop and E. J. Harris (1950), Rev. Scient. Instr. *21*, 366.
. Bonne and R. Margoloff (1951), Ann. Radioél. *6*, 318.
. J. Caldecourt (1949), Rev. Scient. Instr. *20*, 748.
. A. Cohen (1943), Phys. Rev. *63*, 219.
avenport, Johnson and Middleton (1952), J. Appl. Phys. *23*, 377.
. M. Dowben (1952), Rev. Scient. Instr. *23*, 506.
. J. Dowling and C. O'Ceallaigh (1935), Phil. Mag. *20*, 532.
. A. DuBridge and H. Brown (1933), Rev. Scient. Instr. *4*, 532.
. Ezoe (1953), J. Scient. Res. Inst. [Tokyo] *47*, 65.
. Gunn (1932), Phys. Rev. *40*, 307.
. R. Hafstad (1933), Phys. Rev. *44*, 201.
. L. Hales (1953), J. Scient. Instr. *30*, 52.
. J. Harris and P. O. Bishop (1949), Electronic Eng. *21*, 332, 355.
ughes and Lander (1953), Rev. Scient. Instr. *24*, 331.
. W. Hull (1932), Physics *2*, 409.
. M. Lafferty and K. H. Kingdon (1946), J. Appl. Phys. *17*, 894.
. T. Leland (1950), Phys. Rev. *77*, 634.
. Lennander (1954), Ark. Fysik *8*, 551.
. McAdam, R. E. Tarpley, and A. J. Williams (1951), Electronics, *Aug.*, 128.
. A. Macdonald (1936), Physics *7*, 265.
. E. Miller (1941), Electronics, *Nov.*, 27, 105.
. E. Nielsen (1947), Rev. Scient. Instr. *18*, 18.
. O. Nier, E. P. Ney, and M. G. Inghram (1947), ibid., 294.
. Nonaka, S. Hirasawa, and K. Tsutsumi (1951), J. Phys. Soc. Japan *6*, 466.
. Nyquist (1928), Phys. Rev. *32*, 110.
. E. O'Meara (1951), Rev. Scient. Instr. *22*, 106.
. Pelchowitch and J. J. Zaalberg van Zelst (1952), ibid., *23*, 73.
. Pelchowitch (1954), Philips Res. Rep. *9*, 2.
. B. Penick (1935), Rev. Scient. Instr. *6*, 115.
. R. Prescott (1949), ibid., *20*, 553.
. J. Reich, Theory and Application of Electron Tubes. McGraw-Hill, New York 1939.

C. Reuterswärd (1951), Ark. Fysik *4*, 203.
—— (1953), Swedish Nat. Conf. Physics, Gothenburg (abstr. in Ark. Fysik *8*, 18).
S. Roberts (1939), Rev. Scient. Instr. *10*, 181.
J. Schintlmeister, Die Elektronenröhre als physikalisches Messgerät. Springer, Wien 1943.
W. Schottky (1918), Ann. Physik *57*, 541.
N. T. Seaton (1948), Canad. J. Res. *F26*, 302.
W. Siri (1947), Rev. Scient. Instr. *18*, 540.
Stevens and Inghram (1953) ibid., *24*, 987.
P. G. Sulzer and A. H. Waynick (1949), ibid., *20*, 320.
W. H. Sutherland (1949), Brit. J. Radiol. *22*, 255.
J. Taïeb (1952), Trans. Instr. Meas. Conf., Stockholm, 144.
Tait and Chalklin (1953), J. Scient. Instr. *30*, 268.
C. Taylor (1954), Ark. Fysik *8*, 201.
Thode, Harkness and Graham (1947), J. Scient. Instr. *24*, 119.
Thomas and Finch (1950), Electronic Eng. *22*, 395.
A. W. Vance (1936), Rev. Scient. Instr. *7*, 489.
J. A. Victoreen (1949), Proc. I. R. E. *37*, 432.
R. K. Wanless and H. G. Thode (1953), J. Scient. Instr. *30*, 395.
F. A. White and T. L. Collins (1954), Appl. Spectrosc. *8*, 17.

Tryckt den 25 april 1956

Uppsala 1956. Almqvist & Wiksells Boktryckeri AB

ARKIV FÖR FYSIK Band 10 nr 38

Communicated 14 March 1956 by Manne Siegbahn and Ivar Waller

On the annihilation of positrons in condensed materials

By T. R. Gerholm

With 9 figures in the text

Summary

The positron annihilation lifetimes in various metals and insulators have been measured with an automatic millimicrosecond coincidence equipment. The lifetimes were found to be the same in all metals and equal to $(2.5 \pm 0.3) \times 10^{-10}$ sec, which is longer than the value hitherto accepted, $(1.5 \pm 0.3) \times 10^{-10}$ sec. The halflife of the first excited state in Pb^{207} was found to be $(0.9 \pm 0.3) \times 10^{-10}$ sec. This result is in accordance with the value $1.0^{+0.4}_{-0.2} \times 10^{-10}$ sec deduced for this halflife from the reduced transition probabilities measured in Coulomb excitation. The annihilation lifetimes in various metals and insulators are in agreement with the theoretical values deduced from a model suggested here. A weak component with a longer lifetime has been observed in aluminium. An interpretation of this component is suggested, based on the same model.

Introduction

In a series of experiments by Deutsch and co-workers [1] the existence of a bound electron–positron state—positronium—was clearly demonstrated. The formation and decomposition of positronium in a variety of gases has been studied. It has been found that the rate of annihilation, measured from the time of the creation of the positron, exhibits a complex behaviour. It generally consists of a pressure-dependent component corresponding to the annihilation of free positrons and two more or less pressure-independent components due to the two ground state positronium modifications. The singlet state, *para-positronium*, annihilates very fast while the triplet state, *ortho-positronium*, has a longer lifetime.

The singlet state annihilates with the emission of two quanta travelling in opposite directions, while for the triplet state energy and momentum conservation requires at least three annihilation quanta. Obviously the two-quantum annihilation corresponds to monochromatic gamma-ray emission, while the three-quantum annihilation gives rise to a continuous spectral distribution.

Since radiative transitions between the two states take place only at a very slow rate (magnetic dipole character) one would expect the triplet state to decay almost completely by three-quantum annihilation, which is about 1000 times slower than the two-quantum process. The theoretical annihilation lifetimes [2] for the para-positronium state is 1.25×10^{-10} sec. and for the ortho-positronium 1.4×10^{-7} sec. The experimental results are in good agreement with these theoretical values.

However, the rate of decay of the longer-lived ortho-positronium is very often considerably enhanced by conversion into the short-lived para-positronium modification. Such triplet to singlet conversion can take place by means of spin exchange in collisions with molecules containing unpaired electrons of the appropriate spin orientation. External magnetic fields, or molecular fields in the presence of paramagnetic ions, also give rise to a partial quenching of the triplet state due to the Zeeman effect.

Although the various modes of interaction between the positronium atom and the surrounding gaseous molecules are not always completely understood, theory and experiment are in excellent agreement as far as the positronium itself is concerned. In fact positronium can be considered one of the physical configurations that are best understood theoretically.

In the past few years a great deal of interest has been focused on the problems connected with the annihilation of positrons in liquids and solids. There exists some experimental evidence for the formation of positronium also in condensed materials, but the situation is more complicated both from the theoretical and the experimental points of view.

The theory must account for the fact that the positron is strongly repelled by Coulomb fields from the neighbouring nuclei. Therefore the positrons are confined to the interstitial space, and the question arises whether there is enough room for the positronium atom to exist. In the case of metal, one also has to consider the interaction between the positronium and the unbound conduction electrons.

The lifetimes to be measured are at the very limit of present delayed coincidence technique. The possibility to distinguish between the triplet and the singlet states by means of their corresponding two-quantum and three-quantum modes of annihilation is of very limited value, since, as will be discussed later, one has to assume that ortho-positronium, if it is formed, decays mainly via conversion to para-positronium, i.e. by two-quantum annihilation.

However, apart from its intrinsic interest, the possible formation of positronium in condensed materials is of importance, since, as has been pointed out in several connections [3, 4], one might anticipate that once the mechanism of its formation and decomposition is understood, the positronium atom will constitute a useful tool for the study of solid state physics and physical chemistry.

Experimental evidence for the formation of positronium in condensed material

The slowing down time of positrons in condensed materials is generally supposed to be short compared to the mean lifetime of the positrons. According to Lee-Whiting [5] the positrons are thermalized in metals within 3×10^{-12} sec. These calculations do not apply to insulators, since the excess momentum is considered to be absorbed by the conduction electrons only. However, in view of the similarity between the experimental results obtained with metals and with many non-conducting materials one feels justified to assume that also in these materials positrons are slowed down to thermal velocities before annihilation.

This assumption is supported by experiment. With a gamma-ray spectrometer of sufficiently good resolution one can determine the center of mass velocity of the electron–positron pair from the Doppler broadening of the annihilation line. Such experiments were made by DuMond and co-workers [6, 7] with a crystal diffraction spectrometer and by Lind and Hedgran [8] with a large double-focusing beta-ray spectrometer. A quite different method was first suggested by DeBenedetti, who pointed out that the deviation from perfect colinearity of the two annihilation quanta is a measure of the momentum of the annihilating pair. From this angular spread DeBenedetti and co-workers [9] have been able to measure the momenta of positrons annihilating in various materials.

The different experiments are all in reasonable agreement. They show that the momentum of the annihilating pair is about $mc/137$ corresponding to $v/c \sim 4 \times 10^{-3}$ or an energy of about 16 eV. This means that at least the majority of the positrons are thermalized before the annihilation. Furthermore it is evident that the inner shell electrons do not participate in the annihilation process.

Having been thermalized the positron was thought [9] to spend some time diffusing through the crystal lattice and finally annihilate as a free particle. This model can be checked in different ways.

Since the ratio of the three-quantum to two-quantum annihilation rates [2] is $4e^2 (\pi^2-9)(9\pi\hbar c)^{-1} = 1/1115$, one would obtain, for electron spins distributed at random, for the ratio between the two corresponding annihilation cross-sections $\sigma_{3q}/\sigma_{2q} = 3/1120 = 1/372$.

If positronium is formed, however, the electron spins become oriented with respect to the positron spins. This means that one would expect the three quantum annihilation process to become more frequent due to the formation and decay of ortho-positronium.

In a series of experiments DeBenedetti and Siegel [10] measured the σ_{3q}/σ_{2q} ratio for various materials. Their experiments confirmed the results for positronium formation in gases, already obtained in a different way by Deutsch and his co-workers. But for aluminium and some non-conducting liquids and solids they got the 1/372 ratio expected for a statistical electron spin distribution. From their experiment they concluded that either positronium is not formed to any considerable extent in condensed materials, or if it is formed, there is a fast triplet to singlet conversion, so that the three-quantum annihilating state becomes quenched.

From the picture of freely diffusing positrons one would expect some of the positrons to escape from the metal surface. These should be possible to collect on a negatively charged electrode. The experiment was tried by Madansky and Rasetti [11], but with a clearly negative result.

This is important, since it shows that either the positrons become bound in some way to the lattice, so that they cannot escape, or they do come out but with electrons attached to them, i.e. as postitronium.

Further evidence for the formation of positronium in solids and liquids has been derived from a measurement of the time distribution of the annihilation quanta, with respect to the time of creation of the positron. DeBenedetti and Richings [12] proved by relative measurements that the lifetimes of positrons in metals and several inorganic chemical compounds are independent of the material (to $\pm 0.5 \times 10^{-10}$ sec), while in certain insulators like quartz, paraffin, water, teflon and polystyrene the mean lifetimes of the positrons are somewhat longer than in aluminium ($\sim 2.5 \pm 10^{-10}$ sec according to their measurements).

Later, Bell and Graham [13] made very careful studies of the rate of annihilation of positrons in condensed materials. They were able to perform absolute measurements of the lifetimes by means of a fast coincidence equipment with a resolving time of about two millimicroseconds. Since these measurements will be discussed in some detail below, we shall quote here only their main results.

For all metals they got a mean lifetime of $(1.5 \pm 0.3) \times 10^{-10}$ sec. In many insulators the lifetimes were of the same order of magnitude. In addition they discovered, however, that some amorphous substances like fused quartz, teflon and polystyrene exhibit a complex decay curve. There is a fast component (τ_1) with a mean life of a few times 10^{-10} sec and a second component (τ_2) with a lifetime about 10 times longer.

The values for the lifetimes of the τ_2 component scatter considerably for different materials and were also found to be temperature-dependent. The τ_2 lifetimes increase with increasing temperature. When present, the τ_2 component was found to be responsible for about one third of the total number of annihilations, independently of the actual value of τ_2.

In an elegant way Bell and Graham were able to prove that the τ_2 component also decayed mainly by two-quantum annihilation.

The existence of a complex decay, very much resembling the annihilation behaviour in gases, strongly favours the positronium formation hypothesis. According to Bell and Graham, the positrons during the slowing-down process pick up electrons and form positronium in some of the cases. The τ_2 component is due to the more long-lived ortho-positronium, but the decay is enhanced by a factor 50 or more by triplet to singlet conversion. This conversion is due to collisions with atoms of the sample material. In metals the conversion rate is expected to be even higher due to the presence of conduction electrons and the triplet state therefore becomes completely quenched. This explains the absence of τ_2 component.

Owing to the fast triplet to singlet conversion, two-quantum annihilation becomes by far the dominating process, also if positronium is formed. However, Bell and Graham have called attention to the fact that, according to their model, one would expect the relative yield of three-quantum events from teflon (at 20°) to be

$$\frac{\sigma_{3q}}{\sigma_{2q}} = \frac{1}{3}\,\frac{3.5 \times 10^{-9}}{1.4 \times 10^{-7}} = 0.8\,\%$$

which is about three times as much as one would get for electron spins distributed at random ($\sigma_{3q}/\sigma_{2q} = 1/372$).

In fact DeBenedetti and Siegel [10] did find about twice as many three-quantum annihilations from teflon as from Al under identical conditions. Further experiments by Graham and Stewart [14] and others [15, 16] have shown a temperature effect in this σ_{3q}/σ_{2q}ratio, in accordance with the temperature dependence of the τ_2 component observed by Bell and Graham.

However, Bell and Graham themselves point out that their theory is not free from objections. The most serious of these are concerned with the values found for the annihilation lifetimes in metals and with the observed intensity ratio between the two components in those cases, where the time distribution of the annihilation quanta shows a complex form.

The value which Bell and Graham found for the positron lifetimes in metals, $(1.5 \pm 0.3) \times 10^{-10}$ sec., is very close to the theoretical mean lifetimes of para-positronium, 1.25×10^{-10} sec. However, one would expect to get a lifetime which is *four times* this value, since, as was first pointed out by Garwin [17], in the case of rapid conversion, the positrons spend three fourths of their life in the slow annihilating triplet state.

The observed constancy of the τ_2 component, in spite of large variations in lifetime, is also difficult to reconcile with the suggested quenching mechanism. It has been shown by Dixon and Trainor [18] that it is impossible, independently of the choice of conversion rate, to account for the lifetimes and intensity ratios obtained by Bell and Graham on the basis of a simple conversion theory.

Alternatively, Dixon and Trainor suggested an interpretation of the τ_2 component in terms of annihilation from the excited 2S state. It seems that this hypothesis must be ruled out, however, since, according to Wallace [41], the 2S state, if it is a bound configuration, will rapidly decay to the ground state by means of P state admixtures.

To summarize, one might say that some qualitative evidence for positronium formation in condensed material has been presented, at least for those materials that show the τ_2 component. However, it has not been possible to account quantitatively for the observed annihilation lifetimes. In view of the discrepancies outlined above it was considered worth while to try to remeasure some of the lifetimes given by Bell and Graham, using a somewhat different technique.

Measurements

1. *The coincidence arrangement*

For the measurements reported here a coincidence arrangement [19] of the fast–slow type was used (Fig. 1). Pulses are taken out from the photomultiplier anodes and are fed, via equalizing circuits, through a variable delay line to a fast coincidence unit. Within the limits set by the resolving time of this circuit, only those pulses will be accepted that have a relative time delay, corresponding to the delay line position. The apparatus is similar to that described by Bell *et al.* [20].

Simultaneously, pulses, coming from one of the last dynodes of each of the two multipliers, are fed to differential discriminators, as shown on the block diagram. By means of the pulse height selection in these side channels a rough energy discrimination is also provided.

Thus pulses that appear at the output of the slow ($5\,\mu s$) triple coincidence unit correspond to coincidence events that have fulfilled the time conditions in the central channel as well as the pulse height conditions in the side channels. These coincidences are recorded by a number of mechanical registers corresponding to different delay line settings.

The coincidence sampling time is limited by an electronic timer. When the timer stops, the carriage with the fast coincidence circuit goes to the next position, where it stops and the timer starts again. In the extreme positions the direction of motion is automatically reversed. The apparatus will therefore continue to scan the delay interval, collecting coincidences, until it is shut down. It is preferable to use a rather short sampling time and scan the interval many times, since in this way small deviations, caused by drifts in the electronic circuits, tend to cancel, and the accuracy will be improved.

Stilbene crystals ($10 \times 10 \times 12$ mm^3), fitted with thin aluminium foils as light reflectors, were used as scintillators. The surfaces facing the photomultipliers were ground. The crystals were fixed to selected 1P21 tubes, normally operated at 2000 volts. The detectors were wrapped in black tape to shield them from external light. This was possible since only gamma-gamma coincidences were of interest. The sam-

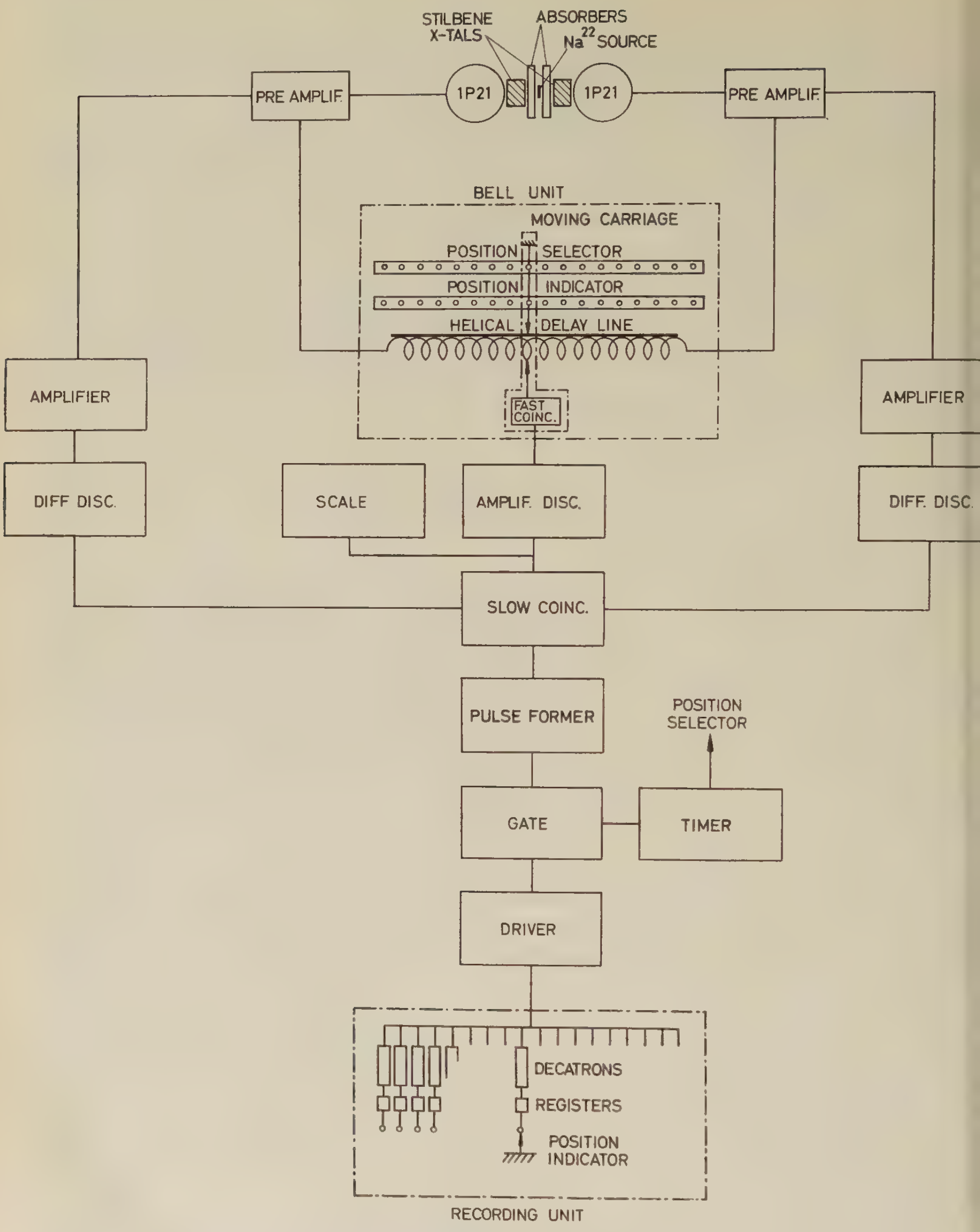

Fig. 1. Automatic millimicrosecond coincidence equipment.

es could be interchanged without switching off the high voltage, which is of advantage nce the measurements become more reproducible.

1P21 multipliers were chosen because the transit time variations in these tubes e smaller than in other types. This means that the ultimate resolving time is shorter. owever, due to the poor light collection efficiency, these tubes are much less favourble than end-cathode types as regards energy resolution. For the measurements ported here the poor energy resolution was not too serious, since the initial and aal quanta differ in maximum Compton electron energy by about a factor three. herefore the discriminators in the side channels could easily be adjusted so that the itial quanta were accepted only in one channel. This arrangement is necessary hen the lifetimes to be measured are shorter than the resolving time of the coindence circuit.

The pulse height versus energy linearity was checked and the detectors were librated with suitable sources. During the course of the experiments, the spectral stribution in both channels was measured several times and found to be stable. he reproducibility after shut-down periods was excellent, provided the electronic mponents were allowed to reach thermal equilibrium before the comparison meas-rements were made.

The instrument gives the coincidence counting rate (N_{coinc}) for various inserted me delays (x). According to Newton [21] one has the following formula, if only one etime is involved

$$F(x) = \lambda\, e^{-\lambda x} \int_{-\infty}^{x} e^{\lambda t}\, P(t)\, dt. \tag{1}$$

(x) is the delayed coincidence curve corresponding to a rate of decay $\lambda = 1/\tau$ (τ is e mean lifetime). $P(x)$, finally, is the instrumental response to prompt coincidences nder otherwise identical conditions.

From this expression one easily obtains

$$\frac{d \log F(x)}{dx} = -\lambda \left\{1 - \frac{P(x)}{F(x)}\right\}. \tag{2}$$

there is a region where $P(x)/F(x) \ll 1$, i.e. if $\tau \gg \tau_0$, the lifetime is simply and ost accurately obtained from the slope of the curve log $F(x)$ versus x. But if $\tau \leq \tau_0$, is necessary to consider the shape of the whole curve. It has been shown by Bay [22] at the mean lifetime is equal to the centroid shift.

$$\tau = \overline{T}_F - \overline{T}_P. \tag{3}$$

It is very often difficult or even impossible to measure the prompt curve. In those ases it is sometimes possible to determine the lifetime by means of a relative measureent, i.e. to compare the centroid shift with the displacement of the resolution curve aused by a similiar sample with a known lifetime. In that case one obviously has

$$\tau = \tau_C + \overline{T}_F - \overline{T}_C \tag{3'}$$

here τ_C and $\overline{T}_C$ are the mean life and x coordinate of the centroid of the comparison urve, respectively. Alternatively, one can compare the curve $F(x)$ with its own inverse $F(-x)$, obtained with the functions of the two detectors interchanged (self comparison method). One then has

$$2\tau = \overline{T}_F - \overline{T}_{-F}. \tag{3''}$$

2. *Instrumental shift*

The comparison and self-comparison methods rest on the assumption that there are no instrumental contributions to the centroid shift, i.e. the centroid of the prompt curve should coincide with its own inverse ($\overline{T}_P = \overline{T}_{-P}$). This, however, is generally not the case. In fact, if the two scintillation crystals absorb different energies, the prompt curve will always be slightly shifted towards the low energy side, i.e. the low energy pulse is artificially delayed with respect to its coincident partner corresponding to higher energy. Depending on the conditions, this instrumental shift can therefore be positive or negative. In our case it will always be positive, since the preceding gamma quantum corresponds to higher energies absorbed in the scintillation crystal

For sufficiently high energies this effect can be neglected, but for energies below 342 keV, which is the maximum Compton recoil energy given to the crystal by an annihilation quantum, the instrumental shift is expected to be of the same order of magnitude as the positron annihilation lifetimes in metals. If the comparison or self-comparison methods are used, this effect should therefore be properly taken into account.

The instrumental shift arises as follows. Suppose that a gamma quantum is absorbed in the scintillation crystal at time $t = 0$. Then the probability that a photoelectron is produced at time t is given by the expression

$$p(t) = R(1 - e^{-\lambda t}), \tag{4}$$

where R is the total number of photoelectrons produced during the light flash and λ is the decay constant of the scintillator. From this expression it is possible to calculate the average time $\bar{t}$ elapsed before the appearance of the first photoelectron at the multiplier photocathode.

According to Post and Schiff [23], $\bar{t}$ is given by

$$\bar{t} \approx \frac{Q}{R\lambda}\left\{1 + \frac{Q+1}{2R} + \cdots\right\} \tag{5}$$

where Q is the number of photoelectrons necessary to trigger the electronics and R is the average total number of photoelectrons per scintillation. If, in accordance with Bell *et al.* [20], we now suppose that our coincidence circuit responds to the first photoelectron produced ($Q = 1$) and for stilbene detectors assume $1/\lambda = 8 \times 10^9$ sec and $R = E/4$ photoelectrons, E being the Compton electron energy in keV, we obtain

$$\bar{t} = \frac{320}{E}\, 10^{-10} \text{ sec.} \tag{5'}$$

To secure a detector efficiency of about 80 % one has to wait a time $2\bar{t}$, i.e., for energies around 300 keV, about 2×10^{-10} sec.

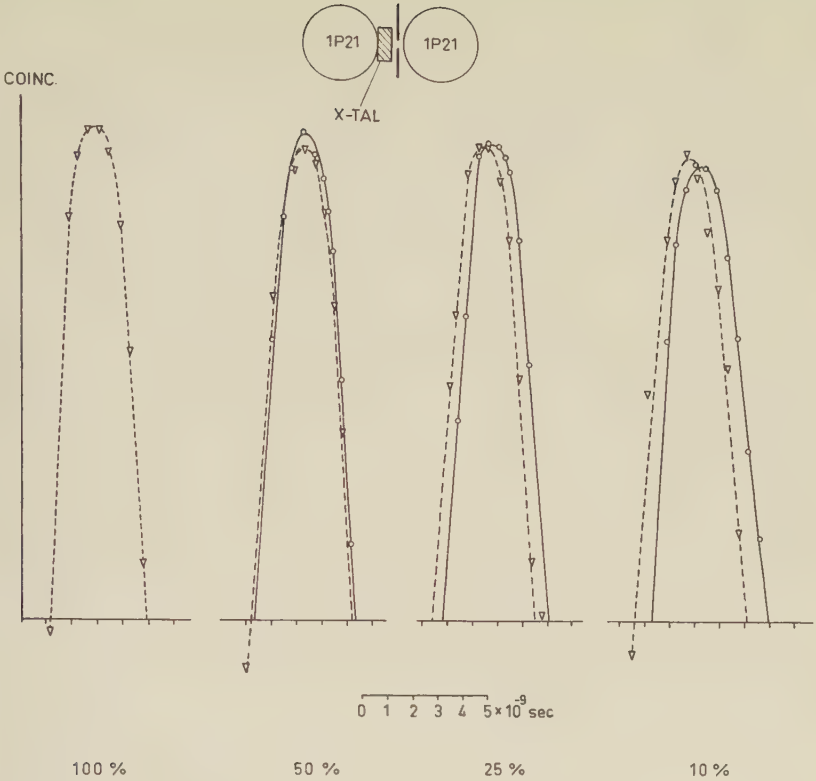

Fig. 2 a.

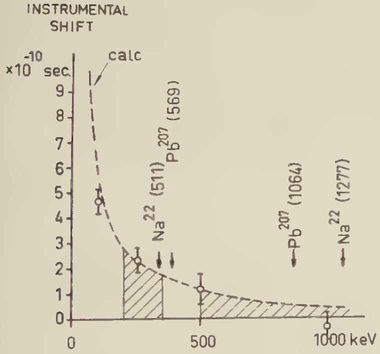

Fig. 2 b.

Fig. 2. (*a*) Single crystal study of the artificial time delay (instrumental shift). (*b*) Instrumental shift versus energy dissipated in the crystal. The points are values obtained by the single crystal method. The dashed curve is the theoretical relation corresponding to the appropriate detector efficiency ($\varepsilon \sim 80$ per cent). The hatched regions correspond to the Compton electron energies accepted by the two side channels during the delayed coincidence experiments described in the text.

To check these calculations one can make an estimate of E from the shape of the prompt coincidence curve, since, for sufficiently large delays, the prompt curve should have an exponential dropping-off rate approximately corresponding to $\bar{t}$. However, $\bar{t}$ will be very inaccurately measured by this method, since the shape of the curve will also be affected in other ways, particularly by transit time variations in the electron multipliers. For 1P21 the transit time spread is known [24] to be about 10^{-10} sec.

In order to determine $\bar{t}$ as a function of E more accurately the following experiment was made. A single scintillation crystal was inserted between the two multipliers, facing the photocathodes on both sides simultaneously. Obviously, practically every gamma quantum that is detected on one side will also be detected on the other, provided the discriminators in the side channels are adjusted in a suitable way. The "genuine coincidence" counting rate will be almost as high as the channel counting rates, whereas there will be no background due to "random coincidences". The coincidence efficiency is easily determined as the ratio between the "coincidence" counting rate and the counting rate in the side channels (the lowest if they are different).

To simulate an energy difference in the two channels the crystal surface facing one of the photomultipliers was partially masked with black paper. The number of photoelectrons produced in this tube will be reduced in proportion to the percentage of masking and this will, at least approximately, give rise to the same change in $\bar{t}$ as would have been caused by a corresponding change in energy.

If the gamma quanta absorbed in the crystal are of sufficiently high energy and the discriminator on the unmasked side is adjusted to accept only the highest pulses, one can neglect the delay on the unmasked side. A Co^{60} (1.2 and 1.3 MeV gamma-rays) source was used, placed at some distance from the crystal. The experiment showed that the resolution curve is shifted towards the unmasked side as expected. The average delay $\bar{t}$ was determined by centroid shift analysis for some different "energies", i.e. different percentage of masking. As shown in the diagram in Fig. 2, the measured points are in reasonable agreement with the curve $2\,\bar{t}$ versus E, calculated from the approximate formula (5′) for a coincidence efficiency of about 80 per cent, corresponding to the measured ratio between coincidence and channel counting rates.

The purpose of this experiment was only to demonstrate the existence of the instrumental shift and to give an idea of the orders of magnitude. In principle it would have been possible to use the single crystal method to calibrate the instrument and determine the lifetimes directly from the self-comparison centroid shift by subtracting the instrumental shift corresponding to the Compton electron energies involved. However, for the sake of accuracy, this method was avoided, and the experimental $\bar{t}$ versus E relation was only used as guidance for the following experiments.

3. *Relative measurements*

The positron emitter Na^{22} (halflife 2.6 year) offers a suitable source for positron lifetime measurements. As shown in Fig. 3 the branching to the 1.277 MeV first excited state of Ne^{22} is nearly 100 per cent.

Transitions to the ground state take place by means of electric quadrupole radiation [25]. Unfortunately the lifetime of the excited state has not yet been measured. The transition has been observed [26] in Coulomb excitation, but no estimate of the transition probability has been published so far. From theory [27, 28] one would expect a lifetime of the order of a few times 10^{-11} sec, but the theoretical estimates of $E2$-transition probabilities are usually too low by considerable factors [29]. The lifetime is therefore very probably less than 10^{-11} sec. This implies that for these experiments the 1.277 MeV gamma quantum can be considered prompt with respect

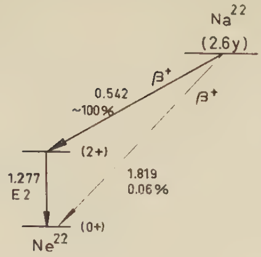

Fig. 3. Decay scheme of Na^{22} according to Hinman, Brower and Leamer [25].

to the emission of the positron. The positron lifetime can therefore be taken to equal the time elapsed between the emission of the 1.277 MeV gamma quantum and the appearance of the annihilation quanta.[1]

A Na^{22} source of high specific activity was deposited in a 2 mg/cm^2 aluminium envelope and placed between two aluminium absorbers. Each of these was 2 mm thick. Since the maximum energy of the positron spectrum is only 542 keV [30] the positrons are completely absorbed in the aluminium and will annihilate in the metal.

The source and the aluminium absorbers were inserted between the scintillation crystals. The geometry was kept fixed by suitable means during the experiments. The discriminator in the left channel was set to accept all pulses corresponding to Compton electron energies larger than 500 keV, which is well above the maximum energy given to the scintillation crystal by an annihilation quantum (342 keV). Since the left channel responds only to the primary, 1.277 MeV, gamma-rays, the delayed annihilation quanta must be recorded in the right channel. The differential discriminator on this side was operated with a rather wide channel, set just below the Compton edge of the annihilation radiation (cf. Fig. 2b). In these experiments one can neglect the three-quantum annihilation, since, as was discussed above, in all metals the three-quantum process accounts only for about 0.3 per cent of the total number of annihilations.

The delayed coincidence resolution curve recorded in this way, should be shifted towards the right. According to (3) the mean lifetime is equal to the displacement of the centroid relative to the centroid of the prompt coincidence resolution curve, obtained under otherwise identical conditions. However, since such a prompt curve is not available, it is necessary to make a comparison measurement, i.e. to measure against a similar source with a known lifetime. In view of the energy dependence of the instrumental shift, discussed in the previous section, such a comparison source should be chosen carefully, to correspond as closely as possible to the same crystal absorbtion.

Bi^{207} (halflife 27 years), which decays by electron capture, is a very suitable reference source. A careful study of the decay scheme has recently been published by Alburger and Sunyar [31] (cf. Fig. 4). Since the weak 1.44–0.90 MeV cascade accounts only for a negligible fraction of all decays, the feeding to the 569 keV first excited state is practically 100 per cent. The transition to the ground state is of electric quadrupole character. From direct lifetime measurements by means of delayed coincidences only an upper limit for the lifetime of the 569 keV level has been obtained [29, 32]. According to Sunyar, the halflife is $< 4 \times 10^{-10}$ sec. However, the transition has also

---

[1] A lifetime of the 1.277 MeV level comparable to the positron mean lifetime would make the experimentally determined values for the annihilation lifetimes correspondingly shorter.

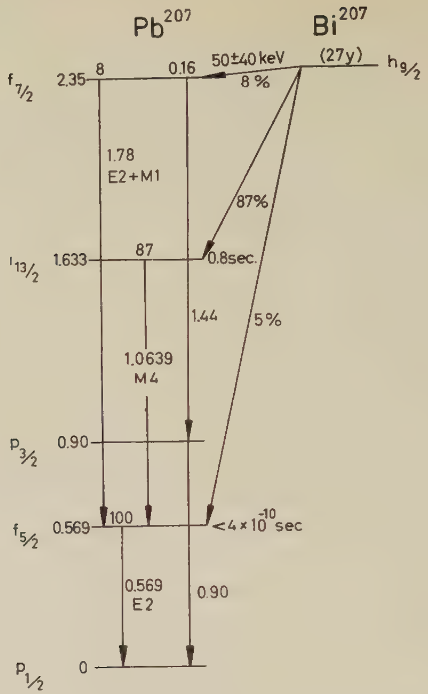

Fig. 4. Decay scheme of Pb^{207} according to Alburger and Sunyar [31]. The halflife of the 569 keV level has been measured in this work to be $(0.9 \pm 0.3) \times 10^{-10}$ sec.

been observed in Coulomb excitation. The reduced transition probabilities determined by Stelson and McGowan [33] indicate a mean life of $1.4^{+0.6}_{-0.3} \times 10^{-10}$ sec. which is indeed very close to the value $(1.5 \pm 0.3) \times 10^{-10}$ sec obtained by Bell and Graham [13] for the mean life of positrons in aluminium.

Thus, if the apparatus is adjusted in exactly the same way in the two experiments one would expect the centroid of the Pb^{207} curve to coincide almost exactly with the centroid of the positron annihilation curve, if the two curves are normalized to the same area. The small energy difference in the two cases gives rise only to a negligible difference in the instrumental shift.

According to the measurements, however, the positron annihilation curve is shifted considerably more towards positive delays (cf. Fig. 5). The centroid displacement obtained from three independent comparison measurements, was found to be

$$T_{\mathrm{Al}} - T_{\mathrm{Pb}^{207}} = (1.1 \pm 0.3) \times 10^{-10} \text{ sec.}$$

Thus, assuming Stelson and McGowan's value for Pb^{207} to be correct, we obtain for the mean lifetimes of positrons in aluminium about 2.5×10^{-10} sec, in disagreemen with Bell and Graham's value $(1.5 \pm 0.3) \times 10^{-10}$ sec. The question then arises whether one is justified to accept Stelson and McGowan's figure. The semi-classica theory of Coulomb excitation due to Alder and Winther [34] is considered to be wel established. In those cases, where a direct comparison is possible, the lifetime

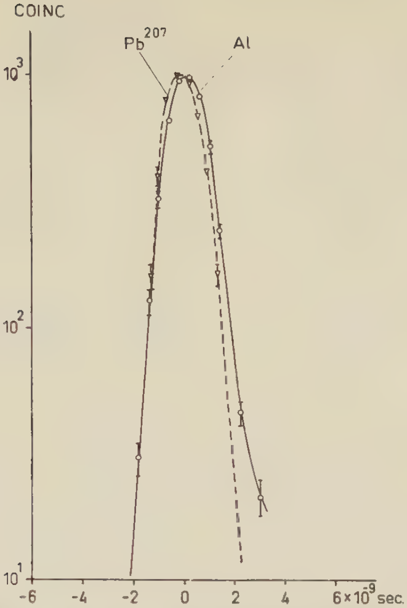

ig. 5. Comparison measurement. The centroid displacement shows that the positron annihilation ifetime in aluminium is about 1.0×10^{-10} sec longer then the mean life of the 569 keV excited in Pb^{207}. Random coincidence background subtracted.

leduced from Coulomb excitation cross-sections have generally been found to be n good agreement with those measured by delayed coincidence technique.

However, the problem whether the observed discrepancy is a real effect or might e due to some error in the Coulomb excitation theory or in the experiments cannot e solved on the basis of these relative measurements only. Therefore it was decided o make an absolute measurement of the positron lifetime in aluminium as well as f the halflife of the 569 keV excited state in Pb^{207}.

. Absolute measurements

For these measurements the comparison-self-comparison method [35] was used. he delayed coincidence resolving curve, obtained from the annihilation of positrons n aluminium ("aluminium curve") was first measured in exactly the same way as lescribed above. Then the inverse aluminium curve was measured, without changing nything but the discriminator settings in the side channels. These were readjusted n such a way that they interchanged the functions of the two detectors, i.e. the rimary gamma-rays were detected in the left channel and the delayed quanta in the ight. Particular care was taken that the same regions of the Compton energy distributions were selected as in the first measurement.

Having obtained the aluminium curve and its inverse, the corresponding two b^{207} curves were measured.

Finally, exactly the same two measurements were made with a Co^{60} source of uitable strength inserted between the two scintillation crystals. Co^{60} was chosen

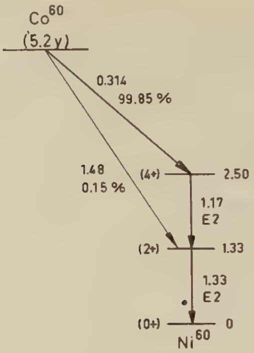

Fig. 6. Decay scheme of Co^{60} according to Keister and Schmidt [36].

as a comparison source for the following reasons. As shown in Fig. 6 the beta-active Co^{60} (halflife 5.3 years) decays [36] almost entirely to the second excited state in Ni^{60}. From this level there is an $E2$-$E2$ cascade down to the ground state. To prevent the beta-rays from being detected, two teflon absorbers of 3 mm thickness were inserted between the source and the two detectors. The coincidences were therefore only due to the 1.17–1.33 MeV gamma-gamma cascade. Under the existing experimental conditions the instrument will not be able to distinguish between the 1.17 MeV and the 1.33 MeV gamma-rays. Therefore, in about one half of the coincidence events the preceding 1.17 MeV quantum is recorded in the left and the following 1.33 MeV quantum in the right channel, giving rise to a centroid displacement towards positive delays. In the remaining one half of all coincidence events the opposite will occur, the 1.17 MeV gamma quantum is recorded in the right and the 1.33 MeV quantum in the left channel with a resulting negative centroid displacement. Possible centroid displacements caused by delayed gamma quanta will therefore cancel. The centroid will coincide with the centroid of the true, prompt curve. A lifetime in the 10^{-11} sec region will only manifest itself as a broadening of the Co^{60} curve. Since no such broadening was observed when the Co^{60} curve was compared with an artificial prompt curve, obtained by the single-crystal method described above, it was concluded that the lifetime of the first excited state was less than a few times 10^{-11} sec. This is in accordance with the results recently published by Bay *et al.* [37] who got an upper limit of 10^{-11} sec for the most long-lived state of Ni^{60}.

Three complete series of measurements were made, each consisting of a set of 3 pairs of self-comparison curves (cf. Fig. 7). The lifetimes were obtained from the experimental curves by means of the following two relations.

$$\tau_{\mathrm{Al}} = \tfrac{1}{2}\left\{(\overline{T}_{\mathrm{Al}} - \overline{T}_{-\mathrm{Al}}) - (\overline{T}_{\mathrm{Co}^{60}} - \overline{T}_{-\mathrm{Co}^{60}})\right\} \tag{6}$$

and

$$\tau_{\mathrm{Pb}^{207}} = \tfrac{1}{2}\left\{(\overline{T}_{\mathrm{Pb}^{207}} - \overline{T}_{-\mathrm{Pb}^{207}}) - (\overline{T}_{\mathrm{Co}^{60}} - \overline{T}_{-\mathrm{Co}^{60}})\right\} \tag{7}$$

where $\overline{T}_{\mathrm{Co}^{60}} - \overline{T}_{-\mathrm{Co}^{60}}$ is taken as a measure of the instrumental shift.

The difference in energies between the Co^{60} coincidence pair and the corresponding pairs in Al and Pb^{207} should not influence the results, since the differential discriminators in the "delayed" channel select out of all coincident events only those that cor

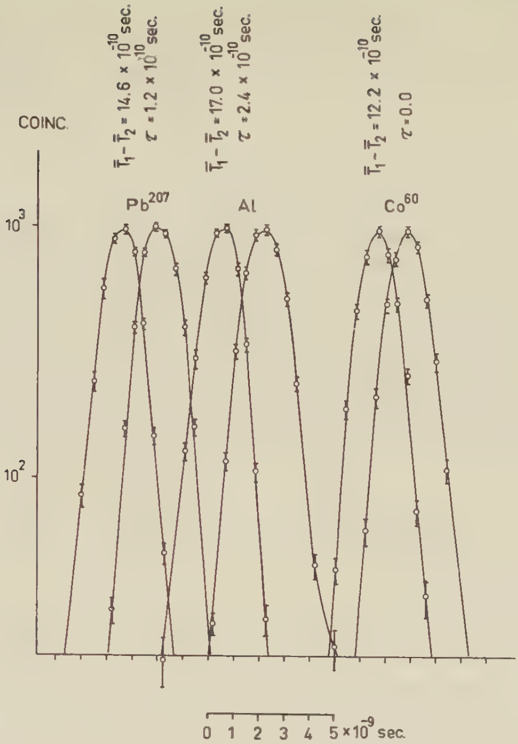

g. 7. Comparison–self-comparison measurements. Random coincidence background subtracted.

spond to approximately the same Compton energies dissipated in the scintillators.) make sure that no systematic error was introduced here, one series of measureents was made with the lower level of the discriminator shifted from 15 volts up 25 volts. As one would expect from formula (5) and Fig. 2 this change caused a nsiderable difference in the instrumental shift. In fact $\overline{T}_{Co^{60}} - \overline{T}_{-Co^{60}}$ was deeased from 12×10^{-10} sec to 6.5×10^{-10} sec, but the lifetimes deduced from relations) and (7) remained unchanged within the statistical errors.

The experimental results can be summarized as follows:

(i) The mean life for positrons in aluminium was found to be $(2.5 \pm 0.3) \times 10^{-10}$ sec.

(ii) The halflife of the 569 keV excited state of Pb^{207} was found to be $(0.9 \pm 0.3) \times 10^{-10}$ sec. This figure is in good agreement with the value $1.0^{+0.4}_{-0.2} \times 10^{-10}$ deduced from the Coulomb excitation cross-sections measured by Stelson and McGowan [33].

It may be worth pointing out that one should expect the single particle model to particularly applicable to the Pb^{207} nucleus, since it consists of only one neutron le in a doubly closed shell configuration. In fact spin and parity assignments are accordance with shell model predictions [31]. However, from the extreme single particle model one would expect for the 569 keV level a halflife considerably longer than the value found experimentally. This is interesting, since it indicates that collective effects probably play a more important rôle for a nucleus like Pb^{207} than one might expect.

5. *Annihilation lifetimes in different materials*

In the next series of measurements the lifetimes, corresponding to the annihilation of positrons in various substances, were measured. For this purpose the sandwich sample arrangement first used by DeBenedetti and Richings [12] was used. The Na^{22} source S was placed in the center of a pile of absorbers arranged in the following order: ABSBA, where B represents absorbers made of the material to be investigated and A represents similar aluminium absorbers. The B absorbers were thick enough to stop the positrons completely and the delayed coincidence resolving curve obtained with this arrangement therefore corresponds to the annihilation of positrons in substance B. The following materials were investigated in this way: Fe, Cu, Pb, perspex and teflon.

A small fraction of the annihilations will take place in the 2 mg/cm² aluminium cover, but, since this fraction is estimated to be less than 10 per cent no corrections were made for this effect.

For each material a reference curve was taken with the absorbers arranged in the order BASAB. Centroid shift analysis gives the annihilation lifetimes for the substance in question referred to the known aluminium lifetime. The method has the advantage that all measurements are made with exactly the same geometry.

In perspex and teflon the decay exhibits a clearly complex behaviour. The lifetimes of the second more long-lived τ_2 component were obtained from the exponentially decaying slope of the curve (cf. Fig. 8).

The complex curve can be resolved into two components, since, if the shape of a prompt curve (i.e. Co^{60}, cf. previous section) is known, the shape of a delayed curve with a lifetime τ_2 is also known (cf. formula (1)). The intensity of this τ_2-curve was then adjusted to fit the exponential slope of the complex curve. By subtracting the τ_2 component from the complex curve the τ_1 component is obtained. The τ_1 lifetime is finally determined in the usual way from the centroid displacement. In view of the uncertainties associated with this analysis the limits of error were taken to be somewhat wider (cf. Table 2).

The results can be summarized as follows:

(i) Earlier observations [12, 13], that in different metals the positron annihilation lifetimes show a remarkable constancy, were confirmed. The small variations obtained, of the order of a few times 10^{-11} sec, cannot be considered significant. They can probably be ascribed to statistical fluctuations, which are estimated to be of this order of magnitude.

(ii) The complex decay found by Bell and Graham [13] in many "amorphous" substances was observed in perspex and teflon. The lifetime of the τ_2 compo nent was found to be about 10 times longer than that of the τ_1 component o the annihilation lifetimes in metals. The τ_2-value for teflon, $(21 \pm 3) \times 10^{-1}$ sec, is somewhat shorter than the lifetime observed by Bell and Graham, $(35 \pm$ $4) \times 10^{-10}$ sec. However, this lifetime might be slightly different for teflon produced by different manufacturers.

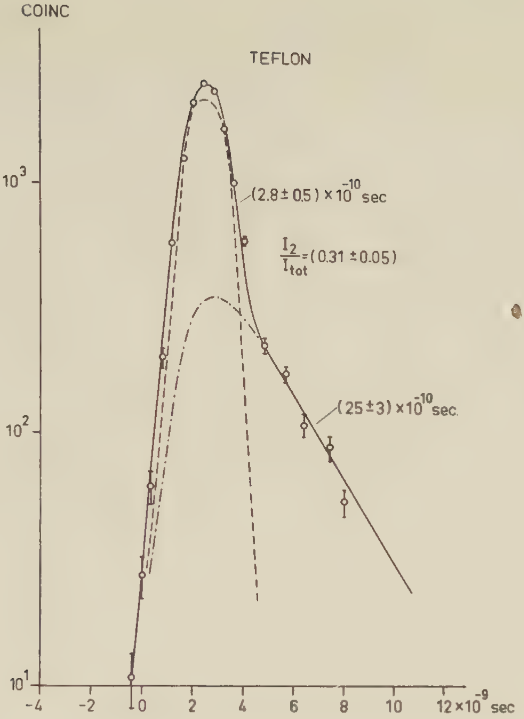

ig. 8. Delayed coincidence curve corresponding to the annihilation of positrons in polytetrafluorethylene $(C_2F_4)n$ (teflon). Random coincidence background subtracted.

(iii) The observation of Bell and Graham [13] that the τ_2 component, when present, is responsible for about 30 per cent of all annihilations, independently of the actual value of the τ_2 lifetime, was confirmed.

Evidence of a veak τ_2 component in metals

It is a consequence of formula (1) that the curvature of the delayed coincidence solving curve must always be negative when the curvature of the prompt curve is gative, unless two or more lifetimes are involved, in which cases formula (1) does t hold. During the course of the previous experiments, however, it became evident at, for all curves corresponding to the annihilation of positrons in metals, there was region of *positive* curvature, indicating the presence of a very weak component ith a longer lifetime. The effect was not attributable to instrumental imperfections, nce it was observed neither in the Pb^{207} and Co^{60} curves nor in the single crystal ns.

Unfortunately the statistical accuracy in this region of the curves is not good enough allow one to draw any definite conclusions. However, since the possible presence a τ_2 component in metals is of fundamental interest, a special experiment was ndertaken to settle this point.

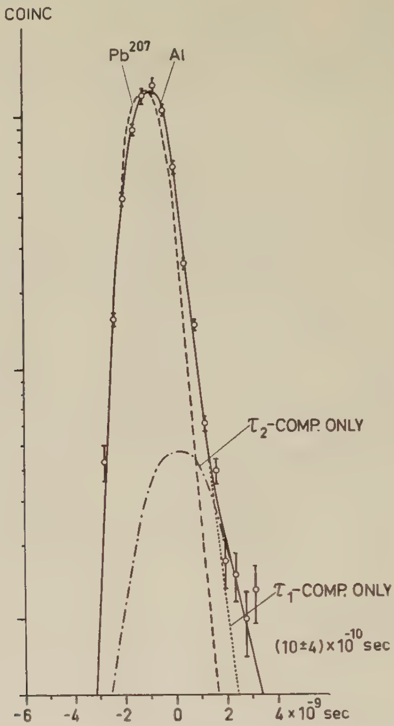

Fig. 9. Experimental evidence of a second, more long-lived component in aluminium. The dashed curve, corresponding to Pb^{207}, is shown for comparison. Random coincidence bacgkround subtracted.

To "resolve" the complex structure of the delayed coincidence curve it is necessary to use a short resolving time. In this experiment the fast coincidence circuit was adjusted to a relative half-width of the prompt curve, $2\tau_0 = 1.5 \times 10^{-9}$ sec. This, of course, implies a low coincidence counting rate. The complete run lasted about 50 hours and in all about 2×10^4 coincidences were registred. Particular care was taken to assure operating stability of the electronic equipment during the measurement. The random coincidence background was taken for several points, corresponding to large delays, inserted on both sides of the curve. The coincidence counting rates on these points were all found to be constant within the statistical errors.

The result (cf. Fig. 9) demonstrates the presence of a weak τ_2 component in the aluminium curve. The lifetime obtained from the exponential slope of the curve is $(10 \pm 4) \times 10^{-10}$ sec and the intensity is estimated to be about 6 per cent. So far, measurements have only been performed with aluminium but very probably the same effect is present in all metals.

Summary of results. Errors

The results are summarized in Tables 1 and 2. The limits of error correspond to the estimated errors due to statistics, about 10^{-11} sec, and to uncertainties in the instrumental shift $\bar{t}$, about 10^{-11} sec. Errors due to inaccuracy in the calibration or operation of the delay line are estimated [38] to be less than 10^{-11} sec. All measurements reported here are found to coincide, within their limits of error, with the corresponding values given in the tables.

As already pointed out, the main features of Bell and Graham's results have been confirmed here, with two important exceptions. The positron annihilation liftime in metals was found to be considerably longer than the value reported by Bell and Graham. Further, the coincidence resolving curve, corresponding to the annihilation of positrons in metals (aluminium), was found to exhibit a complex behaviour, indicating the presence of a more long-lived component.

Since these discrepancies are of importance for the interpretation of the results in terms of any particular model, a few comments on Bell and Graham's measurements may be justified.

The method for an absolute measurement of the positron annihilation lifetimes used here is quite different from the technique developed by Bell and Graham. Their experiments were made with a beta-ray spectrometer. The light originating in the scintillation crystals was collected on the photomultiplier cathode by means of light guides of suitable shape. A Na^{22} source was inserted between one of the light guides and a thin stilbene crystal. Positrons penetrated through the crystal and produced light flashes giving a time $t = 0$ indication. These positrons were then focused by means of the beta-ray spectrometer onto the second scintillation crystal. In front of this second crystal an absorber of the material to be investigated was inserted. The positrons stopped and annihilated in this sample, and the delayed annihilation quanta were detected by the corresponding scintillation detector in a fraction of all cases. To achieve a reasonable detection efficiency, a rather big (1 cm^3) crystal was used for this detector. The scintillator material chosen for this counter was diphenylacetylene.

In this way the delayed coincidence curve $F(x)$ was obtained. A comparison curve $P(x)$, considered to be prompt, was measured with the sample removed. In this case the positrons were detected directly in the diphenylacetylene crystal. Finally the lifetimes were deduced by centroid shift analysis, from formula (3).

The main difficulties encountered in this method are related to the fact that the comparison is made between positron-gamma and positron-positron coincidence curves. Bell and Graham assume that the positron curve, obtained with the sample removed, will be exactly equal to the prompt curve that corresponds to the measured time distribution of delayed annihilation quanta.

However, according to formula (5) and Fig. 2, for scintillation crystal excitation energies around 200 keV, which was the energy region of interest in these measurements, the instrumental shift varies considerably with energy. It might therefore become necessary to consider the intensity distribution within the energy interval. The positron measurements correspond to a discrete energy of 220 keV, since this was the energy focused by the spectrometer. However, the annihilation measurements correspond to energies ranging from 150 keV up to 342 keV, which is the maximum Compton electron energy. The discriminator bias level was adjusted to accept only pulses corresponding to energies above 150 keV. It is not impossible that this difference in energy between the two measurements might give rise to a change in the instrumental delay of about 10^{-10} sec.

Another possible effect that could explain the experimental discrepancy can arise due to the fact that, while the positrons are all absorbed in the very surface of the scintillation crystal, the Compton electrons will be more or less uniformly produced within the scintillator. The transit time of the light is therefore slightly different, particularly since the optical action of the light guides will depend on the geometrical origin of the light flash.

It has also been suggested [39] that the de-excitation mechanism of a scintillator might be somewhat different in the surface layers and deeper inside the crystal lattice.

Other undesirable effects of varying importance that could influence the shape of the curves might also be mentioned, e.g. a possible admixture of positron- (or electron-) gamma coincidences, caused by the 1.277 MeV gamma-rays emitted in coincidence with the positrons in the decay of Na^{22}. Some coincidences in the positron runs might also be due to delayed annihilation quanta originating from positrons that have escaped detection and then have annihilated inside the scintillation crystal itself or in the lucite light guide.

As discussed below, the existence of a longer-lived component in metals points to interesting features of the annihilation mechanism. There is probably also some evidence for this effect in Bell and Graham's published curves. However, the statistical accuracy in these regions of the curves are not good enough to permit any definite statements. In the curves obtained with the spectrometer method outlined above, there is probably an instrumental asymmetry. This is due to the fact that the signals produced by positrons penetrating through the thin crystal are supposed to be more uniform in size than those produced in the second crystal.[1] This effect, if present, makes the search for a weak component on the flank of the curve somewhat dubious.

Discussion

Let $g(t)$ be the probability that a positron, created at time $t = 0$, will be found at time t. Then $g(t)$ decreases with time according to the differential equation

$$\frac{1}{g} \cdot \frac{dg}{dt} = C_s\,|\psi_s|^2 + C_t\,|\psi_t|^2. \tag{8}$$

The fundamental annihilation constants C_s and C_t correspond to singlet and triplet states respectively. According to detailed calculations [40, 2] in the plane wave approximation, they are given by

$$C_s = \sigma_{2q}\, v = 4\pi \left(\frac{e^2}{m c^2}\right)^2 c \tag{9}$$

$$C_s = 3 \times 10^{-14}\ \text{cm}^3/\text{sec}$$

and

$$C_t = \sigma_{3q} \cdot v = \frac{4}{9\pi} \cdot (\pi^2 - 9) \cdot \frac{e^2}{\hbar c} \cdot C_s \tag{10}$$

$$C_t = 2.7 \times 10^{-17}\ \text{cm}^3/\text{sec}.$$

According to (8) the rate of positron annihilation is governed by the squares of the electron wave-functions $|\psi_s|^2$ and $|\psi_t|^2$, corresponding to the singlet and to the triplet states respectively, i.e. by the average densities of electrons with the corresponding spin orientations. The problem is then how to adjust the squares of the wave-functions in such a way that the corresponding lifetimes are in agreement with the experimental values.

---

[1] Cf. R. E. Bell, Beta and Gamma Ray Spectroscopy (K. Siegbahn), Ch. XVIII (1) p. 511.

a. Annihilation of positrons in metals

Let us first consider annihilation in metals. The Coulomb attraction between the positron and the surrounding conduction electrons very probably gives rise to polarization. The effective electron density, as seen by the positron, is therefore higher than the average electron density in the metal. As pointed out by Wallace [41] this effect tends to shorten the lifetimes and smear out the differences between the different elements.

Recent calculations by Ferrell [42] show, that the Coulomb attraction enhances the annihilation considerably. So far calculations have only been published for sodium, but in that particular case the theory indicates a mean life of 13×10^{-10} sec. This is much larger than the experimental values for metals reported in this and other works.

As an alternative it is suggested here, that the net result of the polarization can be described in terms of positronium formation. One particular electron becomes bound to the positron in a positronium atom. In this way the charge of the positron is neutralized and the presence of a positron will not influence the distribution of the remaining conduction electrons in the metal. The wave-functions then split up into two parts, one corresponding to the positronium electron $\{|\psi|^2\}_{\text{pos}}$ and the other to the average density of "free" (conduction) electrons in the metal $\{|\psi|^2\}_{\text{free}}$. Obviously these two parts represent competing annihilation processes: annihilation with the positronium partner (partial lifetime τ_{pos}) and annihilation with an external "free" electron (partial lifetime τ_{free}). The positrons can be considered free in collisions with the conduction electrons, since the Fermi energy of these electrons is generally higher than the binding energy of the positronium atom (6.8 eV). The total lifetime simply becomes

$$\frac{1}{\tau} = \frac{1}{\tau_{\text{pos}}} + \frac{1}{\tau_{\text{free}}}. \tag{11}$$

It is quite conceivable that positrons form positronium in metals. It is known [43,44] that the electron capture cross-section is high, provided the relative velocities correspond to the Bohr orbit velocity $e^2/\hbar$. For thermalized positrons this is about 13.6 eV electron energy, which is not far from the Fermi energies of the electrons. In aluminium for instance the Fermi energy is about 12 eV. If the electrons are captured in one of the outer Bohr orbits they will rapidly cascade down to one of the ground states, triplet or singlet.

Positronium formation also seems to be the most reasonable explanation of the negative outcome of the experiment by Madansky and Rasetti [11]. It is also interesting to recall here the observed complex shape of the coincidence resolving curve for annihilation in aluminium (cf. Fig. 9). The presence of a more long-lived component implies, that the corresponding positrons are somehow (see below) prevented from taking part in the fast annihilation process. It is difficult to explain this effect unless one assumes that at least in a fraction of all cases positronium is formed.

As suggested by Bell and Graham, the σ_{3q}/σ_{2q} ratio for metals (1/372) can be understood if rapid triplet to singlet conversion due to spin exchange is assumed. The order of magnitude of the conversion rate can be estimated on the basis of the following arguments. The conversion rate γ is given by the formula

$$\gamma = n_{\text{eff}}\, v\, \sigma_c \tag{12}$$

where n_{eff} is the effective density of electrons with velocity v, i.e.

$$n_{\text{eff}} = 6 \times 10^{23} \frac{\varrho}{A} \nu \tag{13}$$

ϱ is the density, A the atomic weight and ν the number of electrons per atom taking part in the annihilation process. Since the positron is strongly repelled by the nuclear Coulomb field it will not be able to penetrate into the inner electron shells but merely annihilate with outer shell electrons, i.e. in metals with the unbound valence electrons. ν is therefore assumed here to equal the number of valence electrons per atom. This is in accordance with experimental determinations [9] of the momenta of the annihilating pairs. The velocity v corresponds to the momenta of the Fermi electrons, i.e. $\sim 10^8$ cm/sec. The spin exchange cross section, finally, should be approximately one half of the geometrical cross-section

$$\sigma_c \sim \tfrac{1}{2}\pi r_0^2 = 1.6 \times 10^{-16}\ \text{cm}^2$$

since the electron spins will become exchanged in about one half of all collisions, unless the spin exchange is not restrained in some way.

The value 1.6×10^{-16} cm^2 for σ_c is in good agreement with the published values of the quenching cross-sections in gases [1] and liquids [15, 45] containing molecules (ions) with unpaired electrons. The quenching mechanism in these cases is generally considered to be due to spin exchange.

According to (12), the rate of ortho-para positronium conversion in aluminium then becomes

$$\gamma = 0.28 \times 10^{12}\ \text{sec}^{-1}.$$

Since this conversion rate is very much higher than the rate of annihilation from the singlet state one should, as already pointed out, expect the positronium lifetime to become nearly four times the singlet lifetime. According to the analysis by Dixon and Trainor [18], the lifetime in the limit of rapid conversion approaches the value

$$\tau_{\text{pos}} = 5 \times 10^{-10}\ \text{sec}.$$

The ortho positronium state is, of course, completely quenched and manifests itself only as a lengthening of the singlet annihilation lifetime.

The positronium annihilation lifetime is about twice the observed values for metals. However, the rate of annihilation is enhanced by the competing process, i.e. annihilation with free electrons. Since the effect of the Coulomb attraction has already been taken into account in the positronium part of the wave-function, the remainder takes the simple form

$$\{|\psi|^2\}_{\text{free}} = \tfrac{1}{4} n_{\text{eff}}$$

where n_{eff} is given by (13). The corresponding lifetime then becomes

$$\tau_{\text{free}} = (C_s \tfrac{1}{4} n_{\text{eff}})^{-1}.$$

And for aluminium one has

$$\tau_{\text{free}} = 7.5 \times 10^{-10} \text{ sec.}$$

Finally we obtain for the total annihilation lifetime of positrons in aluminium, according to formula (11)

$$\tau = 3 \times 10^{-10} \text{ sec.}$$

As shown in Table 1 the annihilation lifetimes calculated in this way for Al, Fe, Cu and Pb are remarkably constant. The absolute values are in reasonable agreement with the experimental results. However, the theoretical values are all somewhat too high. In fact this was to be expected, since we have only taken into account the valence electrons and completely neglected any possible contribution from the inner shells. If, for aluminium, some 10 per cent of all annihilations were attributable to bound inner shell electrons, the theoretical value would be in exact agreement with experiment. One would expect the nuclear repulsion to become less effective for heavier elements, which in turn would increase the probability of annihilation with bound electrons. In fact, this assumption is supported by experiment. In more recent measurements of angular correlation between annihilation quanta with improved instrumental resolution Stewart [46] discovered that for heavier elements a component corresponding to higher momenta appears, which is very probably due to an increased number of annihilations with bound electrons. The same effect has also been observed by DeBenedetti *et al.* [47].

Let y be the ratio between the number of annihilations with bound electrons and the number of annihilations with free electrons. Then the annihilation lifetimes will be reduced according to

$$\tau_{\text{calc}}^{\text{corr}} = (1+y)^{-1} \cdot \tau_{\text{calc}}\,.$$

We assume now, that y is proportional to the fractional volume occupied by the ionic core and that it is about 7 per cent for aluminium. This seems to be in accordance with experiments [46, 47]. As shown in Table 1 the lifetimes corrected in this way are all in agreement with the experimental results within the limits of error. The $\tau_{2\text{calc}}^{\text{corr}}$ lifetimes given in the table correspond to the fractional lifetime τ_{free}, corrected for annihilation with bound electrons.

In this connection it may be mentioned that the low value 1.5×10^{-10} sec given by Bell and Graham for the annihilation lifetime in metals cannot be brought into accordance with the model suggested here. To account for a total lifetime of 1.5×10^{-10} sec in aluminium it is necessary to assume that about 10 electrons per atom take part in the annihilation process. This means that not only the three valence electrons (M-shell) but also the majority of the L-shell electrons contribute to the same extent. This is of course impossible.

It is interesting to consider the mean time $\tau_{\text{ex}} = \gamma^{-1}$, spent by the positronium atom in one state before it is converted into another by spin exchange. From the estimated conversion rate it follows that

$$\tau_{\text{ex}} \sim 3.5 \times 10^{-12} \text{ sec.}$$

Since this lifetime is substantially longer than the time necessary to describe a complete Bohr orbit ($\sim 3 \times 10^{-16}$ sec), one is justified in speaking of positronium. However the estimated value for τ_{ex} shows that the positron will exchange its electron partner (spin) 100 times or more before annihilation. This may explain, why the positronium atom is not thermalized, but found to annihilate with a momentum equal to the momentum of the Fermi electrons.

However, according to Lee-Whiting [5] positrons are slowed down to thermal energies in a time which is of the same order of magnitude as τ_{ex}. If it is assumed that these calculations apply to the positronium atom as well, it seems possible that at least a few of the positronium atoms do reach thermal energies.

If this happens, however, one would expect the triplet to singlet conversion due to spin exchange to become much less effective, probably negligible, since for these low electron energies all states are already occupied. The Pauli principle therefore limits spin exchange. As far as the triplet state is concerned one is then left with the "free" annihilation process only.[1] The lifetime should then be lengthend to correspond to τ_{free}.

This may be the explanation of the observed longer-lived weak τ_2 component in aluminium. In this particular case one has

$$\tau_2 = \tau_{\text{free}} = 7.5 \times 10^{-10} \text{ sec}$$

or with correction for annihilation with bound electrons

$$\tau_{2\text{calc}}^{\text{corr}} = 6.4 \times 10^{-10} \text{ sec}$$

while the observed value is

$$\tau_2 = (10 \pm 4) \times 10^{-10} \text{ sec.}$$

Of course, more experimental material must be collected before any conclusions can be drawn about this point.

We will finally add a few words on the experiments on positron annihilation in superconductors and their bearings on the model discussed here. It was first suggested by Dresden [4] that a study of annihilation in superconductors might disclose some interesting features of the annihilation mechanism. Measurements of the positron annihilation in lead at liquid helium temperature have been reported by Stump and Talley [48] who got $\tau = (5.7 \pm 0.7) \times 10^{-10}$ sec, and by Millett [49], $\tau = (3.5 \pm 0.5) \times 10^{-10}$ sec, indicating an annihilation rate different from that reported by Bell and Graham for the annihilation lifetime in lead at room temperature, $(1.5 \pm 0.3) \times 10^{10}$ sec. No such change in lifetime was observed between normally conducting and superconducting tin. Experiments on the frequency of two-quantum annihilation [50] did not show any difference between the normally conducting and superconducting states. Investigations by Schönberg and Heer [51] of the influence of external fields on the angular correlation between nuclear gamma-rays have shown that the density distribution of the superconducting electrons is the same as that of the normally conducting electrons.

With the new value for the annihilation lifetime found in this work, $(2.5 \pm 0.3) \times 10^{10}$ sec, the discrepancy is almost removed. However, it is not impossible that

---

[1] We neglect here, as throughout this discussion, the three-quantum annihilation process.

Table 1.

	τ_{obs}	τ_{calc}	$\tau_{\text{calc}}^{\text{corr}}$	$\tau_{2\text{obs}}$	$\tau_{2\text{calc}}^{\text{corr}}$	I_2/I_{tot}
Al	2.5 ± 0.3	3.0	2.8	10 ± 4	6.4	0.06
Fe	2.3 ± 0.3	3.1	2.3	—	4.3	—
Cu	2.7 ± 0.3	3.8	2.3	—	4.3	—
Pb	2.5 ± 0.3	4.0	2.6	—	5.4	—

Lifetimes in 10^{-10} sec.

further experiments with improved accuracy will reveal some interesting features. On the basis of the model suggested her, one would expect the spin exchange cross section to depend in some way on the Fermi function. For very low temperatures the longer-lived component would become more intense and the complexity of the coincidence curve would show up more markedly. In fact, there seems to be some evidence for this effect in the curves published by Stump and Talley.

Their value for the annihilation lifetime in superconducting lead is also in agreement with the calculated $\tau_{2\text{calc}}^{\text{corr}}$ lifetime shown in Table 1.

b. *Annihilation of positrons in certain insulators*

To interpret the annihilation mechanism in metals and other conducting media, it is necessary to consider only the interaction between the positron and the conduction electrons. The contribution from the bound electrons is of minor importance. However, in those insulators, where the τ_2 component appears, the situation is more complicated and it is necessary to take into consideration the chemical structure of the material in question. Nevertheless it seems to be possible to account for at least the main features of the annihilation process by means of a simple model, essentially the same as first suggested by Bell and Graham [13].

It seems to be certain that positronium is formed in these materials in a fraction of all cases. The presence of a complex annihilation curve is in itself an indication of positronium formation, since the existence of the triplet positronium state is the most reasonable interpretation of the fact that the positrons contributing the longer-lived component τ_2 are somehow prevented from participating in the fast annihilation process. As already mentioned, Bell and Graham have pointed out the fact that if the τ_2 component is a remainder of an almost completely quenched ortho-positronium state, one would expect a somewhat higher three-quantum yield than would correspond to statistically distributed spin orientations. In teflon, for instance, σ_{3q}/σ_{2q} should be ~ 0.8 per cent as compared to ~ 0.3 per cent for random distributions of spins. Measured values seem to be in reasonable agreement with this prediction. Graham and Stewart [14] have shown that there is an obvious correlation between the σ_{3q}/σ_{2q} ratio as a function of the sample temperature and the corresponding temperature dependence of the τ_2 lifetime.

It has recently been found [46, 52] that the angular correlation curves obtained with samples of fused quartz and teflon exhibit a complex behaviour. Nearly 20 per cent of all annihilations contribute to a narrow component corresponding to a thermalized or nearly thermalized electron–positron pair, while the remaining frac-

Table 2.

Sample	Formula	ϱ	A	ν	$\tau_{1\mathrm{calc}}$	$\tau_{1\mathrm{obs}}$	$\tau_{2\mathrm{obs}}$	$\frac{\tau_{2\mathrm{obs}}}{\tau_{1\mathrm{obs}}}$
Plastic sulfur	S_8	1.92	256	48	6.1	1.5 ± 0.4	4.5 ± 0.6	3
Water	H_2O	1.00	18	8	5.0	—	17 ± 2	—
Ice	H_2O	0.92	18	8	5.4	—	12 ± 2	—
Fused quartz	SiO_2	2.65	60	16	3.1	3.5 ± 0.5	18 ± 2	5
Borax	$Na_2B_4O_7 \cdot 10H_2O$	1.7	381	236	2.1	2.6 ± 0.5	9 ± 2	3
Cellulose nitrate	$C_{12}H_{17}(ONO_2)_3O_7$	1.66	459	176	3.5	—	23 ± 4	—
Isopropylalcohol	$CH_3CHOHCH_3$	0.79	60	26	6.4	—	23 ± 4	—
Polystyrene	$(C_6H_5CH : CH_2)n$	1.1	104	40	5.2	3.7 ± 0.5	23 ± 2	6
Polyethylene	$(CH_2 : CH_2)n$	0.9	28	12	5.7	3.0 ± 0.5	24 ± 3	8
Teflon	$(CF_2 : CF_2)n$	2.2	100	36	2.8	—	35 ± 4	—
Teflon*	$(CF_2 : CF_2)n$	2.2	100	36	2.8	2.3 ± 0.5	21 ± 3	9
Perspex*	$(CH_2 : C(CH_3)COOCH_3)n$	1.2	100	40	4.6	1.4 ± 0.5	14 ± 3	10

Lifetimes in 10^{-10} sec (quoted from Bell and Graham).
* This work.

tion gives a somewhat broader distribution indicating center of mass momenta of the electron–positron pair of about 0.8×10^{-2} in units of 2 mc.

It is reasonable to correlate these two components with the τ_1 and τ_2 components found in the lifetime measurements. Because the narrow component shows a temperature effect and because the relative intensities are best explained in this way, it is most plausible to identify the narrow component with the τ_2 component, which implies that if the τ_2 component is due to the annihilation of ortho-positronium, the positronium atom must be practically thermalized before annihilation.

The remaining annihilations should then be due to free positrons, which do not necessarily have thermal velocities. However, the angular spread of annihilation quanta for this component seems to agree roughly with the expected momenta of the electrons in the corresponding outer Bohr orbits.

Table 2 gives the τ_1 and τ_2 lifetimes for some different materials. The outstanding feature of this summary is the remarkable similarity in lifetimes for very different kinds of elements. For all materials studied so far, the τ_1 lifetimes have been found to be about 2.5×10^{-10} sec. Furthermore, there seems to be a correlation between the τ_1 and the τ_2 lifetimes. As shown in the table, the τ_2/τ_1 ratios are all about 6. The limits of experimental error are very wide. There is perhaps a tendency for "simple" materials like plastic sulfur, water and fused borax to give somewhat lower value.

In view of these trends it seems reasonable to assume that the τ_1 lifetimes and the τ_2/τ_1 ratios are determined mainly by the effective electron densities as seen by the positron. Neglecting the three-quantum annihilation process, one has for the short-lived component, according to (8)

$$\lambda_1 = \tfrac{1}{4} \cdot \frac{\varrho \nu}{A}\, 6 \times 10^{23} \cdot 3 \times 10^{-14} \ \mathrm{sec}^{-1}$$

or

$$\tau_1 = \frac{A}{\varrho \nu}\, 2.2 \times 10^{-10} \ \mathrm{sec}. \tag{14}$$

In this expression A is the molecular weight, ϱ the density and ν the effective number of electrons per atom. ν is taken equal to the sum of the number of electrons in the external shell in each atom (valence electrons). This seems to be a reasonable assumption, since the strong nuclear repulsion will prevent the positrons from penetrating into the atomic core.

As seen in the table, the values calculated from this simple formula are all found to be surprisingly close to each other for all these different kinds of materials. The mean value is about 4.5×10^{-10} sec, which is somewhat higher than the mean value of the experimental τ_1 lifetime, 2.6×10^{-10} sec.[1] However it should be noted that, in the calculations, only annihilation with the outer shell electrons has been taken into account and the contribution of internal shells is completely neglected. Coulomb attraction will probably also enhance the annihilation somewhat.

Let us finally consider the longer-lived component. This is thought to be due to ortho-positronium. The relative intensities of the τ_2 component then show that positronium is formed in about 30 per cent of all cases, which happens to be about the same as has been observed in gases under normal conditions [1].

Once formed, the positronium atom will probably persist and slow down to thermal energies. It is easily seen that the spin exchange, so efficient in metals, will generally not take place in these materials, since the electrons are all bound in closed shell configurations and will therefore not be able to interact with the positronium atom. "Pick off" annihilations, i.e. annhihilations in collisions with bound electrons of the appropriate spin orientation (singlet), will be the quenching mechanism, as first suggested by Garwin [17]. This process is much less likely to occur, but it is possible to show that it is of the right order of magnitude to account for the observed τ_2 lifetimes.

Let σ_e be the *electronic* quenching cross section for "pick off" annihilation. An estimate of the magnitude of σ_e can be derived from the following arguments. In one half of all collisions the external electron will have the antiparallel spin orientations. The probability that annihilation will occur during the collision is then roughly given by (8) with $|\psi|^2 = 1/\pi r_0^3$ multiplied by the "time of contact" $2\, r_0/v'$, v' being the velocity of the external electron, i.e.

$$\sigma_e \sim \pi r_0^2 \tfrac{1}{2} C_s \frac{1}{\pi r_0^3} \frac{2 r_0}{v'} = \frac{C_s}{v'}. \tag{15}$$

For v' one would expect $v' \sim (1/137)(Z/n)c$.

For L-shell electrons in carbon, for instance, $v' \sim 0.02\, c$. However, this seems to be a little too high. From angular correlation data a value of $v' \sim 0.008\, c$ is obtained. Making use of this experimental value we get

$$\sigma_e = 1.2 \times 10^{-22}\ \mathrm{cm}^2.$$

It is interesting to see what the corresponding molecular quenching cross-section σ_m would be

$$\sigma_m = \nu\, \sigma_e. \tag{16}$$

---

[1] Values quoted from Bell and Graham are either obtained from measurements with the spectrometer or from relative measurement against aluminium. In both cases they should be increased by about 1×10^{-10} sec if the value for the annihilation lifetime in metals reported here is accepted. The average value of τ_1 for the elements listed would then be 3.3×10^{-10} sec.

In the case of teflon (polyfluorethylene $(C_2F_4)_n$) one has $\nu = 36$ and

$$\sigma_m = 4.5 \times 10^{-21}\ \mathrm{cm}^2$$

which is not too different from the published values [10, 53] for the molecular quenching cross-sections in gases like CCl_2F_2 (freon) $\sigma_m = 0.8 \times 10^{-21}$ and SF_6, $\sigma_m = 0.97 \times 10^{-21}\ \mathrm{cm}^2$.

Having obtained the quenching cross-section σ_e, we can at once write down the rate of annihilation which becomes

$$\lambda_2 \sim n_{\mathrm{eff}}\, v\, \sigma_e = \tfrac{1}{4} n_{\mathrm{eff}}\, C_s \frac{v}{v'}\, 4 \tag{17}$$

or

$$\frac{\lambda_1}{\lambda_2} = \frac{\tau_2}{\tau_1} = \frac{1}{4} \cdot \frac{v'}{v} \tag{18}$$

where v is the velocity of the positronium atom, presumably thermal, i.e., at 20°C.

$$v = c\sqrt{\frac{kT}{mc^2}} \sim 2 \times 10^{-4}\, c.$$

We finally obtain for the τ_2/τ_1 ratio

$$\frac{\tau_2}{\tau_1} \sim 10,$$

to be compared with the experimental ratio of about 6.

This must, of course, be considered a very crude estimate. However, the τ_2/τ_1 ratio is found to have the correct order of magnitude. In fact, one would expect the experimental figure to be lower than the value 10 obtained here, since obviously the positronium atom is less strongly repelled by the nuclear Coulomb field than the free positron. Therefore one would expect the inner shell electrons to contribute relatively more to the "pick off" annihilation rate than to the direct annihilation with free positrons. This effect tends to improve the agreement.

One would perhaps expect the "pick off" annihilation to give rise to a broader angular correlation curve, since the bound electrons have rather high momenta. However, it is easily seen that the electron partner released in the annihilation process will replace—i.e. be exchanged with—the annihilated bound electron in the molecule. This electron will therefore carry away the excess momentum.

It should also be mentioned that the model discussed here does not, in its present form, explain the temperature effect. According to (16) one would expect the τ_2 lifetime to decrease as $\sqrt{T}$, but, as mentioned earlier, the experiments show the opposite trend. To account for the temperature effect it seems necessary to consider in more detail the quenching mechanism and probably also the slowing-down process. It would be interesting to know whether the short-lived component also shows the temperature effect.

Conclusions

To summarize, one can say that, according to the model discussed here, positrons ehave in solids and liquids just as they do in gases. The effects that are known to e responsible for the formation and decomposition of positronium in gases are present lso in condensed materials, but here the net result of these effects is very different. he high electron density in these media gives rise to a strong perturbation of the ositronium atom. Therefore the long-lived triplet state becomes more or less comletely quenched. The quenching is particularly effective when unpaired electrons re present, as is the case for instance in metals, since then an exchange of electron pins takes place.

ACKNOWLEDGEMENTS

The author is much indebted to Professor Kai Siegbahn for his interest in this work and for his nfailing support. Further my thanks are due to Professor I. Waller and to Docent S. Lundqvist t the Institute of Theoretical Physics at this University, for valuable discussions concerning ome of the theoretical problems. I also wish to thank Mr Y. Jonsson, who assisted me during the xperiments, and E. Sokolowski, B.S., who has corrected the English.

Physics Department, University of Uppsala, Sweden.

REFERENCES

1. M. Deutsch, Beta and Gamma Ray Spectroscopy (editor Kai Siegbahn), Ch. XXI (V). North-Holland Publishing Company (1955).
2. A. Ore and J. L. Powell, Phys. Rev. *75*, 1696, 1963 (1949).
3. S. DeBenedetti and H. C. Corben, Annual Review of Nuclear Science *4*, 191 (1954).
4. M. Dresden, Phys. Rev. *93*, 1413 (1954).
5. G. E. Lee-Whiting, Phys. Rev. *97*, 1557 (1955).
6. D. E. Muller, H. C. Hoyt, D. J. Klein, and J. W. M. DuMond, Phys. Rev. *88*, 775 (1952).
7. J. W. M. DuMond, D. A. Lind, and B. B. Watson, Phys. Rev. *75*, 1226 (1949).
8. D. Lind and A. Hedgran, Ark. Fys. *5*, 29 (1952).
9. S. DeBenedetti, C. E. Cowan, W. R. Konneker, and H. Primakoff, Phys. Rev. *77*, 205 (1950).
0. S. DeBenedetti and R. T. Siegel, Phys. Rev. *94*, 955 (1954).
1. L. Madansky and F. Rasetti, Phys. Rev. *79*, 397 (1950).
2. S. DeBenedetti and H. J. Richings, Phys. Rev. *85*, 377 (1952).
3. R. E. Bell and R. L. Graham, Phys. Rev. *90*, 644 (1953).
4. R. L. Graham and A. T. Stewart, Can. J. Phys. *32*, 678 (1954).
5. T. A. Pond, Phys. Rev. *93*, 478 (1954).
6. R. T. Wagner and F. L. Hereford, Phys. Rev. *99*, 593 (1955).
7. R. L. Garwin, Phys. Rev. *91*, 1571 (1953).
8. W. R. Dixon and L. E. H. Trainor, Phys. Rev. *97*, 733 (1955).
9. H. de Waard and T. R. Gerholm, Nuc. Phys. *1*, 281 (1956).
0. R. E. Bell, R. L. Graham, and H. E. Petch, Can. J. Phys., *30*, 35 (1952).
1. T. D. Newton, Phys. Rev. *78*, 490 (1950).
2. Z. Bay, Phys. Rev. *77*, 419 (1950).
3. R. F. Post and L. I. Schiff, Phys. Rev. *80*, 1113 (1950).
4. Z. Bay, M. R. Cleland, and F. McLernon, Phys. Rev. *87*, 901 (1952).
5. G. Hinman, D. Brower, and R. Leamer, Phys. Rev. *90*, 370 (1953).
R. D. Leamer and G. W. Hinman, Phys. Rev. *96*, 1607 (1954).
6. N. P. Heydenburg and G. M. Temmer, Phys. Rev. *94*, 1252 (1954).

27. V. F. Weisskopf, Phys. Rev. *83*, 1073 (1951).
28. S. A. Moszkowski, Phys. Rev. *83*, 1071 (1951).
29. A. W. Sunyar, Phys. Rev. *98*, 653 (1955).
30. P. A. Macklin, L. J. Lidofsky, and C. S. Wu, Phys. Rev. *78*, 318 (1950).
31. D. E. Alburger and A. W. Sunyar, Phys. Rev. *99*, 695 (1955).
32. F. K. McGowan and E. C. Campbell, Phys. Rev. *92*, 523 (1953).
33. P. H. Stelson and F. K. McGowan, Phys. Rev. *99*, 112 (1955).
34. K. Alder and A. Winther, Phys. Rev. *96*, 237 (1954); Dan. Mat. Fys. Medd. *29*, nr 19 (1955).
35. H. de Waard, Phys. Rev. *99*, 1045 (1955).
36. G. L. Keister and F. H. Schmidt, Phys. Rev. *93*, 140 (1953).
37. Z. Bay, V. P. Henri, and F. McLernon, Phys. Rev. *97*, 561 (1955).
38. R. L. Graham and R. E. Bell, Can. J. Phys. *31*, 377 (1953).
39. J. B. Birks, Scintillation Counters. Pergamon Press, London (1953), p. 93.
40. P. A. M. Dirac, Proc. Camb. Phil. Soc. *26*, 361 (1930).
41. P. R. Wallace, Phys. Rev. *100*, 738 (1955).
42. R. A. Ferrell, Phys. Rev. *100*, 973, 953 (1955).
43. N. Bohr, Dan. Mat. Fys. Medd. *18*, nr 8 (1948).
44. T. Hall, Phys. Rev. *79*, 504 (1950).
45. H. S. Landes, S. Berko, and A. J. Zuchelli, Bull. Am. Phys. Soc. *1*, 68 (1956).
46. A. T. Stewart, Phys. Rev. *99*, 594 (1955).
47. G. Lang, S. DeBenedetti, and R. Smoluchowski, Phys. Rev. *99*, 596 (1955).
48. R. Stump and H. E. Talley, Phys. Rev. *96*, 904 (1954); Phys. Rev. *94*, 809 (1954).
49. W. E. Millett, Phys. Rev. *94*, 809 (1954).
50. S. M. Shafroth and J. A. Marcus, Phys. Rev. *99*, 644 (1955).
51. H. Albers-Schönberg and E. Heer, Helv. Phys. Acta *28*, 389 (1955).
52. L. A. Page, M. Heinberg, J. Wallace, and T. Trout, Phys. Rev. *98*, 206 (1955).
53. J. Wheatley and D. Halliday, Phys. Rev. *88*, 424 (1952).

Tryckt den 21 april 1956

Uppsala 1956. Almqvist & Wiksells Boktryckeri AB

ARKIV FÖR FYSIK Band 10 nr 39

Read 25 January 1956

The spectrum of singly-ionized calcium, Ca II

By Bengt Edlén and Percy Risberg

With 2 figures in the text

Summary

The spectrum of ionized calcium has been observed from 3000 to 12,000 Å by using a hollow-cathode light source and a large concave-grating spectrograph. A list of improved wave-lengths is given. Several new multiplets, mainly in the infrared, have been found, permitting the identification of a number of fairly strong lines in the solar spectrum.

A complete recalculation of the term system on the basis of the new data gives a significantly improved and fairly uniform accuracy of about 0.03 cm^{-1} for both relative and absolute term values. By suitably extending the Ritz formula and by applying the polarization theory for nearly hydrogen-like terms simple extrapolation formulae have been derived, by means of which the observed term system may be arbitrarily extended. From the revised term values accurate wave-lengths have been calculated for use as standards in the Schumann region.

The investigation gives a reminder of the fact that our knowledge of many simple and seemingly well known atomic spectra still leaves much to be desired and may be usefully improved by relatively simple means, especially by reobserving the photographic infrared.

Introduction

The last comprehensive paper on Ca II, published by Saunders and Russell in 1925, gave a rather complete account of the term system, and additional observations have been furnished by Shenstone (1930, 1946). However, in her introduction to "A Multiplet Table" Moore (1945) comments on Ca I and Ca II as follows: "Although the analyses of these spectra are almost completed, the spectra require further laboratory observation. Accurate wave-lengths, especially of the fainter lines are urgently needed. It is surprisingly difficult to obtain accordant term values." The significance of these remarks was confirmed when in the course of some experiments with hollow cathodes we found that several new multiplets of Ca II could be easily observed, especially in the near infrared, and that the wave-lengths found deviated considerably from the predicted values. Consequently, it was found worth while to carry through a re-investigation of Ca II by means of the available equipment. As an immediate result of the new observations a number of lines in the infrared solar spectrum could be identified, as was reported some time ago (Edlén 1953). The investigation was essentially completed at the beginning of 1953.

The observations

The light source was a water-cooled hollow cathode of simple design. The cathode consisted of a brass tube into which was fitted a tube of calcium metal having an inner diameter of 0.7 cm and a length of 2.5 cm. Argon was circulated at a pressure of about 1 mm Hg. Small quantities of other rare gases were occasionally admitted to obtain reference lines. The current ranged from 1 to 1.8 amperes and the voltage from 200 to 300 volts. The ability of the hollow cathode to produce undisturbed radiation is illustrated by the fact that even the highest observed members of the *4f–ng* series showed no noticeable broadening.

The spectra were photographed with a concave grating (radius = 6 meters, 10,000 lines/inch, a total of 60,000 lines) in a stigmatic mounting described by Lidén (1949). Wave-lengths shorter than 8000 Å were measured both in the first and in the second order (at 7.5 and 3.7 Å/mm, respectively), the longer wave-lengths only in the first order. Eastman spectroscopic plates of different kinds were used. Care was taken to obtain optimum conditions for accurate measurements by choosing a suitable density of each line to be measured and by securing a favourable distribution of reference lines. The latter requirement often presented a problem in the infrared region. Selected lines of the rare gases were generally used for standards and also some calcium lines measured interferometrically by Wagman (1937).

The final wave-lengths, which are given in Table 1, are as a rule means from three or more spectrograms. The deviation from the mean was always less than 0.02 Å and for the shorter wave-lengths generally less than 0.01 Å. The intensity figures, given in parentheses after the wave-length, are rough estimates on a logarithmic scale and are uncorrected for the variation in sensitivity of the photographic plates. In the same column are included the wave-lengths measured interferometrically by Wagman (1937) for the four multiplets connecting the five deepest terms.[1] Wagman used a vacuum arc, which may give values slightly different from those of a hollow cathode, but as the terms involved are relatively low it has been assumed that the difference will be less than our experimental errors for the same lines. They have accordingly been preferred to the values obtained in the present investigation. The third column thus contains the complete observational material that has been utilized in the recalculation of the term system. Calculated wave-lengths are given for some unobserved multiplets, including the quadrupole transition *4s–3d* from the metastable *3d* state.

In Table 1 are also collected for comparison the best wave-length values from earlier investigations, a dash indicating that the line was not observed before. Some systematic differences between the old and the new data may be real and due to the use of different light sources. This applies especially to transitions involving high quantum numbers, which could be appreciably shifted in the arcs formerly employed. For this reason, in order to have a homogeneous material, the new results have been generally preferred, although, for instance, the careful measurements by Crew and McCauley (1914) should be of at least a comparable accuracy. The wave-lengths given by Saunders and Russell for the two lines at 4721–4716 Å are about 1.5 Å too large. It is evident that by mistake the vacuum values have been listed in place of the air values, but for the first line some further inconsistency remains, the reciprocal of the

---

[1] Jackson's values for λλ 3968–3933, given in the next column, might be more accurate than Wagman's. The small difference is of no consequence for the present purpose.

Table 1. Ca II, spectrum lines.

Under the heading "Present investigation" are included also the interferometric observations by Wagman (1937), marked W.

The references to previous observations are abbreviated as follows: CC = Crew & McCauley (1914), M = Meggers (1918), SR = Saunders & Russell (1925), J - Jackson (1932), Sh = Shenstone (1930, 1946).

The solar data are from St. John, Moore, Ware, Adams & Babcock (1928), Babcock & Moore (1947), and Mohler (1955).

Term combination	Present investigation			Previous observations, λ	Solar spectrum data λ, intens., ident.		
	σ, cm^{-1}	λ (air), intensity					
$4f\ ^2F_3 - 5d\ ^2D_2$	4 665.32	21 428.90	calc.		21 428.72	30	⊙
$^2F_4 -\ \ ^2D_3$	4 674.02	21 389.00	calc.		21 389.08	33	⊙
$5s\ ^2S_1 - 5p\ ^2P_1$	8 366.11	11 949.72	(1)	—	11 949.77	1*n*	Ti
$^2S_1 -\ \ ^2P_2$	8 444.36	11 838.99	(2)	—	11 839.00	2*N*	⊙
$5p\ ^2P_2 - 6s\ ^2S_1$	10 066.32	9 931.39	(9)	—	9 931.45	3*n*	⊙
$^2P_1 -\ \ ^2S_1$	10 144.62	9 854.74	(8)	—	9 854.66	1*N*	⊙
$4f\ ^2F\ - 5g\ ^2G$	10 107.81	9 890.63	(11)	—	9 890.67	3*n*	⊙
$4d\ ^2D_3 - 4f\ ^2F_4$	11 198.45	8 927.36	(11)	7.34 Sh	8 927.392	7	Ca II
$^2D_2 -\ \ ^2F_3$	11 217.66	8 912.07	(10)	2.10 Sh	8 912.101	7	Ca II
$3d\ ^2D_2 - 4p\ ^2P_1$	11 541.32	8 662.140 W	(16)	2.10 M	8 662.170	23	Ca II
$^2D_3 -\ \ ^2P_2$	11 703.52	8 542.089 W	(17)	2.06 M	8 542.144	25	Ca II
$^2D_2 -\ \ ^2P_2$	11 764.22	8 498.018 W	(13)	7.98 M	8 498.062	20	Ca II
$5p\ ^2P_2 - 5d\ ^2D_2$	12 110.94	8 254.725	(7)	—	8 254.681	1	⊙
$^2P_2 -\ \ ^2D_3$	12 119.65	8 248.797	(11)	—	8 248.802	4	⊙
$^2P_1 -\ \ ^2D_2$	12 189.21	8 201.720	(10)	—	8 201.695	2	⊙ Atm
$4f\ ^2F_3 - 6d\ ^2D_2$	12 464.62	8 020.504	(2)	—			
$^2F_4 -\ \ ^2D_3$	12 469.28	8 017.502	(2)	—			
$4s\ ^2S_1 - 3d\ ^2D_2$	13 650.19	7 323.89	calc.				
$^2S_1 -\ \ ^2D_3$	13 710.88	7 291.47	calc.				
$4f\ ^2F\ - 6g\ ^2G$	15 483.09	6 456.874	(8)	6.907 CC	6 456.874	−1*N*	Fe
$4f\ ^2F_3 - 7d\ ^2D_2$	16 876.69	5 923.69	(1)	—			
$^2F_4 -\ \ ^2D_3$	16 879.46	5 922.72	(1)	—			
$4f\ ^2F\ - 7g\ ^2G$	18 724.23	5 339.189	(5)	9.29 SR	5 339.222	−2	
$5p\ ^2P_2 - 7s\ ^2S_1$	18 837.00	5 307.223	(7)	7.30 SR	5 307.229	−2	
$^2P_1 -\ \ ^2S_1$	18 915.25	5 285.268	(6)	5.34 SR	5 285.262	−2	
$5p\ ^2P_2 - 6d\ ^2D_2$	19 910.25	5 021.138	(4)	1.141 CC	5 021.153	−3	Ca$^+$?
$^2P_2 -\ \ ^2D_3$	19 914.88	5 019.971	(8)	9.981 CC	masked Ti		
$^2P_1 -\ \ ^2D_2$	19 988.51	5 001.479	(7)	1.489 CC	5 001.479	−2	Ca$^+$?
$4f\ ^2F\ - 8g\ ^2G$	20 827.63	4 799.973	(4)	0.16 SR			
$4d\ ^2D_3 - 5f\ ^2F_4$	21 175.90	4 721.028	(4)	2.58* SR	masked Fe		
$^2D_2 -\ \ ^2F_3$	21 195.17	4 716.736	(3)	8.16* SR			
$4f\ ^2F\ - 9g\ ^2G$	22 269.54	4 489.178	(2)	9.22 SR			
$5s\ ^2S_1 - 6p\ ^2P_1$	22 319.02	4 479.226	(1)	9.29 SR	4 479.242	−1	
$^2S_1 -\ \ ^2P_2$	22 354.87	4 472.043	(2)	2.09 SR	4 472.080	−2	

---

* Evidently, Saunders and Russell have listed their vacuum values for these lines.

Table 1 (*cont.*)

Term combination	Present investigation		Previous observations, λ	Solar spectrum data λ, intens., ident.
	σ, cm^{-1}	λ (air), intensity		
$5p\,^2P_2 - 8s\,^2S_1$	23 689.59	4 220.074 (5)	0.13 SR	
$^2P_1 - {}^2S_1$	23 767.87	4 206.175 (4)	6.21 SR	
$5p\,^2P_2 - 7d\,^2D_2$	24 322.39	4 110.279 (3)	0.330 CC	
$^2P_2 - {}^2D_3$	24 325.13	4 109.816 (6)	9.825 CC	masked Fe
$^2P_1 - {}^2D_2$	24 400.61	4 097.102 (5)	7.12 SR	masked Fe
$4s\,^2S_1 - 4p\,^2P_1$	25 191.51	3 968.468 W (22)	8.470 J	3 968.494 700 Ca$^+$
$^2S_1 - {}^2P_2$	25 414.40	3 933.663 W (23)	3.664 J	3 933.684 1000 Ca$^+$
$4d\,^2D_3 - 6f\,^2F_4$	26 599.61	3 758.386 (3)	8.36 Sh	
$^2D_2 - {}^2F_3$	26 618.86	3 755.668 (2)	5.61 Sh	
$5p\,^2P_2 - 9s\,^2S_1$		masked by Ca I	—	
$^2P_1 - {}^2S_1$	26 734.84	3 739.375 (1)	—	
$4p\,^2P_2 - 5s\,^2S_1$	26 752.54	3 736.901 W (18)	6.903 CC	3 736.919 5 Ca$^+$
$^2P_1 - {}^2S_1$	26 975.41	3 706.026 W (17)	6.022 CC	3 706.038 6*d* Ca$^\pm$Mn
$5p\,^2P_2 - 8d\,^2D_2$	27 060.62	3 694.355 (1)	4.31 SR	
$^2P_2 - {}^2D_3$	27 062.43	3 694.108 (4)	4.108 CC	
$^2P_1 - {}^2D_2$	27 138.92	3 683.696 (3)	3.714 CC	
$5p\,^2P_2 - 10s\,^2S_1$	28 602.84	3 495.156 (1)		
$5p\,^2P_2 - 9d\,^2D_3$	28 877.84	3 461.871 (2)	1.896 CC	
$^2P_1 - {}^2D_2$	28 954.91	3 452.657 (1)	2.67 SR	
$4d\,^2D_3 - 7f\,^2F_4$	29 868.60	3 347.035 (1)	6.99 Sh	
$4p\,^2P_2 - 4d\,^2D_2$	31 424.85	3 181.275 W (15)	1.283 CC	3 181.277 3 Ca$^+$
$^2P_2 - {}^2D_3$	31 444.05	3 179.332 W (18)	9.340 CC	3 179.343 5*d* Ca$^+$
$^2P_1 - {}^2D_2$	31 647.74	3 158.869 W (17)	8.877 CC	3 158.887 2 Ca$^+$
$4p\,^2P_2 - 6s\,^2S_1$	45 263.22	2 208.611 calc.	8.606 CC	
$^2P_1 - {}^2S_1$	45 486.11	2 197.787 calc.	7.791 CC	
$3d\,^2D_2 - 5p\,^2P_1$	46 882.83	2 132.304 calc.	2.25 SR	
$^2D_3 - {}^2P_2$	46 900.40	2 131.505 calc.	1.43 SR	
$^2D_2 - {}^2P_2$	46 961.10	2 128.750 calc.	8.733 Sh	
$4p\,^2P_2 - 5d\,^2D_2$	47 307.83	2 113.146 calc.	3.19 CC	
$^2P_2 - {}^2D_3$	47 316.53	2 112.757 calc.	2.763 CC	
$^2P_1 - {}^2D_2$	47 530.72	2 103.235 calc.	3.239 CC	

tabulated wave-number being 4722.48 as compared to 4722.58 for the listed wave-length.

The wave-numbers σ in the second column of Table 1 have been derived from the wave-lengths in the third column by using the internationally adopted dispersion formula (Edlén, 1953). They were calculated to three decimals which were retained during the calculation of the term system. The estimated uncertainty in σ is on the average two or three units in the second decimal.

In the last column of Table 1 is collected the available information on the appearance of Ca II in the solar spectrum. The four new multiplets in the region 8200–12,000 Å are all clearly present with a fair intensity, the reason why their origin had not been previously recognized being, evidently, that the errors in the predicted wavelengths were just too large. Of several transitions now predictable for the lead-sulphide region only 4*f*–5*d* can be definitely recognized in the solar spectrum.

The calculation of term values

The term values have been derived exclusively from the lines in the region 3100–12,000 Å listed in Table 1. Most effective links are provided by the infrared multiplets, in particular by 5*s*–5*p* which fixes the position of the key term 5*p* ^2P, as may be seen from the Grotrian diagram in Fig. 1. The accuracy of the measurements is checked by means of recurring intervals of ^2P and ^2D terms and by the combination cycles 4*p*–5*s*–5*p*–6*d*, 7*d*, –4*f*–4*d*–4*p*. The derived relative values *E* are collected in Table 2. Their error limits are estimated to be a few units in the second decimal. When comparing these values with those given in *Atomic Energy Levels* (Moore 1949) one finds for the lowest configurations, 3*d*, 4*p*, 5*s*, and 4*d*, only the small systematic difference due to the use of different dispersion formulae, the maximum deviation being 0.06 cm^{-1}. The values for 5*p* and those directly depending on 5*p*, viz. $ns\,(n \geq 7)$ and $nd\ (n \geq 6)$, are all about 2.0 cm^{-1} too large in the A.E.L. The error can be traced to λ 2131 which was previously used for connecting 5*p* to the lower terms. The large deviation of 5*f*, amounting to about 6.6 cm^{-1}, derives from the erroneous listing of vacuum values for $\lambda\lambda$ 4721–4716 already mentioned.

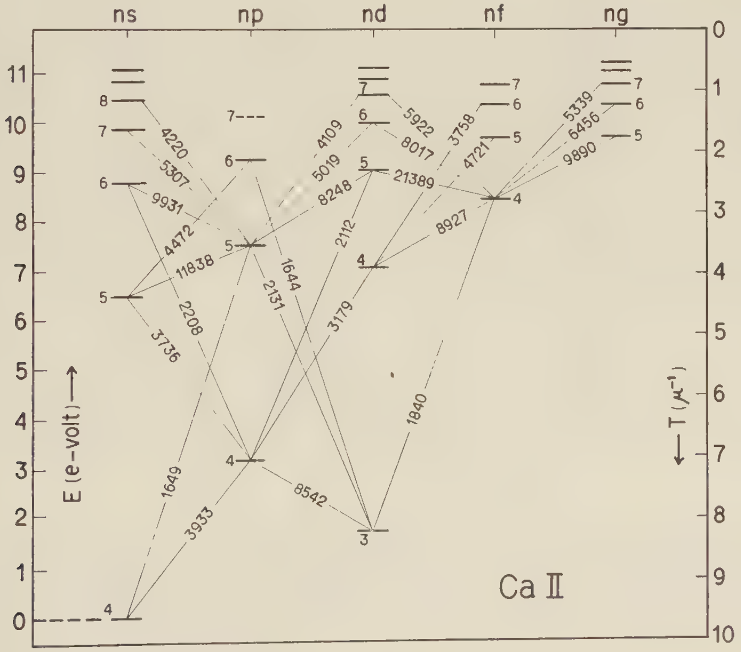

Fig. 1. Term diagram for Ca II. The figures give the approximate wave-length of the leading line in each multiplet.

Table 2. Ca II, terms.

Symbol	E, cm^{-1}	ΔE	T, cm^{-1}	n^*	Δn^*
$4s\ ^2S_1$	0.00		95 751.87	2.141 068	
$5s\ ^2S_1$	52 166.93		43 584.94	3.173 480	
$6s\ ^2S_1$	70 677.62		25 074.25	4.183 985	
$7s\ ^2S_1$	79 448.28		16 303.59	5.188 746	
$8s\ ^2S_1$	84 300.89		11 450.98	6.191 311	
$9s\ ^2S_1$	87 267.86		8 484.01	7.192 891	
$10s\ ^2S_1$	89 214.13		6 537.74	8.193 892	
$4p\ ^2P_1$	25 191.51	222.89	70 560.36	2.494 156	0.003 949
$^2P_2$	25 414.40		70 337.47	2.498 105	
$5p\ ^2P_1$	60 533.02	78.26	35 218.85	3.530 340	0.003 929
$^2P_2$	60 611.28		35 140.59	3.534 269	
$6p\ ^2P_1$	74 485.95	35.85	21 265.92	4.543 202	0.003 834
$^2P_2$	74 521.80		21 230.07	4.547 036	
$7p\ ^2P_1$	(81 498)	(20)	(14 254)		
$^2P_2$	(81 517)		(14 234)		
$3d\ ^2D_2$	13 650.19	60.69	82 101.68	2.312 214	0.000 855
$^2D_3$	13 710.88		82 040.99	2.313 069	
$4d\ ^2D_2$	56 839.25	19.21	38 912.62	3.358 604	0.000 829
$^2D_3$	56 858.46		38 893.41	3.359 433	
$5d\ ^2D_2$	72 722.23	8.70	23 029.64	4.365 766	0.000 825
$^2D_3$	72 730.93		23 020.94	4.366 591	
$6d\ ^2D_2$	80 521.53	4.63	15 230.34	5.368 455	0.000 816
$^2D_3$	80 526.16		15 225.71	5.369 271	
$7d\ ^2D_2$	84 933.65	2.76	10 818.22	6.369 805	0.000 813
$^2D_3$	84 936.41		10 815.46	6.370 618	
$8d\ ^2D_2$	87 671.93	1.78	8 079.94	7.370 553	0.000 813
$^2D_3$	87 673.72		8 078.15	7.371 366	
$9d\ ^2D_2$	89 487.93	1.20	6 263.94	8.371 056	0.000 802
$^2D_3$	89 489.13		6 262.74	8.371 858	
$4f\ ^2F$	68 056.91		27 694.96	3.981 105	
$5f\ ^2F$	78 034.39		17 717.48	4.977 406	
$6f\ ^2F$	83 458.08		12 293.79	5.975 320	
$7f\ ^2F$	86 727.06		9 024.81	6.974 050	
$8f\ ^2F$	(88 847.19)		(6 904.68)		
$9f\ ^2F$	(90 299.69)		(5 452.18)		
$5g\ ^2G$	78 164.72		17 587.15	4.995 815	
$6g\ ^2G$	83 540.00		12 211.87	5.995 328	
$7g\ ^2G$	86 781.14		8 970.73	6.995 038	
$8g\ ^2G$	88 884.54		6 867.33	7.994 844	
$9g\ ^2G$	90 326.45		5 425.42	8.994 717	

The terms $5g$, $9s$, and $10s$ are new. The higher np terms ($n \geq 7$), although sufficiently well predictable, have still defied observation. The intensity in the series $5s$–np seems to decrease rapidly. It is also remarkable that the transition $4d$–$6p$ is too faint to be observed. Presumably the np states are too heavily drained by direct transitions to the ground state.

Table 3. Ca II, calculated wave-lengths.

Combination	σ, cm^{-1}	λ vac	Combination	σ, cm^{-1}	λ vac
$4p\,^2P_2 - 6s\,^2S_1$	45 263.22	2209.299	$4p\,^2P_2 - 8s\,^2S_1$	58 886.48	1698.183
$^2P_1 - \quad ^2S_1$	45 486.11	2198.473	$^2P_1 - \quad ^2S_1$	59 109.37	1691.779
$3d\,^2D_2 - 5p\,^2P_1$	46 882.83	2132.977	$4p\,^2P_2 - 7d\,^2D_2$	59 519.25	1680.129
$^2D_3 - \quad ^2P_2$	46 900.40	2132.178	$^2P_2 - \quad ^2D_3$	59 522.01	1680.051
$^2D_2 - \quad ^2P_2$	46 961.10	2129.422	$^2P_1 - \quad ^2D_2$	59 742.14	1673.860
$4p\,^2P_2 - 5d\,^2D_2$	47 307.83	2113.815	$4s\,^2S_1 - 5p\,^2P_1$	60 533.02	1651.991
$^2P_2 - \quad ^2D_3$	47 316.53	2113.426	$^2S_1 - \quad ^2P_2$	60 611.28	1649.858
$^2P_1 - \quad ^2D_2$	47 530.72	2103.903	$3d\,^2D_3 - 6p\,^2P_2$	60 810.92	1644.441
$4p\,^2P_2 - 7s\,^2S_1$	54 033.88	1850.691	$^2D_2 - \quad ^2P_1$	60 835.76	1643.770
$^2P_1 - \quad ^2S_1$	54 256.77	1843.088	$^2D_2 - \quad ^2P_2$	60 871.61	1642.802
$3d\,^2D_3 - 4f\,^2F$	54 346.03	1840.061	$3d\,^2D_3 - 5f\,^2F$	64 323.51	1554.642
$^2D_2 - \quad ^2F$	54 406.72	1838.008	$^2D_2 - \quad ^2F$	64 384.20	1553.176
$4p\,^2P_2 - 6d\,^2D_2$	55 107.13	1814.647	$3d\,^2D_3 - 6f\,^2F$	69 747.20	1433.749
$^2P_2 - \quad ^2D_3$	55 111.76	1814.495	$^2D_2 - \quad ^2F$	69 807.89	1432.503
$^2P_1 - \quad ^2D_2$	55 330.02	1807.337	$4s\,^2S_1 - 6p\,^2P_1$	74 485.95	1342.535
			$^2S_1 - \quad ^2P_2$	74 521.80	1341.889

Calculated wave-lengths in the Schumann region

The possibilities for calculating accurate wave-lengths for use as standards in the ultra-violet are particularly good in Ca II owing to the favourable positions of the deep terms. As may be seen from Fig. 1 the terms due to $4s$, $3d$, and $4p$ are all connected with each other and with the higher terms through lines having relatively long and accurately measureable wave-lengths. Table 3 gives the vacuum wave-lengths for 13 multiplets calculated from the terms of Table 2 and covering the range 2209–1341 Å. The air wave-lengths for the three multiplets falling above 2000 Å are given in Table 1. An estimated error limit of 0.05 cm^{-1} corresponds to 0.001 Å for wave-lengths around 1400 Å. It must be remembered, however, that the values will be strictly applicable only when a hollow cathode or a similarly undisturbed excitation is being used. In other light sources, as for instance an arc or a vacuum spark, the wave-lengths may be shifted, in particular when high quantum numbers are involved and the lines are noticeably broadened.

Most of these lines have been observed, the latest measurements being those of Lang (1926) and Selwyn (1929) who used as a light source a vacuum spark and an arc in nitrogen, respectively. Their wave-lengths—given to two decimals—are in fair agreement with the values now calculated.

The series limit and series formulae

The series limit of the CaII term system can best be derived from the ng series which contains five well observed members, reaches closer to the limit than any of the other series, and can be safely assumed to obey the simple Ritz formula.

Denoting by E the relative term value, counted upwards from the ground term, and by E_l the ionization energy, we define the absolute term value as $T = E_l - E$. The "effective quantum number" n^* is then defined by $T = RZ_0^2/(n^*)^2$, where R

is the Rydberg constant[1] and Z_0 is the net charge of the atom core (here $Z_0 = 2$). Introducing the "quantum defect" $\delta = n - n^*$, n being the principal quantum number, we write the Ritz formula

$$\delta = a + \beta T. \tag{1}$$

In order to determine the correct value of E_l we start with an approximate value E_l^0 and the corresponding values T^0 and δ^0. From (1) and the definition of δ then follows the approximate relation

$$\delta^0 + \Delta T \frac{n^*}{2T} = a + \beta T, \tag{2}$$

by means of which the correction $\Delta T = E_l - E_l^0$ can be determined from three series members (distinguished by indices 1, 2, 3) by solving for ΔT

$$\frac{\Delta T}{2} = \frac{(T_1 - T_2)(\delta_2^0 - \delta_3^0) - (T_2 - T_3)(\delta_1^0 - \delta_2^0)}{(T_1 - T_2)(n_3^*/T_3 - n_2^*/T_2) - (T_2 - T_3)(n_2^*/T_2 - n_1^*/T_1)}. \tag{3}$$

By applying formula (3) to 5*g*, 6*g*, and 7*g* it is found that the limit given by Saunders and Russell should be increased by 4.0 cm^{-1}. However, in order to make full use of available data we may determine ΔT by using all five members of the *ng* series. Assuming a constant wave-number uncertainty (which gives, however, a slightly too high weight to the highest members) and multiplying the equations (2) by an appropriate weight factor, $p = T/n^*$, we get five equations from which ΔT is obtained by the method of least squares. This gives the result $E_l = 95{,}751.87$ cm^{-1} with a possible error of only a few units in the last decimal.

At the same time the parameters of the Ritz formula may be obtained. It is convenient to write the formula in terms of a "reduced" term value, t,

$$\delta = a + bt, \tag{4}$$

where

$$t = T/RZ_0^2 \equiv (n^*)^{-2}, \tag{5}$$

and the parameter b will be independent of the choice of wave-number unit. The formula for *ng* and its performance are shown in Table 4. The differences $T_{\text{obs}} - T_{\text{calc}}$ were obtained by using the three-decimal values for T_{obs} as the differences appear only in the third decimal. Though the remarkably close agreement may be fortuitous, it confirms that the simple Ritz formula indeed represents the *ng* series exactly—that is, within the limits of the experimental error.

The absolute values for all the terms have been calculated with respect to the new limit and collected in Table 2 together with the corresponding effective quantum numbers. This material gives a good occasion to investigate the possibilities of representing unperturbed term series by series formulae. A bird's-eye view of the five observed series is given by the diagram in Fig. 2 where δ is plotted against T and the simple Ritz formula will be a straight line. The diagram shows directly that *ns*, *np*, and especially *nd* deviate significantly from this formula, though they approach it

---

[1] In the following calculations a rounded-off value 438,943 cm^{-1} has been used for RZ_0^2, cf. p. 564, footnote 2.

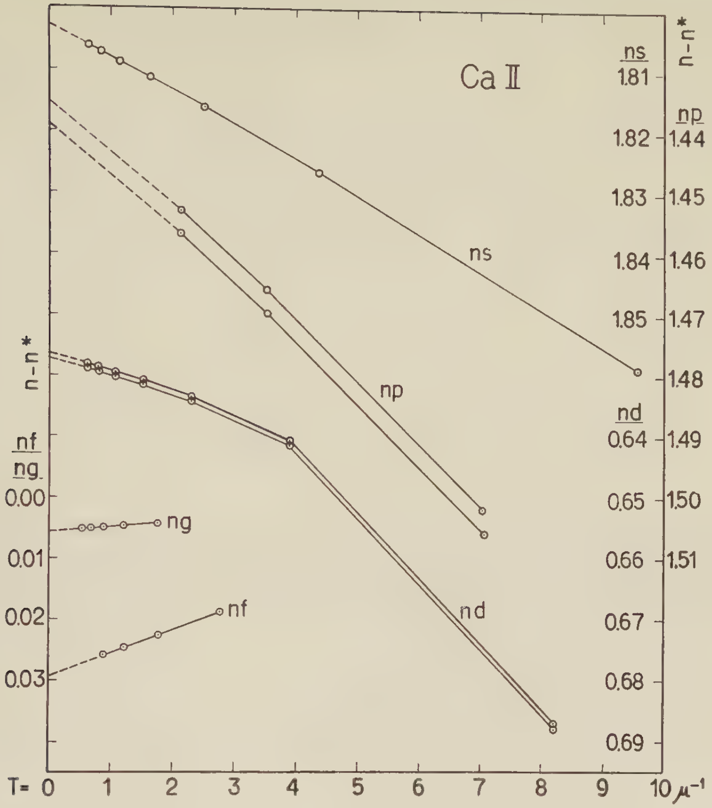

Fig. 2. Series diagram showing the five term series observed in Ca II.

asymptotically with increasing n. If we want to represent accurately the whole of these series it will be necessary to amend formula (4), the natural way being to extend it into a power series of t:

$$\delta = a + bt + ct^2 + dt^3 + \cdots \qquad (6)$$

This form is contained already in the work of Ritz and was later deduced by Sommerfeld and quantum-mechanically by Hartree (1928). As a 3-parameter formula it has actually been used on a few occasions, for instance by Shenstone (1948). The parameters will here be determined from the lowest series members (distinguished by indices 1, 2, 3, 4), and the higher members, as far as they have been observed, will serve as a check. The calculation presents no difficulties, but it may be found useful to have the following explicit expressions at hand. We introduce the abbreviations

$$k_{12} = \frac{\delta_1 - \delta_2}{t_1 - t_2}, \quad k_{23} = \frac{\delta_2 - \delta_3}{t_2 - t_3}, \quad k_{34} = \frac{\delta_3 - \delta_4}{t_3 - t_4}$$

$$q_{13} = \frac{k_{12} - k_{23}}{t_1 - t_3}, \quad q_{24} = \frac{k_{23} - k_{34}}{t_2 - t_4}$$

and obtain for formulae with 2, 3, or 4 terms, respectively:

$$\text{I} \qquad \delta = a + bt, \qquad \begin{cases} b = k_{12} \\ a = \delta_1 - bt_1 \end{cases}$$

$$\text{II} \qquad \delta = a + bt + ct^2, \qquad \begin{cases} c = q_{13} \\ b = k_{12} - c(t_1 + t_2) \\ a = \delta_1 - bt_1 - ct_1^2 \end{cases}$$

$$\text{III} \qquad \delta = a + bt + ct^2 + dt^3, \qquad \begin{cases} d = (q_{13} - q_{24})/(t_1 - t_4) \\ c = q_{13} - d(t_1 + t_2 + t_3) \\ b = k_{12} - c(t_1 + t_2) - d(t_1^2 + t_1 t_2 + t_2^2) \\ a = \delta_1 - bt_1 - ct_1^2 - dt_1^3 \end{cases}$$

Results of the calculation of series formulae are shown in Tables 4, 5, and 6. As appears from the figures given in Table 4 the series *nf* deviates slightly from the simple Ritz formula but is well represented by a formula of type II, the deviation for 7*f* being of the order of the expected experimental error. It may be inferred from several examples in Tables 5 and 6 that the error in T_{calc} which is due to the failure of a formula will almost reach its maximum in the first extrapolated term. Therefore, the higher terms of the *nf* series extrapolated by means of formula II should have about the same accuracy as the observed terms. In any case they will form a more consistent continuation to the series as observed in a hollow cathode than would the values actually observed in other light sources.

The series *ns* shows, as may be seen from Fig. 2, a clear though not excessive departure from the Ritz formula. It appears from the figures given in Table 5 that the formula of type II is still not quite capable of representing the series (col. 3) unless the lowest term is sacrificed (col. 5). Only the formula III gives a perfect fit to the entire series as seen from col. 4 where the residuals for the last three terms can be

Table 4. Series formulae for the *ng* and *nf* series of Ca II.

$$T = 438\,943/(n-\delta)^2, \quad t = (n-\delta)^{-2}.$$

ng, $\delta = 0.0057744 - 0.03966\ t$

nf $\begin{cases} \text{I}, & \delta = 0.029162 - 0.16273\ t \\ \text{II}, & \delta = 0.029606 - 0.18075\ t + 0.1742\ t^2 \end{cases}$

ng	T_{calc}, cm^{-1}	obs − calc	*nf*	T_{obs} − (I)	T_{obs} − (II)	(II), cm^{-1}
			4*f*	(0)	(0)	27 694.96
5*g*	17 587.151	0.000	5*f*	(0)	(0)	17 717.48
6*g*	12 211.868	+0.002	6*f*	+0.31	(0)	12 293.79
7*g*	8 970.739	−0.005	7*f*	+0.35	−0.03	9 024.84
8*g*	6 867.330	+0.003	8*f*			6 904.68
9*g*	5 425.419	−0.002	9*f*			5 452.18

Table 5. Series formulae for the *ns* series of Ca II.

$T = 438\,943/(n-\delta)^2, \quad t = (n-\delta)^{-2}.$

$$\begin{aligned}
&\text{I}, && \delta = 1.799439 + 0.27273\,t \\
&\text{II}, && \delta = 1.8026179 + 0.226140\,t + 0.14676\,t^2 \\
&\text{III}, && \delta = 1.8028028 + 0.220194\,t + 0.20273\,t^2 - 0.1494\,t^3 \\
&\text{II}', && \delta = 1.8027714 + 0.221908\,t + 0.17381\,t^2 \\
&\text{I}'', && \delta = 1.802403 + 0.23829\,t
\end{aligned}$$

ns	$T_{\text{obs}}-(\text{I})$	$T_{\text{obs}}-(\text{II})$	$T_{\text{obs}}-(\text{III})$	$T_{\text{obs}}-(\text{II}')$	$T_{\text{obs}}-(\text{I}'')$
4*s*	(0)	(0)	(0)	−46.3	+405.5
5*s*	(0)	(0)	(0)	(0)	+ 12.5
6*s*	+11.9	(0)	(0)	(0)	(0)
7*s*	+10.6	+0.21	(0)	(0)	(0)
8*s*	+ 7.9	+0.26	+0.02	+ 0.03	+ 0.25
9*s*	+ 5.7	+0.15	−0.06	− 0.04	+ 0.24
10*s*	+ 4.2	+0.14	−0.03	− 0.01	+ 0.25

attributed to experimental errors. For comparison are also shown (col. 2 and 6) the results obtained by fitting the simple Ritz formula to two different pairs of terms.

Of the *np* series only three members have been observed. They permit the derivation of a formula II,

$$np\,^2P_2, \quad \delta = 1.435145 + 0.34761\,t + 0.4302\,t^2, \tag{7}$$

but no check on the accuracy is provided. The residuals of the corresponding formula for *ns* suggest, however, that the extrapolated values, which are given in Table 2, could not be in error by more than about one wave-number unit.

The large departure from a straight line shown by the *nd* series in Fig. 2 gives reason to expect difficulties in finding an accurate formula, and the figures in Table 6 (col. 6) show that even formula III is insufficient. As there would seem to be little point in going beyond four adjustable parameters, an attempt has been made to modify III by replacing the term in t^3 by one in t^4, giving a formula IIIa which indeed fits the observations satisfactorily (col. 5).[1] The term values thus extrapolated for $n \geq 10$ will at any rate be more accurate than those derived from existing observations.

---

[1] We give the expressions for deriving the parameters of this and a corresponding form IIa, using the same notation as before:

$$\text{II a} \qquad \delta = a + b\,t + d\,t^3, \qquad \begin{cases} d = q_{13} \big/ (t_1 + t_2 + t_3) \\ b = k_{12} - d\,(t_1^2 + t_1\,t_2 + t_2^2) \\ a = \delta_1 - b\,t_1 - d\,t_1^3 \end{cases}$$

$$\text{III a} \qquad \delta = a + b\,t + c\,t^2 + e\,t^4, \qquad \begin{cases} e = (q_{13} - q_{24}) \big/ (t_1 - t_4)\,(t_1 + t_2 + t_3 + t_4) \\ c = q_{13} - e\,(t_1^2 + t_2^2 + t_3^2 + t_1\,t_2 + t_1\,t_3 + t_2\,t_3) \\ b = k_{12} - c\,(t_1 + t_2) - e\,(t_1 + t_2)\,(t_1^2 + t_2^2) \\ a = \delta_1 - b\,t_1 - c\,t_1^2 - e\,t_1^4 \end{cases}$$

Table 6. Series formulae for $nd\ ^2D_3$ of Ca II.

$T = 438\,943/(n-\delta)^2, \quad t = (n-\delta)^{-2}.$

II, $\delta = 0.632486 - 0.08918\ t + 2.0356\ t^2$
II a, $\delta = 0.6270939 + 0.103321\ t + 6.2067\ t^3$
II′a, $\delta = 0.6262828 + 0.122203\ t + 4.9678\ t^3$
III a, $\delta = 0.6264903 + 0.106610\ t + 0.42445\ t^2 + 21.05\ t^4$
III, $\delta = 0.6258523 + 0.147674\ t - 0.46921\ t^2 + 7.6377\ t^3$

nd	$T_{\rm obs}$ – (II)	$T_{\rm obs}$ – (II a)	$T_{\rm obs}$ – (II′a)	$T_{\rm obs}$ – (III a)	$T_{\rm obs}$ – (III)
3*d*	(0)	(0)	+ 379.7	(0)	(0)
4*d*	(0)	(0)	(0)	(0)	(0)
5*d*	(0)	(0)	(0)	(0)	(0)
6*d*	− 6.3	− 1.18	(0)	(0)	(0)
7*d*	− 7.3	− 1.19	+ 0.05	0.00	+ 0.21
8*d*	− 6.4	− 0.88	+ 0.15	+ 0.07	+ 0.38
9*d*	− 5.2	− 0.69	+ 0.15	+ 0.06	+ 0.38

The hydrogen-like terms and the polarizability of Ca^{++}

No terms of the *nh* series have been observed, but their values may be deduced from the *ng* series by applying the theory for "non-penetrating" orbits. According to this theory, developed by Born and Heisenberg (1924) and Waller (1926), the departure from the hydrogenic values is due principally to a polarization of the atom core, and the "term defect" ΔT may be written[1]

$$\Delta T = T - T_0 = \frac{\alpha R Z_0^4}{2 a_0^3} \cdot \frac{3n^2 - l(l+1)}{n^5 (l-\frac{1}{2})\, l\, (l+\frac{1}{2})(l+1)(l+\frac{3}{2})}, \tag{8}$$

where $T_0 = RZ_0^2/n^2$, a_0 the first Bohr radius of hydrogen, and α the polarizability of the core. The factor

$$C = \frac{\alpha R Z_0^4}{2 a_0^3} \tag{9}$$

will be constant for a given spectrum and may be determined by (8) from any term for which the effect of "penetration" is sufficiently small to be neglected. As shown in Table 7 the values derived from the different *ng* terms ($l = 4$) are in fact nearly constant as expected.[2] Adopting a mean value $C = 2905 \times 10^3\ \mathrm{cm}^{-1}$ we obtain $\alpha = 0.490 \times 10^{-24}\ \mathrm{cm}^3$ for the polarizability[3] of the ion Ca^{++}. This value of C reproduces the *ng* terms almost within the experimental errors (Table 7, col. 5), only the first member deviating significantly. Considering that the term defect decreases rapidly with increasing quantum number l we may assume that formula (8) will yield term values for $l \geq 5$ with at least the same accuracy as for the *ng* series. The values for *nh* ($l = 5$) have been calculated and are included in Table 7.

---

[1] From a discussion by K. Bockasten (to be published).

[2] When calculating T_0 we have used $4R_{\rm Ca} = 438{,}943.24$ obtained from $R_{\rm Ca} = 109{,}737.31 - 60.22/40.07 = 109{,}735.81$.

[3] Mayer and Mayer (1933) obtained $\alpha = 0.46 \times 10^{-24}$ from the old data for the same series.

Table 7. The polarization formula for „non-penetrating'' orbits applied to the *ng* and *nh* series of Ca II.

n	T_0, cm^{-1}	$ng\ ^2G$			$nh\ ^2H$	
		ΔT_{obs}	C, cm^{-1}	ΔT_{calc}	ΔT_{calc}	T_{calc}
5	17 557.73	29.42	2896×10^3	29.51		
6	12 192.87	19.00	2909×10^3	18.98	6.04	12 198.91
7	8 958.03	12.70	2912×10^3	12.67	4.19	8 962.22
8	6 858.49	8.84	2918×10^3	8.80	2.98	6 861.47
9	5 419.05	6.37	2922×10^3	6.33	2.17	5 421.22

Fine-structure intervals

As is shown by Fig 2 and the last column of Table 2 the series $np\ ^2P$ and $nd\ ^2D$ give a good illustration of a regularity first pointed out by Bohr, namely that the difference Δn^* for the two components of a doublet term is nearly constant through a Rydberg series. This property was deduced by Landé (1924) from his formula

$$\Delta T = \frac{R\alpha^2 Z_0^2 (Z-s)^2}{(n^*)^3 l(l+1)} = \frac{T\alpha^2 (Z-s)^2}{n^* l(l+1)}, \tag{10}$$

where α is the Sommerfeld fine-structure constant ($\alpha^{-1} = 137.037$), and $Z-s$ is an average effective charge acting on the penetrating part of the orbit. In fact, from (10) and the definition of n^* one finds directly

$$-2\Delta n^* = n^* \frac{\Delta T}{T} = \frac{\alpha^2 (Z-s)^2}{l(l+1)}, \tag{11}$$

showing that Δn^* will be constant to the same extent as $Z-s$. The function $n^* \Delta T/T$ is convenient to use for extrapolating ΔT.

For the spin-doublet splitting of nearly hydrogen-like terms the Sommerfeld formula

$$\Delta T = \frac{R\alpha^2 Z_a^4}{n^3 l(l+1)} \tag{12}$$

is applicable. For $4f\ ^2F$, with $l = 3$, $n = 4$, $Z_0 = 2$, this formula gives $\Delta T = 0.12$ cm^{-1}. However, from the observed combinations of $4f\ ^2F$ it appears that $|\Delta T|$ must be less than about 0.04 cm^{-1}, which shows that the interval must be affected by a similar perturbation as causes the inversion of the ^2D terms in the alkali metals.

Conclusion

The investigation has yielded a description of the term system of Ca II as accurate as can be obtained with a large grating and a hollow-cathode light source. Excepting the np series, where one or two more members still need to be observed, the description is complete in the sense that the term system can be extended, whenever necessary, to arbitrary values of n and l by means of simple extrapolation formulae derived from the observed part of the system. It has been confirmed that the term values and their intervals are—within the experimental errors—perfectly smooth functions of the quantum numbers, a result which, though theoretically expected, deserves mentioning. It supports the suspicion that any irregularities in observed term values of alkali-like spectra may eventually be traced to experimental errors.

The fact that several lines with appreciable intensity in the infrared solar spectrum could be immediately identified by means of the new observations, once again calls attention to the fact that our knowledge of even very simple and supposedly well-known atomic spectra may still be far from adequate for astrophysical needs.

The results obtained for Ca II have incited further investigations along the same lines of similar spectra. A revision of Mg II was recently published (Risberg, 1955), and a study of Na I and K I is in progress.

Physics Department of the University, Lund, January, 1956.

REFERENCES

Babcock, H. D. and Moore, Ch. E., *The Solar Spectrum, λ 6600 to λ 13,495*. Carnegie Inst. Wash. Publ. *579* (1947).
Born, M. and Heisenberg, W., Z. Phys. *23*, 388 (1924).
Crew, H. and McCauley, G. V., Astroph. J. *39*, 29 (1914).
Edlén, B., J. Opt. Soc. Amer. *43*, 339 (1953).
—— Atti dell'XI Convegno Volta, Accad. Lincei, Roma (1953), p. 56.
Hartree, D. R., Proc. Camb. Phil. Soc. *24*, 426 (1928).
Jackson, C. V., M. N. Roy. Astr. Soc. *93*, 98 (1932).
Landé, A., ZS. f. Phys. *25*, 46 (1924).
Lang, R. J., Astroph. J. *64*, 167 (1926).
Lidén, K., Arkiv f. Fysik *1*, 229 (1949).
Mayer J. E., and Goeppert-Mayer, M., Phys. Rev. *43*, 605 (1933).
Meggers, W. F., Sc. Papers, Bur. Stand. No. 312 (1918).
Mohler, O. C., *A Table of Solar Spectrum Wave Lengths, 11984 A to 25578 A*. The Univ. of Michigan Press, Ann Arbor (1955).
Moore, Ch. E., *A Multiplet Table of Astrophysical Interest*. Contrib. Princeton Univ. Obs., No. 20, Princeton (1945).
—— *Atomic Energy Levels*, Vol. I. Bur. Stand. Circular 467, Washington (1949).
—— *An Ultraviolet Multiplet Table*, Section 1. Nat. Bur. Stand. Circular 488, Washington (1950).
Risberg, P., Arkiv f. Fysik *9*, 483 (1955).
Saunders, F. A. and Russell, H. N., Astroph. J. *62*, 1 (1925).
Selwyn, E. W. H., Proc. Phys. Soc. *41*, 392 (1929).
Shenstone, A. G., unpublished results from 1930 and 1945, quoted by Moore (1945, 1950).
—— Phil. Trans. Roy. Soc. (London) *A 241*, 297 (1948).
St. John, Ch. E., Moore, Ch. E., Ware, L. M., Adams, E. F., and Babcock, H. D., *Revision of Rowland's Preliminary Table of Solar Spectrum Wavelengths*. Carnegie Inst. Wash. Publ. *396* (1928).
Wagman, N. E., Univ. Pittsburgh Bull. *34*, 1 (1937).
Waller, I., Z. f. Phys. *38*, 635 (1926).

Tryckt den 23 april 1956

Uppsala 1956. Almqvist & Wiksells Boktryckeri AB

ARKIV FÖR FYSIK Band 10 nr 40

Communicated 14 March 1956 by MANNE SIEGBAHN and BENGT EDLÉN

A study of C IV: Term values, series formulae, and Stark effect

By KJELL BOCKASTEN

With 2 plates and 5 figures in the text

Summary

The spectrum of C IV has been studied in the region 9950-1900 Å by means of a sliding vacuum spark. Thirty-five lines have been measured, twenty-two of which had not been observed before. The resonance doublet, λ 1548, has been remeasured on some old plates. On the basis of this material and the wavelengths of ten lines in the region 1250–380 Å given by EDLÉN the term system has been recalculated.

The hydrogen-like terms are strongly affected by Stark effect from the ionic field in the light source, and the Stark effect patterns of the transitions 5–6, 5–7, 5–8, 6–7, 6–8, and 6–9 are found to agree closely with those of the Balmer lines of hydrogen having the same difference in principal quantum number. The polarization formula for hydrogen-like terms was tested on term series of Mg II and Li I and then used for calculating unaffected values of hydrogen-like terms in C IV. From these values the Stark effect levels have been computed and are given in graphs as functions of the field strength for $n = 5$, 6, and 7. The transition 5–7 has been studied graphically. The observed Stark effect displacements correspond to an effective ionic field of about 25 kV/cm. The unaffected term values deduced from the observations are given in a special table.

Introduction

In an earlier investigation (BOCKASTEN, 1955) C III was studied by means of a sliding vacuum spark. The purpose was originally to provide the laboratory data in the red and infrared region needed for the interpretation of stellar spectra. As the light source was found to produce C III and C IV more intensely and with much better line quality than the ordinary vacuum spark which had been used in previous investigations, the work was extended to cover the whole accessible region from 9950 down to 1900 Å. Details about the light source, the spectrograms, the standard lines, and the measuring procedure have been given in the paper on C III.

1. Wavelengths and intensities

A list of the C IV lines observed in the sliding vacuum spark is given in Table 1. The intensities are estimated on a logarithmic scale and refer to the most intense spectrogram of the particular region. The shape of the lines is indicated by symbols explained in the head of the table. The considerable width and asymmetry of certain lines can be traced to Stark effect perturbations which will be discussed in detail in section 4.

Table 1. C IV lines in the region 9950–1500 Å.

Abbreviations in column 1:

bl = blended by
h = hazy
h u l = hazy, unsymmetrical, shaded to longer waves
h u s = hazy, unsymmetrical, shaded to shorter waves
m = masked by
u l = unsymmetrical, shaded to longer waves
unr = unresolved (= separation very uncertain)
u s = unsymmetrical, shaded to shorter waves
w = wide
w h = wide, hazy

References to previous measurements:

BI = I. S. Bowen and S. B. Ingram (1926)
BR = J. C. Boyce and C. A. Rieke (1935)
E = B. Edlén (1934)
M = T. R. Merton (1915)

Intensity	λ_{air}, Å	Previous measurements	σ_{obs}, cm^{-1}	σ_{calc}	Combination
6 very w	7 726.2		12 939.5		$6fgh - 7fghi$
9	5 811.98	2.14 E; 2.0 M	17 201.08	1.1	$3s\,^2S_1 - 3p\,^2P_1$
10	5 801.33	1.51 E; 1.4 M	17 232.64	2.7	$^2S_1 - {}^2P_2$
2	5 018.39		19 921.16	1.1	$5p\,^2P_2 - 6s\,^2S_1$
1	5 016.58		19 928.36	8.2	$^2P_1 - {}^2S_1$
0 } unr	4 786.7		20 885.5	6.8	$5d\,^2D_2 - 6p\,^2P_1$
1 }	4 785.88		20 888.95	9.0	$^2D_3 - {}^2P_2$
1 very w	4 685.4[1]		21 336.8		$6fgh - 8fghik$
9 very w	4 658.30	8.64 E	21 461.1		$5fg - 6fgh$
m C III	4 646.				$5d\,^2D - 6f\,^2F$
3 ul	4 441.49	}1.81 E	22 508.64	8.6	$5p\,^2P_2 - 6d\,^2D_3$
2 ul	4 440.34		22 514.46	4.5	$^2P_1 - {}^2D_2$
1	3 934.89		25 406.51	6.5	$5s\,^2S_1 - 6p\,^2P_1$
2	3 934.29		25 410.34	0.4	$^2S_1 - {}^2P_2$
2 very w	3 689.6		27 095.5		$6fgh - 9fghikl$
1	2 953.95		33 843.1	3.1	$5p\,^2P_2 - 7s\,^2S_1$
0	2 953.4		33 849.	50.2	$^2P_1 - {}^2S_1$
1	2 935.12		34 060.2	0.2	$5d\,^2D_{3,2} - 7p\,^2P_{2,1}$
5 very w	2 906.29[1]	5.97 E	34 398.1		$5fg - 7fghi$
2 w h	2 901.60	1.65 E	34 453.6	3.6	$5d\,^2D - 7g\,^2G$
1 ul	2 819.24		35 460.0	0.1	$5p\,^2P_{2,1} - 7d\,^2D_{3,2}$
4	2 698.67	8.70 E	37 044.3	4.3	$4p\,^2P_2 - 5s\,^2S_1$
4 bl C III	2 697.75	7.73 E	37 057.0	7.4	$^2P_1 - {}^2S_1$
3	2 595.295	}5.14 E	38 519.75	9.7	$4d\,^2D_2 - 5p\,^2P_1$
4	2 595.089		38 522.80	2.8	$^2D_3 - {}^2P_2$
2 ul	2 533.77		39 455.0	5.0	$4f\,^2F - 5d\,^2D_{3,2}$
6 h u l	2 530.6		39 505.	5.6	$4f\,^2F - 5f\,^2F$
11 u s	2 529.98	9.97 E	39 514.1	4.2	$4f\,^2F - 5g\,^2G$
1 h	2 527.7		39 549.	50.7	$4d\,^2D_{3,2} - 5d\,^2D_{3,2}$

---

[1] The wavelength corresponds to the intensity minimum in the centre of the Stark effect pattern.

Table 1 (cont.)

Intensity	λ_{air}, Å	Previous measurements	σ_{obs}, cm^{-1}	σ_{calc}	Combination
9 ul	2 524.41	4.40 E	39 601.3	1.3	$4d\ {}^2D_{3,2} - 5f\ {}^2F$
4 hus	2 523.7		39 613.	09.9	$4d\ {}^2D_{3,2} - 5g\ {}^2G$
6 ul	2 405.10	5.18 E	41 565.6	5.7	$4p\ {}^2P_2 - 5d\ {}^2D_3$
5	2 404.44	4.46 E	41 577.1	7.1	${}^2P_1 - {}^2D_2$
2 very w	2 335.9		42 796.		$5fg - 8fghik$
1	2 104.24		47 508.0	7.7	$4s\ {}^2S_1 - 5p\ {}^2P_1$
2	2 103.94		47 514.8	4.8	${}^2S_1 - {}^2P_2$
	λ_{vac}				
19[2]	1 550.771[3]	BR 0.790; E 0.768; BI 0.774	64 484.05	4.0	$2s\ {}^2S_1 - 2p\ {}^2P_1$
20[2]	1 548.185[3]	BR 8.214; E 8.195; BI 8.189	64 591.76	1.7	${}^2S_1 - {}^2P_2$

[2] Intensity from EDLÉN (1934).

[3] From measurements on plates taken by Edlén in 1937. Details are given in the paper on C III (BOCKASTEN, 1955).

The tabulated wavelengths are weighted means of measurements on several spectrograms. The electric data determining the current density of the spark have varied and the wavelength means correspond to an average condition which may be different for different lines. Thus, the strong lines have been measured on spectrograms taken with large self-inductance, where they are sharp, while the weakest lines could be observed only on spectrograms taken with little self-inductance. Therefore, the Stark effect displacements of the weak lines may correspond to a somewhat higher field strength than those of the strong lines. The wavelengths have been rounded off so that the estimated uncertainty will be from one to ten units in the last figure. The wave numbers were calculated before the rounding-off.

By using EDLÉN's (1934) term table for C IV the new lines were easily classified. The combinations are given in his notation. For the line λ 2901 the classification $5d\,{}^2D$–$7f\,{}^2F$ has been changed to $5d\,{}^2D$–$7g\,{}^2G$. The reason for this change is given in section 4.

Most of the observed lines correspond to quantum number transitions 4–5, 5–6, and 5–7. The intensities within such a group cover a wide range, as can be seen from the values in Table 1. The intensity is strongly concentrated to the most hydrogen-like transitions for which n and l change in the same sense. Since the deviations from the hydrogenic term values are small, the most intense lines fall in a very narrow wavelength band. In a paper on the identification of emission lines in Wolf-Rayet spectra EDLÉN (1956) has pointed out these facts and has given an instructive diagram of the theoretical intensities for the group 5–6 of C IV, based on hydrogenic transition probabilities.

For the transition group 4–5 of C IV the theoretical intensities I_s, corresponding to the excitation conditions at a high temperature, have been calculated in a similar way. According to BETHE (1933) I_s for the transition $nl \rightarrow n'l'$ is proportional to $\max(l, l')(R_n^{n'}{}_l^{l'})^2\sigma^4$, where $R_n^{n'}{}_l^{l'}$ is the dipole strength and σ the wave number of

Table 2. Calculated (I_s) and observed (I_{obs}) intensities for the transition group 4–5 of C IV.

Combination	λ, Å	$(R_{n\,l}^{n'l'})^2$	I_s (%)	I_{obs}
$4s-5p$	2104	72.6	6.5	0.2
$4p-5d$	2405	121.9	12.7	2.5
$4d-5f$	2524	197.8	25.5	13.4
$4f-5g$	2530	314.0	53.5	53.5
$4f-5d$	2534	2.8	0.4	0.1
$4d-5p$	2595	9.3	0.7	0.6
$4p-5s$	2698	21.2	0.7	0.6

the transition. In Table 2 are listed for each allowed combination the approximate wavelength, the square of the dipole strength, the calculated intensity I_s in per cent, and the observed relative intensity I_{obs}, adjusted to make the values equal for the strongest line. The observed intensities were obtained by assuming them proportional to 2^n, n being the figure given in the intensity column of Table 1. In view of the considerable uncertainty of at least a factor 2 in the observed values, the agreement with the calculated intensities is satisfactory except for the first two transitions in Table 2. Especially λ 2104 but also λ 2405 is much fainter than expected. This may be partly due to a reduced photographic response in the short-wave region. The reduced reflecting power of the grating and the aluminized mirror in the spectrograph as well as the increased absorption in the quartz-fluorite projection lens and the quartz window of the spark chamber will work in the same direction. All the transitions 4–5 fall in the region 2700–2100 Å and can be seen on Plate I, showing three different spectrograms taken with various amounts of self-inductance in the spark circuit.

The observed lines can be divided into three groups: (a) lines having a very small Stark effect, usually observed as sharp lines, (b) lines which are broadened and displaced by Stark effect, observed as wide, hazy, and unsymmetrical lines, (c) groups of hydrogen-like transitions forming wide patterns on the spectrograms. Only the first two groups of lines have been used for calculating the term values.

The measurements on the hydrogen-like patterns have been made on the intensity maximum except for λ 2906 and λ 4685 for which the wavelength of a central minimum is given. All transitions of this type are listed separately in Table 3 where the corresponding hydrogenic wave numbers σ_0 are included for comparison. The position

Table 3. Observed hydrogen-like transitions in C IV.

σ_0 is the calculated hydrogenic wave number.

Transition	λ_{obs}, Å	σ_{obs}, cm^{-1}	σ_0	$\sigma_{\text{obs}}-\sigma_0$
5–6	4658.30	21 461.1	21 458.8	+2.3
5–7	2906.29	34 398.1	34 397.7	+0.4
5–8	2335.9	42 796.	42 795.6	0.
6–7	7726.2	12 939.5	12 939.0	+0.5
6–8	4685.4	21 336.8	21 336.8	0.0
6–9	3689.6	27 095.5	27 094.4	+1.1

f λ 2906 has been measured on spectrograms taken with widely different current ensity but no displacement of the centre of the pattern was observed. Plate II 1ows exposures of λ 7726, λ 2906, and λ 3689 at different current densities. Above ach spectrogram is a microphotometer record of its photographic density.

2. The term system as obtained from the observations

Most of the observed lines correspond to transitions between levels with the prin- ipal quantum numbers 4, 5, 6, and 7. Starting with a preliminary value of $4s\,^2S$ ie terms $6s$, $7s\,^2S$, $5p\,^2P$, $4d$, $6d$, $7d\,^2D$, and $5f\,^2F$ were determined relative to $4s\,^2S$. imilarly, assuming a preliminary value of $5s\,^2S$, the rest of the observed levels with rincipal quantum number 4, 5, 6, and 7 were determined relative to $5s\,^2S$. The level $p\,^2P_1$ cannot be directly determined since λ 2697 is blended by C III. It was obtained y extrapolating the fine-structure splitting of $4p\,^2P$ from that of $2p$ and $3p\,^2P$, the xtrapolation being based on the relation $\Delta T \sim (n^*)^{-3}$.

To attach the levels having principal quantum number 2 or 3, wavelengths in the acuum region are needed. Ten lines from EDLÉN's (1934) list have been chosen for his calculation. They are collected in Table 4 with intensities, wavelengths, wave umbers, and combination notations as given by EDLÉN. The four shortest wave- engths were measured in the sixth to the tenth order against iron standards. By neans of the doublets λ 1230 and λ 1107, weighted in the ratio 2 to 1, $3p\,^2P$ is attached o the system based on $4s\,^2S$, the fine-structure splitting being taken from the doublet 5801. Then, $3s\,^2S$ is obtained from λ 5801, $2p\,^2P$ from λ 419, and, finally, $2s\,^2S$ from 1548, which also gives the fine-structure splitting of $2p\,^2P$. All these low terms are hus connected to the $4s\,^2S$ system.

The terms have now been obtained in two separate systems which have to be oined together. The faint transition $3s\,^2S$–$4p\,^2P$ observed by EDLÉN at λ 948 could e used for this purpose, and the two transitions $2p\,^2P$–$3d\,^2D$ and $3d\,^2D$–$4f\,^2F$ give nother possibility. In this way the uncertainty of the relative position of the two ystems may be reduced to perhaps 2 cm^{-1}. The normally forbidden transitions in he group 4–5 which come forth in the electric field in the light source also provide

able 4. C IV lines in the region 1500–380 Å used for the calculation of term values.

Intensities, wavelengths and combination notations from EDLÉN (1934).

Intensity	λ_{vac}, Å	σ_{obs}, cm^{-1}	σ_{calc}	Combination
3	1 230.511	81 267.1	6.4	$3p\,^2P_2$–$4s\,^2S_1$
2	1 230.046	81 297.8	8.0	$^2P_1$– $^2S_1$
4	1 168.990	85 543.9	4.8	$3d\,^2D_3$–$4f\,^2F_4$
3+	1 168.873	85 552.5	3.3	$^2D_2$– $^2F_3$
2	1 107.933	90 258.2	8.4	$3p\,^2P_2$–$4d\,^2D_3$
1	1 107.600	90 285.3	6.0	$^2P_1$– $^2D_2$
14	419.714	238 257.5	7.3	$2p\,^2P_2$–$3s\,^2S_1$
13	419.525	238 364.8	5.0	$^2P_1$– $^2S_1$
17	384.178	260 296.0	8.6	$2p\,^2P_2$–$3d\,^2D_3$
16	384.032	260 395.0	5.8	$^2P_1$– $^2D_2$

a connection. However, being hazy and sometimes unsymmetrical they would give no better precision than the lines in the vacuum region.

In these circumstances the best way to combine the two systems is no doubt by means of series formulae. Suitably extended Ritz formulae have been shown to give a very accurate representation of term series in alkali-like spectra (RISBERG, 1955; EDLÉN and RISBERG, 1956). They will be applied here. The terms $n = 2, 3, 4, 6, 7$ of the $ns\,^2S$ series and the terms $n = 2, 3, 5$ of the $np\,^2P$ series all belong to the system based on $4s\,^2S$. The series limit was determined by fitting the terms $n = 2, 3, 4, 6$ of the $ns\,^2S$ series to the three-parameter formula

$$\delta = a + bt + ct^2,$$

where δ is the quantum defect $n - n^*$, and $t = (n^*)^{-2} = T_n/16R$, T_n being the term value and R the Rydberg constant for carbon. The value $16R = 1755716.8$ cm^{-1} has been used. The $ns\,^2S$ series can be assumed to give the best value of the series limit since it is less perturbed by Stark effect than any other term series. By the formula thus obtained the terms $5s\,^2S$ and $7s\,^2S$ can be calculated. For $7s\,^2S$ the deviation $T_{\text{obs}} - T_{\text{calc}}$ is smaller than the experimental uncertainty.

The limit being fixed from the $ns\,^2S$ series, it is now possible to derive three-parameter formulae for the $np\,^2P$ series from the terms $n = 2, 3, 5$ and to calculate $4p\,^2P$ and $6p\,^2P$ from these formulae. The correction to be applied to the $5s\,^2S$ system is finally obtained as the average shift required to make $5s\,^2S$, $4p\,^2P$, and $6p\,^2P$ agree with the values calculated from the series formulae.

The term $3d\,^2D$ has been calculated from the doublets λ 384 and λ 1168, weighted in the ratio 1 to 2. The splitting was calculated from λ 1168, assuming $4f\,^2F$ as a doublet with the hydrogenic splitting 2.0 cm^{-1}.

In Table 5 are collected the term values finally obtained. The effective quantum numbers n^* are also included. The differences Δn^* for resolved doublets are seen to be remarkably constant through each series. $T_{\text{obs}} - T_{\text{calc}}$ refer to term values calculated from the series formulae given in section 3. The last column contains an estimate of the Stark effect displacements in the light source.

The uncertainty of the series limit may be estimated to be 0.5 cm^{-1}. The wavelength values on which the term system is based are of very different accuracy. As a rough estimate the uncertainty of the relative values of terms with principal quantum numbers 4, 5, and 6 may be given as 0.5 cm^{-1}, while in other cases it may reach 1 or 2 cm^{-1}.

3. The calculation of unaffected term values

A rough calculation shows that all the observed ^2S and ^2P terms as well as $3d$, $4d\,^2D$, and $4f\,^2F$ are practically unaffected by Stark effect at moderate electric fields. The unaffected values of $ns\,^2S$ and $np\,^2P$ can therefore be calculated by means of the following series formulae derived from supposedly unperturbed terms:

$$\begin{aligned}
ns\,^2S_1&:\ \delta = 0.1543569 + 0.025936\,t + 0.008877\,t^2,\ (n = 2, 3, 4, 6)\\
np\,^2P_2&:\ \delta = 0.0383751 - 0.003943\,t - 0.00671\,t^2,\ (n = 2, 3, 4)\\
np\,^2P_1&:\ \delta = 0.0386066 - 0.003913\,t - 0.00681\,t^2,\ (n = 2, 3, 4).
\end{aligned}$$

The n-values of the terms used for calculating the constants are given in brackets. The four terms of the ^2S series were needed for determining the series limit in addition to the three constants.

Table 5. The term system of C IV as obtained from the observations.

Term symbol	Term value, T, cm^{-1}		n^*		$T_{\text{obs}} - T_{\text{calc}}$	Stark effect displacement for 25 kV/cm
$2s\,^2S_1$	520 177.0		1.837 180		—	—
$3s\,^2S_1$	217 328.0		2.842 297		—	—
$4s\,^2S_1$	118 828.9		3.843 847		—	—
$5s\,^2S_1$	74 808.5		4.844 532		−0.3	—
$6s\,^2S_1$	51 393.0		5.844 876		—	—
$7s\,^2S_1$	37 471.0		6.845 092		−0.1	+0.1
$2p\,^2P_2$	455 585.3	107.7	1.963 100	0.000 232	—	—
$^2P_1$	455 693.0		1.962 868		—	—
$3p\,^2P_2$	200 095.3	31.56	2.962 162	0.000 234	—	—
$^2P_1$	200 126.9		2.961 928		—	—
$4p\,^2P_2$	111 852.8	13.2	3.961 903	0.000 233	—	—
$^2P_1$	111.865.9		3.961 670		—	—
$5p\,^2P_2$	71 314.1	7.1	4.961 802	0.000 246	−0.2	—
$^2P_1$	71 321.2		4.961 556		+0.2	—
$6p\,^2P_2$	49 398.1	3.8	5.961 724	0.000 231	+0.3	+0.1
$^2P_1$	49 402.0		5.961 493		+0.3	+0.1
$7p\,^2P_{2,1}$	36 227.6		6.961 57		+0.6	+0.2
$3d\,^2D_3$	195 286.7	10.5	2.998 409	0.000 081	—	—
$^2D_2$	195 297.2		2.998 328			
$4d\,^2D_3$	109 836.9	4.0	3.998 094	0.000 073	—	—
$^2D_2$	109 840.9		3.998 021			
$5d\,^2D_3$	70 287.1	1.7	4.997 921	0.000 061	+0.6	+0.3
$^2D_2$	70 288.8		4.997 860			
$6d\,^2D_3$	48 805.5	1.2	5.997 812	0.000 076	+0.9	+1.0
$^2D_2$	48 806.7		5.997 736			
$7d\,^2D_{3,2}$	35 856.4		6.997 51		+2.8	+3.0
$4f\,^2F$	109 742.8		3.999 809		−0.3	—
$5f\,^2F$	70 237.2		4.999 69		+2.3	+1.1
$5g\,^2G$	70 228.6		5.000 00		−1.5	−1.0
$7g\,^2G$	35 834.2		6.999 69		+2.6	+3.4

For the hydrogen-like terms the polarization formula for non-penetrating orbits gives a possibility of calculating unaffected term values. BOHR (1923) was the first to point out that the polarization of the atom core in the field of the valence electron will produce a quantum defect for non-penetrating orbits in alkali-like spectra. BORN and HEISENBERG (1924) treated this effect on the basis of the old quantum theory, and WALLER (1926) gave the quantum-mechanical theory. Waller obtains from the perturbation theory a relation that can be written:

$$T = T_0 + R\alpha a_0 \langle r^{-4} \rangle, \tag{1}$$

where T is a hydrogen-like term value, T_0 the corresponding hydrogenic term value RZ_0^2/n^2, R the Rydberg constant, α the polarizability of the atom core, a_0 the radius of the first Bohr orbit of hydrogen, and $\langle r^{-4}\rangle$ the average of r^{-4} taken over the unperturbed system, r being the distance from the nucleus to the valence electron. For this average Waller derived the expression:

$$\langle r^{-4}\rangle = \frac{Z_0^4[3n^2 - l(l+1)]}{2a_0^4 n^5 (l-\frac{1}{2})\,l\,(l+\frac{1}{2})\,(l+1)\,(l+\frac{3}{2})}, \tag{2}$$

where Z_0 is the net charge of the core, and n and l are the quantum numbers of the valence electron.

The formula (1) is based on the assumption that the core is in a homogeneous electric field, i.e. that the valence electron is at a large distance from the core. MAYER and MAYER (1933) have calculated polarizabilities of ions from spectroscopic term values corresponding to orbits that are no longer strictly non-penetrating. They apply two corrections to the simple formula, one for quadrupole distortion of the ion, corresponding to a field gradient at the atom core, and one for the penetration effect. A term corresponding to the quadrupole distortion can easily be added. Following STERNHEIMER (1954) the equation may then be written:

$$T = T_0 + R\alpha a_0\langle r^{-4}\rangle + R\alpha_q a_0\langle r^{-6}\rangle, \tag{3}$$

where α_q is the quadrupole polarizability.

The quantum-mechanical expression of $\langle r^{-6}\rangle$ has been calculated by VAN VLECK (1934) in terms of certain parameters. It can be given explicitly in terms of the quantum numbers n and l as

$$\langle r^{-6}\rangle = \frac{Z_0^6\{35n^4 - 5n^2[6l(l+1)-5] + 3(l-1)\,l\,(l+1)\,(l+2)\}}{8a_0^6 n^7 (l-\frac{3}{2})\,(l-1)\,(l-\frac{1}{2})\,l\,(l+\frac{1}{2})\,(l+1)\,(l+\frac{3}{2})\,(l+2)\,(l+\frac{5}{2})}. \tag{4}$$

Introducing the expressions for $\langle r^{-4}\rangle$ and $\langle r^{-6}\rangle$ in (3) one gets the final formula:

$$T = T_0 + A\varphi(n, l) + B\psi(n, l), \tag{5}$$

where $\varphi(n, l) = a_0^4\langle r^{-4}\rangle/Z_0^4$ and $\psi(n, l) = a_0^6\langle r^{-6}\rangle/Z_0^6$. A and B are connected with α and α_q by the relations

$$A = R\alpha Z_0^4/a_0^3, \qquad B = R\alpha_q Z_0^6/a_0^5.$$

In order to facilitate the use of the polarization formula (5) the functions $\varphi(n, l)$ and $\psi(n, l)$ have been tabulated in an Appendix to this paper.

To get an estimate of the accuracy with which the polarization formula can represent an unperturbed term series it was tested on Mg II. After the recent observations by RISBERG (1955) this spectrum offers long series of accurately determined hydrogen-like terms. It was found (BOCKASTEN, 1956) that the ^2G and ^2H series of Mg II are accurately reproduced by the simple formula (1), containing as single parameter the polarizability α of the Mg^{+2} ion. The ^2F series can be represented within the experimental uncertainty of 0.02 cm^{-1} by the complete formula (5) with the constants A and B determined from $4f$ and $5f\,^2F$. The same values of the parameters give the ^2H series correctly and the ^2G series with only a very slight syste-

Table 6. Residuals ($T_{\text{obs}} - T_{\text{calc}}$) in cm^{-1} for Mg II, T_{calc} being obtained from the polarization formula (5) with $A = 829\,700$ and $B = 4\,305\,000$.

n	$nf\,^2F$	$ng\,^2G$	$nh\,^2H$
4	(0.000)	—	—
5	(0.000)	+0.042	—
6	+0.009	−0.006	—
7	+0.001	−0.008	−0.001
8	+0.002	−0.014	+0.010
9	−0.016	−0.012	+0.010
10	−0.004	−0.023	−0.055
11	—	−0.035	—

Table 7. Hydrogenic term values $T_0 = 1\,755\,716.8/n^2$, and term defects $T - T_0$, calculated for C IV from the polarization formula (5) with $A = 280\,250$ and $B = 471\,500$.

n	T_0, cm^{-1}	$nd\,^2D$	$nf\,^2F$	$ng\,^2G$	$nh\,^2H$	$ni\,^2I$	$nk\,^2K$	$nl\,^2L$
3	195 079.64	211.3	—	—	—	—	—	—
4	109 732.30	106.2	10.79	—	—	—	—	—
5	70 228.67	58.5	6.25	1.44	—	—	—	—
6	48 769.91	35.2	3.84	0.93	0.29	—	—	—
7	35 830.96	22.7	2.51	0.62	0.20	0.08	—	—
8	27 433.08	15.4	1.72	0.43	0.14	0.06	0.03	—
9	21 675.52	10.9	1.22	0.31	0.11	0.04	0.02	0.01

matic deviation as shown in Table 6. The calculations are based on observed term values with three decimals supplied by RISBERG from his working list.

For Li I-like spectra the orbits must be less penetrating than the corresponding orbits of Mg II. EDLÉN and LIDÉN (1949) have shown that the $nd\,^2D$ series of Li I, $n = 3, 4, 5, 6$, as given by the precision measurements of MEISSNER, MUNDIE and STELSON (1948, 1949), can be represented by a simple Ritz formula to within 0.002 cm^{-1}. The two-constant formula (5) applied to this series gives the same accuracy as the Ritz formula.

The results of these tests indicate that the polarization formula will give the terms with $L \geq 2$ of C IV with an ample accuracy. As the formula neglects the fine-structure splitting, the centre of gravity has been used for separated doublets. A calculation of the parameters in formula (5) from the observed values of $3d$ and $4d\,^2D$ gives $A = 280\,250$ cm^{-1} and $B = 471\,500$ cm^{-1}, by means of which the term "defects" $T - T_0$ shown in Table 7 are obtained. The observed value of $4f\,^2F$, which is supposed not to be appreciably affected by Stark effect, agrees within the estimated experimental error with the calculated value. The differences $T_{\text{obs}} - T_{\text{calc}}$ in Table 5 for the ^2D, ^2F, and ^2G terms refer to the calculations shown in Table 7.

Theoretical values of α for rare-gas-like ions have been calculated by several investigators, e.g. PAULING (1927) and STERNHEIMER (1954), and theoretical values of α_q can be obtained from MAYER and MAYER (1933) and Sternheimer. Sternheimer's

Table 8. Comparison between theoretical and experimental values of dipole (α) and quadrupole (α_q) polarizabilities of some ions.

Ion	Experimental value based on	$\alpha \times 10^{24}$, cm^3			$\alpha_q \times 10^{40}$, cm^5		
		Experimental value	STERNHEIMER (1954)	PAULING (1927)	Experimental value	STERNHEIMER (1954)	MAYER and MAYER (1933)
Li^{+1}	$3d$ and $4d\,{}^2D$	0.0283	0.0316	0.0293	0.0016	0.00477	0.0018
C^{+4}	$3d$ and $4d\,{}^2D$	0.00148	0.00139	0.00135	0.0000435	0.0000431	0.000024
Mg^{+2}	$4f$ and $5f\,{}^2F$	0.0700	—	0.094	0.0254	—	0.0061

values of α_q are on the average about twice as large as those of Mayer and Mayer. The best experimental values of α are obtained from spectroscopic data. The strictly non-penetrating orbits, for which the last term of formula (5) is small, will probably give the best values, because no penetration effect is present. As the term defects are small, however, it is important that the limit be correctly determined. To get spectroscopic values of α_q it is necessary to use less hydrogen-like term series, for which the quadrupole term of (5) is not too small. As the penetration effect has been neglected it is possible that some part of the constants A and B are in this case due to penetration. It has been considered interesting, however, to compare in Table 8 the theoretical results with the values of α and α_q derived for some ions from the formula (5).

4. The Stark effect in C IV

The Stark effect in the sliding vacuum spark is manifested in C IV by: (a) displaced lines, (b) violation of the selection rule $\Delta l = \pm 1$ and (c) wide patterns on the spectrograms where hydrogen-like transitions are expected.

To get a quantitative picture of the Stark effect perturbations the positions of the Stark effect levels for $n = 5$, 6, and 7 have been calculated for various field strengths following the account of the quantum-mechanical theory of the Stark effect given by RYDE (1956). The spin interaction has been neglected since the fine-structure splitting of the hydrogen-like terms of C IV is very small. The calculations have been made in polar coordinates and the quantum numbers are, therefore, n, l, and m. The Stark effect perturbations will act as a mutual repulsion of two levels with the same m-values and adjacent values of l. Quantum-mechanically the perturbation may be considered as a mixing of eigenfunctions of different l-values, at first between terms with adjacent l-values. This explains why the transition $\Delta l = +1$ is accompanied in the first place by the transitions $\Delta l = 0$ and $\Delta l = +2$.

In C IV the terms occur in close groups for each n-value, and at moderate fields perturbations only between terms with the same n-value are important. Furthermore, for $n = 5$, 6, and 7 the ${}^2S$ and ${}^2P$ terms are so distant from the more hydrogen-like terms, that their influence can be neglected at the field strengths for which the present calculations have been made.

Starting with the calculated unperturbed term values T_l, the perturbed values t are obtained as roots to the secular equation with the principal diagonal elements $(T_l - t)$. The elements of the adjacent diagonals on both sides are the hydrogenic matrix elements

$$\varepsilon_{n,\,l,\,m}^{n,\,l-1,\,m} = -\frac{C\,n\,F}{Z_0}\sqrt{\frac{(n^2-l^2)\,(l^2-m^2)}{4\,l^2-1}}\,.$$

All the other elements of the determinant are zero. C is the splitting factor, F the field strength, and Z_0 the net charge of the core. The theoretical value $C = 0.0640$ cm^{-1}/kV/cm has been used. Each combination of n, F, and m gives one secular equation.

Perturbed term values have been calculated for $F = 100$, 60, 25, and 10 kV/cm. The results are given in Fig. 1–3 in the form of graphs showing the positions of the Stark effect levels versus field strength.[1] From these curves the approximate displacements of the terms can be derived as the average of the displacements of the individual m-states.

In the present case the Stark effect arises from ionic fields in the spark and the field strengths are, therefore, statistically distributed. As the spark discharge is oscillating, the distribution is varying with time as well. The effective field strength will here be defined as the strength of a constant field that will displace the terms so that the lines fall where the intensity maximum has been observed on the plates.

From a study of the transition 5–7 it has been estimated that the effective field strength on the plates that have been used for measurements is about 25 kV/cm. In the last column of Table 5 are listed the term displacements at this field strength. They explain fairly well the differences between the observed and the calculated term values.

In order to see if the characteristic intensity minimum at the centre of the pattern at λ 2906 can be explained by the Stark effect calculations, the hydrogen-like transitions 5–7 have been studied. Using the matrix amplitude of KUPPER (1928) it can be shown that at zero field the two transitions $5g$–$7h$ and $5f$–$7g$ are responsible for about 80 per cent of the intensity falling near the hydrogenic position. In Fig. 4 is shown the position of the line components satisfying the selection rule for Stark effect, $\Delta m = 0, \pm 1$, for the transitions $5g$–$7ghi$ and $5f$–$7fgh$, assuming that the intensities of the transitions with $\Delta l = +1$ are mainly distributed into the transitions $\Delta l = 0, +1, +2$. Components appearing only in electric fields have been dashed for small values of the field strength. Although the line components in Fig. 4 will have different intensities the diagram gives a rough idea about the distribution of the intensity in the neighbourhood of the calculated hydrogenic position σ_0. The observed position of the central minimum is marked by a circle on the wave number axis. From a purely qualitative analysis of this diagram a profile with two maxima can be deduced. By identifying them with the two maxima seen on the microphotometer tracings, an effective field strength of about 25 kV/cm is obtained for the spark conditions normally used.

The six Stark effect patterns corresponding to the hydrogen-like transitions 5–6, 5–7, 5–8, 6–7, 6–8, and 6–9 agree closely with those of the Balmer lines of hydrogen having the same difference in principal quantum number. As mentioned previously the transitions 5–7 and 6–8 show the characteristic central intensity minimum of H_β. The agreement in line form with H_α, H_β, and H_γ, respectively, is illustrated by the microphotometer records of the transitions 6–7, 5–7, and 6–9 shown in Plate II.

---

[1] The calculations for Fig. 1–3 were actually based on values of the unperturbed ^2D terms slightly different from the more accurate values given in Table 7. The graphs of the D-levels should, therefore, be displaced by 0.9, 0.9, and 0.7 cm^{-1} towards the left in the diagrams for $n = 5$, 6, and 7.

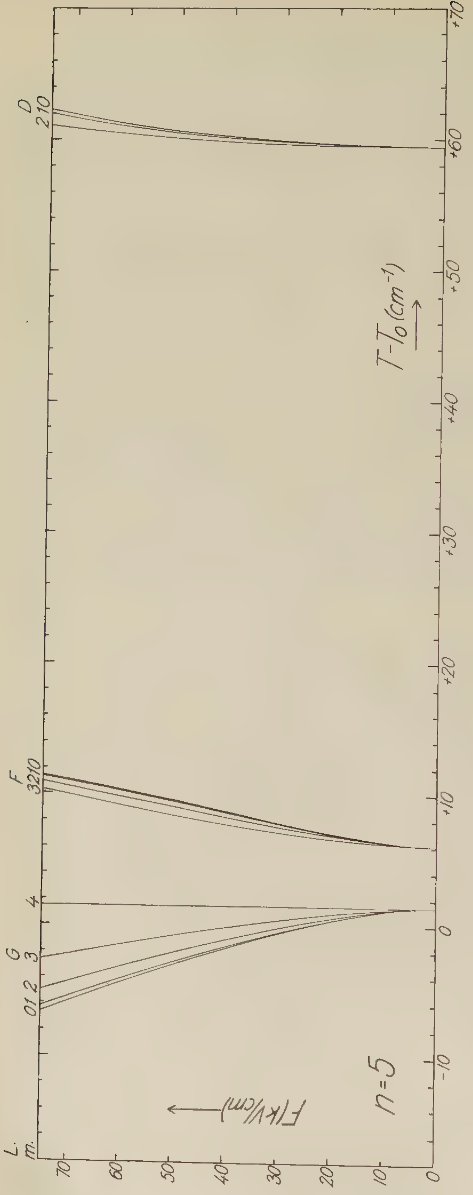

Fig. 1. Calculated Stark effect displacements of terms with $n = 5$ in C IV.

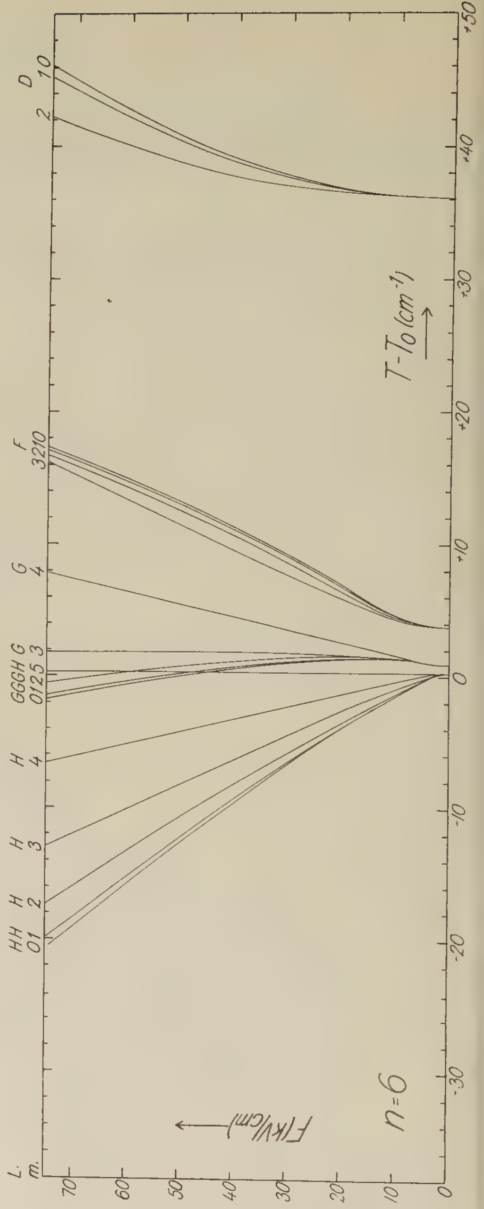

Fig. 2. Calculated Stark effect displacements of terms with $n = 6$ in C IV.

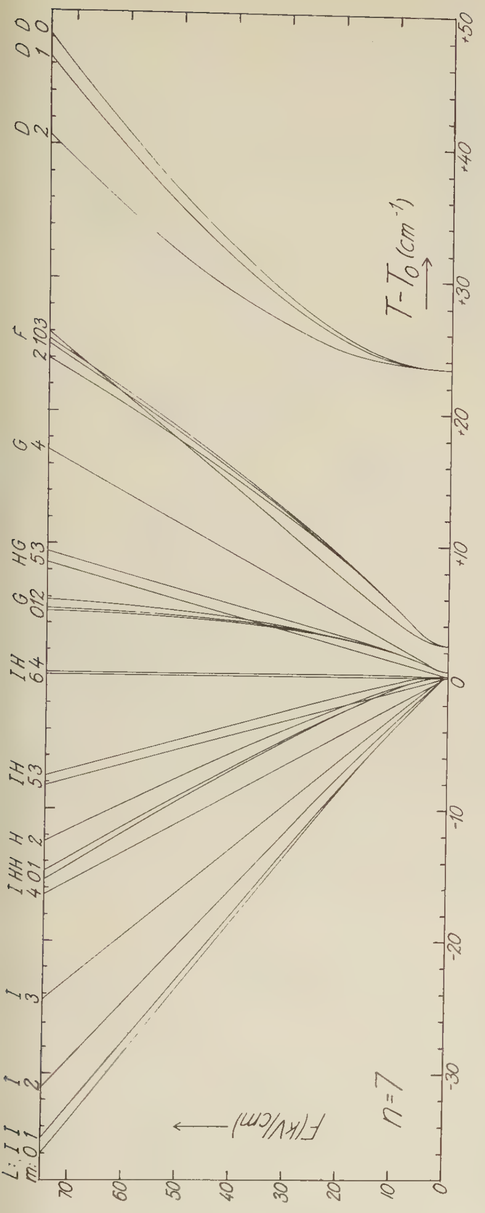

Fig. 3. Calculated Stark effect displacements of terms with $n = 7$ in C IV.

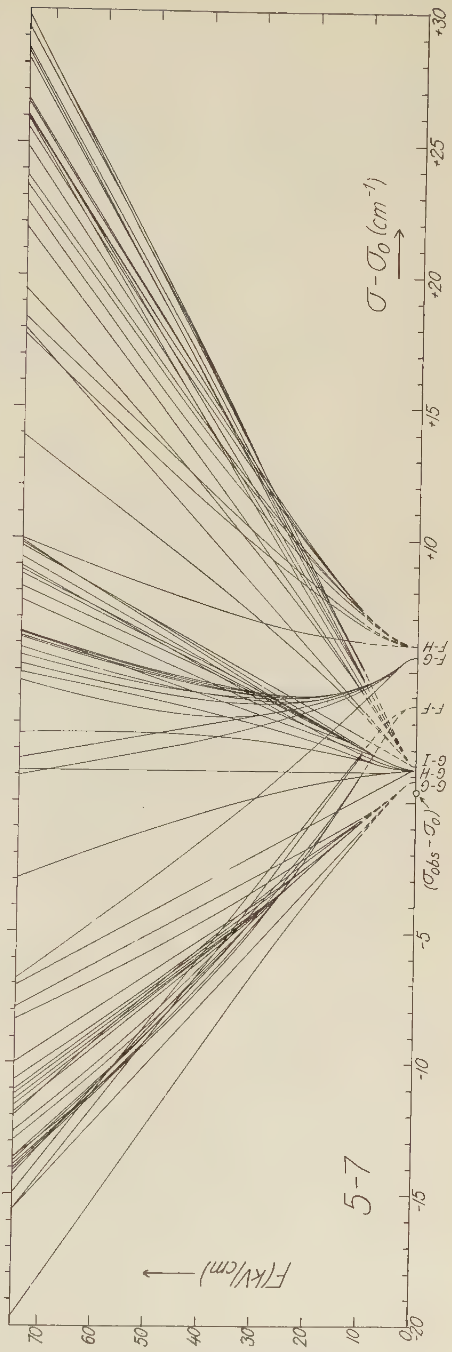

Fig. 4. Calculated displacements of the Stark effect components of $5f$–$7fgh$ and $5g$–$7ghi$ in C IV.

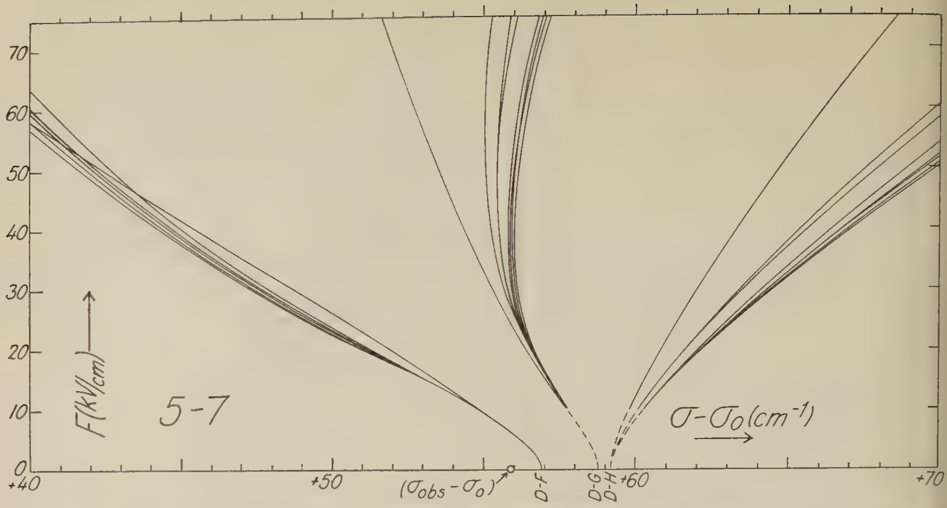

Fig. 5. Calculated displacements of the Stark effect components of $5d$–$7fgh$ in C IV. The zero of the wave number axis is the hydrogenic value σ_0.

The line λ 2901 (see Plate IId), classified by EDLÉN (1934) as $5d\,^2D$–$7f\,^2F$, is situated near the unperturbed position of this transition. At a field strength of 25 kV/cm it ought to be displaced about 8 cm^{-1}, however. A study of the Stark effect displacements of the line components given in Fig. 5 shows that the identification must be $5d\,^2D$–$7g\,^2G$. The transition $5d\,^2D$–$7f\,^2F$ cannot be seen on the plates, evidently because its intensity is distributed over a large area, while the position of $5d\,^2D$–$7g\,^2G$ is rather insensitive to variations in the electric field.

For astrophysical purposes the unperturbed term values of C IV may be of principal interest. In Table 9 have been collected for convenient reference the term values obtained from Table 7 and from the extended Ritz formulae given in section 3. The observed fine-structure splittings for the ^2D terms have been smoothed by means of the relation $\Delta T \sim n^{-3}$.

Table 9. Unperturbed term values of C IV.

Term symbol	$n=2$	$n=3$	$n=4$	$n=5$	$n=6$	$n=7$	$n=8$	$n=9$
$ns\,^2S_1$	520 177.0	217 328.0	118 828.9	74 808.8	51 393.0	37 471.1	28 526.2	22 440.3
$np\,^2P_2$	455 585.3	200 095.3	111 852.8	71 314.3	49 397.9	36 226.2	27 697.7	21 861.3
$^2P_1$	455 693.0	200 126.9	111 865.9	71 321.0	49 401.7	36 228.6	27 699.3	21 862.4
$nd\,^2D_3$	—	195 287.1	109 836.9	70 286.4	48 804.6	35 853.6	27 448.5	21 686.4
$^2D_2$	—	195 296.6	109 840.9	70 288.4	48 805.8			
$nf\,^2F$	—	—	109 743.1	70 234.9	48 773.8	35 833.5	27 434.8	21 676.7
$ng\,^2G$	—	—	—	70 230.11	48 770.84	35 831.58	27 433.51	21 675.83
$nh\,^2H$	—	—	—	—	48 770.20	35 831.16	27 433.22	21.675.63
$ni\,^2I$	—	—	—	-	—	35 831.04	27 433.14	21 675.56
T_0	438 929.20	195 079.64	109 732.30	70 228.67	48 769.91	35 830.96	27 433.08	21 675.52

APPENDIX

Tables of $\varphi(n,l)$ and $\psi(n,l)$ in the polarization formula $T=T_0+A\,\varphi(n,l)+B\,\psi(n,l)$

$$\varphi(n,l)=\frac{3n^2-l(l+1)}{2n^5(l-\tfrac{1}{2})\,l\,(l+\tfrac{1}{2})(l+1)(l+\tfrac{3}{2})},$$

$$\psi(n,l)=\frac{35n^4-5n^2[6l(l+1)-5]+3(l-1)l(l+1)(l+2)}{8n^7(l-\tfrac{3}{2})(l-1)(l-\tfrac{1}{2})\,l\,(l+\tfrac{1}{2})(l+1)(l+\tfrac{3}{2})(l+2)(l+\tfrac{5}{2})}.$$

Table 1. $\varphi(n,l)\times 10^{10}$.

n	D	F	G	H	I	K	L	M
3	5 486 968	—	—	—	—	—	—	—
4	2 604 167	372 024	—	—	—	—	—	—
5	1 401 905	213 333	50 794	—	—	—	—	—
6	832 843	130 642	32 661	10 392	—	—	—	—
7	532 658	84 999	21 808	7 212	2 774	—	—	—
8	360 398	58 129	15 149	5 122	2 032	894	—	—
9	254 833	41 397	10 899	3 737	1 511	682	332	—
10	186 667	30 476	8 081	2 797	1 146	526	261	138

Table 2. $\psi(n,l)\times 10^{10}$.

n	D	F	G	H	I	K	L	M
3	1 219 326	—	—	—	—	—	—	—
4	705 295	7 750	—	—	—	—	—	—
5	407 975	5 689	271	—	—	—	—	—
6	251 078	3 856	227	21	—	—	—	—
7	163 855	2 647	171	19	3	—	—	—
8	112 281	1 870	127	15	2	0	—	—
9	80 072	1 360	95	12	2	0	0	—
10	59 007	1 016	72	9	2	0	0	0

Description of plates I–II

The spectrograms are of a sliding vacuum spark with graphite electrodes and an insulating disk of porcelain. A stigmatic 21-foot concave grating spectrograph has been used in the first order (5 Å/mm). The spectrograms on Plate I have been enlarged 2.5 times and those on Plate II 3.9 times. Spark data and time of exposure for each spectrogram were as follows:

Spectrogram	Condenser, μF	Auxiliary spark gap, mm	Induction coil, number of turns	Exposure time, minutes
I a	0.30	4.5	0	85
I b	0.30	4.5	5	70
I c	0.30	4.5	15	60
II a	0.30	2.5	2	95
II b	0.30	2.5	2	140
II c	0.30	5	0	60
II d	0.30	3	3	70
II e	0.30	10	5	6
II f	0.30	10	0	6
II g	0.30	10	5	6
II h	0.30	10	0	6

ACKNOWLEDGEMENTS

I wish to express my sincere gratitude to Professor Bengt Edlén for his stimulating advice and sustained interest during this investigation.

I am greatly indebted to Fil. Dr. Lennart Minnhagen for his expert help and valuable suggestions as to the Stark effect calculations and to Fil. Lic. Percy Risberg for having placed at my disposal his working lists of Mg II term values.

Finally I wish to acknowledge, with thanks, the financial support received from the Swedish Natural Science Research Council.

The Physical Laboratory, University of Lund, March 1956.

REFERENCES

Bethe, H., Handbuch d. Phys., Vol. XXIV/1, pp. 431–442 (1933).
Bockasten, K., Ark. Fys. *9*, 457 (1955).
—— Phys. Rev. (in press) (1956).
Bohr, N., Ann. der Phys. [4], *71*, 262 (1923).
Born, M. and Heisenberg, W., Z. Phys. *23*, 388 (1924).
Bowen, I. S. and Ingram, S. B., Phys. Rev. *28*, 444 (1926).
Boyce, J. C. and Rieke, C. A., Phys. Rev. *47*, 653 (1935).
Edlén, B., Nova Acta Reg. Soc. Sci. Ups. *9*, No. 6, pp. 14–18, 40–49 (1934).
— Vistas in Astronomy, Vol. II. Pergamon Press Ltd., London (1956).
Edlén, B. and Lidén, K., Phys. Rev. *75*, 890 (1949).
Edlén, B. and Risberg, P., Ark. Fys. (in press) (1956).
Kupper, A., Ann. der Phys. [4], *86*, 511 (1928).
Mayer, J. E. and Goeppert-Mayer, M., Phys. Rev. *43*, 605 (1933).
Meissner, K. W., Mundie, L. G., and Stelson, P. H., Phys. Rev. *74*, 932 (1948).
—— Phys. Rev. *75*, 891 (1949).
Merton, T. R., Proc. Roy. Soc. London *A 91*, 498 (1915).
Pauling, L., Proc. Roy. Soc. London *A 114*, 181 (1927).
Risberg, P., Ark. Fys. *9*, 483 (1955).
Ryde, N., Atoms and Molecules in Electric Fields. A.B. Gleerup Bokförlag, Lund (in press) (1956).
Sternheimer, R. M., Phys. Rev. *96*, 951 (1954).
Van Vleck, J. H., Proc. Roy. Soc. London *A 143*, 679 (1934).
Waller, I., Z. Phys. *38*, 635 (1926).

Tryckt den 26 april 1956

Uppsala 1956. Almqvist & Wiksells Boktryckeri AB

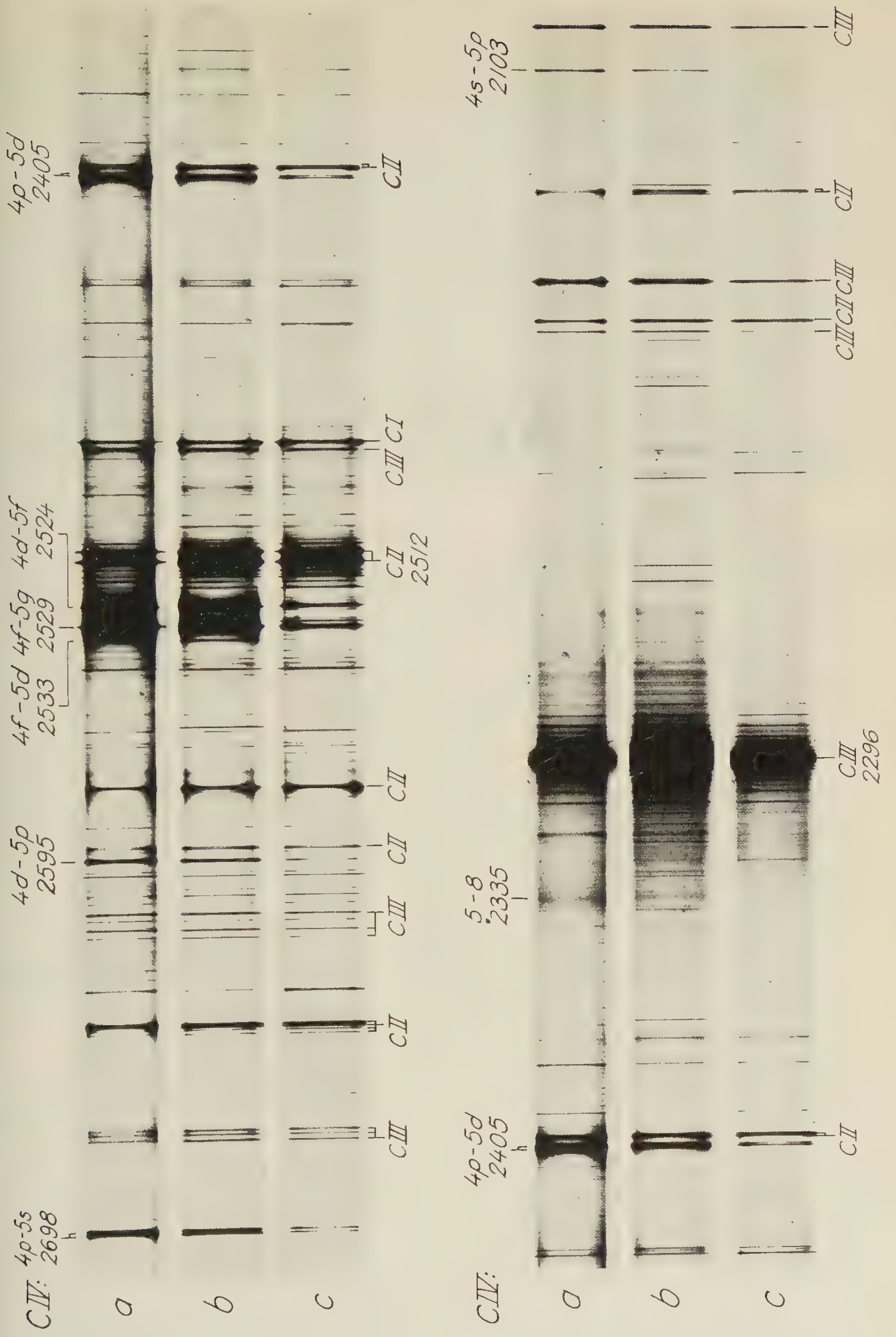
CIV:
4p-5s 2698
4p-5d 2405
4d-5p 2595
4f-5d 2533
4f-5g 2529
4d-5f 2524
CII
CIII CI
CII 2512
CII
CII
CIII
CII
CIII
a
b
c
CIV:
4s-5p 2103
4p-5d 2405
5-8 2335
CIII
CII
CIIICIICIII
CIII 2296
CII
a
b
c

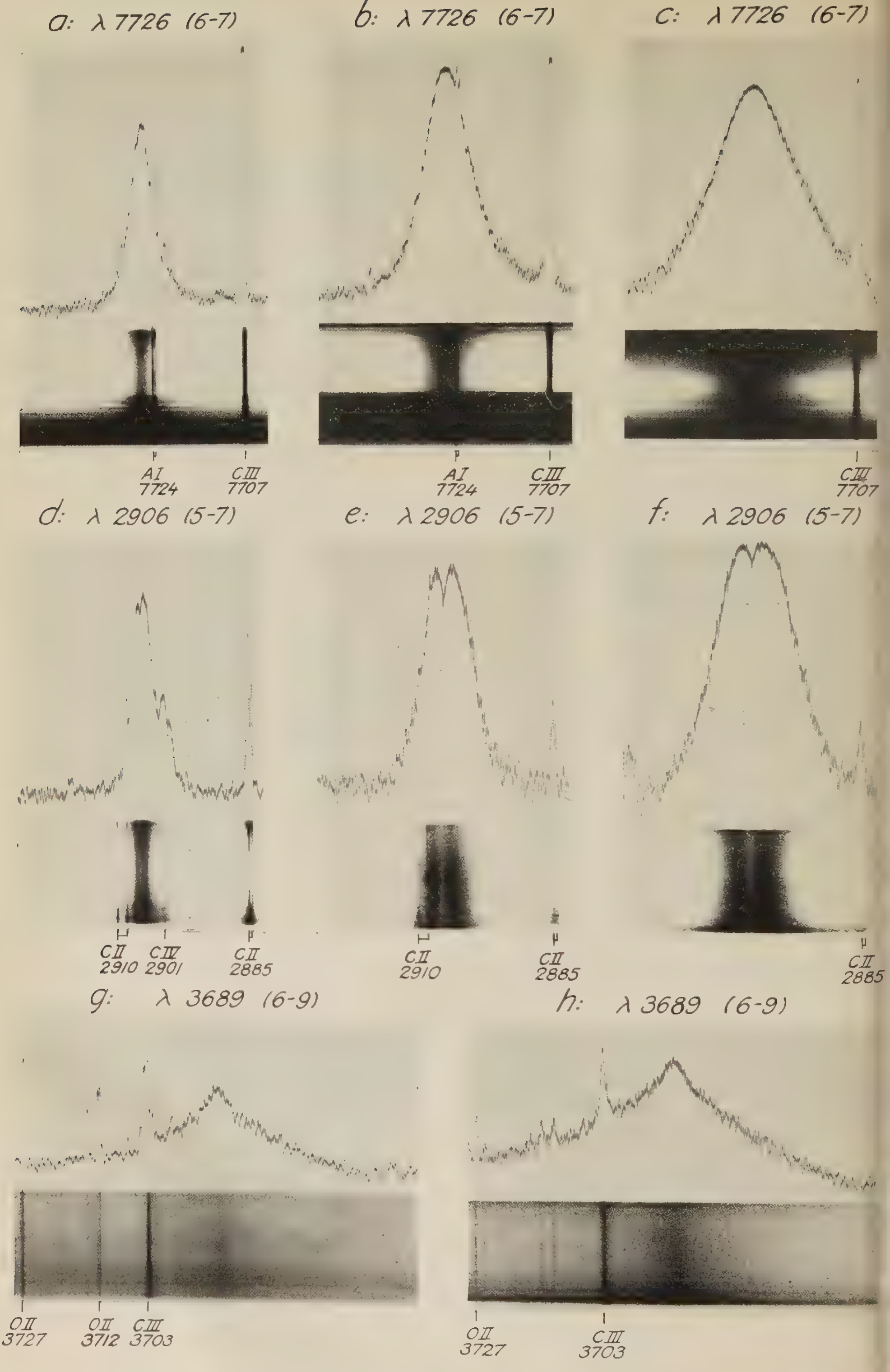
a: λ 7726 (6-7)
AI 7724
CIII 7707
b: λ 7726 (6-7)
AI 7724
CIII 7707
c: λ 7726 (6-7)
CIII 7707
d: λ 2906 (5-7)
CII 2910
CIV 2901
CII 2885
e: λ 2906 (5-7)
CII 2910
CII 2885
f: λ 2906 (5-7)
CII 2885
g: λ 3689 (6-9)
OII 3727
OII 3712
CIII 3703
h: λ 3689 (6-9)
OII 3727
CIII 3703

ARKIV FÖR FYSIK Band 10 nr 41

Communicated 14 March 1956 by MANNE SIEGBAHN and BENGT EDLÉN

A revision of the term systems for Na I and K I based on hollow-cathode observations

By PERCY RISBERG

With 2 plates and 8 figures in the text

Summary

By using a hollow-cathode discharge as a light source wavelengths have been determined by means of concave grating spectrographs for forty-five lines in Na I in the region 11 403–2852 Å, and for seventy-nine lines in K I in the region 11 772–3101 Å. On the basis of these data and those of Meissner and Luft for Na I, as well as some wavelengths determined in this laboratory by I. Johansson in the lead-sulfide region, the term systems have been recalculated, the series limits precisely determined, and accurate series formulae derived.

Introduction

The arc spectra of sodium and potassium are well known since the early days of spectrum analysis. The knowledge was summarized by Fowler (1922) and by Paschen and Götze (1922). Although new data have since been added there has remained a need for further observations, especially in the infrared, and the results of a recent revision of Ca II (Edlén and Risberg, 1956) and Mg II (Risberg, 1955) suggested that it would be of interest to make a similar investigation of Na I and K I.

Light source, spectrographs, and measurements

The hollow-cathode discharge tube used in the present work on sodium and potassium is shown in Fig. 1 in its final and most suitable form. The anode part consists of a brass tube and is separated from the cathode part by means of a glass plate. Joints between metal and glass are made vacuum-tight with O-rings. Anode part, glass plate, and cathode part are held together by electrically isolated clamps not shown in the figure. The quartz window at the front end of the anode is attached with apiezon grease. The cathode itself is a copper cylinder having the following dimensions: inner length 65 mm, inner diameter 15 mm, diameter of opening 6 mm, wall thickness 1.5 mm. Copper was chosen because of its great heat conductivity which ensures the uniform wall temperature necessary for obtaining an alkali-metal discharge filling the whole of the cathode.

The alkali metal is introduced through the front of the discharge tube and pressed on to the bottom of the cathode. The metal evaporating from the cathode will deposit

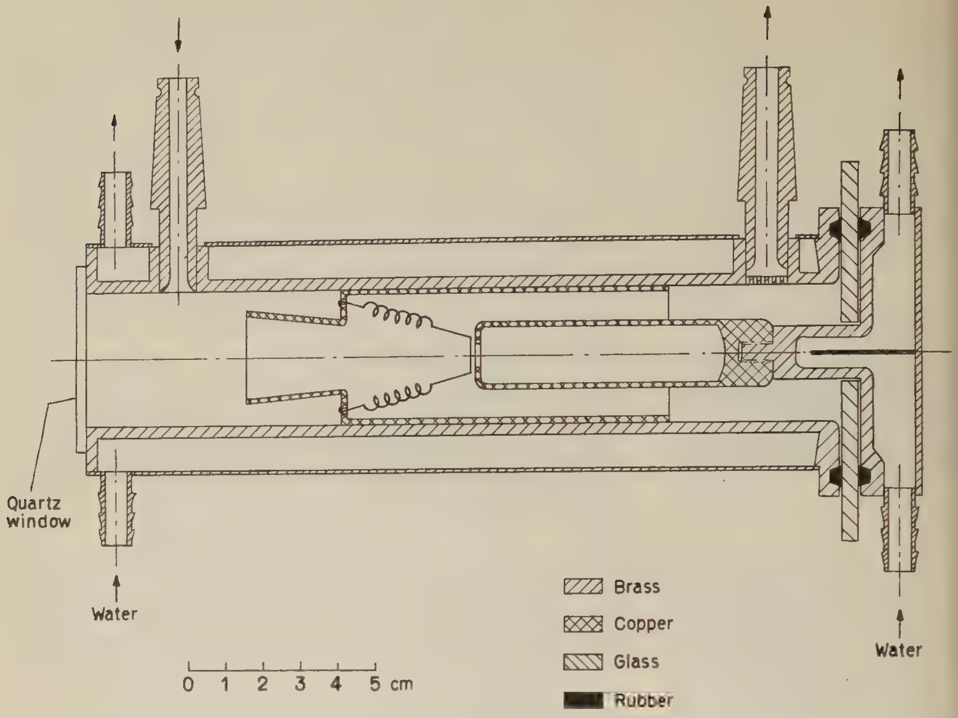

Fig. 1. The hollow-cathode discharge tube.

on a copper tube which fits in the anode tube and is easy to pull out and clean. To keep the discharge entirely inside the hollow cathode a ring made of an iron wire and having a diameter of 8 mm is placed in front of the opening of the cathode. The ring is thermally insulated by a coiled supporting wire and will therefore acquire a high enough temperature to prevent a deposit of alkali metal which could cause a short circuit.

The discharge was run in a mixture of helium and neon at a total pressure of 1 mm of mercury or less. The voltage was about 200 V for sodium and about 120 V for potassium, and the current varied between 200 mA and 600 mA, its value being chosen in every case so as to obtain a suitable intensity relation between the lines to be measured and the reference lines.

Two grating spectrographs, both in Wadsworth's mounting, have been used. The one which is described in detail by Lidén (1949) has a 21-foot concave grating with 60000 lines and gives a dispersion of about 7.5 Å/mm in the first order. The upper wavelength limit is here set by the sensitivity of the photographic emulsions. The other spectrograph (JA 70–15 m, Jarrell-Ash Company), having a 21-foot concave grating with 90000 lines, gives a dispersion of about 5 Å/mm in the first order and reaches to 10000 Å. The first spectrograph was used mainly for wavelengths above 5000 Å and the second for wavelengths below 9500 Å. Measurements were made in the second order when possible.

The spectrograms were taken on Eastman spectroscopic plates and were measured in a Zeiss Abbe comparator. The measurements were reduced by using standard lines n the same order. Above 9500 Å, however, the first-order standards were in some ases supplemented with standards from the second or third order. The reference ines were mainly interferometrically measured rare-gas or iron lines, the latter being btained by putting some iron powder into the hollow cathode.

With few exceptions the wavelengths determined in the present investigation are nean values from at least four spectrograms, and the error limits are estimated to e about 0.03 Å at λ 11500 and 0.004 Å at λ 3000. Wave numbers were calculated y means of the internationally adopted dispersion formula (Edlén, 1953).

Observations in the lead-sulfide region

In Na I and K I it is not possible to determine the lower ^2F terms by photographic bservations since the corresponding transitions have too long wavelengths. The uthor is greatly obliged to Mr. I. Johansson for having made available unpublished neasurements of these and some other transitions in sodium and potassium made vith a lead-sulfide-cell spectrograph in this laboratory. The light source was a hollow-athode discharge similar to the one used in the photographic region. Johansson stimates the error in his observations to be less than 0.03 Å.

Na I. Wavelengths

Meissner and Luft (1937) have published very accurate interferometric measure-nents of eighteen lines in Na I obtained with an atomic-beam light source. In addition o the resonance doublet $3s$–$3p$, they measured lines belonging to the sharp and the liffuse series. Their wavelengths are included in Table 1 and marked ML. The wave umbers have been recalculated in accordance with the new dispersion formula. Some f these lines were observed by Meissner and Ebbinghaus (1937) by using a Geissler ube. They measured also the transition $3p$–$7d$, and their result is found to agree well vith the present grating values. A few more interferometric observations in Na I have een reported, especially by Hetzler, Boreman, and Burns (1935) who observed in a acuum arc ten of the lines measured by Meissner and Luft.

Observations in the photographic infrared have been made by Meggers (1933) vho used an arc in air and later (1935) a Geissler tube. Rood and Sawyer (1938) ised the positive column of a discharge tube, but their optical equipment did not ermit precise determinations. Of previous measurements in the visible region those nade by Datta (1921) show varying deviations up to 0.25 Å when compared with he wavelengths given in Table 1. The observations in absorption made by Thackeray 1949) will be discussed later.

The present observations of forty-five lines are given in Table 1. In the same column re included two lines measured by Johansson in the lead-sulfide region and all the ines measured by Meissner and Luft. A few additional members which were observed n some of the series have not been included in the table since the lines were too faint o be accurately measured. Special attention was directed to the forbidden transitions isted in Fowler's report (1922) but only $3s$–$3d$ and $3s$–$4d$ could be found, the latter ransition being faint and measured on two plates only. On overexposed pictures of d–$8f$ and $3d$–$9f$ there is a very faint satellite on the short wavelength side, which nay possibly be identified as $3d$–ng.

The intensity figures are based on visual estimates and the scale is consistent over imited regions only. Intensities in parenthesis are the theoretical values which Meiss-ier and Luft found to agree within each doublet with their observations.

Table 1. Wavelengths in Na I.

In the column for λ_{air} are included the observations of Meissner and Luft (1937), marked ML, and those made by I. Johansson with a lead-sulfide spectrometer, marked J.

References to previous measurements:

D = Datta (1921).
E = Edlén (1936).
HBB = Hetzler, Boreman, and Burns (1935)
M(1) = Meggers (1933).
M(2) = Meggers (1935).
ME = Meissner and Ebbinghaus (1937).
P = Paschen (1908).
RS = Rood and Sawyer (1938).
T = Thackeray (1949).
Z = Zickendraht (1910).
WF = Wood and Fortrat (1916).

Intensity	λ_{air}, Å	Previous measurements	σ_{obs}, cm^{-1}	σ_{calc}	Combination	Solar data		
						λ	Intensity	Ident.
	23 379.13 calc	23 391.3 P	4 276.	.15	$4p\ ^2P_2 - 4d\ ^2D_3$	9.28	240	Na
	23 348.41 calc	23 361.0 P	4 281.	.78	$^2P_1 - \ ^2D_2$	8.82	237	Na
	22 083.67 calc	22 084.2 P	4 527.	.00	$4s\ ^2S_1 - 4p\ ^2P_1$	3.93	276	Na
	22 056.44 calc	22 056.9 P	4 532.	.59	$^2S_1 - \ ^2P_2$	6.62	300	Na
	18 465.25 J	18 459.5 P	5 414.10	$F\dagger$	$3d\ ^2D - 4f\ ^2F$			
	16 388.85 calc		6 100.	.04	$4p\ ^2P_2 - 6s\ ^2S_1$	8.93	27	Na
	16 373.85 calc		6 105.	.63	$^2P_1 - \ ^2S_1$	(4.15)	(30)	(CH_4)
	14 779.73 calc		6 764.	.18	$4p\ ^2P_2 - 5d\ ^2D_3$	9.89	36	Na
	14 767.48 calc		6 769.	.79	$^2P_1 - \ ^2D_2$	(7.05)	(1155)	(HOH)

2	11 197.21	—	8 928.35	.36	$4p\ ^2P_2 - 7d\ ^2D_3$			
1	11 190.19	—	8 933.96	.95	$^2P_1 - \ ^2D_2$			
8	10 834.87	4.4 RS	9 226.93	*F*	$3d\ ^2D - 6f\ ^2F$	4.99	−1, 1	⊙
9	10 749.29	8.7 M(1)	9 300.39	.39	$4s\ ^2S_1 - 5p\ ^2P_1$			
10	10 746.44	5.9 M(1)	9 302.86	.86	$^2S_1 - \ ^2P_2$			
3	10 572.28	—	9 456.11	.12	$4p\ ^2P_2 - 8d\ ^2D_3$			
1	10 566.00	—	9 461.73	.71	$^2P_1 - \ ^2D_2$			
7	9 961.281	1.0 RS	10 036.12	*F*	$3d\ ^2D - 7f\ ^2F$	1.38	0N, 4	Na
6	9 465.938	—	10 561.30	*F*	$3d\ ^2D - 8f\ ^2F$	5.98	−2, 0	Na
4	9 153.878	4.7 RS	10 921.34	*F*	$3d\ ^2D - 9f\ ^2F$			
2	8 942.962	3.6 RS	11 178.91	*F*	$3d\ ^2D - 10f\ ^2F$			
6	8 650.889	49.6 RS	11 556.33	*P*	$4s\ ^2S_1 - 6p\ ^2P_1$			
7	8 649.922		11 557.62	*P*	$^2S_1 - \ ^2P_2$			
(9)	8 194.8237 ML	4.811 HBB 4.817 E	12 199.471	.471	$3p\ ^2P_2 - 3d\ ^2D_3$	4.836	12 N, 18 N	Na
(1)	8 194.7905 ML		12 199.521	.521	$^2P_2 - \ ^2D_2$			
(5)	8 183.2556 ML	3.270 HBB 3.247 E	12 216.717	.717	$^2P_1 - \ ^2D_2$	3.30	11 N, 15 N	Na
3	7 810.237	09.4 RS	12 800.19	*P*	$4s\ ^2S_1 - 7p\ ^2P_1$			
4	7 809.781		12 800.93	*P*	$^2S_1 - \ ^2P_2$			
1	7 373.491	—	13 558.36	*P*	$4s\ ^2S_1 - 8p\ ^2P_1$			
2	7 373.229	—	13 558.84	*P*	$^2S_1 - \ ^2P_2$			
(2)	6 160.7470 ML	0.760 HBB; 0.725 D	16 227.307	.307	$3p\ ^2P_2 - 5s\ ^2S_1$	0.759	3, 10	Na
(1)	6 154.2253 ML	4.229 HBB; 4.214 D	16 244.503	.503	$^2P_1 - \ ^2S_1$	4.235	2, 7	Na
(16)	5 895.9236* ML	5.923 HBB	16 956.172	.172	$3s\ ^2S_1 - 3p\ ^2P_1$	5.944	20, 60	Na
(32)	5 889.9504* ML	9.953 HBB	16 973.368	.368	$^2S_1 - \ ^2P_2$	9.977	30, 95	Na

† A letter in this column indicates that the high level was determined from this line alone.
* Centre of gravity of hyperfine structure.

Table 1 (*continued*)

Intensity	λ_{air}, Å	Previous measurements	σ_{obs}, cm^{-1}	σ_{calc}	Combination	Solar data		
						λ	Intensity	Ident.
(9)	5 688.2046 ML	8.224 HBB; 8.222 D	17 575.363	.363	$3p\ ^2P_2 - 4d\ ^2D_3$	8.220	6, 12	Na
(1)	5 688.1934 ML		17 575.398	.398	$^2P_2 - \ ^2D_2$			
(5)	5 682.6333 ML	2.657 HBB; 2.675 D	17 592.594	.594	$^2P_1 - \ ^2D_2$	2.650	5, 10	Na
(2)	5 153.4024 ML	3.645 D	19 399.252	.252	$3p\ ^2P_2 - 6s\ ^2S_1$	3.417	−1, −1	
(1)	5 148.8381 ML	9.090 D	19 416.448	.448	$^2P_1 - \ ^2S_1$	8.846	−2	
(2)	4 982.8134 ML	2.845 HBB; 2.864 D	20 063.386	*D*	$3p\ ^2P_2 - 5d\ ^2D_3$	2.827	2, 4	−Na
(1)	4 978.5414 ML	8.585 HBB; 8.608 D	20 080.602	*D*	$^2P_1 - \ ^2D_2$	8.559	0	Na
(2)	4 751.8218 ML	1.891 D	21 038.677	.676	$3p\ ^2P_2 - 7s\ ^2S_1$	1.829	−1, 3	Na?
(1)	4 747.9410 ML	8.016 D	21 055.872	.872	$^2P_1 - \ ^2S_1$	7.984	−2, 1	Na?
(2)	4 668.5595 ML	8.597 D	21 413.889	*D*	$3p\ ^2P_2 - 6d\ ^2D_3$	8.574	1N, 3	Na
(1)	4 664.8107 ML	4.858 D	21 431.098	*D*	$^2P_1 - \ ^2D_2$	4.796	3, 5	−Cr Na?
8	4 545.186	5.218 D	21 995.14	.14	$3p\ ^2P_2 - 8s\ ^2S_1$			
7	4 541.633	1.671 D	22 012.34	.34	$^2P_1 - \ ^2S_1$			
11	4 497.658	7.657 ME; 7.724 D	22 227.56	.57	$3p\ ^2P_2 - 7d\ ^2D_3$	7.682	0N, 2	−Na?
10	4 494.177	4.180 ME; 4.266 D	22 244.77	.76	$^2P_1 - \ ^2D_2$	4.194	−1N, 0	−Na?
7	4 423.246	3.31 D	22 601.48	.48	$3p\ ^2P_2 - 9s\ ^2S_1$			
6	4 419.885	9.94 D	22 618.67	.68	$^2P_1 - \ ^2S_1$			
9	4 393.340	3.45 D	22 755.33	.33	$3p\ ^2P_2 - 8d\ ^2D_3$			
8	4 390.029	0.14 D	22 772.49	.53	$^2P_1 - \ ^2D_2$			
5	4 344.736	4.8 D	23 009.89	.90	$3p\ ^2P_2 - 10s\ ^2S_1$			
4	4 341.489	1.5 D	23 027.10	.09	$^2P_1 - \ ^2S_1$			
7	4 324.615	4.3 Z	23 116.94	*D*	$3p\ ^2P_2 - 9d\ ^2D_3$			
6	4 321.400	1.1 Z	23 134.15	*D*	$^2P_1 - \ ^2D_2$			
3	4 291.006	0.6 Z	23 298.00	.01	$3p\ ^2P_2 - 11s\ ^2S$			

1	4 249.410	9.3 Z	23 526.06	.05	$^2P_1$ – $^2S_1$			
3	4 242.082	1.6 Z	23 566.69	*D*	$3p\ ^2P_2 - 11d\ ^2D_3$			
2	4 238.987	8.8 Z	23 583.90	*D*	$^2P_1$ – $^2D_2$			
6	3 426.862	6.858 T	29 172.85	.86	$3s\ ^2S_1 - 3d\ ^2D$			
18	3 302.979	2.987 T	30 266.99	.99	$3s\ ^2S_1 - 4p\ ^2P_1$	2.983	5	Na
19	3 302.369	2.375 T	30 272.58	.58	$^2S_1$ – $^2P_2$	2.384	6	Na
1	2 893.618	3.619 T	34 548.69	.75	$3s\ ^2S_1 - 4d\ ^2D$			
15	2 853.013	3.023 T	35 040.37	.38	$3s\ ^2S_1 - 5p\ ^2P_1$			
16	2 852.811	2.816 T	35 042.85	.85	$^2S_1$ – $^2P_2$			
	2 680.433 calc	0.421 T	37 296.	.32	$3s\ ^2S_1 - 6p\ ^2P_1$			
	2 680.340 calc	0.331 T	37 297.	.61	$^2S_1$ – $^2P_2$			
	2 593.919 calc	3.927 WF	38 540.	.18	$3s\ ^2S_1 - 7p\ ^2P_1$			
	2 593.869 calc	3.828 WF	38 540.	.93	$^2S_1$ – $^2P_2$			
	2 543.872 calc	3.875 WF	39 298.	.35	$3s\ ^2S_1 - 8p\ ^2P_1$			
	2 543.841 calc	3.817 WF	39 298.	.84	$^2S_1$ – $^2P_2$			

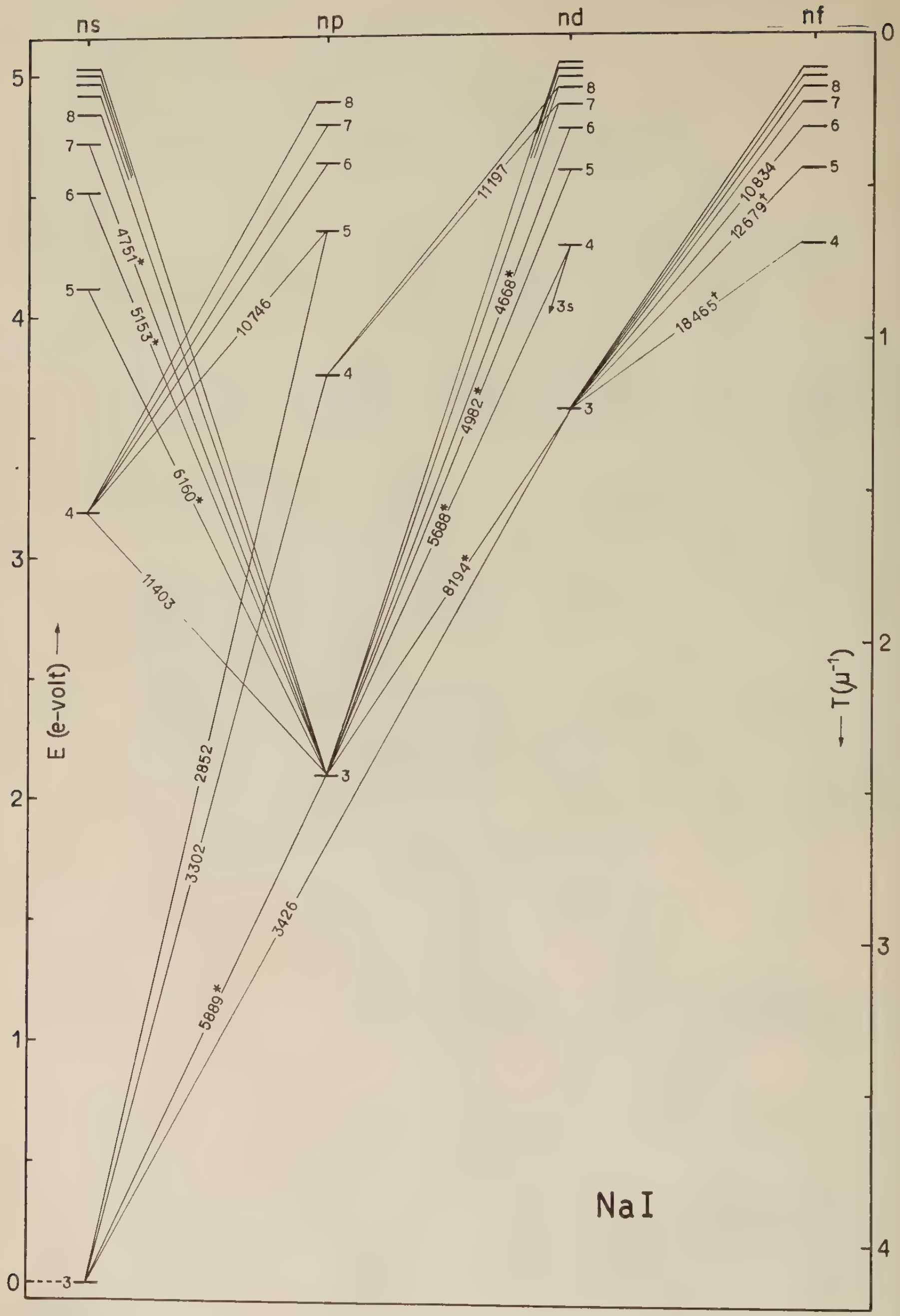

Fig. 2. The term system of Na I. Transitions observed by Meissner and Luft are marked with * and those observed by Johansson in a lead-sulfide spectrometer with †.

Table 2. Term values of Na I.

Term symbol	E, cm^{-1}	ΔE	T, cm^{-1}	n^*	Δn^*
$3s\ ^2S_1$	0.000		41 449.44	1.627 094	
$4s\ ^2S_1$	25 739.991		15 709.45	2.642 966	
$5s\ ^2S_1$	33 200.675		8 248.77	3.647 351	
$6s\ ^2S_1$	36 372.620		5 076.82	4.649 177	
$7s\ ^2S_1$	38 012.044		3 437.40	5.650 114	
$8s\ ^2S_1$	38 968.51		2 480.93	6.650 66	
$9s\ ^2S_1$	39 574.85		1 874.59	7.651 01	
$10s\ ^2S_1$	39 983.27		1 466.17	8.651 26	
$11s\ ^2S_1$	40 271.38		1 178.06	9.651 35	
$12s\ ^2S_1$	40 482.22		967.22	10.651 46	
$3p\ ^2P_1$	16 956.172	17.196	24 493.27	2.116 648	0.000 743
$^2P_2$	16 973.368		24 476.07	2.117 391	
$4p\ ^2P_1$	30 266.99	5.59	11 182.45	3.132 589	0.000 783
$^2P_2$	30 272.58		11 176.86	3.133 373	
$5p\ ^2P_1$	35 040.38	2.47	6 409.06	4.137 851	0.000 797
$^2P_2$	35 042.85		6 406.59	4.138 648	
$6p\ ^2P_1$	37 296.32	1.29	4 153.12	5.140 258	0.000 799
$^2P_2$	37 297.61		4 151.83	5.141 057	
$7p\ ^2P_1$	38 540.18	0.75	2 909.26	6.141 59	0.000 79
$^2P_2$	38 540.93		2 908.52	6.142 37	
$8p\ ^2P_1$	39 298.35	0.48	2 151.09	7.142 38	0.000 80
$^2P_2$	39 298.84		2 150.61	7.143 18	
$3d\ ^2D_2$	29 172.889	−0.050	12 276.58†	2.989 739	−0.000 006
$^2D_3$	29 172.839				
$4d\ ^2D_2$	34 548.766	−0.035	6 900.70†	3.987 728	−0.000 010
$^2D_3$	34 548.731				
$5d\ ^2D_2$	37 036.774	−0.020	4 412.68†	4.986 787	−0.000 011
$^2D_3$	37 036.754				
$6d\ ^2D_2$	38 387.270	−0.013	3 062.18†	5.986 276	−0.000 013
$^2D_3$	38 387.257				
$7d\ ^2D$	39 200.93		2 248.51	6.985 94	
$8d\ ^2D$	39 728.70		1 720.74	7.985 72	
$9d\ ^2D$	40 090.31		1 359.13	8.985 49	
$10d\ ^2D$	40 348.83		1 100.61	9.985 18	
$11d\ ^2D$	40 540.07		909.37	10.985 02	
$4f\ ^2F$	34 586.96		6 862.48	3.998 816	
$5f\ ^2F$	37 057.65		4 391.79	4.998 633	
$6f\ ^2F$	38 399.79		3 049.65	5.998 562	
$7f\ ^2F$	39 208.98		2 240.46	6.998 47	
$8f\ ^2F$	39 734.16		1 715.29	7.998 41	
$9f\ ^2F$	40 094.19		1 355.25	8.998 35	
$10f\ ^2F$	40 351.77		1 097.67	9.998 52	

† The T-values correspond to the centre of gravity of the separate E-values.

The last three columns of Table 1 give a comparison with the solar spectrum. Solar data are from Mohler (1955), Babcock and Moore (1947), and St. John, Moore, Ware, Adams, and Babcock (1928). Below 12000 Å the first figure in the intensity column refers to the disk and the second to the spot spectrum.

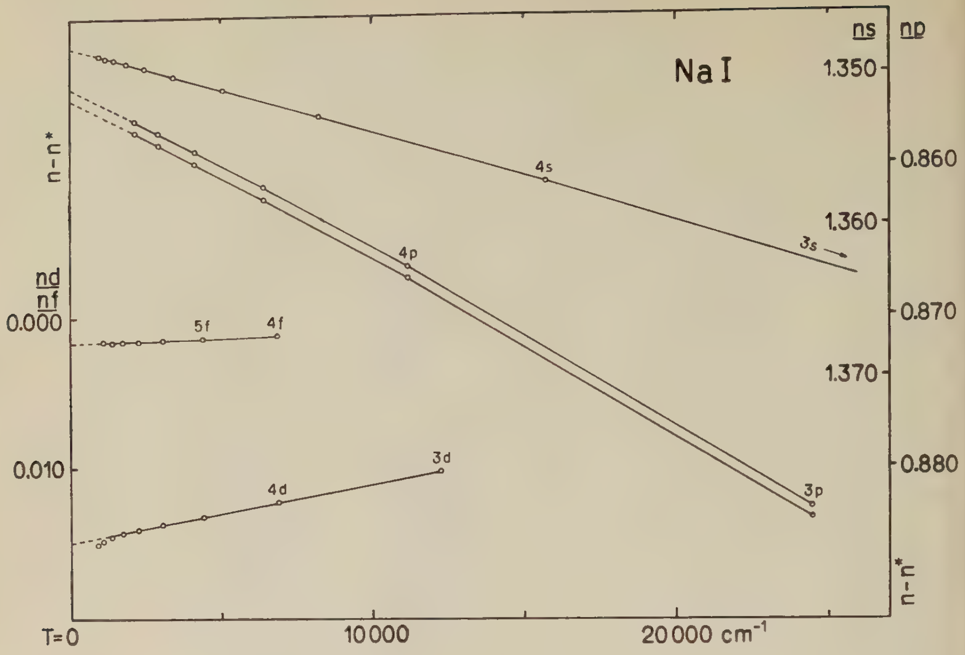

Fig. 3. Quantum defects n–n^* in Na I.

Na I. The term system

The diagram in Fig. 2 serves to show how the terms are connected through the observed transitions which have been used for determining the relative term values E, collected in Table 2. The series limit might have been most easily determined from the ^2F series by applying the simple Ritz formula, $\delta = n - n^* = a + bt$, $t = (n^*)^{-2}$. Before the first two ^2F terms had become available, however, it was considered better to use the ^2S series for this purpose by fitting it to an extended Ritz formula of the form $\delta = a + bt + ct^2 + dt^3$ which had been found to serve remarkably well in Ca II and Mg II.[1] The value 41449.44 cm⁻¹ thus obtained was later checked and confirmed by applying the formula $\delta = a + bt$ to the ^2F series when this series had been extended with 4*f* and 5*f* from Johansson's observations in the lead-sulfide region. This limit gives the absolute term values T shown in Table 2 and the effective quantum numbers, computed with $R_{\mathrm{Na}} = 109734.69$ cm⁻¹. The diagram in Fig. 3 shows the quantum defects $\delta = n - n^*$, for which the following formulae have been derived:

$$^2S\ : \delta = 1.347\,950\,6 + 0.061\,369\,t + 0.015\,852\,t^2 - 0.009\,033\,t^3$$
$$^2P_2 : \delta = 0.854\,629\,6 + 0.111\,669\,t + 0.058\,813\,t^2 + 0.013\,13\,t^3$$
$$^2P_1 : \delta = 0.855\,409\,2 + 0.112\,453\,t + 0.048\,139\,t^2 + 0.039\,99\,t^3$$
$$^2D\ : \delta = 0.014\,897\,2 - 0.042\,146\,t + 0.006\,323\,t^2$$
$$^2F\ : \delta = 0.001\,692\,3 - 0.008\,123\,t.$$

As shown by the differences $T_{\mathrm{obs}} - T_{\mathrm{calc}}$ in Table 3 these formulae reproduce very well the observed term values with the exception of the two highest ^2D terms. The

---

[1] Edlén and Risberg (1956); Risberg (1955).

Table 3. Differences $T_{obs} - T_{calc}$ in cm^{-1} between the observed term values and those calculated from the series formulae for Na I given in the text.

n	^2S	$^2P_2$	$^2P_1$	^2D	^2F
3	(0)	(0)	(0)	(0)	
4	(0)	(0)	(0)	(0)	(0)
5	(0)	(0)	(0)	(0)	(0)
6	(0)	+0.01*	+0.01*	0.00	−0.03
7	0.00	−0.01*	−0.01*	+0.02	0.00
8	0.00	−0.01	−0.01	+0.02	+0.01
9	−0.01			+0.04	+0.02
10	−0.01			+0.08	−0.03
11	+0.01			+0.07	
12	+0.01				

* Formula contains four constants; $n = 6$ and 7 were both used for the calculation.

lines determining 10*d* and 11*d* were measured on several plates in the second order of the Jarrell-Ash spectrograph, and the deviations 0.08 and 0.07 cm^{-1}, respectively, would seem to exceed the possible errors of measurements. The sign of the deviation would suggest a Stark effect shift,[1] but this explanation meets with the difficulty that the *nf* series, which should be more sensitive to Stark effect, is apparently unaffected.

From the residuals shown in Table 3, especially for the long ^2S series, it would seem safe to conclude that the error in the value 41449.44, adopted for the series limit, could not exceed 2 or 3 units in the second decimal. There is a clear contradiction, therefore, with the value 41449.65 ± 0.02 derived from Thackeray's (1949) observations of the resonance series in absorption. In order to find some explanation for the discrepancy the wave numbers of the resonance series have been computed from the

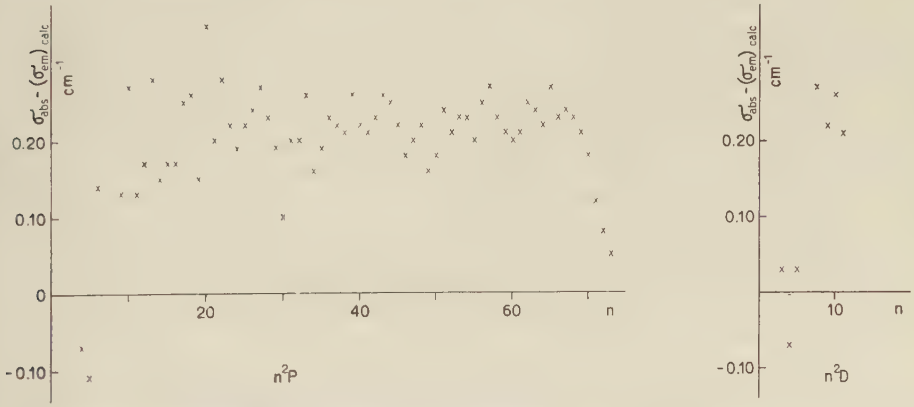

Fig. 4. Differences between σ_{abs} obtained by Thackeray for Na I in absorption and $(\sigma_{em})_{calc}$ obtained from the series formulae for the present emission data, plotted against the quantum number n for the series $3s\ ^2S$–$np\ ^2P$ and $3s\ ^2S$–$nd\ ^2D$.

---

[1] For a discussion of the Stark effect in Na I se Olbers, W., Ann. der Phys. (5) *33*, 708 (1938).

formulae for $np\ ^2P$ given above and compared with the wave numbers observed by Thackeray, corrected for the change of dispersion formula. The differences $\Delta\sigma$ are plotted in Fig. 4. For resolved members the mean of the $\Delta\sigma$'s for the two components is given, and for unresolved members it was assumed that Thackeray's values refer to the centre of gravity of the two components. The $\Delta\sigma$'s scatter around $+0.2$ for large n-values (for $n > 65$ the observations are from one plate only), while for small n they show irregular variations, changing for instance from -0.11 for $5p$ to $+0.14$ for $6p$. Since the difference $5p - 6p$ was determined in the present investigation from the transitions $4s$–$5p$ and $4s$–$6p$, which have been accurately measured in the photographic infrared, an error of 0.25 cm^{-1} in this difference is practically excluded. This would indicate that there may be errors of this order of magnitude in Thackeray's measurements. A similar comparison with his observations of $3s$–nd, also shown in Fig. 4, points in the same direction. It seems not impossible, however, that part of the systematic difference for high series members may be due to a pressure shift of the kind described by Füchtbauer, Schulz, and Brandt (1934).

K I. Wavelengths

Wavelengths for eighty-five lines are given in Table 4, including six lines measured by Johansson in the lead-sulfide region. The only forbidden transitions observed were those from $3d$ and $4d$ to the ground state, the same as in sodium. In column 3 the results of some selected previous measurements are shown for comparison. Observations in the photographic infrared have been reported by Meggers (1933, 1935) and Edlén (1936). Most of Meggers values are from an arc in air which causes excessive broadening and shifts in transitions involving high quantum numbers. The line 9591.8, classified by Meggers as a component of $3d$–$6f$, must be the forbidden $3d$–$6g$ which is likely to appear in the arc. Edlén's observations of $3d$–nf were made with a hollow cathode and agree on the whole satisfactorily with the present ones.

The only interferometric determinations of potassium wavelengths seem to be those by Hetzler, Boreman, and Burns (1935) of $4s$–$4p$ and $4p$–$6s$, and by Wagman (1937) of $4s$–$5p$. In both cases a vacuum arc was used. Their values agree well with the present measurements. The latter have been preferred, however, in order to avoid a possible inconsistency due to the difference in light sources. Among the most extensive of the numerous measurements in the ordinary photographic region are those made by Datta (1921, 1922) who observed both in emission and absorption. The results are remarkably erratic, however, showing in some cases inexplicable deviations up to one ångström unit while in other cases they are quite good. Edlén's values in this region agree closely with the present values except for the group of four lines from λ 5359 to λ 5323 where they are about 0.10 Å too large. The very extensive and accurate observations by Kratz on the resonance series in absorption will be discussed below. His wavelengths are marked K in Table 4, and it is seen that the agreement is excellent for the four members which have been observed also in the present investigation.

In K I the transitions $4p$–nd and $4p - (n+2)s$ fall close together forming characteristic groups of four lines. The intensity ratio of corresponding members of the diffuse and the sharp series show remarkable variations which must be ascribed to intensity anomalies in the diffuse series. These anomalies have recently been discussed theoretically by Villars (1952). Most conspicuous is the extreme faintness of the transition $4p$–$4d$, which remained unobserved for a long time (Edlén, 1936). It is of

Table 4. Wavelengths measured in K I.

Lines Marked J have been observed by I. Johansson with a lead-sulfide spectrometer.

References to previous measurements:

D(1) = Datta (1921).
D(2) = Datta (1922).
E = Edlén (1936).
EH = Exner and Haschek (1911).
HBB = Hetzler, Boreman, and Burns (1935).
K = Kratz (1949).
M(1) = Meggers (1933).
M(2) = Meggers (1935).
P = Paschen (1908).
SB = Segrè and Bakker (1931).
VG = de Vaucouleurs and Glaser (1949).
W = Wagman (1937).

Intensity	λ_{air}, Å	Previous measurements		σ_{obs}, cm^{-1}	σ_{calc}	Combination
	15 168.40 J	5.8 P		6 590.85	.86	$3d\ ^2D_2 - 4f\ ^2F_3$
	15 163.08 J			6 593.16	.16	$^2D_3 - {}^2F_4$
	13 397.09 J		—	7 462.26	.27	$3d\ ^2D_2 - 6p\ ^2P_1$
	13 377.86 J		—	7 472.99	3.02	$^2D_3 - {}^2P_2$
	12 522.11 J	3.0 P		7 983.69	.69	$4p\ ^2P_2 - 5s\ ^2S_1$
	12 432.24 J	4.3 P		8 041.40	.41	$^2P_1 - {}^2S_1$
17	11 772.83	3.05 M(1);	2.66 M(2)	8 491.81	.81	$4p\ ^2P_2 - 3d\ ^2D_3$
16	11 769.62	9.41 M(1)		8 494.13	.12	$^2P_2 - {}^2D_2$
17	11 690.21	0.17 M(1);	89.76 M(2)	8 551.83	.83	$^2P_1 - {}^2D_2$
16	11 022.67	2.3 M(1)		9 069.73	.73	$3d\ ^2D_2 - 5f\ ^2F_3$
17	11 019.87			9 072.03	.03	$^2D_3 - {}^2F_4$
8	10 487.11	7.7 M(1)		9 532.90	.90	$3d\ ^2D_2 - 7p\ ^2P_1$
5	10 482.15			9 537.41	.40	$^2D_2 - {}^2P_2$
9	10 479.63	80.3 M(1)		9 539.71	.71	$^2D_3 - {}^2P_2$
5	9 954.141	5.2 M(1)		10 043.32	.32	$5s\ ^2S_1 - 7p\ ^2P_1$
6	9 949.668	50.5 M(1)		10 047.83	.83	$^2S_1 - {}^2P_2$
14	9 597.829	7.1 M(1)	7.76 E	10 416.17	.17	$3d\ ^2D_2 - 6f\ ^2F_3$
15	9 595.704		5.60 E	10 418.47	.47	$^2D_3 - {}^2F_4$
6	9 351.590		—	10 690.44	.44	$3d\ ^2D_2 - 8p\ ^2P_1$
3	9 349.248		—	10 693.11	.11	$^2D_2 - {}^2P_2$
7	9 347.235		—	10 695.42	.41	$^2D_3 - {}^2P_2$
4	8 925.436		—	11 200.86	.87	$5s\ ^2S_1 - 8p\ ^2P_1$
5	8 923.312		—	11 203.53	.53	$^2S_1 - {}^2P_2$
12	8 904.017		4.04 E	11 227.80	.81	$3d\ ^2D_2 - 7f\ ^2F_3$
13	8 902.188		2.20 E	11 230.11	.11	$^2D_3 - {}^2F_4$
3	8 767.053		—	11 403.21	*P*	$3d\ ^2D_2 - 9p\ ^2P_1$
4	8 763.955		—	11 407.24	.24	$^2D_3 - {}^2P_2$
10	8 505.112		5.19 E	11 754.41	.40	$3d\ ^2D_2 - 8f\ ^2F_3$
11	8 503.449		3.51 E	11 756.70	.71	$^2D_3 - {}^2F_4$
1	8 419.996		—	11 873.23	*P*	$3d\ ^2D_2 - 10p\ ^2P_1$
2	8 417.535		—	11 876.70	*P*	$^2D_3 - {}^2P_2$

Table 4 (*Continued*)

Intensity	λ_{air}, Å	Previous measurements	σ_{obs}, cm^{-1}	σ_{calc}	Combination
masked	8 391.44 calc		11 913.	.63	$5s\ ^2S_1 - 9p\ ^2P_1$
3	8 390.223	—	11 915.36	.36	$^2S_1 - \ ^2P_2$
8	8 251.743	—	12 115.32	.32	$3d\ ^2D_2 - 9f\ ^2F_3$
9	8 250.180	0.22 E	12 117.62	.62	$^2D_3 - \ ^2F_4$
6	8 079.618	—	12 373.42	.42	$3d\ ^2D_2 - 10f\ ^2F_3$
7	8 078.114	—	12 375.73	.73	$^2D_3 - \ ^2F_4$
4	7 956.832	—	12 564.36	.36	$3d\ ^2D_2 - 11f\ ^2F_3$
5	7 955.371	—	12 566.67	.67	$^2D_3 - \ ^2F_4$
24	7 698.959	8.979 HBB	12 985.20	.17	$4s\ ^2S_1 - 4p\ ^2P_1$
25	7 664.899	4.907 HBB	13 042.90	.88	$^2S_1 - \ ^2P_2$
12	6 964.672	4.69 E	14 354.22	.22	$4p\ ^2P_2 - 4d\ ^2D_3$
7	6 964.18	4.18 E	14 355.23	.25	$4p\ ^2P_2 - 4d\ ^2D_2$
20	6 938.767	9.50 D(1); 8.76 E; 8.774 HBB*	14 407.81	.81	$4p\ ^2P_2 - 6s\ ^2S_1$
12	6 936.284	6.27 E	14 412.97	.97	$4p\ ^2P_1 - 4d\ ^2D_2$
19	6 911.084	1.80 D(1); 1.08 E; 1.087 HBB*	14 465.52	.52	$4p\ ^2P_1 - 6s\ ^2S_1$
17	5 831.887	2.31 D(1); 1.89 E	17 142.36	*D*	$4p\ ^2P_2 - 5d\ ^2D_3$
15	5 812.148	2.71 D(1); 2.15 E	17 200.58	*D*	$^2P_1 - \ ^2D_2$
17	5 801.752	2.16 D(1); 1.74 E	17 231.39	.39	$4p\ ^2P_2 - 7s\ ^2S_1$
16	5 782.384	2.77 D(1); 2.37 E	17 289.11	.11	$^2P_1 - \ ^2S_1$
14	5 359.574	9.521 D(1); 9.66 E	18 653.01	*D*	$4p\ ^2P_2 - 6d\ ^2D_3$
12	5 342.970	2.974 D(1); 3.07 E	18 710.98	*D*	$^2P_1 - \ ^2D_2$
13	5 339.688	9.670 D(1); 9.79 E	18 722.48	.48	$4p\ ^2P_2 - 8s\ ^2S_1$
12	5 323.276	3.228 D(1); 3.38 E	18 780.20	.20	$^2P_1 - \ ^2S_1$
12	5 112.249	2.204 D(1)	19 555.41	*D*	$4p\ ^2P_2 - 7d\ ^2D_3$
11	5 099.200	9.180 D(1)	19 605.46	.47	$4p\ ^2P_2 - 9s\ ^2S_1$
11	5 097.171	7.144 D(1)	19 613.26	*D*	$4p\ ^2P_1 - 7d\ ^2D_2$
10	5 084.226	4.212 D(1)	19 663.20	.19	$4p\ ^2P_1 - 9s\ ^2S_1$
10	4 965.031	5.038 D(1)	20 135.24	*D*	$4p\ ^2P_2 - 8d\ ^2D_3$
9	4 956.146	6.043 D(1)	20 171.34	.33	$4p\ ^2P_2 - 10s\ ^2S_1$
9	4 950.815	0.816 D(1)	20 193.06	*D*	$4p\ ^2P_1 - 8d\ ^2D_2$
8	4 942.015	1.964 D(1)	20 229.02	.05	$4p\ ^2P_1 - 10s\ ^2S_1$
9	4 869.757	9.70 D(1)	20 529.17	*D*	$4p\ ^2P_2 - 9d\ ^2D_3$
8	4 863.483	3.61 D(1)	20 555.65	.65	$4p\ ^2P_2 - 11s\ ^2S_1$
8	4 856.090	6.03 D(1)	20 586.95	*D*	$4p\ ^2P_1 - 9d\ ^2D_2$
7	4 849.865	9.88 D(1)	20 613.37	.37	$4p\ ^2P_1 - 11s\ ^2S_1$
8	4 804.348	5.19 D(1); 4.76 VG	20 808.66	*D*	$4p\ ^2P_2 - 10d\ ^2D_3$
6	4 799.754	0.16 D(1)	20 828.58	.58	$4p\ ^2P_2 - 12s\ ^2S_1$
7	4 791.049	1.08 D(1); 1.46 VG	20 866.42	*D*	$4p\ ^2P_1 - 10d\ ^2D_2$
5	4 786.491	6.89 D(1)	20 886.29	.29	$4p\ ^2P_1 - 12s\ ^2S_1$

* The wavelengths for these two lines were incorrectly given in the reference cited. The correct values given here were communicated by Dr. Burns in a private letter to Prof. Edlén.

le 4 (*Continued*)

tenity	λ_{air}, Å	Previous measurements	σ_{obs}, cm^{-1}	σ_{calc}	Combination
7	4 757.389	9.31 D(1); 7.73 VG	21 014.06	*D*	$4p\ ^2P_2 - 11d\ ^2D_3$
5	4 753.934	4.5 D(1)	21 029.33	.33	$4p\ ^2P_2 - 13s\ ^2S_1$
6	4 744.345	5.58 D(1); 4.69 VG	21 071.83	*D*	$4p\ ^2P_1 - 11d\ ^2D_2$
4	4 740.914	1.6 D(1)	21 087.08	.05	$4p\ ^2P_1 - 13s\ ^2S_1$
11	4 642.373	2.172 D(1); 2.42 EH; 2.27 SB	21 534.68	.70	$4s\ ^2S_1 - 3d\ ^2D_3$
10	4 641.876	1.585 D(1); 1.92 EH; 1.77 SB	21 536.99	7.00	$^2S_1 - {}^2D_2$
17	4 047.206	7.201 D(1); 7.214 W; 7.208 K	24 701.43	*P*	$4s\ ^2S_1 - 5p\ ^2P_1$
18	4 044.136	4.140 D(1); 4.145 W; 4.136 K	24 720.17	*P*	$^2S_1 - {}^2P_2$
4	3 648.981	8.971 D(2)	27 397.10	.10	$4s\ ^2S_1 - 4d\ ^2D_3$
3	3 648.841		27 398.16	.14	$^2S_1 - {}^2D_2$
10	3 447.375	7.701 D(1); 7.40 EH; 7.376 K	28 999.27	.27	$4s\ ^2S_1 - 6p\ ^2P_1$
11	3 446.372	6.722 D(1); 6.37 EH; 6.376 K	29 007.71	.71	$^2S_1 - {}^2P_2$
6	3 217.621	7.50 D(1); 7.633 (D2); 7.615 K	31 069.89	.90	$4s\ ^2S_1 - 7p\ ^2P_1$
7	3 217.155	7.01 D(1); 7.176 D(2); 7.151 K	31 074.39	.40	$^2S_1 - {}^2P_2$
3	3 102.043	2.023 D(2); 2.051 K	32 227.47	.44	$4s\ ^2S_1 - 8p\ ^2P_1$
4	3 101.790	1.806 D(2); 1.791 K	32 230.10	.11	$^2S_1 - {}^2P_2$
	3 034.920 calc	4.911 K	32 940.	.21	$4s\ ^2S_1 - 9\text{p}\ ^2P_1$
	3 034.761 calc	4.751 K	32 941.	.94	$^2S_1 - {}^2P_2$
	2 992.223 calc	2.215 K	33 410.	.23	$4s\ ^2S_1 - 10p\ ^2P_1$
	2 992.118 calc	2.108 K	33 411.	.39	$^2S_1 - {}^2P_2$

interest, therefore, to note that the intensity ratio of $4p$–$3d$ to $4p$–$5s$, as found in the present work, is normal, the member of the diffuse series being stronger than that of the sharp series, as is the case for large n-values. This is shown in Fig. 5 which is a recording made by Johansson by means of the lead-sulfide spectrometer. The satellite in $4p$–$3d$ is abnormally strong however. Moreover, conspicuous variations in its relative intensity have been found. On one spectrogram the intensity of the satellite is actually equal to that of the adjacent main line. No explanation for this strange behaviour has been found. It seems hardly possible to explain it as an absorption effect, and an exact coincidence with a strong foreign line of unknown origin would be extremely improbable.

The wavelengths of K I have been compared with the solar spectrum, using the same sources of solar data as for sodium, and the result is given in Table 5. No lines of K I in the lead-sulfide region seem to appear in the solar spectrum.

K I. The term system

The energy levels have been computed from weighted wave numbers, all obtained from the present measurements. The levels are collected in Table 6, and the term diagram in Fig. 6 shows all transitions used in the computations. Masaki and Kobayakawa (1936) have observed interferometrically the separations of some ^2D terms

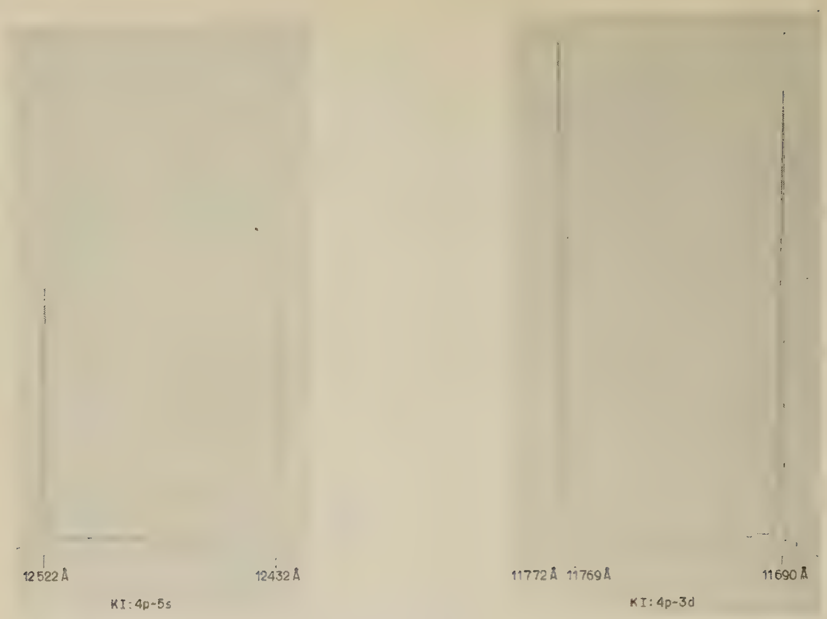

Fig. 5. A record showing the relative intensities of $4p$–$5s$ and $4p$–$3d$ in K I.

Table 5. Comparison of some K I lines with solar data.

Combination	Present investigation		Solar data		
	Intensity	λ_{air}, Å	λ	Intensity disk, spot	Identification
$4p\,^2P_2 - 5s\,^2S_1$		12 522.11	2.16	3*ns*	K? C?
$^2P_1 - \ ^2S_1$		12 432.24	2.25	– 1	Atm
$4p\,^2P_2 - 3d\,^2D_3$	17	11 772.83	2.77	15	Atm (K)
$^2P_2 - \ ^2D_2$	16	11 769.62	9.72	– 2N	K
$^2P_1 - \ ^2D_2$	17	11 690.21	(. . .)		(K)
$4s\,^2S_1 - 4p\,^2P_1$	24	7 698.959	8.977	11, 16	K
$^2S_1 - \ ^2P_2$	25	7 664.899	4.872	12, 20	K
$4p\,^2P_2 - 6s\,^2S_1$	20	6 938.767	8.737	– 2NN, 0	⊙
$^2P_1 - \ ^2S_1$	19	6 911.084			
$4p\,^2P_2 - 5d\,^2D_3$	17	5 831.887	1.944	– 2N, 1	
$^2P_1 - \ ^2D_2$	15	5 812.148	2.133 2.206	– 3N – 3	
$4p\,^2P_2 - 7s\,^2S_1$	17	5 801.752	1.753	– 2N	Atm –
$^2P_1 - \ ^2S_1$	16	5 782.384	2.372	– 2N	
$4p\,^2P_2 - 6d\,^2D_3$	14	5 359.574	9.528	– 2	K?
$^2P_1 - \ ^2D_2$	12	5 342.970	2.967	– 3, 2	Sc
$4p\,^2P_2 - 8s\,^2S_1$	13	5 339.688	9.697	3	
$^2P_1 - \ ^2S_1$	12	5 323.276			
$4s\,^2S_1 - 5p\,^2P_1$	17	4 047.206	7.191	– 1*d*?, 0	K
$^2S_1 - \ ^2P_2$	18	4 044.136	4.147	0, 0	K

Table 6. Term values of K I.

Term symbol	E, cm^{-1}	ΔE	T, cm^{-1}	n^*	Δn^*
$4s\ ^2S_1$	0.00		35 009.77	1.770 433	
$5s\ ^2S_1$	21 026.58		13 983.19	2.801 373	
$6s\ ^2S_1$	27 450.69		7 559.08	3.810 128	
$7s\ ^2S_1$	30 274.28		4 735.49	4.813 838	
$8s\ ^2S_1$	31 765.37		3 244.41	5.815 761	
$9s\ ^2S_1$	32 648.35		2 361.42	6.816 91	
$10s\ ^2S_1$	33 214.22		1 795.56	7.817 62	
$11s\ ^2S_1$	33 598.54		1 411.23	8.818 09	
$12s\ ^2S_1$	33 871.46		1 138.31	9.818 47	
$13s\ ^2S_1$	34 072.22		937.56	10.818 72	
$4p\ ^2P_1$	12 985.17	57.72	22 024.60	2.232 133	0.002 931
$^2P_2$	13 042.88		21 966.89	2.235 064	
$5p\ ^2P_1$	24 701.43	18.75	10 308.34	3.262 719	0.002 971
$^2P_2$	24 720.17		10 289.60	3.265 690	
$6p\ ^2P_1$	28 999.27	8.45	6 010.51	4.272 860	0.003 005
$^2P_2$	29 007.71		6 002.06	4.275 865	
$7p\ ^2P_1$	31 069.90	4.51	3 939.87	5.277 558	0.003 020
$^2P_2$	31 074.40		3 935.37	5.280 578	
$8p\ ^2P_1$	32 227.44	2.67	2 782.33	6.280 15	0.003 01
$^2P_2$	32 230.11		2 779.66	6.283 16	
$9p\ ^2P_1$	32 940.21	1.73	2 069.56	7.281 74	0.003 04
$^2P_2$	32 941.94		2 067.83	7.284 78	
$10p\ ^2P_1$	33 410.23	1.17	1 599.54	8.282 78	0.003 03
$^2P_2$	33 411.39		1 598.38	8.285 80	
$3d\ ^2D_2$	21 537.00	−2.31	13 472.77	2.853 945	−0.000 244
$^2D_3$	21 534.70		13 475.08	2.853 701	
$4d\ ^2D_2$	27 398.14	−1.04	7 611.63	3.796 953	−0.000 259
$^2D_3$	27 397.10		7 612.67	3.796 694	
$5d\ ^2D_2$	30 185.74	−0.50	4 824.03	4.769 460	−0.000 248
$^2D_3$	30 185.24		4 824.53	4.769 212	
$6d\ ^2D_2$	31 696.15	−0.25	3 313.63	5.754 697	−0.000 218
$^2D_3$	31 695.89		3 313.88	5.754 479	
$7d\ ^2D_2$	32 598.43	−0.13	2 411.35	6.745 97	−0.000 18
$^2D_3$	32 598.30		2 411.47	6.745 79	
$8d\ ^2D_2$	33 178.23	−0.10	1 831.55	7.740 43	−0.000 21
$^2D_3$	33 178.12		1 831.65	7.740 22	
$9d\ ^2D_2$	33 572.11	−0.06	1 437.66	8.736 68	−0.000 17
$^2D_3$	33 572.06		1 437.71	8.736 51	
$10d\ ^2D_2$	33 851.59	−0.05	1 158.18	9.733 89	−0.000 19
$^2D_3$	33 851.55		1 158.22	9.733 70	
$11d\ ^2D_2$	34 057.00	−0.06	952.77	10.731 97	−0.000 31
$^2D_3$	34 056.94		952.83	10.731 66	
$4f\ ^2F$	28 127.85		6 881.92	3.993 185	
$5f\ ^2F$	30 606.73		4 403.04	4.992 266	
$6f\ ^2F$	31 953.17		3 056.60	5.991 763	
$7f\ ^2F$	32 764.80		2 244.97	6.991 48	
$8f\ ^2F$	33 291.40		1 718.37	7.991 27	
$9f\ ^2F$	33 652.32		1 357.46	8.991 07	
$10f\ ^2F$	33 910.42		1 099.35	9.990 93	
$11f\ ^2F$	34 101.36		908.41	10.990 90	

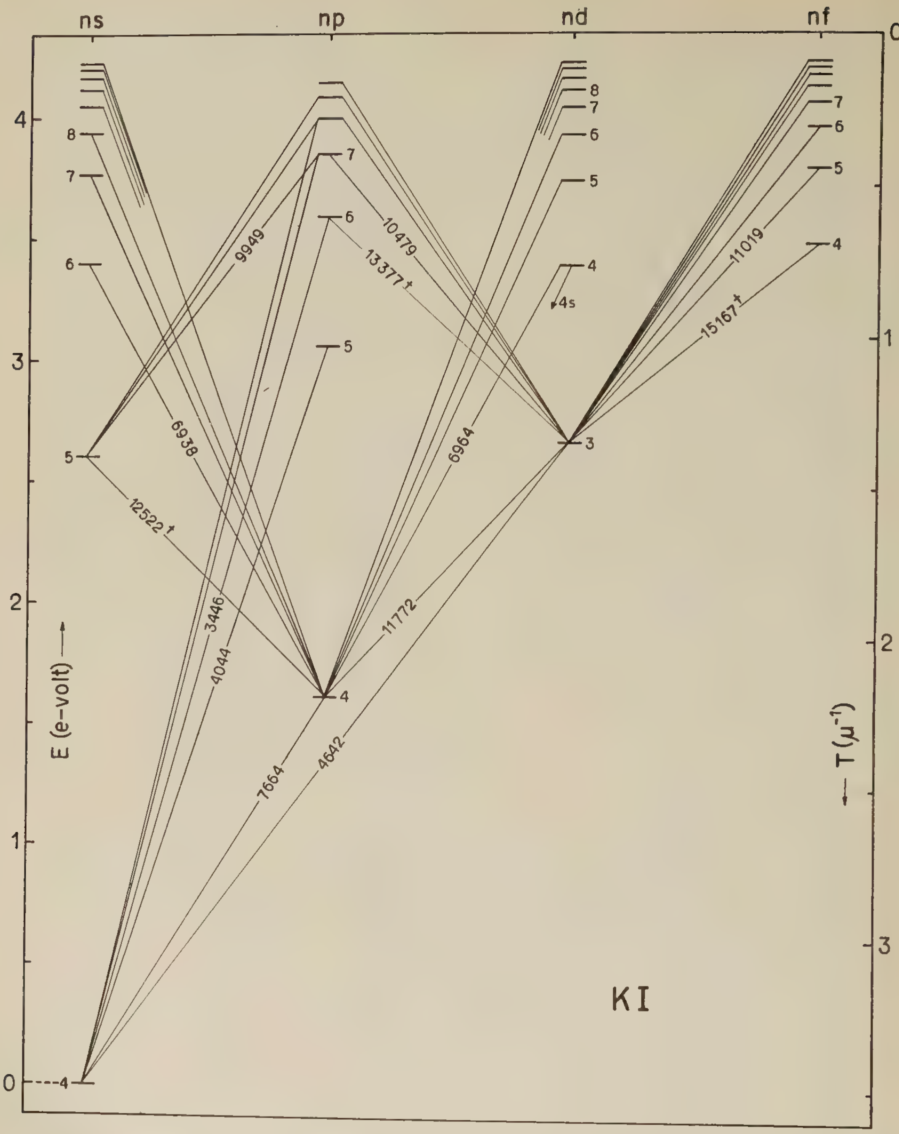

Fig. 6. The term system of K I. Wavelengths measured by Johansson in a lead-sulfide spectrometer are marked with †.

by using a modified Geissler tube. Although their wavelengths do not agree with the present ones, and the separation for $4p\ ^2P$ is quite wrong, their values for the separations of the ^2D terms, determined from the very small distance between satellite and main line in $4p$–nd, may well be correct. They are given in Table 7 and confirm the present results within their limits of error. As regards the ^2F terms, the present investigation shows that the separations are probably less than ± 0.01 cm^{-1}.

Table 7. Separations of $nd\,^2D$ terms in K I as observed by Masaki and Kobayakawa (1936).

n	5	6	7	8
$\Delta\sigma$ Δn^*	-0.503 $-0.000\,249$	-0.262 $-0.000\,227$	-0.158 $-0.000\,221$	-0.096 $-0.000\,203$

Table 8. Differences $T_{\text{obs}} - T_{\text{calc}}$ in cm^{-1} between observed term values and those calculated from the series formulae for K I given in the text.

n	^2S	$^2P_2$	$^2P_1$	$^2D_3$	$^2D_2$	^2F
3				(0)	(0)	
4	(0)	(0)	(0)	(0)	(0)	(0)
5	(0)	(0)	(0)	(0)	(0)	(0)
6	(0)	(0)	(0)	(0)	(0)	0.00
7	(0)	(0)	(0)	-0.01	-0.01	-0.01
8	0.00	0.00	-0.01	0.00	-0.02	0.00
9	-0.02	-0.03	-0.02	-0.01	-0.02	$+0.02$
10	-0.01	-0.02	-0.02	$+0.04$	$+0.02$	$+0.02$
11	0.00			$+0.04$	$+0.01$	$+0.01$
12	-0.01					
13	-0.01					

In order to determine the series limit the ^2S series was fitted to a formula $\delta = a + bt + ct^2 + dt^3$, and the ^2F series to a simple Ritz formula $\delta = a + bt$. The two determina-ions gave almost identical results, the difference being only 0.03 cm^{-1}. The mean value 35009.77 cm^{-1} was adopted as the absolute value for 4s ^2S. This gives the T values and the effective quantum numbers $n^*(R_{\text{K}} = 109735.77$ cm$^{-1})$ shown in Table 6. The quantum defects, $\delta = n - n^*$, are plotted in Fig. 7. It may be noted that he slope of the $nd\,^2D$ curve is unusually steep though it still has the sign characteristic or a "non-penetrating" series in contrast to Ca II where the same series is typically 'penetrating". The following series formulae have been derived:

$S\ \ : \delta = 2.180\,151\,3 + 0.136\,029\,t + 0.077\,805\,t^2 - 0.058\,568\,t^3$
$P_2 : \delta = 1.710\,779\,9 + 0.235\,080\,t + 0.162\,159\,t^2 + 0.074\,83\,t^3$
$P_1 : \delta = 1.713\,819\,5 + 0.234\,589\,t + 0.151\,407\,t^2 + 0.106\,99\,t^3$
$D_3 : \delta = 0.276\,981\,0 - 1.015\,372\,t - 1.028\,774\,t^2 + 5.138\,03\,t^3$
$D_2 : \delta = 0.276\,926\,2 - 1.023\,500\,t - 0.929\,723\,t^2 + 4.756\,51\,t^3$
$F\ \ : \delta = 0.009\,367\,0 - 0.040\,692\,t.$

As shown in Table 8 the agreement between observed and calculated term values s quite good,[1] indicating that the error in the series limit is probably less than 0.03 m^{-1}.

Kratz (1949) has observed the principal series in absorption and gives the wave-

---

[1] Pertubations in the *ns* and *nd* series as reported by de Vaucouleurs and Glaser (1949) are learly not existent.

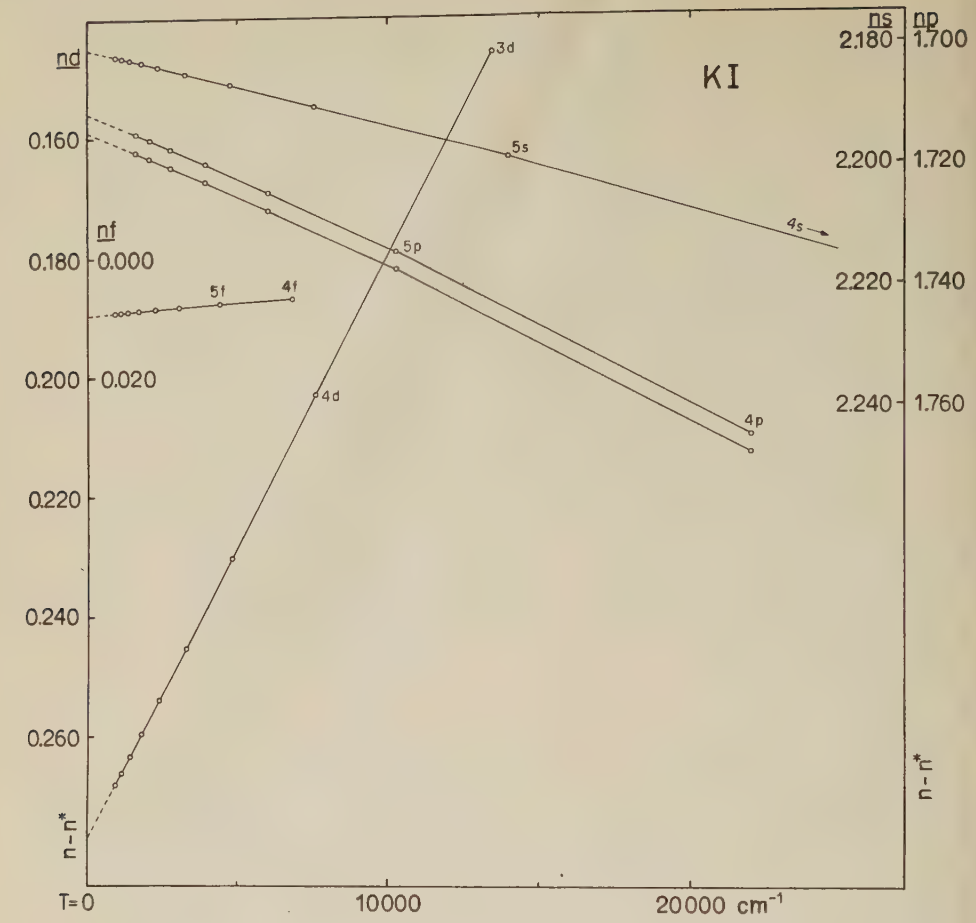

Fig. 7. Quantum defects n–n^* in K I.

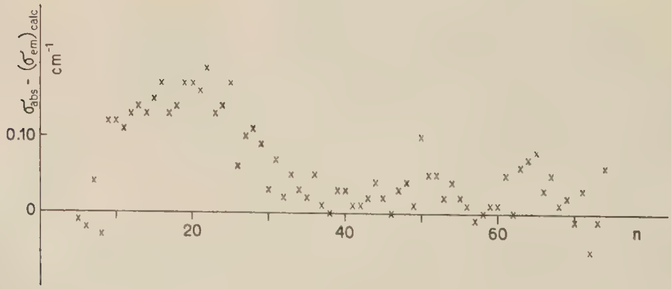

Fig. 8. Differences between σ_{abs} obtained by Kratz for K I in absorption and $(\sigma_{\mathrm{em}})_{\mathrm{calc}}$ obtained from the series formulae for the present emission data, plotted against the quantum number n for the series $4s\ {}^2S$–$np\ {}^2P$.

lengths of $4s$–np from $n=5$ to $n=79$, the doublets being resolved up to $n=17$. The value of the series limit, when corrected for the error in Kayser's *Tabelle der Schwingungszahlen*, is 35009.80 ± 0.03 cm^{-1}, in excellent agreement with the value 35009.77 found in the present work. In the same way as was described above for sodium the wave numbers measured by Kratz have been compared with those obtained from the emission data of the present work, represented by the formulae given above. The differences $\sigma_{\mathrm{abs}}-(\sigma_{\mathrm{em}})_{\mathrm{calc}}$ are shown in Fig. 8. For $n \leq 17$ the mean value of the differences for the two fine structure components was plotted and for $n > 17$ it was assumed that Kratz's values refer to the centre of gravity of the components. The agreement is seen to be quite satisfactory for the low members as well as for the end of the series, while there is a significant difference in the intermediate region from $n=9$ to $n=25$. In particular, there is a jump of 0.15 cm^{-1} from $n=8$ to $n=9$. This definitely exceeds the error limits in the present work in which the interval between $8p$ and $9p$ was determined from combinations with both $3d$ and $5s$ in a favourable region of the photographic infrared. It may be mentioned in this connection that the helium pressure of 10 mm Hg used by Kratz would be expected to increase the wave numbers of the higher members of the principal series by an amount of about 0.08 cm^{-1}.[1]

Polarization formulae for non-penetrating orbits in Na I and K I

Following a treatment by Bockasten (1956) the "term defect" for non-penetrating orbits may be written

$$\Delta T = T - T_0 = A\varphi(n, l) + B\psi(n, l)$$

where T_0 is the hydrogenic term value RZ_0^2/n^2, and $A = R\alpha Z_0^4/a_0^3$, $B = R\alpha_q Z_0^6/a_0^5$, a_0 being the first Bohr radius of hydrogen, α the dipole polarizability and α_q the quadrupole polarizability of the atom core. The expressions for φ and ψ and their numerical values for different values of the quantum numbers n and l are given in Bockasten's paper. This formula has been applied to the nf series in Na I and K I. The constants A and B, determined from $4f$ and $5f$, are given in Table 9 which also contains the values obtained for α and α_q. In view of the perfect agreement between observed and calculated term defects, shown in Tables 10 and 11, it may be assumed that the formulae will give accurate values of the term defects also for $l > 3$. The term values thus calculated for the ng series are included in Tables 10 and 11.

Table 9. Polarization constants of Na$^+$ and K$^+$ derived from $4f$ and $5f\,^2F$ of Na I and K I.

	Na	K
A, cm^{-1}	97.31×10^3	600.46×10^3
B, cm^{-1}	571.6×10^3	1407.7×10^3
α, cm^3	0.131×10^{-24}	0.811×10^{-24}
α_q, cm^5	0.216×10^{-40}	0.532×10^{-40}

---

[1] Füchtbauer, Schulz, and Brandt (1934).

Table 10. The polarization formula applied to the $nf\,^2F$ and $ng\,^2G$ series in Na I.

n	T_0, cm^{-1}	$nf\,^2F$		$ng\,^2G$	
		ΔT_{obs}	ΔT_{calc}	ΔT_{calc}	T_{calc}
4	6858.42	4.06	(4.06)		
5	4389.39	2.40	(2.40)	0.51	4389.90
6	3048.19	1.46	1.49	0.33	3048.52
7	2239.48	0.98	0.98	0.22	2239.71
8	1714.61	0.68	0.67	0.15	1714.76
9	1354.75	0.50	0.48	0.11	1354.86
10	1097.35	0.33	0.36	0.08	1097.43

Table 11. The polarization formula applied to the $nf\,^2F$ and $ng\,^2G$ series in K I.

n	T_0, cm^{-1}	$nf\,^2F$		$ng\,^2G$	
		ΔT_{obs}	ΔT_{calc}	ΔT_{calc}	T_{calc}
4	6858.49	23.43	(23.43)		
5	4389.43	13.61	(13.61)	3.09	4392.52
6	3048.22	8.39	8.39	1.99	3050.21
7	2239.51	5.46	5.48	1.33	2240.84
8	1714.62	3.75	3.75	0.93	1715.55
9	1354.76	2.69	2.68	0.67	1355.43
10	1097.36	1.99	1.97	0.50	1097.85
11	906.91	1.50	1.49	0.38	907.28

ACKNOWLEDGEMENTS

The author is deeply indebted to Professor Bengt Edlén who suggested this investigation and gave generously of his time in valuable discussions. Thanks are due also to Dr. Lennart Minnhagen for great interest and encouraging support, and to Mr Ingmar Johansson for generous contribution of data from the lead-sulfide spectrometer.

The work has been financially supported by the Swedish Natural Science Research Council, which is gratefully acknowledged.

The Physical Laboratory, University of Lund, March 1956.

REFERENCES

Babcock, H. D. and Moore, Ch. E., Carnegie Inst. Wash. Publ. *579* (1947).
Bockasten, K., Arkiv för Fysik (in press) (1956).
Datta, S., Proc. Roy. Soc. London (A) *99*, 69 (1921).
—— Proc. Roy. Soc. London (A) *101*, 539 (1922).
Edlén, B., Zeit. Phys. *98*, 445 (1936).
—— J. Opt. Soc. Am. *43*, 339 (1953).
Edlén, B. and Risberg, P., Arkiv för Fysik *10*, 553 (1956).

EXNER, F. and HASCHEK, E., *Die Spektren der Elemente bei normalem Druck* II:114. Franz Deuticke, Leipzig and Wien, 1911.
FOWLER, A., *Report on Series in Line Spectra.* Fleetway Press, London, 1922.
FÜCHTBAUER, CHR., SCHULZ, P., and BRANDT, A. F., Zeit. Phys. *90*, 403 (1934).
HETZLER, C. W., BOREMAN, R. W., and BURNS, K., Phys. Rev. *48*, 656 (1935).
KAYSER, H., *Tabelle der Schwingungszahlen.* S. Hirzel, Leipzig, 1925.
KRATZ, H. R., Phys. Rev. *75*, 1844 (1949).
LIDÉN, K., Arkiv för Fysik *1*, 229 (1949).
MASAKI, O. and KOBAYAKAWA, K., J. Sci. Hiroshima Univ. (A) *6*, 217 (1936).
MEGGERS, W. F., J. Res. Nat. Bur. Stand. *10*, 669 (1933).
—— J. Res. Nat. Bur. Stand *14*, 487 (1935).
MEISSNER, K. W. and EBBINGHAUS, E., Ann. der Phys. (5) *29*, 713 (1937).
MEISSNER, K. W. and LUFT, K. F., Ann. der Phys. (5) *29*, 698 (1937).
MOHLER, O. C., *A Table of Solar Spectrum Wave Lengths 11984 A to 25578 A.* The University of Michigan Press, Ann Arbor, 1955.
PASCHEN, F., Ann. der Phys. (4) *27*, 537 (1908).
PASCHEN, F. and GÖTZE, R., *Seriengesetze der Linienspektren.* Julius Springer, Berlin, 1922.
RISBERG, P., Arkiv för Fysik *9*, 483 (1955).
ROOD, P. and SAWYER, R. A., Astrophys. J. *87*, 68 (1938).
SEGRÈ, E. and BAKKER, C. J., Zeit. Phys. *72*, 724 (1931).
ST. JOHN, CH. E., MOORE, CH. E., WARE, L. M., ADAMS, E. F., and BABCOCK, H. D., Carnegie Inst. Wash. Publ. *396* (1928).
THACKERAY, E. R., Phys. Rev. *75*, 1840 (1949).
VAUCOULEURS, A. DE and GLASER, L., C. R. Acad. Sci. (Paris) *228*, 1714 (1949).
VILLARS, D. S., J. Opt. Soc. Am. *42*, 552 (1952).
WAGMAN, N. E., Univ. Pittsburgh Bull. *34*, 1 (1937).
WOOD, R. W. and FORTRAT, R., Astrophys. J. *43*, 73 (1916).
ZICKENDRAHT, H., Ann der Phys. (4) *31*, 233 (1910).

Description of Plates I–II

The spectrograms shown in Plate I (sodium) and Plate II (potassium) were obtained by using a hollow-cathode discharge and two stigmatic grating spectrographs described in the text, one having a Rowland grating and the other being a Jarrell-Ash instrument, designated in the list below by R and Ja, respectively. The accompanying figure denotes the diffraction order used. In some cases second and third order lines were superimposed on the first order spectrum as remarked in column 4. When argon and xenon lines were used as standards they were obtained by means of a separate discharge (Col. 5). The Z, M, and N plates were hypersensitized, except for the spectrogram IIe. Spectrograms If and IIi were enlarged 5.7 times and all the others 4 times.

Spectrogram	Spectrograph	Plate type	Discharge in He and/or Ne	Supplementary discharge
I a*	R, 1	I–Z	3 hours, 1 amp.	
I b, c	R, 1	I–Z(2)	9 hours, 0.50 amp. (2nd and 3rd order 45 min)	
I d	R, 1	I–Z(2)	1 hour, 0.15 amp.	
I e	Ja, 1	I–M	5 hours, 0.40 amp.	Ar 10 sec 0.15 amp. Xe 7 sec 0.08 amp.
I f	Ja, 2	103a–O	1.5 hours, 0.23 amp.	
II a	R, 1	I–Z(2)	1.5 hours, 0.30 amp.	
II b	Ja, 1	I–N	30 min, 0.22 amp.	
II c	Ja, 1	I–N	1.5 hours, 0.20 amp.	Ar 10 sec 0.10 amp.
II d	R, 1	I–Z(2)	3.5 hours, 0.40 amp. (2nd and 3rd order 7 min)	
II e	R, 1	I–N	2 hours, 0.30 amp.	
II f	R, 1	I–Z(2)	4 hours, 0.20 amp. (2nd and 3rd order 30 min)	Ar 20 min 0.35 amp.
II g	R, 1	I–M	8 hours, 0.20 amp. (2nd and 3rd order 2 hours)	Ar 20 min 0.30 amp. Xe 2 min 0.25 amp.
II h	R, 2	103a–F(3)	10 min, 0.33 amp.	
II i	Ja, 1	I–N	2 hours, 0.40 amp.	
II j	Ja, 2	103a–O	5 min, 0.20 amp.	
II k	Ja, 1	103a–O	75 min, 0.47 amp.	

* Spectrogram I a was obtained with a water-cooled hollow cathode of aluminium.

Tryckt den 21 april 1956

Uppsala 1956. Almqvist & Wiksells Boktryckeri AB

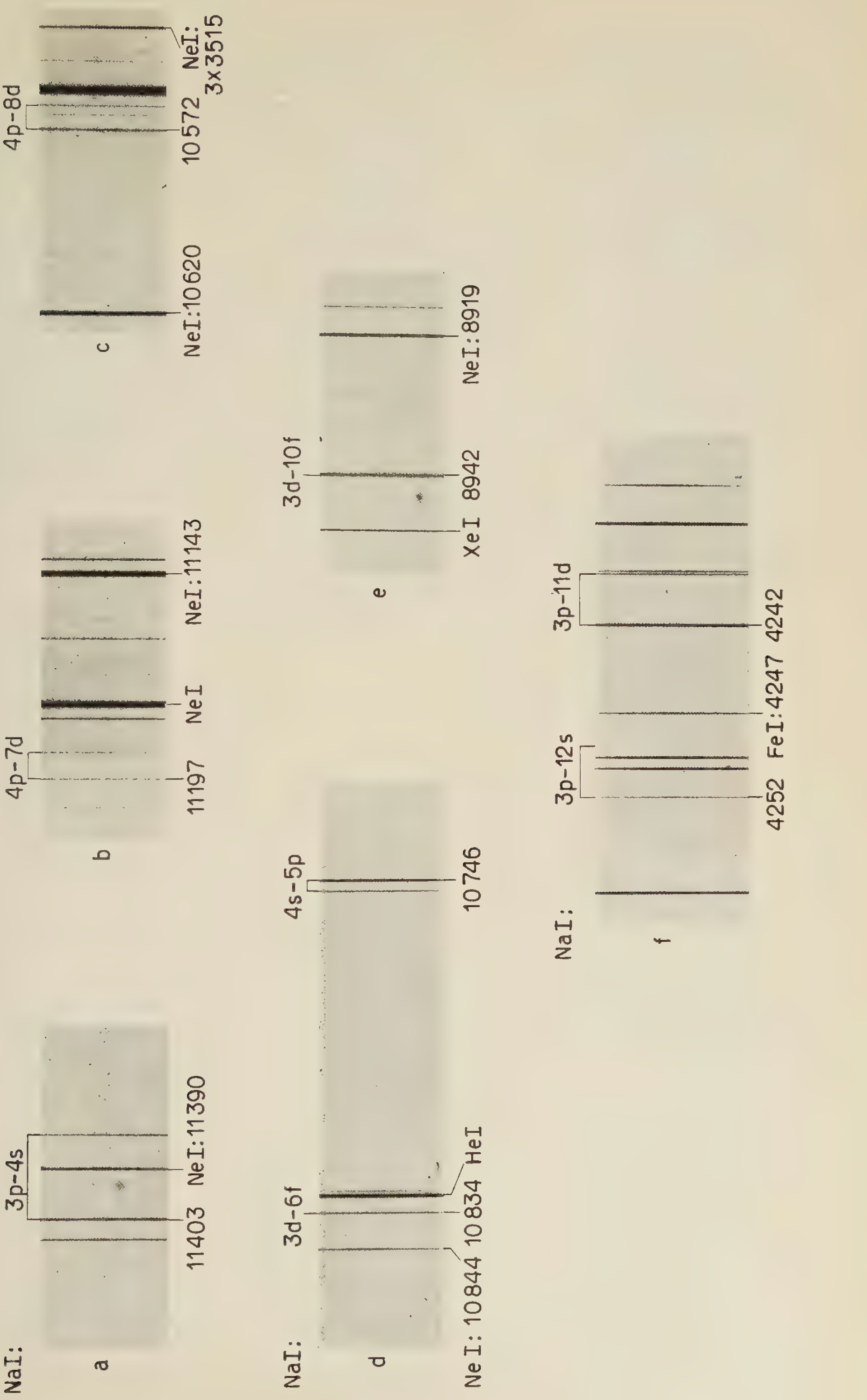
NaI:
a
3p-4s
11403
NeI:11390
b
4p-7d
11197
NeI
NeI:11143
c
4p-8d
NeI:10620
10572
NeI:
3x3515
NaI:
d
3d-6f
NeI:10844
10834
HeI
4s-5p
10746
e
3d-10f
XeI 8942
NeI:8919
NaI:
f
3p-12s
4252
FeI:4247
3p-11d
4242

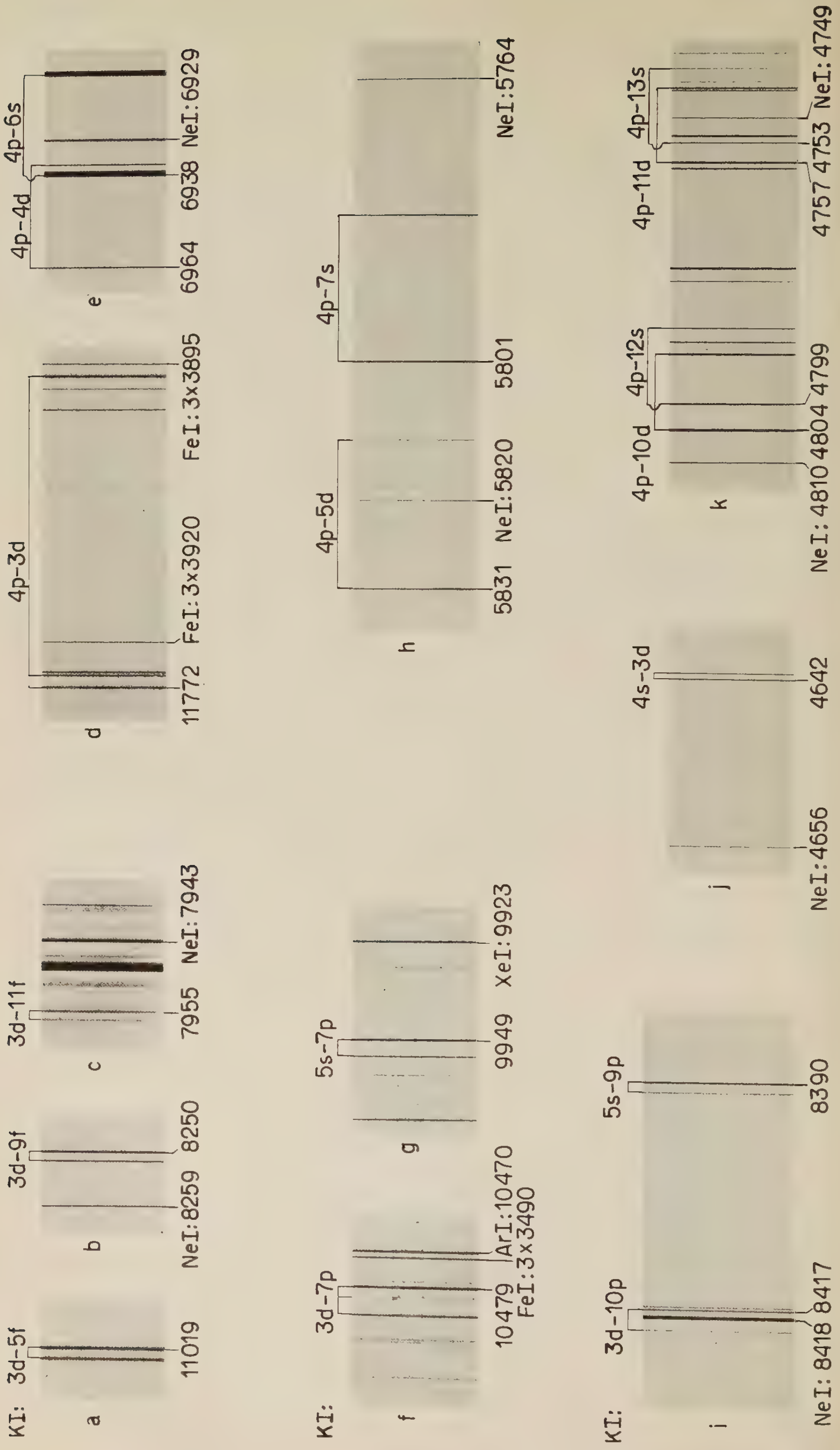
KI:
3d-5f
a
11019
3d-9f
b
NeI:8259
8250
3d-11f
c
7955
NeI:7943
4p-3d
d
11772
FeI:3x3920
FeI:3x3895
4p-4d
4p-6s
e
6964
6938
NeI:6929
KI:
3d-7p
f
10479
FeI:3x3490
ArI:10470
5s-7p
g
9949
XeI:9923
4p-5d
4p-7s
h
5831
NeI:5820
5801
NeI:5764
KI:
3d-10p
i
NeI: 8418
8417
5s-9p
8390
4s-3d
j
NeI:4656
4642
4p-10d
4p-12s
4p-11d
4p-13s
k
NeI: 4810
4804
4799
4757
4753
NeI: 4749

DATE DUE

SCI.	LIB	MAR 19 '79 MAR 16 1979	

DEMCO 38-297

CHICAGO
3 8198 314 370 097